



NAVAL FACILITIES ENGINEERING SERVICE CENTER
Port Hueneme, California 93043-4328

Contract Report CR 96.003

USE OF MICROTREMORS FOR SITE RESPONSE CHARACTERIZATION

An Investigation Conducted by

Leighton and Associates, Inc.
17781 Cowan
Irvine, CA 92714

February 1996

19960319 126

DTIC QUALITY INSPECTED 1

19960319 126

FIGURES 2.2, 2.3, & 2.4 ARE LISTED ON PAGE 28.

PAGES E-35 AND H-7 ARE MISSING BECAUSE PAGES

WERE MISNUMBERED PER JOHN FERRITTO (805

982-1243 AT NAVAL FACILITIES ENGINEERING

SERVICE CENTER - PORT HUENEME, CALIF.

MAY 14, 1996

DISCLAIMER NOTICE



THIS DOCUMENT IS BEST QUALITY AVAILABLE. THE COPY FURNISHED TO DTIC CONTAINED A SIGNIFICANT NUMBER OF PAGES WHICH DO NOT REPRODUCE LEGIBLY.

REPORT DOCUMENTATION PAGE			Form Approved OMB No. 0704-018	
Public reporting burden for this collection of information is estimated to average 1 hour per response, including the time for reviewing instructions, searching existing data sources, gathering and maintaining the data needed, and completing and reviewing the collection of information. Send comments regarding this burden estimate or any other aspect of this collection information, including suggestions for reducing this burden, to Washington Headquarters Services, Directorate for Information and Reports, 1215 Jefferson Davis Highway, Suite 1204, Arlington, VA 22202-4302, and to the Office of Management and Budget, Paperwork Reduction Project (0704-0188), Washington, DC 20503.				
1. AGENCY USE ONLY (Leave blank)		2. REPORT DATE February 1996		3. REPORT TYPE AND DATES COVERED Final; Jan 1994 through Feb 1996
4. TITLE AND SUBTITLE USE OF MICROTREMORS FOR SITE RESPONSE CHARACTERIZATION			5. FUNDING NUMBERS Navy Project Contract No. N4708-94-C-7416 Leighton Project No. 2940013-01	
6. AUTHOR(S)				
7. PERFORMING ORGANIZATION NAME(S) AND ADDRESS(ES) Leighton and Associates, Inc. 17781 Cowan Irvine, CA 92714			8. PERFORMING ORGANIZATION REPORT NUMBER CR 96.003	
9. SPONSORING/MONITORING AGENCY NAME(S) AND ADDRESSES Naval Facilities Engineering Service Center 560 Center Drive Port Hueneme, CA 93043-4328			10. SPONSORING/MONITORING AGENCY REPORT NUMBER	
11. SUPPLEMENTARY NOTES				
12a. DISTRIBUTION/AVAILABILITY STATEMENT Approved for public release; distribution unlimited.			12b. DISTRIBUTION CODE	
13. ABSTRACT (Maximum 200 words) <p>The primary objective of this project was to investigate the feasibility of using microtremors to obtain information on the local site conditions for site-specific ground motion analysis. Microtremors and microseisms have been used by many investigators for site response investigation. One of the old and rather neglected techniques is Aki's (1957) "Circular Array" method. It uses microtremor data on a small scale circular array to infer information on the wave propagation properties of the local site materials. Aki successfully used this technique at a site in the University of Tokyo to obtain the information on the shear wave velocity profile for the site. The most attractive feature of this technique is its simplicity in data requirement and field operation. Theoretical, numerical, and field investigations of the Circular Array technique were conducted to evaluate its potential for site investigation. The results of this study clearly indicate that the Circular Array technique can provide general information on the seismic wave propagation properties of the local site materials. The data requirements (i.e., microtremors) and the field instrumentation are fairly simple. The data processing and interpretation can be simple or sophisticated depending upon the detail of the velocity model that is desired for a particular application. However, it is possible to automate different aspects of the data processing in order to make the interpretation the least time consuming.</p>				
14. SUBJECT TERMS Microtremors, circular array, wave propagation, shear wave velocity, site investigation			15. NUMBER OF PAGES 573	
			16. PRICE CODE	
17. SECURITY CLASSIFICATION OF REPORT Unclassified	18. SECURITY CLASSIFICATION OF THIS PAGE Unclassified	19. SECURITY CLASSIFICATION OF ABSTRACT Unclassified	UL	

Use of Microtremors for Site Response Characterization

Project Summary

U.S. Navy Contract No. N47408-94-C-7416

Leighton and Associates, Inc. Project No. 2940013-01

Principal Investigator: Dr. Mehrdad Mahdyiar, Vortex Rock Consultants, Inc.

The primary objective of this project is to investigate the feasibility of using microtremors to obtain information on the local site conditions for site-specific ground motion analysis. Microtremors and microseisms have been used by many investigators for site response investigation. One of the old and rather neglected techniques is Aki's (1957) "Circular Array" method. It uses microtremor data on a small scale circular array to infer information on the wave propagation properties of the local site materials. Aki successfully used this technique at a site in the University of Tokyo to obtain the information on the shear wave velocity profile for the site. The most attractive feature of this technique is its simplicity in data requirement and field operation. We conducted theoretical, numerical, and field investigations of the Circular Array technique to evaluate its potential for site investigation. The results of this study clearly indicate that the Circular Array technique can provide general information on the seismic wave propagation properties of the local site materials. the data requirements, i.e. microtremors, and the field instrumentation are fairly simple. The data processing and interpretation can be simple or sophisticated depending upon the detail of the velocity model that is desired for a particular application. However, it is possible to automate different aspects of the data processing in order to make the interpretation the least time consuming. It is our conclusion that the Circular Array technique has the potential to be a practical method for site investigation.

The ultimate objective of any site response investigation is to predict site-specific ground motions for future earthquakes. Therefore, we formulated a methodology that simplifies the integration of the weak motion and nonlinear strong motion site response into the ground motion simulation of large earthquakes. The proposed methodology is a practical way of simulating the response spectra and time histories of scenario earthquakes under controlled rupture mechanisms, path effects, and local site response. The final chapter of this report looks into the site response of sites in the Los Angeles area during the Northridge, 1994, earthquake. The objective of this aspect of the study is to evaluate the application of the soil-to-rock site spectral ratio technique for site investigation. The results indicate that the spectral ratio analysis of ground motions of earthquakes at pairs of soil-rock sites could provide general information on the possible ground motion amplification at soil sites. However, the information is site-specific and in many ways earthquake-specific and cannot be easily applied to other sites for site response analysis of engineering applications.

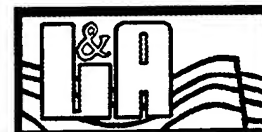


VortexRock Consultants, Inc.



Table of Contents

<i>Description</i>	<i>Page No.</i>
<i>Transmittal Letter</i>	
<i>Abstract</i>	<i>i</i>
<i>Executive Summary</i>	<i>3</i>
 <i>Chapter 1. Introduction</i>	 <i>6</i>
 <i>Chapter 2. Application of Circular Array Technique in Site Investigation</i>	 <i>13</i>
2.1 Theoretical Formulation of the Circular Array Technique	14
2.2 Simulation of Circular Array Experiments by Two Instruments	21
2.3 Simulation of Circular Array Experiments by Two Fixed Instruments	24
2.4 Numerical Simulation: Case Studies of the Application of Circular Array Technique for Site Investigation	26
2.5 Interpretation of the Correlation Coefficient-Frequency Data for Site Investigation	37
2.6 Construction of Shear Wave Velocity Profile from the Apparent Velocity of Microtremors	42
2.7 Semi-Theoretical Approach to the Inversion of Phase Velocities to Shear Wave Velocity Profiles	44
2.8 Theoretical Simulation of the Dispersion Curves for Rayleigh Waves in Flat Layered Medium	53
 <i>Chapter 3. Field Experiments</i>	 <i>81</i>
3.1 Experiments No. 1 & 2: The Parking Lot of the St. Aidams Episcopal Church Malibu California	83
3.2 Experiment No. 3: The Mazda Parking Lot Port of Huenemi Oxnard California	99
3.3 Experiment No. 4: The basketball Court of the McBride School Los Angeles California	105
3.4 Experiment No. 5: The Palm Spring Site	112
 <i>Chapter 4. Simulation of Strong Ground Motion Parameters Based on Weak Motion Site Response</i>	 <i>177</i>



*Chapter 5. Soil site response analysis of sites in Los Angeles area based
on Northridge, 1994 earthquake data*

Chapter 6. Computer Programs

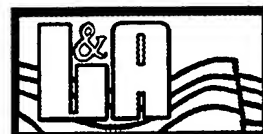
Bibliography

Appendix A

Appendix B

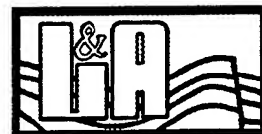
Appendix C

Appendix D



Executive Summary

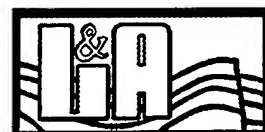
The primary objective of this study is to identify a practical technique for site investigation for seismic engineering analysis. We seek techniques that can be applied locally, are not based on the availability of earthquake data, and are relatively inexpensive and simple to apply in both data gathering and processing. Most site-specific seismic hazard analyses rely on simple models of wave propagation through layered medium to account for the response of local site materials to earthquake ground motions. However, methods that use earthquake data for site response characterization are preferable since such data include the most realistic information on site response to earthquake ground motions. The major problem with using earthquake-related data, either strong motions or weak motions such as coda waves, for routine site response studies is that earthquake data are not readily available at specific sites of interest. Microtremors and microseisms have been used by many investigators for site response investigations. The results of studies that use spectral amplitudes of microtremors to determine the site characteristic period have not been conclusive to have practical applications in seismic engineering analysis. However, microtremor data on two-dimensional arrays have provided useful information on the direction and velocity of wave propagation on regional and local scales. Aki (1957) introduced a site investigation technique based on the recordings of microtremors on a small scale circular array. He successfully used this technique at a site in the University of Tokyo to obtain information on the phase velocities for Rayleigh waves and then interpreted the results in terms of the shear wave velocity profile for the site. The



most attractive feature of this technique is its simplicity in data requirement and field operation.

We have conducted theoretical, numerical, and field investigations of Aki's (1957) "Circular Array" technique to evaluate its potential for site investigation. The results of this study clearly indicate that the Circular Array technique can provide general information on the shear wave velocity for the site of investigation. The results also indicate that under ideal situations the interpretation of data from a Circular Array experiment can lead to the construction of the shear wave velocity-depth profiles for the site. The data requirements, microtremors, and the field instrumentation are fairly simple. The data processing and interpretation can be simple or sophisticated depending upon the detail of the velocity model that is desired for a particular application. However, it is possible to automate different aspects of the data processing in order to make the interpretation the least time consuming. It is our conclusion that the Circular Array technique has the potential to be a practical method for site investigation.

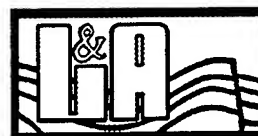
The ultimate objective of any site response investigation is to predict site-specific ground motions for future earthquakes. Therefore, our second issue of concern is to integrate the site response information into the response spectral analysis of earthquakes for site-specific studies. We have formulated a methodology for ground motion simulation of large earthquakes based on the weak motion site response, such as coda waves amplifications. The propose methodology is a practical way of simulating the response spectra and time histories of scenario



earthquakes on faults with specific consideration for the rupture mechanisms, path effects, and local site response.

The final chapter of this report looks into the site response of sites in the Los Angeles area during the Northridge, 1994, earthquake. The objective of this aspect of the study is to evaluate the application of the soil-to-rock site spectral ratio technique for site investigation. The results indicate that the spectral ratio analysis of ground motions of earthquakes at pairs of soil-rock sites could provide general information on the possible ground motion amplification at soil sites. However, the information is site-specific and in many ways earthquake-specific and can not be easily applied to other sites for site response analysis of engineering applications.

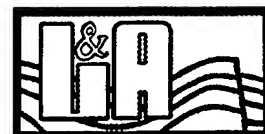
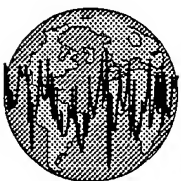
Dr. Mehrdad Mahdyiar of Vortex Rock Consultants, Inc., is the Principal Investigator of this study. Mr. Gan Mukhopadhyay of Leighton and Associates, Inc., is the Project Manager.



Chapter 1

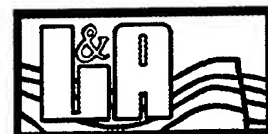
Introduction

The dramatic effects of local site conditions on the damage potential of earthquakes have been observed and documented for almost all major earthquakes around the world. The most recent examples are the 1985 Michoacan, Mexico, earthquake (Singh et al., 1988), 1988 Armenian earthquake (Borcherdt et al., 1989), 1989 Loma Prieta, California, earthquake (Borcherdt and Glassmoyer, 1992) and Northridge, California, earthquake (EERI Report, 1994). Yet, the issue of site response analysis for engineering design purposes has remained as one of the major challenges in engineering seismology. The earthquake ground motions at a site reflect the nature of the ground motions at the source, the wave propagation through the Earth between the source and the site, possible focusing or defocusing effects of large scale geologic structures on seismic waves, topography of the site, possible resonating effects of shallow reflectors, and the nonlinear response of the local site materials. Isolating the effects of the local site materials on earthquake ground motions from other effects is a major problem in all site response studies. The technique of spectral ratio analysis of ground motions at soil sites to the related adjacent rock sites is the most common technique to isolate the site effects from the source and path effects (Borcherdt, 1970; Andrews, 1986; Jarpe et al., 1989; Shakal et al., 1990; Darragh and Shakal, 1991; Field et al., 1992, Field, 1994; Steidle, 1993). Methods that use earthquake data are specially attractive since such data include the most realistic information on the site response to earthquake ground motions. The basic assumptions are that 1) the earthquake radiation pattern at the adjacent sites are similar and 2) the rock site has relatively flat site response as a function



of frequency. However, in reality most pairs of soil-rock sites with earthquake data are kilometers apart and depending upon the epicentral locations of earthquakes may experience ground motions of different radiation patterns. Furthermore, earthquake recordings are not available for most sites of engineering interest. This makes the spectral ratio technique mostly useful for understanding the phenomena of soil site response rather than for site response characterization for engineering design purposes.

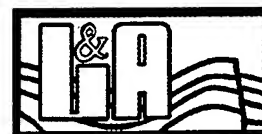
In recent years, attempts have been made to use coda waves to develop maps of regional site amplification factors (Phillips and Aki, 1986; Sue et al., 1992; Mayeda et al., 1991; and Chin and Aki 1991). Coda waves are the late arrivals of earthquake ground motions, tails of seismograms, at a site. They carry information on both the regional attenuation properties and the local site response to earthquake weak ground motions. Phillips and Aki (1986) and Chin and Aki (1991) used earthquake recordings at northern, central, and southern California and developed maps of coda waves amplification factors for different frequency bands. Earthquake data at rock sites were used to establish the reference coda waves amplitudes for the region. The amplification factors at soil sites were determined by comparing their corresponding coda waves amplitudes with the reference values. They used the correlation between the surface geology and the coda waves amplification factors at the sites with and without earthquake data to construct the site amplification maps. An important issue with using coda waves amplification values for earthquake strong ground motion simulation is that coda waves represent the site response to weak ground motions. There is ample evidence that the soil materials show strong nonlinear behavior under strong



ground shaking that should be taken into consideration for strong ground motion simulations (Seed & Idriss, 1969; Idriss, 1990; Hryciw et al., 1991, and Chin and Aki; 1991)

The characterization of site response based on soil to rock site spectral ratio or coda waves require earthquake data that are not readily available for many regions and at specific sites of interest. Microtremors and microseisms, long period microtremors with $T \geq 2$ s, have been used by many investigators for site response studies. The early work by Kanai (1957) and Kanai and Tanaka (1961) and subsequent work by Udvardia and Trifunac (1973), Ohta et al. (1978), Kagami et al. (1982 and 1986), Celebi et al. (1987), Field et al (1990), and Dravinski et al. (1992) have not yet produced a conclusive result that could be used in practical applications. It is argued, Udvardia and Trifunac (1973), that the nature and the propagation path of earthquake ground motions are totally different from those of microtremors and thus the spectral amplitudes of microtremors can not provide meaningful information on site response to earthquake ground motions.

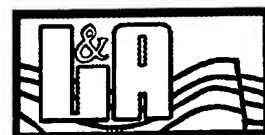
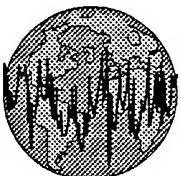
Another approach to the use of microtremors for site investigation has been to record microtremors on two-dimensional arrays to obtain information on the direction and velocity of wave propagation on regional and local scales (Capon, 1969; Lacoss et al., 1969; Asten and Henstridge, 1984; Horike, 1985; and Okada and Matsushima, 1986). In this type of studies the recordings of microtremors are used to determine the frequency-wave number, F-K ($k = 2\pi/\lambda$, where λ is wavelength), content of microtremors. The F-K data provide information on the direction and the apparent velocities of different frequency components of



microtremors. Assuming that microtremors are mainly composed of surface waves the apparent velocities are translated into models of shear wave velocity-depth profiles. The array-recording technique because of the results that it produces is very attractive. However, the required instrumentation and the dimension of the array make it less suitable for most typical engineering analysis.

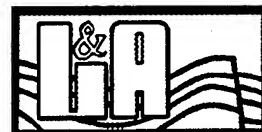
Aki (1957) introduced a site investigation technique based on microtremor data on a circular array. He showed that the azimuthal average of the spatial correlation coefficients of microtremors on a circular array can provide information on the propagation velocity of microtremors across the array as a function of frequency. Assuming that microtremors are dominantly composed of surface waves, he successfully used this technique at a site in the University of Tokyo to determine the phase velocities for Rayleigh waves. He interpreted the results in terms of the shear wave velocity profile for the site. The results of recent studies of Aki's technique at sites in Italy and Hawaii (Ferrazzini et al., 1991; Hough et al., 1992; and Malagnini et al., 1993) are encouraging. The most attractive feature of this technique is its simplicity in data requirement and field operation.

Nakamura (1989) suggested an alternative method for site characterization by dividing the horizontal to vertical spectral components of microtremors. He argued that taking the ratio of the horizontal to vertical spectral components will remove the effects of the source and Rayleigh waves from the records and thus provides information on site response to the S-waves. Theoretical and numerical studies by Lachet and Bard (1994) and Dravinski (personal communication)



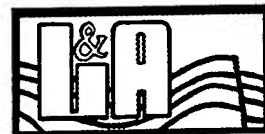
suggests that Nakamura's hypothesis is not strictly valid for all situations. Lachet and Bard (1994) indicated that the peak amplitudes in the horizontal to vertical spectral ratios are more related to the polarization of Rayleigh waves rather than the site response. However, there are reports of successful applications of this method to microtremors and microseisms data in identifying the site characteristic period (Nakamura, 1989; Omachi et al., 1991; and Field et al, 1993, Field, 1994). Field et al. (1993) used Nakamura's technique to study the site response in Giumri, Armenia, using the aftershocks of the 1988 Spitak earthquake and the recorded ambient noise at the corresponding sites. Theodulidis et al. (1994) studied the application of Nakamura's technique by using microseisms data from a downhole array in Garner Valley in the San Jacinto fault zone. These studies reported good agreements between the observed resonant frequencies based on Nakamura's technique and the theoretical S-wave transfer functions derived from the geotechnical profile. However, they also reported strong differences in the levels of site amplification for the S-waves and those from the Nakamura's technique.

The primary objective of this study is to identify a practical technique for site investigation that can provide reliable information on site conditions for routine seismic engineering analysis. This requires to identify techniques that can be applied locally, are not based on the availability of earthquake data since such data are not available for most sites, and are relatively inexpensive and simple in both data gathering and processing. Certainly, these criteria limit the choices. However, first it is necessary to characterize what is meant by the reliable information on site conditions. The state-of-the-practice for site response



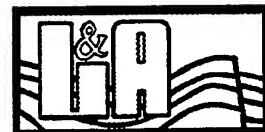
analysis is to use the results of one dimensional SH-wave propagation in a layered medium with known shear wave velocity-depth profile. In recent reports by Borchardt (1994), that reflects the view of the USGS and to some degree the CDMG, the site response to earthquake ground motions is characterized based on the average shear wave velocity of the top 30 m of the site materials. This concept is also taken by different authors of attenuation equations for the purpose of categorizing site conditions, e.g. Boore et al. (1994). Borchardt (1994) has developed a series of graphs and tables for the site amplification values for short period (0.1 - 0.5 s) and mid-period (0.4-2.0 s) in terms of the input ground motions and the average shear wave velocity of the top 30 m of the site materials. This set of data and, in general, this type of data are being accepted by the geotechnical earthquake community and are being used for routine site response characterization and analysis. In that respect, our objectives becomes to obtain the most representative value for the shear wave velocity of the shallow materials and if possible to construct a general picture of the local shear wave velocity profile for one-dimensional site response analysis.

Nakamura's technique because of its simplicity is very attractive for site response characterization. However, the results are controversial, its theoretical basis is questionable, and the type of results that it provides can not be easily used for the site response analysis. Aki's (1957) "Circular Array" technique is also attractive in the sense that it provides information on the velocity of wave propagation for the investigation site, it is based on microtremor data that can be obtained from surface measurements, the instrumentation for data gathering is relatively simple, and there is a theoretical basis for the methodology that can be tested. It is our



believe that the Circular Array technique has the potential to be a practical method for site investigation.

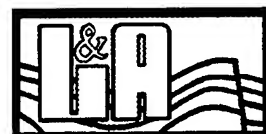
The first three chapters of this report review the theoretical basis of the Circular Array technique, validate the theory based on both numerical simulation of typical case studies and field investigations at different sites. Chapter 4 will discuss the integration of site response into the site-specific time history and response spectral analysis. A methodology for using the weak motion site response, such as coda waves amplification values, for ground motion simulation of large earthquakes will be discussed. In Chapter 5 the results of the site response investigation of the Northridge, California 1994 earthquake at few selected soil-rock sites will be discussed. The manual for the computer programs that are prepared for data processing and interpretation of typical Circular Array experiment are documented in Chapter 6.



Chapter 2

Application of the Circular Array Technique for Site Investigation

Aki (1957 and 1965) demonstrated that microtremor data on a set of instruments with a circular array configuration, with an instrument at the center, can be used to obtain information about the wave propagation properties of the recording site. The primary assumptions in formulating the "Circular Array" technique are that microtremors are temporally and spatially stationary within the time period and over the region of observation. Based on these assumptions it can be shown that the azimuthal average of spatial correlation coefficients of microtremors on the peripheral instruments, circular array, with respect to the center station would have predictable patterns as a function of frequency that could be used to obtain information on the seismic properties of the medium. Assuming that microtremors are composed of surface waves the Circular Array technique could provides information on the phase velocity, dispersion curve, of surface waves which can be translated into the shear wave velocity-depth profile for the site. This is a very attractive scenario that from the measurements of microtremors at a site one could obtain information on the shear wave velocity profile for that site. In this report we examine the application of the Circular Array technique for site response characterization. We present the theoretical formulation of the problem and evaluate its application to site investigation through both numerical simulation, this chapter, and field investigation, that will be discussed in the next chapter.



2.1. Theoretical Formulation of the Circular Array Technique

The setting is a circular array of instruments with one instrument at the center recording microtremors. Here, we refer to the circular array and the station at the center as the peripheral and reference instruments, respectively. Let us assume that for the time period of observation microtremors are stationary. From the mathematical point of view, a stationary ground motion can be modeled as the sum of an infinite number of plane waves of different frequency and wave numbers. For a single frequency and wave number the equation for propagating plane waves can be written as

$$g(\tilde{x}, t) = G(\omega, k, \phi) \cdot e^{i(\omega t - \tilde{k} \cdot \tilde{x})} \quad (2.1)$$

where $G(\omega, k, \phi)$ is the amplitude at frequency ω and wave number $k = 2\pi/\lambda$ (λ is the wavelength) and ϕ is the direction of wave propagation. The \sim sign on x and k is used to indicate that these terms are vectors and that the equation represents one, two, or three-dimensional wave propagation. For a two dimensional case equation (2.1) can be written as

$$g(x, y, t) = G(\omega, k, \phi) \cdot e^{i[\omega t - k \cdot \cos(\phi) \cdot x - k \cdot \sin(\phi) \cdot y]} \quad (2.2)$$

Microtremors, in general, are composed of waves of different frequencies and wave numbers traveling in different directions. Equation (2.2) can be generalized to represent such wave forms:

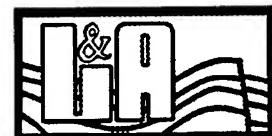


$$g(x, y, t) = \int_0^{2\pi} \int_{-\infty}^{\infty} \int_{-\infty}^{\infty} G(\omega, k, \phi) e^{i[\omega t - k \cdot x \cos(\phi) - k \cdot y \sin(\phi) + \theta(\omega, \phi)]} k \cdot dk \cdot d\phi \cdot d\omega \quad (2.3)$$

where the integration over the wave number domain is taken in polar coordinate system. $\theta(\omega, \phi)$ is a random phase that represents the statistical independence of the wave components of microtremors. The range of variation for $\theta(\omega, \phi)$ is 2π and as a random variable it is assumed to have a uniform probability density function:

$$\begin{cases} p[\theta(\omega, \phi)] = \frac{1}{2\pi}, & 0 \leq \theta(\omega, \phi) \leq 2\pi \\ = 0, & \text{otherwise} \end{cases} \quad (2.4)$$

Microtremors are assumed to be predominantly composed of surface waves (Aki, 1957; Lacoss et al., 1969; Tokimatsu et al., 1992). Surface waves, in general, propagate with frequency dependent phase velocities and could have different modes of propagation. However, obtaining information on the direction and modes of propagation for surface waves requires data on a relatively large aperture array for F-K analysis. Here, as is common in most practical applications, it is assumed that microtremors are predominantly composed of single mode surface waves. This gives a unique relationship between the frequency and wave number that is essential for relating the spatial and temporal spectral parameters. Based on this assumption, the spectral density function can be simplified as



$$G(\omega, k, \phi) = G'(\omega, \phi) \cdot \delta(k - \omega / C) \quad (2.5)$$

where $\delta(.)$ is delta function

$$\begin{aligned} \delta(k - \omega / c) &= 1 & k &= \omega / c \\ &= 0 & k &\neq \omega / c \end{aligned}$$

Substituting for $G(\omega, k, \phi)$ in equation (2.4) and defining

$$G(\omega, \phi) = (\omega / C) \cdot G'(\omega, \phi) \quad (2.6)$$

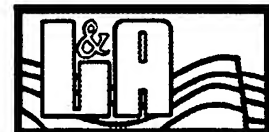
gives

$$g(x, y, t) = \int_0^{2\pi} \int_{-\infty}^{\infty} G(\omega, \phi) e^{i[\alpha t - k x \cos(\phi) - k y \sin(\phi) + \theta(\omega, \phi)]} d\phi \cdot d\omega \quad (2.7)$$

Equation (2.7) describes microtremors as composition of statistically independent waves of different frequencies traveling in different directions. The spatial autocorrelation function $\gamma(r, \phi)$ is defined as

$$\gamma(r, \phi) = E[g(x, y, t) * g(x + r \cdot \cos(\phi), y + r \cdot \sin(\phi), t)] \quad (2.8)$$

where $E[.]$ represents the expected value for the terms in the bracket, r is the distance between the two observation sites, ϕ is the direction between the two sites with respect to the x axis, and $*g(x, y, t)$ is the complex conjugate of $g(x, y, t)$



as is defined by equation (2.7). Substituting for $g(x, y, t)$ with appropriate modification for the complex conjugate gives

$$\gamma(r, \phi) = \int_{\omega=-\infty}^{\infty} \int_{\phi=0}^{2\pi} \int_{\omega'=-\infty}^{\infty} \int_{\phi'=0}^{2\pi} G(\omega, \phi) \cdot G(\omega', \phi') \quad (2.9)$$

$$\begin{aligned} & e^{i(\omega t - kx \cos(\phi) - ky \sin(\phi))} \\ & e^{-i(\omega' t - k'x \cos(\phi') - k'y \sin(\phi'))} \\ & E\{e^{i[\theta(\omega, \phi) - \theta(\omega', \phi')]} \} \\ & e^{i(k'r \cos(\phi) \cdot \cos(\phi') + k'r \sin(\phi) \cdot \sin(\phi'))} d\omega d\phi d\omega' d\phi' \end{aligned}$$

After carrying out the double integration with respect to ω' and ϕ' and taking into consideration that

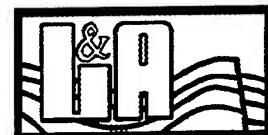
$$E\{e^{i[\theta(\omega, \phi) - \theta(\omega', \phi')]} \} = \begin{cases} 0, & \text{for } \omega \neq \omega' \text{ and } \phi \neq \phi' \\ 1, & \text{for } \omega = \omega' \text{ and } \phi = \phi' \end{cases} \quad (2.10)$$

the spatial autocorrelation function can be simplified as

$$\gamma(r, \phi) = \int_{-\infty}^{\infty} \int_0^{2\pi} [G(\omega, \phi) d\omega d\phi]^2 e^{ikr \cos(\phi - \phi)} \quad (2.11)$$

Equation (2.11) in terms of spectral power density function can be written as

$$\gamma(r, \phi) = \int_{-\infty}^{\infty} \int_0^{2\pi} S(\omega, \phi) e^{ikr \cos(\phi - \phi)} d\omega d\phi \quad (2.12)$$



where

$$S(\omega, \phi) = G(\omega, \phi)^2 d\omega d\phi. \quad (2.13)$$

The average of the spatial correlation function over different azimuths is

$$\bar{\gamma}(r) = \frac{1}{2\pi} \int_0^{2\pi} \left\{ \int_{-\infty}^{\infty} \int_0^{2\pi} S(\omega, \phi) e^{ikr \cos(\varphi - \phi)} d\omega d\phi \right\} d\varphi \quad (2.14)$$

The azimuthal integration of the exponential term is a zero order Bessel function of the first kind, i.e.

$$\int_0^{2\pi} e^{ikr \cos(\varphi - \phi)} d\varphi = 2\pi J_0(kr) \quad (2.15)$$

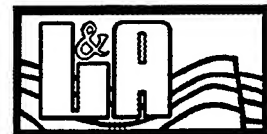
Therefore, equation (2.14) for a dispersive medium with $k = \omega / C(\omega)$ can be simplified as

$$\bar{\gamma}(r) = \begin{cases} (1 / 2\pi) \int_{-\infty}^{\infty} S_0(\omega) J_0[r\omega / C(\omega)] d\omega \\ (1 / \pi) \int_0^{\infty} S_0(\omega) J_0[r\omega / C(\omega)] d\omega \end{cases} \quad (2.16)$$

where $S_0(\omega)$ is the azimuthal average of the power spectral density

$$S_0(\omega) = (1 / 2\pi) \int_0^{2\pi} S(\omega, \phi) d\phi. \quad (2.17)$$

For a narrow frequency band with the center frequency of ω_0 the power spectral density can be approximated as a constant value. Defining $S_0(\omega_0)$ as



$$S_0(\omega_0) = \pi S_0(\omega) \quad \text{for} \quad \omega_0 - \delta\omega < \omega < \omega_0 + \delta\omega \quad (2.18)$$

equation (2.16) for a narrow frequency band can be written as

$$\bar{\gamma}(r, \omega_0) = S_0(\omega_0) J_0\left(r \frac{\omega_0}{C(\omega_0)}\right) \quad (2.19)$$

Accordingly, the equation for the autocorrelation coefficient

$$\bar{\rho}(r, \omega_0) = \bar{\gamma}(r, \omega_0) / \bar{\gamma}(0, \omega_0) \quad (2.20)$$

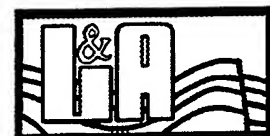
can be written as

$$\bar{\rho}(r, \omega_0) = J_0\left(r \frac{\omega_0}{C(\omega_0)}\right) \quad (2.21)$$

Equation (2.21) is the basis for Aki's (1957) formulation of the Circular Array technique. Equation (2.21) is for the case where the waves are not polarized such as the vertical ground motions. The horizontal ground motions are polarized either parallel or perpendicular to the direction of propagation. For the case of parallel polarization, that corresponds to P, SV, or Rayleigh waves, equations for the radial and tangential components of correlation coefficients, similar to equation (2.21), can be developed as

$$\bar{\rho}_r(r, \omega_0) = J_0[r\omega_0 / C(\omega_0)] - J_2[r\omega_0 / C(\omega_0)] \quad (2.22)$$

$$\bar{\rho}_\phi(r, \omega_0) = J_0[r\omega_0 / C(\omega_0)] + J_2[r\omega_0 / C(\omega_0)] \quad (2.23)$$



where $\bar{\rho}_r$ and $\bar{\rho}_\phi$ are the radial and tangential correlation coefficients, respectively, and $J_2[.]$ is the second order Bessel function of the first kind. For the case of perpendicular polarization, that corresponds to SH waves and Love waves, the correlation coefficients are

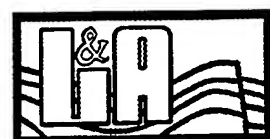
$$\bar{\rho}_r(r, \omega_0) = J_0[r\omega_0 / C(\omega_0)] + J_2[r\omega_0 / C(\omega_0)] \quad (2.24)$$

$$\bar{\rho}_\phi(r, \omega_0) = J_0[r\omega_0 / C(\omega_0)] - J_2[r\omega_0 / C(\omega_0)] \quad (2.25)$$

Equations (2.21) to (2.25) indicate that in an ideal situations the average of the spatial correlation coefficients of microtremors on peripheral instruments of a circular array with respect to the reference station at the center would have predictable patterns as a function of frequency as are shown on Figure 2.1. The interpretation of the average correlation coefficients, from a Circular Array experiment, in terms of the Bessel functions, equations (2.21) to (2.25), provides information on the apparent velocity of microtremor waves as a function of frequency that can be used to develop velocity-depth profile for the site.



This page intentionally left blank.



2.2. Simulation of the Circular Array Experiments by Two Instruments

Equations (2.21) to (2.25) are developed based on the concept that the recordings of microtremors on all instruments of the circular array are simultaneous. Let us examine the case where only two instruments are available for data collection. This may be the situation for most typical site investigation for engineering projects. By fixing one instrument and moving the other one on a circle one could simulate a circular array configuration. However, the recorded ground motions at different azimuths would not be simultaneous. This configuration was used by Aki (1957) for his experiment at the University of Tokyo.

The equation for the correlation coefficients in the frequency domain (Bracewell, 1978) at a particular azimuth φ can be written as

$$\rho(r, \omega_0, \varphi) =$$

$$\frac{2 \int_{\omega_0 - \delta\omega}^{\omega_0 + \delta\omega} \text{Re}[\mathfrak{I}(x, y, \omega) \mathfrak{I}^*(x + r \cos \varphi, y + r \sin \varphi, \omega)] d\omega}{\left(2 \int_{\omega_0 - \delta\omega}^{\omega_0 + \delta\omega} \mathfrak{I}^2(x, y, \omega) d\omega \cdot 2 \int_{\omega_0 - \delta\omega}^{\omega_0 + \delta\omega} \mathfrak{I}^2(x + r \cos \varphi, y + r \sin \varphi, \omega) d\omega \right)^{1/2}} \quad (2.26)$$

where $\mathfrak{I}(x, y, \omega)$ is the Fourier transformation of $g(x, y, t)$ and $\text{Re}[\cdot]$ indicates the real component of the complex quantity. Malagnini et al (1993) in their site amplification study in central Italy used similar equation to calculate the correlation coefficients in different azimuths and then took the average of all



azimuths to interpret the results in terms of equation (2.21). Substituting for $\mathfrak{I}(x, y, \omega)$ in terms of the inverse of equation (2.7), equation (2.26) can be simplified as

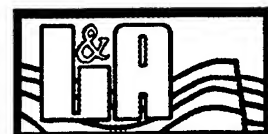
$$\rho(r, \omega_0, \varphi) = \frac{\operatorname{Re} \left[\int_0^{2\pi} G^2(\omega_0, \phi) \cdot e^{ik_0 r \cos(\phi - \varphi)} \cdot d\phi \right]}{\int_0^{2\pi} G^2(\omega_0, \phi) \cdot d\phi} \quad (2.27)$$

where $G(\omega_0, \phi)$ is the average amplitude spectrum, assumed to be constant, over the frequency band of $\omega - \delta\omega$ to $\omega + \delta\omega$ and $k_0 = \omega_0 / C(\omega_0)$. Taking the average of $\rho(r, \omega_0, \varphi)$ over the azimuth gives

$$\bar{\rho}(r, \omega_0) = \int_0^{2\pi} \operatorname{Re} \left(\frac{\int_0^{2\pi} G^2(\omega_0, \phi) \cdot e^{ik_0 r \cos(\phi - \varphi)} \cdot d\phi}{\int_0^{2\pi} G^2(\omega_0, \phi) \cdot d\phi} \right) d\varphi \quad (2.28)$$

If $\bar{\rho}_0(r, \omega_0)$, equation (2.28), is to be interpreted in terms of $J_0(kr)$, equation (2.21), the terms in the parenthesis in equation (2.28) should be approximated as

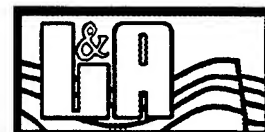
$$\frac{\int_0^{2\pi} G^2(\omega_0, \phi) \cdot e^{ik_0 r \cos(\phi - \varphi)} \cdot d\phi}{\int_0^{2\pi} G^2(\omega_0, \phi) \cdot d\phi} \cong e^{ik_0 r \cos(u)} \quad (2.29)$$



In that case, substituting for the left side of equation (2.29) in equation (2.28) gives

$$\overline{\rho}(r, \omega_0) \cong \int_0^{2\pi} e^{ik_0 r \cos(u)} du = 2\pi J_0(k_0 r) \quad (2.30)$$

The degree of approximation in equation (2.29) depends upon the azimuthal distribution of $G(\omega_0, \phi)$. Equation (2.29) holds true for all frequencies if $G(\omega_0, \phi)$ is independent of azimuth or is unidirectional. For all other cases, the equality in equation (2.29) is an approximation.



2.3. Simulation of Circular Array Experiments by Two Fixed Instruments

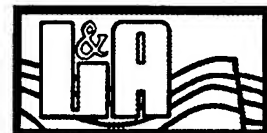
Let us examine the case where instead of moving one instrument on a circle around the other one to simulate a circular array configuration, the locations of both instruments are fixed and the averaging of the correlation coefficients are performed over different time windows rather than azimuths. We examine this configuration since its field requirement is very simple and practical. For each time window $\rho(r, \omega_0, \varphi)$ can be formulated by equation (2.27) as it represents one azimuthal realization of the circular array data. However, in this case the averaging of $\rho(r, \omega_0, \varphi)$ is performed over different time windows rather than different azimuths

$$\bar{\rho}(r, \omega_0) = \langle \rho(r, \omega_0, \varphi) \rangle = \left(\sum_{j=1}^n \rho_j(r, \omega_0, \varphi) \right) / n \quad (2.31)$$

where $\langle . \rangle$ indicates averaging over time windows. Using a similar approximation for equation (2.27) as was described by equation (2.29), $\bar{\rho}(r, \omega_0)$ can be formulated as

$$\bar{\rho}(r, \omega_0) \cong \langle e^{ik_r r \cos(u)} \rangle = \left(\sum_{j=1}^n e^{i[k_r r \cos(u)]_j} \right) / n \quad (2.32)$$

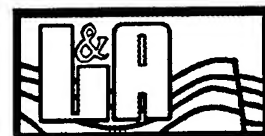
If equation (2.32) is to be interpreted in terms of $J_0(kr)$, equation (2.21), the following approximation should hold



$$\left(\sum_{j=1}^n e^{i[k_0 r \cos(u)]_j} \right) / n \cong \int_0^{2\pi} e^{ik_0 r \cos(u)} du = 2\pi J_0(k_0 r) \quad (2.33)$$

This requires that the average of the correlation coefficients over different time windows to be statistically the same as the average values over azimuth.

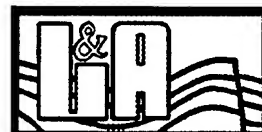
Both the azimuthal and time window averaging of the correlation coefficients for two-instruments configuration can simulate a circular array with certain level of approximation. It is not immediately apparent the degree of uncertainties in the estimation of the apparent velocities because of these approximation. In the next section we examine the application of these field configurations to site investigation through numerical simulations of microtremor data under different conditions.



2.4. Numerical Simulation: Case Studies of the Application of the Circular Array Technique for Site Investigation

In the previous section we discussed the formulation of the Circular Array technique. We also reviewed the possibility that the data for a Circular Array experiment can be collected using only two instruments. Two scenarios for data collection were presented: 1) having one instrument fixed and moving the other one on a circle and 2) having both instruments fixed and recording for a relatively long period of time for time window averaging of the correlation coefficients. In an ideal Circular Array experiment there are simultaneous recordings of microtremors on all instruments. However, since the proposed alternatives use only two instruments the recordings of microtremors at different azimuths or over different time windows will not be simultaneous. In the first scenario the correlation coefficients are averaged over different azimuths to simulate an ideal Circular Array experiment. In the second scenario this objective is achieved by averaging the correlation coefficients over different time windows. In order to understand the effects of these different field configurations on the interpretation of data we performed numerical simulation of microtremors on typical circular arrays of specific configurations that were described. The results of the numerical simulations also help to understand and evaluate the application of Circular Array technique for site investigation.

Figures 2.2, 2.3, and 2.4 show the schematic diagrams for the three field configurations that are considered in this study.



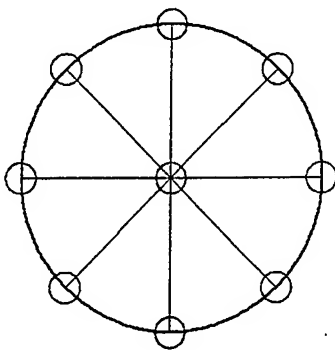


Figure 2.2. *The configuration of an ideal Circular Array experiment. The recording of microtremors on all instruments are simultaneous.*

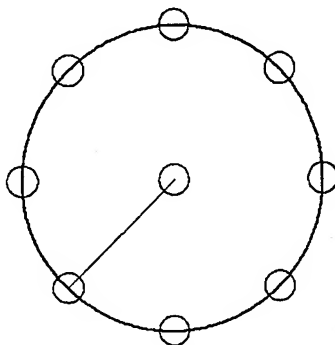


Figure 2.3. *The configuration of a Circular Array experiment with two instruments. The location of the instrument at the center is fixed. The other instrument is moved on a circular path to simulate the configuration of an ideal Circular Array experiment. Obviously, the recordings of microtremors on different pairs of reference-peripheral instruments are not simultaneous.*

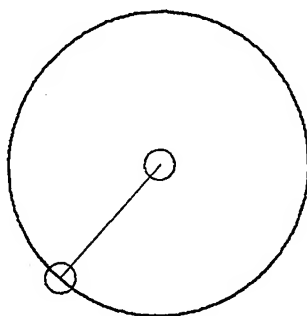
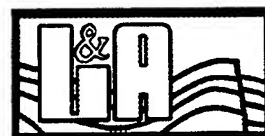


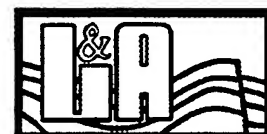
Figure 2.4. *The configuration of a Circular Array experiment with two fixed instruments. The locations of both instruments are fixed. The averaging of the correlation coefficients are performed over different time windows rather than azimuths.*



Here, we refer to these three configurations as case I, II, and III, respectively. In our numerical simulation and for all cases, microtremors are simulated by integrating statistically independent wave forms from different directions. Figure 2.5 shows typical time histories. Considering the stochastic nature of microtremors, they are simulated using a random number generator. In case I, Figure 2.2, the same set of time histories, each time history within a set represents microtremors from different direction, are used to simulate microtremors on each instrument. In cases II and III different sets of time histories are used for different pairs of reference-peripheral instruments or time windows. For each pair of reference-peripheral instruments and each direction for wave propagation appropriate phase shifts are applied to the time histories to account for the passage of the wave front at these sites. The amount of the phase shift depends upon the assumed direction for the wave propagation, azimuth and the distance between the two stations, and the assumed apparent velocity of the wave front.

Let us denote $g(x_1, y_1, \phi, t)$ as a component of microtremors at location (x_1, y_1) traveling in direction ϕ . Let us denote the Fourier transformation of $g(x_1, y_1, \phi, t)$ as $\mathfrak{I}(x_1, y_1, \phi, \omega)$. Assuming that this wave form is not generated in the immediate vicinity of the recording instruments, the frequency domain amplitudes of this wave form at a site at (x_2, y_2) , see the diagram, can be written as

$$\mathfrak{I}(x_2, y_2, \phi, \omega) = \mathfrak{I}(x_1, y_1, \phi, \omega) \cdot e^{i \cdot \omega \cdot \delta t} \quad (2.34)$$



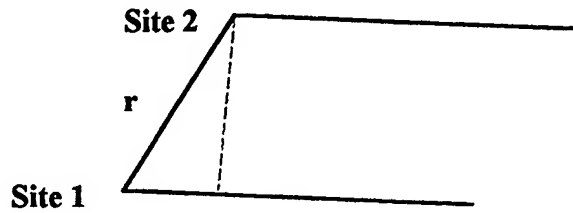


Diagram 2.1. The phase difference in the wave forms at two sites is the function of the distance between the sites the relative direction of the wave propagation with respect to the sites and the velocity of wave propagation.

where $\delta t = r \cdot \sin(\phi) / C(\omega)$ is the phase shift, r is the distance between the sites, ϕ is the angle, and $C(\omega)$ is the apparent velocity of the wave front. The ground motions at the reference site is the sum of all ground motions arriving at that site from different directions, i.e.

$$g(x_1, y_1, t) = \sum_{\phi} g(x_1, y_1, \phi, t) \quad \text{in time domain} \quad (2.35)$$

$$\mathfrak{I}(x_1, y_1, \omega) = \sum_{\phi} \mathfrak{I}(x_1, y_1, \phi, \omega) \quad \text{in the frequency domain} \quad (2.36)$$

The ground motions at site 2 in the frequency domain can be written as

$$\mathfrak{I}(x_2, y_2, \omega, \phi) = \sum_{\phi} \mathfrak{I}(x_1, y_1, \phi, \omega) \cdot e^{i \cdot \omega \cdot \delta t(\phi, \phi)} \quad (2.37)$$

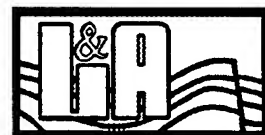


where $\delta t(\phi, \varphi)$ is the time shift for each direction. The symbol φ identifies the direction between the reference and peripheral site. Based on equations (2.36) and (2.37) and for assumed values for r , φ , the apparent velocity as a function of frequency, and the azimuthal distribution of microtremors $\mathfrak{I}(x_1, y_1, \omega)$ and $\mathfrak{I}(x_2, y_2, \omega)$ in the frequency domain can be simulated. Using this information and equation (2.26) the correlation coefficients for each pair of reference-peripheral sites can be calculated. This procedure is common to all three configurations; i.e. case I, II, and III. In the numerical simulation for case I the same set of input time histories are used for all pairs of reference-peripheral sites. For cases II and III different sets of time histories are used for different pairs of reference-peripheral sites. In case II the time shift, $\delta t(\phi, \varphi)$ in equation (2.37), varies with φ . In case III, $\delta t(\phi, \varphi)$ does not vary with φ since the locations of the instruments are fixed.

We will discuss the results of numerical simulation in terms of the plots of the correlation coefficients versus frequency, CC-F curves or data. In the following discussion the term "results of the analysis" means the average of CC-F for different cases. Three types of input parameters could be identified:

Azimuthal distribution of microtremors

Ideally microtremors are composed of statistically independent wave forms with a uniform azimuthal distribution. This might not always be the case. For this reason, we allow for non-uniform azimuthal distribution of microtremors, i.e. limiting the arrival of waves to certain azimuths.



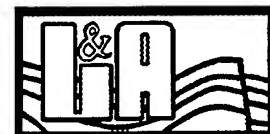
Wave propagation properties of the medium

The wave propagation properties of the medium comes into play when calculating the phase differences between the Fourier spectral amplitudes of waves at two stations, $\delta t(\phi, \varphi) = r \cdot \sin(\varphi) / C(\omega)$ in equation (2.37). In our simulation, as is apparent from equation (2.37), $C(\omega)$ is defined as a function of frequency.

The configuration of the Circular Array experiment

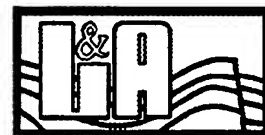
The configuration of the Circular Array determines the distance, r , and angle, φ , that are used for the phase shift analysis. It also determines how the averaging of the correlation coefficients over the azimuth is performed.

In this report, we are using both metric and English units. We apologize for this. However, since some of the analyses are performed using distances and velocities in ft and ft/s, respectively, translating them to metric units would not be whole numbers and look awkward. Therefore, we use English units in this chapter. First, let us examine an ideal Circular Array configuration, i.e. case I. Figure 2.6 shows the results of the simulation of a typical Circular Array, case I, experiment with the radius of 45 ft. In this example, uniform azimuthal distribution for microtremors and a constant apparent velocity of 1000 ft/s for wave propagation in the medium are assumed. The solid line is the plot of $J_0(\omega \cdot r / C(\omega))$ and the jagged line is the plot of the averaged correlation coefficients, equations (2.26) and (2.28), versus frequency. There is an excellent agreement between



$J_0(\omega.r / C(\omega))$ and the average correlation coefficients that is what we expect based on theory. Figure 2.7 shows CC-F for two different cases with $C=100$ ft/s and $C=2000$ ft/s. Again there are excellent agreements between the CC-F results and the expected $J_0(\omega.r / C(\omega))$ values for both cases. Comparing the results on Figures 2.6 and 2.7 indicates an increase in the correlation coefficients within the frequency range of the first half cycle of the curve with increasing the apparent velocity. This is expected since with increasing the apparent velocity of the medium the time differences between the arrivals of wave fronts at the two sites decrease which means a better correlation between the ground motions at the sites. It is worth mentioning that the increase in the apparent velocity has the same effects on the correlation coefficients as the decrease in the distance between the recording sites. Figure 2.8 demonstrates this point. This figure shows the results of the simulation for two different radii, $r = 45$ ft and $r = 90$ ft with the apparent velocity of $C = 2000$ ft/s. The case of $r = 90$ ft and $C = 2000$ ft/s is similar to the case of $r = 45$ ft and $C = 1000$ ft/s. Compare the results on Figures 2.6 and 2.7.

Let us examine the effects of non-uniform azimuthal distribution of microtremors on the estimation of the correlation coefficients from a typical Circular Array experiment. Figures 2.9 and 2.10 show the results of two such cases where the azimuthal distribution of microtremors are limited to 180 and 90 degrees rather than 360 degrees. All other parameters are the same as those that are used in the simulation of Figure 2.7. Both cases show practically no recognizable effects on the results. This is interesting and needs explanation. The term $J_0(k.r)$ appears in the formulation of the Circular Array technique due to averaging the



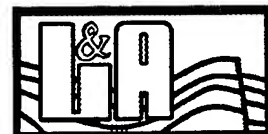
correlation coefficients over different azimuths as a part of recording process rather than the azimuthal distribution of microtremors. This was shown in equation (2.15) as

$$\int_0^{2\pi} e^{ikr \cos(\varphi - \phi)} d\varphi = 2\pi J_0(kr) \quad (2.15)$$

$d\varphi$ identifies the variation in the azimuthal distribution of the reference-peripheral instruments. The averaging on the azimuthal distribution of the wave propagation was used to formulate the average power spectral density, equation (2.17)

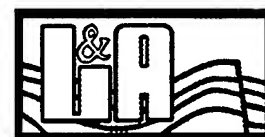
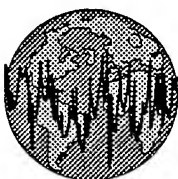
$$S_0(\omega) = (1/2\pi) \int_0^{2\pi} \bar{S}(\omega, \phi) d\phi. \quad (2.17)$$

Therefore, the azimuthal distribution of microtremors would primarily affect the power spectral amplitude rather than the shape of the correlation coefficients as a function of frequency. To further demonstrate this point let us show the results of two simulations for a single pair of instruments without any azimuthal averaging. It should be emphasized that in these two simulations microtremors are assumed to be uniformly distributed. Figure 2.11 shows the results of these simulations. All parameters are the same as those that are used in the simulation of Figure 2.7. Figure 2.11 clearly shows that although the general pattern of the correlation coefficients follow $J_0(k.r)$ for each case, there are strong randomness in the correlation coefficients. In other words, it is through azimuthal averaging that the randomness of the correlation coefficients smooth itself out. This point is also



related to the observed randomness of the correlation coefficients at high frequencies in all previous figures. As ω increases the rate of variation of the exponential term in equation (2.15) increases. Therefore, in order to obtain a smooth correlation coefficients for high frequency ranges the averaging must be done over many more azimuths than is necessary for the low frequency ranges.

Let us examine the cases where only two instruments are available for data gathering, i.e. cases II and III. Figure 2.12 shows the results of simulation for case II configuration with the same input parameters that are used in Figure 2.7 simulation. Figure 2.13 shows similar results for case III configuration where the averaging of the correlation coefficients are performed over different time windows. A comparison between these two figures and Figure 2.7 indicate that both field configurations could provide very reasonable approximation of an ideal Circular Array set up. Apparently, the randomness in the CC-F values are smoothed out through the averaging process over different time windows or azimuths. The effects of different time histories for each azimuth or time window is apparent in Figure 2.12 and 2.13. However, it does not overshadow the expected pattern for the CC-F in the context of the Circular Array experiment. It is necessary to mention that the agreement between the results of case III, Figure 2.13, with the ideal Circular Array simulation, Figure 2.7, should not be taken as a general rule. Under certain circumstances, due to the azimuthal distribution and/or temporal variation of microtremors, the time window averaging might not provide the adequate smoothing for the CC-F curve to simulate an ideal Circular Array experiment. Figure 2.14 shows the CC-F curve for a case III experiment where the results of an ideal Circular Array could not be simulated. The results



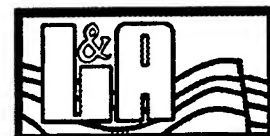
of these simulation suggest that when there are only two instruments available a combination of case II and Case III experiments, i.e. taking both azimuthal and time window averaging, could provide the best results.

Let us examine a case where the phase velocity is frequency dependent. Figure 2.15 shows the results of CC-F for case I configuration with $r = 45$ ft and the following phase velocity profile

$$\begin{aligned} C(\omega) &= 1000 \text{ ft / s} \quad \text{for } 3.0 \text{ Hz} \geq f \\ C(\omega) &= 2000 \text{ ft / s} \quad \text{for } 12.0 \text{ Hz} \geq f > 3.0 \\ C(\omega) &= 1500 \text{ ft / s} \quad \text{for } 12.0 \text{ Hz} < f \end{aligned}$$

Figures 2.16 and 2.17 show similar results for the Case II and III configurations, respectively. All figures show excellent agreements between the expected pattern for $J_0(k.r)$ and the calculated CC-F.

The results of these simulations indicate that the Circular Array technique, even under less than ideal field configuration, show a very predictable pattern that could be used for site investigation. However, it is necessary to emphasize that the results of numerical analyses characterize ideal situations where the phase shift between any two recording sites can be predicted by the distance between the sites, the relative direction of the wave propagation with respect to the sites, and frequency dependent apparent velocities that do not change with azimuth. Furthermore the waves are assumed to be single mode, i.e. all waves of given frequency band propagate with a unique apparent velocity. Certainly, the real Earth does not comply. All these assumptions, in one way or another, could be violated. Therefore, whatever information that could be obtained from the



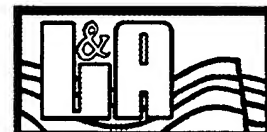
Circular Array technique is only an approximation of the reality. Nevertheless, the results of numerical simulation are very encouraging.



2.5. Interpretation of the Correlation Coefficient-Frequency Data for Site Investigation

The objective of a Circular Array experiment, as is formulated here, is to obtain information on the shear wave velocity profile for the site of experiment. Let us examine how the correlation coefficient data as a function of frequency, CC-F curve, can lead to the construction of the velocity depth profile for a site. We demonstrate the proposed interpretation methodology through an example. In the first part, for a known frequency dependent apparent velocity we simulate the CC-F curve. Assuming that the simulated CC-F curve is the result of a Circular Array experiment we reconstruct the input apparent velocity model. In the second part, assuming that microtremors are composed of surface waves the apparent velocities are used to construct shear wave velocity profile for the medium. We review both theoretical and empirical techniques for interpreting the phase velocity of surface waves into the shear wave velocity profile. The discussion on the data interpretation is limited to the case of non-polarized components of ground motions, i.e. the vertical components. The reason is that in real Earth situation it is rather difficult to determine the polarization of microtremor waves that is necessary for the interpretation of the horizontal components. The determination of such information requires data on a rather large scale array and a full scale frequency-wave number analysis.

Let us consider a hypothetical situation where the apparent velocities for microtremors as a function of frequency are known, as shown in the following diagram.



Apparent Velocity

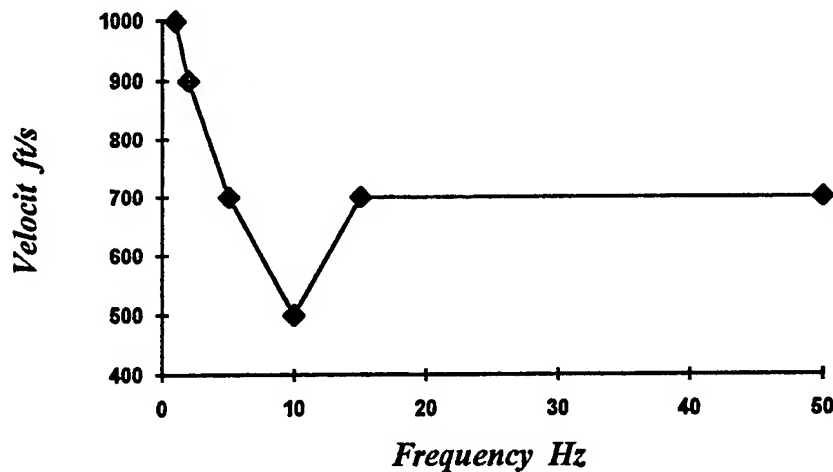
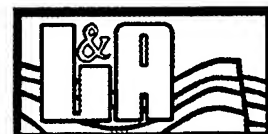


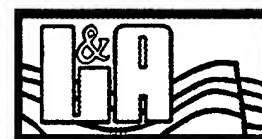
Figure 2.18 shows the CC-F curve and the expected Bessel function values, equation (2.21), as a function of frequency for $r=45$ ft and using the apparent velocities that are shown on the diagram. In order to demonstrate the methodology of data interpretation, let us assume that Figure 2.18 is the CC-F curve from a Circular Array experiment for a site with the apparent velocities that are shown on the Diagram. Each value in Figure 2.18 represents an average correlation coefficient $\bar{\rho}(\omega)$ over a narrow frequency band. $\bar{\rho}(\omega)$ can be interpreted in terms of the Bessel function $J_0(x = \omega.r / C(\omega))$. Using the tables of Bessel functions the values for variable x can be determined in such a way that $J_0(x) = \bar{\rho}(\omega)$. Knowing the radius and the frequency, the apparent velocities are calculated as $C(\omega) = \omega.r / x$. The procedure is simple. However, since the function $J_0(x)$ is not a single valued function the determination of x for a given value of $J_0(x)$ needs special attention. Figure 2.19 shows a typical example. For certain ranges of $J_0(x)$ different cycles of Bessel function give different estimates of x . Therefore, the interpretation of CC-F curves in terms of the



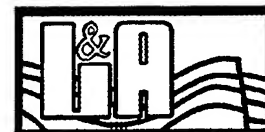
Bessel function requires that the half cycles of the Bessel function to which different values of $\bar{\rho}(\omega)$ belong are identified. A practical approach to this problem is to identify the maximum and minimum values on CC-F curves. Table 2.1 shows the $\bar{\rho}(\omega)$ values that are shown on Figure 2.18. The thick solid lines identify where the maximum and minimum $\bar{\rho}(\omega)$ -values occur. Table 2.1 also shows the x -values corresponding to each $J_0(x) = \bar{\rho}(\omega)$ over four cycles. The cells without any value indicate that there is no possibility of having $J_0(x)$ value on that cycle for the given $\bar{\rho}(\omega)$. The first minimum for $\bar{\rho}(\omega)$ occurs at $f = 7.75$ Hz. Without knowing the cycles and half cycles of the Bessel function to which $\bar{\rho}(\omega)$ belongs, $\bar{\rho}(\omega)$ at $f = 8.25$ Hz could be interpreted as $J_0(x|x=3.577)$ or $J_0(x|x=4.092)$. However, knowing that $\bar{\rho}(\omega)$ at $f = 8.25$ Hz falls between the first minimum and second maximum enables us to correctly select $x = 4.092$ for this frequency.

Table 2.1. The CC-F values and the estimated phase velocities for the first four modes.

f Hz	$\bar{\rho}(\omega)$ ↓ $J_0(x)$	x	$C_1(\omega)$	x_2	$C_2(\omega)$	x_3	$C_3(\omega)$	x_4	$C_4(\omega)$
.25	.999	.069	1019						
.75	.989	.212	1000						
1.25	.967	.362	975						
1.75	.930	.535	925						
2.25	.874	.720	883						
2.75	.801	.915	850						
3.25	.708	1.125	816						
3.75	.592	1.354	783						
4.25	.454	1.602	750						
4.75	.297	1.874	716	6.871	195	7.161	187		
5.25	.138	2.151	690	5.954	249	8.140	182	12.445	119.3

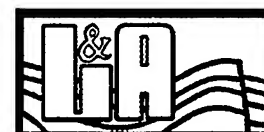


f Hz	$\bar{\rho}(\omega)$ ↓ $J_0(x)$	x	$C_1(\omega)$	x_2	$C_2(\omega)$	x_3	$C_3(\omega)$	x_4	$C_4(\omega)$
5.75	-.011	2.427	670	5.487	296	8.695	187	11.743	138.4
6.25	-.151	2.719	650	5.081	347	9.266	190	11.111	159.0
6.75	-.270	3.029	630	4.698	406				
7.25	-.357	3.361	610	4.323	474				
7.75	-.400	3.715	589	3.950	554				
8.25	-.389	3.577	652	4.092	570				
8.75	-.321	3.203	772	4.498	550				
9.25	-.199	2.834	922	4.935	530	9.530	274	10.831	241
9.75	-.039	2.482	1110	5.405	510	8.800	313	11.623	237
10.25	.054	2.302	1258	5.683	510	8.455	342	12.030	240
10.75	.071	2.271	1338	5.735	530	8.393	362	12.107	251
11.25	.087	2.243	1418	5.783	550	8.336	381	12.179	261
11.75	.101	2.218	1498	5.829	570	8.283	401	12.248	271
12.25	.113	2.195	1578	5.871	590	8.235	420	12.313	281
12.75	.125	2.174	1658	5.910	610	8.189	440	12.375	291
13.25	.136	2.155	1738	5.947	630	8.148	459	12.434	301
13.75	.145	2.137	1818	5.981	650	8.109	479	12.491	311
14.25	.154	2.122	1899	6.014	670	8.072	499	12.546	321
14.75	.163	2.107	1979	6.044	690	8.038	518	12.600	331
15.25	.192	2.055	2098	6.160	700	7.910	545	12.832	336
15.75	.236	1.979	2250	6.362	700	7.691	579		
16.25	.269	1.922	2391	6.564	700	7.477	614		
16.75	.291	1.885	2512	6.766	700	7.268	651		
17.25	.300	1.869	2609	6.969	699	7.063	690		
17.75	.297	1.875	2677	6.863	731	7.169	700		
18.25	.282	1.900	2715	6.666	774	7.371	700		
18.75	.256	1.945	2725	6.473	819	7.573	700		
19.25	.220	2.006	2712	6.283	866	7.775	700		
19.75	.177	2.082	2682	6.099	915	7.977	700	12.703	439
20.25	.128	2.169	2639	5.919	967	8.179	700	12.389	462
20.75	.074	2.266	2589	5.744	1021	8.381	700	12.121	484
21.25	.019	2.368	2537	5.577	1077	8.583	700	11.874	506
21.75	-.035	2.474	2485	5.417	1135	8.783	700	11.640	528
22.25	-.087	2.580	2438	5.267	1194	8.987	700	11.414	551
22.75	-.134	2.682	2398	5.129	1254	9.189	700	11.193	574
23.25	-.175	2.776	2367	5.007	1312	9.391	700	10.977	598
23.75	-.208	2.857	2350	4.905	1368	9.593	700	10.765	623
24.25	-.232	2.920	2347	4.829	1420	9.795	700	10.557	649
24.75	-.246	2.959	2364	4.782	1463	9.998	700	10.350	676
25.25	-.250	2.970	2403	4.769	1497	10.152	703	10.196	700
25.75	-.243	2.952	2466	4.790	1519	9.948	731	10.401	700
26.25	-.227	2.908	2552	4.843	1532	9.750	761	10.603	700
26.75	-.203	2.844	2659	4.923	1536	9.555	791	10.805	700



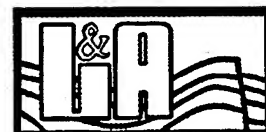
f Hz	$\bar{\rho}(\omega)$ ↓ $J_0(x)$	x	$C_1(\omega)$	x_2	$C_2(\omega)$	x_3	$C_3(\omega)$	x_4	$C_4(\omega)$
27.25	-.170	2.764	2787	5.023	1533	9.363	822	11.007	700
27.75	-.131	2.675	2933	5.139	1526	9.175	855	11.209	700
28.25	-.088	2.581	3094	5.265	1517	8.990	888	11.411	700
28.75	-.042	2.487	3269	5.399	1505	8.809	922	11.613	700
29.25	.005	2.395	3453	5.536	1493	8.634	957	11.815	700
29.75	.051	2.308	3645	5.674	1482	8.465	993	12.017	700
30.25	.095	2.229	3838	5.809	1472	8.305	1029	12.219	700
30.75	.133	2.159	4026	5.938	1464	8.157	1065	12.421	700
31.25	.166	2.101	4205	6.056	1458	8.024	1101	12.623	700
31.75	.191	2.057	4365	6.156	1458	7.914	1134	12.825	700
32.25	.209	2.026	4499	6.230	1463	7.833	1164	13.027	700
32.75	.217	2.011	4603	6.270	1476	7.790	1188	13.229	700
33.25	.217	2.012	4673	6.269	1499	7.791	1206	13.218	711
33.75	.208	2.027	4706	6.228	1532.2	7.835	1217	13.018	733
34.25	.191	2.057	4706	6.154	1573.5	7.916	1223	12.820	755
34.75	.166	2.101	4676	6.057	1622.1	8.023	1224	12.624	778
35.25	.135	2.156	4623	5.945	1676.5	8.150	1223	12.431	801
35.75	.099	2.221	4552	5.824	1735.7	8.289	1219	12.240	825
36.25	.059	2.293	4470	5.698	1798.6	8.436	1215	12.053	850
36.75	.018	2.370	4383	5.573	1864.4	8.588	1210	11.869	875

Finding the maximum and minimum values for the CC-F curve that is shown on Figure 2.18 is simple since the curve is fairly smooth. In real situations the CC-F curves might not be necessarily smooth. The local maximum and minimum values, due to the raggedness of the results, could be misleading in terms of finding the appropriate cycle of the Bessel function. Figure 2.20 shows a typical example where certain degree of randomness is introduced to the CC-F curve of Figure 2.18. In order to interpret this data in terms of the Bessel function, the CC-F curve must be smoothed. We use 3-poles Butterworth filter for this purpose. The solid line on Figure 2.20 shows the filtered CC-F curve. The smoothed curve has well defined maximum and minimum values that can be used for data interpretation.

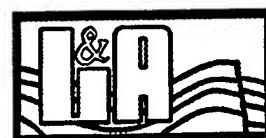


2.6. Construction of Shear Wave Velocity Profile from the Apparent Velocity of Microtremors

Microtremors are assumed to be predominantly composed of surface waves. The vertical components of microtremors are often modeled as Rayleigh waves. Accordingly, the estimated apparent velocities from the CC-F curves of the vertical components of microtremors can be interpreted as the phase velocities, dispersion curve, for the Rayleigh wave propagation across the site of investigation. The inversion of the dispersion curve for shear wave velocity profile is a complex and non-unique problem that has attracted a good amount of research (e.g., Haskell, 1953; Harkrider, 1964; Nazarian, 1984; and Hossein and Drnevich, 1989). There are different sophisticated techniques for inverting phase velocities of surface waves. However, considering the degree of uncertainties in the formulation of the Circular Array technique adopting a very sophisticated methodology for the phase velocity inversion is not warranted. Furthermore, the state-of-the-practice of the site amplification analysis, i.e. one-dimensional SH wave propagation through layered medium, is overly simplified. The recent reports by Borcherdt (1994) that reflects the view of the USGS and to some degree the CDMG suggest characterizing the site conditions based on the average shear wave velocity of the top 30 m (100 ft) materials. In that respect, our objectives are to obtain the most representative value for shear wave velocity of the top 100 ft materials and if possible to construct a general picture of the local shear wave velocity profile for one-dimensional site amplification analysis. Therefore, for converting the phase velocities to the shear wave velocity profile we seek a practical approach that could provide reasonable results with minimum amount of time and effort.



There are both theoretical and empirical approaches to the surface wave phase velocity inversion to shear wave velocity profiles. The theoretical approach relies on rigorous mathematical formulation of Rayleigh wave propagation in layered medium. The optimum shear wave velocity profile is constructed by minimizing the mismatch between the simulated and observed phase velocities. The empirical or semi-theoretical approach simplify the inversion problem by making assumptions about the effective depths that control the phase velocities of different frequency bands. This assumption provides a tool for transforming the phase velocity-frequency curves directly into a phase velocity-depth profile. Assuming that the phase velocity is a fraction of the shear wave velocity of the site, the phase velocity-depth profile is translated into the shear wave velocity-depth profile for the site. This is a practical approach that can be used for our analysis. However, for the purpose of fine tuning the results and also for better understanding the relationship between the velocity-depth profiles and phase velocities, we also present the theoretical formulation and software for the phase velocity simulation of Rayleigh waves in layered medium.

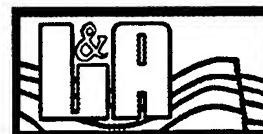


2.7. Semi-Theoretical Approach to the Inversion of Phase Velocities to Shear Wave Velocity Profiles

The semi-theoretical approach to the phase velocity inversion relies on two types of information: 1) the relationship between the phase velocities and the shear wave velocity of a site and 2) the effective depths that control the phase velocities of different frequencies. Theory indicates that the ratio of the phase velocity of Rayleigh waves to the effective shear wave velocity, $C(\omega) / \beta$, that control the phase velocity of that frequency band has a relatively narrow range of variation. Satoh et al (1991) reported the range of $C(\omega) / \beta$ between 0.874 to 0.955 for a wide range of Poisson's ratios. Verttos and Prange (1990) reported $C(\omega) / \beta = 0.932$ for Poisson's ratio of 0.33. Satoh (1989), based on data from surface wave experiments at many Japanese sites, developed the following empirical relationship

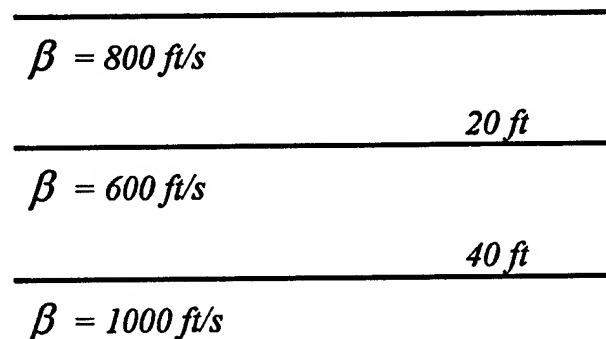
$$C(\omega) = 0.89 * \beta + 4 \quad (2.38)$$

where the units are in m/s. On the issue of the effective penetration depth of Rayleigh waves, it is commonly assumed that the effective depth is about half of the wave length at any given frequency. However, recent studies by Verttos (1990) and Verttos and Prange (1991) on surface wave propagation in medium with depth-dependent stiffness indicate that the effective depth of penetration for Rayleigh waves may be less than half of the wavelength. These studies show that the effective depth as a fraction of wavelength increases with increasing the frequency and Poisson's ratio. Their results suggest that the effective depth may be about 30% rather than 50% of the wavelengths. The information on $C(\omega) / \beta$



ratio and the effective depth of penetration for Rayleigh waves are sufficient to invert the Rayleigh waves phase velocities into a shear wave velocity-depth profile. Following, we demonstrate the application of this approach through an example.

Let us consider a layered medium with known shear wave velocity profile as shown in the following diagram.



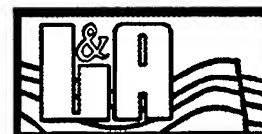
The phase velocities for the first four modes of the Rayleigh waves for this medium are shown on Figure 2.21. The velocities for the p-waves are assumed to be 1.73 times the shear wave velocities. We use the phase velocities for the first mode to simulate the CC-F curve for a typical Circular Array experiment. Random values are directly introduced to the simulated CC-F values, Figure 2.22, to simulate a real field situation. As was discussed in the previous section the CC-F curve on Figure 2.22 should be filtered to obtain a smooth representative CC-F curve for the medium. Figure 2.23 shows plots of both simulated and filtered CC-F curves. The values of the filtered CC-F curve are shown in Table 2.2. The table also



shows the interpretation of $J_0(x) = \bar{\rho}_0(\omega)$ on four different half cycles of the Bessel function.

Table 2.2. The CC-F values, from Figure 2.23, and the corresponding apparent velocities.

f Hz	$\bar{\rho}(\omega)$ ↓ $J_0(x)$	x	$C_1(\omega)$	x_2	$C_2(\omega)$	x_3	$C_3(\omega)$	x_4	$C_4(\omega)$
.25	.988	.21	329.						
.75	.983	.26	807.						
1.25	.937	.51	698.						
1.75	.922	.56	878.						
2.25	.912	.60	1062.						
2.75	.824	.86	906.						
3.25	.735	1.07	862.						
3.75	.648	1.25	851.						
4.25	.555	1.42	845.						
4.75	.451	1.61	835.						
5.25	.334	1.81	820.						
5.75	.204	2.03	799.	6.21	262.	7.85	207.	12.96	125.
6.25	.069	2.28	777.	5.73	309.	8.40	210.	12.10	146.
6.75	-.061	2.53	756.	5.34	357.	8.88	215.	11.53	166.
7.25	-.174	2.77	739.	5.01	409.	9.38	218.	10.99	187.
7.75	-.262	3.01	729.	4.73	464.				
8.25	-.323	3.21	726.	4.49	520.				
8.75	-.354	3.35	739.	4.34	570.				
9.25	-.358	3.37	777.	4.32	606.				
9.75	-.343	3.29	837.	4.40	627.				
10.25	-.314	3.18	912.	4.53	640.				
10.75	-.274	3.04	999.	4.68	649.				
11.25	-.224	2.90	1097.	4.86	655.	9.72	327.	10.64	299.
11.75	-.168	2.76	1205.	5.03	660.	9.35	355.	11.02	301.
12.25	-.105	2.62	1323.	5.22	664.	9.06	382.	11.33	306.
12.75	-.038	2.48	1454.	5.41	666.	8.80	410.	11.63	310.
13.25	.027	2.35	1592.	5.60	669.	8.56	438.	11.91	315.
13.75	.088	2.24	1735.	5.79	672.	8.33	467.	12.18	319.
14.25	.145	2.14	1884.	5.98	674.	8.11	497.	12.49	323.
14.75	.196	2.05	2035.	6.17	676.	7.89	528.	12.87	324.
15.25	.233	1.98	2174.	6.35	679.	7.71	559.		
15.75	.257	1.94	2292.	6.48	687.	7.57	589.		
16.25	.272	1.92	2397.	6.59	698.	7.45	616.		



f Hz	$\bar{\rho}(\omega)$ ↓ $J_0(x)$	x	$C_1(\omega)$	x_2	$C_2(\omega)$	x_3	$C_3(\omega)$	x_4	$C_4(\omega)$
16.75	.289	1.89	2509.	6.75	702.	7.29	650.		
17.25	.313	1.85	2642.						
17.75	.336	1.81	2779.						
18.25	.339	1.80	2864.						
18.75	.314	1.84	2874.						
19.25	.271	1.92	2837.	6.58	828.	7.46	729.		
19.75	.220	2.01	2783.	6.28	889.	7.78	718.		
20.25	.165	2.10	2723.	6.05	946.	8.03	713.	12.62	454.
20.75	.114	2.19	2674.	5.87	999.	8.23	713.	12.31	476.
21.25	.076	2.26	2657.	5.75	1045.	8.37	718.	12.13	495.
21.75	.053	2.30	2669.	5.68	1083.	8.46	727.	12.03	511.
22.25	.018	2.37	2653.	5.57	1129.	8.59	732.	11.87	530.
22.75	-.050	2.50	2570.	5.37	1197.	8.84	728.	11.58	556.
23.25	-.134	2.68	2452.	5.13	1281.	9.19	716.	11.20	587.
23.75	-.201	2.84	2366.	4.93	1362.	9.54	704.	10.82	621.
24.25	-.233	2.92	2346.	4.83	1421.	9.80	699.	10.55	650.
24.75	-.235	2.93	2389.	4.82	1452.	9.83	712.	10.52	665.
25.25	-.221	2.89	2469.	4.86	1468.	9.69	737.	10.66	670.
25.75	-.205	2.85	2554.	4.91	1482.	9.57	760.	10.79	675.
26.25	-.194	2.82	2629.	4.95	1500.	9.50	781.	10.86	683.
26.75	-.187	2.81	2696.	4.97	1522.	9.46	800.	10.91	694.
27.25	-.177	2.78	2770.	5.00	1541.	9.40	819.	10.97	703.
27.75	-.154	2.73	2878.	5.07	1547.	9.28	845.	11.09	707.
28.25	-.111	2.63	3035.	5.20	1537.	9.09	879.	11.30	707.
28.75	-.054	2.51	3237.	5.36	1516.	8.86	918.	11.56	703.
29.25	.008	2.39	3461.	5.54	1492.	8.62	959.	11.83	699.
29.75	.061	2.29	3675.	5.70	1475.	8.43	998.	12.06	697.
30.25	.100	2.22	3854.	5.83	1468.	8.29	1032.	12.24	699.
30.75	.126	2.17	4002.	5.91	1470.	8.19	1062.	12.38	702.
31.25	.143	2.14	4127.	5.97	1479.	8.12	1089.	12.48	708.
31.75	.151	2.13	4219.	6.00	1496.	8.09	1110.	12.53	717.
32.25	.148	2.13	4276.	5.99	1522.	8.10	1126.	12.51	729.
32.75	.144	2.14	4327.	5.98	1549.	8.11	1141.	12.48	742.

The shaded cells identify the accepted values, based on the appropriate half cycle on the Bessel function, for different frequency ranges. Table 2.3 shows the summary of the apparent velocities versus frequency. The apparent velocities for frequency ranges less than about 1 Hz should not be considered since they are



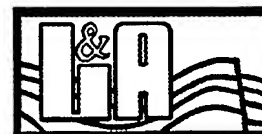
sensitive to the size of time window that is used for data processing. Certain frequency ranges do not show values for apparent velocities. This is due to the uncertainties in the CC-F curve that the estimated $\bar{\rho}(\omega)$ values at these frequency ranges are higher than the maximum or lower than the minimum values for $J_0(x)$ over the related cycle of the Bessel function. For these cases we assume linear transition for the values of the apparent velocities between the lower and higher frequency ranges.

Table 2.3. The estimated apparent velocities from Table 2.2.

f Hz	$C_1(\omega)$	f Hz	$C_1(\omega)$	f Hz	$C_1(\omega)$	f Hz	$C_1(\omega)$
.25	329.	8.25	726.	16.25	698.	24.25	699.
.75	807.	8.75	739.	16.75	702.	24.75	712.
1.25	698.	9.25	777.	17.25		25.25	670.
1.75	878.	9.75	627.	17.75		25.75	675.
2.25	1062.	10.25	640.	18.25		26.25	683.
2.75	906.	10.75	649.	18.75		26.75	694.
3.25	862.	11.25	655.	19.25	729.	27.25	703.
3.75	851.	11.75	660.	19.75	718.	27.75	707.
4.25	845.	12.25	664.	20.25	713.	28.25	707.
4.75	835.	12.75	666.	20.75	713.	28.75	703.
5.25	820.	13.25	669.	21.25	718.	29.25	699.
5.75	799.	13.75	672.	21.75	727.	29.75	697.
6.25	777.	14.25	674.	22.25	732.	30.25	699.
6.75	756.	14.75	676.	22.75	728.	30.75	702.
7.25	739.	15.25	679.	23.25	716.	31.25	708.
7.75	729.	15.75	687.	23.75	704.	31.75	717.

At each frequency the wave length of the Rayleigh waves can be calculated as $\lambda = C(\omega) / f$.

Let us consider the effective depth of Rayleigh waves as half of the wave length, i.e. $d_{\text{effective}} = 0.5 * \lambda = C(\omega) / 2f$. Based on this assumption the apparent

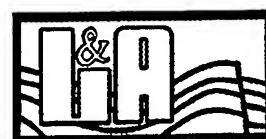
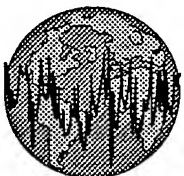


velocity-frequency data can be transformed into the apparent velocity-depth profile, Table 2.4. Figure 2.24 shows the plots of the apparent velocities versus depth. Each point on Figure 2.24 shows the apparent velocity for the Rayleigh waves over the entire depth from the point of half wave length to the surface. Here, we refer to this type of data as $\bar{C} - D$ data or curve.

The $\bar{C} - D$ data should be translated into a velocity-depth profile. Satoh (1989) developed a simple technique for this purpose. Satoh's methodology is based on the premise that the change in the material properties of different strata would cause changes in the slope of $\bar{C} - D$ curve. He proposed two different equations for estimating the Rayleigh wave velocity of different strata from different sections of $\bar{C} - F$ curve with increasing or decreasing values with depth. Figure 2.25 shows a hypothetical example of $\bar{C} - F$ curve with three sections each having different slope. For the segment of the curve with increasing \bar{C} -values with depth Satoh proposed the following equation to estimate the Rayleigh wave velocity for a single representative strata

$$C_n = \frac{\bar{C}_n \cdot D_n - \bar{C}_{n-1} \cdot D_{n-1}}{D_n - D_{n-1}} \quad (2.38)$$

$$C_n = \frac{D_n - D_{n-1}}{(D_n / \bar{C}_n) - (D_{n-1} / \bar{C}_{n-1})} \quad (2.39)$$



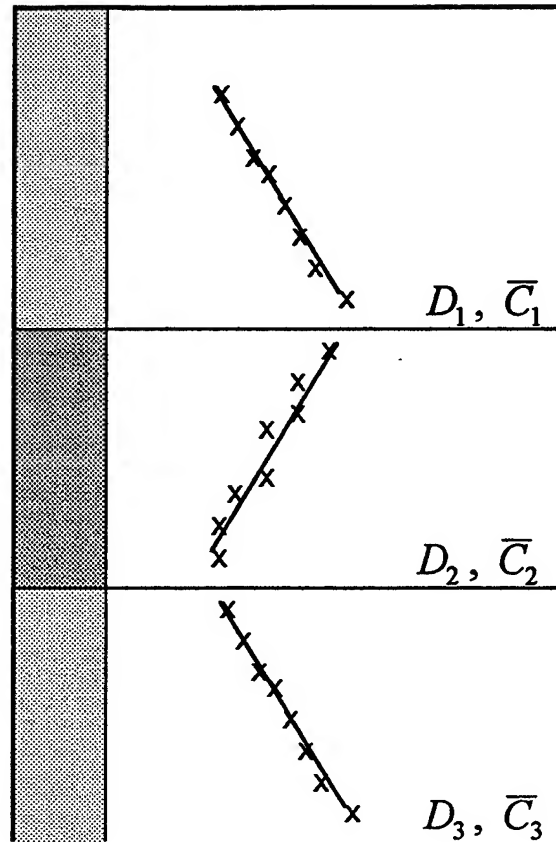


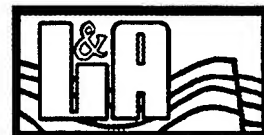
Figure 2.25. A hypothetical phase velocity-depth profile to demonstrate Satoh's empirical phase velocity inversion technique.

For the segment of the curve with decreasing \bar{C} -values with depth the equation is

For example, from Figure 2.25

$$C_1 = \bar{C}$$

$$C_2 = \frac{\bar{C}_2 \cdot D_2 - \bar{C}_1 \cdot D_1}{D_2 - D_1}$$



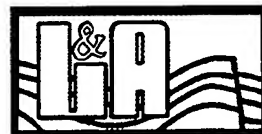
$$C_3 = \frac{D_3 - D_2}{D_3 / \bar{C}_3 - D_2 / \bar{C}_2}$$

Let us use Satoh's methodology to interpret the $\bar{C} - F$ curve in our example. The shallow segment of the curve show increasing \bar{C} -values with depth. The first change of slope occurs at depth of 20 ft at $\bar{C}_1 = 800$ ft/s. Assuming that this slope extends to the surface, from equation 2.38 $\bar{C}_1 = 800$ ft/s. The location for the second change of slope is not very clear but it should be at a depth below 35 ft. Let us use $D_2 = 35$ ft and $\bar{C}_2 = 674$ ft/s. From equation 2.39, $C_2 = 568$. The third segment of the curve extends to the depth of about 162 ft with increasing velocity with depth. Using $D_3 = 162$ ft and $\bar{C}_3 = 974$ ft/s in equation 2.38 gives $C_3 = 1053$ ft/s. The depths and the estimated phase velocities are shown in Table 2.4. Using Satoh's (1989) empirical equation the Rayleigh wave phase velocities can be translated into the shear wave velocities as are shown in Table 2.4.

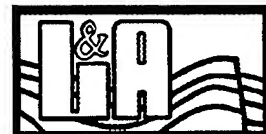
Table 2.4. The phase velocities and shear wave velocities of the three layers based on Satoh's empirical phase velocity inversion.

Depth ft	C ft/s (m/s)	β ft/s (m/s)
0 - 20	770 (235)	849 (259)
20 - 35	568 (173)	623 (190)
> 35	1053 (321)	1168 (356)

The excellent agreement between the estimated velocity-depth profile, Table 2.4, and the input model attests to the usefulness of Satoh's methodology for interpreting the $\bar{C} - D$ data. It is specially interesting to notice the fact that the



hidden low velocity layer was detected. However, in real situation the estimated velocity depth profile from Satoh's simple methodology needs to be verified, i.e. the model should simulate the observed phase velocities as a function of frequency. This requires the capability of simulating phase velocity of Rayleigh waves, dispersion curve, for layered medium.



2.8 Theoretical Simulation of the Dispersion Curves for Rayleigh Waves in Flat Layered Medium

Thompson (1950) and Haskell (1953) formulated the characteristic equations for the dispersion of the Rayleigh waves. Haskell's approach is based on the matrix formulation of the wave propagation in layered medium. This approach because of its elegance and the efficiency in the numerical calculation has been the bases for most other later studies (Knopoff, 1964, Dunkin, 1965, Thrower, 1965, and Watson, 1970). Following, we present the necessary formulation of the dispersion characteristic equation for the Rayleigh waves.

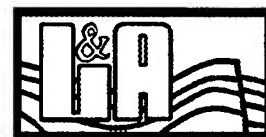
Consider an elastic medium consisting of N parallel horizontal and homogeneous layers overlying a homogeneous half space, Diagram 2.2. The plane waves (SH, SV, and P waves) are incident on the (N-1)th interface from below. Each layer will sustain an upgoing and down going waves in such a way that the following boundary conditions are met:

The traction on the free surface vanishes

The displacement and stresses at each interface are continuos.

Based on these assumptions and boundary conditions it can be shown (Haskell, 1953) that the dispersion characteristic equation for the Rayleigh waves satisfies the following relationship

$$\frac{\dot{u}_0}{\dot{w}_0} = \frac{K}{L} = \frac{M}{N} \quad (2.40)$$



where \dot{u}_0 and \dot{w}_0 are the velocity components at the surface in the x and z directions, respectively, and

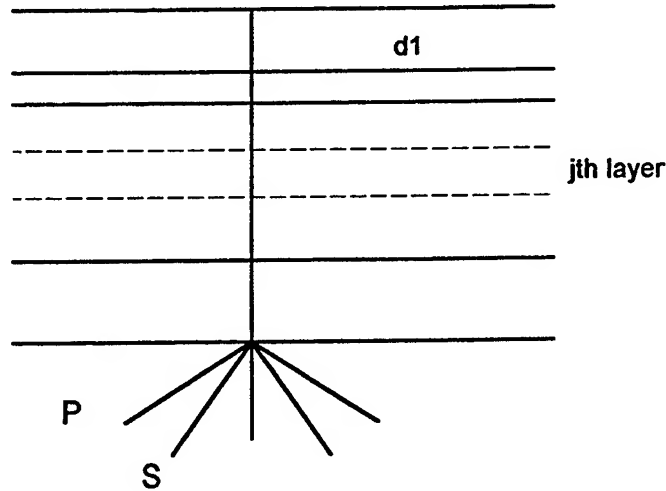
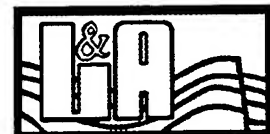


Diagram 2.2. A schematic diagram of a multi-layer model

$$\begin{aligned}
 K &= \gamma_N \eta_{\alpha N} A_{12} + (\gamma_N - 1) A_{22} - \frac{\eta_{\alpha N} A_{32}}{\rho_N c^2} + \frac{A_{42}}{\rho_N c^2}, \\
 L &= \gamma_N \eta_{\alpha N} A_{11} + (\gamma_N - 1) A_{21} - \frac{\eta_{\alpha N} A_{31}}{\rho_N c^2} + \frac{A_{41}}{\rho_N c^2}, \\
 M &= -(\gamma_N - 1) A_{12} + \gamma_N \eta_{\beta N} A_{22} + \frac{A_{32}}{\rho_N c^2} + \frac{\eta_{\beta N} A_{42}}{\rho_N c^2}, \\
 N &= -(\gamma_N - 1) A_{11} + \gamma_N \eta_{\beta N} A_{21} + \frac{A_{31}}{\rho_N c^2} + \frac{\eta_{\beta N} A_{41}}{\rho_N c^2}.
 \end{aligned}$$

(2.41)



The symbols α and β identify parameters related to the P- and S-waves, respectively. The other symbols are defined as follows

$$c = \frac{\beta_j}{\sin(f_j)} = \frac{\alpha_j}{\sin(e_j)}, \quad (j = 1, 2, \dots, N)$$

where α_j and β_j are the S- and P-wave velocities of the j th layer respectively.

$$\eta_{\alpha_j} = \begin{cases} \sqrt{[(c/\alpha_j)^2 - 1]}, & c > \alpha_j \\ -i\sqrt{[1 - (c/\alpha_j)^2]}, & c < \alpha_j \end{cases} \quad (2.42)$$

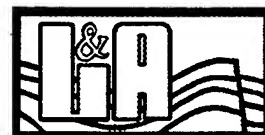
$$\eta_{\beta_j} = \begin{cases} \sqrt{[(c/\beta_j)^2 - 1]}, & c > \beta_j \\ -i\sqrt{[1 - (c/\beta_j)^2]}, & c < \beta_j \end{cases}$$

$$\gamma_j = \frac{2\beta_j^2}{c^2} \quad (2.43)$$

$$k = \frac{\omega}{c}$$

A_{kl} ($k = 1, 4$ and $l = 1, 4$) are components of a four by four matrix that is defined as the product of $N-1$ four by four matrices as

$$\tilde{A} = \tilde{a}_{N-1} \cdot \tilde{a}_{N-2} \dots \tilde{a}_j \dots \tilde{a}_1 \quad (2.44)$$



The components of the matrix \tilde{a}_j for each layer is defined as

$$\begin{aligned}
 (a_j)_{11} &= \gamma_j \cos(P_j) - (\gamma_j - 1) \cos(Q_j), \\
 (a_j)_{12} &= i[(\gamma_j - 1) \eta_{\alpha j}^{-1} \sin(P_j) + \gamma_j \eta_{\beta j} \sin(Q_j)], \\
 (a_j)_{13} &= -(\rho_j c^2)^{-1}[(\cos(P_j) - \cos(Q_j))], \\
 (a_j)_{14} &= i(\rho_j c^2)^{-1}[(\eta_{\alpha j}^{-1} \sin(P_j) + \eta_{\beta j} \sin(Q_j))],
 \end{aligned} \tag{2.45}$$

$$\begin{aligned}
 (a_j)_{21} &= -i[\gamma_j \eta_{\alpha j} \sin(P_j) + (\gamma_j - 1) \eta_{\beta j}^{-1} \sin(Q_j)], \\
 (a_j)_{22} &= -(\gamma_j - 1) \cos(P_j) + \gamma_j \cos(Q_j), \\
 (a_j)_{23} &= i(\rho_j c^2)^{-1}[\eta_{\alpha j} \sin(P_j) + \eta_{\beta j}^{-1} \sin(Q_j)], \\
 (a_j)_{24} &= (a_j)_{13}
 \end{aligned}$$

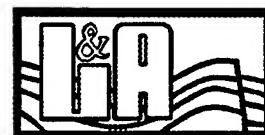
$$\begin{aligned}
 (a_j)_{31} &= \rho_j c^2 \gamma_j (\gamma_j - 1)[(\cos(P_j) - \cos(Q_j))], \\
 (a_j)_{32} &= i \rho_j c^2 [(\gamma_j - 1)^2 \eta_{\alpha j}^{-1} \sin(P_j) + \gamma_j^2 \eta_{\beta j}^{-1} \sin(Q_j)], \\
 (a_j)_{33} &= (a_j)_{22} \\
 (a_j)_{34} &= (a_j)_{12}
 \end{aligned}$$

$$\begin{aligned}
 (a_j)_{41} &= i \rho_j c^2 [\gamma_j^2 \eta_{\alpha j} \sin(P_j) + (\gamma_j - 1)^2 \eta_{\beta j}^{-1} \sin(Q_j)] \\
 (a_j)_{42} &= (a_j)_{31} \\
 (a_j)_{43} &= (a_j)_{21} \\
 (a_j)_{44} &= (a_j)_{11}
 \end{aligned}$$

where $P_j = k \eta_{\alpha j} d_j$, $Q_j = k \eta_{\beta j} d_j$, and d_j is the thickness of the j th layer.



A computer program, based on the above formulation, is prepared for the simulation of Rayleigh waves dispersion curves in layered medium. Figure 2.26 shows the simulated dispersion curves for the estimated velocity-depth profile model in the previous example, Table 2.4, and the plots of the phase velocities that are used for the simulation. The results on Figure 2.26 suggest slight modifications to the velocity depth profile of table 2.4. Comparisons between the simulated and observed phase velocities allow fine tuning the inverted velocity-depth models.



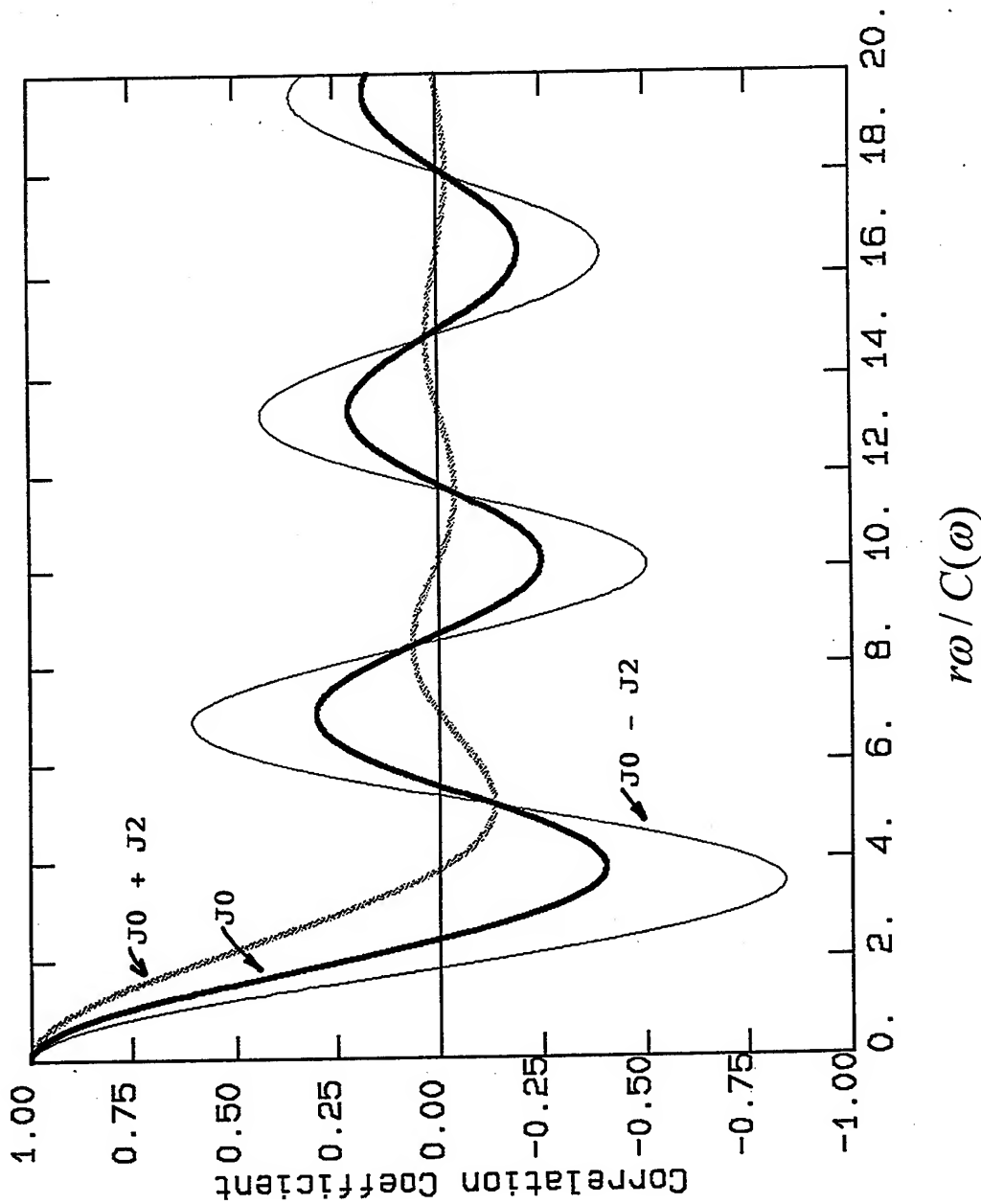
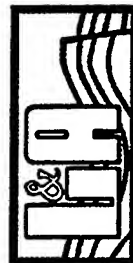


Figure 2.1. Plots of the expected patterns for the correlation coefficients from a Circular Array experiment, equations (2.21) through (2.25), for the non-polarized and polarized components.



VortexRock Consultants, Inc.



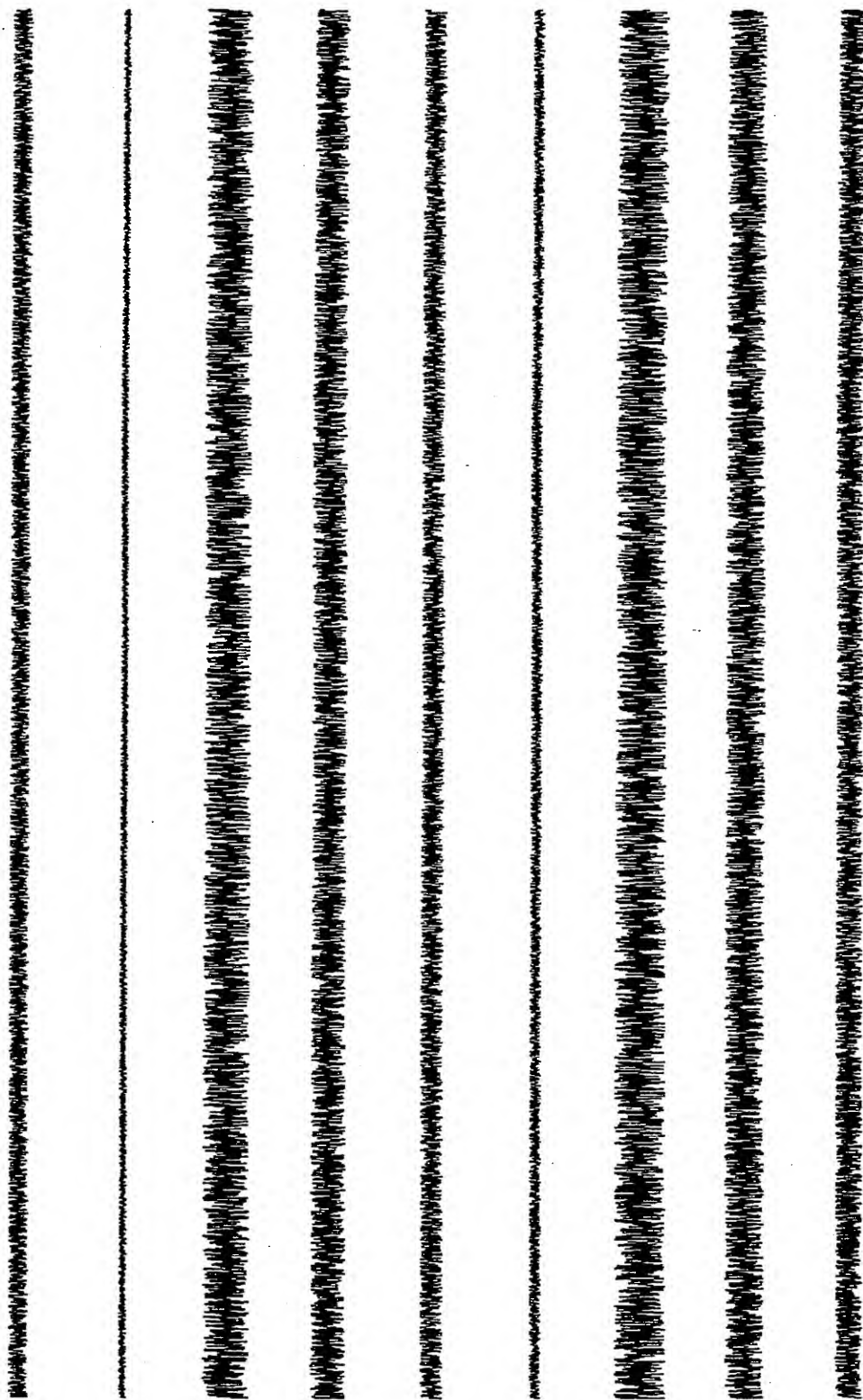


Figure 2.5. Plots of the simulated time histories representing microtremors that are propagating in different directions. Time histories, with random peak amplitudes for different azimuths, are developed using a random number generator.



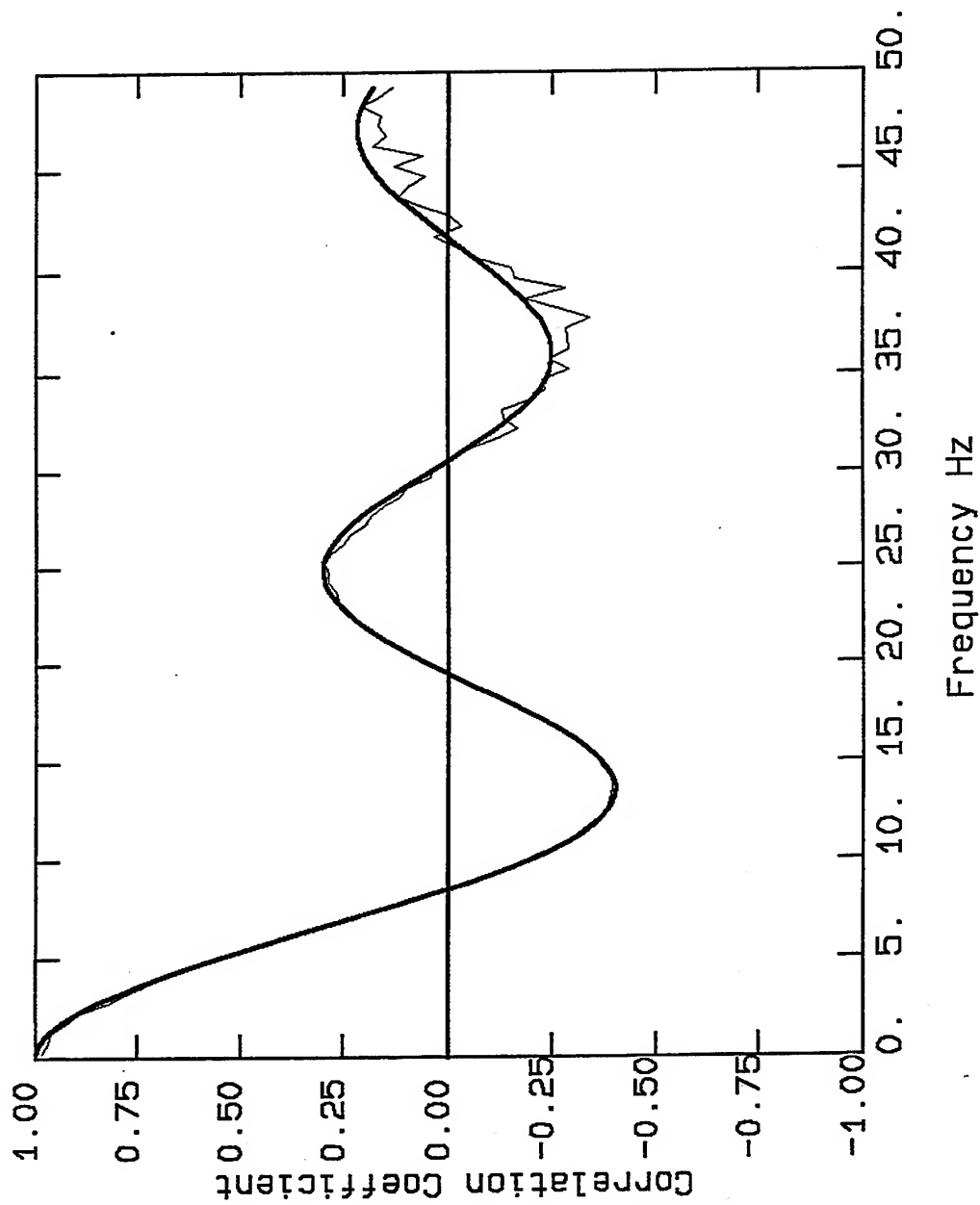


Figure 2.6. Results of numerical simulations of an ideal Circular Array experiment. The jagged line represents the average correlation coefficients for the case of constant apparent velocity $C = 1000$ ft/s, radius $r = 45$ ft, 50 different azimuthal directions for microtremors, and 10 recording sites. The solid line shows the expected pattern for the correlation coefficients based on equation (2.21).



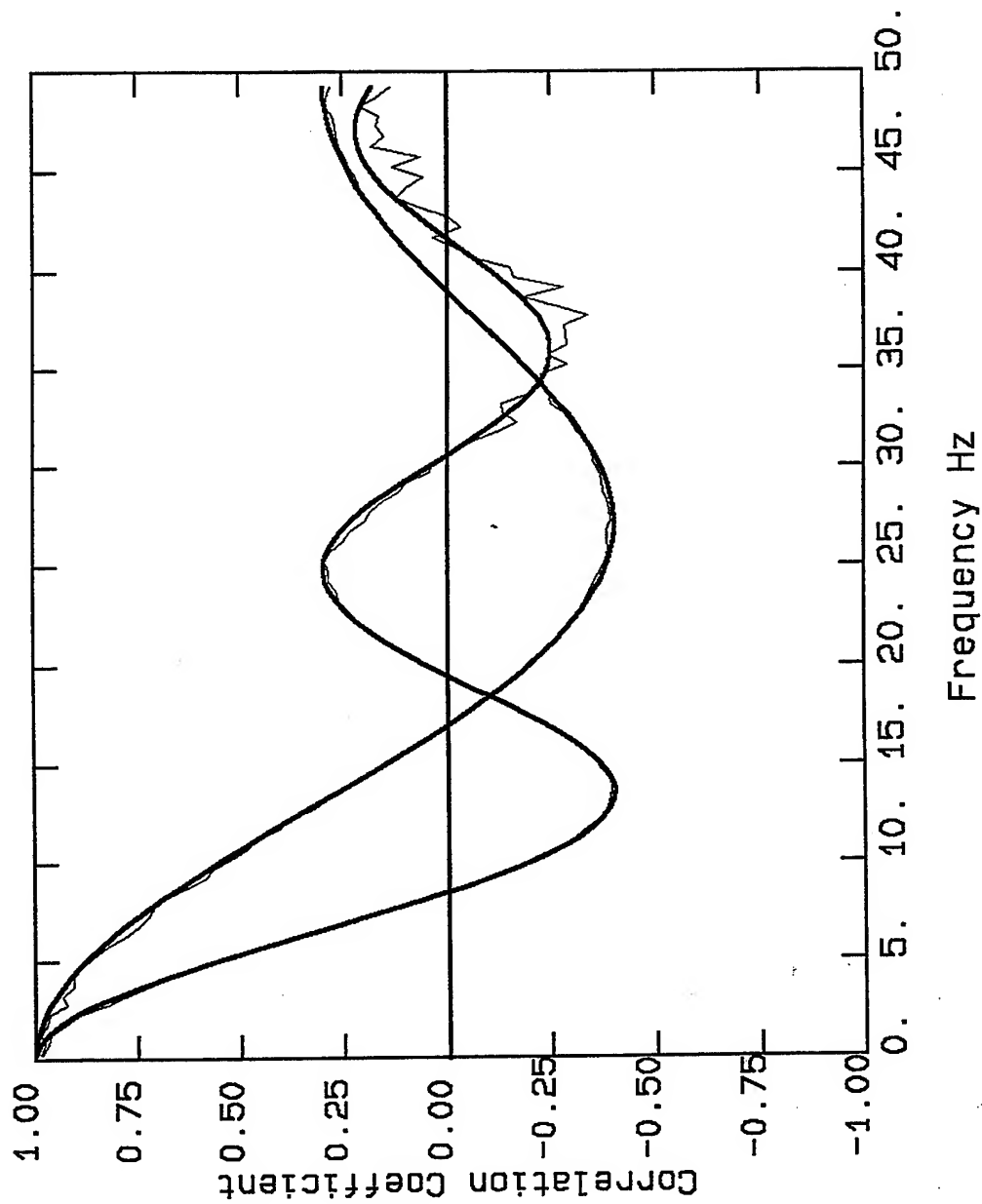


Figure 2.7. Results of a numerical simulation of an ideal Circular Array experiment for two cases of constant apparent velocities of $C = 1000$ ft/s and $C = 2000$ ft/s. All other parameters are similar to those on Figure 2.6.



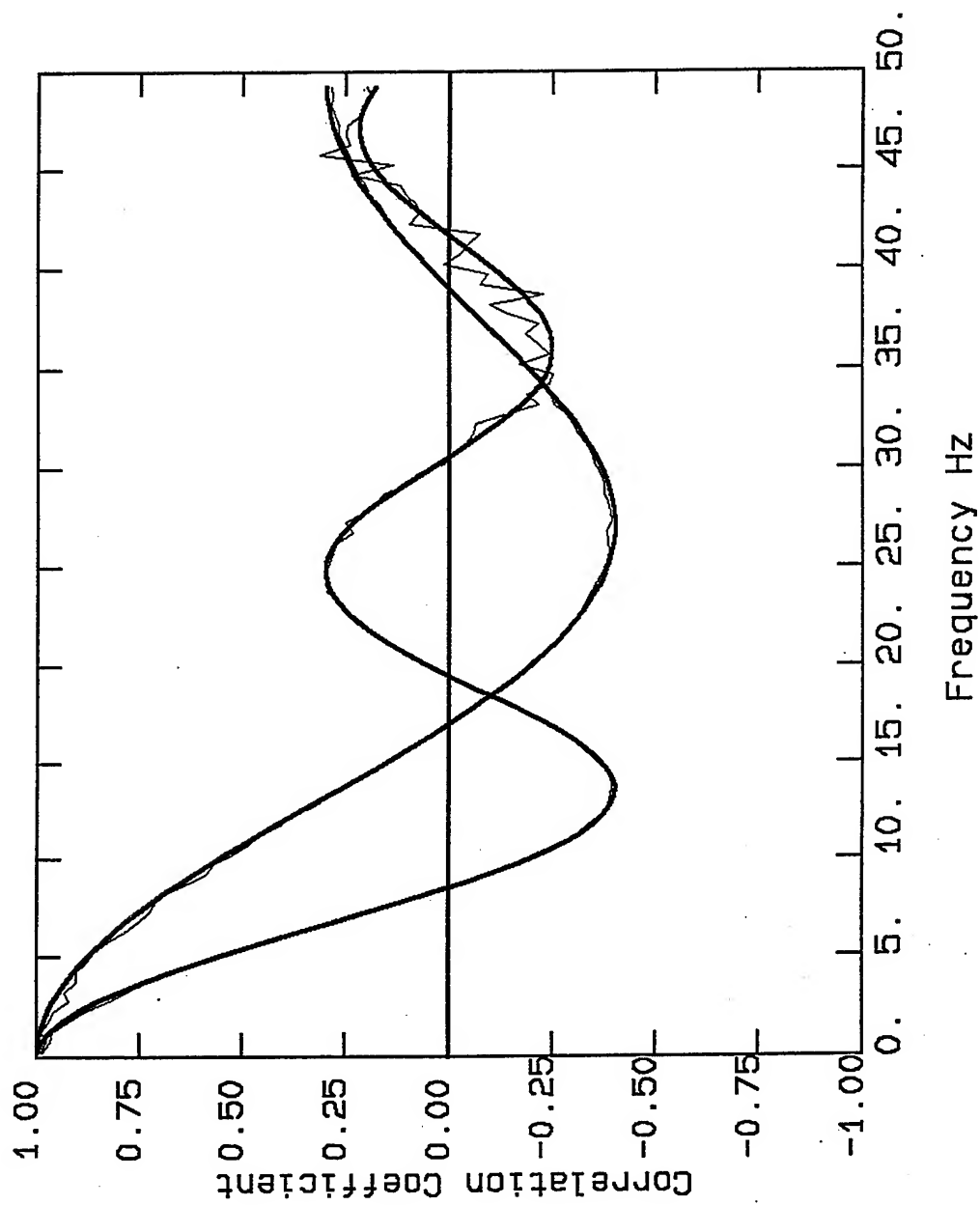


Figure 2.8. Results of a numerical simulation of an ideal Circular Array experiment for two different radii $r = 45$ ft and $r = 90$ ft and constant apparent velocities of $C = 2000$ ft/s and $C = 2000$ ft/s. All other parameters are similar to those on Figure 2.6. Increasing the radius of the array have the same effect as decreasing the apparent velocity.



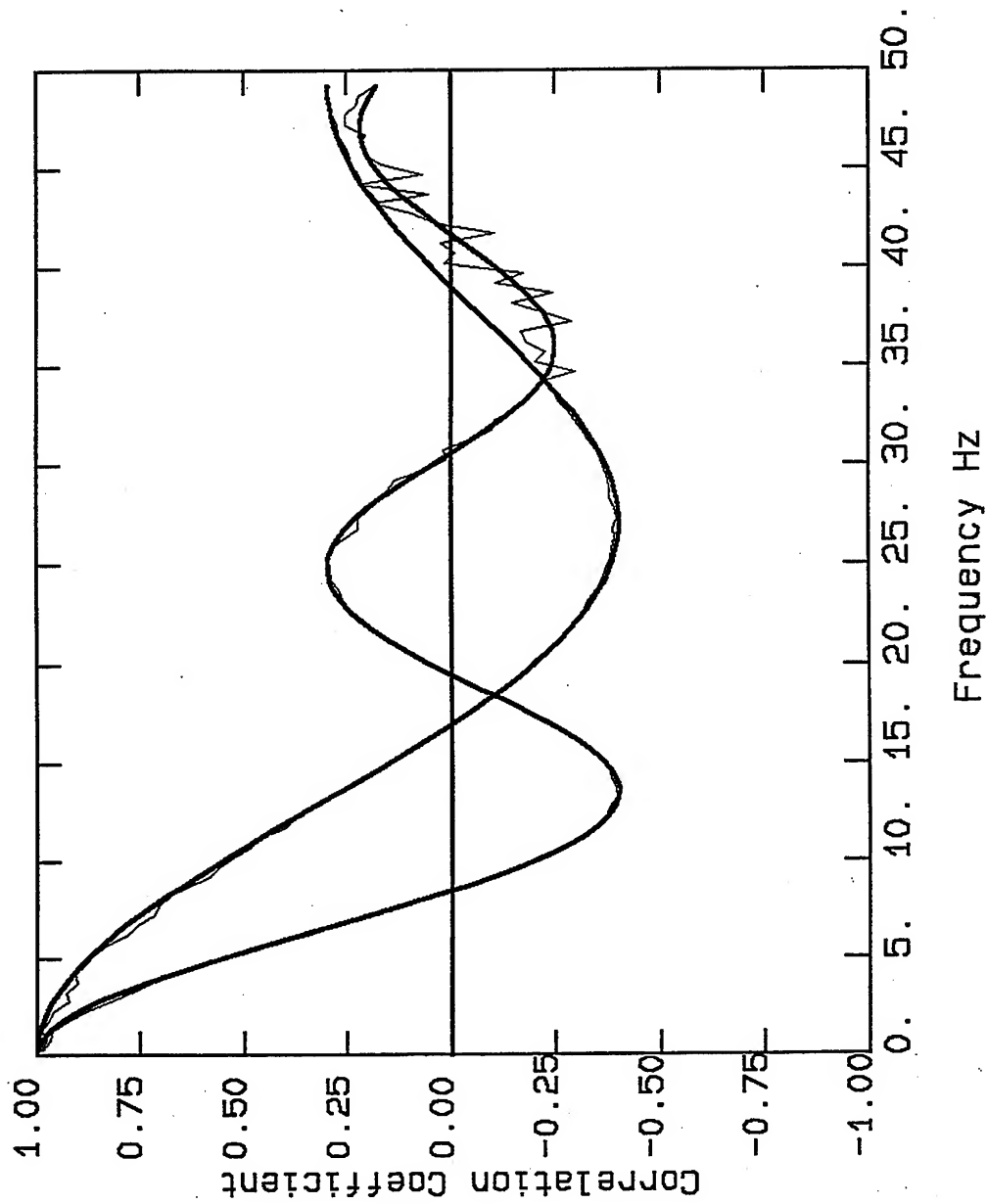


Figure 2.9. Similar to Figure 2.8 except that the azimuthal distribution of microtremors is restricted to the range of 180 rather than 360 degrees.



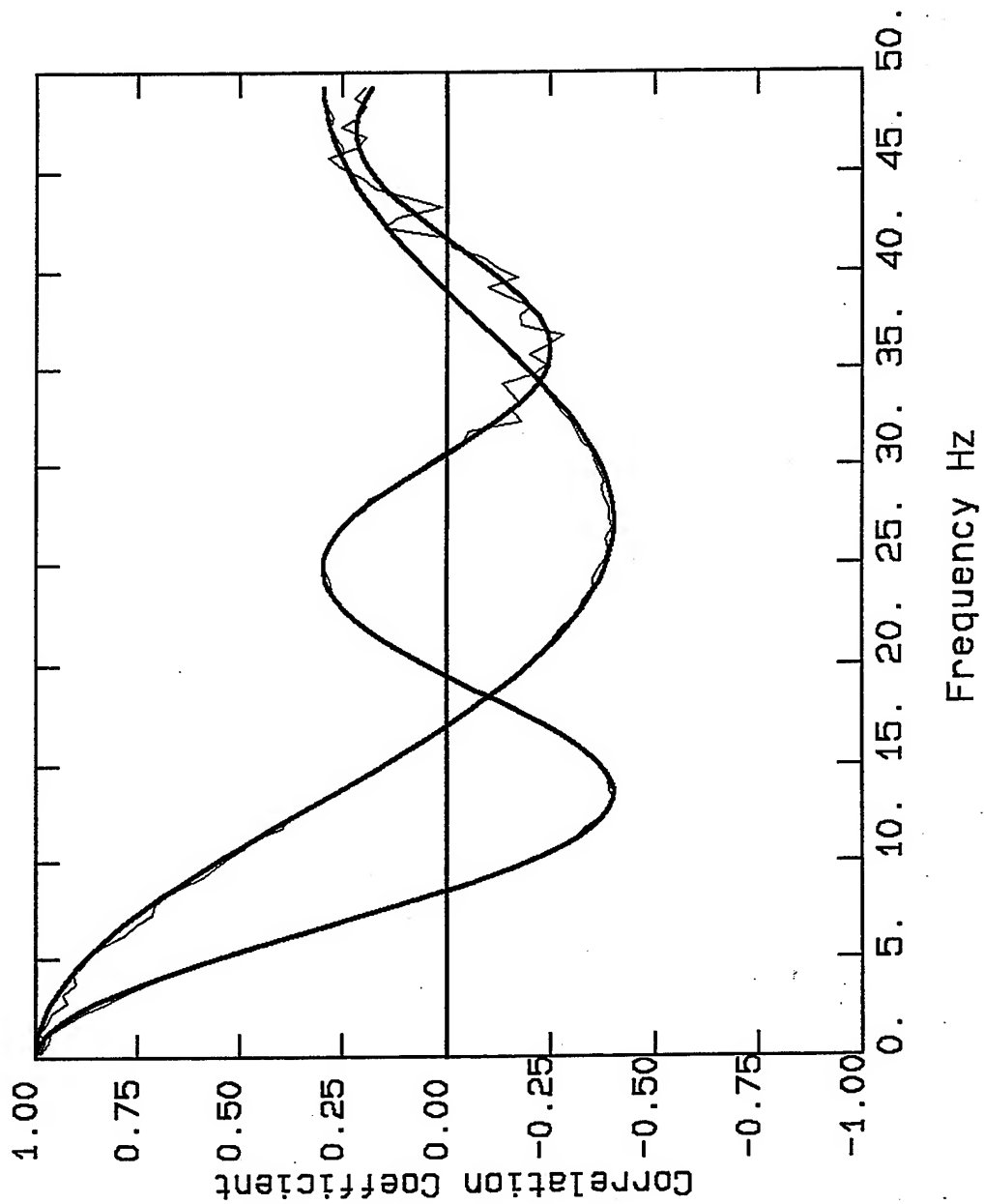


Figure 2.10. Similar to Figure 2.8 except that the azimuthal distribution of microtremors is limited to the range of 90 rather than 360 degrees.



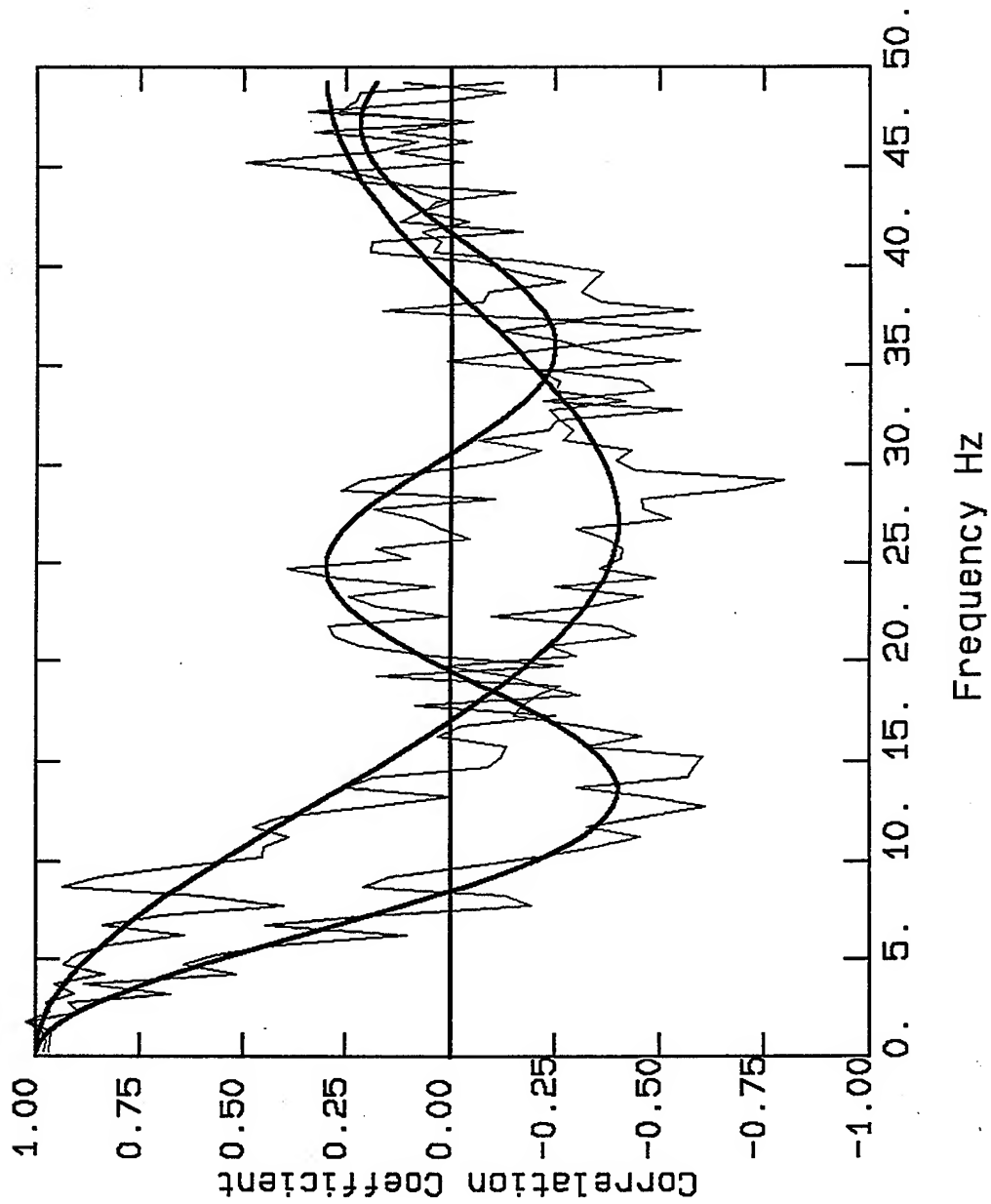


Figure 2.11. Similar to Figure 2.8 except that only one pair of instruments, without any azimuthal averaging, is used for the analysis.



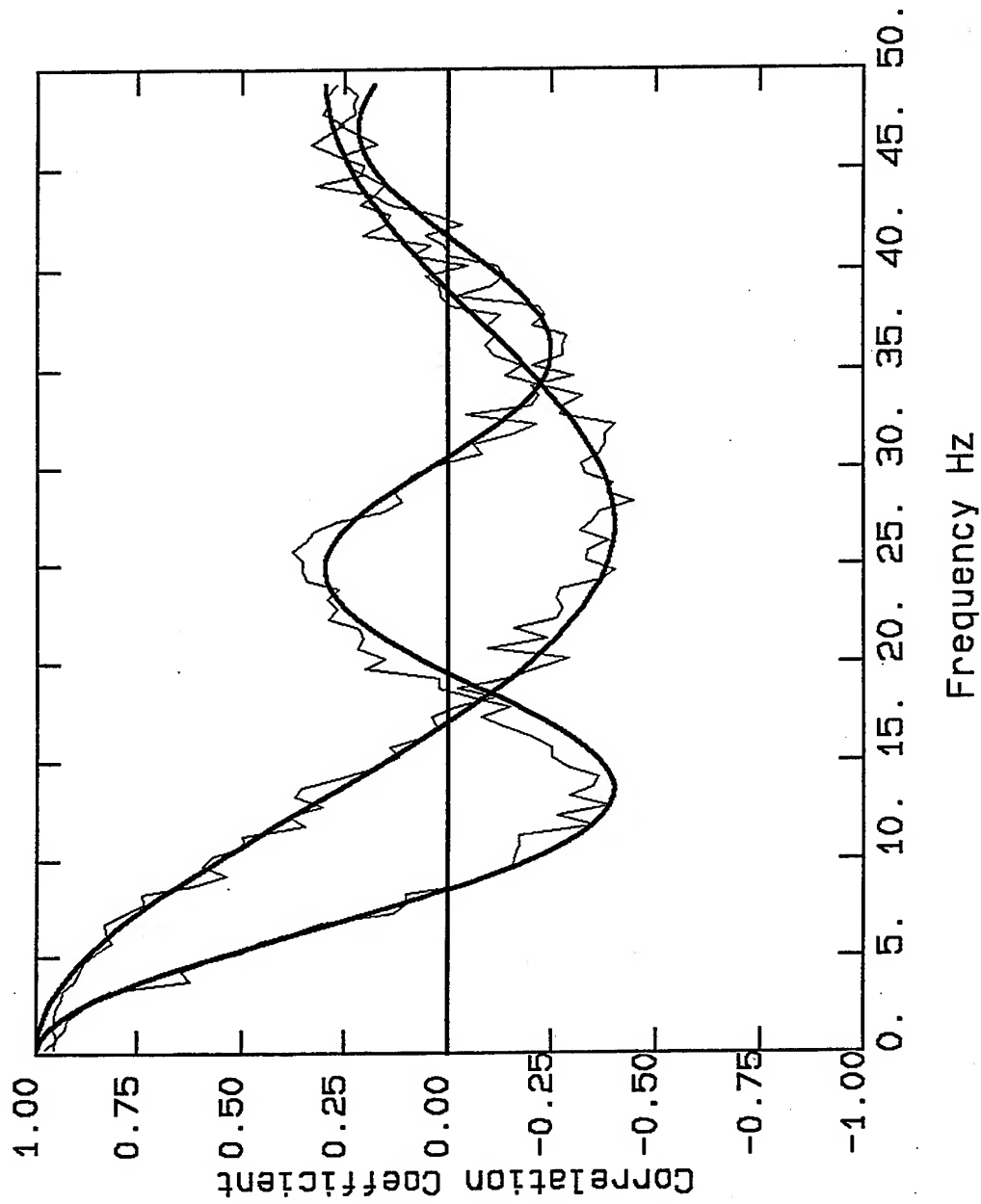
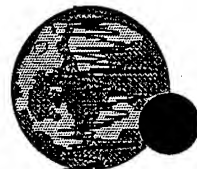


Figure 2.12. Similar to Figure 2.8 but for case II configuration. The simulated time histories for different reference-peripheral sites are different. The plots represent the average correlation coefficients over azimuth.



VortexRock Consultants, Inc.

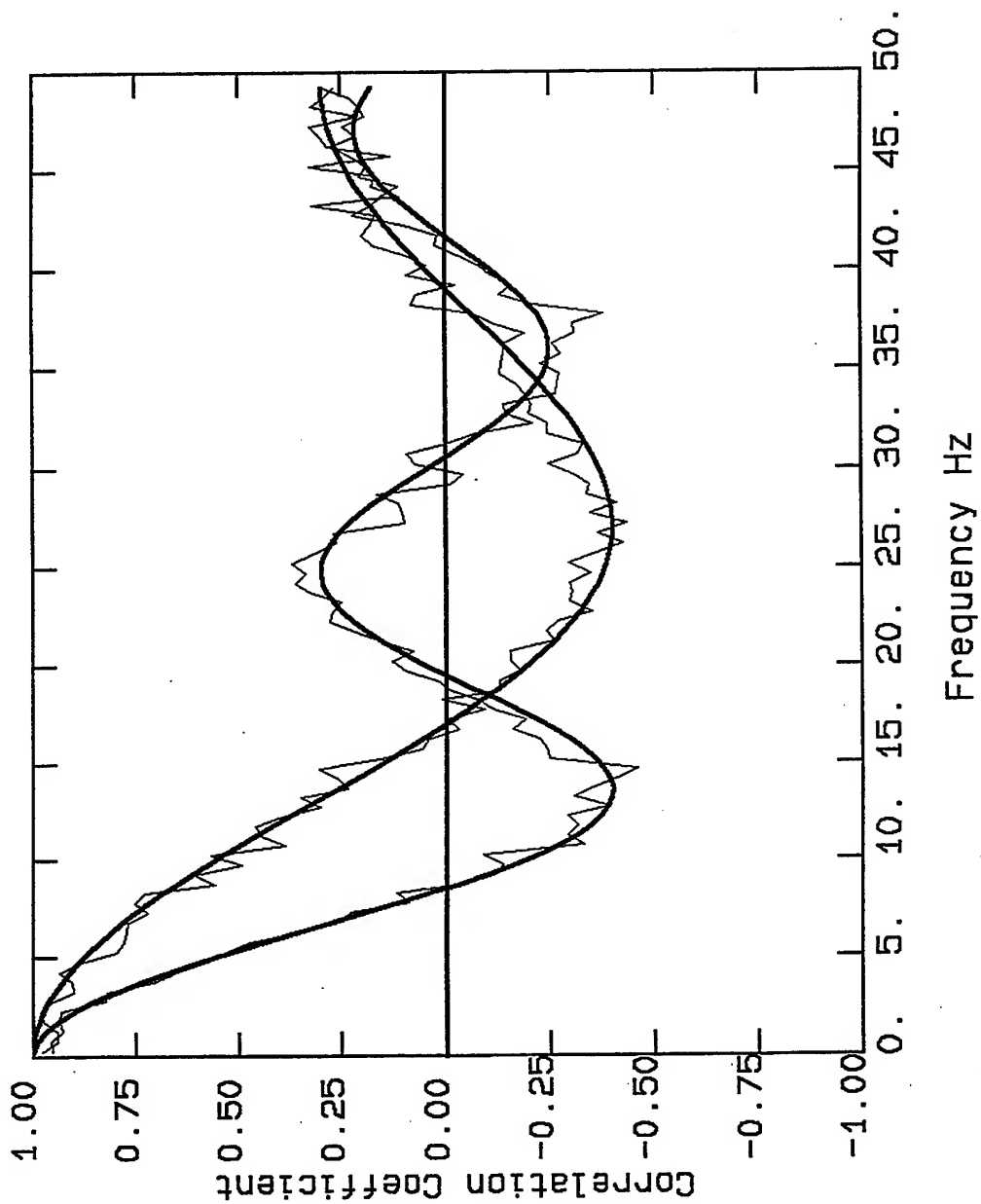


Figure 2.13. Similar to Figure 2.8 but for case III configuration. The simulated time histories for different reference-peripheral sites are different. The plots represent the average correlation coefficients over different time windows.



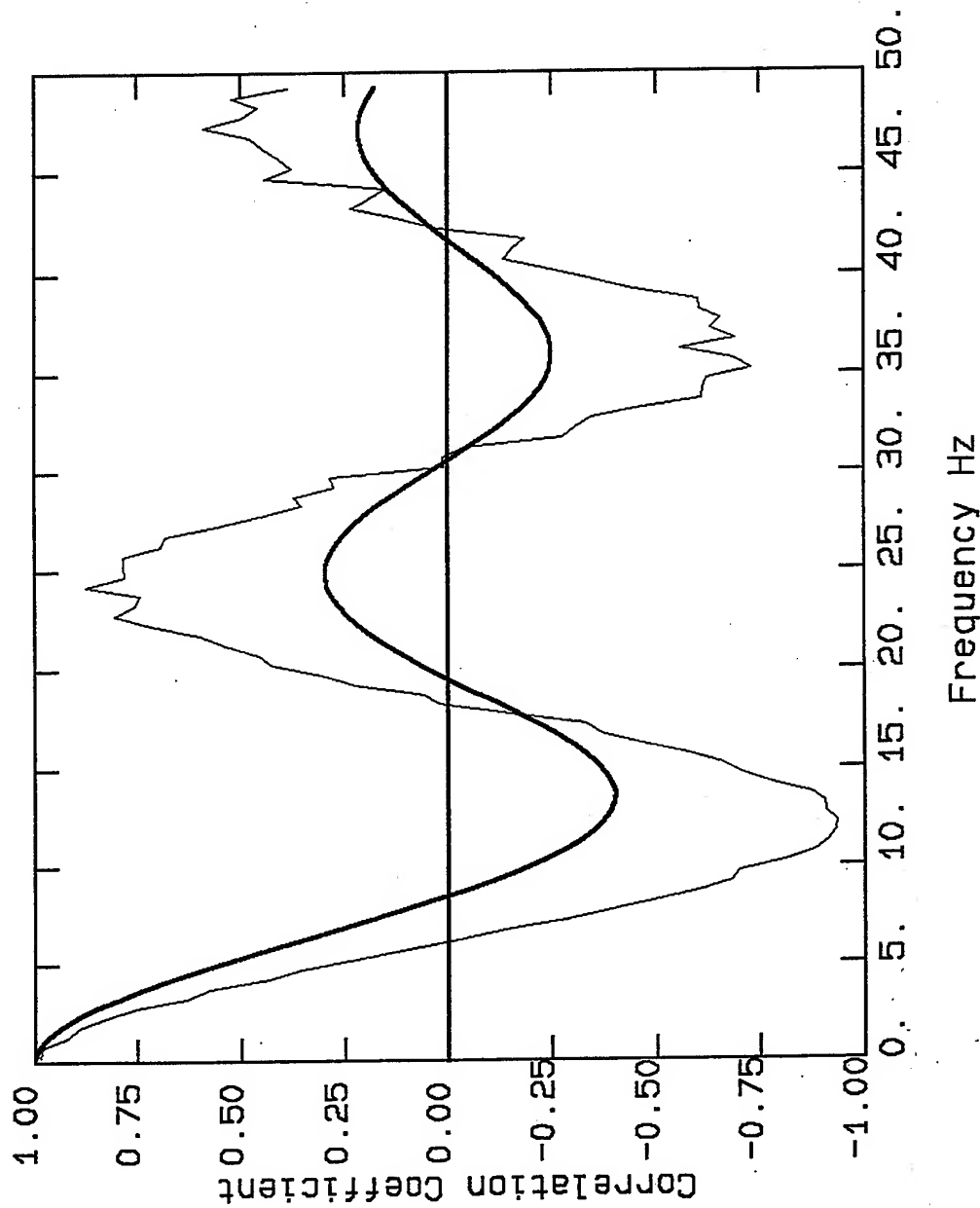


Figure 2.14. Similar to Figure 2.13 except that the azimuthal distribution of microtremors, ϕ , is limited to 90 degrees. The results of the case III configuration is sensitive to the azimuthal distribution, ϕ , of microtremors. The results of different simulations suggest that for $\phi > 180$ degrees case III configuration is a reasonable alternative for an ideal Circular Array experiment.



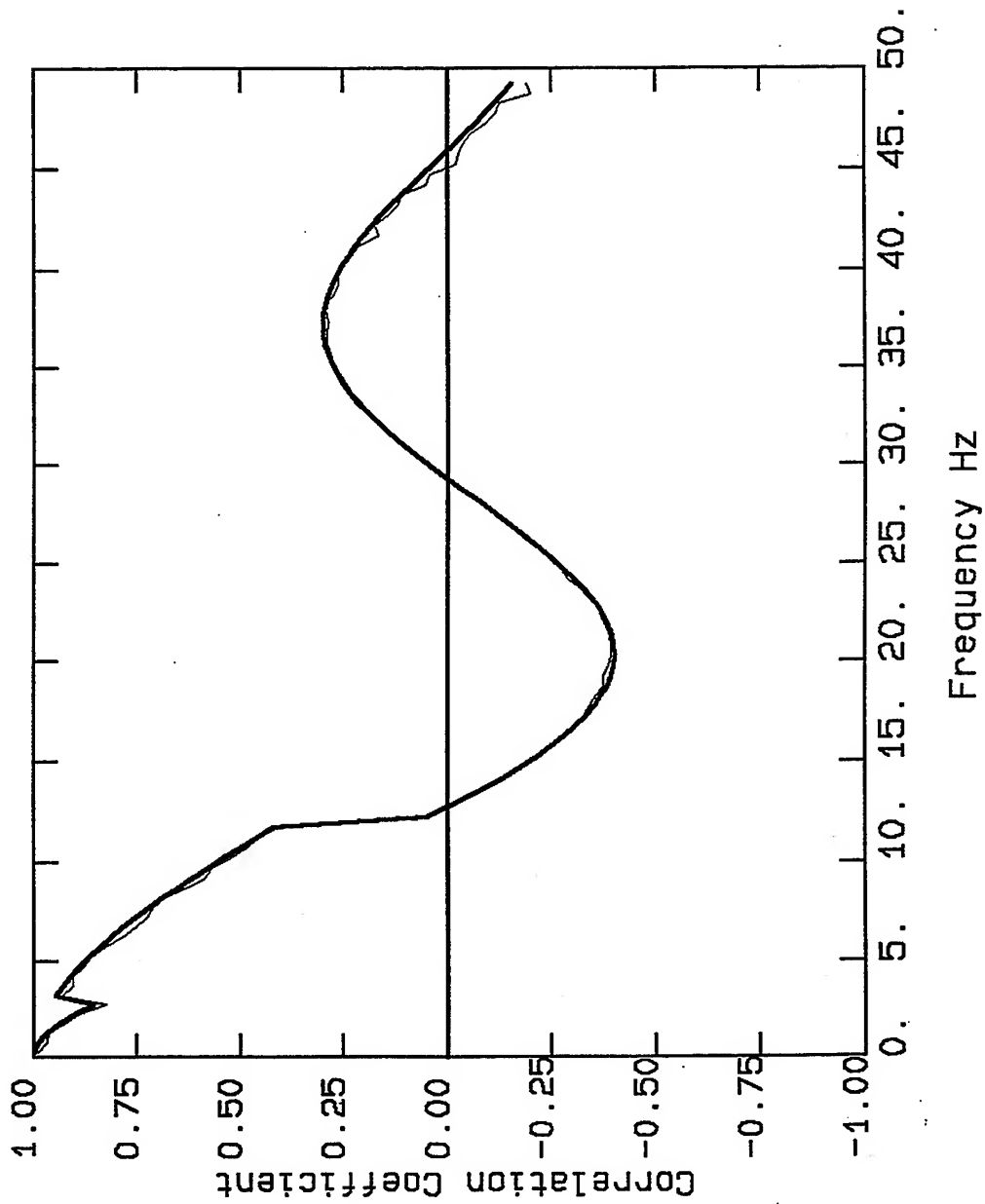


Figure 2.15. Plot of CC-F curve for case I configuration with $r = 45$ ft. Frequency dependent apparent velocities of $C(\omega) = 1000$ ft/s for $f < 3$ Hz, $C(\omega) = 2000$ ft/s for $12 \text{ Hz} > f > 3.0$ Hz, and $C(\omega) = 1500$ ft/s for $f > 12$ Hz are assumed.



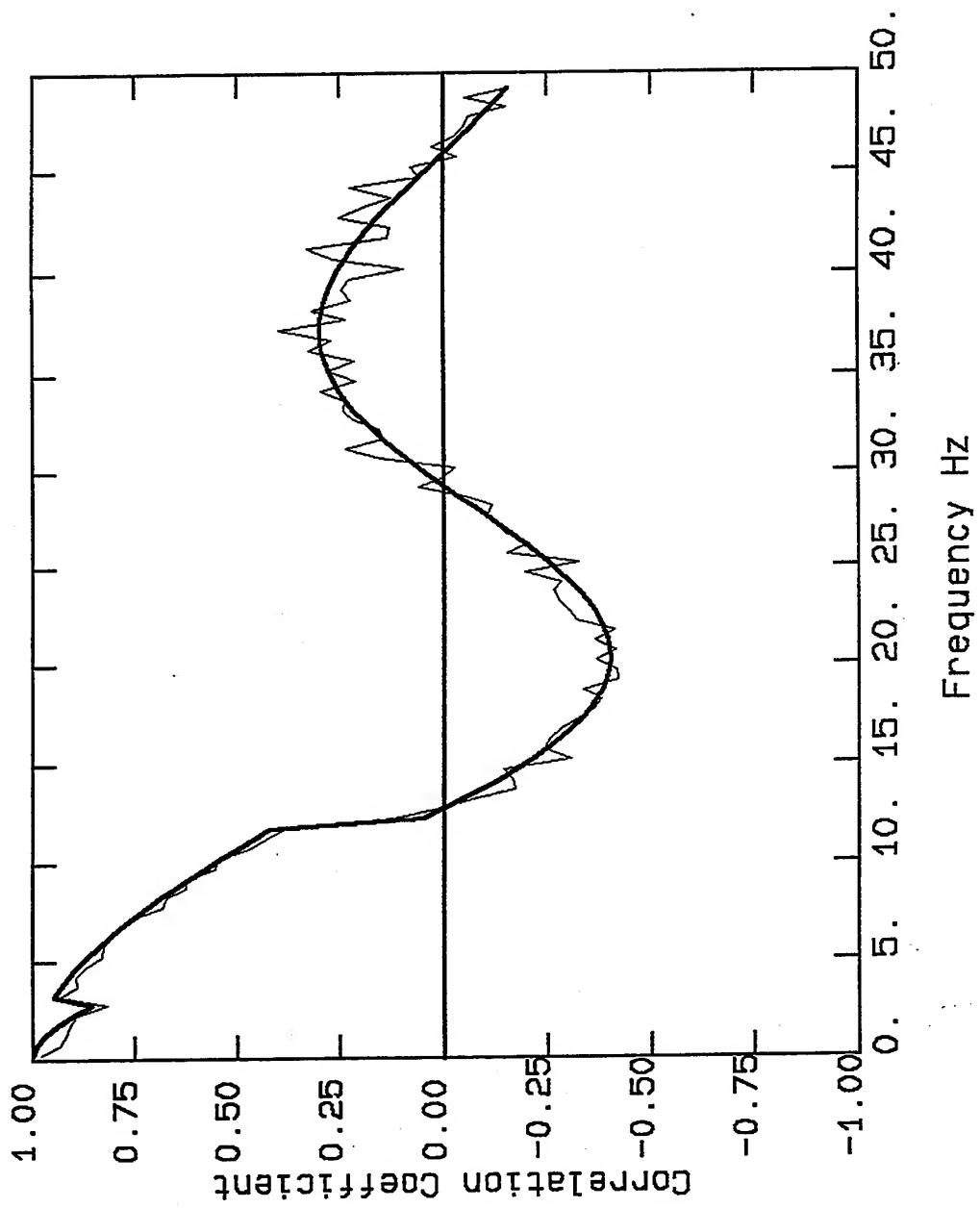


Figure 2.16. Similar to Figure 2.15 but for case II configuration.



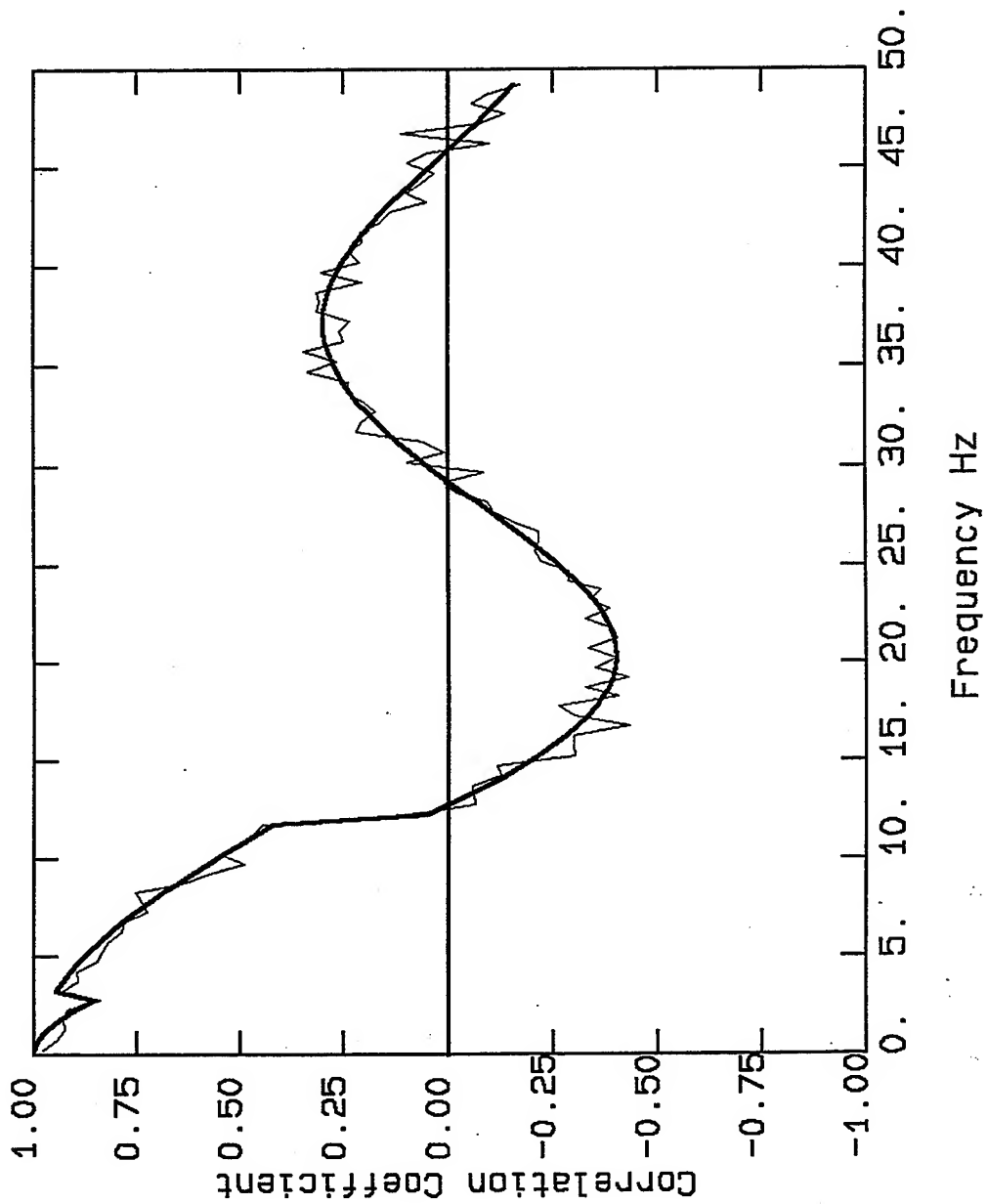


Figure 2.17. Similar to Figure 2.15 but for case III configuration. A uniform azimuthal distribution of microtremors over 360 degrees is assumed.



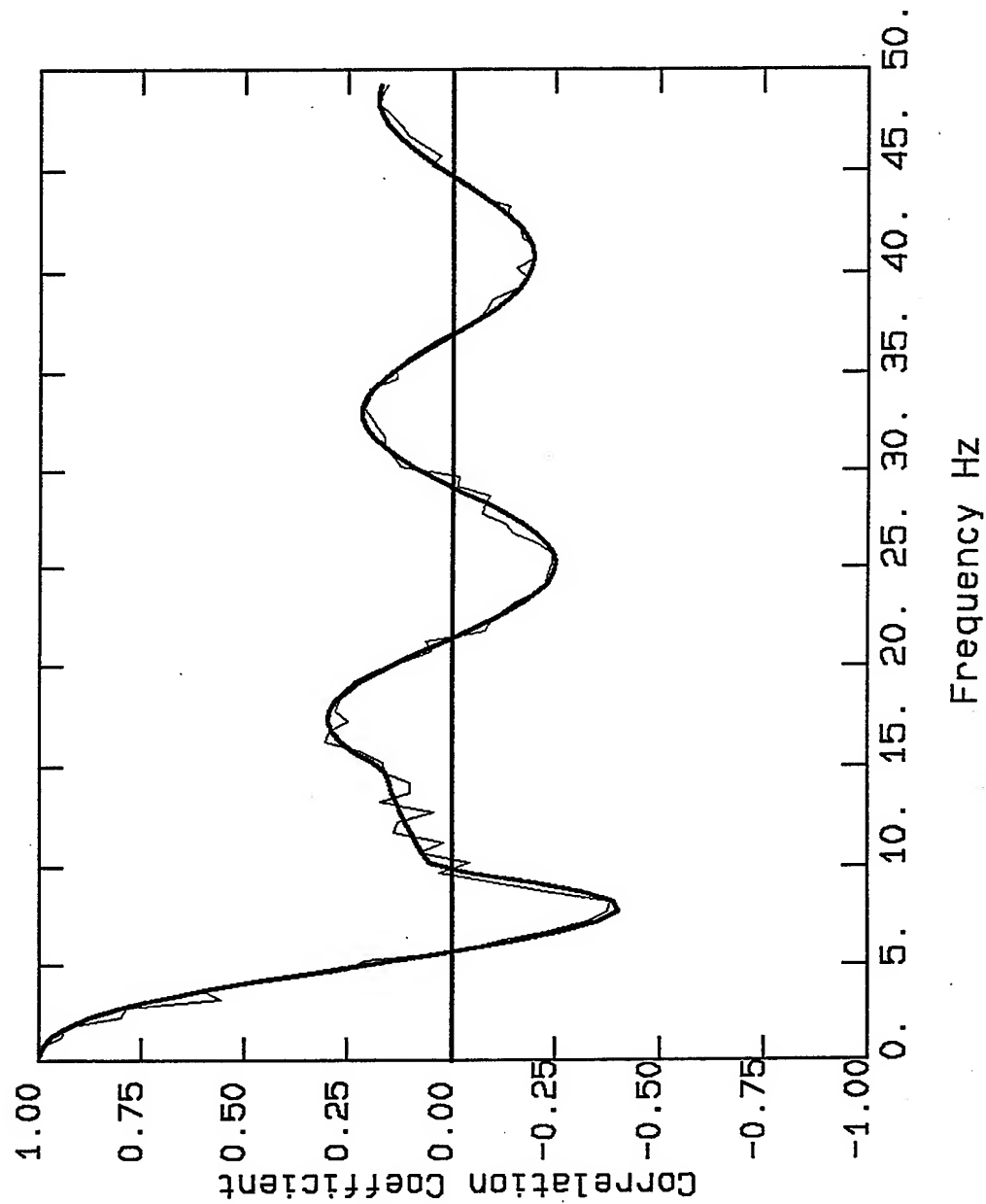


Figure 2.18. Plot of simulated and expected CC-F for a Circular Array experiment with $r = 45$ ft and for the apparent velocity-frequency values that are shown on the Diagram.



VortexRock Consultants, Inc.

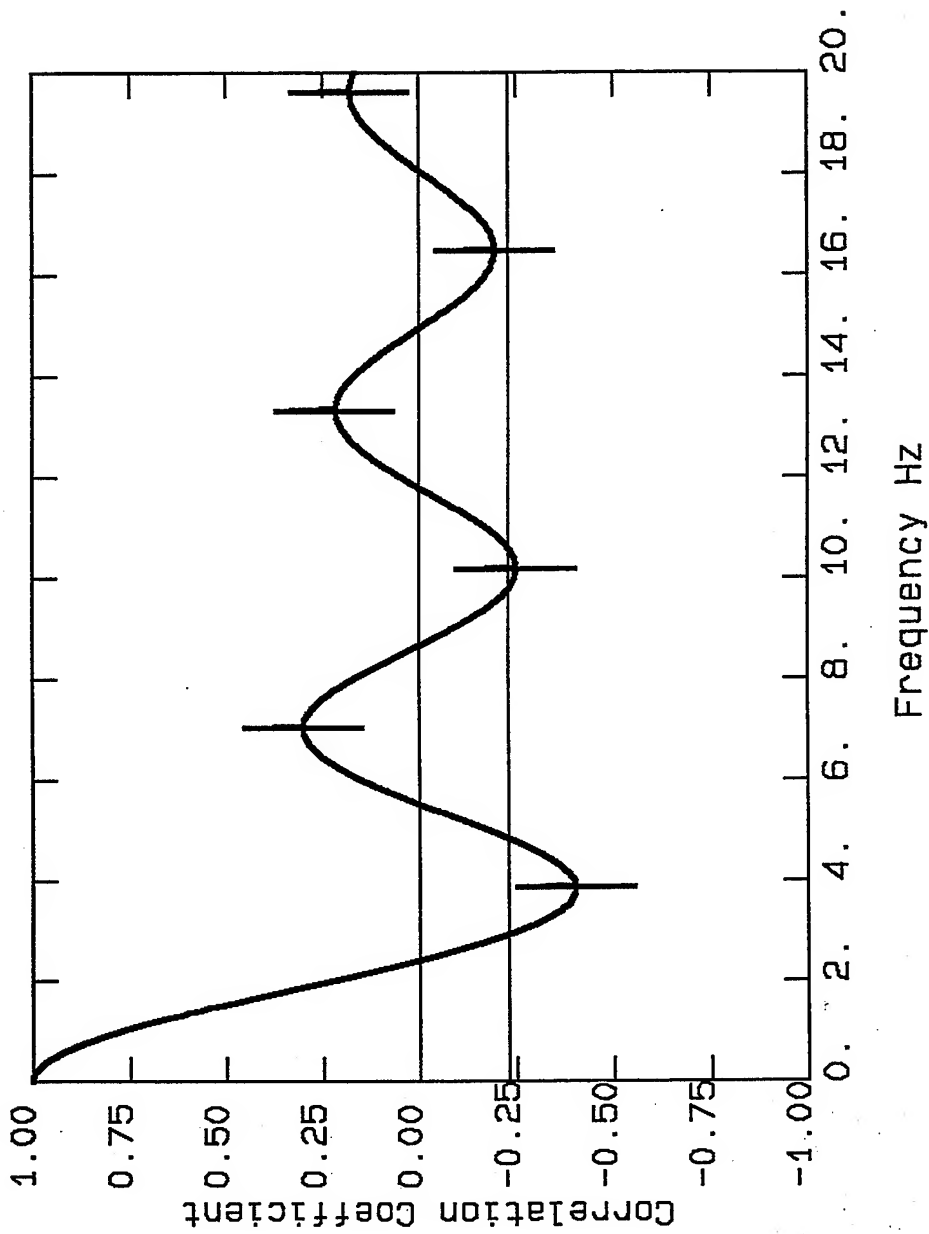


Figure 2.19. The Bessel function $J_0(x)$ is not a single valued function, i.e. a given value of $J_0(x)$ may not correspond to a single value of x . For example, as is shown on the figure, there are four different x -values, on different half cycle of the Bessel function, that satisfy the equation $J_0(x) = -0.23$.



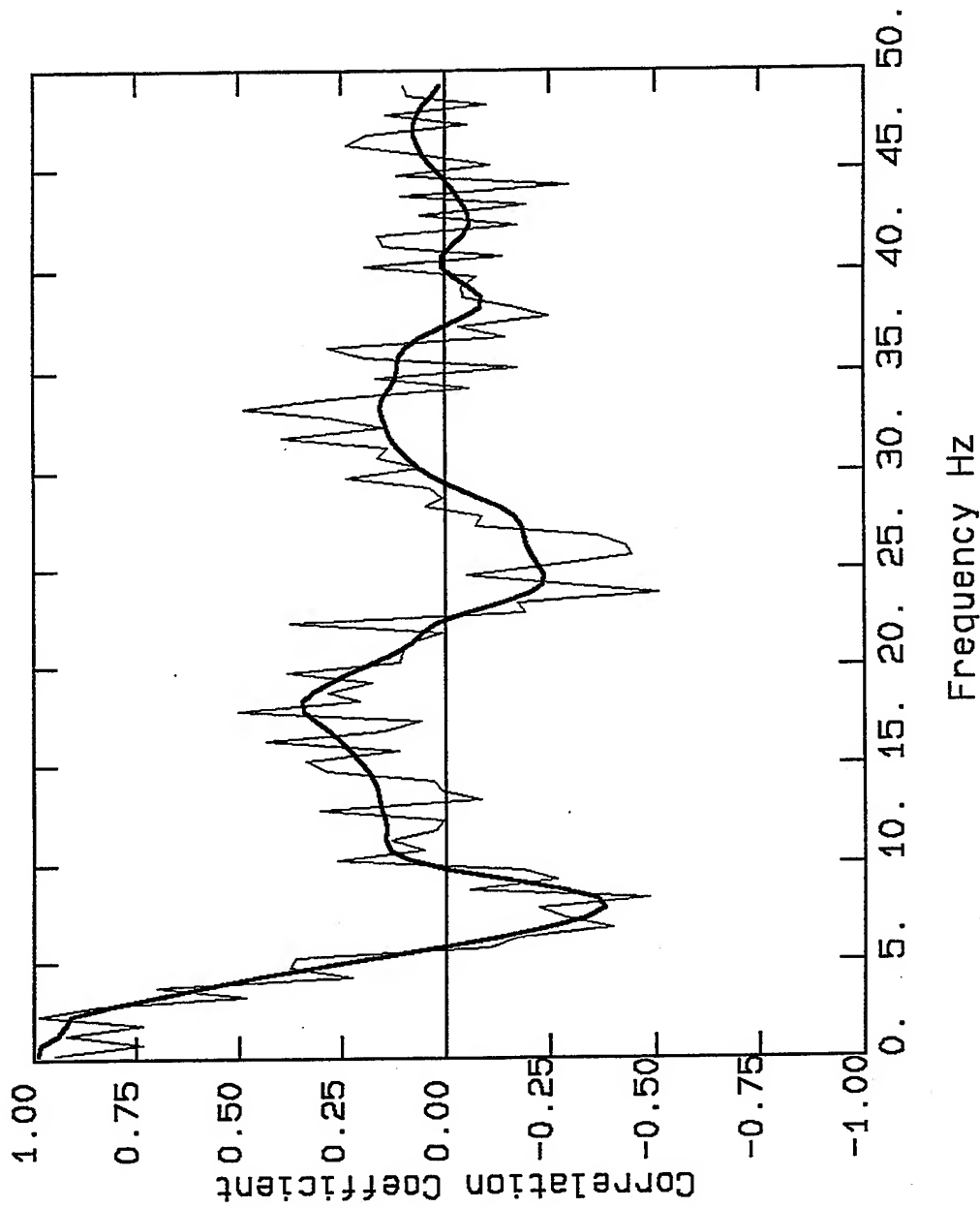


Figure 2.20. Similar to Figure 2.18 except that random values are directly introduced into the correlation coefficients. Interpreting the raw data in terms of $J_0(x)$ could be very difficult if the general pattern and the cycles of the CC-F curve are not identified. The solid line shows the filtered data using 3 Poles Butterworth filter, the should be used for interpretation.



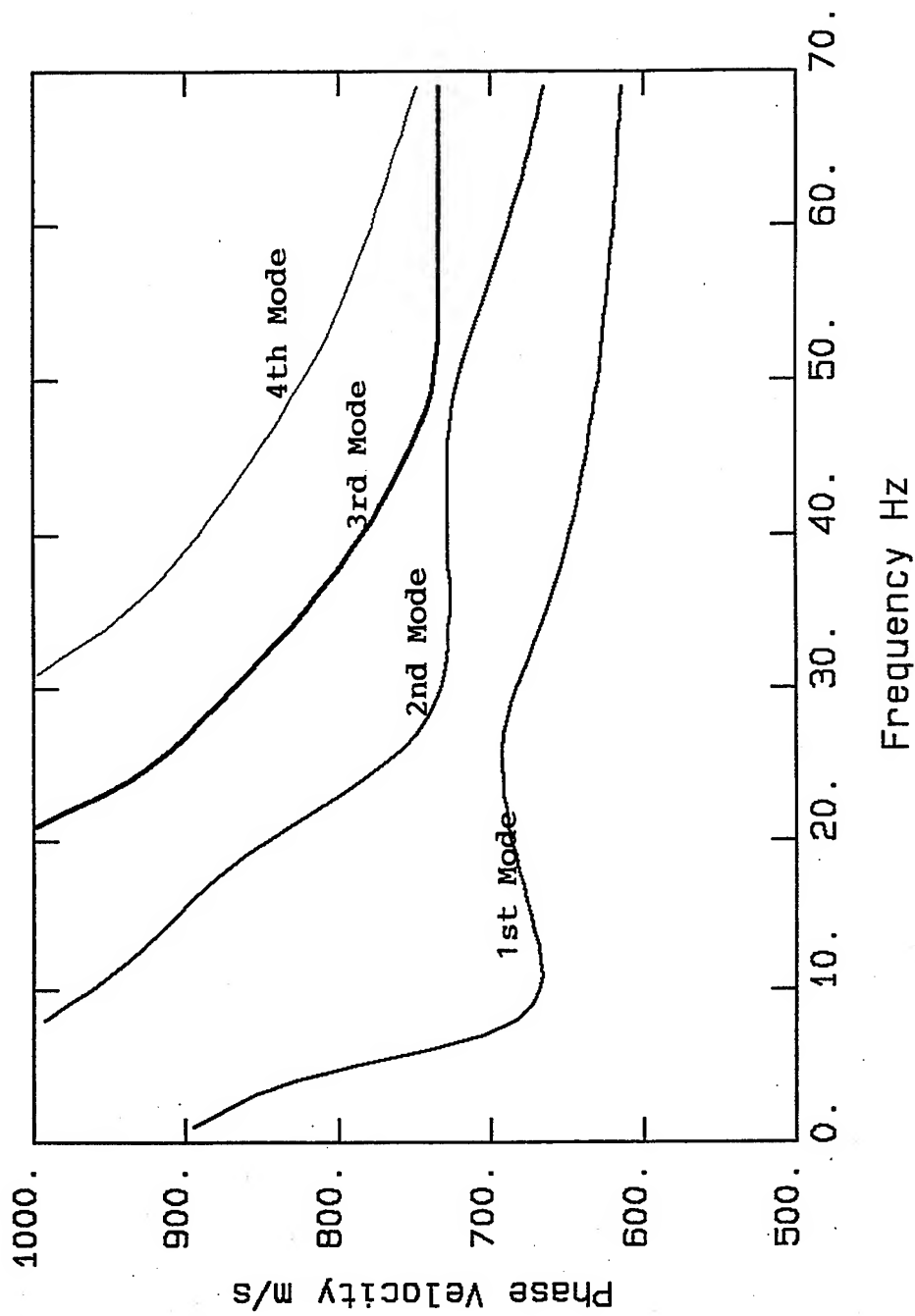


Figure 2.21. The phase velocities for the first four modes of Rayleigh waves for the velocity-depth profile that is shown on the diagram in the text.



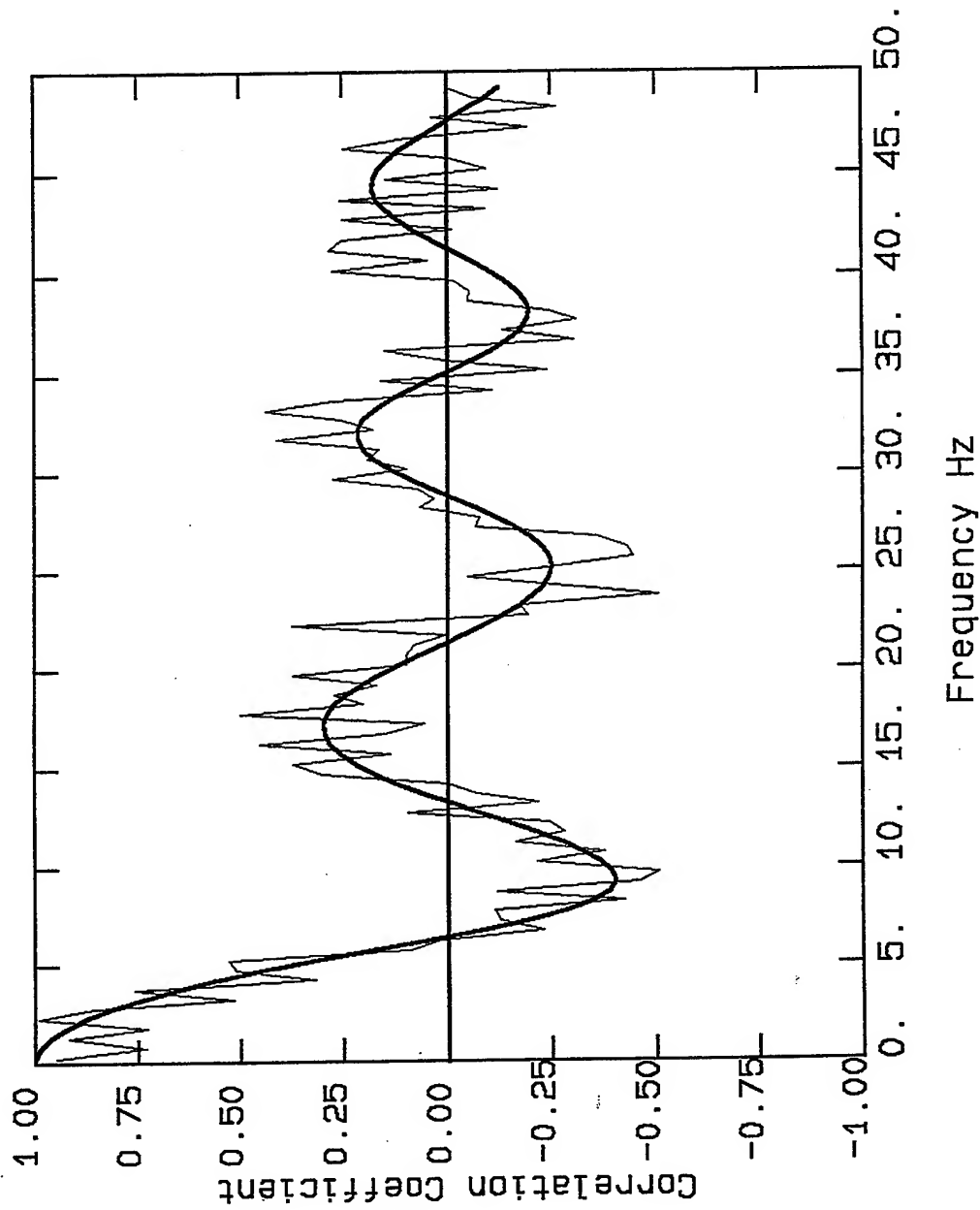


Figure 2.22. Simulated CC-F curve based on the phase velocities of the first mode on Figure 2.21. Random values are directly introduced to the simulated CC-F curve to simulate a real field situation. The solid line shows the expected pattern for the CC-F curve based on the input phase velocities.



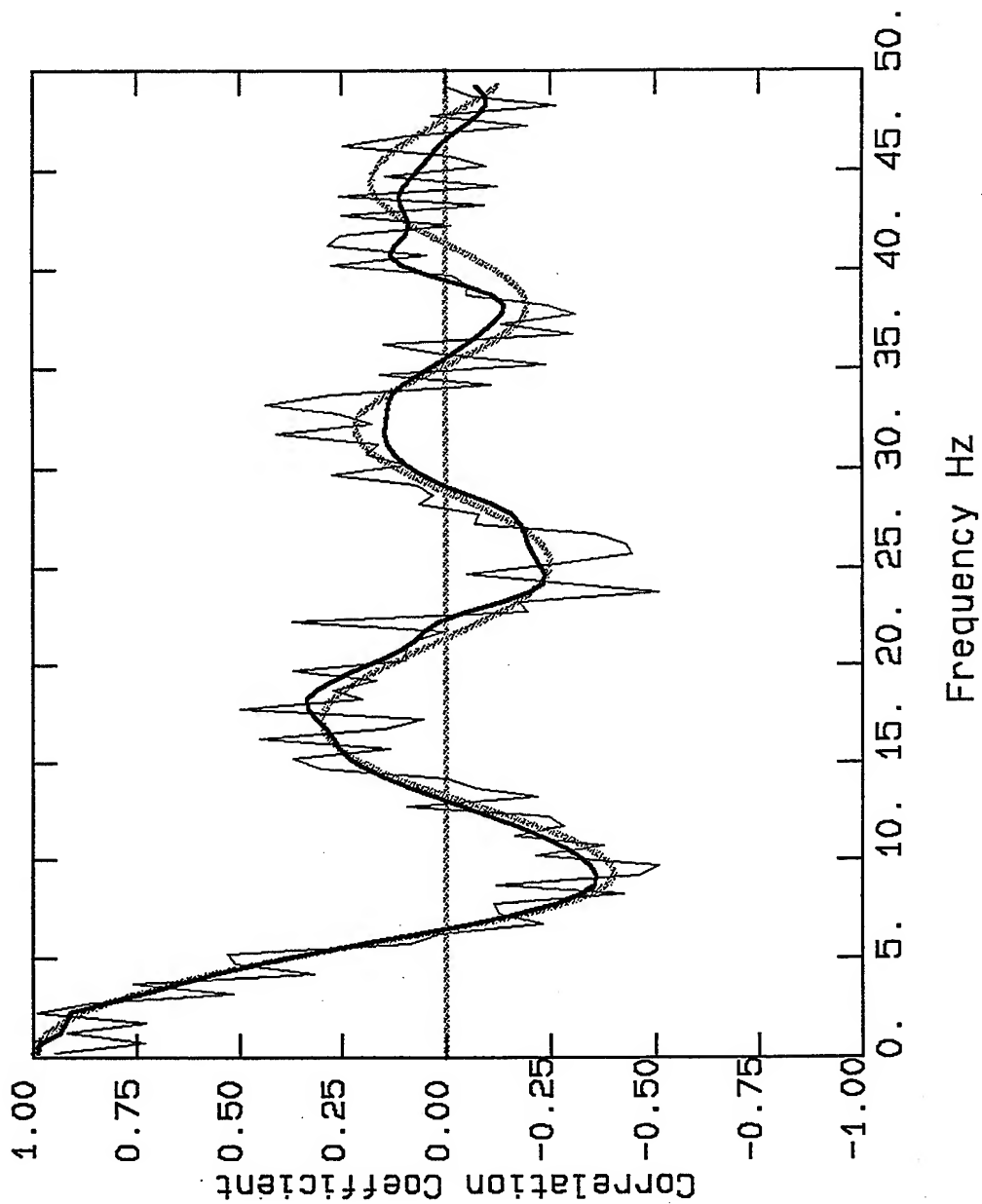


Figure 2.23. Similar to Figure 2.22 showing the filtered CC-F curve, the thick solid line. The shaded line is the expected pattern for the CC-F curve based on the input phase velocities.



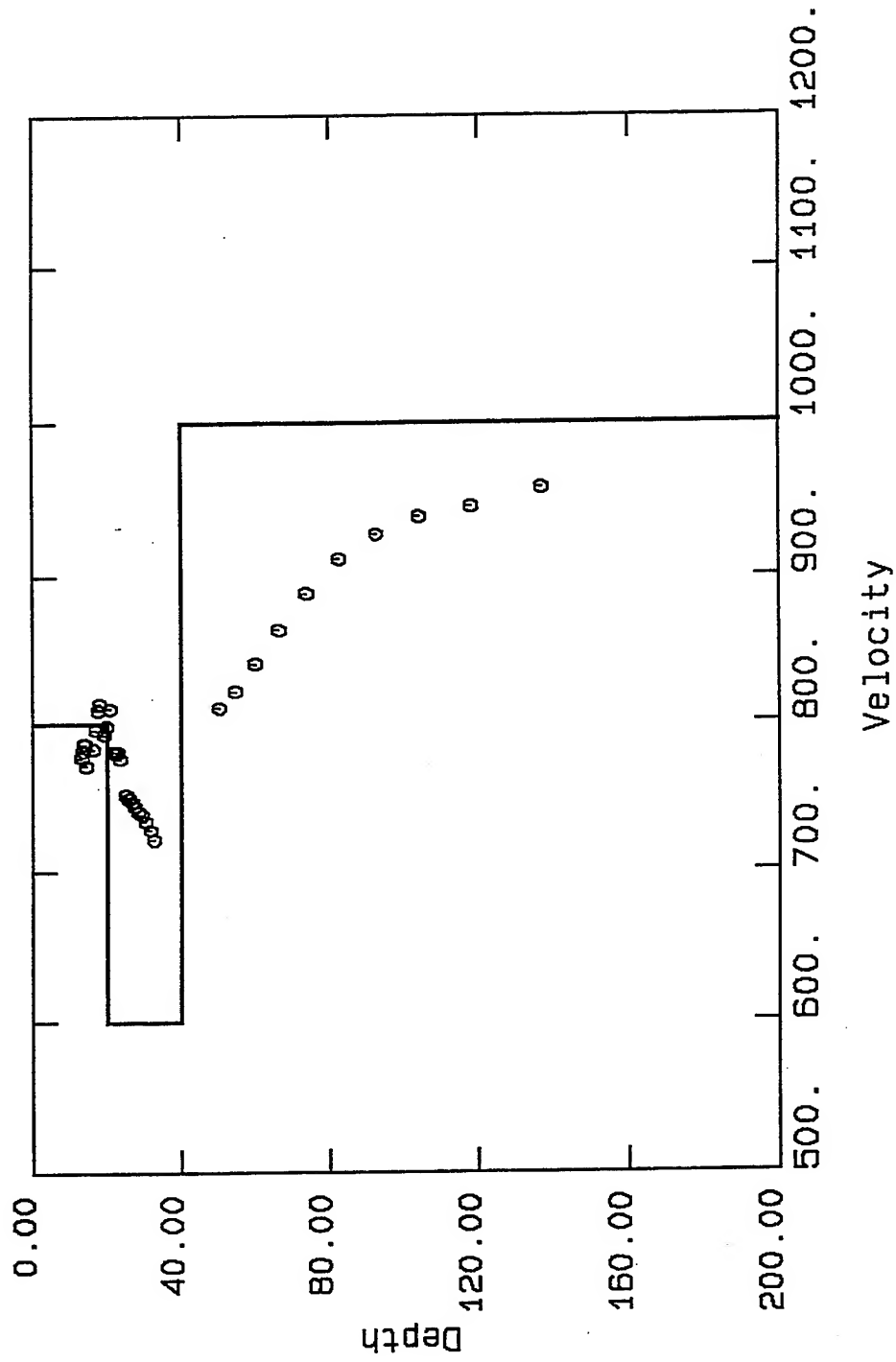
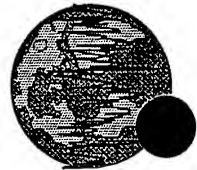


Figure 2.24. Plots of the apparent velocities verses the effective depth based on the data in Table 2.4. The plot also shows the assumed velocity-depth profile that is used for simulation.



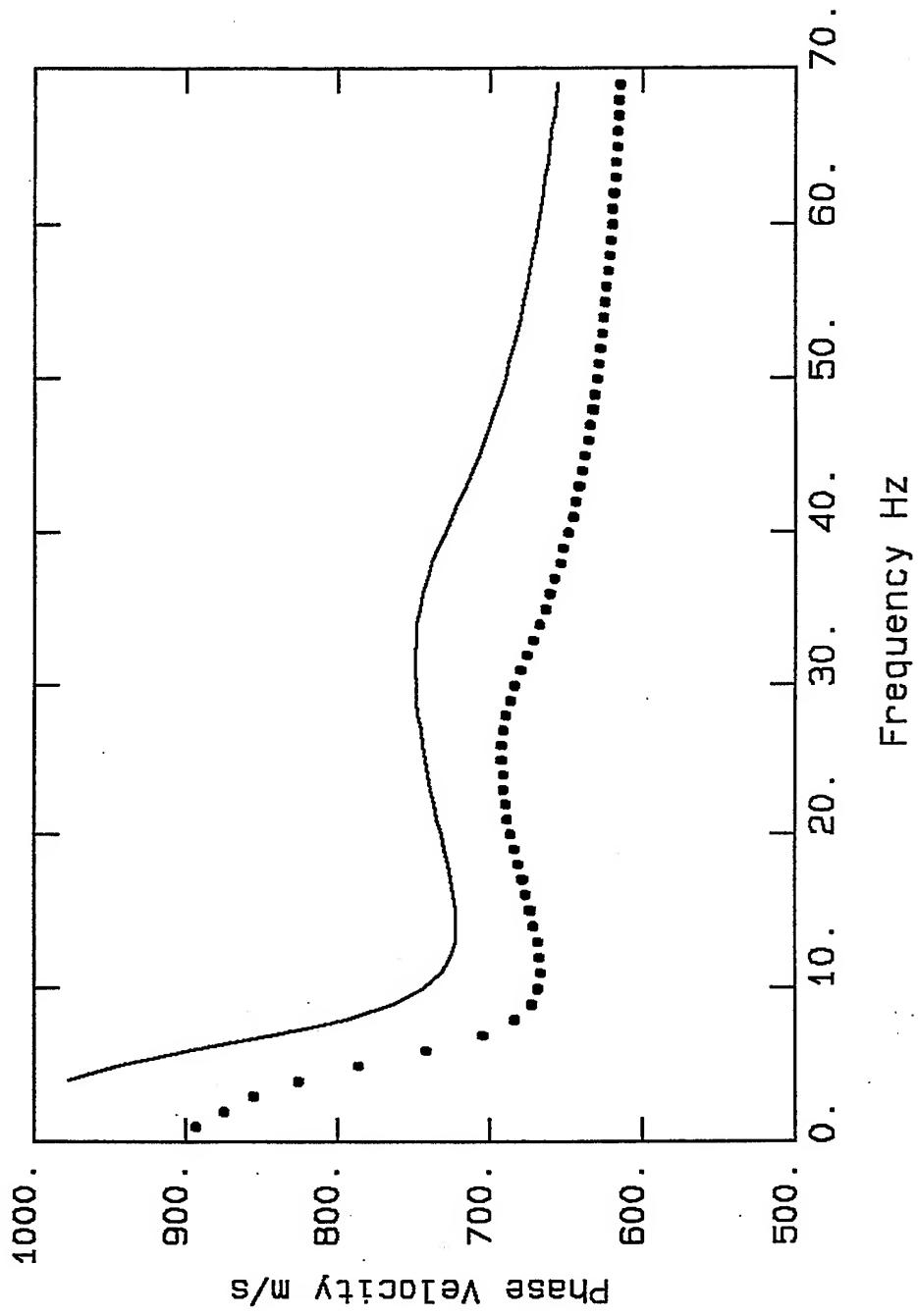


Figure 2.26. Plots of Simulated and input dispersion curves corresponding to Figure 2.21 and Table 2.4.



(This page intentionally left blank)



Chapter 3

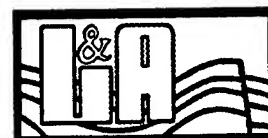
Field Experiments

In the previous chapter we reviewed the theoretical basis of the Circular Array technique and through numerical simulations demonstrated its application and limitation for site investigation. However, the Circular Array technique, like any other methodology, must be validated through field experiments. We conducted five different field investigations at four different sites in order to examine and evaluate the application of the Circular Array technique to real Earth situations. All filed experiments were conducted using two instruments, i.e. case II and III configurations as were discussed in the previous chapter. The selections of the sites were based on the availability of data on site conditions such as the velocity-depth profile, phase velocity for surface waves, surface geology, and the geotechnical boring logs.

All experiments were conducted using two three-components 2.0 Hz L-22E Mark Products geophones and Terra Technology IDS-3602 16 Bit digital recording systems. The sensors were mounted on small platforms allowing vertical adjustments for leveling. In all experiments channels one, two, and three were the vertical, north-south, and east-west directions, respectively. Before each experiment the internal clocks of the instruments were synchronized by one-shot signal, see the IDS-manual for the detail, for accurate timing. At each setting, the instruments were manually timed to start recording at the same time for about five to ten minutes. Data was directly stored on the IDS' 2 MB internal memory with



the sampling rate of 250 sample per second. A Lap-Top computer was used to communicate with the IDS units and for data transfer.



3.1. Experiments No. 1 & 2: The Parking Lot of the St. Aidams Episcopal Church, Malibu, California

The St. Aidams Episcopal Church is located at 28211 W. Pacific Coast Highway, Malibu, California. In 1993, Vibration Instrument Company, VIC, conducted a surface wave measurement survey at this site for the Department of Civil Engineering of the University of Southern California. The VIC report provides Rayleigh wave phase velocity-frequency information for the site. The VIC experiment was based on spectral analysis of surface waves generated by controlled sources, referred to as CXW. The CXW uses a powerful electromagnetic vibration source to generate different forms of surface waves. The vibration source generates frequency swap of repeated amplitude modulated harmonic pulses at preselected frequency intervals. The recorded data, discretized in the frequency domain, is a measure of the dispersion curve for the Rayleigh waves in the medium. Figure 3.1 and 3.2 are from the VIC report showing the estimated Rayleigh wave phase velocities and the phase velocity-depth profile from a CXW experiment at the parking lot of the church. It should be mentioned that the results presented on these figures are not the raw data but gone through different levels of smoothing. The dots on these figures are based on measured data and the lines on Figure 3.1 show the simulated phase velocities for the first three modes of the velocity-depth profiles that are shown on Figure 3.2.

The parking lot of the church is sitting on a bluff about 30 to 40 meters away from and above the Pacific Coast Highway (PCH). A day-care center is very close to the parking lot and there are occasional car traffic through the parking lot from 8:30 a.m. till 4:00 p.m. The site was instrumented at three different days. Each



survey took about eight to ten hours. The setting of the experiment was a combination of case II and III configurations, i.e. keeping one instrument fixed and moving the other one on a circle around the first one to simulate an ideal Circular Array experiment.

The useful width of the parking lot is about 15 m that determined the radius of the circular array. However, in two different directions data were collected with the instruments-spacing of 27 and 37 m (90 and 120 ft, respectively). The following diagrams show the topography of the site and the setting of the experiments. The diagrams are not in scale.

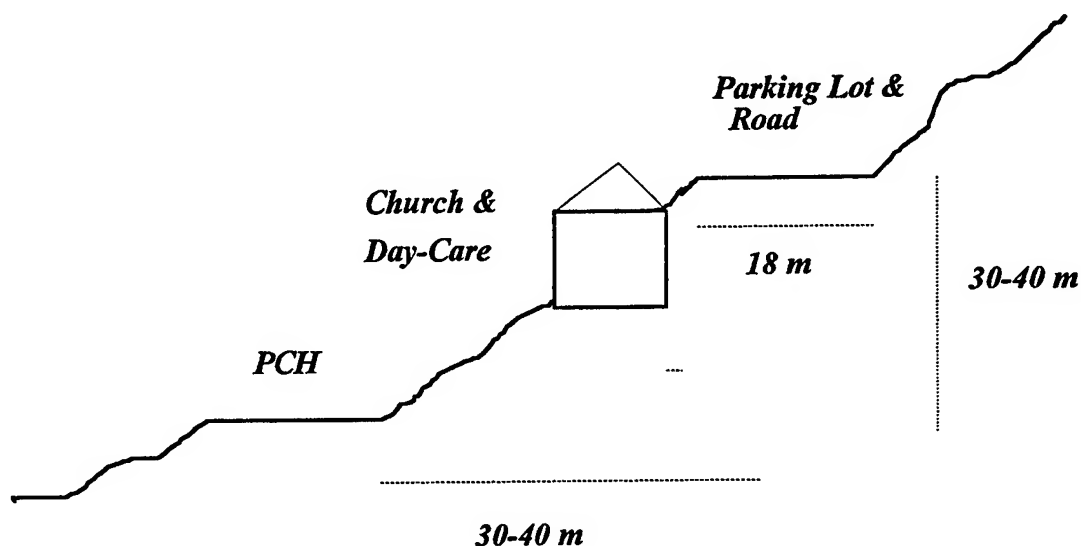
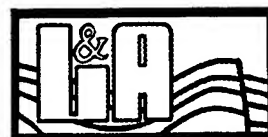


Diagram 3.1. Topography of the site of the St. Aidams Episcopal Church



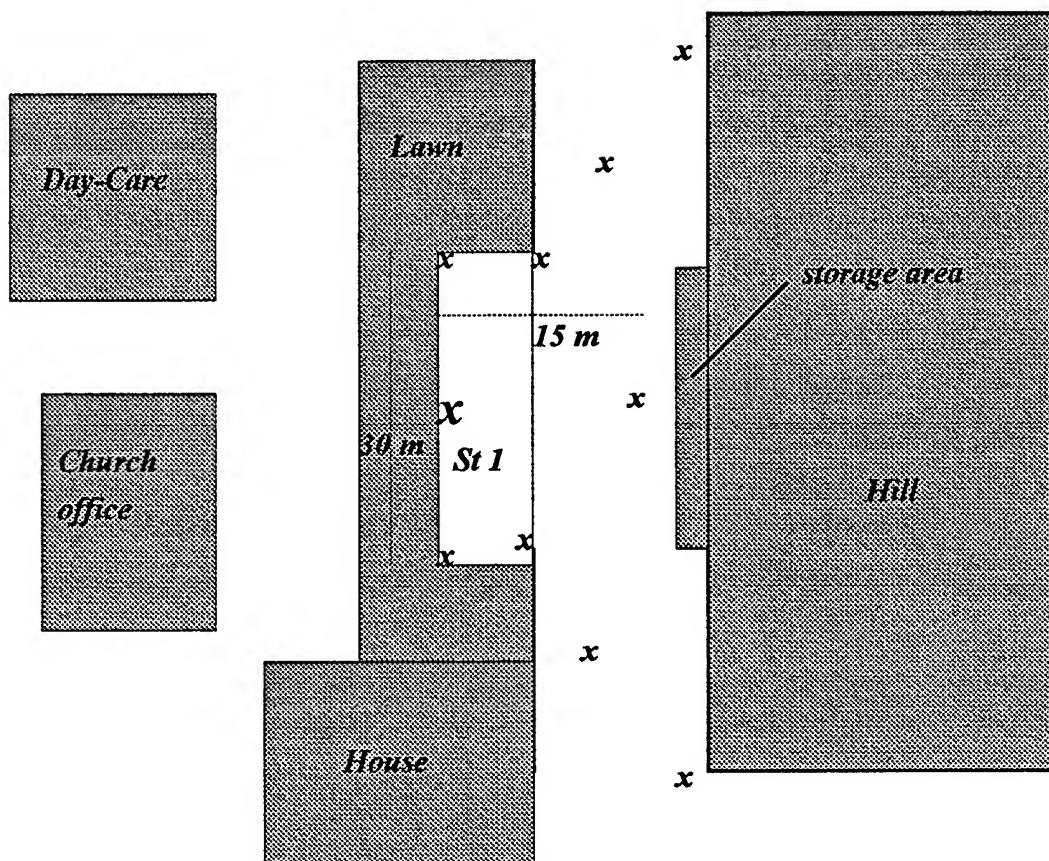
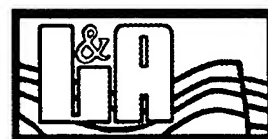


Diagram 3.2. The setting of the parking lot and the data collection sites for the Circular Array experiments. Station 1 refers to the fixed instrument.



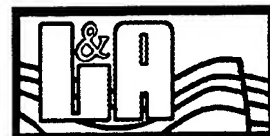
Data Processing

The first five minutes of each record is selected for data processing. Each record is divided into nine overlapping one minute windows with 30 seconds of overlap between the adjacent windows. The horizontal components are rotated to obtain the radial and tangential components, parallel and perpendicular to the direction connecting each pair of instruments, respectively. The Fourier transformation of all time histories are calculated from which the spatial correlation coefficients, equation (2.26), over different frequency bands are obtained. The correlation coefficients are averaged over different time windows and azimuths to obtain the CC-F curves. The setting of the experiments and the averaging represent a combination of the case II and III configurations that were discussed earlier. The plots of the selected time histories, spectral parameters, and correlation coefficients from individual time windows are shown in Appendix A. Figures 3.3 and 3.4 show the CC-F curves for the vertical components of microtremors for two Circular Array experiments with $r=1$ m that were conducted at two different days. Figures 3.5 and 3.6 show similar results for the cases of $r=27$ and $r=37$ m, respectively. The solid line on each figure represents the expected pattern for the vertical component of the CC-F curve based on equation (2.21) using $r = 15$ m and the VIC's frequency dependent first mode phase velocities on Figure 3.1. The vertical components are not polarized and have only one expected pattern. The VIC's data do not cover frequencies below about 5 Hz. Therefore, the CC-F values for $f < 5$ Hz can not be directly compared with the expected pattern from the VIC data. All CC-F curves at the frequency of about 6 to 7 Hz show abrupt jumps in values. However, it is interesting to note that the CC-F



curves at frequencies below about 6 Hz, for all cases, show similar trends as the expected pattern from the VIC data if the VIC-related curves are extended to the low frequency region. The observed jump in the CC-F values is specially clear on Figures 3.3 and 3.4. On these figures the CC-F curves show higher values than the VIC-related curve up to the frequency of about 12 Hz. At this frequency the CC-F curve follows the VIC-related curve but only over a short frequency band. The latter observation is not very clear on Figures 3.5 and 3.6 because of the many cycles of the Bessel function for these cases. The CC-F curves on Figures 3.3 and 3.4, that are based on data collected at two different days, show remarkable similarity. This suggests that there could be a physical reason for the unusual shape of the CC-F curve for the frequency band of 6 to 12 Hz.

Let us examine a possible scenario to explain the behavior of the CC-F curves for the frequency range of 6 to 12 Hz. As mentioned earlier, the parking lot is sitting on a bluff about 30 to 40 meters away from and above the PCH. The observation of the time histories and the related spectral amplitudes, Appendix A, indicate that the traffic-related ground motions dominate the spectral amplitudes of most records in the frequency range of 5 to 12 Hz. Figure 3.7 shows a typical example from the Appendix A. The high spectral amplitudes at the frequency range of 6 to 12 Hz are dominantly from traffic. Our analyses show that the waves from traffic disappear on low pass filtered, $f_c = 5$ Hz, time histories. Also comparisons between the spectra of time windows with and without traffic signals indicate that the high spectral amplitudes in the frequency band of 5 to 12 Hz are from traffic.



The propagation paths of the waves from traffic on PCH to the site of the experiment are not horizontal as is the assumption in the formulation of the Circular Array technique for the wave propagation of surface waves. The CC-F curves, in general, reflect the amount of phase shift that microtremor waves of different frequencies experience traveling the distance between the reference site to each of the peripheral stations. The phase shift in the frequency domain, as was discussed in the previous chapter, can be formulated as $x = r \cdot \omega / C(\omega)$. A decrease in the value of x means a better correlation between the ground motions at recording sites and below certain frequencies, i.e. within the frequency range of the first half cycle of the CC-F curve, cause higher CC-F values. This can occur either due to shorter propagation-distance for the wave fronts or higher propagation velocity for waves. The probable propagation paths for traffic on PCH to the parking lot suggest shorter propagation distances for the wave front from one site to another than the radius of the circular array, see Diagram 3.3.

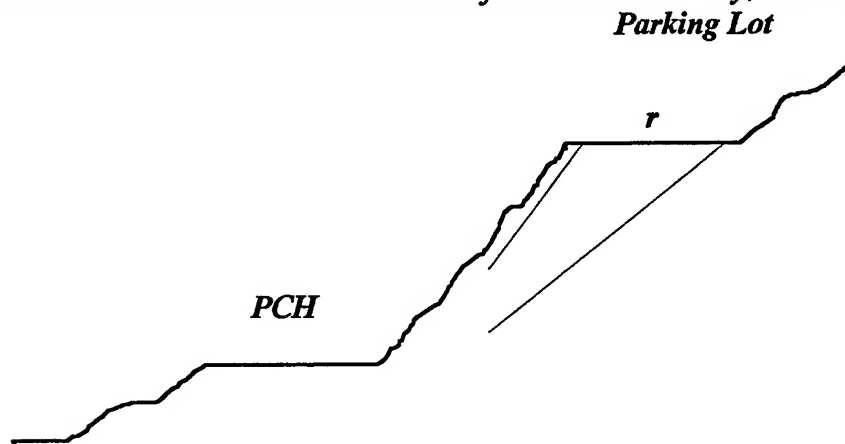
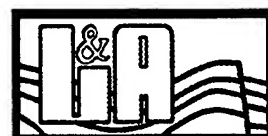
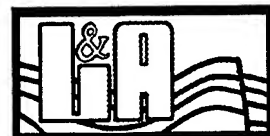


Diagram 3.3. Possible propagation paths for seismic waves from traffic on PCH to the site of the parking lot of the church. The differences in the propagation path for the traffic-related waves are shorter than the horizontal distance between any two stations.



Furthermore, the traffic waves may be predominantly composed of body waves with higher propagation velocities than those of Rayleigh waves. Both conditions would reduce the phase difference between the ground motions at the recording sites and thus increase the related correlation coefficients. For example, reducing the $r / C(\omega)$ ratio by 50% over the frequency band of 6 to 12 Hz, implying changes in either r or $C(\omega)$, can explain the observed behavior of the CC-F curve for the parking lot, Figures 3.8 and 3.9. However, from the practical point of view, the segments of the CC-F curves for the frequency range of 7 to 12 Hz do not have any interpretation value. In general, we should not expect sudden increase or decrease in the CC-F values under normal conditions if microtremors are composed of horizontally propagating surface waves. Theory indicates that the phase velocity of surface waves at a given frequency is controlled by the seismic properties of materials to the depth of about half the wave length corresponding to that frequency. Therefore, phase velocities represent the average seismic properties over depth and are not expected to show rapid change over a narrow frequency band. Assuming that $C(\omega)$ is constant over a narrow frequency band or changes very little the term $r \cdot \omega / C(\omega)$ for a given value of r should increase with increasing frequency. Within the first half cycle of the Bessel function, this means a decrease in the values of the correlation coefficients with frequency. In general, segments of the CC-F curves with rapid increase or decrease in values with frequency, different from the expected randomness for this type of data, should be treated very carefully or be rejected completely.

Our objective is to interpret the CC-F values in terms of the velocity-depth profile for the site. Because of the abnormal pattern of the CC-F curves for $f > 7$ Hz, the



interpretation of the data is limited to the frequency ranges of $f < 7$ Hz. The interpretation procedure as was discussed in the previous chapter is as follows

- Filter the CC-F data to obtain a smooth CC-F curve*
- Interpret the CC-F curve as $J_0(x)$ to obtain the corresponding x -values*
- Calculate the phase velocity as $C(\omega) = r \cdot \omega / x$ using the radius and the estimated value for x for each frequency band*
- Transform the phase velocity-frequency values to phase velocity-depth values*
- Interpret the phase velocity-depth values to phase velocity of layered medium*
- Construct a shear wave velocity-depth profile*
- Theoretically simulate the phase velocities for the constructed model*
- Compare the simulated and calculated phase velocities and if necessary repeat the cycle*

Figures 3.10 to 3.13 show the filtered CC-F curves corresponding to Figures 3.3 to 3.6, respectively. Table 3.1 shows the CC-F values and the estimated phase velocities for these four cases.

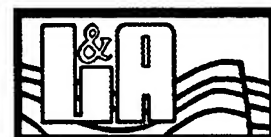
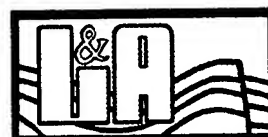


Table 3.1. The CC-F values and the corresponding phase velocities over different frequency bands.

	$r=15\text{ m}$		$r=15\text{ m}$		$r=27\text{ m}$		$r=37\text{ m}$	
f Hz	$J_0(x)$	$C(\omega)$ m/s	$J_0(x)$	$C(\omega)$ m/s	$J_0(x)$	$C(\omega)$ m/s	$J_0(x)$	$C(\omega)$ m/s
.25	.83	31	.35	14	.49	30	.24	31
.75	.85	99	.97	237	.91	227	.97	565
1.25	.91	221	.96	344	.92	424	.96	777
1.75	.93	350	.94	372	.91	551	.92	792
2.25	.96	613	.97	678	.92	753	.90	872
2.75	.93	558	.92	501	.85	656	.77	705
3.25	.91	549	.87	459	.77	616	.64	645
3.75	.88	565	.82	458	.69	608	.52	631
4.25	.86	578	.78	464	.61	608	.41	634
4.75	.82	580	.73	465	.52	603	.30	637
5.25	.79	581	.68	468	.42	595	.19	640
5.75	.77	602	.65	485	.34	600	.11	654
6.25	.76	653	.65	523	.30	628	.07	690
6.75	.78	732	.66	577	.29	676	.08	749

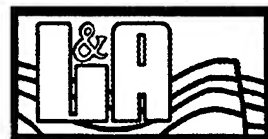
The estimations of the phase velocities below 2 Hz are not reliable. This is specially the case for $r=15\text{m}$ experiments. The small aperture of the array can not provide information on long period waves. In fact, the larger size arrays show more stable results for frequencies below 2 Hz. However, for the purpose of interpretation we do not use the phase velocities below $f < 2\text{ Hz}$. Assuming that at each frequency the phase velocity of Rayleigh wave is predominantly controlled by the seismic properties of materials to the depth of about half the wavelength at that frequency, the phase velocity-frequency values in Table 3.1 can be translated into the phase velocity-depth as



$$d_{\text{effective}} = \lambda / 2 = C(\omega) / 2f$$

Figure 3.14 shows the plots of phase velocities versus depth, $d_{\text{effective}}$, for the four cases. The line on the figure represents the average of the four phase velocity-depth profiles. The values for the cases of $r=15$ m show very similar results about 100 m/s lower values than the cases of $r=27$ and 37 m. It appears that the estimated phase velocities from experiments with larger radius arrays systematically are higher than those from the smaller radius arrays. However, the pattern of the phase velocities with depth for all cases are very similar. Figure 3.15 and 3.16 show the plots of phase velocities versus depth for the two cases of $r=15$ m and for $r=27$ and 37 m, respectively. The shallowest depth with phase velocity information is about 46 m. This is based on the assumption that the effective depth is about half of the wave length at each frequency. A study by Satoh (1989) suggests that the effective depth for surface waves may be about 30% of the wavelength rather than 50%. This puts the shallowest depth to about 28 m. In our interpretation we assume the effective depth to be 50% of the wavelength with the understanding that this assumption requires more investigation.

In order to interpret the phase velocity-depth information into phase velocity of layered medium we have to identify the depths at which significant changes in the slope of such data occurs. For the cases of $r=15$ m, Figure 3.15, two breaking points on the average phase velocity-depth profile at $d = 46$ and 74 m with the phase velocities of 500 and 483 m, respectively, are identified. Using the appropriate empirical equations, equation 2.38 or 2.39, the data on Figure 3.15



can be interpreted as phase velocities for layered medium as are shown in Table 3.2. The table also shows the shear wave velocity profile using $C(\omega) / \beta = 0.9$ for all frequencies.

Table 3.2. The velocity-depth profile for a layered medium based on the observed phase velocity-depth profile that is shown on Figure 3.15.

<i>Depth</i> <i>m</i>	<i>Phase Velocity</i> <i>m/s</i>	<i>Shear Wave Velocity</i> <i>m/s</i>
<46	500	556
46-74	457	508
>74	775	861

In a similar way we can interpret the phase velocity-depth values for the cases of $r=27$ and 37 m, Figure 3.16, and the average of all four cases, Figure 3.14. The results are shown in Tables 3.3 and 3.4, respectively.

Table 3.3. The velocity-depth profile for a layered medium based on the observed phase velocity-depth profile that is shown on Figure 3.16.

<i>Depth</i> <i>m</i>	<i>Phase Velocity</i> <i>m/s</i>	<i>Shear Wave Velocity</i> <i>m/s</i>
< 94	618	687
>94	920	1022

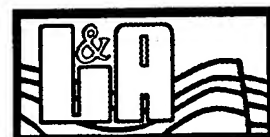


Table 3.4. *The velocity-depth profile for a layered medium based on the observed phase velocity-depth profile that is shown on Figure 3.14.*

<i>Depth</i> <i>m</i>	<i>Phase Velocity</i> <i>m/s</i>	<i>Shear Wave Velocity</i> <i>m/s</i>
< 86	550	611
> 86	872	969

The estimated velocity-depth profiles should be validated against their related phase velocities. Figures 3.17 and 3.18 show the results of phase velocity simulation of Rayleigh waves for the velocity-depth profiles in Tables 3.3 and 3.4, respectively. The simulated phase velocities based on the empirical data are good approximation of the observed phase velocities, however, they are not the best possible fit to the data. The primary reason may be that there is no information on the velocity depth profile at shallow depths. The detail of the velocity depth profile at shallow depths would affect the shape of the phase velocity curve. Using a low velocity layer at shallow depths would reduce the phase velocities and bring them closer to the observed values. Tables 3.5 and 3.6 show two examples of the velocity-depth profiles and Figures 3.19 and 3.20 show the simulated and observed phase velocity values, respectively.



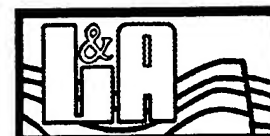
Table 3.5. *A modified velocity-depth profile corresponding to the model in Table 3.2.*

<i>Depth</i> <i>m</i>	<i>Shear Wave Velocity</i> <i>m/s</i>	<i>P-Wave Velocity</i> <i>m/s</i>
< 40	600	1038
40-74	400	692
>74	861	1489

Table 3.6. *A modified velocity-depth profile corresponding to the models in Tables 3.3 and 3.4.*

<i>Depth</i> <i>m</i>	<i>Shear Wave Velocity</i> <i>m/s</i>	<i>P-Wave Velocity</i> <i>m/s</i>
< 40	800	1384
40-94	550	951
> 94	1022	1768

The simulated phase velocities for these models are in very good agreement with the observed values. However, if we add a low velocity layer at the surface to these models the shape of the simulated phase velocity curve would change drastically, Figure 3.21. This figure shows the effect of adding a surface layer with the depth of 14 m with the shear wave velocity of 270 m/s, as suggested by the VIC's velocity-depth profile, to the model in Table 3.6.



Let us examine how the phase velocities from the VIC's velocity-depth profile compare with those from our experiment. However, before making such comparison it is necessary to mention that the VIC's velocity-depth profiles at depth because of the limitation in their frequency range is not well constrained. For this site, the VIC's shear wave velocity-depth profile, the table on Figure 3.2, shows a high velocity layer at the depth of 34.6 m. It is not immediately clear how this depth is calculated. The fact that VIC data do not show any phase velocity values below the depth of 50 m suggests that perhaps the depth and velocity of the last layer; i.e. 34.7 m and 1500 m/s, respectively; are not well constrained. To demonstrate this point, we simulated the phase velocities for two modified VIC's velocity-depth profiles that are shown in Table 3.7.

Table 3.7. The VIC's and two related modified velocity-depth profiles. β and α are the shear and pressure wave velocities.

VIC Model			Model I			Model II		
Depth m	β m/s	α m/s	Dept h m	β m/s	α m/s	Dept h m	β m/s	α m/s
<1.6	113	185	<1.6	113	185	<1.6	113	185
<14.1	270	441	<14.1	270	441	<14.1	270	441
<34.6	753	1229	<94	753	1229	<74	753	1229
> 34.6	1500	2449	> 94	1200	2449	> 74	1200	2076

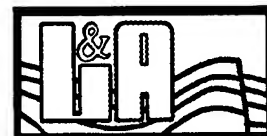
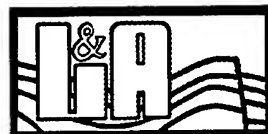
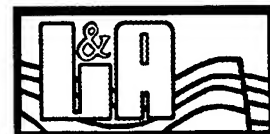


Figure 3.22 shows the plot of the first mode phase velocities for these three velocity-depth profiles. The phase velocities are different at low frequency ranges below about 5 Hz. However, there are no significant differences between the phase velocities for frequencies above 5 Hz where all VIC phase velocity data exist. This means that all models are reasonable scenarios to VIC data. However, the phase velocities from the Circular Array experiment at low frequencies, as are shown on Figures 3.22, support the choice of either model I or II for the velocity-depth profile of the site. Except for the shallow low velocity layers the velocity-depth models I and II in Table 3.7 are fairly similar to the velocity-depth profile models that are constructed from the Circular Array experiment, Tables 3.5 and 3.6.

Figures 3.23 and 3.24 show plots of the CC-F curves for the radial and tangential components of microtremors. The thick and thin solid lines on these figures show the expected patterns for the radial and tangential components, equations (2.22) to (2.25), depending upon the predominant direction of polarization for the horizontal components of microtremors. The CC-F curves for the horizontal components do not resemble either of the expected patterns. It is practically impossible to characterize the direction and the degree of polarization for the horizontal components of microtremor ground motions without a full scale frequency-wave number analysis. However, assuming that the horizontal components of microtremors are composed of some combination of Rayleigh and Love waves it is possible to infer the probable fraction of the polarization of the horizontal components and the phase velocities of the Love waves, Ferrazzini et al (1991). The procedure is rather involved and require a more in-depth analysis



that might not be warranted for a routine site investigation studies. Here, we limit our interpretation to the CC-F curves from the vertical components of microtremors with the understanding that the interpretation of the horizontal components needs further investigation.



3.2. Experiment No. 3: The Mazda Parking Lot, Port of Hueneme, Oxnard, California

This site was suggested by Mr. Ferritto, the project manager of this project. A boring log with SPT blow counts and a soil-depth classification for the site are available, Table 3.8. A Circular Array experiment at this site with $r = 14$ m (45 ft) was conducted. The general description of the field investigation is very similar to what was described for the experiment at St. Aidams Episcopal Church. Unfortunately, due to the unexpected malfunction of one of the vertical sensors only a small portion of the collected data is usable that will be presented here. The site of the experiment is located in the parking lot of the Mazda storage area. The parking lot is a paved flat open space that is located relatively close to the shore. The experiment was conducted using two instruments. Microtremors at five different azimuths were simultaneously recorded on the two instruments for six to ten minutes.

The plots of time histories and the related spectra for selected records are shown in Appendix B. Figure 3.25 shows the average CC-F curve for the vertical component of microtremor ground motions. The immediate observation on this figure is that it does not show the abnormal pattern for the frequency ranges above 6 Hz that were observed on the CC-F plots for the St. Aidams Episcopal Church. This supports our arguments regarding the effects of topography and traffic on PCH at that site. The solid line on Figure 3.25 is the best fit to the data. Following the same procedure for the data interpretation, as was described in the previous section, the CC-F values are transformed to the phase velocities. Table 3.9 shows the estimated phase velocities as a function of frequency. We

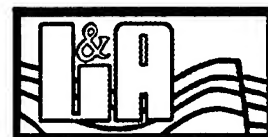


Table 3.8. The boring log information

TEST BORING LOG							1P2/393/100-	
Taber <small>Taber Consultants Engineers and Geologists 530 Sherman Street San Francisco, CA 94102 (415) 371-1230 Fax (415) 371-7283</small> TYPE: 4-Inch Auger to 10ft/3-inch Rotary							BORING No 5 Continu	
ELEVATION: 11.5±								
1			79	1.4	8		SP	Very dense gray very fine-fine and very fine-coarse SAND
0	86	34	8	1.4	9		CL	Soft dark gray CLAYEY SILT
3	97	27	25	1.4	10		ML	Compact gray very fine SANDY SILT to SILT with very fine SAND
6			22	1.4	11			
6			40	1.4	12		SP / SM	Dense gray very fine-fine SAND and SILTY SAND
6			51	1.4	13			
8	93	31	25	1.4	14		CL	Very stiff gray CLAYEY SILT
			106+	1.4	15		SP	Very dense gray very fine-coarse SAND
3			125+	1.4	16			
								Groundwater measured at 8.0ft depth; Boring grout backfilled 8-10-93.
PID READING (ppm)	OTHER TESTS	DRY DENSITY (lbs/cu. ft.)	Moisture (%)	BLOWS/FOOT 350 ft-lb	SAMPLE SIZE (inches)	SAMPLE No.	DEPTH IN FEET	MATERIAL SYMBOL UNIFIED SOIL CLASS THE BORING LOGS SHOW SUBSURFACE CONDITIONS AT THE DATES AND LOCATIONS INDICATED AND IT IS NOT WARRANTED THAT THEY ARE REPRESENTATIVE OF SUBSURFACE CONDITIONS AT OTHER LOCATIONS AND TIMES LOGGED BY: T.A.K. DATE: 8-10-93

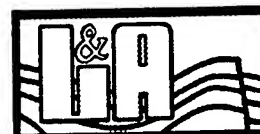


Table 3.8. Continued

Taber Consultants
Engineers and Geologists
836 Colman Street
San Francisco, CA 94101
(415) 371-1000 Fax (415) 371-7285

TEST BORING LOG

1P2/393/100-

TYPE: 4-inch Auger to 10ft/3-inch Rotary ELEVATION: 11.5± BORING No 5

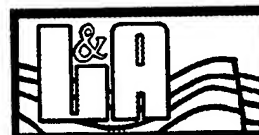
PID READING (ppm)	OTHER TESTS	DRY DENSITY (lb/cu. ft.)	Moisture (%)	BLOWS/FOOT 350 ft-lb	SAMPLE SIZE (inches)	SAMPLE No.	DEPTH IN FEET	MATERIAL SYMBOL	UNIFIED SOIL CLASS	DESCRIPTION
11		104	23	18	1.4	1	0	SM		AC to 0.4ft over (compact) brown fine GRAVELLY SILTY SAND (fill)
							5	SM / ML		Semicompact brown very fine SANDY SILT to SILTY very fine-fine SAND
14		115	16	38	1.4	2	10			Dense and compact gray very fine-coarse SAND
6				35	1.4	3	15	SP		
6	C.S.	97	26	18	2.5	4	20			(Stiff) to soft gray CLAYEY SILT
10		82	39	6	1.4	5	25	CL		
5		93	28	9	1.4	6	30			
3		122	13	74	1.4	7	35	SP		Very dense gray very fine-fine and very fine-coarse SAND
						8	40			

SEE NEXT PAGE

---CONTINUED---

THE BORING LOGS SHOW SUBSURFACE CONDITIONS AT THE DATES AND LOCATIONS INDICATED AND IT IS NOT WARRANTED THAT THEY ARE REPRESENTATIVE OF SUBSURFACE CONDITIONS AT OTHER LOCATIONS AND TIMES

LOGGED BY: T.A.K. DATE: 8-10-93



limit the interpretation of data to the first cycle of the CC-F curve. The high frequency components are less reliable. As was demonstrated in the chapter on the numerical simulation, obtaining a reliable data for high frequency components of the CC-F curve requires averaging the correlation coefficients over many azimuths and time windows, more than what is necessary for getting stable results for low frequency components of the CC-F curves.

Table 3.9. The estimated phase velocities for different frequency bands based on the CC-F values on Figure 3.25.

<i>f</i> Hz	Phase Velocity m/s	<i>f</i> Hz	Phase Velocity m/s	<i>f</i> Hz	Phase Velocity m/s
2.25	251.18	7.25	194.18	12.25	132.96
2.75	277.61	7.75	196.01	12.75	137.64
3.25	274.64	8.25	197.85	13.25	142.34
3.75	272.72	8.75	199.68	13.75	111.22
4.25	272.61	9.25	201.51	14.25	114.39
4.75	266.79	9.75	191.67	14.75	116.65
5.25	252.44	10.25	188.81	15.25	118.33
5.75	233.59	10.75	189.54	15.75	120.12
6.25	214.04	11.25	193.59	16.25	122.94
6.75	192.35	11.75	200.83		

The estimated phase velocities are transformed into the phase velocity-depth profile using $d_{\text{effective}} = \lambda / 2$. Figure 3.26 shows the results. Two break points on this figure at the depths of 9.4 m and 15.3 m can be identified. Using Satoh's (1989) empirical interpretation of the phase velocity-depth profile the data on Figure 3.26 are interpreted as a three-layered medium, Table 3.10.

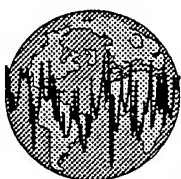
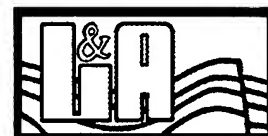


Table 3.10 *The velocity depth profile of a three-layered medium representing the phase velocities that are shown on Figure 3.26.*

<i>Depth</i> <i>m</i>	<i>Phase Velocity</i> <i>m/s</i>	<i>Shear Wave Velocity</i> <i>m/s</i>
< 9.4	193	214
<15.3	177	197
>15.3	364	404

A comparison between the simulated phase velocities for this model, the top curve on Figure 3.27, and the observed values suggest that slight modification for the velocity-depth profile is needed. Lowering the shear wave velocity of the second layer to 170 m/s gives phase velocities with very good agreements with the observed values, the bottom curve on Figure 3.27.

The velocity-depth models of Table 3.10 are constructed based on the initial assumption that the effective depth for the phase velocities are about half of their corresponding wave lengths. Let us consider the case where, as Satoh (1989) suggested, the effective depth is about 30% of the wave length. In that case the estimated velocities for the layers remain the same but the depths of boundaries between different layers change, Model I of Table 3.11. The top curve on Figure 3.28 shows the simulated phase velocities for this model. The simulated and the observed values are not in good agreement. Increasing the thickness of the low velocity layer bring the simulated values closer to the observed values. The simulated values for two cases are shown. Table 3.11, Models II and III, show the velocity-depth profiles for these two cases. The results from Model III are in



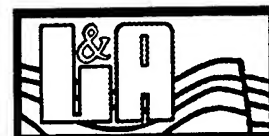
very good agreement with the observed values. Both Model III and the model in Table 3.10 with $\beta=170$ m/s for the second layer are reasonable scenarios for the velocity-depth profile of the site based on the observed phase velocities. This shows the non-uniqueness of the phase velocity inversion process. Both models identify a low velocity layer, a shallow and thick layer in one model and a deeper and relatively thin layer in the other model.

Table 3.11. Model I is the velocity-depth profile for a layered medium based on the assumption that the effective depth that controls the phase velocity of Rayleigh wave is about 30% of the wavelength at all frequency ranges. Models II and III are the modified version of Model I with phase velocities that better fit the observed data than those of Model I.

Model I			Model II			Model III		
Depth m	β m/s	α m/s	Depth m	β m/s	α m/s	Depth m	β m/s	α m/s
<5.7	214	370	<5.7	214	370	<5.7	214	370
<9.2	197	341	<15.3	197	341	<17	197	341
>9.2	404	699	>15.3	404	699	>17	404	699

The thickness of the low velocity layer for these two models are different but both models have similar site response to ground motions. Figure 3.29 and 3.30 show one-dimensional site response for these two models to weak and strong, magnitude 6.5 earthquake at distance of 15 km, ground motions.

Let us compare the two constructed velocity-depth profiles with the boring log information for the site. The SPT blow counts, Table 3.8, can be translated to the



shear wave velocity profile for the site using one of the empirical equations for such conversion. It is a common knowledge that the estimation of the shear wave velocities based on the SPT blow counts are not very precise. However, it could provide us with the general picture of the velocity depth profile for the site. Table 3.11 shows a representative velocity-depth profile based on the SPT blow counts and the velocity-depth profiles from the Circular Array experiment. The results are in fairly good agreements specially for the velocity-depth profile of Table 3.11.

Figures 3.31 and 3.32 show the CC-F curves for the radial and tangential components of microtremor ground motions. The CC-F curves on these figures show remarkable similarities that may suggest that the horizontal components of microtremors consist of waves equally polarized parallel and perpendicular to their directions of propagation. In that case, it is expected that the CC-F curves of the horizontal components have similar patterns as the vertical component, i.e. the zero order Bessel function $J_0(x)$. The radial and tangential CC-F curves show relatively similar pattern with the vertical CC-F curve on figure 3.25. However, the match is not perfect and requires interpretation.

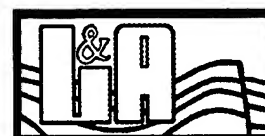


Table 3.12. Shear wave velocity-depth profiles based on the boring-log data and the Circular Array experiments.

<i>Model Based on Boring Log Data</i>	<i>Model from Table 3.11</i>	<i>Model from Table 3.10</i>
$\beta = 300 \text{ ft/s}$ 15'	$\beta = 214 \text{ ft/s}$ 18.7'	$\beta = 214 \text{ ft/s}$ 31'
$\beta = 170 \text{ ft/s}$ 35'	$\beta = 197 \text{ ft/s}$ 56'	$\beta = 197 \text{ ft/s}$ 50'
$\beta > 500 \text{ ft/s}$ 45'		
$\beta = 180 \text{ ft/s}$ 50'		
$\beta = 360 \text{ ft/s}$ 75'	$\beta = 404 \text{ ft/s}$	$\beta = 404 \text{ ft/s}$
<i>Bedrock Type materials</i>	?	?



3.3. Experiment No. 4: The basketball Court of the McBride School, Los Angeles, California

The McBride school is located at 3960 Centinela St., Los Angeles, California. The school is located in a very busy section of town. About 30 m from the site of experiment there is a main road with heavy traffic. The basketball court is located within a large open area. There is a swimming pool in one corner of the school. We were assured by the maintenance people that the water pump was not operating during our experiment. However, the recorded data show strong high frequency component of ground motions. The effects of this high frequency oscillation is clear on the recorded time histories. However, since our analysis is in the frequency domain and the pump oscillation is limited to a very narrow frequency band beyond the frequency range of our interest we processed the data and will present the results.

Similar to the site of the St. Aidams Episcopal Church the Vibration Instrument Company in 1993 conducted a surface wave measurement survey at this site. Figures 3.33 and 3.34 are from the VIC report showing the estimated Rayleigh wave phase velocities and the phase velocity-depth profile for the site. The time histories and the Fourier spectra of selected records are shown in Appendix C. Two Circular Array experiments with $r=15$ and $r=30$ m were conducted. Figures 3.35 and 3.36 show the plots of CC-F curves for the vertical components of the ground motions for these two cases, respectively. The thick solid lines are the expected pattern based on the VIC data and the thin solid lines are the best fit to the observed data. The VIC-related data are limited to frequencies higher than about 5 Hz. The CC-F and VIC-related curves show similar values for the

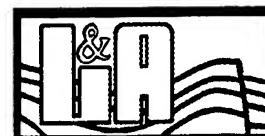


frequency range of 5 to 7 Hz. However, they show different values and patterns for higher frequencies. It should be mentioned that the VIC data, Figure 3.34, shows rather strong scattering in the measured phase velocities for frequencies below 10 Hz. This would affect the expected patterns that are shown on Figures 3.35 and 3.36, i.e. $J_0[r.\omega / C(\omega)]$. Tables 3.13 shows the estimated phase velocities from the CC-F values on Figures 3.35 and 3.36.

Table 3.13 The estimated phase velocities based on the CC-F values shown on Figures 3.35 and 3.36.

Case of $r = 15$ m		Case of $r = 15$ m		Case of $r = 30$ m	
f Hz	Phase Velocity m/s	f Hz	Phase Velocity m/s	f Hz	Phase Velocity m/s
2.25	549	8.75	382	2.25	410
2.75	432	9.25	391	2.75	380
3.25	401	9.75	396	3.25	372
3.75	393	10.25	394	3.75	376
4.25	390	10.75	383	4.25	383
4.75	385	11.25	369	4.75	391
5.25	381	11.75	354	5.25	399
5.75	375	12.25	325	5.75	411
6.25	368	12.75	327	6.25	436
6.75	363	13.25	320		
7.25	363	13.75	313		
7.75	367	14.25	303		
8.25	374	14.75	293		

The CC-F values for the case of $r=15$ m are within the first cycle of the Bessel function up to the frequency of 15 Hz. This makes the interpretation of data up to this frequency relatively easy. We use the phase velocities from this case, construct the velocity-depth profile for the site, and then validate the phase velocities against the observed phase velocities for both cases. Figure 3.37 shows



the phase velocity-depth profile for the site using $d_{\text{effective}} = \lambda / 2$. Two break points at 19.5 and 26.3 m with the phase velocities of 400 and 363 m/s, respectively, can be identified. Using Satoh's (1989) empirical inversion method a velocity depth model, Table 3.14, is constructed.

Table 3.14. The phase velocity and shear wave velocity-depth profiles for the layered medium based on the phase velocity-depth profile on Figure 3.37.

Depth m	Phase Velocity m/s	β m/s
< 10	270	300
< 19.5	400	444
< 26.3	287	319
> 26.3	550	610

Figure 3.37 shows decreasing phase velocities with decreasing depth with the velocity as low as 290 m/s at the depth of about 10 m. This indicates low velocity layers at shallow depths. However, no information is available to identify these layers. Arbitrarily, we included a 10 m layer with the shear wave velocity of 300 m/s to the model. Using the information in Table 3.14, the phase velocities for Rayleigh waves, Figure 3.38, are simulated. Obviously, the velocity-depth profile in table 3.14 needs modification. The changes in the velocity-depth profile should be in such a way that it gives high phase velocities at low frequencies. This implies a high velocity layer at depth. Figure 3.39 shows simulated phase velocities for three velocity-depth profiles that are shown in Table 3.15.



Table 3.15. Three velocity-depth models for simulating and testing the estimated phase velocities.

<i>Model I</i>		<i>Model II</i>		<i>Model III</i>	
<i>Depth</i> <i>m</i>	β <i>m/s</i>	<i>Depth</i> <i>m</i>	β <i>m/s</i>	<i>Depth</i> <i>m</i>	β <i>m/s</i>
< 10	300	< 10	300	< 10	300
< 26	444	< 40	444	< 60	444
> 26	610	< 80	610	< 80	610
		> 80	1200	> 80	1200

The phase velocities for the original model are also shown. Model II and III give the best fit the observed phase velocities. Figure 3.40 shows the same results on Figure 3.39 with the added data points from the Circular Array experiment with $r=30$ m. This data adds to the scattering of the observed phase velocities with respect to the simulated values. However, models II and III still can be considered as reasonable scenarios for the velocity-depth profile for the site based on the observed phase velocities.

The VIC's velocity-depth profile for this site, the table on Figure 3.34 shows similar values as those for Models II and III on Table 3.15. However, the transition depths for the high velocity layers are very different. It can be shown that because of the limitation in the frequency range of the observation in the VIC data their velocity-depth model at depths is not well constrained. Figure 3.41 shows the simulated phase velocities for the VIC's alternative model, the table on

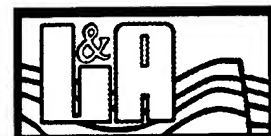


Figure 3.34, and for another model with similar velocities but different transition depths for the layers, Table 3.16.

Table 3.16. The VIC's velocity-depth profile and an alternative model with the same velocity values but different thickness for layers.

VIC Model		Alternative Model	
Depth	β	Depth	β
m	m/s	m	m/s
< 1.1	100	< 1.1	100
< 5.6	180	< 5.6	180
> 22.2	410	< 60	410
> 272.	610	< 80	610
< 27.2	1220	> 80	1220

The scattering in the VIC's phase velocities, Figure 3.33, are well within the range of the simulated phase velocities on Figure 3.41. Figure 3.42 shows the simulated phase velocities based on the VIC's velocity-depth profile and two modified profiles as are shown in Table 3.17.

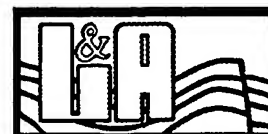
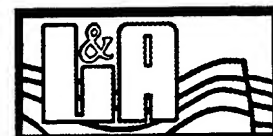


Table 3.17. The VIC's velocity-depth profile and two alternative models with the same velocity values but different thickness for layers.

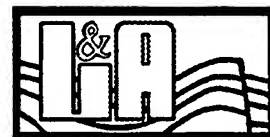
VIC Model		Model I		Model II	
Depth <i>m</i>	β <i>m/s</i>	Depth <i>m</i>	β <i>m/s</i>	Depth <i>m</i>	β <i>m/s</i>
< 1.1	100	< 1.1	100	< 1.1	100
< 5.6	180	< 5.6	180	< 5.6	180
> 22.2	410	< 40	410	< 60	410
> 272.	610	< 60	610	< 80	610
< 27.2	1220	> 60	1220	> 80	1220

The simulated velocities from these three models give similar results as the estimated phase velocities from the Circular Array experiment for frequencies below about 5 to 6 Hz. The estimated phase velocities at high frequencies show much higher values than the simulated results. If the observed phase velocities are accepted the velocity-depth profiles in Table 3.17 without the low velocity layers are reasonable scenarios for the site, Figure 3.43. However, if the VIC data are accepted then there should be an explanation for the higher phase velocity values from the Circular Array experiment with respect to the VIC data, Figure 3.43. The site of experiment is close to a major road with heavy traffic and is exposed to traffic related ground motions. The situation is similar to the case of the St. Aidams Episcopal Church experiment except that the site in this case has a flat topography. The microtremors at the site of experiment for certain frequency ranges might have been composed of body and surface waves. This means that the estimated apparent velocities for those frequencies are representative of that state



and will be higher than the expected phase velocities for Rayleigh waves. For example, just for the purpose of demonstration, reducing the calculated apparent velocities by 50%, implying the possibility of contamination of microtremors by body waves, brings the "modified phase velocities" much closer to the simulated phase velocity curves, Figure 3.44.

Figures 3.45 and 3.46 show the CC-F curves for the radial and tangential components of microtremor ground motions. The CC-F curves on these figures, similar to the previous case, show remarkable similarities that may suggest that the horizontal components of microtremors consist of waves equally polarized parallel and perpendicular to their directions of propagation. In that case, it is expected that the CC-F curves of the horizontal components have similar patterns as the vertical component. The radial and tangential CC-F curves show relatively similar pattern with the vertical CC-F curve on figure 3.25. However, the match is not perfect and requires interpretation.



3.4. Experiment No. 5: The Palm Spring Site

The selection of this site was based on the general information about the surface geology of the area that it is characterized as the region with stiff soil/bedrock site conditions, Chin and Aki (1994) coda waves database. The site is located about one mile north of Highway 10 near the Palm Spring area. The experiment at this site included three circular array configurations with radii of 15, 27, and 37 meters. Figures 3.47 to 3.49 show the CC-F curves for the vertical components of microtremors for these three cases, respectively. The estimated phase velocities are shown in Table 3.18. The phase velocities for the case of $r=1$ m do not show stable values up to the frequency of 4 Hz. In other experiments similar pattern was observed for frequencies below about 2 Hz. Apparently the higher phase velocities for this region cause relatively smaller phase shift to microtremors crossing the reference and the peripheral sites. The phase shift is not large enough to give stable correlation coefficients at low frequencies. It is interesting to notice that the frequency below which this instability is observed decreases with increasing the radius of the array, Table 3.18.

Figure 3.50 shows the phase velocity-depth profiles for the three experiments. The slopes of two of the velocity-depth profiles are very similar and are in a relatively good agreements with the slope of the third velocity-depth profile. This is expected since they all represent the same region. Two of the profiles suggest a low velocity layer at the possible depth of 40 m. Using the most representative break points for the phase velocity profiles, velocity models for a layered medium with two layers is constructed, Table 3.19.



Table 3.18. *The estimated phase velocities based on the CC-F data on Figures 3.47 to 3.49.*

	<i>r = 15 m</i>	<i>r = 27 m</i>	<i>r = 37 m</i>
<i>f</i> <i>Hz</i>	<i>Phase</i> <i>Velocity</i> <i>m/s</i>	<i>Phase</i> <i>Velocity</i> <i>m/s</i>	<i>Phase</i> <i>Velocity</i> <i>m/s</i>
.25	16	28	40
.75	49	90	137
1.25	82	189	319
1.75	156	296	741
2.25	209	466	982
2.75	282	612	1025
3.25	374	694	942
3.75	497	712	874
4.25	642	700	816
4.75	741	680	758
5.25	740	659	698
5.75	689	644	644
6.25	638	635	600
6.75	600	628	562
7.25	573	621	526
7.75	557	616	526
8.25	552	619	
8.75	554		
9.25	561		
9.75	564		
10.25	563		
10.75	559		
11.25	559		

Table 3.19. *The phase velocity and shear wave velocity for layered medium based on the phase velocity-depth profile on Figure 3.50.*

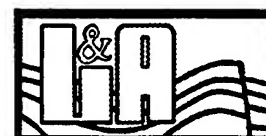
<i>Depth</i> <i>m</i>	<i>Phase Velocity</i> <i>m/s</i>	β <i>m/s</i>
< 20	600	667
<40	466	518



> 40	1177	1310
------	------	------

Figure 3.51 shows the plot of the simulated phase velocities, the top curve on the figure, for the above model. The bottom curve shows the phase velocities for a similar model except that moving the boundary of the second layer to the depth of 50 m. The simulated phase velocities for these model are in good agreements with the calculated phase velocities. The estimated shear wave velocity profile for the site certainly supports the stiff soil/bedrock site characterization.

Figures 3.52 to 3.54 show the CC-F curves for the radial and tangential components of microtremors for the cases of $r = 15, 27$, and 37 m. The CC-F curves for the radial and tangential components show remarkable similarities with each other and with the CC-F curves for the vertical components of the ground motions. As was discussed earlier this can be the case if the horizontal components of microtremors consist of waves equally polarized parallel and perpendicular to their direction of propagation.



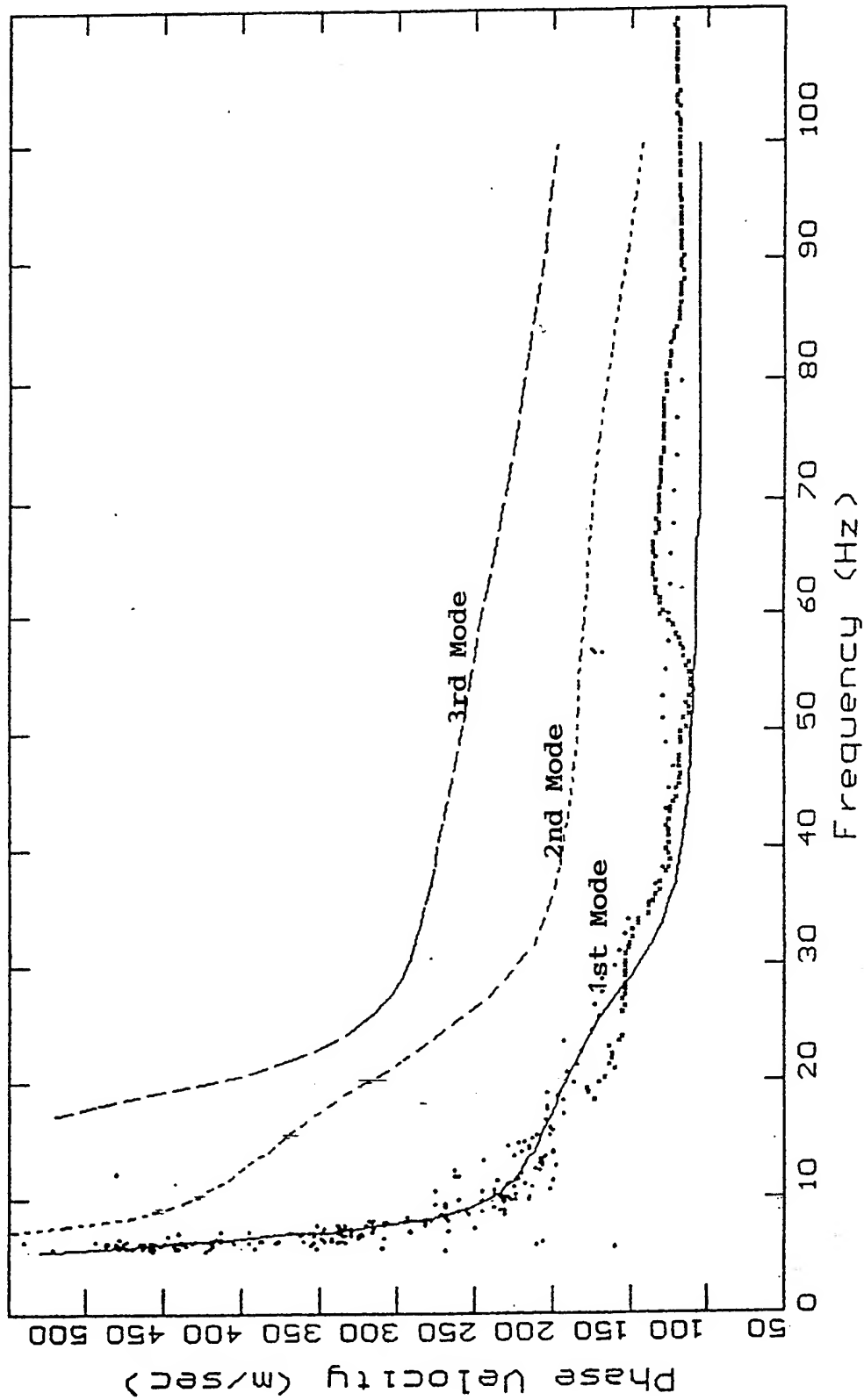


Figure 3.1. The observed, dots, and simulated dispersion curves for the first three modes of Rayleigh waves for the parking lot of St. Aidams Episcopal Church. This figure is from the VIC report.



VortexRock Consultants, Inc.

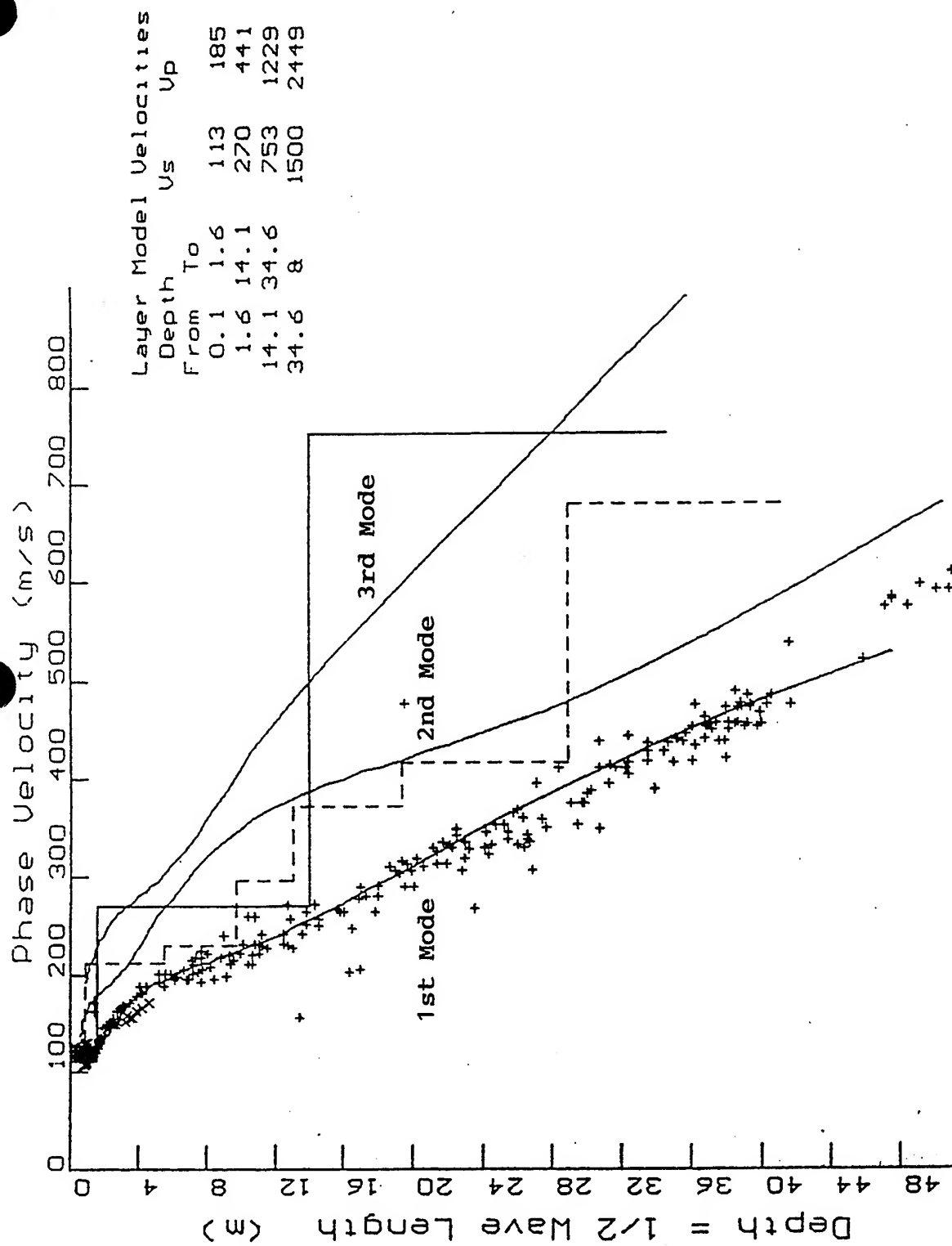


Figure 3.2. Plots of the phase velocity-depth profiles based on the observed and simulated data. The continuous lines are based on the simulated phase velocities on Figure 3.1. This figure is from the VIC report.



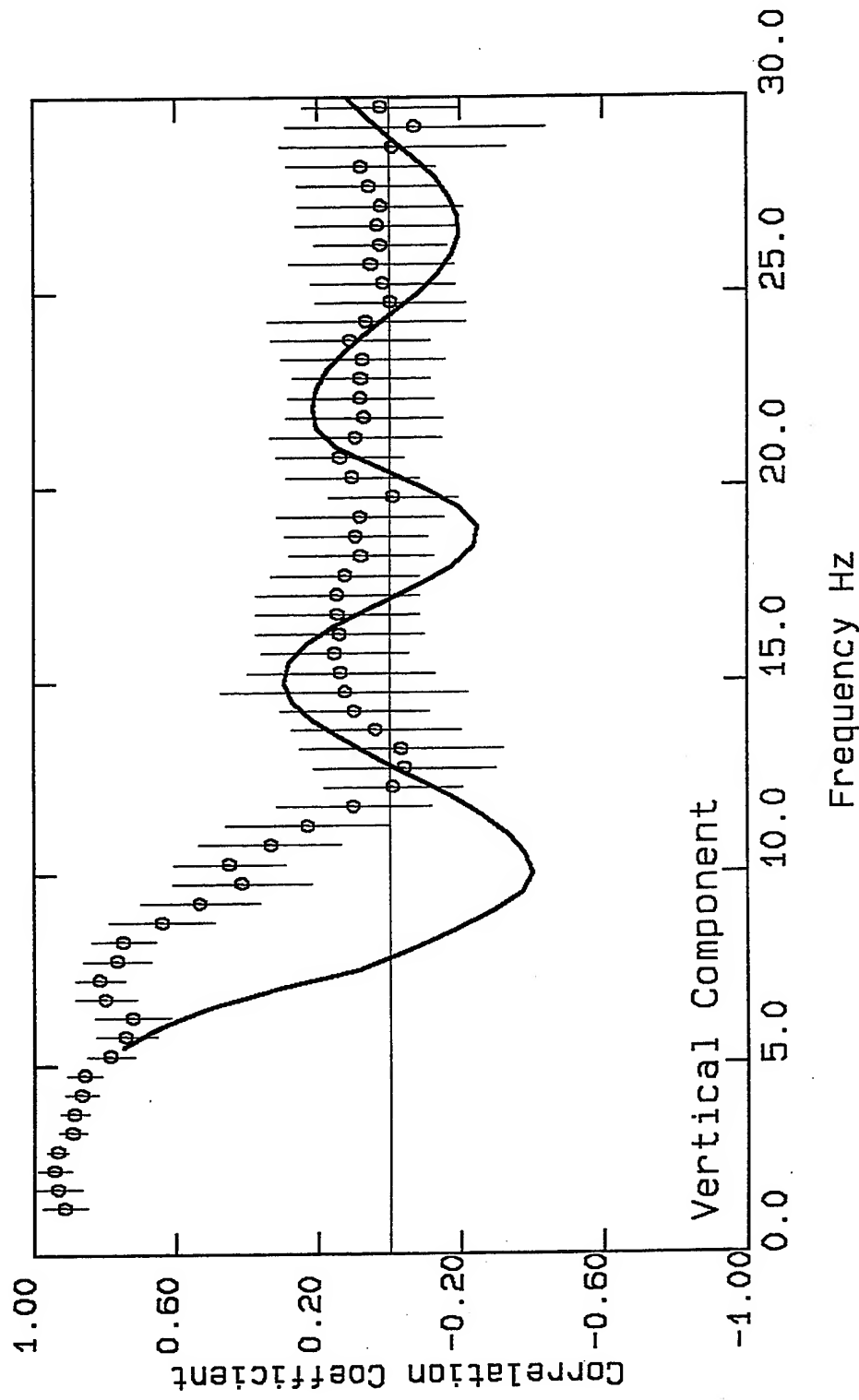
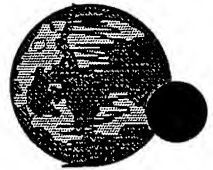


Figure 3.3. The CC-F values from the Circular Array experiment with $r = 15$ m. The solid line shows the expected pattern for the CC-F values based on the phase velocities from the VIC report.



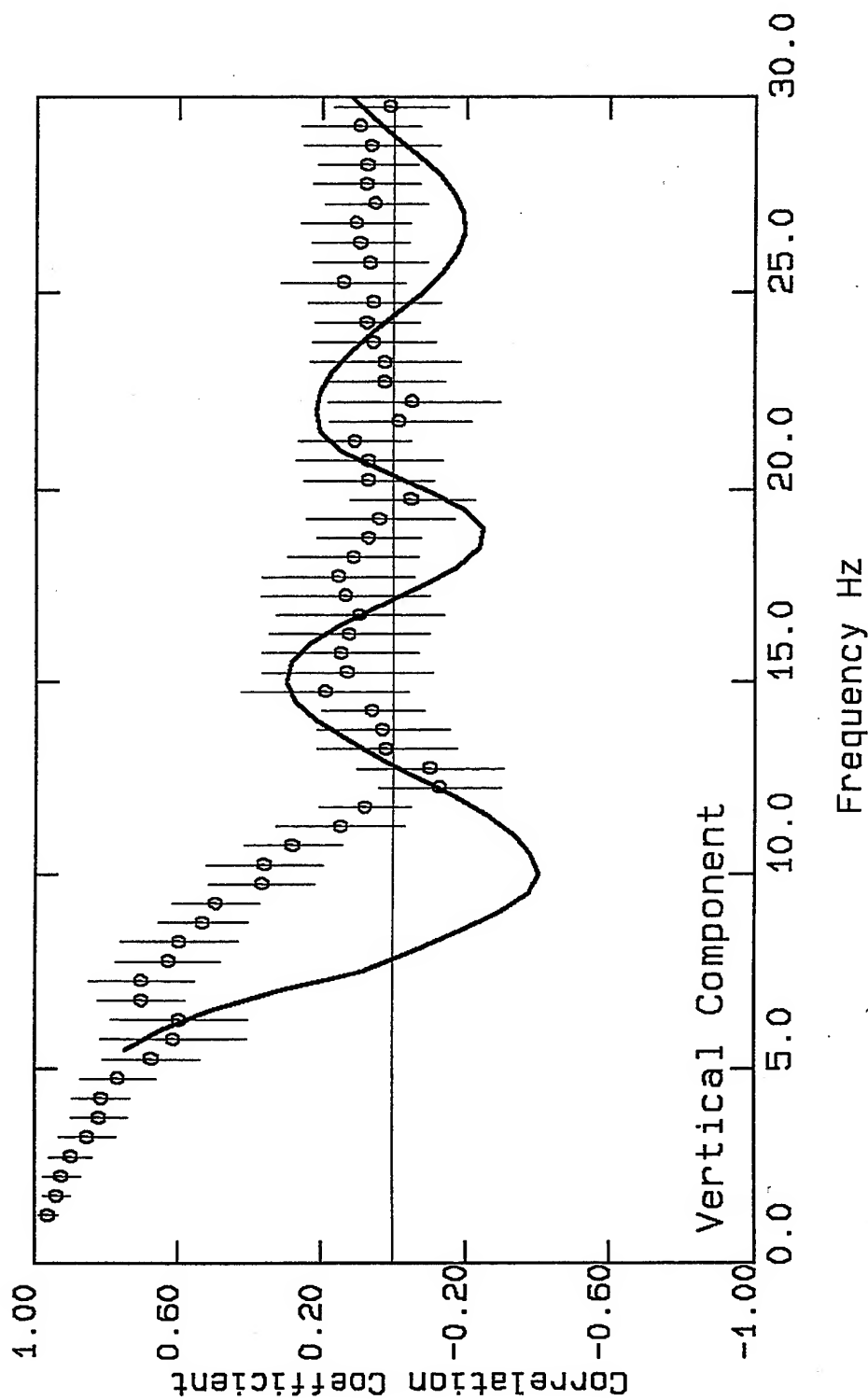


Figure 3.4. Similar to Figure 3.3 except that the data for this figure was collected at a different day.



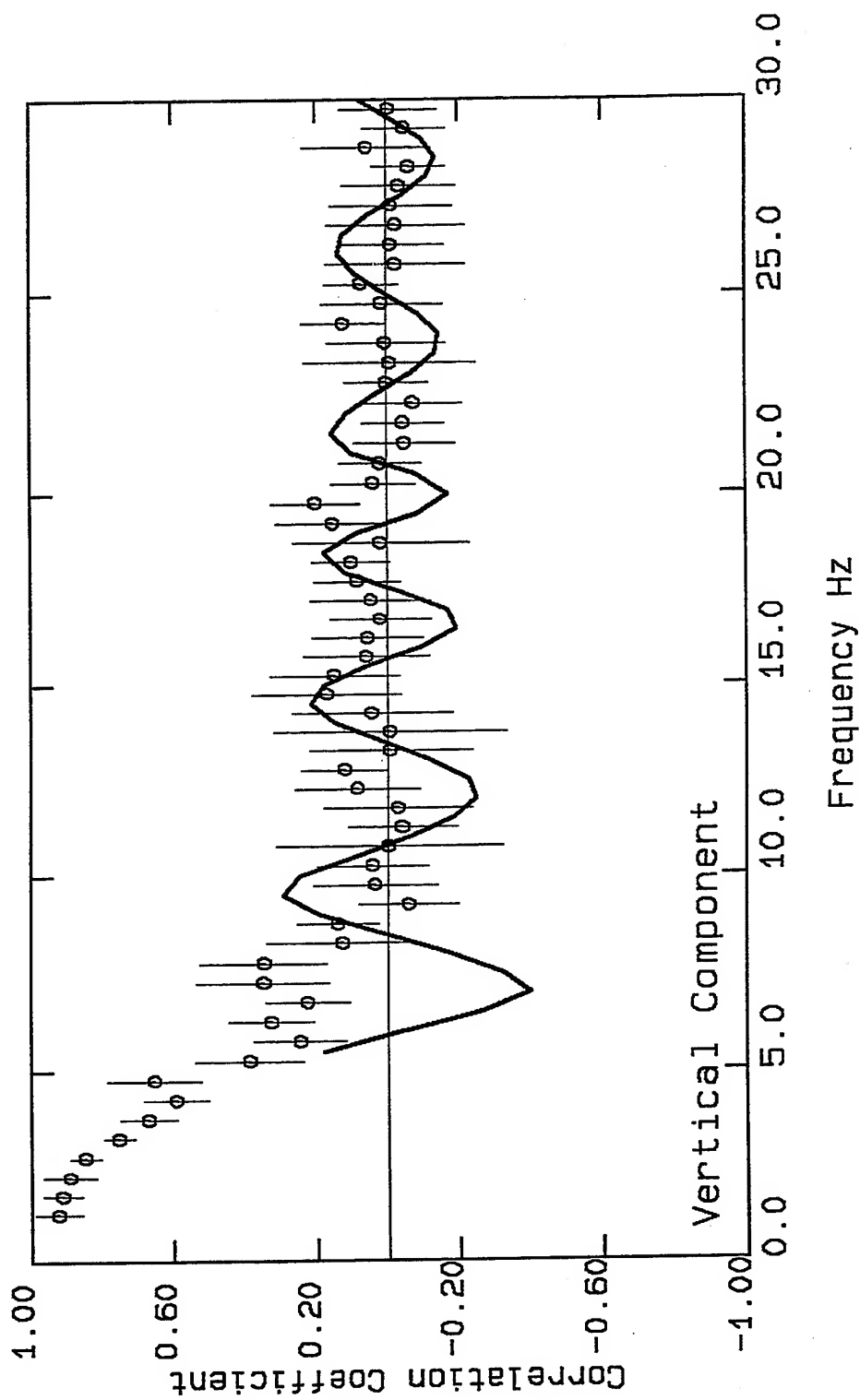


Figure 3.5. The CC-F values from the Circular Array experiment with $r = 27$ m. The solid line shows the expected pattern for the CC-F values based on the phase velocities from the VIC report.



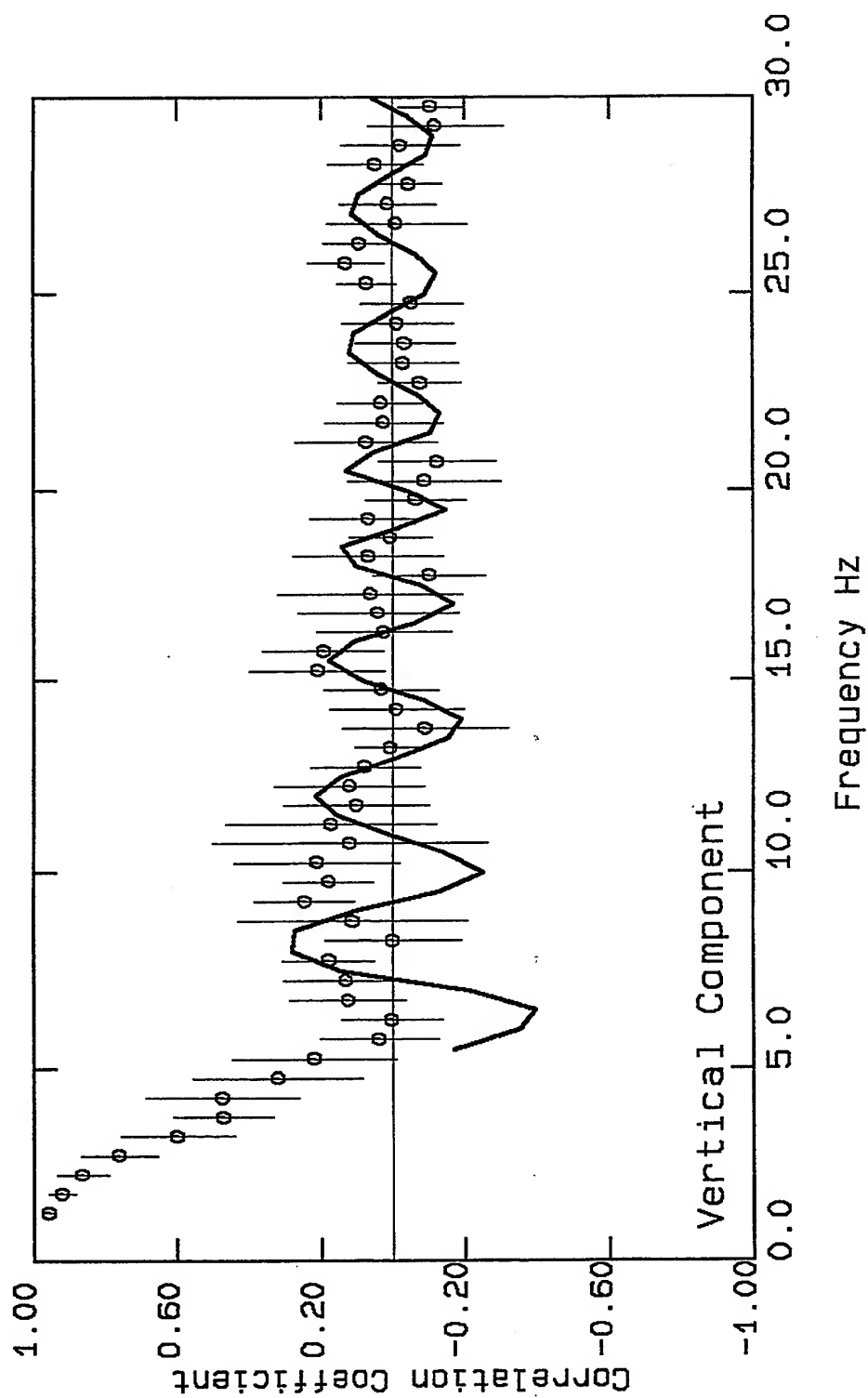


Figure 3.6. The CC-F values from the Circular Array experiment with $r = 37$ m. The solid line shows the expected pattern for the CC-F values based on the phase velocities from the VIC report.



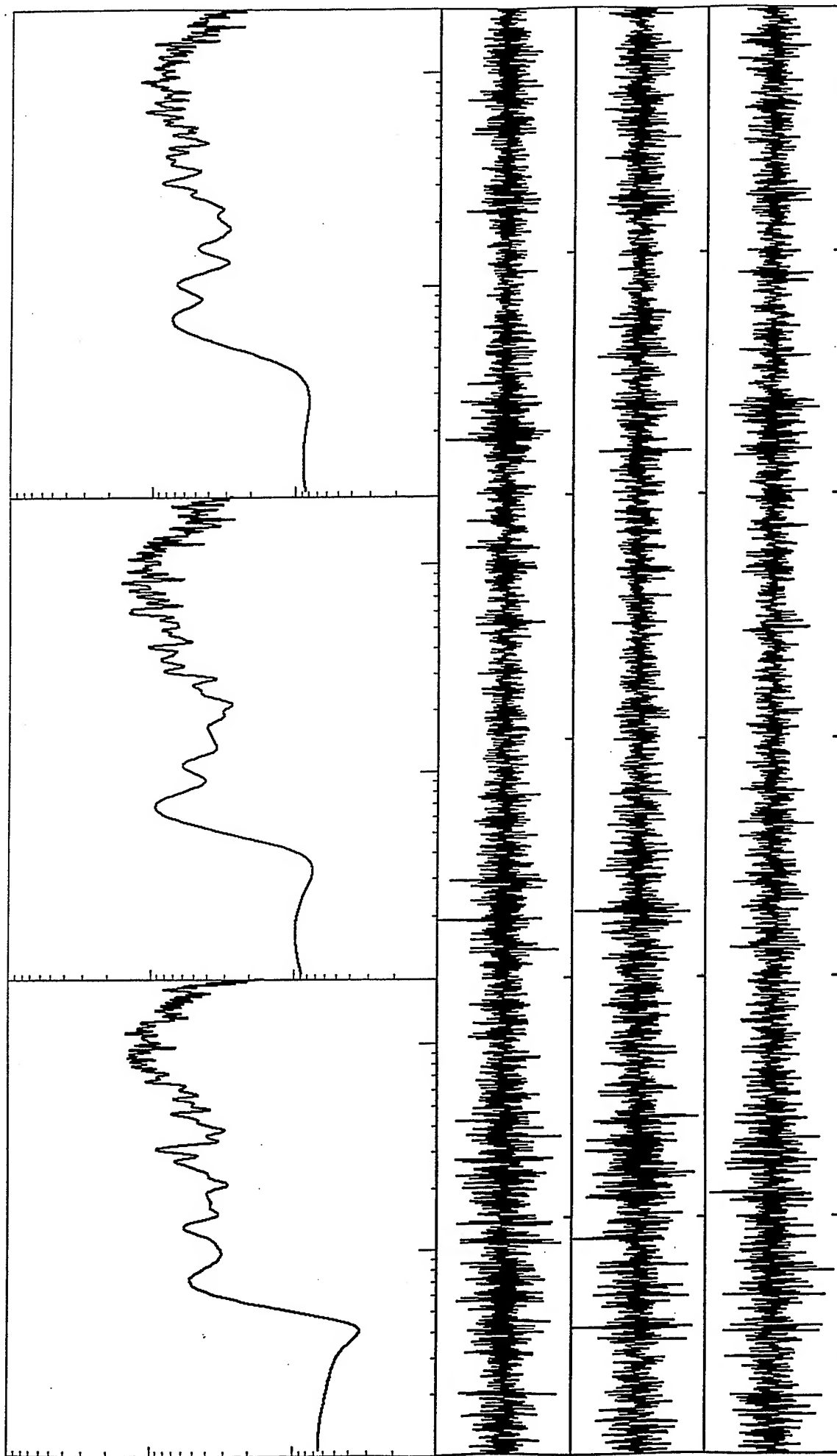


Figure 3.7.a. Typical examples of the ground motion time histories and response spectra of the cases with the least amount of disturbances from traffic on PCH.



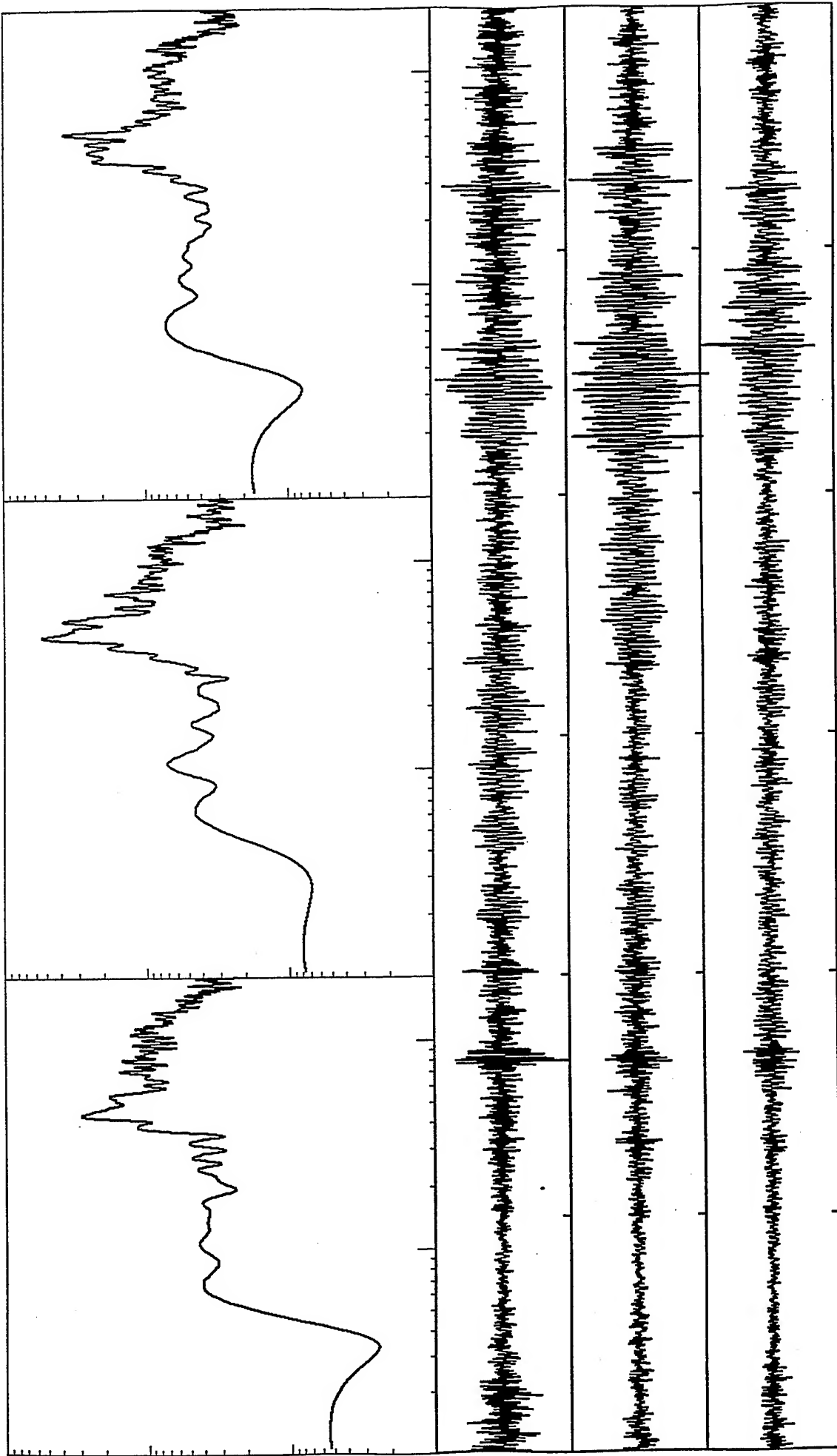


Figure 3.7.b. Typical examples of the ground motion time histories and response spectra showing the disturbances from traffic on PCH.



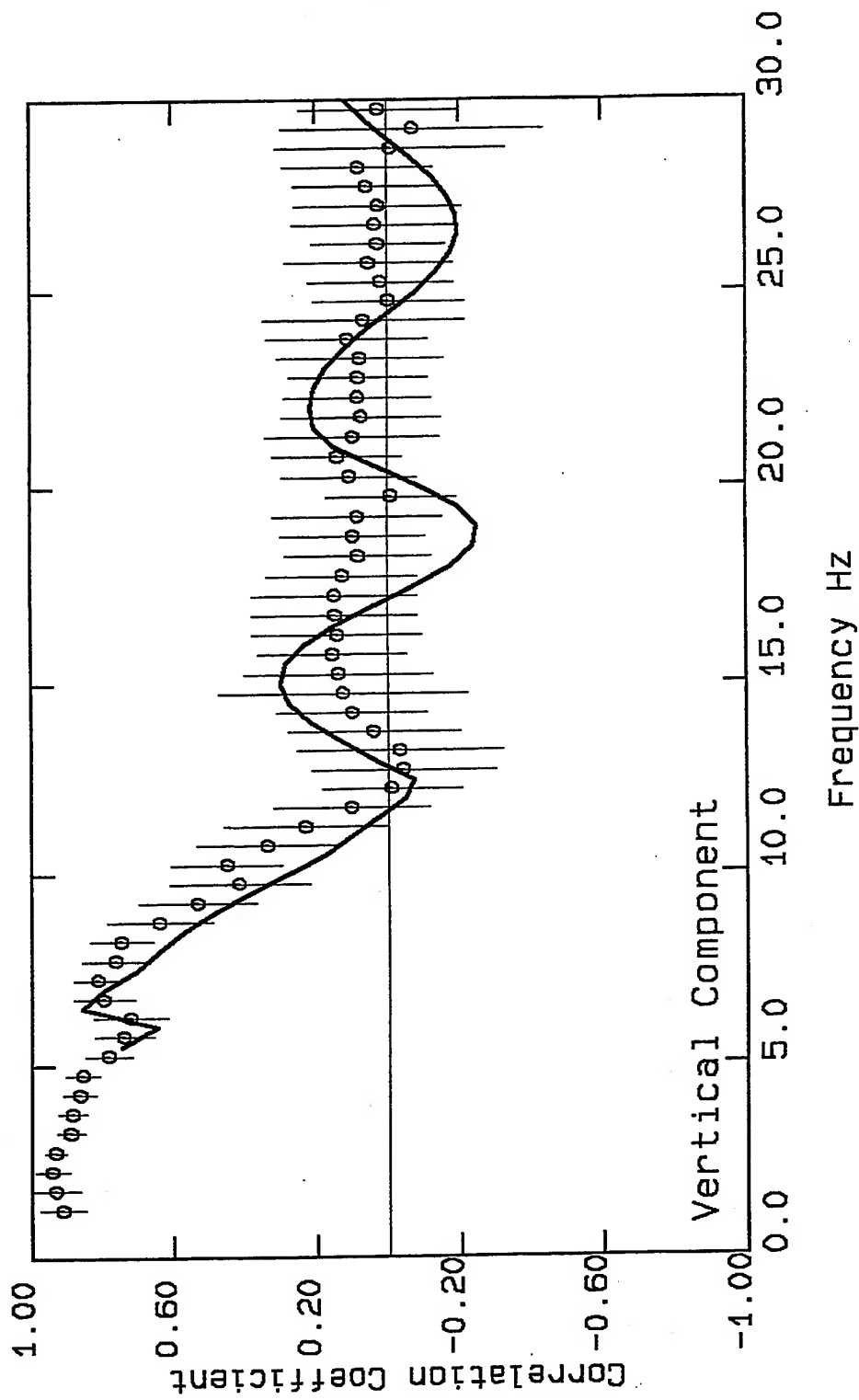
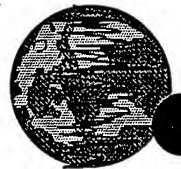


Figure 3.8. Similar to Figure 3.3 except that the expected pattern, $J_0(r \cdot \omega / C(\omega))$, for the frequency range of 6.5 to 12 Hz are modified to reflect reduction in r or increase in $C(\omega)$ with the total effect of 50% reduction in $r / C(\omega)$.



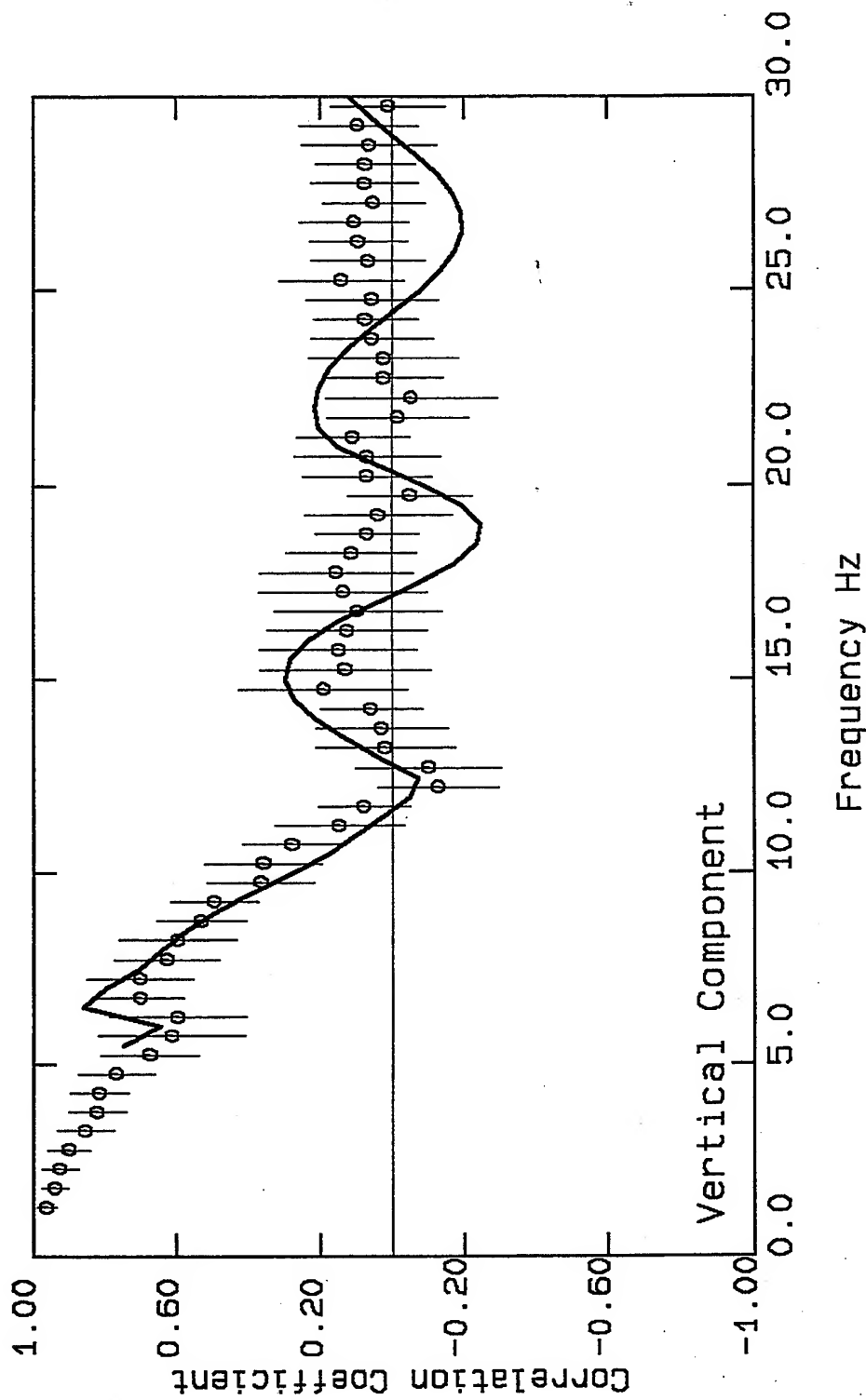


Figure 3.9. Similar to Figure 3.4 except that the expected pattern, $J_0(r \cdot \omega / C(\omega))$, for the frequency range of 6.5 to 12 Hz are modified to reflect reduction in r or increase in $C(\omega)$ with the total effect of 50% reduction in $r / C(\omega)$.



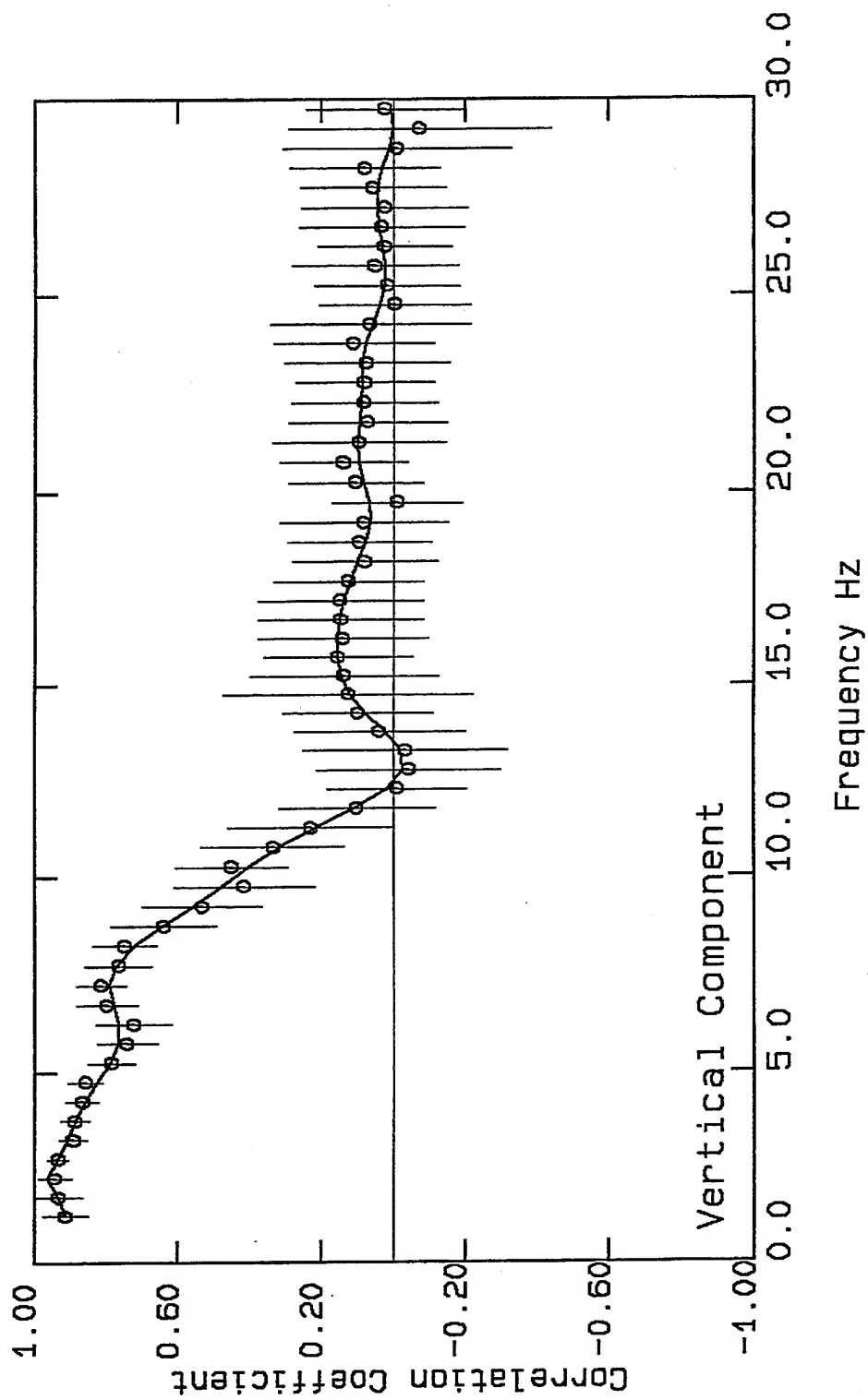


Figure 3.10. The best fit to the CC-F values for the case of $r = 15$ m, Figure 3.3.



VortexRock Consultants, Inc.

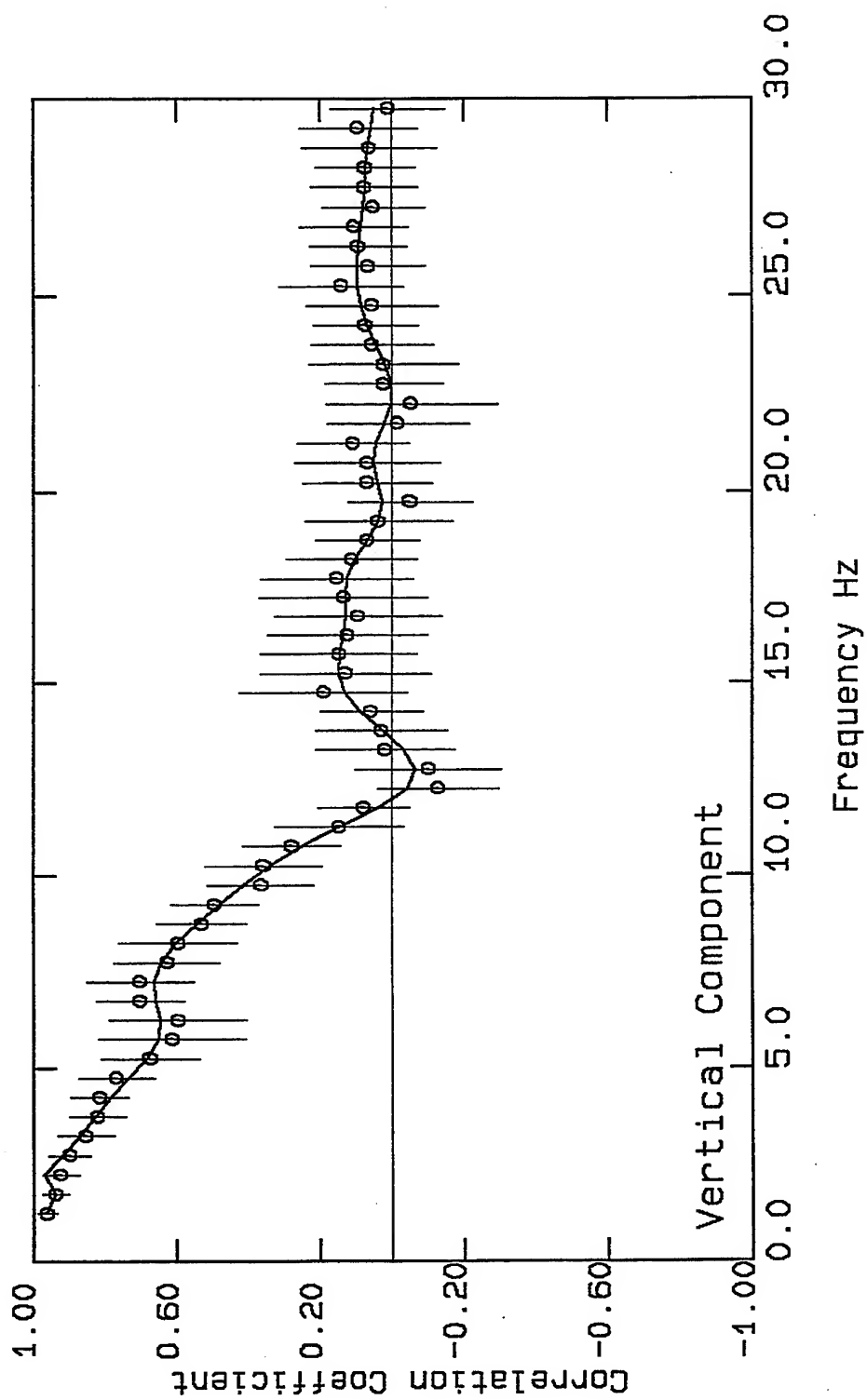


Figure 3.11. The best fit to the CC-F values for the case of $r = 15$ m, Figure 3.4.



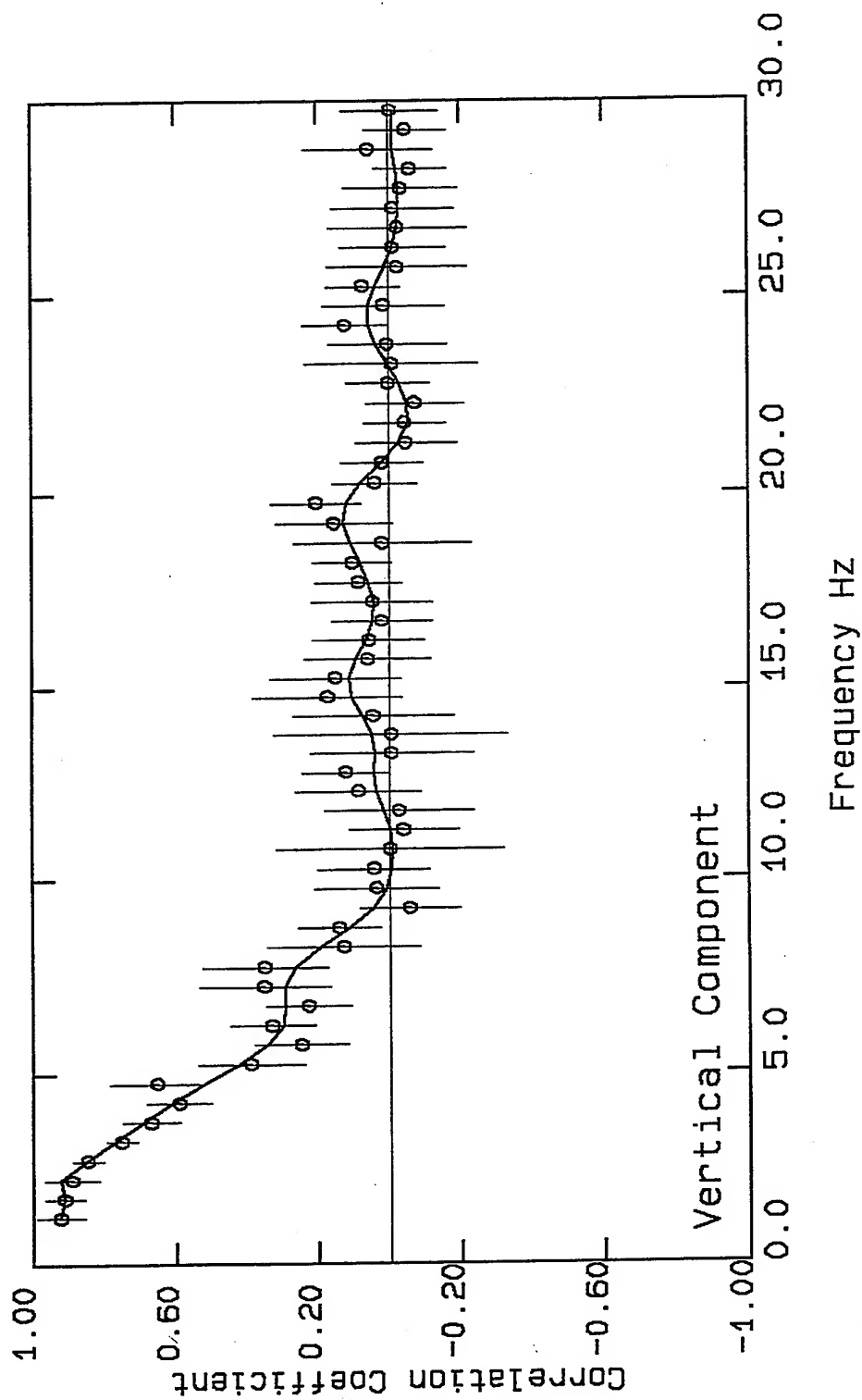


Figure 3.12. The best fit to the CC-F values for the case of $r = 27$ m, Figure 3.5.



VortexRock Consultants, Inc.

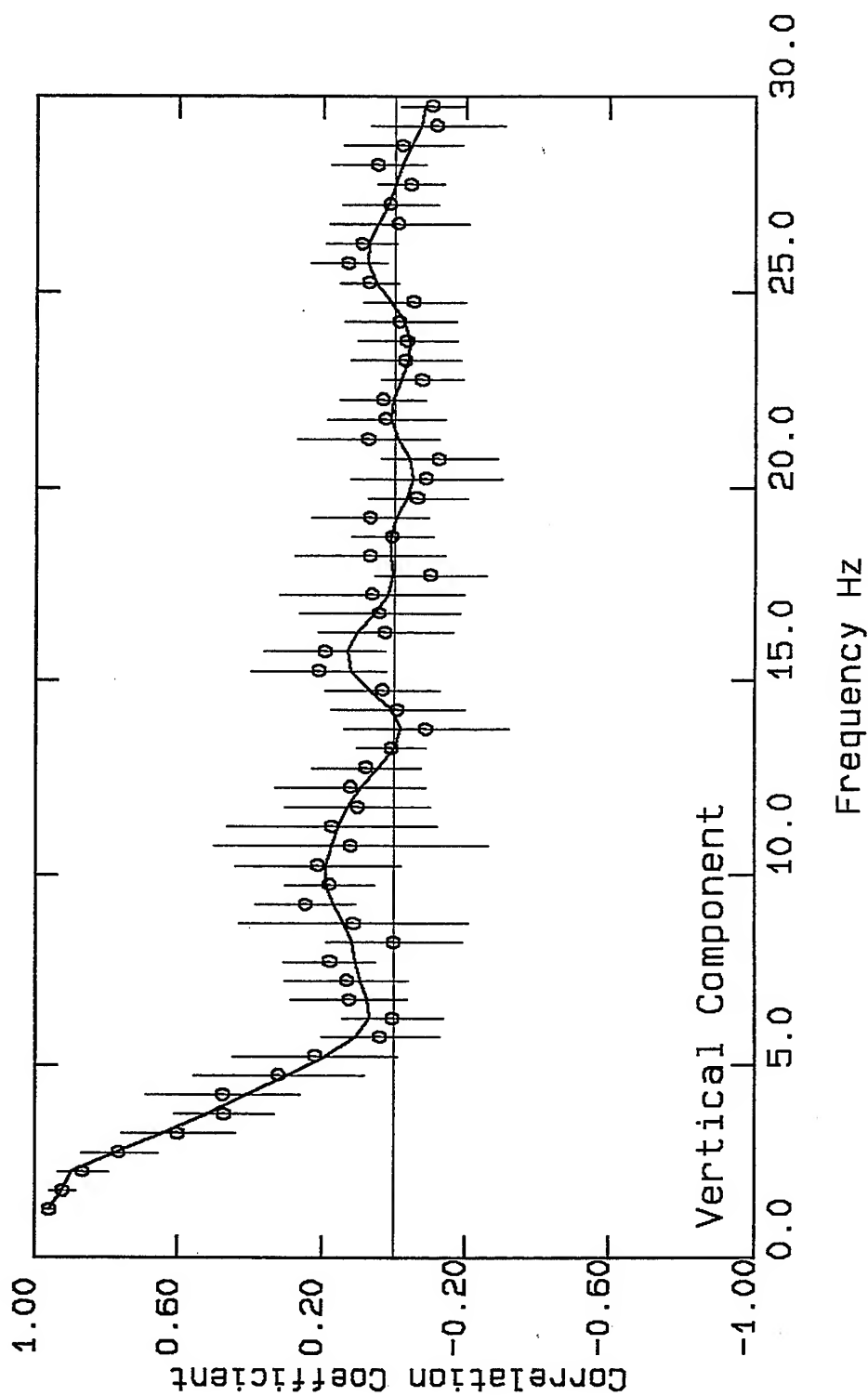


Figure 3.13. The best fit to the CC-F values for the case of $r = 37$ m, Figure 3.6.



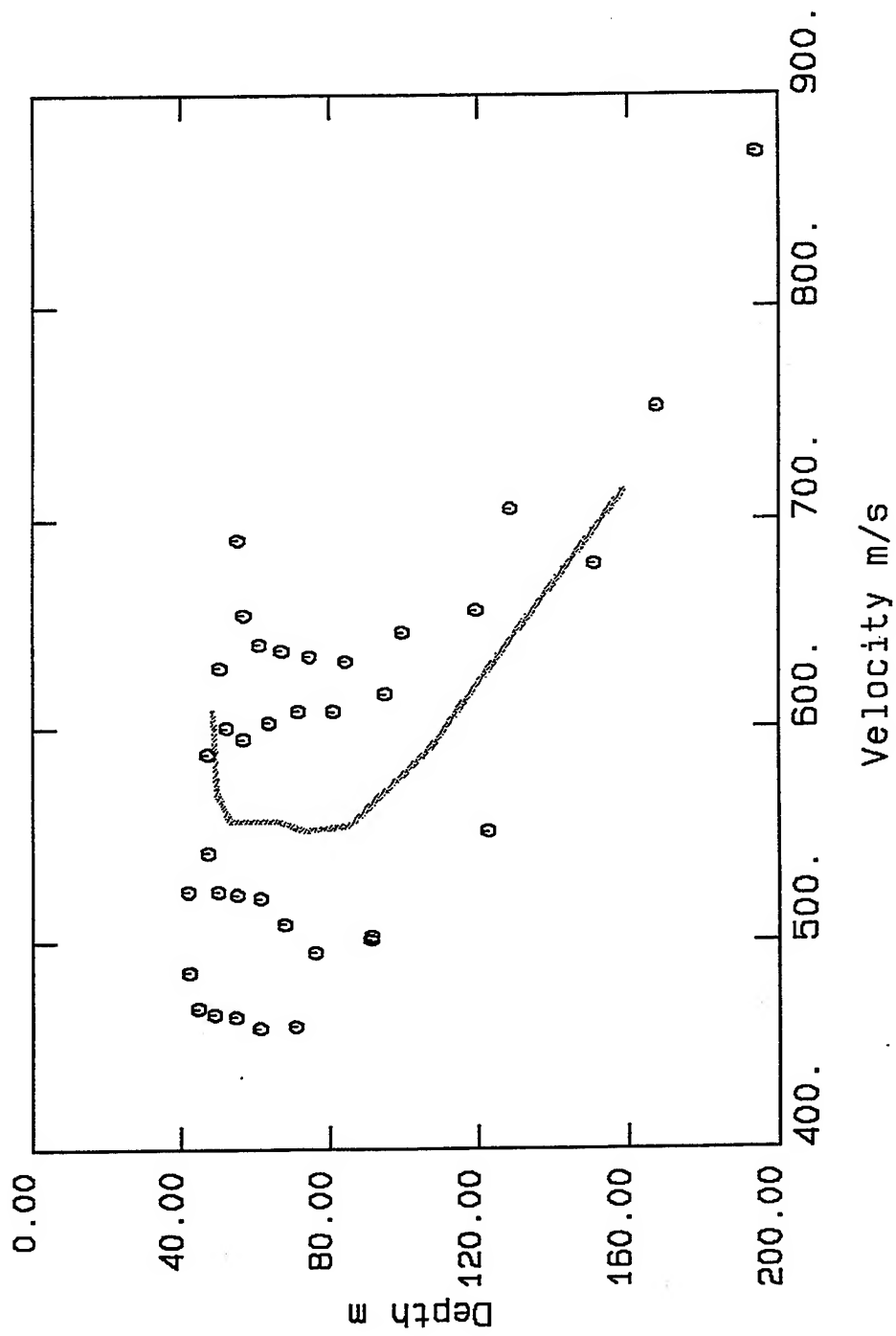


Figure 3.14. Plots of the phase velocities versus depth corresponding to the data on Figures 3.10 to 3.13. The effective depths are calculated as half the wavelengths for the given frequencies and velocities in Table 3.1.



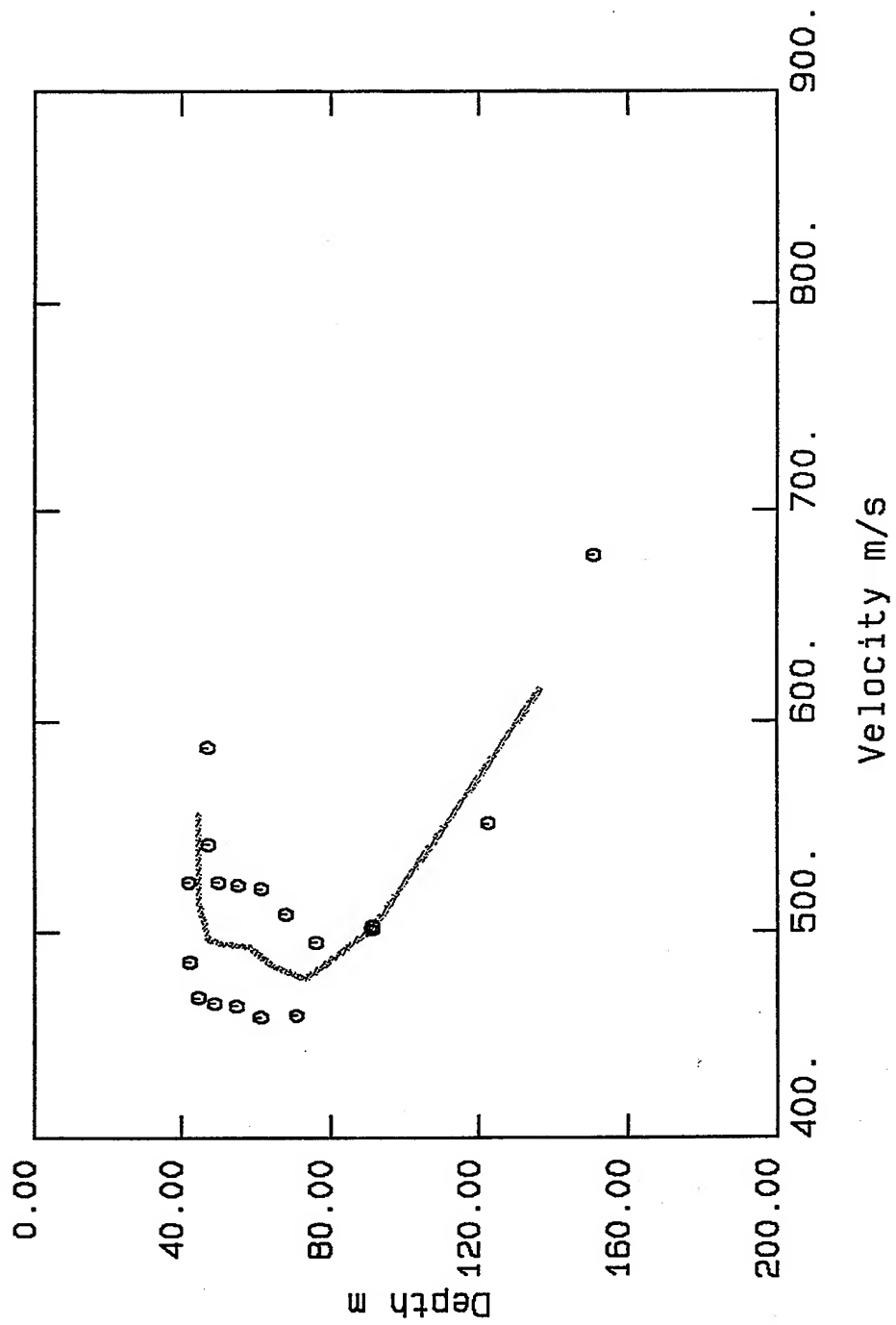


Figure 3.15 Plots of the phase velocities versus depth corresponding to the data on Figures 3.10 and to 3.11 for the two cases of $r = 15$ m.



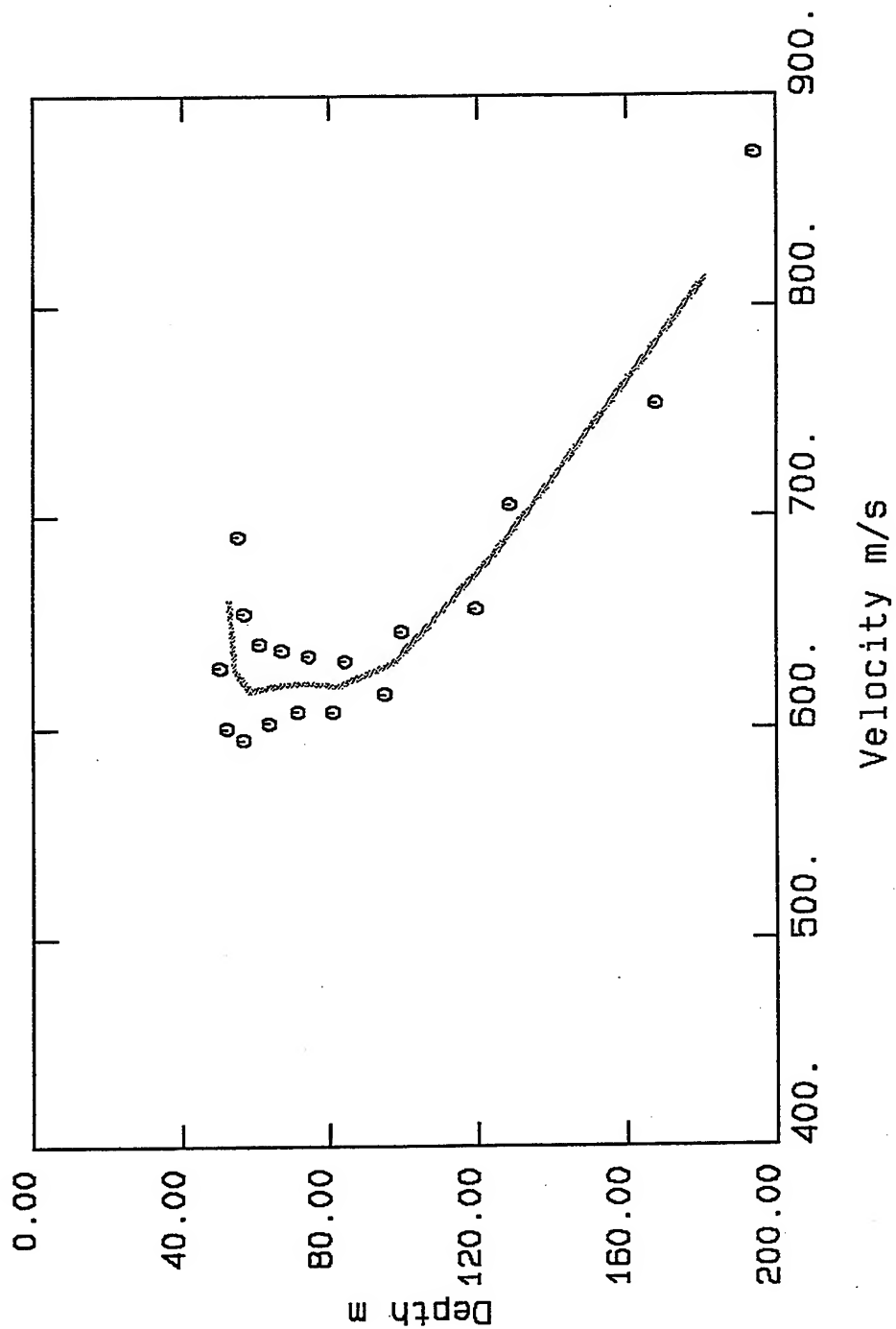
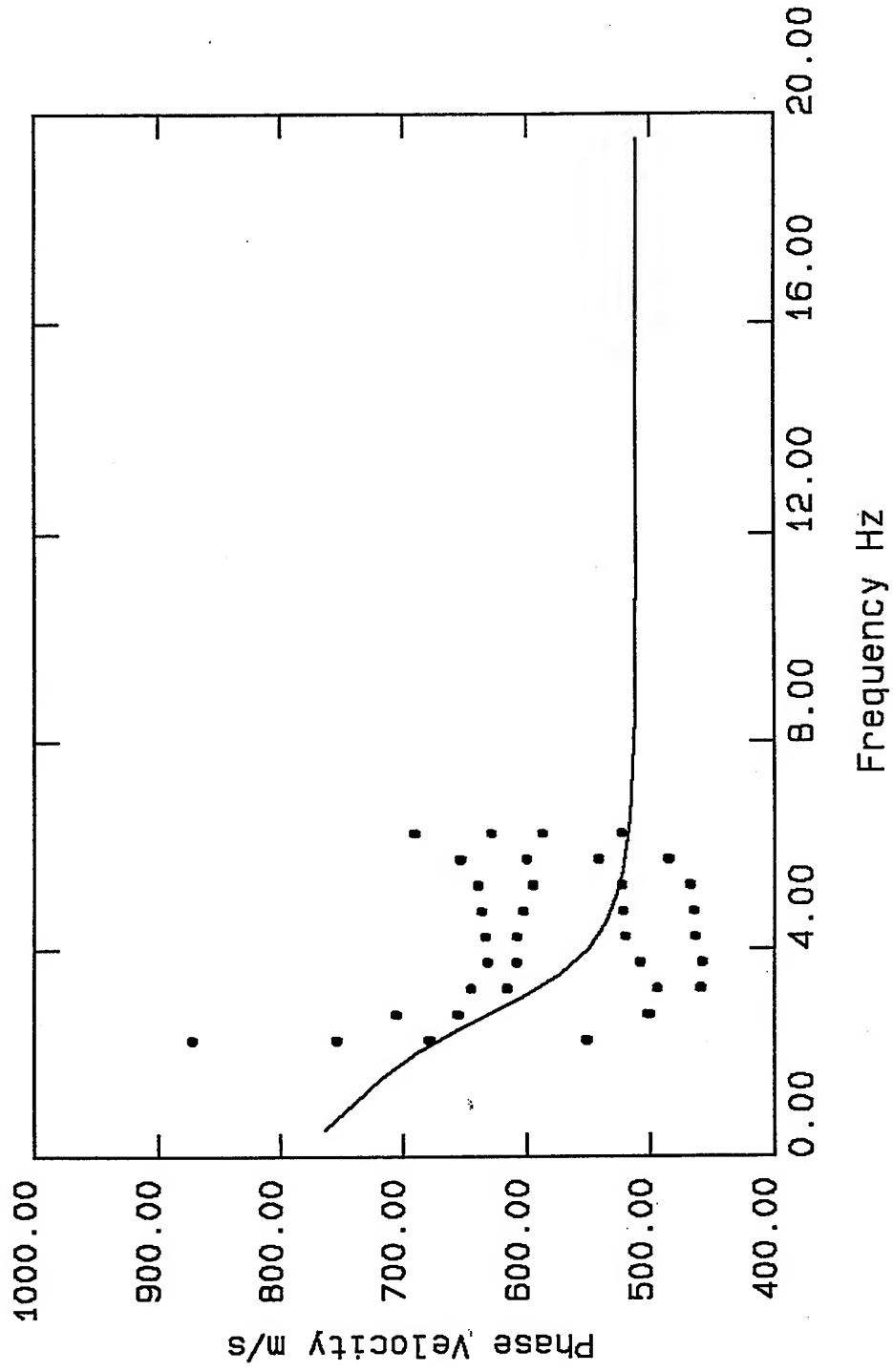


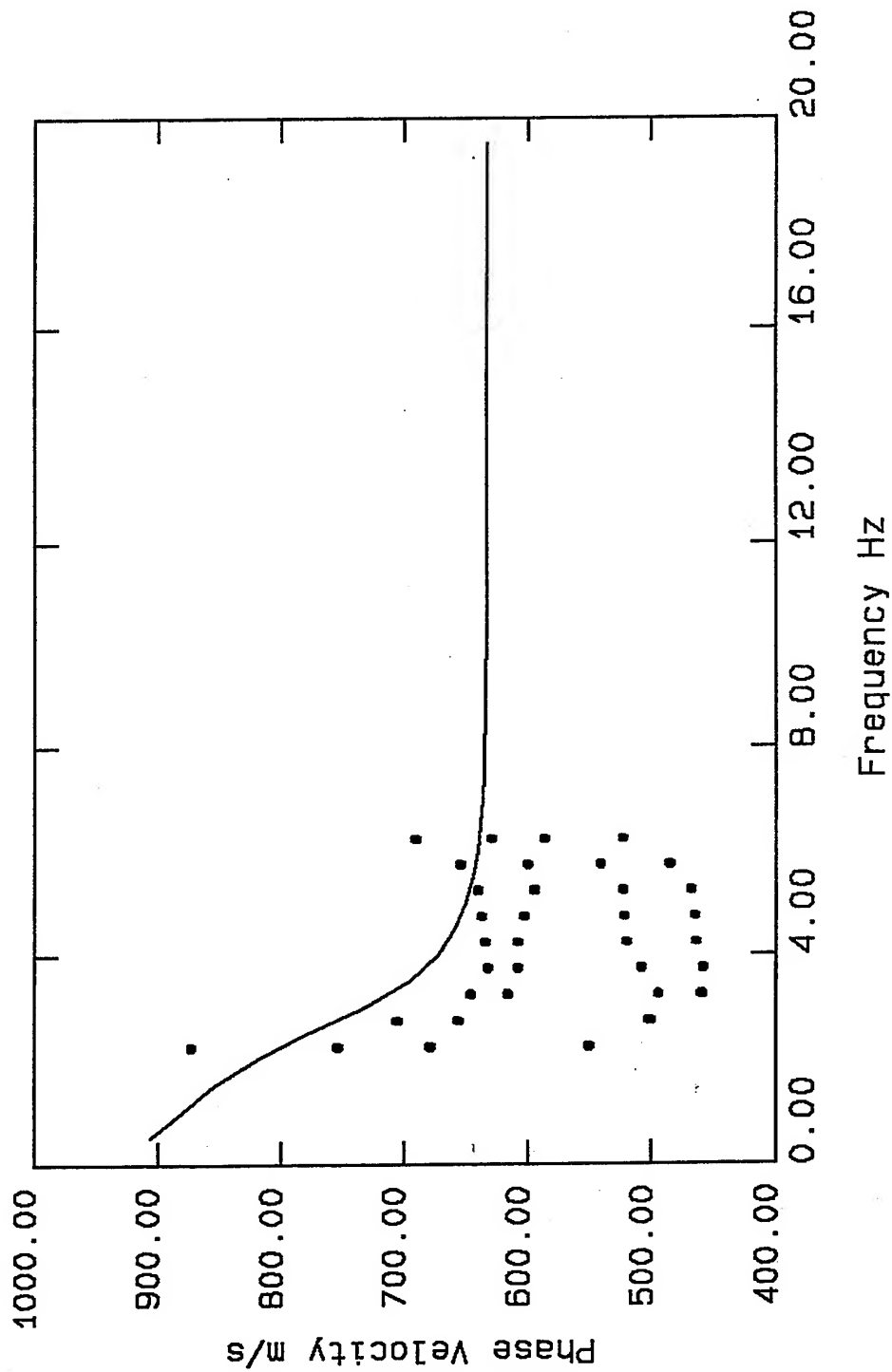
Figure 3.16 Plots of the phase velocity-depth profiles corresponding to the data on Figures 3.12 and to 3.13 for the two cases of $r = 27$ and 37 m.





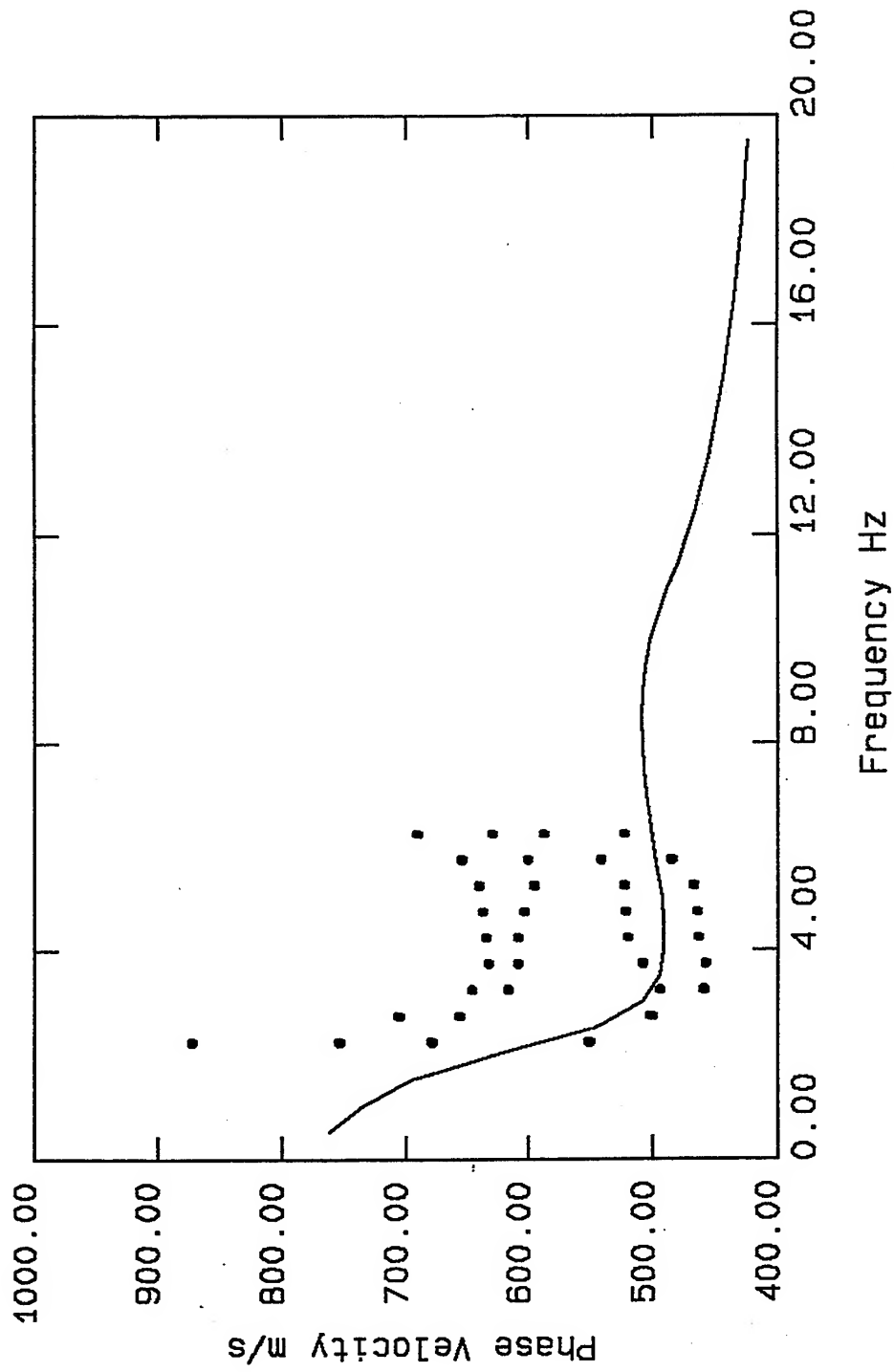
Figures 3.17. Plots of the calculated and simulated phase velocities corresponding to the velocity-depth profiles in Tables 3.3. The calculated phase velocities for all cases are shown.





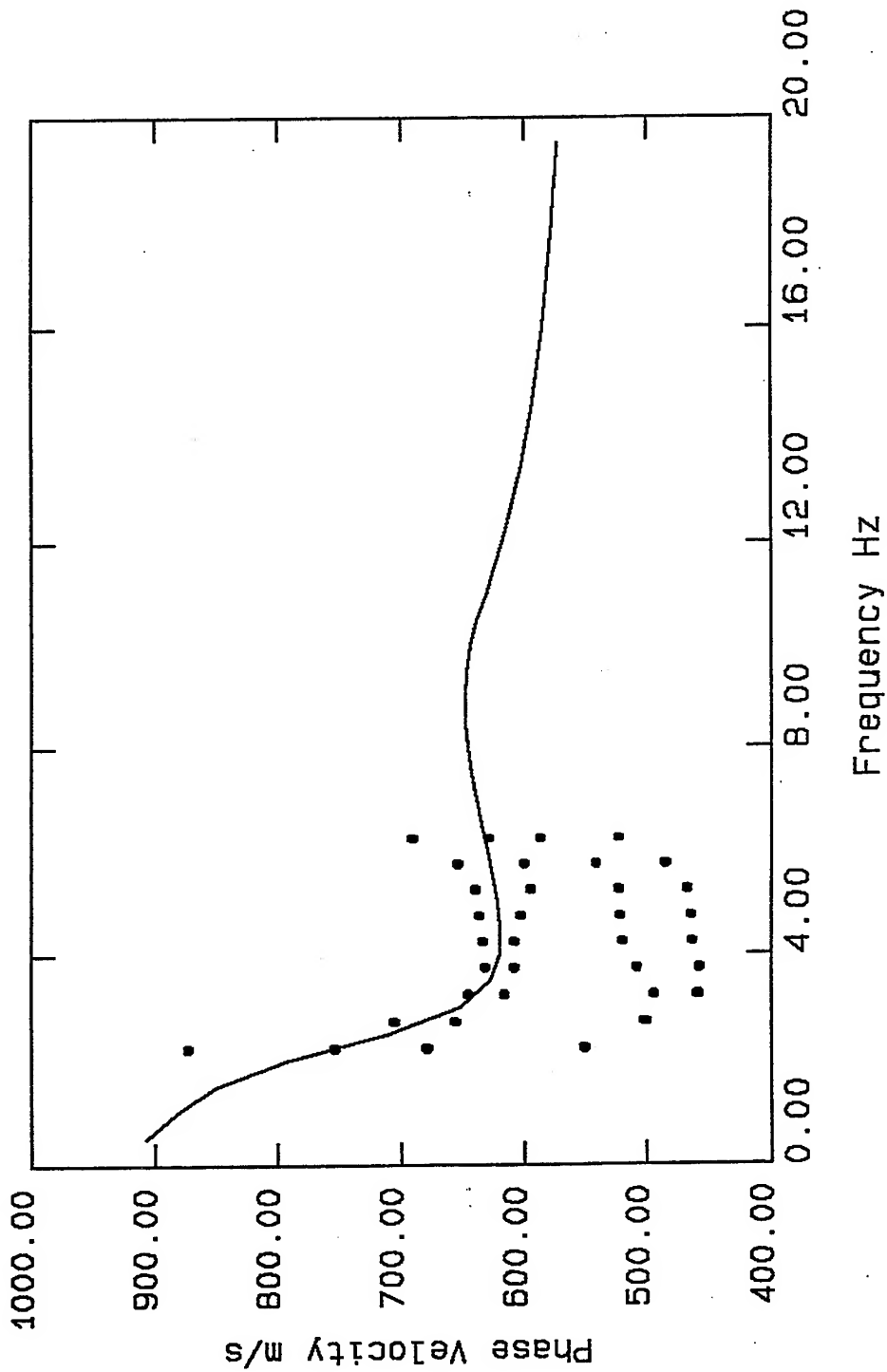
Figures 3.18. Plots of the calculated and simulated phase velocities corresponding to the velocity-depth profiles in Tables 3.4. The calculated phase velocities for all cases are shown.





Figures 3.19. Plots of the calculated and simulated phase velocities corresponding to the velocity-depth profiles in Tables 3.5. The calculated phase velocities for all cases are shown.





Figures 3.20. Plots of the calculated and simulated phase velocities corresponding to the velocity-depth profiles in Tables 3.6. The calculated phase velocities for all cases are shown.



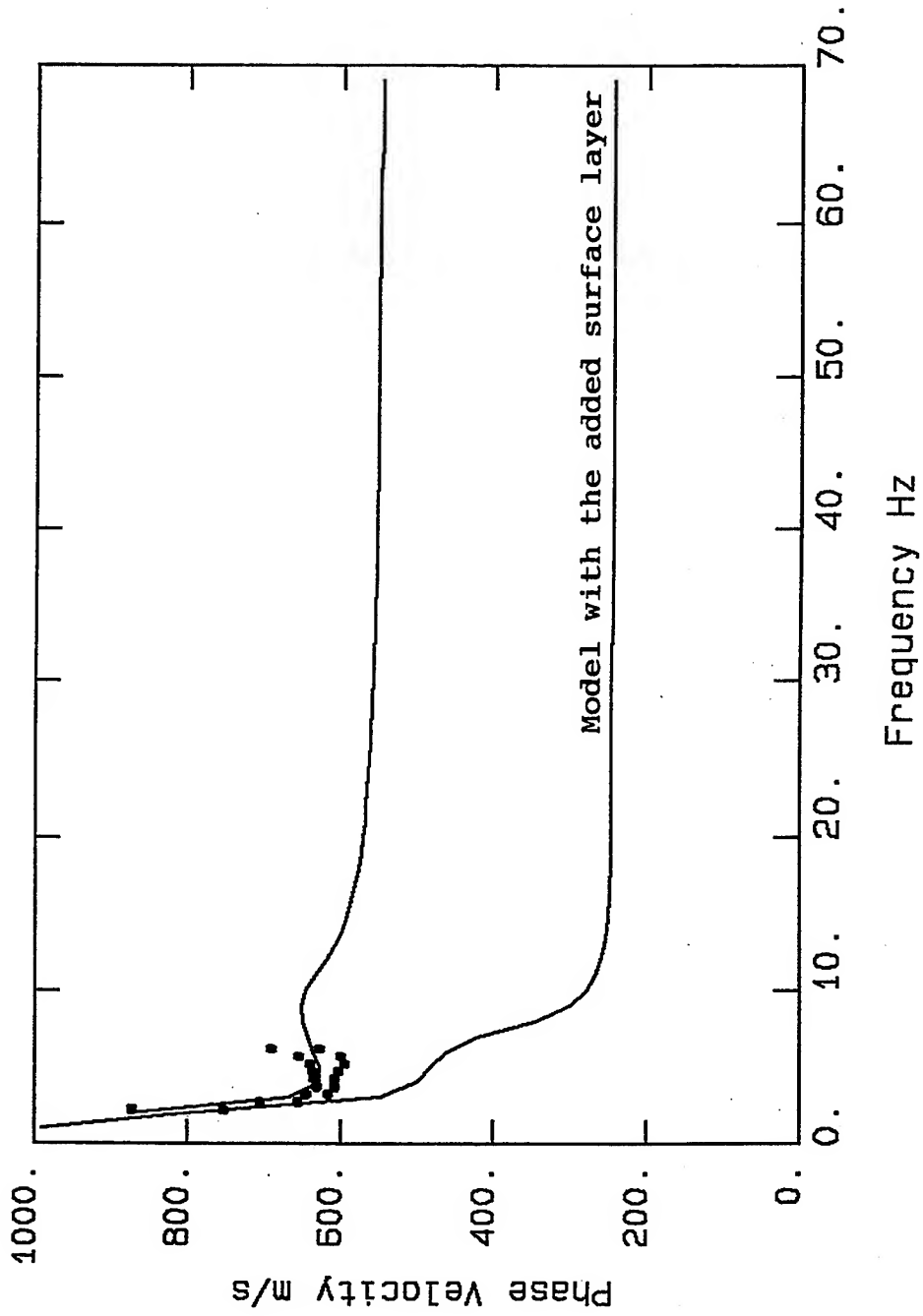


Figure 3.21. Plots of two simulated phase velocities showing the effects of adding a surface layer with the depth of 14 m with the shear wave velocity of 270 m/s, as suggested by the VIC's velocity-depth profile, to the model in Table 3.6.



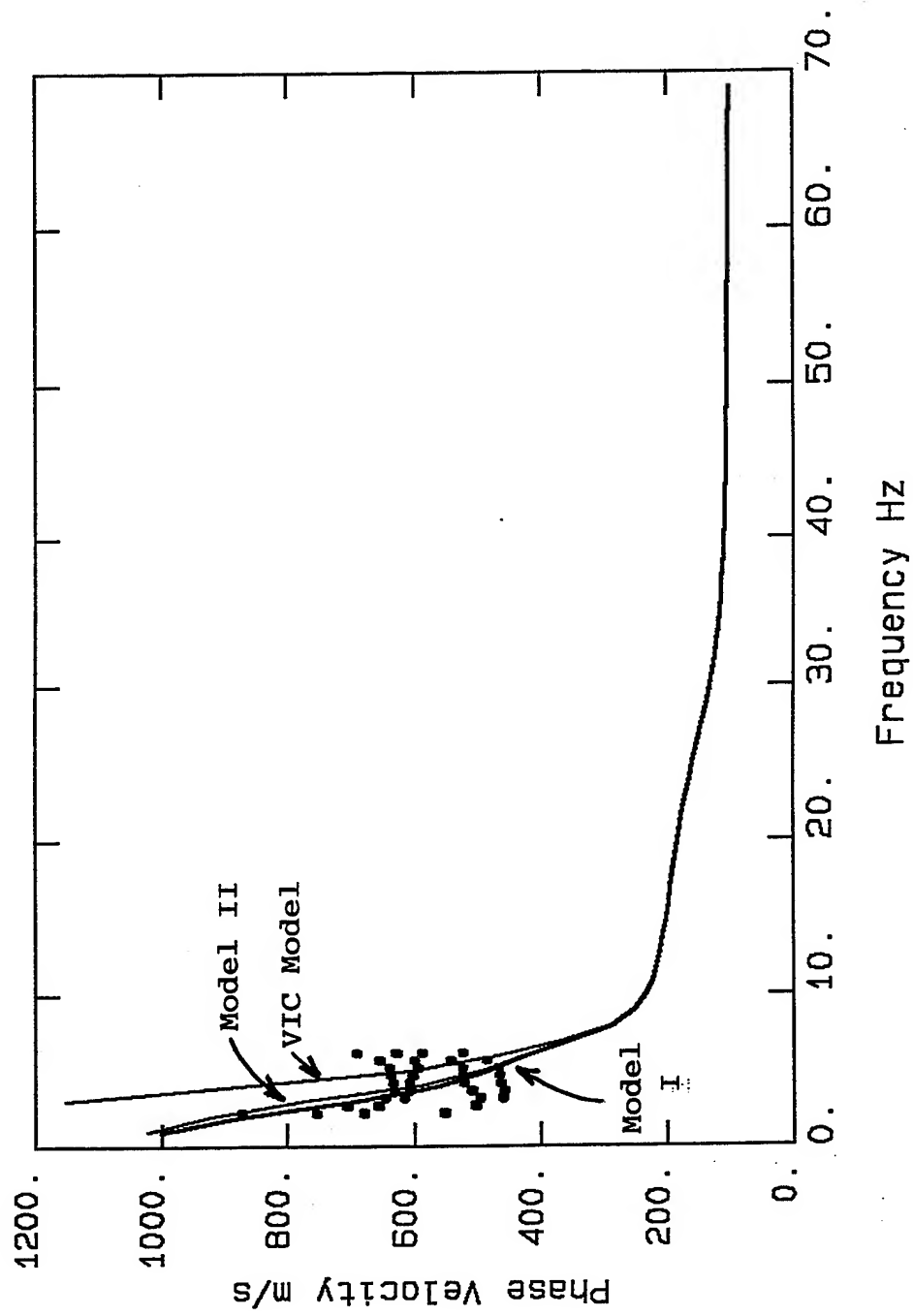
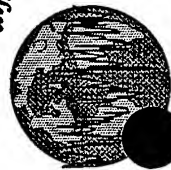
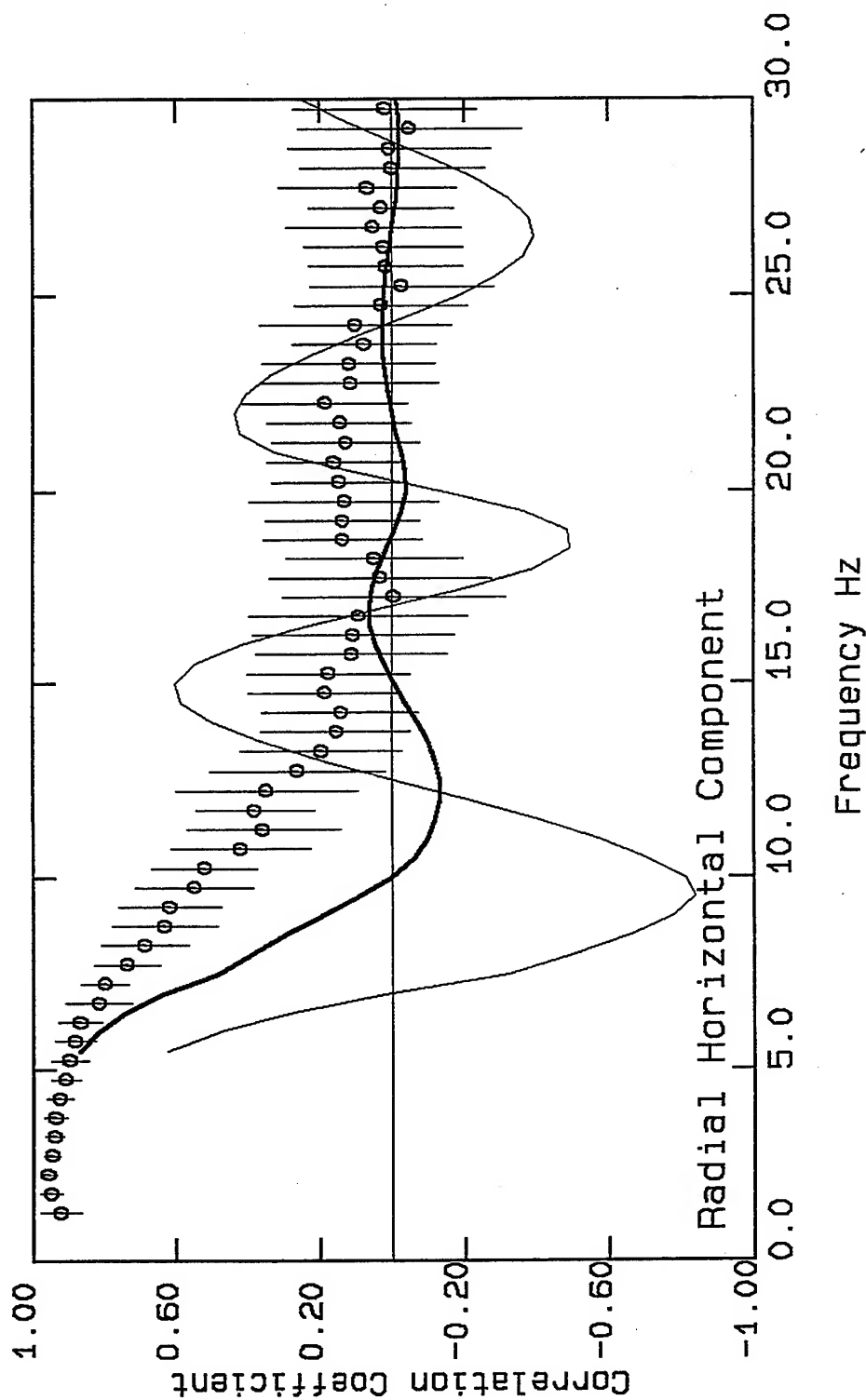


Figure 3.22. Plots of the first mode-phase velocities for three velocity-depth profiles in Table 3.7. The phase velocities are different at low frequency ranges below about 5 Hz. However, there are no significant differences between the phase velocities for frequencies above 5 Hz where all VIC phase velocity data exist.





Figures 3.23.a. Plots of the CC-F values for the radial components of microtremors for the case of $r = 15$ m. The thick and thin solid lines on these figures show the expected patterns for the radial and tangential components, equations (2.22) to (2.25), depending upon the predominant direction of polarization for the horizontal components of microtremors.



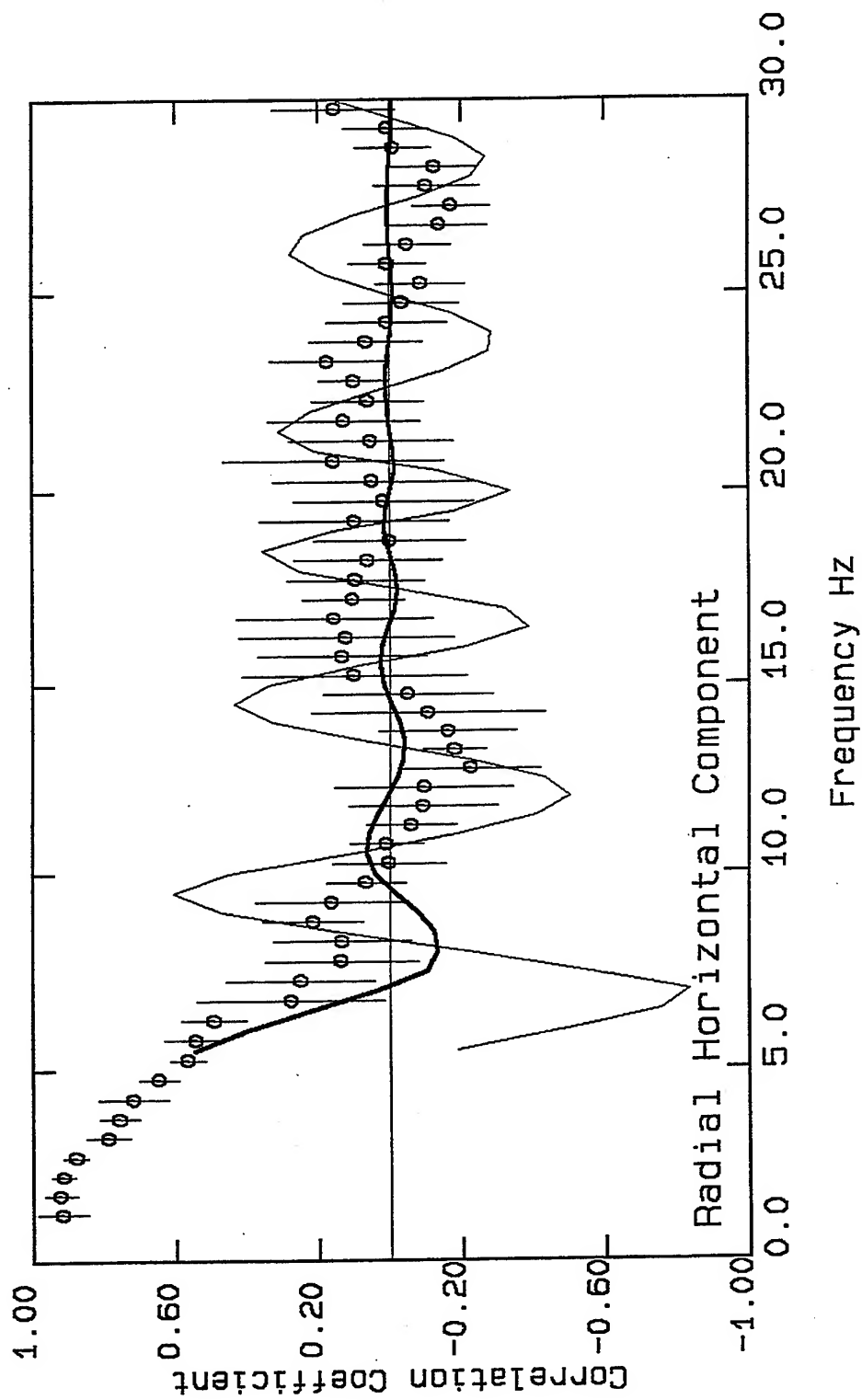


Figure 3.23.b. Similar to Figure 2.23.a but for the case of $r = 27$ m.



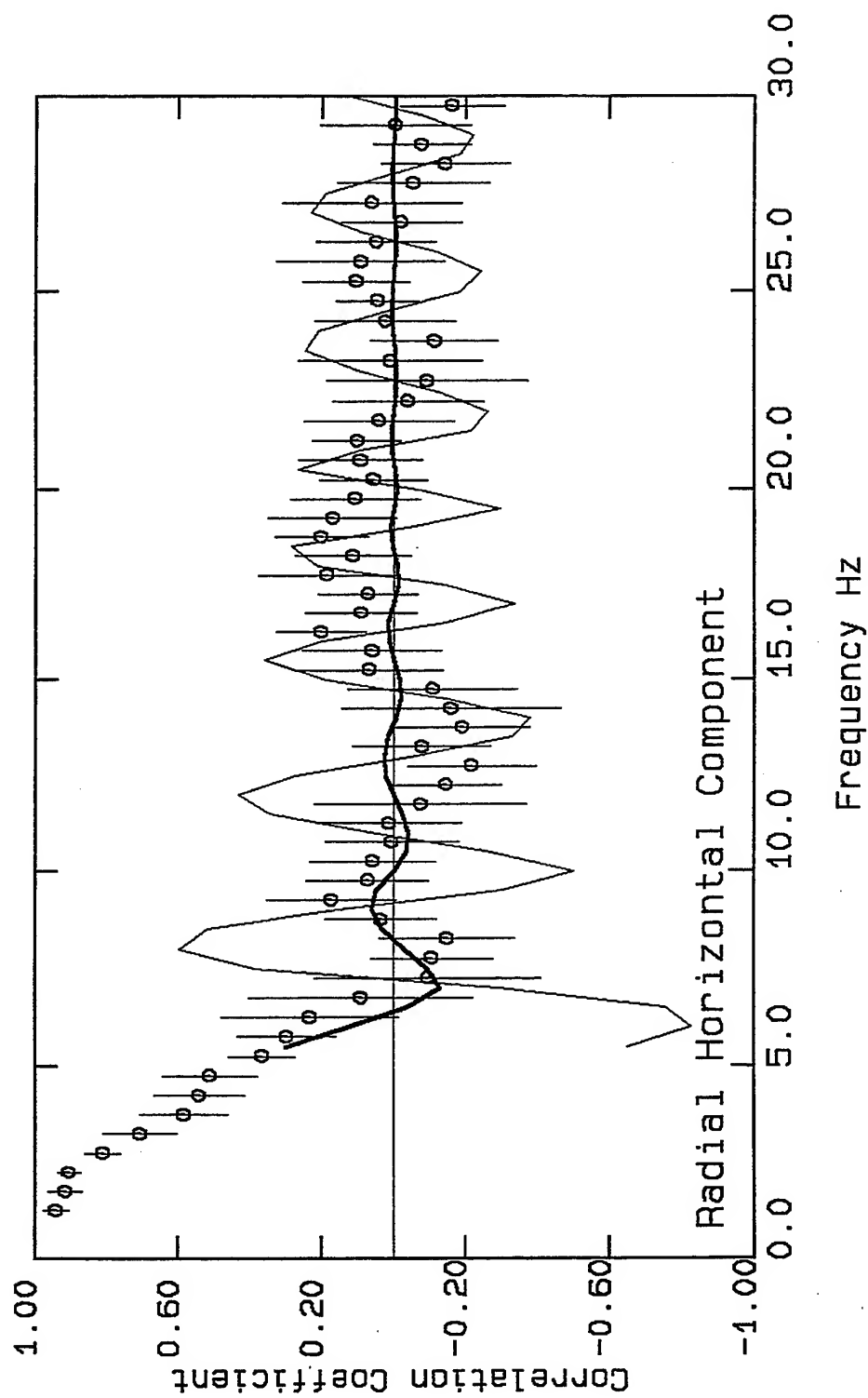
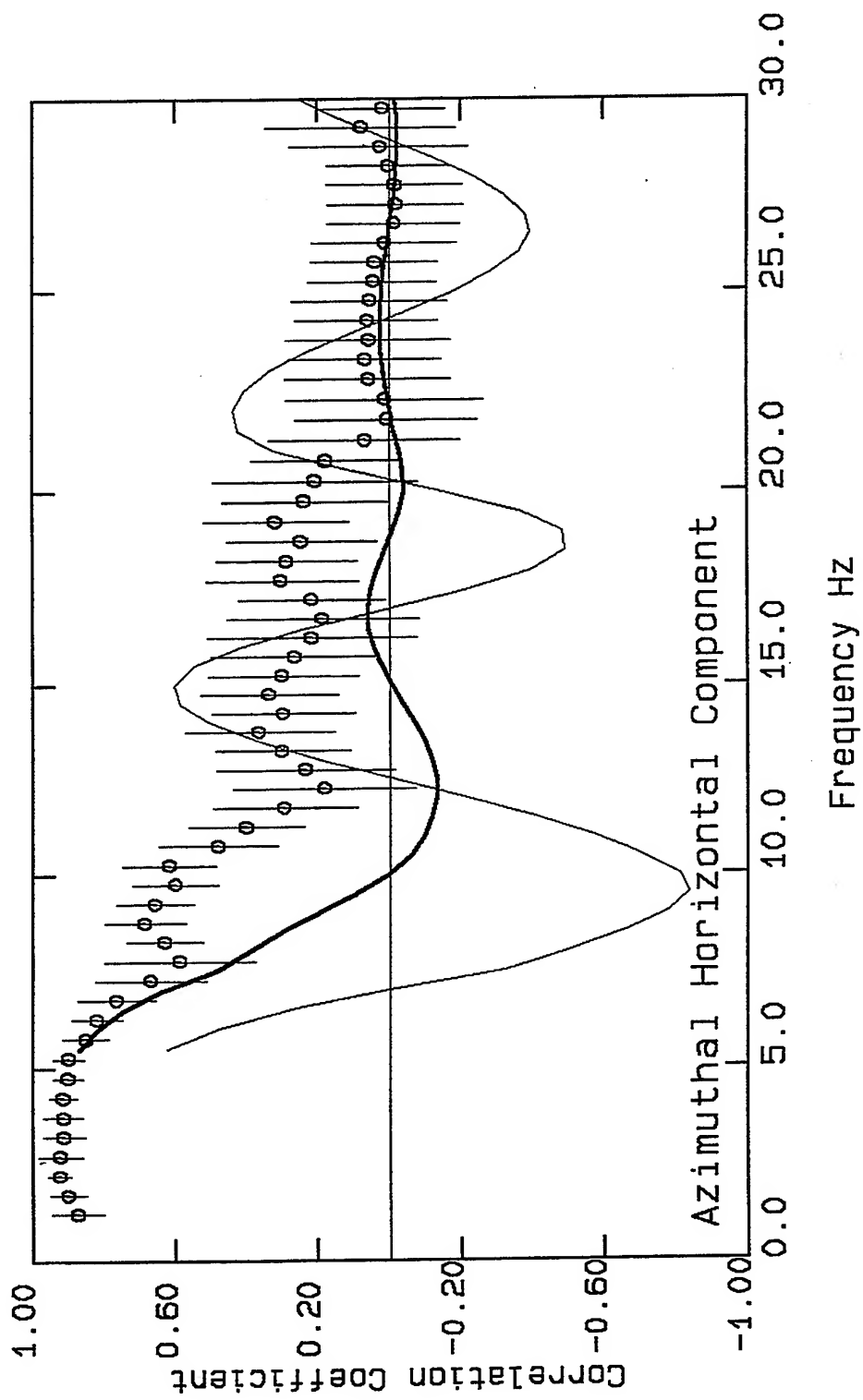
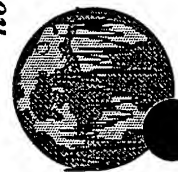


Figure 3.23.c. Similar to Figure 2.23.a but for the case of $r = 37$ m.





Figures 3.24.a. Plots of the CC-F values for the tangential components of microtremors for the case of $r = 15$ m. The thick and thin solid lines on these figures show the expected patterns for the radial and tangential components, equations (2.22) to (2.25), depending upon the predominant direction of polarization for the horizontal components of microtremors.



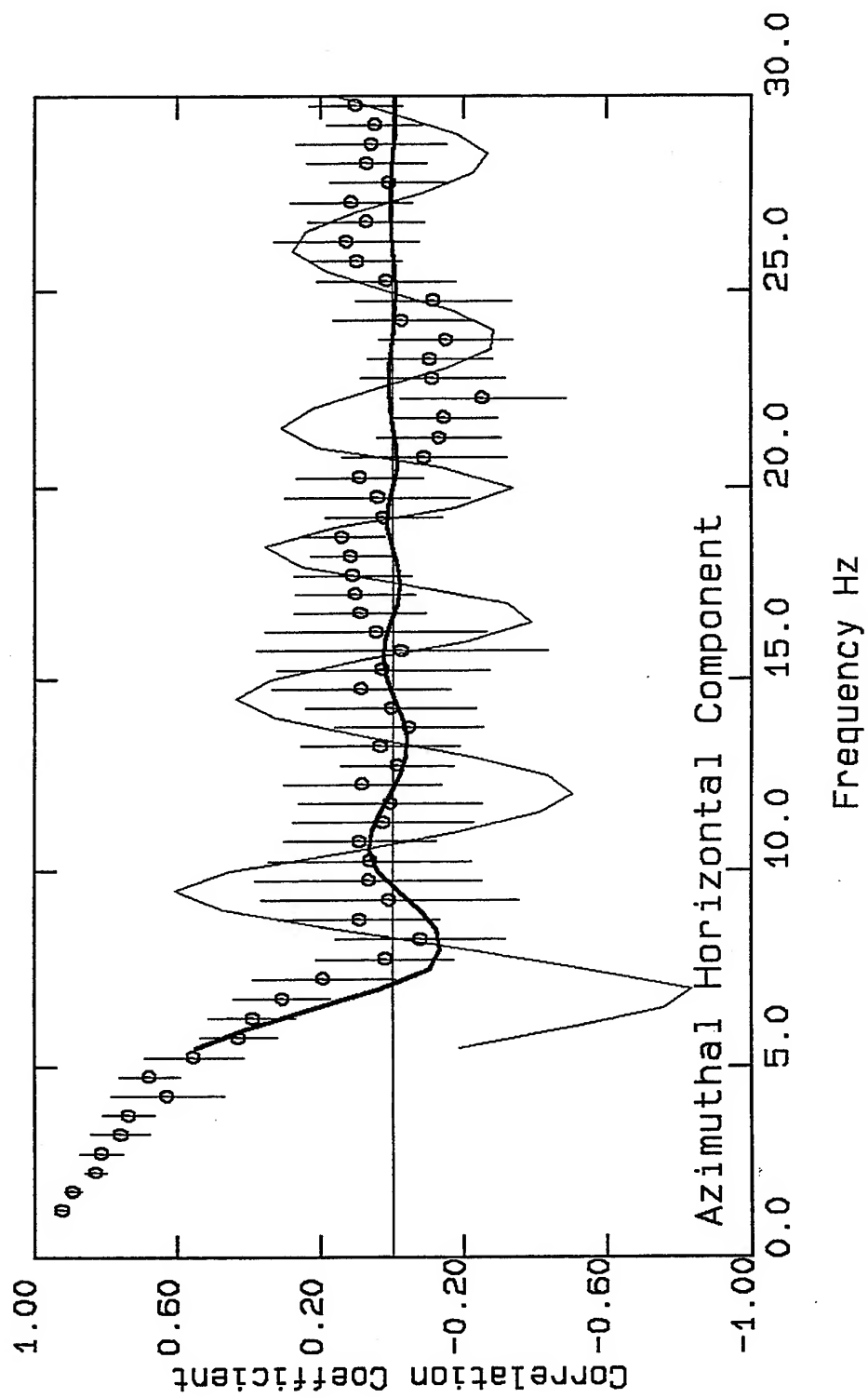


Figure 3.24.b. Similar to Figure 2.23.a but for the case of $r = 27$ m.



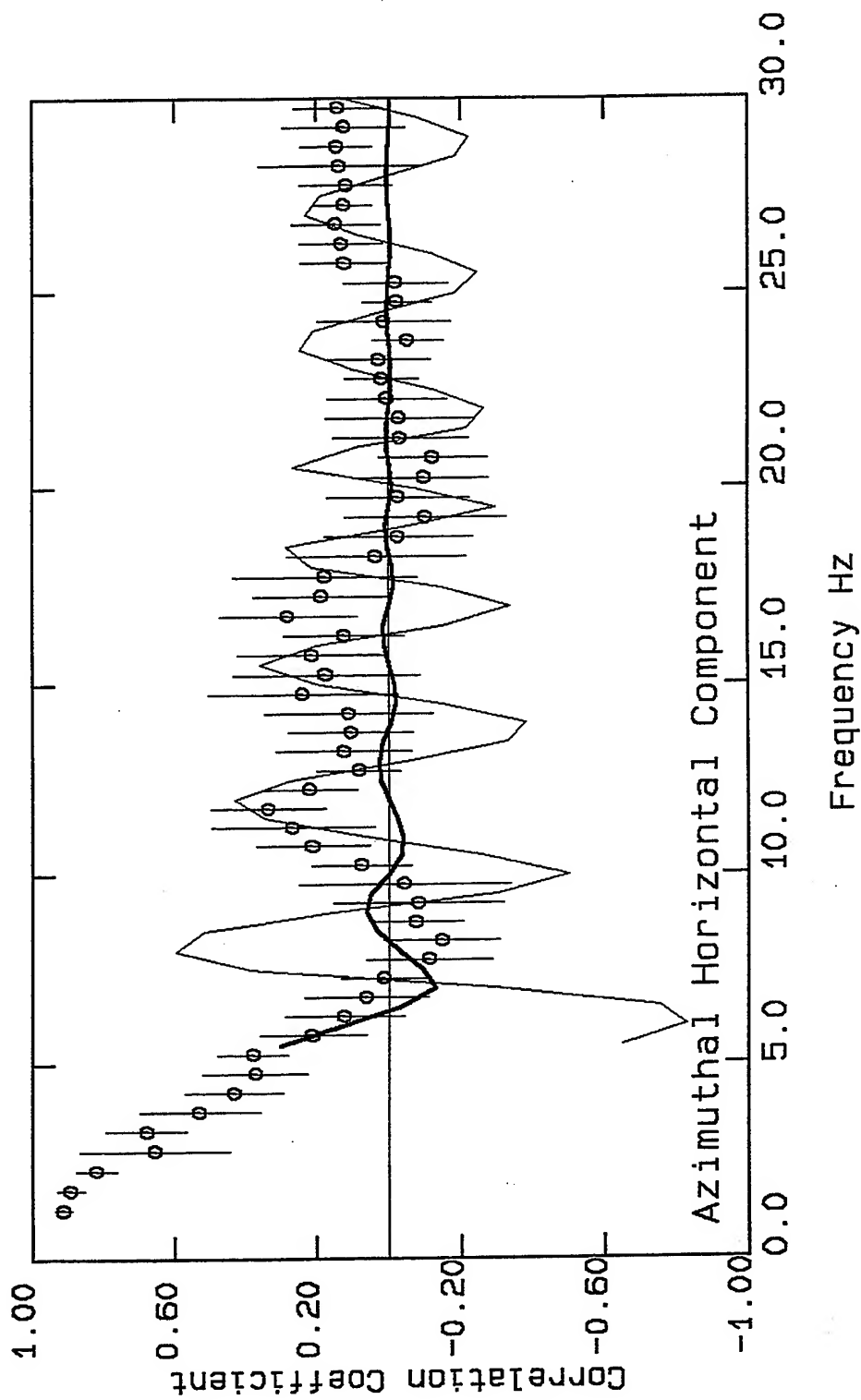


Figure 3.24.c. Similar to Figure 2.23.a but for the case of $r = 37$ m.



VortexRock Consultants, Inc.

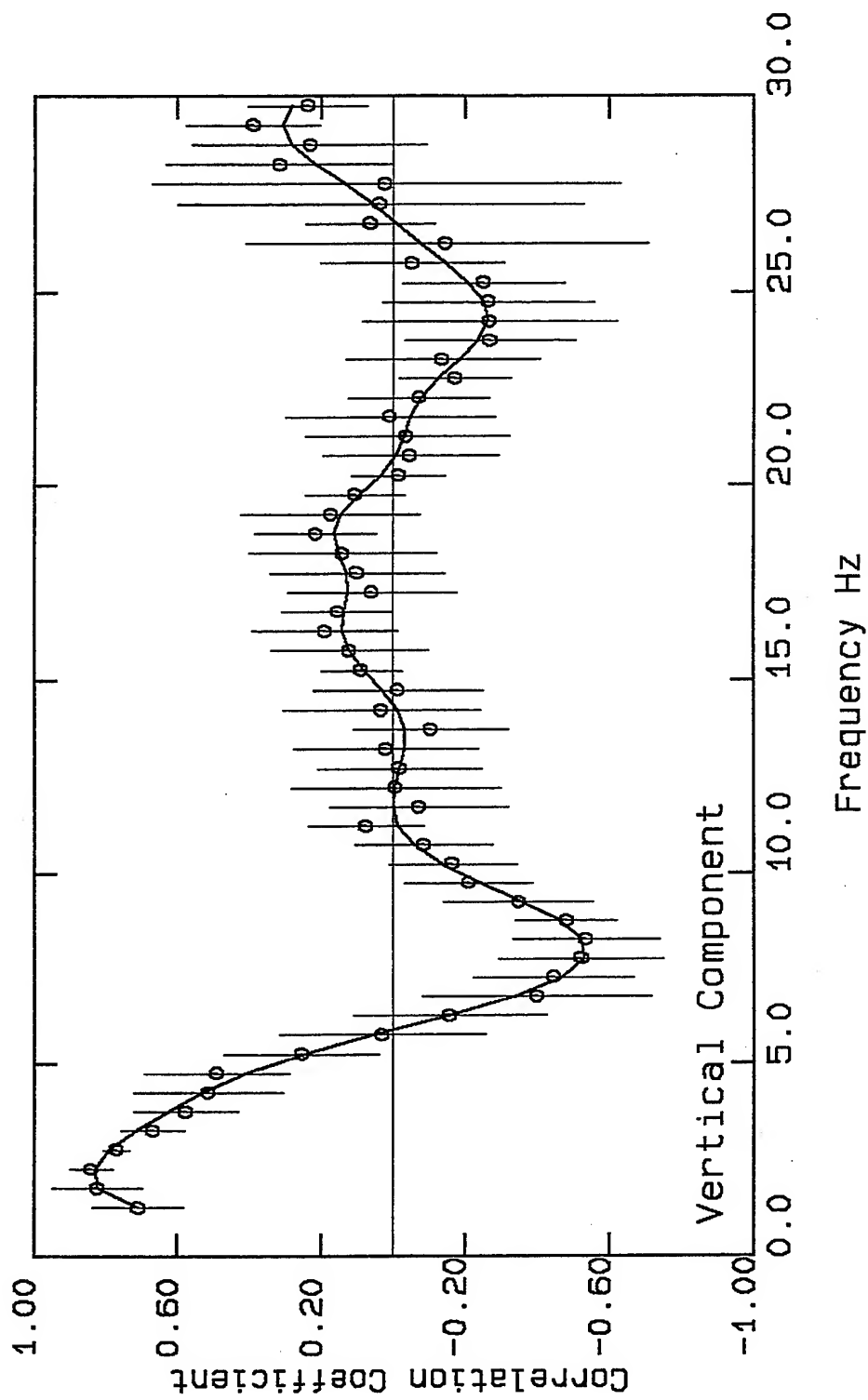


Figure 3.25 Plots of the CC-F values and the best fit to the data for the vertical components of microtremor ground motions.



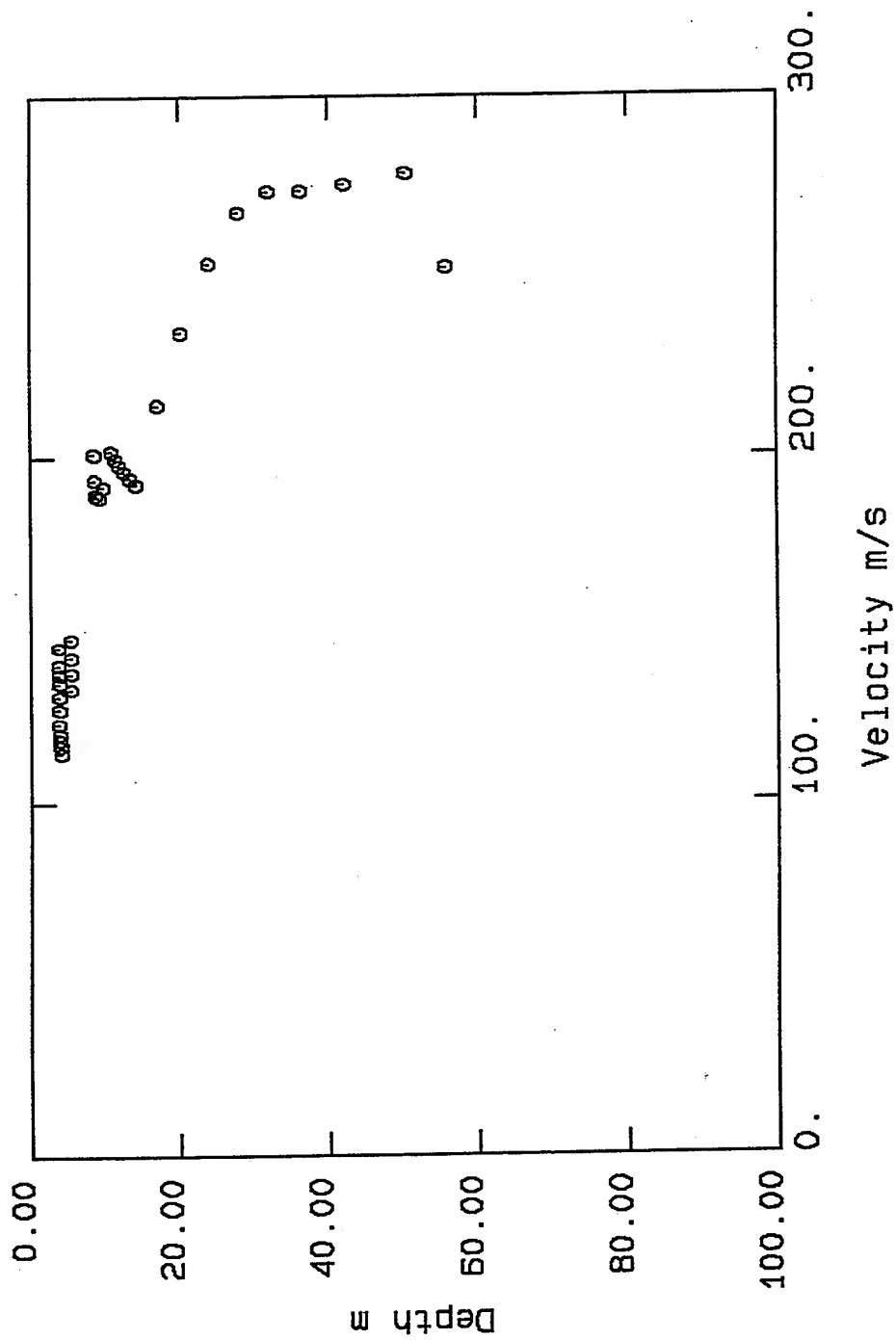


Figure 3.26. Plots of the phase velocities versus depth based on data in Table 3.9. Two break points on this figure at the depths of 9.4 and 15.3 m can be identified.



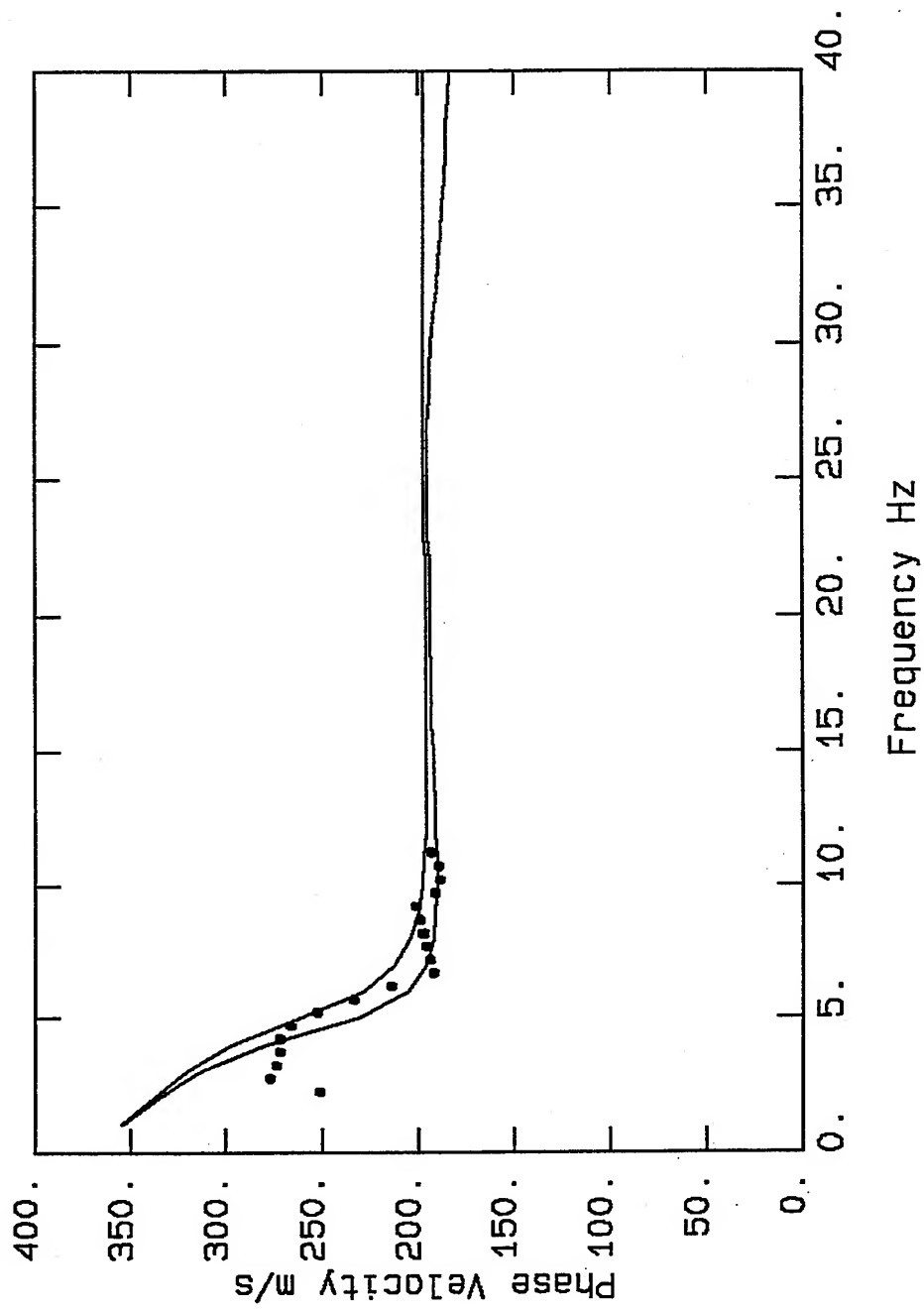


Figure 3.27. Plots of the calculated and simulated phase velocities for the velocity-depth models in Table 3.10, the top curve on this figure. The bottom curve shows the simulated phase velocities using 170 m/s as the shear wave velocity of the second layer.



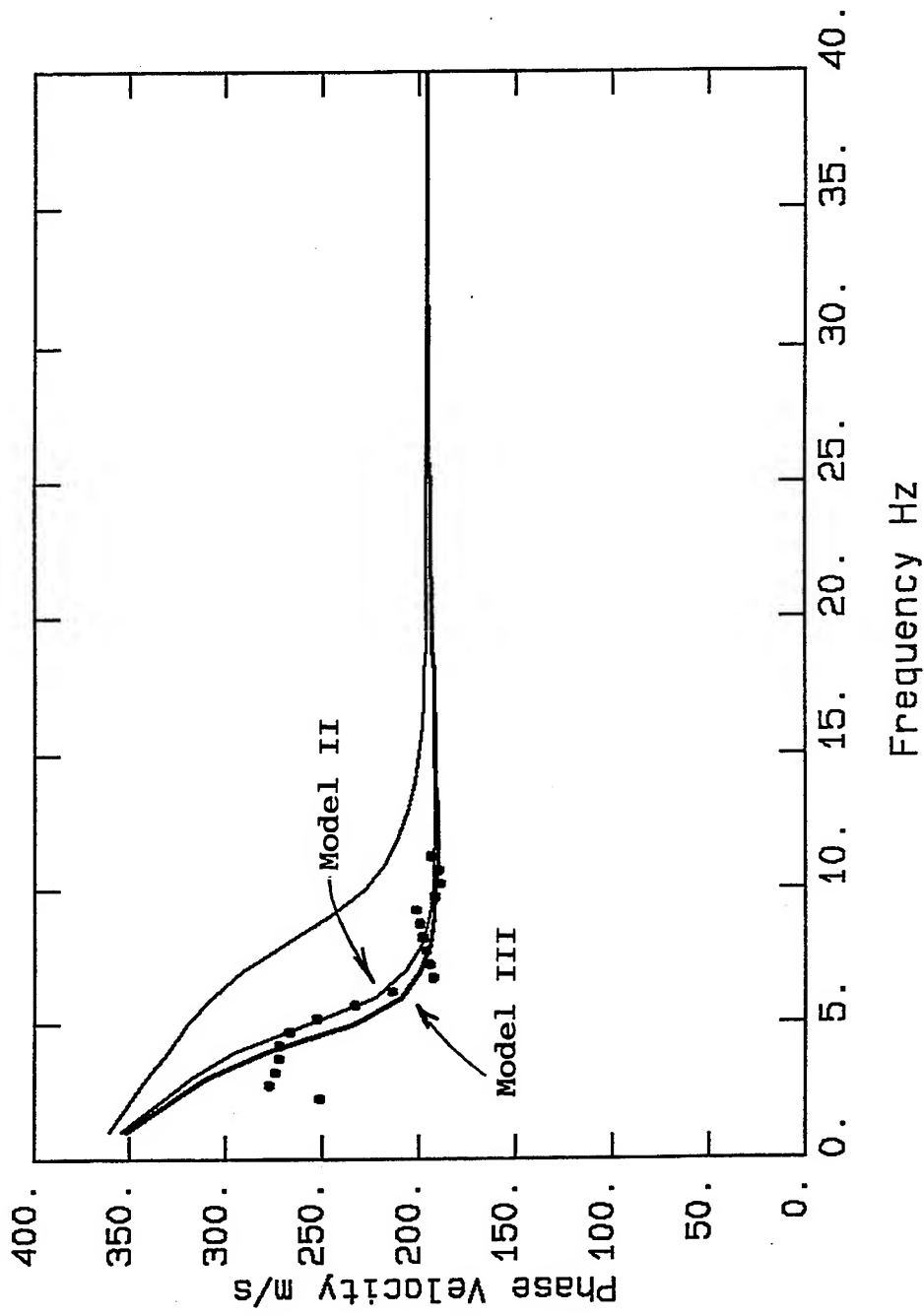
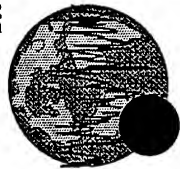


Figure 3.28. plots of the calculated and simulated phase velocities. The top curve corresponds to the velocity model in Table 3.10 but with shallower depths for the layers, see the text for explanation. The bottom curves show the phase velocities for models in Table 3.11.



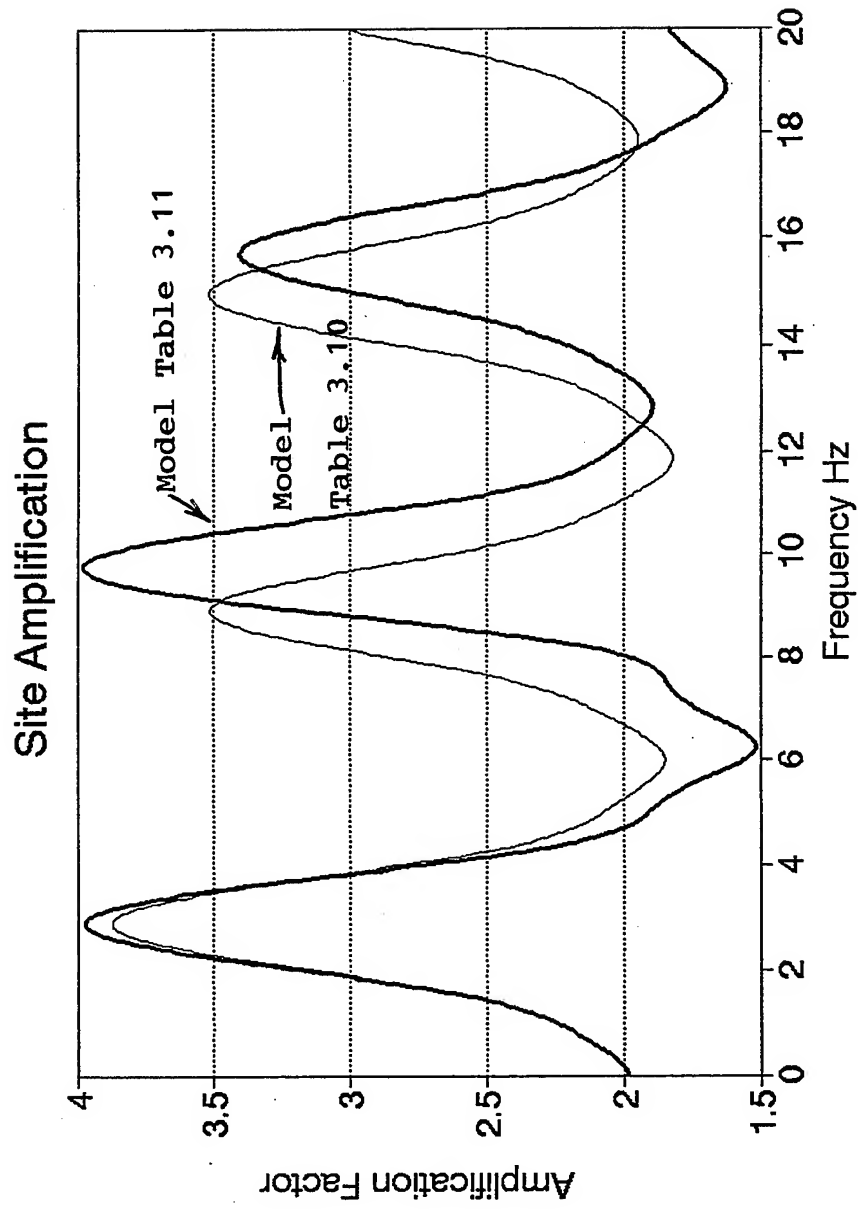


Figure 3.29. Plots of one-dimensional weak motion site amplification values for Model III in Table 3.11 and the model in Table 3.10 with reduced velocity for the second layer.



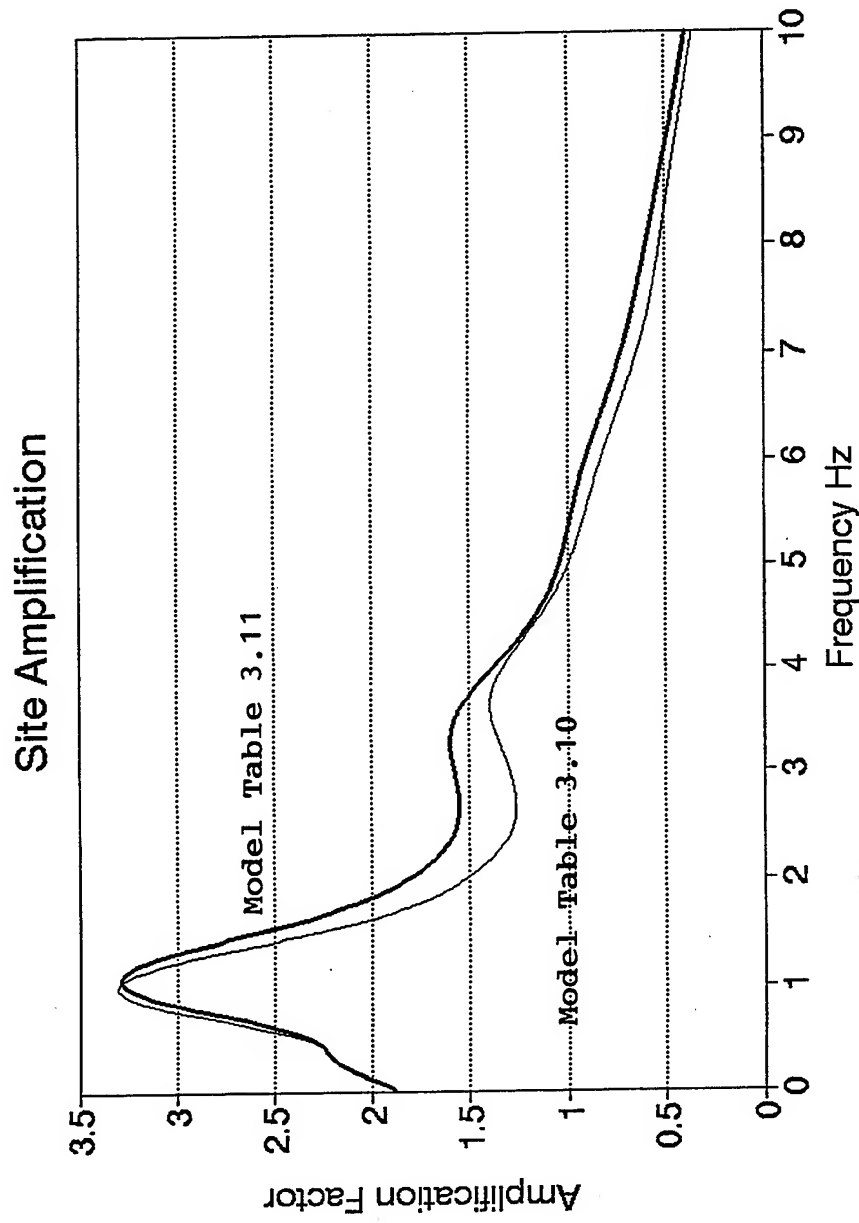
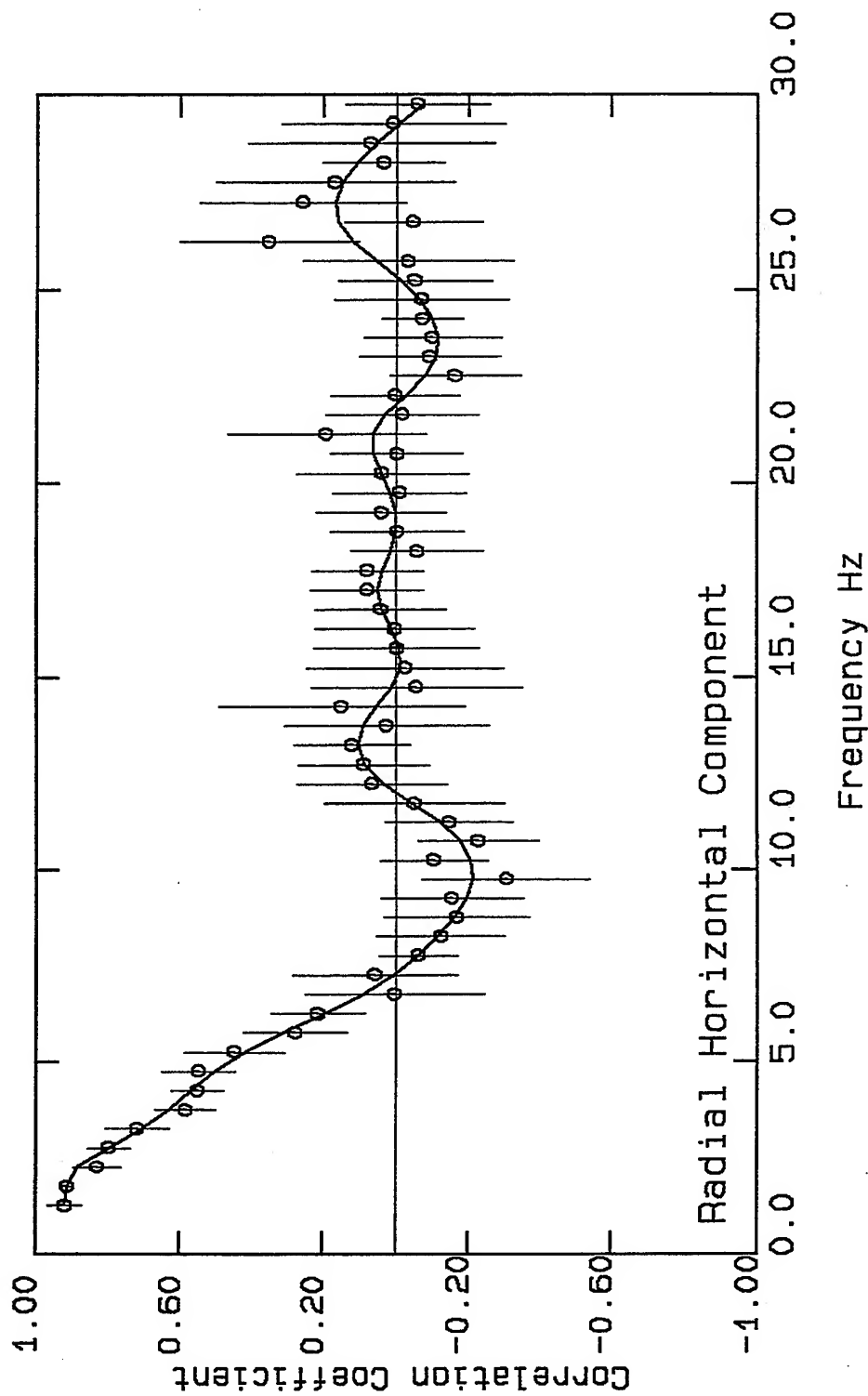


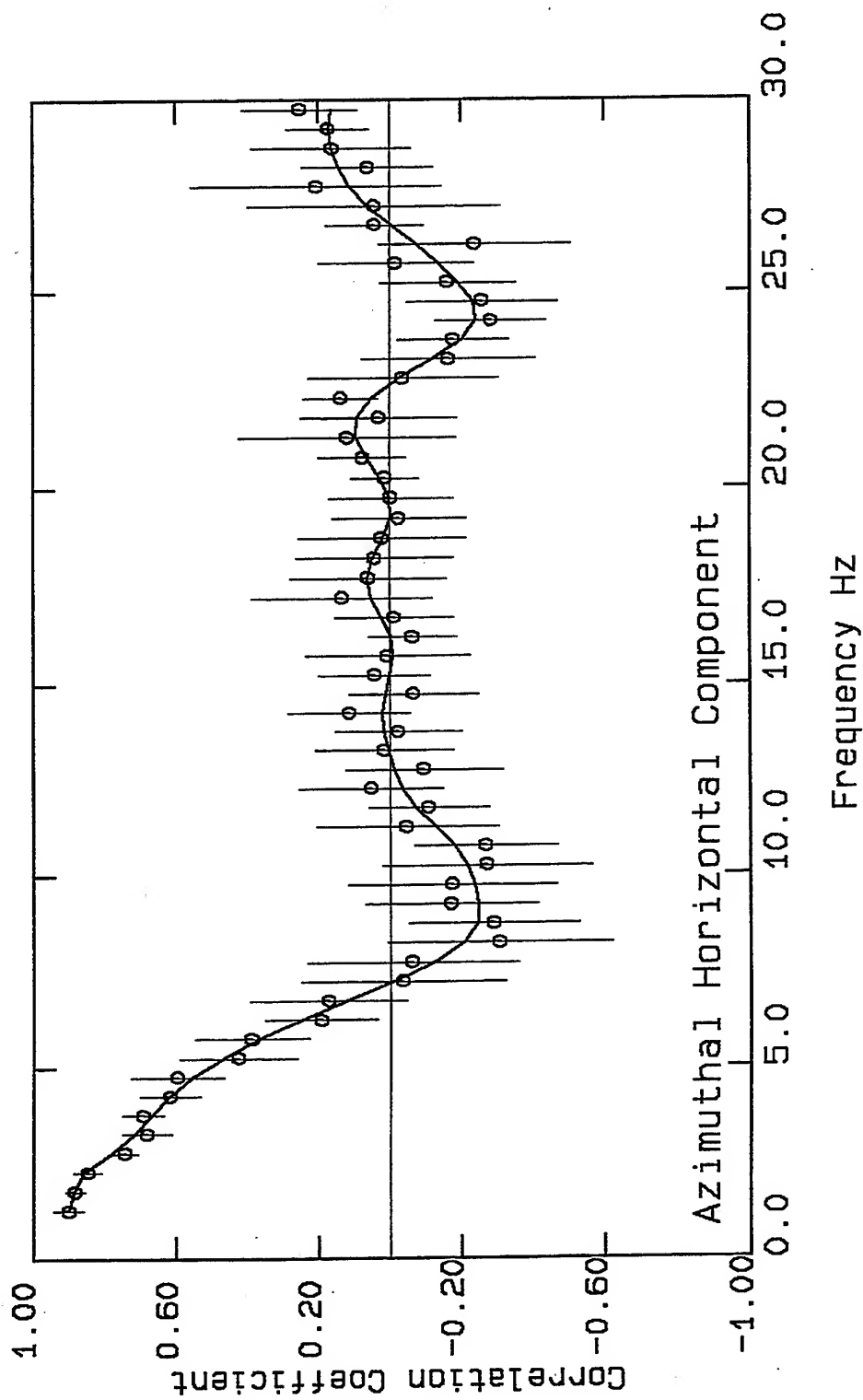
Figure 3.30. Plots of one-dimensional strong motion site amplification values for Model III in Table 3.11 and the model in Table 3.10 with reduced velocity for the second layer.





Figures 3.31. Plots of the CC-F values for the radial components of microtremors. The thick and thin solid lines on these figures show the expected patterns for the radial and tangential components, equations (2.22) to (2.25), depending upon the predominant direction of polarization for the horizontal components of microtremors.





Figures 3.32. Plots of the CC-F values for the tangential components of microtremors. The thick and thin solid lines on these figures show the expected patterns for the radial and tangential components, equations (2.22) to (2.25), depending upon the predominant direction of polarization for the horizontal components of microtremors.



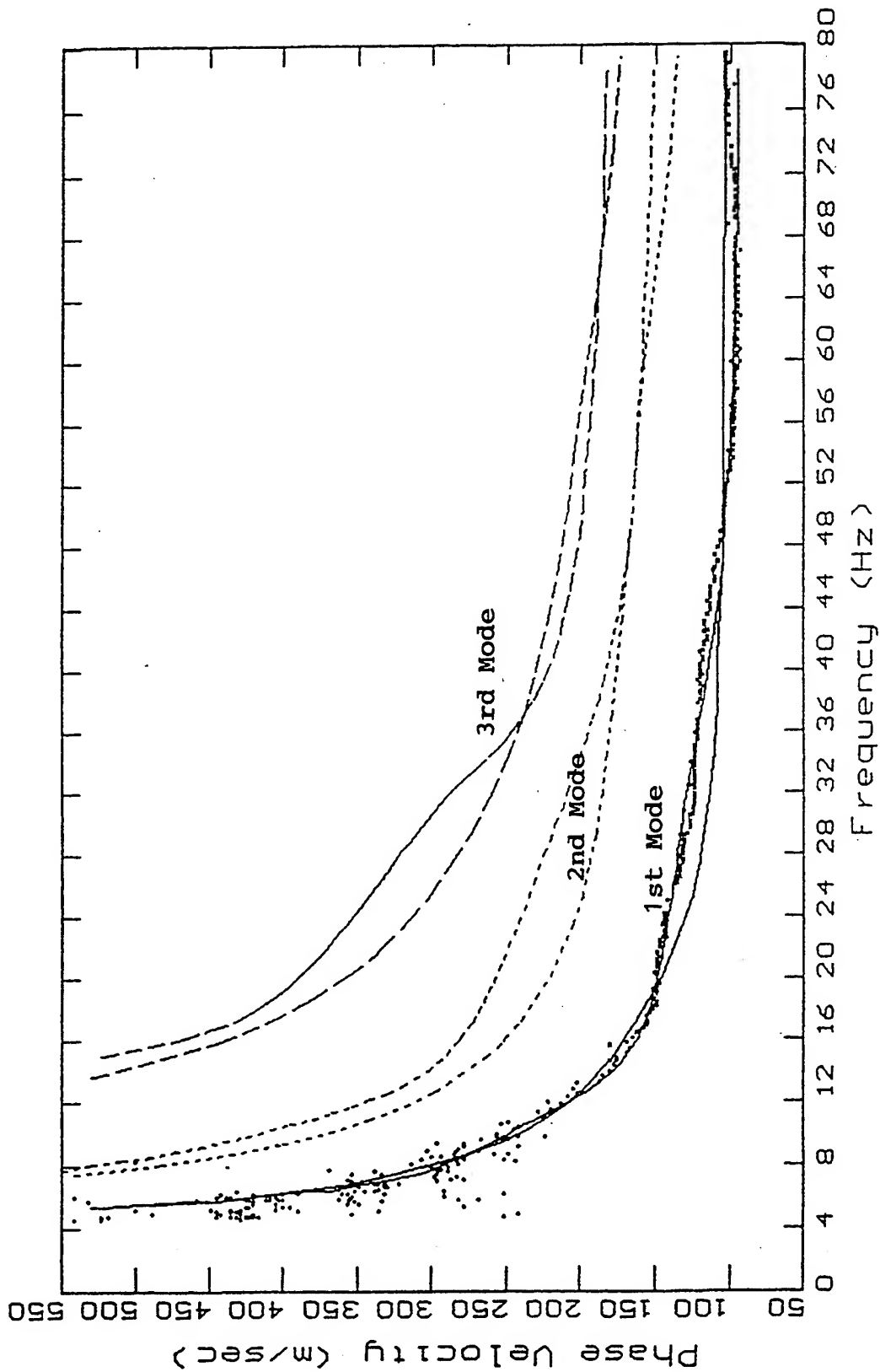


Figure 3.33. The observed, dots, and simulated dispersion curves for the first three modes of Rayleigh waves for the basketball court of McBride School. This figure is from the VIC report.



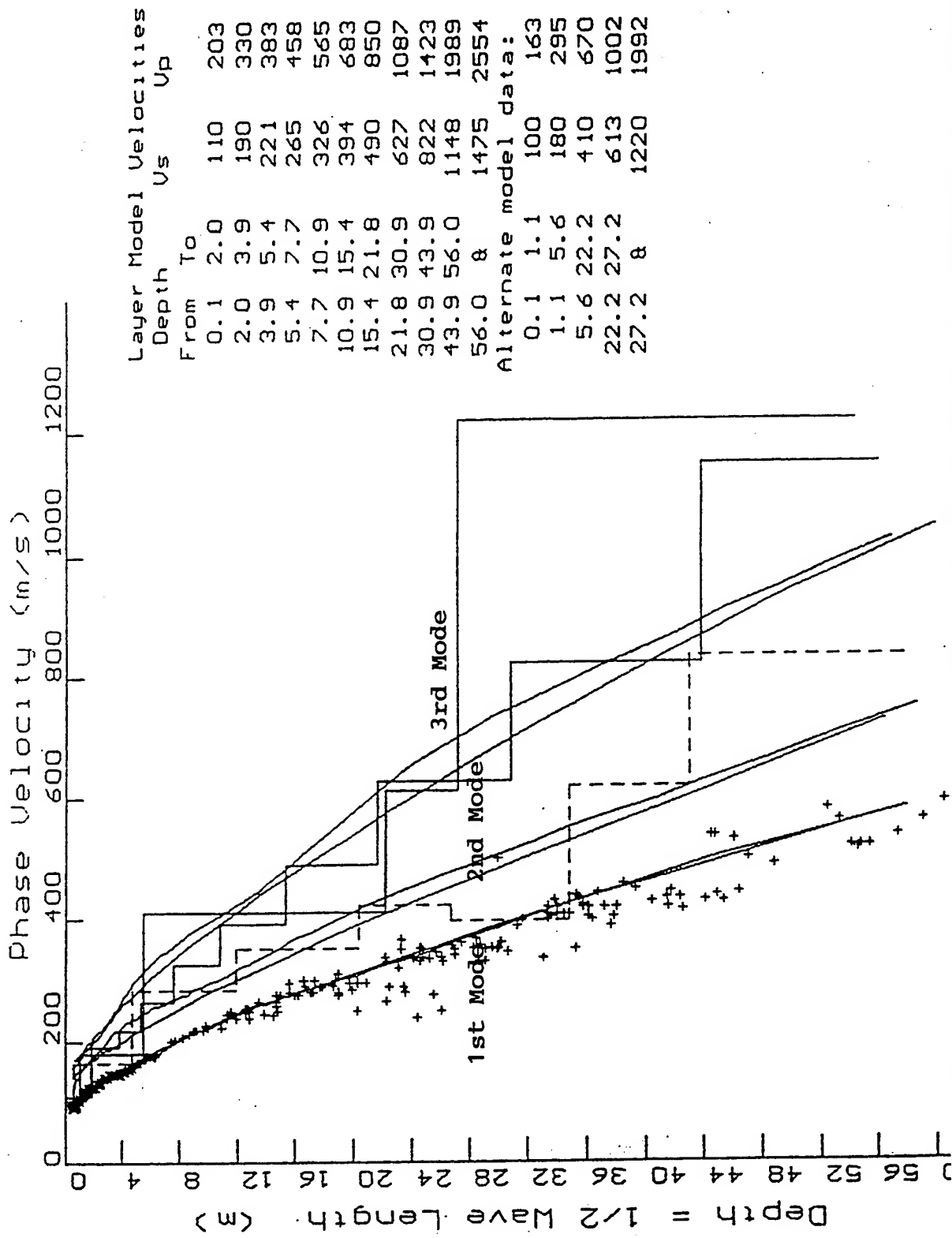
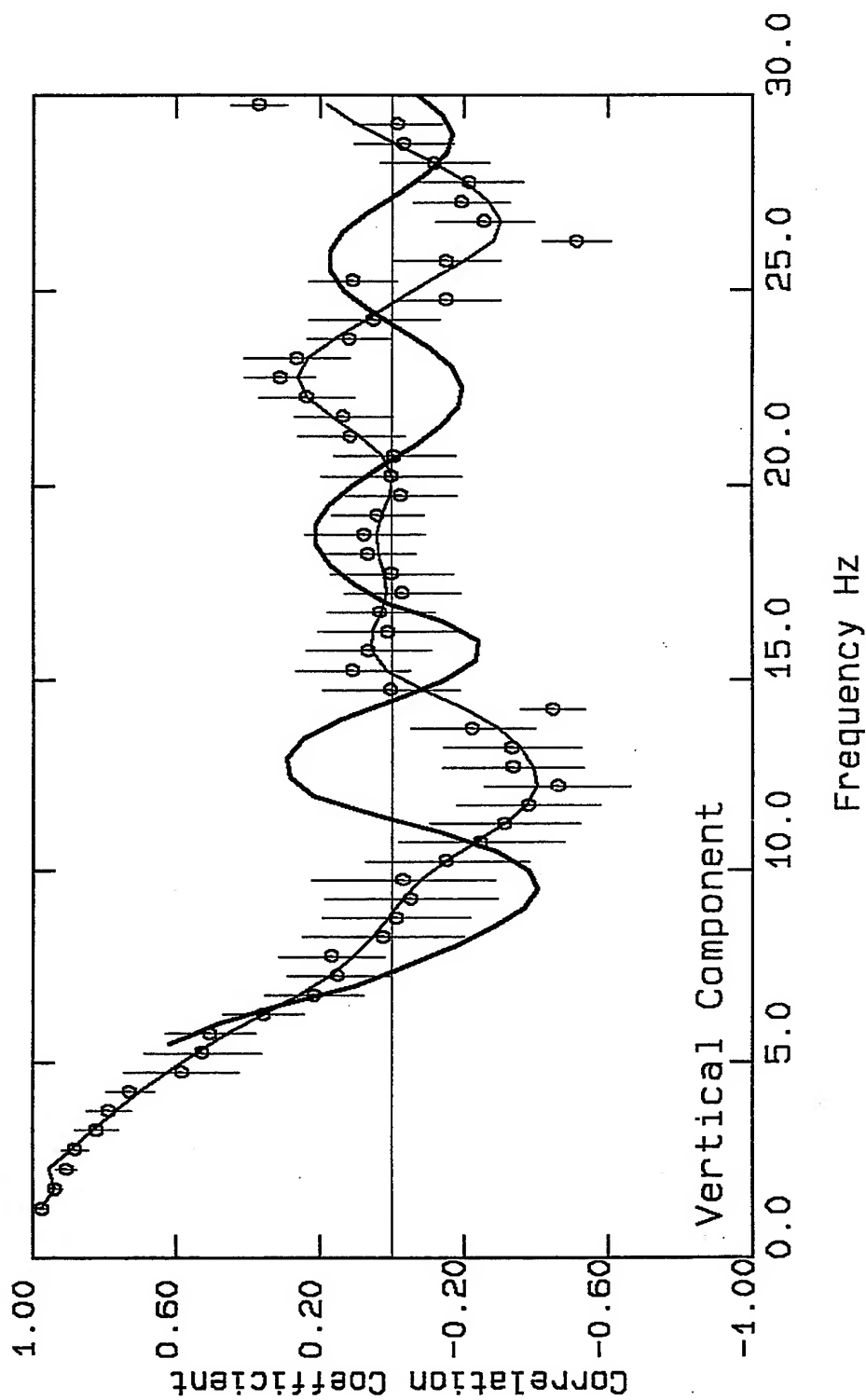


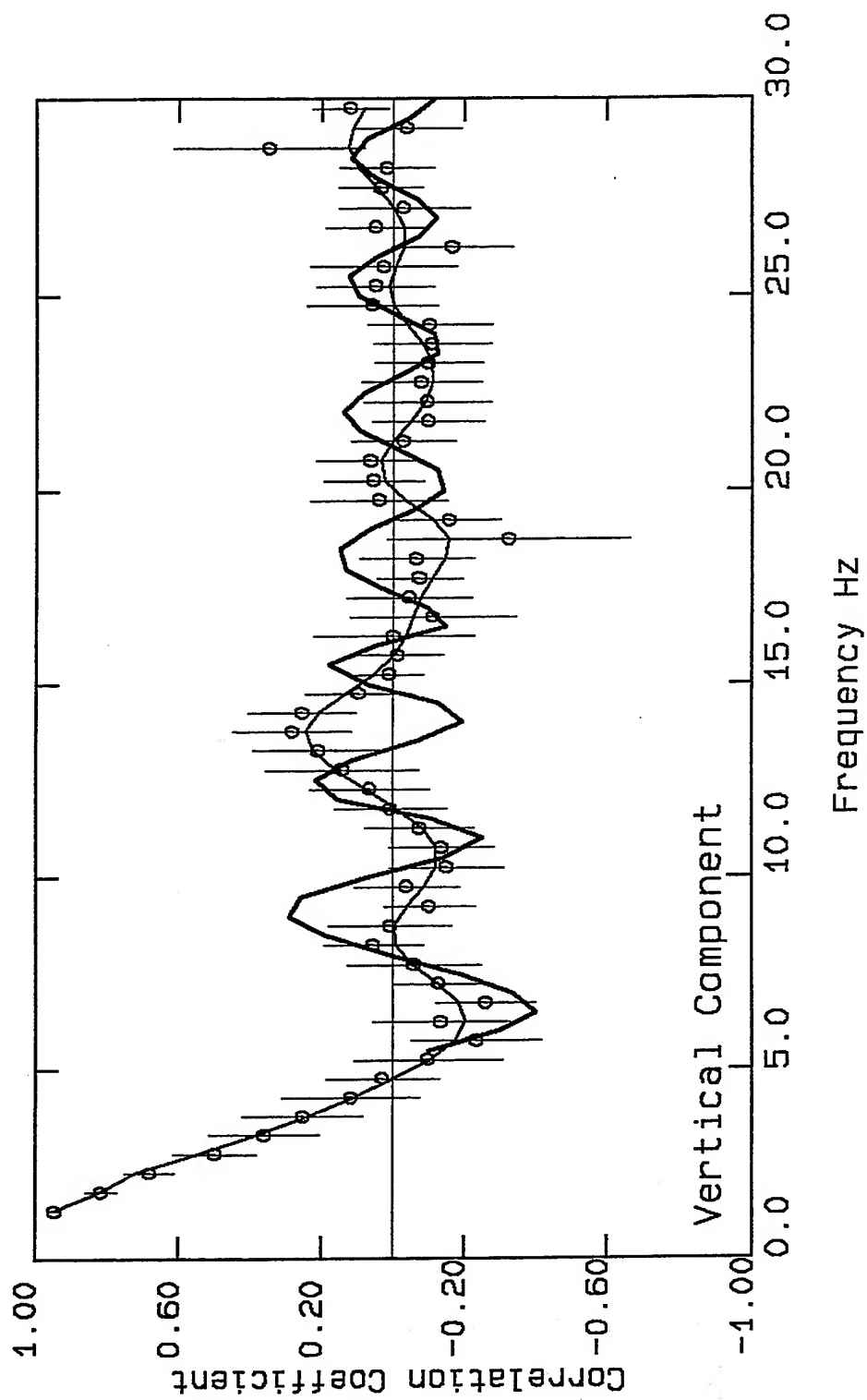
Figure 3.34. Plots of the phase velocity-depth profiles based on the observed and simulated data. This figure is from the VIC report.





Figures 3.35. Plots of the calculated CC-F values and the best fit, thin solid line, to the data for the case of $r = 15$ m. The thick solid line is the expected pattern based on the VIC phase velocity data.





Figures 3.36. Plots of the calculated CC-F values and the best fit, thin solid line, to the data for the case of $r = 30$ m. The thick solid line is the expected pattern based on the VTC phase velocity data.



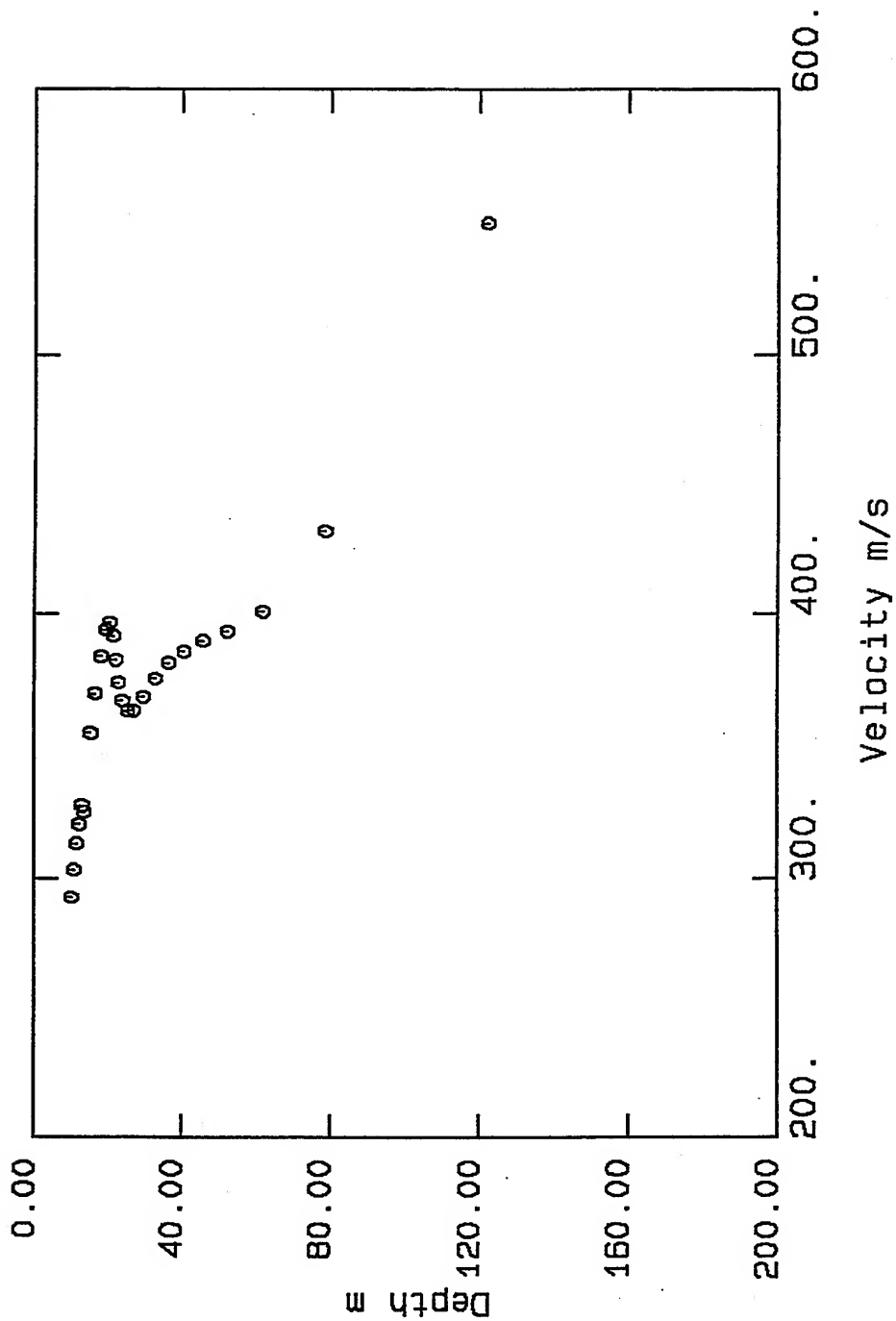


Figure 3.37. Plots of the phase velocities versus depth based on data in Table 3.13 for the case of $r = 15$ m. Two break points at 19.5 and 26.3 m can be identified.



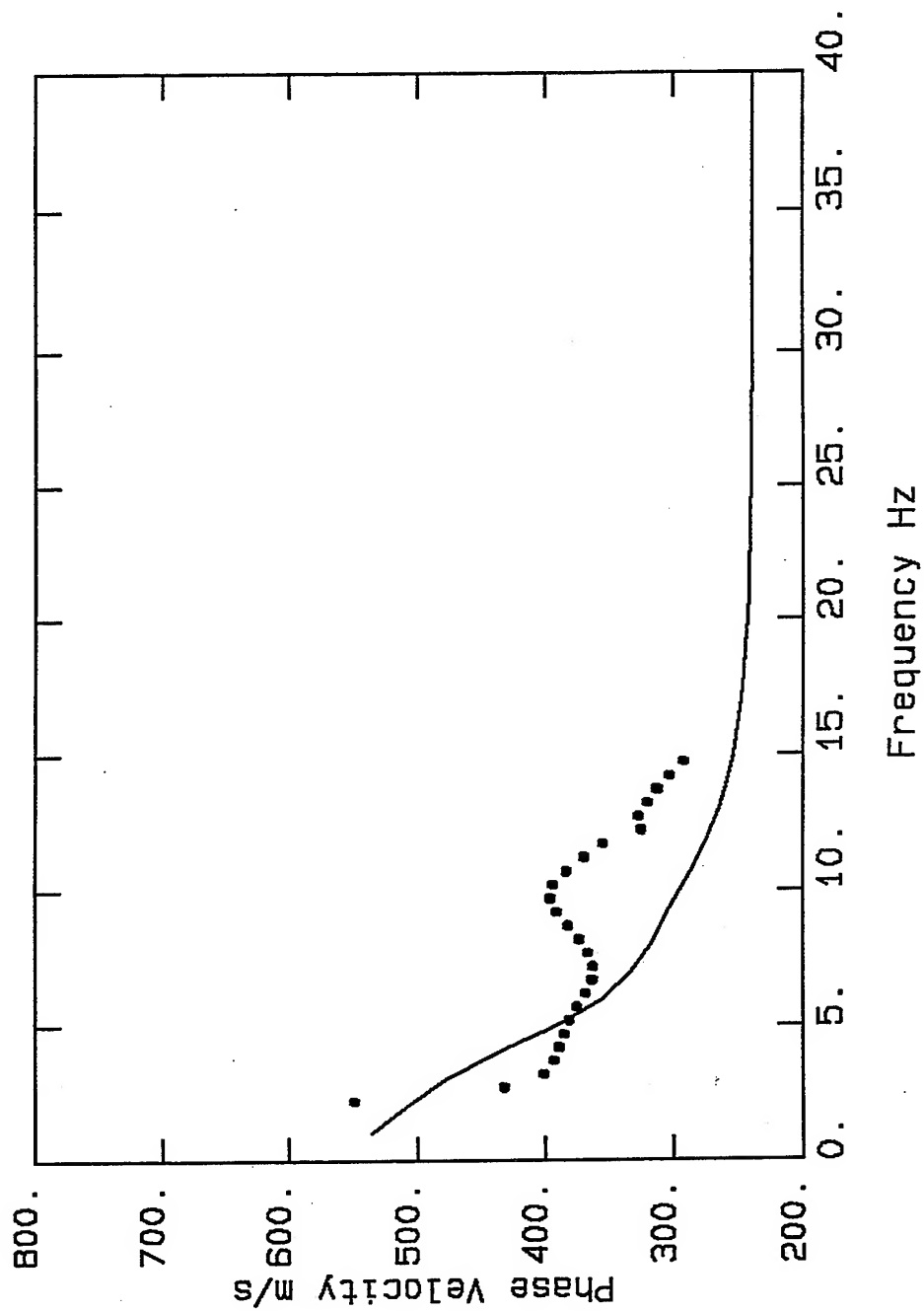


Figure 3.38. Plots of the calculated, from the case of $r = 15$ m, and simulated phase velocities, for the model in Table 3.14.



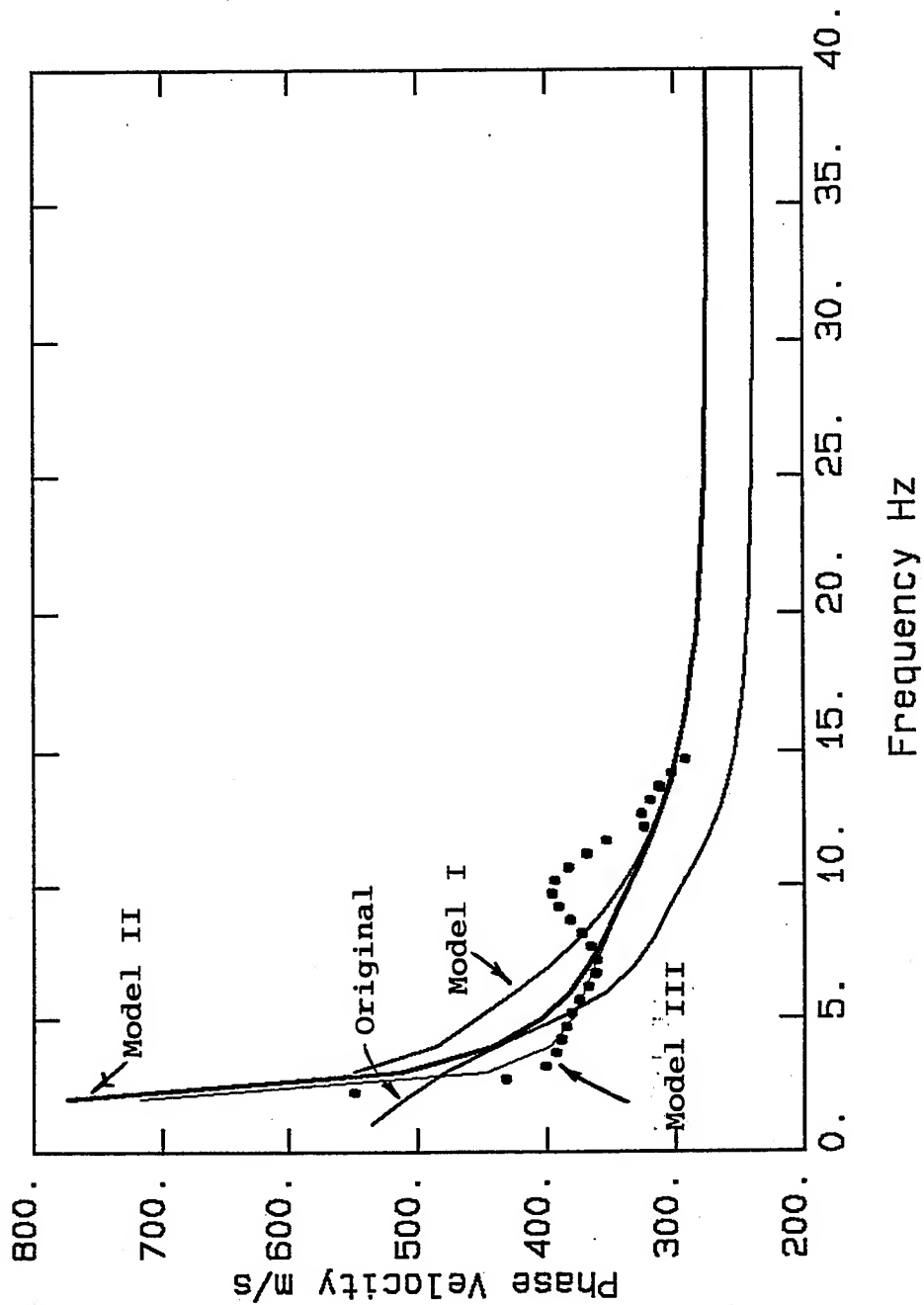


Figure 3.39. Plots of the calculated, from the case of $r = 15$, and simulated phase velocities for the three velocity-depth profiles that are shown in Table 3.15.



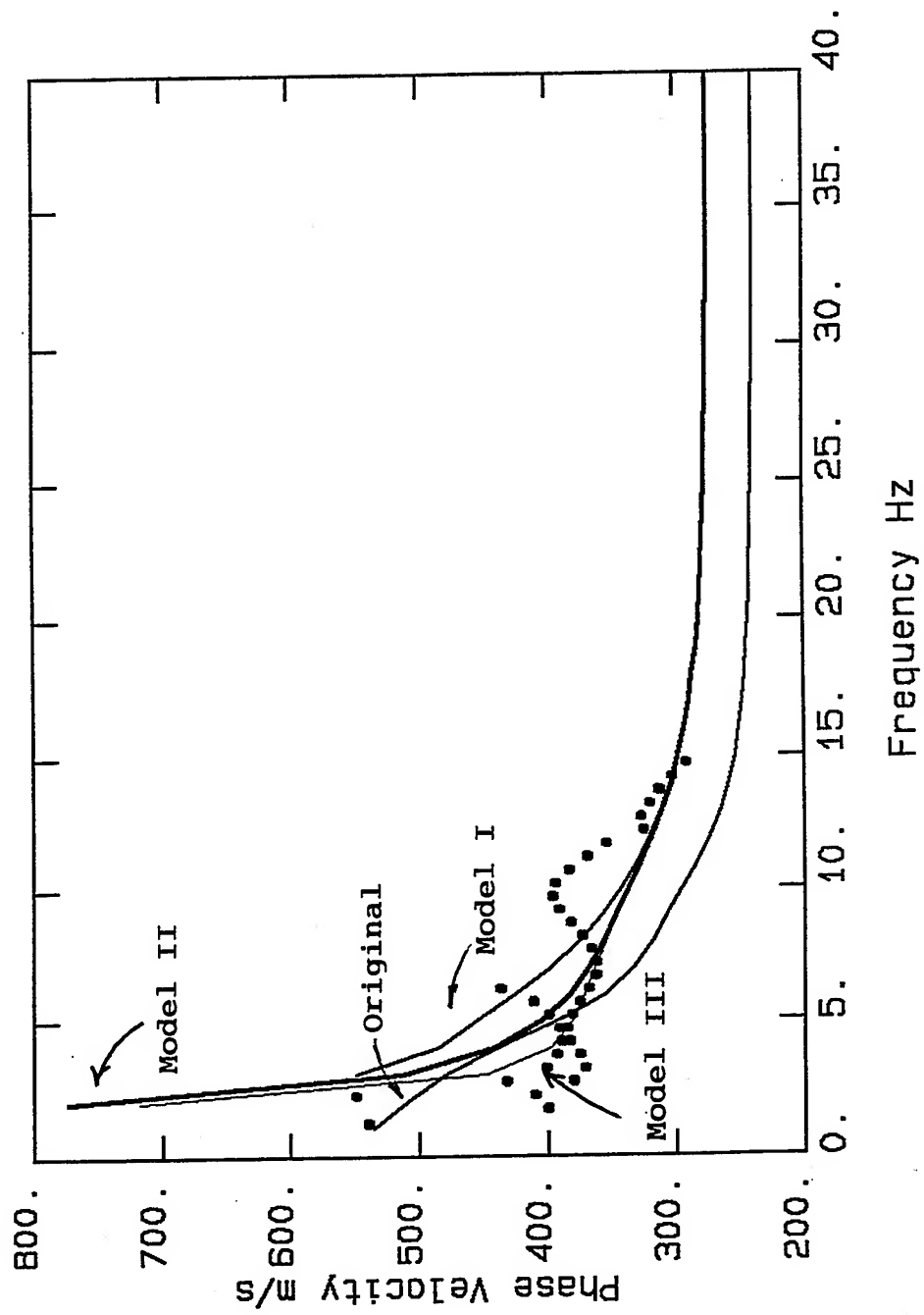
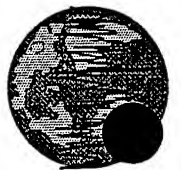


Figure 3.40. Similar to Figure 3.39 with added phase velocities from the Circular Array experiment with $r = 30$ m.



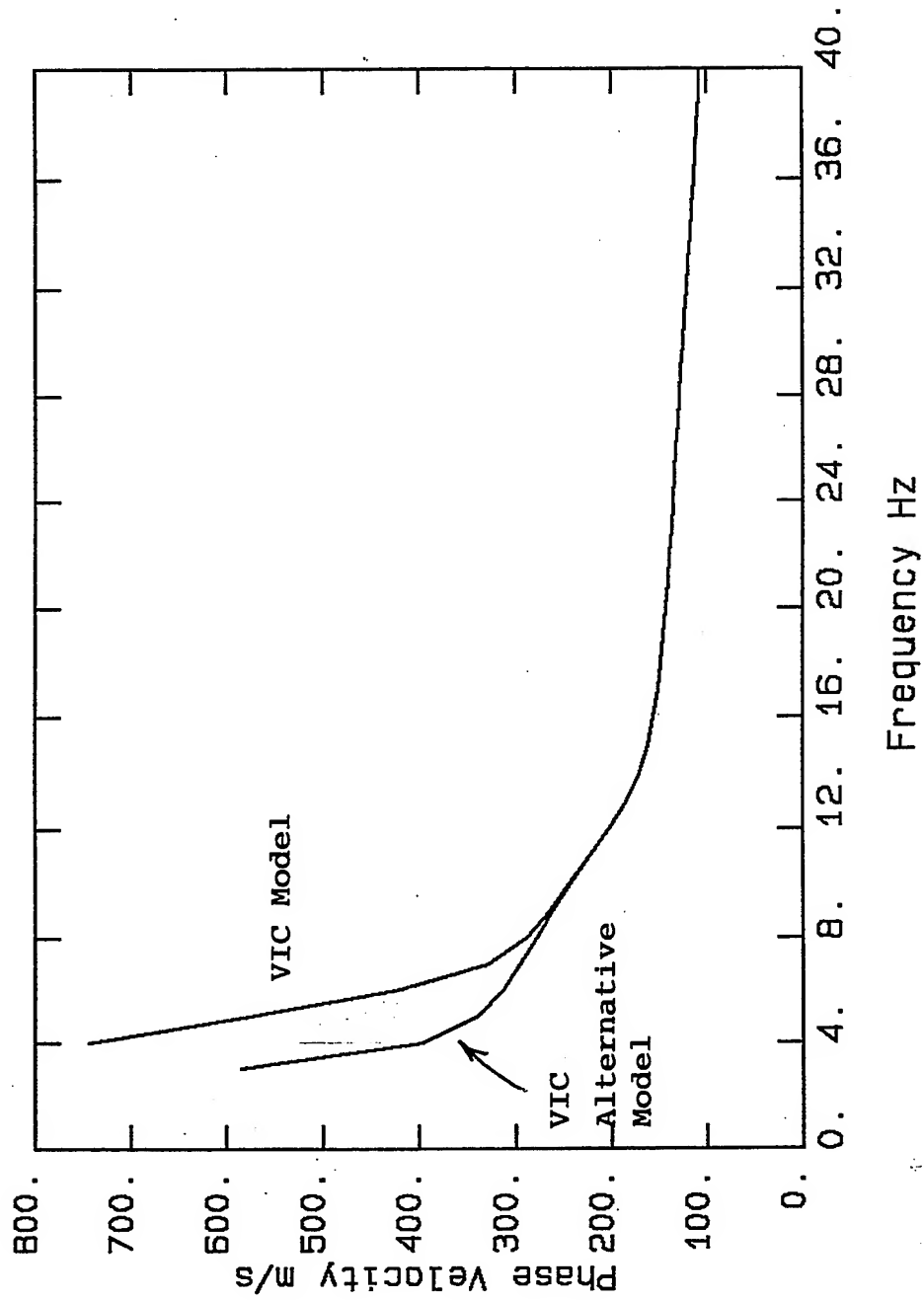


Figure 3.41. Plots of the simulated phase velocities for the VIC's alternative model, the table on Figure 3.34, and for the model in Table 3.16.



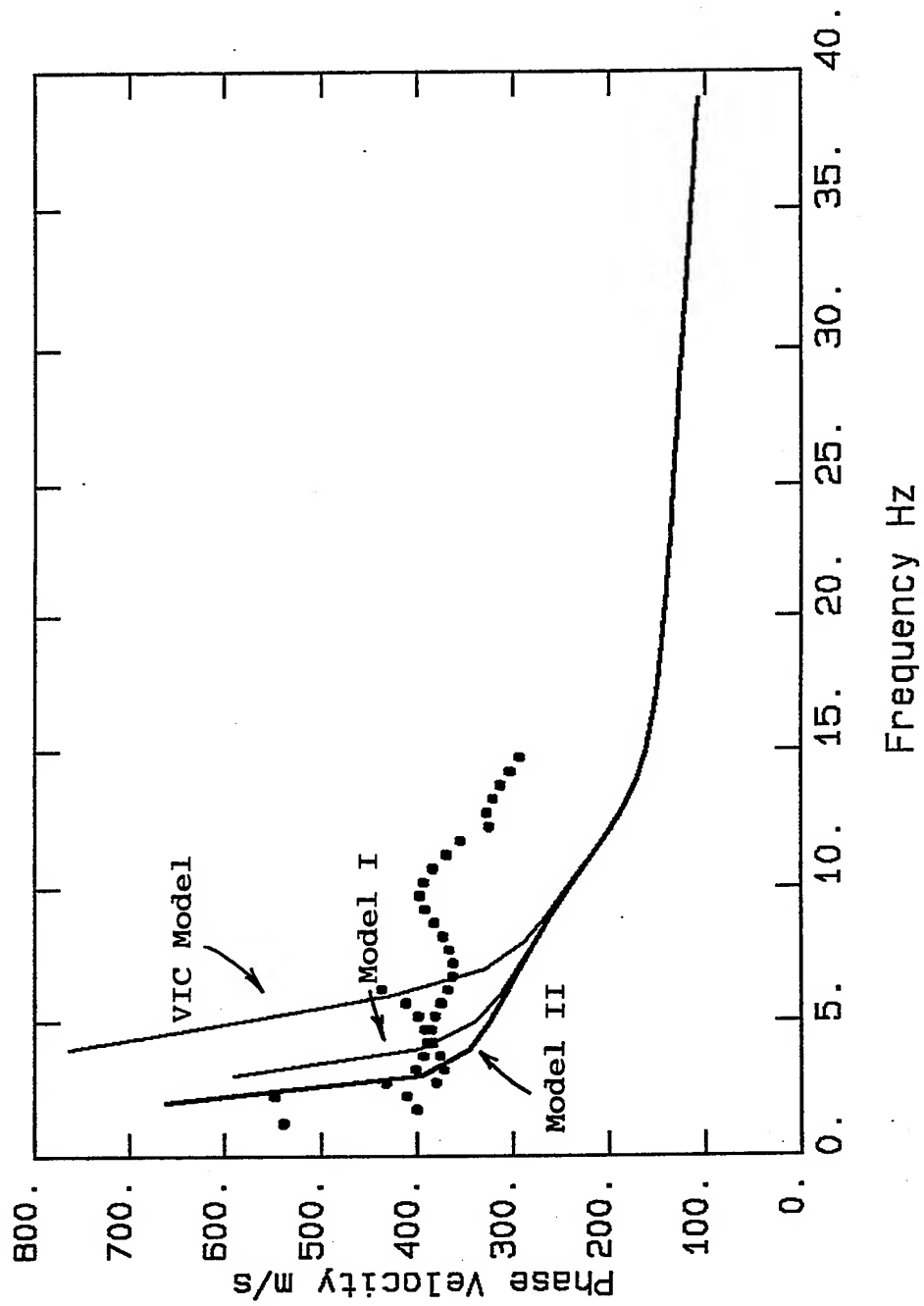


Figure 3.42. Plots of the simulated phase velocities based on the VIC's model, the table on Figure 3.34, and two profiles in Table 3.17.



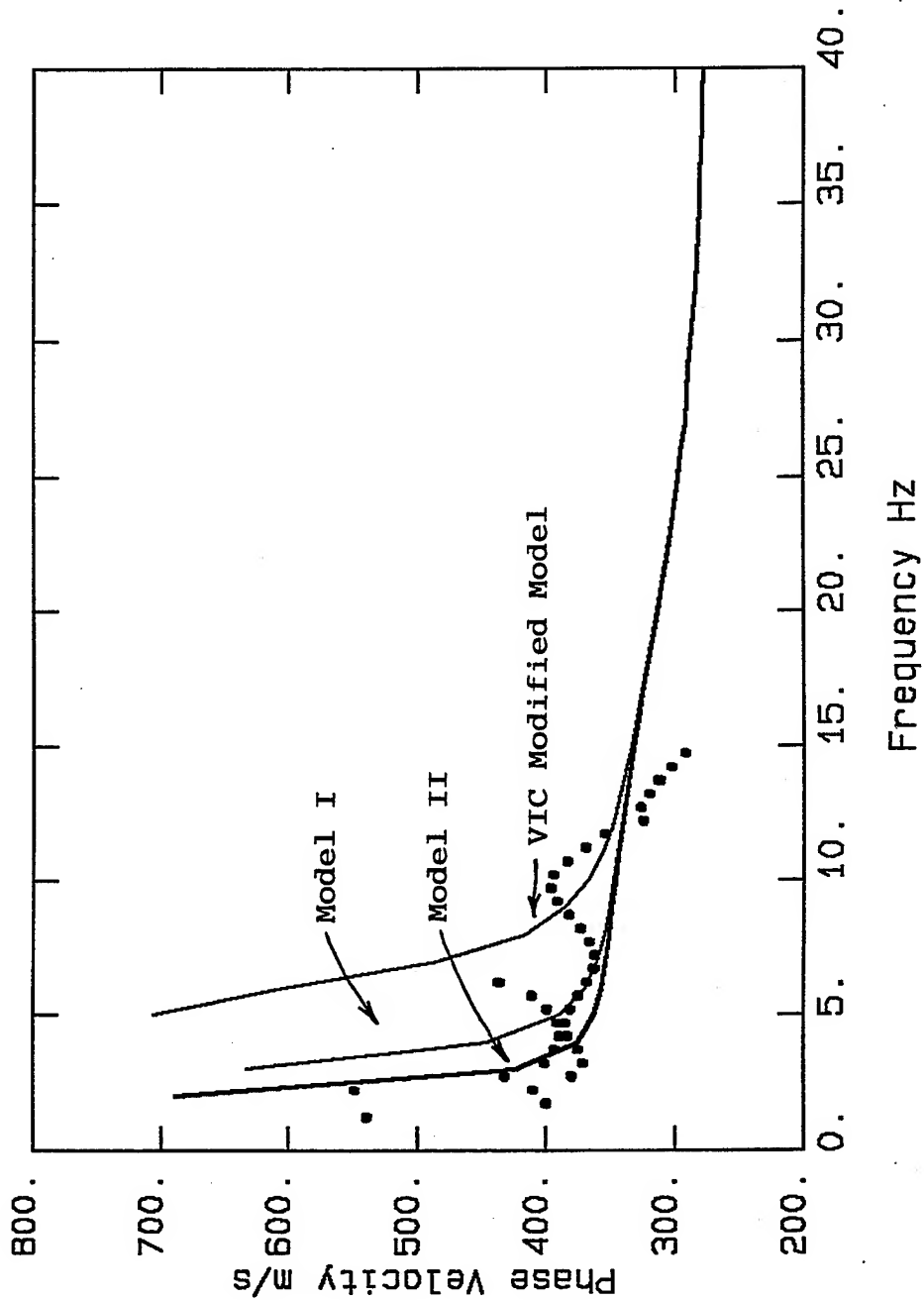


Figure 3.43. Plots of the simulated phase velocities based on the VIC's model, the table on Figure 3.34, without the low velocity layers. The simulated phase velocities for the two profiles in Table 3.17 are also shown.



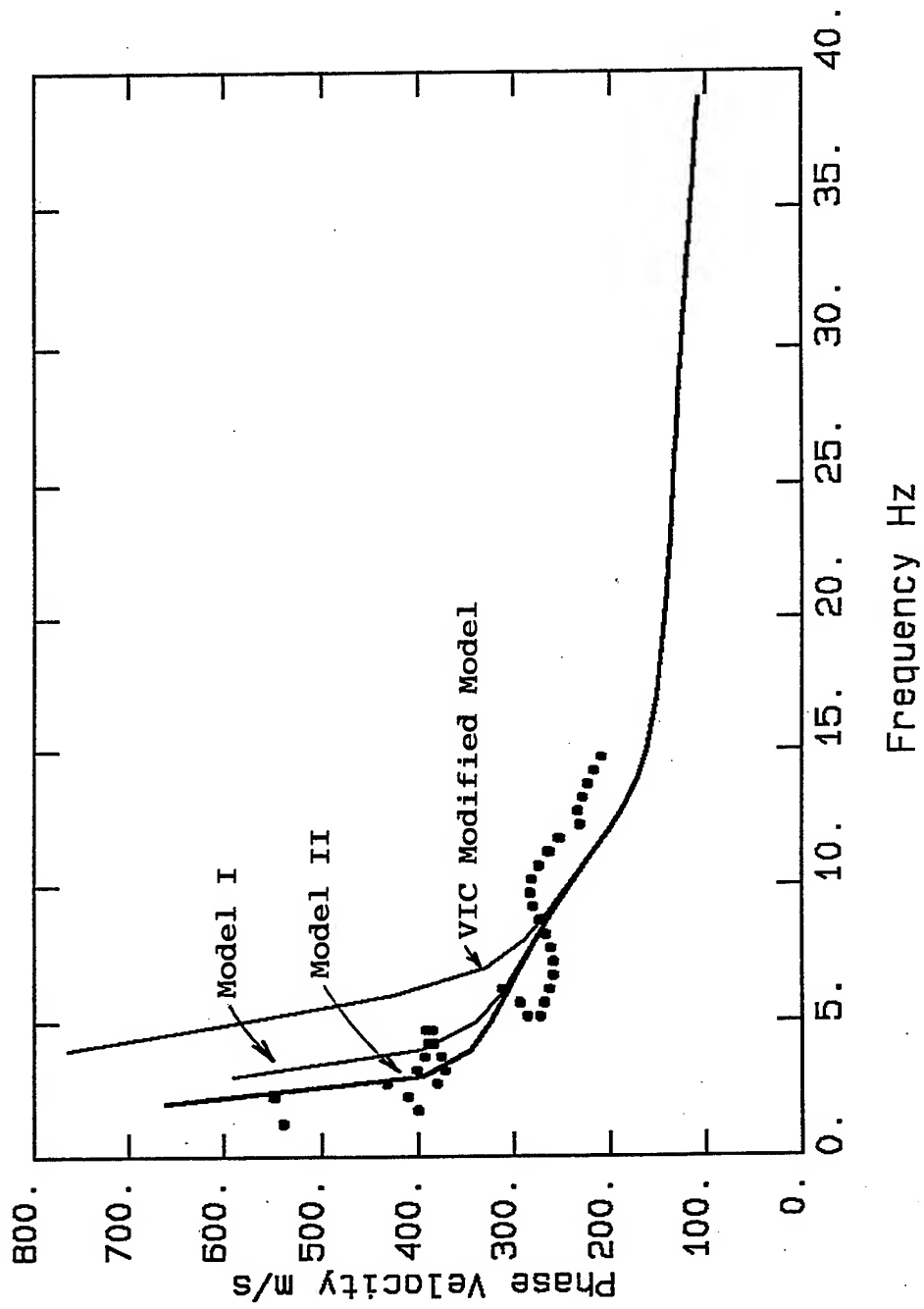
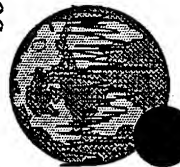
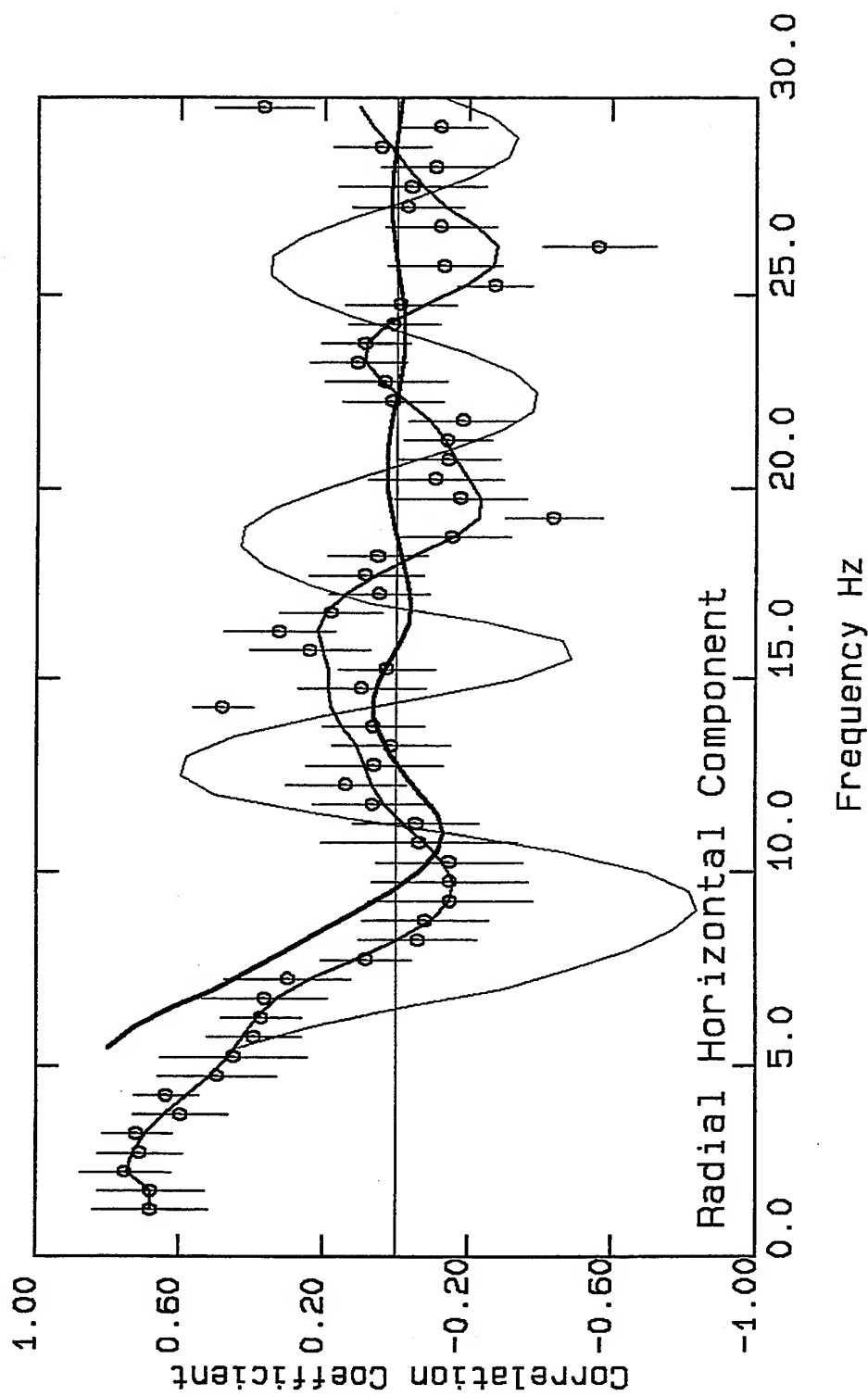


Figure 3.44. Similar to Figure 3.42 except that the calculated phase velocities for frequencies greater than 5 Hz are reduced by 50% to demonstrate the possibility that microtremors for these frequencies are composed of both body and surface waves.





Figures 3.45.a. Plots of the CC-F values for the radial components of microtremors for the case of $r = 15$ m. The thick and thin solid lines on these figures show the expected patterns for the radial and tangential components, equations (2.22) to (2.25), depending upon the predominant direction of polarization for the horizontal components of microtremors.



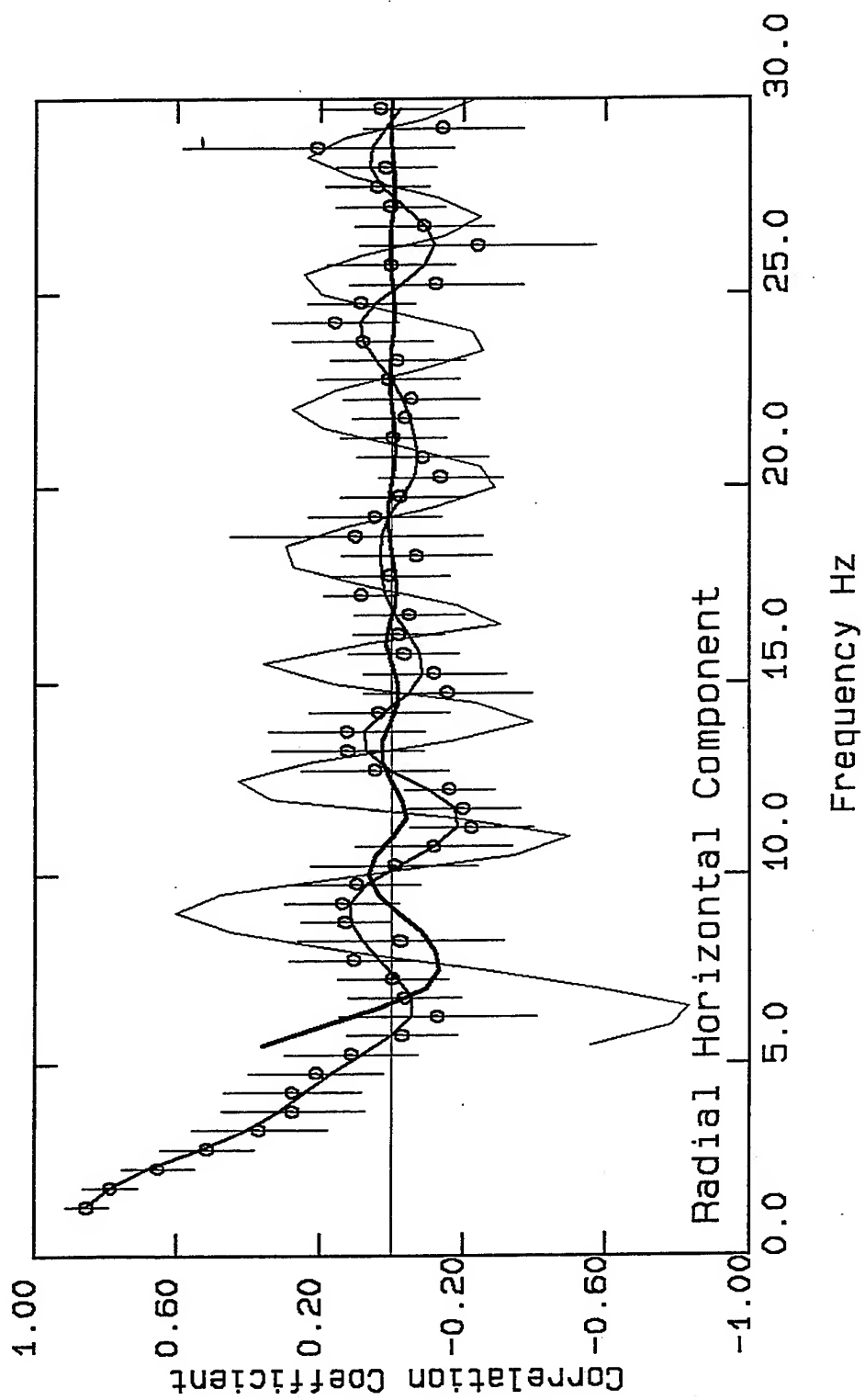
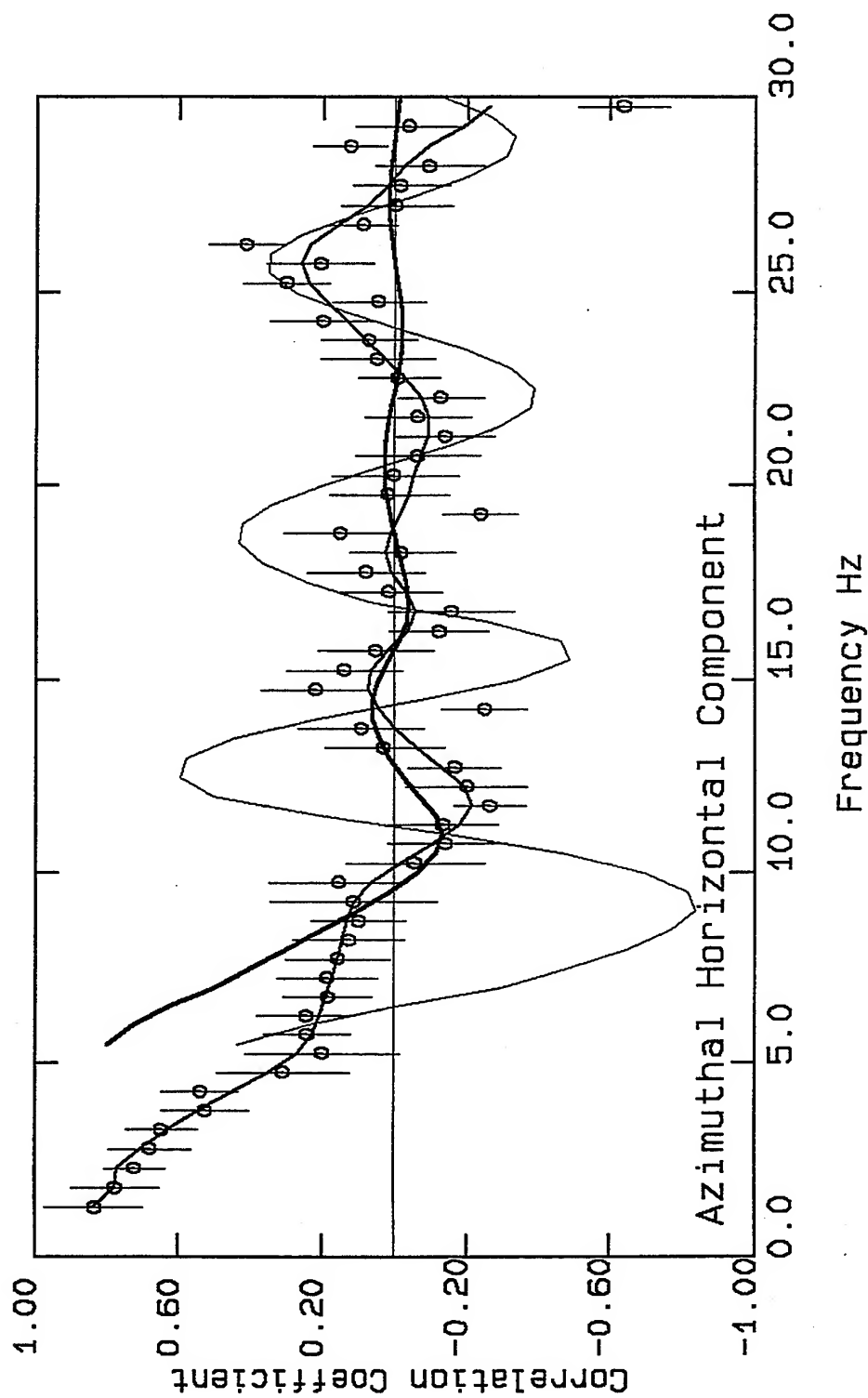


Figure 3.45.b. Similar to Figure 2.23.a but for the case of $r = 30$ m.





Figures 3.46.a. Plots of the CC-F values for the tangential components of microtremors for the case of $r = 15$ m. The thick and thin solid lines on these figures show the expected patterns for the radial and tangential components, equations (2.22) to (2.25), depending upon the predominant direction of polarization for the horizontal components of microtremors.



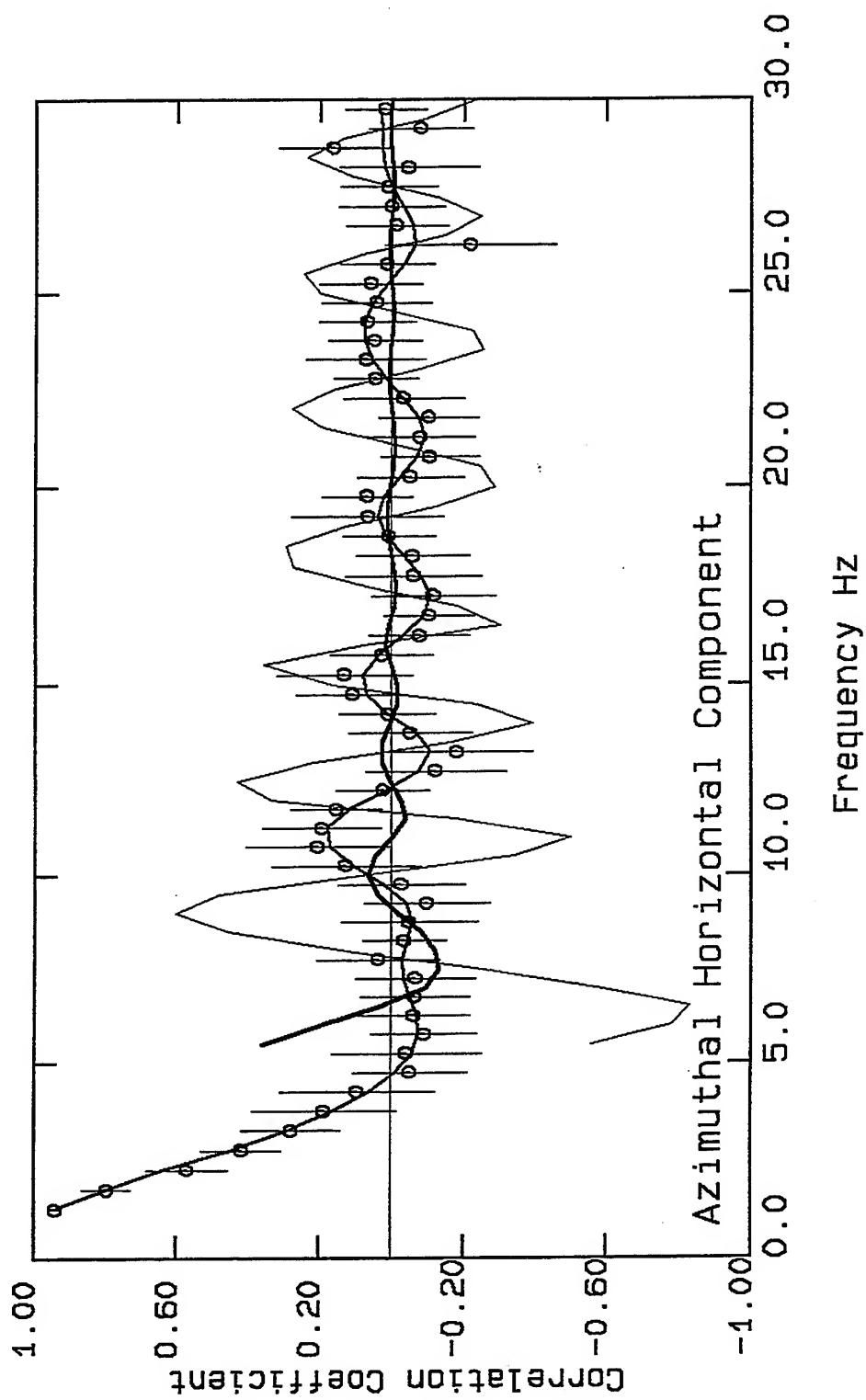
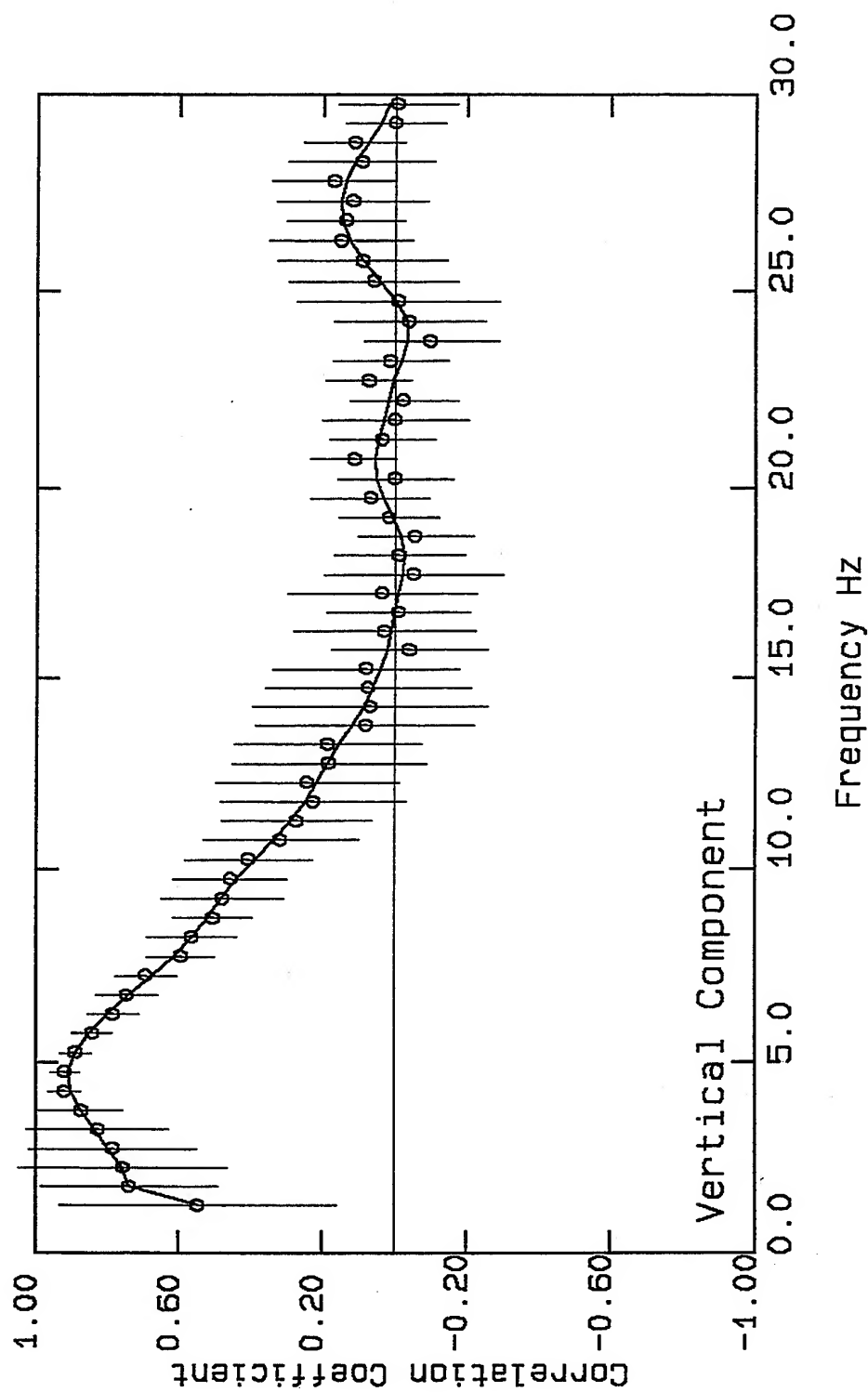


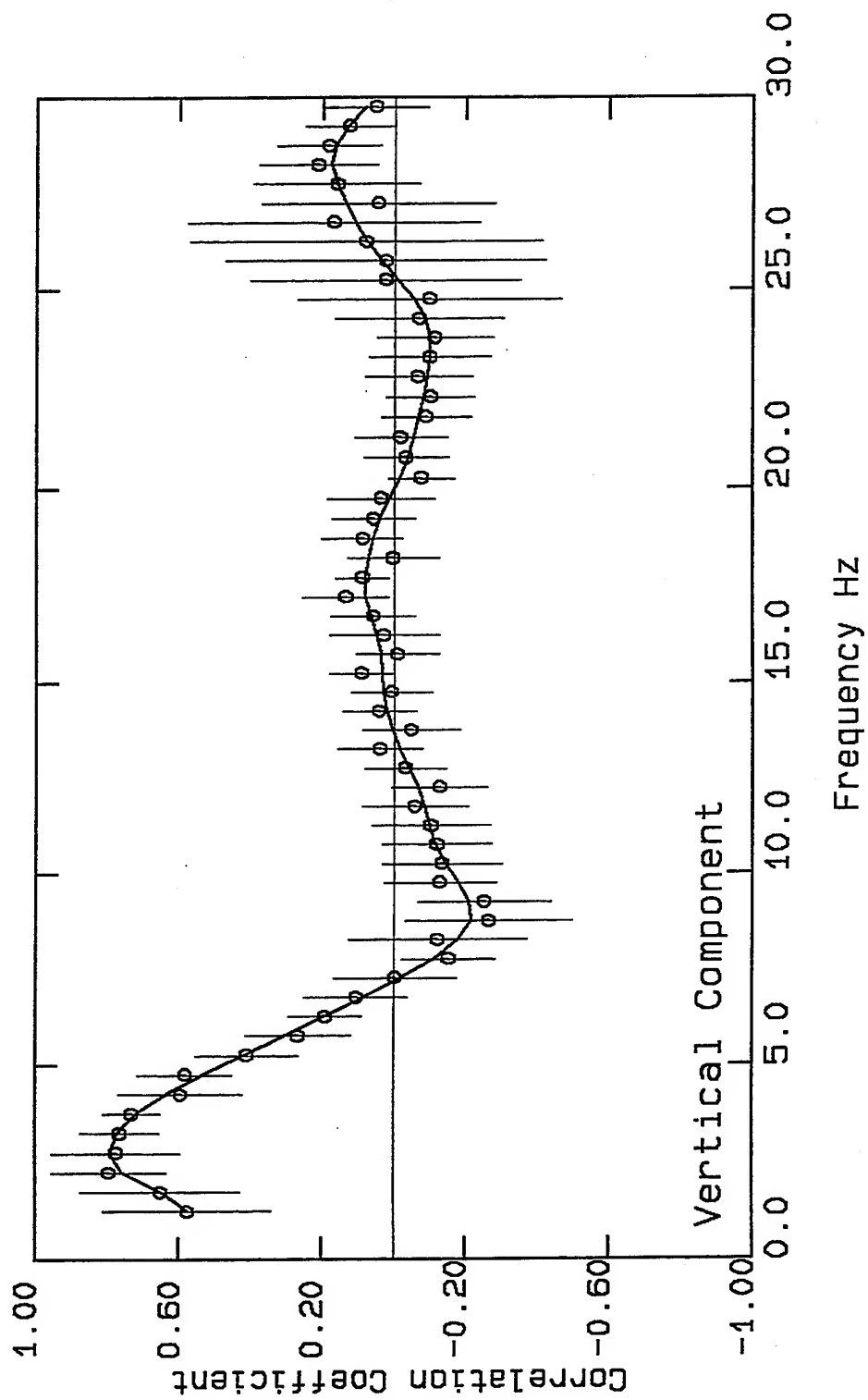
Figure 3.46.b. Similar to Figure 2.23.a but for the case of $r = 30$ m.





Figures 3.47. Plots of the CC-F values for the vertical components of microtremors and the best fit to the data for the case of $r = 15$ m.

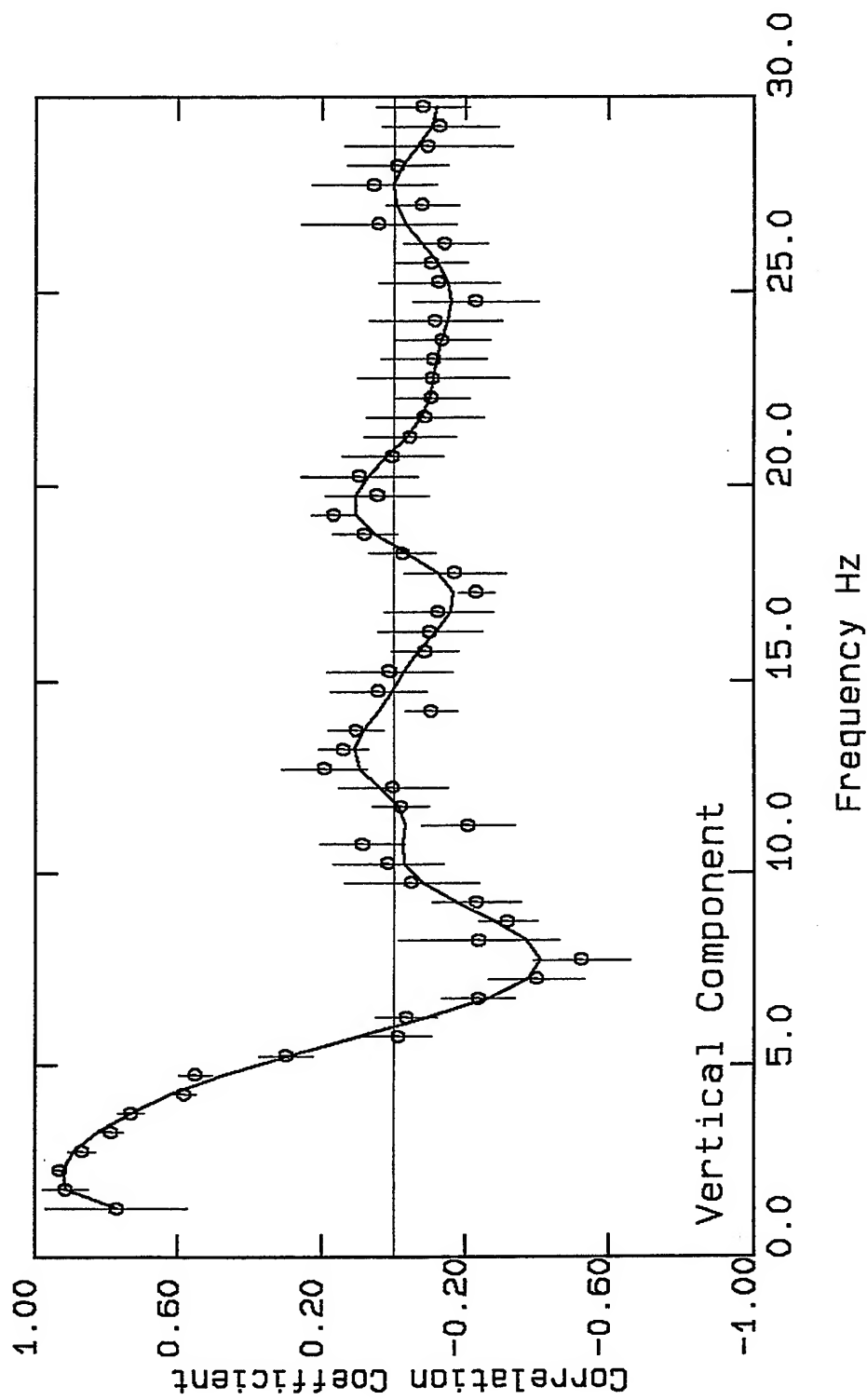




Figures 3.48. Plots of the CC-F values for the vertical components of microtremors and the best fit to the data for the case of $r = 30$ m.



VortexRock Consultants, Inc.



Figures 3.49. Plots of the CC-F values for the vertical components of microtremors and the best fit to the data for the case of $r = 37$ m.



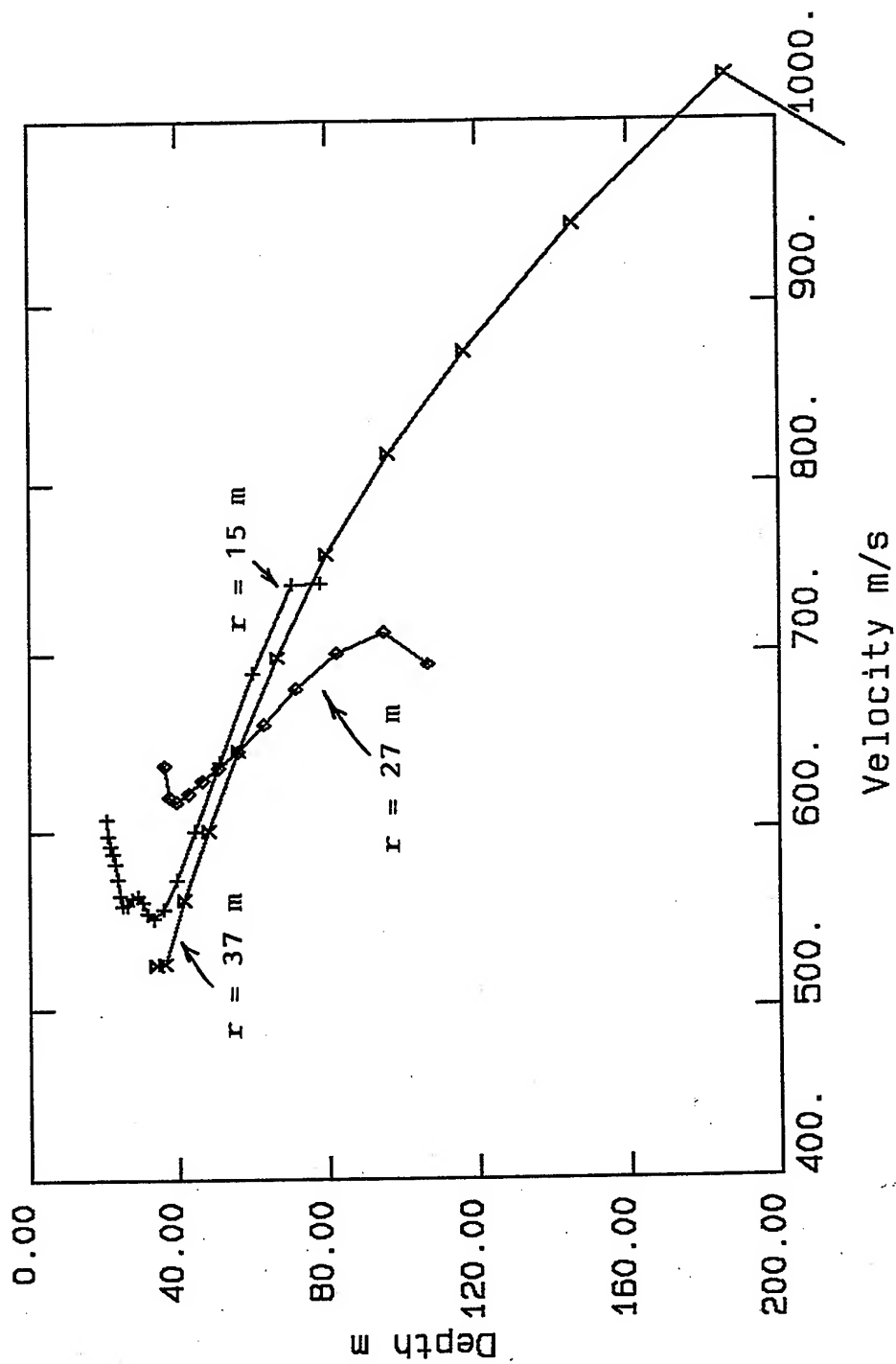


Figure 3.50. Plots of the phase velocities versus depth for the three phase velocity data sets in Table 3.18.



VortexRock Consultants, Inc.

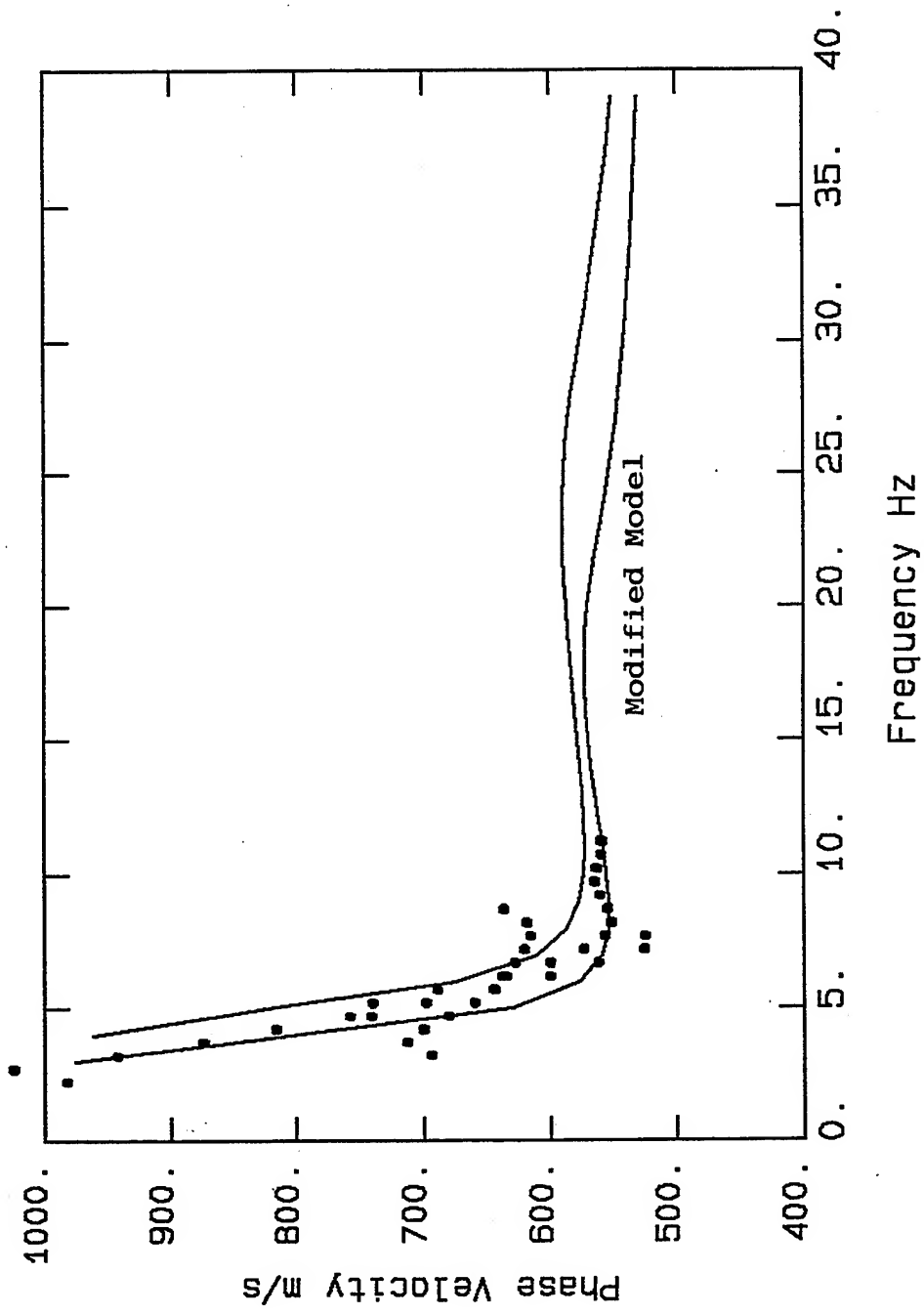
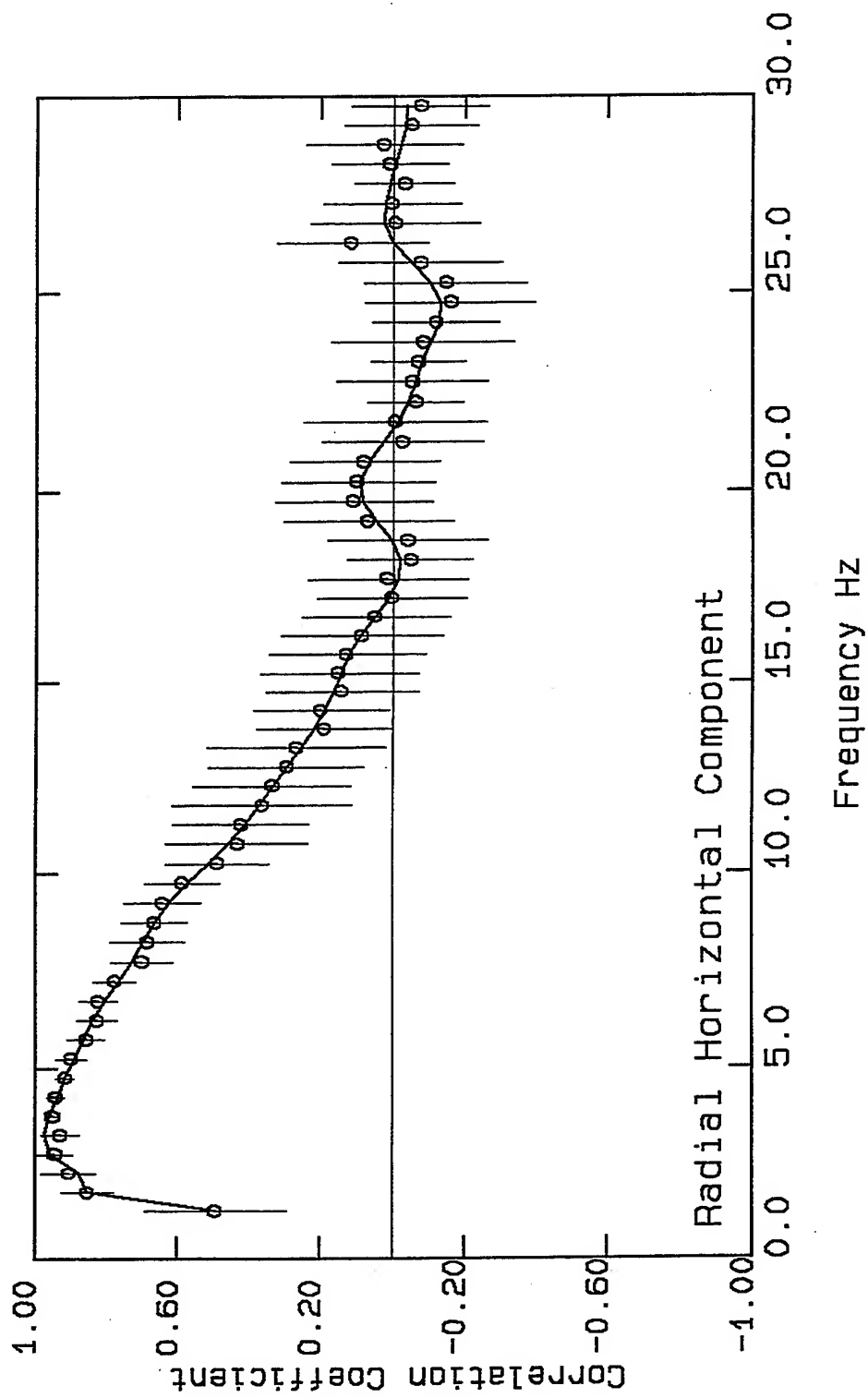
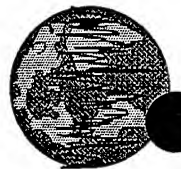


Figure 3.51 Plots of the calculated and simulated phase velocities for the model in Table 3.19, the top curve, and for a modified model with the depth of the second layer at 50 m.





Figures 3.52.a. Plots of the CC-F values and the best fit to the data for the radial components of microtremors for the case of $r = 15$ m.



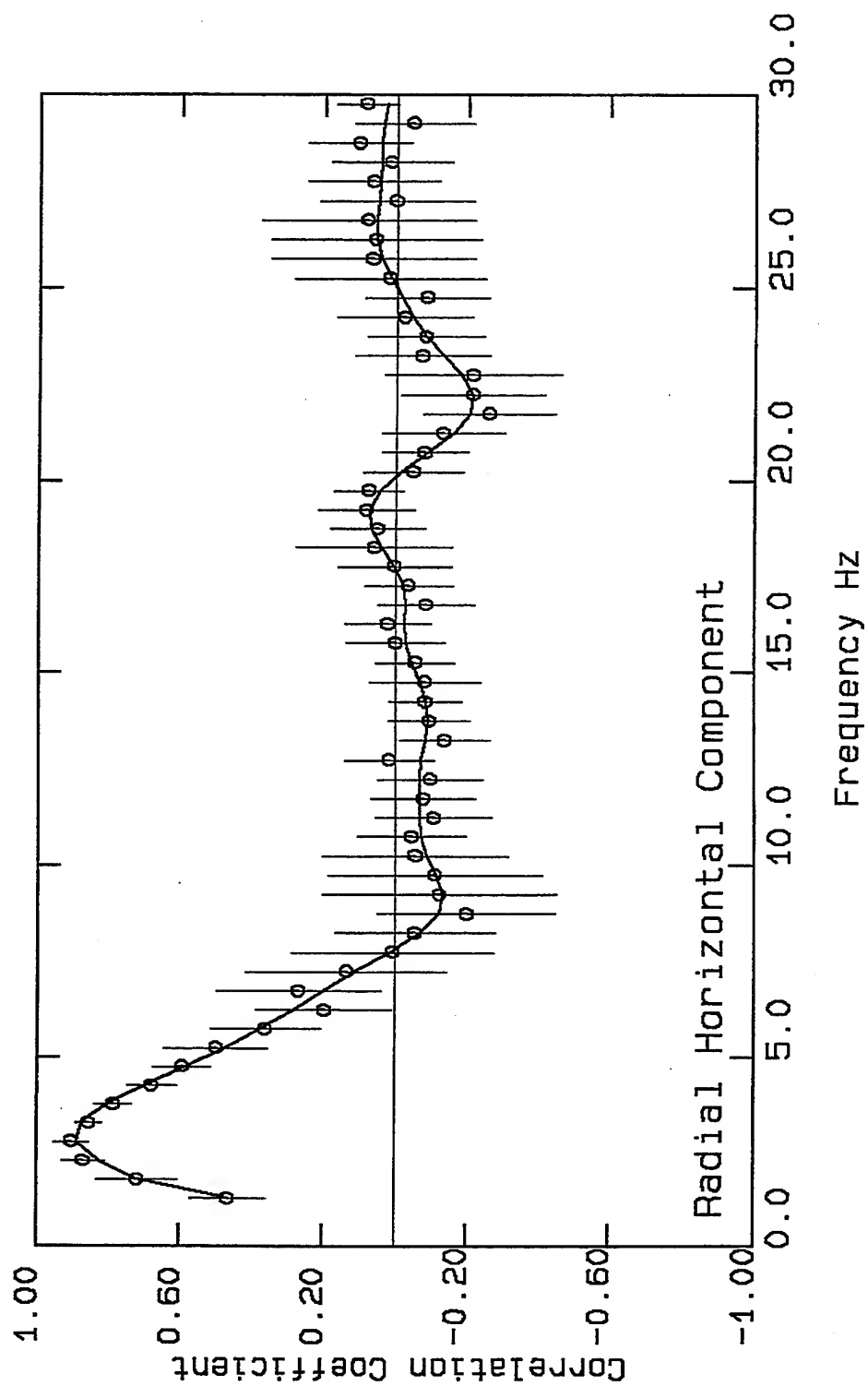


Figure 3.52.b. Similar to Figure 2.23.a but for the case of $r = 30$ m.



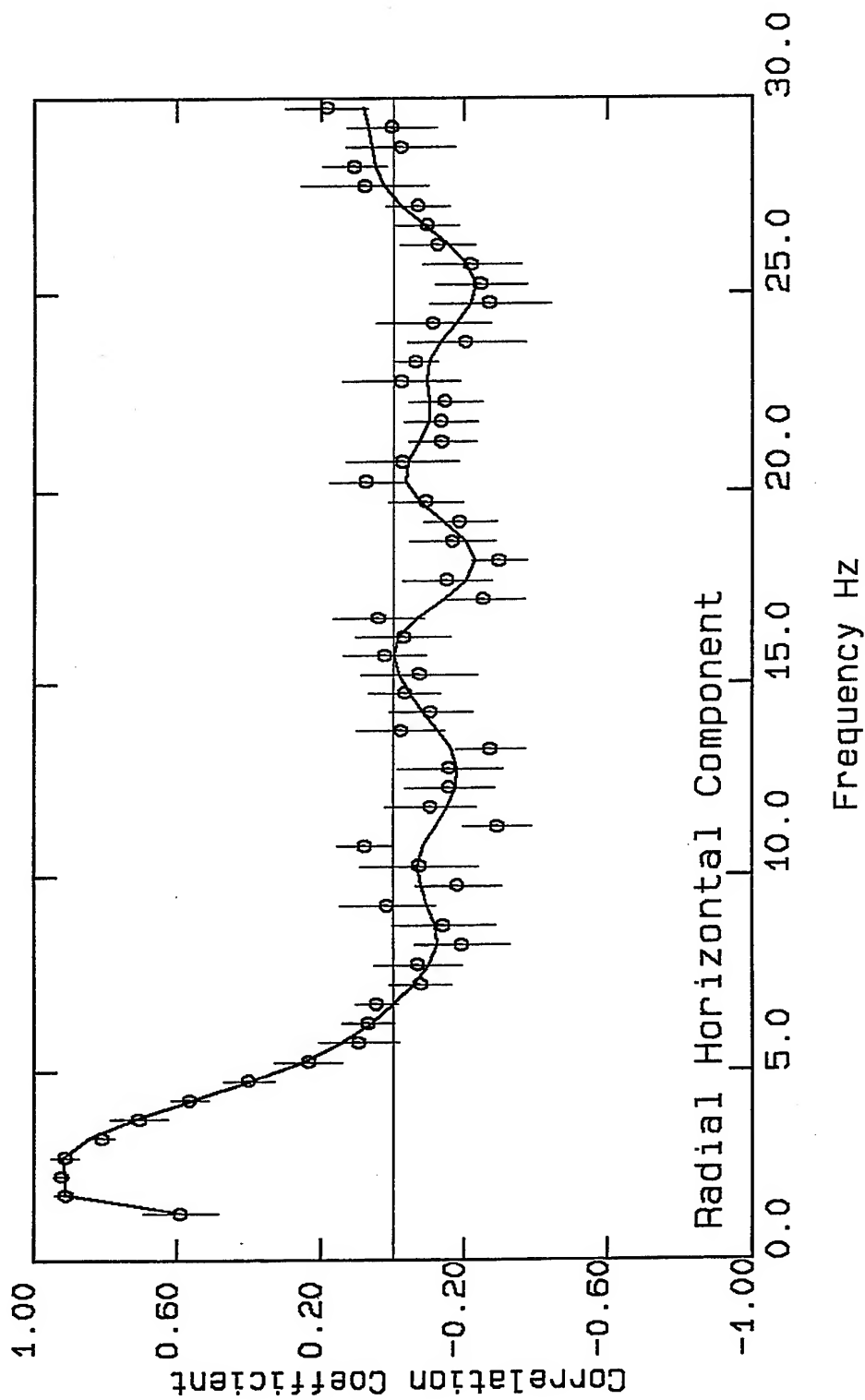
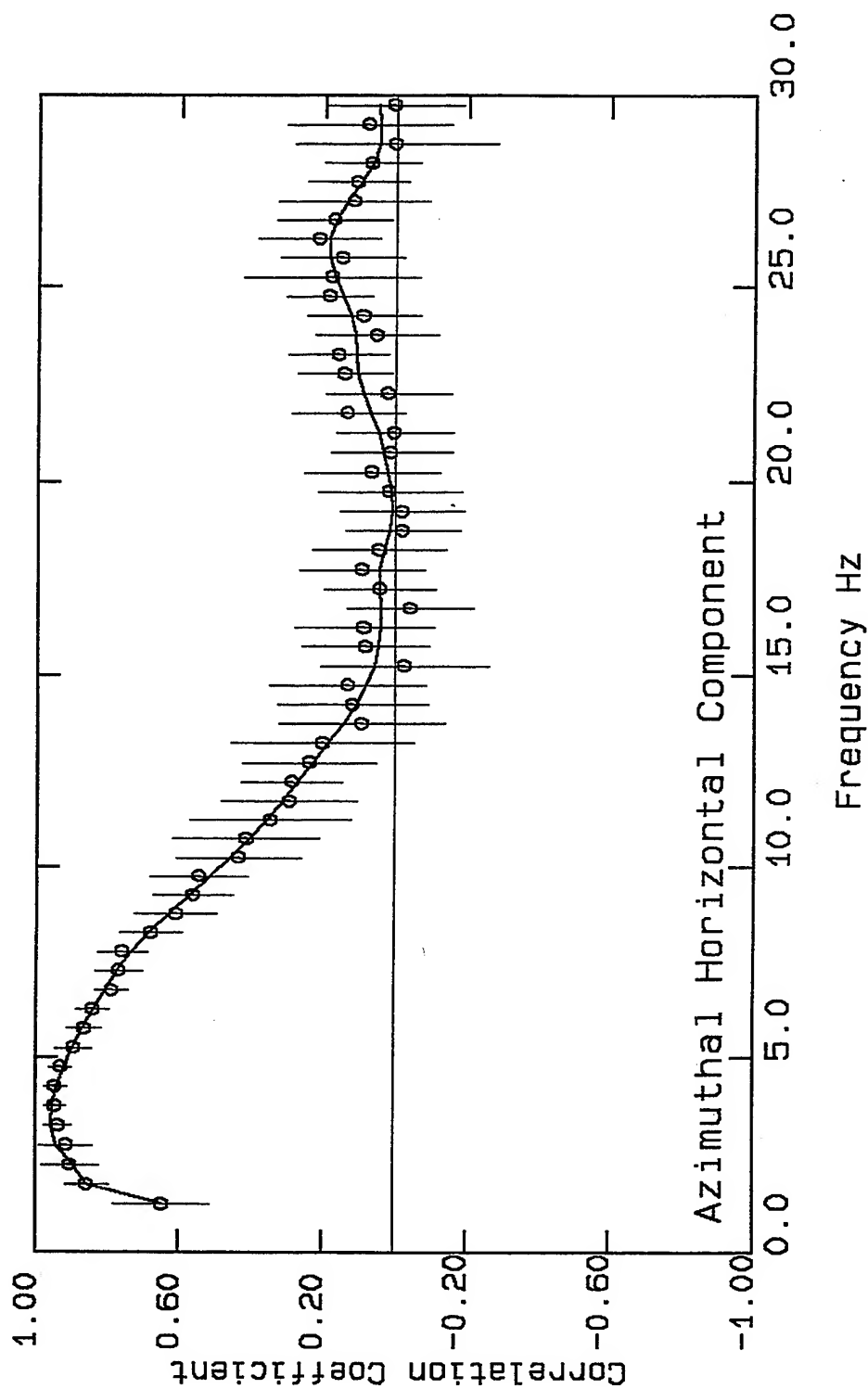


Figure 3.52.c. Similar to Figure 2.23.a but for the case of $r = 37$ m.



VortexRock Consultants, Inc.



Figures 3.53.a. Plots of the CC-F values and the best fit to the data for the tangential components of microtremors for the case of $r = 15$ m. The tangential and radial CC-F curves are very similar and resemble the CC-F curve for the vertical components. This suggests that microtremors are composed of waves that are equally polarized parallel and perpendicular to their directions of propagation.



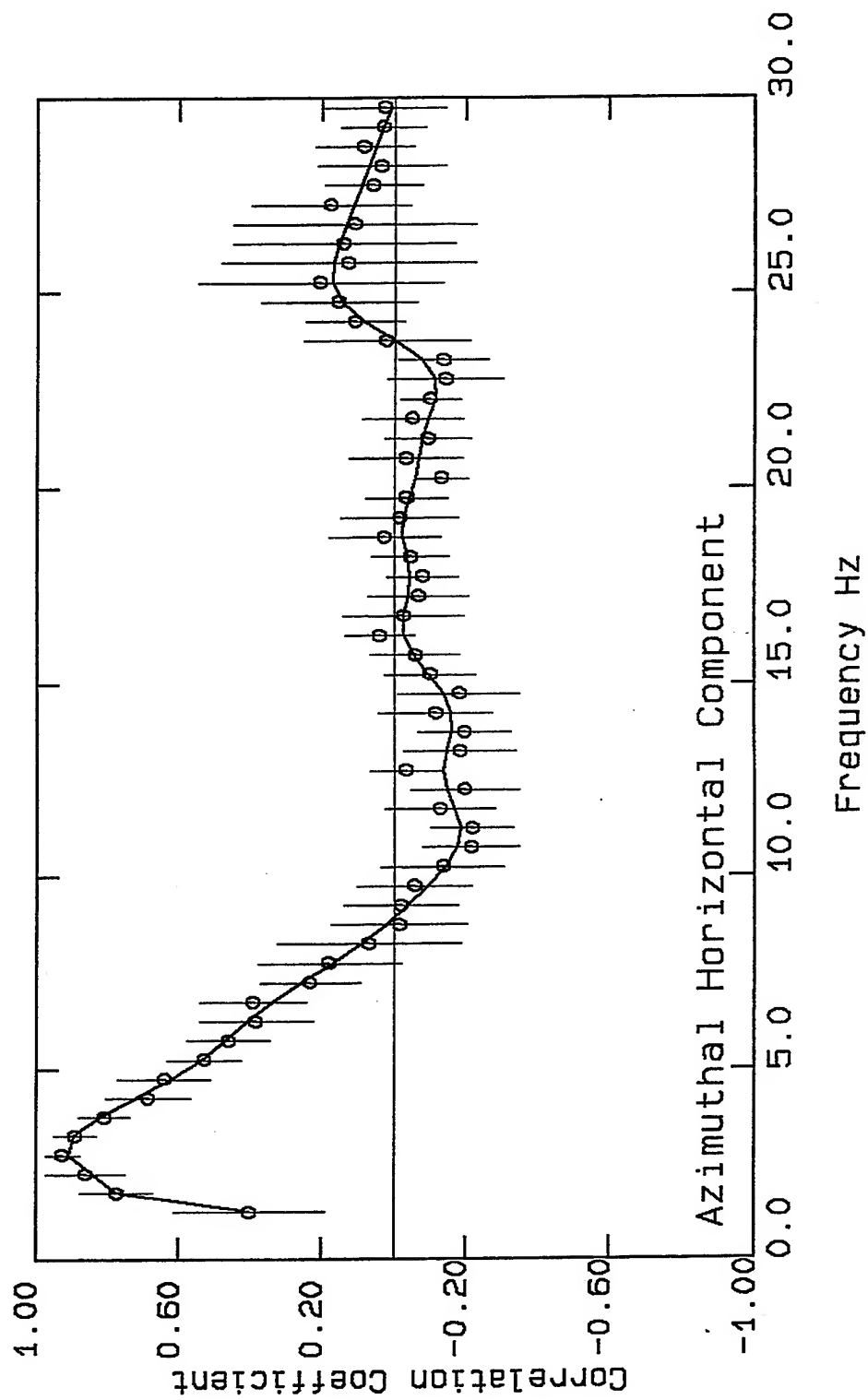


Figure 3.53.b. Similar to Figure 2.23.a but for the case of $r = 30$ m. The CC-F curves for this case also show very good similarity with the CC-F curves for the radial and vertical components.



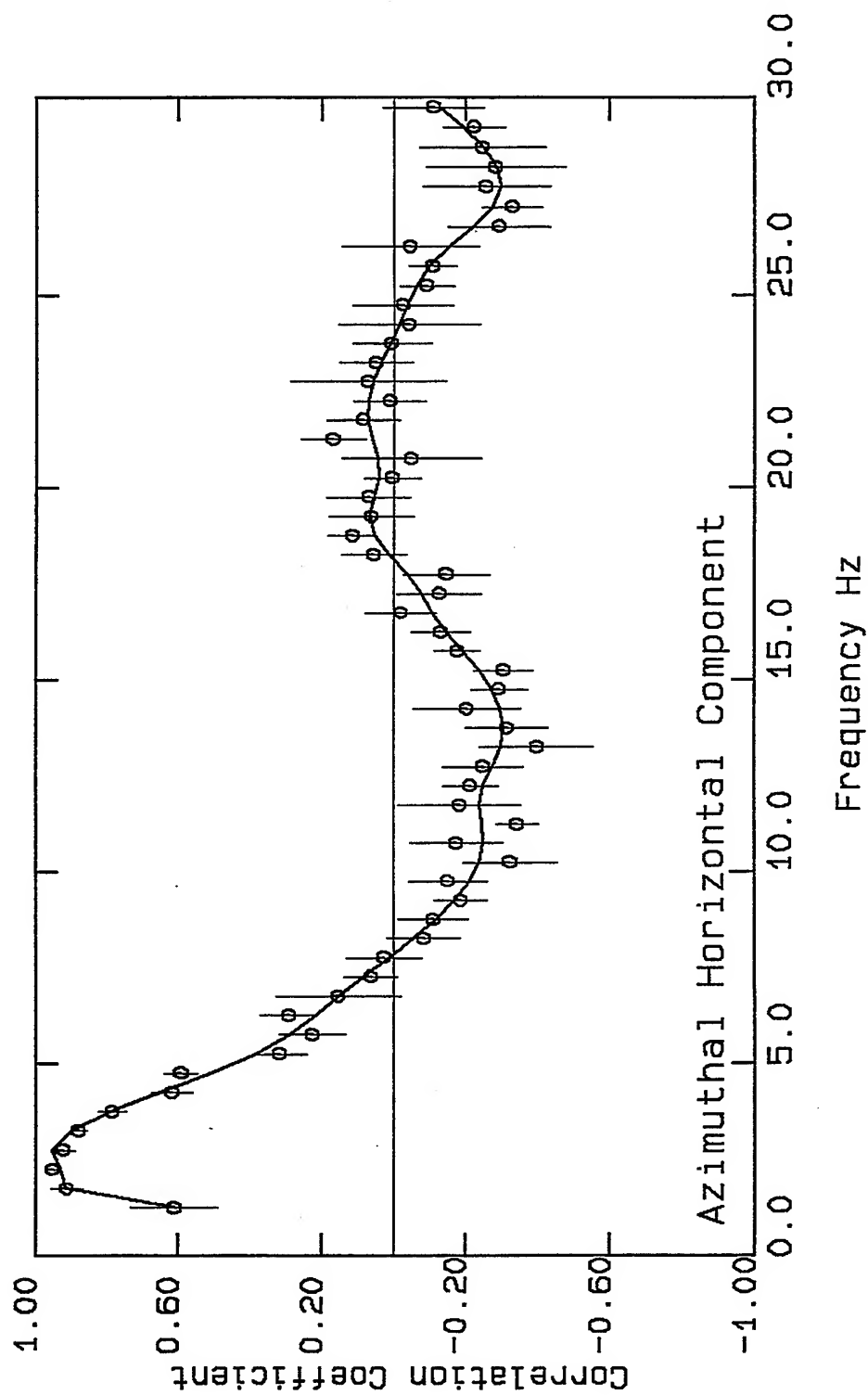


Figure 3.53.c. Similar to Figure 2.23.a but for the case of $r = 37$ m. The CC-F curves for this case also show very good similarity with the CC-F curves for the radial and vertical components.



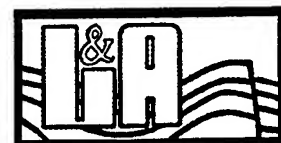
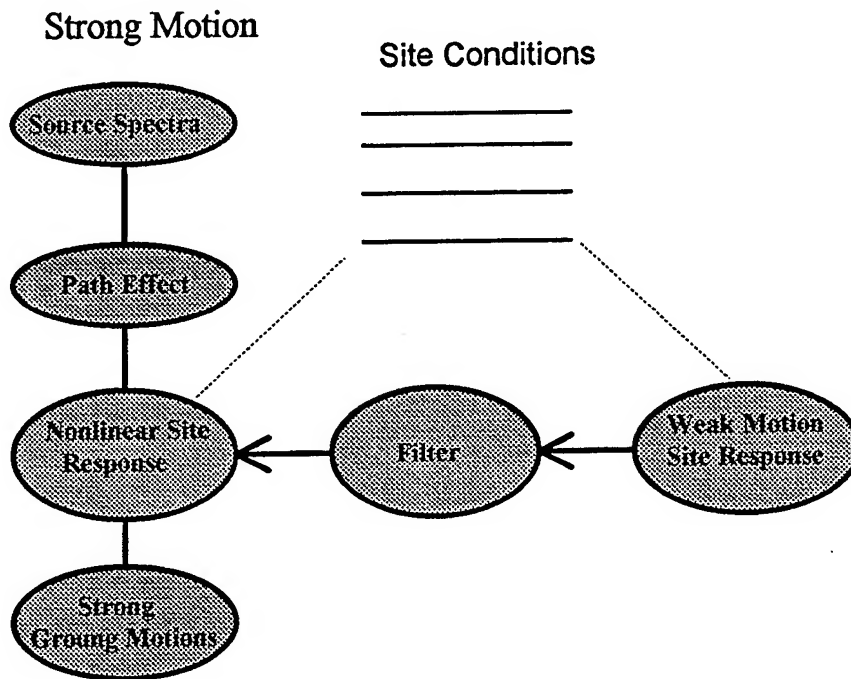
Chapter 4

Simulation of Strong Ground Motion Parameters Based on Weak Motion Site Response

There are ample evidence from theoretical, experimental, and earthquake observation studies that soil materials under strong ground shaking show nonlinear behavior (Boore et al., 1989; Darragh and Shakal, 1991a ,b, Jarpe et al., 1988, 1989; Seed, 1988; Chang et al., 1990; and Chin and Aki, 1991; Mohamadian and Pecker, 1992). The state-of-the-practice for site response analysis is to model the site as layered medium and calculate the strong motion site response by one-dimensional SH wave propagation through the medium. In general, the results of such analysis may not adequately represent the complexity of the wave propagation through the local subsurface materials. In that respect, methods that use real earthquake data to characterize the site response, such as coda waves amplification technique, could provide a more realistic information on the site response to earthquake ground motions. However, except for sites that have been instrumented and recorded moderate or large earthquakes, most available information on site-response including those from the coda waves represent the weak ground motions and thus are the linear site response. The weak motion site response (WMSR) can not be directly translated into the strong motion site response (SMSR) unless the nonlinear mechanisms that control the amplitude and the frequency content of strong ground motions are known.

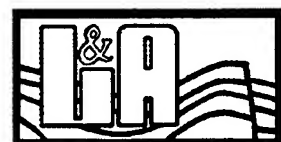


The SMSR is a nonlinear problem that depends upon the frequency content and amplitudes seismic waves. The earthquake ground motions at a site reflect the nature of the ground motions at the source, the wave propagation through the Earth between the source and the site, possible focusing or defocusing effects of large scale geologic structures on seismic waves, topography of the site, possible resonating effects of shallow reflectors, and the nonlinear response of the local site materials. Therefore, the SMSR analysis can not be separated from the detail of the earthquake source parameters and path effects. Following is a block diagram of a typical earthquake ground motion phenomena.



The left column shows the simplified block diagrams of the major parameters that control earthquake strong ground motions. In a typical strong ground motion simulation the missing link is the nonlinear site response. Although, there are uncertainties in all other parameters, we can make reasonable assumptions about the source, path effects in terms of the quality factor, and weak motion site response such as coda waves amplification factors. However, we do not know how the site would respond to earthquake strong ground shaking. Therefore, the issue becomes how to simulate the strong ground motions using the weak motion site response information. As is shown in the diagram, we need to design a filter to transform the WMSR to the SMSR. However, as it will be shown shortly the design of such filter depends upon the source and path parameters and thus requires to be integrated into the whole process of ground motion simulation. Following we will discuss the state of the practice of the ground motion simulation within which we will introduce a simple methodology for transforming the WMSR to SMSR.

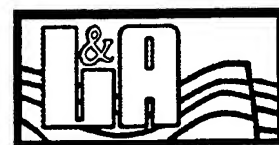
During the last fifteen years, a number of modeling techniques for earthquake rupture mechanisms and earthquake ground motion simulation have been developed that have direct application in engineering seismology. The most notables are the Barrier and Asperity models for fault rupture mechanisms (Papageorgiou and Aki 1983a and 1983b; Kanamori, 1978; and Lay and Kanamori, 1981), the empirical Green's function technique (EGFT) for simulating ground motion time histories (Hartzel, 1978), and the random vibration technique to predict the statistical mean of peak ground motion and response spectra based on an assumed earthquake source spectrum (Hanks and McGuire, 1981 and Boore, 1983). The EGFT is a practical way of simulating ground



motions from a large earthquake (target earthquake) by using the recorded ground motions of smaller events (sub-events) which share the common propagation paths as the target earthquake. However, for most site locations and fault systems, strong motion recordings are not available. To overcome this difficulty, one could take the advantage of the coherent deterministic properties of the long period spectral components of the sub-events and treat the high frequency components as the results of a stochastic process. Therefore, peak ground motions and response spectra could be determined by using the random vibration technique (RVT). Such a procedure could have a broad engineering applications because it could efficiently incorporate the complexities of the rupture mechanisms, the regional and local site effects, and the structural response into the ground motion analysis. Furthermore, the use of RVT is specially suitable to determine the design seismic parameters, since it eliminates the need for performing the analysis for different input motions. Following, we present a model for earthquake strong ground motion simulation based on the concept of empirical Green's function and random vibration techniques.

Based on the concept of the empirical Green's function technique, the Fourier amplitude spectrum of ground motions for a target earthquake at a site can be formulated as

$$y(\omega) = \sum_{j=1}^J Y_j(\omega) e^{-i\omega t_j} G(\omega) \quad (4.1)$$



where $Y_j(\omega)$ is the Fourier amplitude spectrum of sub-event j at the site, ω is the natural frequency, t_j is the delay time for the arrival of the seismic waves from sub-event j to the site; $t_j = X_j / V + R_j / \beta$, where X_j is the distance from the rupture initiation point to the element j , R_j is the distance from the element j to the site, V is the rupture propagation velocity, β is the shear wave velocity for the medium, and $G(\omega)$ is the response of the local site materials.

Using the ω^2 - model for the source spectrum (Hanks and McGuire, 1981) and including the terms for the path effects and f_{\max} (Papageorgiou and Aki, 1983; and Hanks, 1982) the spectral amplitudes for each sub-event can be written as

$$Y_j(\omega) = \frac{K_j}{4\pi\rho\beta^3 R_j} \frac{(M_0)_j (2\pi f)^n}{1+(f/f_{0j})^2} \frac{e^{-\pi f R_j / \beta Q}}{\sqrt{1+(f/f_{mj})^8}} \quad (4.2)$$

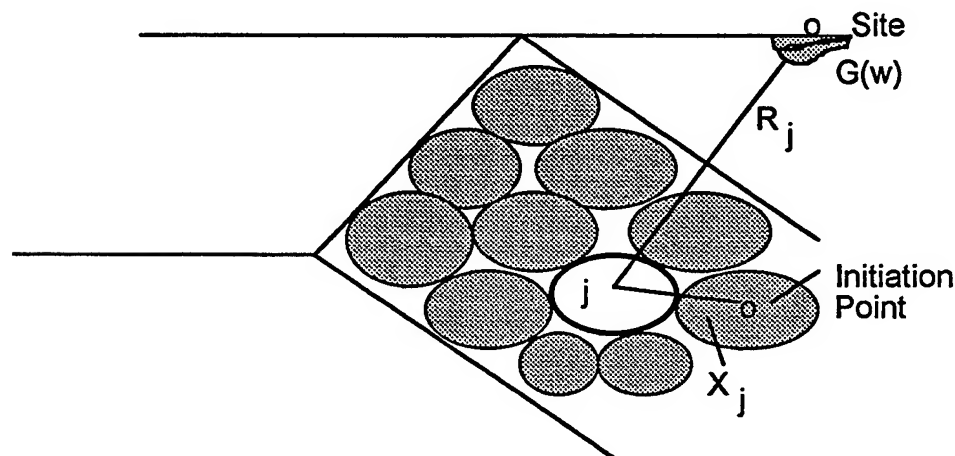


Diagram 4.1. A schematic diagram of the sub-event model as is formulated in equation (1)



where K is a coefficient representing the combined effects of the radiation pattern, free surface effect, and the partition of energy; ρ is the density; M_0 is the seismic moment; f_0 is the corner frequency; Q is the quality factor; and f_m is the high frequency cut-off. M_0 , f_0 , and f_m are defined for each sub-event. The power factor n takes the value of 0, 1, or 2 for displacement, velocity, or acceleration, respectively.

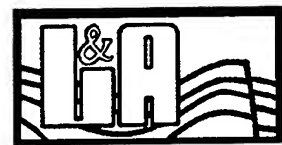
The displacement spectrum of a structure with a single-degree-of-freedom and linear damping properties can be written as

$$RS(\omega) = \left| \frac{\omega^2}{(\omega_0 - \omega^2) - (2\xi\omega_0\omega)i} \right| Y_g(\omega) \quad (4.3)$$

where $RS(\omega)$ is the displacement spectrum of the structure, $Y_g(\omega)$ is the displacement spectrum of the ground motion, and ω_0 and ξ are the natural frequency and the damping ratio of the structure, respectively. Substituting for $Y_g(\omega)$ from equation (4.2), using $n=0$ for displacement, the displacement spectrum of an oscillator with a single-degree-of-freedom could be written as

$$RS(\omega) = \sum_{j=1}^J Y_j(\omega) e^{-i\omega t_j} G(\omega) \left| \frac{\omega^2}{(\omega_0 - \omega^2) - (2\xi\omega_0\omega)i} \right| \quad (4.4)$$

For most engineering analysis the design structures should be checked against many different input ground motions. In that respect, the random vibration technique is an



effective way to determine the design peak ground motions and response spectral parameters. Results of a number of investigations have indicated that RVT successfully predicts the peak ground motion at both local and regional distances (Hanks and McGuire, 1981; Boore, 1983; Hanks and Boore, 1984; Joyner, 1984). The RVT relies on relating the root-mean-square (rms) amplitude, in time domain, to the peak ground motions as a function of the number of cycles of vibration over the strong motion duration.

Cartwright and Longuet-Higgins (1956) derived an asymptotic expression for the ratio of the expected peak ground motions to the corresponding root-mean-square amplitude for the case of large number of extrema in a time interval T as

$$\frac{E(y_{\max})}{y_{\text{rms}}} = [2 \ln(N)]^{1/2} + \gamma / [2 \ln(N)]^{1/2} \quad (4.5)$$

where $E(y_{\max})$ is the expected value of the largest of N extrema, y_{rms} is the root-mean-square amplitude, and $\gamma = 0.5772..$ is Euler's constant. Boore (1983) stated that this equation is good approximation even for small values of N . From the Parseval's theorem y_{rms} can be written as

$$y_{\text{rms}} = \frac{1}{\pi} \int_0^{\infty} |y(\omega)|^2 d\omega \quad (4.6)$$



where $|y(\omega)|$ is the absolute spectral amplitude. The expected number of extrema for N can be estimated from

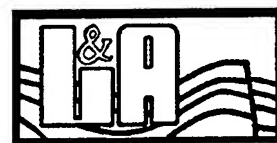
$$N = 2 \tilde{f} T \quad (4.7)$$

where \tilde{f} is the predominant frequency of the motion and T is the duration of the motion. The factor 2 appears because there are two extrema in each cycle of motion. However, for the asymptotic equation (4.5) N is the number of zero crossings and \tilde{f} can be estimated from the following expression

$$\tilde{f} = \frac{1}{2\pi} \left[\frac{\int_0^\infty \omega^2 |y(\omega)|^2 d\omega}{\int_0^\infty |y(\omega)|^2 d\omega} \right]^{1/2} \quad (4.8)$$

Boore and Joyner (1984) proposed two different time windows to estimate the number of extrema (N) and rms amplitudes for the response spectral estimation based on RVT. They obtained corrections for the rms duration of a damped oscillator in terms of the earthquake source duration and the natural period and damping properties of the oscillator.

Equation (4.4) is the basis for the strong motion response spectral simulation of large earthquakes using sub-event models. The term $G(\omega)$ represents the overall local site response. We write $G(\omega)$ in terms of linear and nonlinear site response as follows



$$G(\omega) = G_l(\omega) e^{-\alpha f} \quad (4.9)$$

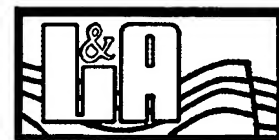
where $G_l(\omega)$ represents the weak motion, linear, site response and $e^{-\alpha f}$ represents the response of the filter in Diagram 4.1 for transforming the WMSR to SMSR. The exponential decay term is equivalent to the response of a dashpot with a constant damping ratio. It also represents a constant Q -model that is commonly used in earthquake seismology for modeling the attenuation properties of materials. It is understood that a simple dashpot model would not capture the complex nature of the nonlinear behavior of the local soil materials. However, the realization of more sophisticated models require information that would not be available in most real case situations. Substituting for $G(\omega)$, equation (4.4) can be written as

$$RS(\omega) = \sum_{j=1}^J Y_j(\omega) e^{-i\omega t_j} G_l(\omega) e^{-\alpha f} \left| \frac{\omega^2}{(\omega_0 - \omega^2) - (2\xi\omega_0\omega)i} \right| \quad (4.10)$$

In a similar way the equation for the free surface ground motion can be written as

$$y(\omega) = \sum_{j=1}^J Y_j(\omega) e^{-i\omega t_j} G_l(\omega) e^{-\alpha f} \quad (4.11)$$

It should be mentioned that the ground motion time histories can be easily calculated from equations (4.10) and (4.11) using the inverse Fourier transformation since these equation provide both the amplitude and phase of the spectral components. Substituting



for $y(\omega)$ and y_{rms} in equation (4.5) the equation for the expected peak ground motion can be written as

$$E(y_{max}) = \frac{1}{\pi} [2 \ln(N)]^{1/2} + \gamma / [2 \ln(N)]^{1/2} \int_0^\infty \left| \sum_{j=1}^J Y_j(\omega) e^{-i\omega t_j} G_i(\omega) e^{-\alpha f} \right|^2 d\omega \quad (4.12)$$

where

$$N = \frac{T}{\pi} \left[\frac{\int_0^\infty \omega^2 \left| \sum_{j=1}^J Y_j(\omega) e^{-i\omega t_j} G_i(\omega) e^{-\alpha f} \right|^2 d\omega}{\int_0^\infty \left| \sum_{j=1}^J Y_j(\omega) e^{-i\omega t_j} G_i(\omega) e^{-\alpha f} \right|^2 d\omega} \right]^{1/2}$$

For a given design earthquake and WMSR the only unknown in the right hand side of equation (4.12) is the coefficient α . Knowing α , the response spectra and time histories for the design earthquake can be simulated. We propose to determine the coefficient α in such a way that equation (4.12) for a given design earthquake and WMSR predicts an assumed peak ground acceleration (PGA) for typical soil sites based on empirical relationships between PGA of soil and rock sites. Shortly, we will discuss the procedure in more detail.

The central point of the proposed methodology is that for any given source-site scenario a reliable estimate of a PGA at the soil site is available. Figure 4.1 shows summary plots of PGA at soil sites versus PGA at rock sites. These curves represent the results of



both the observed and simulated data and could be used for our purpose. However, in order to gain more insight on the nonlinear behavior of soil materials we complement this data with the results of strong ground motion simulation of various source-site scenarios. For this purpose we use the ω^2 - point source model, equation (4.2), for earthquakes and randomize the source and site parameters by using the Monte Carlo simulation technique. The ω^2 - point source model, equation (4.2), is

$$Y_j(\omega) = \frac{K_j}{4\pi\rho\beta^3 R_j} \frac{(M_0)_j (2\pi f)^n}{1+(f/f_{0j})^2} \frac{e^{-\pi f R_j / \beta Q}}{\sqrt{1+(f/f_{mj})^8}} \quad (4.13)$$

The subscript j in equation (4.13) identifies the variables that are used in the Monte Carlo Simulation of the ground motions. The variation in the corner frequency is controlled by the stress drop and the magnitude as follows (Kanamori, 1977; Knopoff, 1957; and Brune, 1970 and 1971)

$$\log(M_0) = 1.5 * M_w + 9.05, \quad (4.14)$$

$$\Delta\sigma = \frac{7}{16} \frac{M_0}{r^3} \quad (4.15)$$

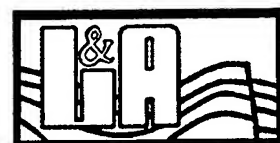
and

$$f_0 = \frac{2.34\beta}{r} \quad (4.16)$$



where M_w is the moment-magnitude, $\Delta \sigma$ is stress drop, and r is the radius of the equivalent circular rupture area for the earthquake. The unit for seismic moment in equation (4.14) is N-m. A single earthquake source model with no direct account of the directivity and rupture propagation is used for the simulation with the idea that statistical variation of different parameters specially the radiation coefficient, K , would account for these effects. The local site condition is modeled by a single layer of soil materials over a base-rock-type materials. It is understood that a single layer model for the site conditions is a very simple representation of a complex system. However, the concept is that each one-layer model is the realization of different multilayer models with similar SMSR. We use the word base-rock instead of rock to emphasize the fact that in the geotechnical earthquake engineering the bedrock-type materials are considered as those with the shear wave velocity of 760 m/s (2500 ft/s). This is very different than the concept of the bedrock in earthquake seismology where the bedrock materials are assumed to have very high shear wave velocities. Table 4.1 shows the list of parameters and the range of values that are considered in the simulation.

The depth of the soil materials is limited to 150 ft since at such a depth the shear wave velocity of different soil type materials, even if normally consolidated, will approach the shear wave velocity of the base-rock materials. The equivalent linear method is used to simulate the nonlinear behavior of the soil materials. The last parameter in the table, the damping factor, is the ratio of the equivalent to peak particle velocities that is used to



obtain the equivalent damping ratio for the soil materials. The total of five thousand simulations are performed. The random vibration technique is used to obtain the peak ground accelerations and 1.0 second spectral acceleration values. For each scenario the

Table 4.1. List of parameters and their range of values that are used in ground motion simulation

<i>Variable</i>	<i>Lower Value</i>	<i>Upper Value</i>
<i>M_w - Moment-Magnitude</i>	<i>6.0</i>	<i>8.0</i>
<i>R - Distance (km)</i>	<i>10.0</i>	<i>30.0</i>
<i>Δσ - Stress Drop (bars)</i>	<i>50.0</i>	<i>100.0</i>
<i>K - Radiation Coefficient</i>	<i>0.8</i>	<i>1.0</i>
<i>Depth - m</i>	<i>3.0 (10 ft)</i>	<i>46 (150 ft)</i>
<i>Shear Wave Velocity m/s</i>	<i>133 (400 ft/s)</i>	<i>457 (1500 ft/s)</i>
<i>Damping Factor</i>	<i>0.6</i>	<i>0.8</i>

ground motion parameters are calculated with and without the effects of the local site materials corresponding to the base-rock and soil site conditions, respectively. A direct comparison between the ground motion parameters of these two site conditions provide information on the nonlinear behavior of the soil site in response to the scenario earthquake. Figure 4.2 shows plots of the PGA values at soil sites versus those at rock sites. The two lines represent the amplification factors of 1.0 and 1.5 for the PGA at the



soil sites. All points above the line with the slope of 1.0 represent the source-site scenarios with relatively linear site amplification. The apparent conclusion from this figure is that the strong motion PGA at soil sites show a broad range of both amplification and de-amplification. However, a close investigation of the results suggests that the depths of the soil materials have dominant effects on the estimation of the PGA values. Figures 4.3-a to 4.3-g are similar to Figure 4.2 except that the data are partitioned based on the depth of the soil materials. Each figure shows a distinctive pattern for the PGA values. The results suggest that at low levels of ground motions, base-rock $PGA < 0.3$ g, the soil site could respond almost linearly with the possibility of ground motion amplification. However, at high level of ground motions the PGA at shallow soil sites, less than about 40 ft, show amplification whereas the PGA at deep soil sites show de-amplification. The results also suggest a definite saturation of the PGA values with increasing the level of the base-rock motions for deep soil sites. However, the degree of saturation of PGA varies with the depth of the soil materials. Figure 4.4 shows the best fit to the simulated soil-base-rock PGA values and the corresponding one standard deviation of error for seven depth intervals. The best fit for the depth range of 100-120 ft show a sudden increase in the soil PGA values. This reflects the lack of data in this depth range rather than the physics of the problem. The plots of 1.0 s acceleration spectral values, Figure 4.5 also show the strong depth dependency. However, the pattern of the behavior for the PGA and 1.0 second spectral acceleration values are different. Considering that 1.0 second spectral acceleration values could be strongly affected by the regional large scale structures, such a basins, that are not related to the local site effects we use soil-rock PGA relationships for WMSR to SMSR purposes.



We propose to characterize the site conditions into three different depth categories as shallow, less than 40 ft, intermediate, between 40 and 80 ft, and deep, greater than 80 ft. Figure 4.6 shows the best fit and one standard deviation of error for the PGA values for the three depth categories. These curves provide predictive relationships for the PGA at soil sites in terms of their corresponding values at base-rock sites. These depth ranges are selected since their lines of one standard deviation of error, for most cases, do not cross each other.

In order to design a nonlinear filter for the soil material, first we estimate the base-rock PGA for the design earthquake from equation (4.12) without any site effects and using RVT. We characterize the soil site as shallow, intermediate, or deep and identify a predictive relationship for rock-soil PGA from Figure 4.6. Using the simulated rock-site PGA and one of the curves on Figure 4.6 we estimate the most probable PGA at the soil site (PGA_S). We estimate the coefficient α , using a trial and error solution of equation (4.12), in such a way that the PGA_S at the site is predicted, see Diagram 4.2. The value for the coefficient α is unique for the given source, WMSR, and the nonlinear PGA scenario. Knowing the value of coefficient α for the given design earthquake the response spectral parameters and time histories for the site could be calculated from equations (4.10) and (4.11) and using the RVT.

Coefficient α is the key parameter that links the linear to nonlinear site response and enables us to estimate the strong ground motion spectral parameters. The fact that the



value for the coefficient α is obtained based on an assumed base-rock-soil site nonlinear PGA relationship does not mean that the estimated response spectra from the subsequent analysis is scaled by the PGA. The determination of the PGA and response spectral parameters from equations (4.10), (4.11), and (4.12) based on RVT takes into consideration the spectral amplitudes of all frequencies. Certainly, the high frequency components of the ground motion make more direct impact on the estimation of the PGA than the long period components. Nevertheless, the shape of the response spectral parameters would change with increasing or decreasing the level of the PGA_S since the nonlinear term, $e^{-\alpha f}$, affects all frequency components.



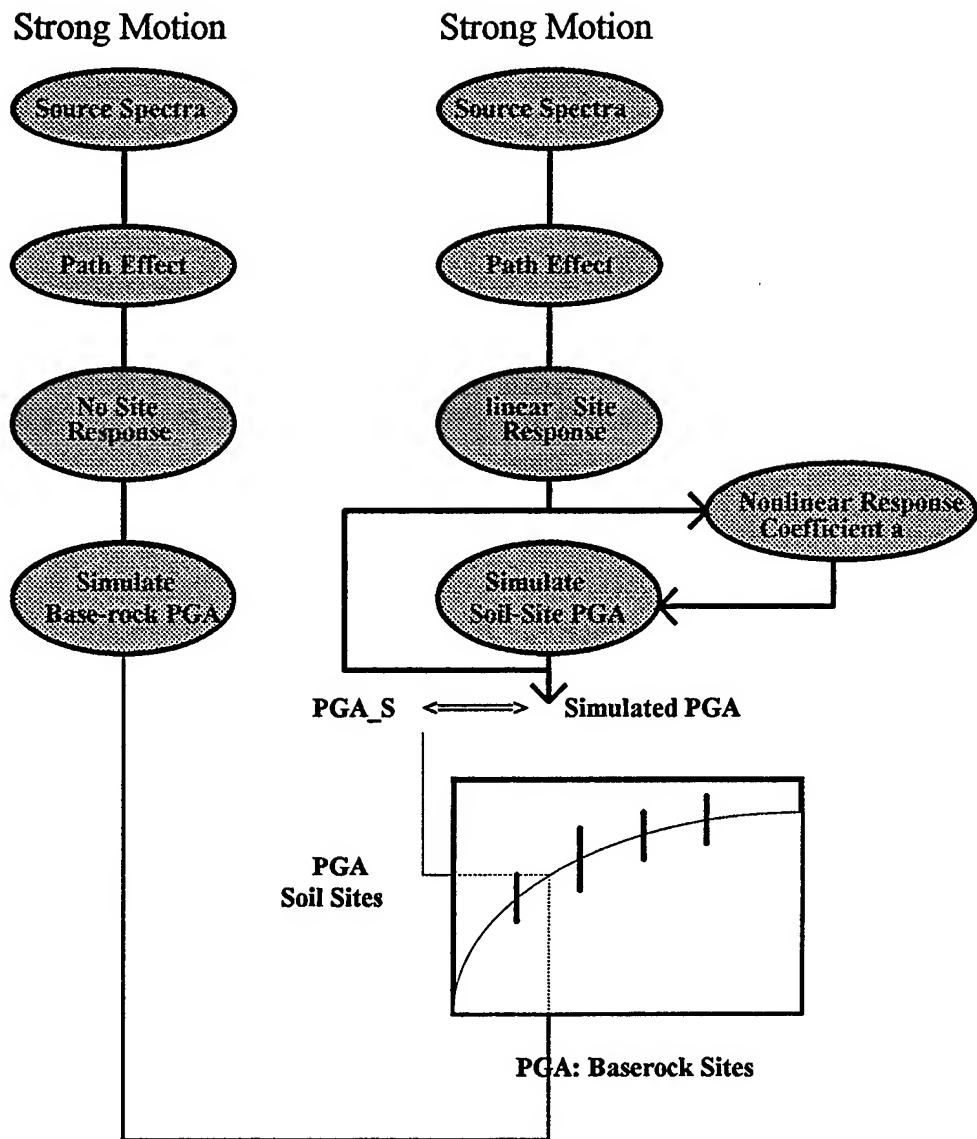
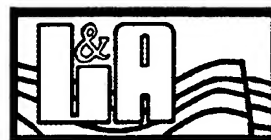


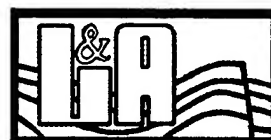
Diagram 4.2. A schematic diagram of the simulation procedure showing the WMSR to SMSR transformation



Application

In order to show the application of the proposed methodology in earthquake ground motion analysis we simulated the response spectral parameters for the Landers (1992) earthquake at five CDMG sites. The selected sites are Barstow, Desert Hot Spring, Joshua Tree, Palm Springs, and Yermo. The weak motion site response of these sites are obtained from a coda wave amplification database for southern California that is compiled by Chin and Aki (1993). The database is a GIS-based map of weak motion amplification factors for southern California based on the coda waves amplification factors and the information on the regional surface geology. Sites are characterized into two general groups namely the alluvium and bedrock. Using the similarity between the surface geology of sites with and without coda waves data a regional distribution of the coda waves amplification factors over 5x5 km grids for four frequency bands with center frequencies of 1.5, 3, 6, and 12 Hz are obtained. Figure 4.7 shows the location of sites underlain by the Quaternary-age alluvial materials. Figures 4.8-a to 4.8-d show the inferred weak motion amplification factors relative to a homogeneous half-space for different frequency bands. Regions of Imperial Valley and central Los Angeles basin show the greatest amplification values in southern California.

The source of the Landers earthquake was modeled by four sub-events with ω^2 -source model. The Landers earthquake has the moment magnitude of $M_w=7.4$ and stress drop of $\Delta\sigma = 100$ bars. The choices of the number of sub-events, stress drop, and f_{max} come from the results systematic studies on these parameters by Papageorgiou and Aki (1983b)



and Chin and Aki (1992). The rupture of the Landers earthquake starts from the southern end of the fault and propagates to the north. The attenuation properties of the region are modeled by a frequency dependent quality factor of $Q = 100 f^{0.9}$ (Chin and Aki, 1992).

Figures 4.9-a to 4.9-e show the horizontal component response spectra for 5% damping ratio at these stations. The CDMG response spectral values are calculated using the published time histories for these sites. The simulated response spectra are shown by symbols. The mid curve in Figure 4.6 is used to estimate the expected PGA at soil sites from those at rock sites. Three sets of response spectra are shown including $f_m = 5$ Hz and $f_m = 10$ Hz with a frequency dependent exponential decay, $e^{-\alpha f}$, and for $f_m = 5$ Hz with a frequency independent exponential decay, $e^{-\alpha}$. The thick line represents Boore et al. (1993) empirical response spectra based on the magnitude of the earthquake and the closest distance from each site to the surface trace of the fault rupture area. Spectral values at 2 seconds (0.5 Hz) are calculated based on coda waves amplification factors at 1.5 Hz. This assumption may not be warranted as the results of the simulation suggest. Table 4.2 shows the summary of observed and simulated PGA and duration parameters at these sites. The Husid duration is defined as the time between 5 and 95% of the cumulative energy of the time history. The simulated PGA and duration values at these sites show excellent agreement with the observed values.

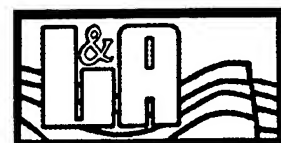
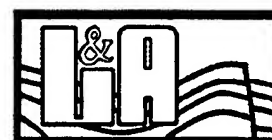


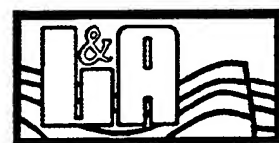
Table 4.2. A comparison between the observed and simulated PGA and the Husid duration at five of the CDMG recording stations.

<i>Station</i>	<i>Observed</i>		<i>Simulated</i>	
	<i>PGA g</i>	<i>Duration Seconds</i>	<i>PGA g</i>	<i>Duration Seconds</i>
<i>Barstow</i>	<i>.14</i>	<i>22</i>	<i>.10</i>	<i>23</i>
<i>Desert Hot Springs</i>	<i>.16</i>	<i>35</i>	<i>.12</i>	<i>41</i>
<i>Joshua Tree</i>	<i>.28</i>	<i>30</i>	<i>.21</i>	<i>35</i>
<i>Palm Springs</i>	<i>.09</i>	<i>43</i>	<i>.08</i>	<i>42</i>
<i>Yermo</i>	<i>.21</i>	<i>20</i>	<i>.14</i>	<i>22</i>

All five CDMG stations reportedly are deployed on alluvial materials. The Boore et al. empirical equation, as expected, represents the regional average response spectra. It appears that for these sites if the estimated PGA based on the empirical equation is in good agreement with the recorded PGA at a site, the empirical and the time history-related response spectra also show good agreement. It must be kept in mind that the results of the simulated response spectra are not strictly site specific. The nonlinear relationships shown in Figure 4.6 do not reflect the effects of a particular local site conditions on the peak ground acceleration. Furthermore, the damping effect of the site materials on seismic waves of different frequencies is possibly different than the simple exponential decay term, $e^{-\alpha f}$ or $e^{-\alpha}$ used in equation (4.5). The details of the local site



conditions will determine the amplification and attenuation of ground motions for different frequency bands. However, the good agreement between the observed and simulated PGA and response spectral values suggests that a "semi-site-specific" response spectra for future earthquakes could be obtained, with reasonable accuracy, by using typical source parameters for a given magnitude earthquake and knowing the WMSR such as coda waves amplification factors for the site. This simulation technique is specially attractive since one could introduce different levels of the complexity on the source parameters, rupture directivity, path effects including the basin response, and local site and structural response into the ground motion analysis. Another interesting aspect of the model is that both the frequency domain spectral parameters and time domain ground motions including the duration of shaking could be estimated. However, in order to fully appreciate the potential of this simulation technique and to evaluate its limitation and shortcomings more investigation on its application on past earthquake data at various sites is needed.



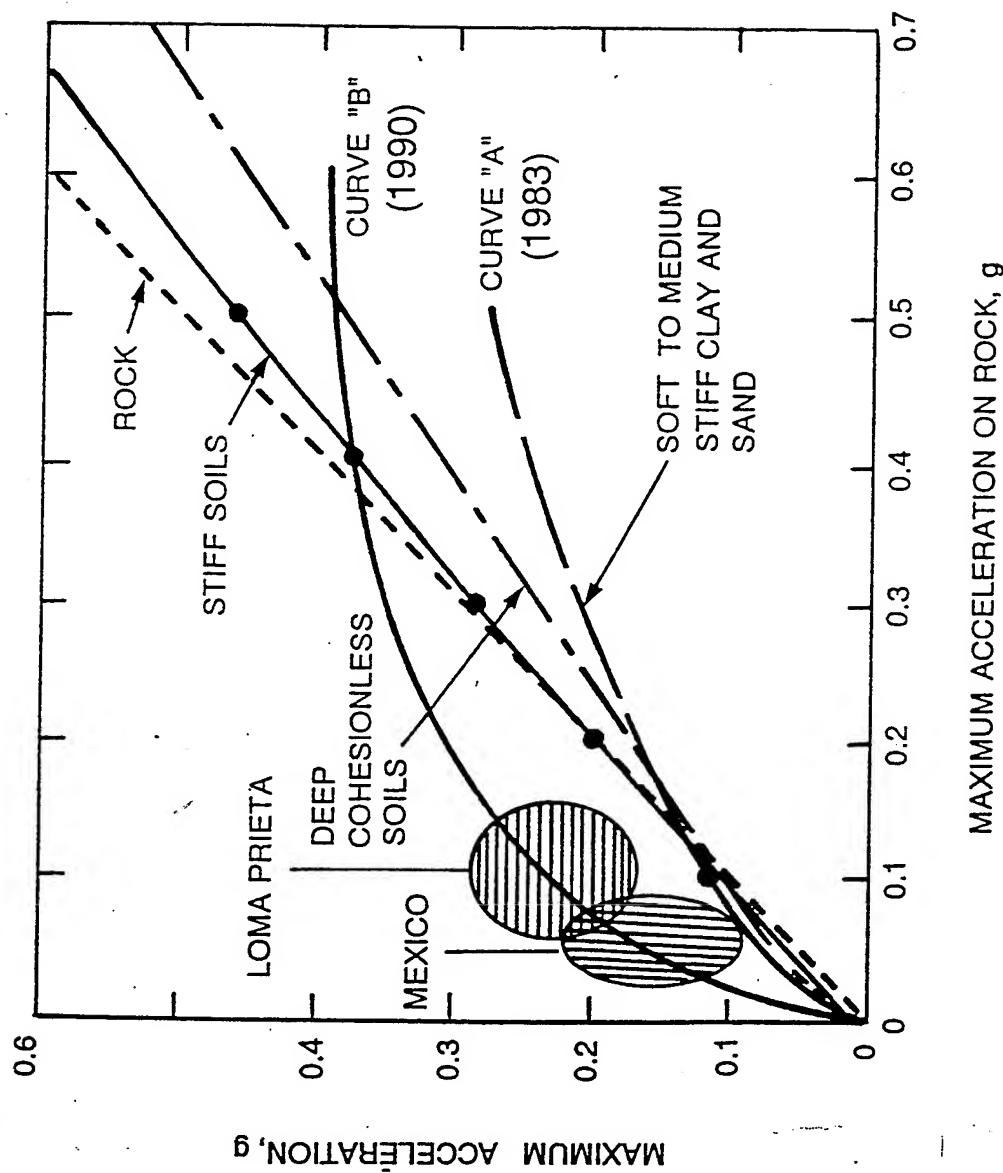


Figure 4.1. Plots of PGA at soil sites versus those at rock sites. The two curves correspond to prediction by Idriss (1990), before and B) after the Mexico and Loma Prieta earthquakes. This figure is taken from Lomintz (1994)



VortexRock Consultants, Inc.

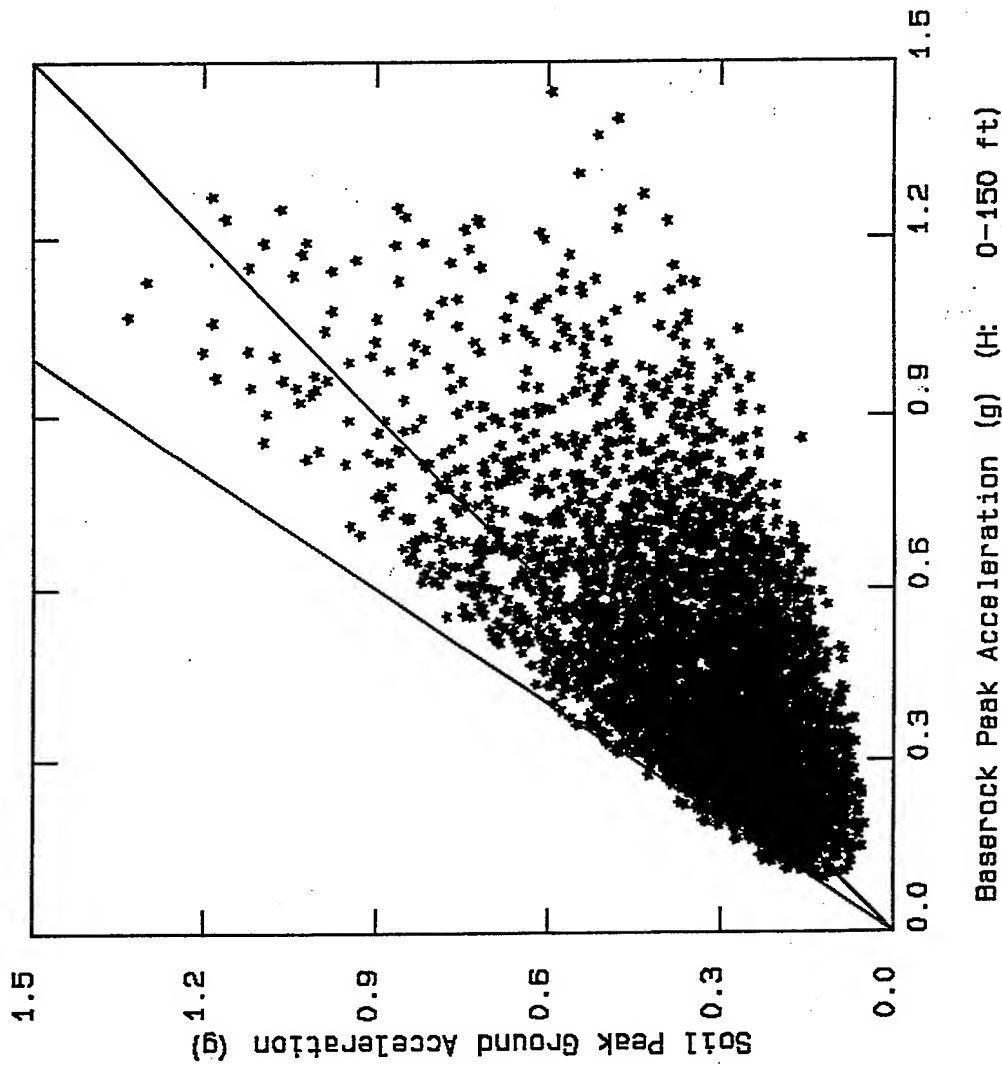


Figure 4.2. plots of PGA values at soil sites versus those at rock sites from 5000 simulations, See text for the detail. The lines for the amplification factors of 1.0 and 1.5 are shown.



VortexRock Consultants, Inc.

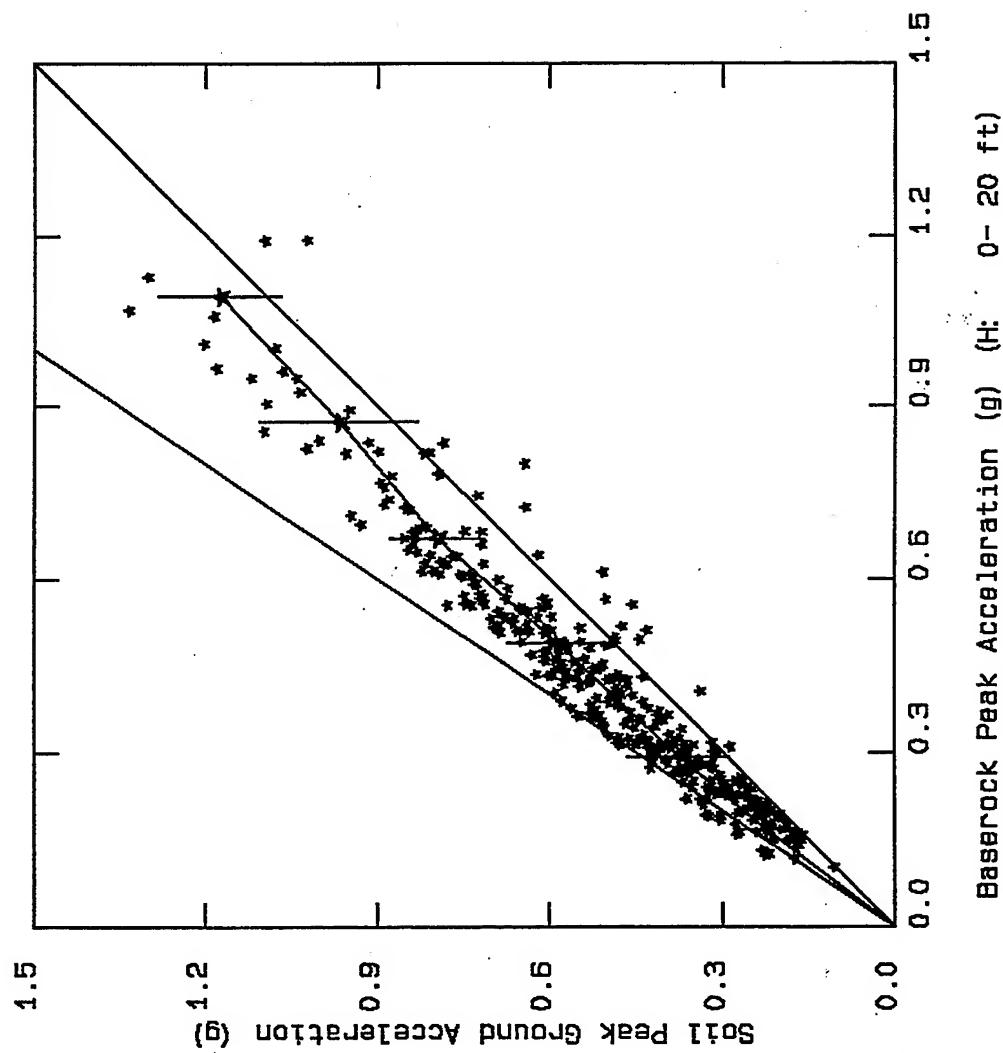


Figure 4.3.a. plots of PGA values at soil sites versus those at rock sites for the selected depths of soil materials. The lines for the amplification factors of 1.0 and 1.5 are shown.



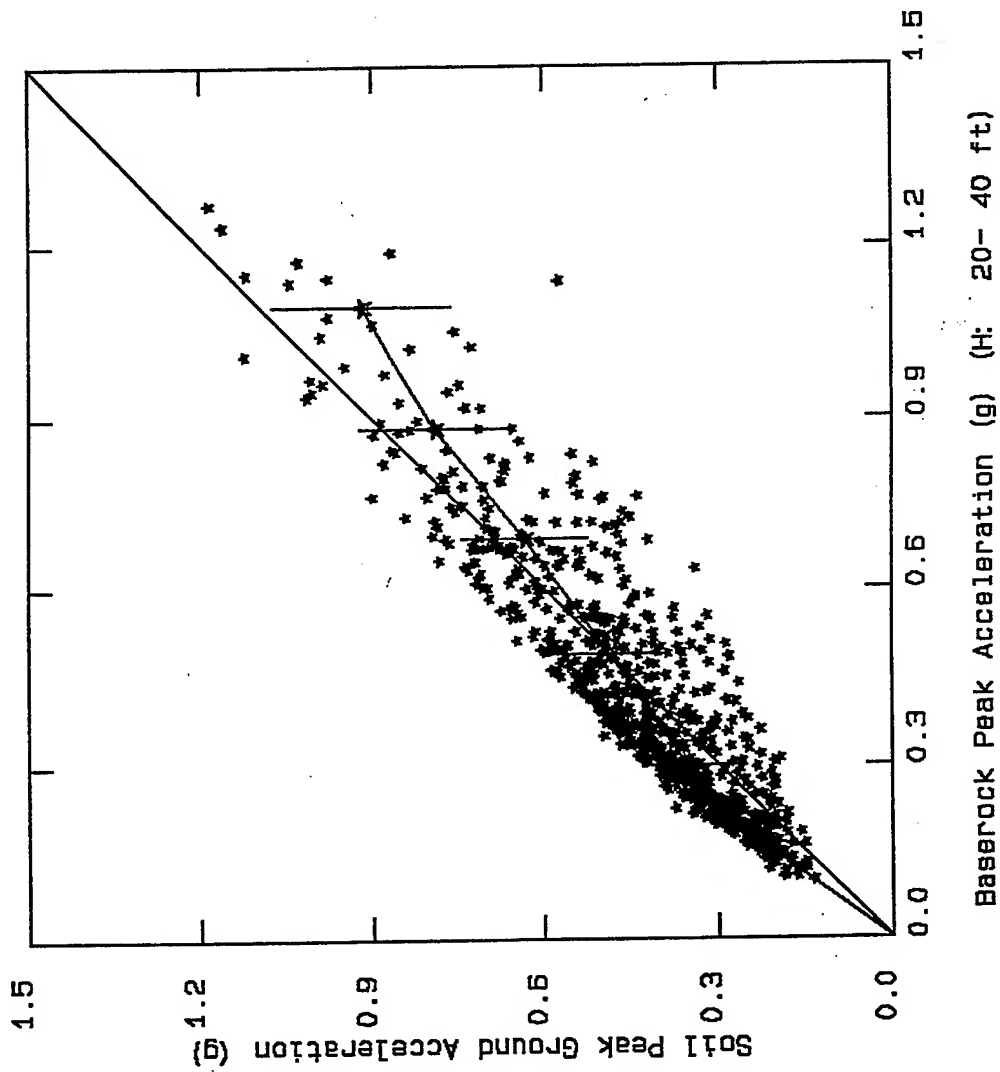


Figure 4.3.b. plots of PGA values at soil sites versus those at rock sites for the selected depths of soil materials.



VortexRock Consultants, Inc.

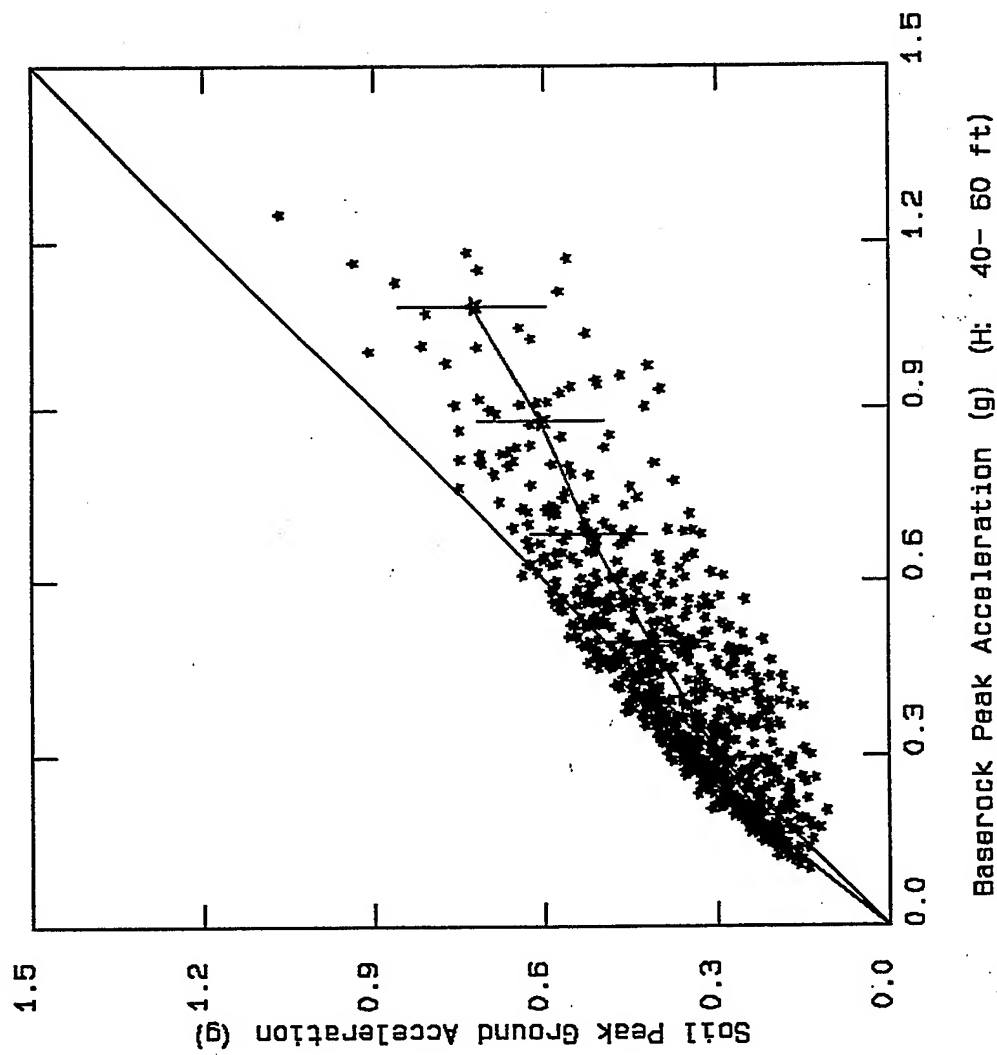


Figure 4.3.c. plots of PGA values at soil sites versus those at rock sites for the selected depths of soil materials.



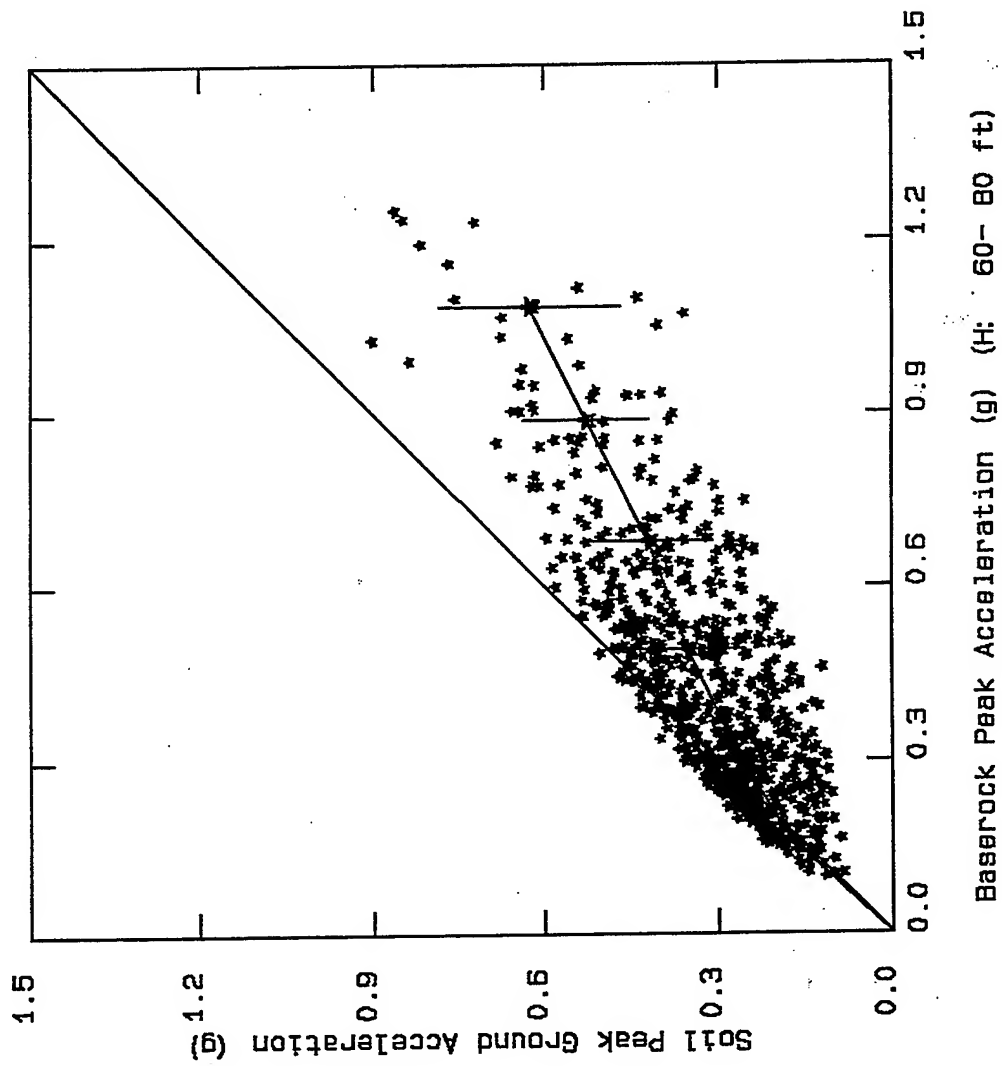


Figure 4.3.d. plots of PGA values at soil sites versus those at rock sites for the selected depths of soil materials.



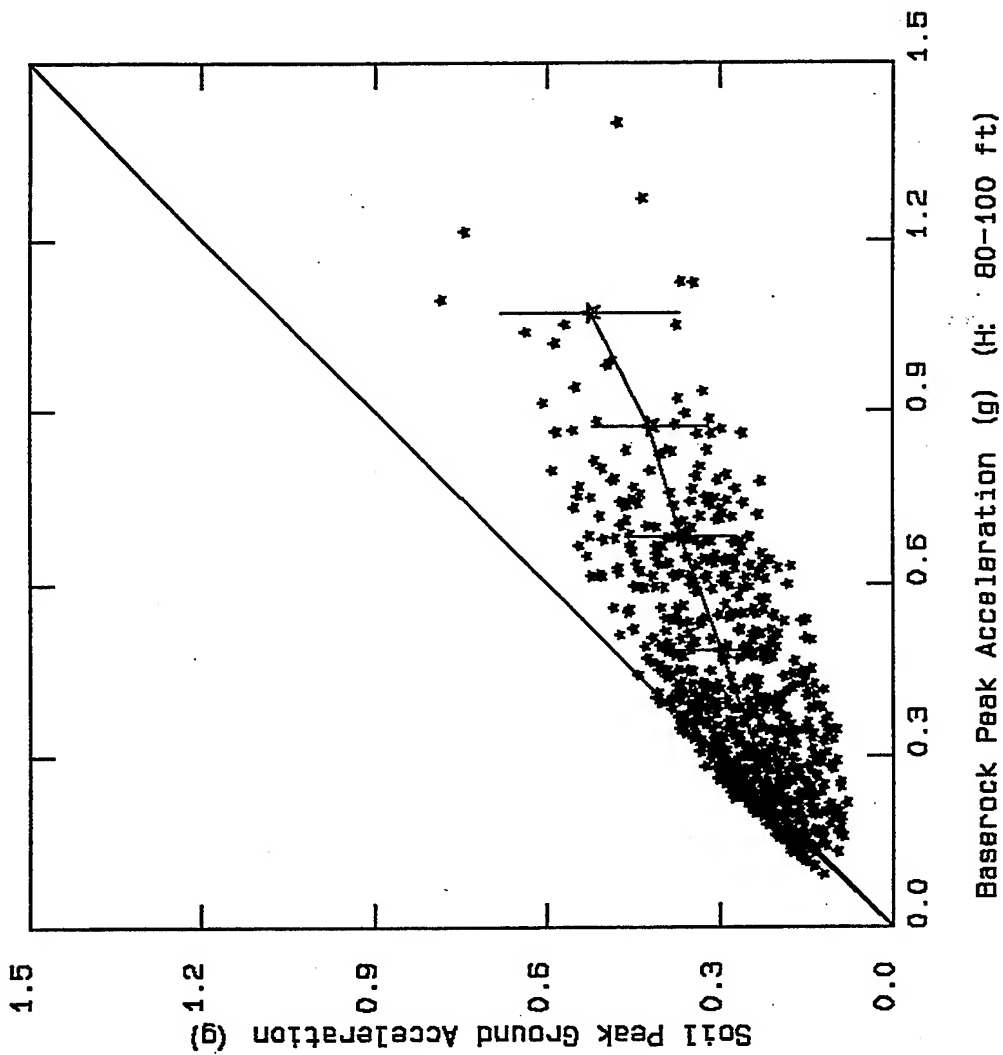


Figure 4.3.e. plots of PGA values at soil sites versus those at rock sites for the selected depths of soil materials.



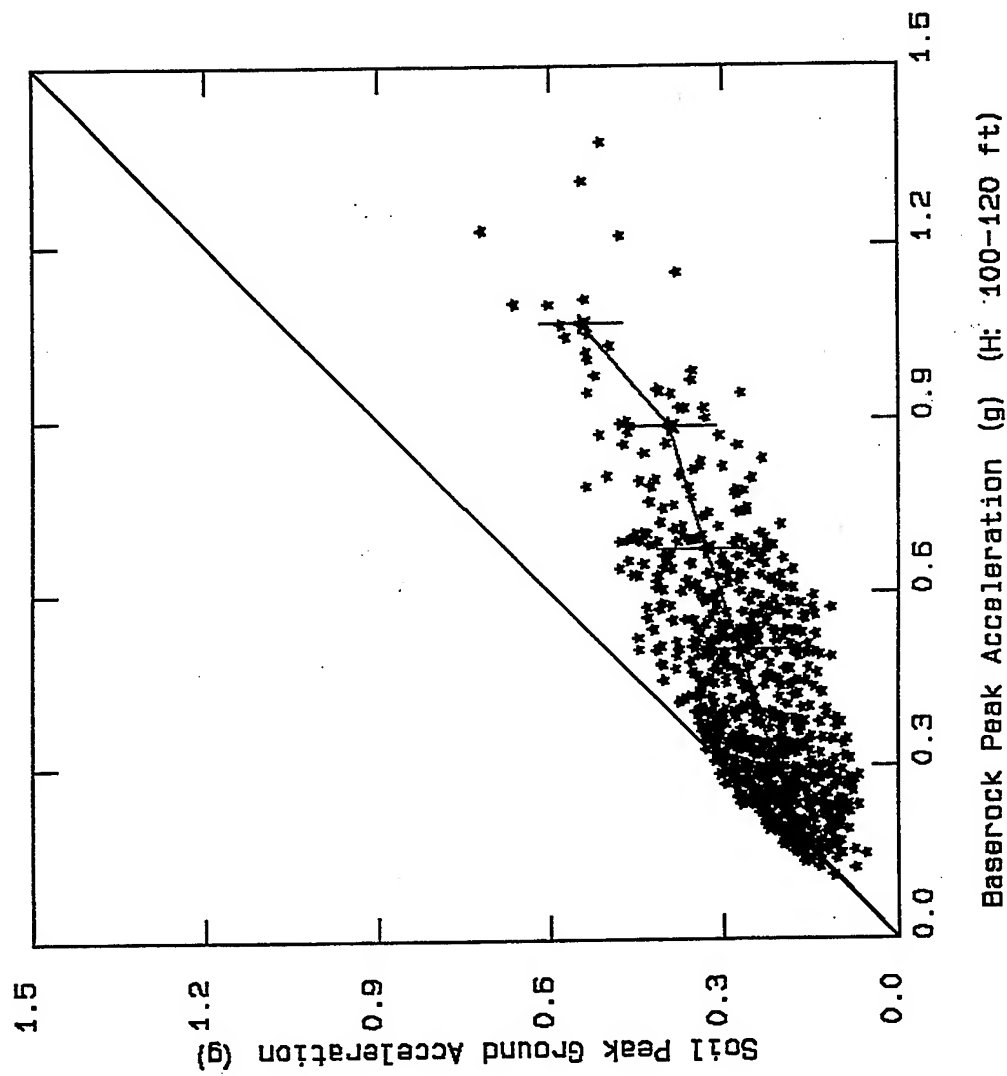


Figure 4.3.f. plots of PGA values at soil sites versus those at rock sites for the selected depths of soil materials.



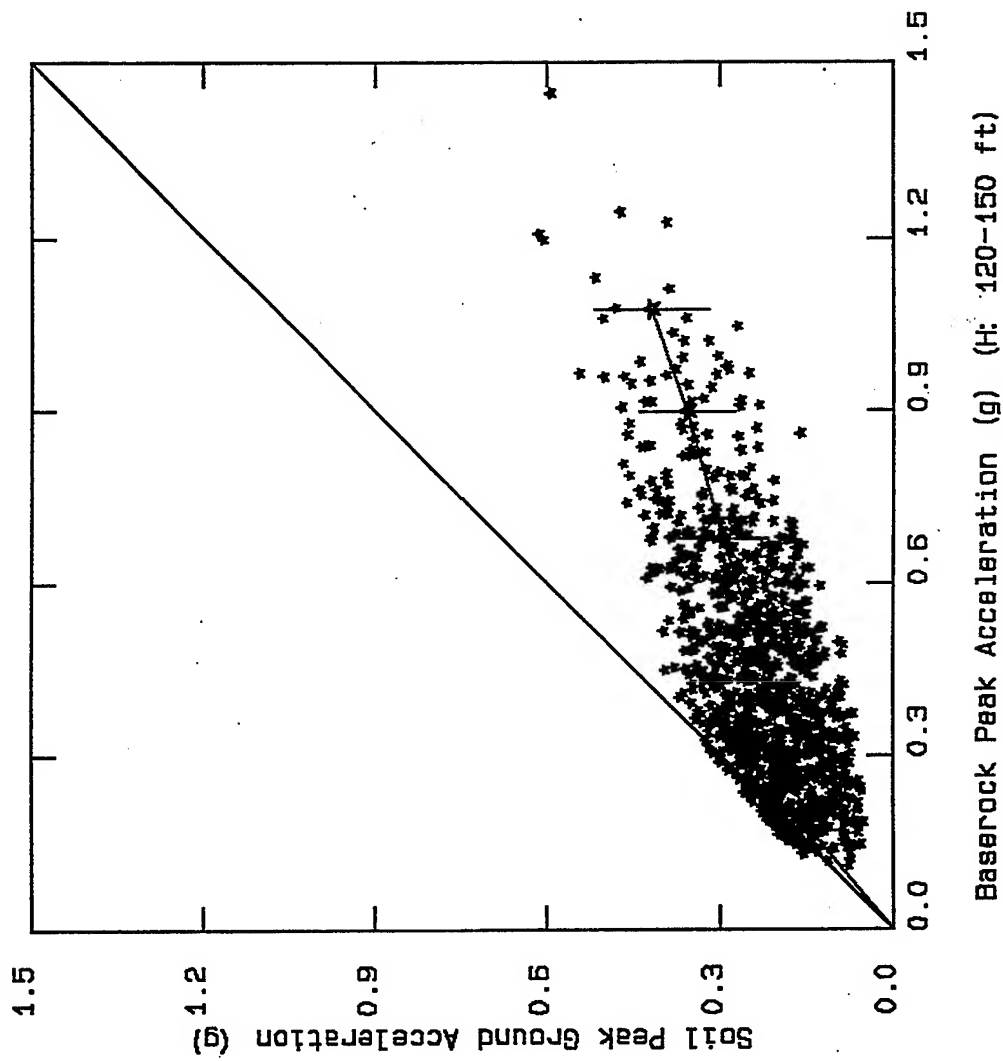


Figure 4.3.g. plots of PGA values at soil sites versus those at rock sites for the selected depths of soil materials.



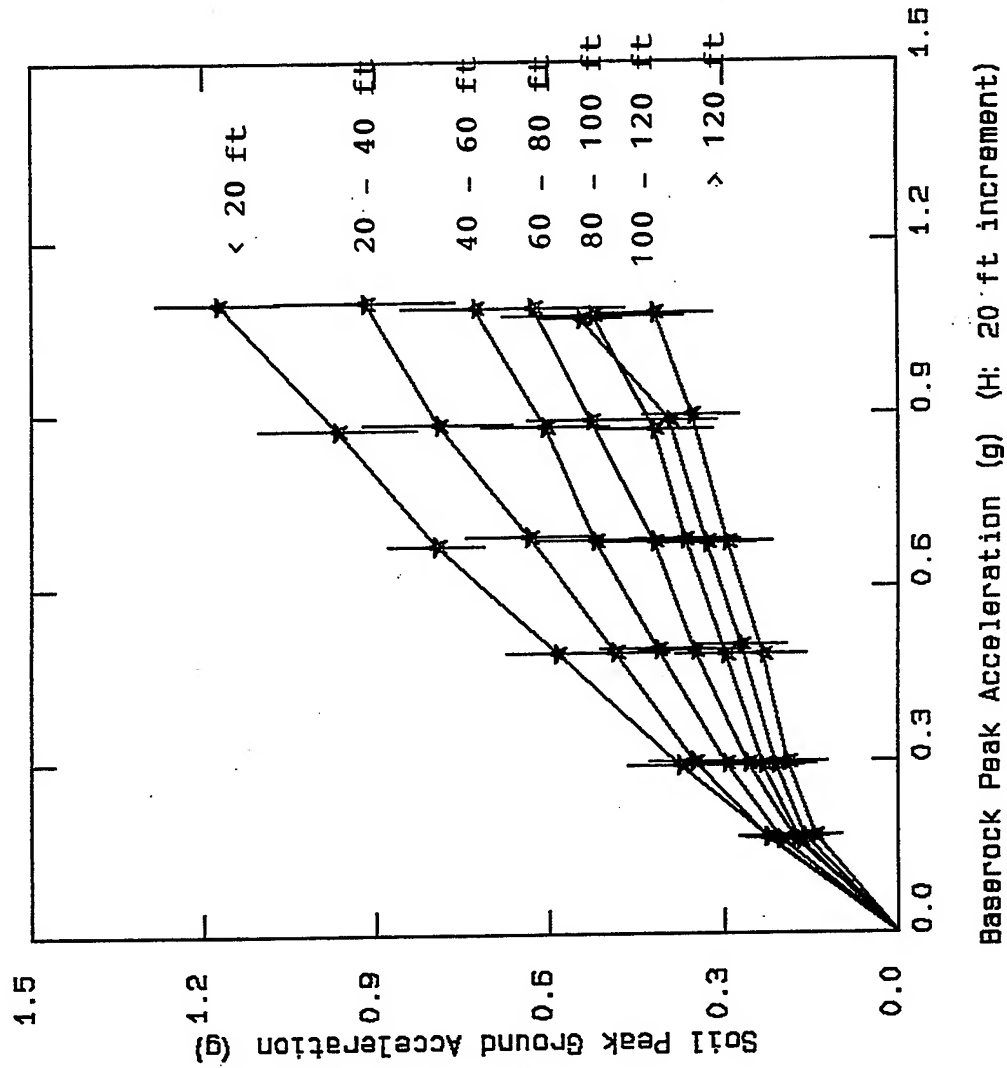


Figure 4.4. The summary plots of the least square fits to the simulated PGA values for different depth categories. The levels of amplification values decrease with increasing the depth of the soil materials.



VortexRock Consultants, Inc.

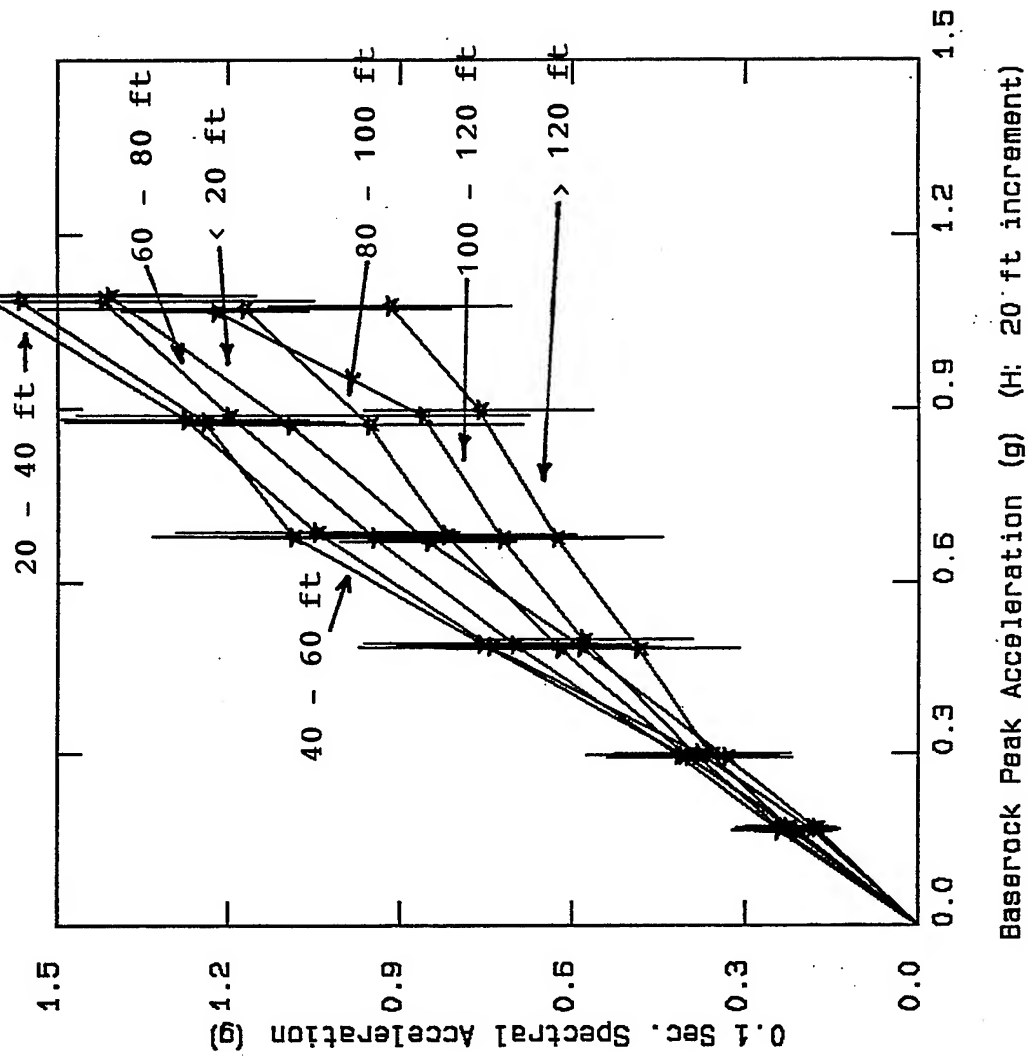


Figure 4.5. The summary plots of the least square fits to the simulated 1.0 s spectral acceleration values for different depth categories. The pattern of amplification as a function of depth is different than those for the PGA values.



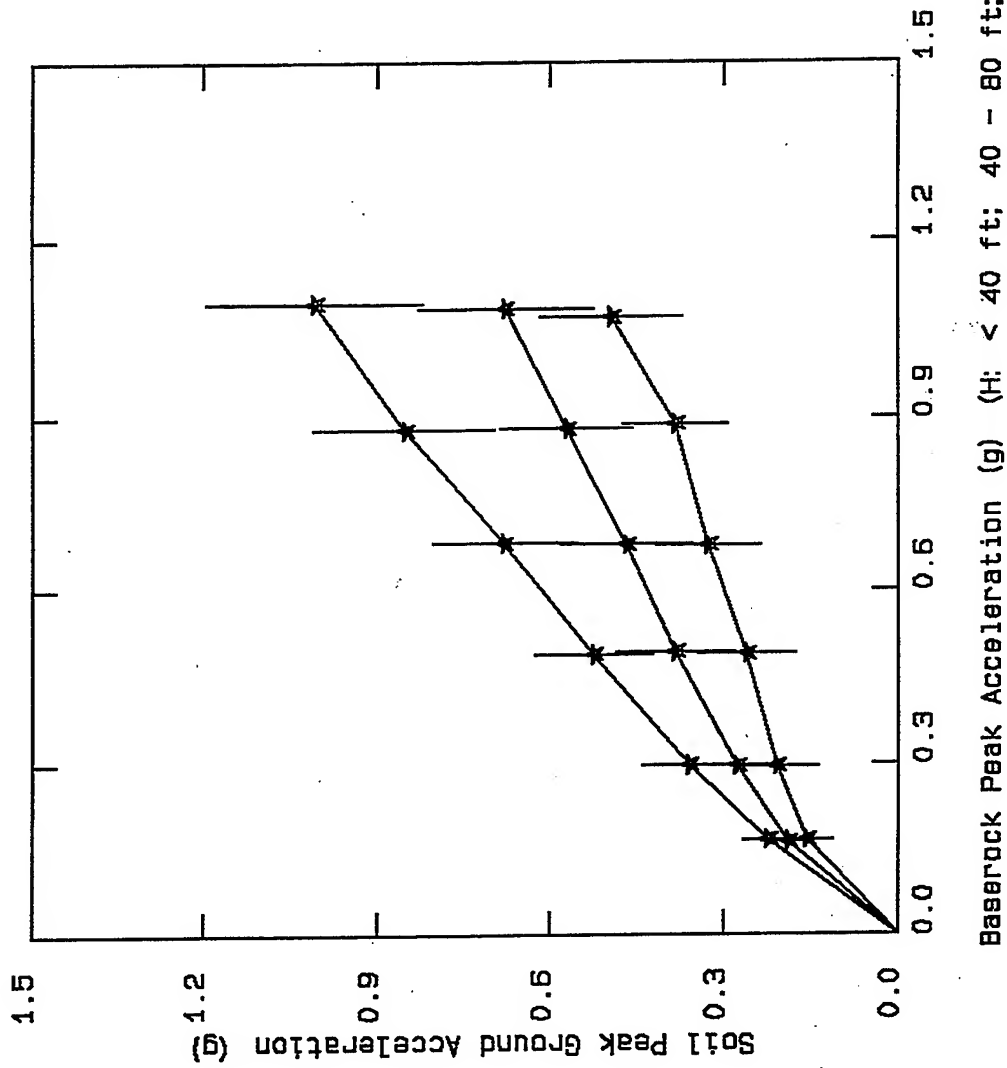
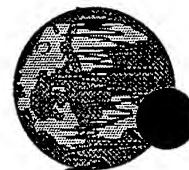


Figure 4.6. The plots of the least square fits to the simulated soil site PGA for three different depth categories that are shown.



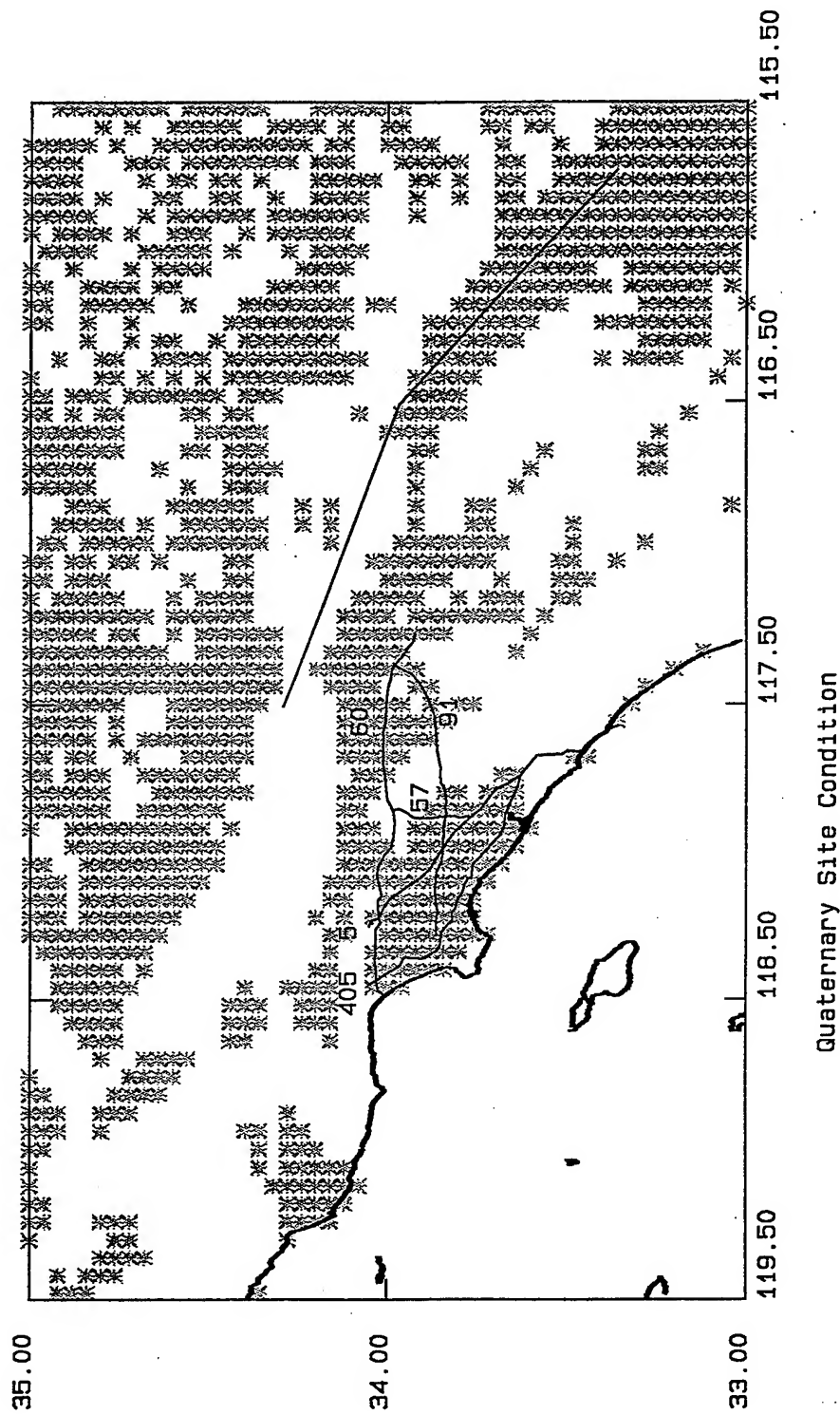
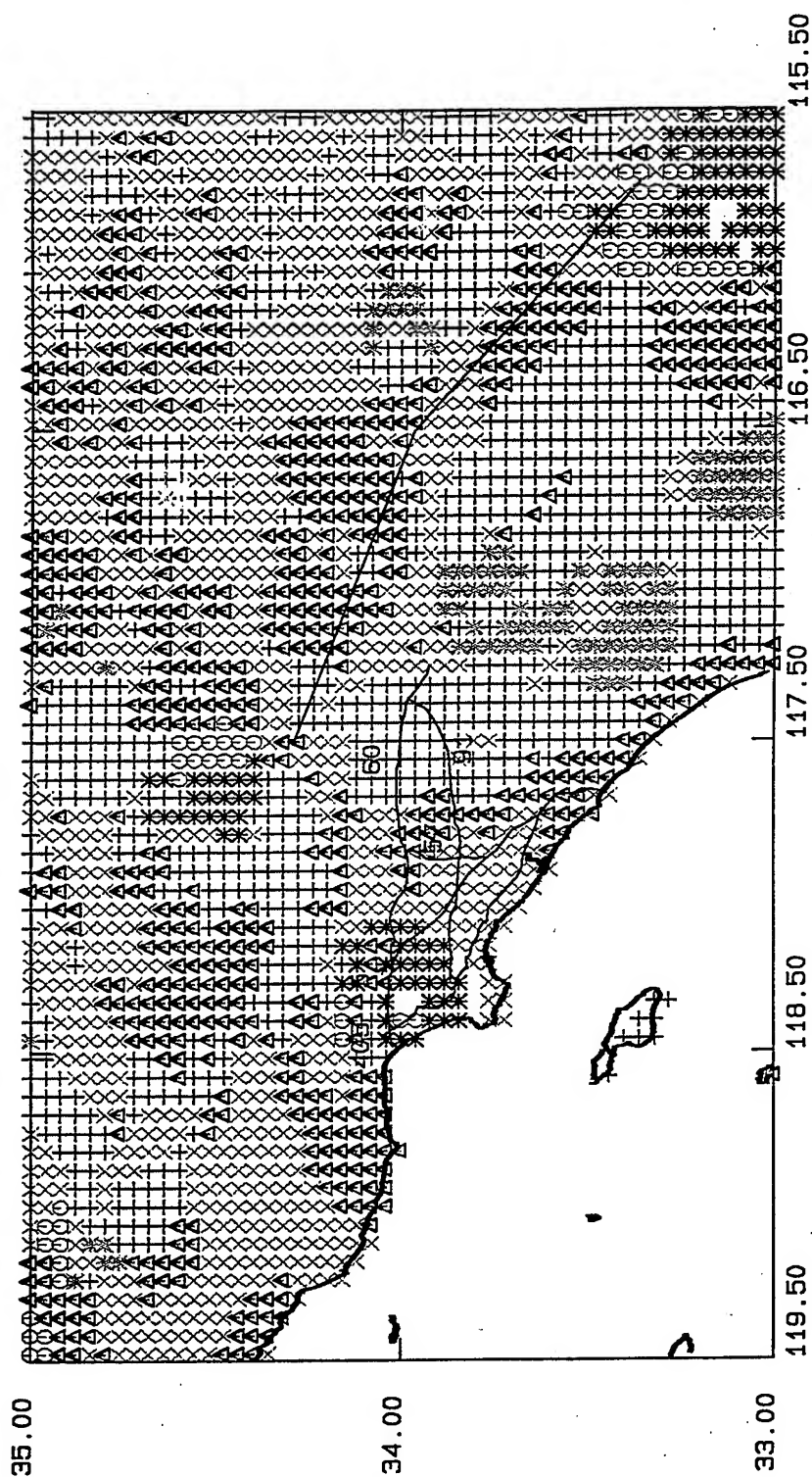


Figure 4.7. Locations of sites underlain by quaternary-age alluvial materials. The site characterization is based on the digitized surface geology data. This information and coda waves amplification factors are obtained from the Southern California Earthquake Center.



.4 - .7 - 1.4 - 2.7 - 5.3 - 10.3 - 20.0

* + Δ X ○ *



Site Amplification; 1.5 Hz; Range: .4 to 20

Figure 4.8.a. Coda waves amplification factors based on earthquake data at several sites in southern California and the surface geology data, Figure 4.7. Few highways and southern segments of the San Andreas fault are shown for references.



VortexRock Consultants, Inc.

.4 - .7 - 1.4 - 2.7 - 5.3 - 10.3 - 20.0

* + Δ × ⊕ *

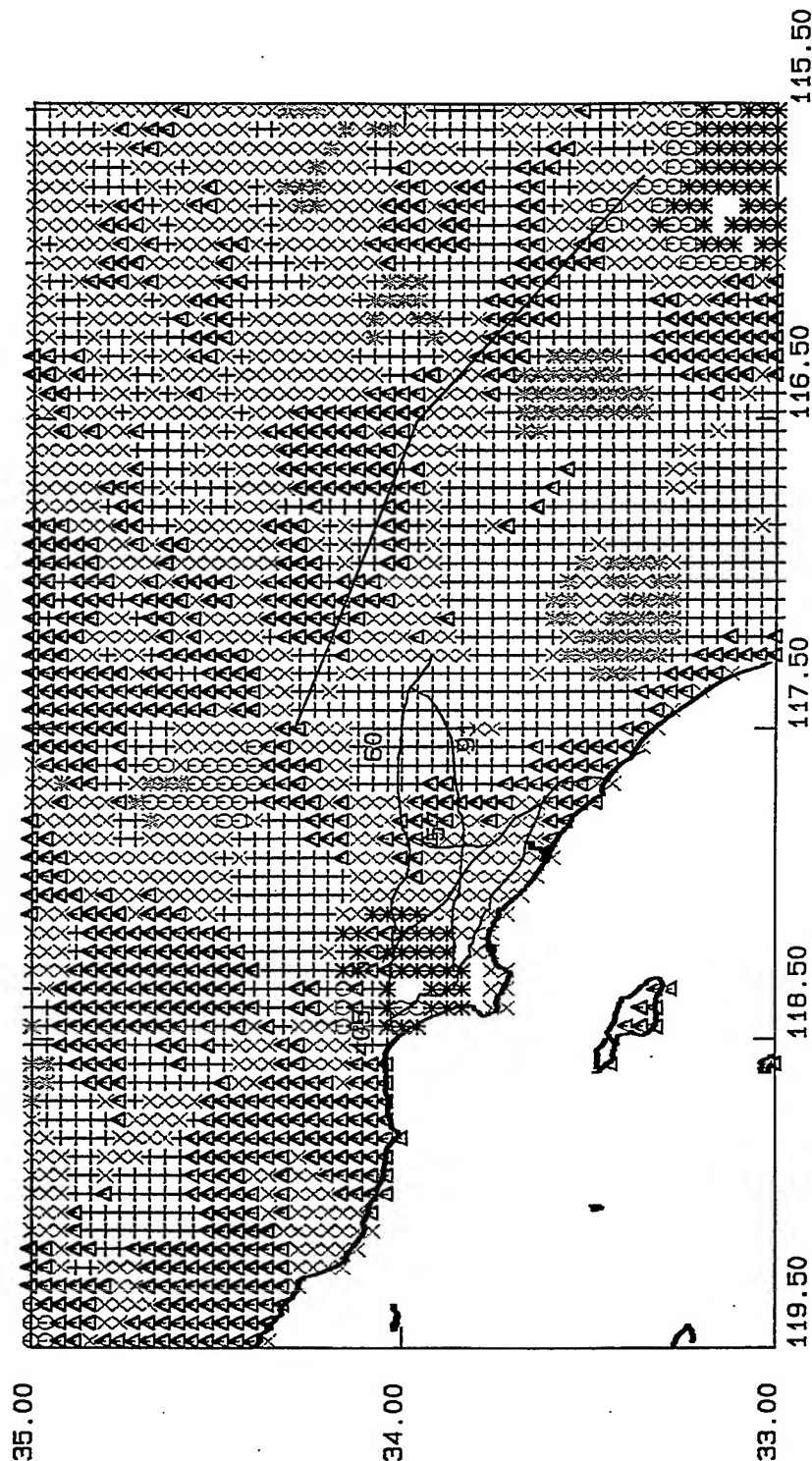


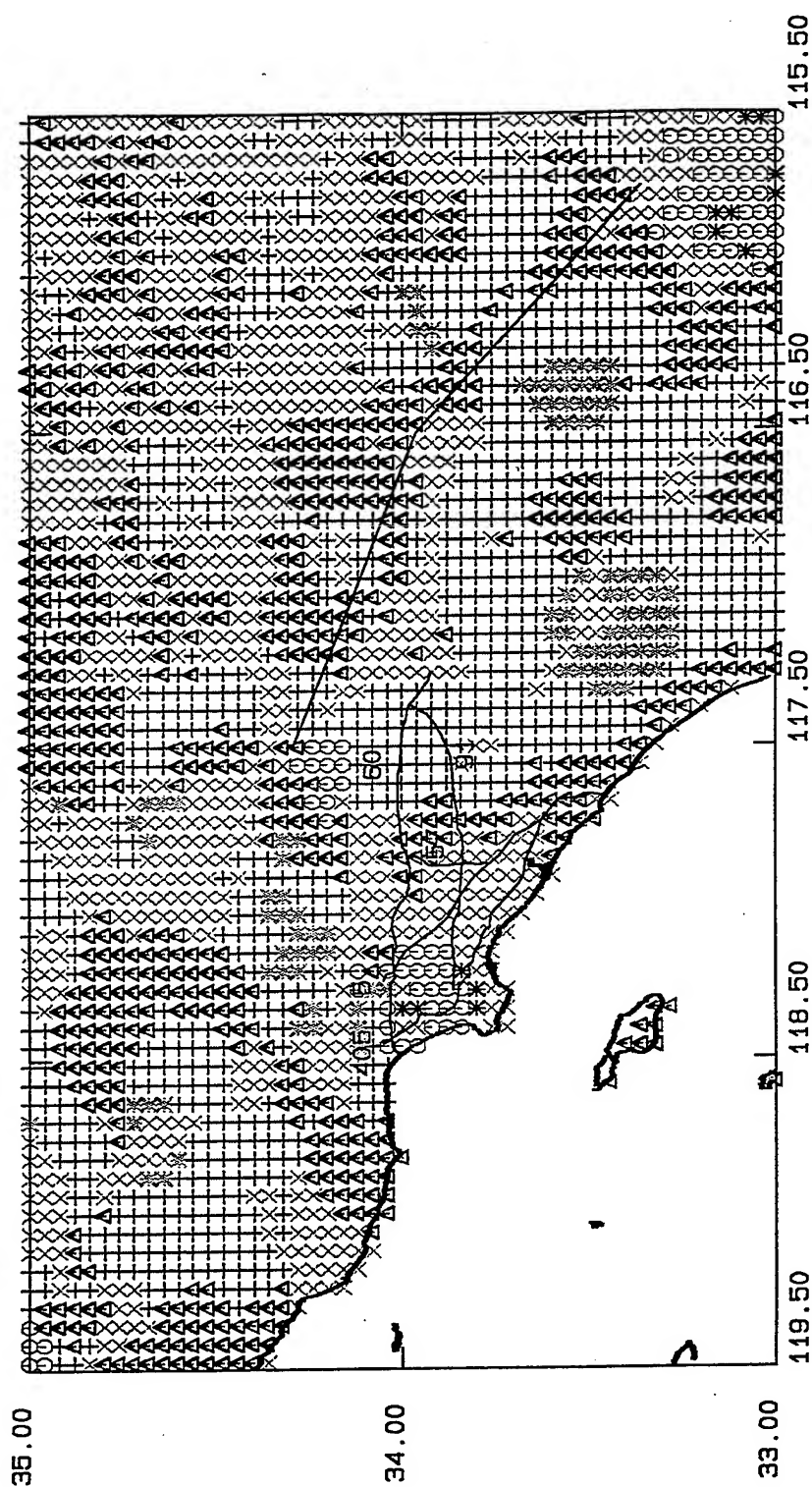
Figure 4.8.b. Coda waves amplification factors based on earthquake data at several sites in southern California and the surface geology data, Figure 4.7. Few highways and southern segments of the San Andreas fault are shown for references.



VortexRock Consultants, Inc.

.4 - .7 - 1.4 - 2.7 - 5.3 - 10.3 - 20.0

✱ + Δ × ○ ✱



Site Amplification; 6.0 Hz; Range: .4 to 20

Figure 4.8.c. Coda waves amplification factors based on earthquake data at several sites in southern California and the surface geology data, Figure 4.7. Few highways and southern segments of the San Andreas fault are shown for references.



VortexRock Consultants, Inc.

.4 - .7 - 1.4 - 2.7 - 5.3 - 10.3 - 20.0

* + Δ × ○ *

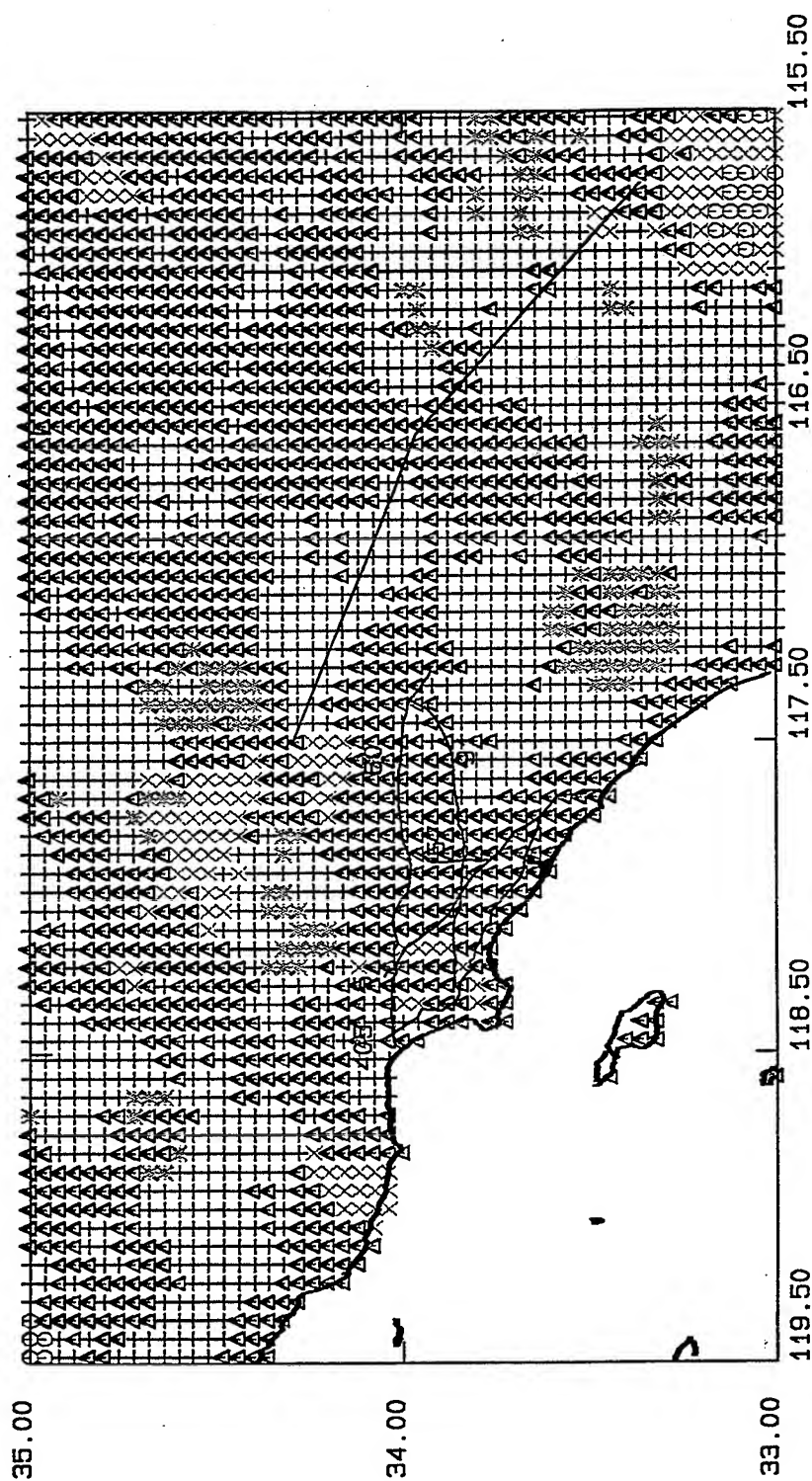


Figure 4.8.d Coda waves amplification factors based on earthquake data at several sites in southern California and the surface geology data, Figure 4.7. Few highways and southern segments of the San Andreas fault are shown for references.



VortexRock Consultants, Inc.

Figure 4.9.a to 4.9.e. Horizontal component response spectra for 5% damping ratio at five CDMG sites. Symbols represent the estimated response spectra based on the sub-event/RVT simulation using the proposed methodology, see the text for detail, to transform the weak motion coda waves amplification factors to strong motion amplification values. Stars are for a nonlinear frequency dependent exponential decay $e^{-\alpha f}$ and $f_m=10$ Hz, triangles are for a nonlinear frequency dependent exponential decay $e^{-\alpha f}$ and $f_m=5$ Hz, and circles are for a nonlinear frequency independent exponential decay $e^{-\alpha}$ and $f_m=5$ Hz. The thick line on each figure shows Boore and Joyner (1993) empirical response spectra for $M_w=7.4$ and using the closest distance from each site to the surface trace of the rupture area.



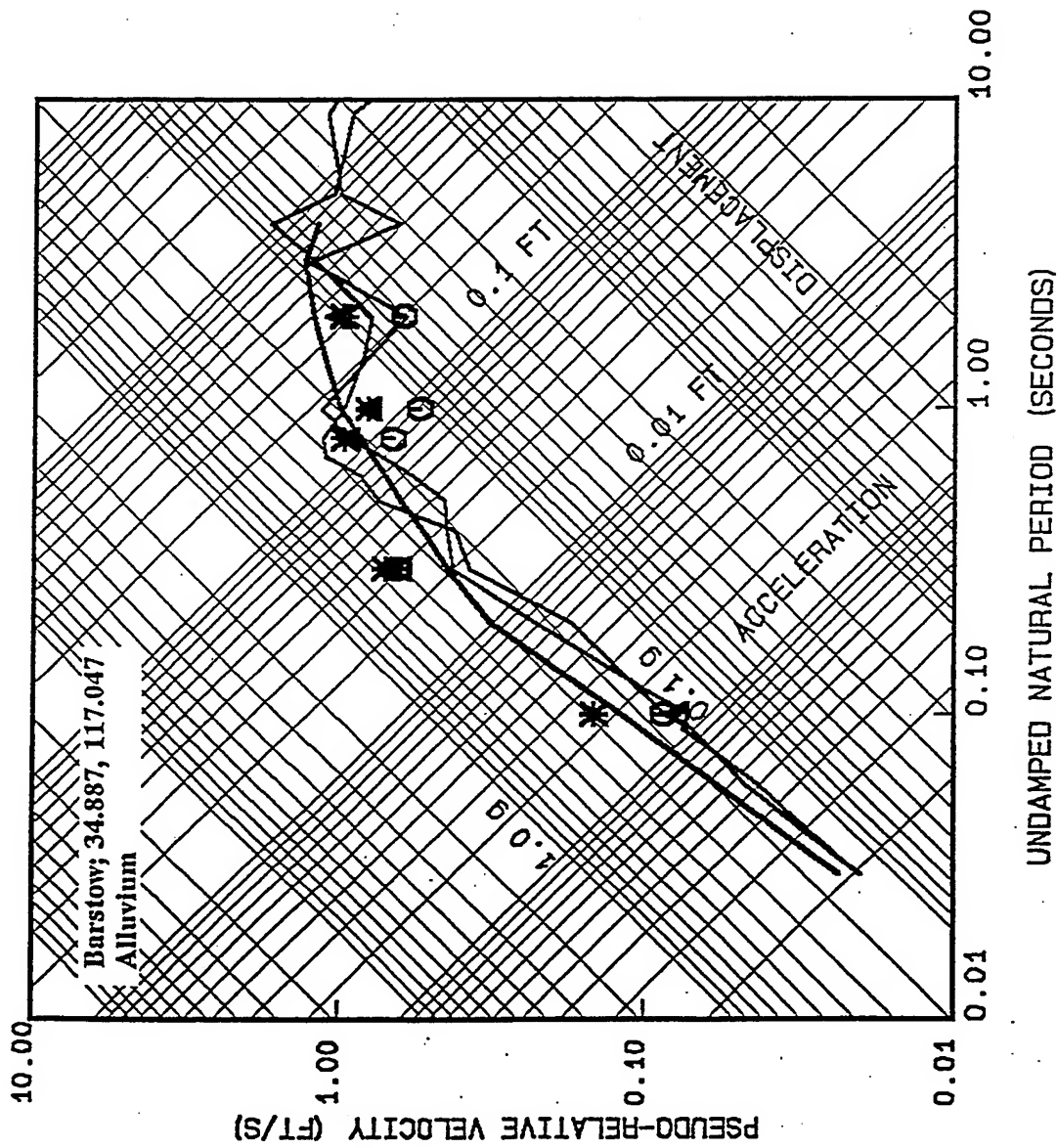


Figure 4.9.a.

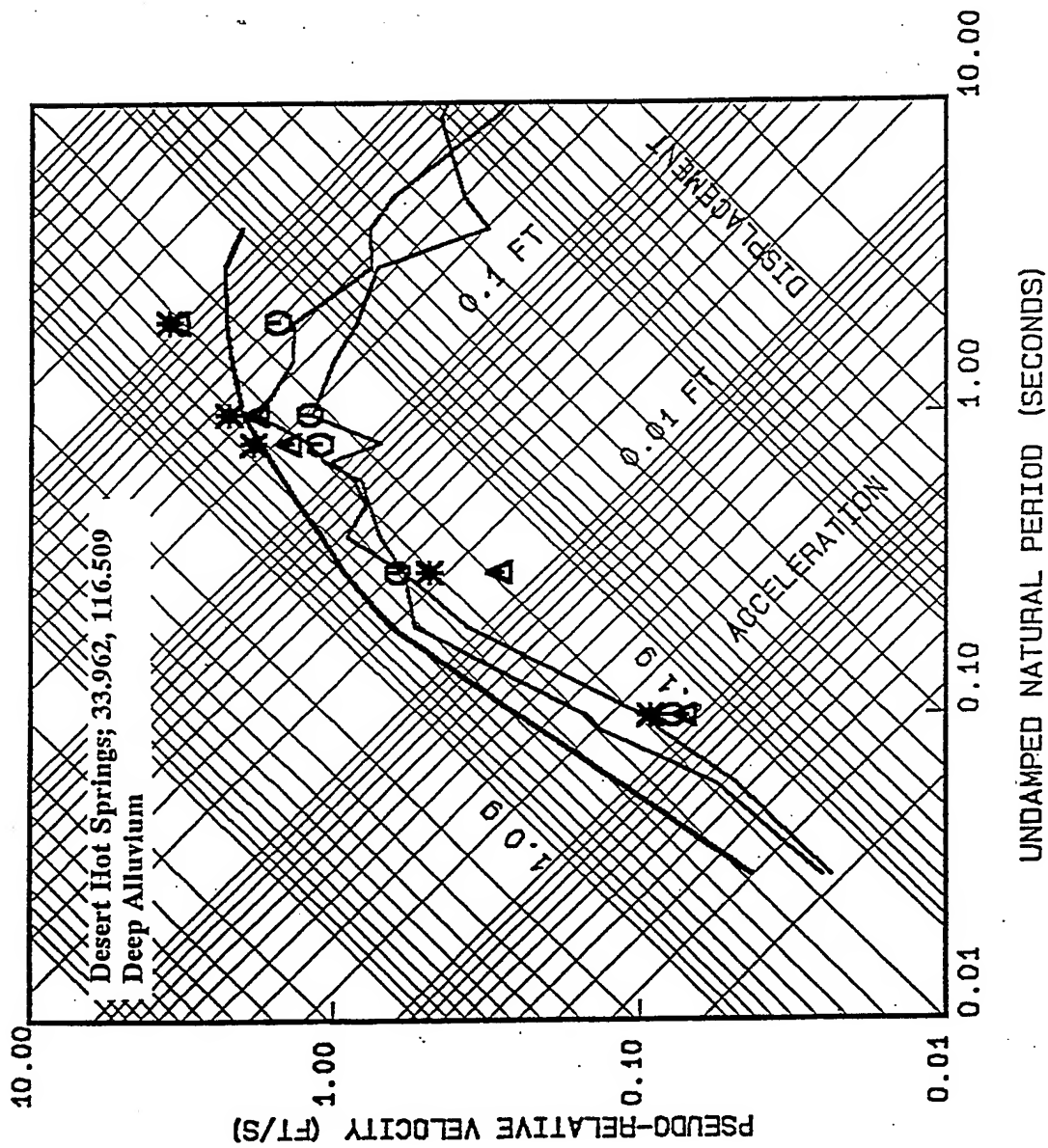


Figure 4.9.b.



VortexRock Consultants, Inc.
 11434 Alder Creek Rd, Corona, CA 91720
 Tel - Fax (714) 692-1443, E-Mail: mahdyiar@codia.usc.edu

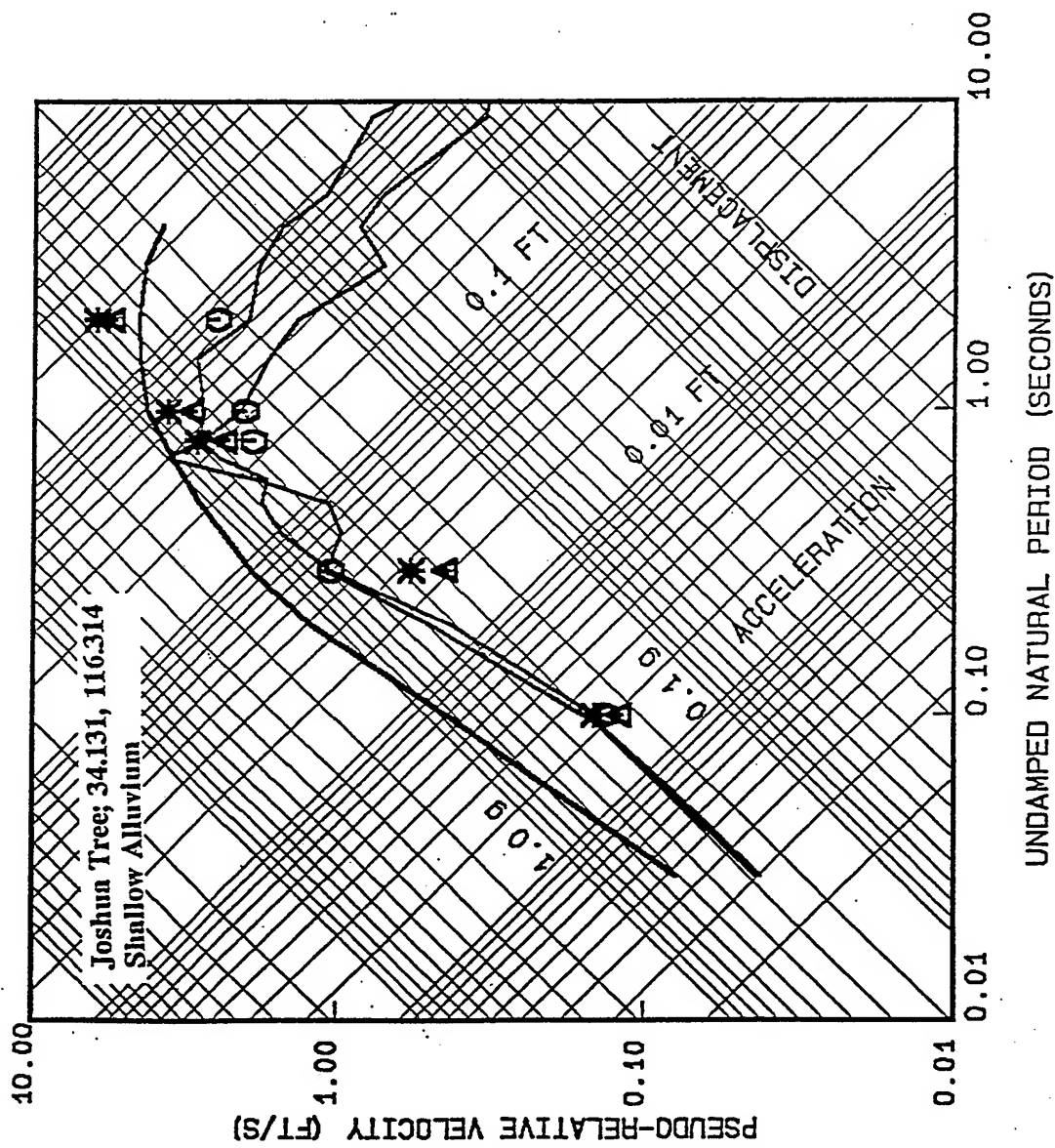


Figure 4.9.c.



VortexRock Consultants, Inc.
11434 Alder Creek Rd, Corona, CA 91720
Tel - Fax (714) 692-1443, E-Mail: mahdyiar@coda.usc.edu

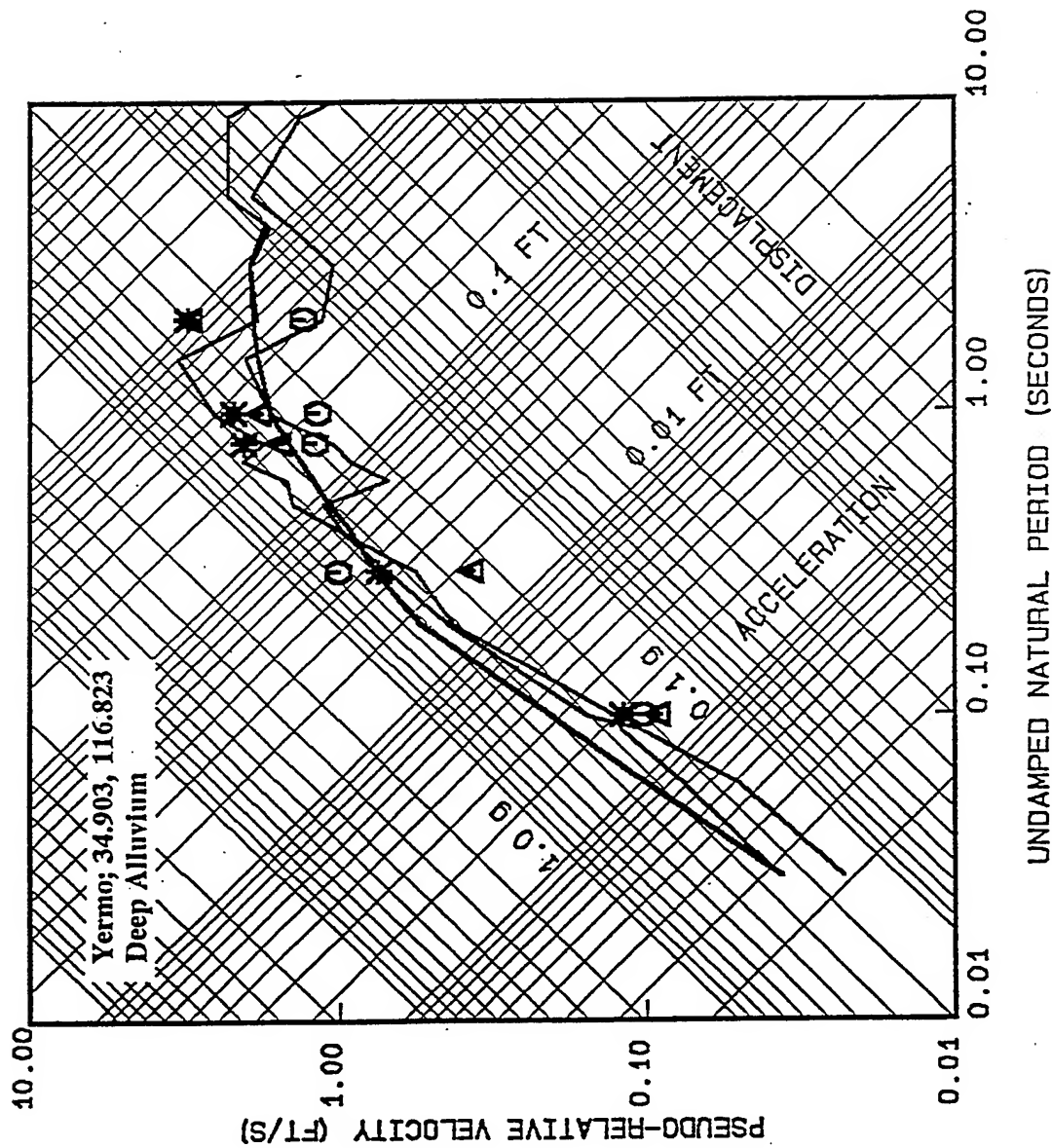


Figure 4.9.e.



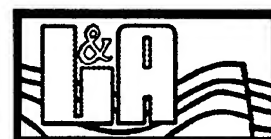
VortexRock Consultants, Inc.
11434 Alder Creek Rd, Corona, CA 91720
Tel - Fax (714) 692-1443, E-Mail: mahdyiar@coda.usc.edu

Chapter 5

Site Response Investigation based on the Spectral Ratio Analysis of the Northridge Earthquake Data

Investigating the response of soil sites to past earthquakes is important for better understanding the phenomena of site response to earthquake ground motions. The Northridge earthquake of January 1994 with moment magnitude 6.7 and its aftershocks have generated good quality data on the USC and Caltech networks at a number of sites in southern California. It is the objective of this study to investigate the response of a number of soil sites in southern California to the ground motions from the Northridge earthquake and its selected aftershocks.

The earthquake ground motions at a site reflect the nature of the ground motions at the source, the wave propagation through the Earth between the source and the site, possible focusing or defocusing effects of large scale geologic structures on seismic waves, topography of the site, possible resonating effects of shallow reflectors, and the nonlinear response of the local site materials. Isolating the effects of the local site materials on earthquake ground motions from other effects is a major problem in all site response studies. In that respect, the spectral ratio technique has been successfully used by many investigators for site response analysis using earthquake data (Borcherdt, 1970; Andrews, 1986; Jarpe et al , 1989; Darragh and Shakal, 1991; Field et al., 1992, Field, 1994; Steidle, 1993). The basic assumptions are that 1) the earthquake radiation pattern at the adjacent sites are similar and 2) the rock site has relatively flat site response as a function of frequency. In this study we use the spectral ratio technique to investigate the response of soil sites to the ground motions of the main shock and few of the aftershocks of the Northridge earthquake.



The Department of Navy provided us with two sets of ground motion data from the USC and California Institute of Technology (Caltech) networks for the Northridge main shock and its aftershocks at different pairs of stations with soil/rock site conditions. Tables 5.1 and 5.2 show general information on the sites and earthquakes from the USC network.

Table 5.1. General information on earthquakes from USC network. The data from earthquake #4 is not used in this study. It is shown here for the consistency in IDs with the Navy Report and original USC data.

Earthquake ID	Latitude	Longitude	Magnitude	Depth km
0	34.2133	118.5369	6.7	18.4
1	34.2786	118.4728	5.9	.0
2	34.2611	118.5339	4.5	14.8
3	34.2544	118.5450	4.6	.0
4	34.2144	118.5094	4.5	17.2
5	34.2314	118.4750	5.3	13.1

Table 5.2. General information on the recording stations of the USC network that are used in this study. The distances from each station to the five earthquakes are shown.

Site ID	Latitude	Longitude	EQ #0 Distance km	EQ #1 Distance km	EQ #2 Distance km	EQ #3 Distance km	EQ #5 Distance km
13	34.1317	118.4394	13	17	17	17	11
16	34.0894	118.4347	17	21	21	21	16
18	34.0875	118.3653	21	23	25	25	19
49	34.0419	118.5536	19	27	24	23	22
60	34.2378	118.2536	26	21	26	27	20
61	34.2864	118.2253	30	23	28	30	24
63	34.2000	118.2311	28	24	29	29	23

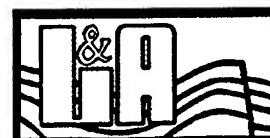


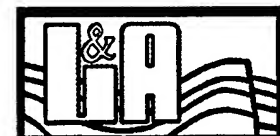
Table 5.3 shows the lists of soil and rock sites and the earthquakes that are recorded by each pair. The general description of the site conditions for the USC recording stations are shown in Table 5.4.

Table 5.4. List of Soil and Rock sites for the USC network that are used in this study.

<i>Soil Site</i>	<i>Rock Site</i>	<i>Events</i>
USC 63	USC 61	Main Shock Aftershock 1 Aftershock 4 Aftershock 5
USC 18	USC 16	Main Shock Aftershock 1 Aftershock 2 Aftershock 5
USC 60	USC 61	Main Shock Aftershock 1 Aftershock 4 Aftershock 5
USC 49	USC 16	Main Shock Aftershock 1 Aftershock 2 Aftershock 5
USC 13	USC 16	Main Shock Aftershock 1 Aftershock 2 Aftershock 3

Table 5.4. The site conditions for the USC stations.

<i>Site ID</i>	<i>Site Classification</i>	<i>Site Conditions</i>
13	C	Stiff soil over sediments
16	B	Rock
18	B	Stiff soil over sediments
49	C	Stiff soil over sediments
60	C	Stiff soil over rock
61	B	Rock
63	C	Stiff soil over rock



* Soil classification are from the Department of Navy's report.

A: $\beta > 760 \text{ m/s}$

B: $360 \text{ m/s} < \beta < 760 \text{ m/s}$

C: $180 \text{ m/s} < \beta < 360 \text{ m/s}$

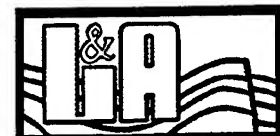
D: $\beta < 180 \text{ m/s}$

Table 5.5 shows the general information on earthquakes from the Caltech network.

Table 5.5. List of earthquakes from the Caltech network that are used in this study.

Earthquake ID	Latitude	Longitude	Magnitude	Soil-Rock Site Pair ID*				
				1	2	3	4	5
1	34.2785	118.4727	5.9	x	x	x	x	x
2	34.3172	118.4548	4.7		x		x	
3	34.2848	118.6238	4.4		x			
4	34.3263	118.6983	5.6				x	
5	34.3425	118.6655	4.0	x	x			
6	34.3787	118.5632	4.4		x			
7	34.3575	118.6223	4.3		x			
8	34.3787	118.5607	4.8	x				
9	34.3785	118.7107	5.1	x		x		
10	34.3010	118.4662	4.6	x				
11	34.2983	118.4523	4.1	x		x		
12	34.2937	118.4613	4.2			x		
13	34.2992	118.4282	4.1					x
14	34.3452	118.5522	4.6					x
15	34.2735	118.5625	4.6					x
16	34.3743	118.4948	4.2					x
17	34.3053	118.5793	5.1				x	
18	34.2782	118.6108	4.3					x
19	34.3570	118.4798	4.1				x	
20	34.3400	118.4800	3.6				x	

* For the description on the ID for the soil-rock sites pairs refer to Table 5.7.



The lists of the stations and their site conditions for the Caltech network are shown in Table 5.6. Table 5.7 shows the list of the pairs of soil-rock sites in terms of their ID number that are shown on Table 5.5. The identification numbers for earthquakes and their distances to the recording sites are shown on Table 5.8.

Table 5.6. List of the selected recording stations from the Caltech network.

Site ID	Latitude	Longitude	Site conditions
1	34.1062	118.4542	Pre-Tertiary Jurassic marine bedrock at dam
2	34.0630	118.4180	Pleistocene non marine terrace deposits
3	34.0900	118.3390	Pleistocene non marine deep alluvium 130 m, sandstone and shale
4	34.0700	118.1500	Pleistocene non marine few hundred feet of alluvium, siltstone
5	34.3120	118.4960	Quaternary sedimentary bedrock Saugus Formation
6	34.3880	118.5332	Alluvium
7	34.148	118.170	Weathered Mesozoic granitic rock tonalite diorite
8	34.019	118.285	400 ft of alluvium over clay and shale
9	33.650	117.009	Rock, Dominigoni Reservoir
10	34.104	117.097	Alluvium, Seven Oaks Dam inside tunnel

Table 5.7. List of soil-rock sites pairs.

Soil-Rock Sites pair ID	Soil Site ID from Table 5.5	Rock Site ID from Table 5.5
1	4	7
2	2	1
3	3	8
4	9	10
5	6	5

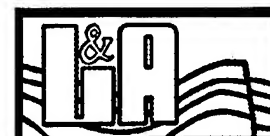
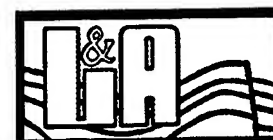


Table 5.8. List of earthquakes and their distances for the recording stations.

<i>Earthquake ID</i>	<i>Station ID</i> (stations are grouped as pairs)							
	<i>4</i>	<i>7</i>	<i>1</i>	<i>2</i>	<i>3</i>	<i>8</i>	<i>5</i>	<i>6</i>
1	37	31	19	24	24	33	4	13
2			23	28				
3			25	31				
4								
5	56	50	32	38				
6			32	37				
7			32	37				
8	51	44						
9	62	56			47	56		
10	39	32						
11	37	31			25	34		
12					3	34		
13							6	14
14							6	5
15							7	13
16							7	4
17								
18							11	14

The epicentral locations of earthquakes that are recorded by each pair of soil-rock sites on the USC network are shown on Figures 5.1. The time histories for this data set, except for the main shock, are mostly less than 30 seconds. For each record the complete time history was used for the spectral ratio analysis. The time histories and spectral amplitudes for all records are shown in Appendix E. The spectral ratios of individual pair of stations are shown in Appendix F. Figures 5.2.a to 5.2.e show the results of spectral ratio analysis for different earthquakes at different pairs of rock-soil sites. The thick shaded lines show the spectral ratios for the main shock and the thick solid lines show the average of the spectral ratios for all earthquakes. The scattering in

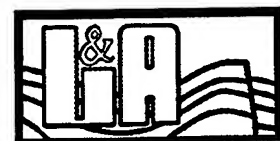


the results for each pair of sites is large. However, the spectral ratios for each pair as a function of frequency show a recognizable pattern. For example, the results on Figure 5.2.a for the station pair 13-16 show a factor of ten amplification for the soil site around 2 Hz on both transverse and vertical components. The average spectral ratios indicate a factor of two amplification for the soil site for most frequency ranges consistent with the C-type site conditions for the station 13, Table 5.4. The average spectral ratios, Figure 5.2.b, for the station pair 16-18 show no significant site amplifications over any frequency range. Station 18 is characterized as a site with B-type site conditions. The spectral ratios show values less than one for the frequency ranges between 1 and 2 Hz. The most consistent parts of the spectral ratio data are for the frequency range of 1 to 2 Hz. This is observed on all records. Station 63 is characterized as a site with C-type site conditions. The spectral ratios for the station pair 63-61 show amplifications at all frequency ranges, except around 1 Hz. All records show consistent results with high amplifications around 2 - 3 Hz and around 5 Hz. Station 60 is characterized as a site with B-type site conditions. The spectral ratios for the station pair 60-61 show amplifications only around 2 Hz with no significant amplifications over other frequency ranges. The spectral ratios for the station pair 49-16 show de-amplifications between the frequency range of 1 to 2 Hz with no significant amplifications over other frequency ranges. Station 49 is characterized as a site with C-type site conditions. The distance ranges for the earthquakes-sites combinations in this study are between 12 and 30 km. The magnitudes of earthquakes range between 4.5 to 6.7. Within these magnitude and distance ranges there are no recognizable consistent differences between the soil-to-rock site spectral ratios for the main shock versus the aftershocks that might indicate any nonlinear site response at these sites.



Figures 5.3 shows the epicentral distribution of earthquakes and site locations for different pairs of stations from the Caltech network. The time histories are mostly 60 s long. On some records there are few seconds of noise before the onset of earthquake ground motions. These records are divided into three time windows for noise, S-waves and coda waves. Other records are identified by S-waves and coda waves. The time histories and the spectral parameters of these records are shown in Appendix G. The spectral ratios for selected records are shown on Appendix I.

The spectral ratios for all pairs show consistent pattern for the records within each pair with very reasonable amount of scattering. However, pair number 4 shows the strongest variation on spectral ratios for the horizontal components. The long period of the vertical component show the least amount of scattering. In general, the vertical components for all cases show less scattering than the horizontal components. It is worth mentioning that earthquakes for pair #4 are close to, within 4 to 12 km, and surrounding the recording stations. This is in contrast to the situation for all other stations where the earthquakes are at distance and to the one side of the recording stations. The strong scattering in the spectral ratios of pair #4 might be due to the effects of the near field radiation pattern. In fact, the coda waves spectral ratios for the pair #4, Figure 5.4.d, show less scattering than the S-wave spectral ratios. The coda waves are the scattered and back scattered waves from heterogeneities in large volume surrounding the source and the recording stations. Therefore coda waves amplitudes are less sensitive, than the S-waves, to the source radiation pattern and the seismotectonic properties of the materials between the source and the recording station. It is interesting to notice that the general patterns and amplitudes of the coda waves amplifications up to the frequency of about 10 Hz are very similar to those of S-waves, Figure 5.4.e. This in part supports the

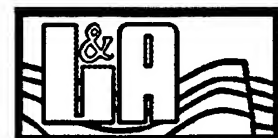
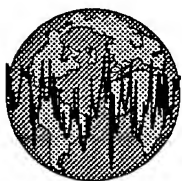


concept that coda waves are composed of S-waves and more importantly that the coda waves amplifications at a site may be good representative for the site response to earthquake ground motions.

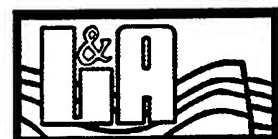
All soil sites show site amplifications over a wide frequency band. Pair #2, Figure 5.3.b, shows strong amplifications for long periods up to about period of .5 s. Similar patterns but with less amplifications at long periods are observed on the coda waves spectral ratios, Figure 5.4.b. The recording stations for pair #2 are close to the edge of the LA basin. The long period amplification of the soil site might be due to the basin effects. However, we do not observe similar response on the spectral ratios of pair 49-16 of the USC network that are at similar locations as the pair #2 of the Caltech network.

The coda waves spectral ratios show very good agreements with the S-waves spectral ratios. This indicates that for the magnitude ranges of earthquakes and the source-site distances the site response to the earthquake ground motions were almost linear, similar to the coda wave weak motion site response. As was discussed earlier, this also supports the hypothesis on the nature of coda waves being of scattered and back scattered S-waves (Phillips and Aki, 1986; Sue et al., 1992; Mayeda et al., 1991; Chin and Aki 1991 and 1994). Furthermore, It supports the idea that coda waves amplifications reflect the weak motion site response to earthquake ground motions and can be used for the earthquake ground motion simulations after taking into the consideration the possible nonlinear site response as was discussed in the previous chapter.

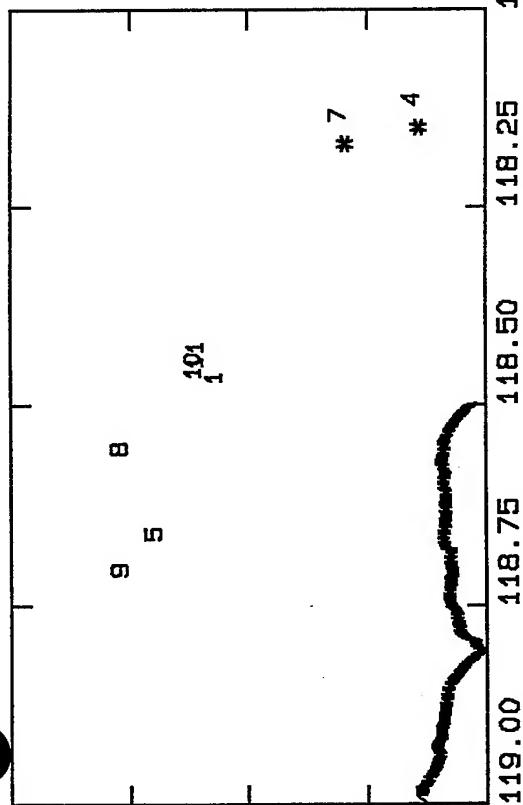
As was discussed in the previous paragraph, the results of this study provides interesting observation on the coda waves and S-waves soil site responses that are useful for better



understanding and formulating the phenomena of site response to earthquake ground motions. However, the variation in the spectral ratios of different earthquakes at each pair of soil/rock sites and the differences in the average spectral ratios among different pairs suggest strong variability for soil site responses to earthquake ground motions. The complexities of the rupture mechanisms, possible focusing or defocusing effects of large scale geologic structures on seismic waves, topography of the site, and the effects of local site materials on ground motions all add to the difficulty of the problem of site response characterization.

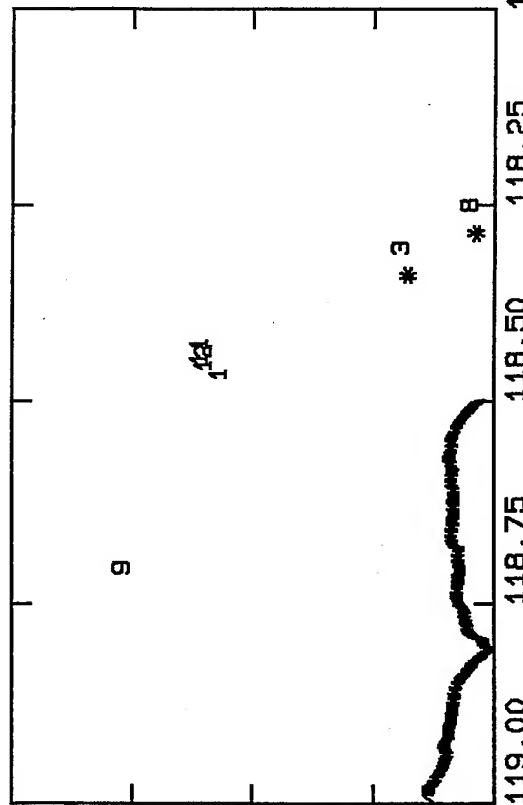


34.50
34.37
34.25
34.12
34.00



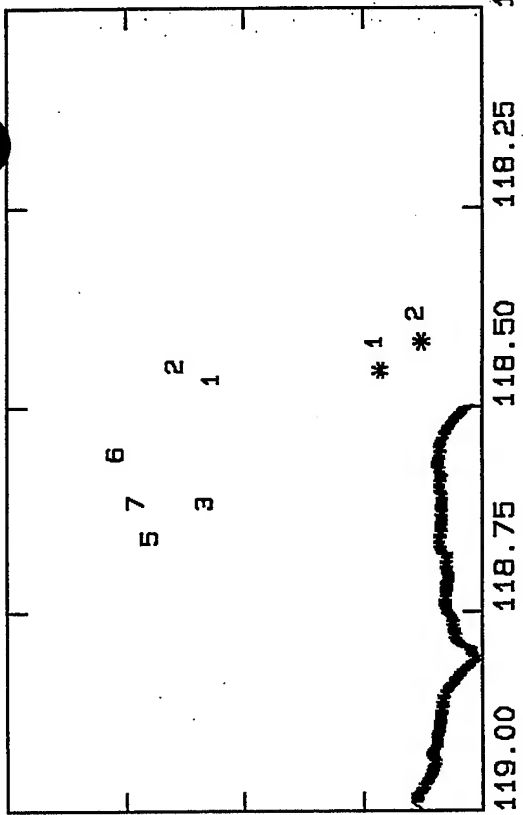
119.00 118.75 118.50 118.25 118.00

34.50
34.37
34.25
34.12
34.00



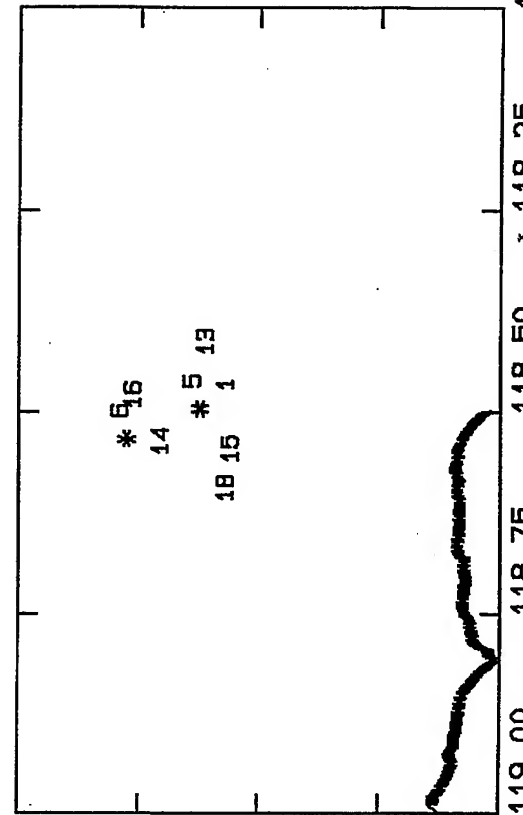
119.00 118.75 118.50 118.25 118.00

34.50
34.37
34.25
34.12
34.00



119.00 118.75 118.50 118.25 118.00

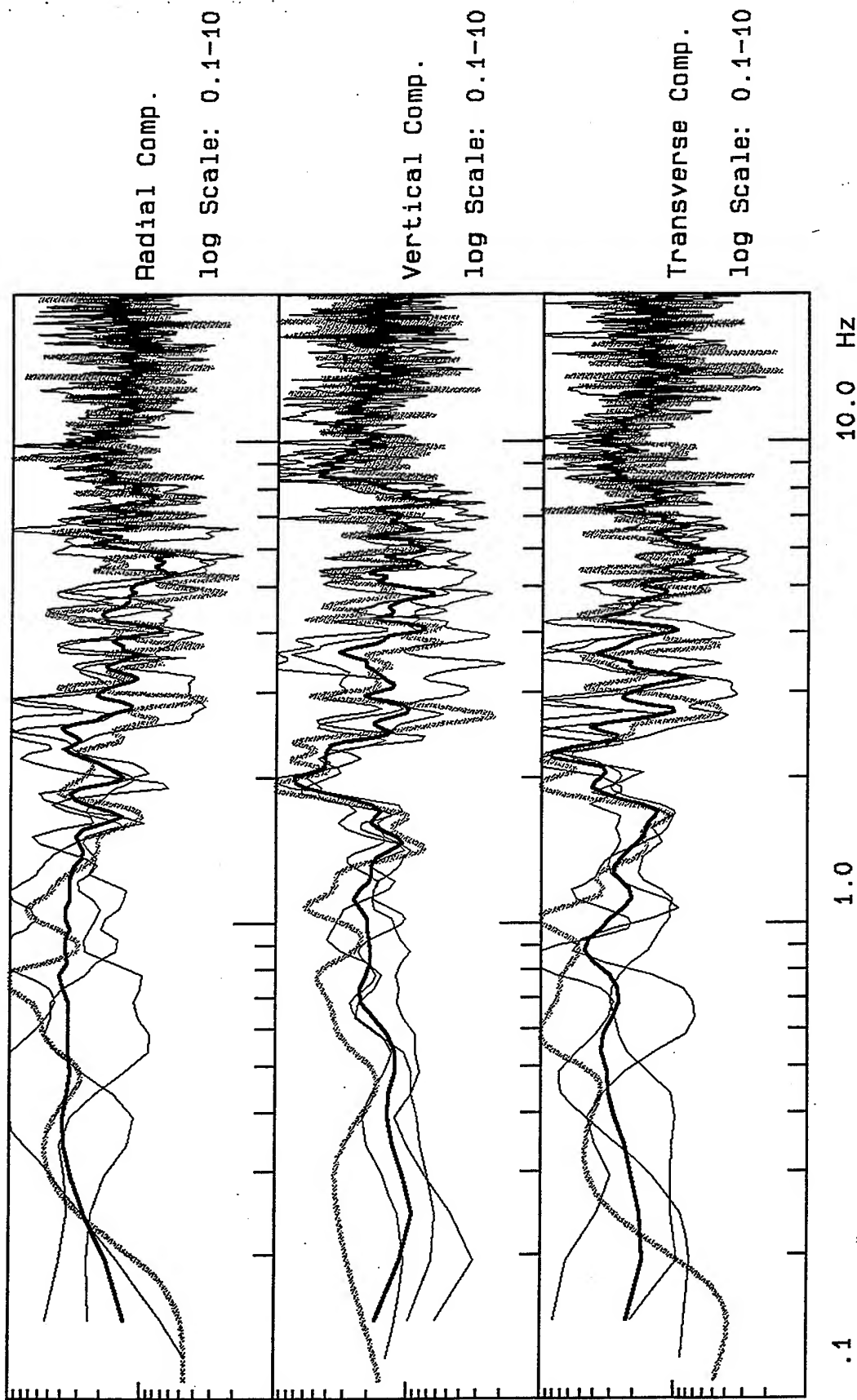
34.50
34.37
34.25
34.12
34.00



119.00 118.75 118.50 118.25 118.00

Figure 5.1. Plots of the locations of pairs of soil-rock sites of the USC network and the epicentral locations of earthquakes that are recorded by different pairs.





.1

Figure 5.2.a. Plots of the soil-to-rock sites spectral ratios for the pair 13-16 of the USC network, see the Appendices E and F. The shaded lines are for the main shock of the Northridge earthquake and the thick lines are the average spectral ratios.



VortexRock Consultants, Inc.

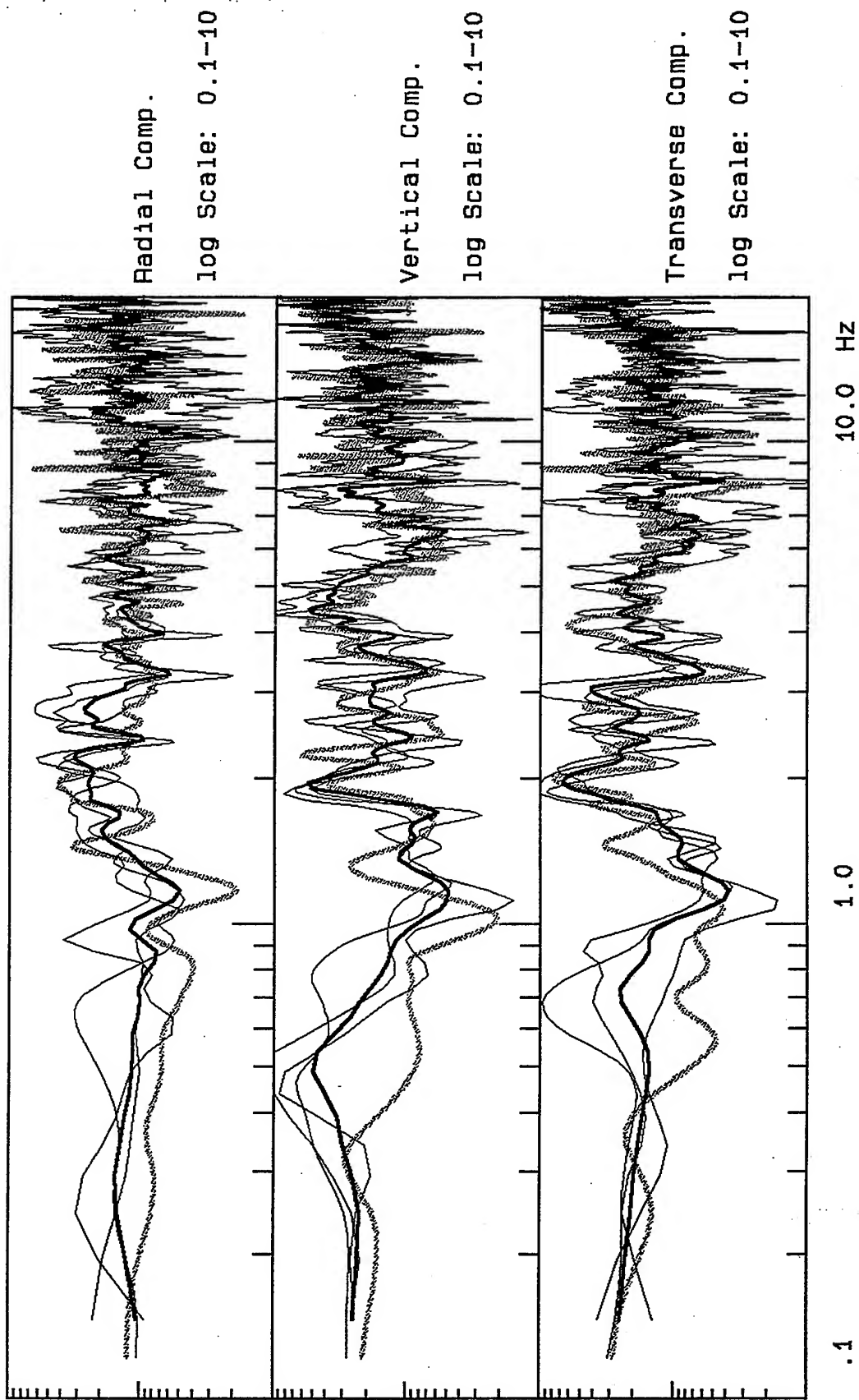


Figure 5.2.b. Plots of the soil-to-rock sites spectral ratios for the pair 63-61 of the USC network, see the Appendices E and F. The shaded lines are for the main shock of the Northridge earthquake and the thick lines are the average spectral ratios.



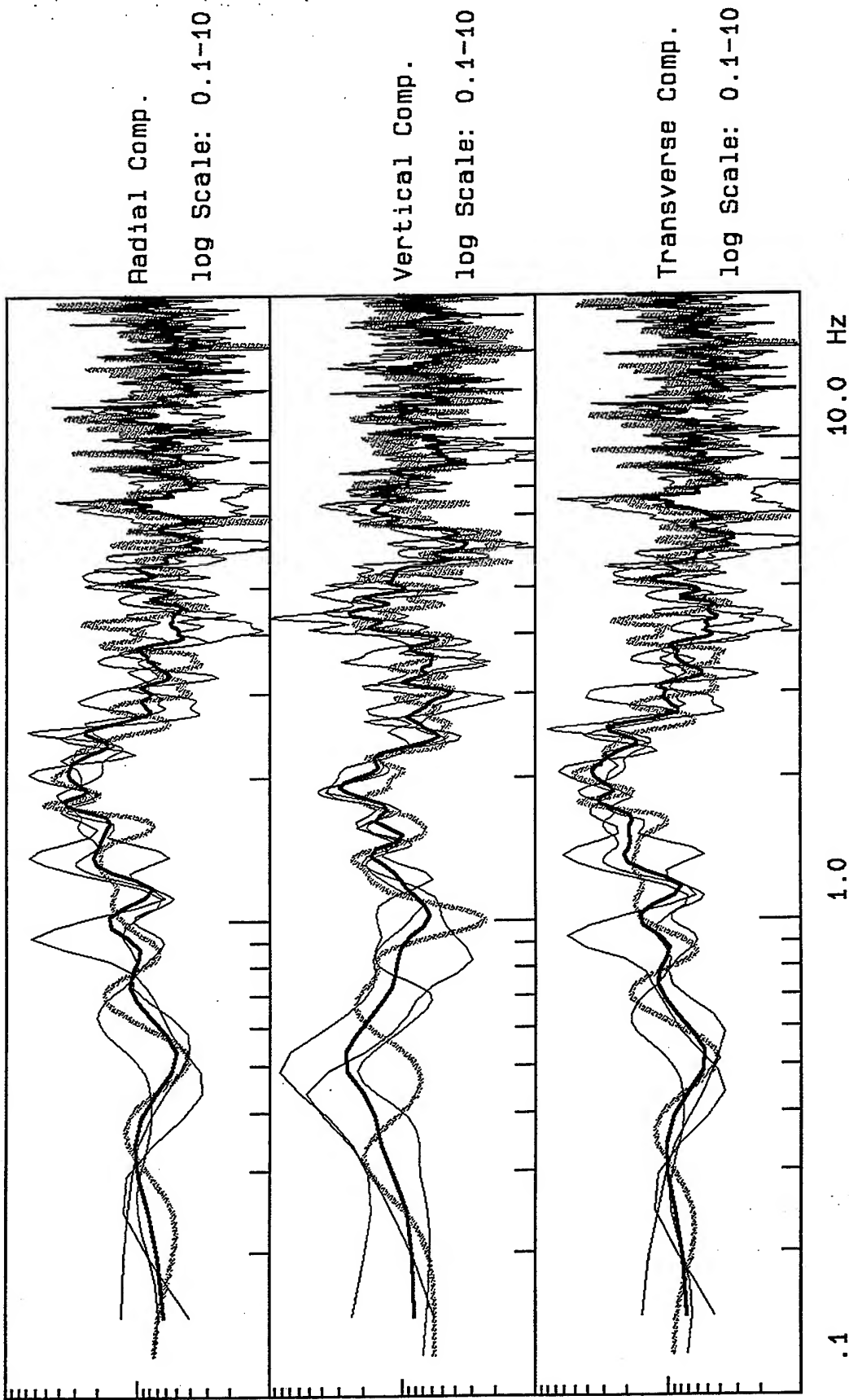


Figure 5.2.c. Plots of the soil-to-rock sites spectral ratios for the pair 60-61 of the USC network, see the Appendices E and F. The shaded lines are for the main shock of the Northridge earthquake and the thick lines are the average spectral ratios.



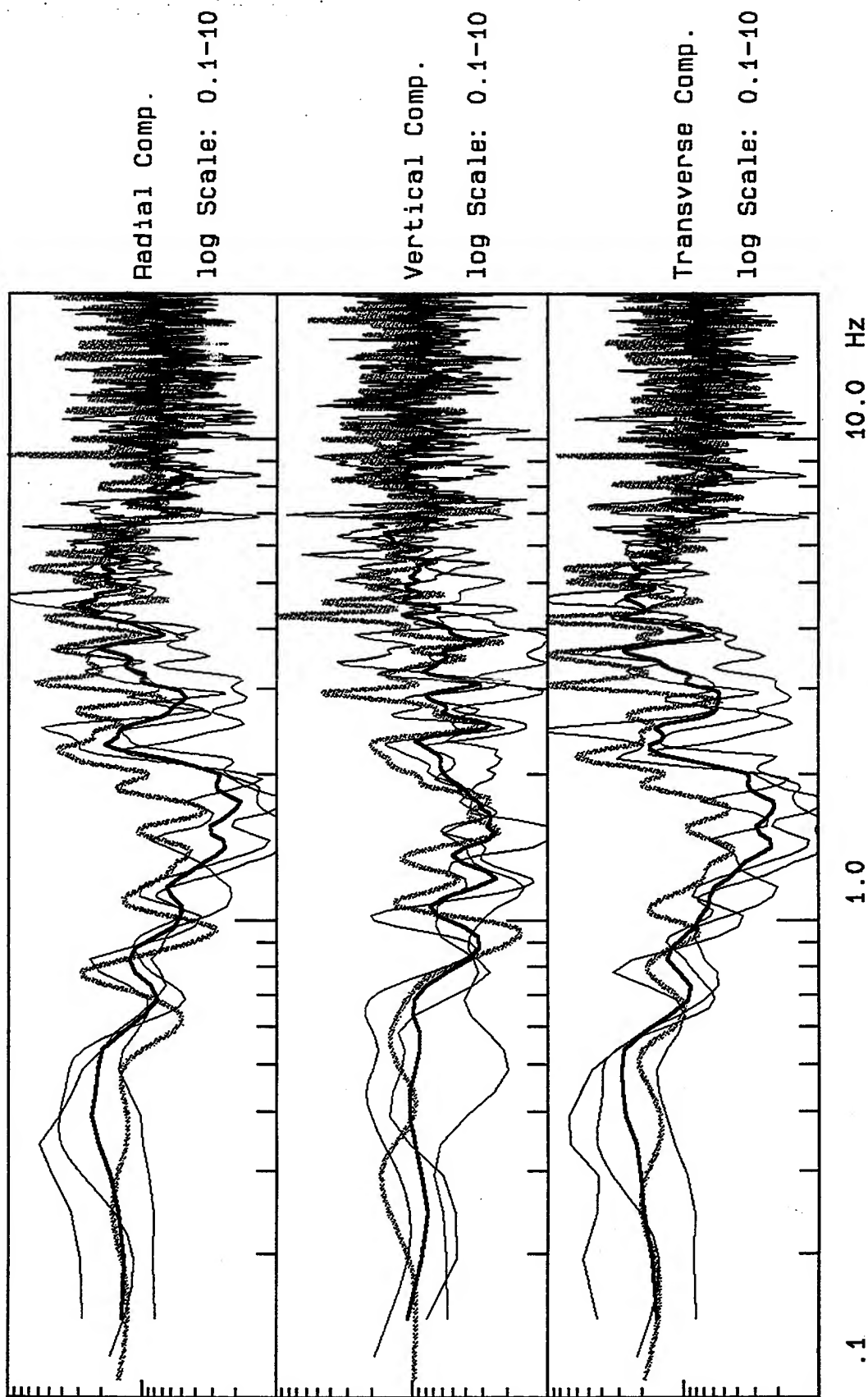


Figure 5.2.d. Plots of the soil-to-rock sites spectral ratios for the pair 49-16 of the USC network, see the Appendices E and F. The shaded lines are for the main shock of the Northridge earthquake and the thick lines are the average spectral ratios.



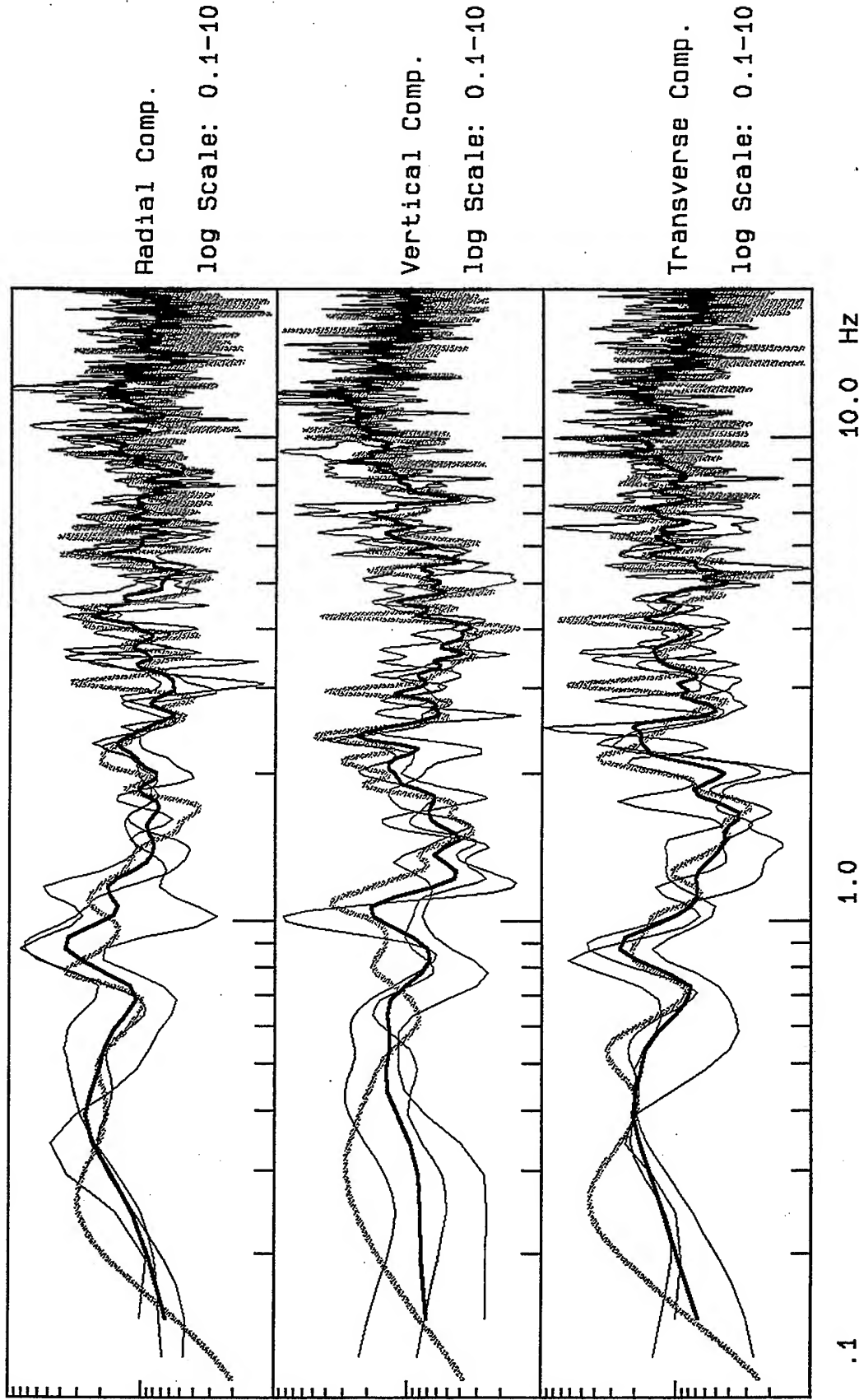


Figure 5.2.e. Plots of the soil-to-rock sites spectral ratios for the pair 16-18 of the USC network, see the Appendices E and F. The shaded lines are for the main shock of the Northridge earthquake and the thick lines are the average spectral ratios.



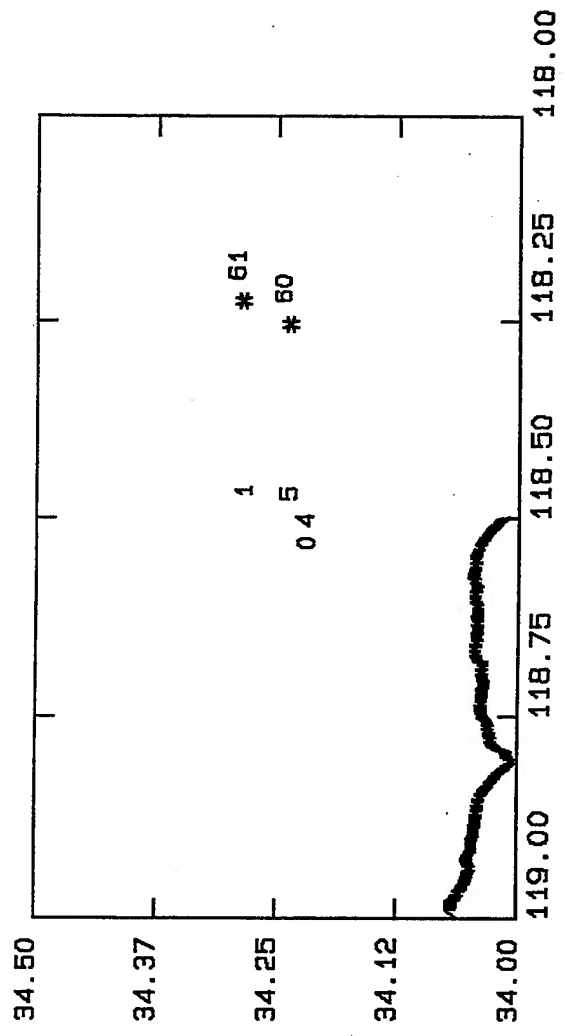
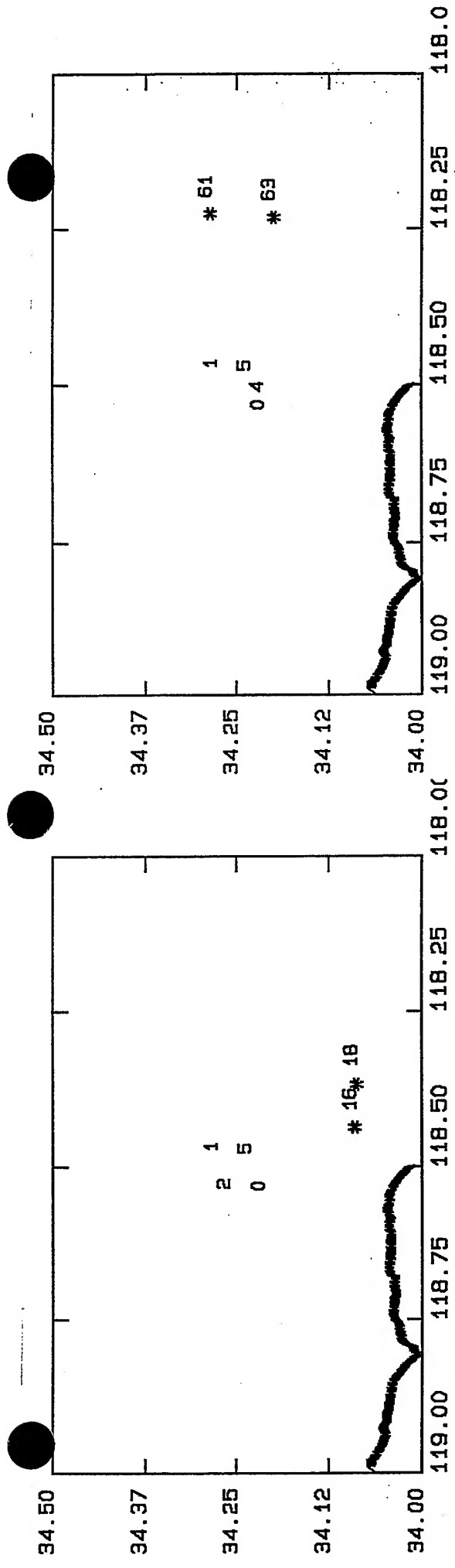


Figure 5.3. Plots of the locations of pairs of soil-rock sites of the Caltech network and the epicentral locations of earthquakes that are recorded by different pairs.



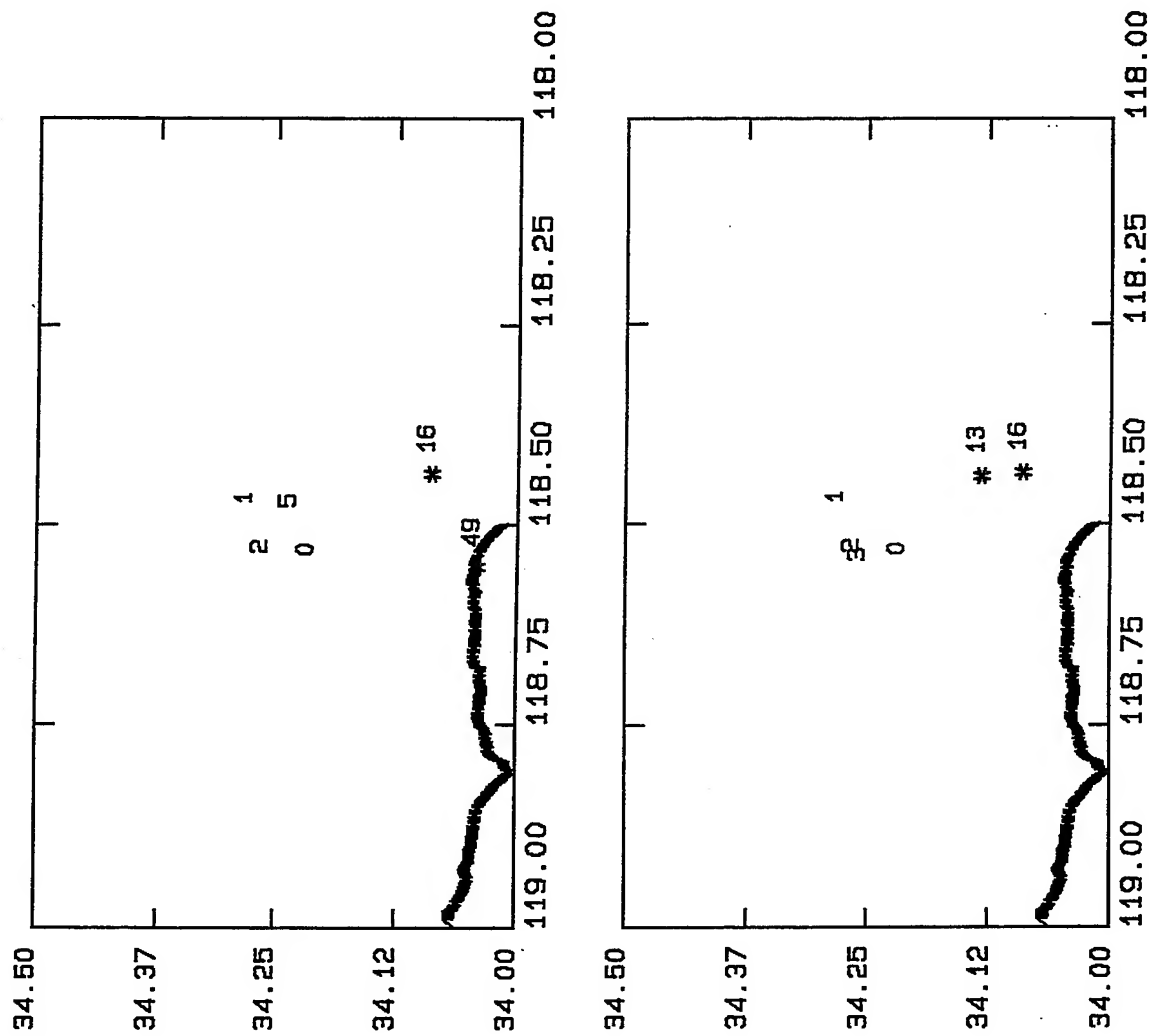


Figure 5.3. Plots of the locations of pairs of soil-rock sites of the Caltech network and the epicentral locations of earthquakes that are recorded by different pairs.



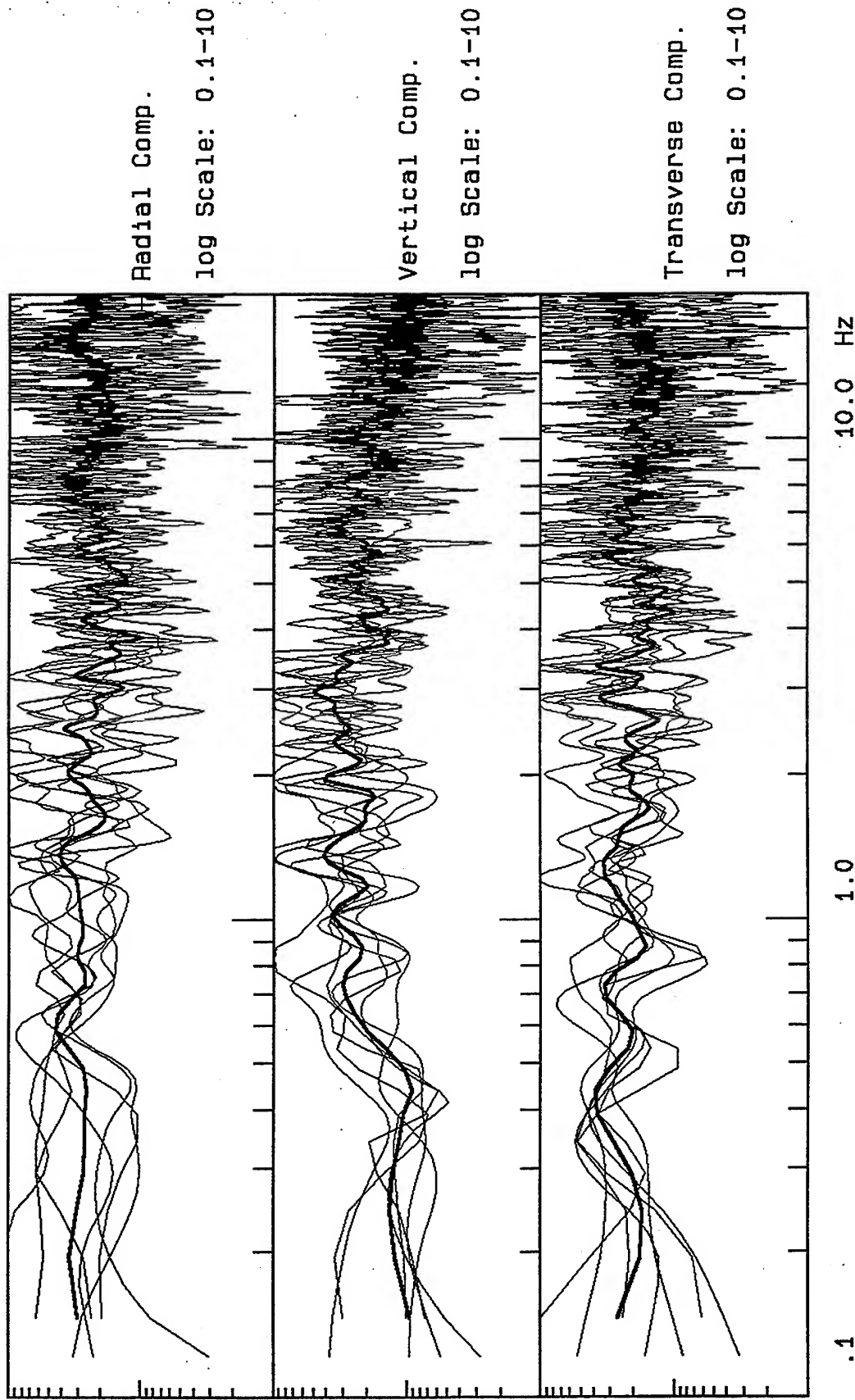


Figure 5.4.a. Plots of the soil-to-rock sites spectral ratios for the pair #1 of the Caltech network, see the Appendices G and H. The shaded lines are for the main shock of the Northridge earthquake and the thick lines are the average spectral ratios.



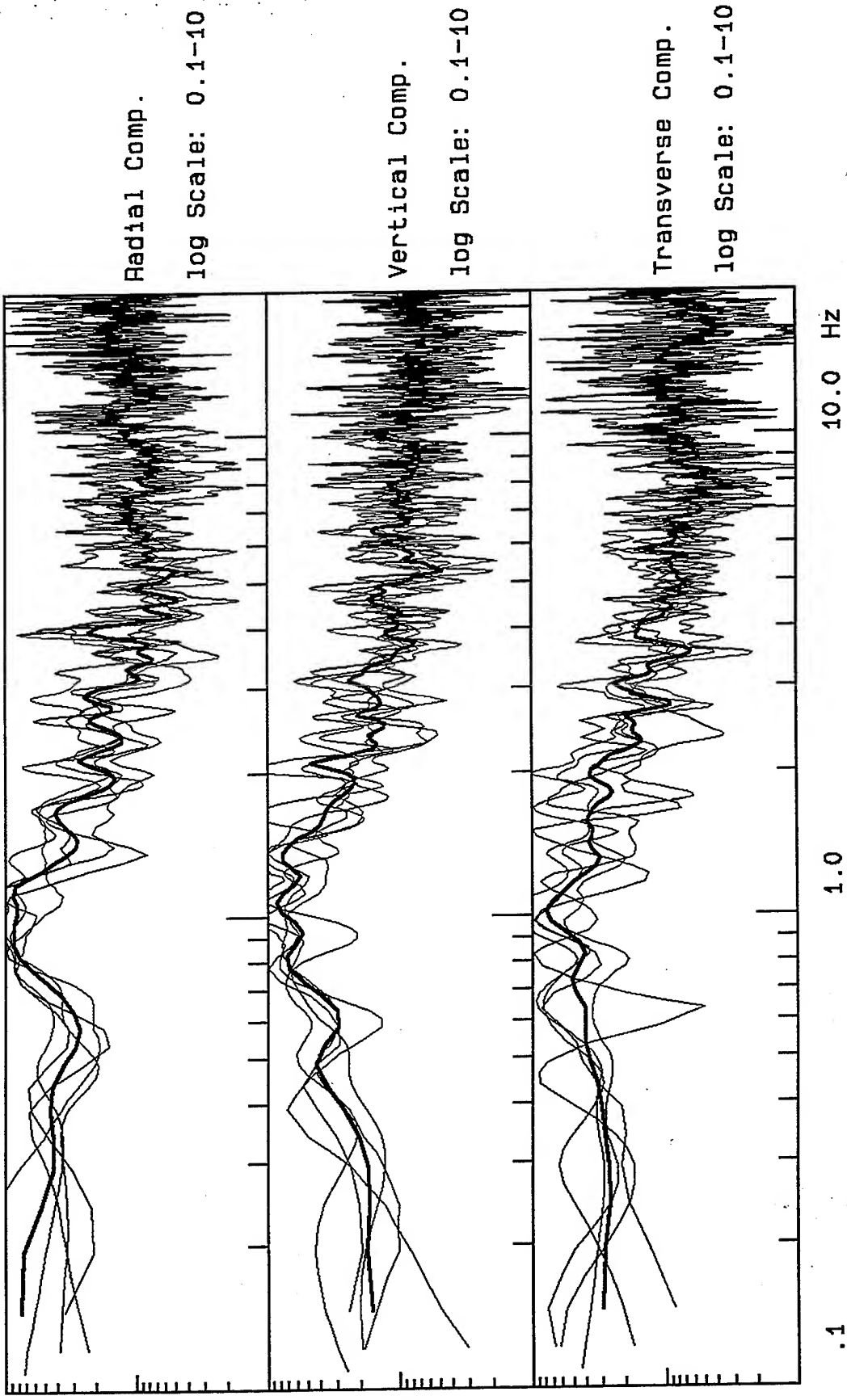


Figure 5.4.b. Plots of the soil-to-rock sites spectral ratios for the pair #2 of the Caltech network, see the Appendices G and H. The shaded lines are for the main shock of the Northridge earthquake and the thick lines are the average spectral ratios.



VortexRock Consultants, Inc.

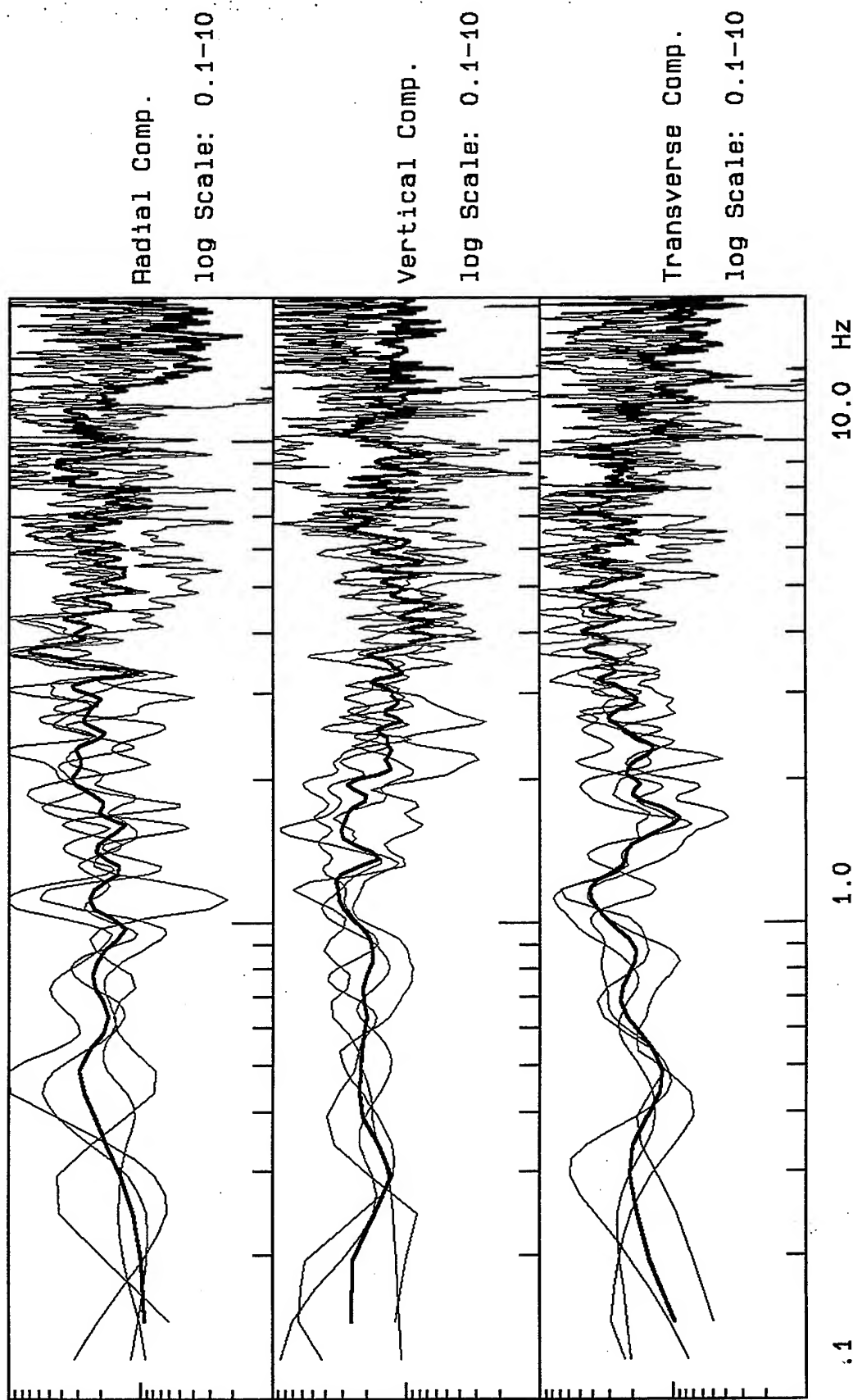


Figure 5.4.c. Plots of the soil-to-rock sites spectral ratios for the pair #3 of the Caltech network, see the Appendices G and H. The shaded lines are for the main shock of the Northridge earthquake and the thick lines are the average spectral ratios.



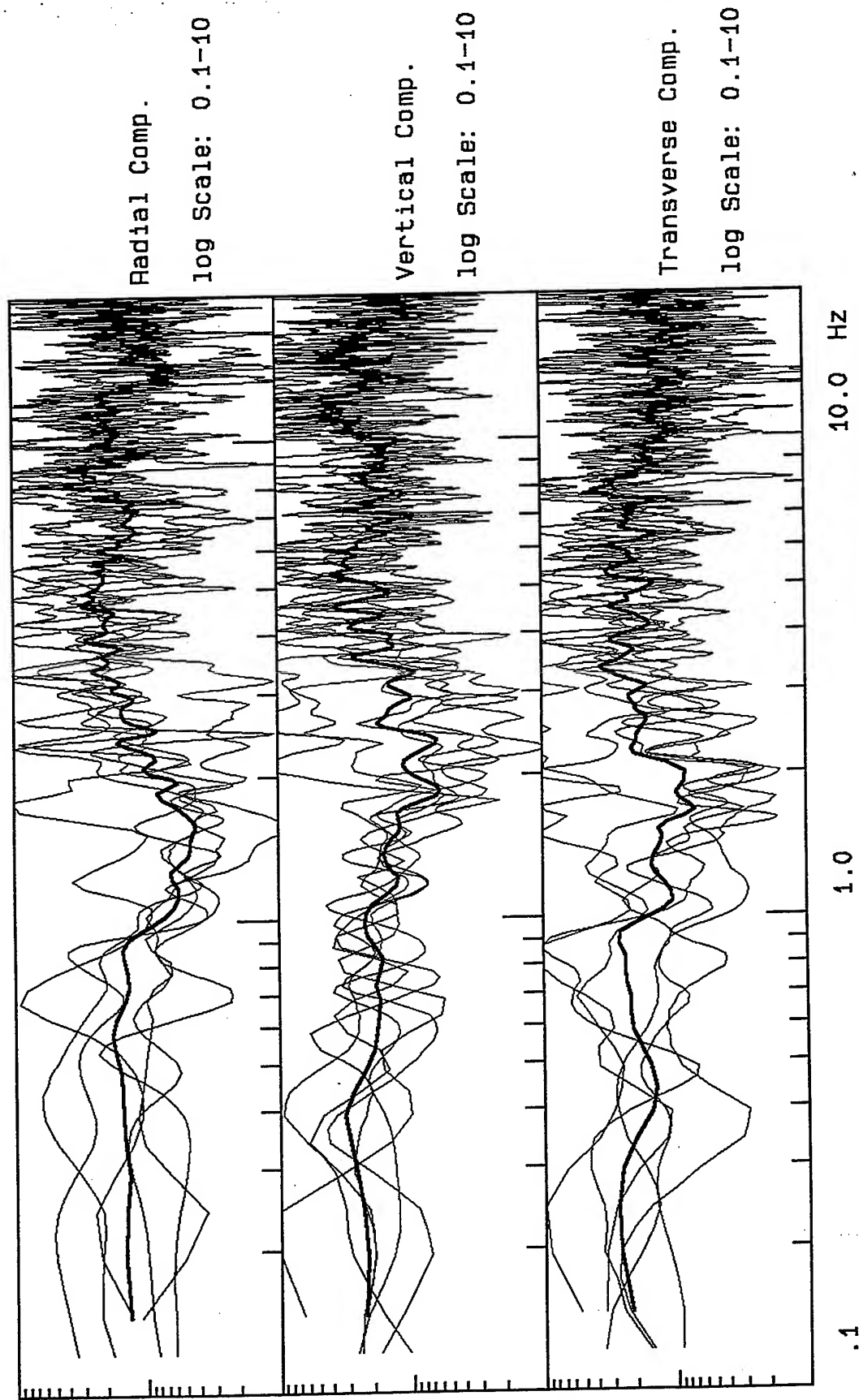


Figure 5.4.d. Plots of the soil-to-rock sites spectral ratios for the pair #4 of the Caltech network, see the Appendices G and H. The shaded lines are for the main shock of the Northridge earthquake and the thick lines are the average spectral ratios.



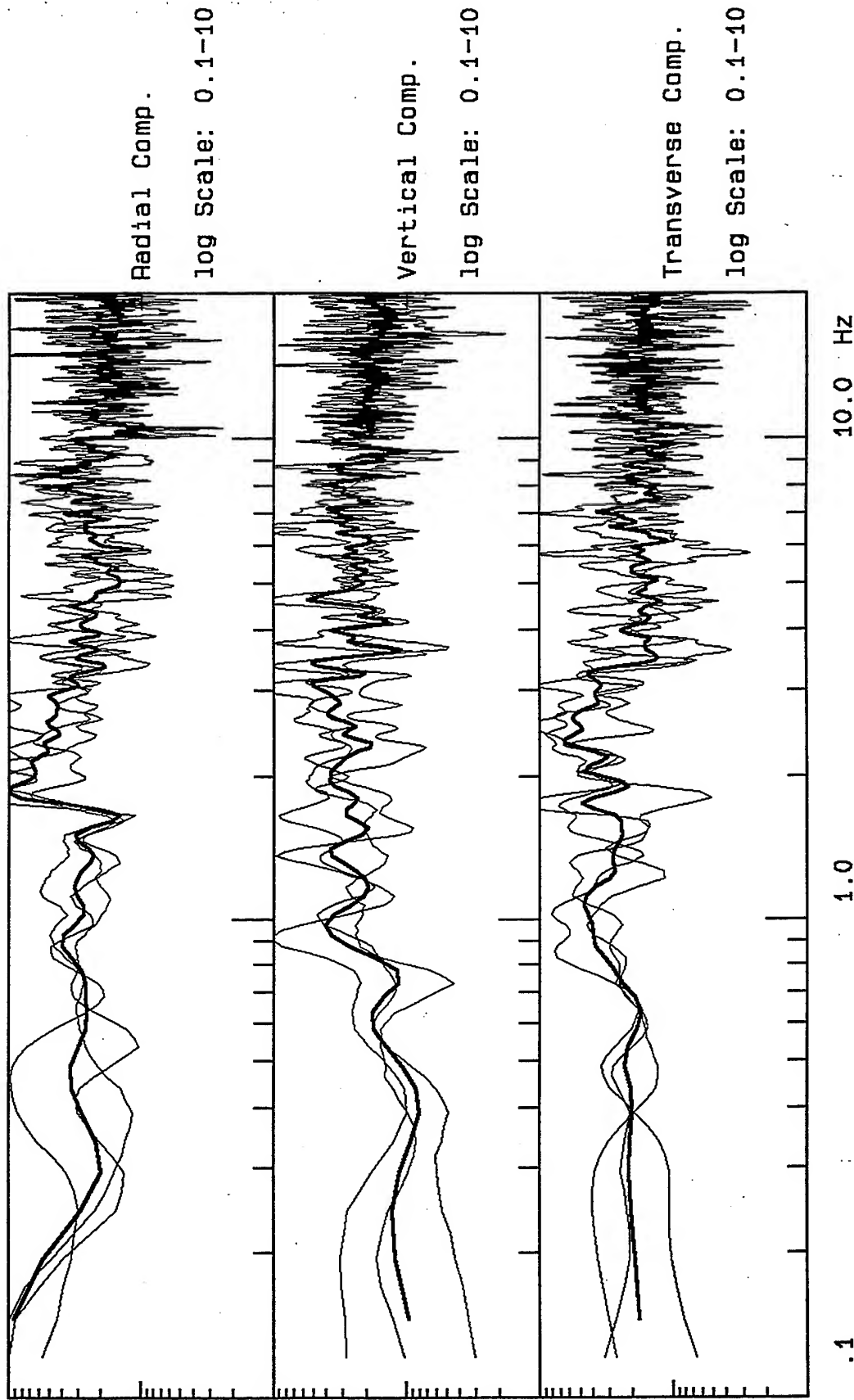


Figure 5.5.a. Plots of the soil-to-rock sites coda waves spectral ratios for the pair #1 of the Caltech network. The shaded lines are for the main shock of the Northridge earthquake and the thick lines are the average spectral ratios.



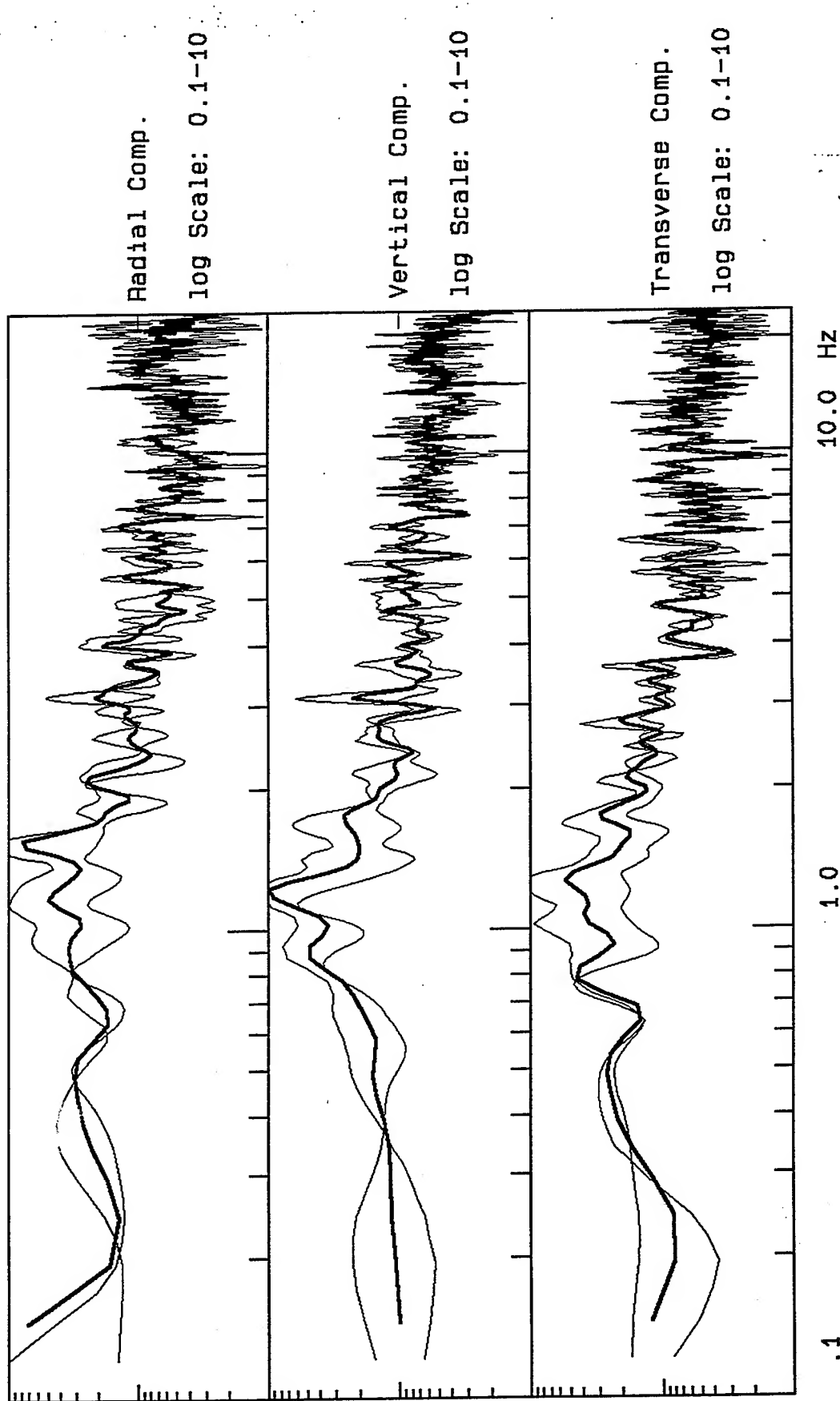


Figure 5.5.b. Plots of the soil-to-rock sites coda waves spectral ratios for the pair #2 of the Caltech network. The shaded lines are for the main shock of the Northridge earthquake and the thick lines are the average spectral ratios.



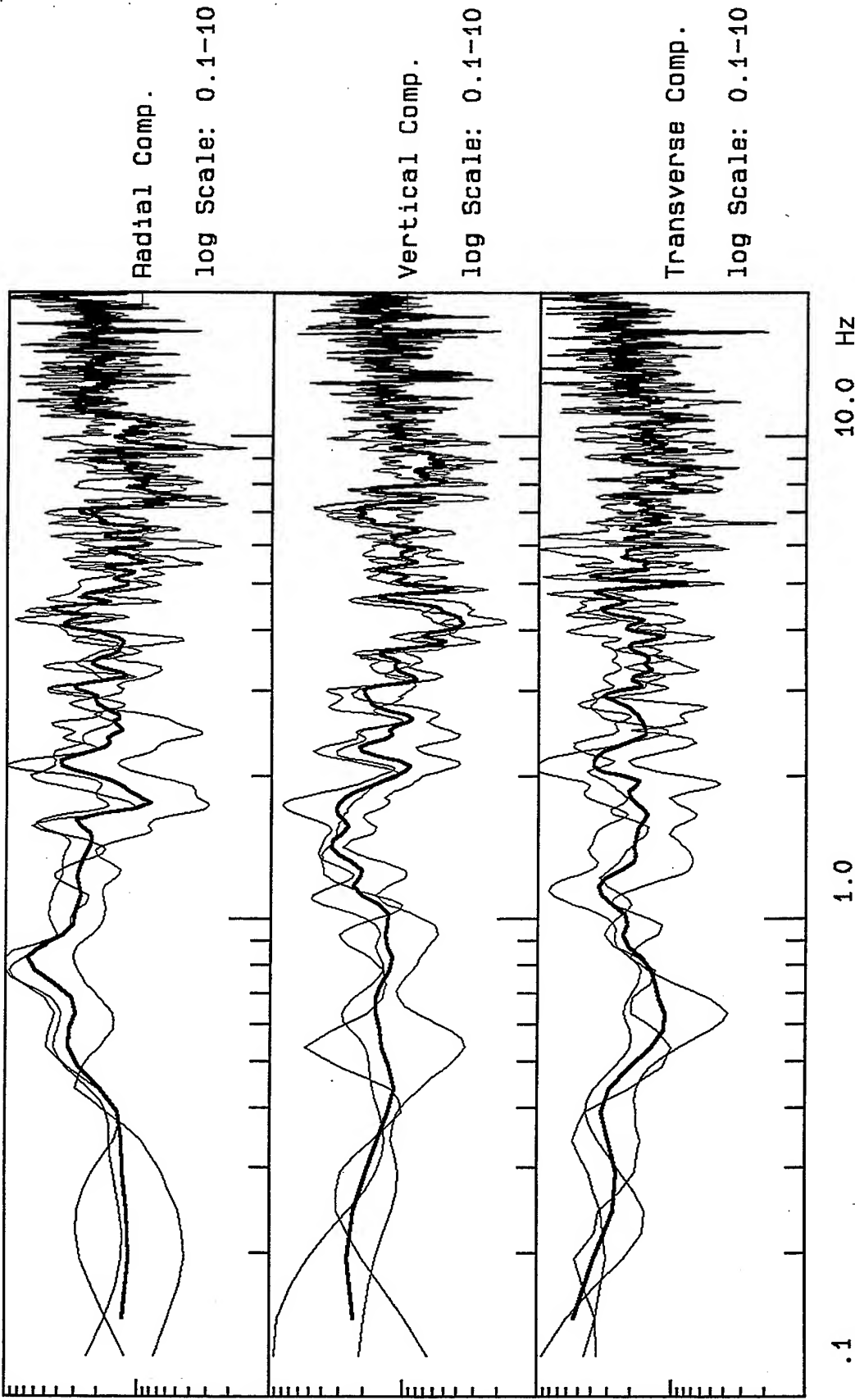


Figure 5.5.c. Plots of the soil-to-rock sites coda waves spectral ratios for the pair #3 of the Caltech network. The shaded lines are for the main shock of the Northridge earthquake and the thick lines are the average spectral ratios.



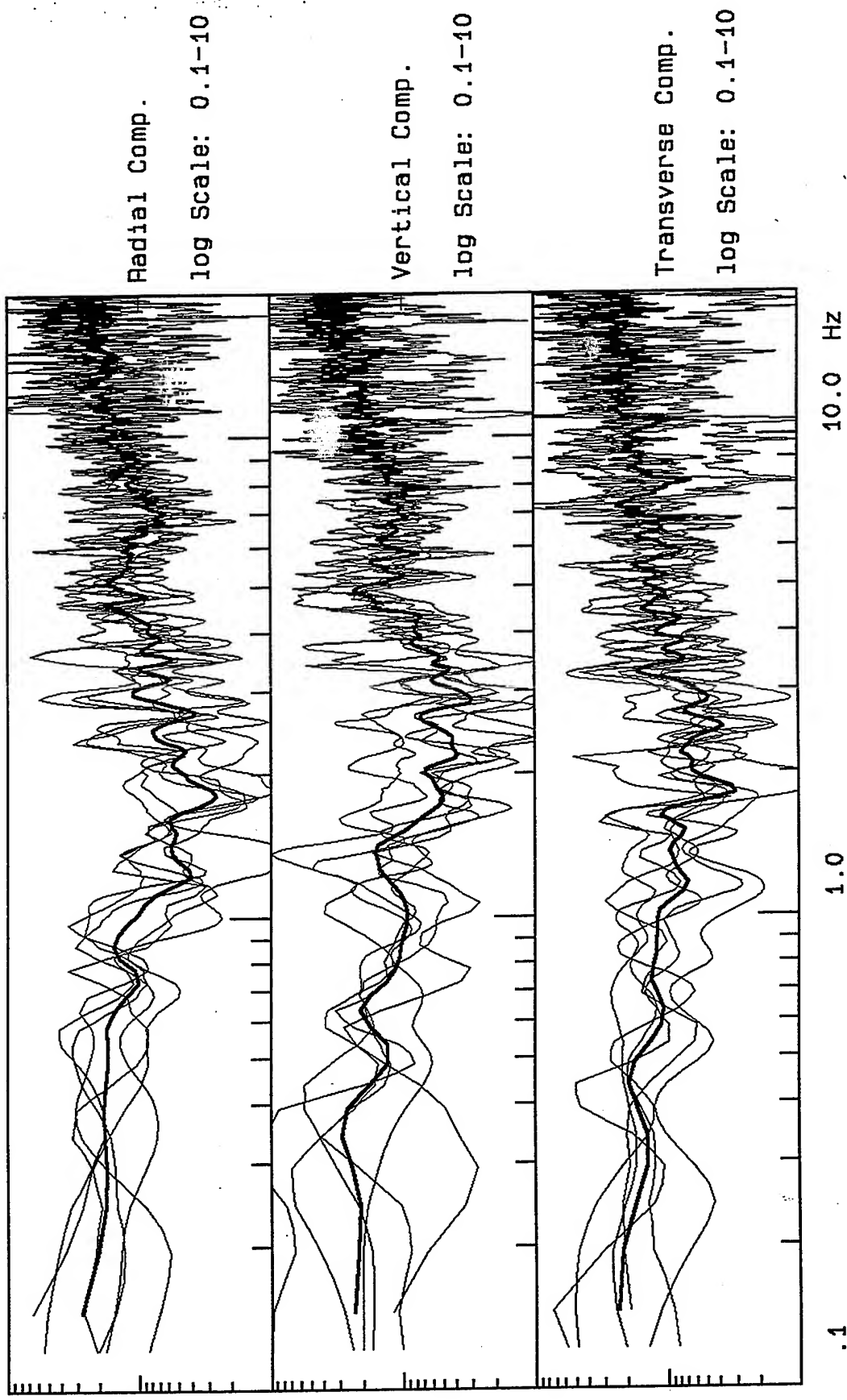


Figure 5.5.d. Plots of the soil-to-rock sites coda waves spectral ratios for the pair #4 of the Caltech network. The shaded lines are for the main shock of the Northridge earthquake and the thick lines are the average spectral ratios.



Chapter 6

Computer Programs for Data Processing and Interpretation

During the course of this study a series of computer programs for data processing and interpretation were developed. These programs can be considered as the basic tools for processing the data from a Circular Array experiment by the instruments that have been used in this study. However, in order to make the programs useful for data processing from other instruments the format of the time history files, that are the primary input data to all programs, are discussed. It should be emphasized that these programs were designed as the necessary tools for our investigation. Therefore, no attempt to automate the data processing or interpretation was made. The user needs to manipulate the input and output data and perform some hand calculation.

Following, a brief description of different steps of data processing and interpretation is presented. Each program and its related input-output data are described in the following section. The application of different programs will be demonstrated by processing a data set from a typical Circular Array experiment.

Data Processing & Interpretation

*Step 1. Transform the IDS binary files of time histories to ASCII files:
Program IDSMENU (This program is provided by the IDS manufacturer)*

Step 2. Resample the recorded time histories and change the format of the IDS ASCII files: Program RESAMPLE

*Step 3. Perform the Fourier spectral analysis of the time histories:
Program FFT (Program FFT_P plots time histories and spectral amplitudes)*



Step 4. Perform the spatial cross correlation analysis of the circular array data: **Program CROSS**

Step 5. Interpret the correlation coefficients in terms of the surface wave phase velocities: **Program PHASE**

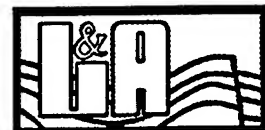
Step 6. Edit the output of the program PHASE to select the appropriate phase velocities for each frequency range: **No Program**

Step 7. Transform the frequency-phase velocity values to depth-phase velocity values: **Program F_DEPTH**

Step 8. Interpret the depth-phase velocity values to the depth- shear wave velocity profile of a layered medium using Satoh's empirical technique: **No Program: Hand Calculation**

Step 9. For the constructed velocity-depth profile simulate the phase velocities for Rayleigh waves: **Program RAYLEIGH (Program R_Plot plots the frequency-phase velocities)**

Step 10. Compare the calculated and simulated phase velocities and if necessary modify the velocity-depth profile. Repeat step 9 if necessary: **No Program**



Step 1. Program IDSMENU

Program IDSMENU is the IDS driver software that allows communicating with the IDS instrument. The IDS instrument stores time histories in a binary format. The binary files can be transformed to ASCII files using the program IDSMENU.

~~~~~

~~~~~

~~

Step 2. Program RESAMPLE

The ASCII files from step 1, in general, require a large amount of computer memory. In order to minimize the memory requirement the time histories are resampled and are stored in a "random access" format.

Input Data:

*Input
Angle
ID-line
output*

Input: Name of the IDS ASCII file

Angle: The azimuth of the connecting line between the center and peripheral sites related to this record. The azimuth is taken with respect to North drawn at the center site. The same angle must be used for both the center and peripheral sites. This angle is used to rotate the horizontal components. Therefore, if the horizontal components are not used or are not rotated then this parameter does not have any significance.

ID-line: One line of site identification

output: Name of the output file

Output file:



The output file is a "random access-unformatted" file with the recording blocks of 5000 Bytes. The first block is used to store the general information. The file has the following format:

1st Block:

ID-line: character*80
 nsample: integer*4
 ksample: integer*4
 ksize: integer*4
 nch: integer*4
 nlast: integer*4
 ang: real*4
 header: 12 lines of character*80

*3*nch Blocks of data each of 5000 Bytes*

nsample: Total number of samples per channel
 ksample: Sampling rate (125 samples per seconds)
 ksize: Size of each block in second ($10\text{ s} \sim 10 \cdot 125 \cdot 4 = 5000$ Bytes)
 nch: No. of blocks per channel
 nlast: No. of samples in the last block
 ang: Azimuthal angle
 header: Header lines read from the IDS file

~~~~~  
 ~~~~~  
 ~~~

**Step 3. Program FFT**

*Program FFT performs Fourier spectral analysis of time windows.*

**Input Data:**

*A file containing the following information:*

name  
 kwin krot  
 kwin set of {win1 win2}



*name:*            *Name of the time history files*  
*kwin:*            *No. of time windows to process*  
*krot:*            *ID to rotate the horizontal components*  
                   *krot <> 0:    Rotate the horizontal components*  
                   *krot = 0:    Do not rotate the horizontal components*

### **Output:**

*Random Access files that contain the Fourier amplitudes of the input time histories. The name of each output file corresponds to the name of each input file and the sequence of the time history window within the list as follows:*

*If "name" includes an extension, i.e. "name = [name].abc", the name of the output file becomes "[name].cij" where "c" is the third letter of the input file extension and ij is the window ID that takes the value from 01 to kwin.*

*If "name" does not include extension, i.e. "name = [name]", the output file becomes "[name].sij".*

~~~~~  
 ~~~~~  
 ~~~

Program FFT_P

Program FFT_P plots the time histories and Fourier amplitude spectra of different channels.

Input Data:

A file containing lines of the following information:

name1 name2

name1: *Name of the spectral amplitude files*
name2: *Name of the time history file corresponding to the file name1*



Output:

Plots of time histories and spectral amplitudes for different channels

~~~~~

~~~~~

~~



Step 4. Program CROSS

Program CROSS calculates the cross correlation of two time histories in the frequency domain

Input Data:

Name

df

f_max

ID

Radius

Output

Name: Name of the file that contains the list of spectral files. Each line of the file should contain the following information:

name1 name2

name1: Name of the 1st spectral amplitude file

name2: Name of the 2nd spectral amplitude file

df: The frequency band over which the correlation coefficients are calculated, equation 2.26 of Chapter 2.

f_max: The maximum frequency to plot the spectral amplitude data

ID: An ID for plotting the results

ID = 1: Plot time histories and correlation coefficients

ID = 2: Only plot the correlation coefficients

ID = 3: Do not plot anything

Radius: Radius of the circular array

Output: Name of the output file that will contain the correlation coefficients as a function of frequency for each set of input time histories



Output:

A file containing the correlation coefficients as a function of frequency for each set of time histories and the corresponding phase velocities based on the first four half cycles of the Bessel function.

Note: For the cases of ID = 1 or 2 the program creates a number of plot files by the names of "TTm.PLT" where m is the sequence number that starts from 01 and increments with each set of records in the input data file. The plot files can be sent to the HP or other compatible printers using the following line command:

pp TTm.PLT set0

The file "set0" includes different plotting information. It can be changed by using the following line command:

pp set0

~~~~~  
~~~~~  
~~

Step 5. Program PHASE

Program PHASE calculates and plots the average of the correlation coefficients of different time windows and the estimated phase velocities based on the first four half cycles of the Bessel function.

Input Data:

Input
output
f_max
ID

Input: Name of the file containing the correlation coefficients for different sets of time histories. This file is the output of program CROSS.

Output: Name of the output file

f_max: The maximum frequency to plot the spectral amplitude data



ID: An ID for filtering the correlation coefficient data

ID = 1: Filter the correlation coefficients and plot the results

ID = 2: Do not filter the correlation coefficients

Note: The interpretation of the correlation coefficients in terms of the first four half cycles of the Bessel function may not always be possible. In such cases the program sets the value of the phase velocity to zero.

Output:

A file that contains the average correlation coefficients and the corresponding phase velocities based on the first four half cycles of the Bessel function. The file will contain four sets of data corresponding to the vertical, horizontal, and the average of the horizontal components of the ground motions.

~~~~~

~~~~~

~~

Step 6. Edit the output of the program PHASE to select the appropriate phase velocities for each frequency range (No Program).

The output of the program PHASE are sets of values for the average correlation coefficients for different frequency bands and the related phase velocities corresponding to the first four half cycles of the Bessel function. The appropriate phase velocity for each frequency band must be determined by identifying the half cycle of the Bessel function to which the correlation coefficient belongs, see Chapter 2 for more detail. For our analysis, we manually examine the output file from the program PHASE to sort out the phase velocities. In cases that the estimated correlation coefficients are beyond the range of Bessel function for the corresponding cycle, the phase velocities are interpolated. The output of step 5 must be a series of frequency-phase velocity values, i.e. a single phase velocity value for each frequency band.

~~~~~

~~~~~

~~



Step 7. Program F_DEPTH

Program F_DEPTH transforms the frequency-phase velocity values to depth-phase velocity values.

Input Data:

Input

ID_velocity

z_max

v_min, v_max, n_div

ID_plt

Input: Name of the input file. The file must have the following format:

np, k, ncol

np lines of {depth, velocity}

Note: np identifies the number of data points for a layered media to be plotted.

k sets of {

ncol lines of {frequency, correlation coefficient, phase velocity}

}

ID_velocity: ID to define the unit of the phase velocities in the file

ID_velocity = 1: Velocities in m/s

ID_velocity = 2: Velocities in ft/s

z_max: Maximum depth to plot

v_min: Minimum velocity to plot

v_max: Maximum velocity to plot

n_div: No. of division for velocity axis

ID_plt: ID to plot individual set or the average of all sets

Output:

Plots of phase velocity-depth profile. A plot file is generated.

~~~~~  
~~~~~  
~~



Step 8. Interpret the depth-phase velocity values to depth-shear wave velocity profile of a layered medium using Satoh's empirical technique (No Program)

The plot of the depth-phase velocity values, from step 7, must be interpreted in terms of the shear wave velocity-depth profile of a layered medium using Satoh's empirical technique, see Chapter 2 for more detail.

~~~~~

~~~~~

~~

Step 9. Program RAYLEIGH

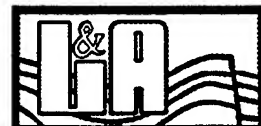
Program RAYLEIGH simulates the phase velocities of the first four modes of Rayleigh waves as a function of frequency for a given velocity-depth profile.

Input Data:

An input file with the following format:

*nlayer
damping, dv
fmax, df, nc
nlayer lines of {depth, density, β , α }*

| | |
|-----------------------------|--|
| <i>nlayer:</i> | <i>Number of layers</i> |
| <i>damping:</i> | <i>% damping ratio for the medium corresponding to the wave related strain level</i> |
| <i>dv:</i> | <i>An increment in the phase velocity to search for the zero crossing of certain equation. Velocities corresponding to different zero crossings are the phase velocities of different modes. $dv = 1$ gives satisfactory results.</i> |
| <i>fmax:</i> | <i>Max frequency to be considered for the analysis</i> |
| <i>df:</i> | <i>frequency increment</i> |
| <i>nc:</i> | <i>Number of modes to be considered</i> |
| <i>depth:</i> | <i>Depth to the top of the layer in an appropriate unit</i> |
| <i>density:</i> | <i>Density of the materials for this layer in an appropriate unit</i> |
| <i>β:</i> | <i>Shear wave velocity for this layer in an appropriate unit</i> |
| <i>α:</i> | <i>P-wave velocity for this layer in an appropriate unit</i> |



Output:

A file that contains the phase velocities of different modes as a function of frequency

~~~~~  
~~~~~  
~~

Program PLOT_R

Program PLOT_R plots the simulated phase velocities versus frequency. The program could also plot individual velocity data points on the same plot.

Input Data:

A file that contains the following information

*ID, n_point, n_column
n_point lines of {frequency, n_column of velocity}
if ID <> 0 lines of
frequency, velocity*

ID: ID that identifies if there are individual velocity points to plot

ID = 0; No data point to plot

ID <> 0 ; There are data points to plot

n_point: No. of frequency values

n_column: No. of different phase velocities for each frequency

~~~~~  
~~~~~  
~~

Step 10. Compare the calculated and simulated phase velocities and if necessary modify the velocity-depth profile. Repeat step 9 if necessary: No Program



6.1 Application

This section demonstrates the application of the programs through processing the data from a typical Circular Array field experiment with the radius of 45 ft. The transformation of the IDS binary files to ASCII files is relatively straight forward. The accompanied floppy disc includes three typical IDS-binary files. In order to convert these files to ASCII files start the program IDSMENU. Under the "SETUP-PC" menu-item select "EVENTS FILE IN PC". Select "TRANSFORM EVENTS" from the menu and under that title select "ASCII OUTPUT". The software brings the list of IDS files in that directory from which different files can be selected for binary to ASCII format transformation. The size of each ASCII file corresponding to the IDS files on the floppy disc is about three to four Mega-Bytes. Using the program RESAMPLE the time histories in the ASCII files will be resampled and the results will be stored in random access unformatted files. Considering the memory requirements for all the IDS and the corresponding ASCII files and the simplicity of the procedure we skip the resampling process and begin the data processing from step 3.

The files P1_3.OU1, P1_4.OU1, P1_10.OU1, P2_3.OU2, P2_4.OU2, and P2_10.OU2 on the floppy disc are the output files of the program RESAMPLE for six different ASCII files. These files contain the resampled time histories from a Circular Array experiment. The files with OU1 extension are for the center station and the files with OU2 extension are for the peripheral sites. The following section demonstrates the application of different programs for data processing and interpretation.



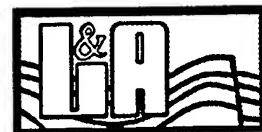
Step 3. Perform the Fourier spectral analysis of the time histories

The file "SPEC.DAT" on the floppy disc contains the input data for program FFT for the Fourier spectral analysis of the time histories. For each time history file nine overlapping time windows for spectral analysis are selected. The beginning and end of each time window in the SPEC.DAT file are in seconds. For each selected time window program FFT performs the spectral analysis and creates an output file. The name of each output file takes the name of the input time history file as its root with an extension that corresponds to the sequence of the time window in the SPEC.DAT file. For example, the third time window corresponding to the file P1_4.OU1 will be P1_4.103. The total of $6 \times 9 = 72$ spectral files will be generated. Program FFT_P plots the time histories and the spectral amplitudes.

~~~~~  
~~~~~  
~~

Step 4. Perform the spatial correlation analysis of the circular array data

Program CROSS performs the cross correlation analysis of two time histories in the frequency domain. The file CROSS.DAT on the floppy disc is constructed as the input file to the program CROSS based on the set of files that will be generated from step 3. Program CROSS can be run with or without plotting the correlation coefficients and time histories. The output of the program CROSS will be a file that contains the correlation coefficient values in terms of frequency and the corresponding phase velocities based on the first four half cycles of the Bessel



function. The file CROSS.OUT on the floppy disc is the output file for our example.

~~~~~  
~~~~~  
~~

Step 5. Average the individual spatial correlation coefficients and interpret the results in terms of the phase velocity

Program PHASE performs the averaging of the spatial correlation coefficients on the output of the program CROSS. The program calculates and plots the mean and the standard deviation of error of the correlation coefficients as a function of frequency. The program filters the correlation coefficient data to obtain an smooth curve. This makes the interpretation of the results easier. The file PHASE.OUT is the output of the program PHASE in our example. The file contains four sets of data one for the vertical, two for the horizontal, and one for the average of the two horizontal components of the ground motions. Each set contains the correlation coefficient values in terms of frequency and the corresponding phase velocities based on the first four half cycles of the Bessel function.

~~~~~  
~~~~~  
~~



Step 6. Edit the output of the program PHASE to select the appropriate frequency-phase velocity values

The output of the program PHASE must be edited to identify the phase velocities corresponding to the appropriate half cycle of the Bessel function to which each correlation coefficient belongs. The following table shows a typical example.

| f
Hz | $\bar{\rho}(\omega)$
↓
$J_0(x)$ | x | $C_1(\omega)$ | x_2 | $C_2(\omega)$ | x_3 | $C_3(\omega)$ | x_4 | $C_4(\omega)$ |
|---|---------------------------------------|-------|---------------|-------|---------------|-------|---------------|--------|---------------|
| .25 | .999 | .069 | 1019 | | | | | | |
| .75 | .989 | .212 | 1000 | | | | | | |
| 1.25 | .967 | .362 | 975 | | | | | | |
| 1.75 | .930 | .535 | 925 | | | | | | |
| 2.25 | .874 | .720 | 883 | | | | | | |
| 2.75 | .801 | .915 | 850 | | | | | | |
| 3.25 | .708 | 1.125 | 816 | | | | | | |
| 3.75 | .592 | 1.354 | 783 | | | | | | |
| 4.25 | .454 | 1.602 | 750 | | | | | | |
| 4.75 | .297 | 1.874 | 716 | 6.871 | 195 | 7.161 | 187 | | |
| 5.25 | .138 | 2.151 | 690 | 5.954 | 249 | 8.140 | 182 | 12.445 | 119.3 |
| 5.75 | -.011 | 2.427 | 670 | 5.487 | 296 | 8.695 | 187 | 11.743 | 138.4 |
| 6.25 | -.151 | 2.719 | 650 | 5.081 | 347 | 9.266 | 190 | 11.111 | 159.0 |
| 6.75 | -.270 | 3.029 | 630 | 4.698 | 406 | | | | |
| 7.25 | -.357 | 3.361 | 610 | 4.323 | 474 | | | | |
| 7.75 | -.400 | 3.715 | 589 | 3.950 | 554 | | | | |
| Beginning of the second half cycle | | | | | | | | | |
| 8.25 | -.389 | 3.577 | 652 | 4.092 | 570 | | | | |
| 8.75 | -.321 | 3.203 | 772 | 4.498 | 550 | | | | |
| 9.25 | -.199 | 2.834 | 922 | 4.935 | 530 | 9.530 | 274 | 10.831 | 241 |
| 9.75 | -.039 | 2.482 | 1110 | 5.405 | 510 | 8.800 | 313 | 11.623 | 237 |
| 10.25 | .054 | 2.302 | 1258 | 5.683 | 510 | 8.455 | 342 | 12.030 | 240 |
| 10.75 | .071 | 2.271 | 1338 | 5.735 | 530 | 8.393 | 362 | 12.107 | 251 |
| 11.25 | .087 | 2.243 | 1418 | 5.783 | 550 | 8.336 | 381 | 12.179 | 261 |
| 11.75 | .101 | 2.218 | 1498 | 5.829 | 570 | 8.283 | 401 | 12.248 | 271 |
| 12.25 | .113 | 2.195 | 1578 | 5.871 | 590 | 8.235 | 420 | 12.313 | 281 |
| 12.75 | .125 | 2.174 | 1658 | 5.910 | 610 | 8.189 | 440 | 12.375 | 291 |
| 13.25 | .136 | 2.155 | 1738 | 5.947 | 630 | 8.148 | 459 | 12.434 | 301 |
| 13.75 | .145 | 2.137 | 1818 | 5.981 | 650 | 8.109 | 479 | 12.491 | 311 |
| 14.25 | .154 | 2.122 | 1899 | 6.014 | 670 | 8.072 | 499 | 12.546 | 321 |



| f
Hz | $\bar{p}(\omega)$
↓
$J_0(x)$ | x | $C_1(\omega)$ | x_2 | $C_2(\omega)$ | x_3 | $C_3(\omega)$ | x_4 | $C_4(\omega)$ |
|--|------------------------------------|-------|---------------|-------|---------------|--------|---------------|--------|---------------|
| 14.75 | .163 | 2.107 | 1979 | 6.044 | 690 | 8.038 | 518 | 12.600 | 331 |
| 15.25 | .192 | 2.055 | 2098 | 6.160 | 700 | 7.910 | 545 | 12.832 | 336 |
| 15.75 | .236 | 1.979 | 2250 | 6.362 | 700 | 7.691 | 579 | | |
| 16.25 | .269 | 1.922 | 2391 | 6.564 | 700 | 7.477 | 614 | | |
| 16.75 | .291 | 1.885 | 2512 | 6.766 | 700 | 7.268 | 651 | | |
| 17.25 | .300 | 1.869 | 2609 | 6.969 | 699 | 7.063 | 690 | | |
| Beginning of the third half cycle | | | | | | | | | |
| 17.75 | .297 | 1.875 | 2677 | 6.863 | 731 | 7.169 | 700 | | |
| 18.25 | .282 | 1.900 | 2715 | 6.666 | 774 | 7.371 | 700 | | |
| 18.75 | .256 | 1.945 | 2725 | 6.473 | 819 | 7.573 | 700 | | |
| 19.25 | .220 | 2.006 | 2712 | 6.283 | 866 | 7.773 | 700 | | |
| 19.75 | .177 | 2.082 | 2682 | 6.099 | 915 | 7.977 | 700 | 12.703 | 439 |
| 20.25 | .128 | 2.169 | 2639 | 5.919 | 967 | 8.179 | 700 | 12.389 | 462 |
| 20.75 | .074 | 2.266 | 2589 | 5.744 | 1021 | 8.381 | 700 | 12.121 | 484 |
| 21.25 | .019 | 2.368 | 2537 | 5.577 | 1077 | 8.583 | 700 | 11.874 | 506 |
| 21.75 | -.035 | 2.474 | 2485 | 5.417 | 1135 | 8.785 | 700 | 11.640 | 528 |
| 22.25 | -.087 | 2.580 | 2438 | 5.267 | 1194 | 8.987 | 700 | 11.414 | 551 |
| 22.75 | -.134 | 2.682 | 2398 | 5.129 | 1254 | 9.189 | 700 | 11.193 | 574 |
| 23.25 | -.175 | 2.776 | 2367 | 5.007 | 1312 | 9.391 | 700 | 10.977 | 598 |
| 23.75 | -.208 | 2.857 | 2350 | 4.905 | 1368 | 9.593 | 700 | 10.765 | 623 |
| 24.25 | -.232 | 2.920 | 2347 | 4.829 | 1420 | 9.795 | 700 | 10.557 | 649 |
| 24.75 | -.246 | 2.959 | 2364 | 4.782 | 1463 | 9.998 | 700 | 10.350 | 676 |
| 25.25 | -.250 | 2.970 | 2403 | 4.769 | 1497 | 10.152 | 703 | 10.196 | 700 |
| Beginning of the fourth cycle | | | | | | | | | |
| 25.75 | -.243 | 2.952 | 2466 | 4.790 | 1519 | 9.948 | 731 | 10.401 | 700 |
| 26.25 | -.227 | 2.908 | 2552 | 4.843 | 1532 | 9.750 | 761 | 10.603 | 700 |
| 26.75 | -.203 | 2.844 | 2659 | 4.923 | 1536 | 9.555 | 791 | 10.805 | 700 |
| 27.25 | -.170 | 2.764 | 2787 | 5.023 | 1533 | 9.363 | 822 | 11.007 | 700 |
| 27.75 | -.131 | 2.675 | 2933 | 5.139 | 1526 | 9.175 | 855 | 11.209 | 700 |
| 28.25 | -.088 | 2.581 | 3094 | 5.265 | 1517 | 8.990 | 888 | 11.411 | 700 |
| 28.75 | -.042 | 2.487 | 3269 | 5.399 | 1505 | 8.809 | 922 | 11.613 | 700 |
| 29.25 | .005 | 2.395 | 3453 | 5.536 | 1493 | 8.634 | 957 | 11.815 | 700 |
| 29.75 | .051 | 2.308 | 3645 | 5.674 | 1482 | 8.465 | 993 | 12.017 | 700 |
| 30.25 | .095 | 2.229 | 3838 | 5.809 | 1472 | 8.305 | 1029 | 12.219 | 700 |
| 30.75 | .133 | 2.159 | 4026 | 5.938 | 1464 | 8.157 | 1065 | 12.421 | 700 |
| 31.25 | .166 | 2.101 | 4205 | 6.056 | 1458 | 8.024 | 1101 | 12.623 | 700 |
| 31.75 | .191 | 2.057 | 4365 | 6.156 | 1458 | 7.914 | 1134 | 12.825 | 700 |
| 32.25 | .209 | 2.026 | 4499 | 6.230 | 1463 | 7.833 | 1164 | 13.027 | 700 |
| 32.75 | .217 | 2.011 | 4603 | 6.270 | 1476 | 7.790 | 1188 | 13.229 | 700 |
| 33.25 | .217 | 2.012 | 4673 | 6.269 | 1499 | 7.791 | 1206 | 13.218 | 711 |



Please see the discussion in Chapter 2 for more detail.

~~~~~  
~~~~~  
~~

Step 7. Transform the frequency-phase velocity values to depth-phase velocity values

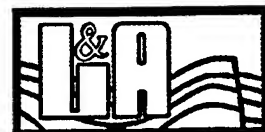
The output of the step 6 is a series of frequency-phase velocity values. This information must be translated into the phase velocity-depth values. Program F_DEPTH performs such transformation and plots phase velocity-depth profile. The file PHASE_V.OUT on the floppy disc contains the input data for the vertical components of ground motions in our example. Figure 6.1 shows the corresponding plot of the phase velocity-depth profile.

~~~~~  
~~~~~  
~~

Step 8. Interpret the depth-phase velocity values to depth-shear wave velocity profile of a layered medium using Satoh's empirical technique

In order to demonstrate the application of Satoh's empirical technique to the velocity-depth data interpretation the data on Figure 6.1 is modeled by two slopes. The phase velocity-depth values for the end points from the shallowest to the deepest points are:

$$\left\{ \begin{array}{l} \overline{C}_1 = 2037 \text{ ft / s} \\ \overline{d}_1 = 40 \text{ ft} \end{array} \right\} \quad \left\{ \begin{array}{l} \overline{C}_2 = 1636 \text{ ft / s} \\ \overline{d}_2 = 99 \text{ ft} \end{array} \right\} \quad \left\{ \begin{array}{l} \overline{C}_3 = 2300 \text{ ft / s} \\ \overline{d}_3 = 232 \text{ ft} \end{array} \right\}$$



Using Satoh's technique the data on Figure 6.1 can lead to the following velocity-depth model.

$$C_1 = 2037 \text{ ft/s}, \beta_1 = 2263 \text{ ft/s}, \text{ and } \alpha_1 = 3915 \text{ ft/s}$$

$$d_1 = 40 \text{ ft}$$

$$C_2 = 1364 \text{ ft/s}, \beta_2 = 1515 \text{ ft/s}, \text{ and } \alpha_2 = 2622 \text{ ft/s}$$

$$d_2 = 99 \text{ ft}$$

$$C_3 = 3295 \text{ ft/s}, \beta_3 = 3661 \text{ ft/s}, \text{ and } \alpha_3 = 6333 \text{ ft/s}$$

where β and α are the shear and pressure wave velocities, respectively. In constructing the above velocity-depth model it is assumed that $c/\beta = 0.9$ and $\alpha/\beta = 1.7$. It is also assumed that the top 40 ft of material, where no data is available, can be modeled by a single layer.

~~~~~  
 ~~~~~  
 ~~~



**Step 9. For the constructed depth-velocity profile of step 8 simulate the phase velocities for the Rayleigh waves**

*Program RAYLEIGH simulates the Rayleigh wave phase velocities for a given velocity-depth profile. The file RAYLEIGH.DAT on the floppy disc is the input data file to the program for our example. The output of the program is a file that contains the simulated phase velocities versus frequency. The corresponding frequency-phase velocity plots can be made using the program PLOT\_R. This program also allows plotting the calculated phase velocities on top of the simulated ones for the purpose of comparison. The file PLOT.DAT on the floppy disc is the input file to the program PLOT-R for our example. Figure 6.2 shows the plots of the simulated and calculated phase velocities. Obviously, the high frequency components of the phase velocities do not agree with the simulated values. It might be the case that the high frequency components of microtremors are dominated by the higher modes of Rayleigh waves.*

~~~~~  
~~~~~  
~~

**Step 10. Compare the calculated and simulated phase velocities and if necessary modify the velocity-depth profile. Repeat step 9 if necessary.**



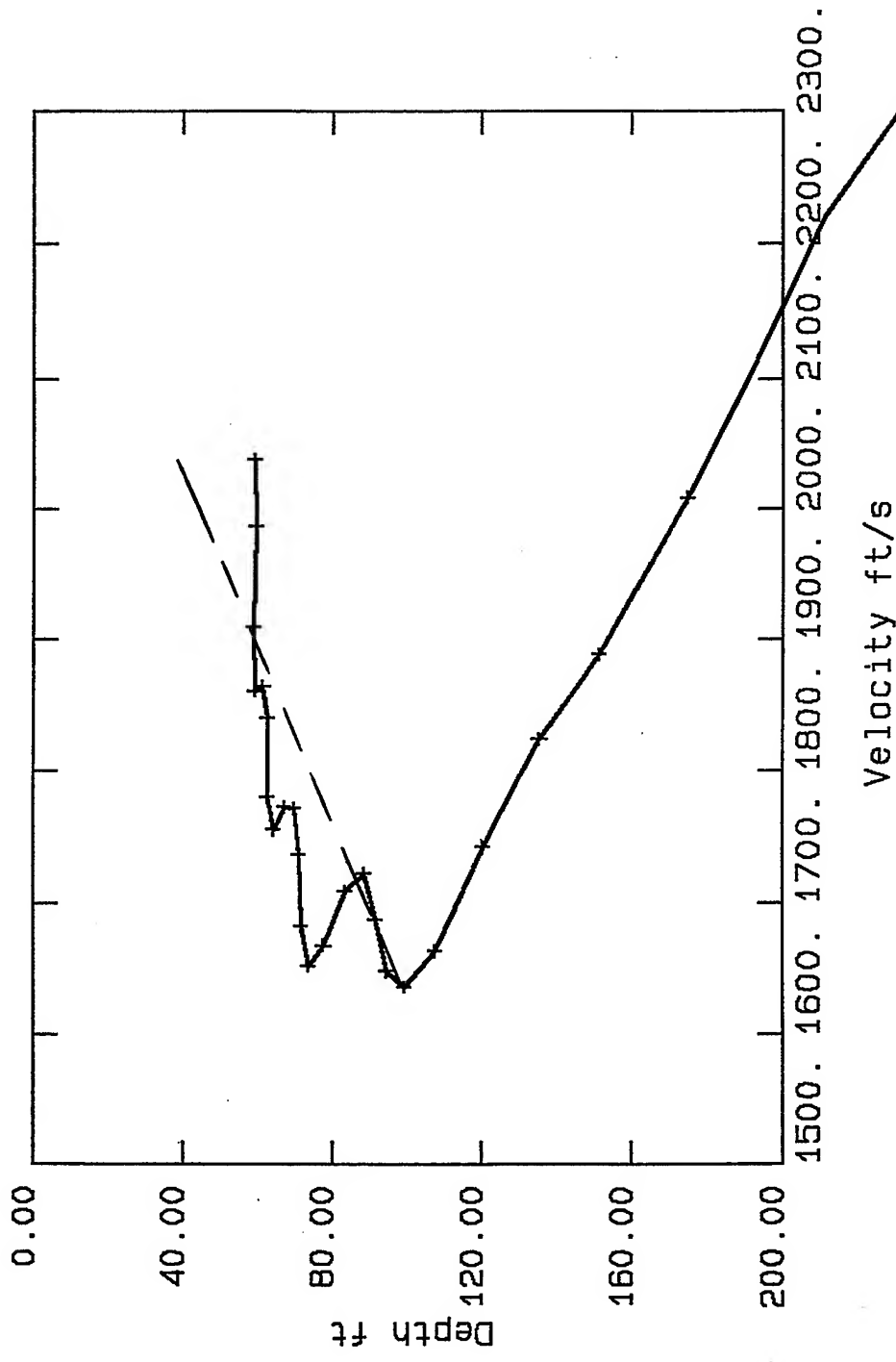


Figure 6.1. Plot of the phase velocity versus depth. According to Satoh's empirical technique this plot should be interpreted in terms of few different segments with constant slopes. The end points of each sloped segment are used to estimate the average phase velocity for that segment.



VortexRock Consultants, Inc.

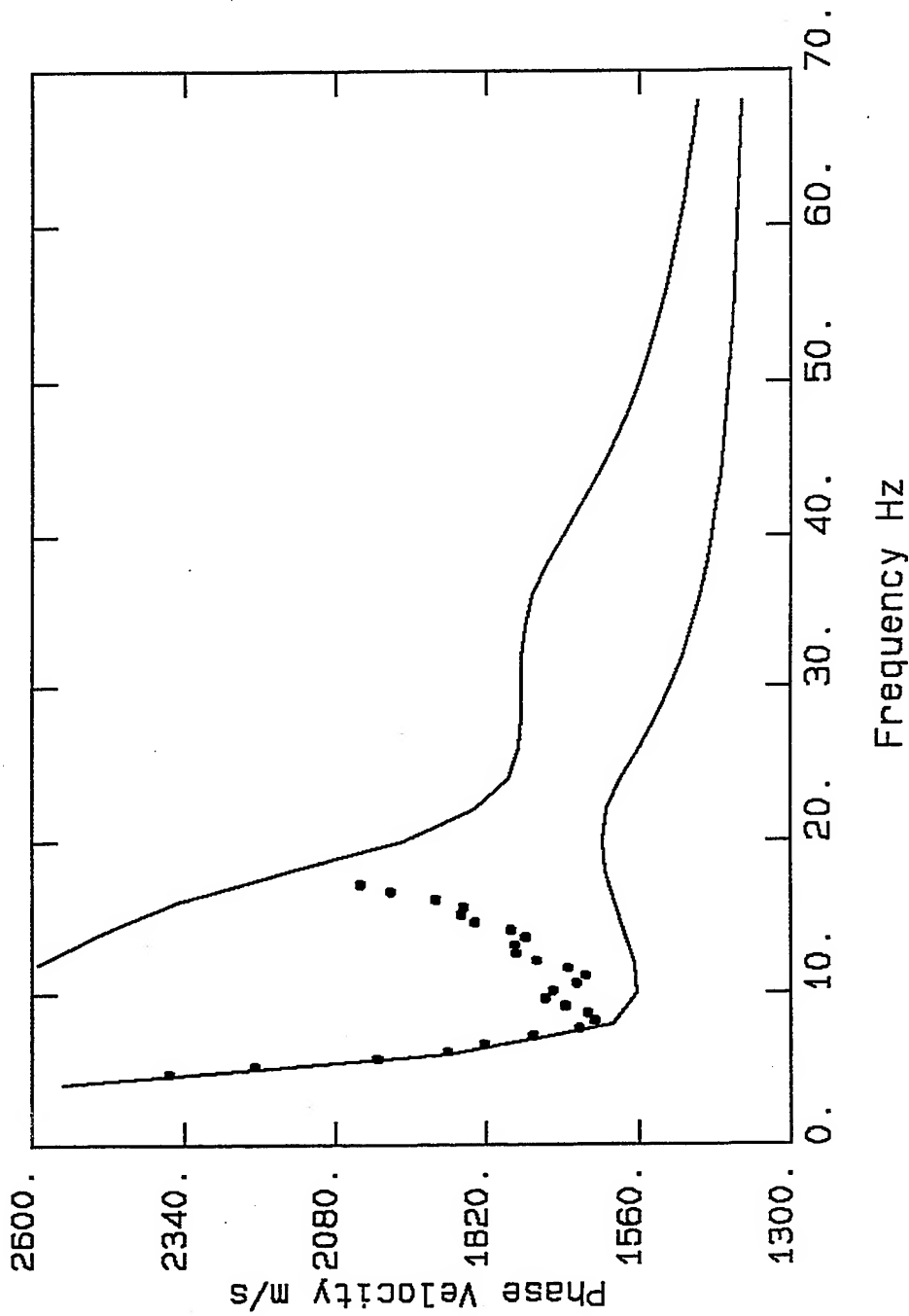


Figure 6.2. Plots of the simulated phase velocities of the first two modes of Rayleigh waves and the calculated phase velocities from the analysis of the circular array data. There are strong disagreement between the results beyond about 10 Hz. This suggests that the high frequency microtremors are dominated by the higher modes of Rayleigh waves and can not be interpreted in terms of only the first mode.



VortexRock Consultants, Inc.

## References

Aki, K., 1957. *Space and time spectra of stationary stochastic waves, with special reference to microtremors*, Bull. Earthq. Res., Inst. Tokyo Univ., 25, 415-457.

Aki, K., 1965. *A note on the use of microseisms in determining the shallow structure of the Earth's crust*, Geophysics 30, 665-666.

Andrews, D.J., 1986. *Objective determination of source parameters and seismicity of earthquakes of different size*, in *Earthquake Source Mechanics*, S. Das, J. Boatwright, and C. H. Scholz (Editors), American Geophys. Union, Washington, D.C., 259-268.

Applied Technology Council, 1978. *Tentative Provisions for the Development of Seismic Regulations for Buildings*, ATC 3-06, National Bureau of Standards, Washington, D.C.

Araya, R., and G. R. Saragoni, 1985. *Earthquake accelerogram destructiveness potential factor*, *Proceedings of the Eight World Conference on Earthquake Engineering*, pp. 835-842, Earthquake Engineering Research Institute, San Francisco, California.

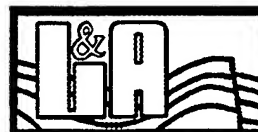
Asten, M.W., and J.D. Henstridge, 1984. *Array estimator and use of microseisms for reconnaissance of sedimentary basins*, Geophysics, 49(11), 1828-1837.

Boatwright, J., 1988. *The seismic radiation from composite models of faulting*, Bull. Seism. Soc. Am. 78, 489-508.

Bolt, B. A., 1973. *Duration of earthquake shaking*, *Fifth World Conference on Earthquake Engineering*, Rome.

Boore, D. M., 1983. *Stochastic simulation of high-frequency ground motions based on seismological models of the radiated spectra*, Bull. Seism. Soc. Am. 73, 1865-1894.

Boore, D. M., and W. B. Joyner, 1984. *A note on the use of random vibration theory to predict peak amplitudes of transient signals*, Bull. Seism. Soc. Am. 74, 2035-2039.



Boore, D. M., L. Seekins, and W. B. Joyner 1989. Peak acceleration form the 17 October 1989 Loma Prieta earthquake, *Seism. Res. Lett.* 60, 151-166.

Boore, D. M., and W. B. Joyner, 1994. Prediction of ground motion in north America, ATC 35-1, *Proceedings of Seminar on New Developments in Earthquake Ground Motion Estimation and Implications for Engineering Design Practice.*

Borcherdt, R.D., 1970. Effects of local geology on ground motion near San Francisco Bay, *Bull. Seism. Soc. Am.*, 60, 29-61.

Borcherdt, R.D., G. Glassmoyer, A. Der Kiureghian, and E. Cranswick, 1989. Results and data from Seismologic and geologic studies following earthquakes of December 7, 1988 near Spitak, Armenia, S.S.R., U.S. Geol. Surv. Open-File Report, 89-163A.

Borcherdt, R.D., G. Glassmoyer, 1992. On the characteristics of local geology and their influence on ground motions generated by the Loma Prieta earthquake in the San Francisco Bay region, California, *Bull. Seis. Soc. Am.*, 82, 603-641.

Borcherdt, R.D., 1994. New developments in estimating site effects on ground motion, ATC 35-1, *Proceedings of Seminar on New Developments in Earthquake Ground Motion Estimation and Implications for Engineering Design Practice.*

Bracewell, R.N., 1978. *The Fourier transform and its applications*, McGraw-Hill New York.

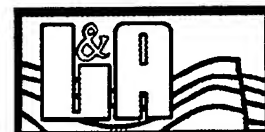
Brune, J.N., 1970. Tectonic stress and the spectra of seismic shear waves from earthquakes, *J. Geophys. Res.*, 75, 4997-5009.

Brune, J.N., 1971. Correction, *J. Geophys. Res.*, 76, 5002.

Capon, J., 1969. High-resolution frequency-wave number spectrum analysis, *proc. IEEE*, 57, 1408-1418.

Cartwright, D.E., and M.S. Longuet-Higgins, 1956. The statistical distribution of maximum of a random function, *Proc. Royal Stat. Soc.*, Vol 237, 212-232.

Celebi, M., C. Dietel, J. Prince, M. Onate and G. Chavez, 1987. Site amplification in Mexico City (determined from 19 September 1985 strong-motion records and



from recordings of weak motions), *Ground Motion and Eng. Seis*, ed. A.S. Cakmak, 141-152, Elsevier.

Chang, C-Y., C. M. Mok, M. S. Power, Y. K. Tank, H. T. Tang, and J. C. Stepp 1990. Equivalent linear versus nonlinear ground response analyses at Lotung Seismic Experiment Site, in *Proc. 4th U.S. Natl. Conf. Earthquake Eng.*, 327-336.

Chin, B.H. and K. Aki, 1991. Simulation study of the source, path, and site effects on strong ground motion during the 1989 Loma Prieta earthquake: a preliminary result on pervasive nonlinear site effects, *Bull. Seism. Soc. Am.* 81, 1859-1884.

Darragh, R. B. and A. F. Shakal 1991a. The site response of two rock and soil station pairs to strong and weak ground motion, in *Proc. 4th Intl. Conf. Seism Zonation*, Vol 3, 359-366.

Darragh, R. B. and A. F. Shakal 1991b. The site response of two rock and soil station pairs to strong and weak ground motion, *Bull. Seism. Soc. Am.* 81, 1885-1899.

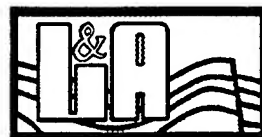
Dobry, R., I. M. Idriss, and E. Ng, 1978. Duration Characteristics of Horizontal Components of Strong Motion Earthquake Records, *Bulletin of the Seismological Society of America*, 68 (5) 1487-1520.

Dravinski, M., H. Yamanaka, H. Kagami, 1992. Site amplification through measurement of long period microtremors: predominant period of motion, *Earthquake Eng. Tenth World Conf. Balkema*, Rotterdam.

Dunkin, J.W., 1965. Computation of modal solutions in layered elastic media at high frequencies, *Bull. Seis. Soc. Am.*, 55, 335-358.

Earthquake Engineering Research Center, 1994. Preliminary report on the seismological and engineering aspects of the January 17, 1994 Northridge earthquake, UCB/EERC Report No. 94/01.

Everden, J. F., and J. M. Thomson, 1988. Predictive model for important ground motion parameters associated with large and great earthquakes, *US Geological Survey Bull.* 1838.



Ferrazzini, V., K. Aki, and B. Chouet, 1991. *Characteristics of seismic waves composing Hawaiian volcanic tremor and gas-piston events observed by a near-source array*, *J. Geophys. Res.*, 96, 6199-6209.

Field, E.H., S.H. Hough, and K.H. Jacob, 1990. *Using microtremors to assess potential earthquake site response: A case study in Flushing Meadow, New York City*, *Bull. Seis. Soc. Am.*, 80, 1456-1480.

Field, E.H., K.H. Jacob, and S.H. Hough, 1992. *Earthquake site response estimation: a weak-motion case study*, *Bull. Seis. Soc. Am.*, 82, 2283-2307.

Field, E.H., and K. Jacob, 1993. *The theoretical response of sedimentary layers to ambient seismic noise*, *Geophysical Res. Letters*, 20-24, 2925-2928.

Field, E.H., 1994. *Earthquake site response estimation*, Ph.D. Thesis, Columbia University, N.Y., N.Y..

Field, E.H., A.C. Clement, K.H. Jacob, V. Aharonian, S.E. Hough, P.A. Friberg, T.O. Babiab, S.S. Karapetian, S.M. Hovanessian, and H.A. Abramian, 1994. *Earthquake site response in Giumri (formerly Leninakan), Armenia using ambient noise observations*, *Bull. Seis. Soc. Am.*

Hanks, T. C., and R. K. McGuire, 1981. *The character of high-frequency strong ground motion*, *Bull. Seism. Soc. Am.* 71, 2071-2095.

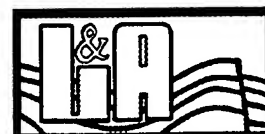
Hanks, T. C., and D. M. Boore, 1984. *Moment-magnitude relations in theory and practice*, *J. Geophys. Res.* 89, 6229-6235.

Hartzell, S.H., 1978. *Earthquake aftershocks as Green's functions*, *Geophys. Res. Letter*, 5, 1-4.

Harkrider, D.G., 1964. *Surface waves in multilayered elastic media I. Rayleigh and Love waves from buried sources in a multilayered elastic half-space.*, *Bull. Seis. Soc. Am.*, 54, 627-679.

Haskell, N.A., 1953. *The dispersion of surface waves on multilayered media*, *Bull. Seis. Soc. Am.*, 43, 17-34.

Horike, M., 1985. *The dispersion of surface waves on multilayered media*, *Bull. seis. Soc. Am.*, 43, 17-34.





Hossain, M.M., and V.P. Drnevich, 1989. Numerical and optimization techniques applied to surface waves for back calculation of layer moduli, *Nondestructive Testing of Pavements and Back calculation of Moduli*, ASTM STP 1026, A.J. Bush and G.Y. Baldi, Eds., Am. Soc. of Testing and materials, Philadelphia, 649-669.

Hough, S.E., L. Seeber, A. Rovell, L. Malagnini, A. DeCesare, G. Selveggi, and A. Lerner-Lam, 1992. Ambient noise and weak-motion excitation of sediment resonance: Results from the Tiber valley, Italy, *Bull. Seis. Soc. Am.*, 82, 1186-1205.

Housner, G. W., 1956. Limit design of structures to resist earthquake, *Proceedings of the First World Conference on Earthquake Engineering*, pp. 5-1 to 5-13, Berkeley, California.

Husid, R. L., 1969. Analisis de terremotos: Analisis general, *Revista del IDIEM*, 8, 21-42, Santiago, Chile.

Hryciw, R.D., K.M. Rollins, M. Homolka, S.E. Shewbridge and M. McHood, 1991. Soil amplification at Treasure Island during the Loma Prieta earthquake, *Proc., 2nd Inter. Conf. on Recent Advances in Geotech. Earthquake Engineering and Soil Dynamics*, St. Louis, Missouri, 2, 1679-1685.

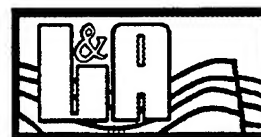
Idriss, I.M., 1990. Response of soft soil sites during earthquakes, *Proc. H. Bolton Seed Memorial Symposium*, Berkeley, California, 2.

Jarpe, S. P., C. H. Cramer, B. E. Tucker, and A. F. Shakal 1988. A comparison of observations of ground response to weak and strong ground motion at Coalinga, California, *Bull. Seism. Soc. Am* 78, 421-435.

Jarpe, S. P., L. J. Hutchings, T. F. Hauk, and A. F. Shakal 1989. Selection strong- and weak-motion data from the Loma Prieta earthquake sequence, *Seism. res. Lett.* 60, 167-176.

Joyner, W. B., and D. M. Boore, 1981. Peak horizontal acceleration and velocity from strong-motion records including records from the 1979 Imperial Valley, California, earthquake, *Bull. Seism. Soc. Am.* 71, 2011-2038.

Joyner, W. B., 1984. A scaling law for the spectra of large earthquakes, *Bull. Seism. Soc. Am.* 74, 1167-1188.



Kagami, H., C. M. Duke, G. C. Liang, and Y. Ohta, 1982. Observation of 1 to 5-second microtremors and their application to earthquake engineering. Part II. Evaluation of site effects upon seismic wave amplification due to extremely deep soil deposits, *Bull., Seism. Soc.* 72, 987-998.

Kanai, K., 1957. The requisite conditions for predominant vibration of ground, *Bull. Earthquake Res. Inst., Tokyo Univ.* 35, 457.

Kanai, K. and T. Tanka, 1961. On microtremors, VIII., *Bull. Earthquake Res. Inst., Tokyo Univ.* 39, 97-115.

Kanamori, H., 1977. The energy release in great earthquakes, *J. Geophys. Res.*, 82, 2981-2987.

Kanamori, H., 1978. Use of seismic radiation to infer source parameters, *Proceedings of Conference IV: Fault mechanics and its relation to earthquake prediction, USGS Open File Report 78-380*, 283-318.

Knopoff, L., 1958. Energy release in earthquakes, *Geophys. J. Roy. Astron. Soc.*, 1, 44-52.

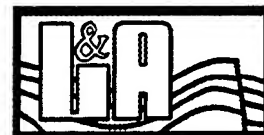
Knopoff, L., 1964. A matrix method for elastic wave problems, *Bull. Seis. Soc. Am.*, 54, 431-438.

Lachet, C. and P.Y. Bard, 1994. Numerical and theoretical investigations on the possibilities and limitations of the Nakamura's technique, *Journal of Physics of the Earth*, accepted.

Lacos, R.T., E. J. Kelly, and M.N. Toksoz, 1969. Estimation of seismic noise structure using array, *Geophysics*, 34: 21-38.

Lay, T. and H. Kanamori 1981. An asperity model of great earthquake sequence in *Earthquake Prediction-An International Review*, Maurice Ewing Series, vol. 4, D. Simpson and P. G. Richards, Editors, American Geophysical Union, Washington, D.C., 579-592.

Malagnini, L., A. Rovelli, S.E. Hough, and L. Seeber, 1993. Site amplification estimates in the Garigliano valley, central Italy, based on dense array measurements of ambient noise, *Bull. Seis. Soc. Am.*, 83, 1744-1755.



Mayeda, K., F. Su and K. Aki, 1991. Site amplification from S-wave coda in the Long Valley Caldera region, California *Bull. Seism. Soc. Am.*

Mohamadian, B. and A. Pecker, 1984. Low-frequency transfer of seismic energy by superficial soil deposit and soft rocks, *Earthquake Eng. Struct. Dynamics* 12, 537-564.

Nakamura, Y., 1989. A method for dynamic characteristics estimation of subsurface using microtremor on the ground surface, *QR of R.T.R.* 30-1.

Nazarian, S., 1984. In situ determination of elastic moduli of soil deposits and pavement systems by spectral-analysis-of-surface-waves method, Ph.D. Dissertation, University of Texas, Austin, Texas.

Ohta, Y.H., H. Kagami, N. Goto, and K. Kudo, 1978. observation of 1- to 5-second microtremors and their application to earthquake engineering. Part I. Comparison with long-period accelerations at the Tokachi-Oki earthquake of 1968, *Bull. Seism. Soc. Am.*, 68, 767-779.

Okada, H. and T. Matsushima, 1986. Estimation of underground structures down to a depth more than several hundreds of meters using long period microtremors, *Proc. 7th Japan Earthquake Eng. Sym.*, 211-216.

Omachi, T., Y. Nakamura, and T. Toshinawa, 1991. Ground motion characteristics in the San Francisco Bay area detected by microtremor measurements, *Proceedings of the Second International Conference on Recent Advances in Geotechnical Earthquake Engineering and Dynamics*, March 11-15, St. Louis, Missouri, 1643-1648.

Papageorgiou, A.S. and K. Aki, 1983a. A specific barrier model for the quantitative description of inhomogeneous faulting and the prediction of strong motion, Part I description of the model, *Bull. Seism. Soc. Am.* 73, 693-722.

Papageorgiou, A.S. and K. Aki, 1983b. A specific barrier model for the quantitative description of inhomogeneous faulting and the prediction of strong motion, Part II applications of the model, *Bull. Seism. Soc. Am.* 73, 953-978.

Phillips, W.S. and K. Aki, 1986. Site amplification of coda waves from local earthquake in central California, *Bull. Seism. Soc. Am.* 76, 627-648.



*Satoh, T., 1989. On the controlled source spectra of Rayleigh wave excitation and measurement system, VIC, Tokyo.*

*Satoh, T., K. Yamagata, C.J. Poran, J.A. Rodriguez, 1991. Soil profiling by spectral analysis of surface waves, Proc. second Inter. Conf. on Recent Advances in Geotechnical earthquake Engineering and Soil Dynamics.*

*Seed, H.B. and I.M. Idriss, 1969. The influence of soil conditions on ground motions during earthquake, J. Soil Mech. Found. Eng. Div., ASCE, No. 94, 93-137.*

*Seed, H. B., I. M. Idriss, and H. Dezfulian, 1970. Relationship between soil conditions and building damage in Caracas earthquake of July 29, 1967, Report No. UCB/EERC-70/2, Earthquake Engineering Research Center, University of California, Berkeley.*

*Seed, H. B., and J. I. Sun, 1989. Implication of site effects in the Mexico City earthquake of Sept. 19, 1985 for earthquake-resistant criteria in the San Francisco Bay area of California, Report No. UCB/EERC-89/03, Earthquake Engineering Research Center, University of California, Berkeley.*

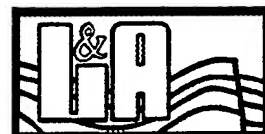
*Seed, H. B. 1988. Discussion on non-linearity, presented at Conf. Earthquake Eng. Soil Dyn. II, Utah.*

*Singh, S.K., J. Lermo, T. Dominguez, M. Ordaz, J.M. Espinosa, E. Mena, R. Quass, 1988. The Mexico earthquake of September 19, 1985--A study of amplification of seismic waves in the valley of Mexico with respect to a hill zone site. Earthquake Spectra, 4, 653-673.*

*Steidl, J.H., 1993. Variation of site response at the UCSB dense array of portable accelerometers, Earthquake Spectra, 9, 289-302.*

*Sue, F., K. Aki, T. Teng, Y. Zeng, S. Koyanagi and K. Mayeda, 1992. The relation between site amplification factor and surfacial geology in central California, Bull. Seism. Soc. Am. 82, 580-602.*

*Theodulidis, N., R.J. Archuleta, P.Y. Bard, and M. Bouchon, 1994. Horizontal to vertical spectral ratio and geological conditions: the case of Garner valley downhole array in southern California, in preparation.*



Thomson, W.T., 1950. *Transmission of elastic waves through a stratified soil medium*, J. Appl. Physics, 21, 89-93.

Tokimatsu, K., Shinzawa, K., and Kuwayama, S., 1992. *Use of short period microtremors for  $s$  profiling*, Journal of Geotech. Eng., ASCE, 118(10), 1544-1558.

Trifunac, M. D., and A. G. Brady, 1975. *A Study on the Duration of Strong Earthquake Ground Motion*, Seismology Society of America Bulletin, Vol. 65, pp. 581-645.

Thrower, E.N., 1965. *The computation of dispersion of elastic waves in layered media*, J. Sound and Vibration, Academic Press, London, 2, 210-226.

Uang, C.-M and V. V. Bertero, 1988. *Implication of recorded earthquake ground motions on seismic design of building structures*, Report No. UCB/EERC-88/13, Earthquake Engineering Research Center, University of California, Berkeley.

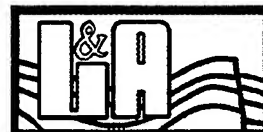
Udwadia, F.E. and M.D. Trifunac, 1973. *Comparison of earthquake and microtremor ground motions in El Centro, California*.

Verttos, C., 1990. *In-plane vibrations of soil deposits with variable shear modulus: I. Surface waves.*, Int. J. Numer. Anal. Methods Geomech.

Verttos, C. and B. Prange, 1990. *Evaluation of in-situ effective shear modulus from dispersion measurements*, ASCE, J. of Geotech. Engrg., 116, 1581-1585,.

VIC Report, 1993. *Shear wave velocity profiling on instrumented sites in the greater Los Angeles area using surface waves measurements*, Vibration Instruments Company, Tokyo, Japan.

Watson, T.H., 1970. *A note on fast computation of Rayleigh waves dispersion in layered elastic half space*, Bull. Seis. Soc. Am., 60, 1761-1766.

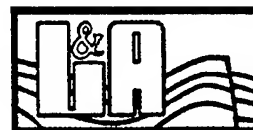


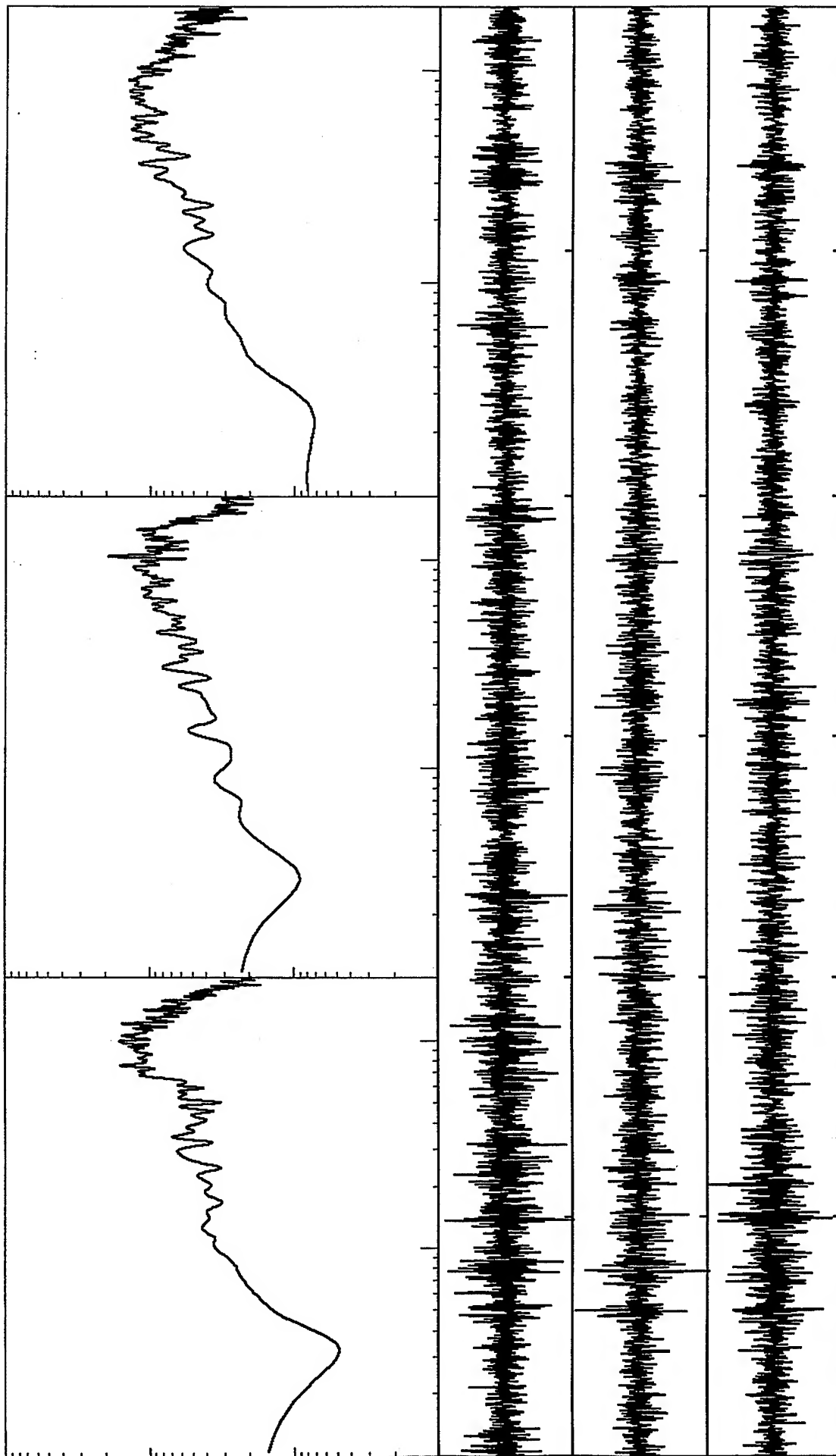
## ***Appendix A Section I***

***Time Histories and Spectral Parameters for Selected  
Records from Experiments 1 & 2 at the Parking Lot of the  
St. Aidams Episcopal Church, Malibu, California***



***VortexRock Consultants, Inc.***

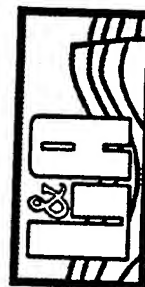


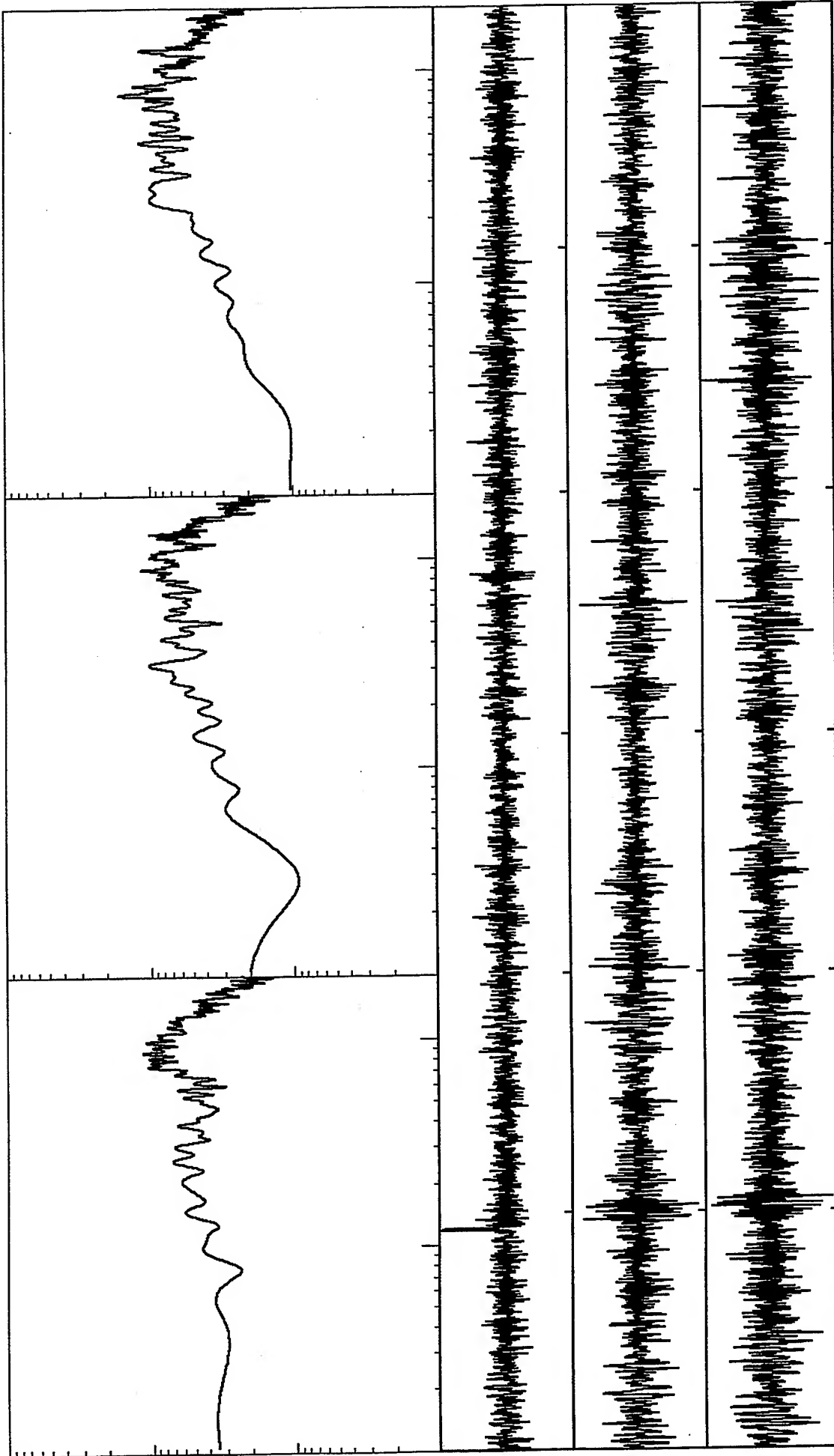


Spectral velocity values 0.1 to 20 Hz. Range: 1.E-6 to 1.E-3 cm/s  
 From top: ch1, 2, & 3: Max values of .322, .407, and .367 1.E-3 cm/s  
 Station 2: 60 s time window

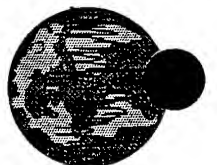


*VortexRock Consultants, Inc.*

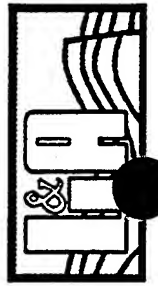




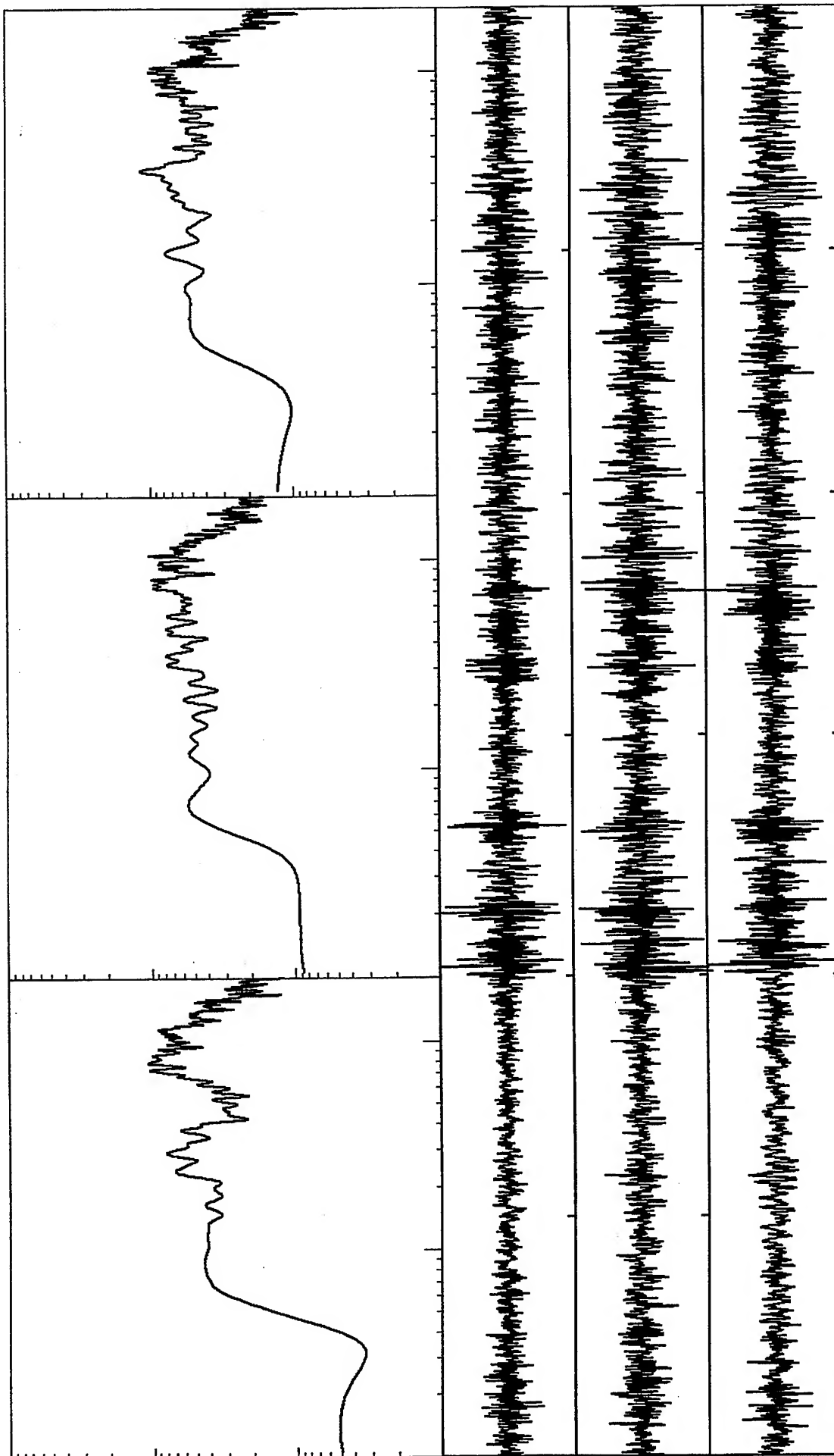
Spectral velocity values 0.1 to 20 Hz. Range: 1.E-6 to 1.E-3 cm/s  
 From top: ch1, 2, & 3: Max values of .351, .291, and .230 1.E-3 cm/s  
 Station 2: 60 s time window



*VortexRock Consultants, Inc.*



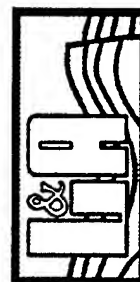


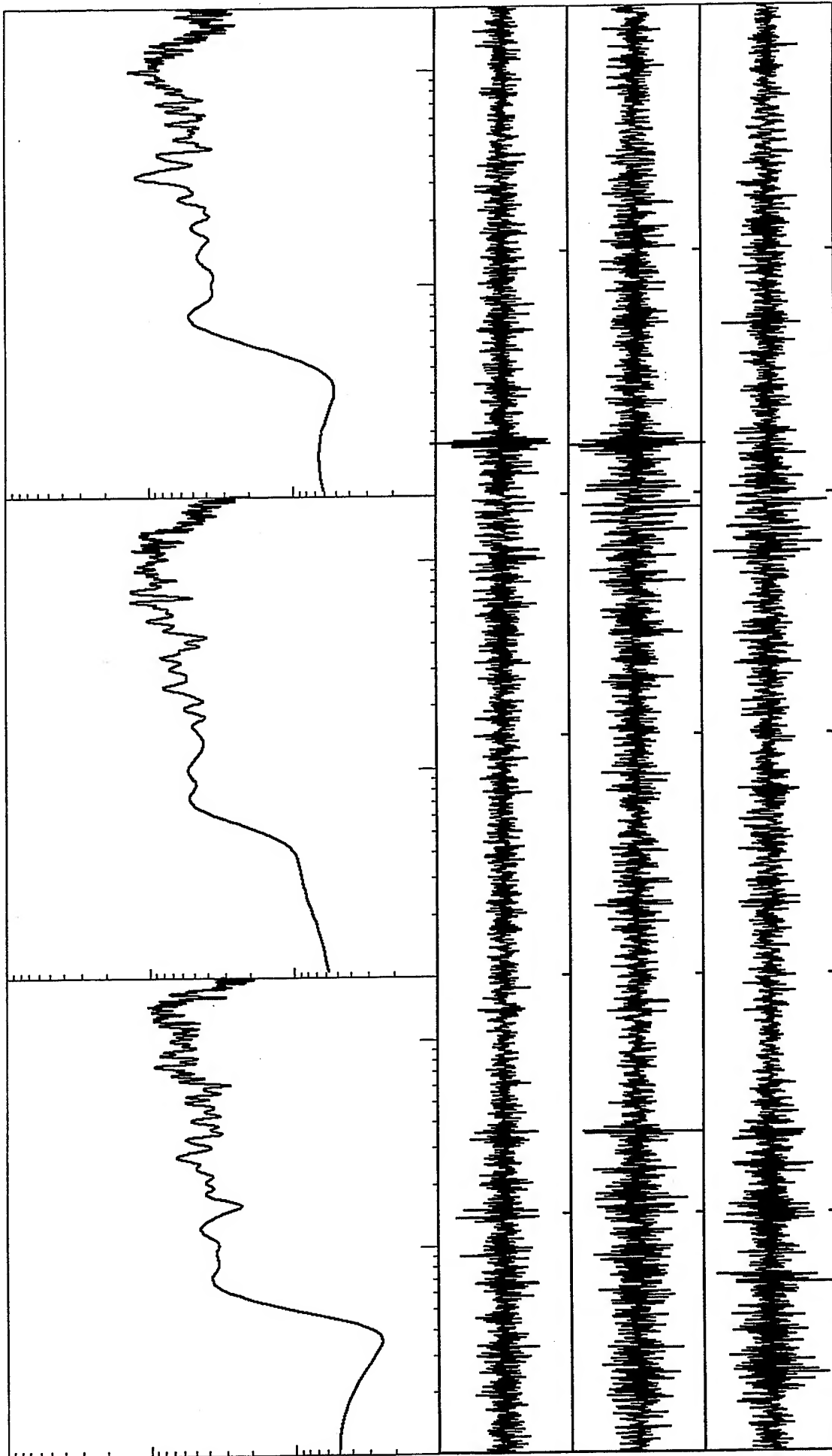


Spectral velocity values 0.1 to 20 Hz. Range: 1.E-6 to 1.E-3 cm/s  
 From top: ch1, 2, & 3: Max values of .261, .205, and .234 1.E-3 cm/s  
 Station 1: 60 s time window

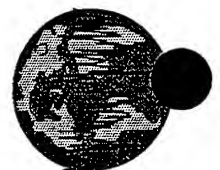


*VortexRock Consultants, Inc.*

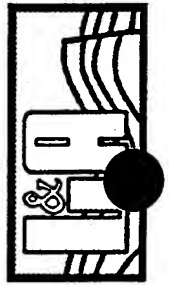


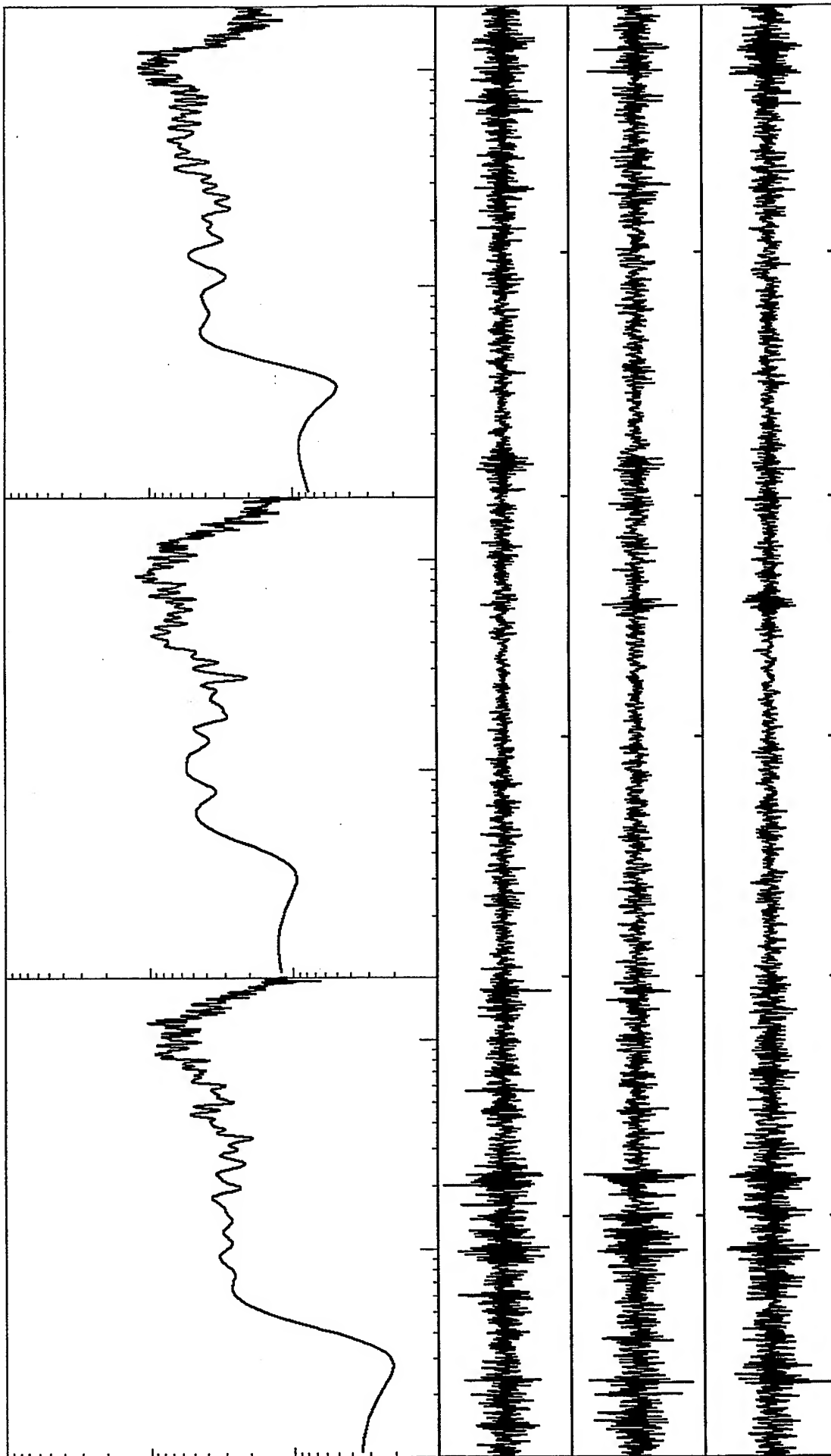


Spectral velocity values 0.1 to 20 Hz. Range: 1.E-6 to 1.E-3 cm/s  
 From top: ch1, 2, & 3: Max values of .330, .301, and .324 1.E-3 cm/s  
 Station 2: 60 s time window



*VortexRock Consultants, Inc.*

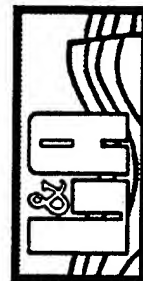


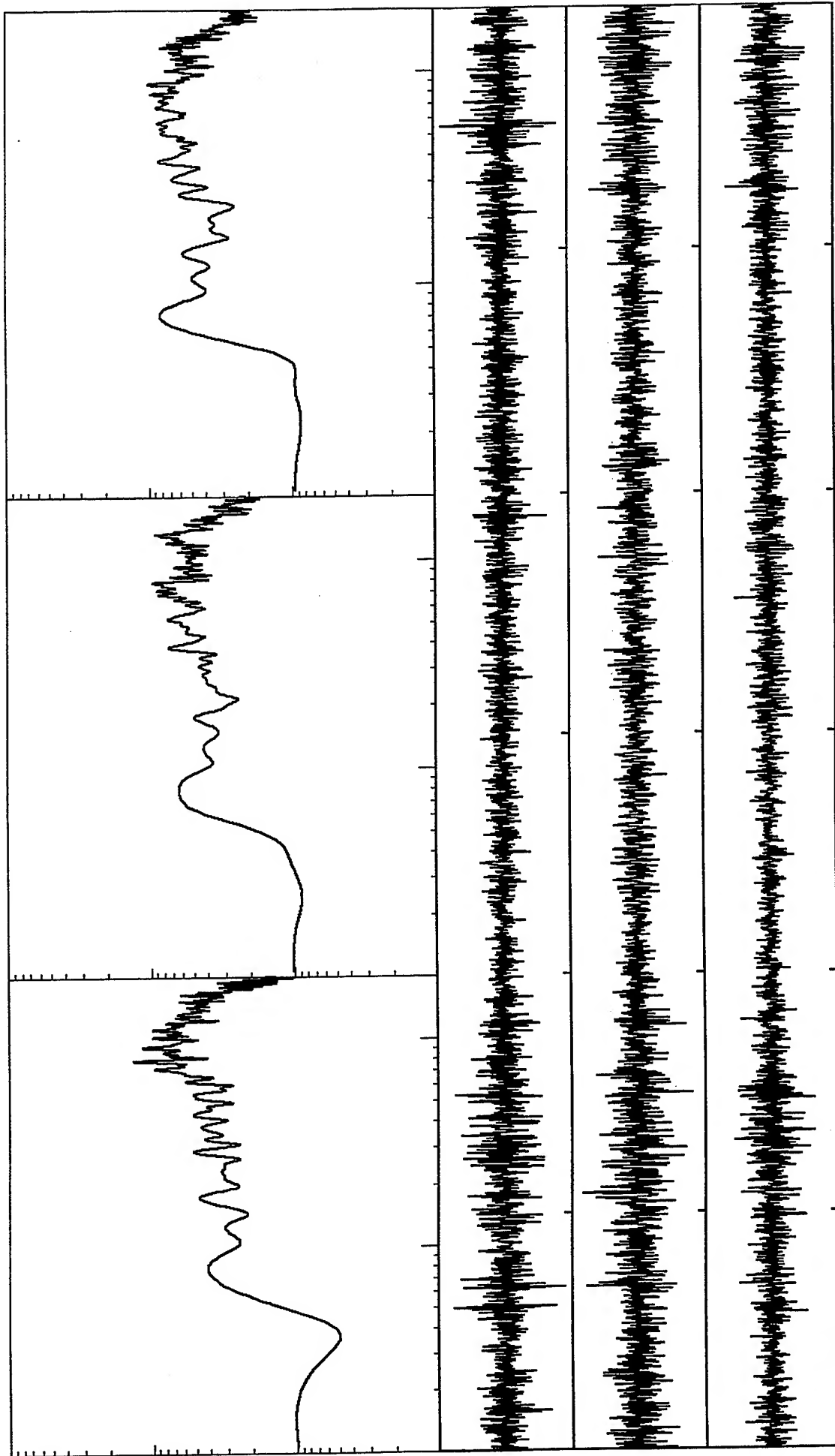


Spectral velocity values 0.1 to 20 Hz. Range: 1.E-6 to 1.E-3 cm/s  
 From top: ch1, 2, & 3: Max values of .270, .332, and .325 1.E-3 cm/s  
 Station 2: 60 s time window



*VortexRock Consultants, Inc.*

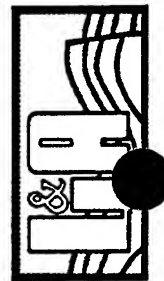


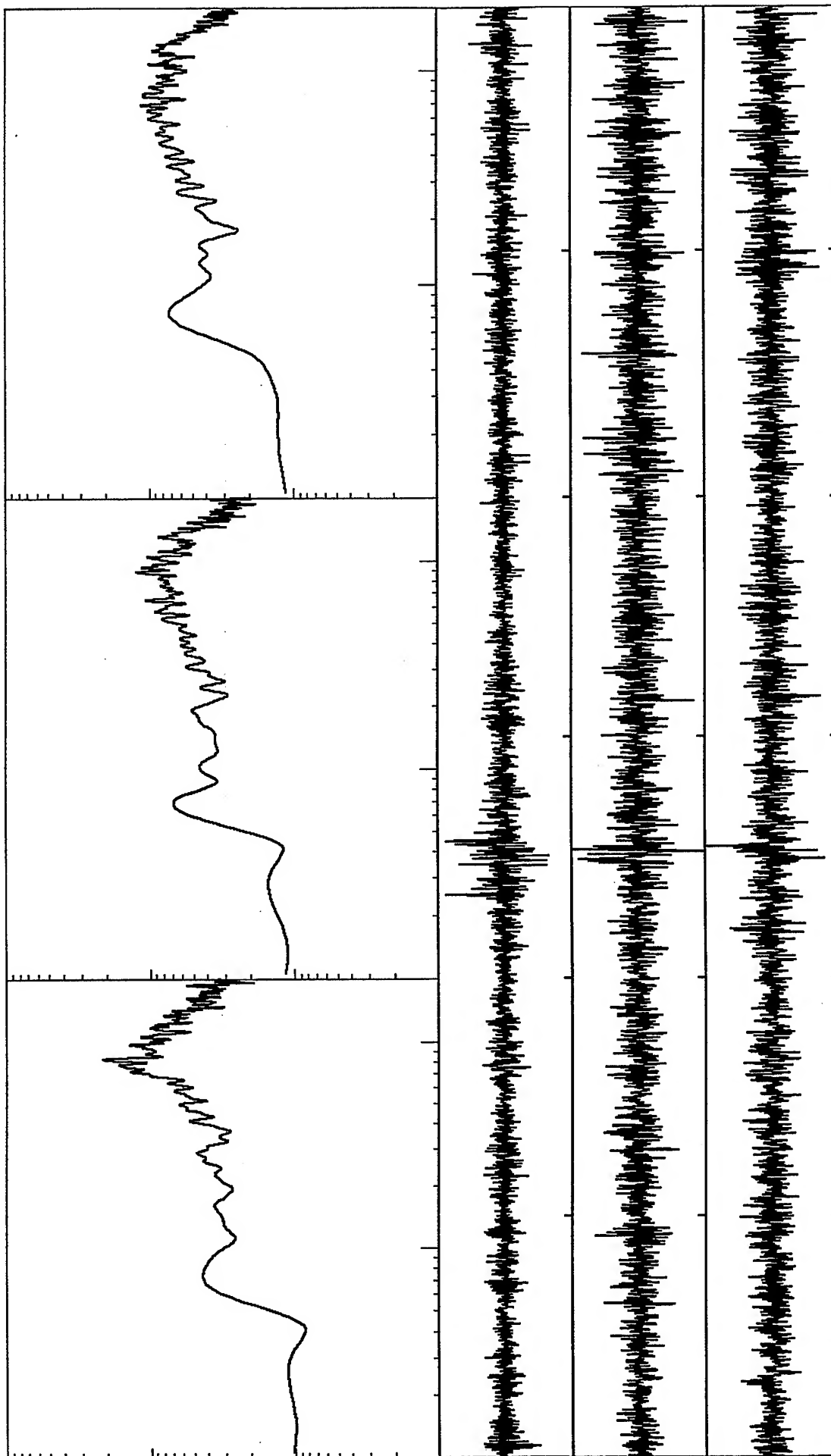


Spectral velocity values 0.1 to 20 Hz. Range: 1.E-6 to 1.E-3 cm/s  
 From top: ch1, 2, & 3: Max values of .282, .270, and .339 1.E-3 cm/s  
 Station 2: 60 s time window



*VortexRock Consultants, Inc.*

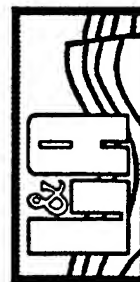


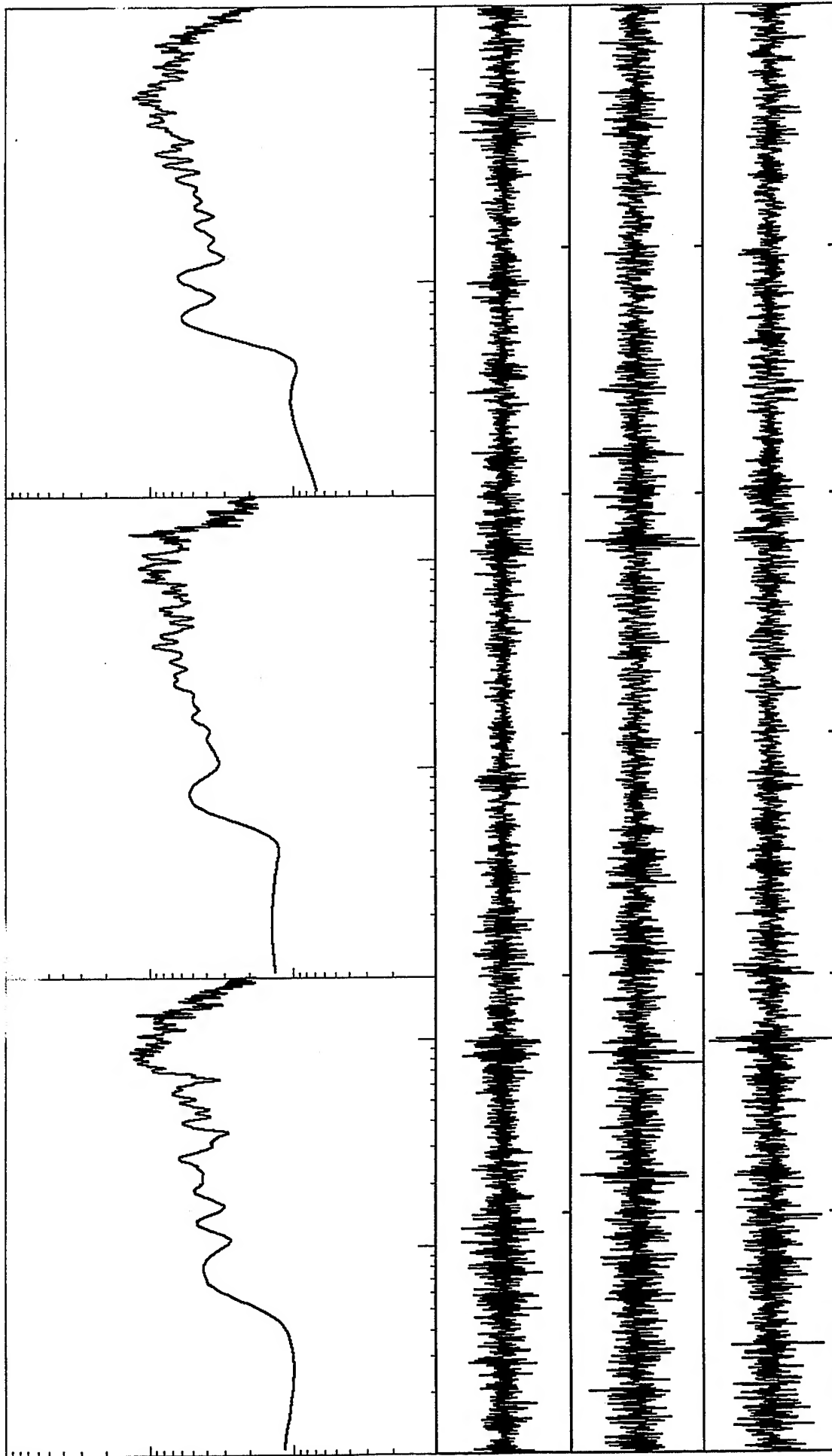


Spectral velocity values 0.1 to 20 Hz. Range: 1.E-6 to 1.E-3 cm/s  
 From top: ch1, 2, & 3: Max values of .543, .301, and .327 1.E-3 cm/s  
 Station 2: 60 s time window



*VortexRock Consultants, Inc.*

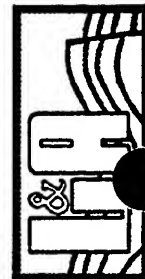


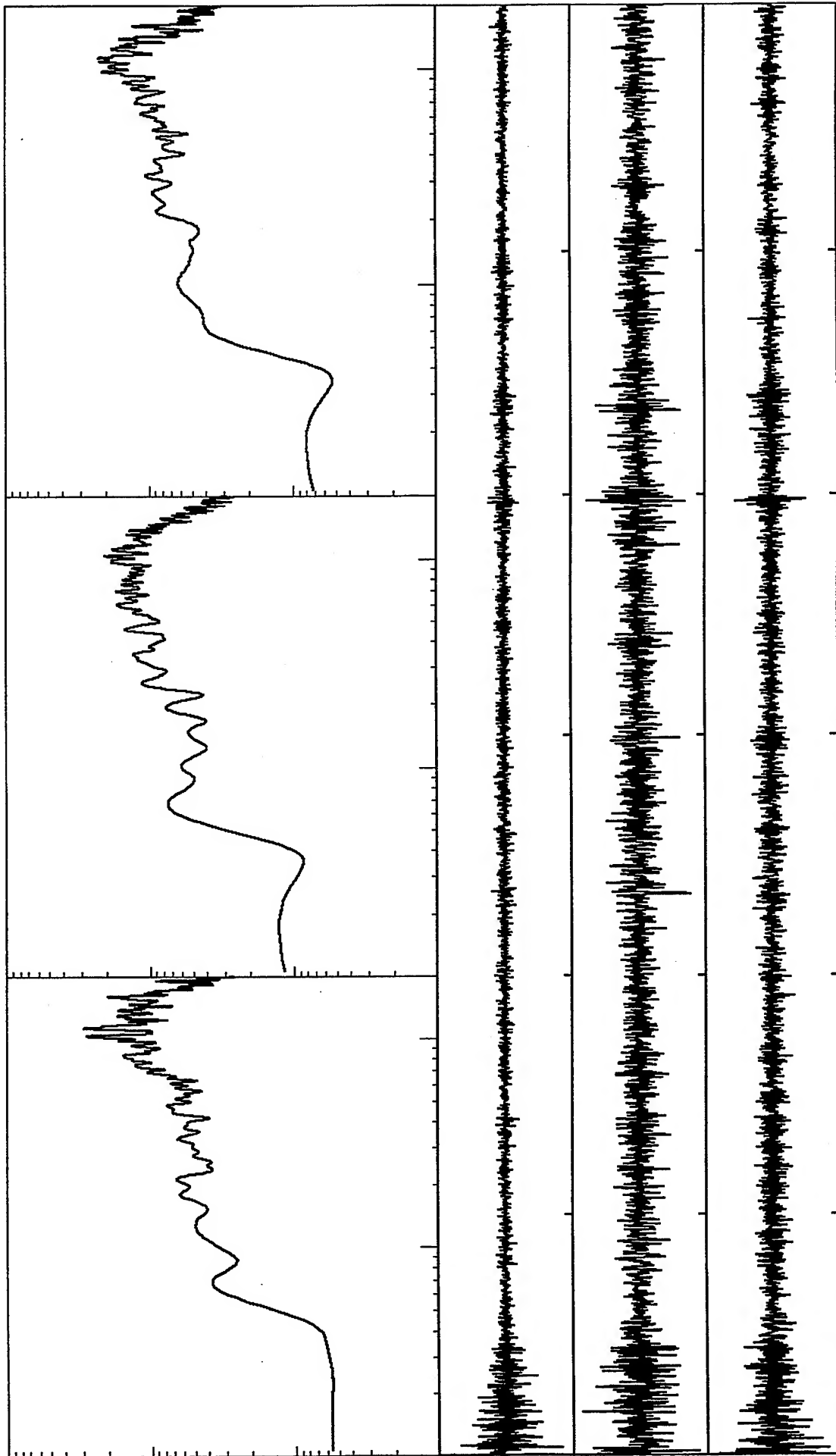


Spectral velocity values 0.1 to 20 Hz. Range: 1.E-6 to 1.E-3 cm/s  
 From top: ch1, 2, & 3: Max values of .379, .301, and .334 1.E-3 cm/s  
 Station 2: 60 s time window



*VortexRock Consultants, Inc.*

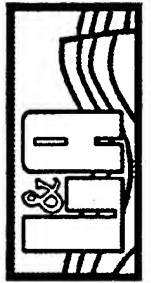


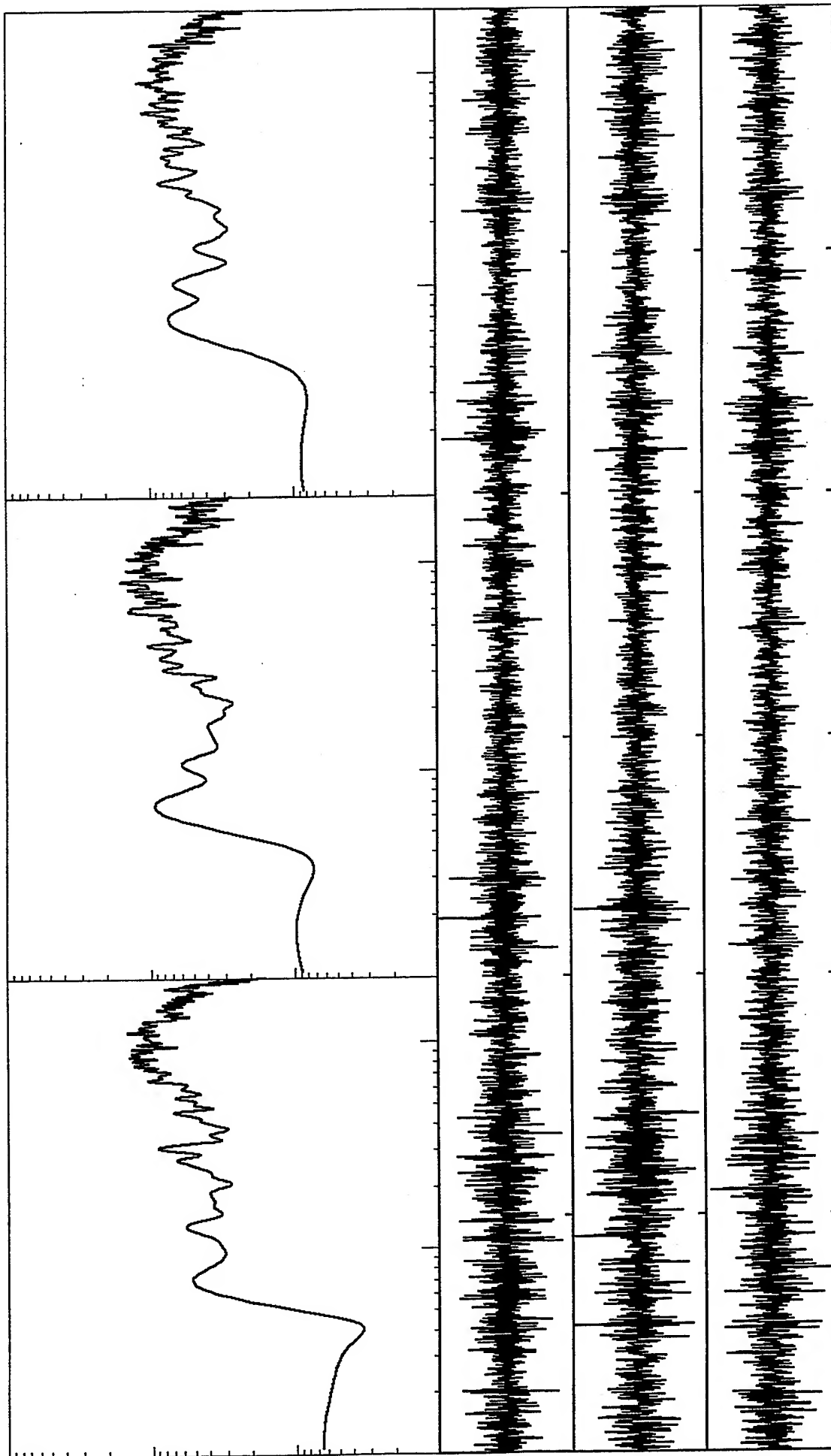


Spectral velocity values 0.1 to 20 Hz. Range: 1.E-6 to 1.E-3 cm/s  
 From top: ch1, 2, & 3: Max values of .128, .053, and .084 1.E-2 cm/s  
 Station 2: 60 s time window



*VortexRock Consultants, Inc.*

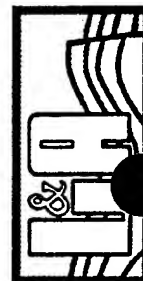




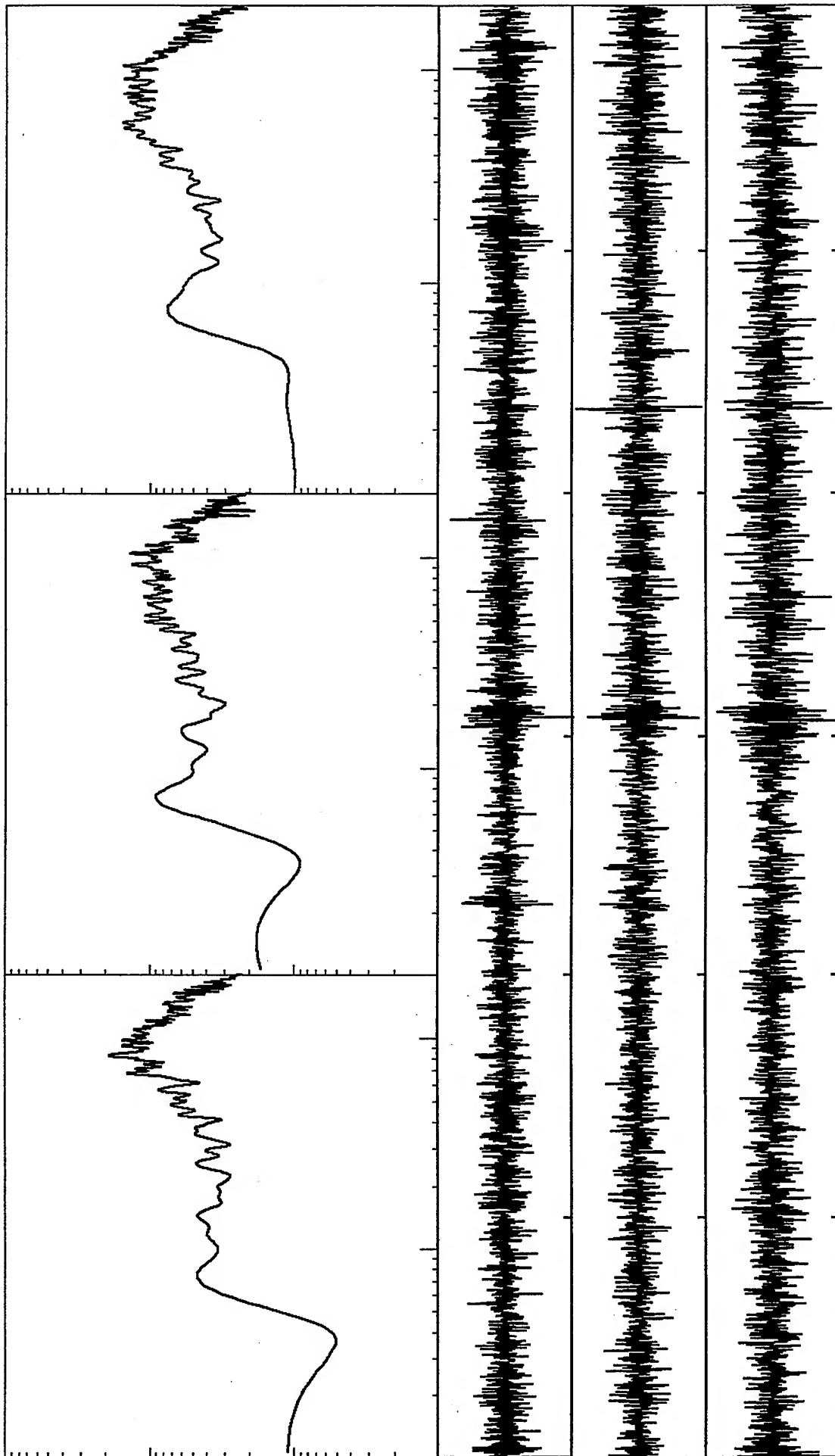
Spectral velocity values 0.1 to 20 Hz. Range: 1.E-6 to 1.E-3 cm/s  
 From top: ch1, 2, & 3: Max values of .332, .318, and .287 1.E-3 cm/s  
 Station 1: 60 s time window



*VortexRock Consultants, Inc.*



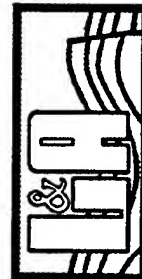


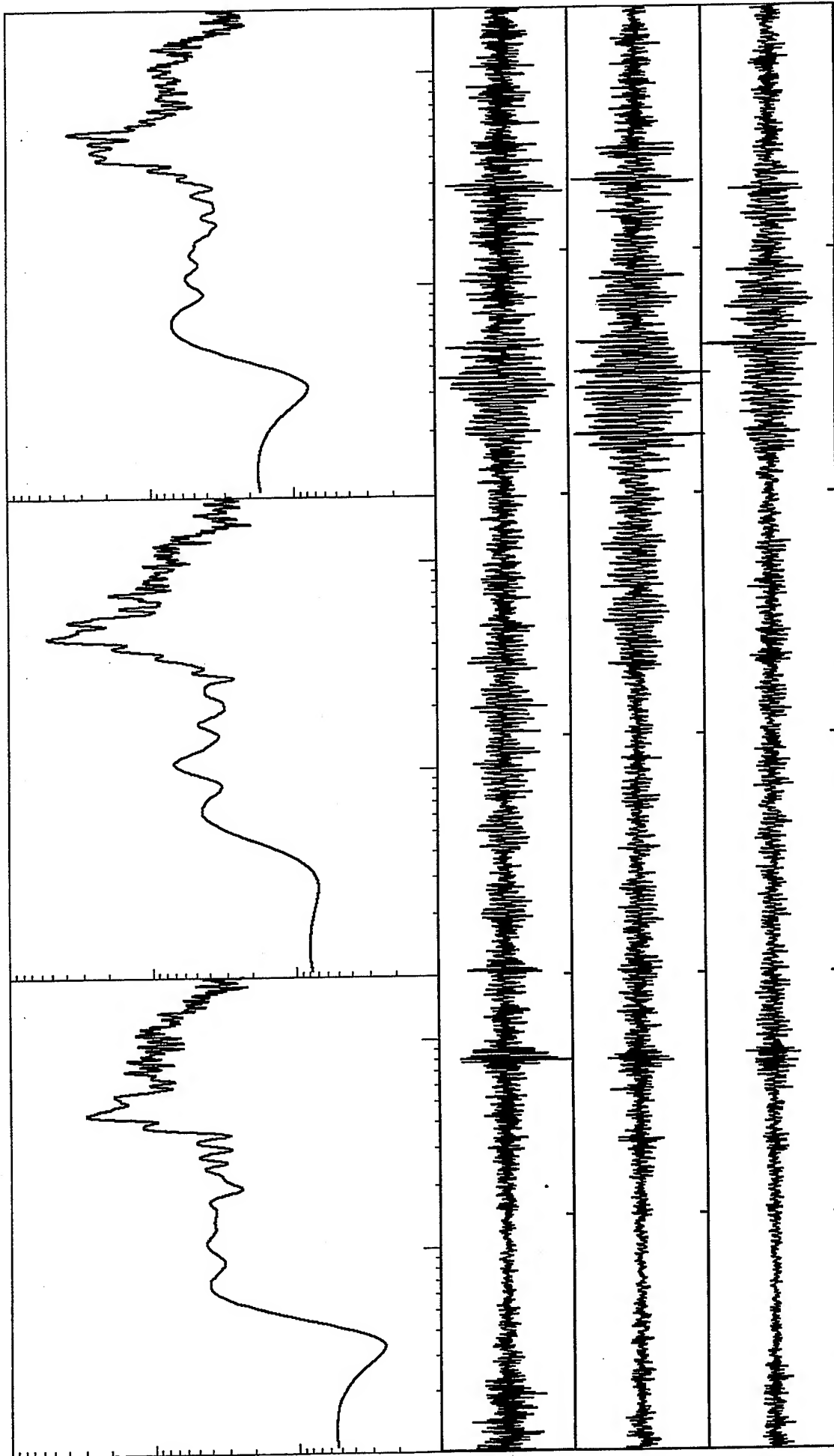


Spectral velocity values 0.1 to 20 Hz. Range: 1.E-6 to 1.E-3 cm/s  
 From top: ch1, 2, & 3: Max values of .346, .368, and .274 1.E-3 cm/s  
 Station 1: 60 s time window

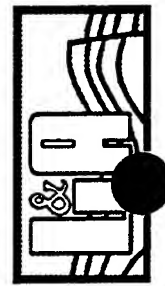


*VortexRock Consultants, Inc.*

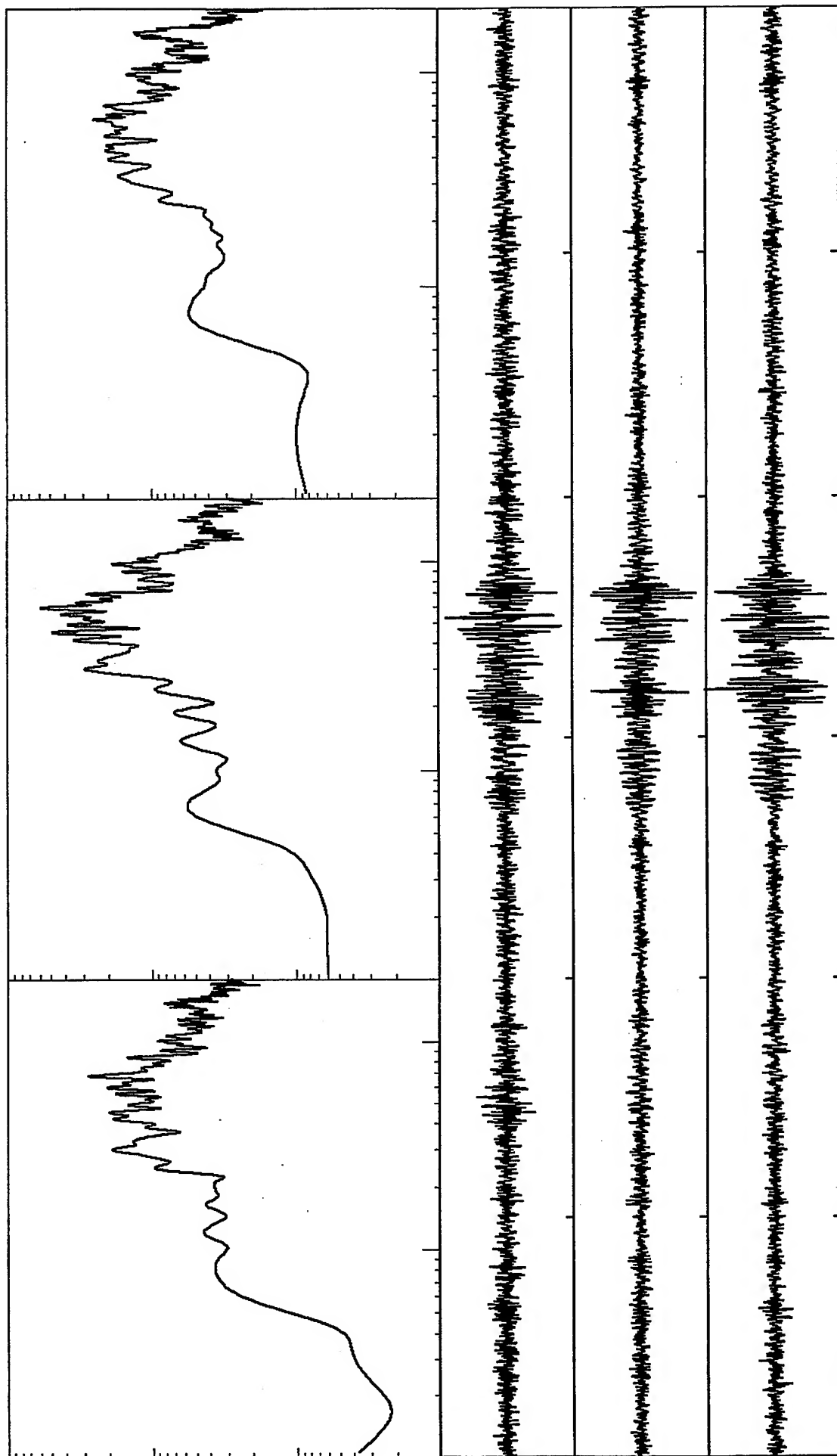




Spectral velocity values 0.1 to 20 Hz. Range: 1.E-6 to 1.E-3 cm/s  
 From top: ch1, 2, & 3: Max values of .413, .501, and .568 1.E-3 cm/s  
 Station 1: 60 s time window



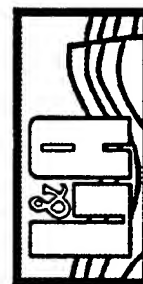
*VortexRock Consultants, Inc.*

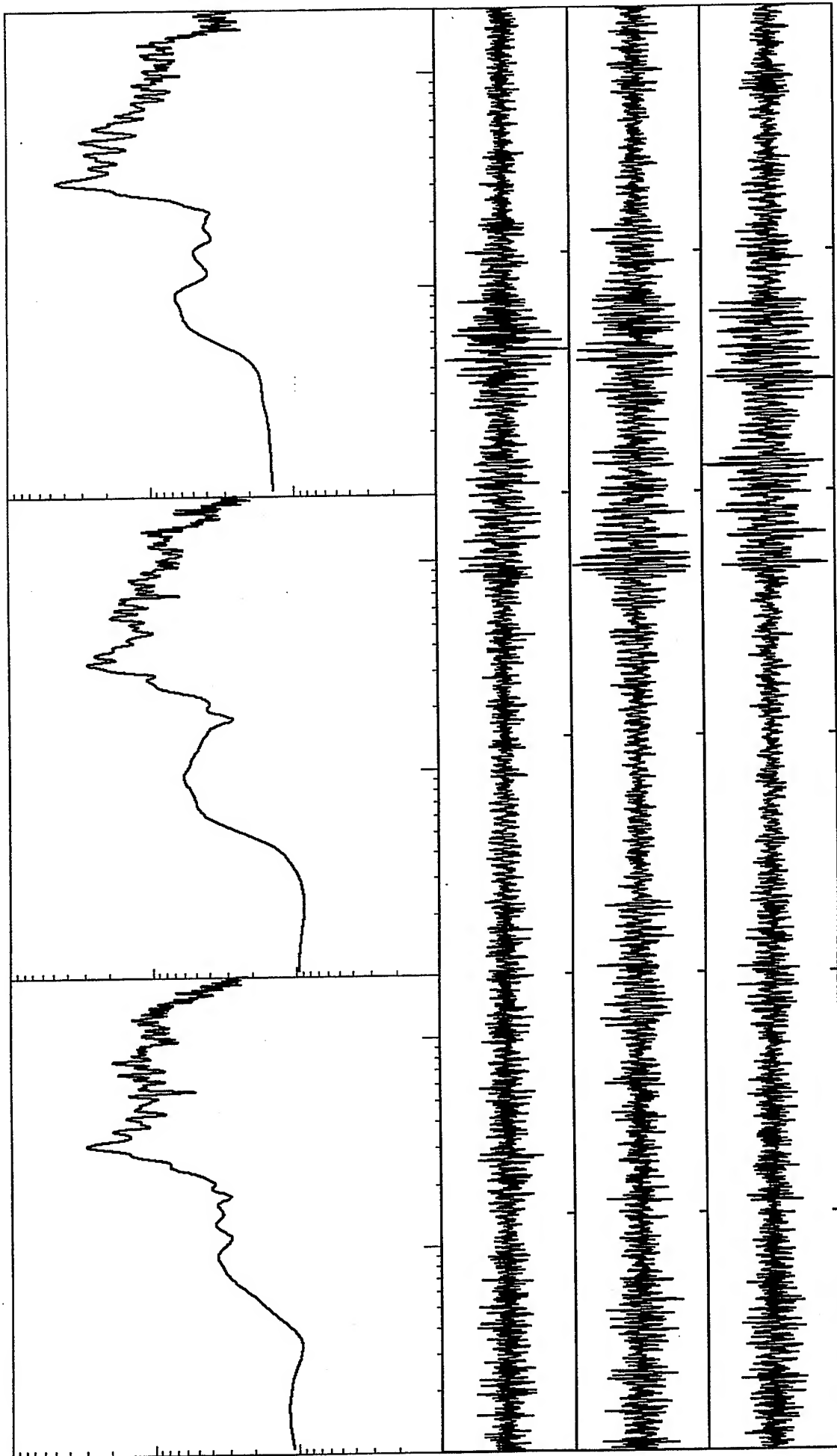


Spectral velocity values 0.1 to 20 Hz. Range: 1.E-6 to 1.E-3 cm/s  
 From top: ch1, 2, & 3: Max values of .060, .104, and .082 1.E-2 cm/s  
 Station 2: 60 s time window



*VortexRock Consultants, Inc.*

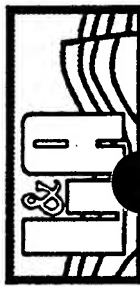


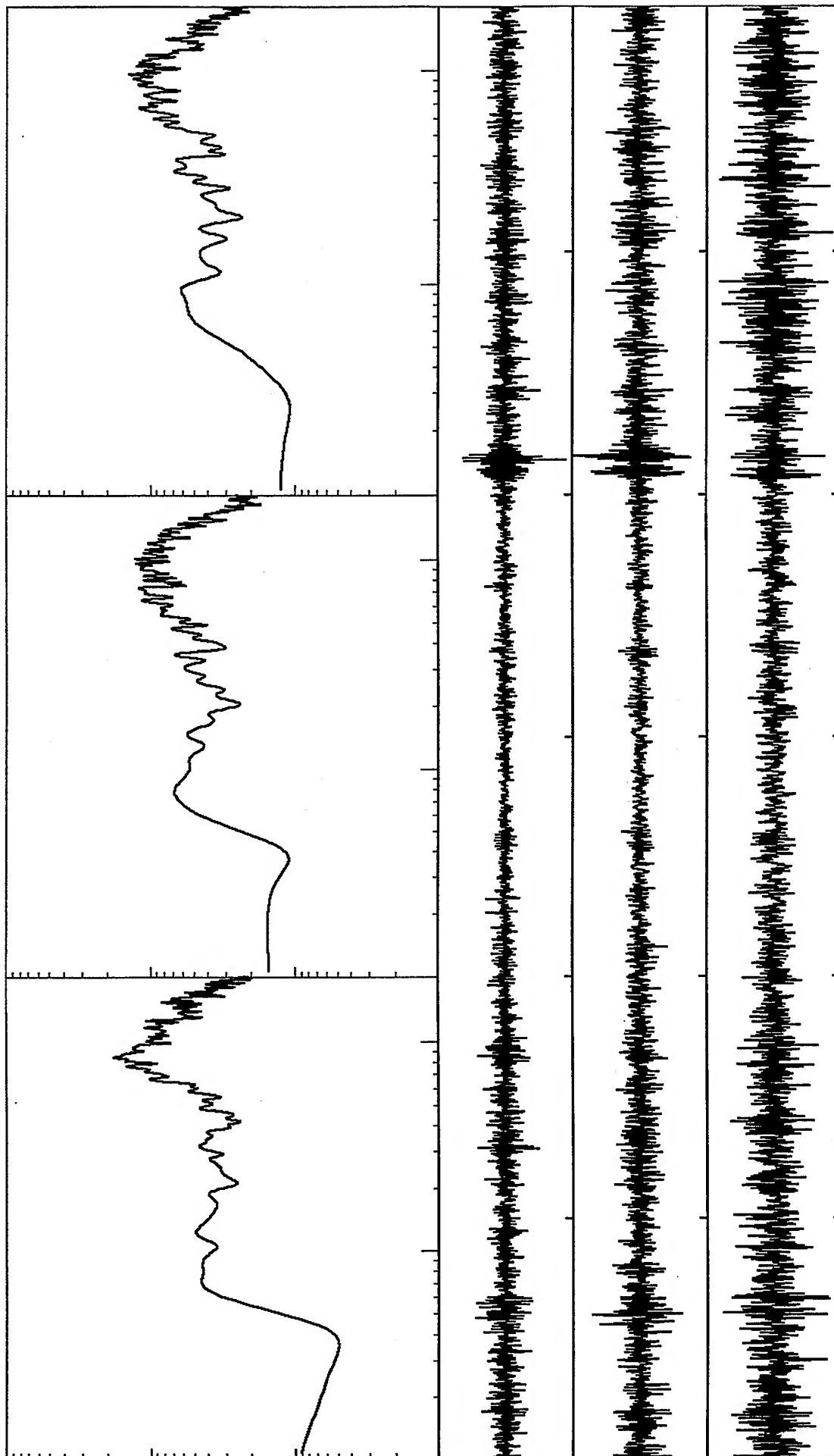


Spectral velocity values 0.1 to 20 Hz. Range: 1.E-6 to 1.E-3 cm/s  
 From top: ch1, 2, & 3: Max values of .531, .511, and .453 1.E-3 cm/s  
 Station 1: 60 s time window



*VortexRock Consultants, Inc.*



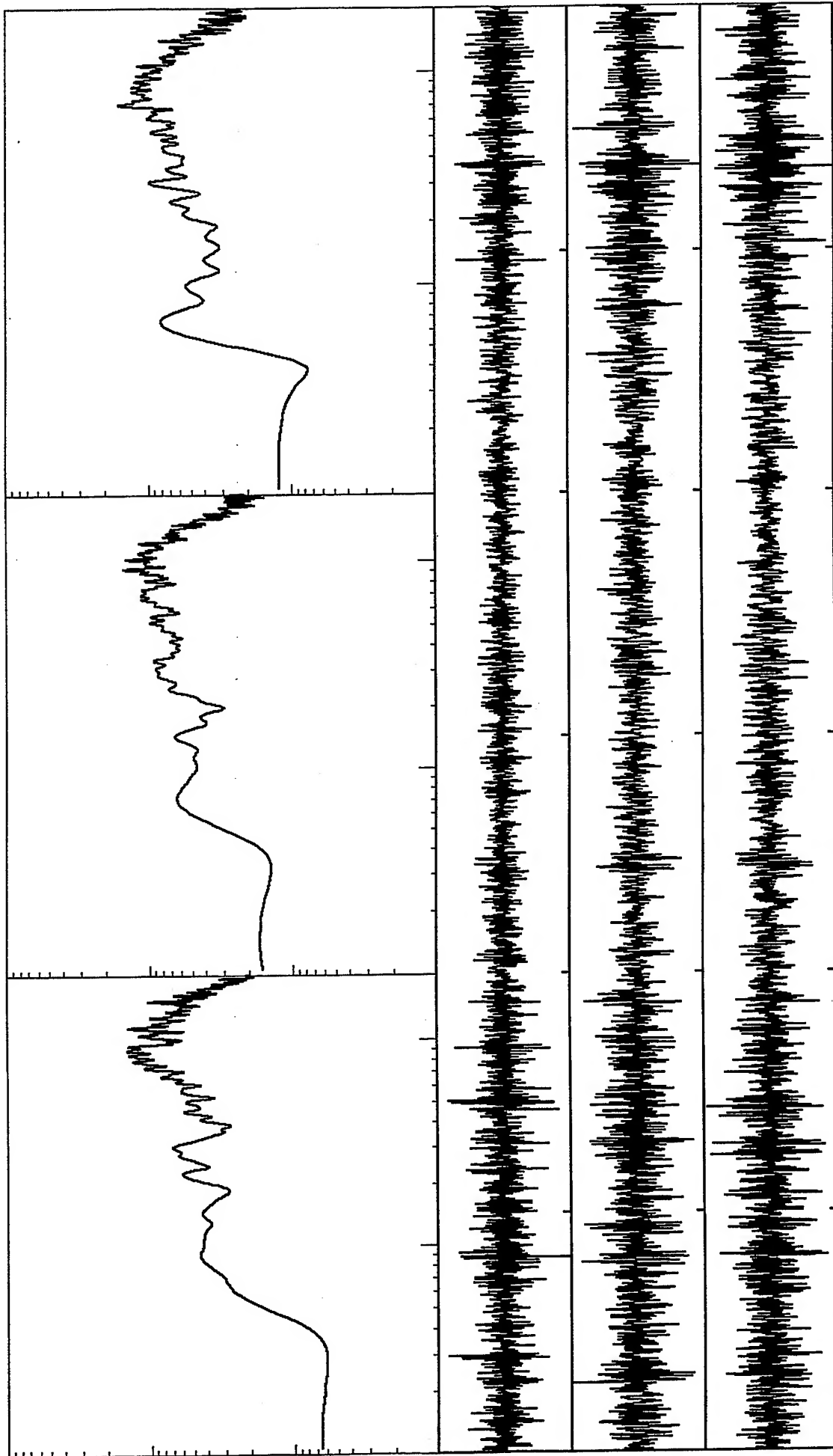


Spectral velocity values 0.1 to 20 Hz. Range: 1.E-6 to 1.E-3 cm/s  
 From top: ch1, 2, & 3: Max values of .575, .479, and .252 1.E-3 cm/s  
 Station 1: 60 s time window



*VortexRock Consultants, Inc.*

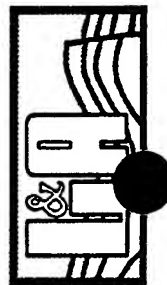


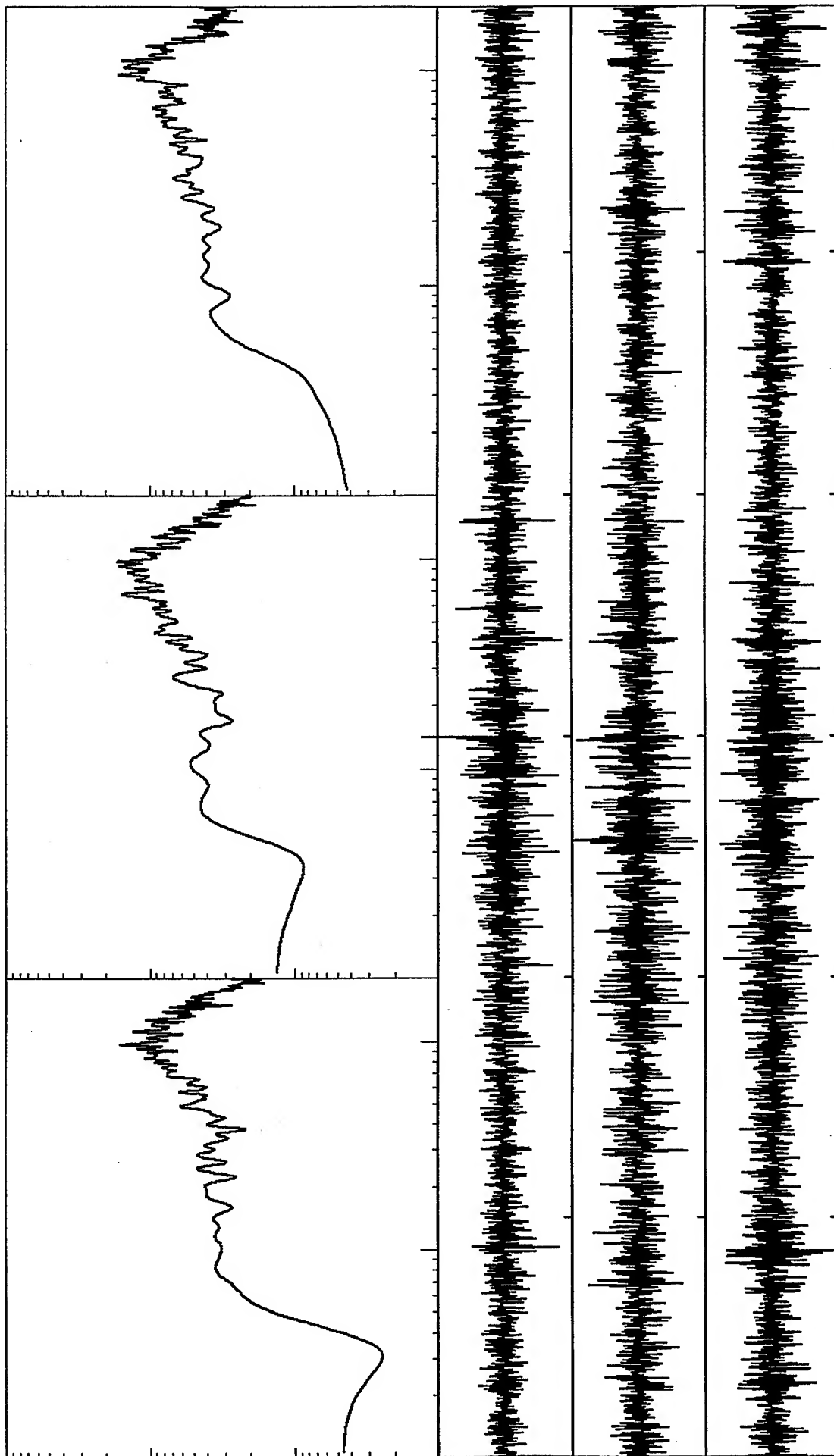


Spectral velocity values 0.1 to 20 Hz. Range: 1.E-6 to 1.E-3 cm/s  
 From top: ch1, 2, & 3: Max values of .339, .307, and .248 1.E-3 cm/s  
 Station 1: 60 s time window



*VortexRock Consultants, Inc.*

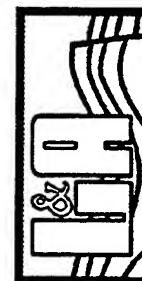




Spectral velocity values 0.1 to 20 Hz. Range: 1.E-6 to 1.E-3 cm/s  
 From top: ch1, 2, & 3: Max values of .302, .309, and .284 1.E-3 cm/s  
 Station 2: 60 s time window



*VortexRock Consultants, Inc.*



***Appendix A  
Section II***

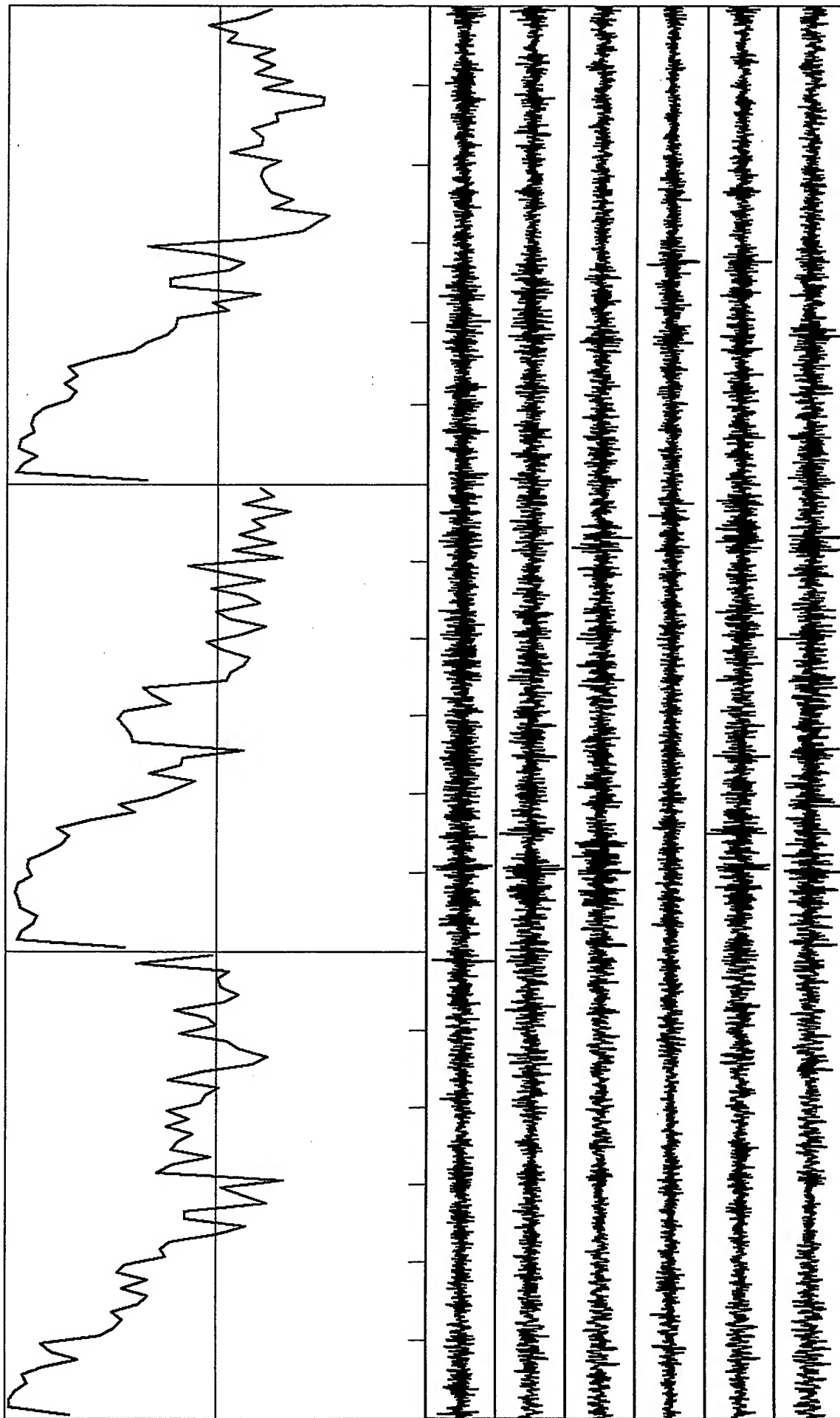
***The Correlation Coefficients for Selected Records from  
Experiments 1 & 2 at the Parking Lot of the St. Aidams  
Episcopal Church, Malibu, California***



***VortexRock Consultants, Inc.***



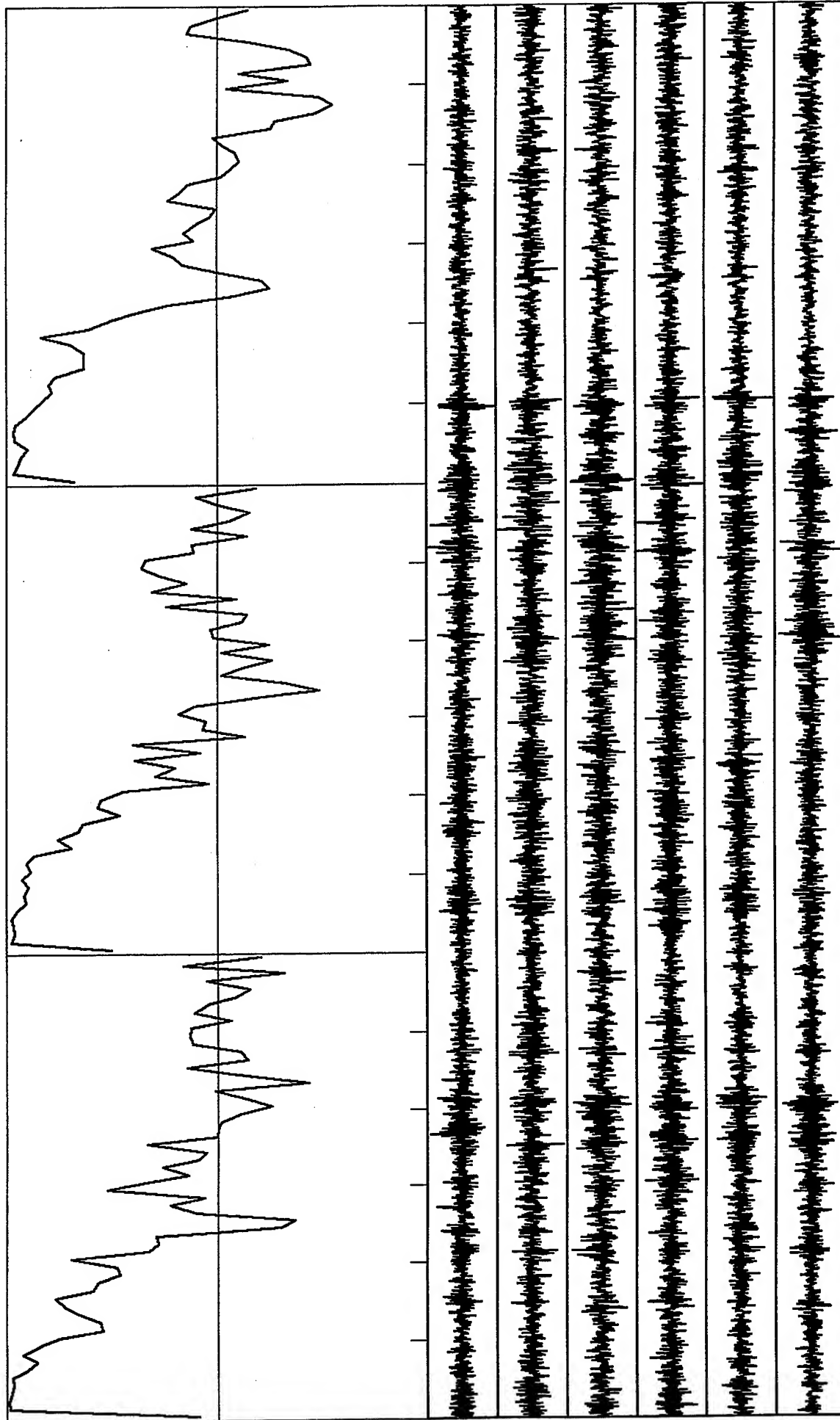




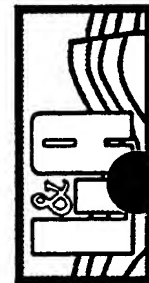
Correlation Coefficients: Scale -1 to +1; freq range: 0 to 30.0 Hz; Radius: 15 m  
 St. 1 & 2: Vertical & horizontal components: 60 s time window



*VortexRock Consultants, Inc.*

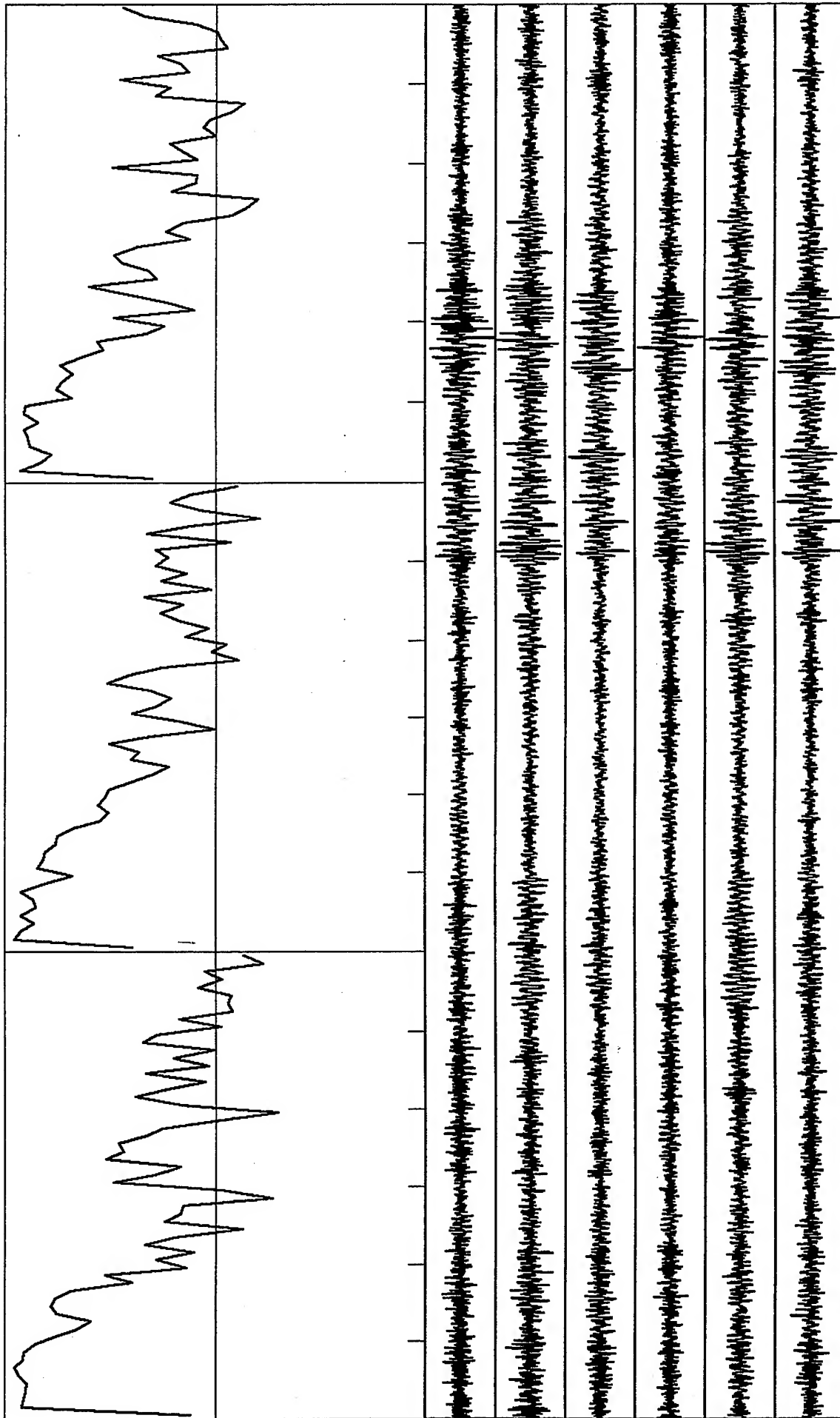


Correlation Coefficients: Scale -1 to +1; freq range: 0 to 30.0 Hz; Radius: 15 m  
 St. 1 & 2: Vertical & horizontal components; 60 s time window



*VortexRock Consultants, Inc.*



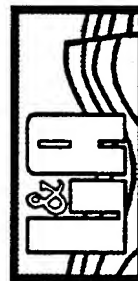


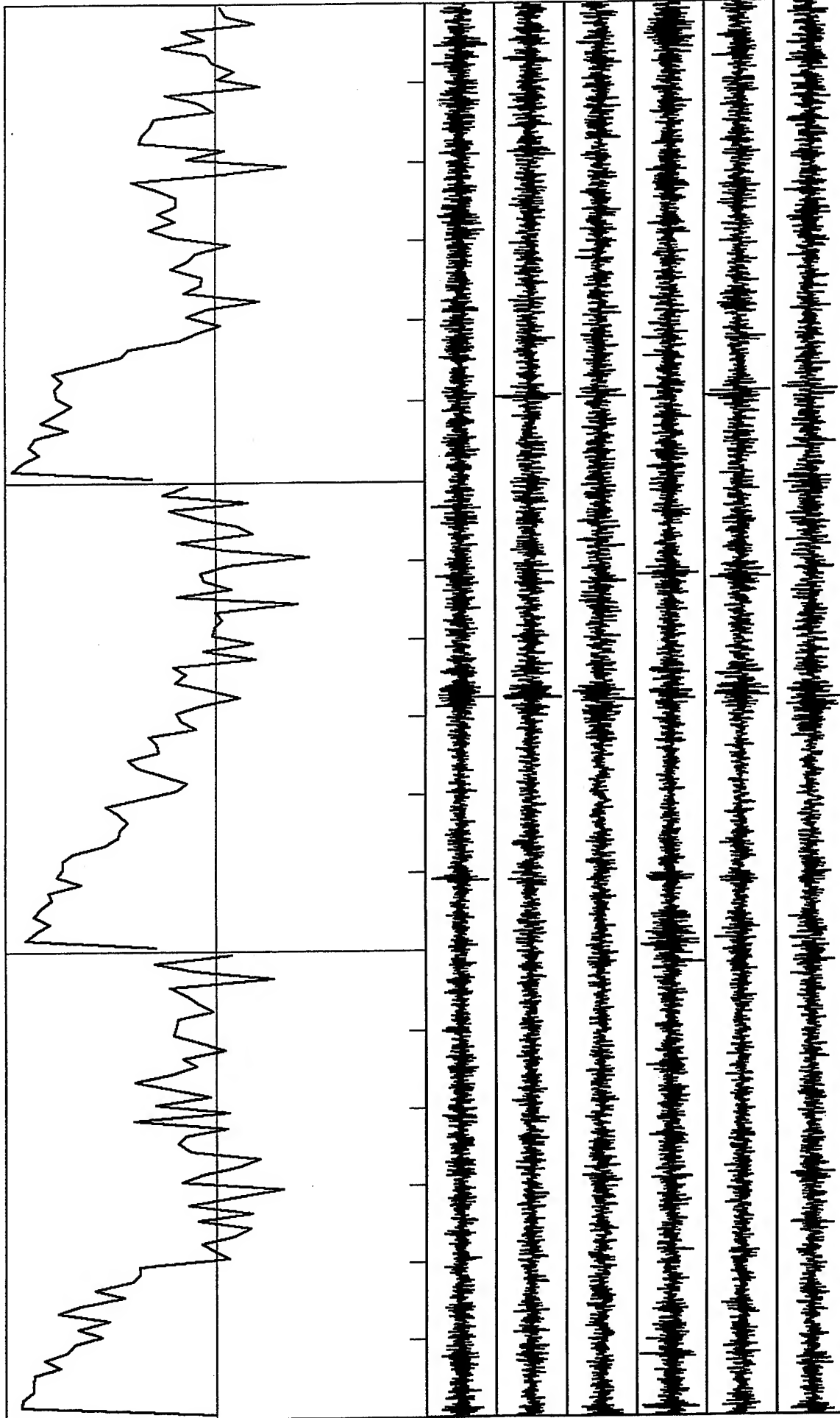
A-II-3



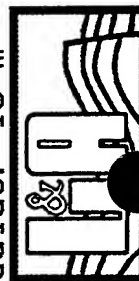
Correlation Coefficients: Scale -1 to +1; freq range: 0 to 30.0 Hz; Radius: 15 m  
 St. 1 & 2: Vertical & horizontal components: 60 s time window

*VortexRock Consultants, Inc.*

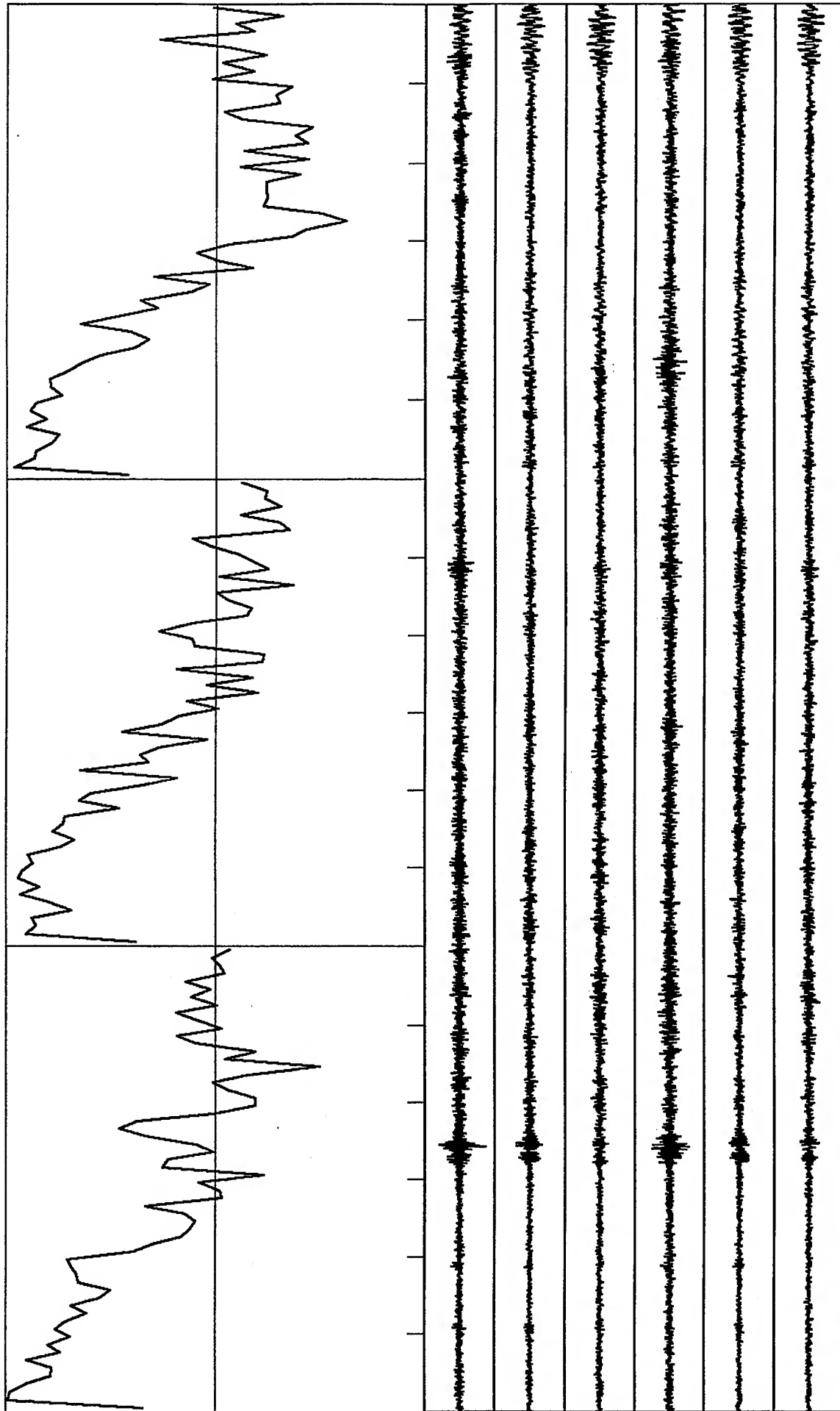




Correlation Coefficients: Scale -1 to +1; freq range: 0 to 30.0 Hz; Radius: 15 m  
 St. 1 & 2: Vertical & horizontal components; 60 s time window



*VortexRock Consultants, Inc.*

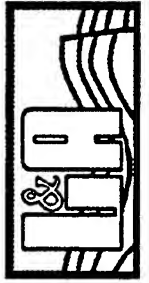


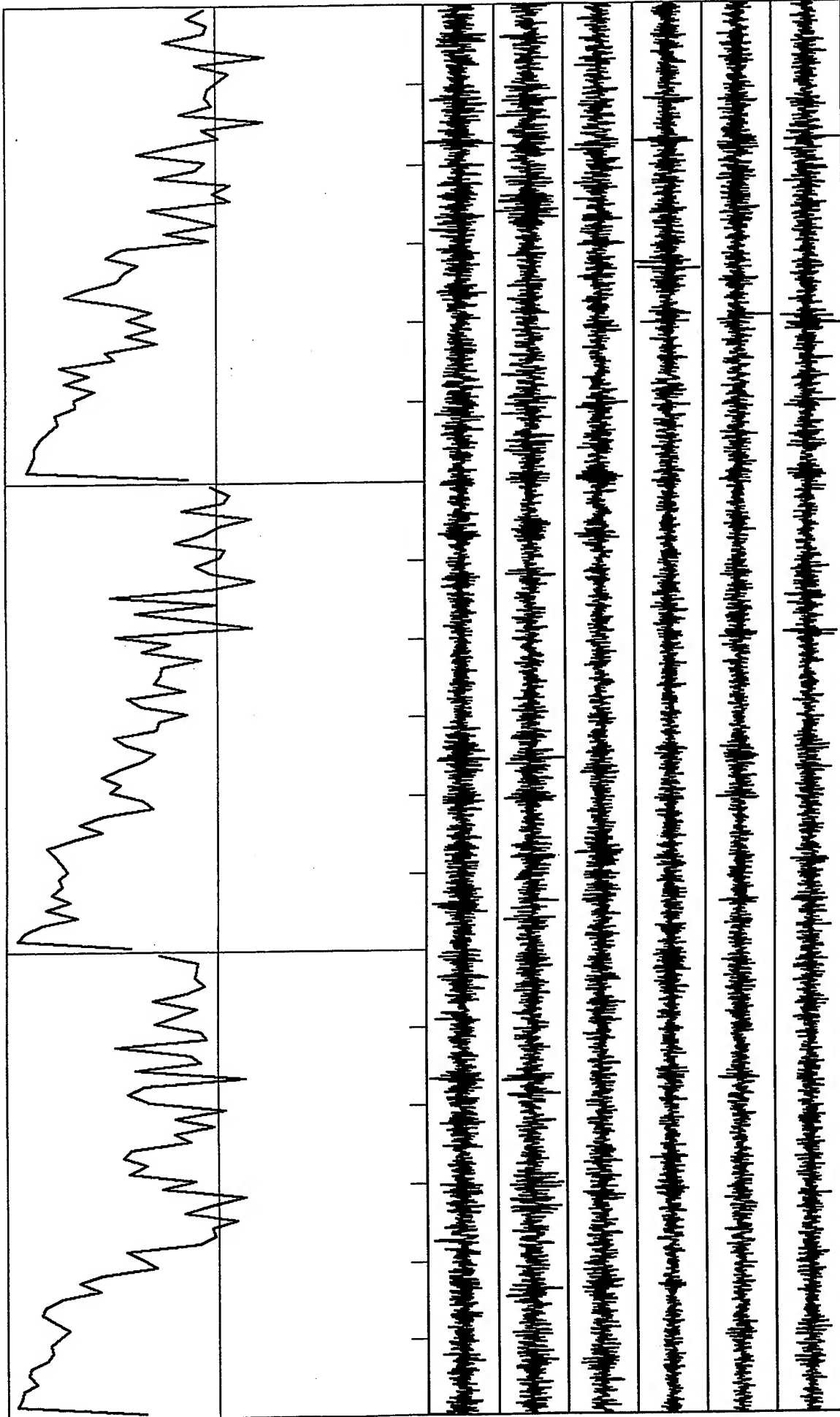
A-II-5



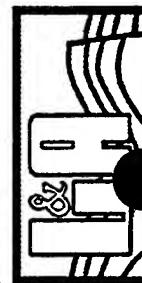
Correlation Coefficients: Scale -1 to +1; freq range: 0 to 30.0 Hz; Radius: 15 m  
 St. 1 & 2: Vertical & horizontal components; 60 s time window

*VortexRock Consultants, Inc.*

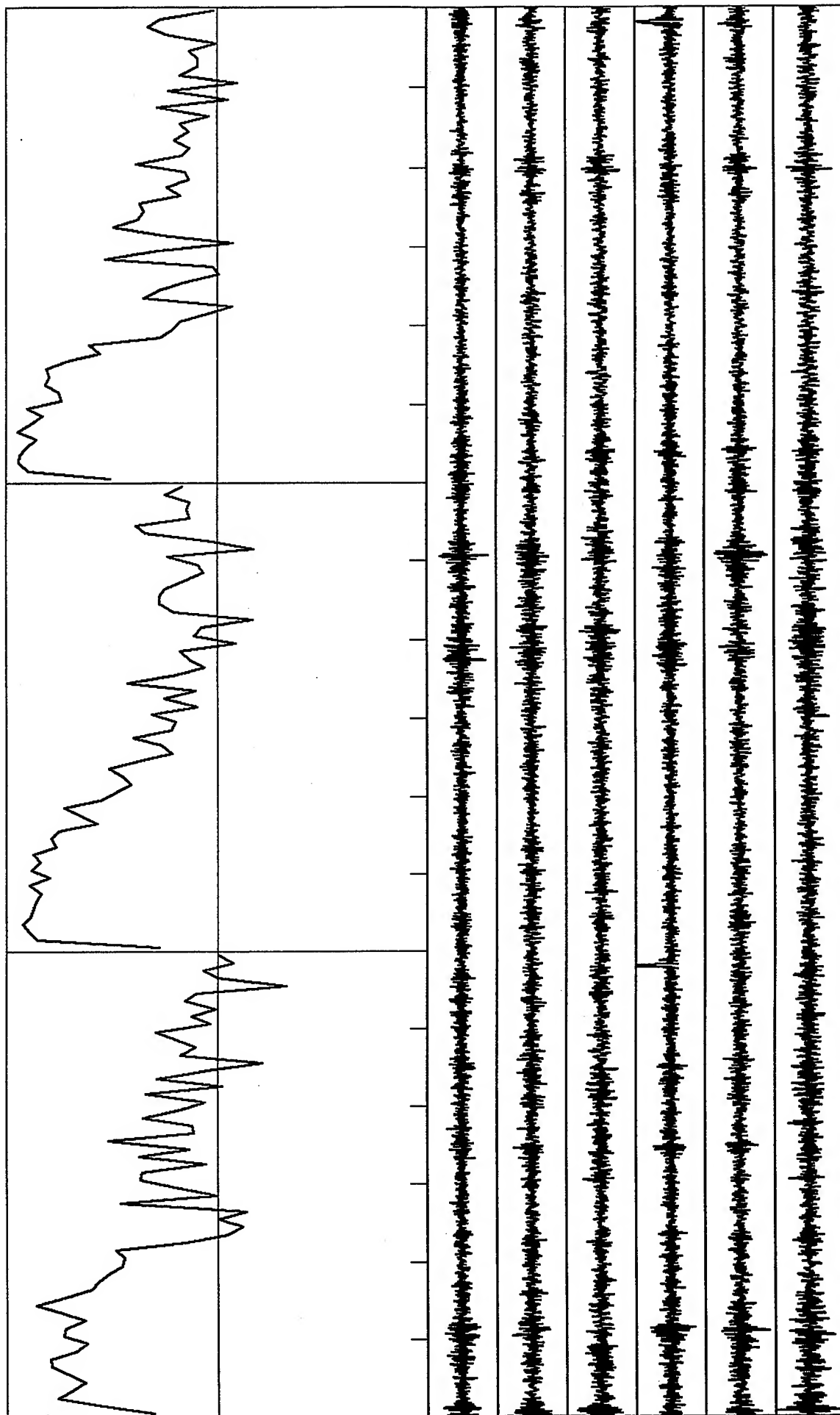




Correlation Coefficients: Scale -1 to +1; freq range: 0 to 30.0 Hz; Radius: 15 m  
 St. 1 & 2: Vertical & horizontal components: 60 s time window



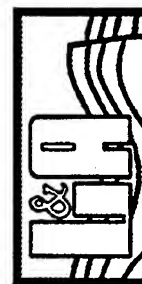
*VortexRock Consultants, Inc.*

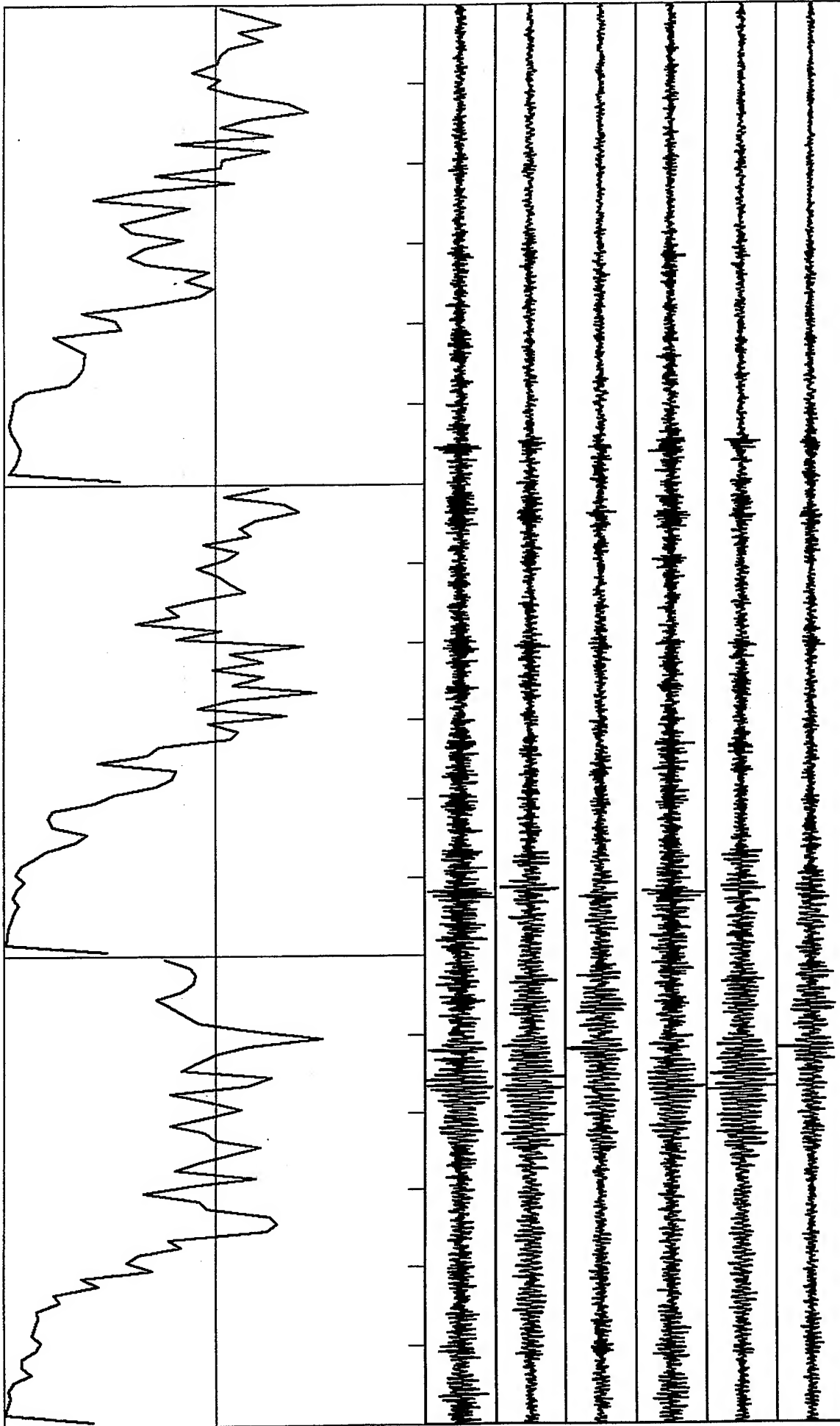


Correlation Coefficients: Scale -1 to +1; freq range: 0 to 30.0 Hz; Radius: 15 m  
 St. 1 & 2: Vertical & horizontal components; 60 s time window



*VortexRock Consultants, Inc.*



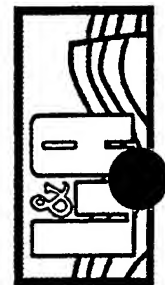


A-II-8

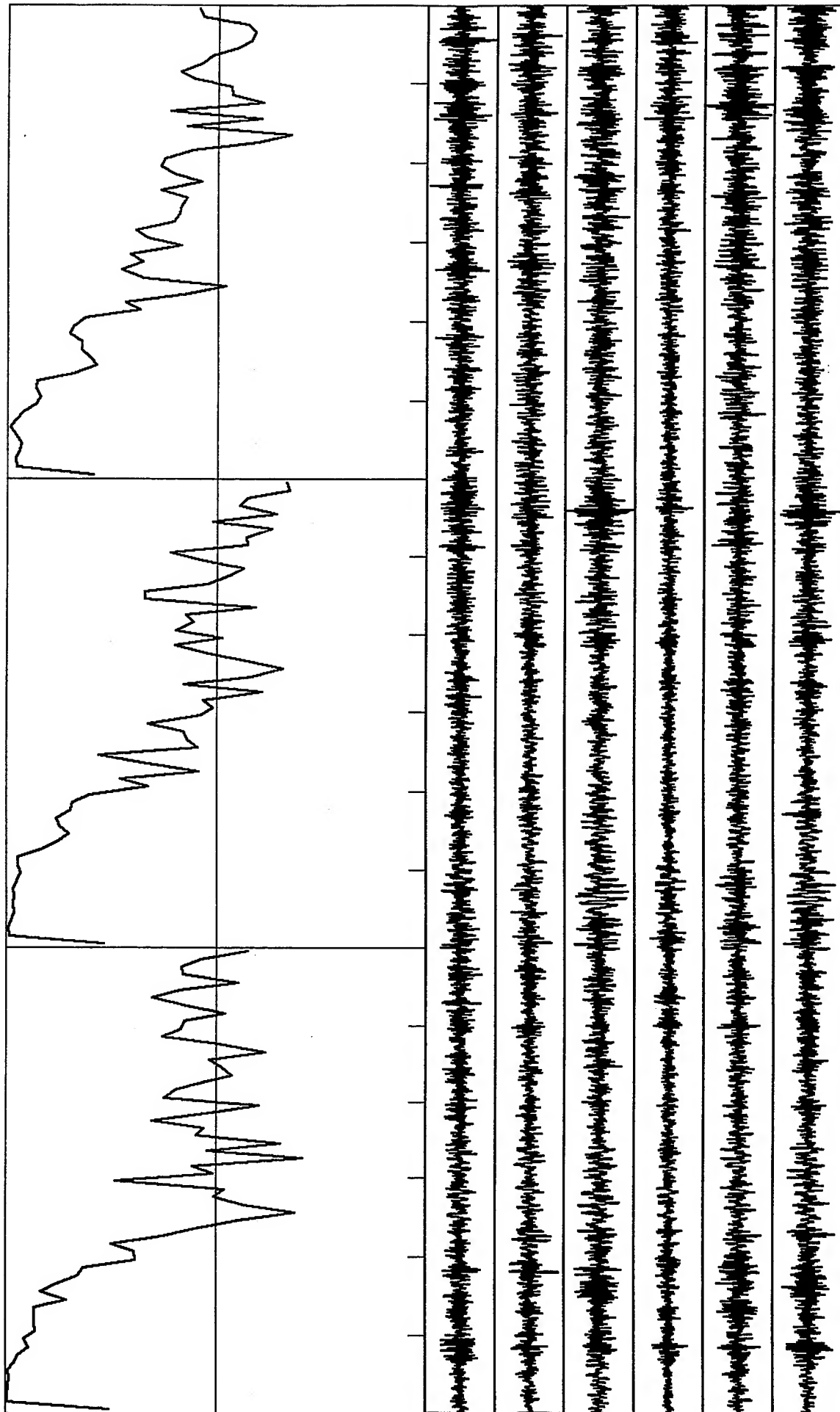
Correlation Coefficients: Scale -1 to +1; freq range: 0 to 30.0 Hz; Radius: 15 m  
 St. 1 & 2: vertical & horizontal components; 60 s time window



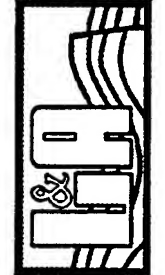
*VortexRock Consultants, Inc.*



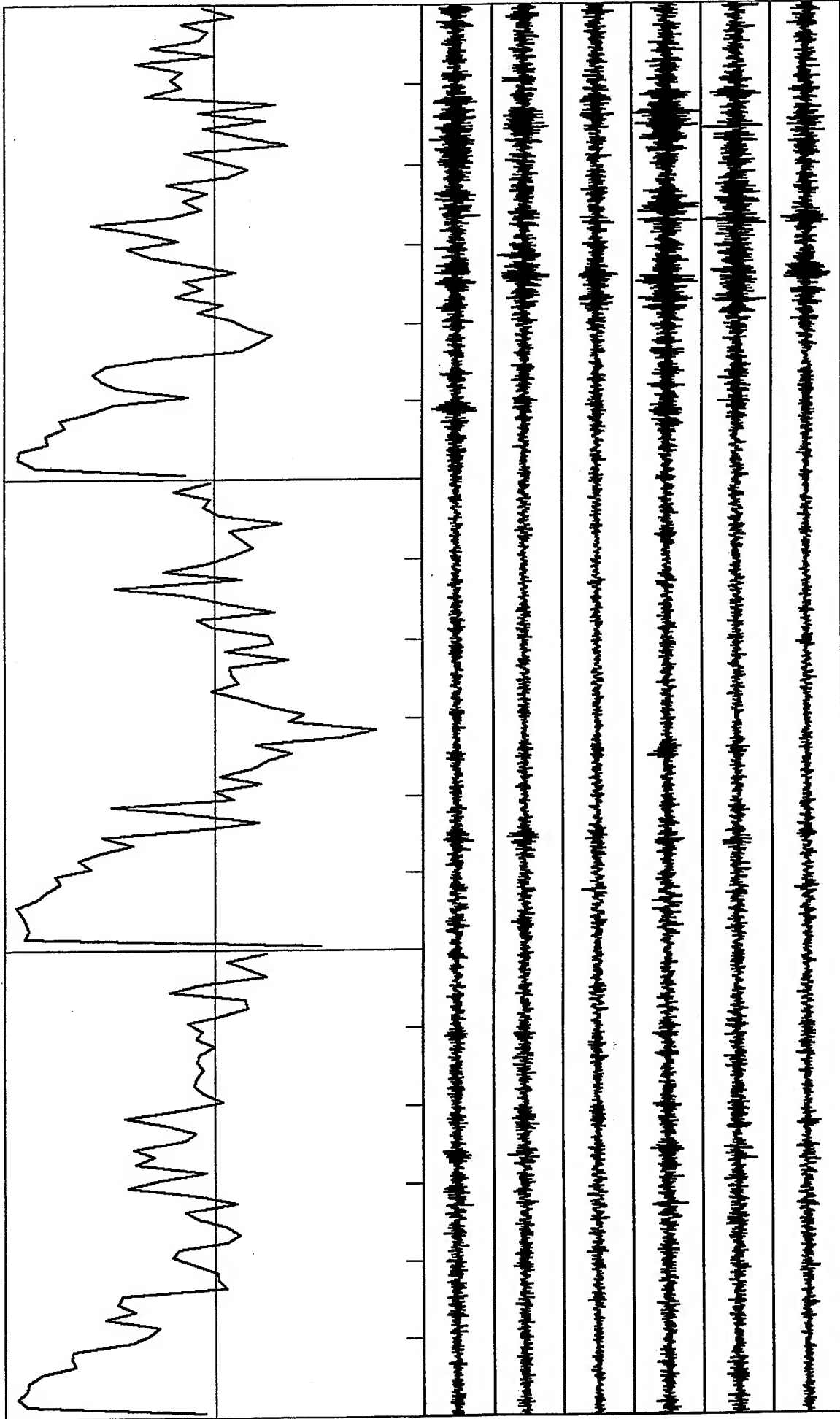




Correlation Coefficients: Scale -1 to +1; freq range: 0 to 30.0 Hz; Radius: 15 m  
 St. 1 & 2: Vertical & horizontal components; 60 s time window



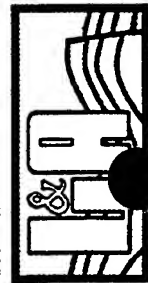
*VortexRock Consultants, Inc.*

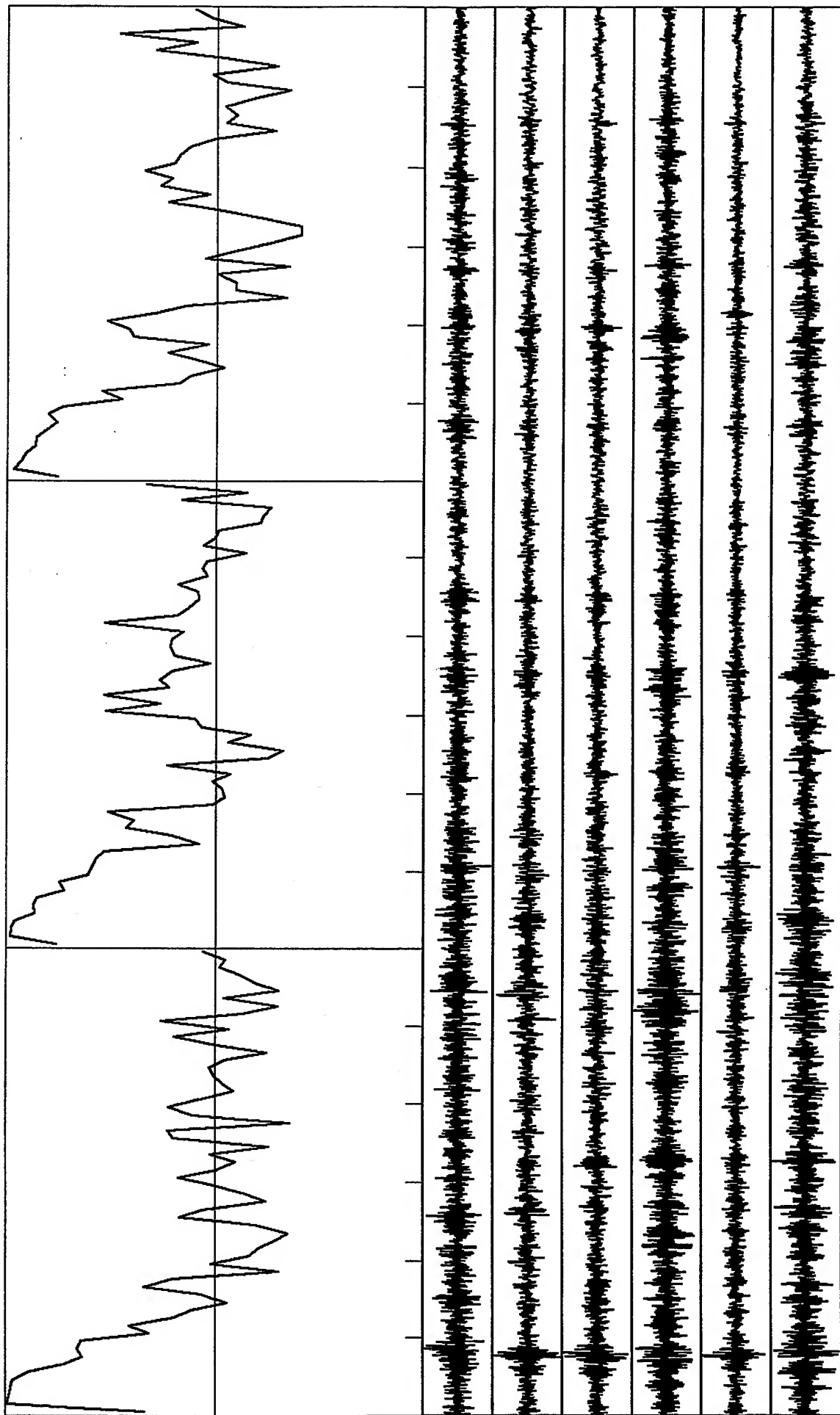


Correlation Coefficients: Scale -1 to +1; freq range: 0 to 30.0 Hz; Radius: 27 m  
 St. 1 & 2: Vertical & horizontal components: 50 s time window

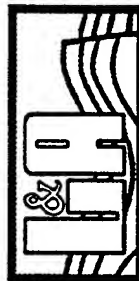


*VortexRock Consultants, Inc.*

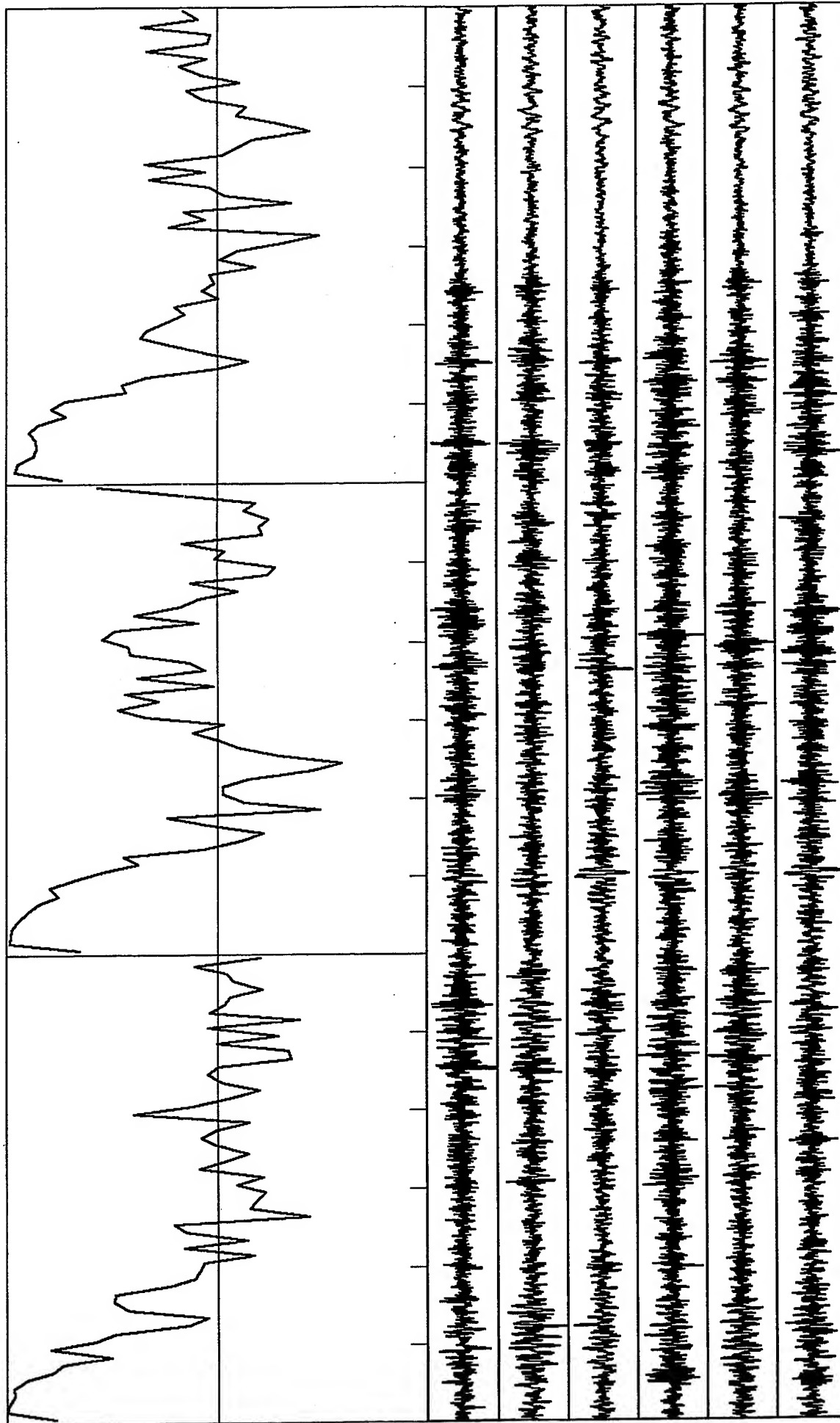




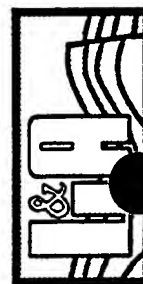
Correlation Coefficients: Scale -1 to +1; freq range: 0 to 30.0 Hz; Radius: 27 m  
 St. 1 & 2: Vertical & horizontal components; 50 s time window



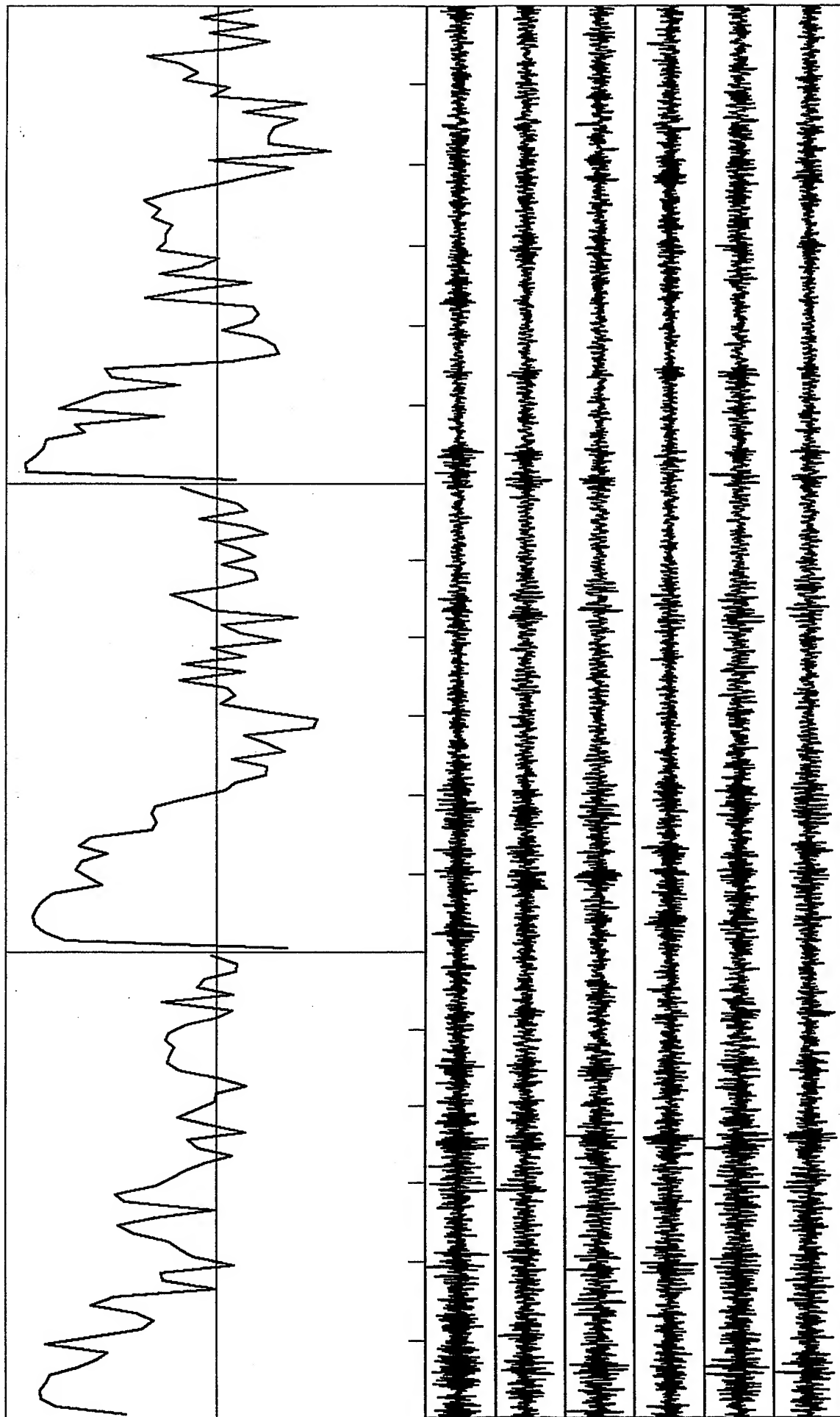
*VortexRock Consultants, Inc.*



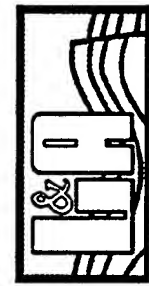
Correlation Coefficients: Scale -1 to +1; freq range: 0 to 30.0 Hz; Radius: 27 m  
 St. 1 & 2: Vertical & horizontal components; 60 s time window



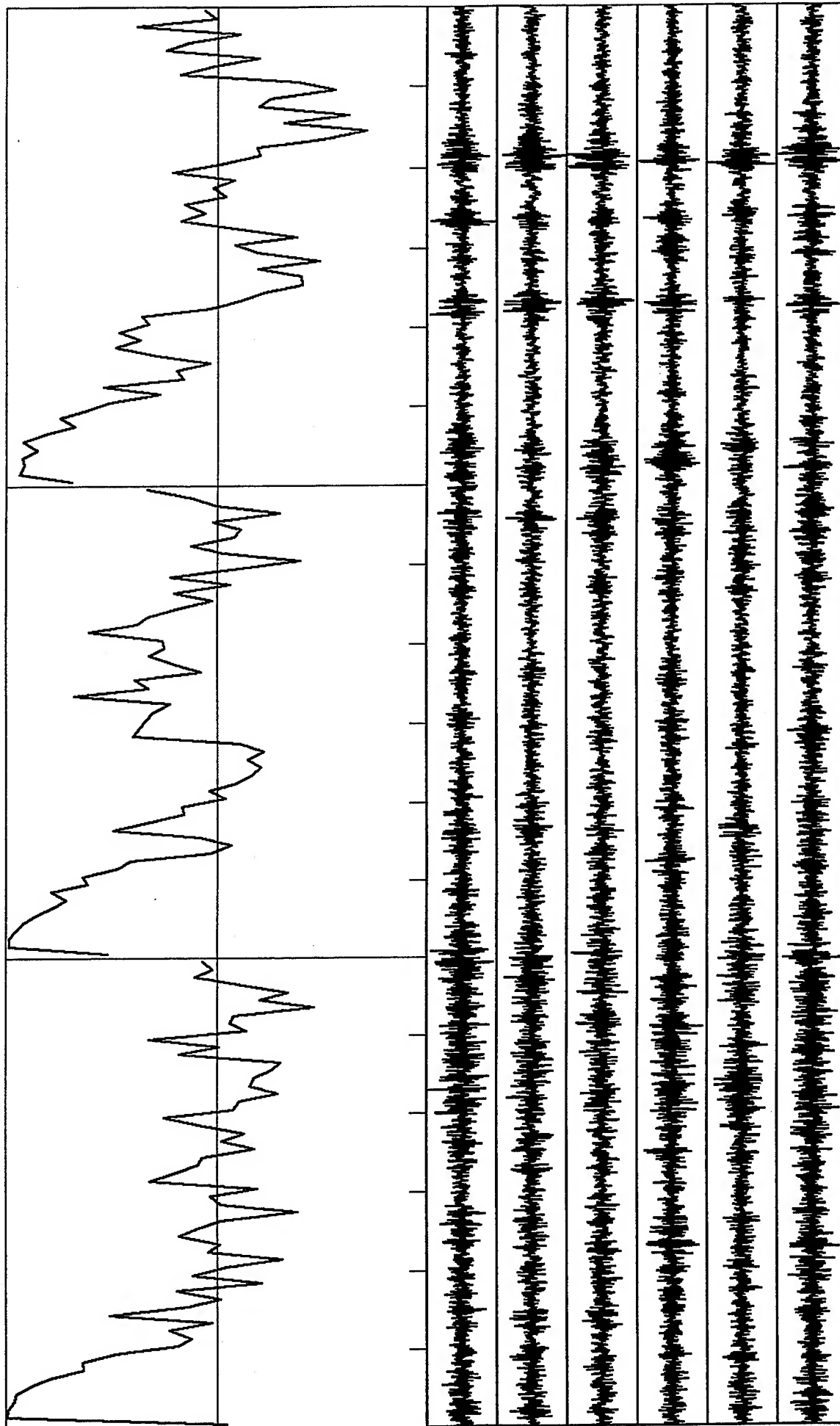
*VortexRock Consultants, Inc.*



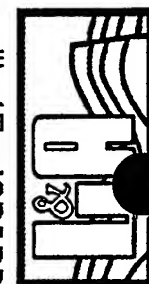
Correlation Coefficients: Scale -1 to +1; freq range: 0 to 30.0 Hz; Radius: 27 m  
 St. 1 & 2: Vertical & horizontal components; 60 s time window



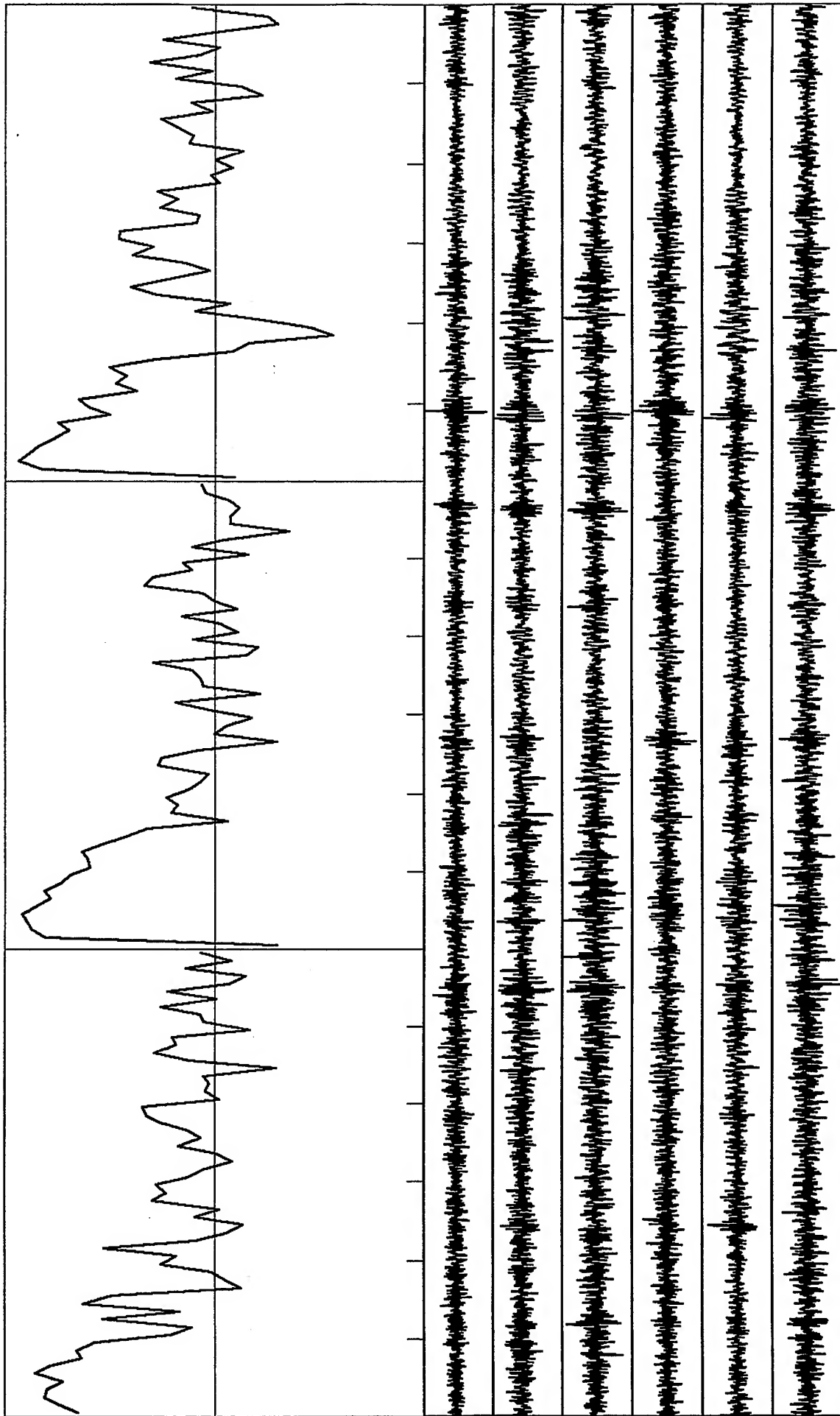
*VortexRock Consultants, Inc.*



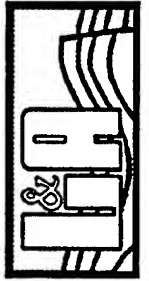
Correlation Coefficients: Scale -1 to +1; freq range: 0 to 30.0 Hz; Radius: 27 m  
 St. 1 & 2: Vertical & horizontal components; 60 s time window



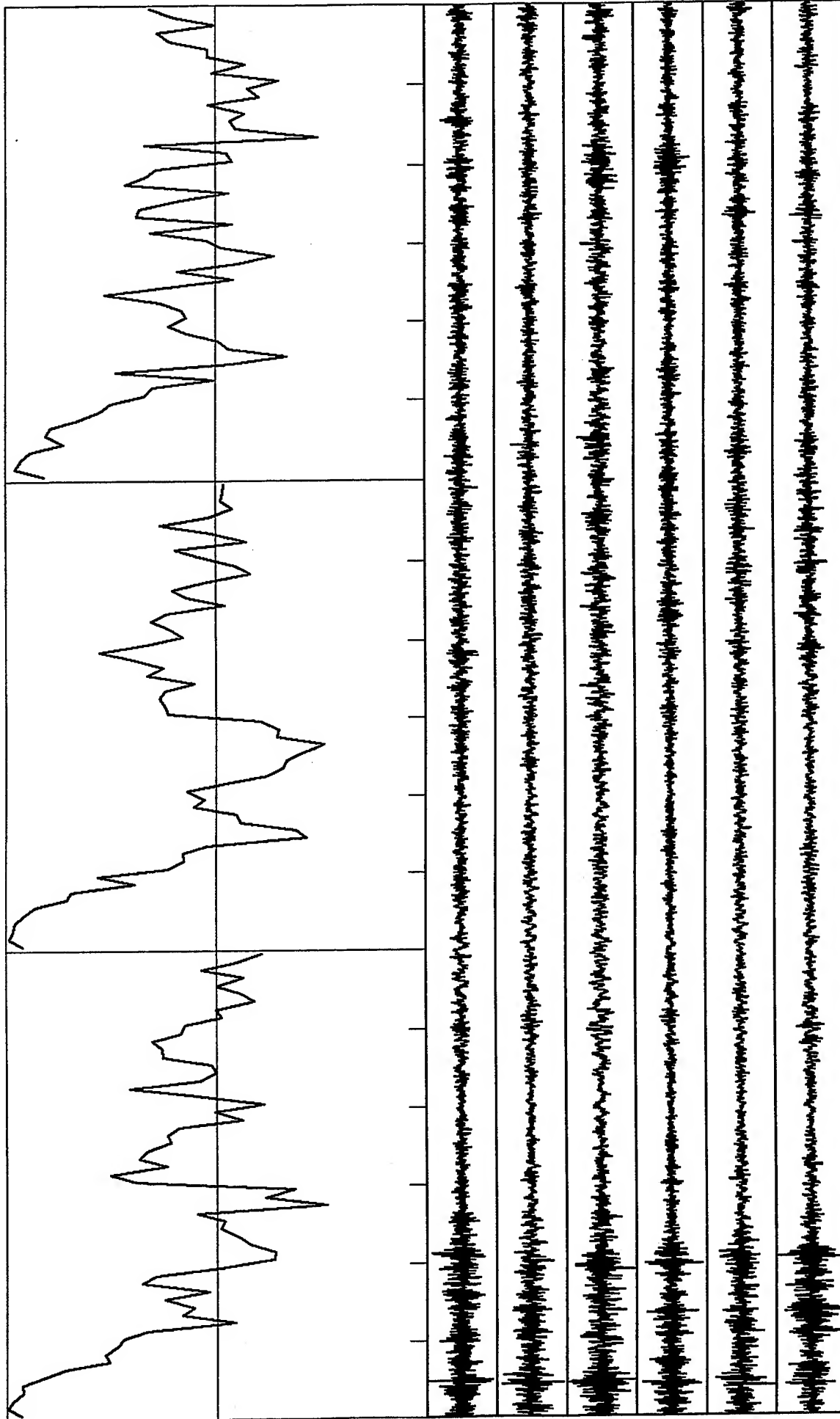
*VortexRock Consultants, Inc.*



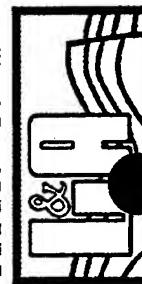
Correlation Coefficients: Scale -1 to +1; freq range: 0 to 30.0 Hz; Radius: 27 m  
 St. 1 & 2: Vertical & horizontal components; 60 s time window



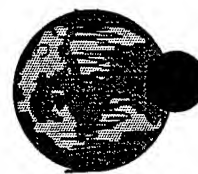
*VortexRock Consultants, Inc.*



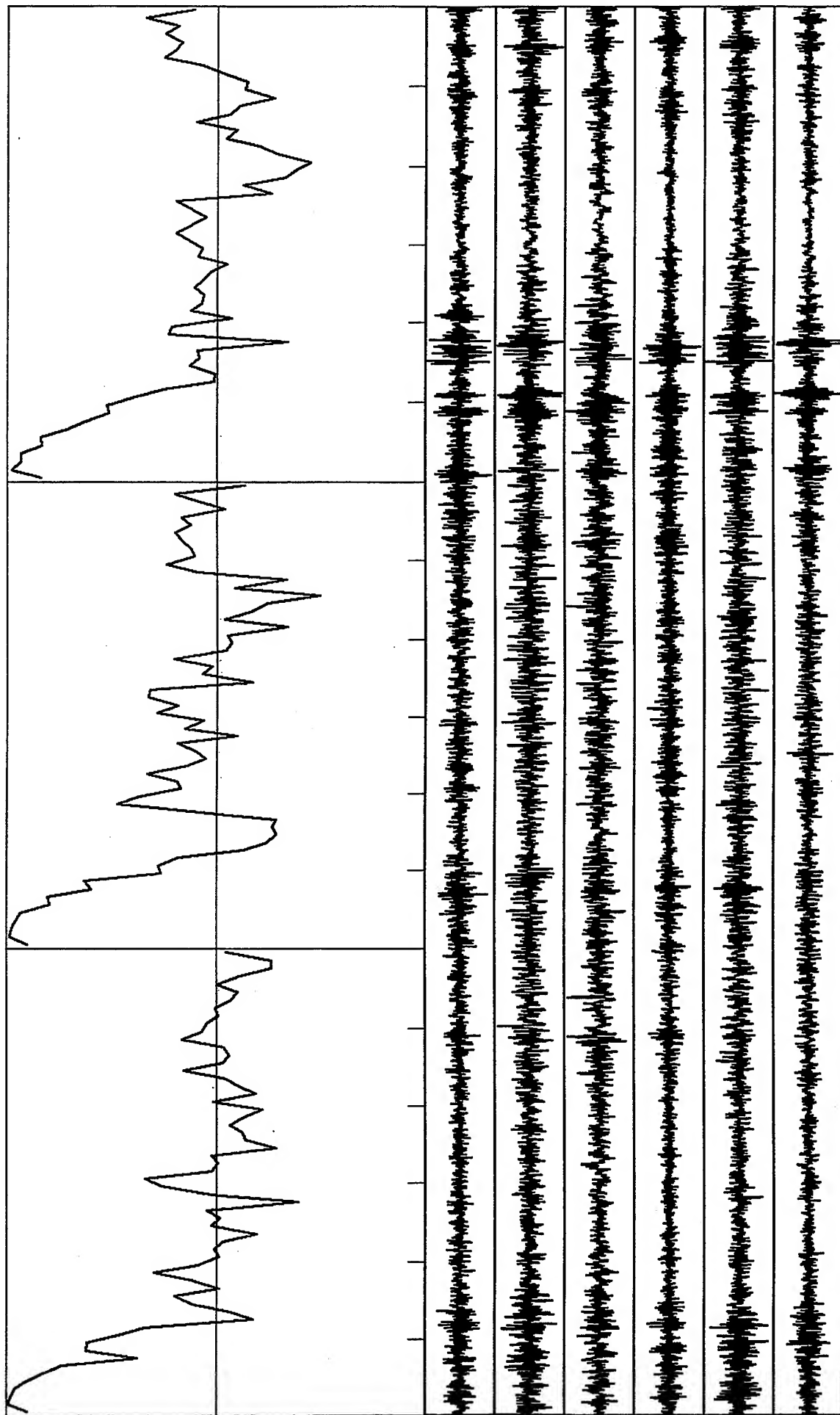
Correlation Coefficients: Scale -1 to +1; freq range: 0 to 30.0 Hz; Radius: 37 m  
 St. 1 & 2: Vertical & horizontal components; 60 s time window



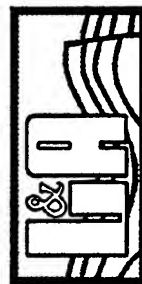
*VortexRock Consultants, Inc.*



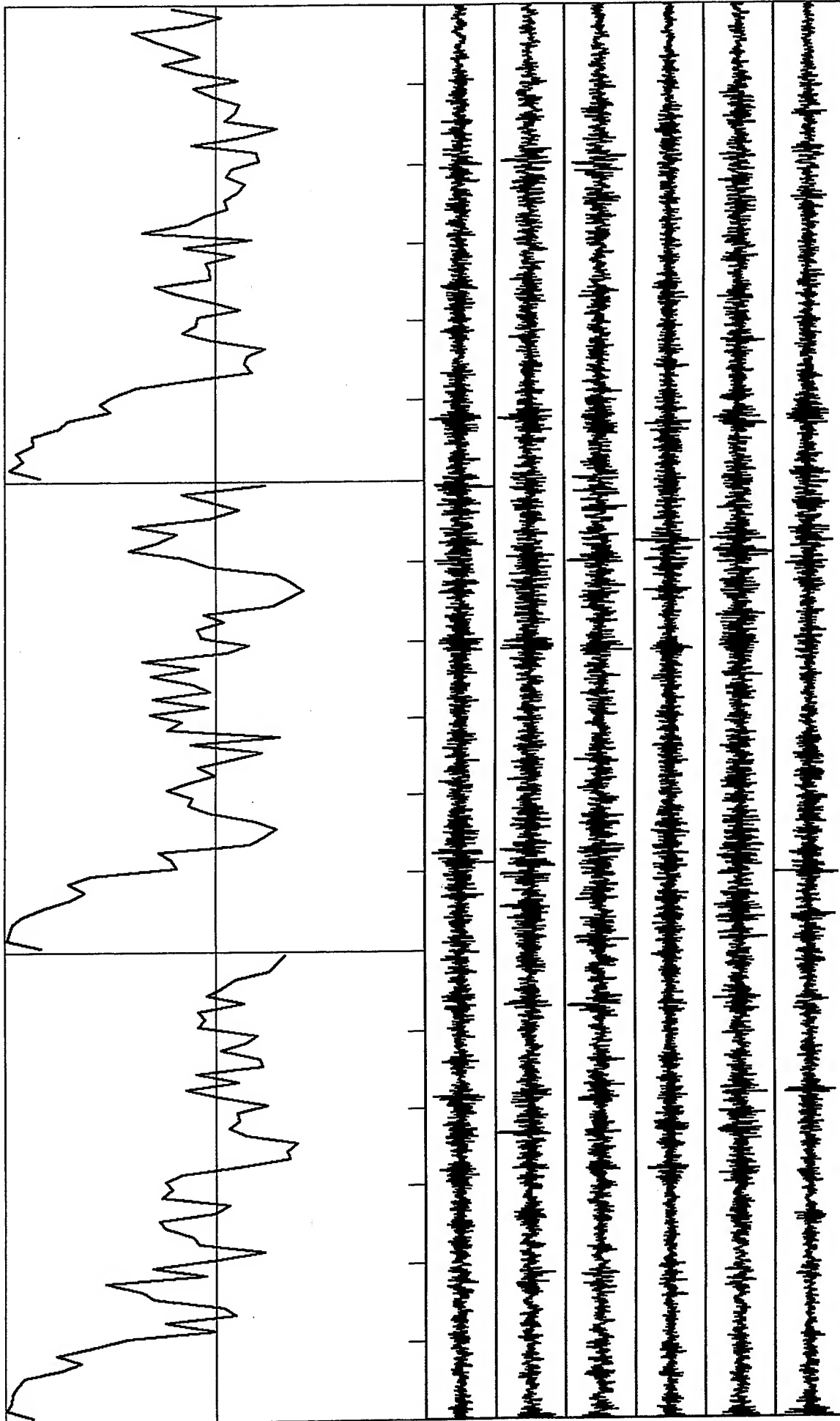




Correlation Coefficients: Scale -1 to +1; freq range: 0 to 30.0 Hz; Radius: 37 m  
 St. 1 & 2: Vertical & horizontal components; 60 s time window



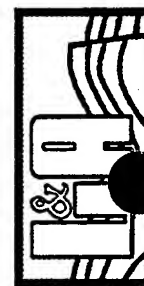
*VortexRock Consultants, Inc.*

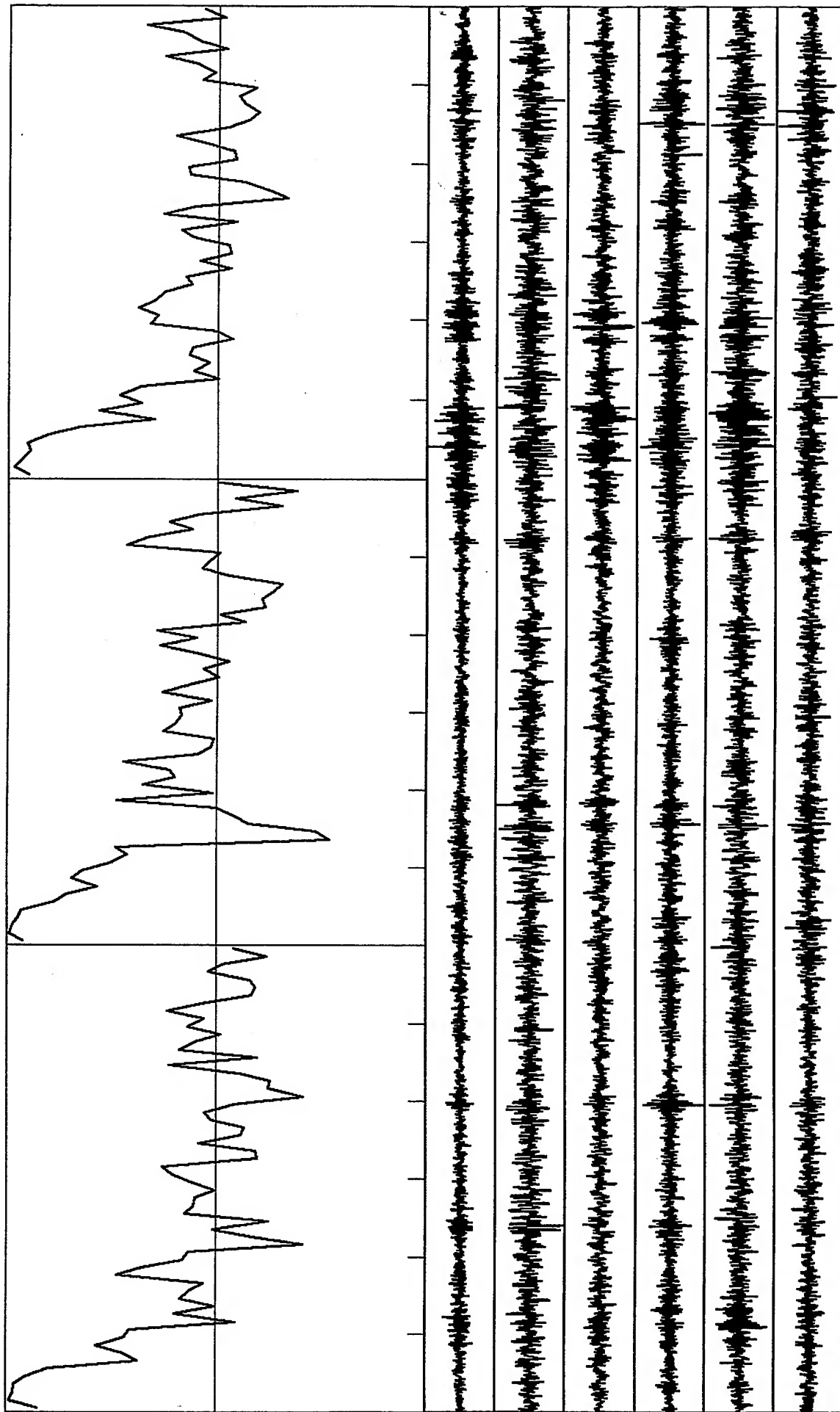


Correlation Coefficients: Scale -1 to +1; freq range: 0 to 30.0 Hz; Radius: 37 m  
 St. 1 & 2: Vertical & horizontal components: 60 s time window

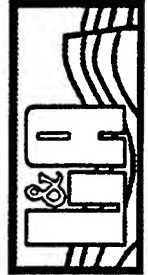


*VortexRock Consultants, Inc.*

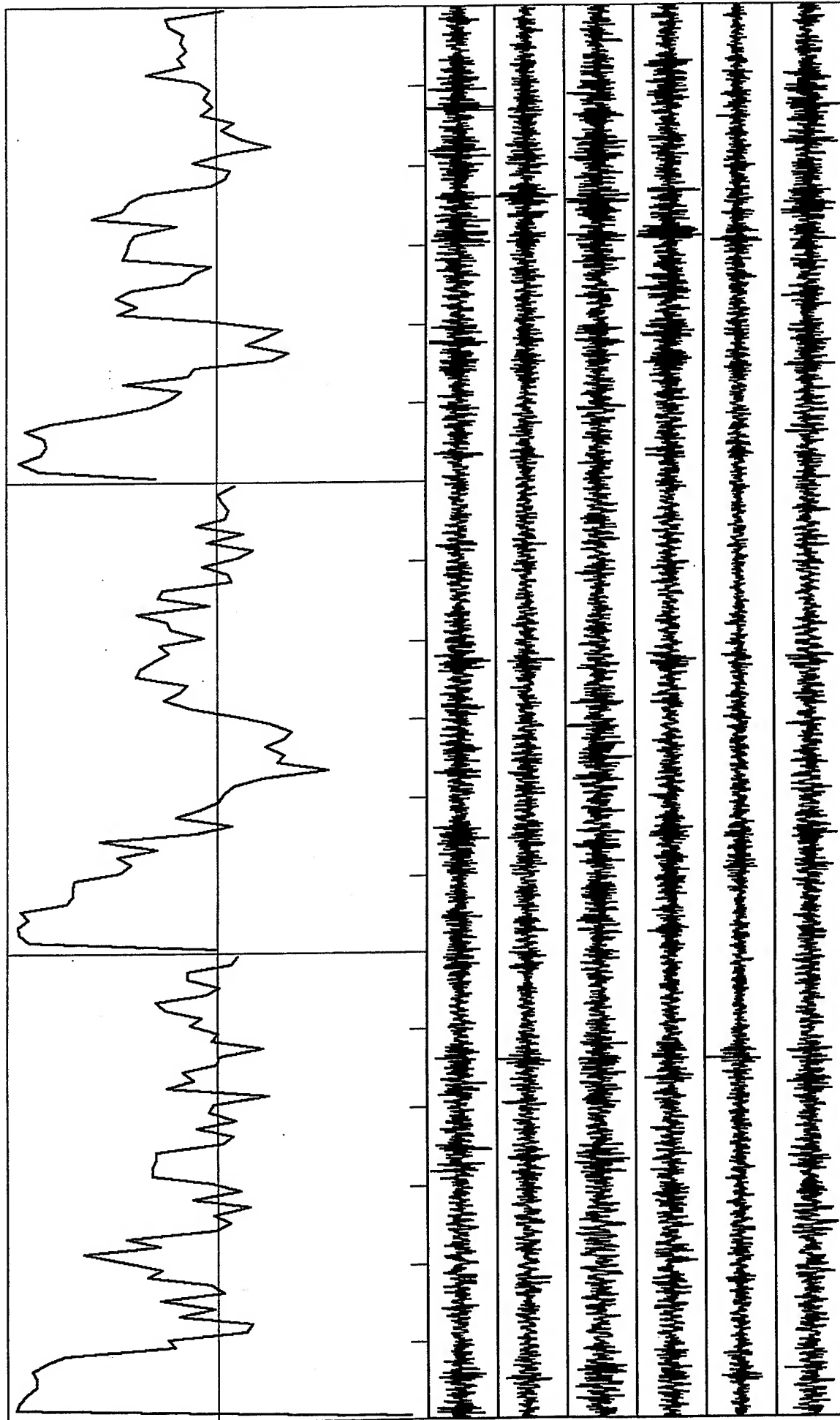




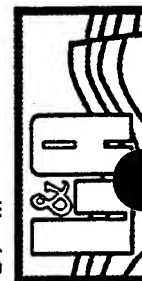
Correlation Coefficients: Scale -1 to +1; freq range: 0 to 30.0 Hz; Radius: 37 m  
 St. 1 & 2: Vertical & horizontal components; 60 s time window



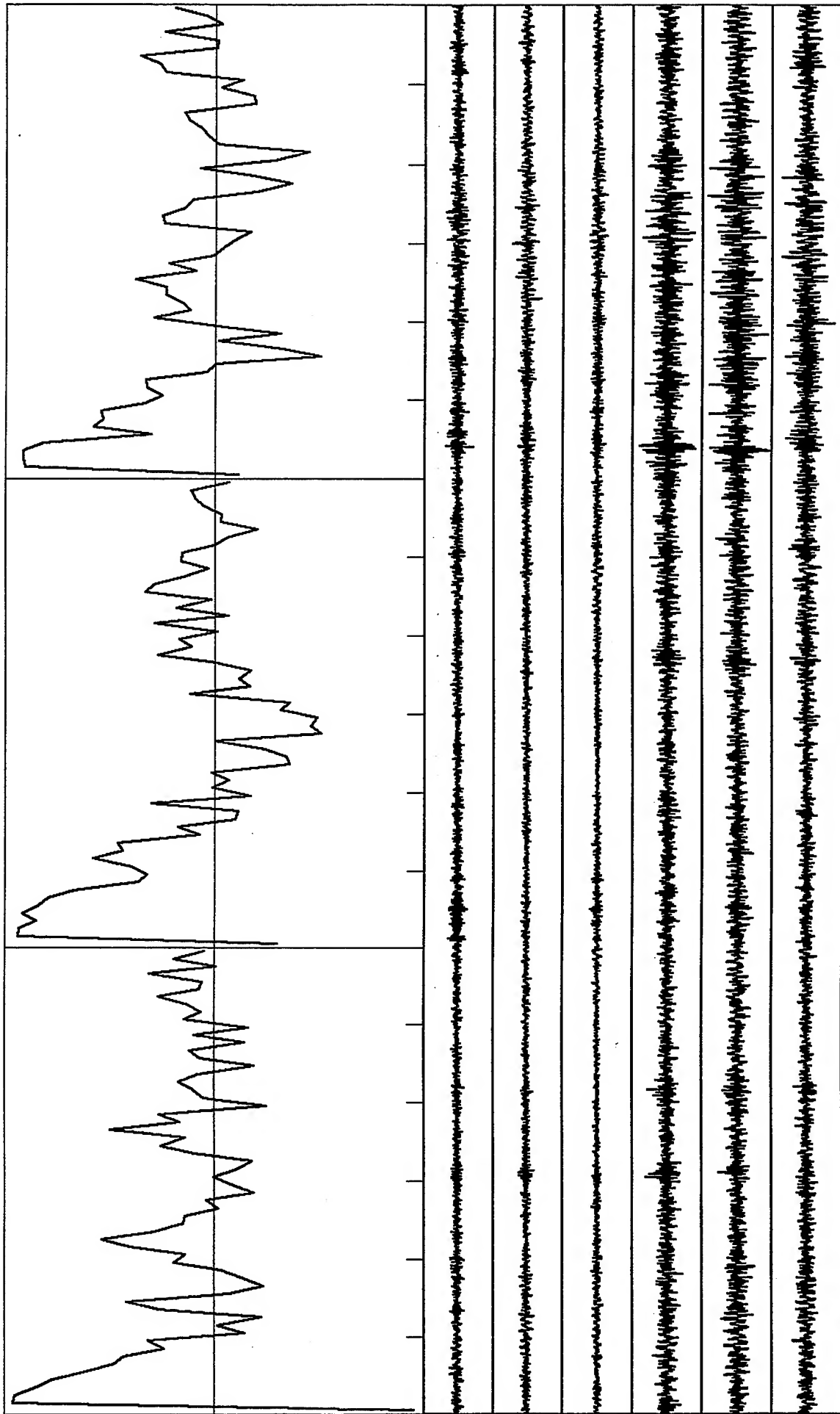
*VortexRock Consultants, Inc.*



Correlation Coefficients: Scale -1 to +1; freq range: 0 to 30.0 Hz; Radius: 37 m  
 St. 1 & 2: Vertical & horizontal components; 50 s time window



*VortexRock Consultants, Inc.*

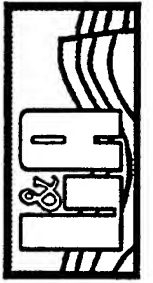


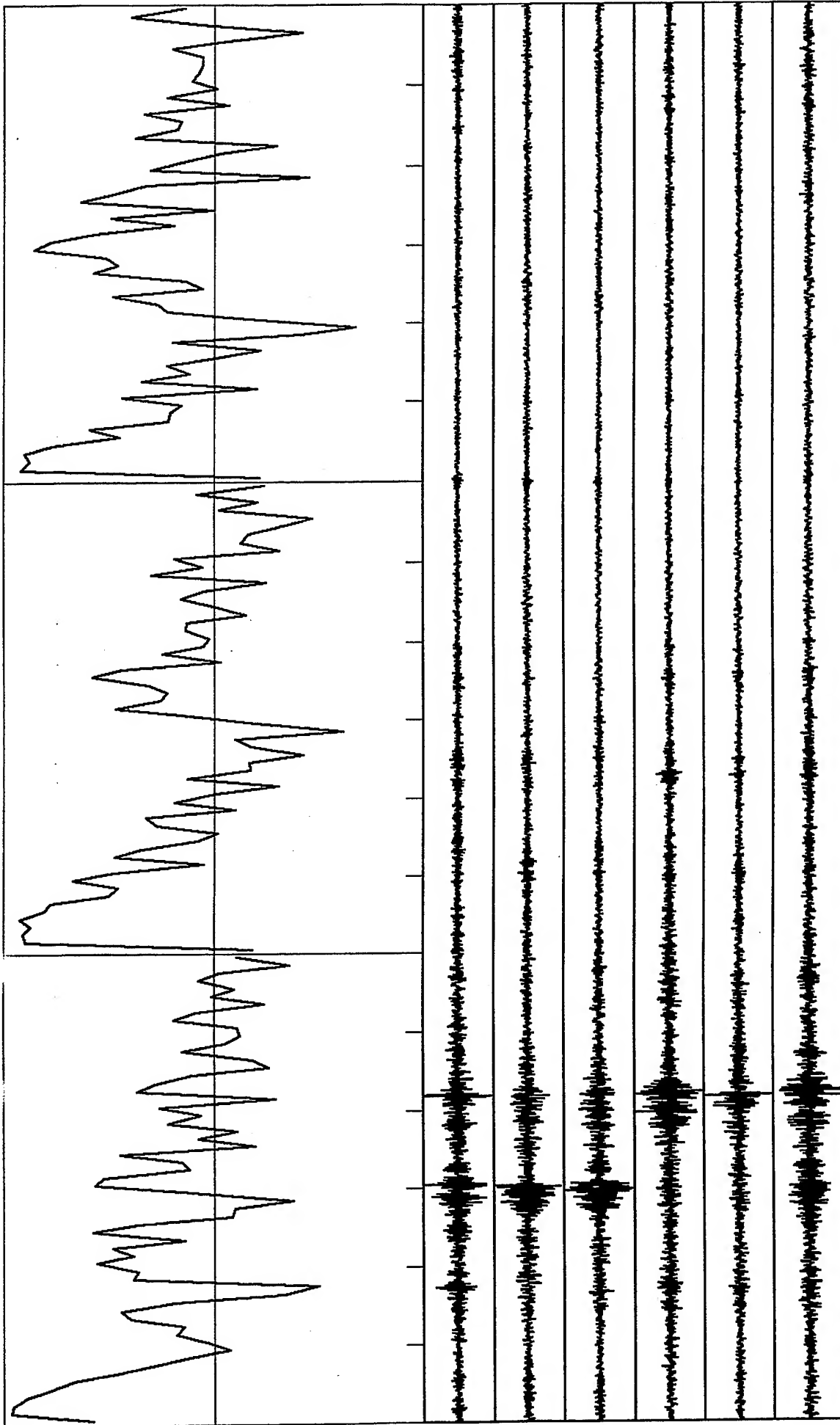
A-II-21



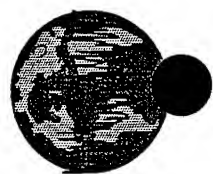
Correlation Coefficients: Scale -1 to +1; freq range: 0 to 30.0 Hz; Radius: 37 m  
 St. 1 & 2: Vertical & horizontal components; 60 s time window

*VortexRock Consultants, Inc.*



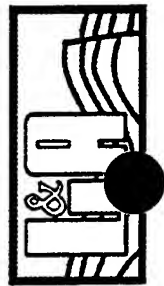


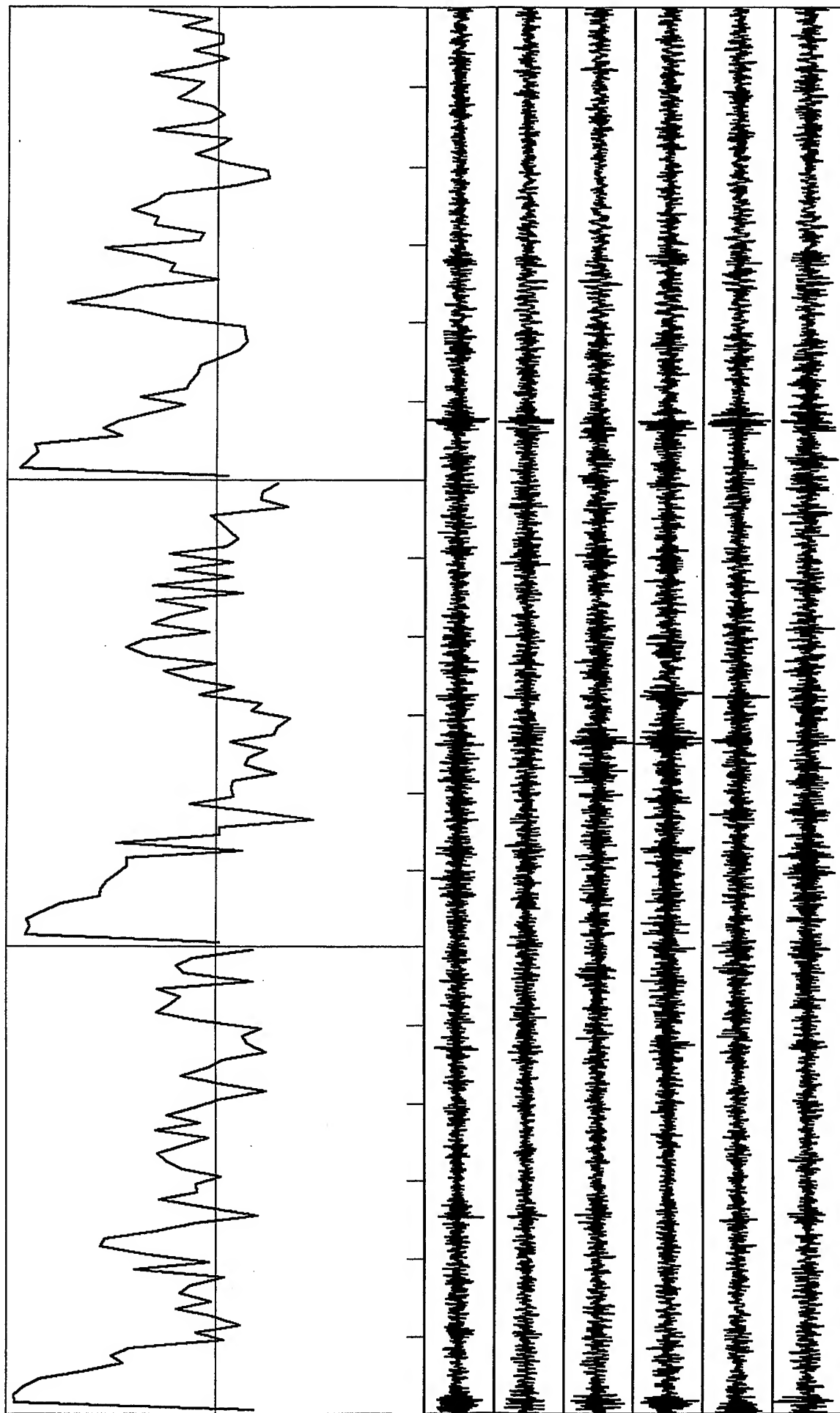
A-II-22



Correlation Coefficients: Scale -1 to +1; freq range: 0 to 30.0 Hz; Radius: 37 m  
St. 1 & 2: Vertical & horizontal components: 60 s time window

*VortexRock Consultants, Inc.*



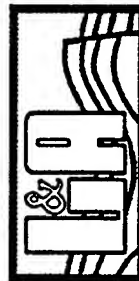


A-II-23



Correlation Coefficients: Scale -1 to +1; freq range: 0 to 30.0 Hz; Radius: 37 m  
 St. 1 & 2: Vertical & horizontal components; 60 s time window

*VortexRock Consultants, Inc.*



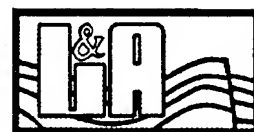
## ***Appendix B***

### ***Section I***

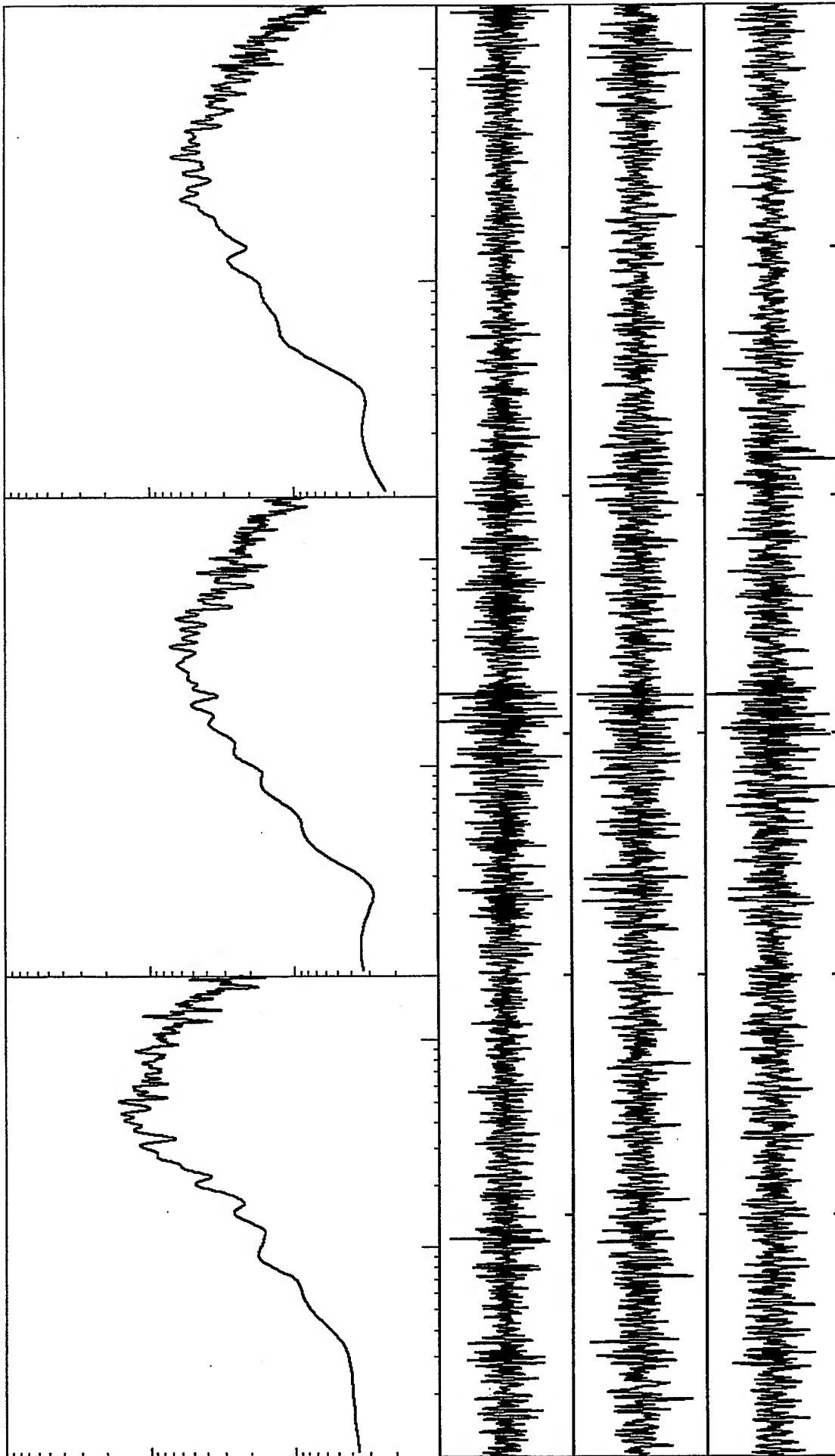
***Time Histories and Spectral Parameters for Selected  
Records from Experiments No. 3 at the Parking Lot of  
Mazda Storage Area, Port Hueneme, Oxnard, California***



***VortexRock Consultants, Inc.***



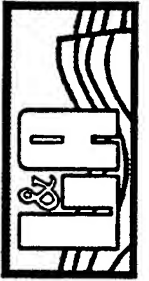


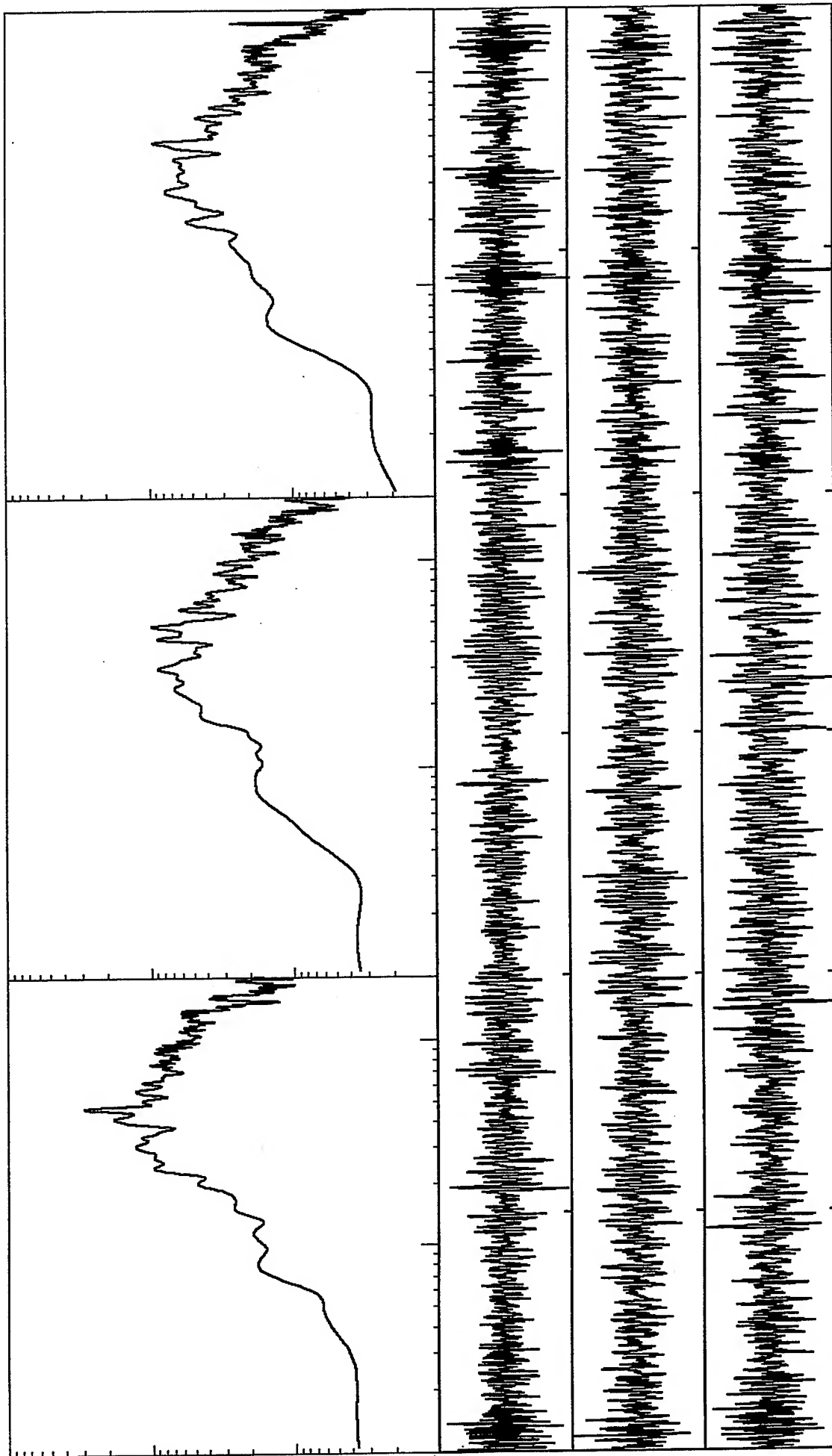


Spectral velocity values 0.1 to 20 Hz. Range: 1.E-5 to 1.E-2 cm/s  
 From top: ch1, 2, & 3: Max values of .315, .123, and .109 1.E-2 cm/s  
 Station 1: 60 s time window



*VortexRock Consultants, Inc.*

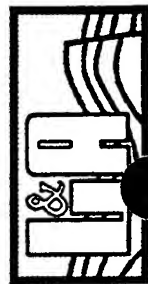


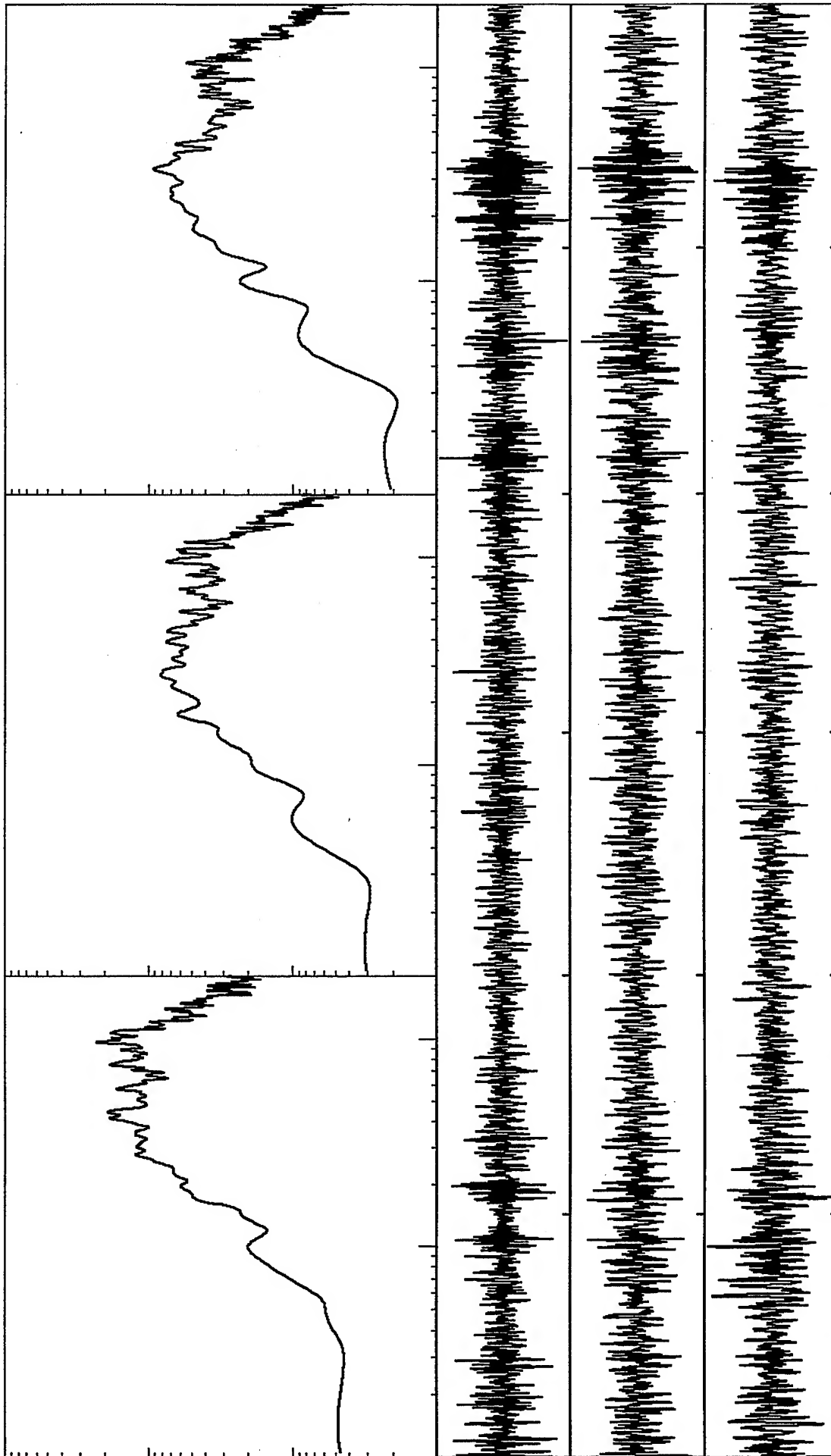


Spectral velocity values 0.1 to 20 Hz. Range: 1.E-5 to 1.E-2 cm/s  
 From tap: ch1, 2, & 3: Max values of .251, .111, and .093 1.E-2 cm/s  
 Station 1: 60 s time window



*VortexRock Consultants, Inc.*

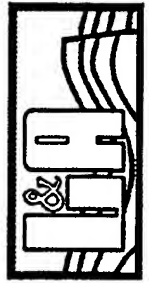


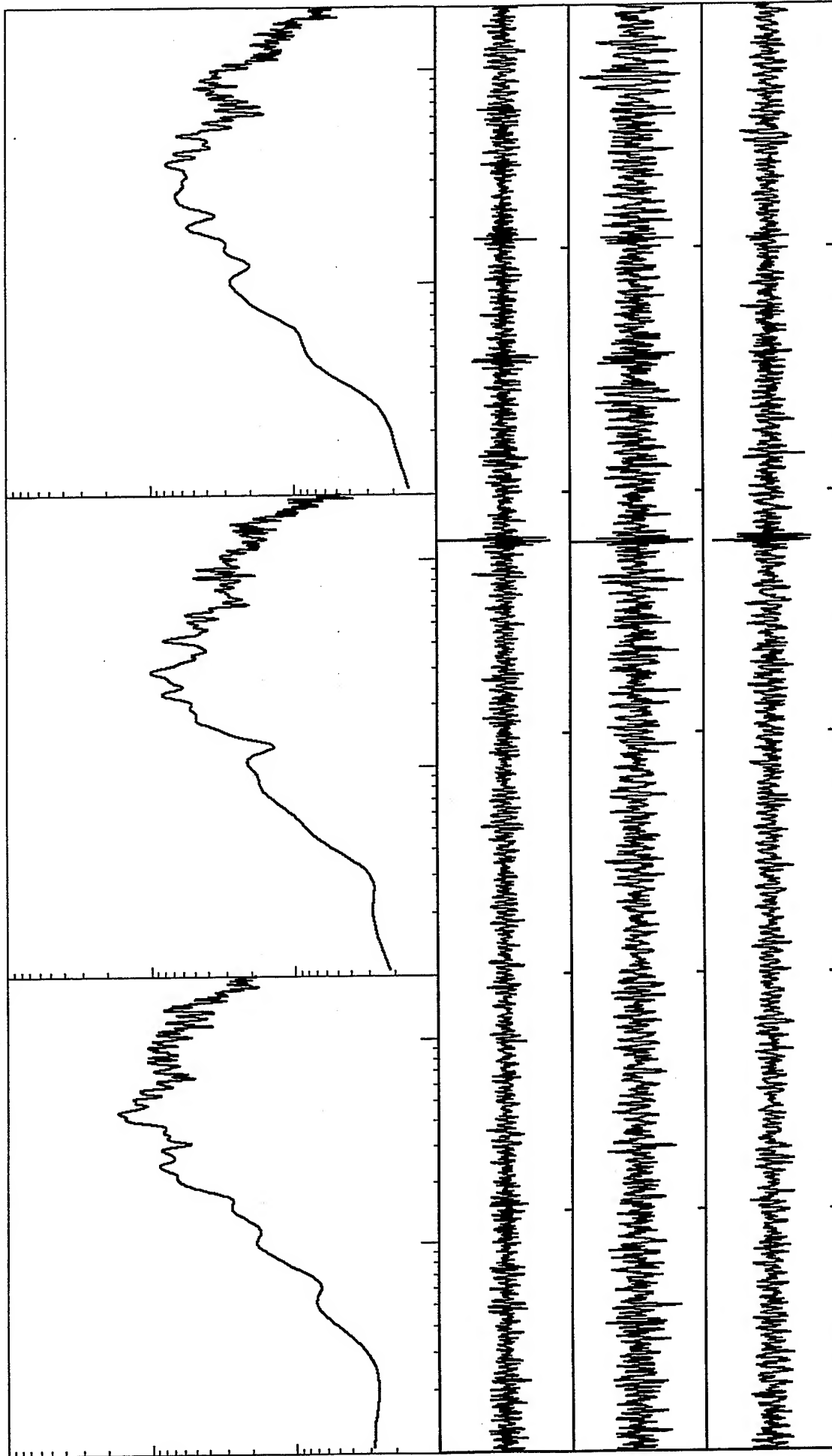


Spectral velocity values 0.1 to 20 Hz. Range: 1.E-5 to 1.E-2 cm/s  
 From top: ch1, 2, & 3: Max values of .395, .150, and .134 1.E-2 cm/s  
 Station 1: 60 s time window



*VortexRock Consultants, Inc.*

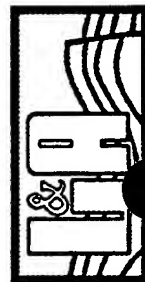


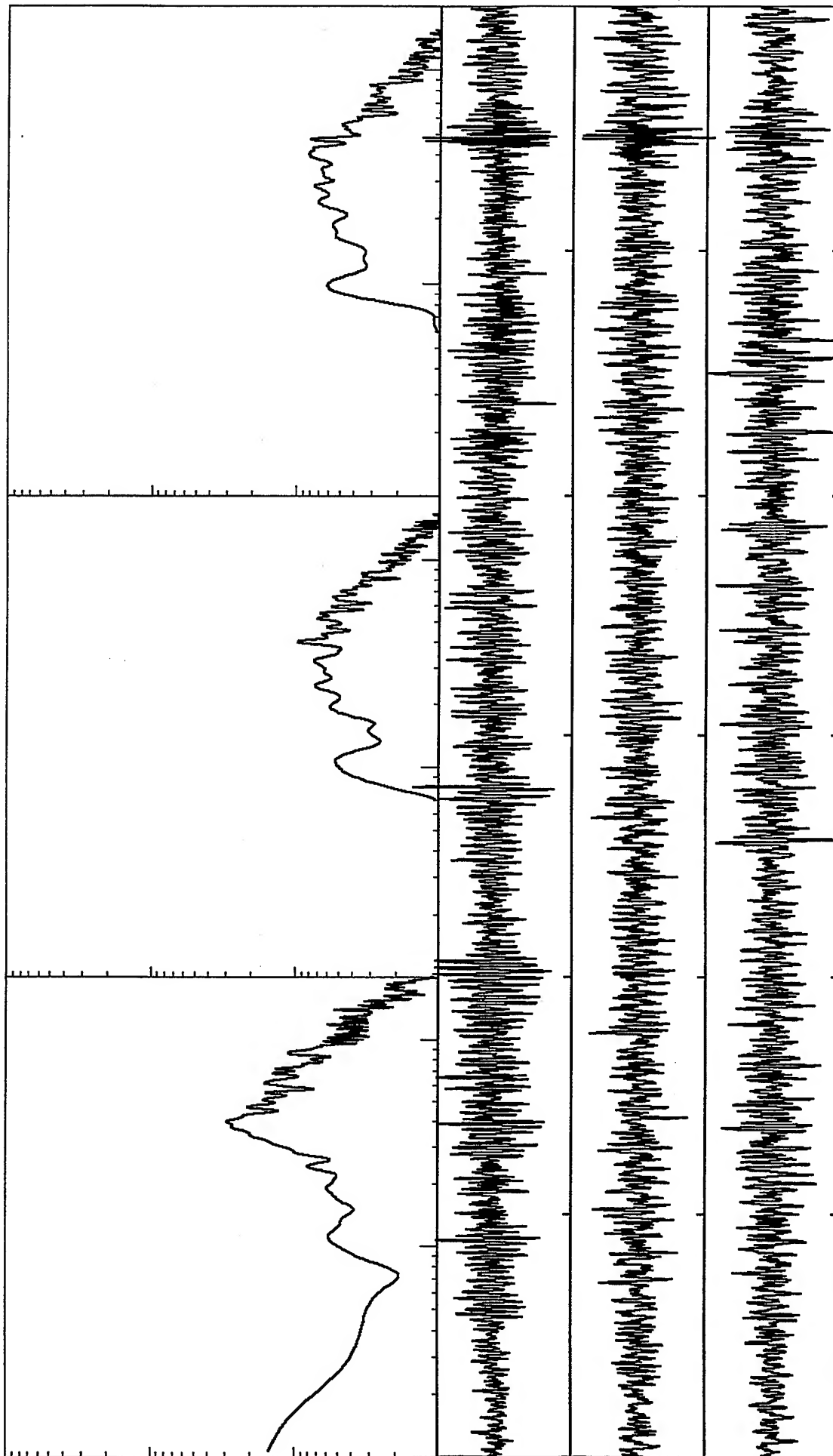


Spectral velocity values 0.1 to 20 Hz. Range: 1.E-5 to 1.E-2 cm/s  
 From top: ch1, 2, & 3: Max values of .531, .153, and .214 1.E-2 cm/s  
 Station 1: 60 s time window



*VortexRock Consultants, Inc.*

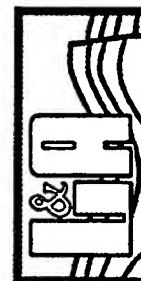


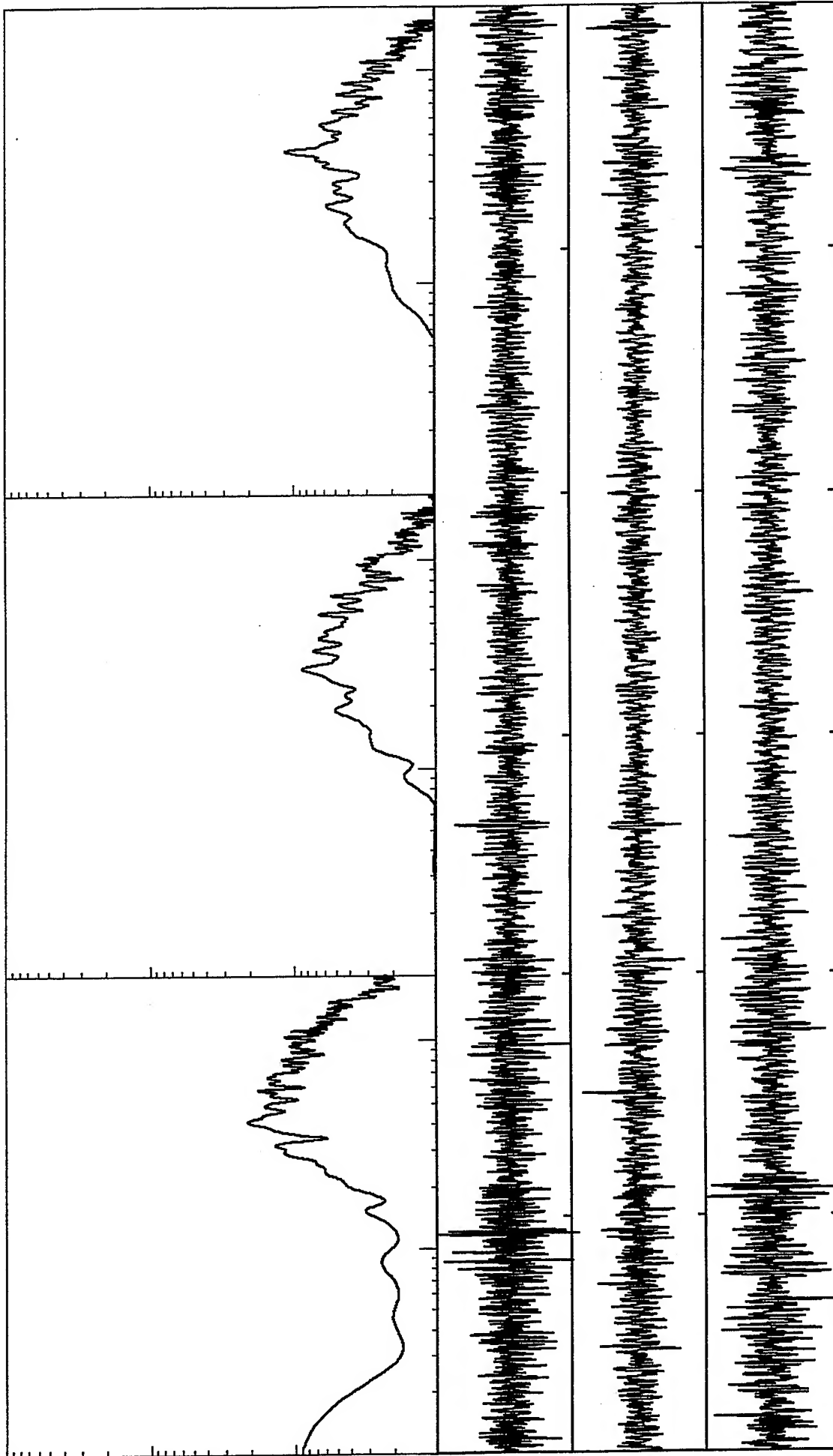


Spectral velocity values 0.1 to 20 Hz. Range: 1.E-4 to 1.E-1 cm/s  
 From top: ch1, 2, & 3: Max values of .295, .122, and .122 1.E-2 cm/s  
 Station 1: 60 s time window

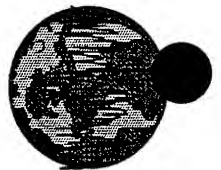


*VortexRock Consultants, Inc.*

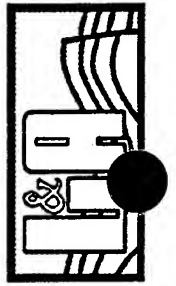


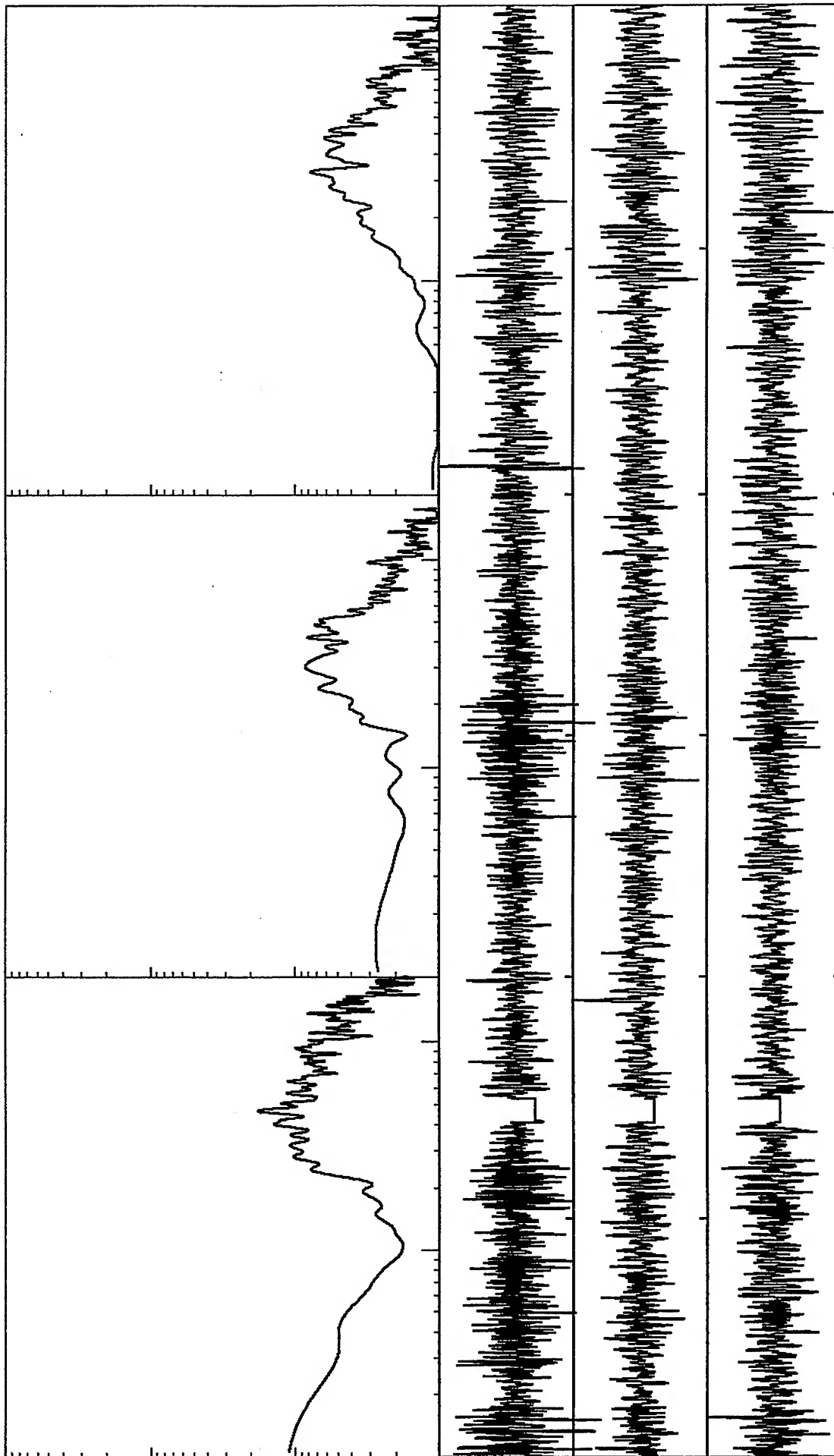


Spectral velocity values 0.1 to 20 Hz. Range: 1.E-4 to 1.E-1 cm/s  
 From top: ch1, 2, & 3: Max values of .341, .184, and .121 1.E-2 cm/s  
 Spectral velocity values 0.



*VortexRock Consultants, Inc.*

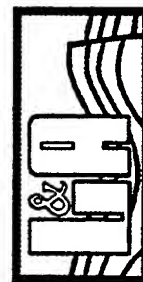


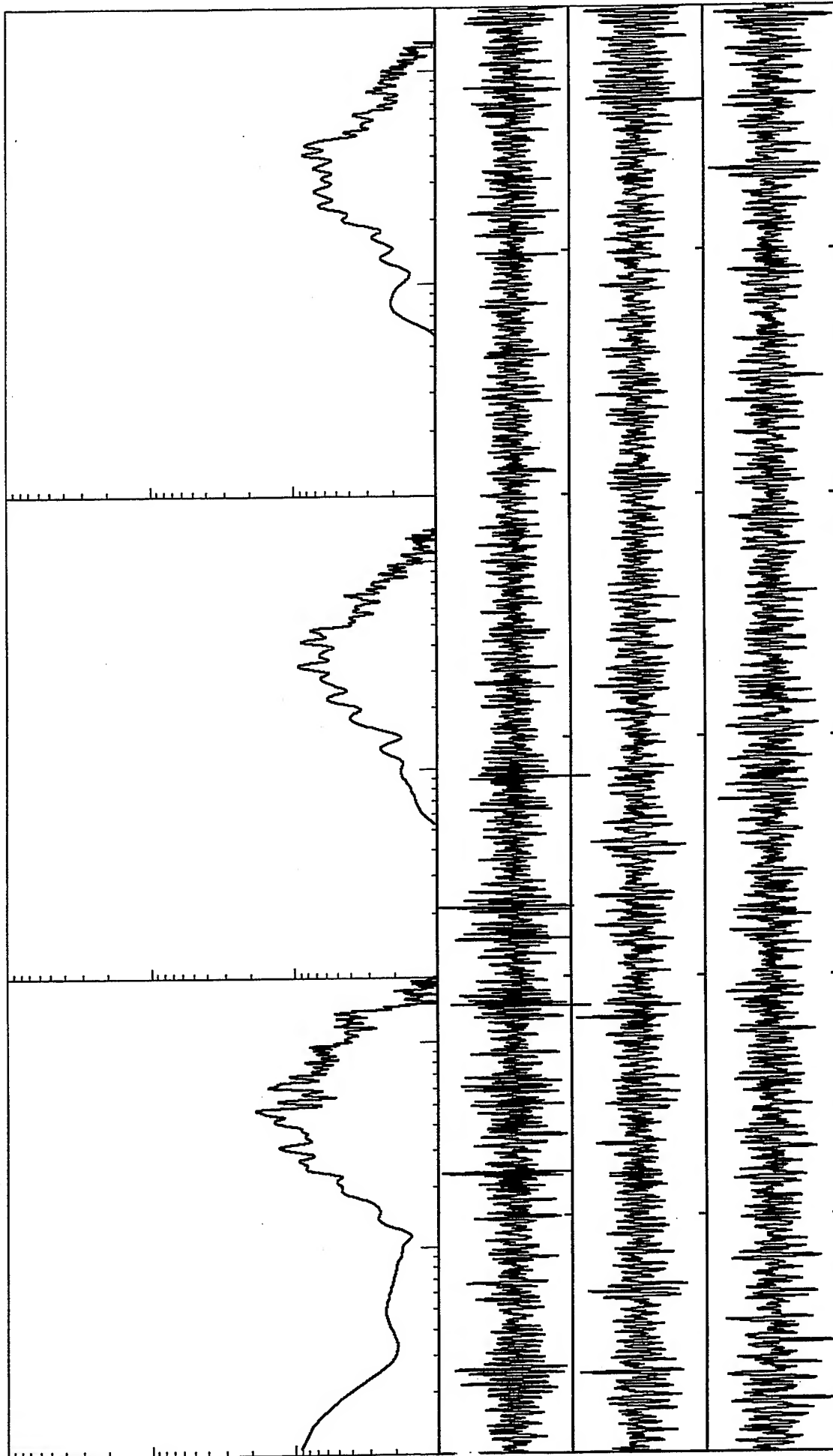


Spectral velocity values 0.1 to 20 Hz. Range: 1.E-4 to 1.E-1 cm/s  
 From top: ch1, 2, & 3: Max values of .220, .130, and .102 1.E-2 cm/s  
 Spectral velocity values 0.



*VortexRock Consultants, Inc.*

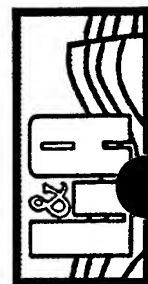




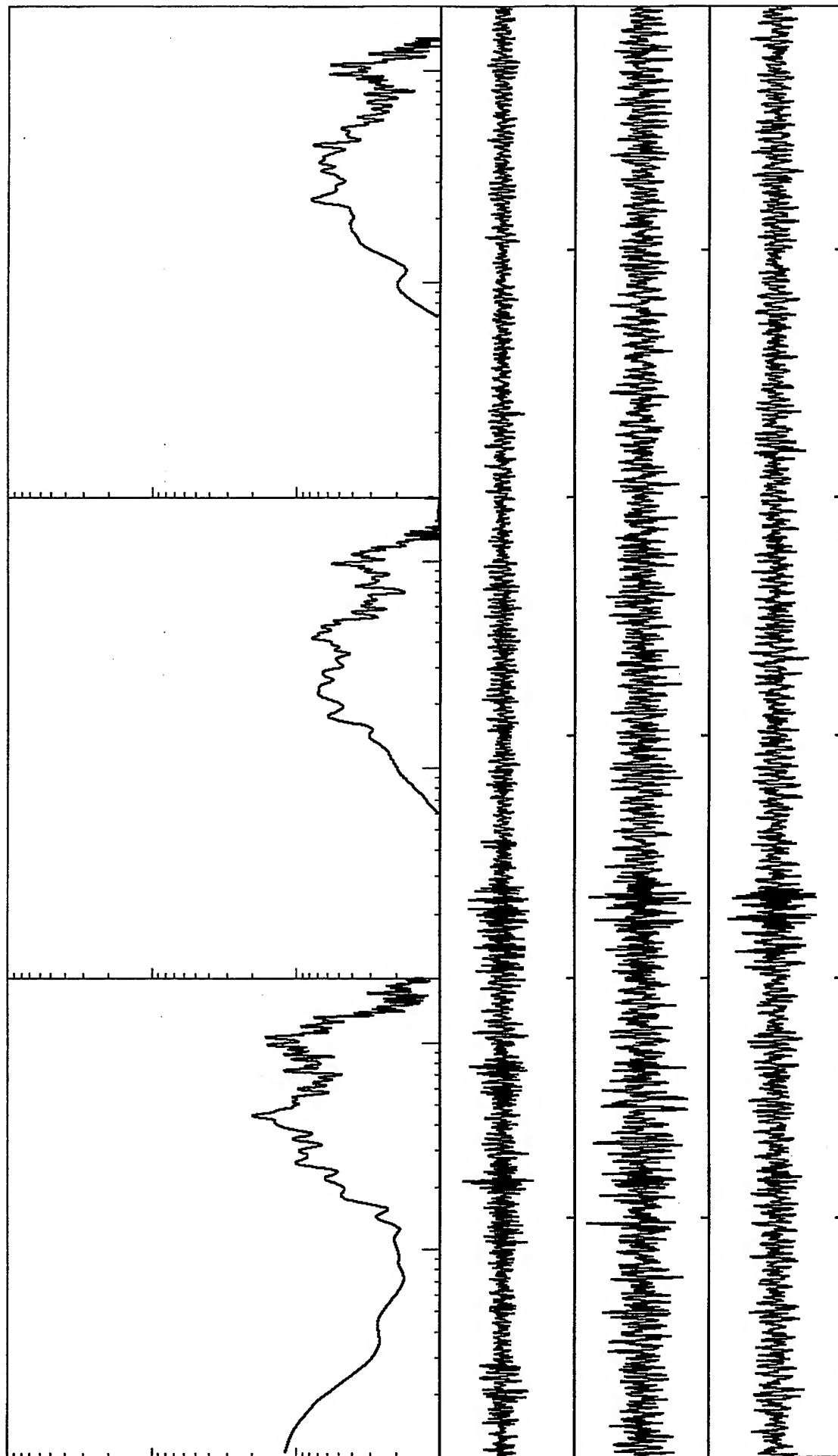
Spectral velocity values 0.1 to 20 Hz. Range: 1.E-4 to 1.E-1 cm/s  
 From top: ch1, 2, & 3: Max values of .221, .124, and .101 1.E-2 cm/s  
 Spectral velocity values 0.



*VortexRock Consultants, Inc.*



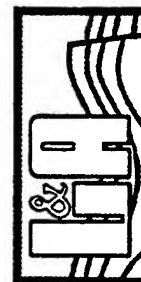


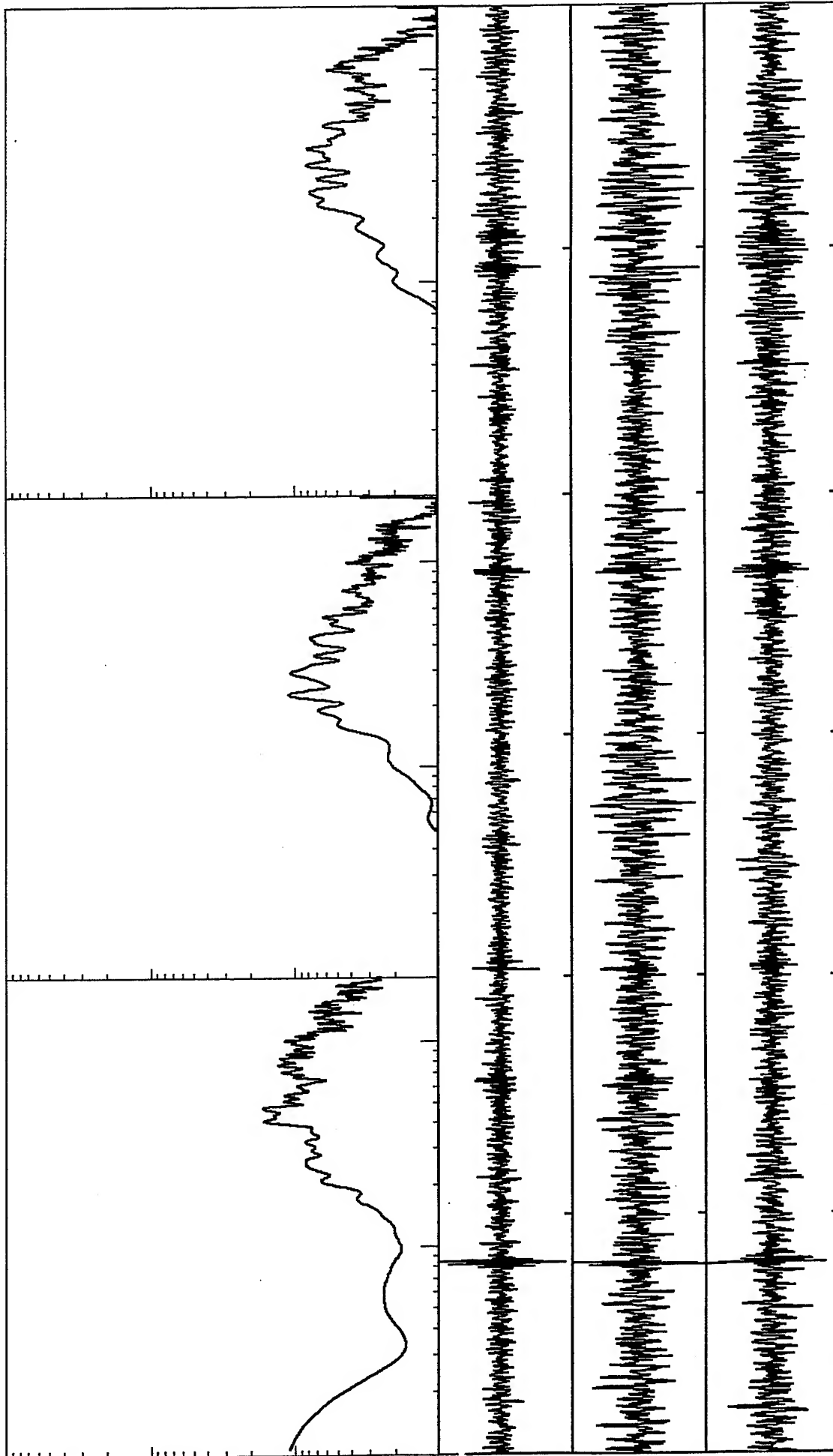


Spectral velocity values 0.1 to 20 Hz. Range: 1.E-4 to 1.E-1 cm/s  
 From top: ch1, 2, & 3: Max values of .588, .151, and .183 1.E-2 cm/s  
 Spectral velocity values 0.

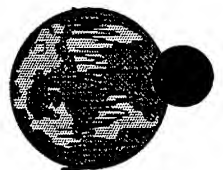


*VortexRock Consultants, Inc.*

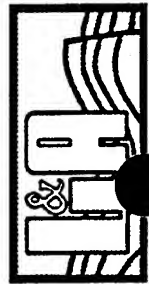




Spectral velocity values 0.1 to 20 Hz. Range: 1.E-4 to 1.E-1 cm/s  
 From top: ch1, 2, & 3: Max values of .588, .151, and .183 1.E-2 cm/s  
 Spectral velocity values 0.



*VortexRock Consultants, Inc.*



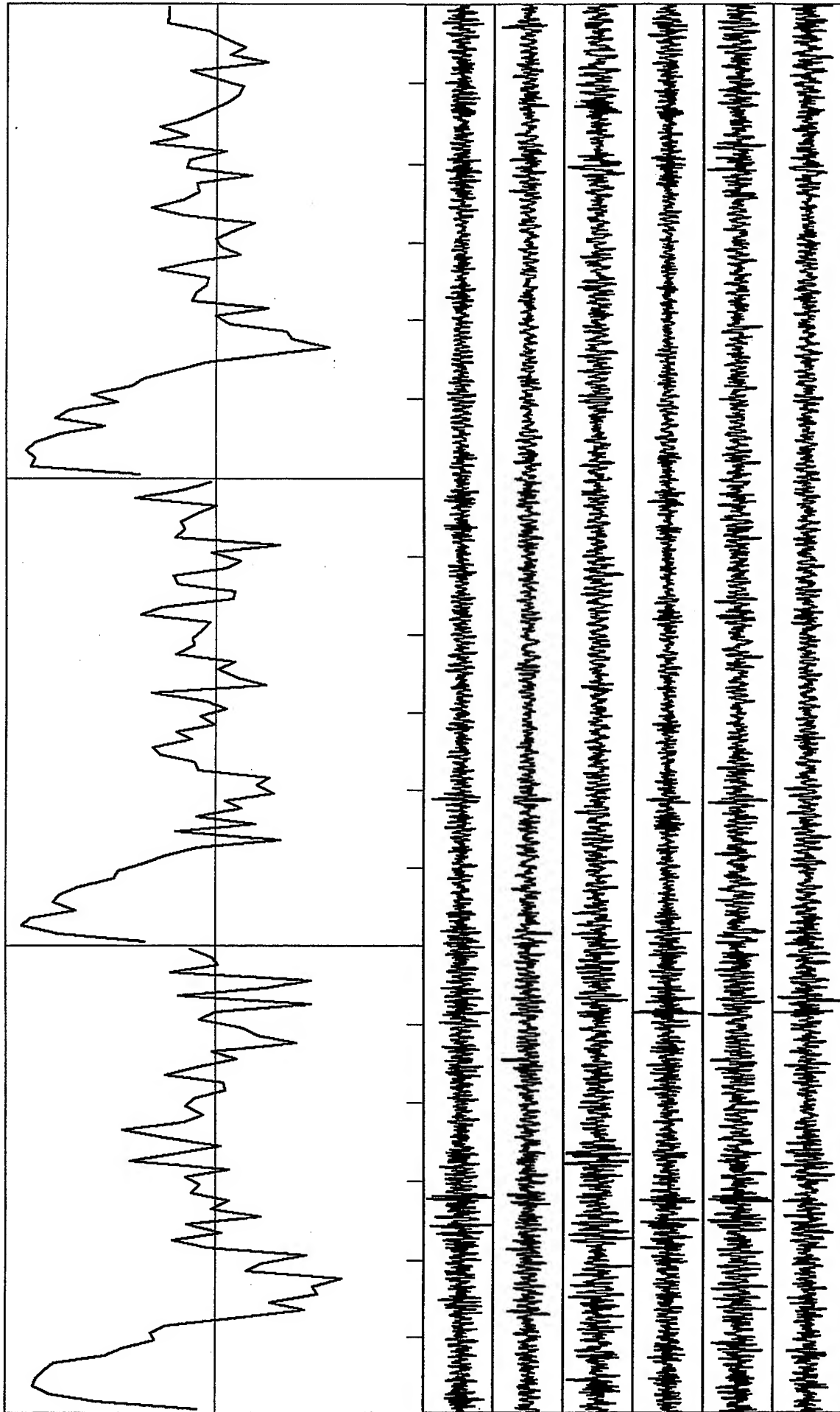
***Appendix B***  
***Section II***

***The Correlation Coefficients for Selected Records from  
Experiments No. 3 at the Parking Lot of Mazda Storage  
Area, Port Hueneme, Oxnard, California***



***VortexRock Consultants, Inc.***



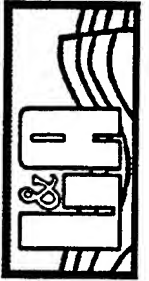


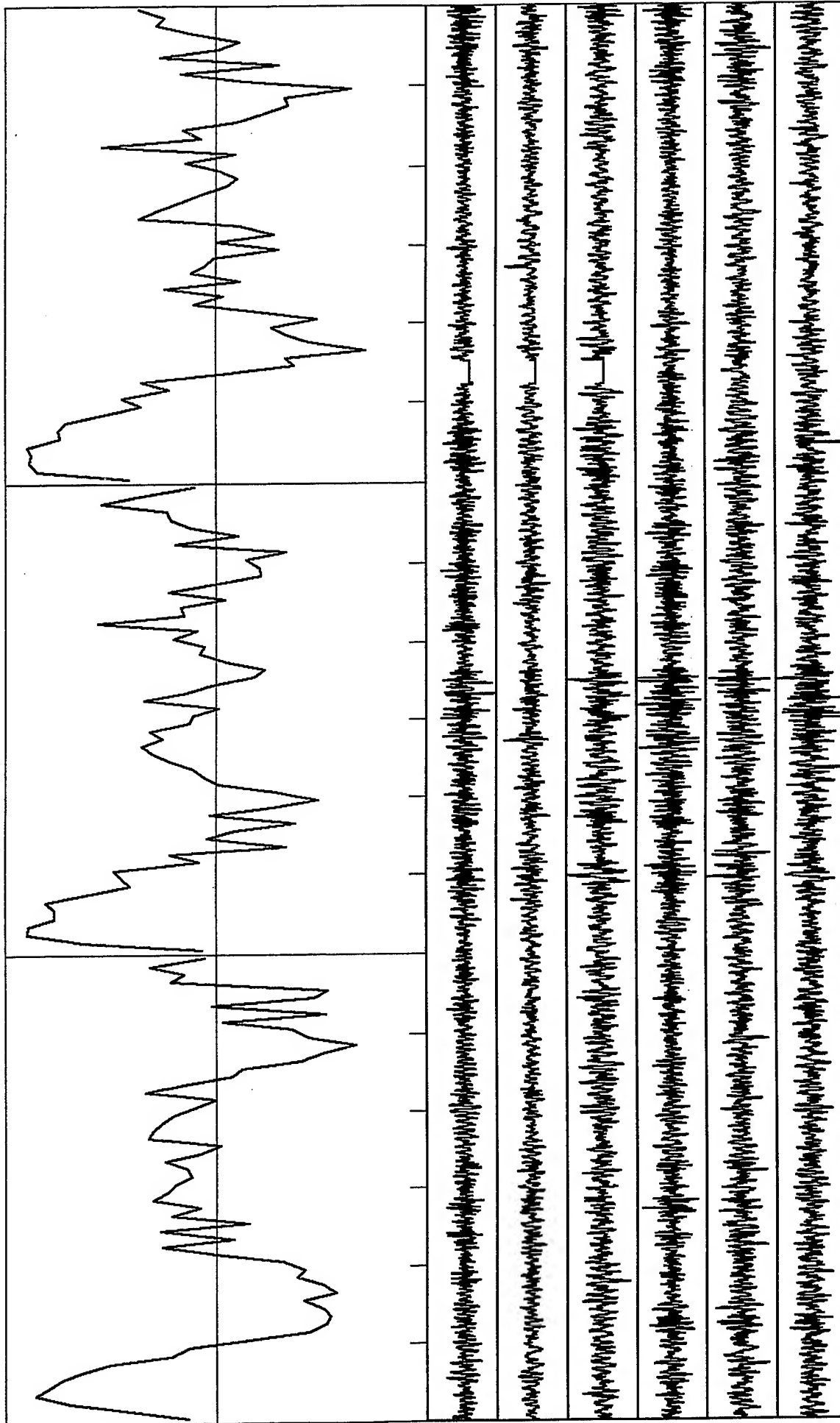
B-II-1

Correlation Coefficients: Scale -1 to +1; freq range: 0 to 30.0 Hz; Radius: 14 m  
 St. 0 & 1: Vertical & horizontal components; 50 s time window



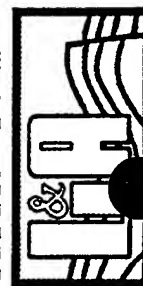
*VortexRock Consultants, Inc.*

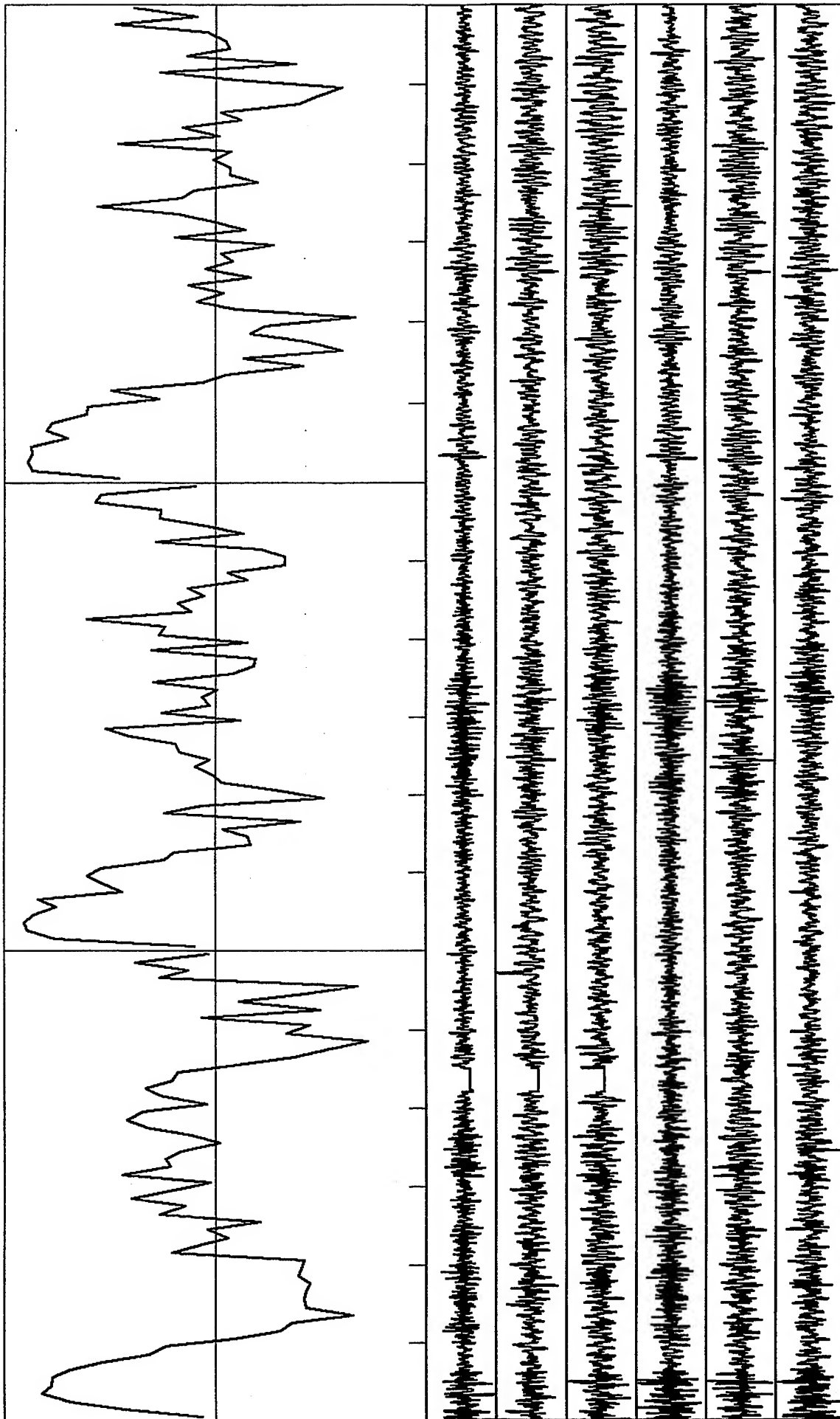




Correlation Coefficients: Scale -1 to +1; freq range: 0 to 30.0 Hz; Radius: 14 m  
 St. 0 & 1: Vertical & horizontal components: 60 s time window

*VortexRock Consultants, Inc.*



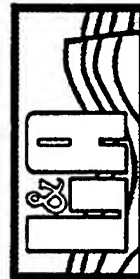


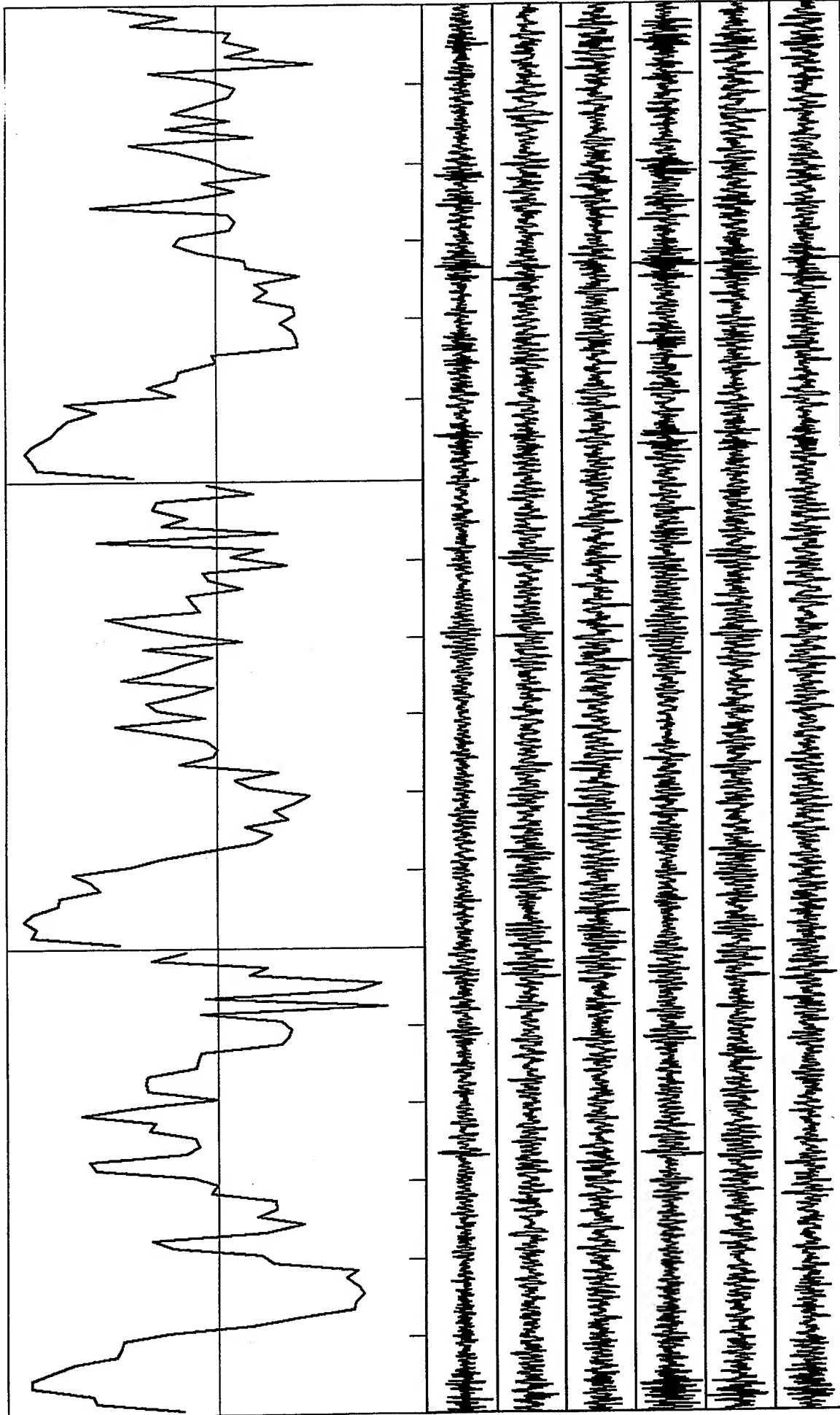
B-13



Correlation Coefficients: Scale -1 to +1; freq range: 0 to 30.0 Hz; Radius: 14 m  
 St. 0 & 1: Vertical & horizontal components; 60 s time window

*VortexRock Consultants, Inc.*

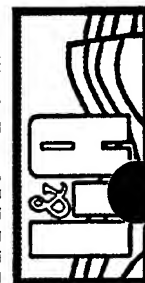


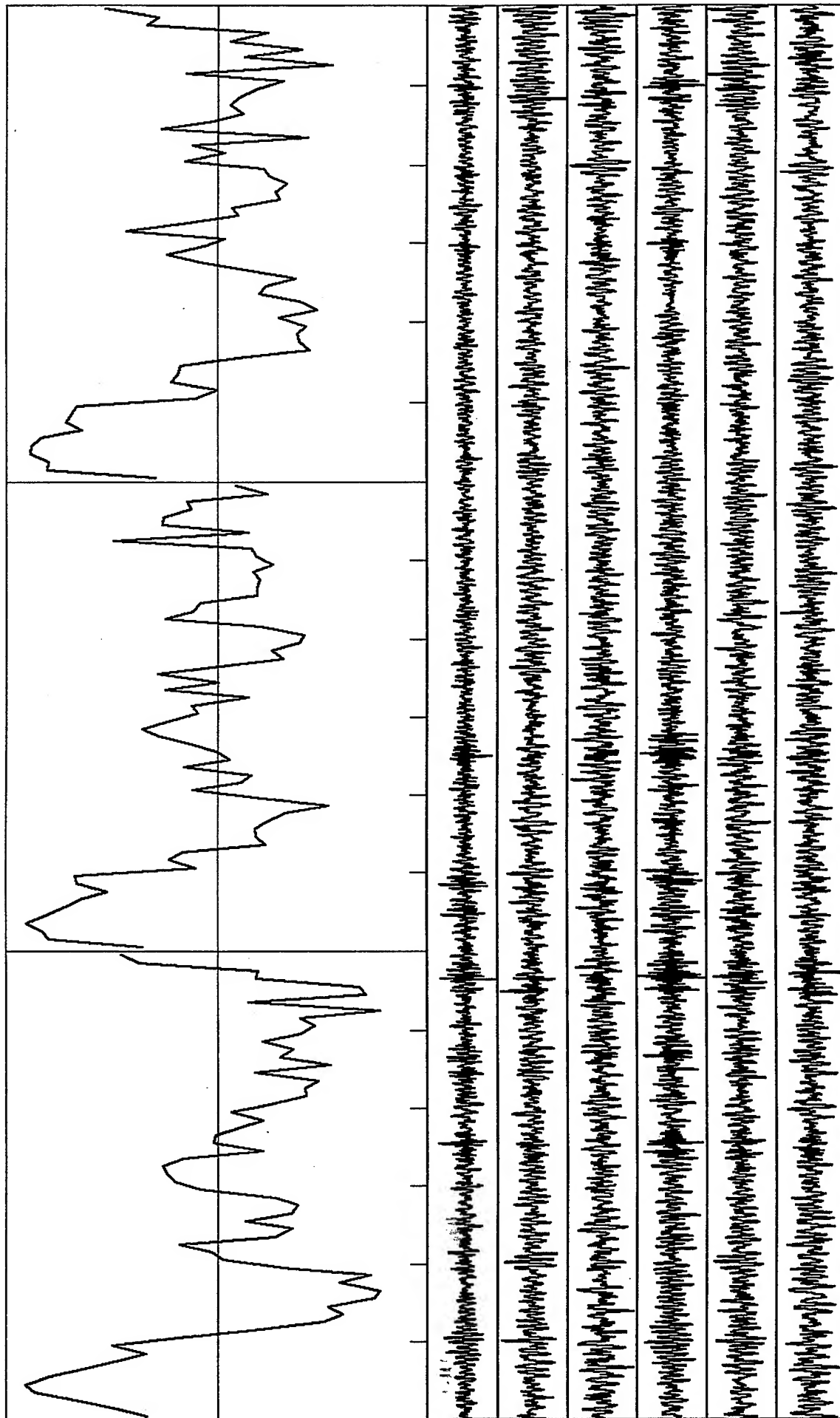


Correlation Coefficients: Scale -1 to +1; freq range: 0 to 30.0 Hz; Radius: 14 m  
 St. 0 & 1: Vertical & horizontal components: 60 s time window



*VortexRock Consultants, Inc.*



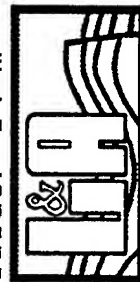


B-II-5

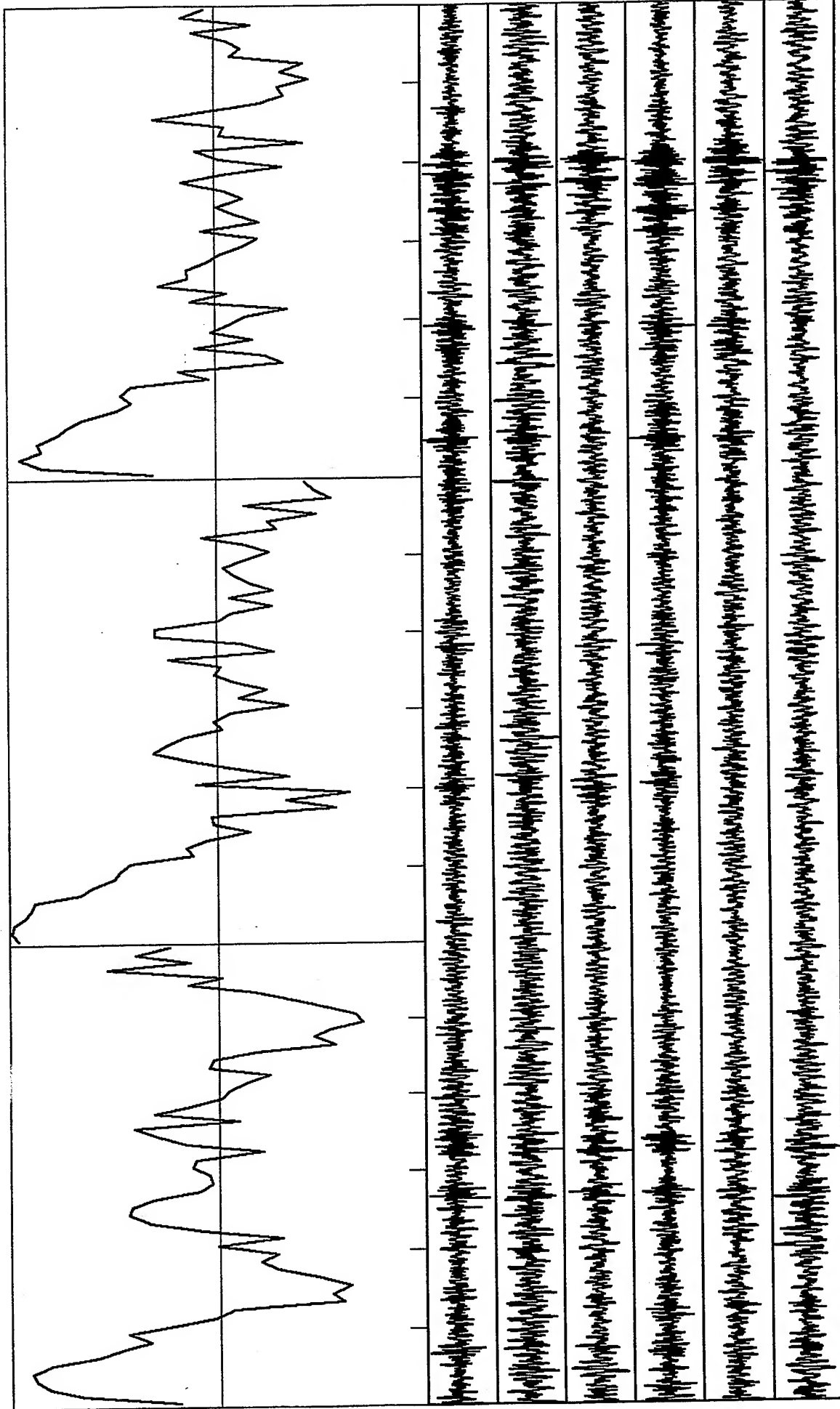


Correlation Coefficients: Scale -1 to +1; freq range: 0 to 30.0 Hz; Radius: 14 m  
 St. 0 & 1: Vertical & horizontal components; 60 s time window

*VortexRock Consultants, Inc.*





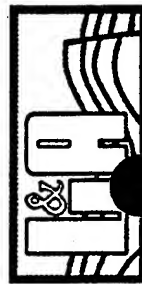


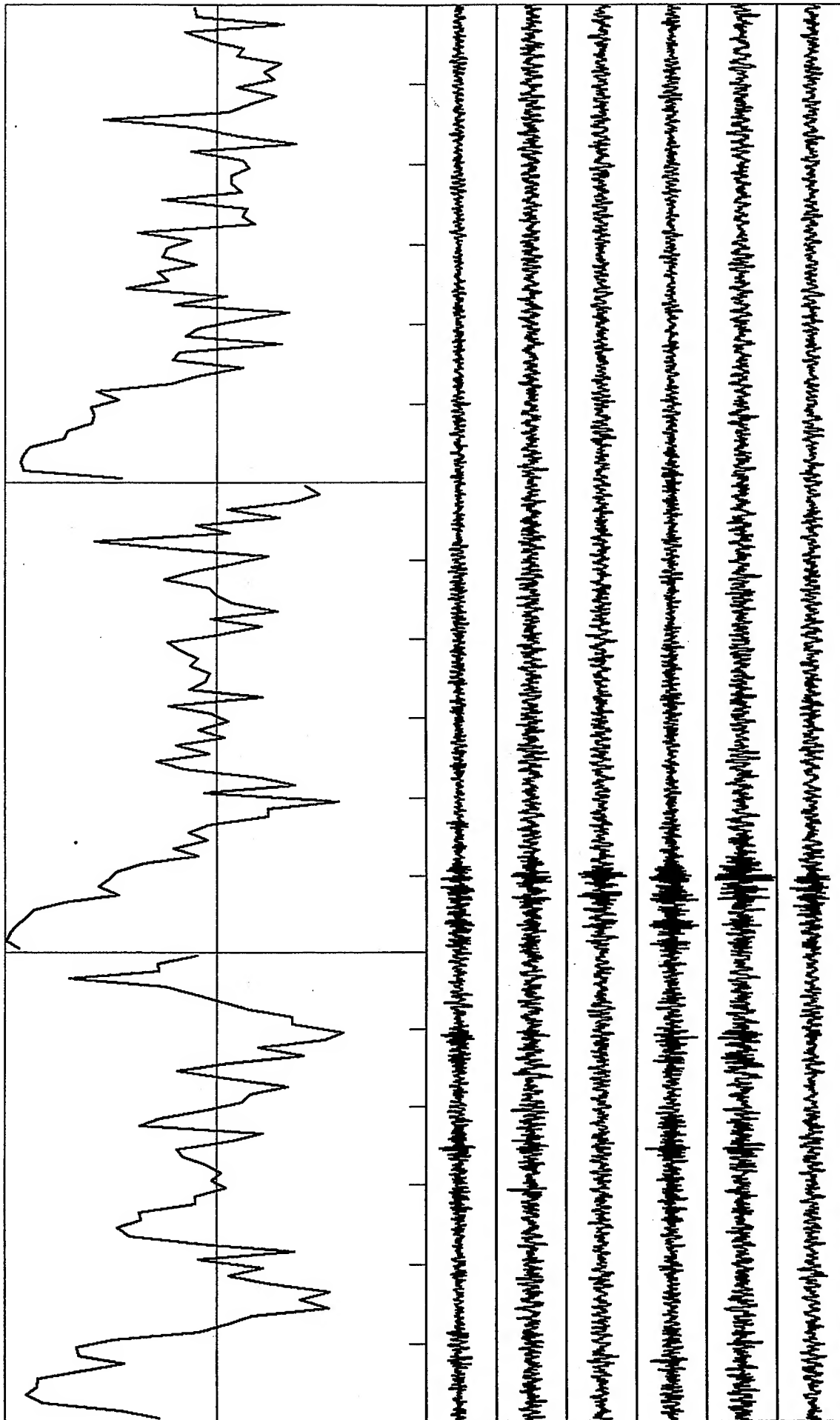
B-4-6



Correlation Coefficients: Scale -1 to +1; freq range: 0 to 30.0 Hz; Radius: 14 m  
 St. 0 & 1: Vertical & horizontal components: 60 s time window

*VortexRock Consultants, Inc.*





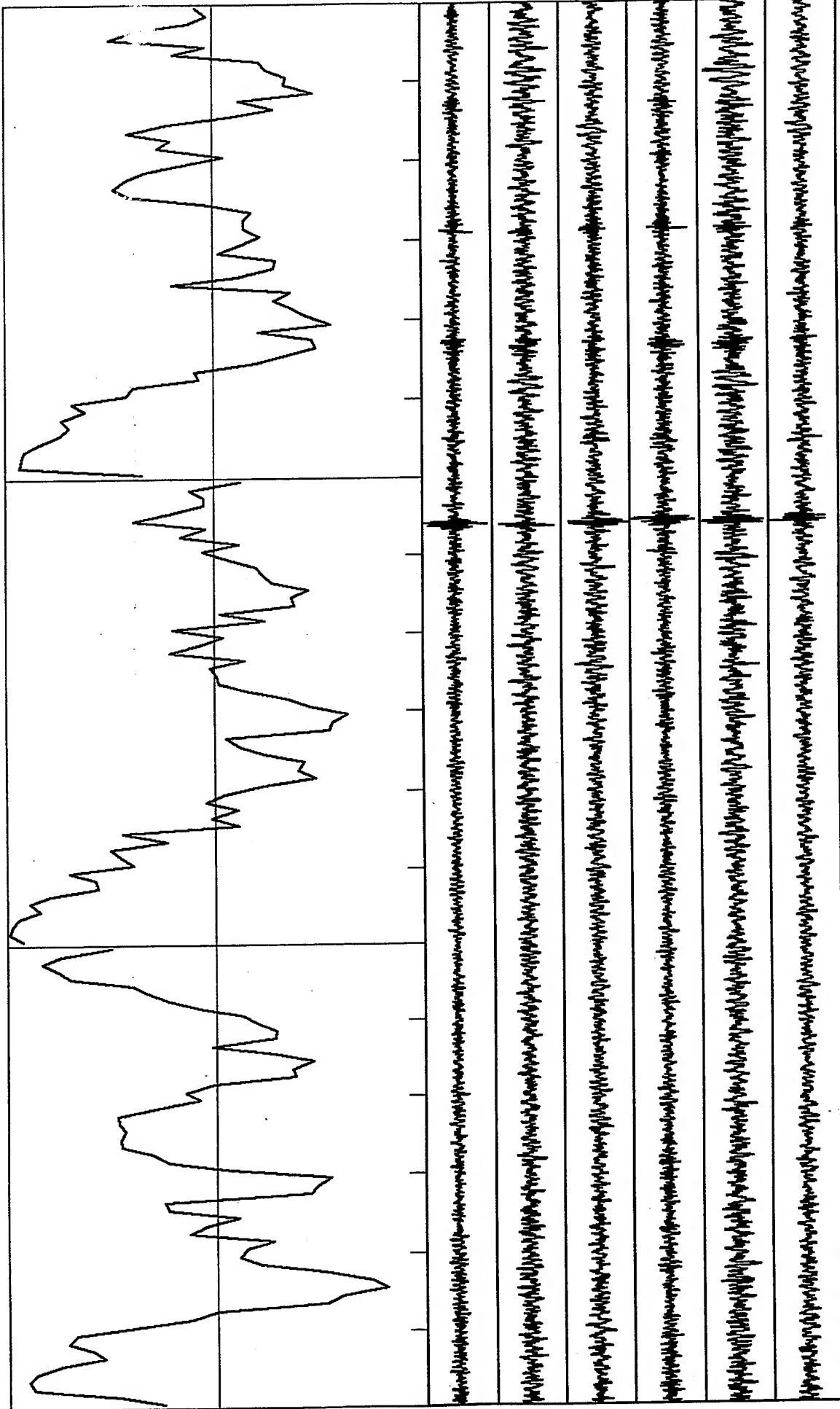
B-17



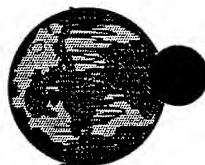
Correlation Coefficients: Scale -1 to +1; freq range: 0 to 30.0 Hz; Radius: 14 m  
 St. 0 & 1: Vertical & horizontal components: 60 s time window

*VortexRock Consultants, Inc.*



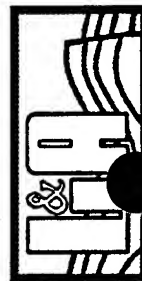


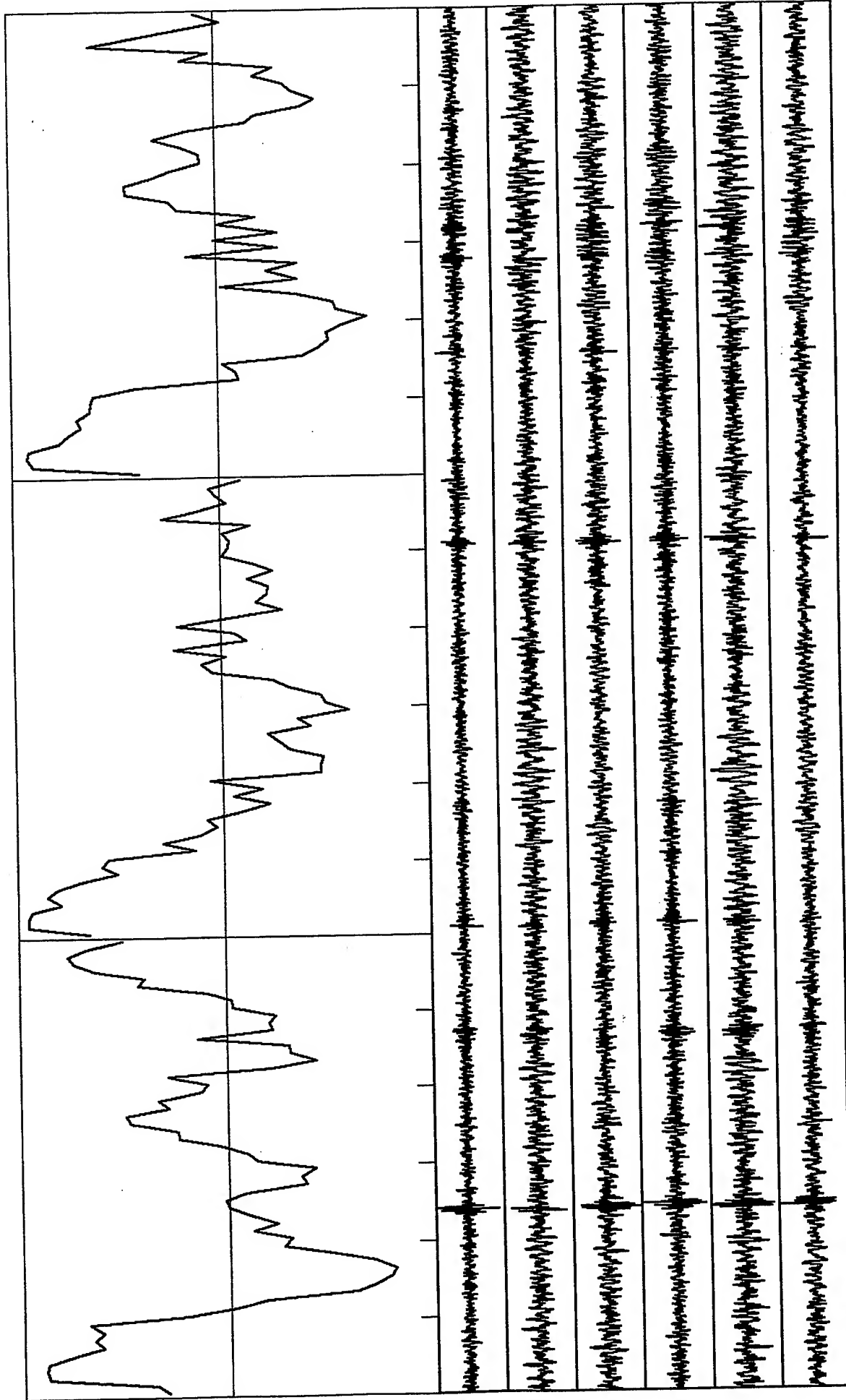
B-1-8



Correlation Coefficients: Scale -1 to +1; freq range: 0 to 30.0 Hz; Radius: 14 m  
 St. 0 & 1: Vertical & horizontal components; 60 s time window

*VortexRock Consultants, Inc.*



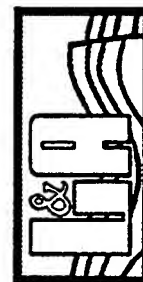


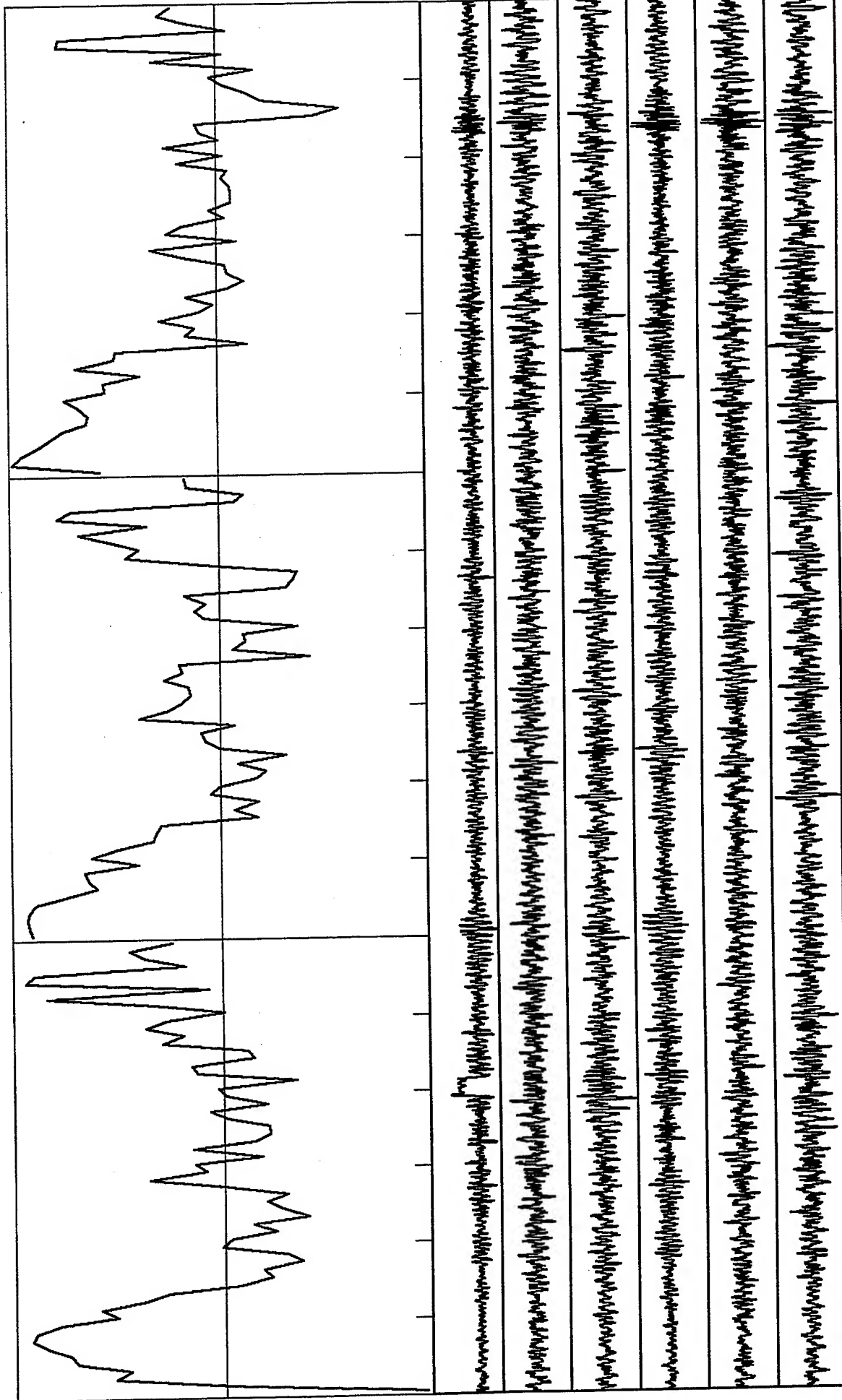
B-9

Correlation Coefficients: Scale -1 to +1; freq range: 0 to 30.0 Hz; Radius: 14 m  
 St. 0 & 1: Vertical & horizontal components: 60 s time window



*VortexRock Consultants, Inc.*



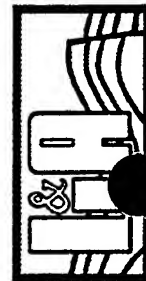


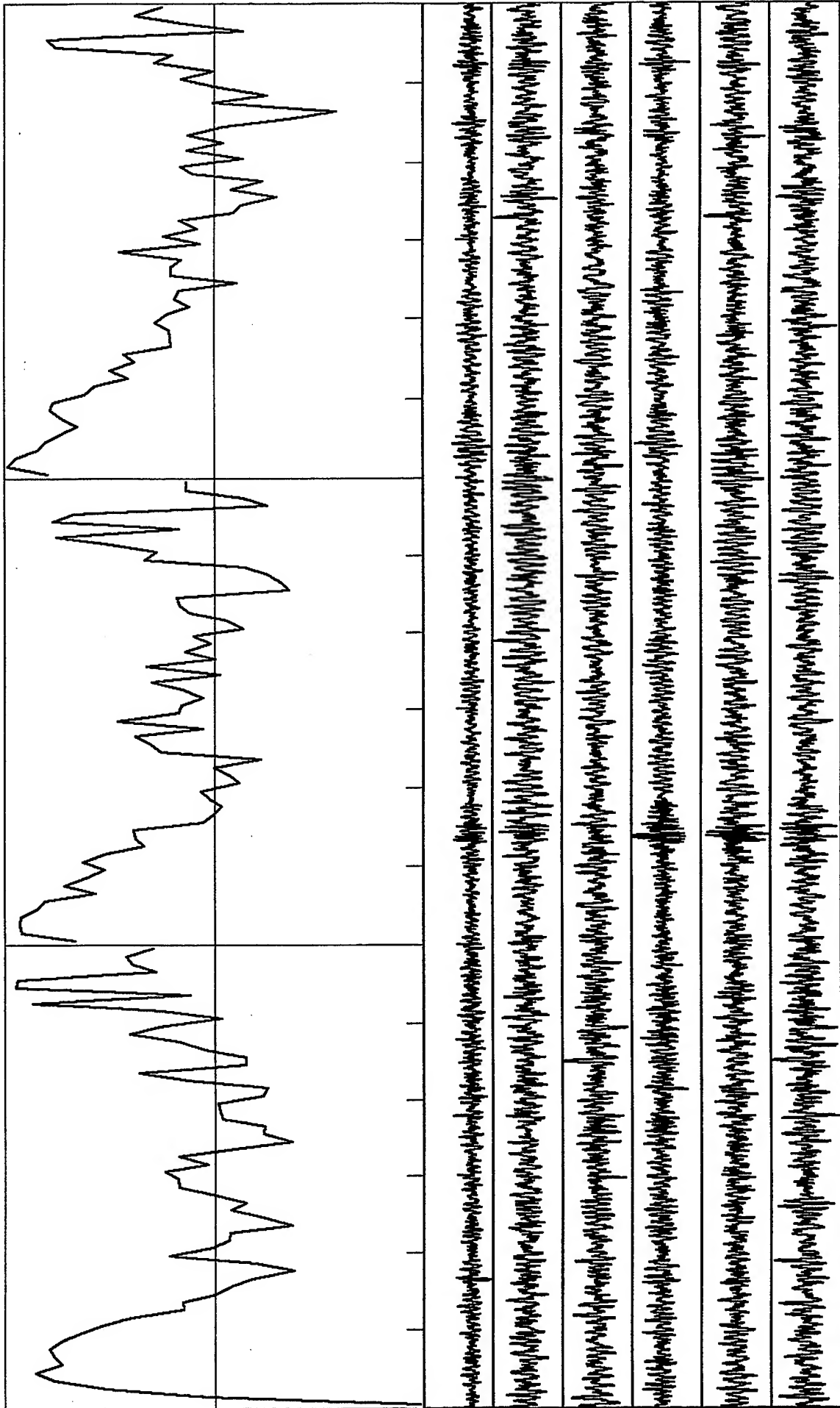
B-#10

Correlation Coefficients: Scale -1 to +1; freq range: 0 to 30.0 Hz; Radius: 14 m  
 St. 0 & 1: Vertical & horizontal components; 60 s time window



*VortexRock Consultants, Inc.*

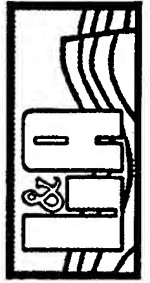




B-II-11



Correlation Coefficients: Scale -1 to +1; freq range: 0 to 30.0 Hz; Radius: 14 m  
 St. 0 & 1: Vertical & horizontal components; 60 s time window



*VortexRock Consultants, Inc.*

## ***Appendix C***

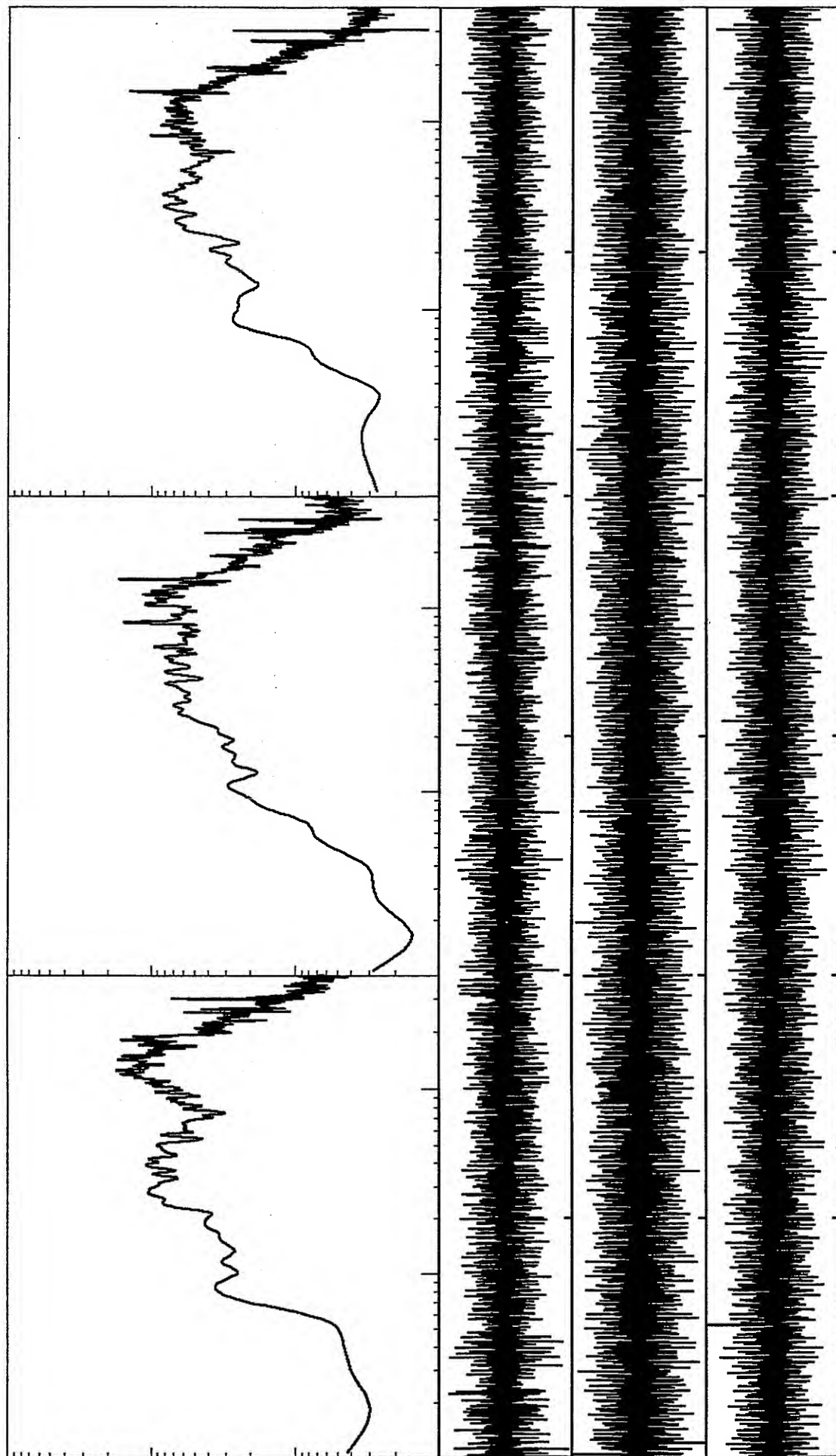
### ***Section I***

***Time Histories and Spectral Parameters for Selected  
Records from Experiments No. 4 t the Basketball Court of  
the McBride School, Los Angeles, California***



***VortexRock Consultants, Inc.***

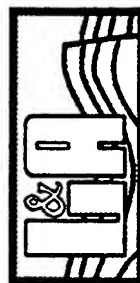




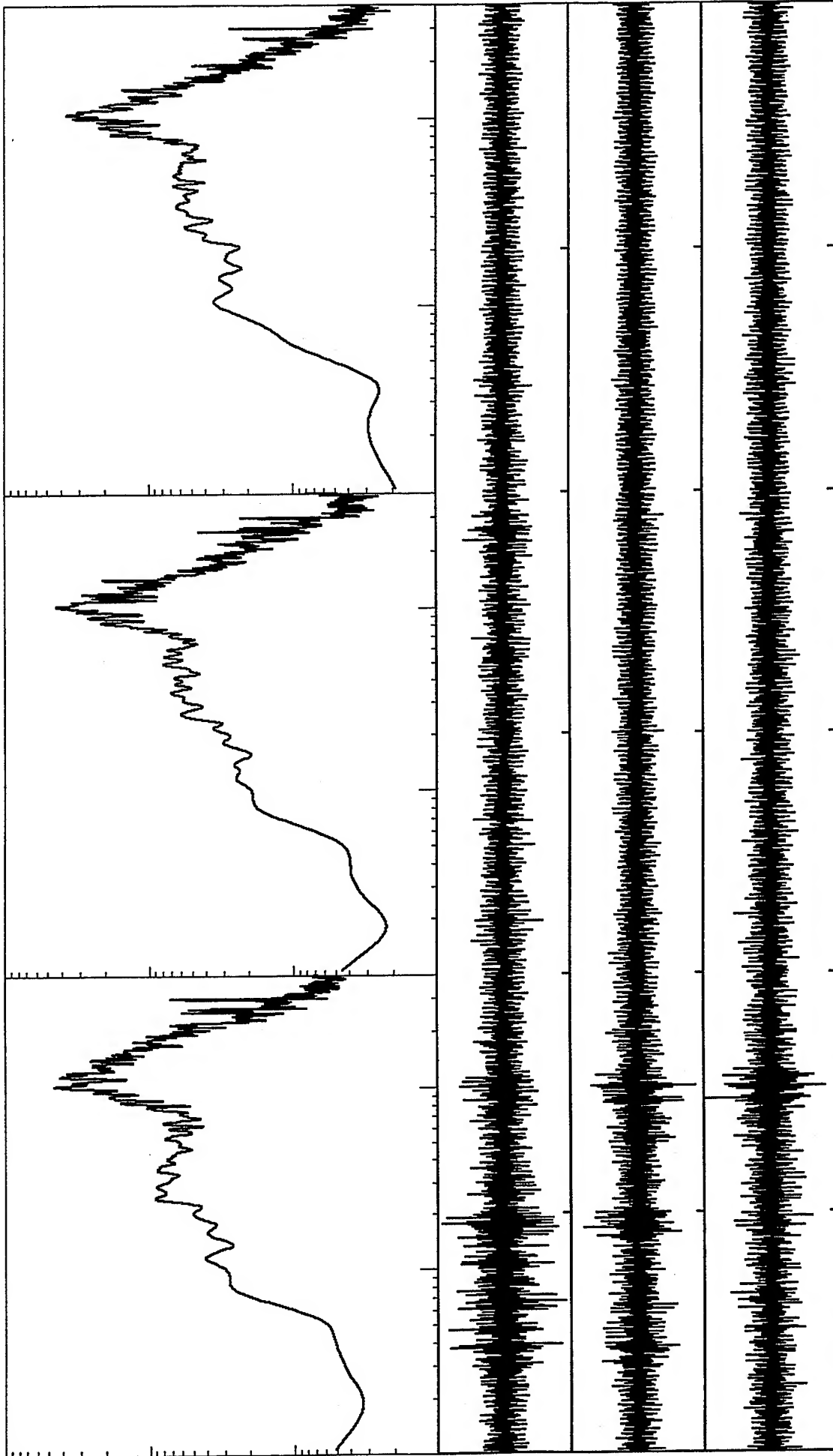
Spectral velocity values 0.1 to 40 Hz. Range: 1.E-6 to 1.E-3 cm/s  
 From top: ch1, 2, & 3: Max values of .567, .539, and .376 1.E-3 cm/s  
 Station 1: 60 s time window



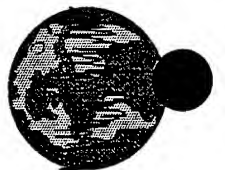
*VortexRock Consultants, Inc.*



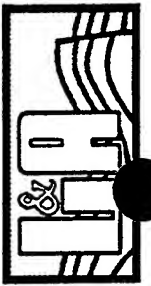


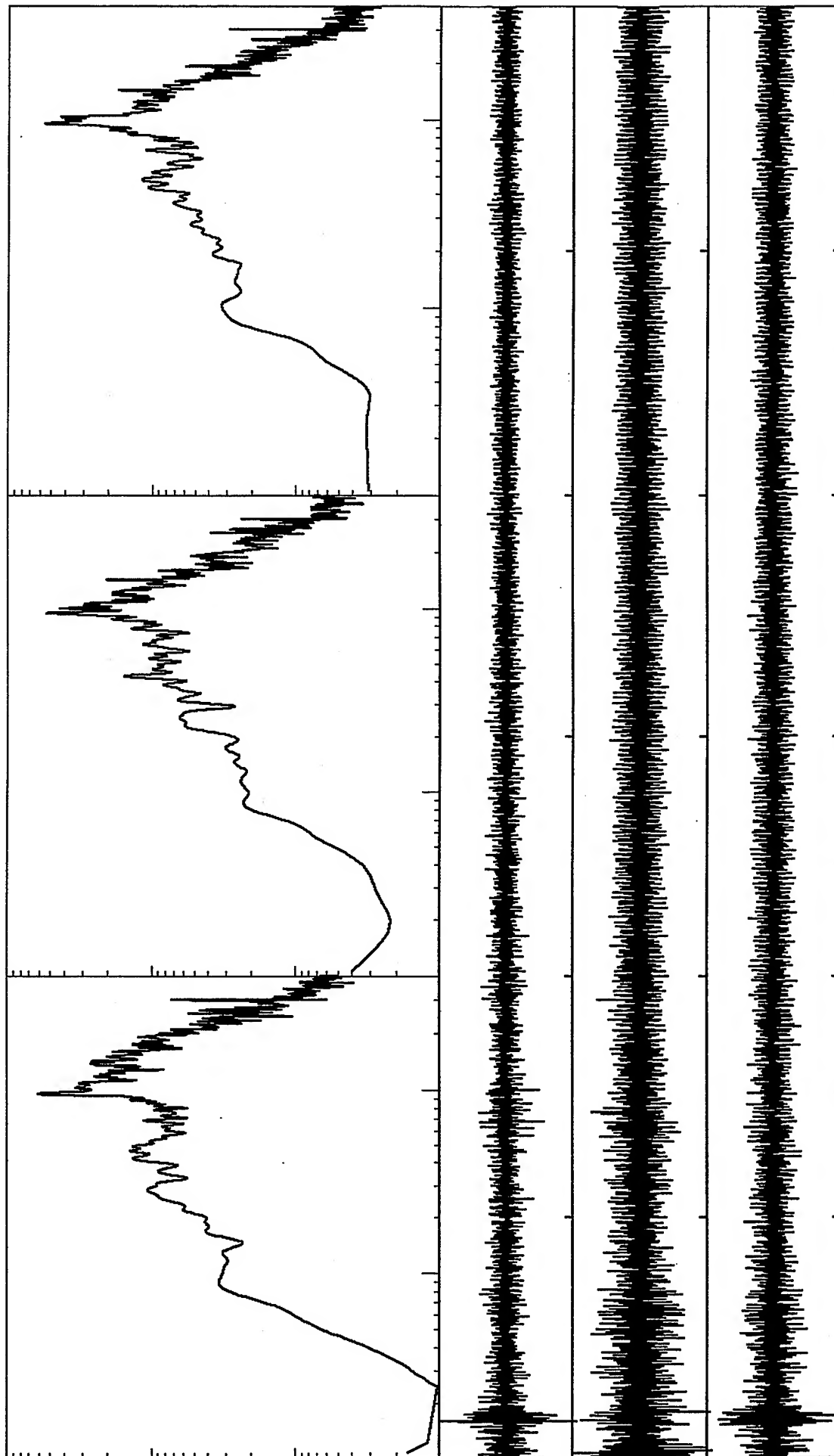


Spectral velocity values 0.1 to 40 Hz. Range: 1.E-6 to 1.E-3 cm/s  
 From top: ch1, 2, & 3: Max values of .104, .133, and .074 1.E-2 cm/s  
 Station 1: 60 s time window



*VortexRock Consultants, Inc.*



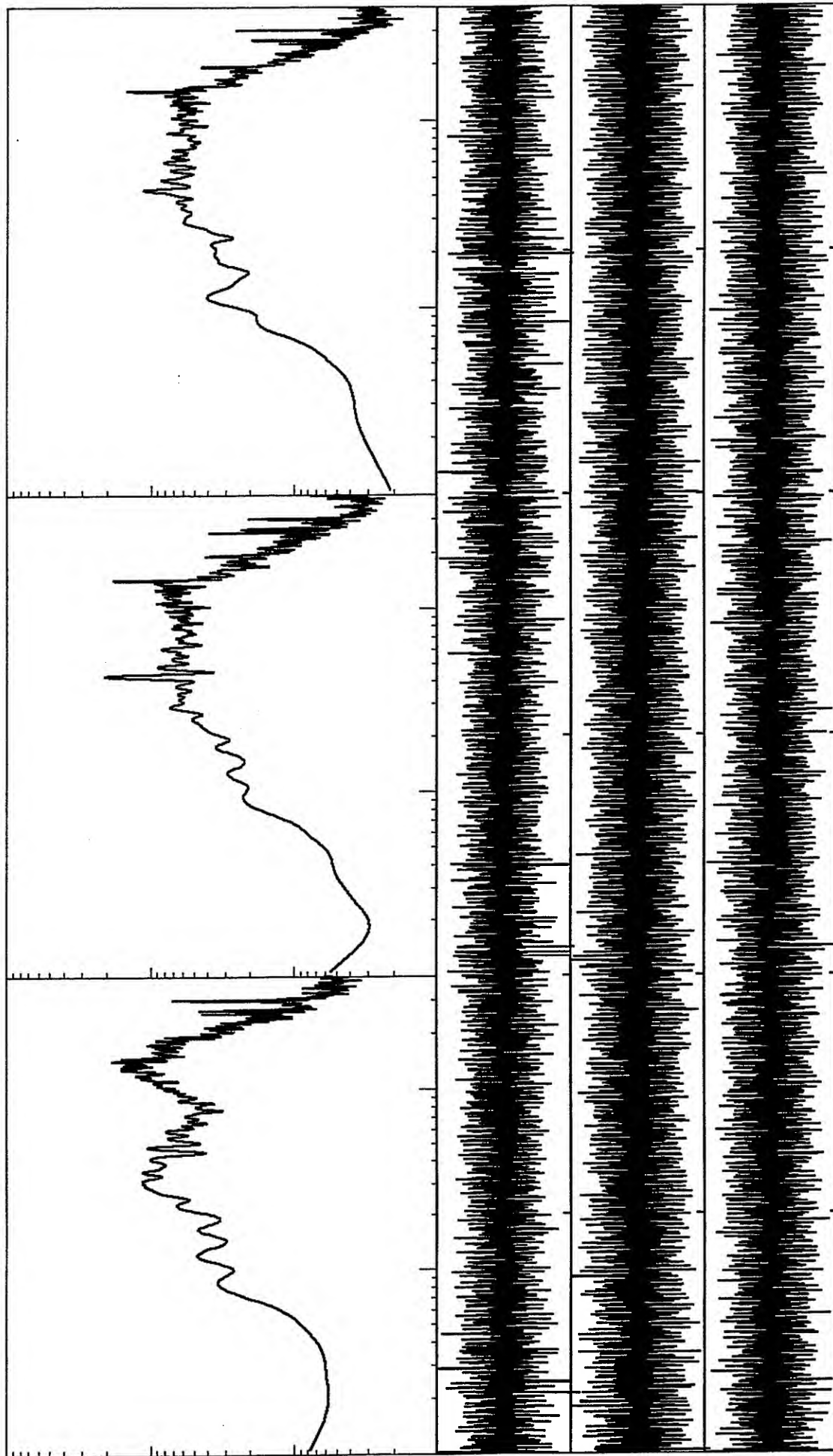


Spectral velocity values 0.1 to 40 Hz. Range: 1.E-6 to 1.E-2 cm/s  
 From top: ch1, 2, & 3: Max values of .154, .104, and .084 1.E-2 cm/s  
 Station 1: 50 s time window



*VortexRock Consultants, Inc.*

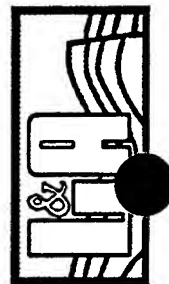


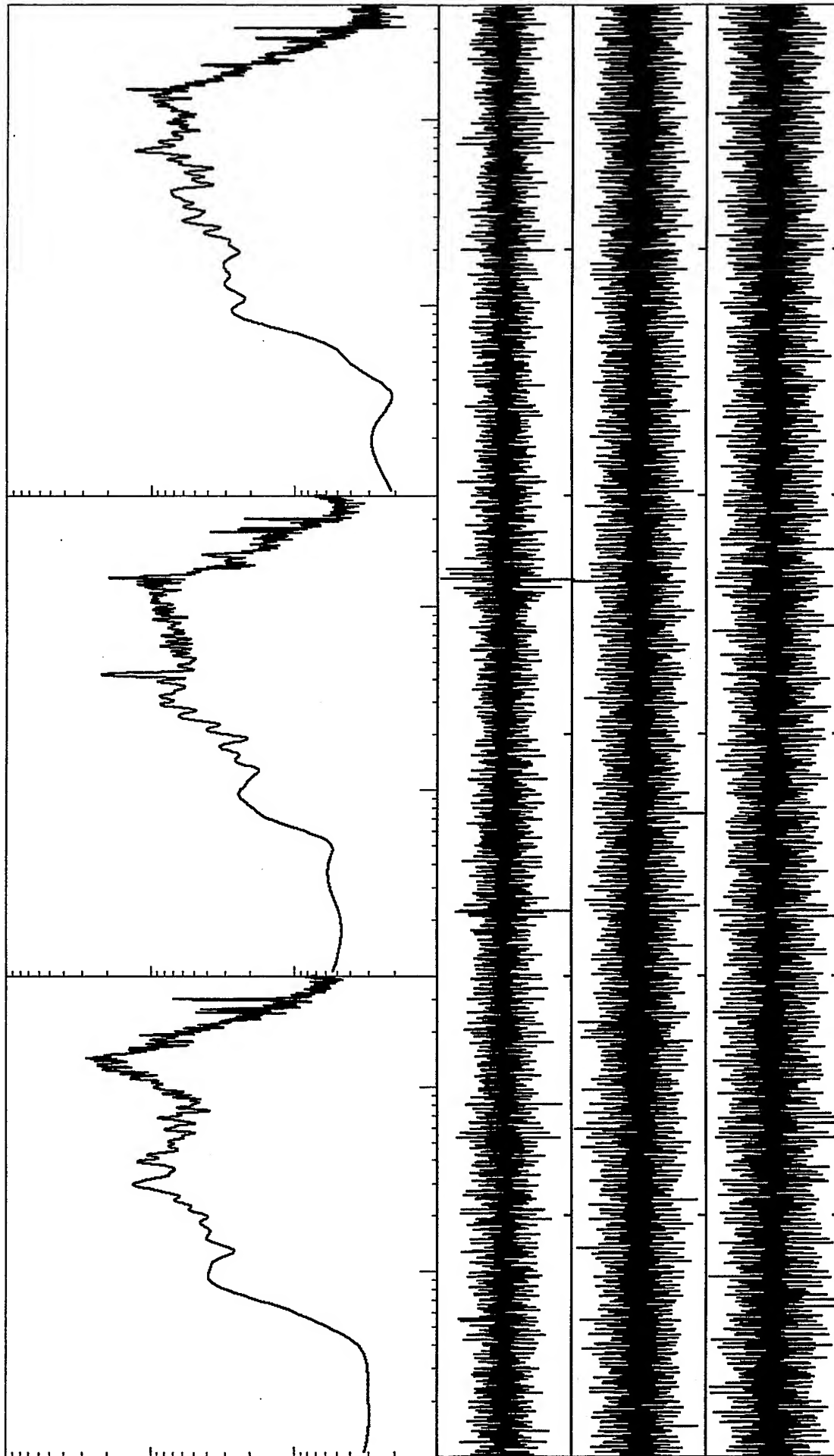


Spectral velocity values 0.1 to 40 Hz. Range: 1.E-6 to 1.E-3 cm/s  
 From top: ch1, 2, & 3: Max values of .485, .500, and .326 1.E-3 cm/s  
 Station 1: 60 s time window



*VortexRock Consultants, Inc.*

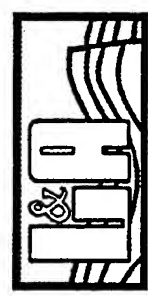


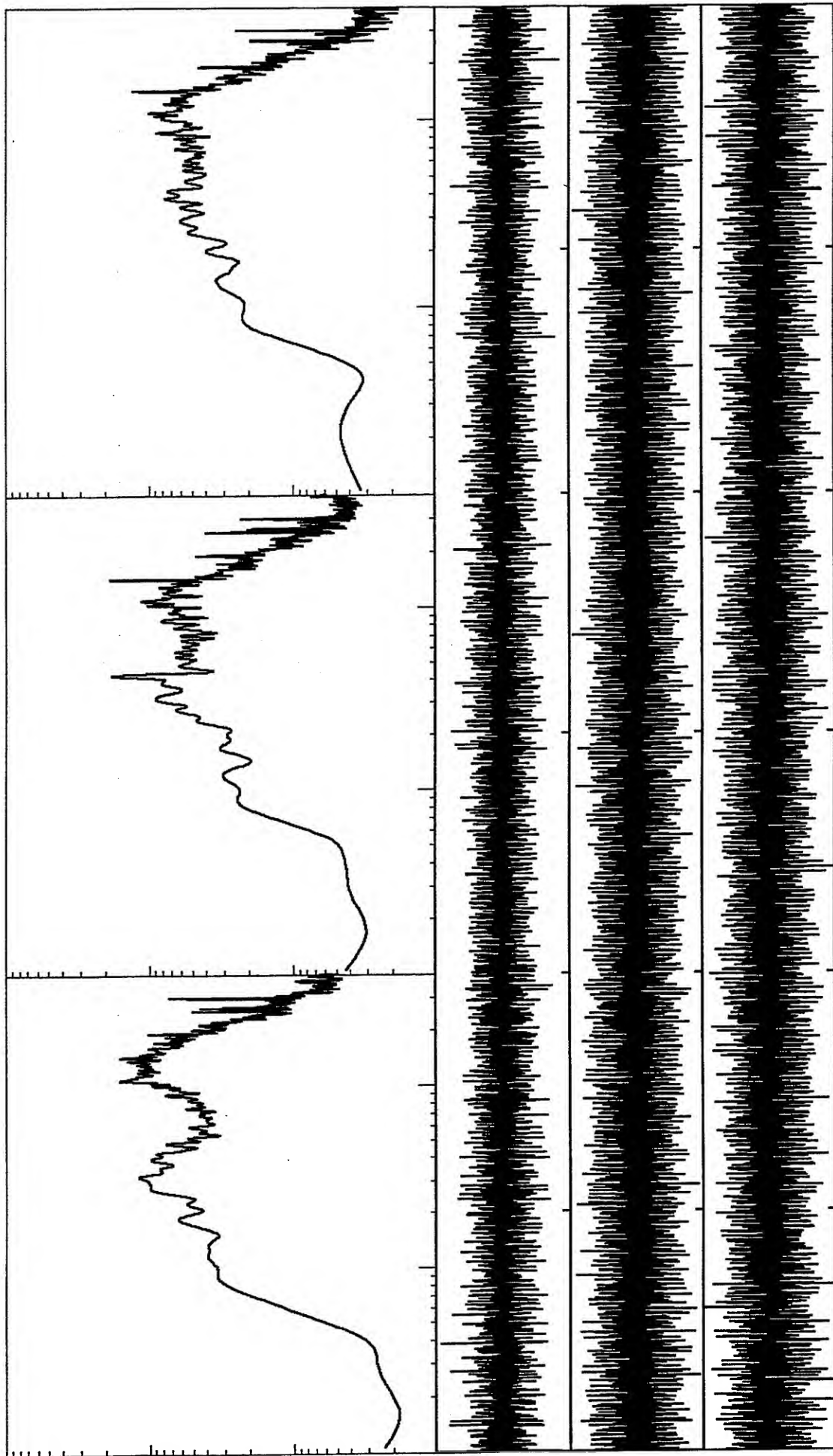


Spectral velocity values 0.1 to 40 Hz. Range: 1.E-6 to 1.E-3 cm/s  
 From top: ch1, 2, & 3: Max values of .678, .597, and .326 1.E-3 cm/s  
 Station 1: 50 s time window



*VortexRock Consultants, Inc.*

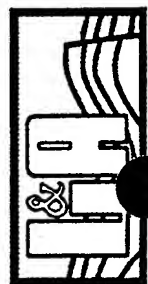


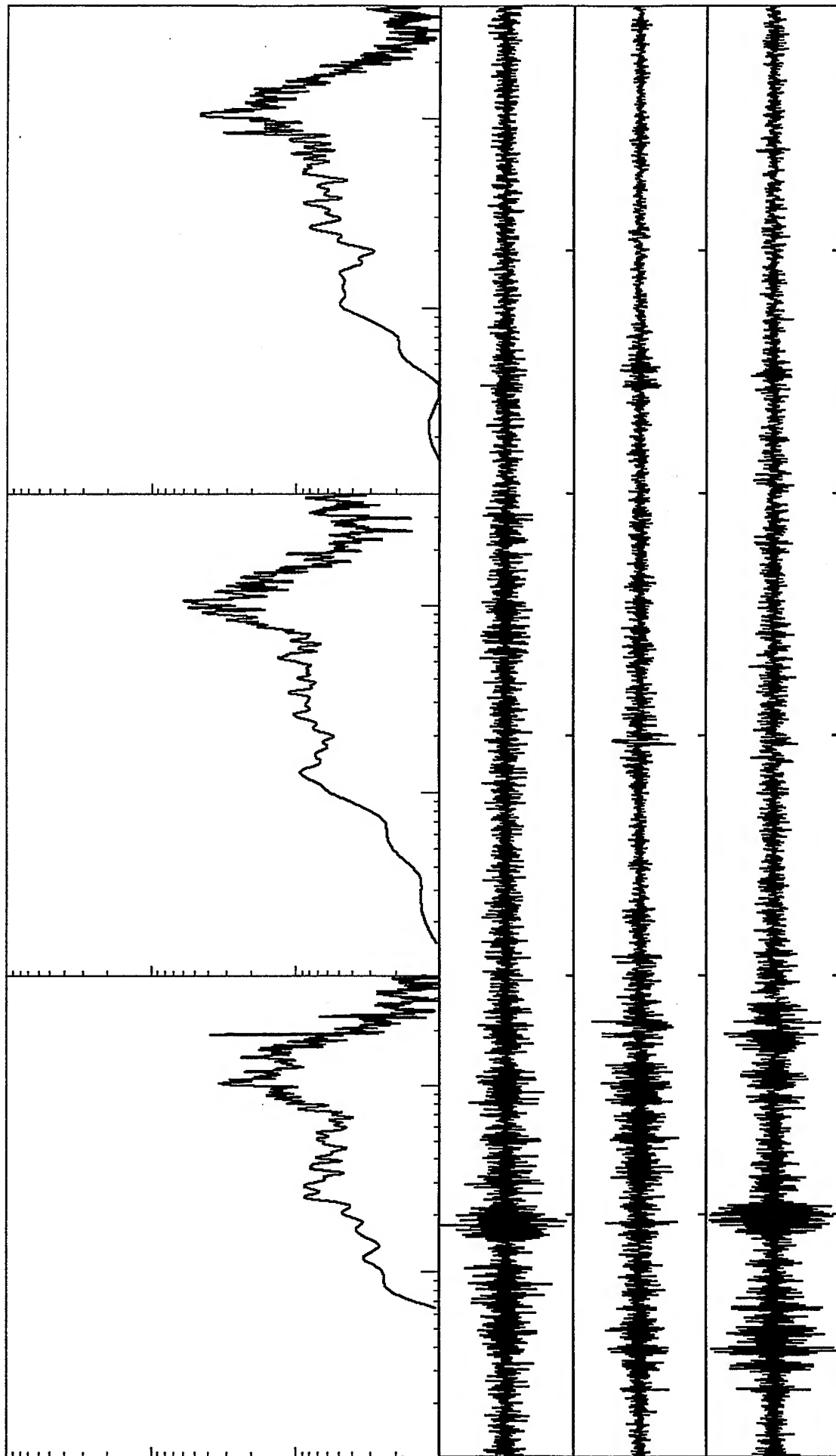


Spectral velocity values 0.1 to 40 Hz. Range:  $1.E-6$  to  $1.E-3$  cm/s  
 From top: ch1, 2, & 3: Max values of .596, .525, and .319  $1.E-3$  cm/s  
 Station 1: 60 s time window



*VortexRock Consultants, Inc.*

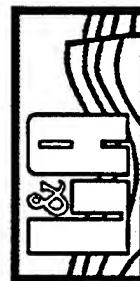


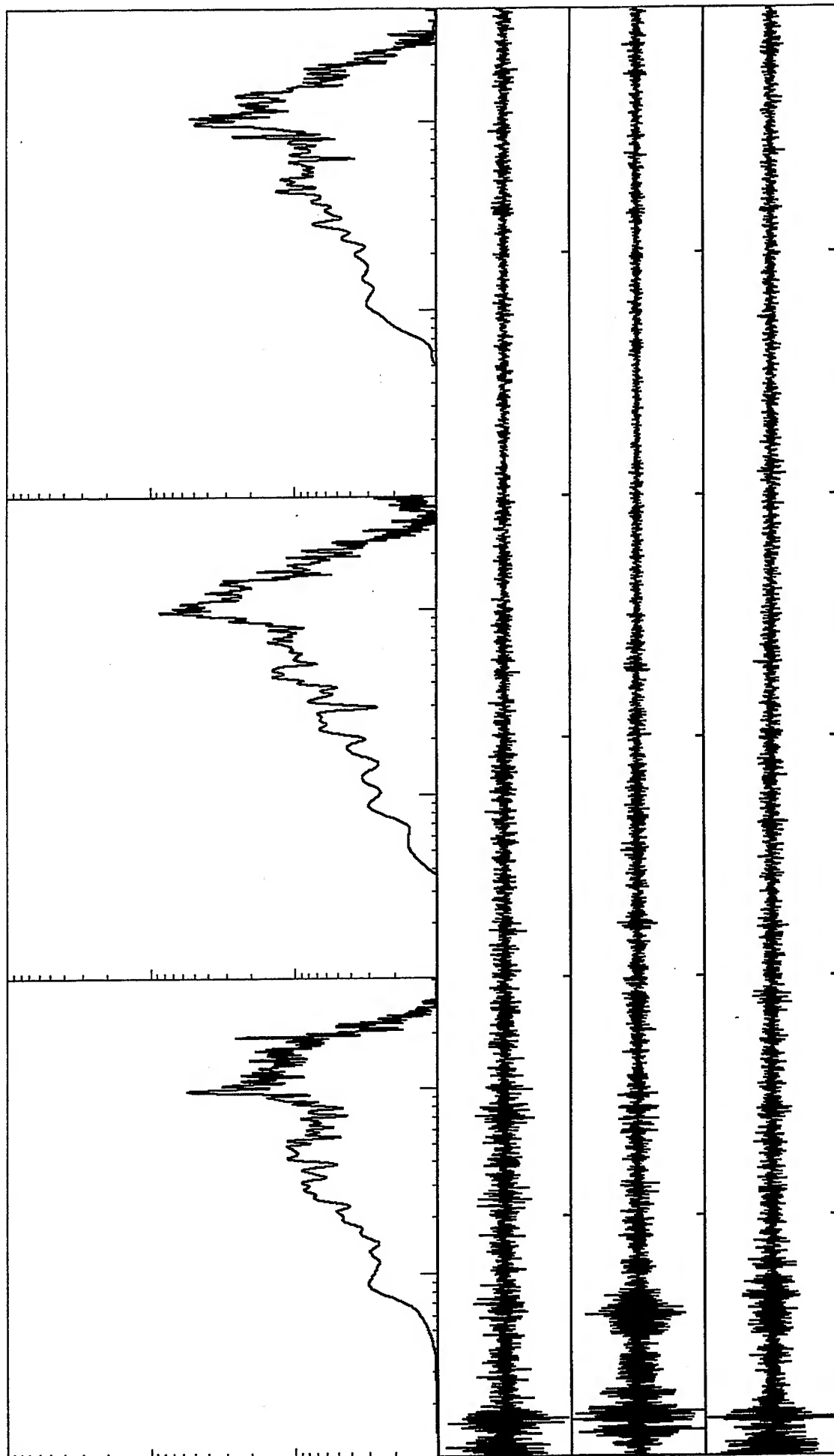


Spectral velocity values 0.1 to 40 Hz. Range: 1.E-5 to 1.E-2 cm/s  
 From top: ch1, 2, & 3: Max values of .071, .120, and .082 1.E-2 cm/s  
 Station 2: 60 s time window



*VortexRock Consultants, Inc.*

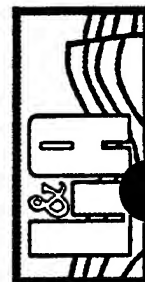


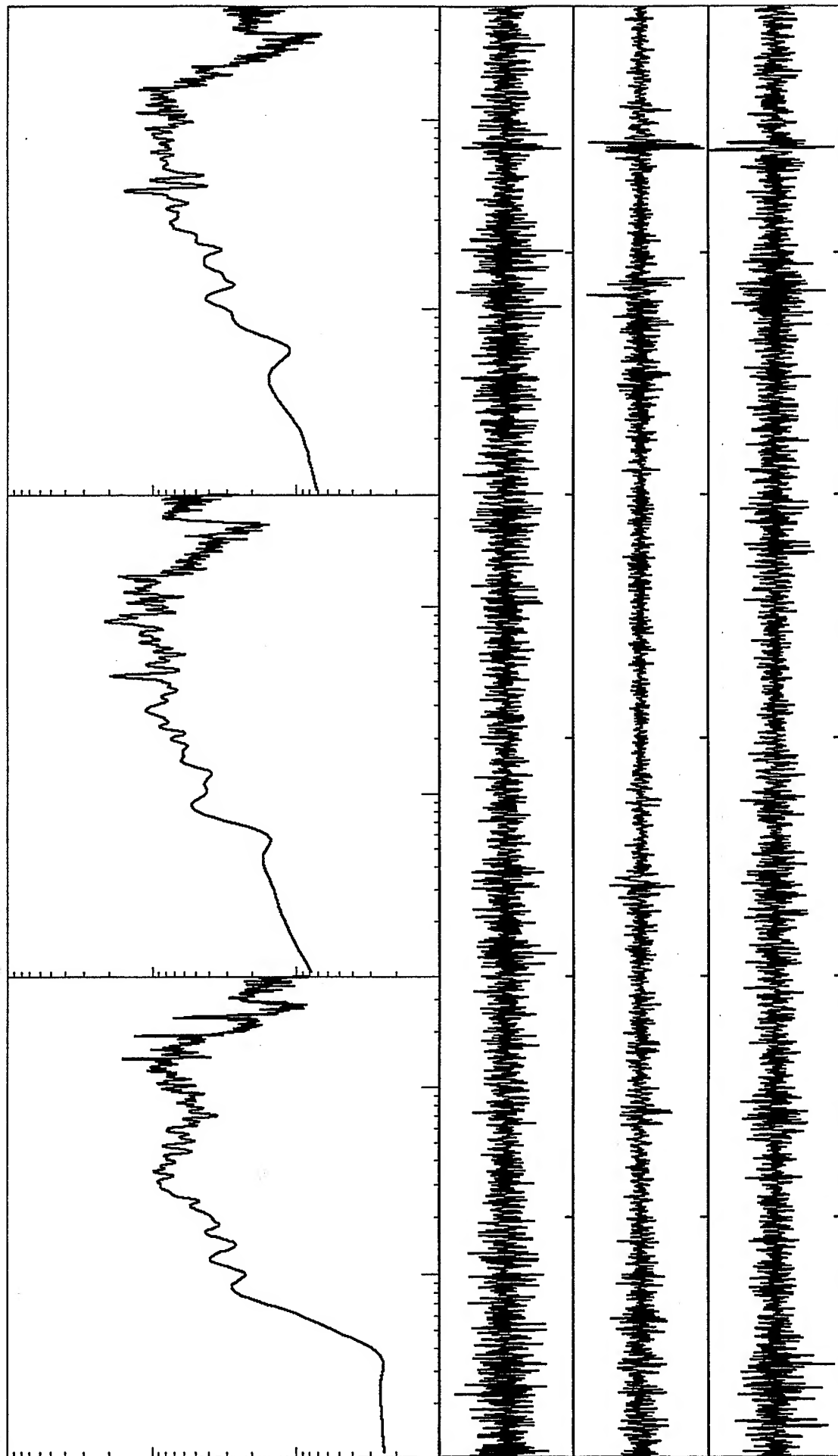


Spectral velocity values 0.1 to 40 Hz. Range: 1.E-5 to 1.E-2 cm/s  
From top: ch1, 2, & 3: Max values of .099, .141, and .119 1.E-2 cm/s  
Station 2: 60 s time window



*VortexRock Consultants, Inc.*

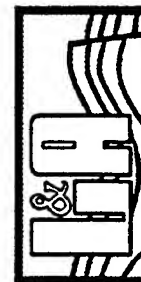




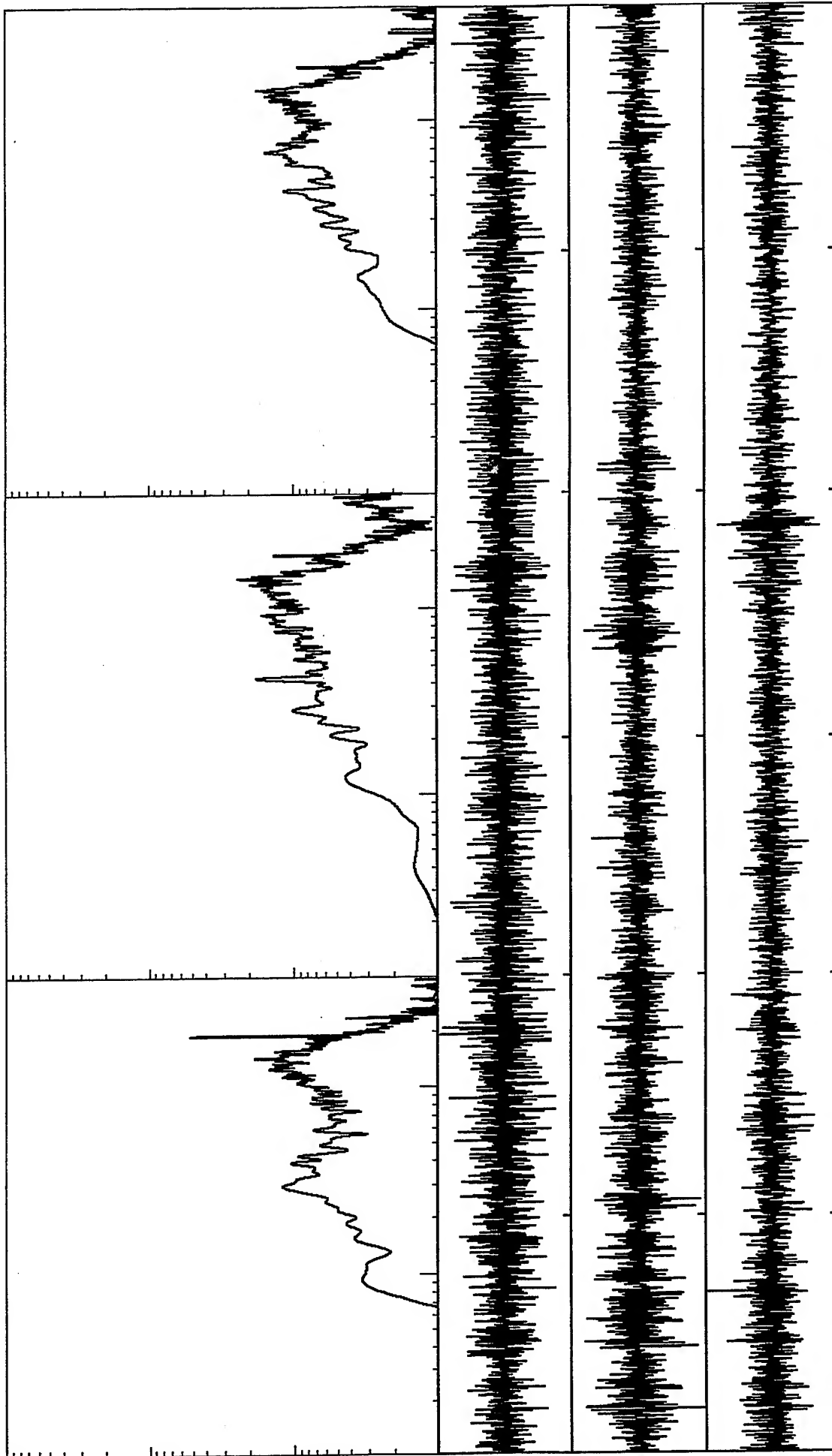
Spectral velocity values 0.1 to 40 Hz. Range: 1.E-6 to 1.E-3 cm/s  
 From top: ch1, 2, & 3: Max values of .310, .772, and .409 1.E-3 cm/s  
 Station 2: 60 s time window



*VortexRock Consultants, Inc.*



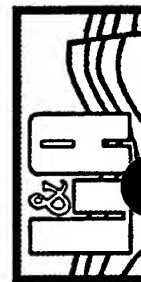


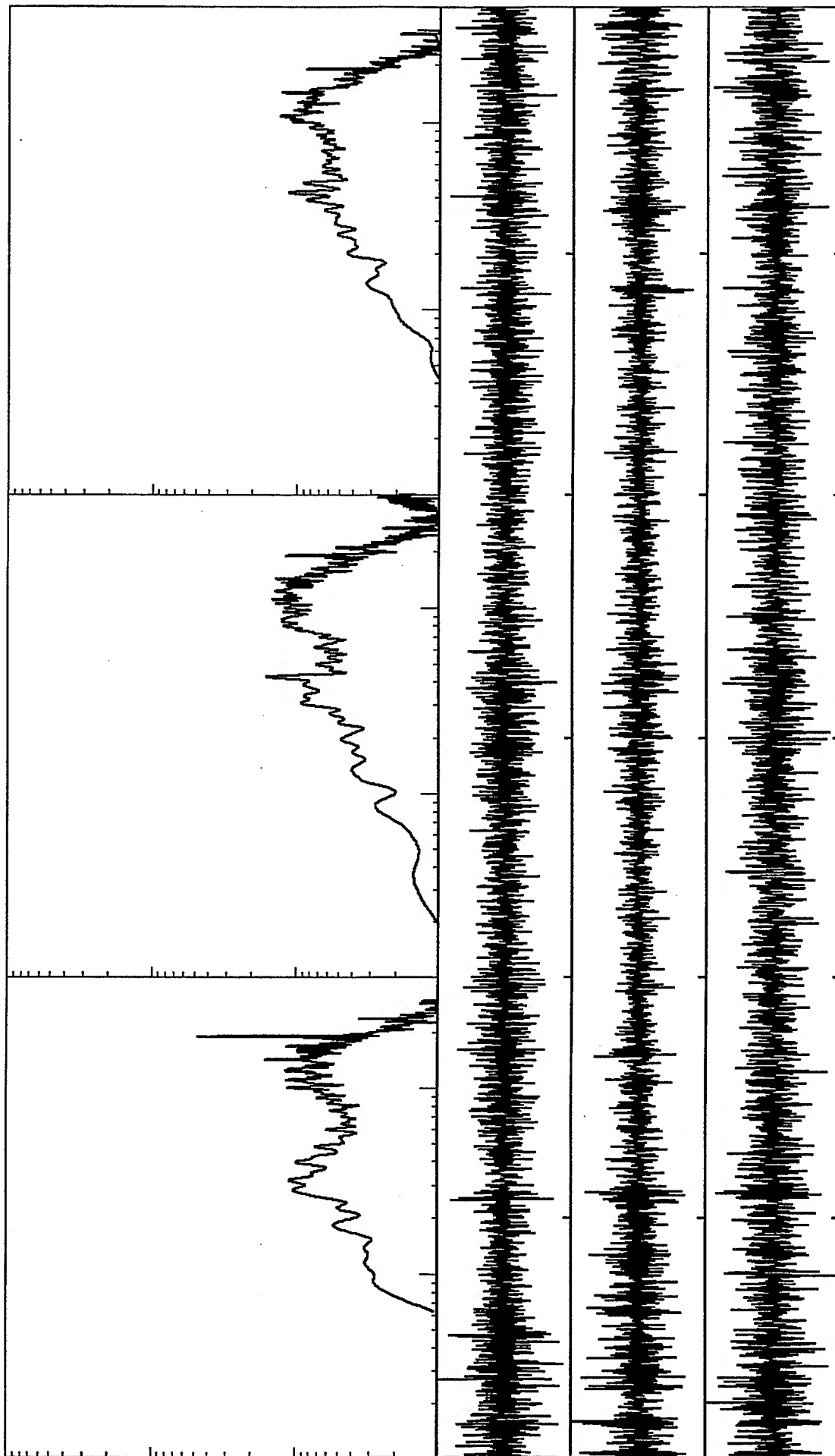


Spectral velocity values 0.1 to 40 Hz. Range: 1.E-5 to 1.E-3 cm/s  
 From top: ch1, 2, & 3: Max values of .347, .421, and .409 1.E-3 cm/s  
 Station 2: 60 s time window



*VortexRock Consultants, Inc.*

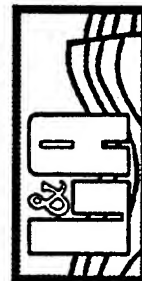


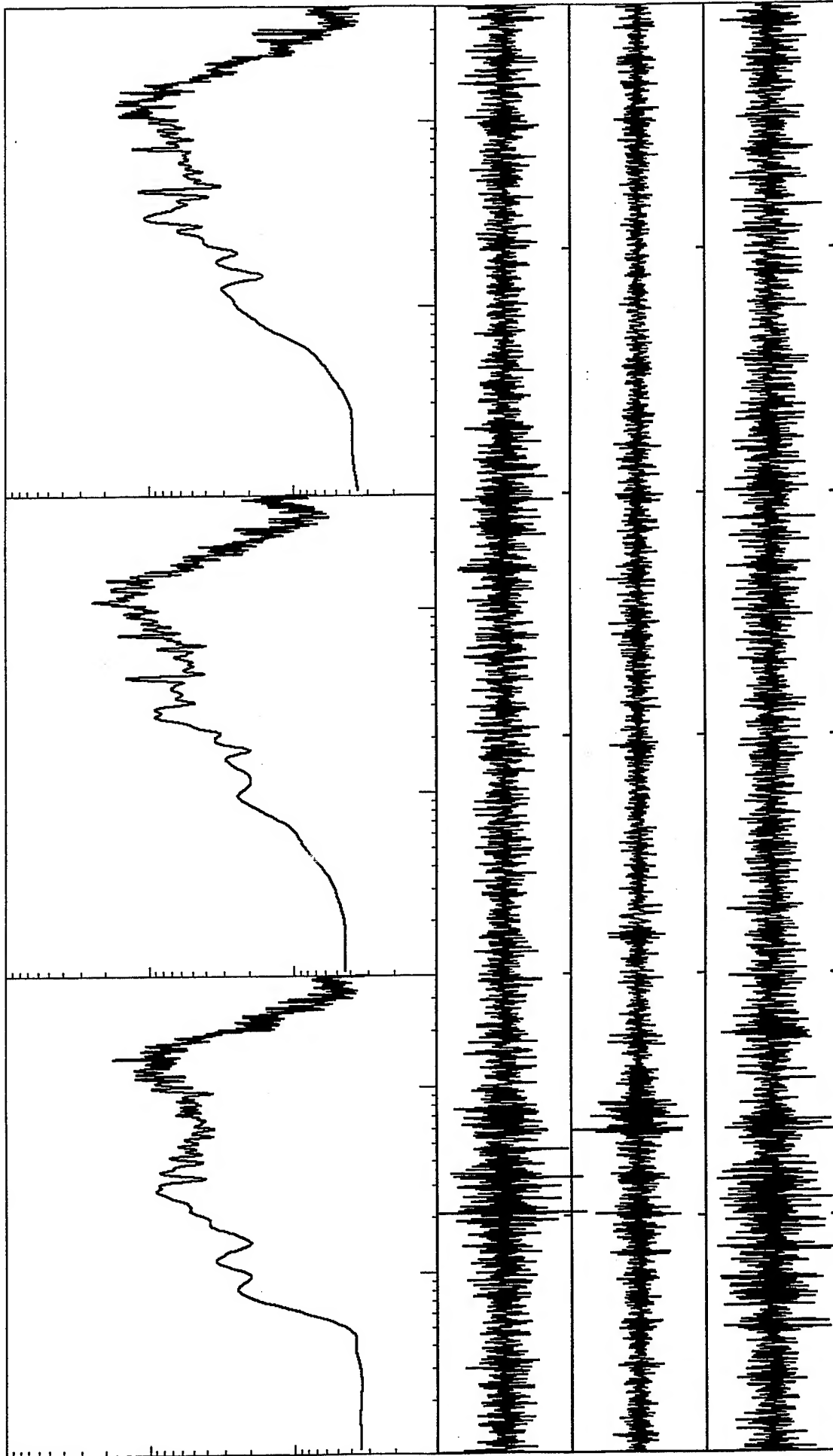


Spectral velocity values 0.1 to 40 Hz. Range: 1.E-5 to 1.E-2 cm/s  
From top: ch1, 2, & 3: Max values of .341, .362, and .237 1.E-3 cm/s  
Station 2: 50 s time window



*VortexRock Consultants, Inc.*

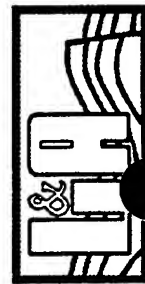


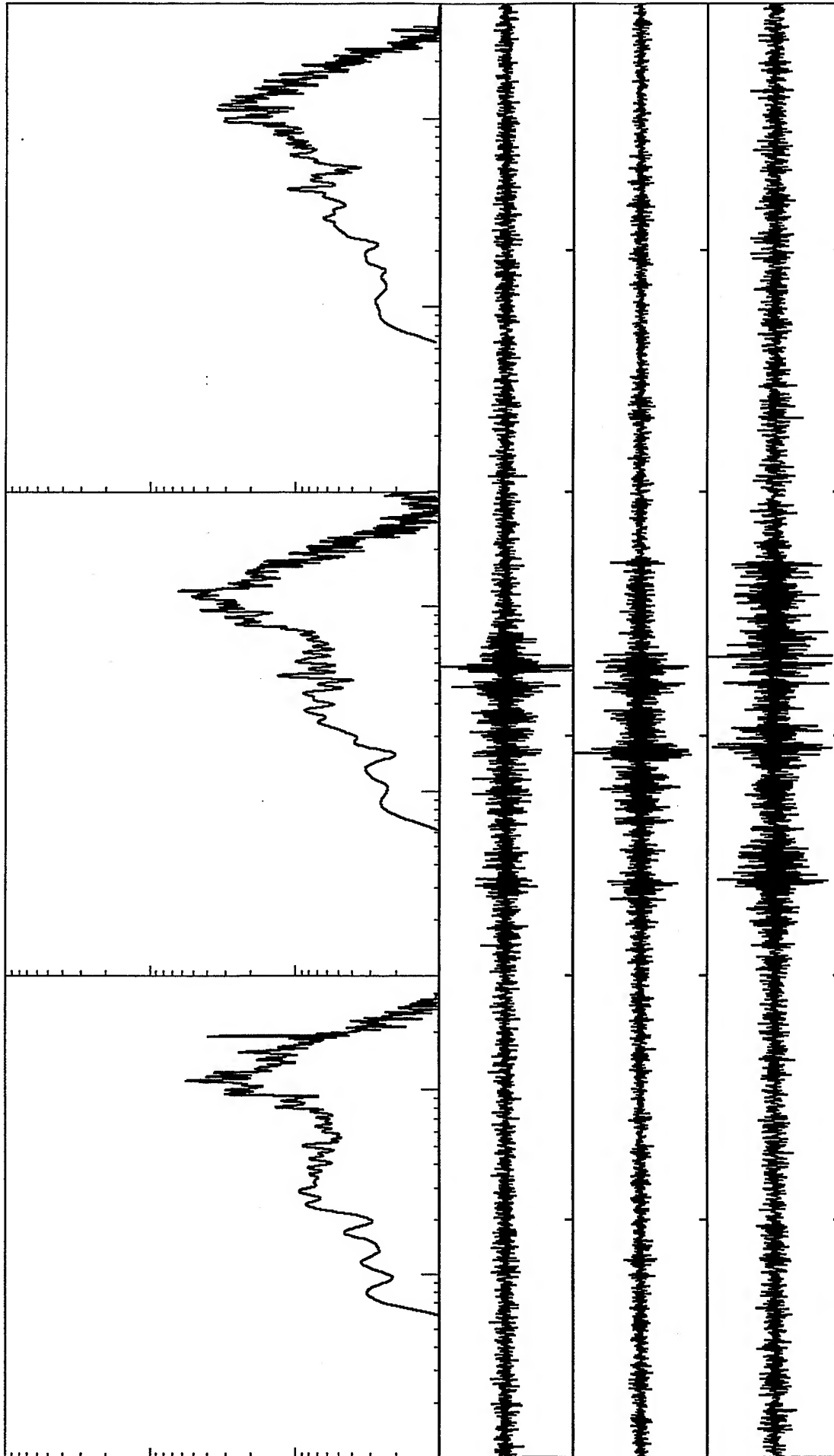


Spectral velocity values 0.1 to 40 Hz. Range: 1.E-6 to 1.E-3 cm/s  
 From top: ch1, 2, & 3: Max values of .286, .611, and .291 1.E-3 cm/s  
 Station 2: 60 s time window



*VortexRock Consultants, Inc.*

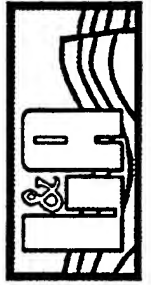




Spectral velocity values 0.1 to 40 Hz. Range: 1.E-5 to 1.E-2 cm/s  
 From top: ch1, 2, & 3: Max values of .108, .130, and .074 1.E-2 cm/s  
 Station 2: 60 s time window



*VortexRock Consultants, Inc.*



## ***Appendix C***

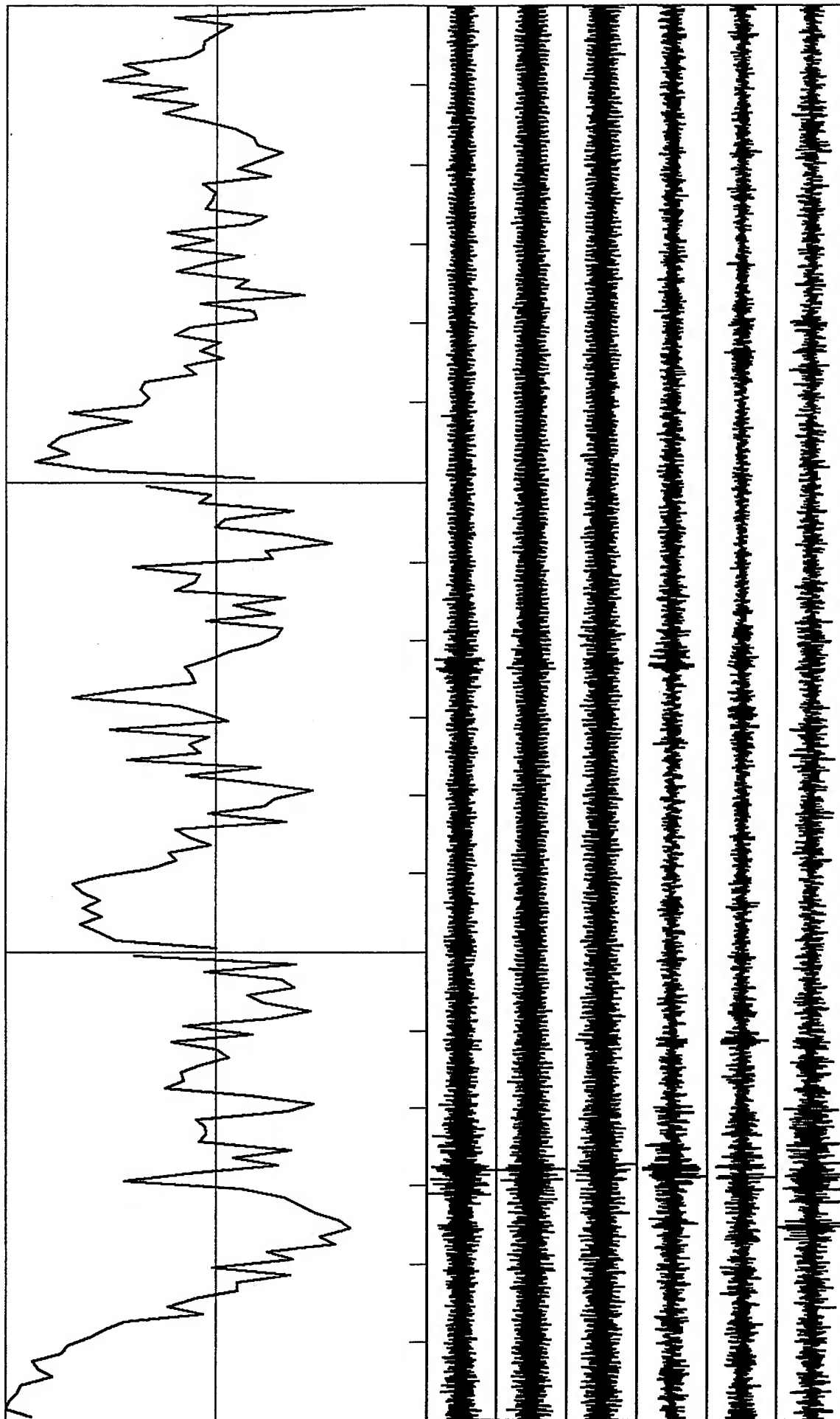
### ***Section II***

***The Correlation Coefficients for Selected Records from  
Experiments No. 4 t the Basketball Court of the McBride  
School, Los Angeles, California***



***VortexRock Consultants, Inc.***





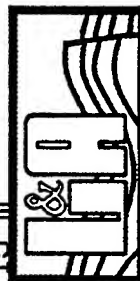
C-#1

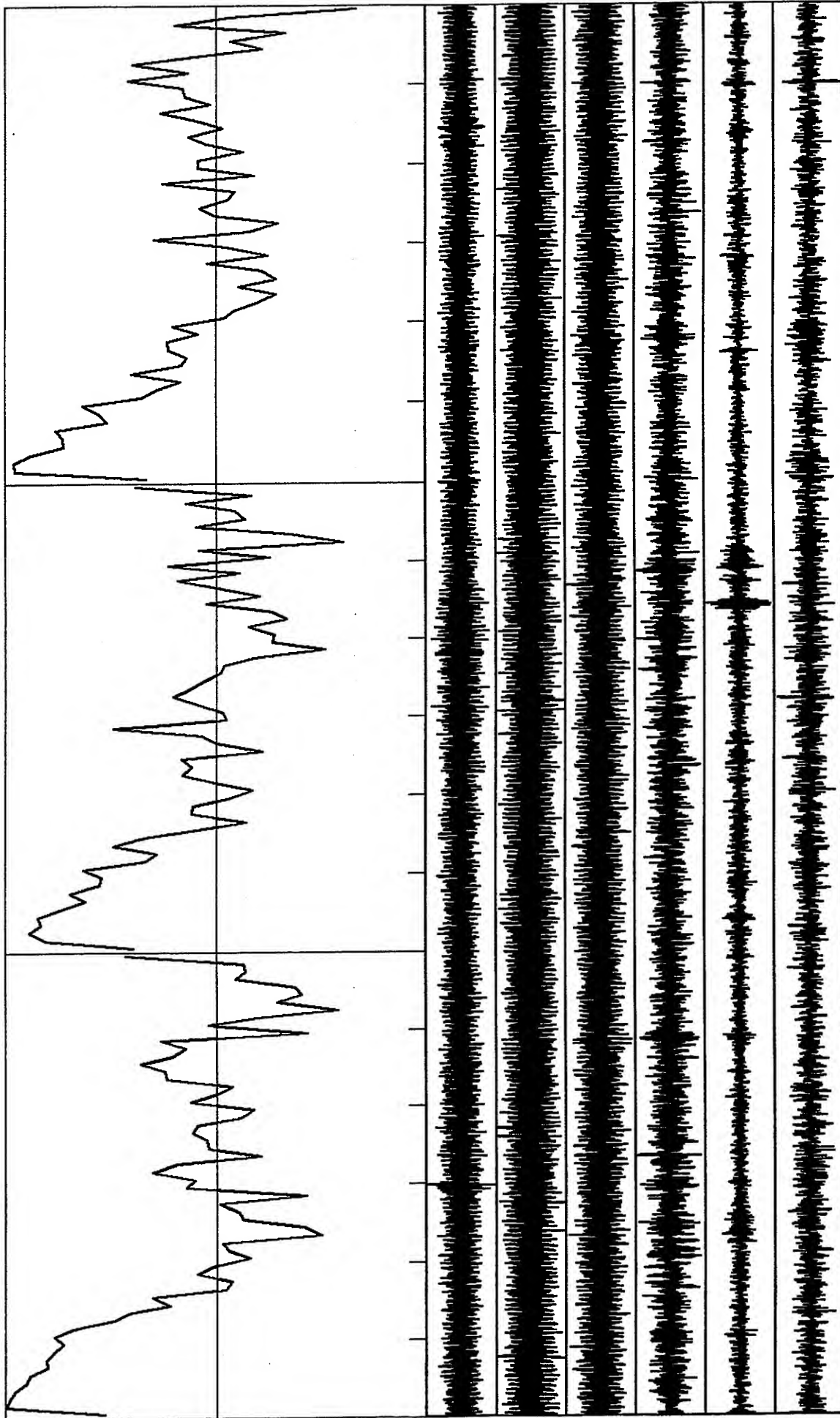


Correlation Coefficients: Scale -1 to +1; freq range: 0 to 30.0 Hz; Radius: 15 m

St. 1 & 2: Vertical & horizontal components; 60 s time window

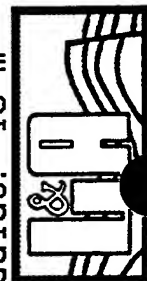
*VortexRock Consultants, Inc.*

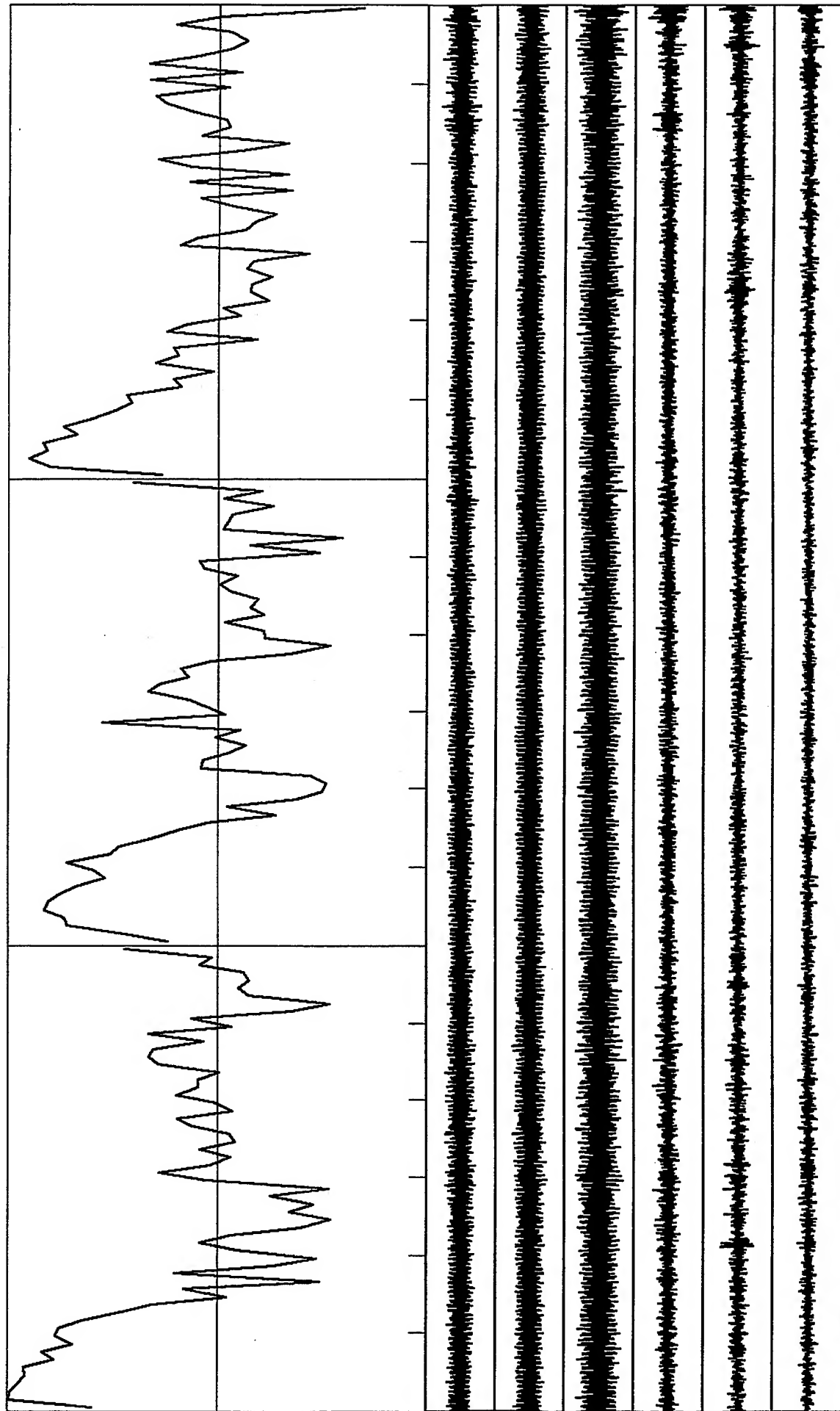




Correlation Coefficients: Scale -1 to +1; freq range: 0 to 30.0 Hz: Radius: 15 m  
 St. 1 & 2: Vertical & horizontal components; 60 s time window

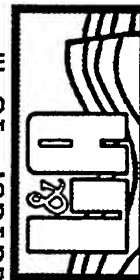
*VortexRock Consultants, Inc.*



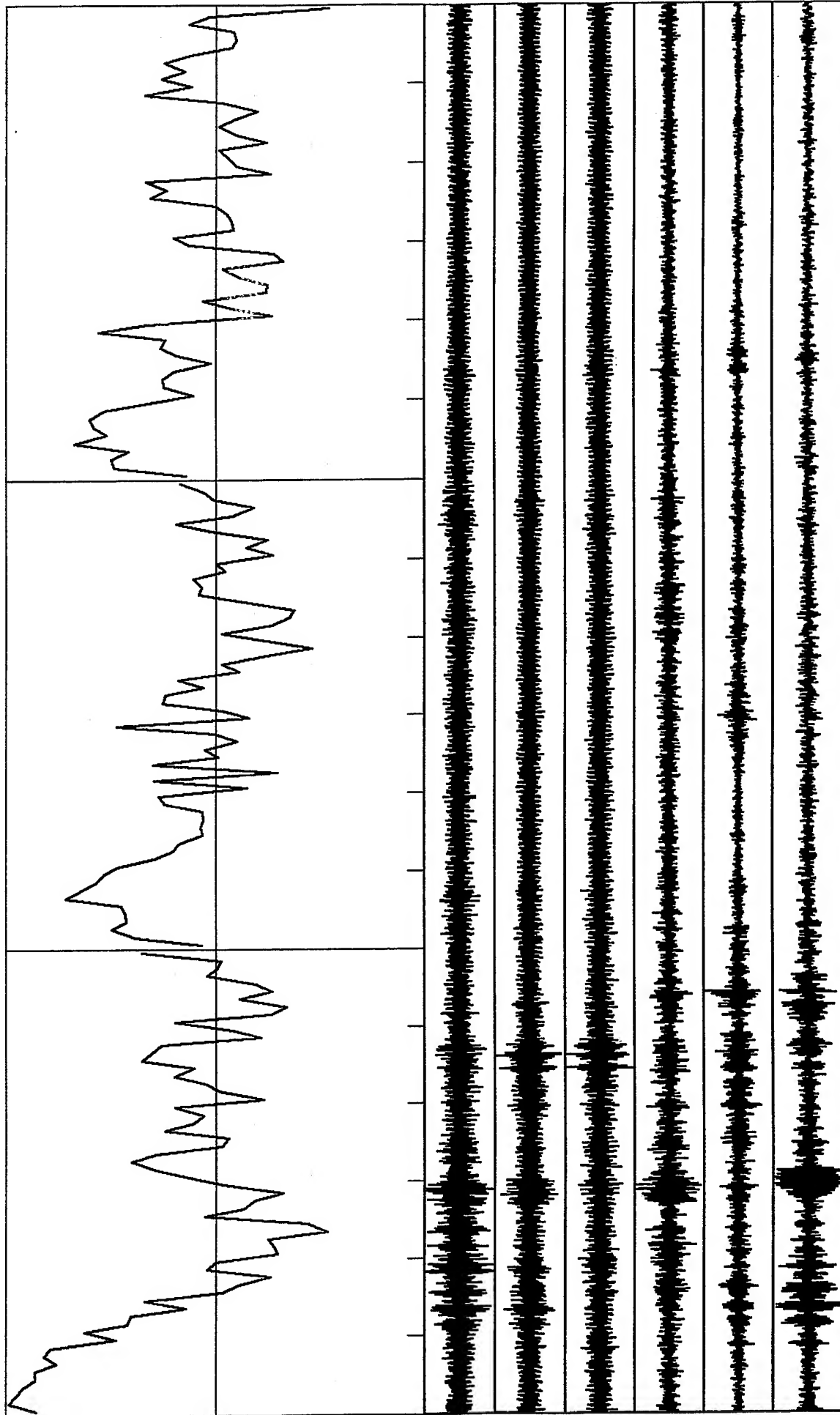


Correlation Coefficients: Scale -1 to +1; freq range: 0 to 30.0 Hz; Radius: 15 m  
 St. 1 & 2: Vertical & horizontal components; 60 s time window

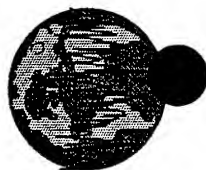
*VortexRock Consultants, Inc.*





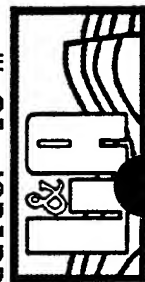


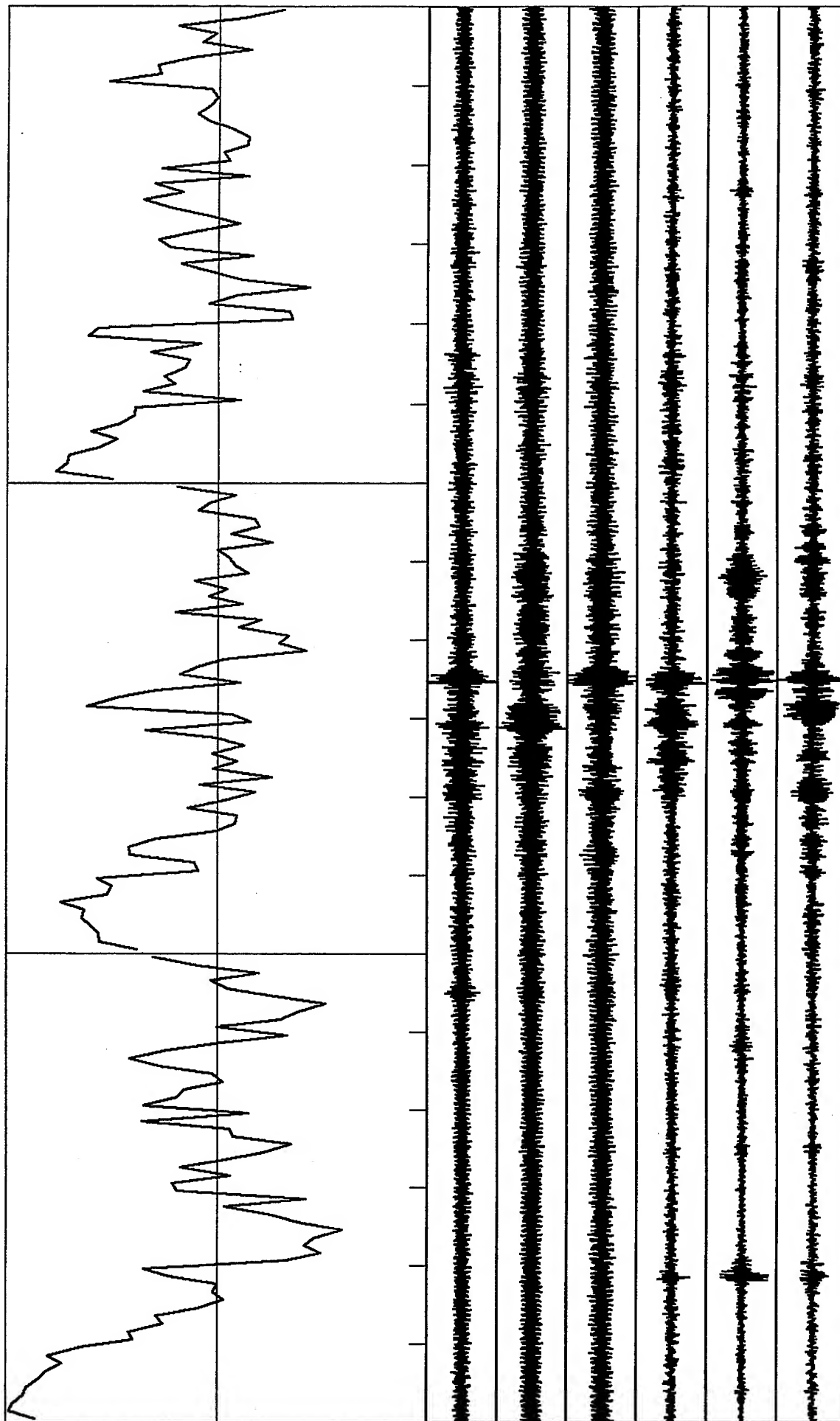
C-4



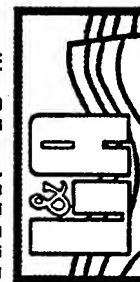
*VortexRock Consultants, Inc.*

Correlation Coefficients: Scale -1 to +1; freq range: 0 to 30.0 Hz; Radius: 15 m  
 St. 1 & 2: Vertical & horizontal components; 60 s time window

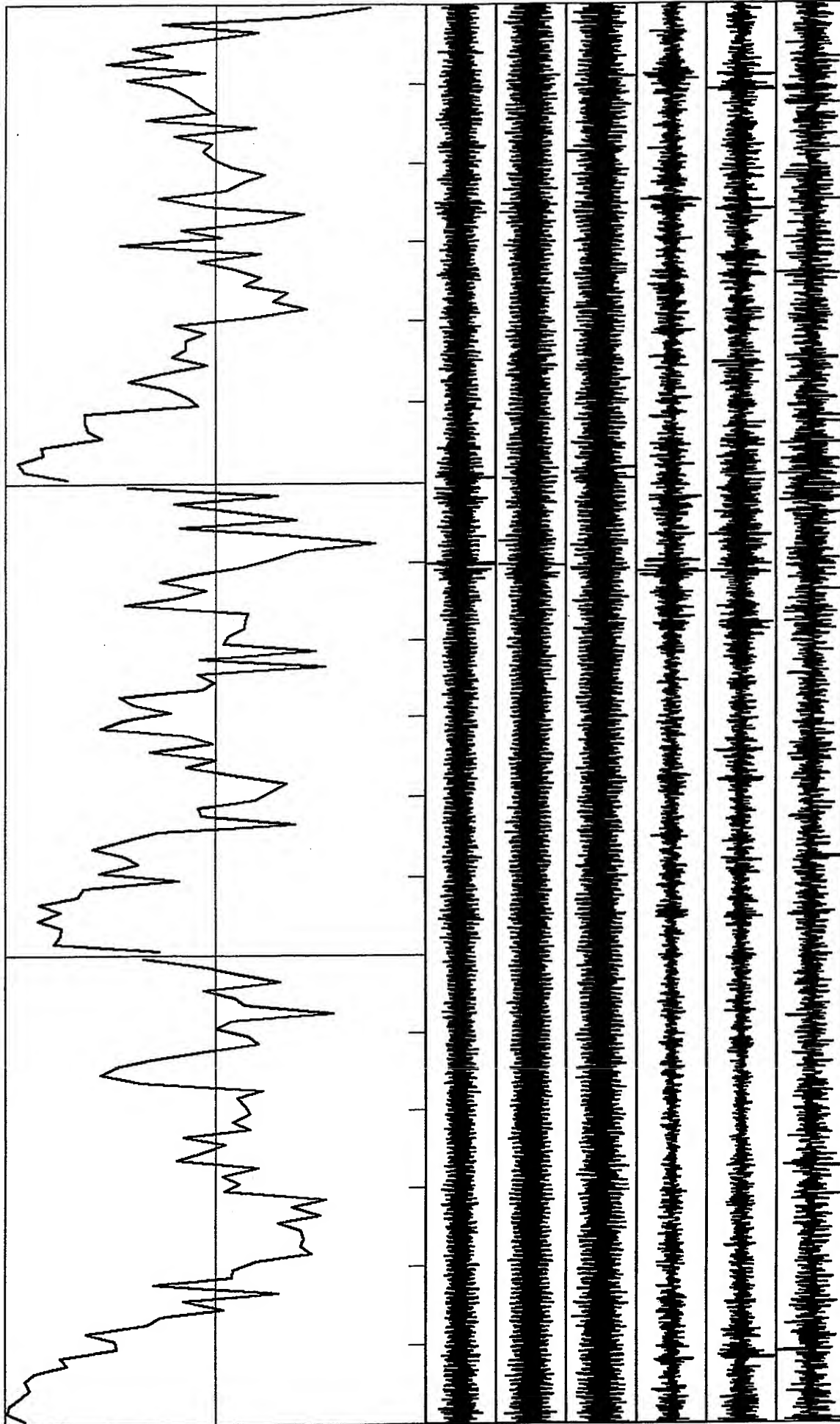




Correlation Coefficients: Scale -1 to +1; freq range: 0 to 30.0 Hz; Radius: 15 m  
St. 1 & 2: Vertical & horizontal components; 60 s time window



*VortexRock Consultants, Inc.*

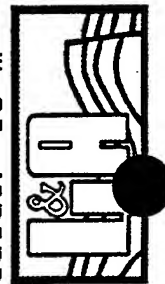


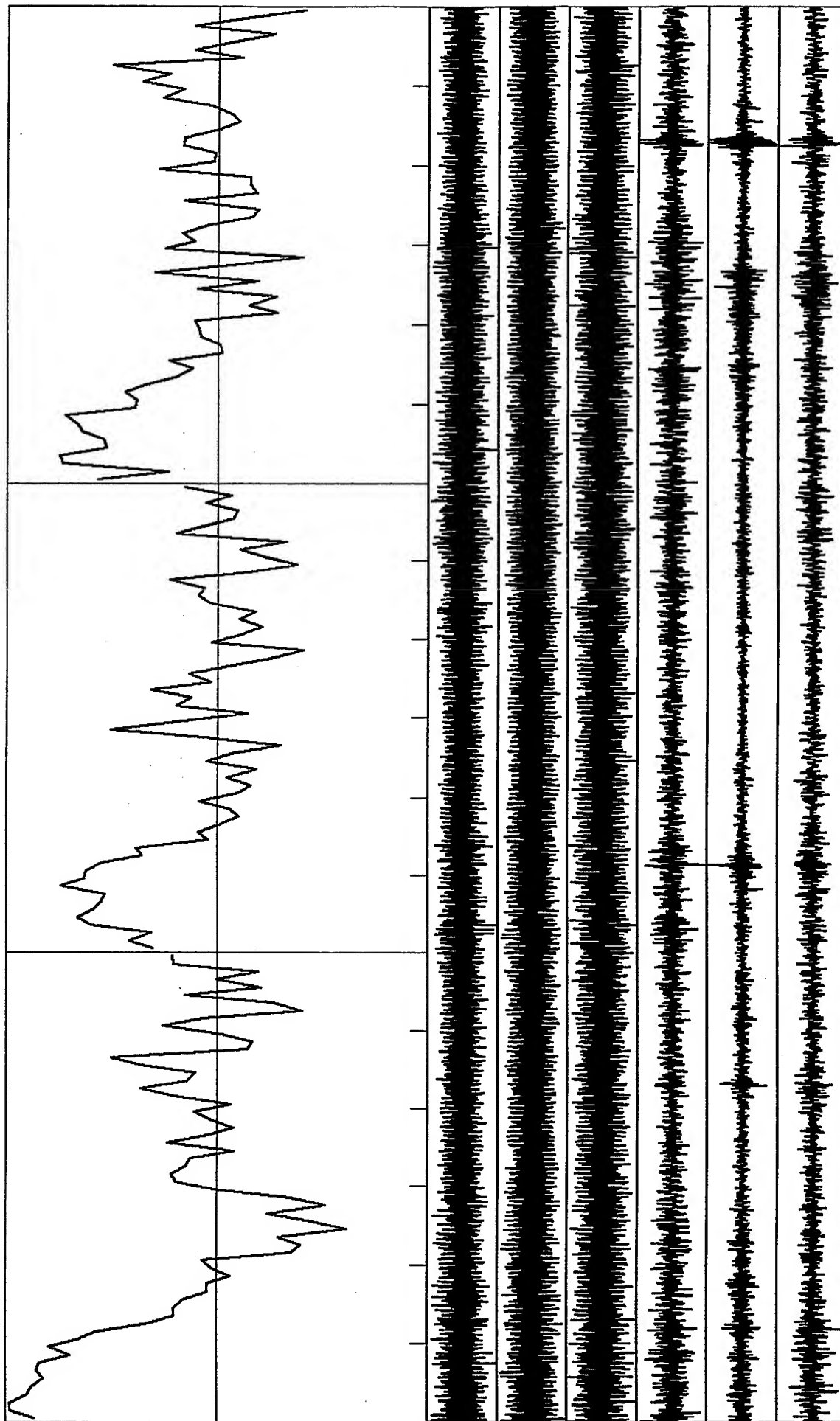
C-6



Correlation Coefficients: Scale -1 to +1; freq range: 0 to 30.0 Hz; Radius: 15 m  
 St. 1 & 2: vertical & horizontal components: 60 s time window

*VortexRock Consultants, Inc.*

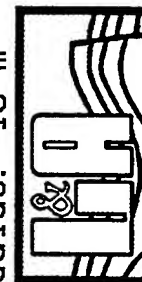




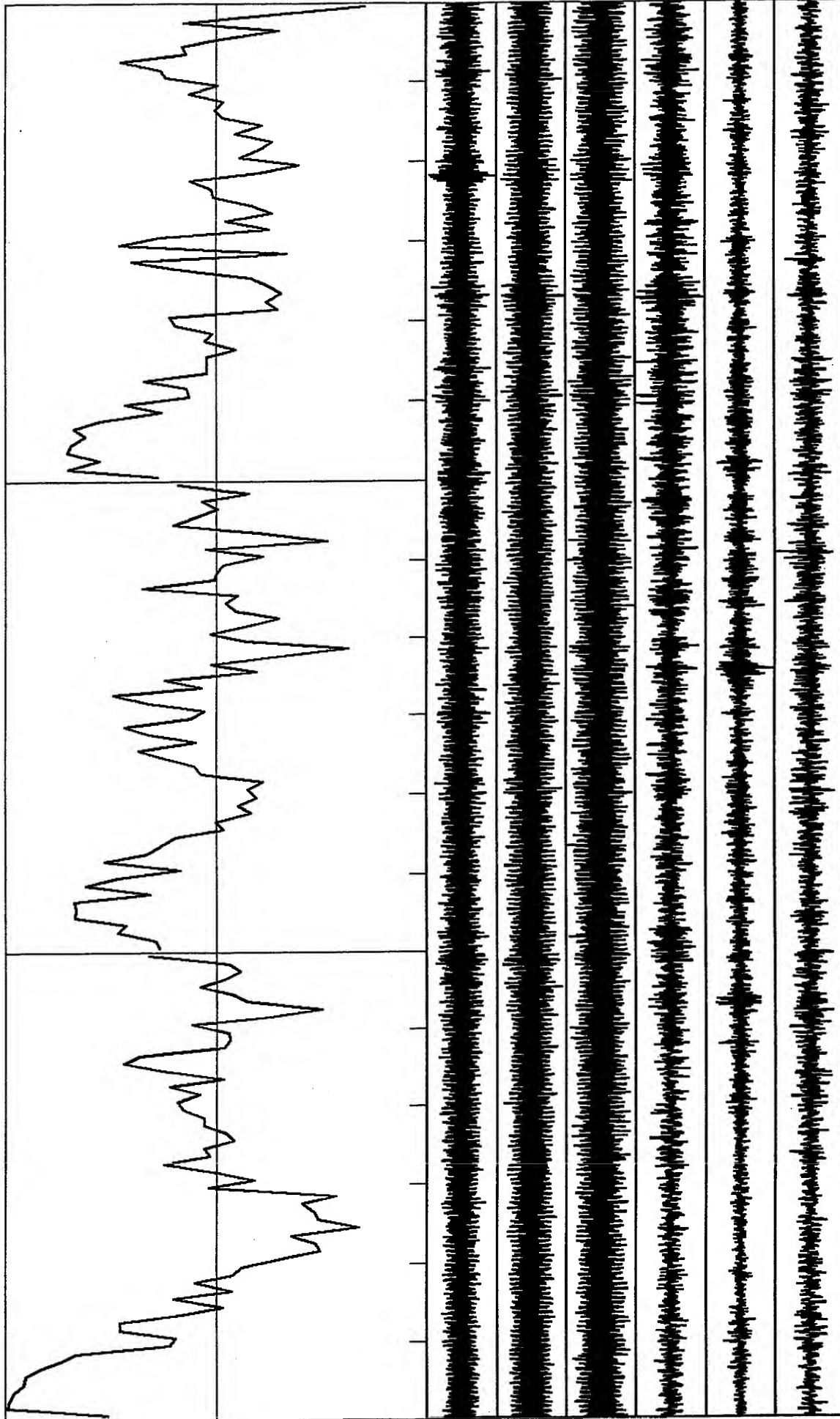
C-17



Correlation Coefficients: Scale -1 to +1; freq range: 0 to 30.0 Hz; Radius: 15 m  
 St. 1 & 2: Vertical & horizontal components; 60 s time window



*VortexRock Consultants, Inc.*

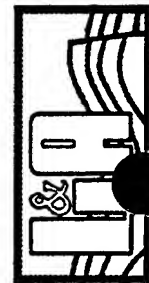


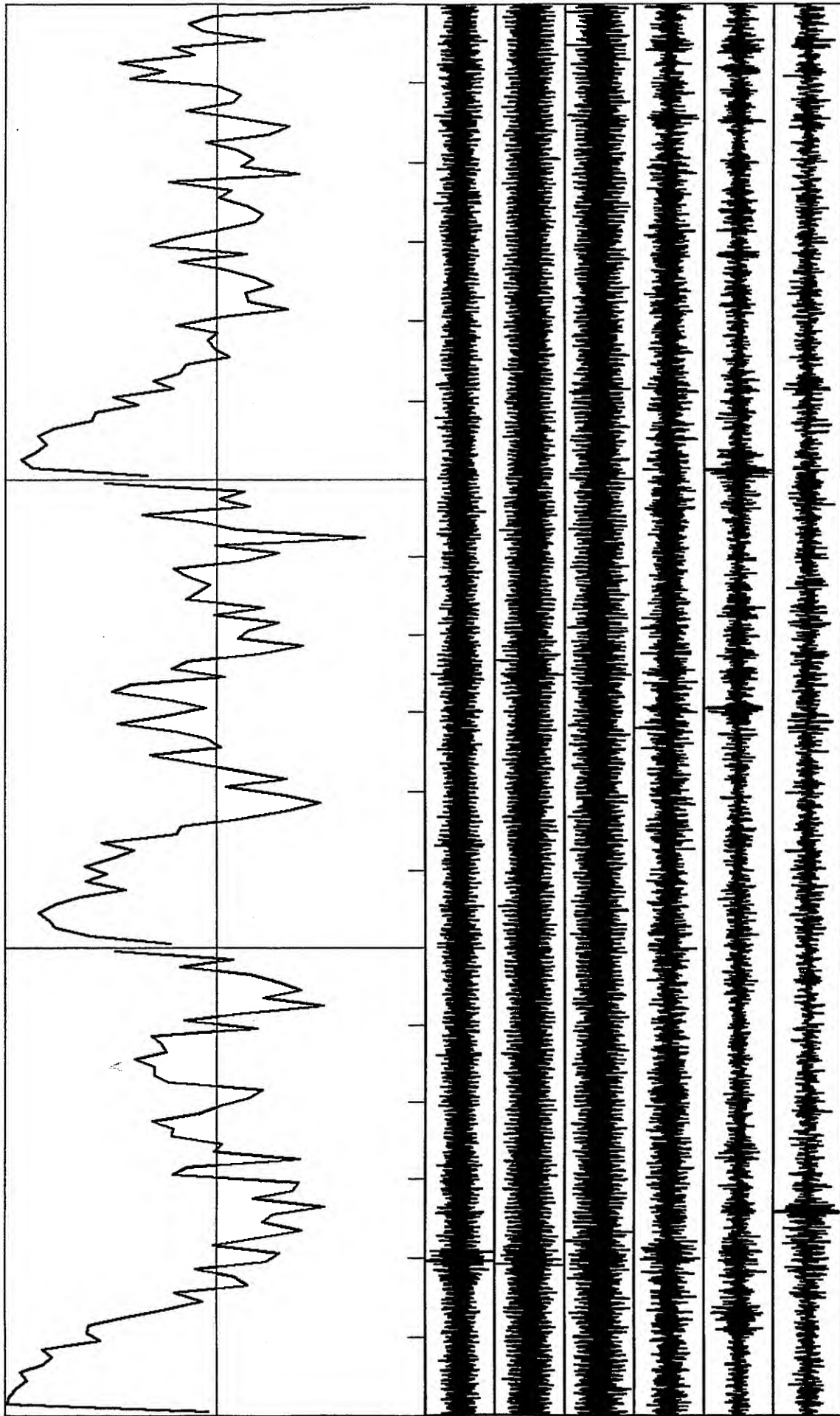
C-8



Correlation Coefficients: Scale -1 to +1; freq range: 0 to 30.0 Hz; Radius: 15 m  
 St. 1 & 2: Vertical & horizontal components; 60 s time window

*VortexRock Consultants, Inc.*

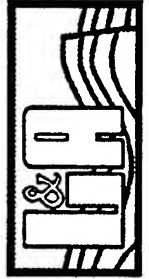




C-9

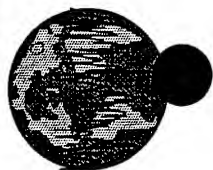
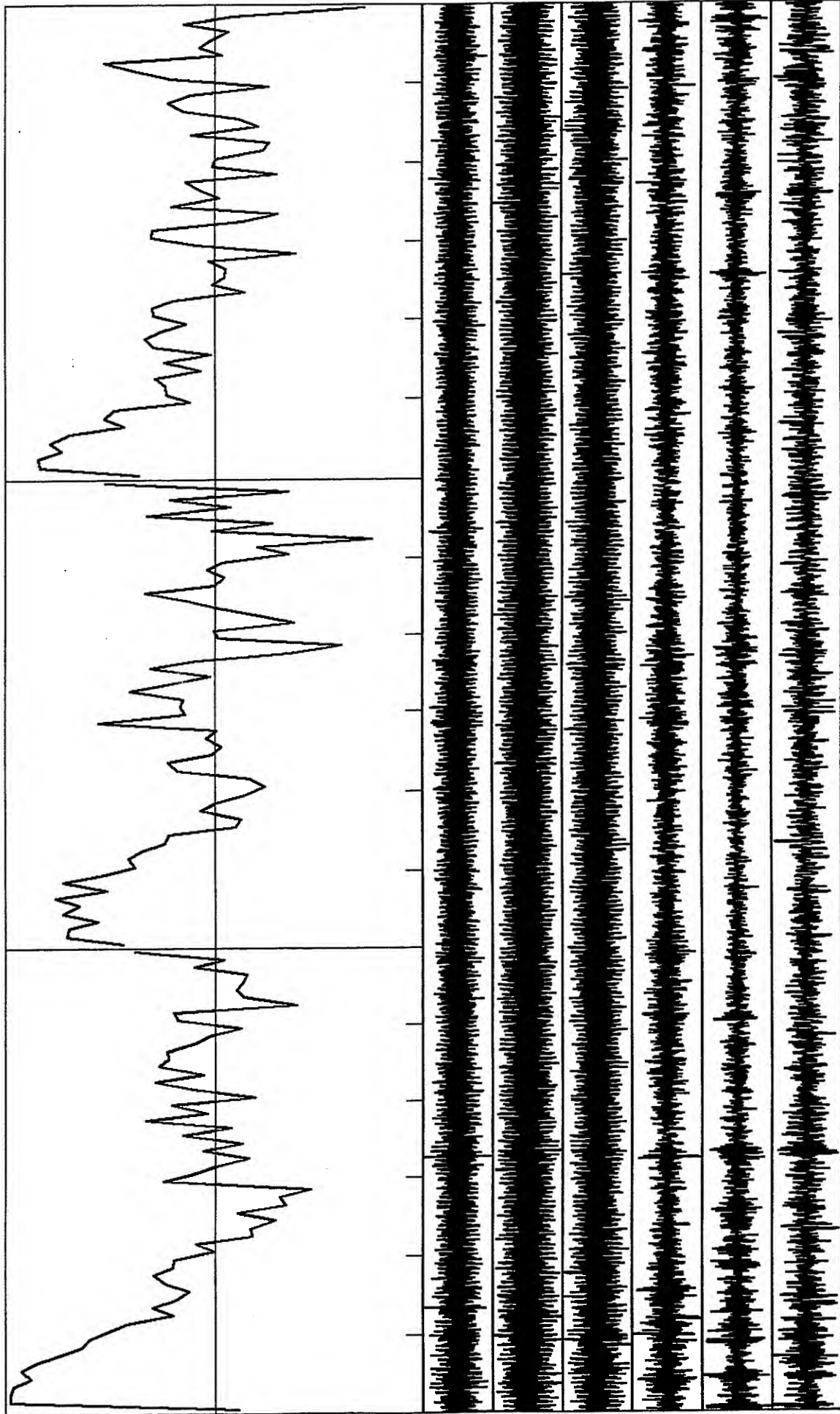


Correlation Coefficients: Scale -1 to +1; freq range: 0 to 30.0 Hz; Radius: 15 m  
 St. 1 & 2: Vertical & horizontal components; 60 s time window



*VortexRock Consultants, Inc.*

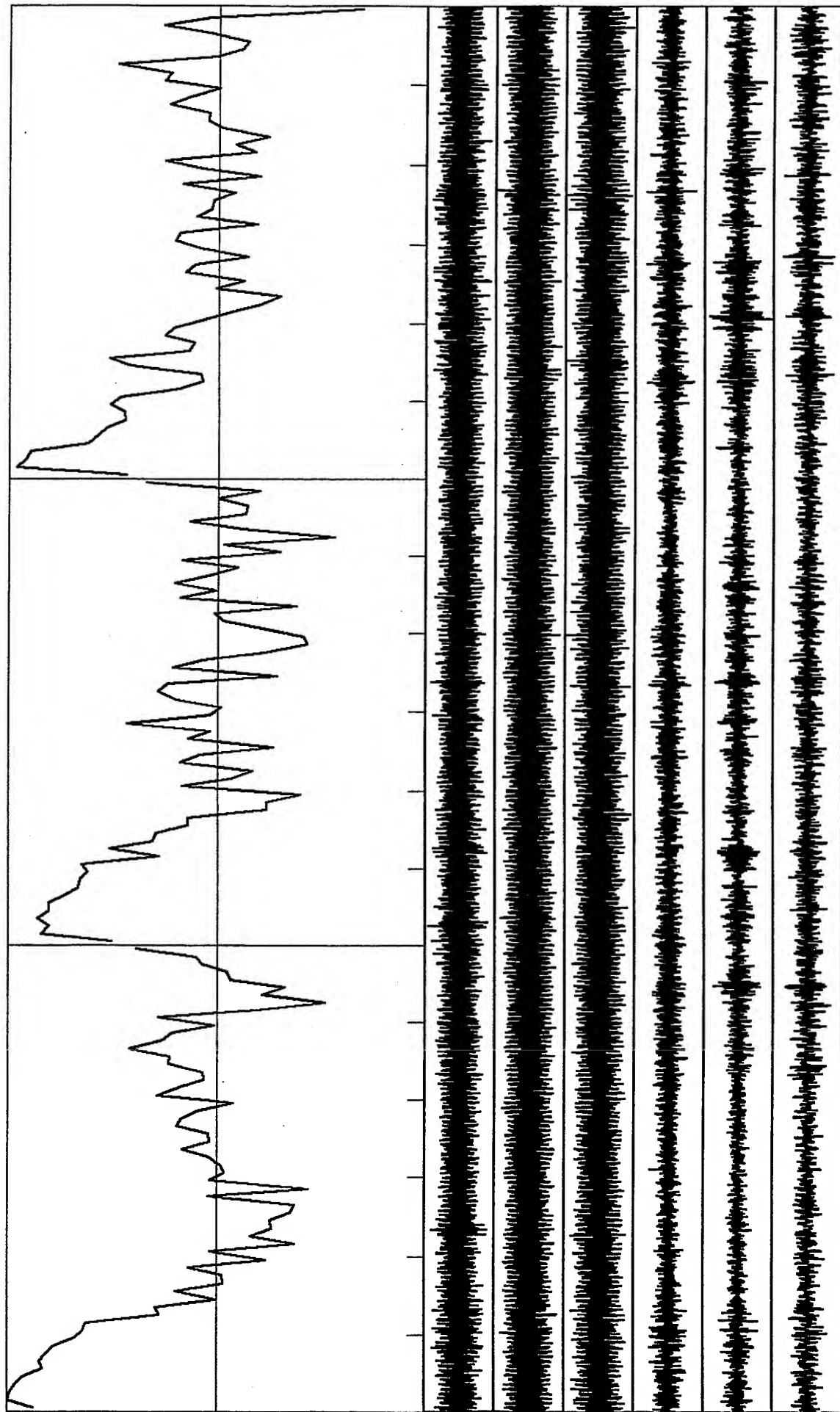




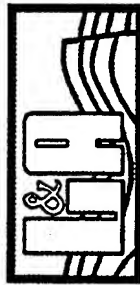
Correlation Coefficients: Scale -1 to +1; freq range: 0 to 30.0 Hz; Radius: 15 m  
 St. 1 & 2: Vertical & horizontal components: 60 s time window

*VortexRock Consultants, Inc.*



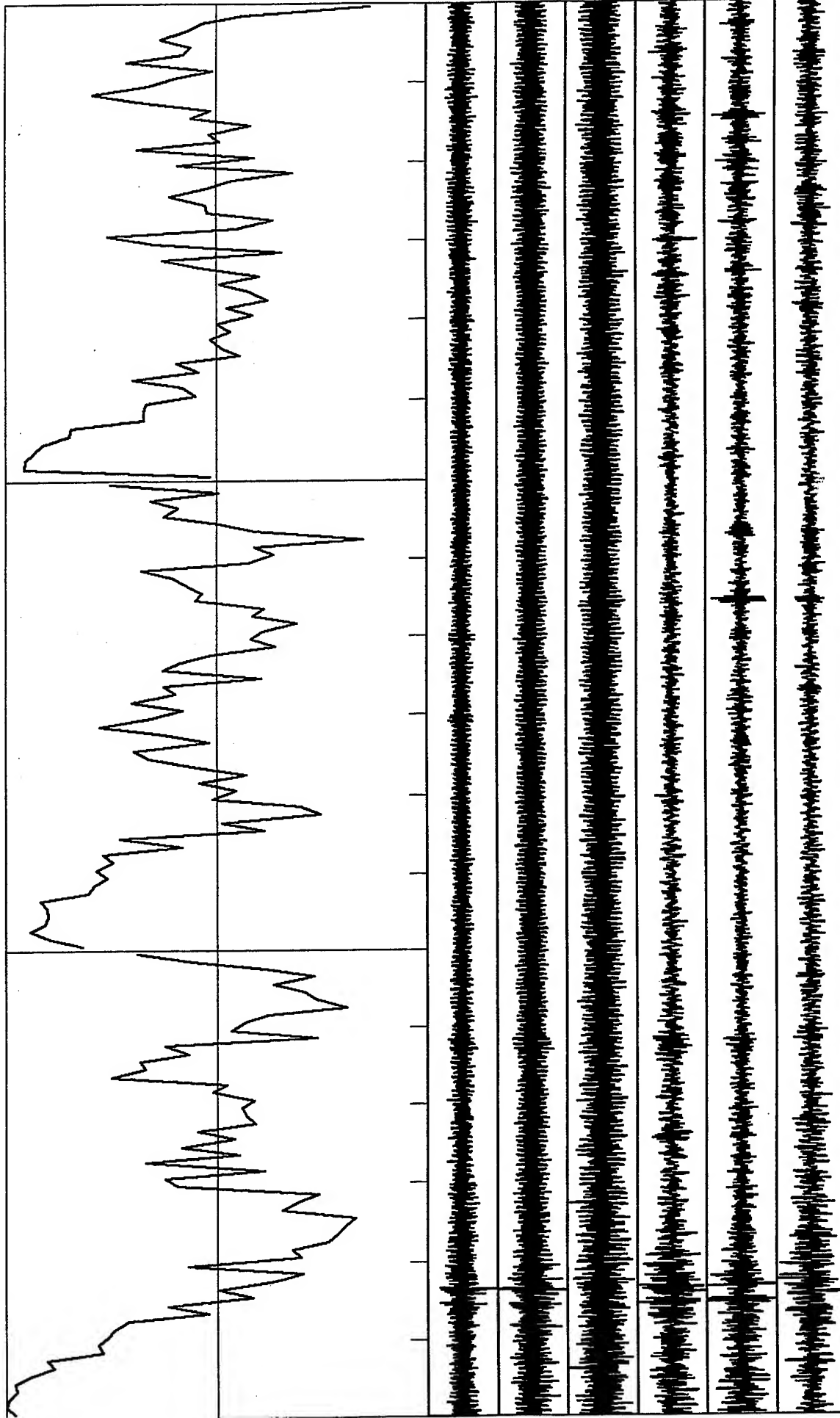


Correlation Coefficients: Scale -1 to +1; freq range: 0 to 30.0 Hz; Radius: 15 m  
St. 1 & 2: Vertical & horizontal components; 60 s time window

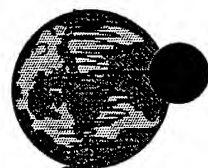


*VortexRock Consultants, Inc.*



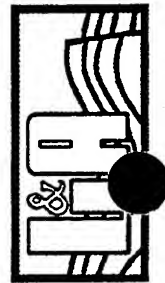


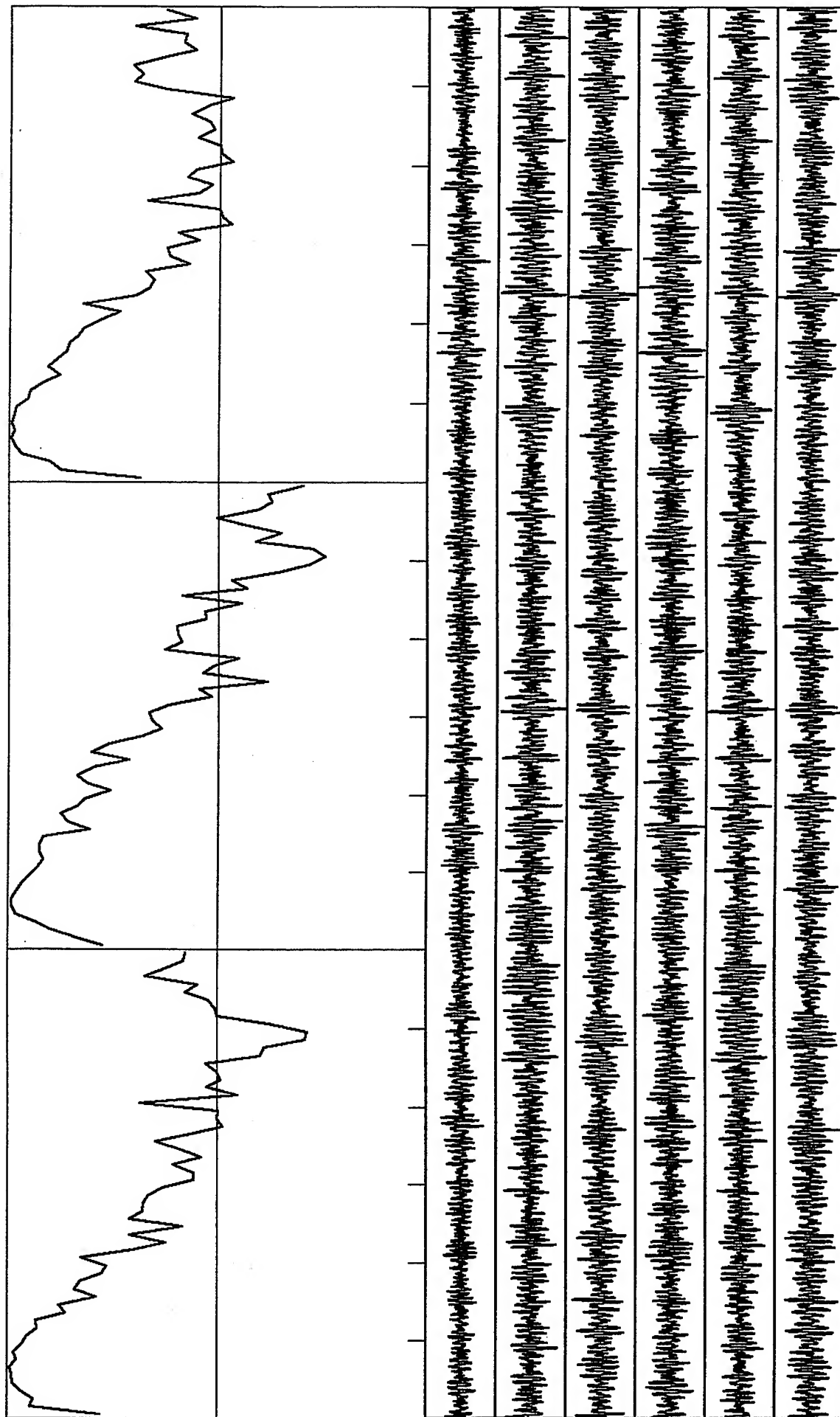
C-12



Correlation Coefficients: Scale -1 to +1; freq range: 0 to 30.0 Hz; Radius: 15 m  
St. 1 & 2: Vertical & horizontal components; 60 s time window

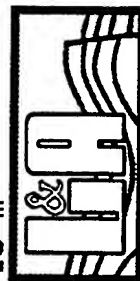
*VortexRock Consultants, Inc.*

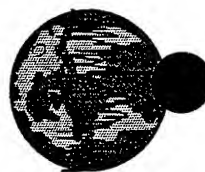
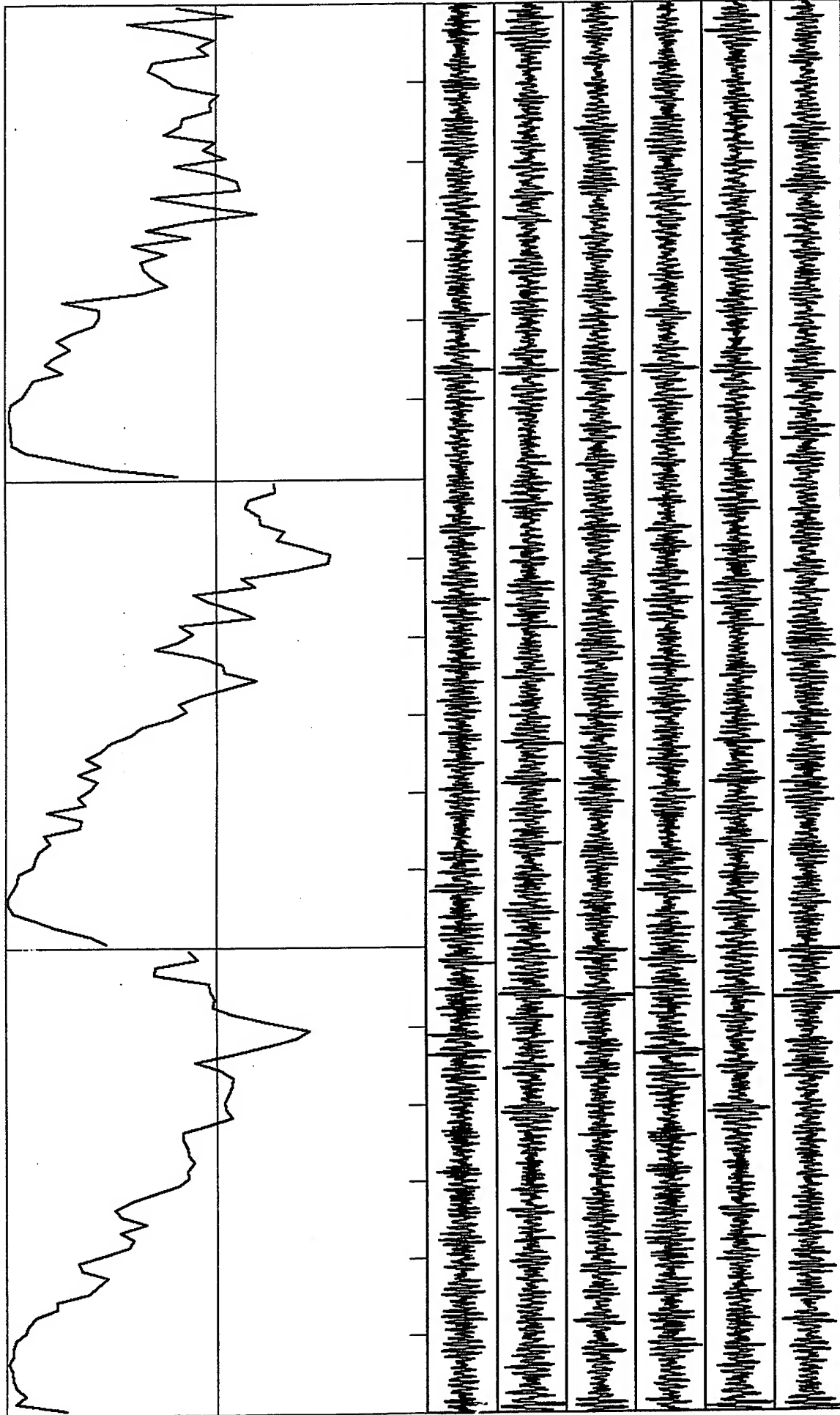




Correlation Coefficients: Scale -1 to +1; freq range: 0 to 30.0 Hz; Radius: 15 m  
 St. 1 & 2: Vertical & horizontal components; 60 s time window

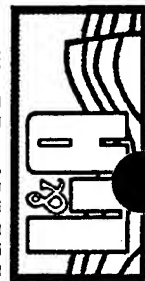
*VortexRock Consultants, Inc.*

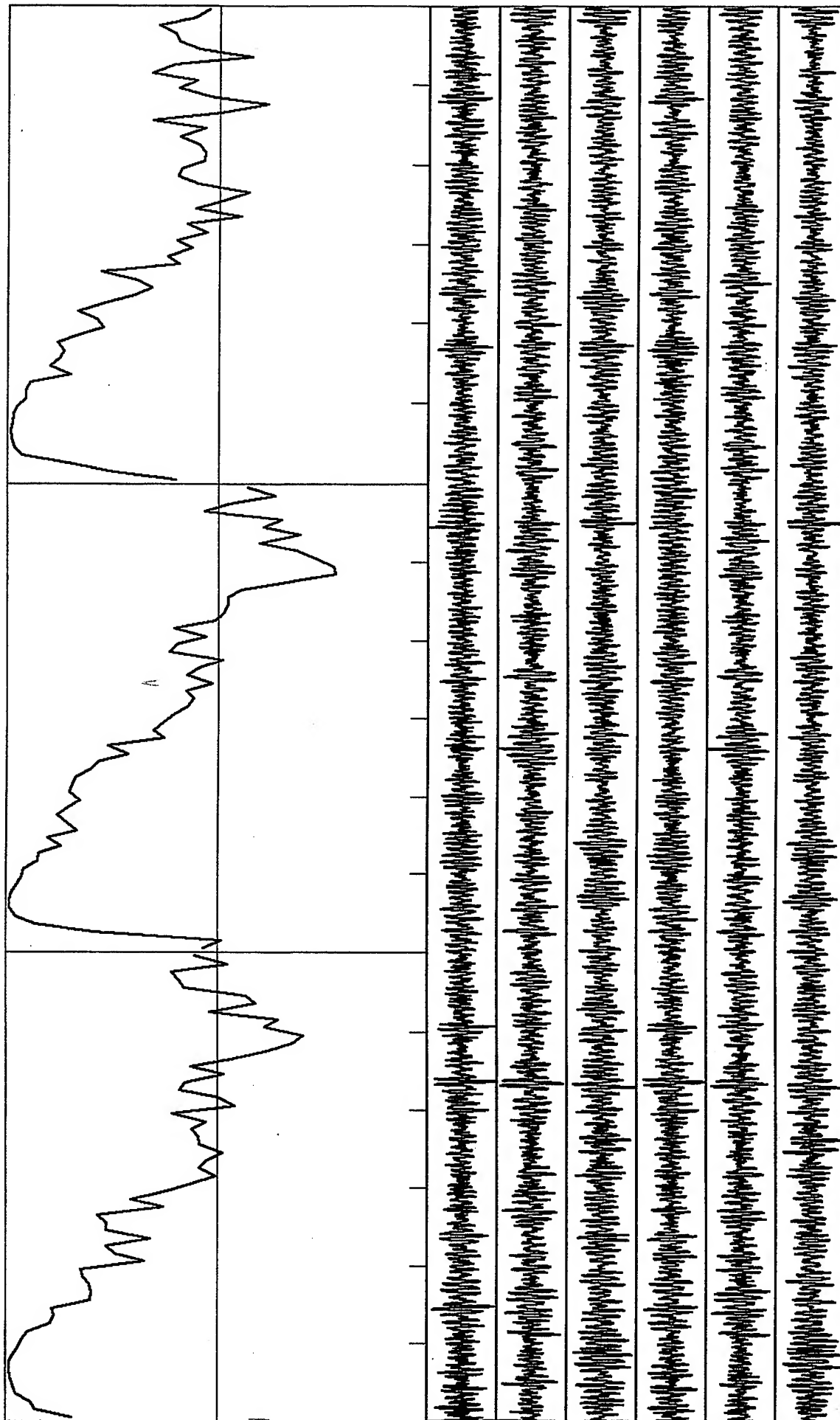




Correlation Coefficients: Scale -1 to +1; freq range: 0 to 30.0 Hz; Radius: 15 m  
 St. 1 & 2: Vertical & horizontal components; 60 s time window

*VortexRock Consultants, Inc.*



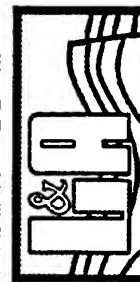


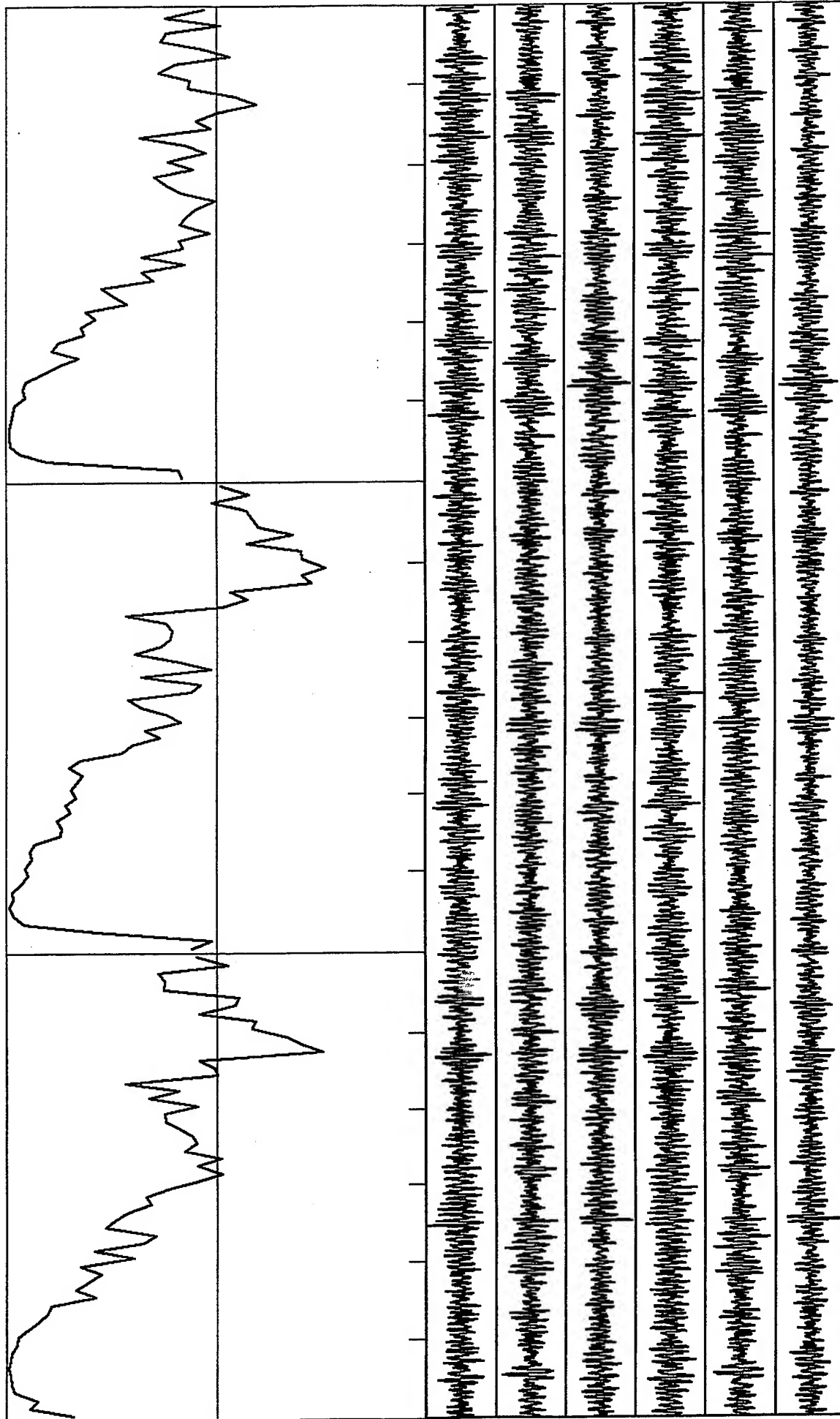
D-3



Correlation Coefficients: Scale -1 to +1; freq range: 0 to 30.0 Hz; Radius: 15 m  
 St. 1 & 2: Vertical & horizontal components; 60 s time window

*VortexRock Consultants, Inc.*

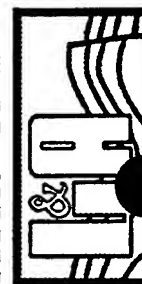


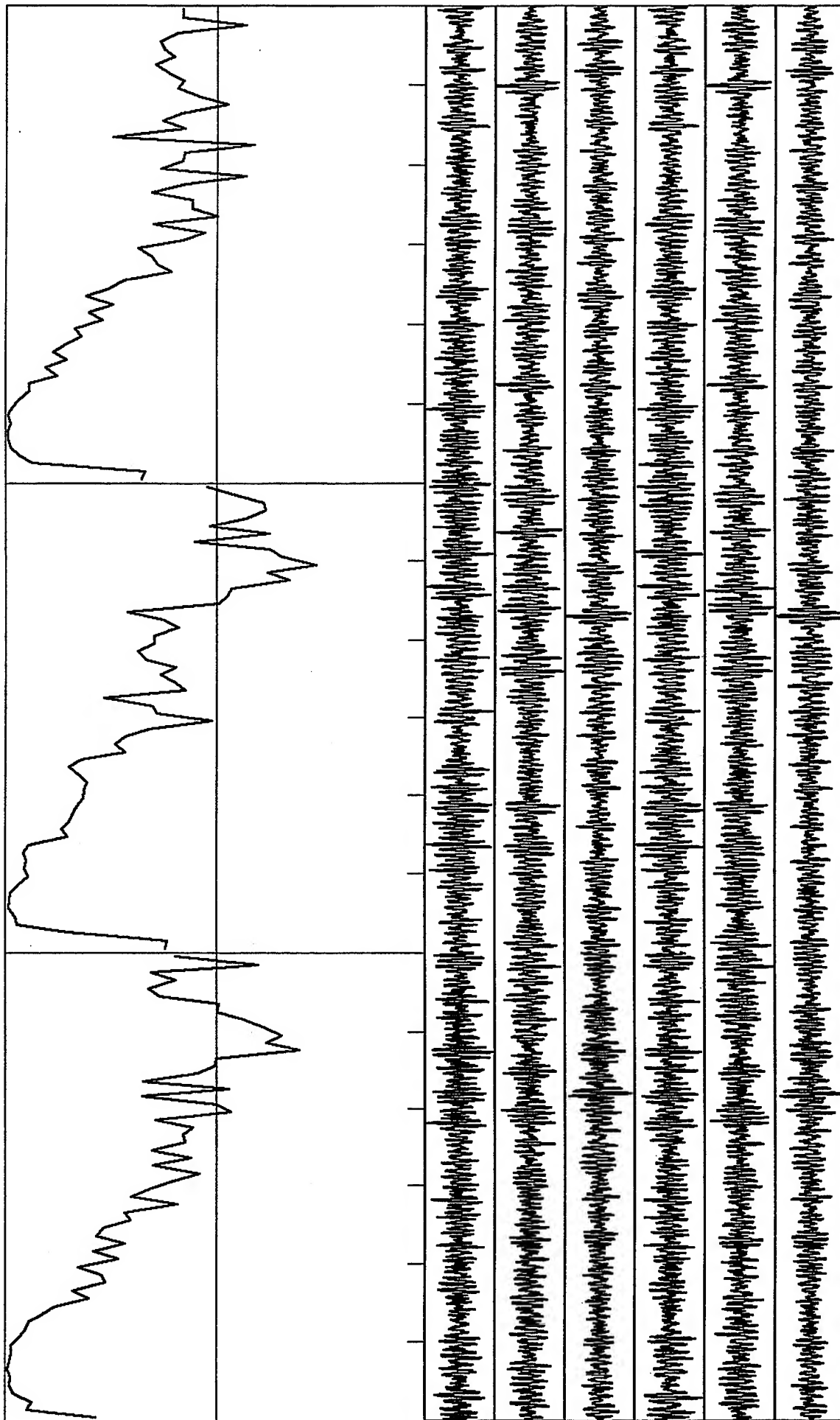


Correlation Coefficients: Scale -1 to +1; freq range: 0 to 30.0 Hz: Radius: 15 m  
 St. 1 & 2: Vertical & horizontal components: 60 s time window

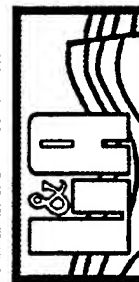


*VortexRock Consultants, Inc.*

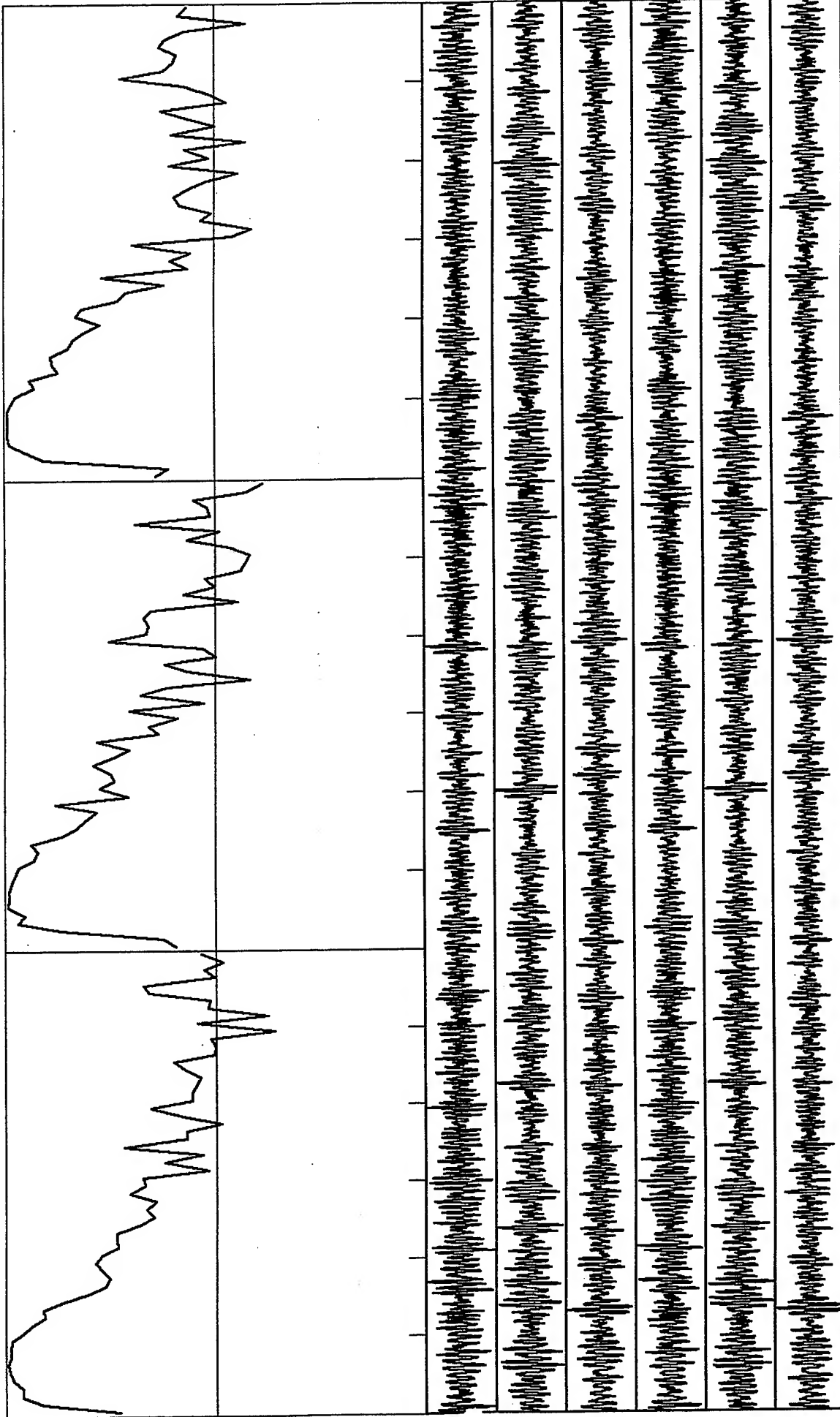




Correlation Coefficients: Scale -1 to +1; freq range: 0 to 30.0 Hz; Radius: 15 m  
St. 1 & 2: Vertical & horizontal components; 60 s time window



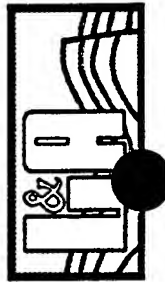
*VortexRock Consultants, Inc.*

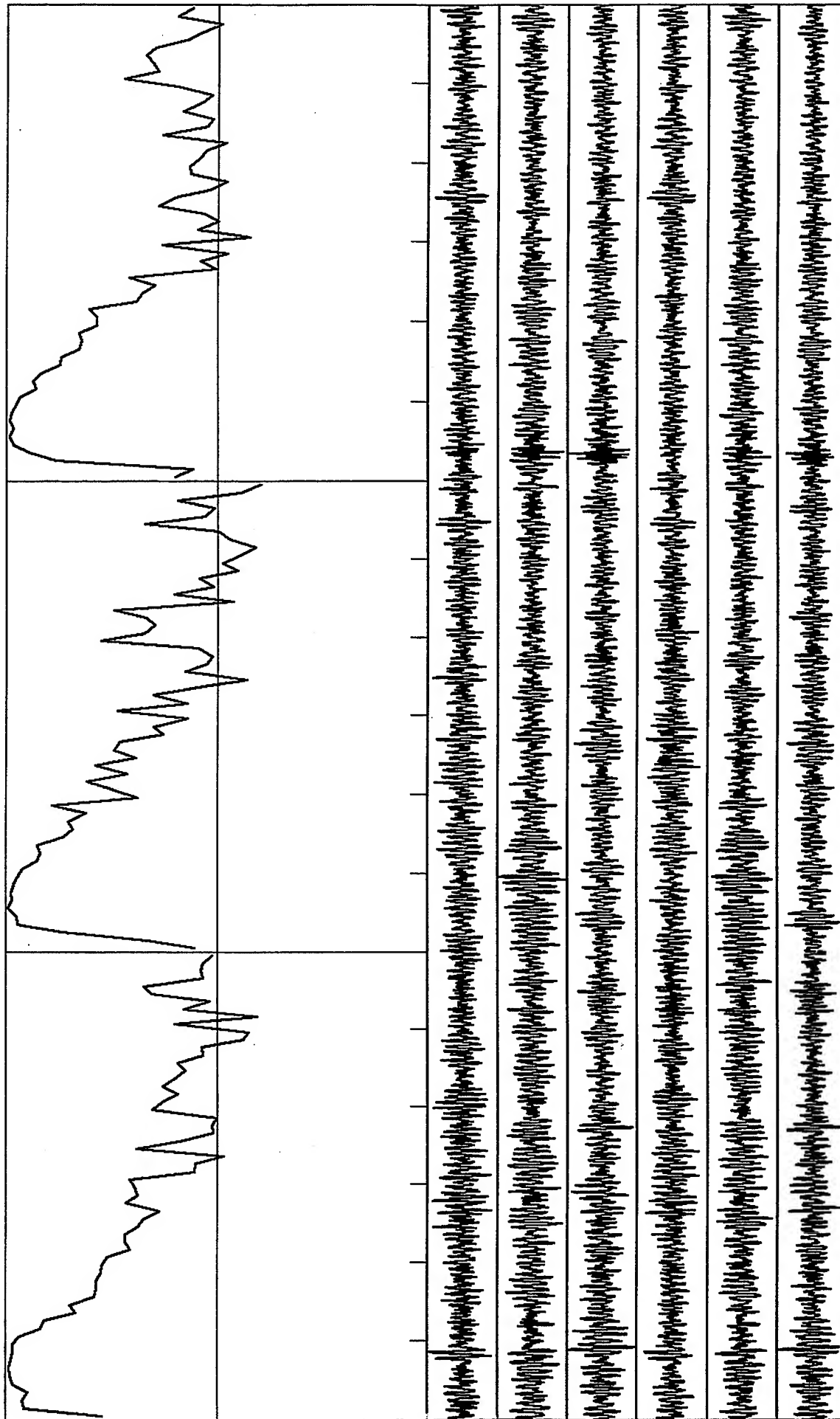


Correlation Coefficients: Scale -1 to +1; freq range: 0 to 30.0 Hz; Radius: 15 m  
 St. 1 & 2: Vertical & horizontal components: 60 s time window

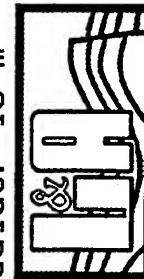


*VortexRock Consultants, Inc.*



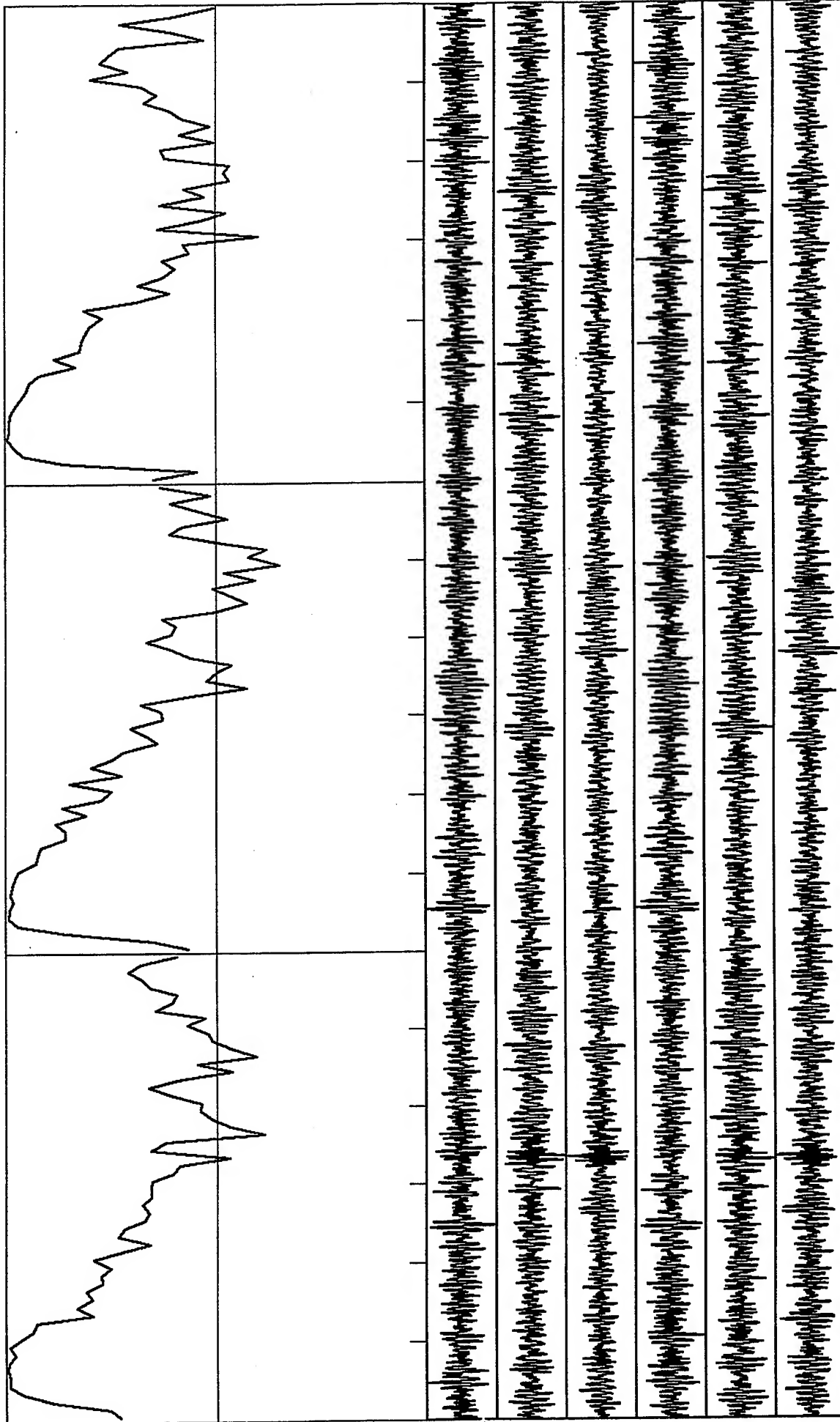


Correlation Coefficients: Scale -1 to +1; freq range: 0 to 30.0 Hz; Radius: 15 m  
 St. 1 & 2: Vertical & horizontal components; 60 s time window



*VortexRock Consultants, Inc.*



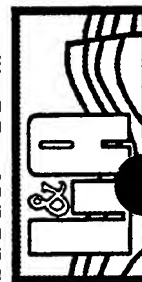


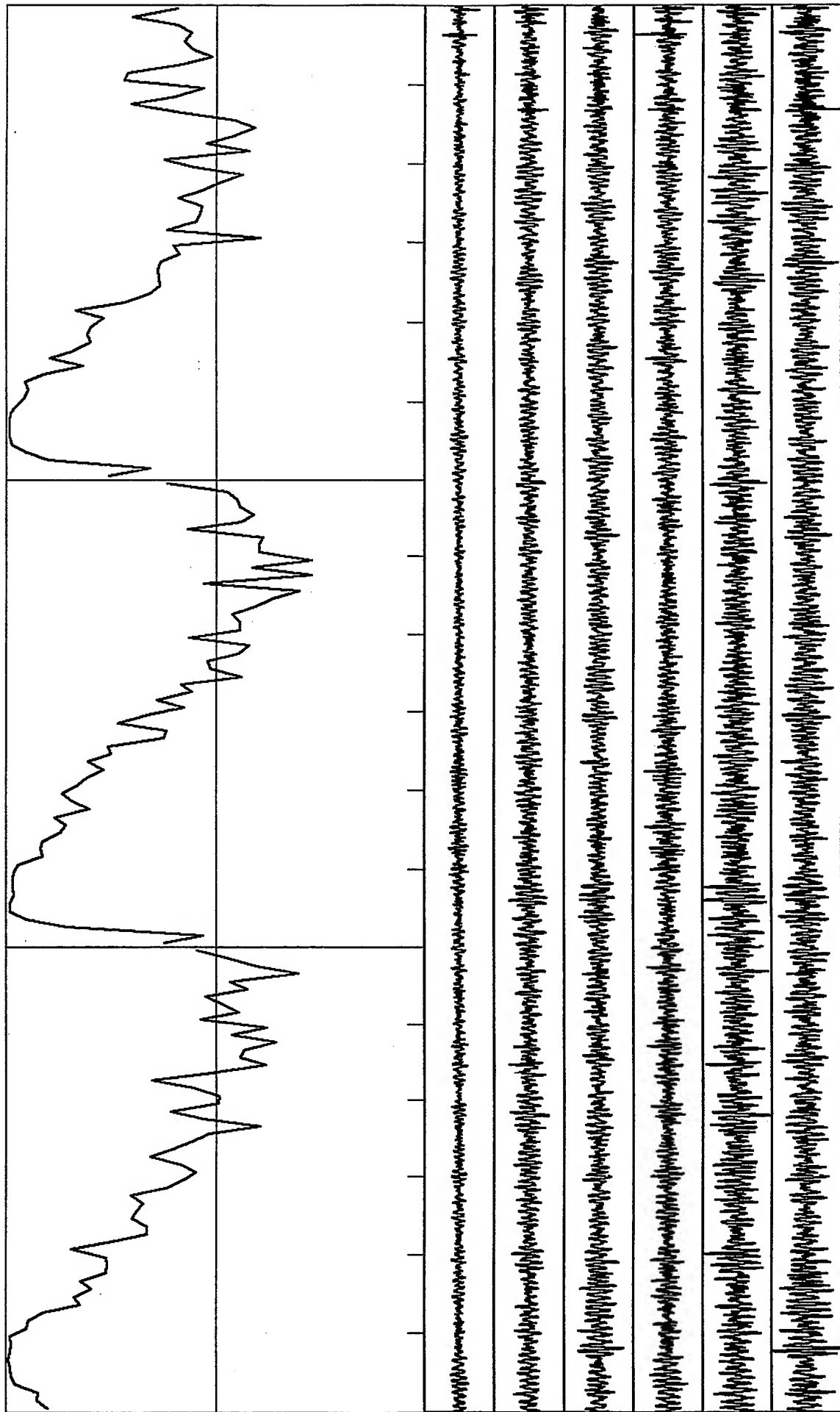
D 8



Correlation Coefficients: Scale -1 to +1; freq range: 0 to 30.0 Hz; Radius: 15 m  
 St. 1 & 2: vertical & horizontal components; 60 s time window

*VortexRock Consultants, Inc.*



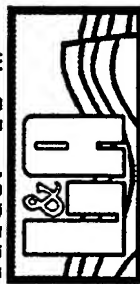


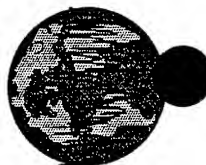
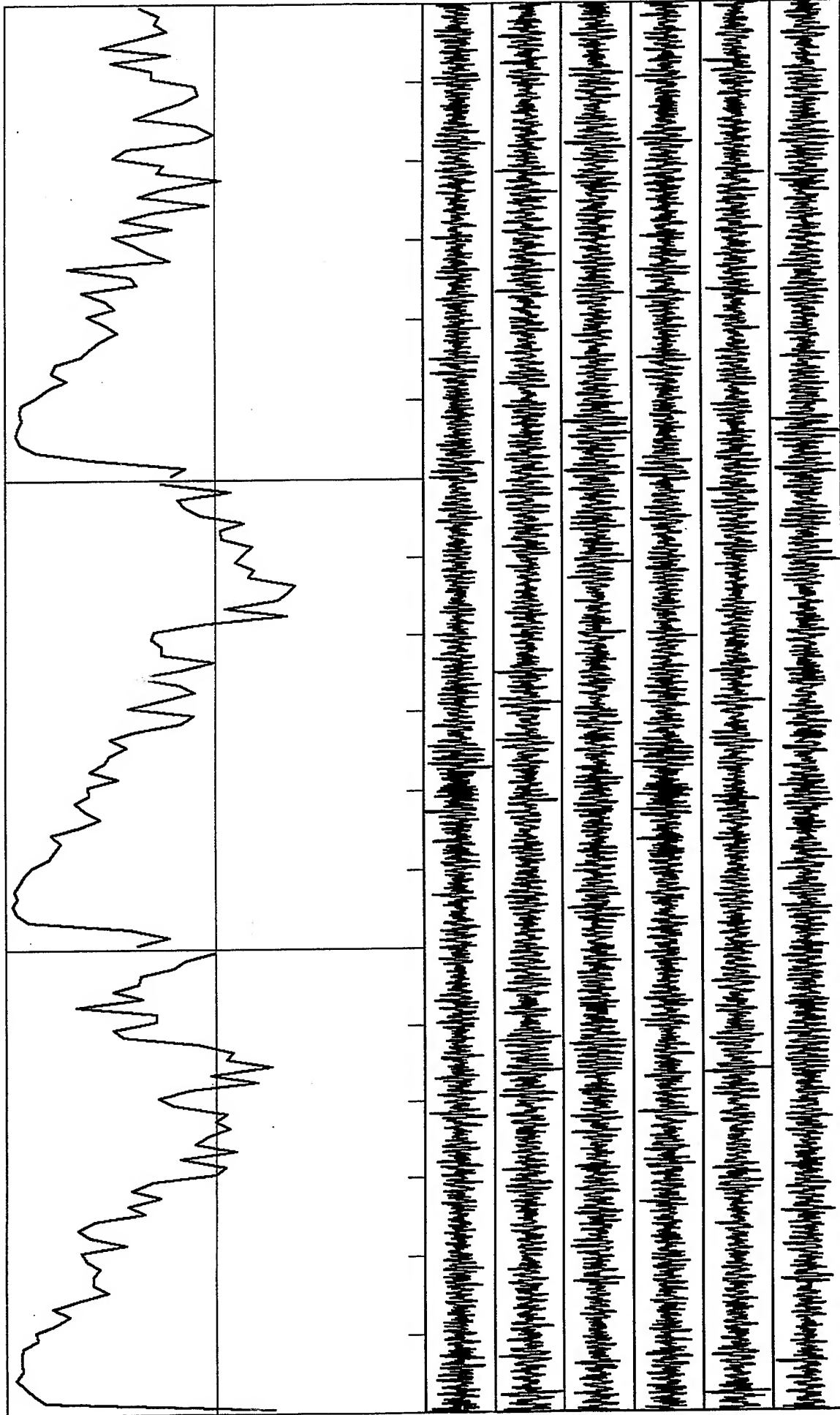
D-9



Correlation Coefficients: Scale -1 to +1; freq range: 0 to 30.0 Hz; Radius: 15 m  
 St. 1 & 2: vertical & horizontal components; 50 s time window

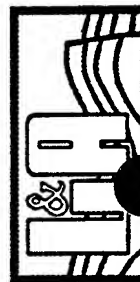
*VortexRock Consultants, Inc.*

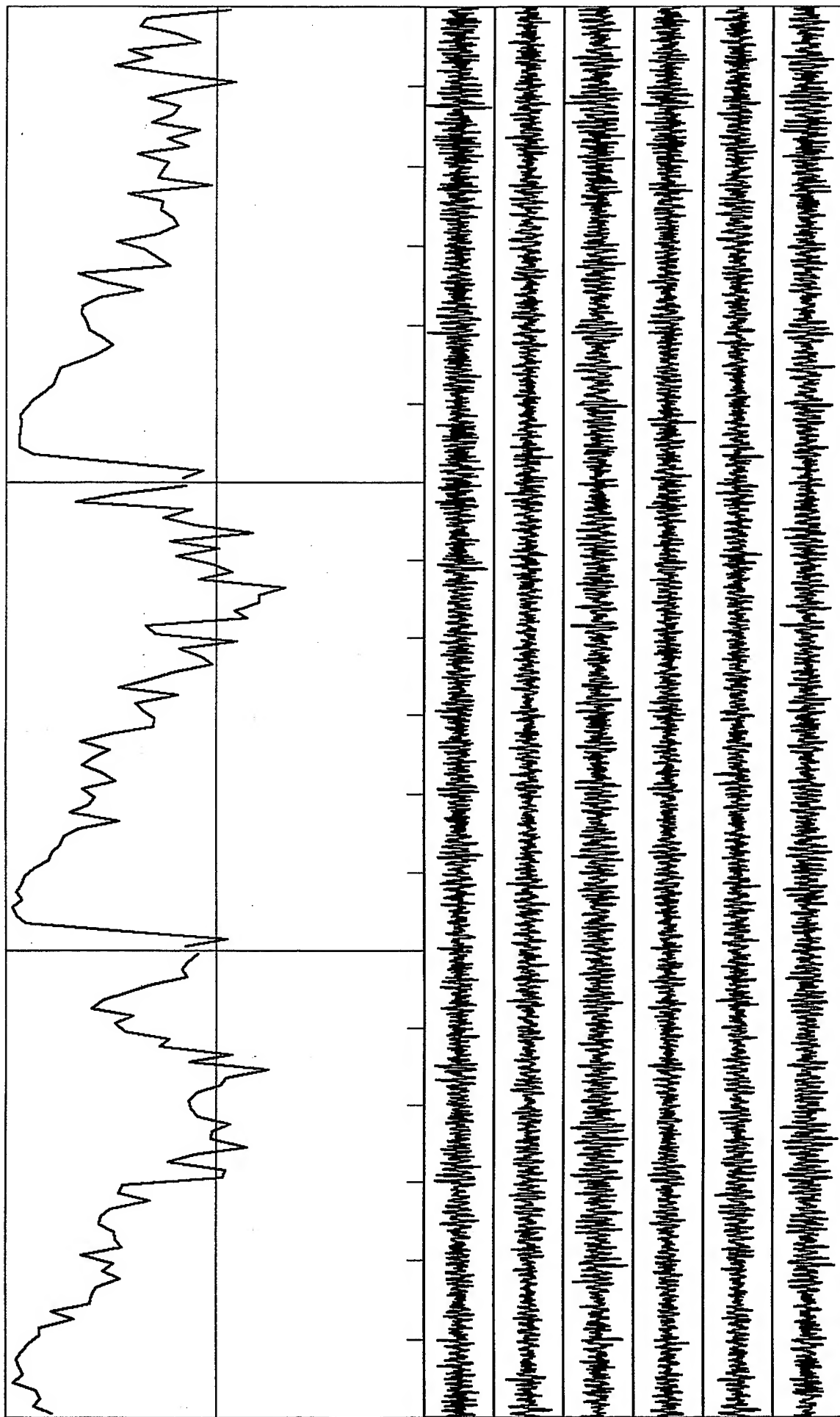




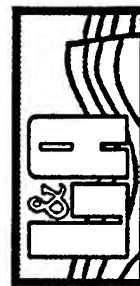
Correlation Coefficients: Scale -1 to +1; freq range: 0 to 30.0 Hz; Radius: 15 m  
 St. 1 & 2: Vertical & horizontal components: 60 s time window

*VortexRock Consultants, Inc.*

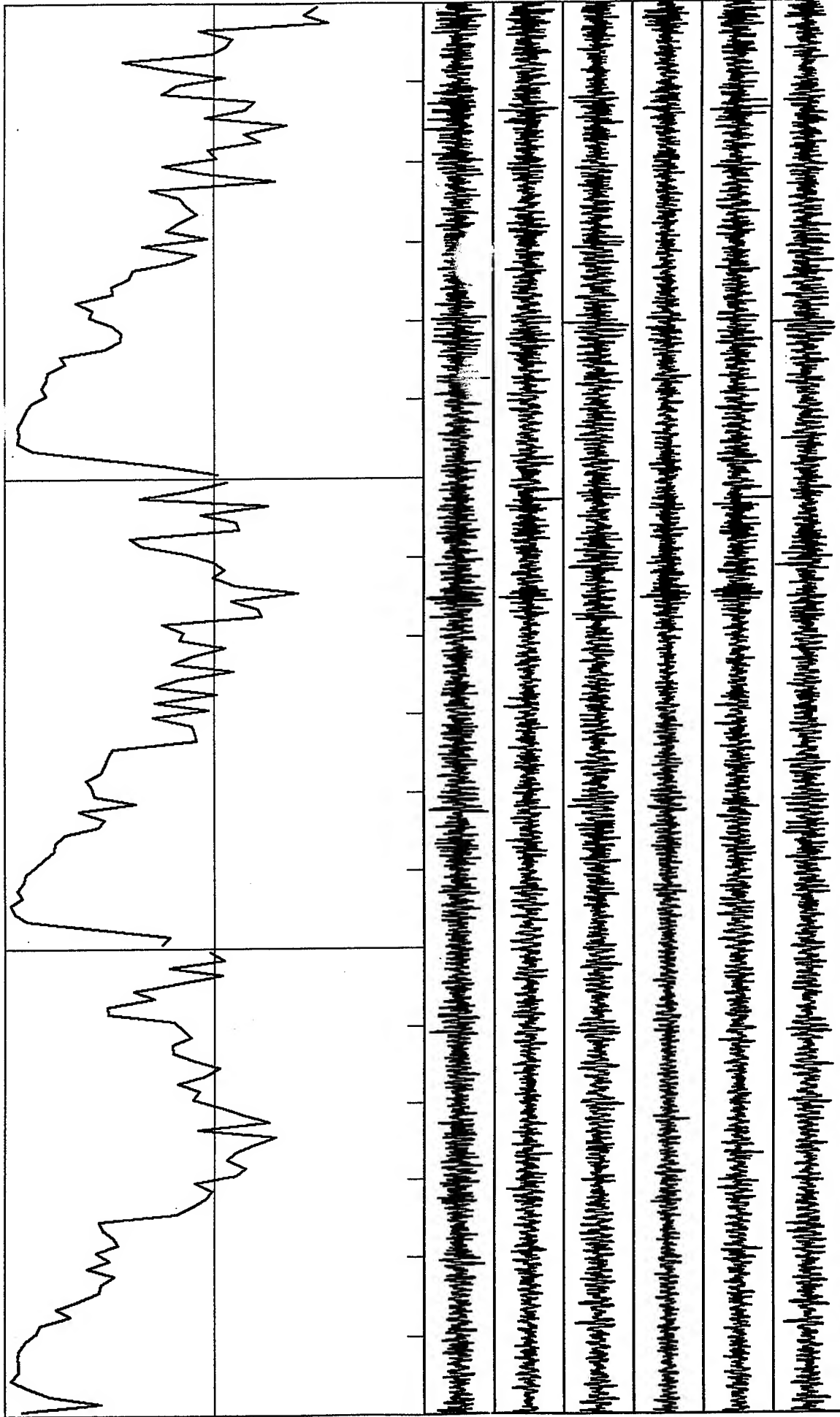




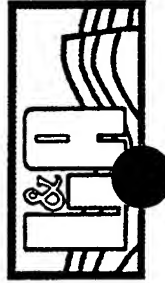
Correlation Coefficients: Scale -1 to +1; freq range: 0 to 30.0 Hz; Radius: 15 m  
 St. 1 & 2: Vertical & horizontal components; 60 s time window



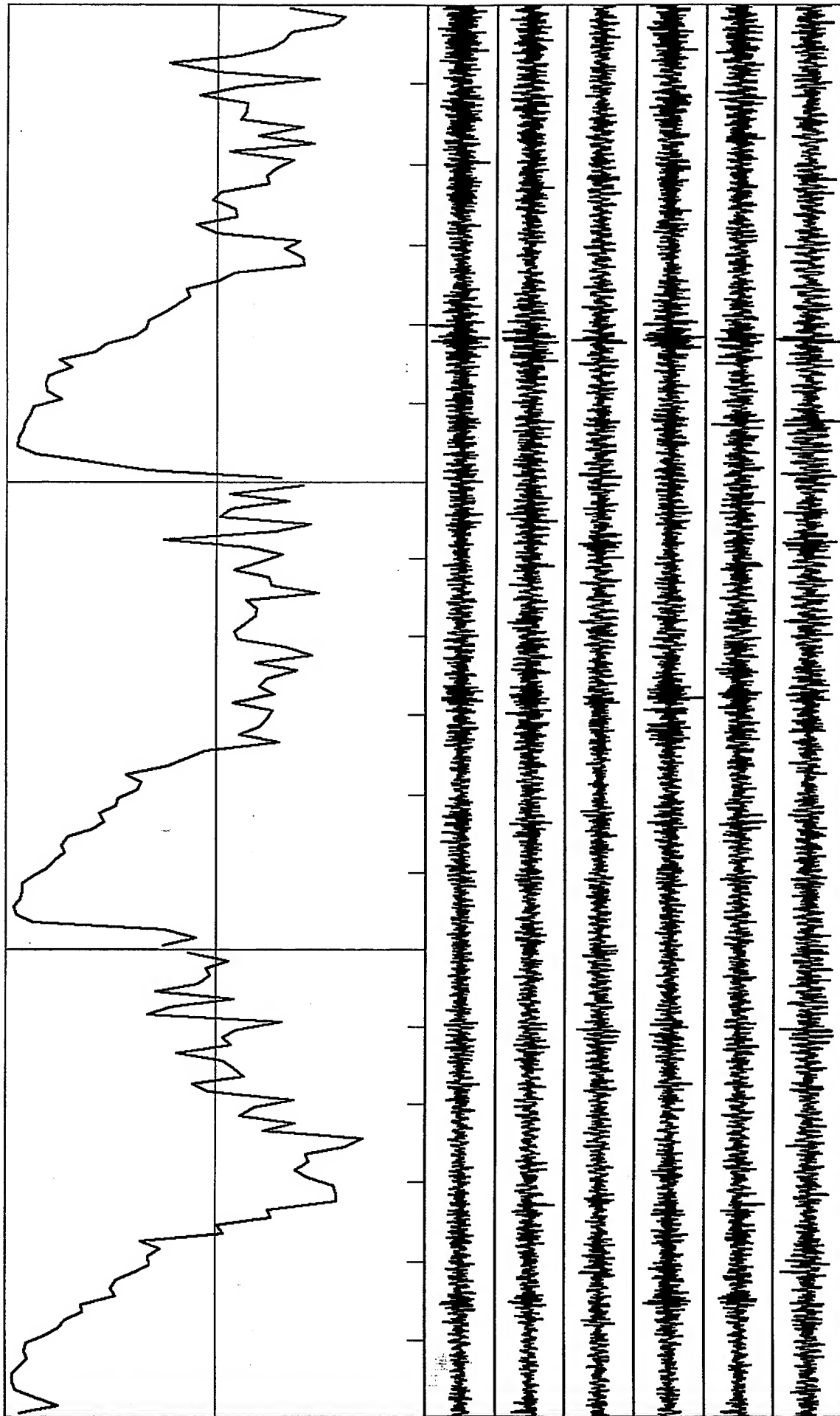
*VortexRock Consultants, Inc.*



Correlation Coefficients: Scale -1 to +1; freq range: 0 to 30.0 Hz; Radius: 15 m  
 St. 1 & 2: Vertical & horizontal components; 60 s time window



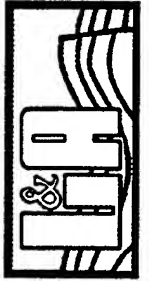
*VortexRock Consultants, Inc.*



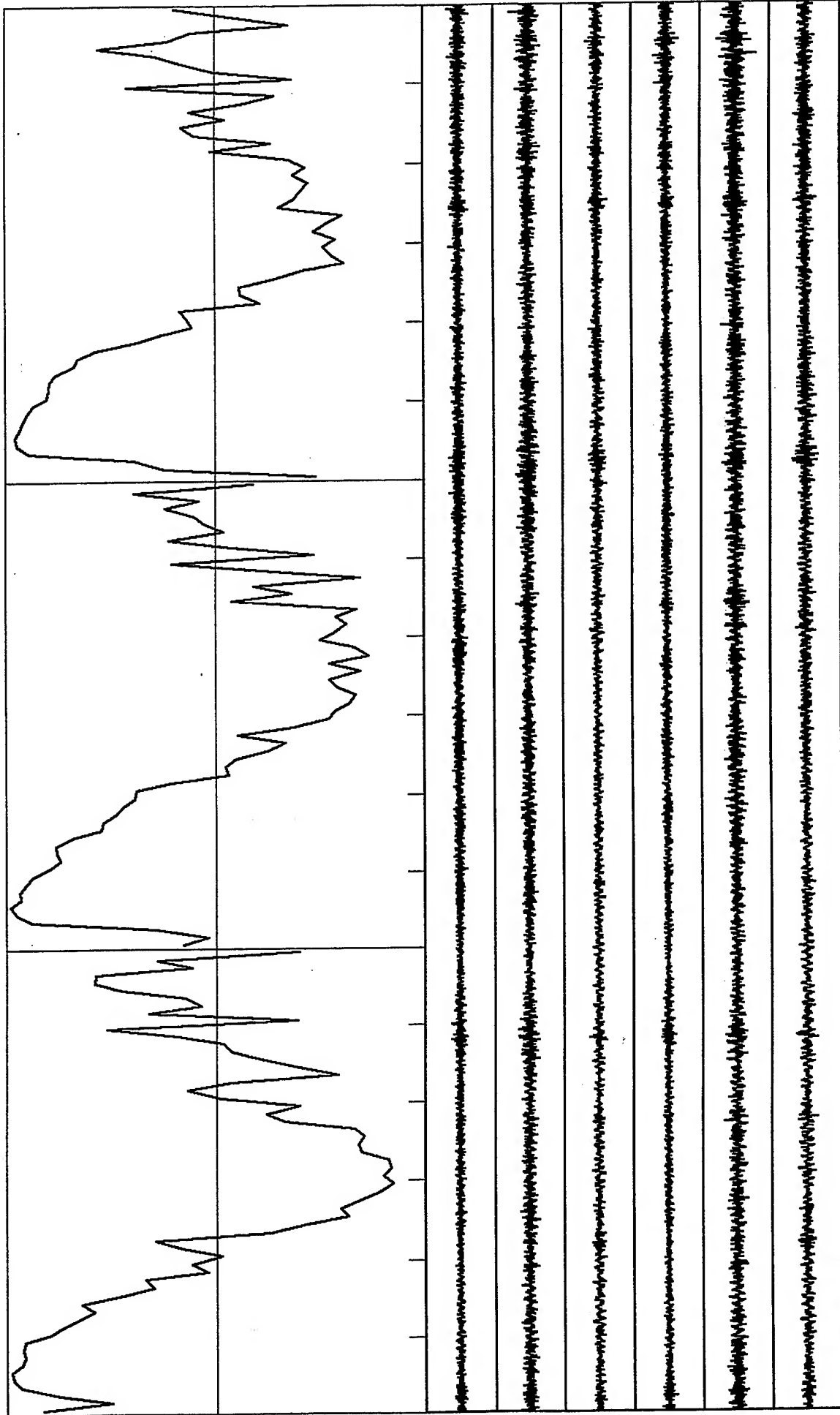
D-13



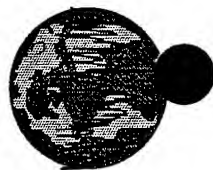
Correlation Coefficients: Scale -1 to +1; freq range: 0 to 30.0 Hz; Radius: 15 m  
 St. 1 & 2: Vertical & horizontal components; 60 s time window



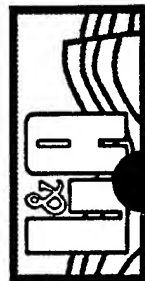
*VortexRock Consultants, Inc.*

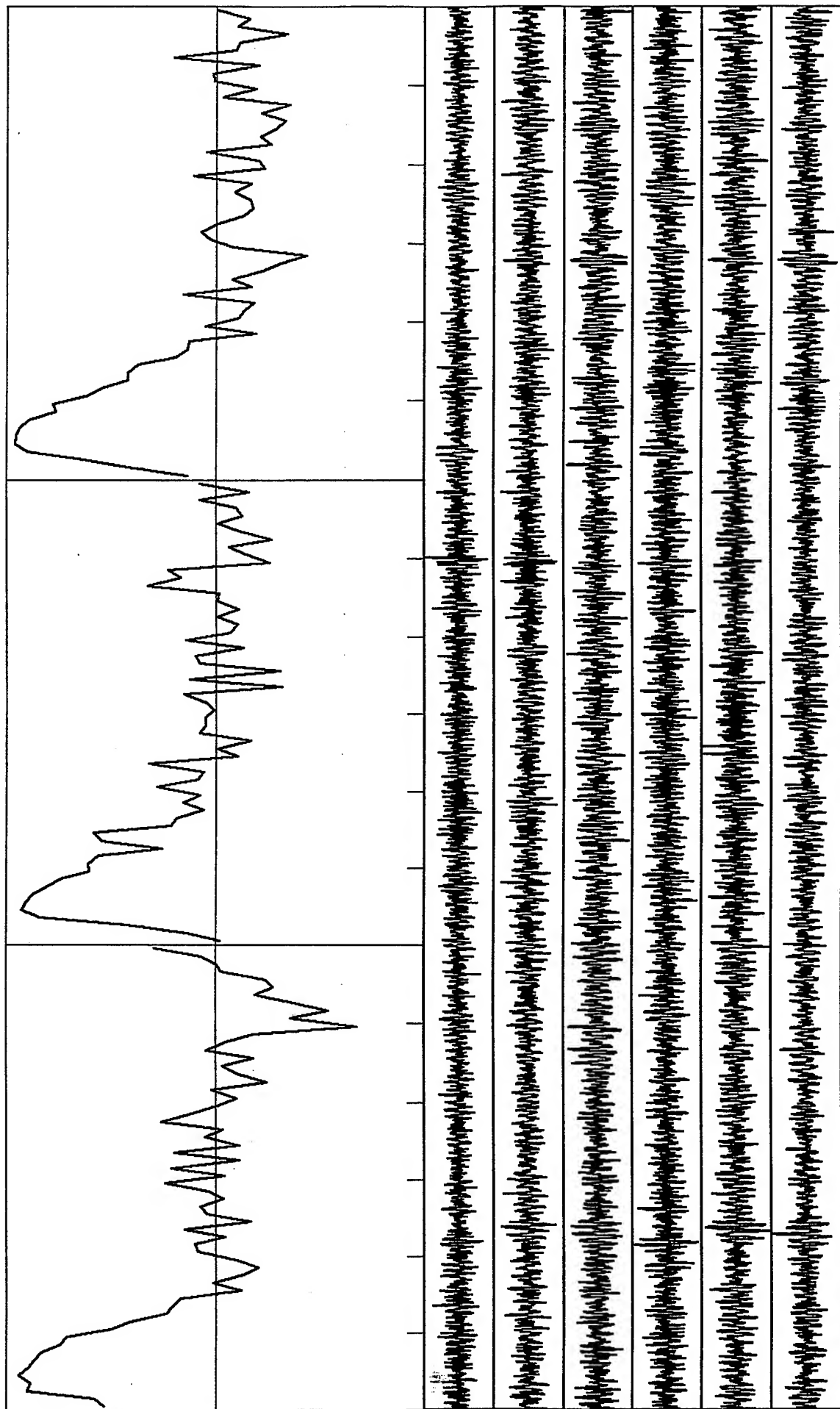


Correlation Coefficients: Scale -1 to +1; freq range: 0 to 30.0 Hz; Radius: 15 m  
 St. 1 & 2: Vertical & horizontal components: 60 s time window



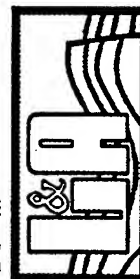
*VortexRock Consultants, Inc.*



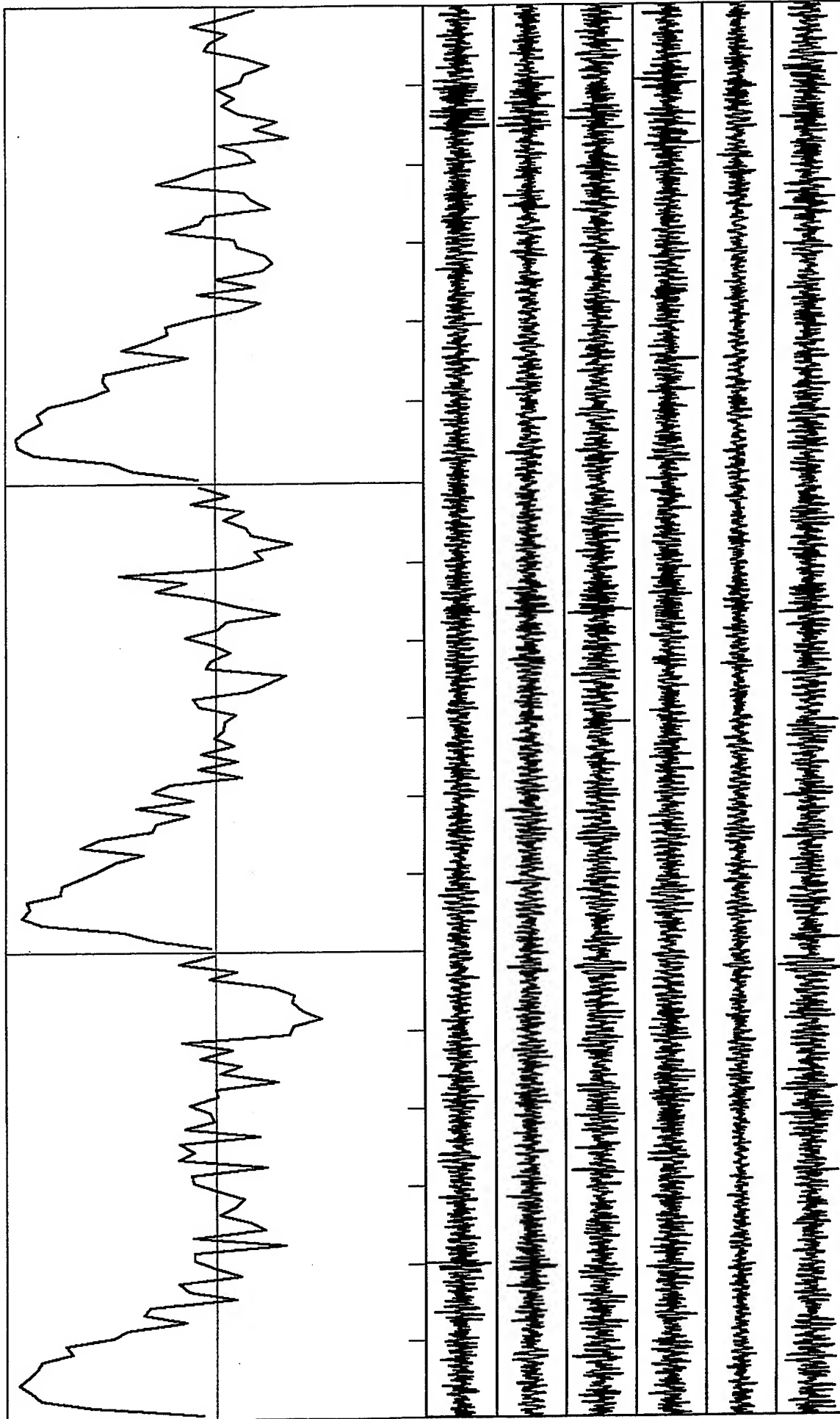


Correlation Coefficients: Scale -1 to +1; freq range: 0 to 30.0 Hz; Radius: 30 m  
 St. 1 & 2: Vertical & horizontal components; 60 s time window

*VortexRock Consultants, Inc.*

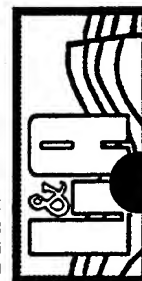


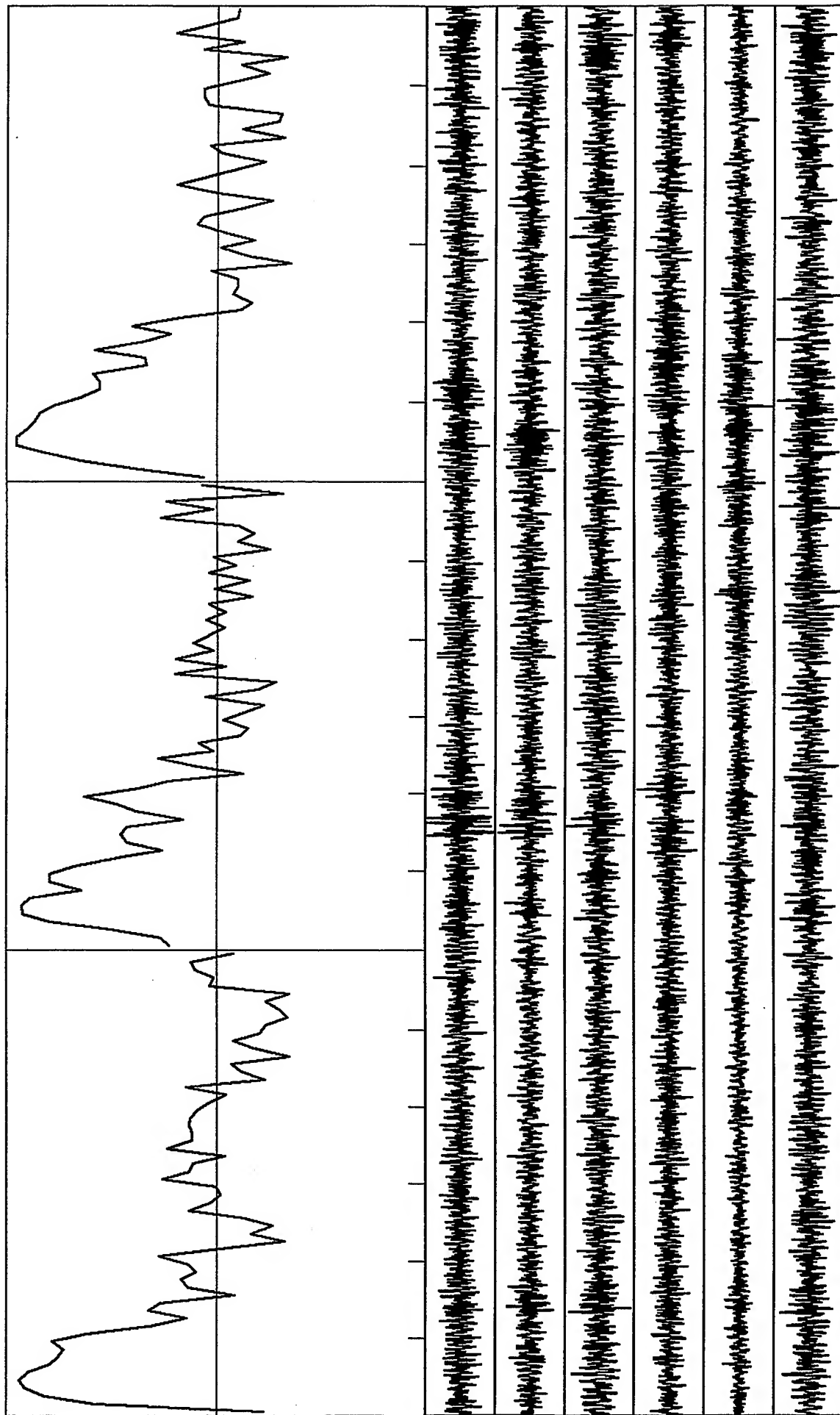




Correlation Coefficients: Scale -1 to +1; freq range: 0 to 30.0 Hz; Radius: 30 m  
 St. 1 & 2: Vertical & horizontal components: 60 s time window

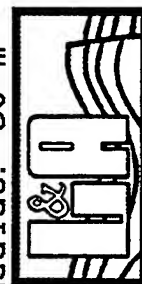
*VortexRock Consultants, Inc.*

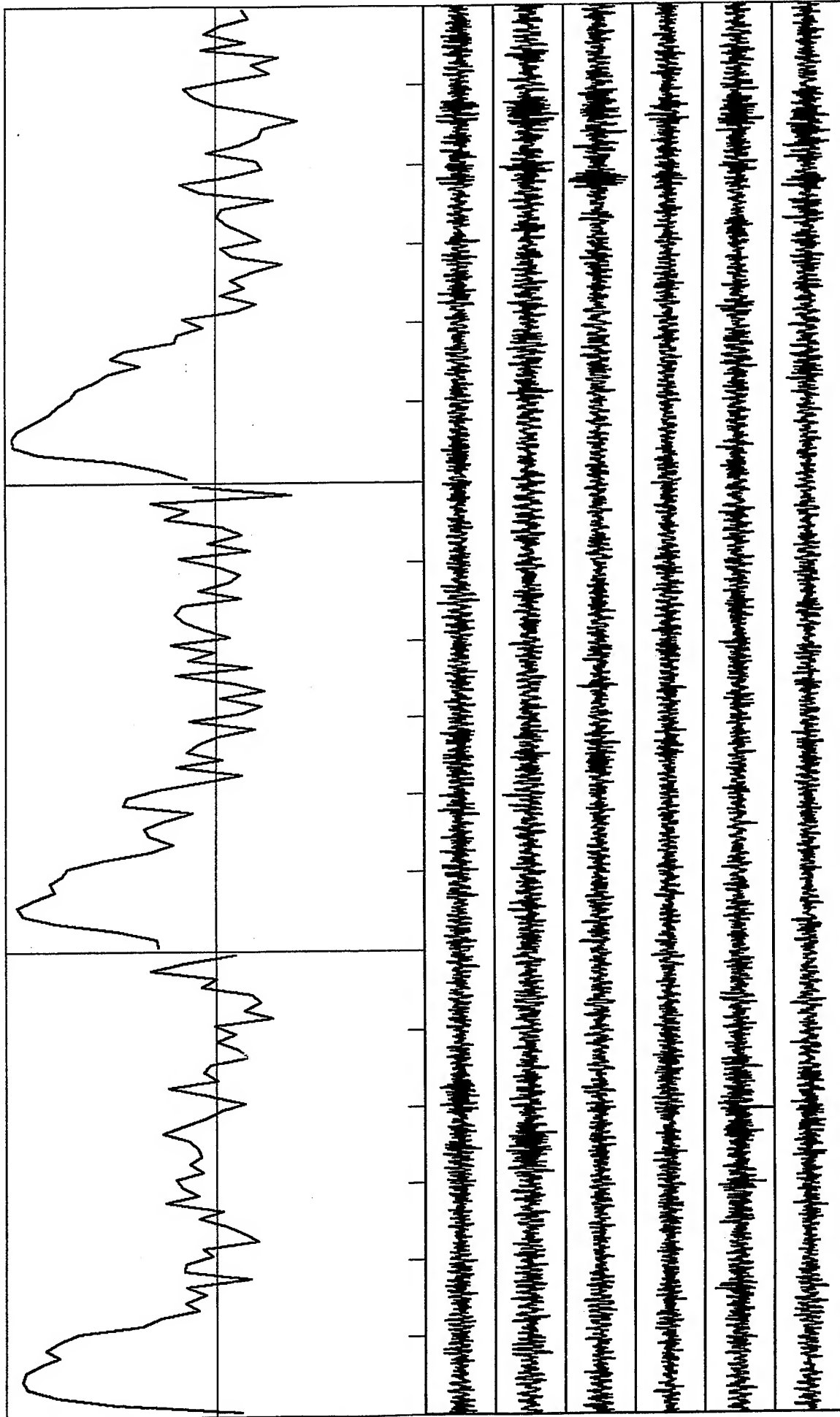




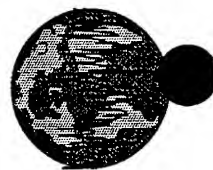
Correlation Coefficients: Scale -1 to +1; freq range: 0 to 30.0 Hz; Radius: 30 m  
 St. 1 & 2: Vertical & horizontal components; 60 s time window

*VortexRock Consultants, Inc.*

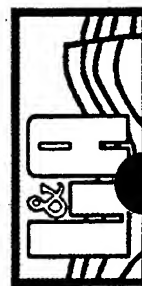


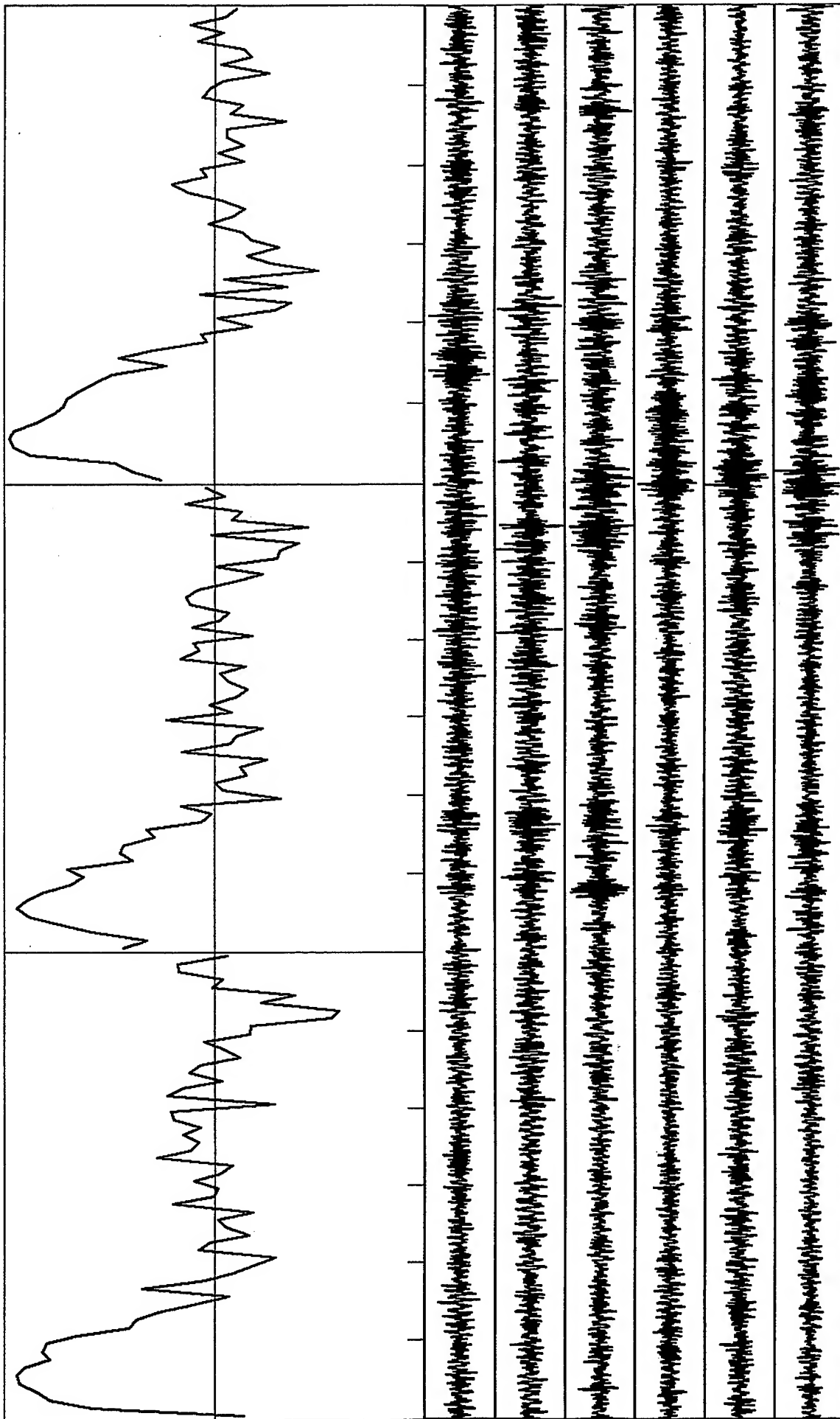


Correlation Coefficients: Scale -1 to +1; freq range: 0 to 30.0 Hz; Radius: 30 m  
 St. 1 & 2: Vertical & horizontal components; 60 s time window

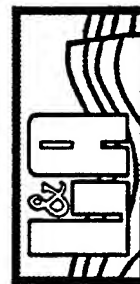


*VortexRock Consultants, Inc.*

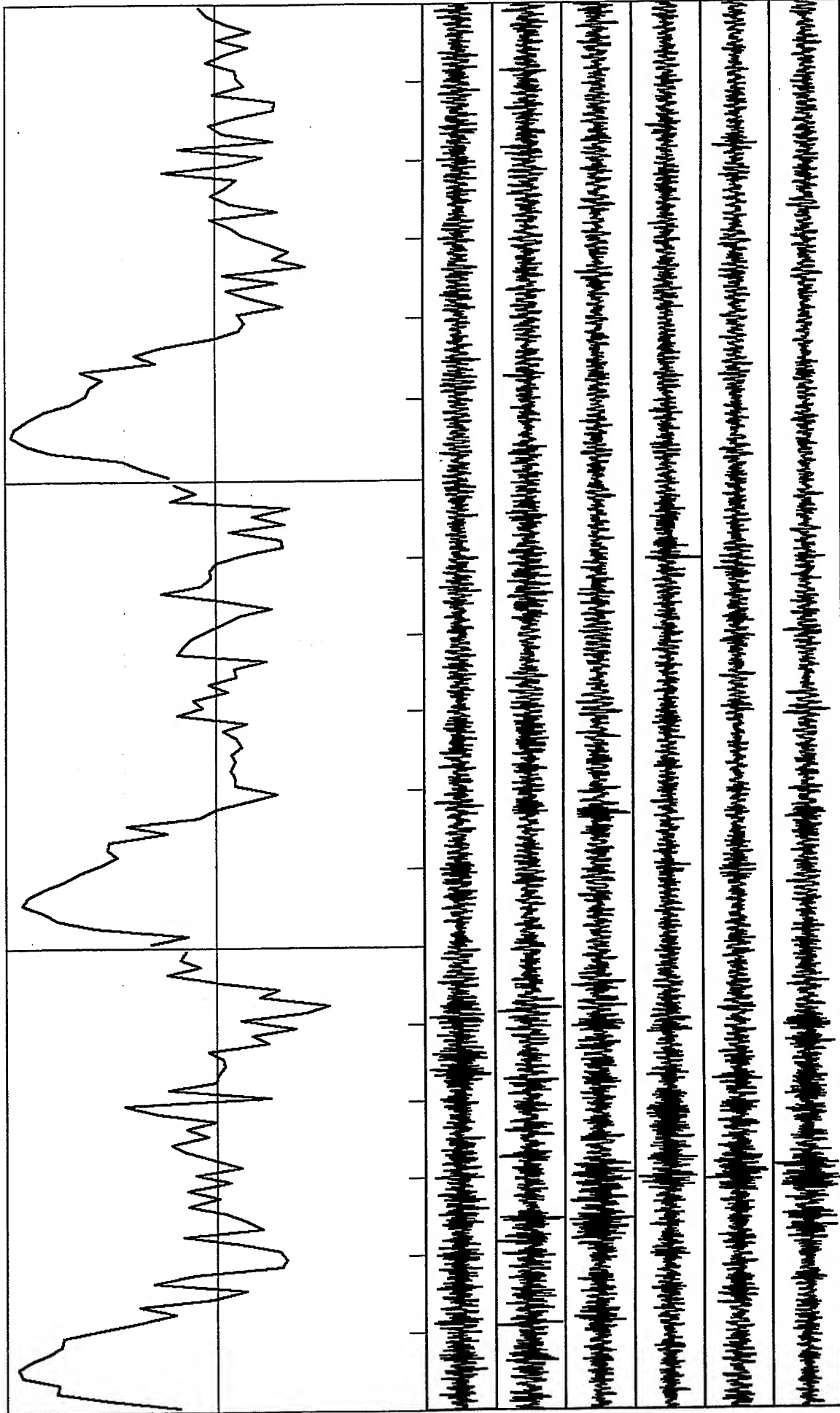




Correlation Coefficients: Scale -1 to +1; freq range: 0 to 30.0 Hz; Radius: 30 m  
 St. 1 & 2: Vertical & horizontal components; 50 s time window



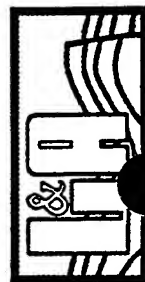
*VortexRock Consultants, Inc.*

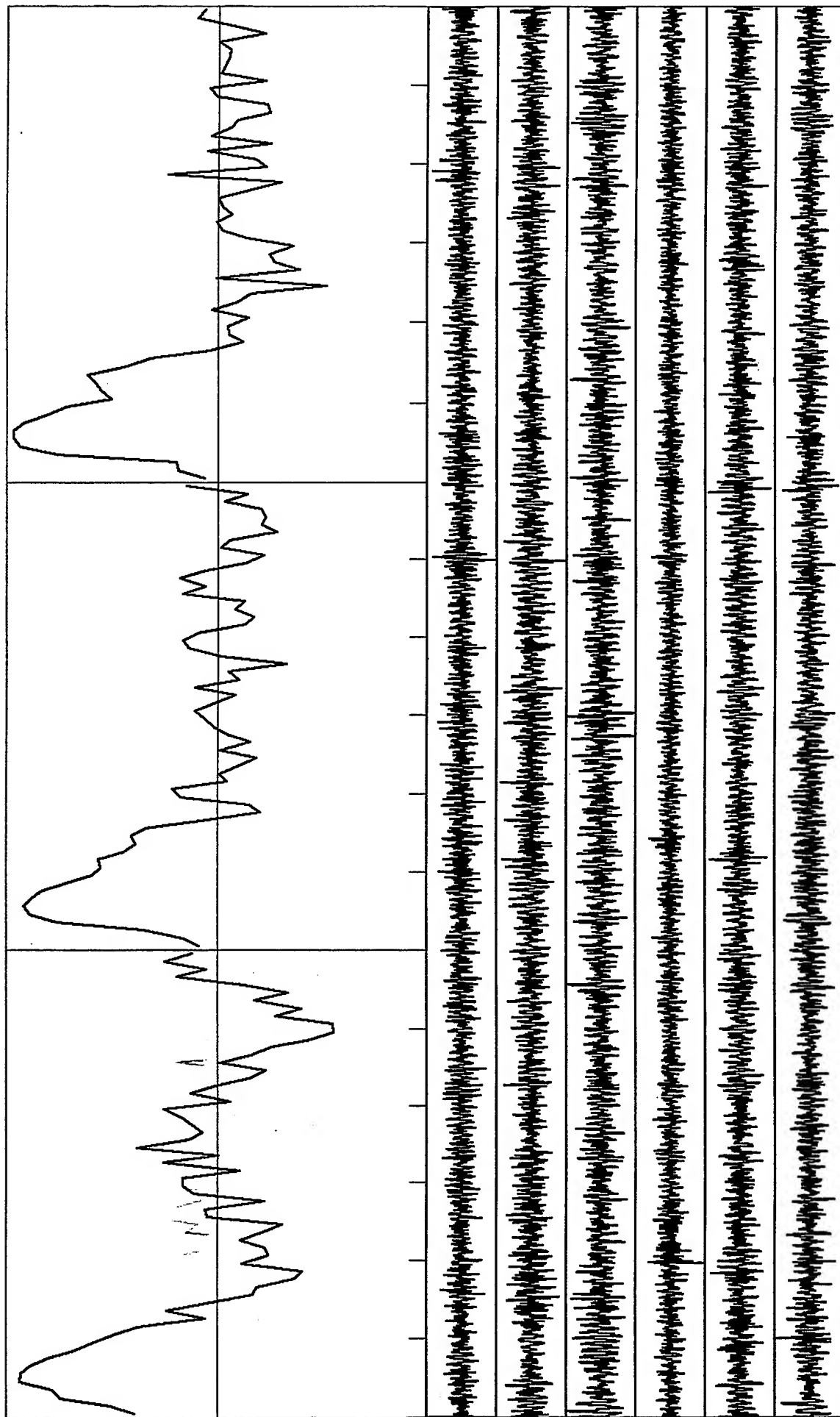


Correlation Coefficients: Scale -1 to +1; freq range: 0 to 30.0 Hz; Radius: 30 m  
 St. 1 & 2: Vertical & horizontal components: 60 s time window



*VortexRock Consultants, Inc.*

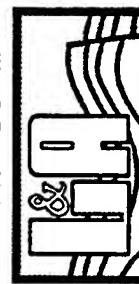




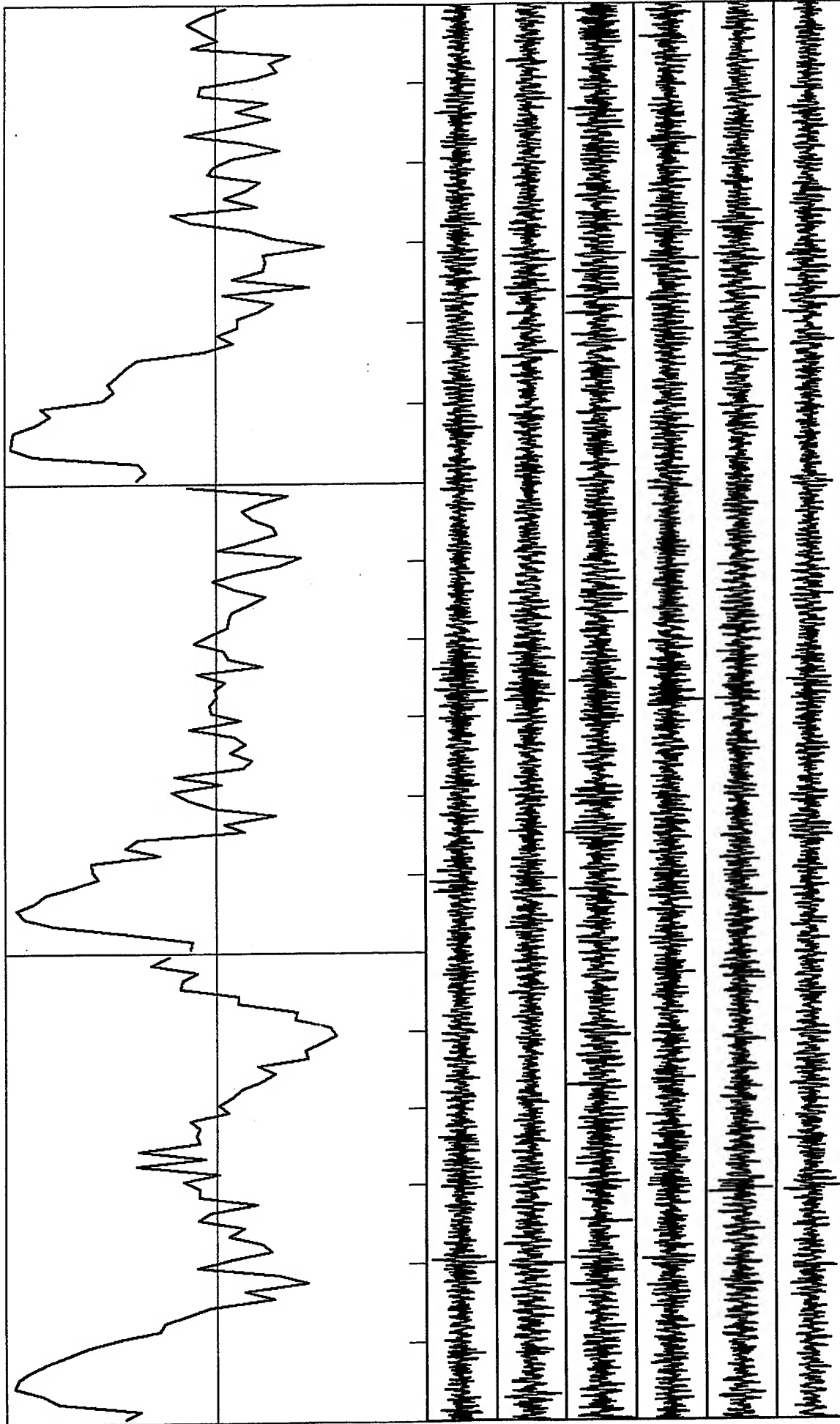
D-21



Correlation Coefficients: Scale -1 to +1; freq range: 0 to 30.0 Hz; Radius: 30 m  
 St. 1 & 2: Vertical & horizontal components; 50 s time window



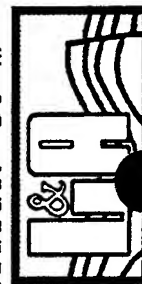
*VortexRock Consultants, Inc.*

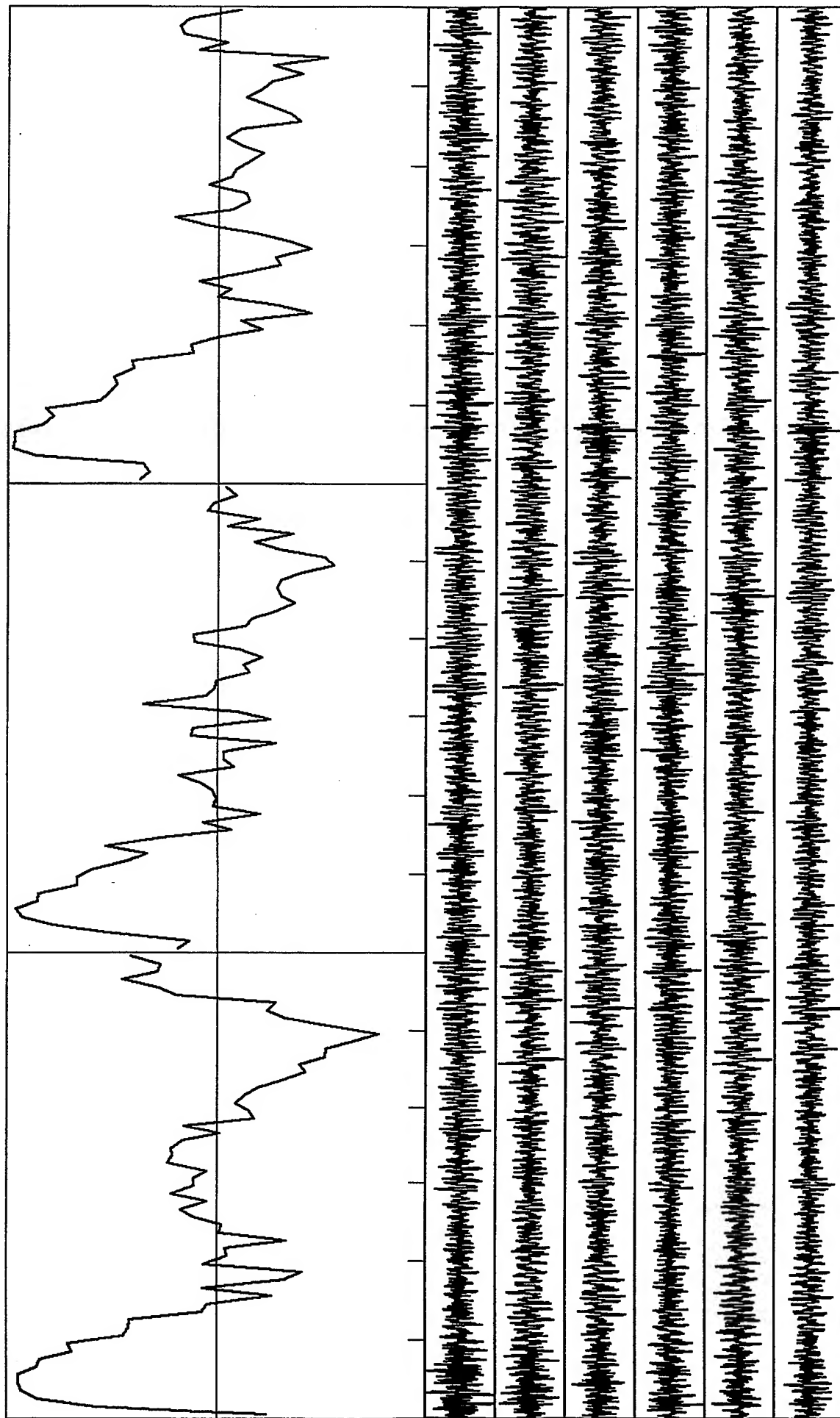


Correlation Coefficients: Scale -1 to +1; freq range: 0 to 30.0 Hz; Radius: 30 m  
 St. 1 & 2: Vertical & horizontal components; 60 s time window



*VortexRock Consultants, Inc.*



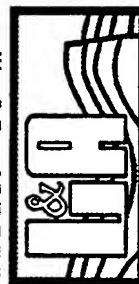


D-23

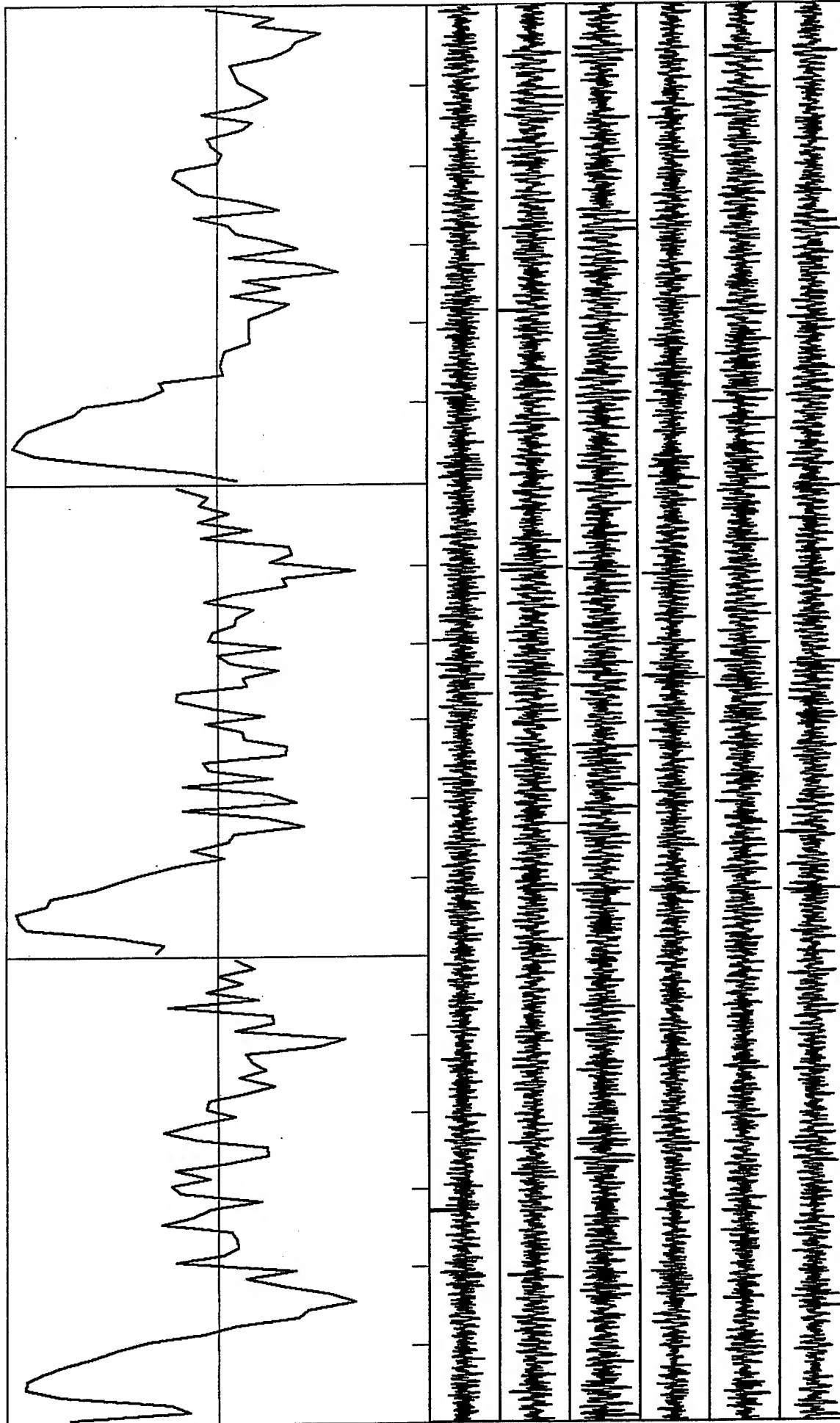


Correlation Coefficients: Scale -1 to +1; freq range: 0 to 30.0 Hz; Radius: 30 m  
 St. 1 & 2: Vertical & horizontal components; 60 s time window

*VortexRock Consultants, Inc.*

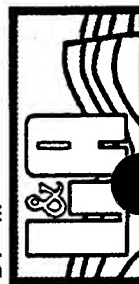
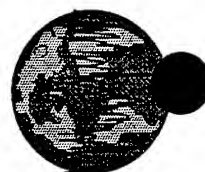




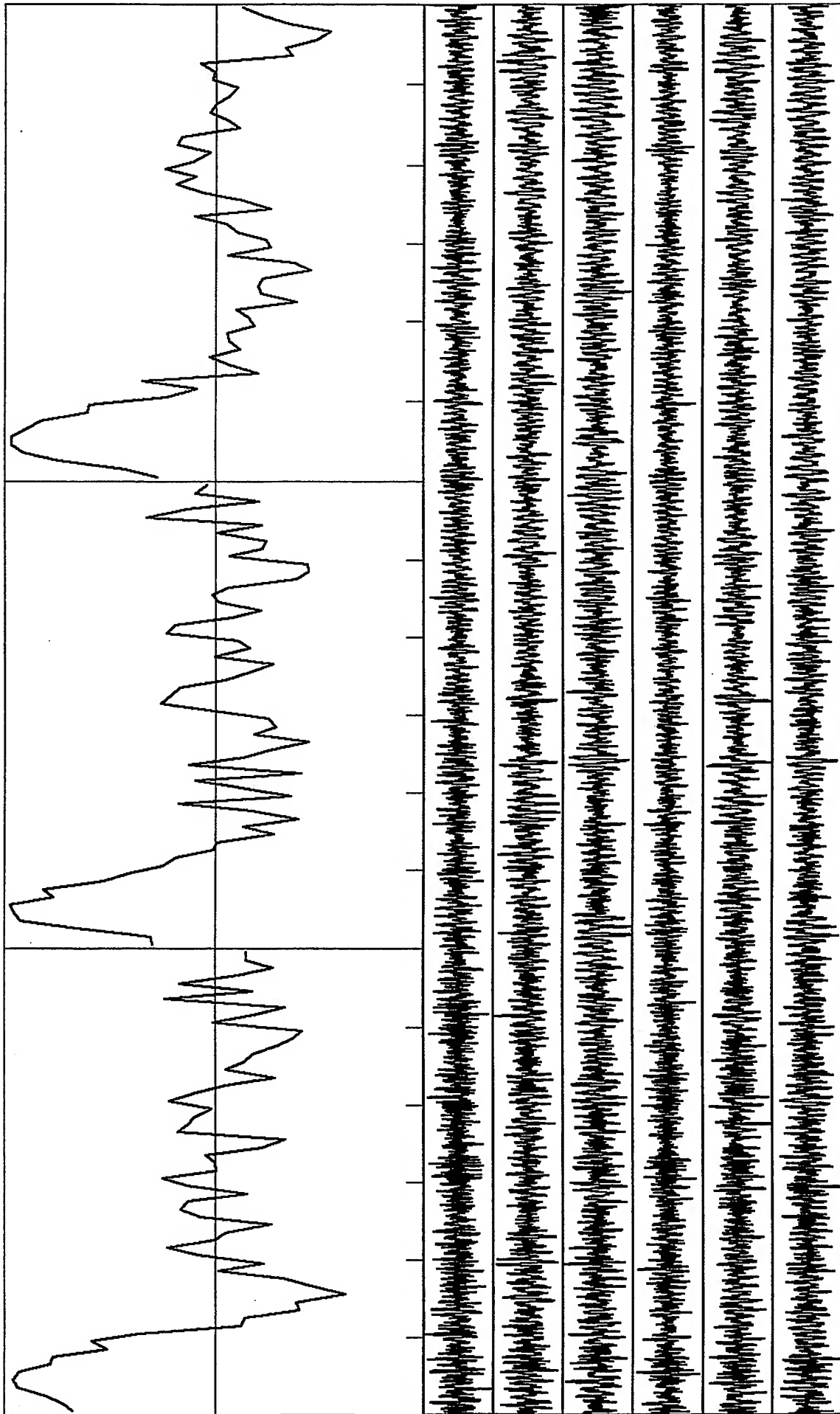


Correlation Coefficients: Scale -1 to +1; freq range: 0 to 30.0 Hz; Radius: 37 m

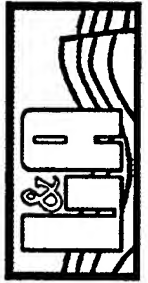
St. 1 & 2: Vertical & horizontal components; 50 s time window



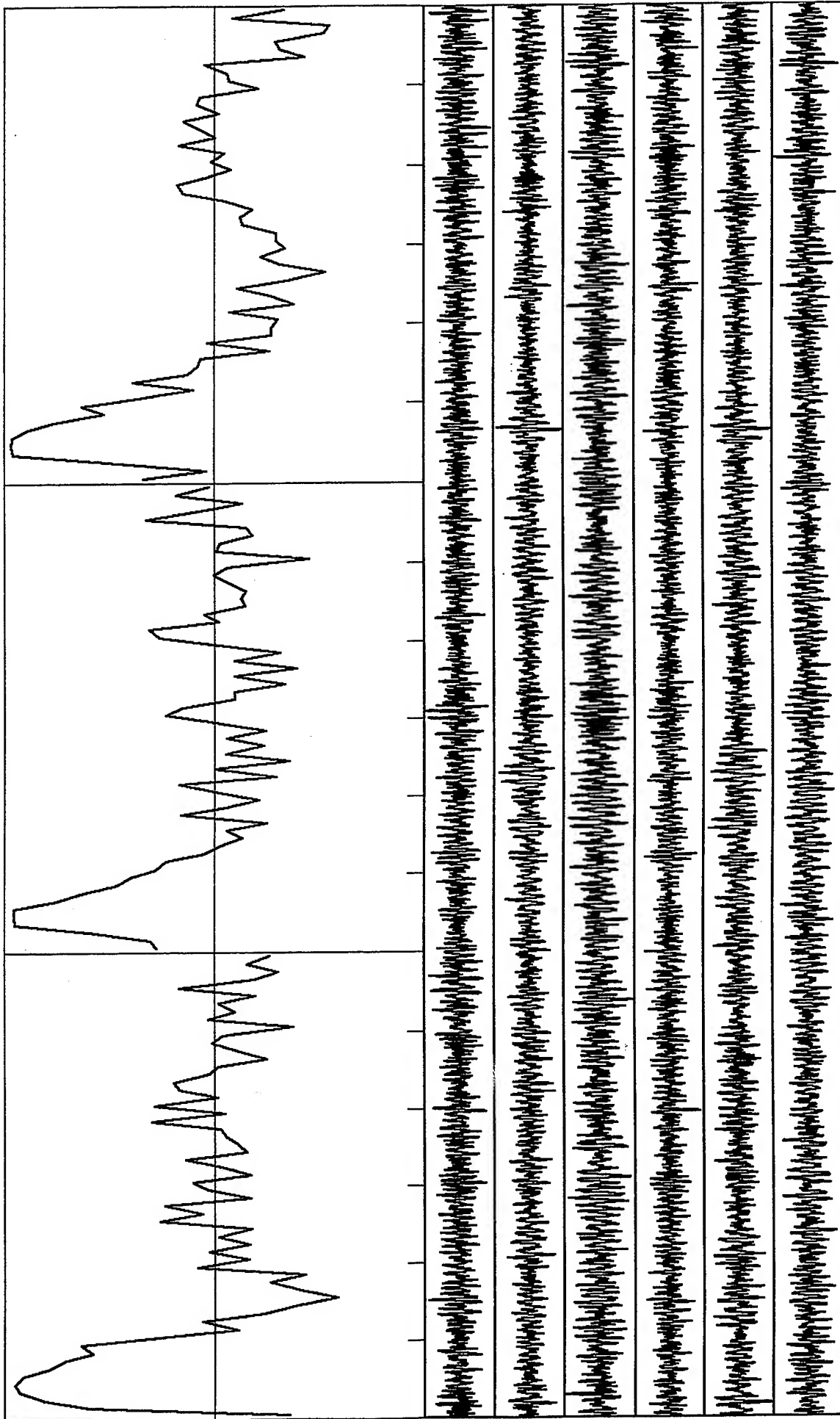
*VortexRock Consultants, Inc.*



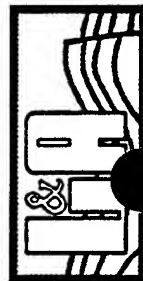
Correlation Coefficients: Scale -1 to +1; freq range: 0 to 30.0 Hz; Radius: 37 m  
 St. 1 & 2: Vertical & horizontal components; 60 s time window



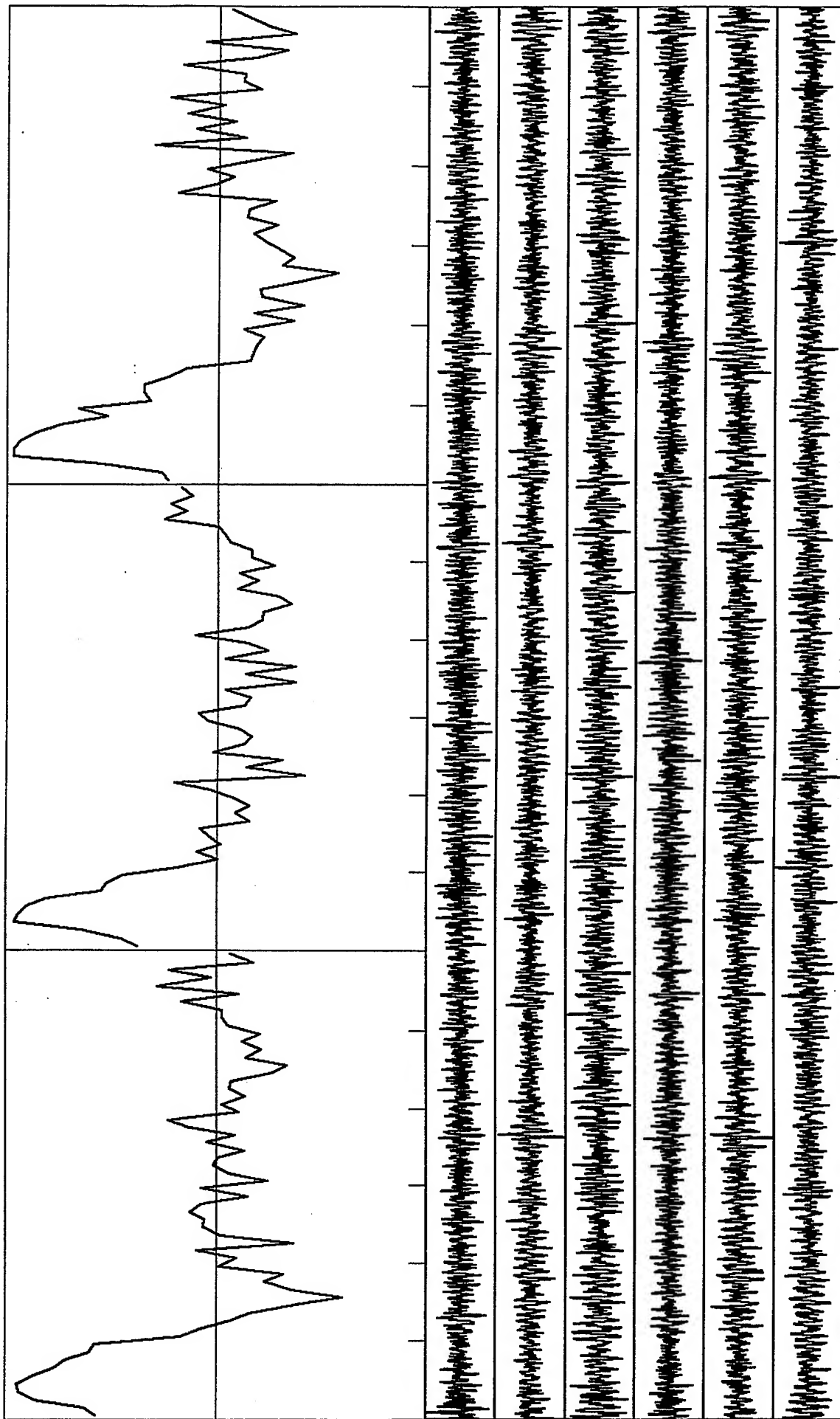
*VortexRock Consultants, Inc.*



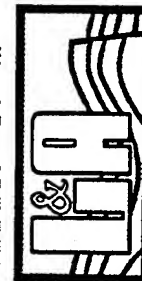
Correlation Coefficients: Scale -1 to +1; freq range: 0 to 30.0 Hz; Radius: 37 m  
 St. 1 & 2: Vertical & horizontal components; 60 s time window



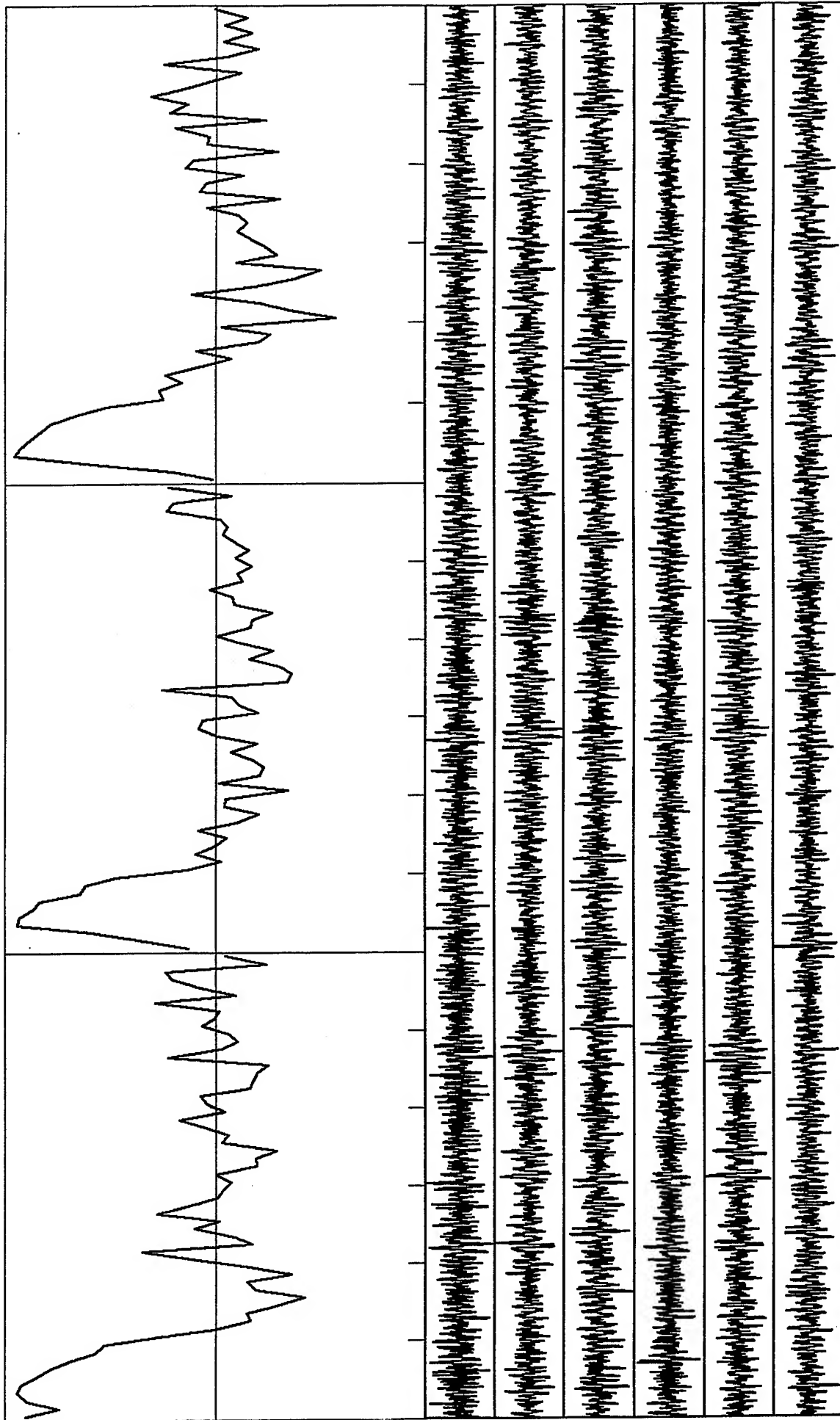
*VortexRock Consultants, Inc.*



Correlation Coefficients: Scale -1 to +1; freq range: 0 to 30.0 Hz; Radius: 37 m  
 St. 1 & 2: Vertical & horizontal components; 50 s time window



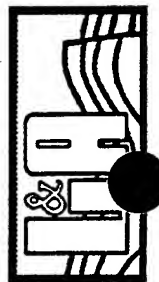
*VortexRock Consultants, Inc.*

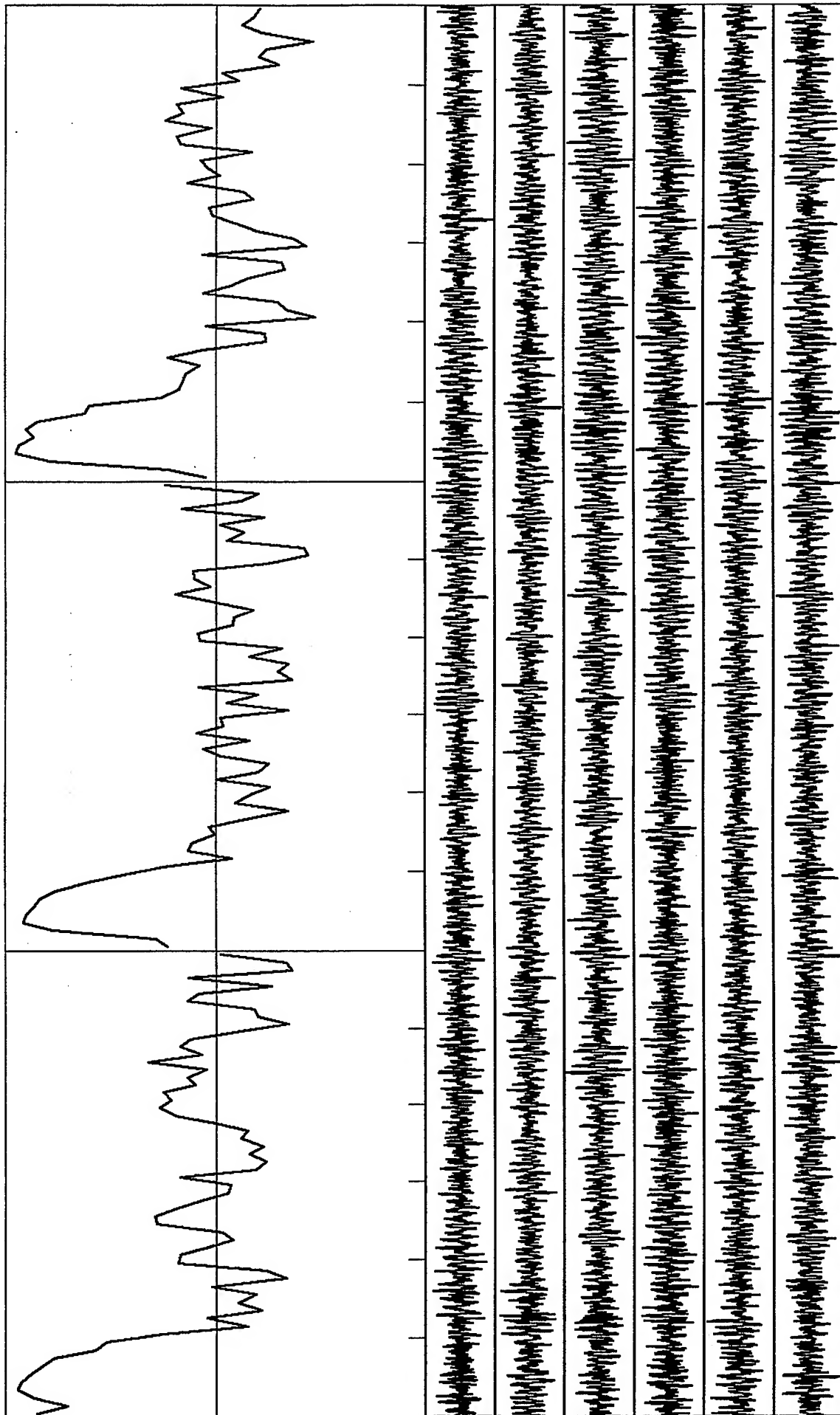


Correlation Coefficients: Scale -1 to +1; freq range: 0 to 30.0 Hz; Radius: 37 m  
 St. 1 & 2: Vertical & horizontal components; 60 s time window



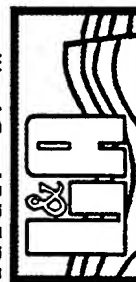
*VortexRock Consultants, Inc.*

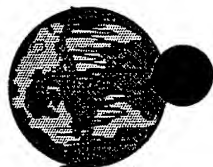
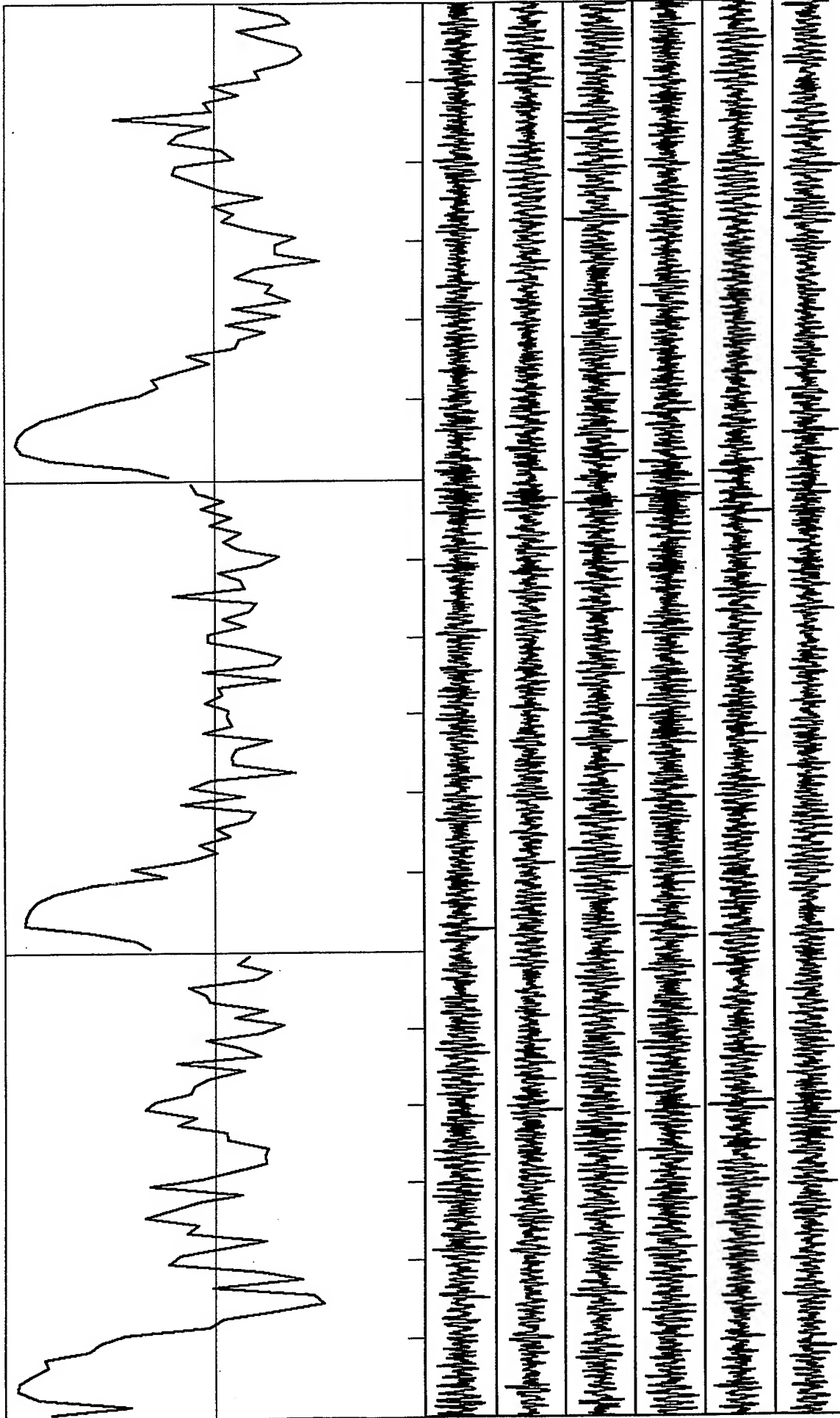




Correlation Coefficients: Scale -1 to +1; freq range: 0 to 30.0 Hz; Radius: 37 m  
 St. 1 & 2: Vertical & horizontal components; 60 s time window

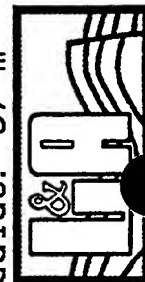
*VortexRock Consultants, Inc.*

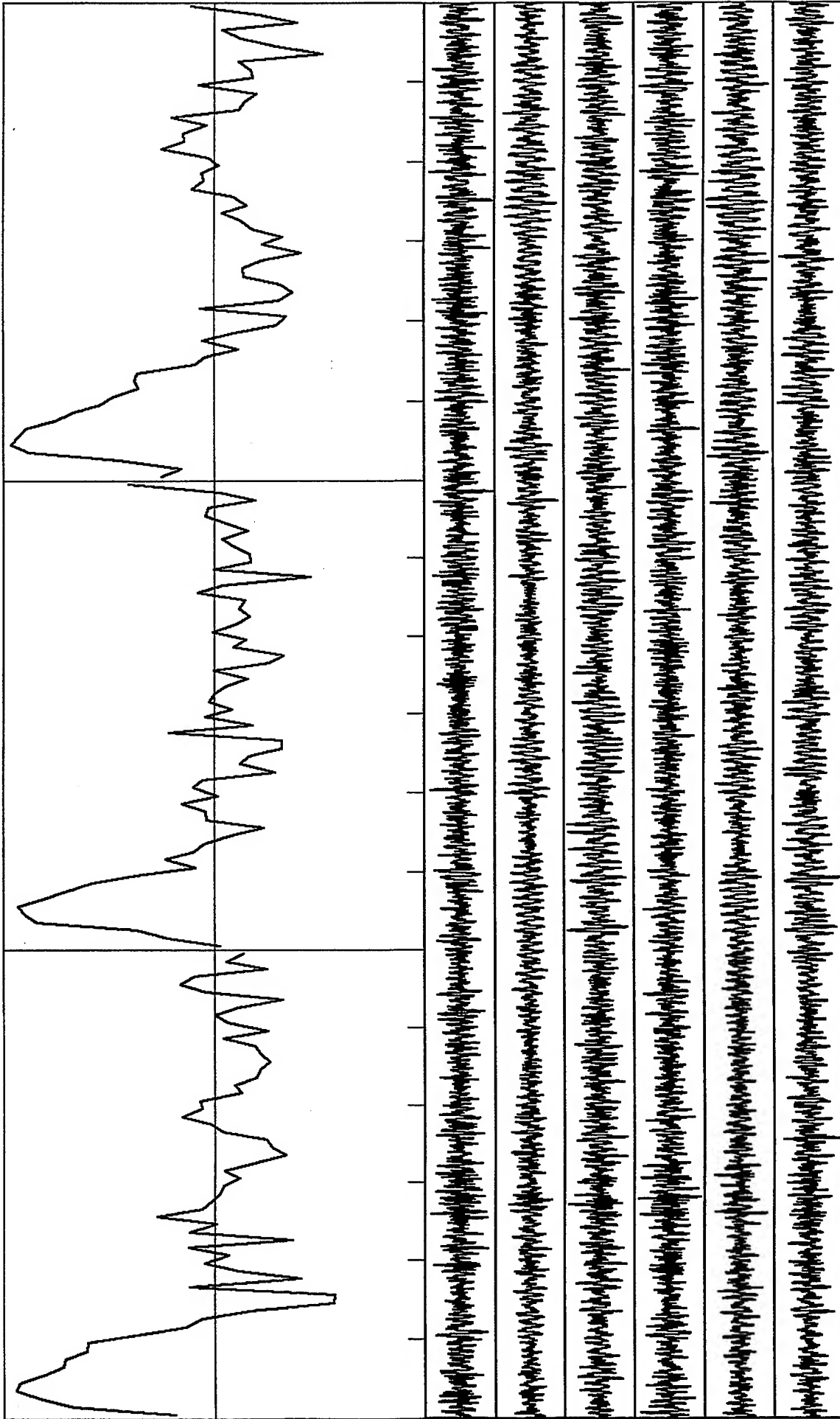




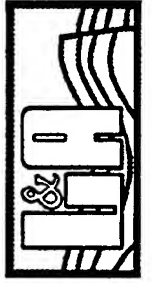
Correlation Coefficients: Scale -1 to +1; freq range: 0 to 30.0 Hz; Radius: 37 m  
 St. 1 & 2: Vertical & horizontal components; 60 s time window

*VortexRock Consultants, Inc.*



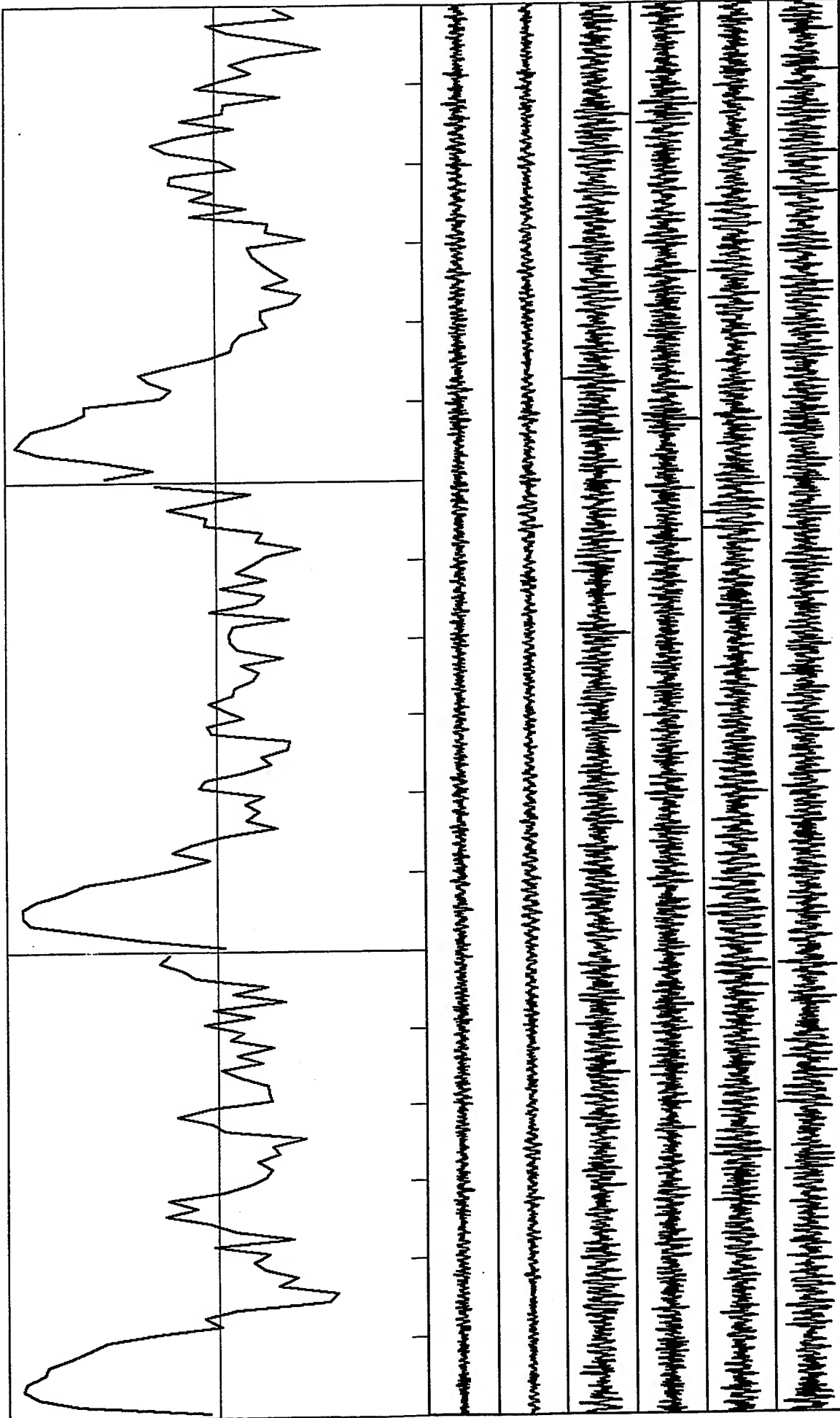


Correlation Coefficients: Scale -1 to +1; freq range: 0 to 30.0 Hz; Radius: 37 m  
 St. 1 & 2: Vertical & horizontal components; 60 s time window



*VortexRock Consultants, Inc.*



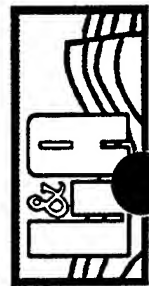


D-32

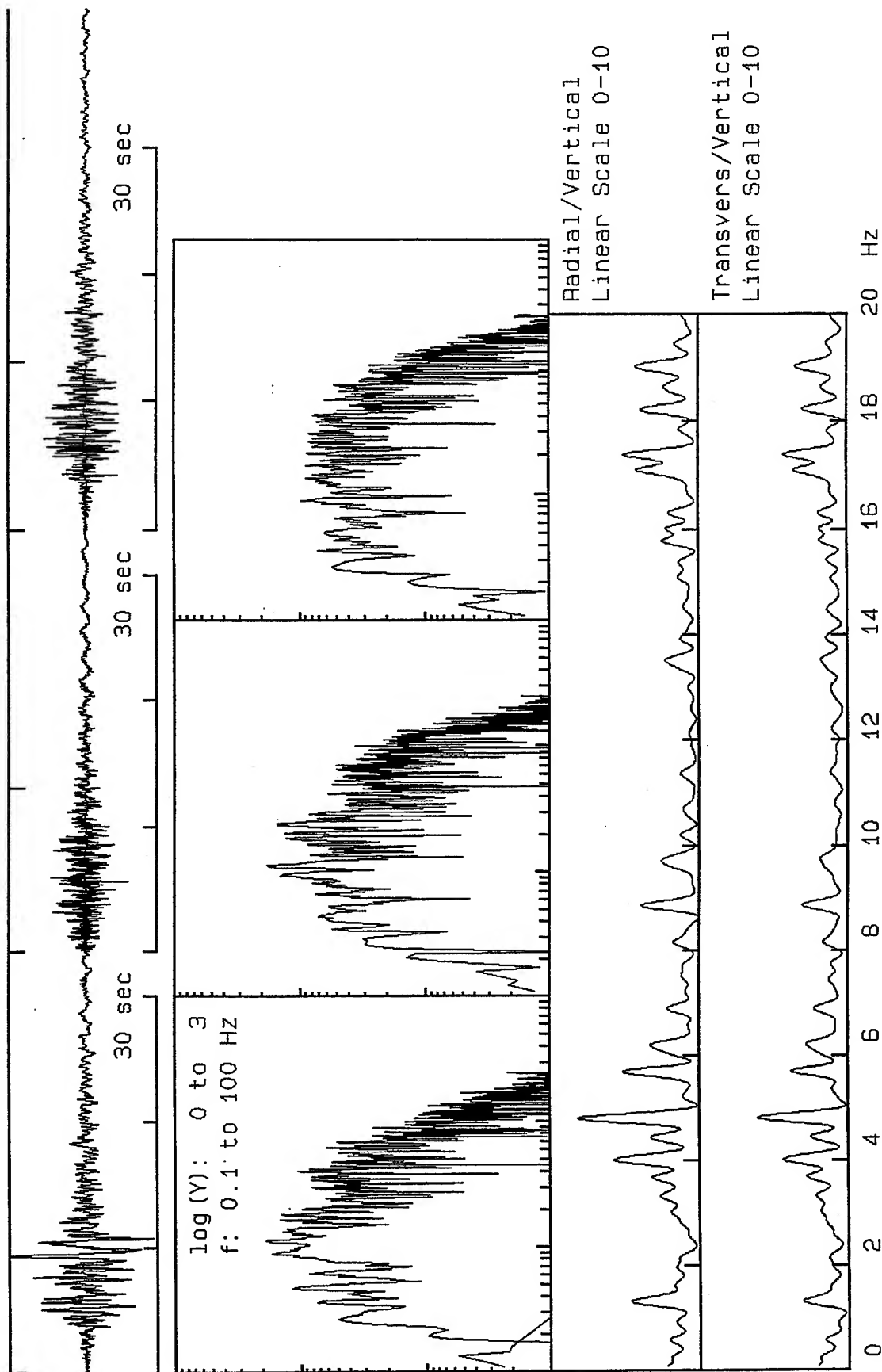
Correlation Coefficients: Scale -1 to +1; freq range: 0 to 30.0 Hz; Radius: 37 m  
 St. 1 & 2: Vertical & horizontal components; 60 s time window



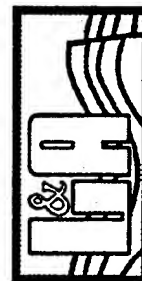
*VortexRock Consultants, Inc.*



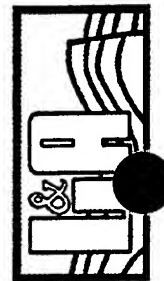
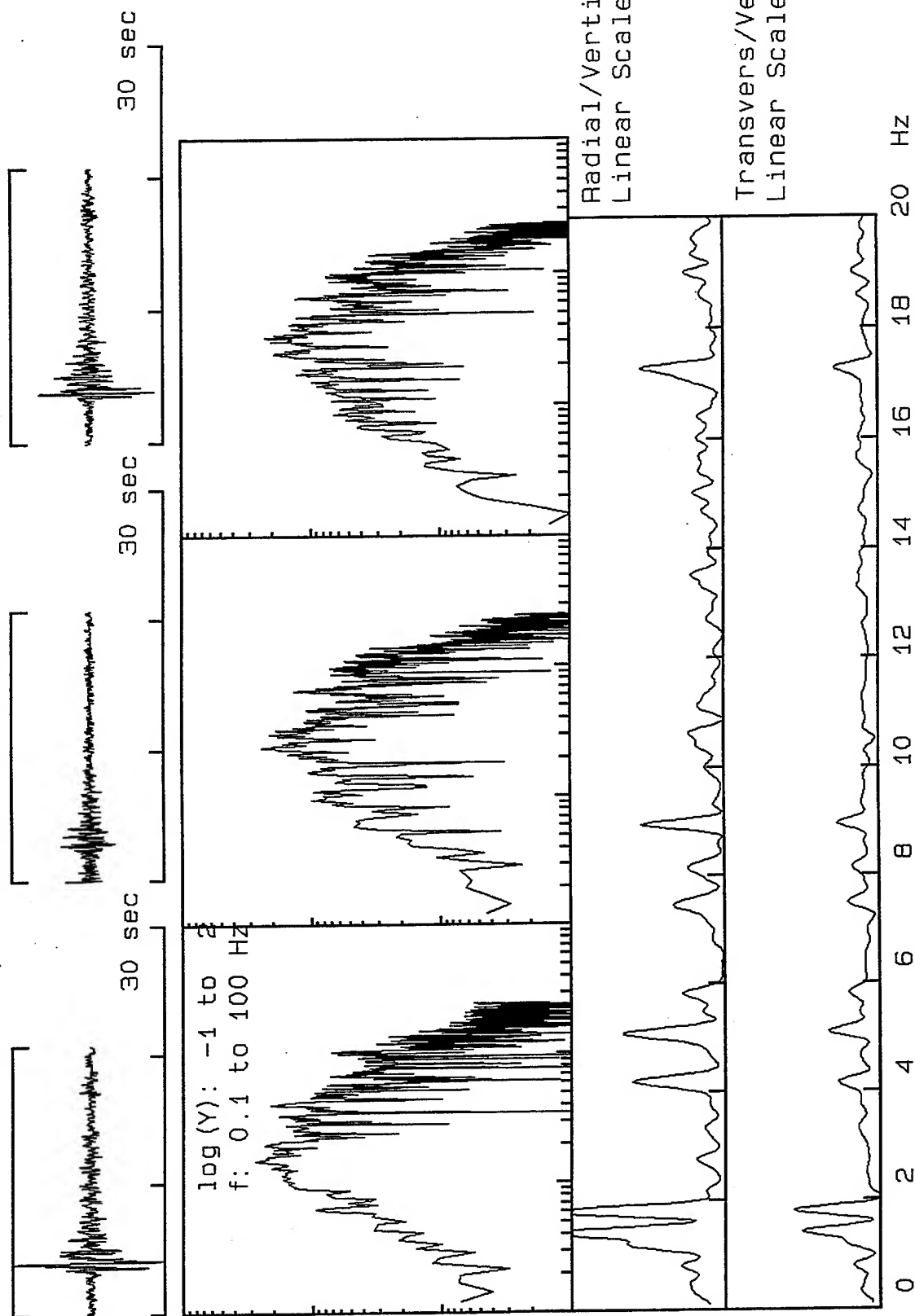
V2X1800, Window: .0 to 46.6 s



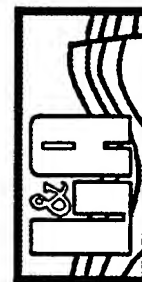
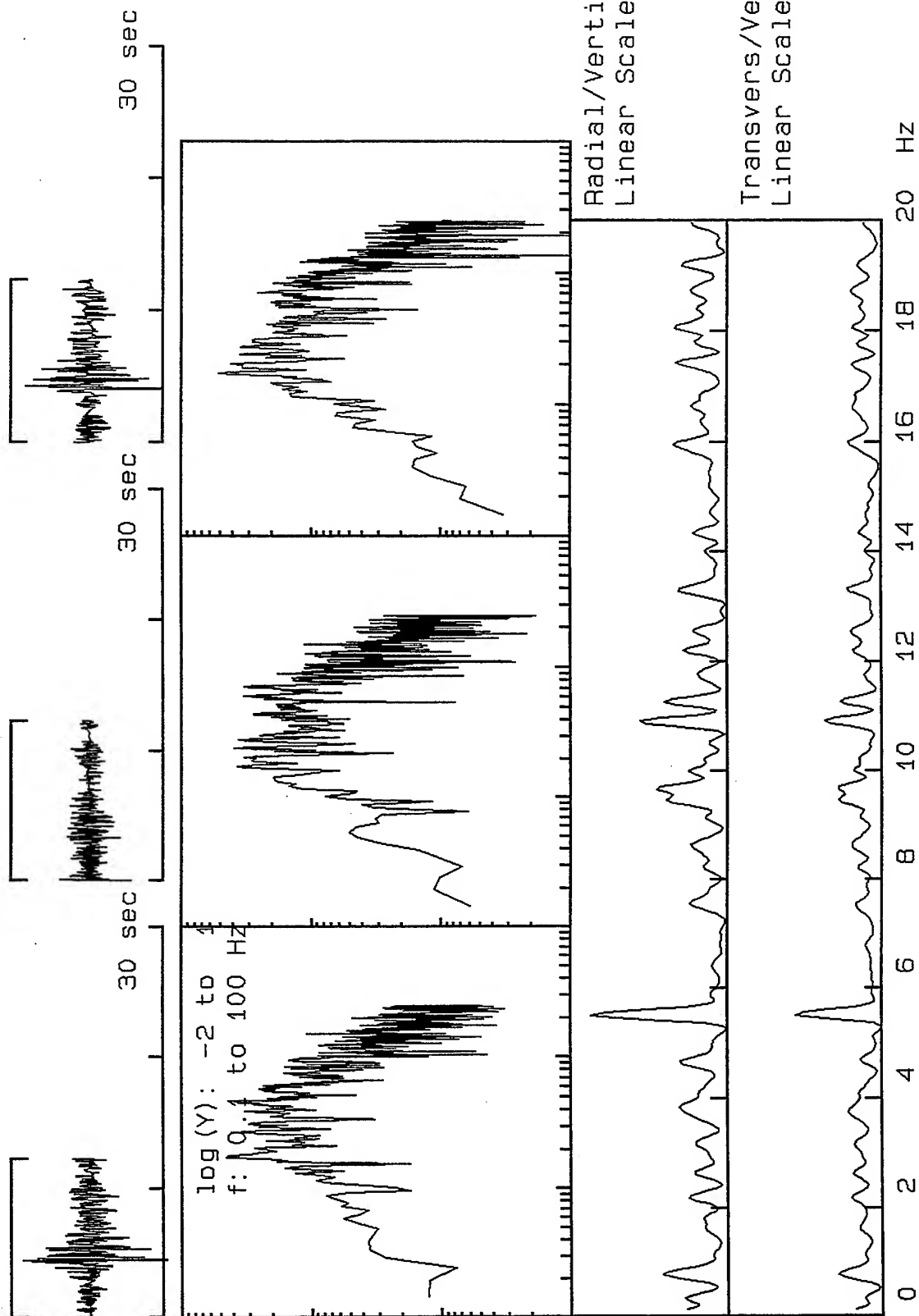
VortexRock Consultants, Inc.



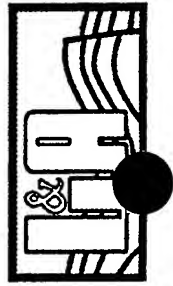
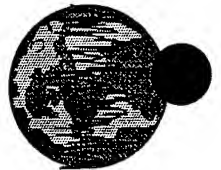
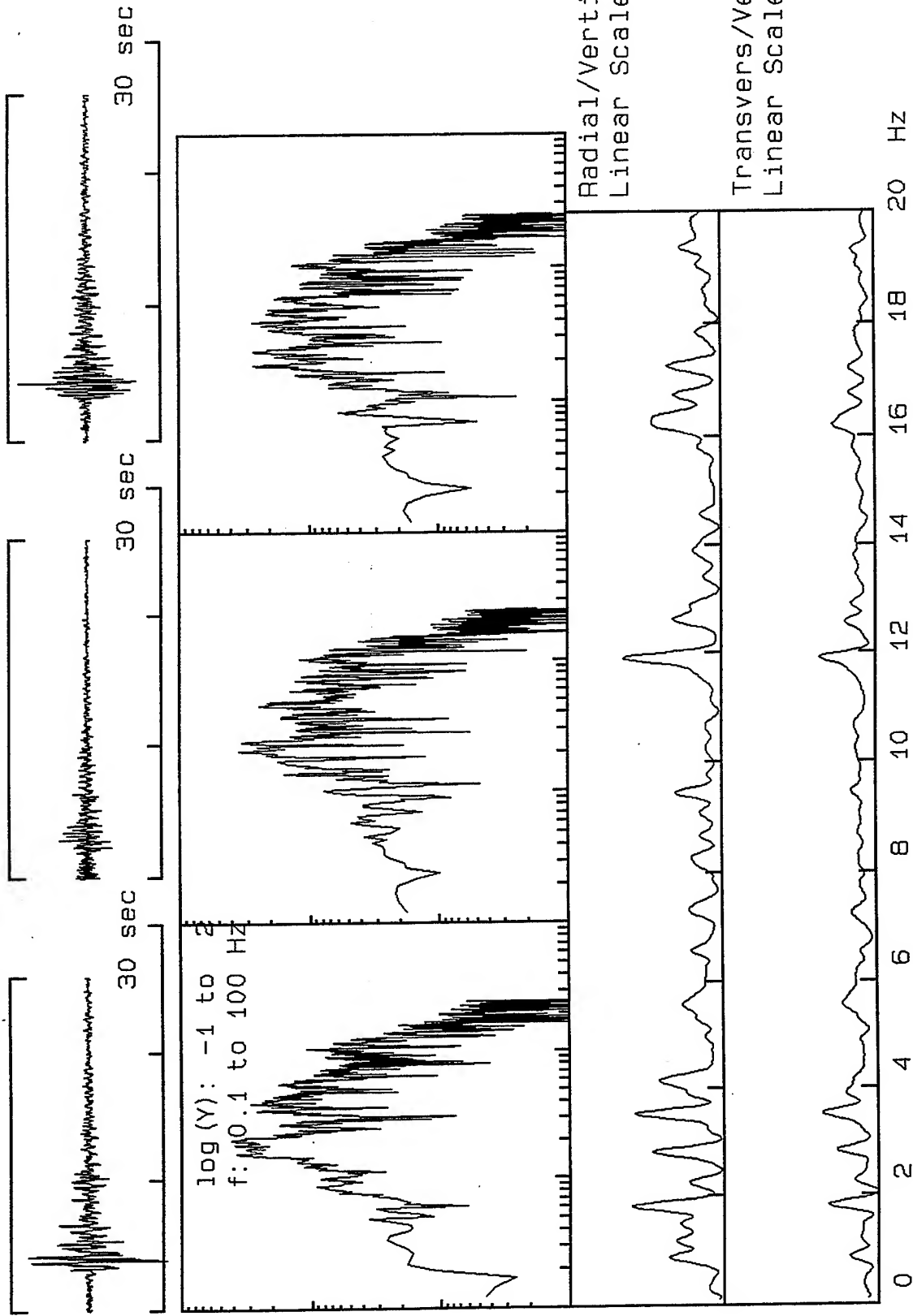
V2X1801, Window: .0 to 20.7 s



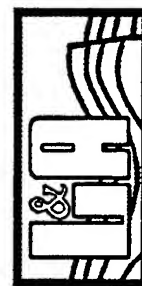
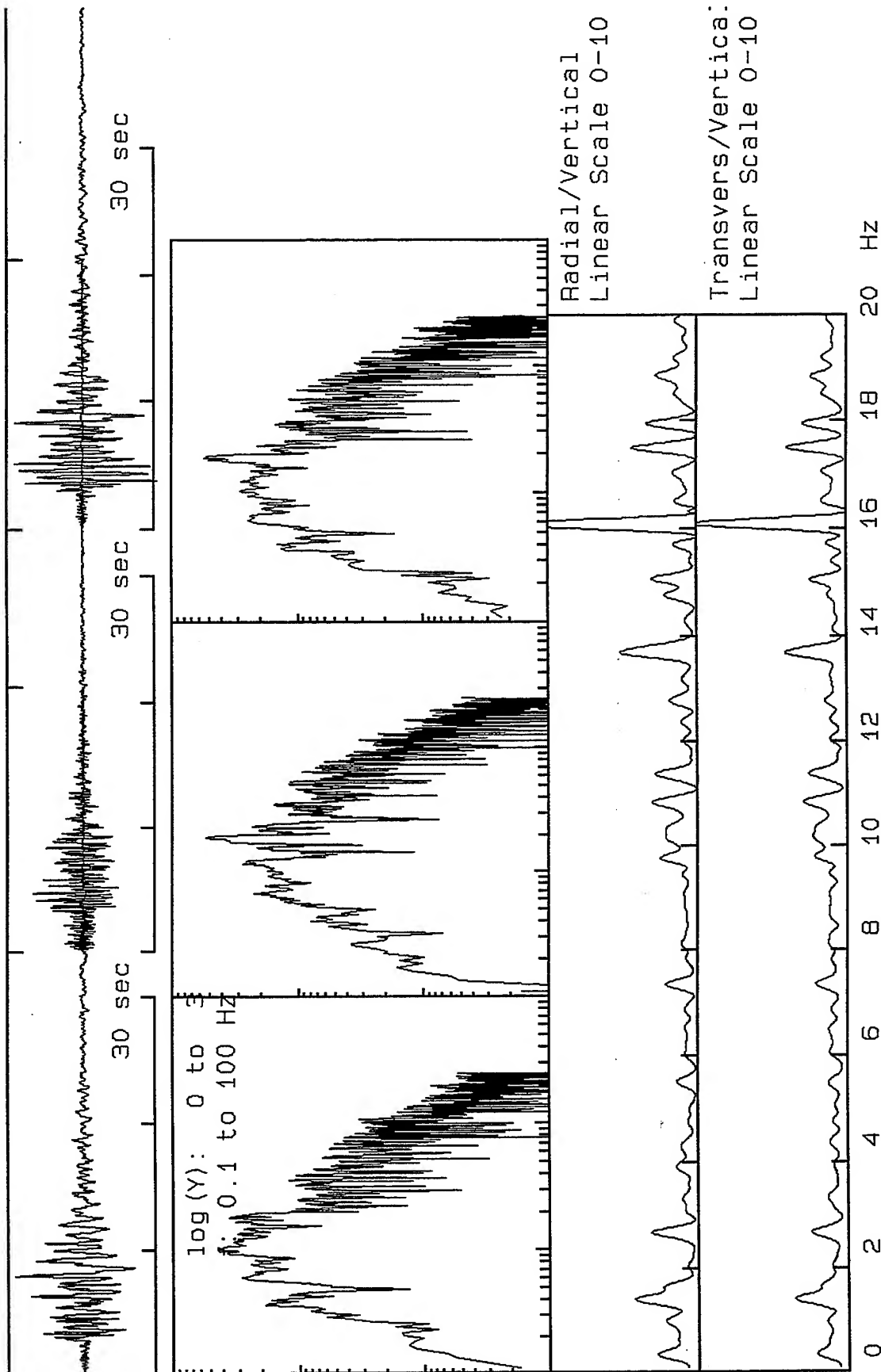
V2X1802, Window: .0 to 12.3 s



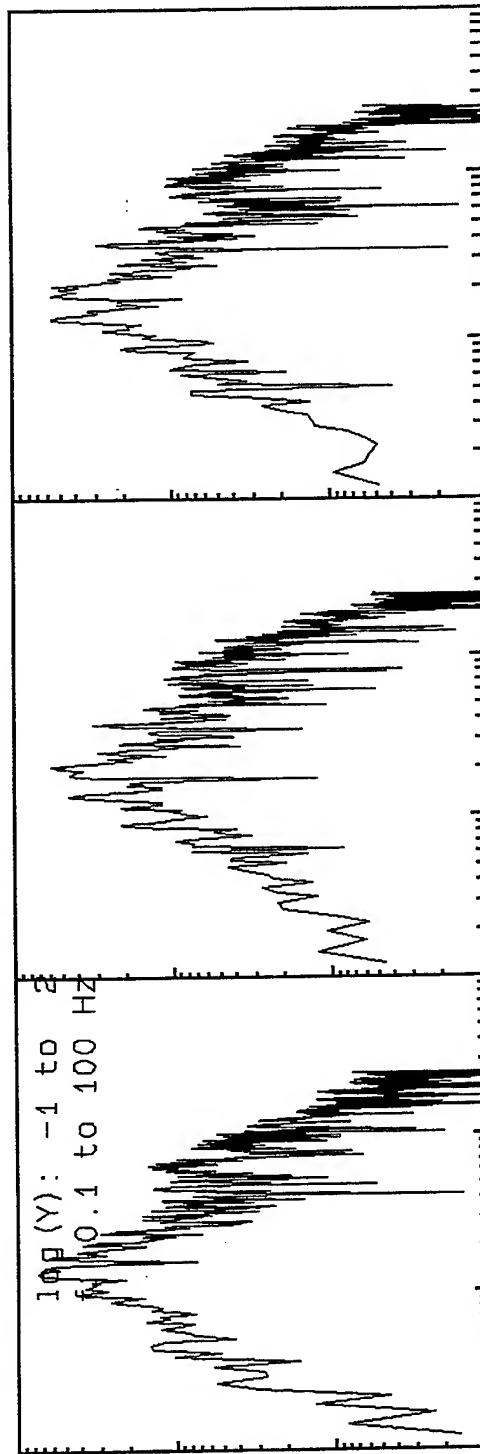
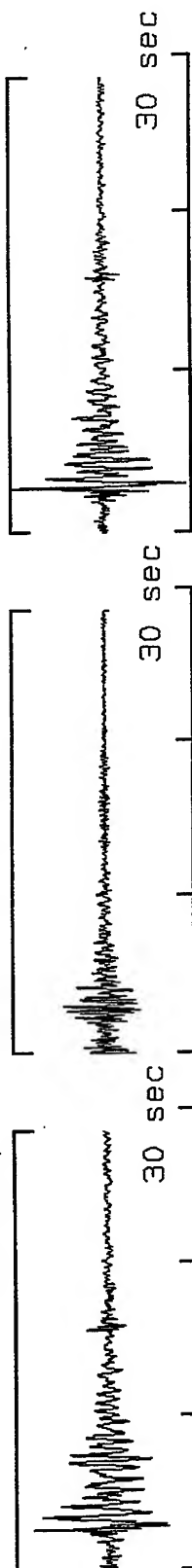
V2X1809, Window: .0 to 26.0 s



V2X1300, Window: .0 to 54.9 s

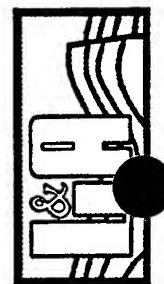


V2X1301, Window: .0 to 28.6 s

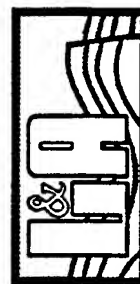
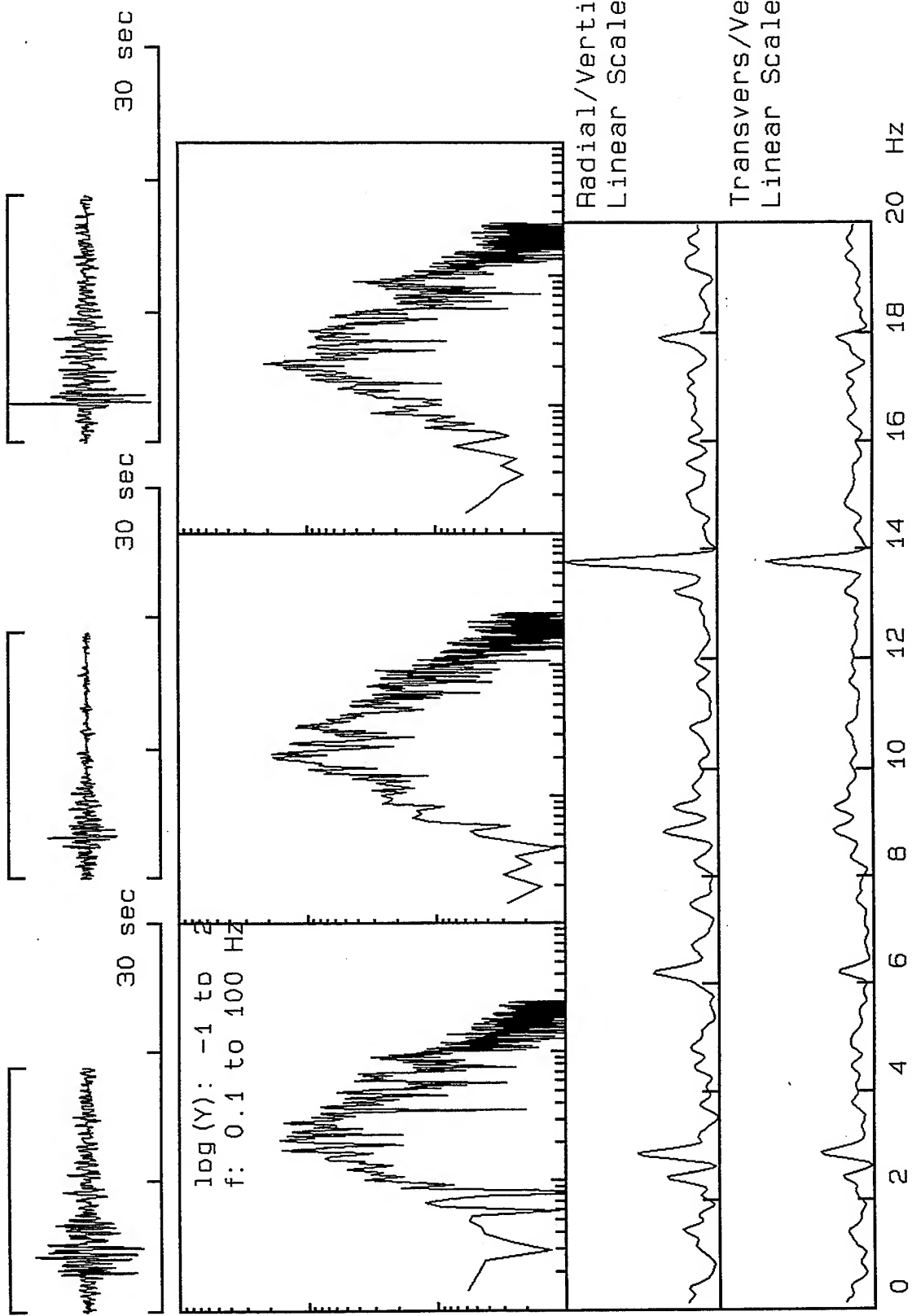


Radial/Vertical  
Linear Scale 0-10

Transvers/Vertical:  
Linear Scale 0-10

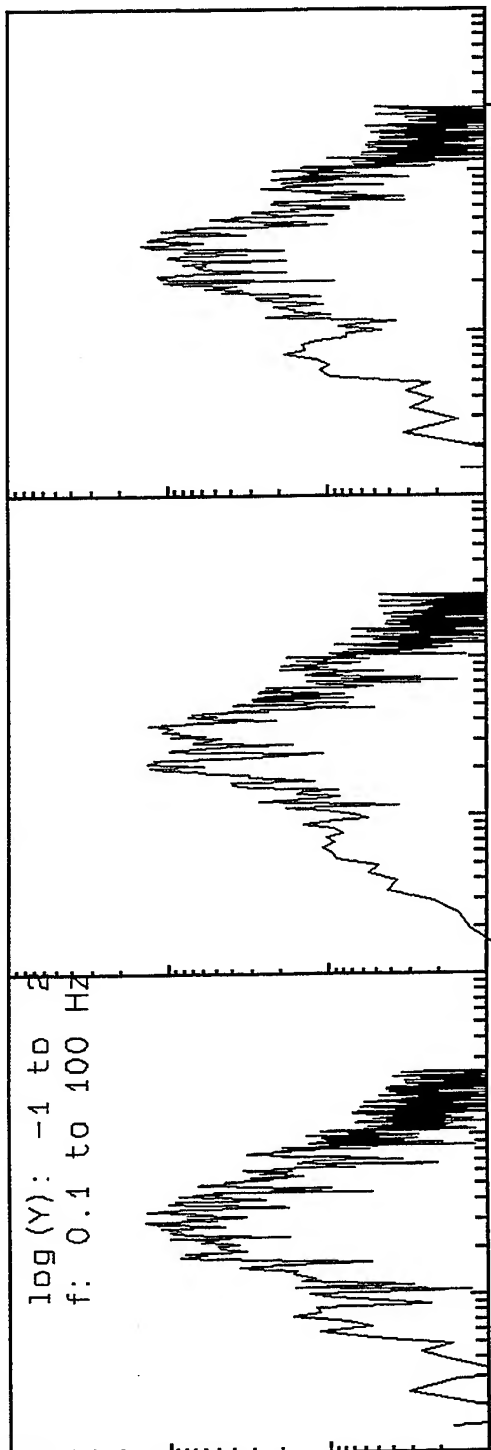
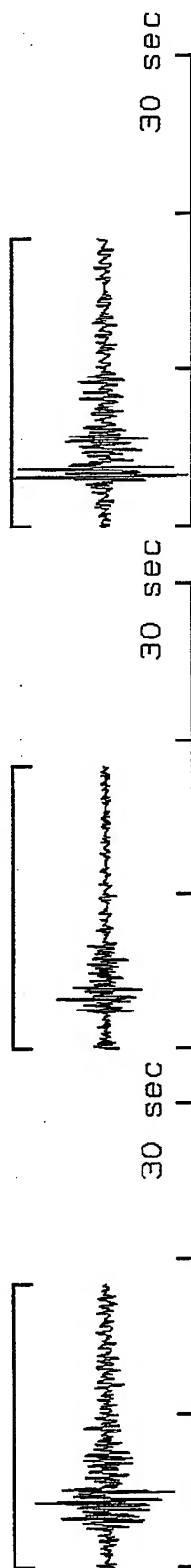


V2X1304, Window: .0 to 18.9 s





V2X1310, Window: .0 to 18.4 s



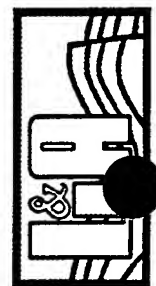
Radial/Vertical  
Linear Scale 0-10

Transvers/Vertical:  
Linear Scale 0-10

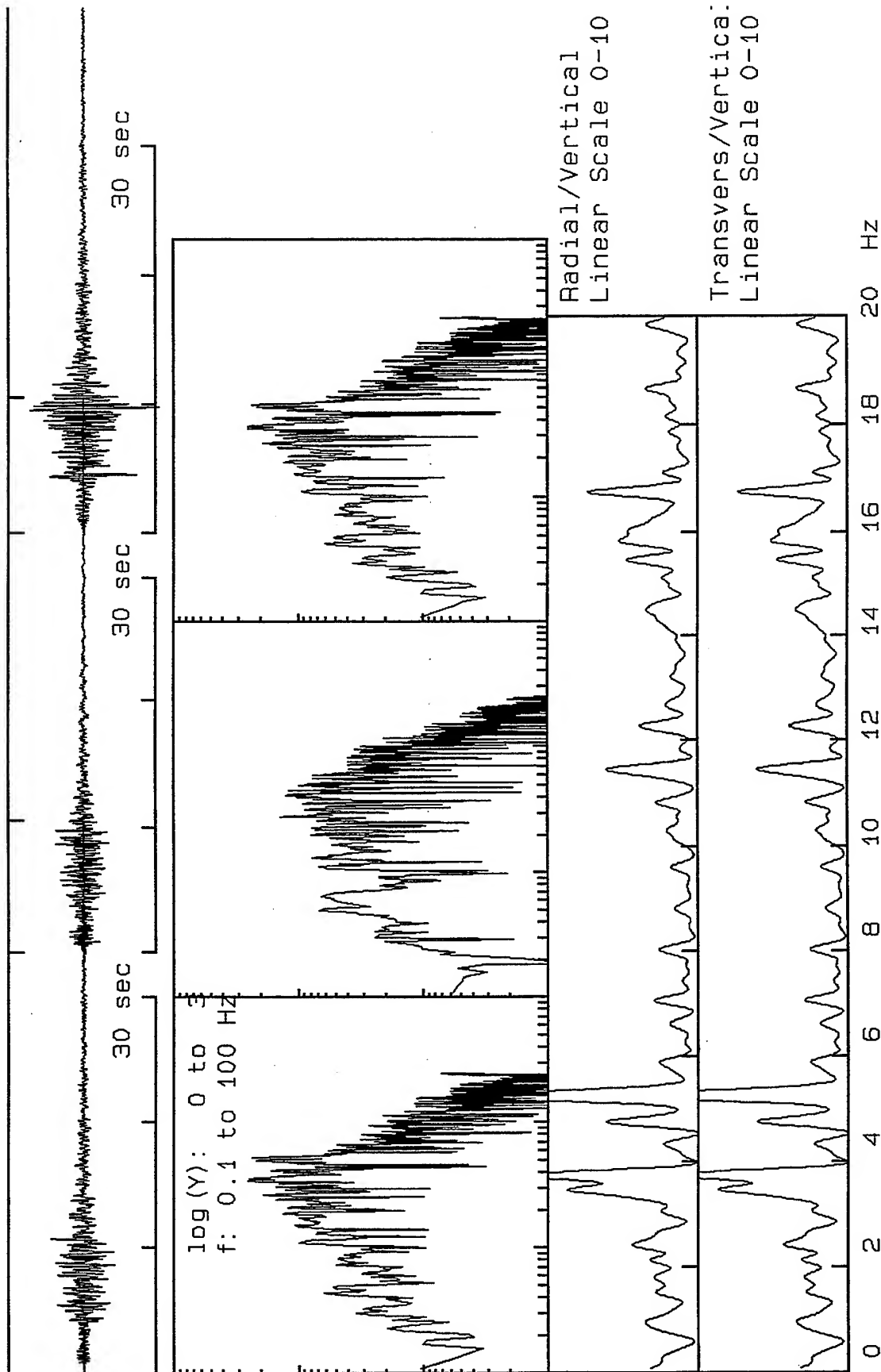
0 2 4 6 8 10 12 14 16 18 20 Hz



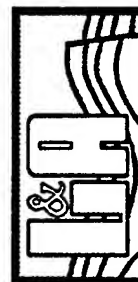
*VortexRock Consultants, Inc.*



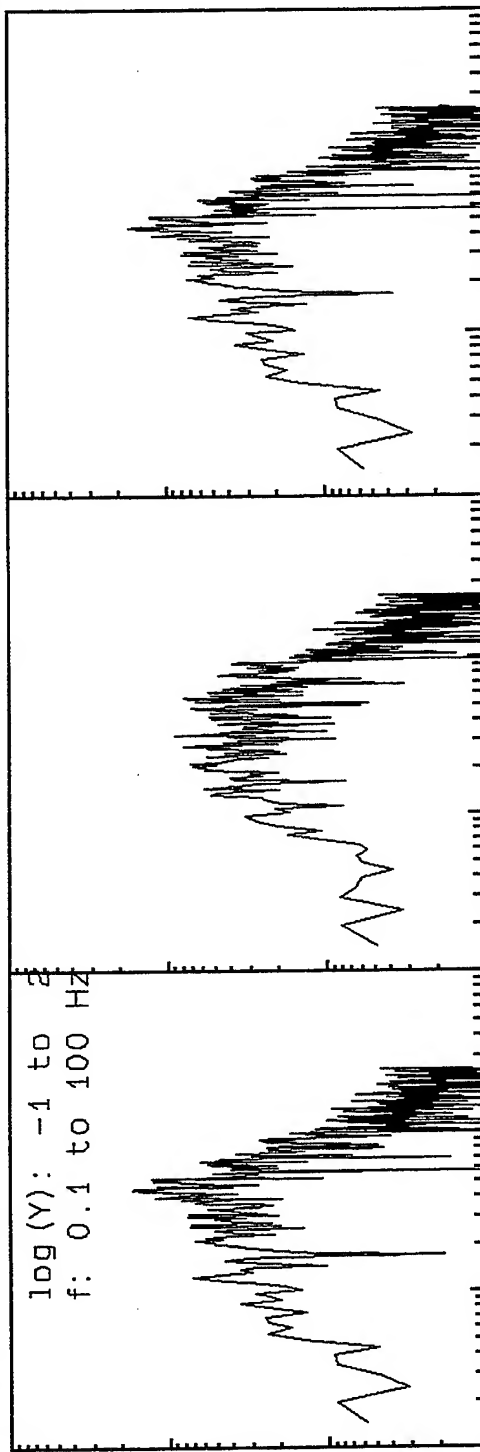
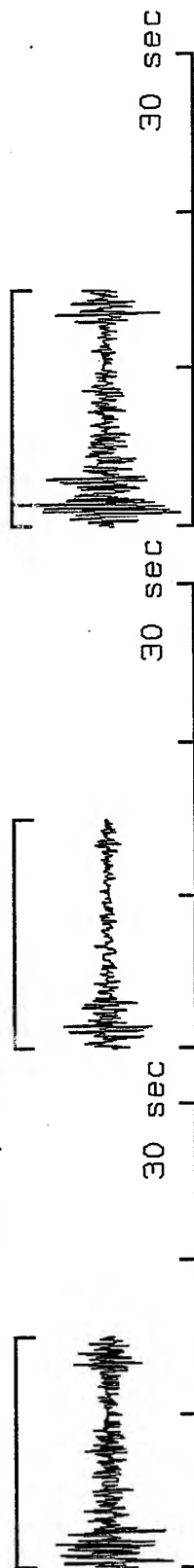
V2X4900, Window: .0 to 44.2 s



*VortexRock Consultants, Inc.*

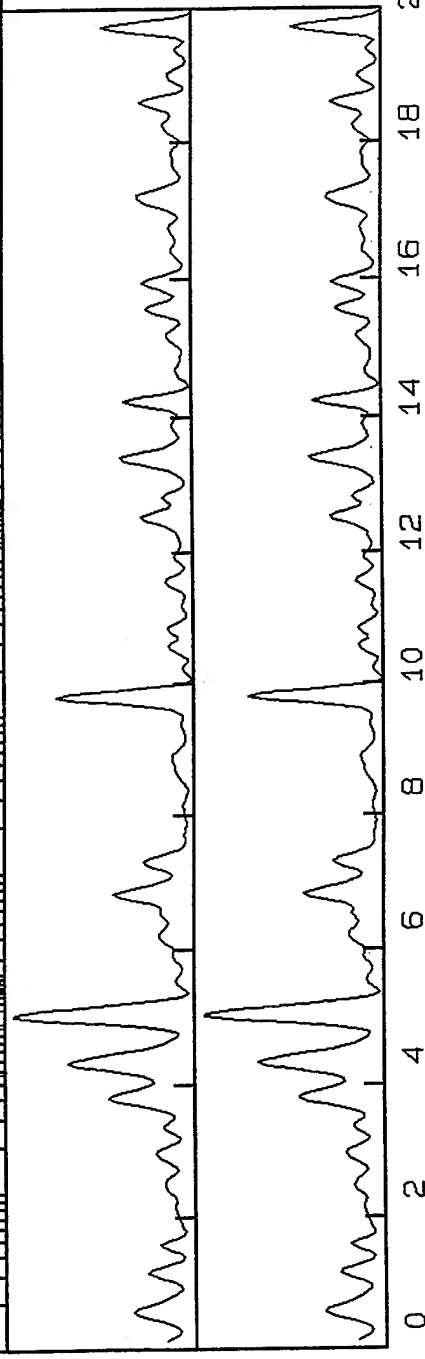


V2X4901, Window: .0 to 15.1 s

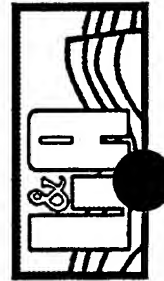


Radial/Vertical  
Linear Scale 0-10

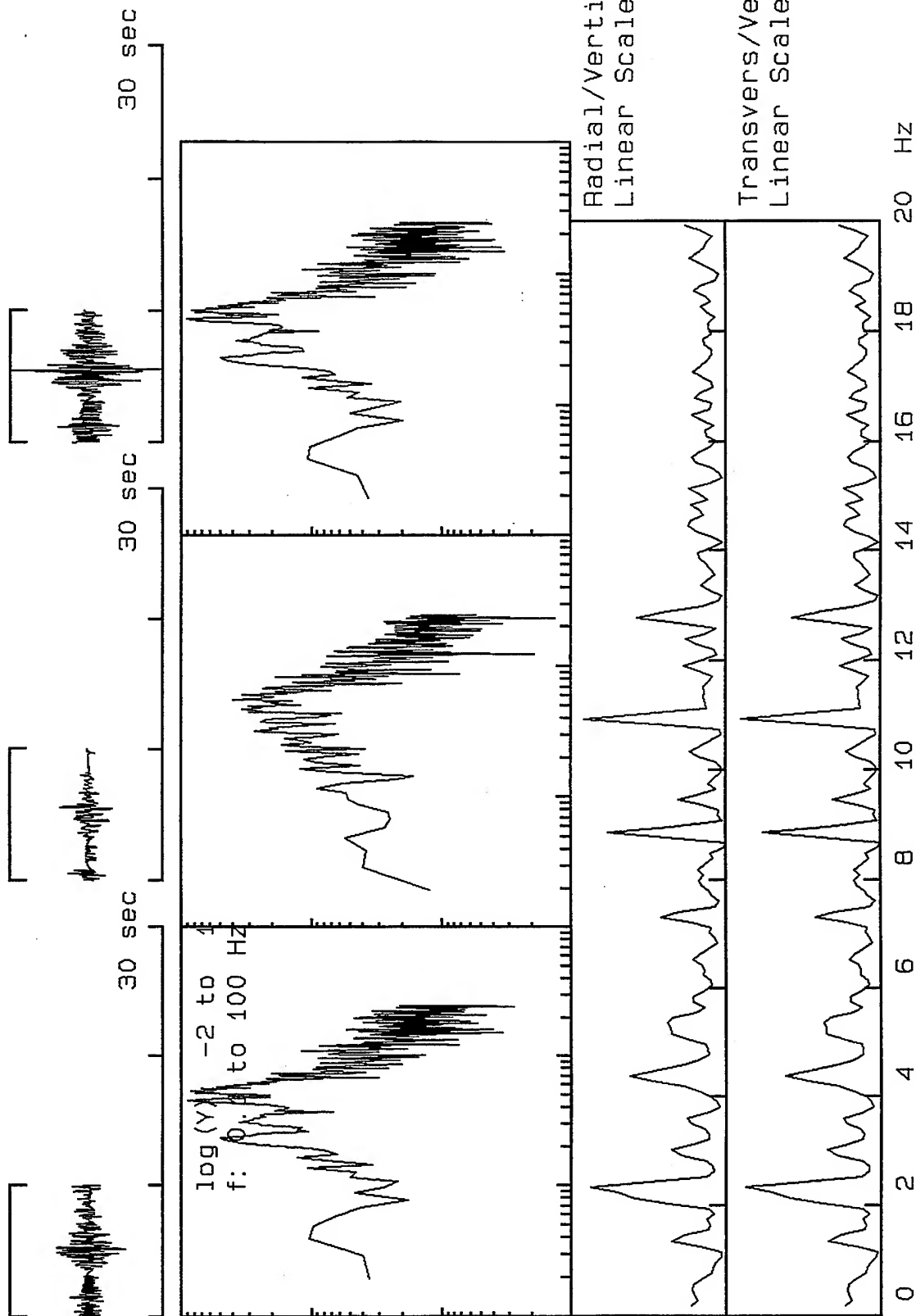
Transvers/Vertical:  
Linear Scale 0-10



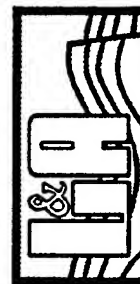
VortexRock Consultants, Inc.



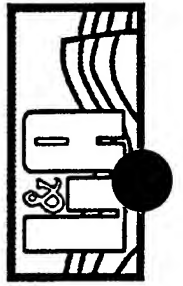
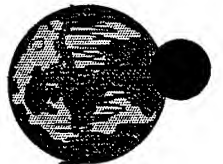
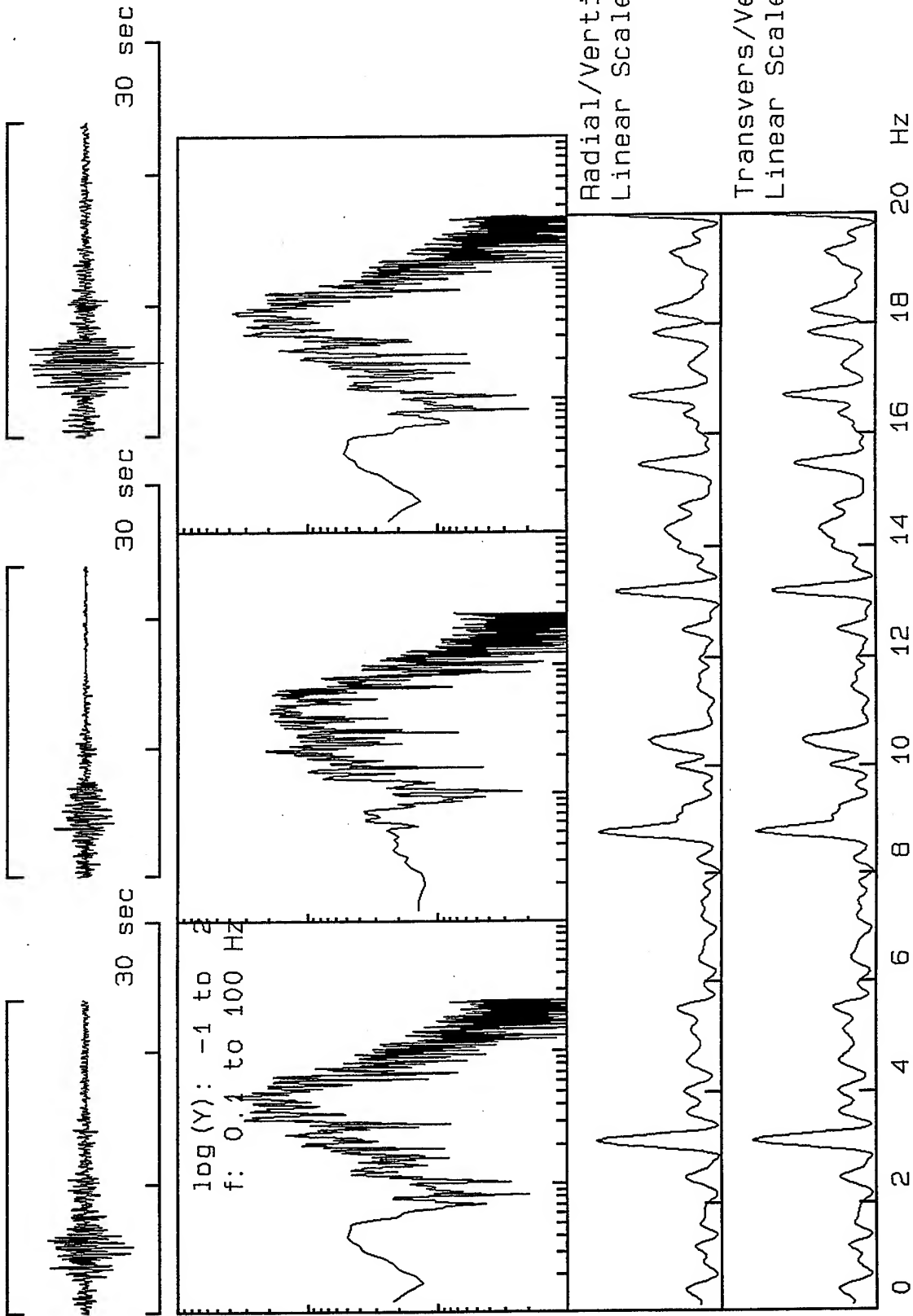
V2X4902, Window: .0 to 10.1 s



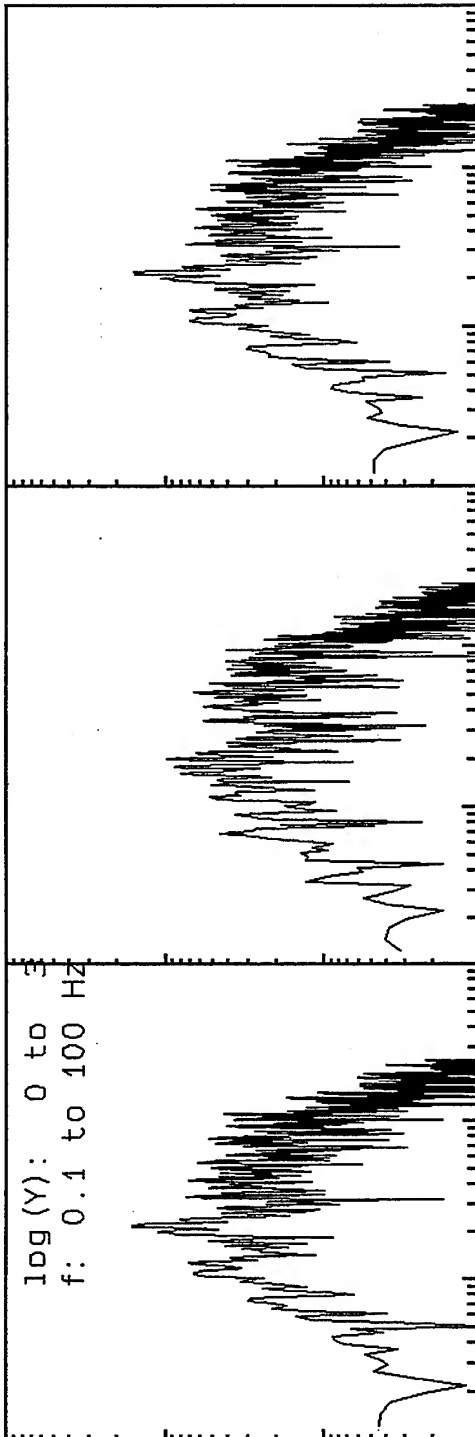
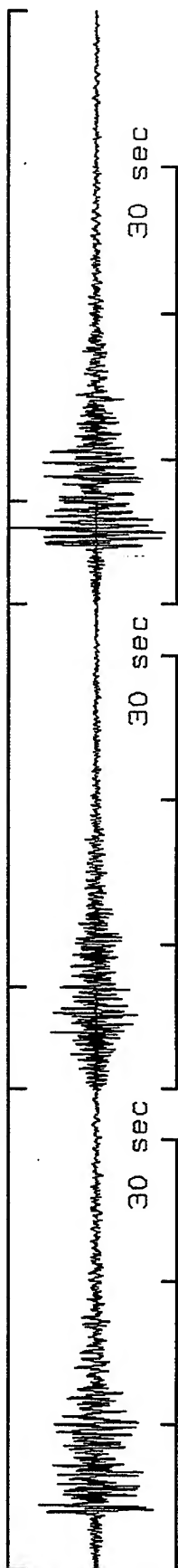
*VortexRock Consultants, Inc.*



V2X4912, Window: .0 to 24.0 s

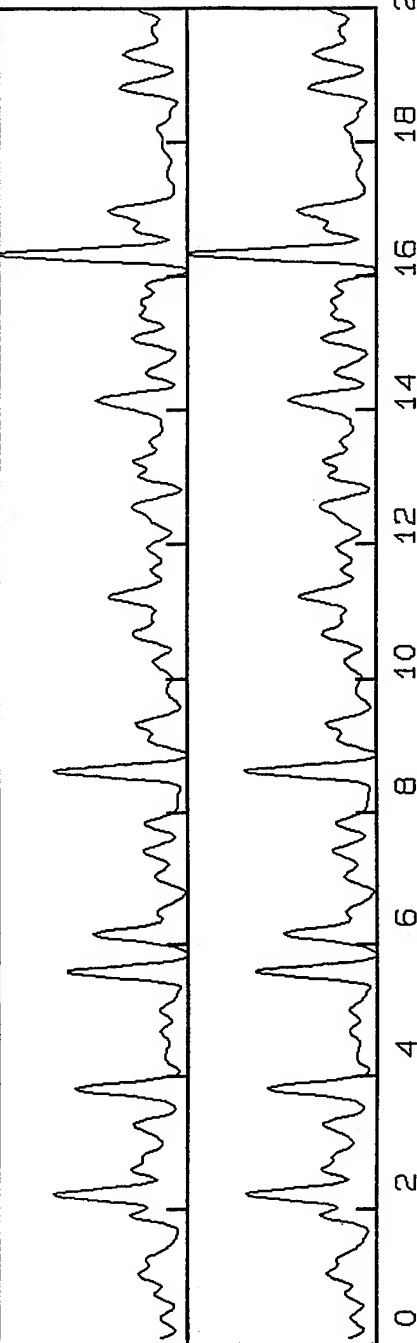


V2X6000, Window: .0 to 40.7 s

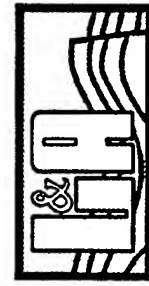


Radial/Vertical  
Linear Scale 0-10

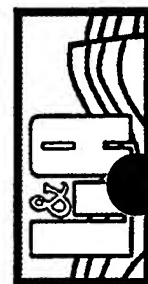
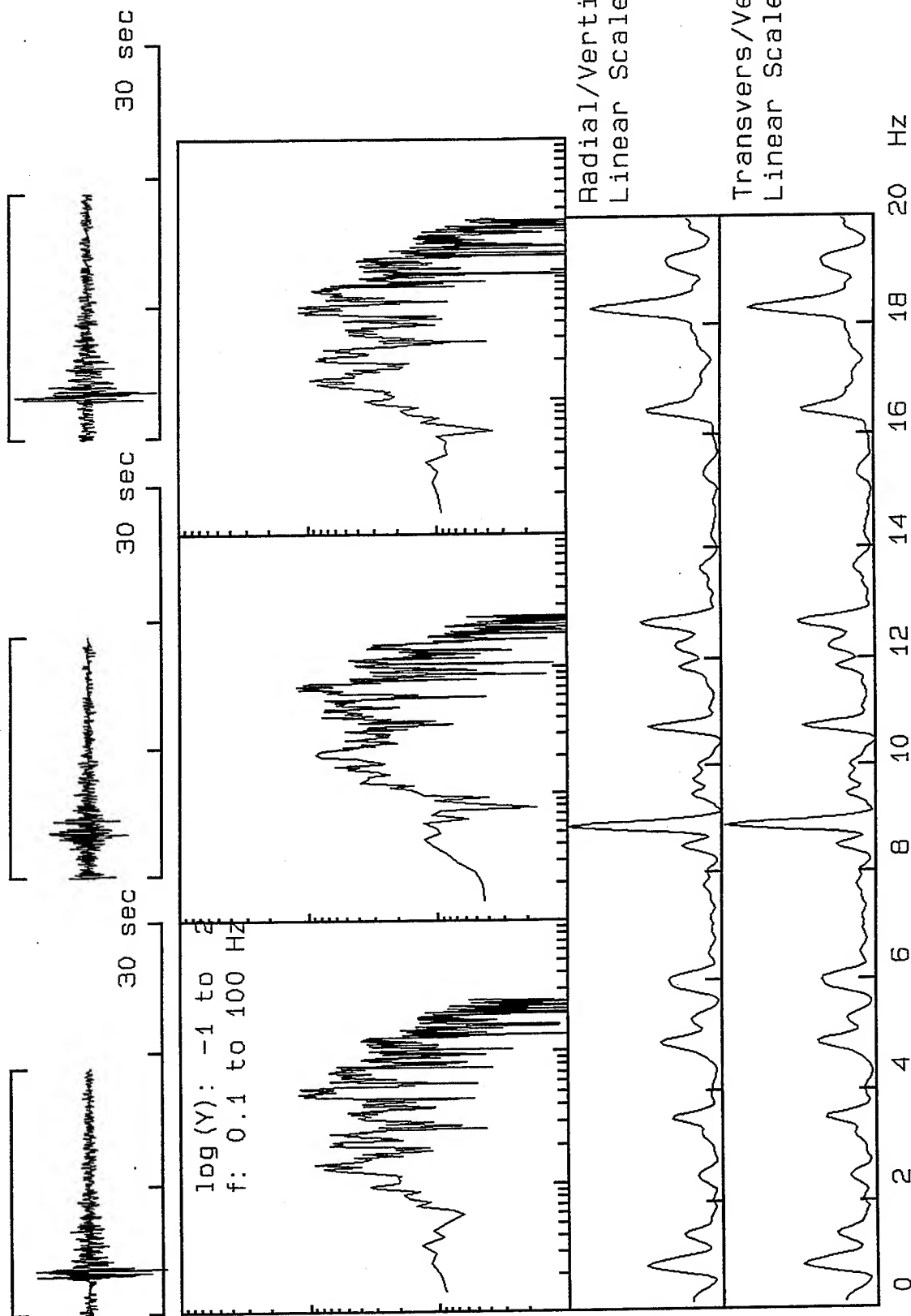
Transvers/Vertical:  
Linear Scale 0-10



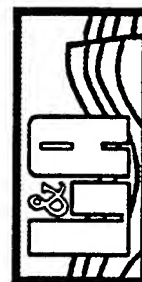
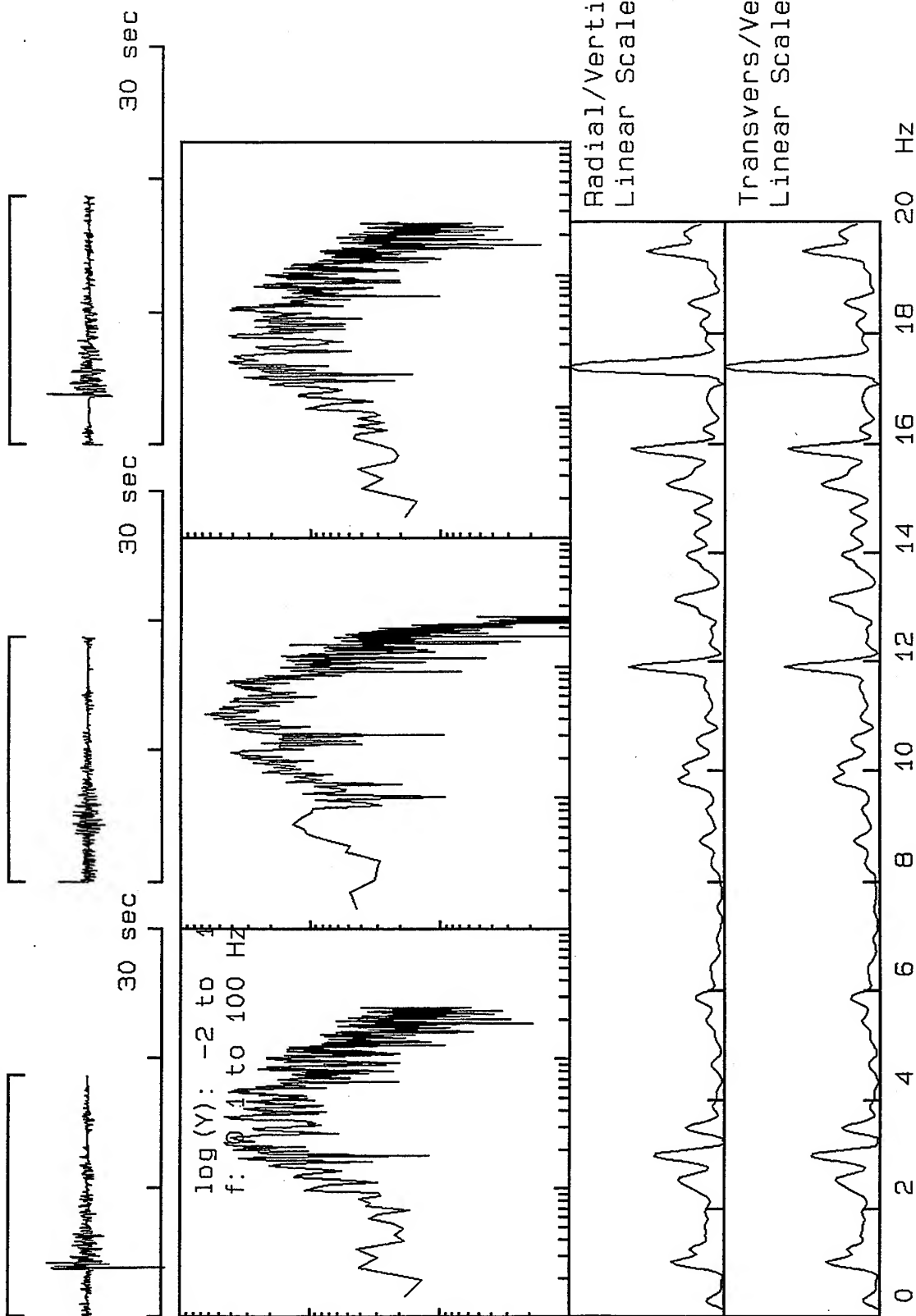
VortexRock Consultants, Inc.



V2X6001, Window: .0 to 18.9 s

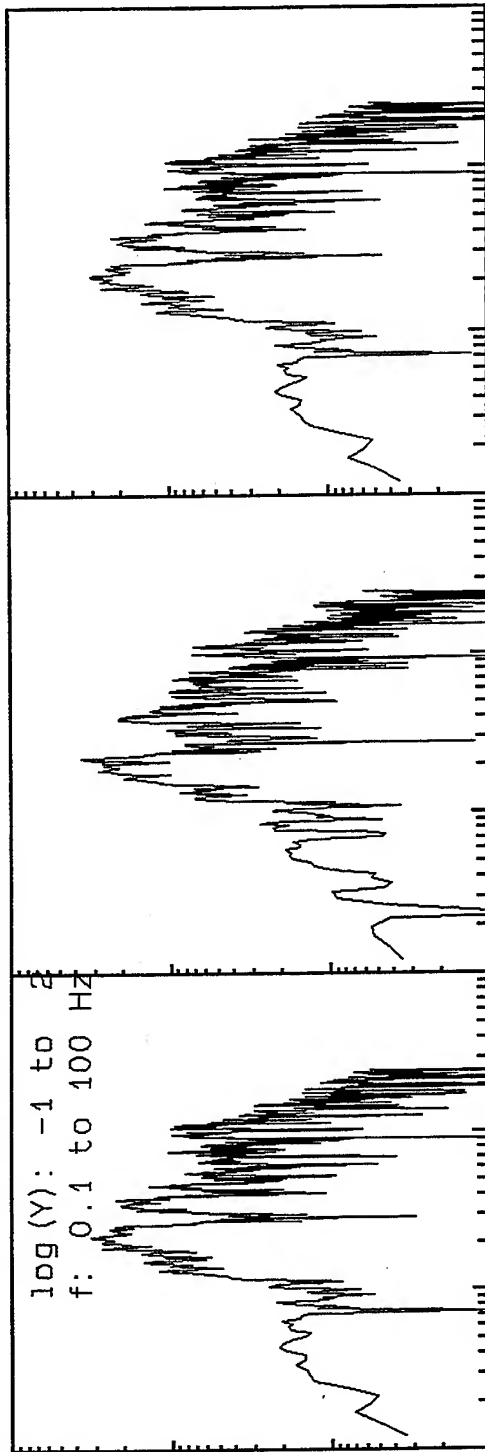
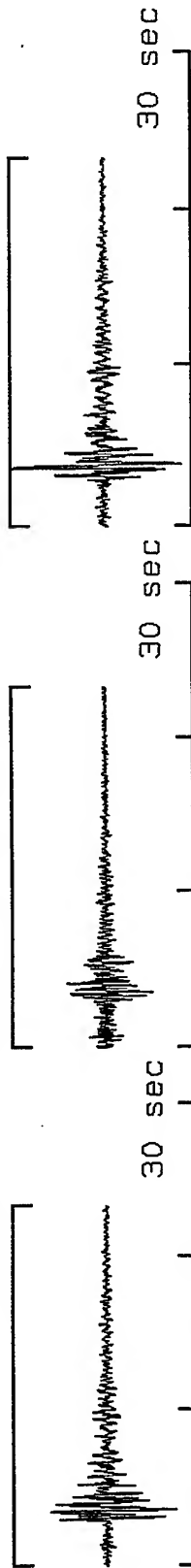


V2X6009, Window: .0 to 18.7 s



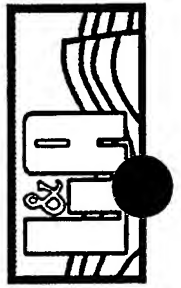
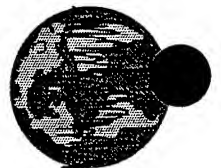
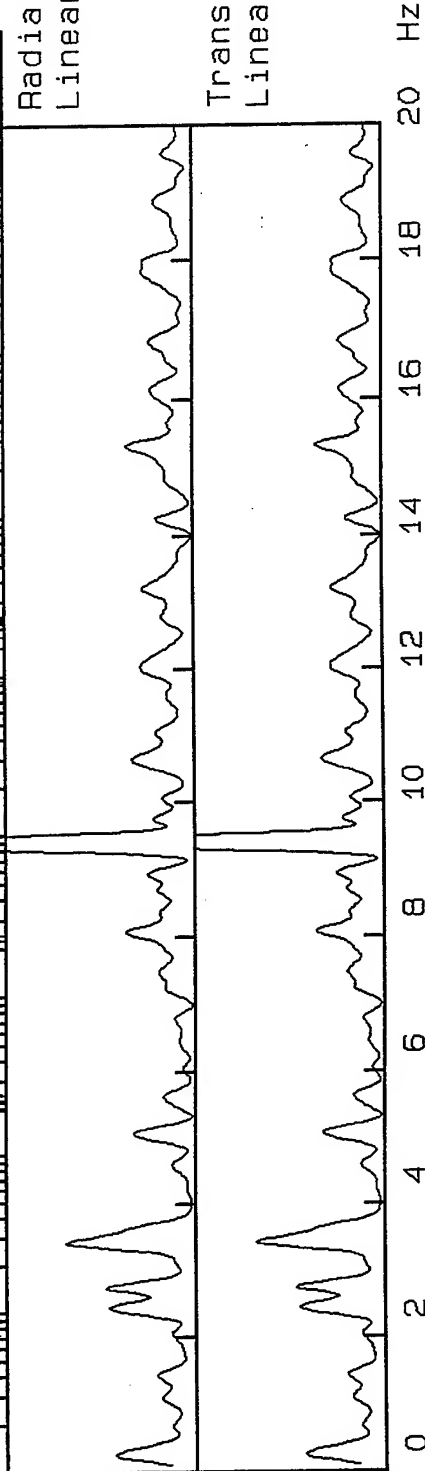


V2X6012, Window: .0 to 23.4 s

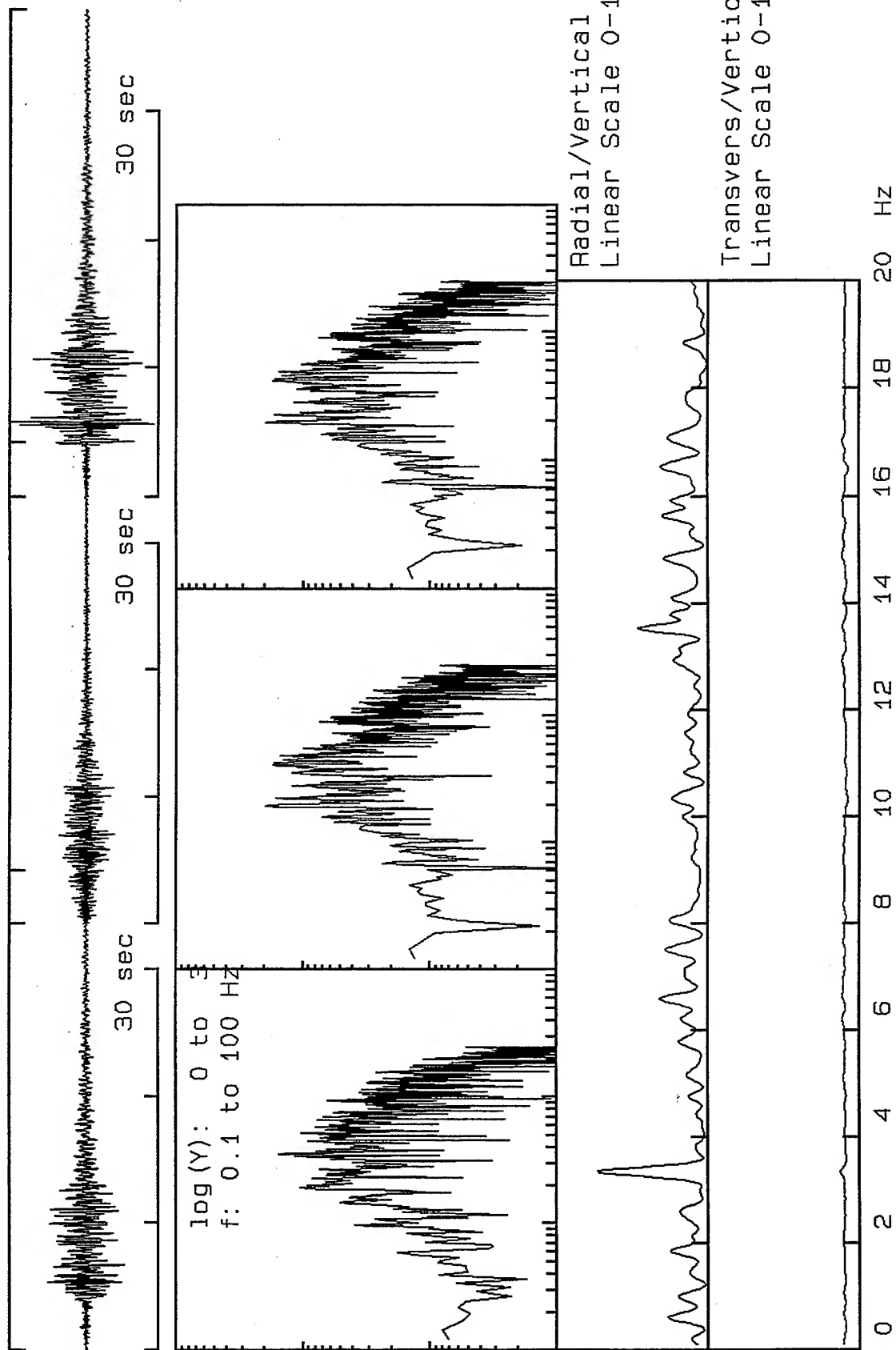


Radial/Vertical  
Linear Scale 0-10

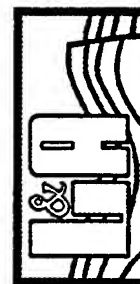
Transvers/Vertical:  
Linear Scale 0-10



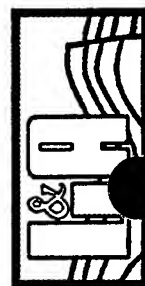
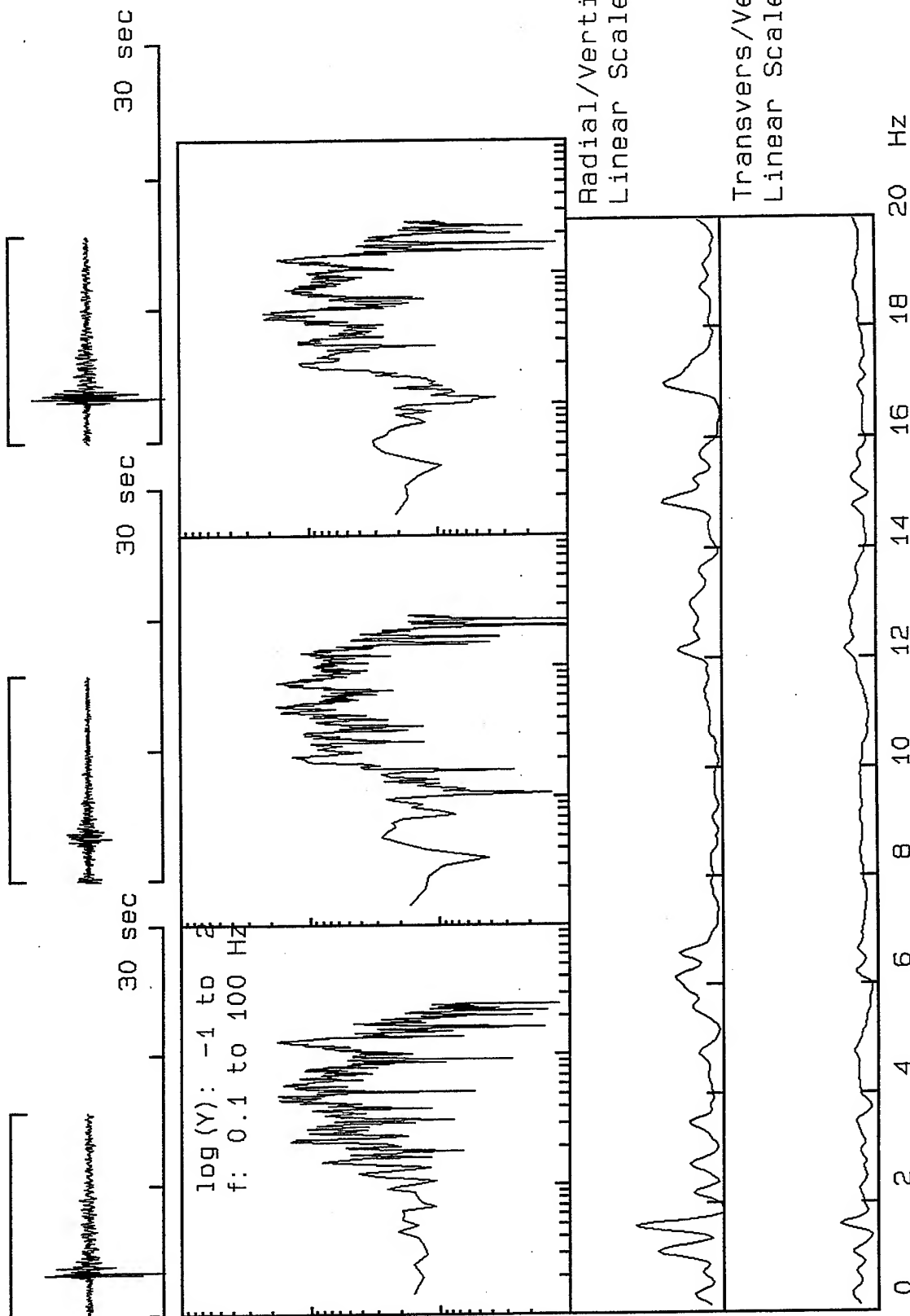
V2X6300, Window: .0 to 37.8 s



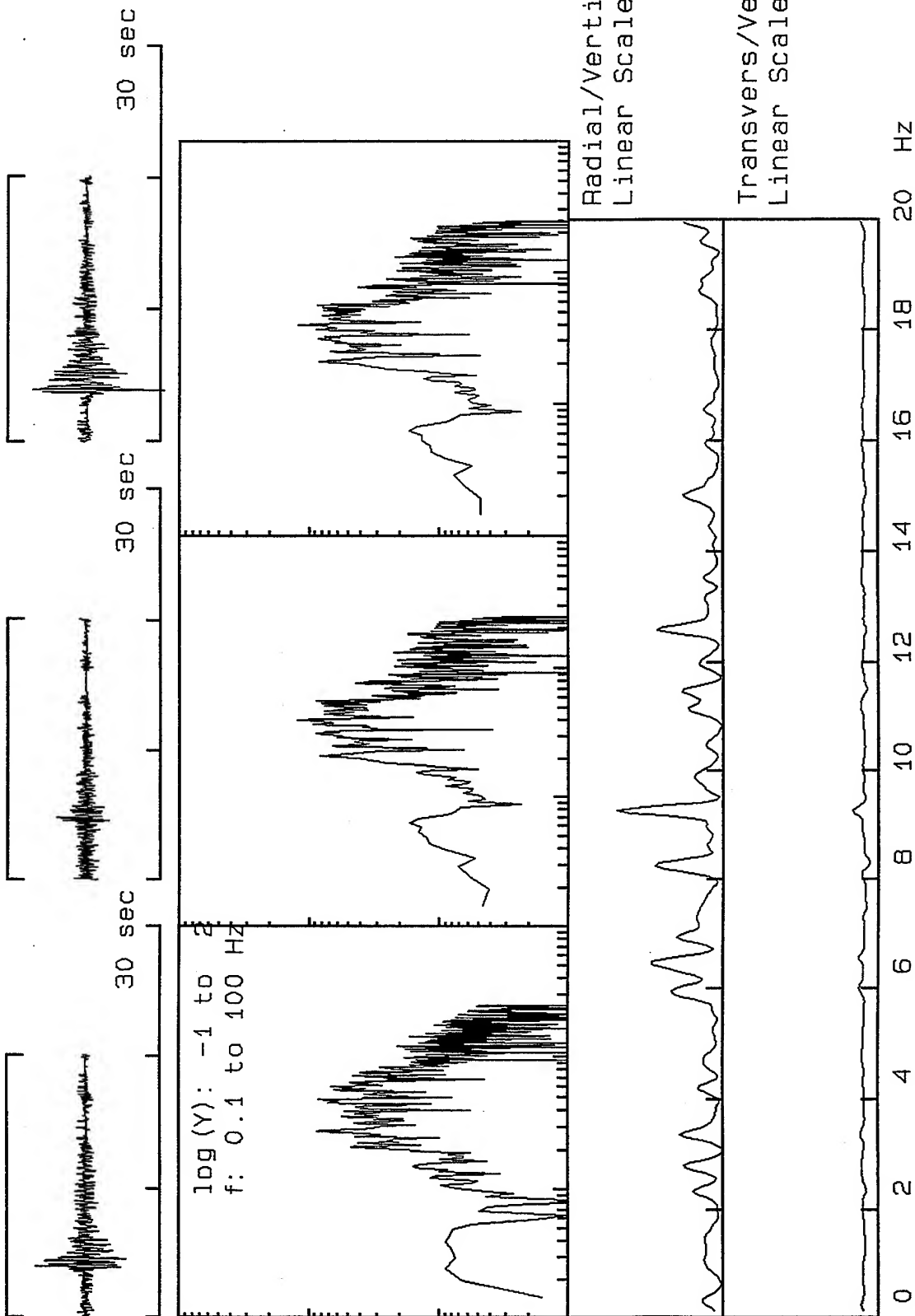
*VortexRock Consultants, Inc.*



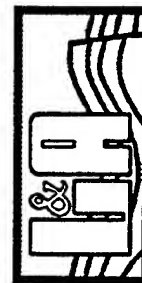
V2X6301, Window: .0 to 15.7 s



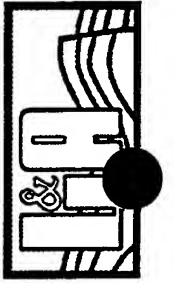
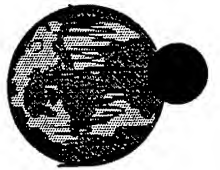
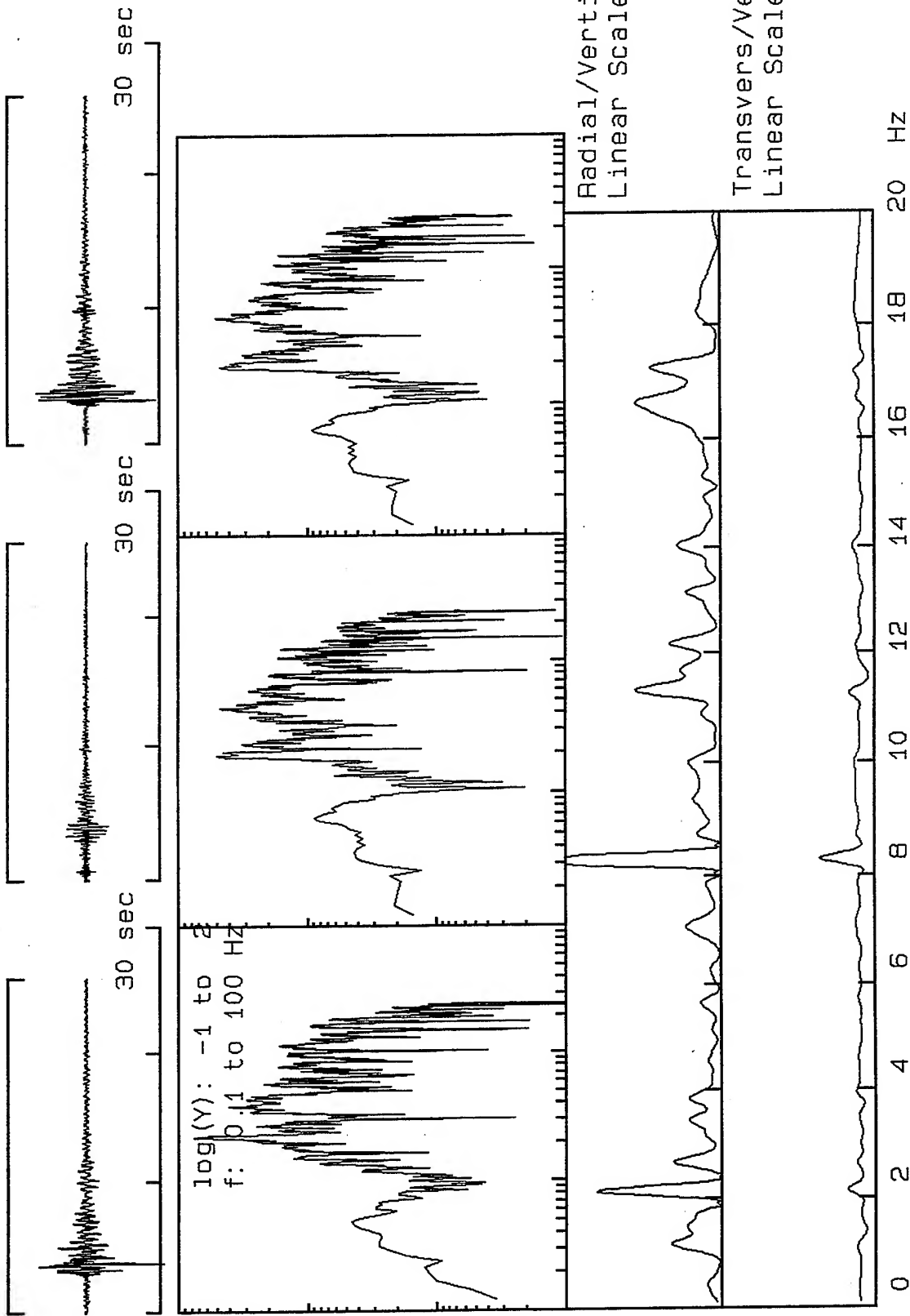
V2X6312, Window: .0 to 20.1 s



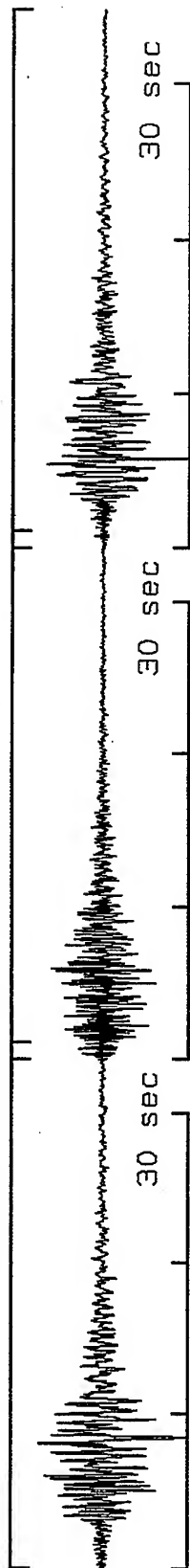
*VortexRock Consultants, Inc.*



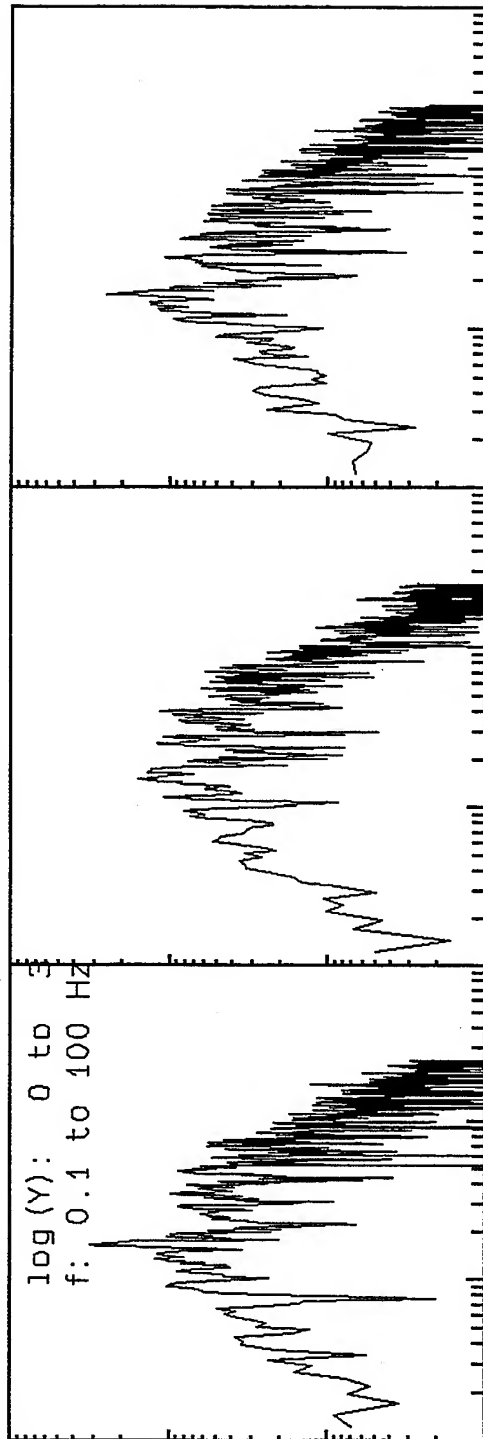
V2X6316, Window: .0 to 26.0 s



V2X1600, Window: .0 to 34.7 s



log (Y): 0 to 3  
f: 0.1 to 100 Hz



Radial/Vertical  
Linear Scale 0-10



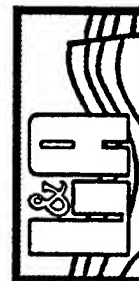
Transvers/Vertical:  
Linear Scale 0-10



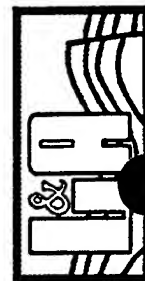
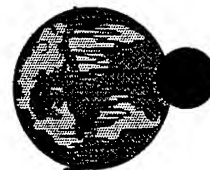
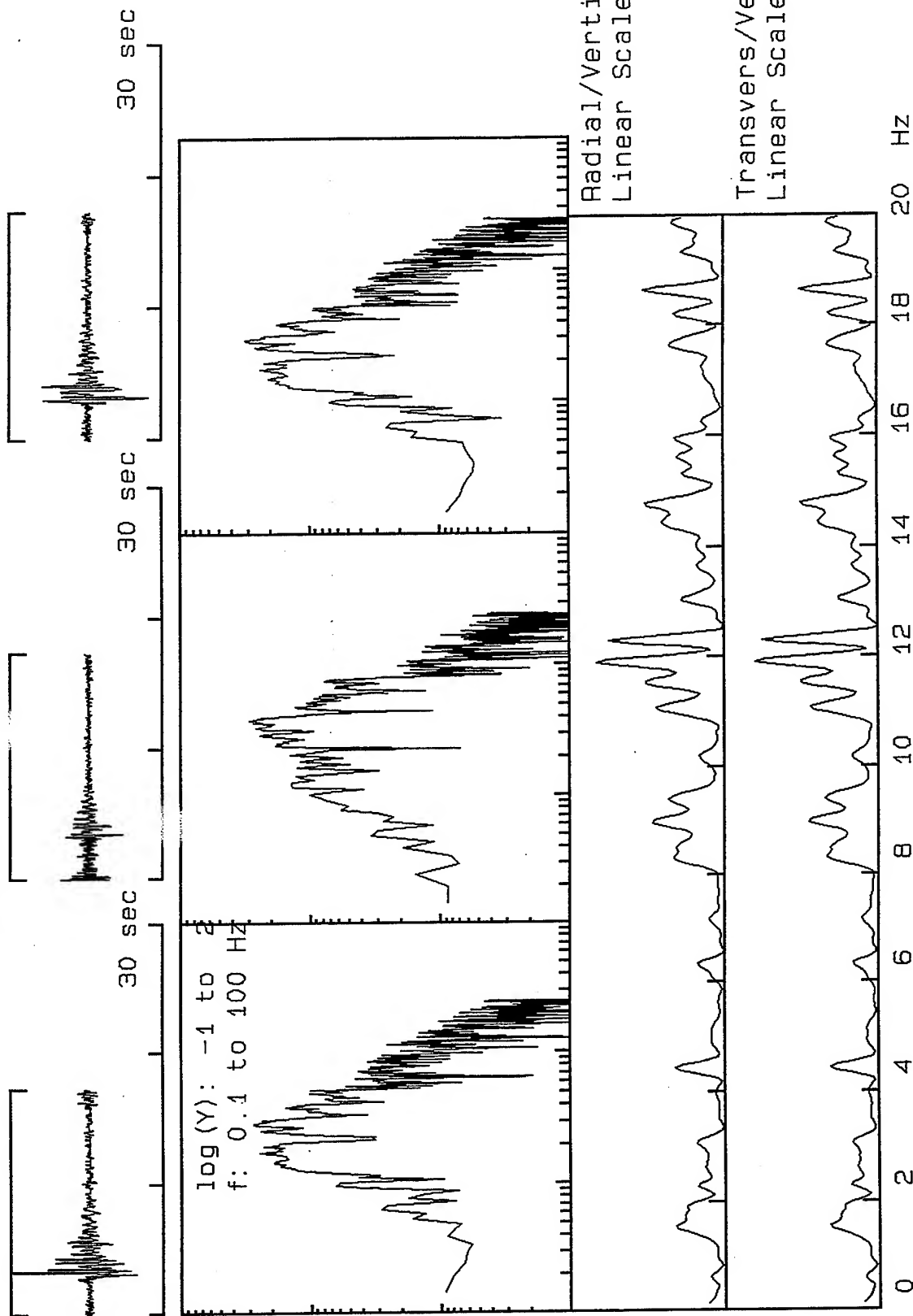
0 2 4 6 8 10 12 14 16 18 20 Hz



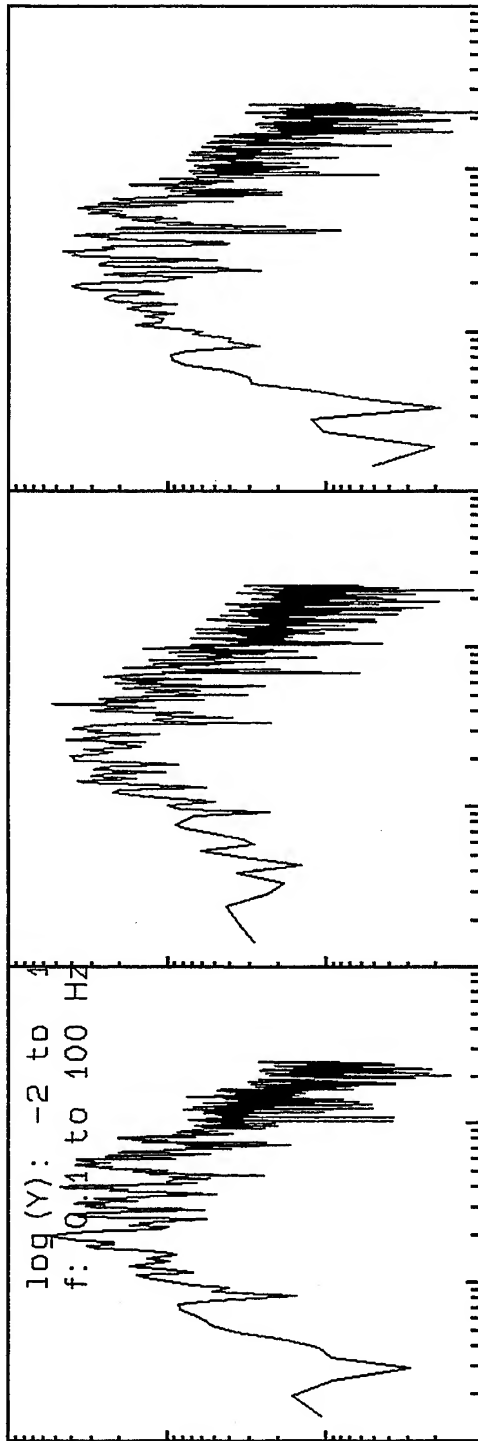
*VortexRock Consultants, Inc.*



V2X1601, Window: .0 to 17.3 s

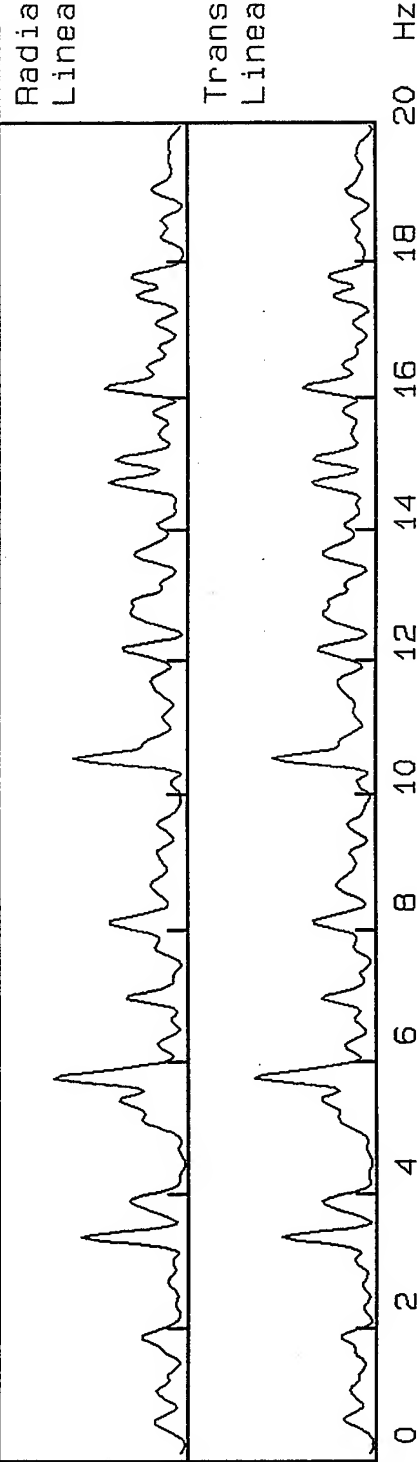


V2X1602, Window: .0 to 11.8 s

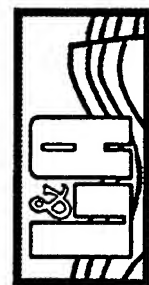


Radial/Vertical  
Linear Scale 0-10

Transvers/Vertical:  
Linear Scale 0-10

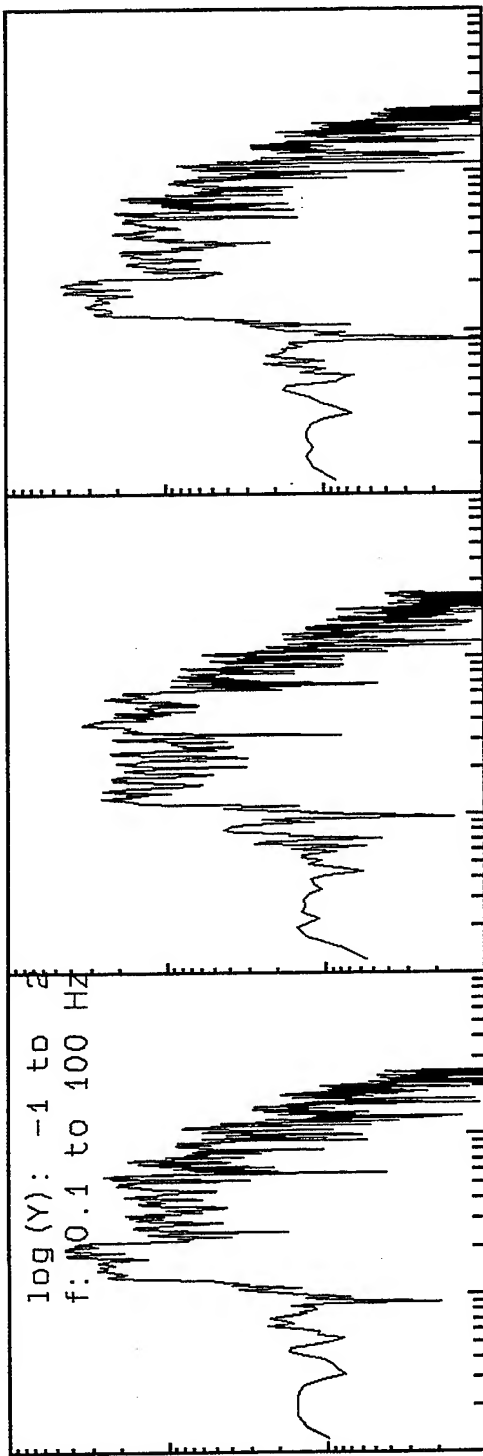
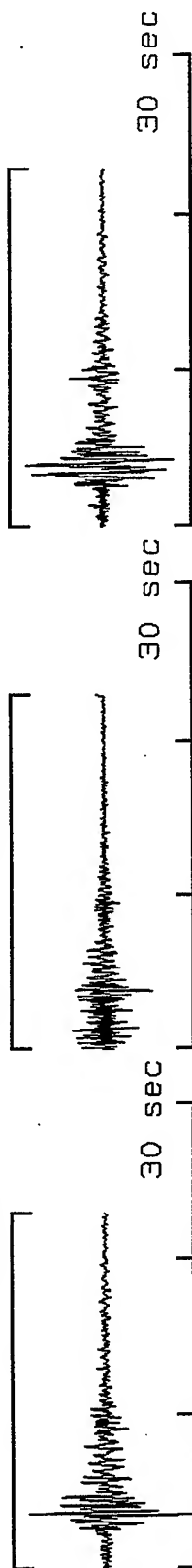


VortexRock Consultants, Inc.





V2X1609, Window: .0 to 22.9 s



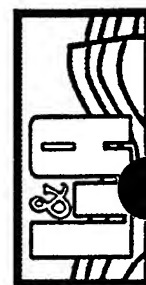
Radial/Vertical  
Linear Scale 0-10

Transvers/Vertical:  
Linear Scale 0-10

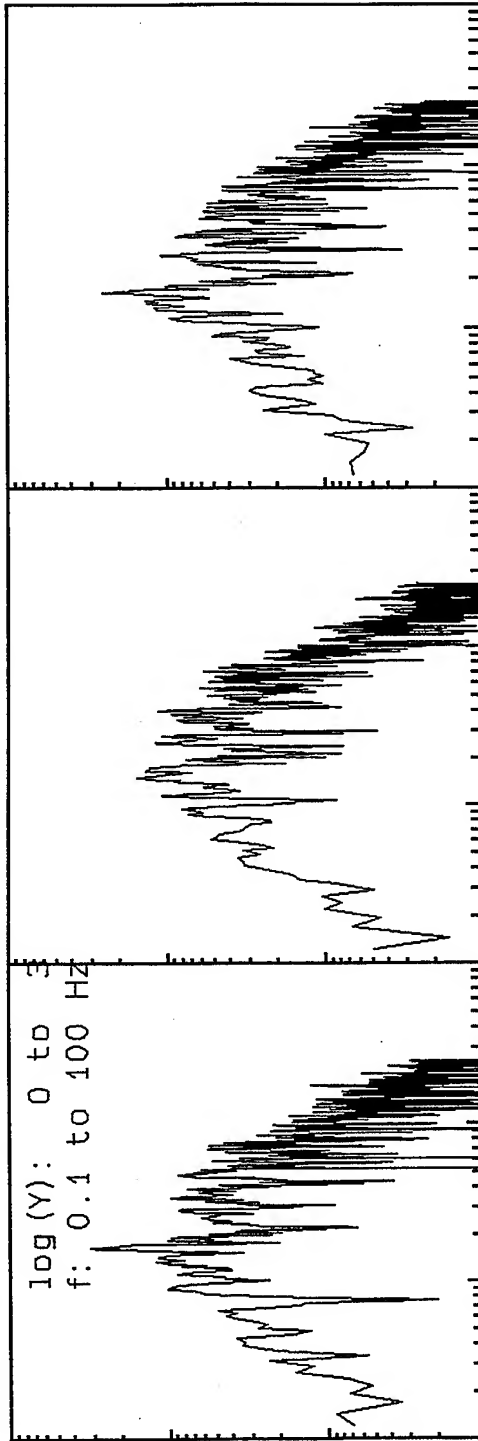
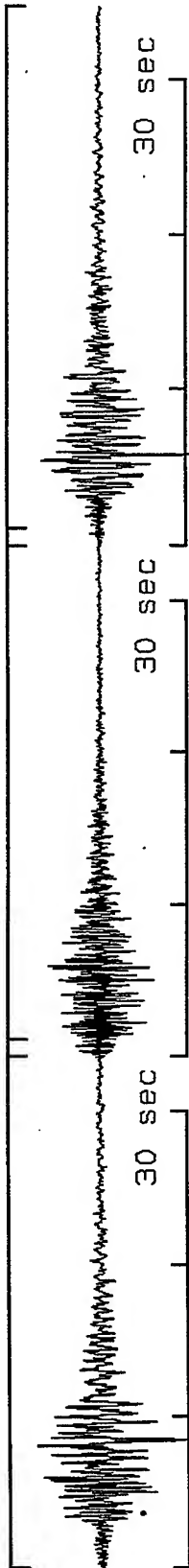
0 2 4 6 8 10 12 14 16 18 20 Hz



VortexRock Consultants, Inc.



V2X1600, Window: .0 to 34.7 s



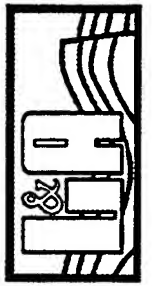
Radial/Vertical  
Linear Scale 0-10

Transvers/Vertical:  
Linear Scale 0-10

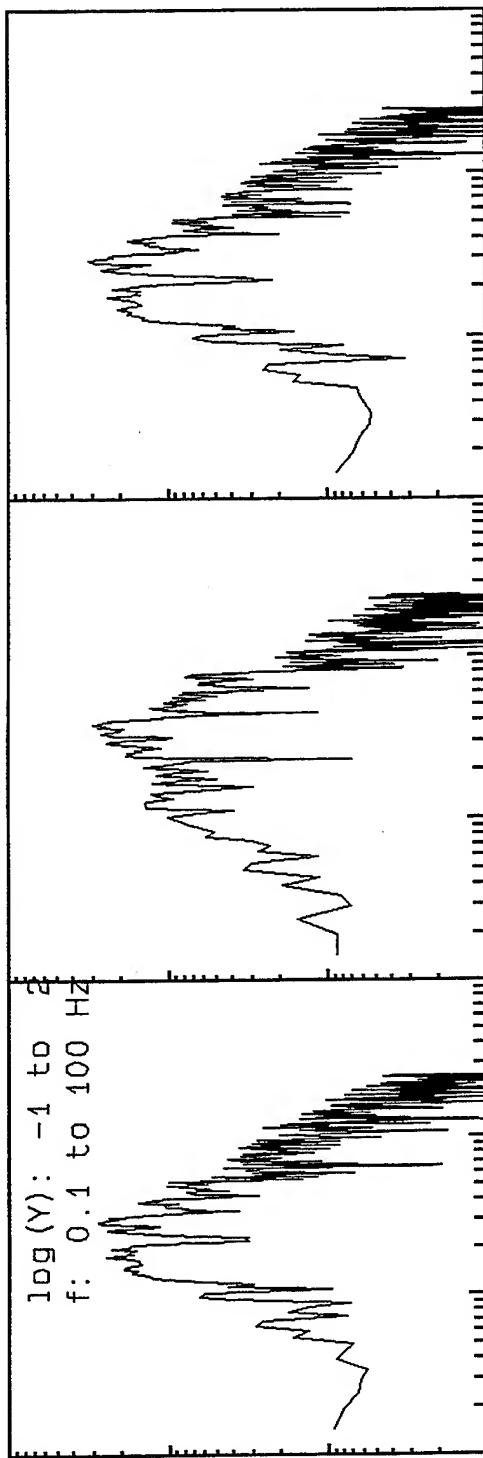
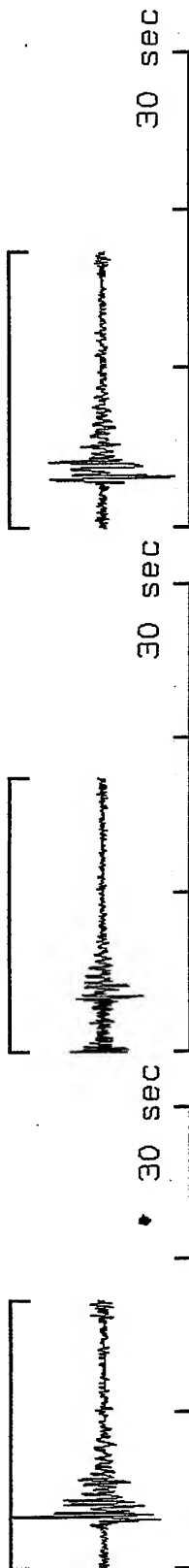
0 2 4 6 8 10 12 14 16 18 20 Hz



VortexRock Consultants, Inc.



V2X1601, Window: .0 to 17.3 s



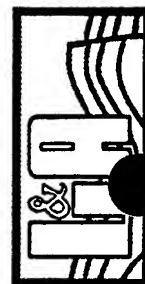
Radial/Vertical  
Linear Scale 0-10

Transvers/Vertical:  
Linear Scale 0-10

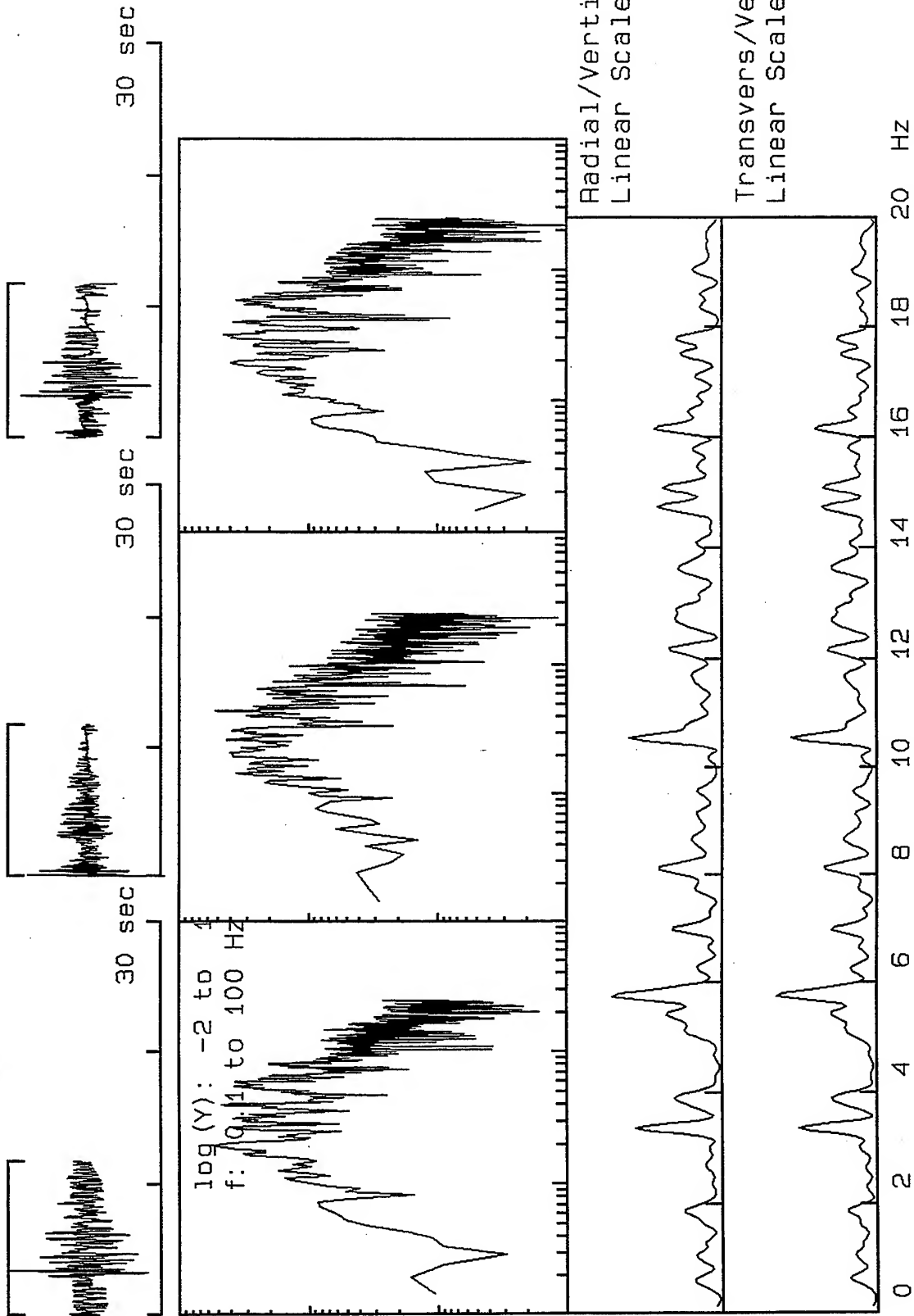
0 2 4 6 8 10 12 14 16 18 20 Hz



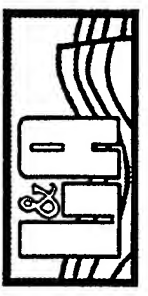
VortexRock Consultants, Inc.



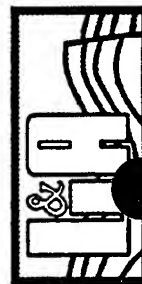
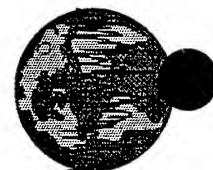
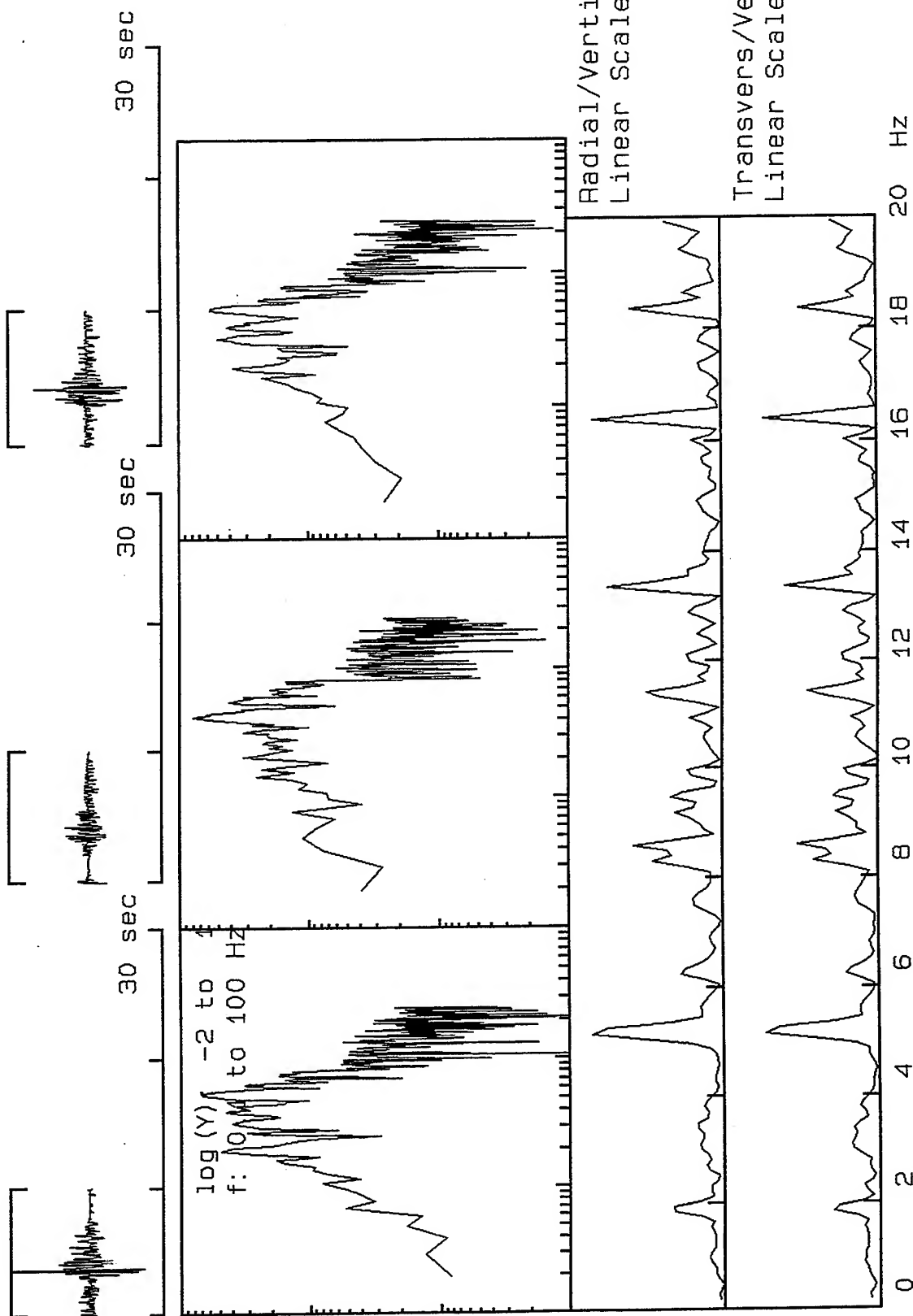
V2X1602, Window: .0 to 11.8 s



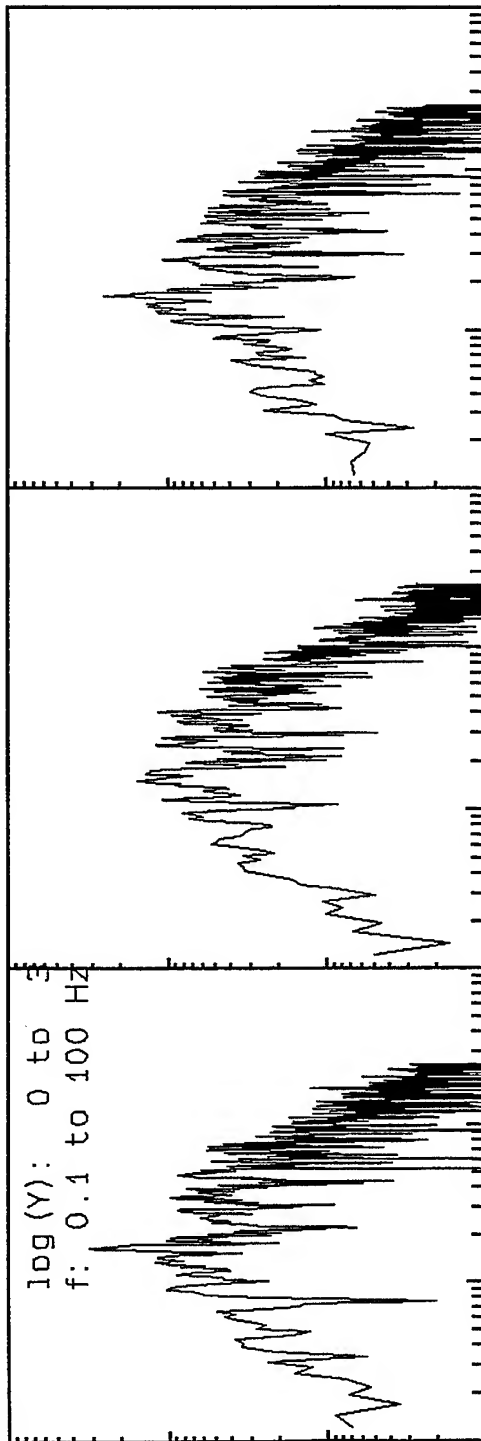
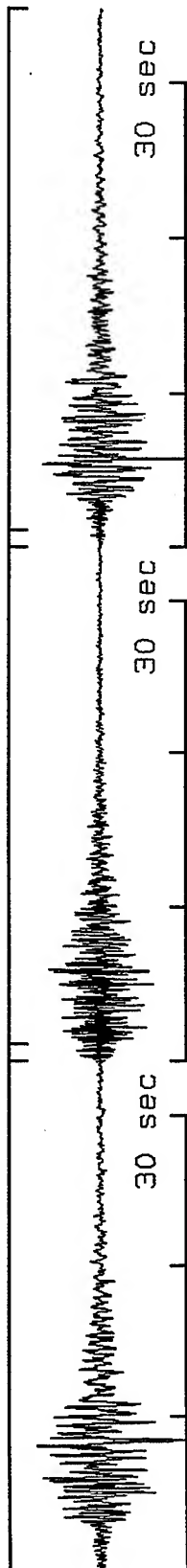
VortexRock Consultants, Inc.



V2X1603, Window: .0 to 10.1 s

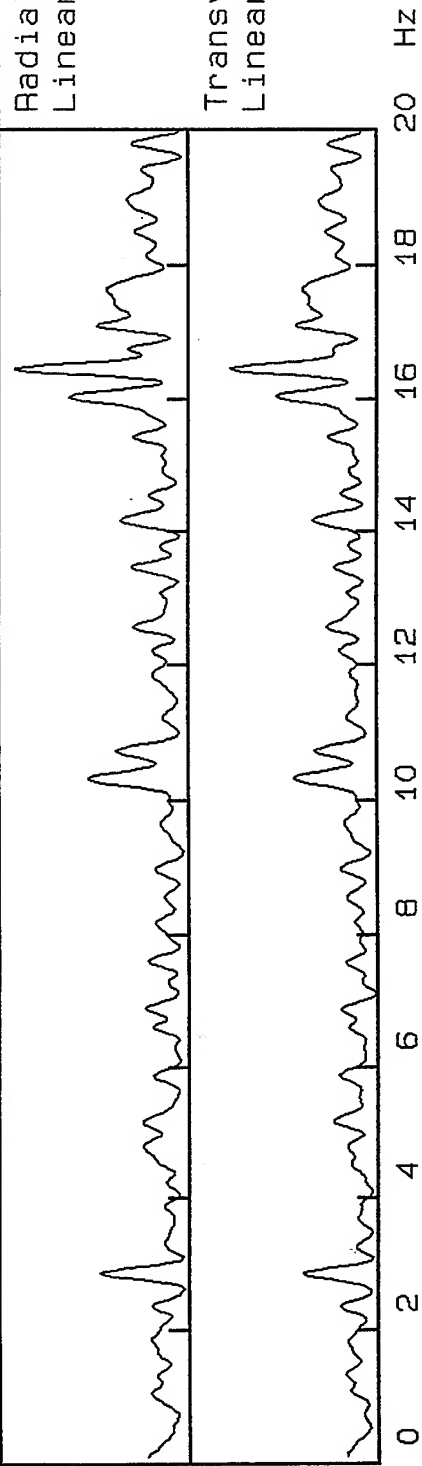


V2X1600, Window: .0 to 34.7 s

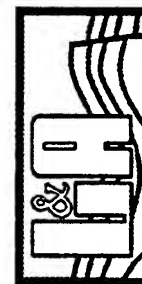


Radial/Vertical  
Linear Scale 0-10

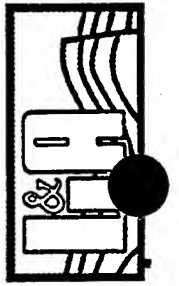
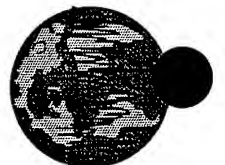
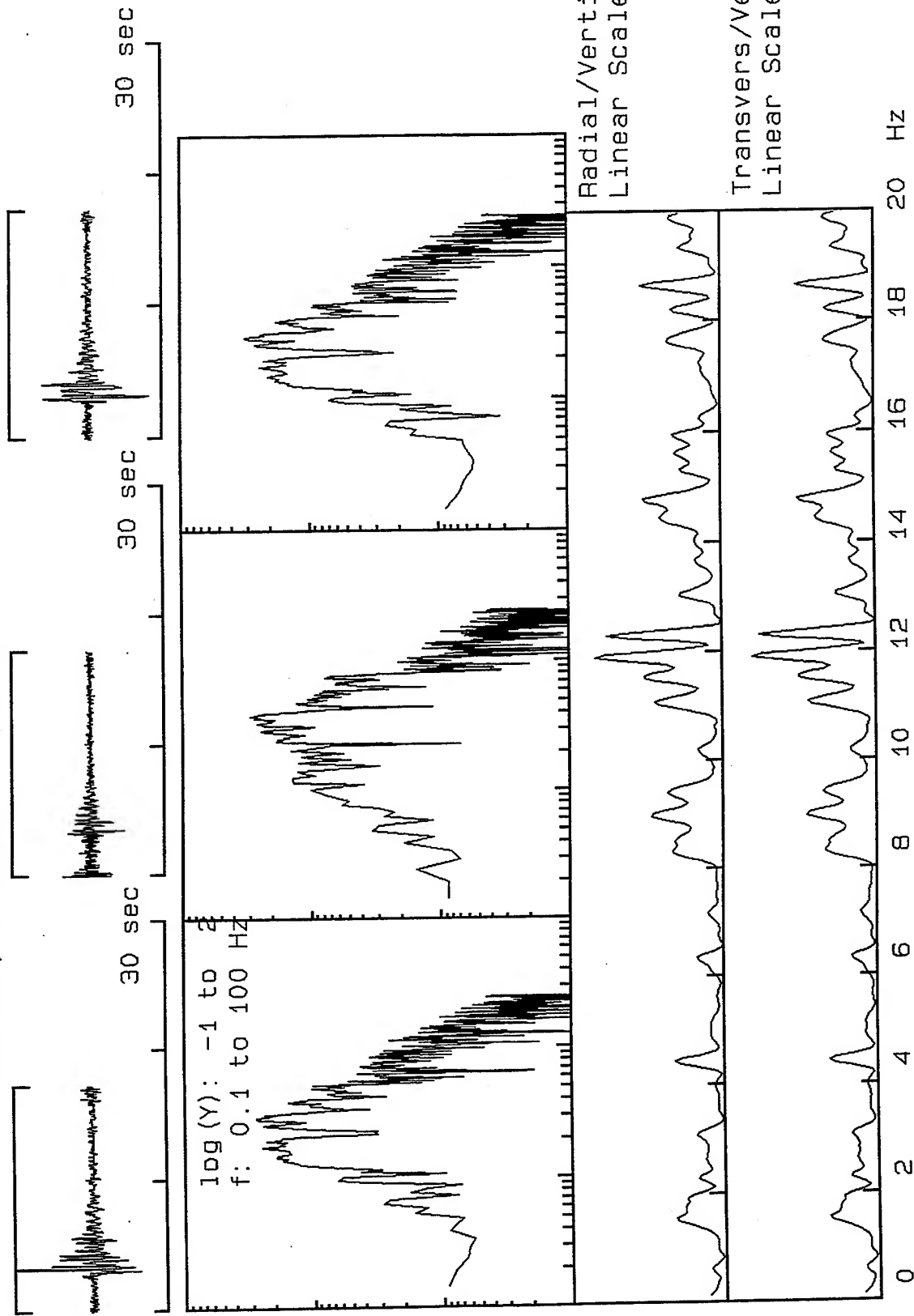
Transvers/Vertical:  
Linear Scale 0-10



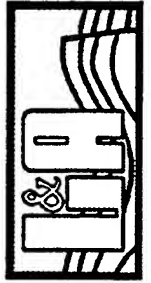
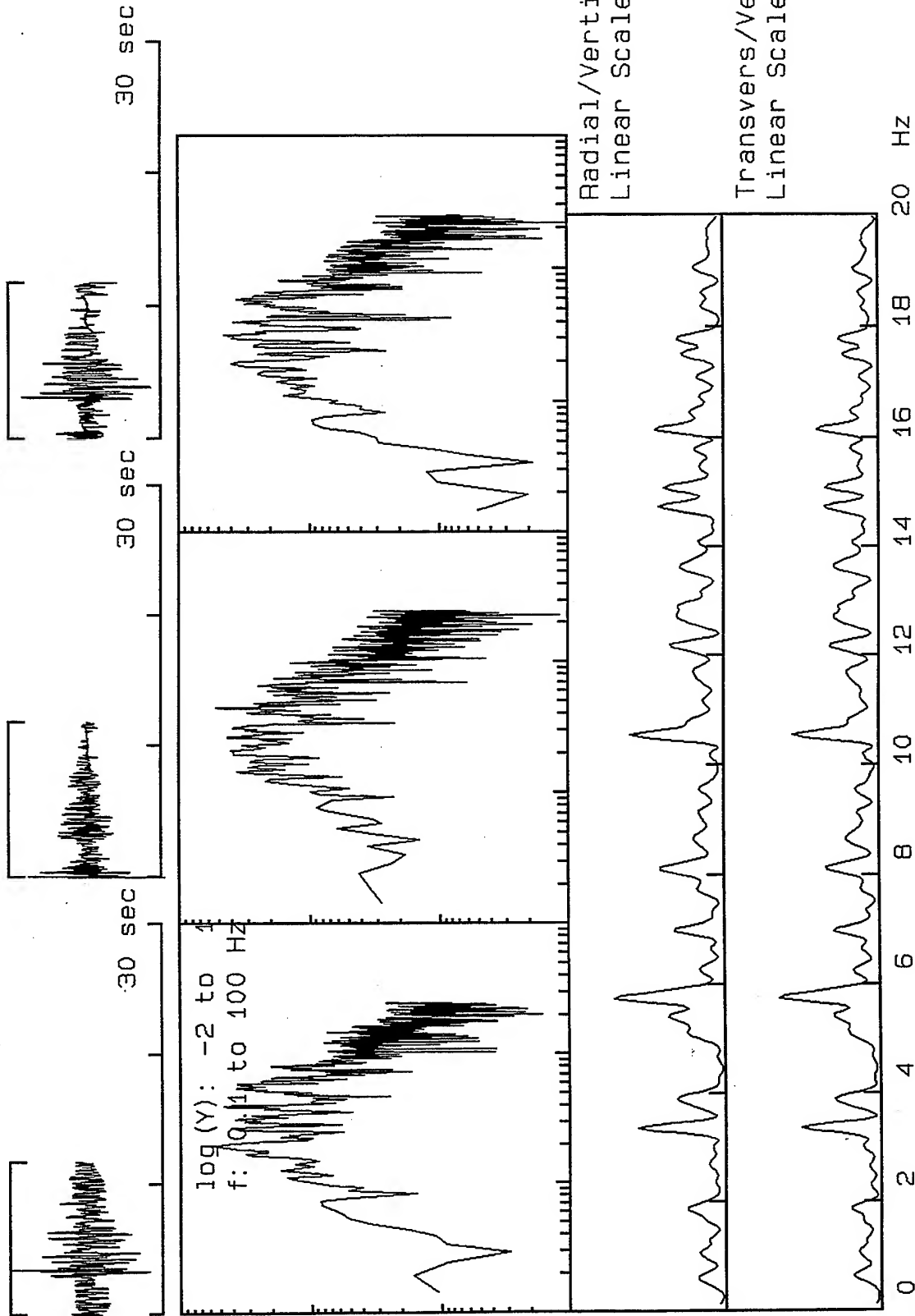
*VortexRock Consultants, Inc.*



V2X1601, Window: .0 to 17.3 s

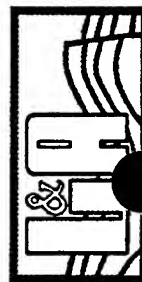
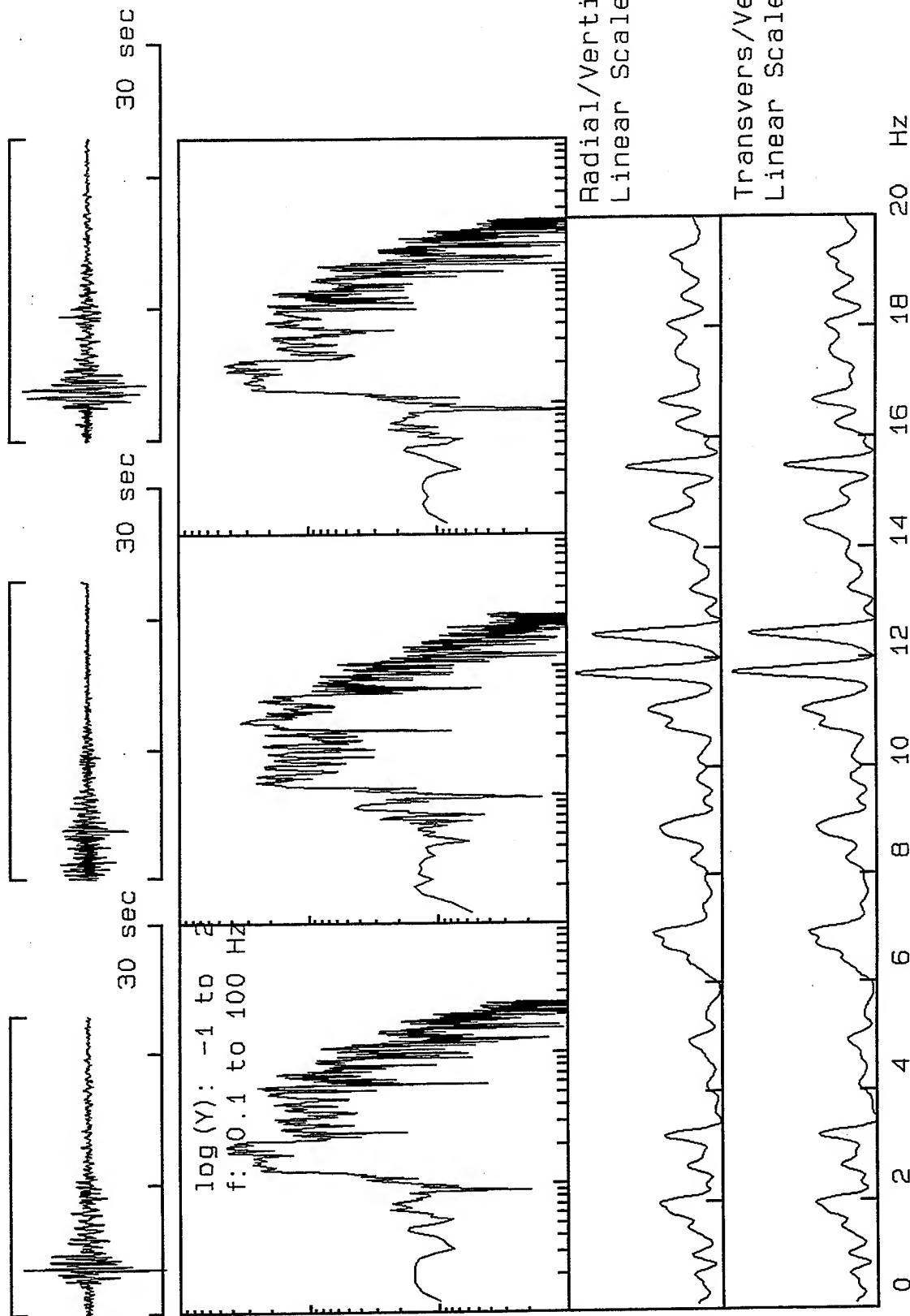


V2X1602, Window: .0 to 11.8 s

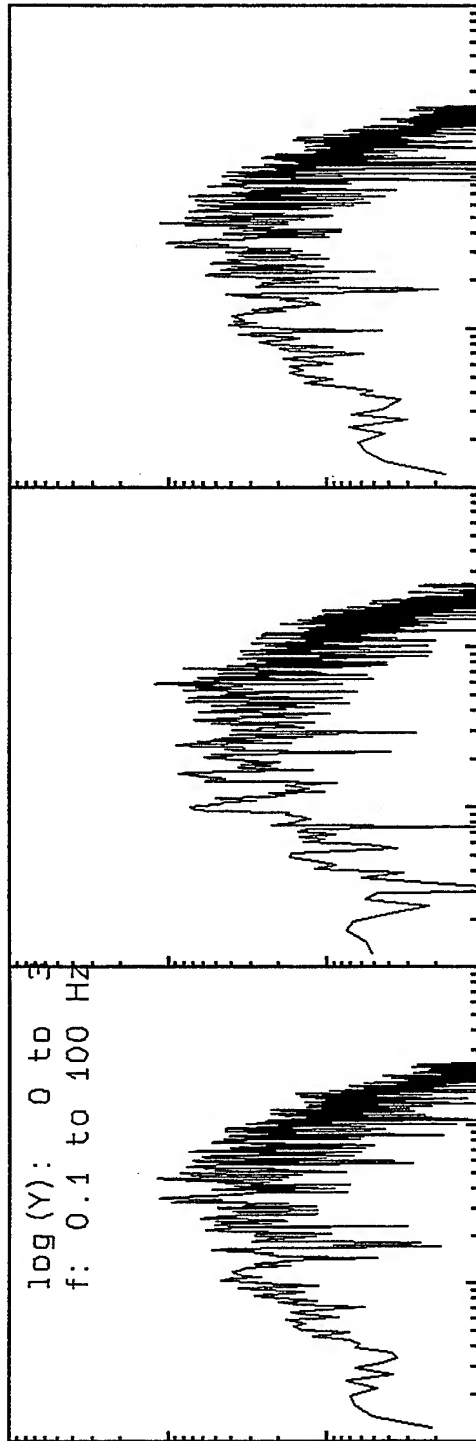
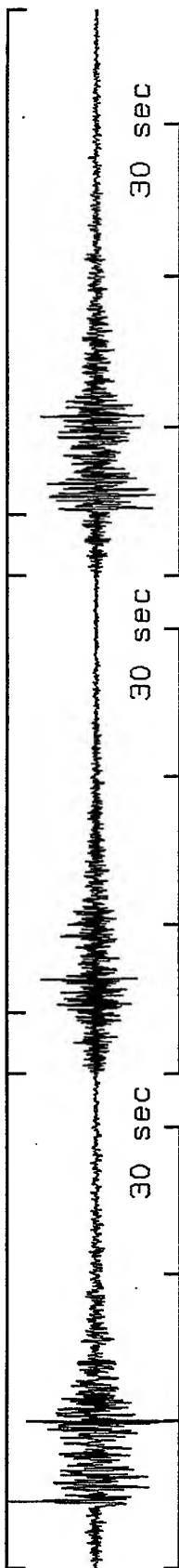




V2X1609, Window: .0 to 22.9 s



V2X6100, Window: .0 to 37.7 s



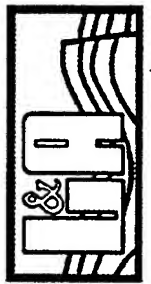
Radial/Vertical  
Linear Scale 0-10

Transvers/Vertical:  
Linear Scale 0-10

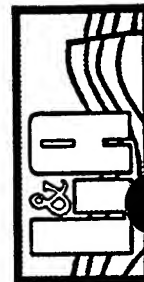
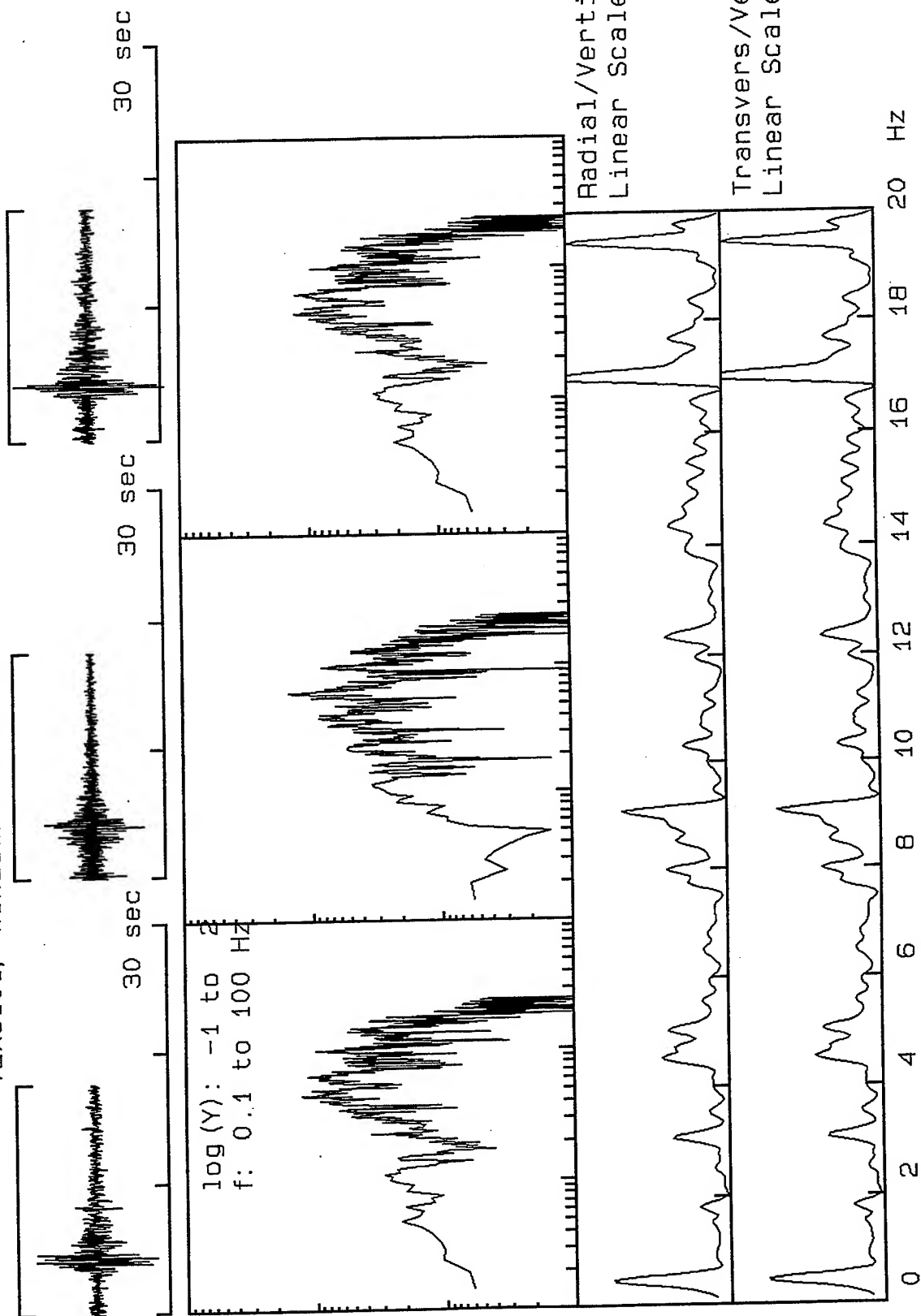
0 2 4 6 8 10 12 14 16 18 20 Hz



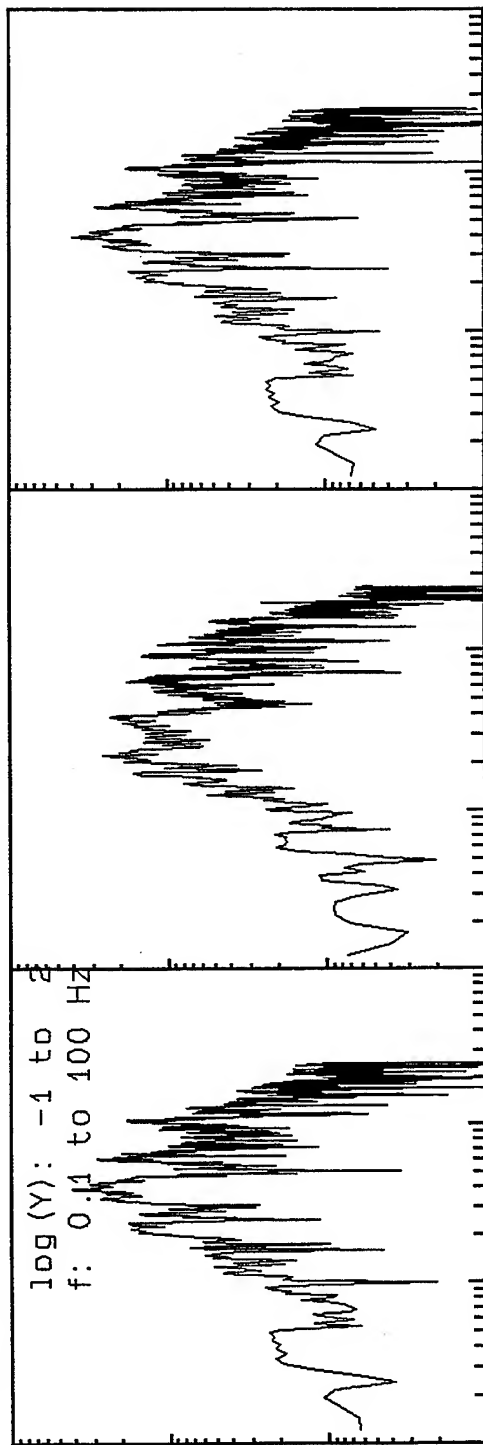
VortexRock Consultants, Inc.



V2X6101, Window: .0 to 17.7 s

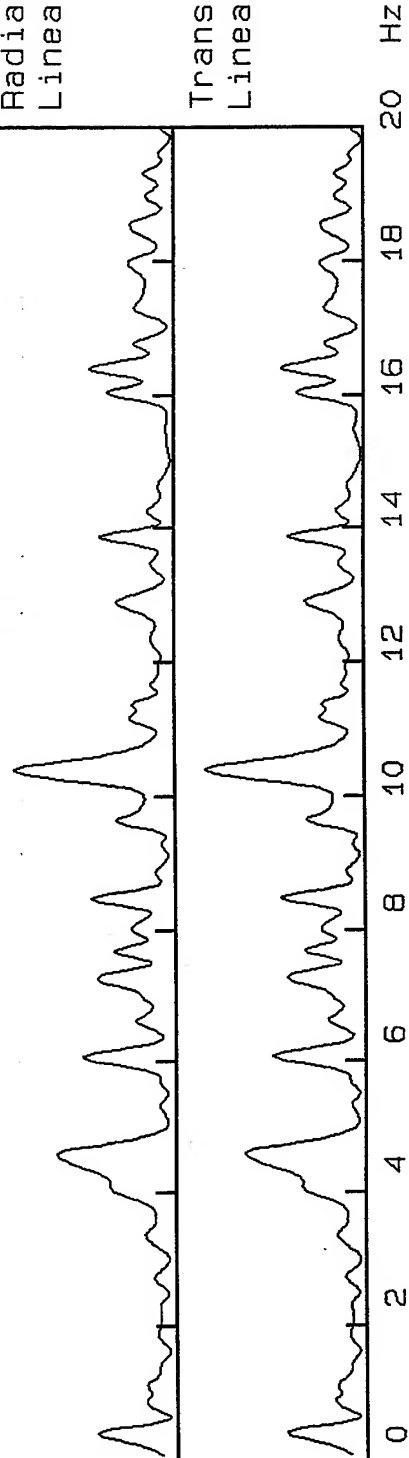


V2X6110, Window: .0 to 23.4 s

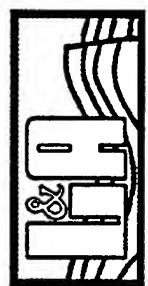


Radial/Vertical  
Linear Scale 0-10

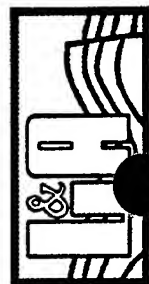
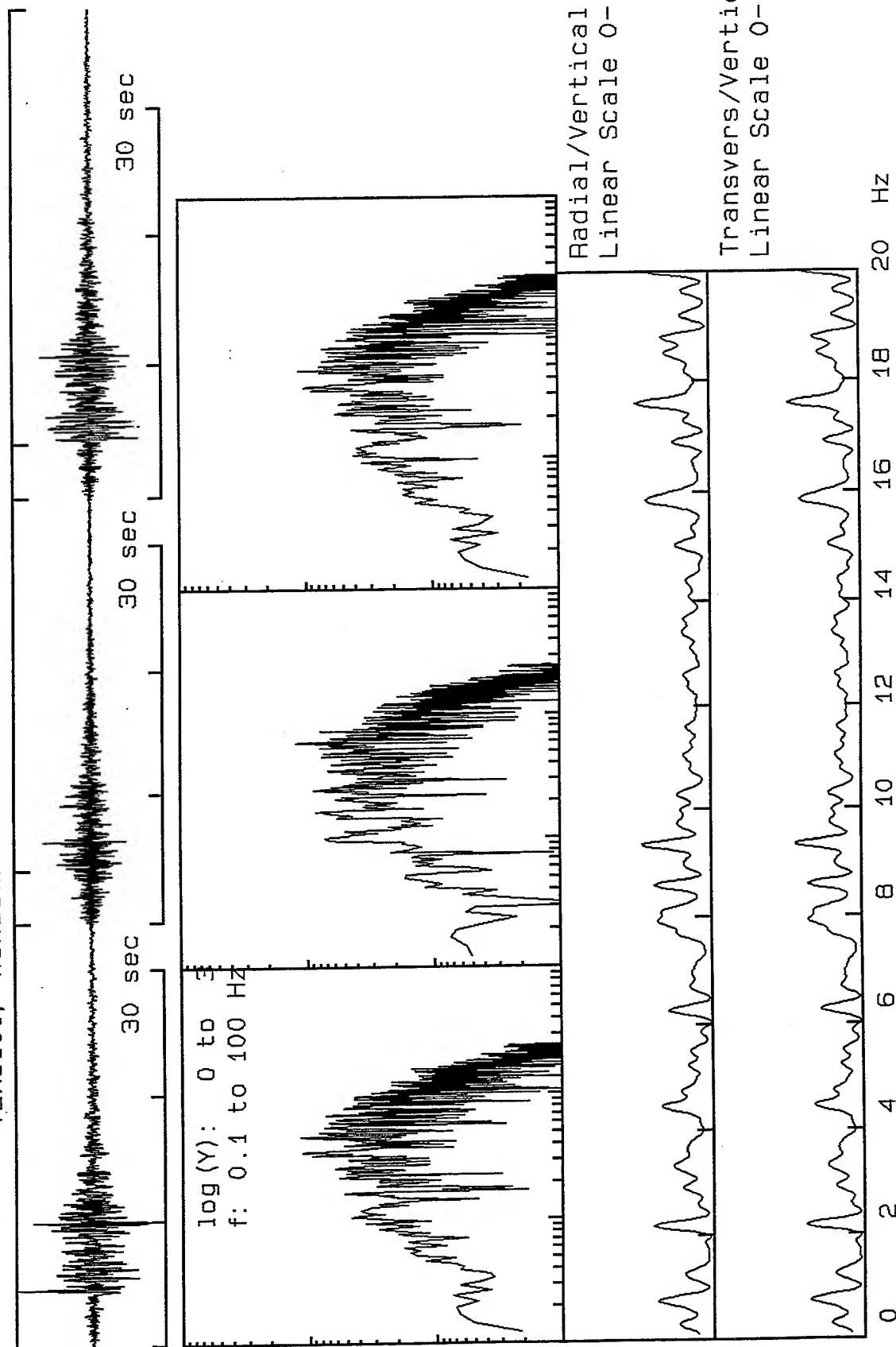
Transvers/Vertical  
Linear Scale 0-10



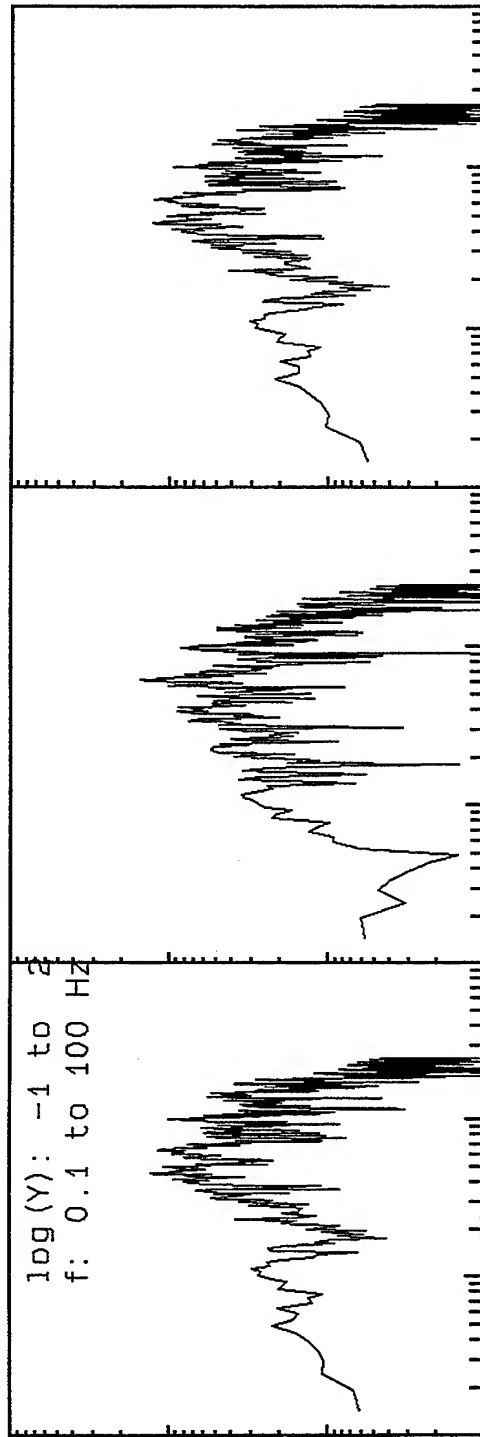
VortexRock Consultants, Inc.



V2X6100, Window: .0 to 37.7 s

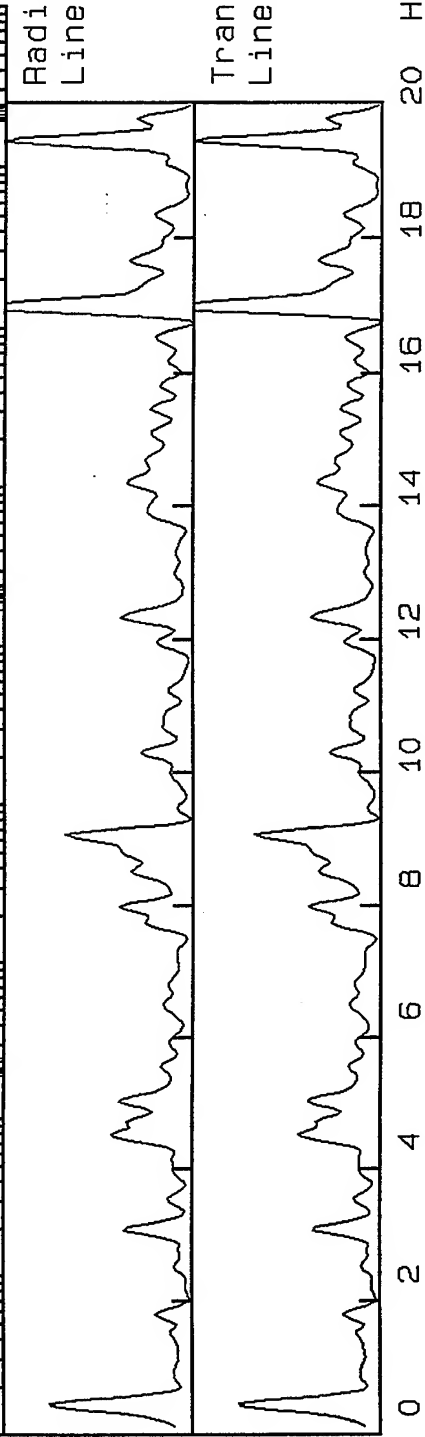


V2X6101, Window: .0 to 17.7 s

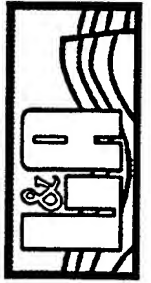


Radial/Vertical  
Linear Scale 0-10

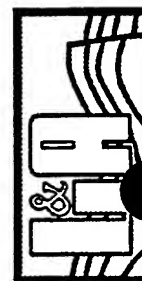
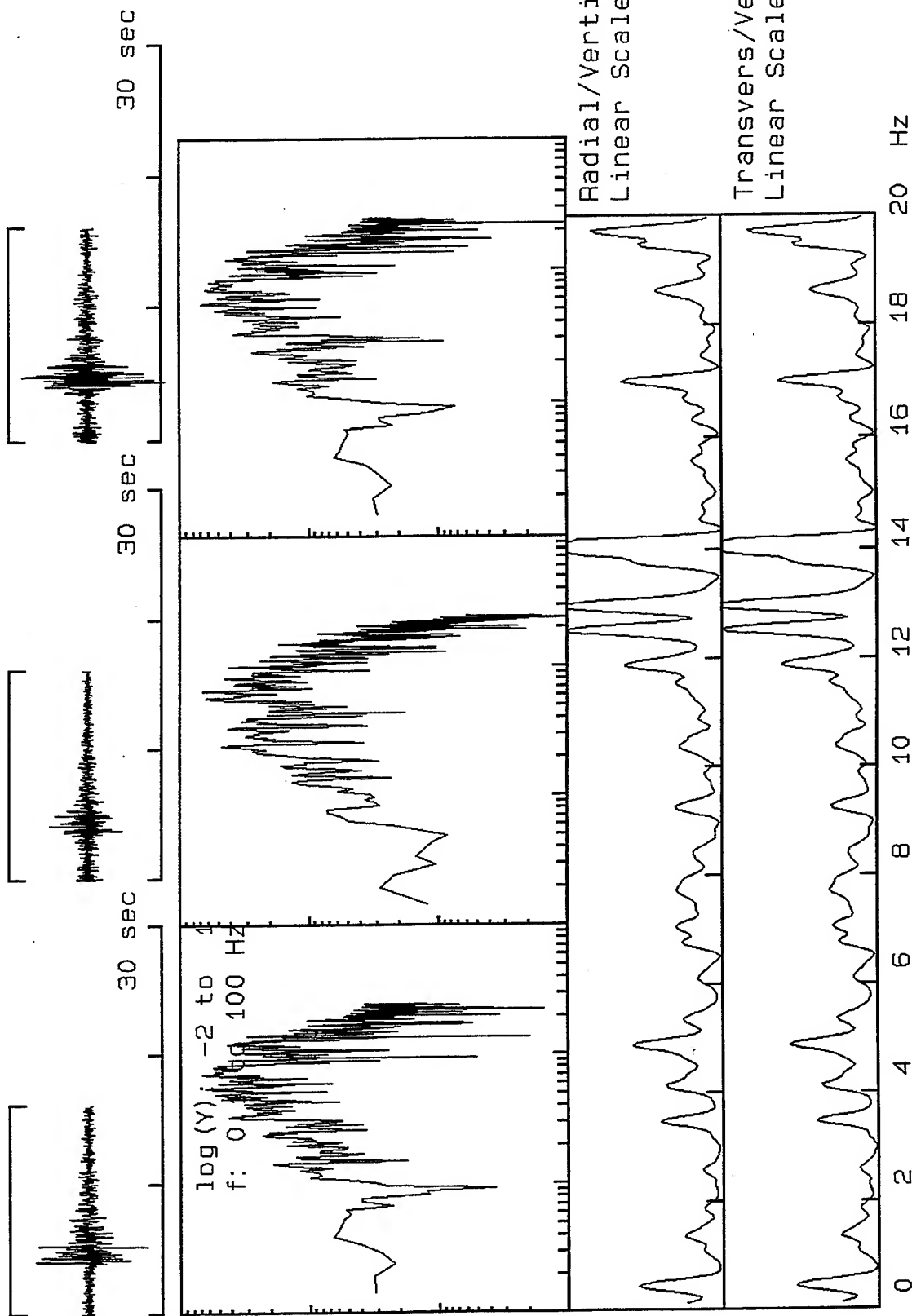
Transvers/Vertical:  
Linear Scale 0-10



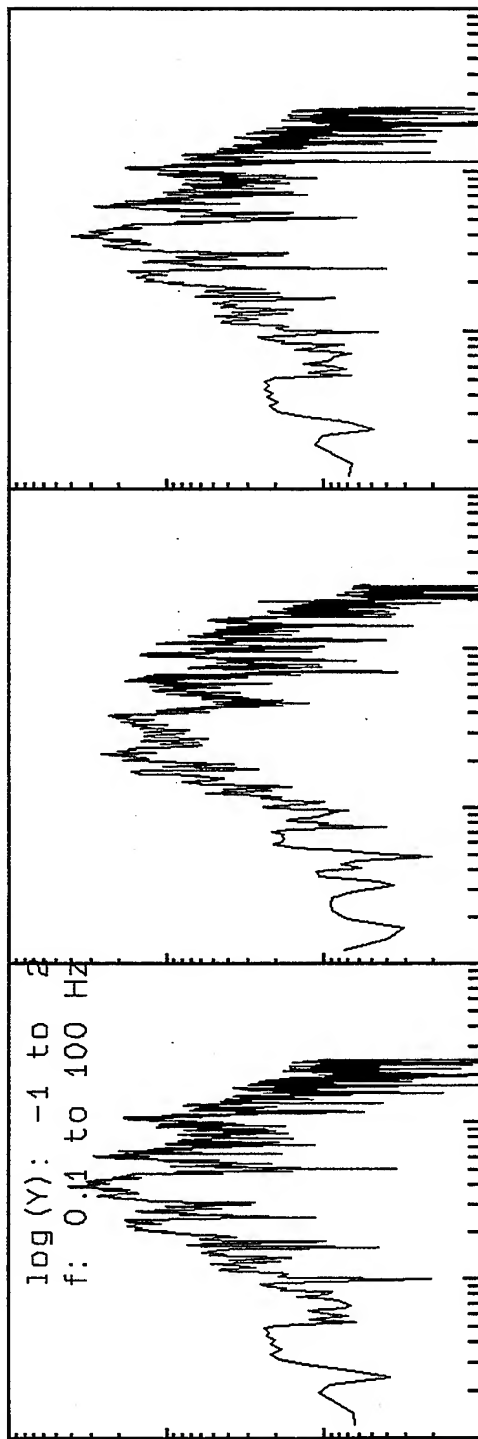
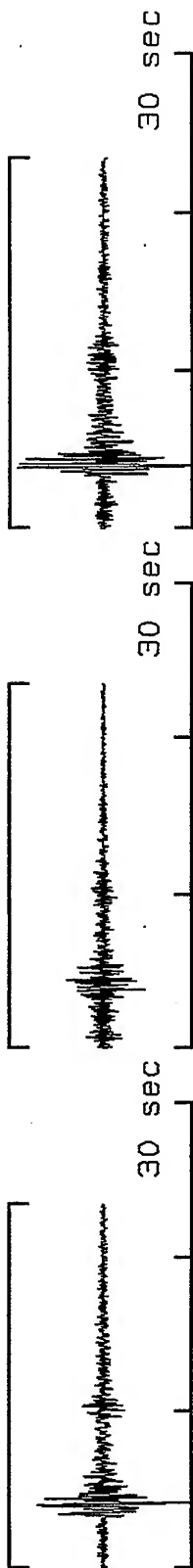
VortexRock Consultants, Inc.



V2X6107, Window: .0 to 16.2 s



V2X6110, Window: .0 to 23.4 s



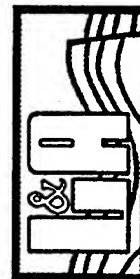
Radial/Vertical  
Linear Scale 0-10

Transvers/Vertical:  
Linear Scale 0-10

0 2 4 6 8 10 12 14 16 18 20 Hz

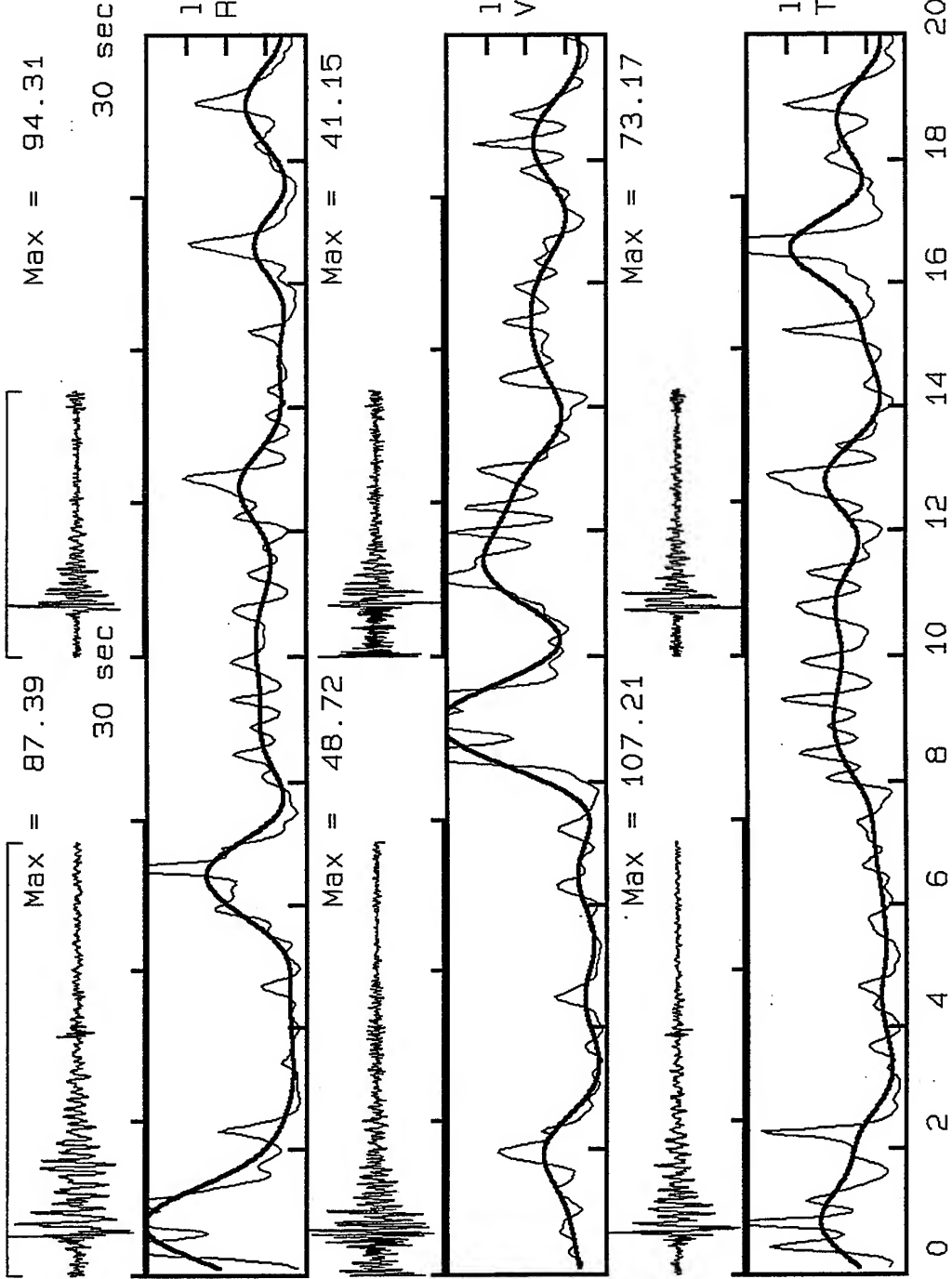


*VortexRock Consultants, Inc.*





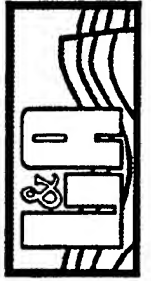
V2X1301, Window: .0 to 28.6 s V2X1601, Window: .0 to 17.3 s



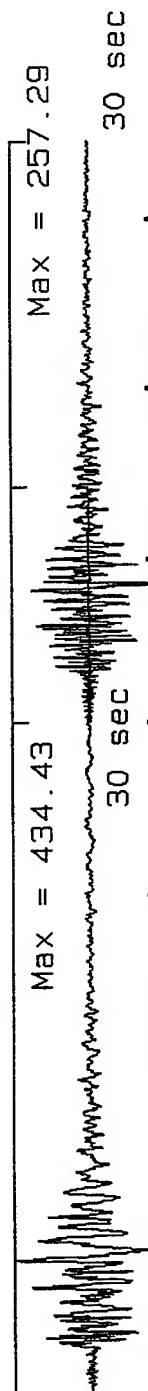
F-1



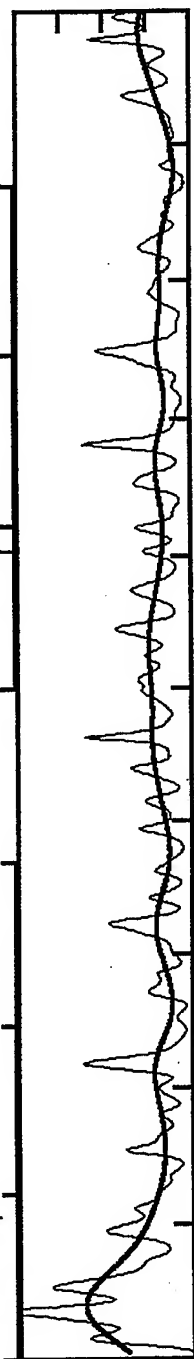
**VortexRock Consultants, Inc.**  
11434 Alder Creek Rd, Corona, CA 91720  
Tel - Fax (714) 692-1443, E-Mail: mahdiyari@coda.usc.edu



V2X1300, Window: .0 to 54.9 s V2X1600, Window: .0 to 34.7 s

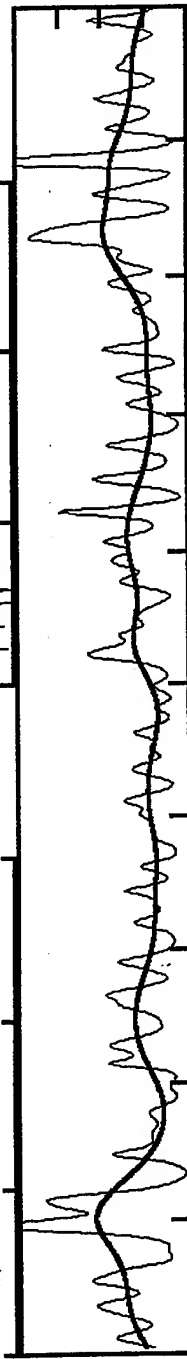


linear Scale: 0-8  
Radial Comp.



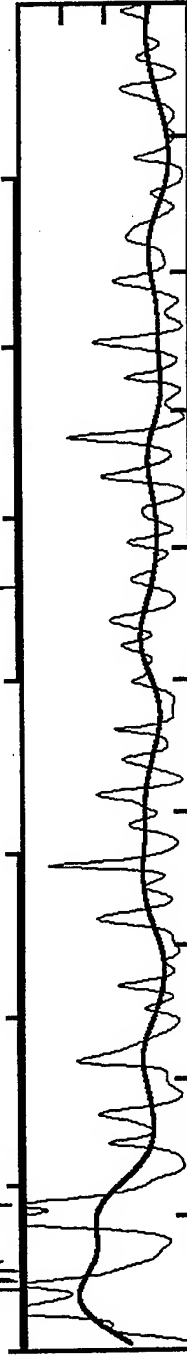
Max = 158.16

linear Scale: 0-8  
Vertical Comp.



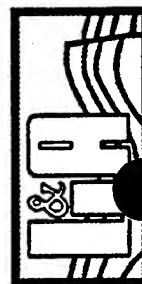
Max = 272.62

linear Scale: 0-8  
Transverse Comp.

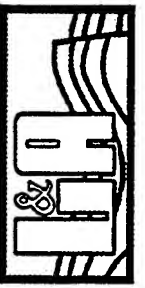
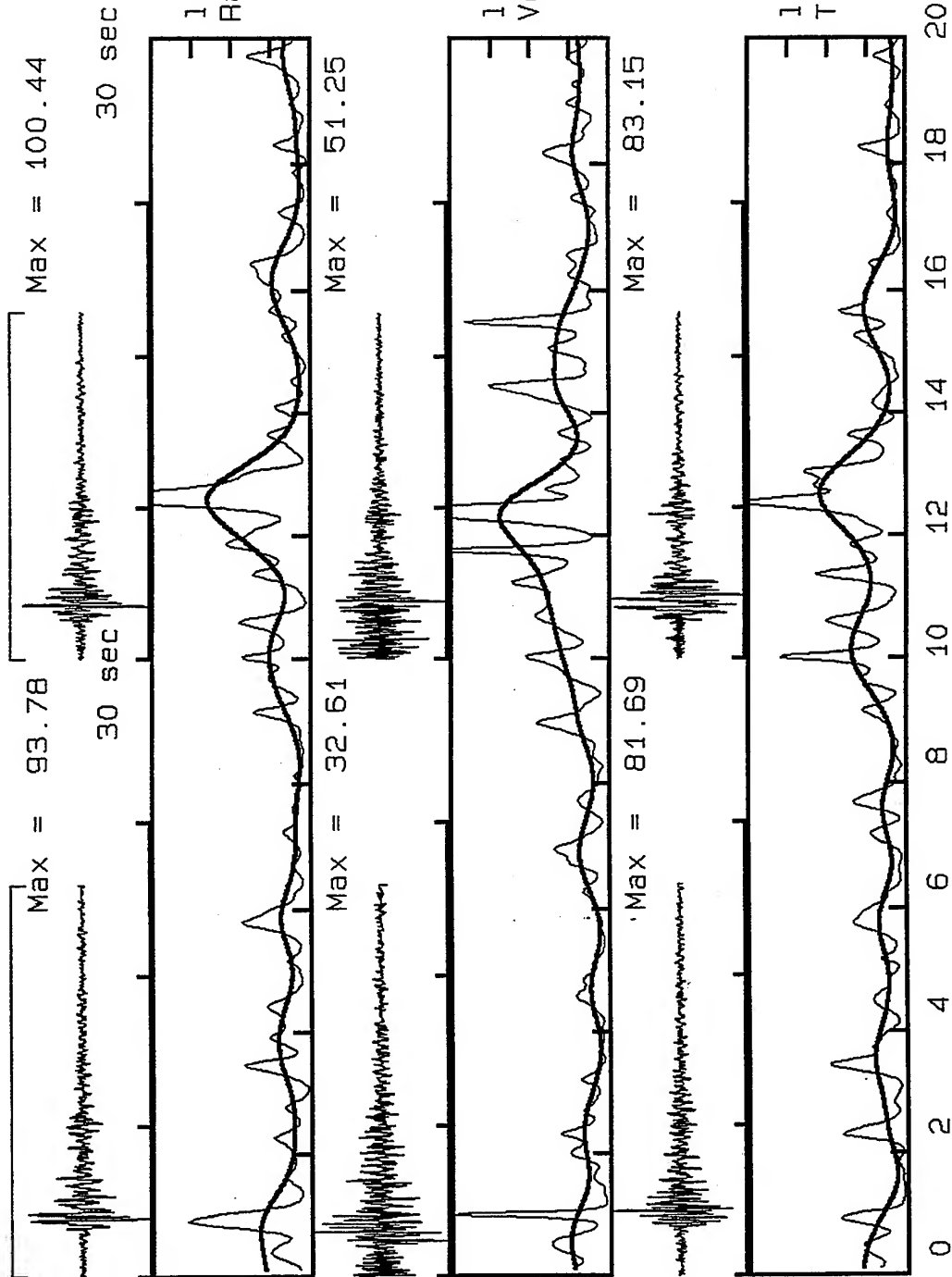


0 2 4 6 8 10 12 14 16 18 20 Hz

**VortexRock Consultants, Inc.**  
11434 Alder Creek Rd, Corona, CA 91720  
Tel - Fax (714) 692-1443, E-Mail: mahdaviar@coda.usc.edu



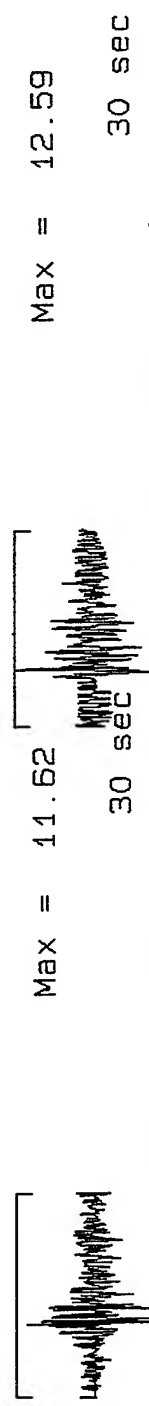
V2X1809, Window: .0 to 26.0 s V2X1609, Window: .0 to 22.9 s



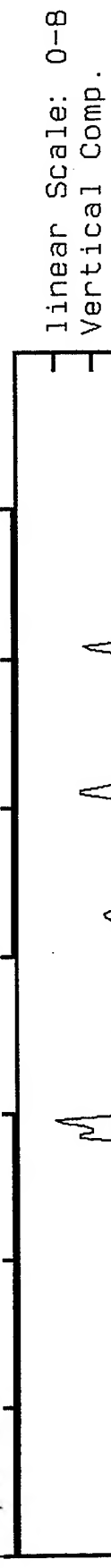
**VortexRock Consultants, Inc.**  
 11434 Alder Creek Rd, Corona, CA 91720  
 Tel - Fax (714) 692-1443, E-Mail: mahdytar@coda.usc.edu



V2X1802, Window: .0 to 12.3 s V2X1602, Window: .0 to 11.8 s



Max = 6.33  
Max = 12.51



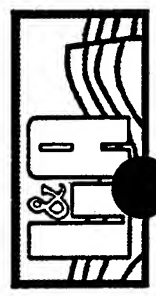
Max = 11.16  
Max = 10.49



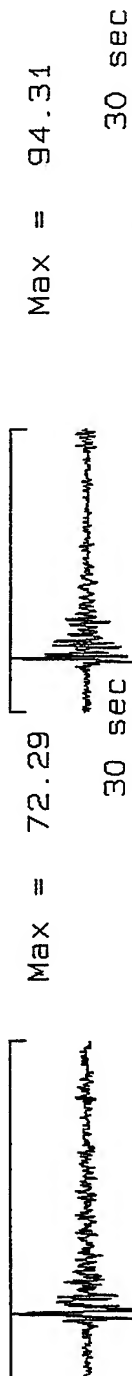
0 2 4 6 8 10 12 14 16 18 20 HZ



**VortexRock Consultants, Inc.**  
11434 Alder Creek Rd, Corona, CA 91720  
Tel - Fax (714) 692-1443, E-Mail: mahdyiar@coda.usc.edu

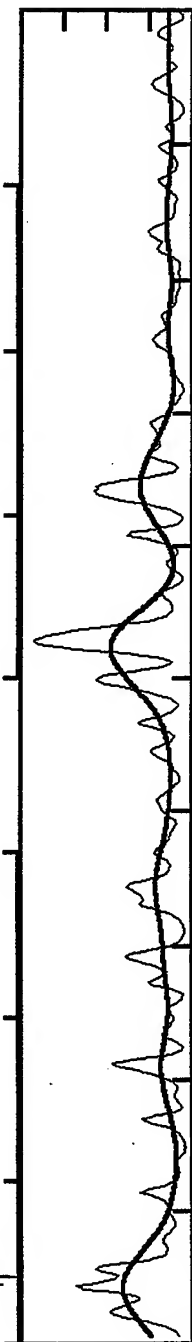


V2X1801, Window: .0 to 20.7 s V2X1601, Window: .0 to 17.3 s



Max = 94.31

30 sec



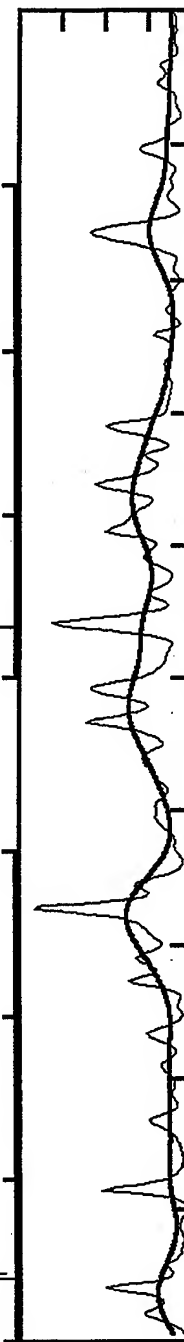
Max = 25.86

Max = 41.15



Max = 60.16

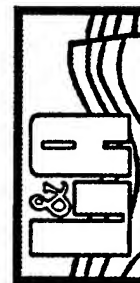
Max = 73.17



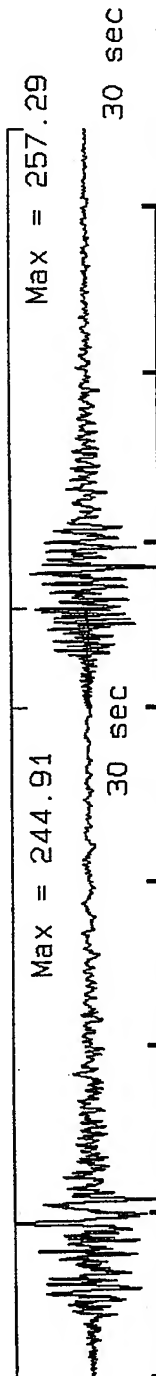
0 2 4 6 8 10 12 14 16 18 20 Hz



**VortexRock Consultants, Inc.**  
11434 Alder Creek Rd, Corona, CA 91720  
Tel - Fax (714) 692-1443, E-Mail: mahdytar@coda.usc.edu

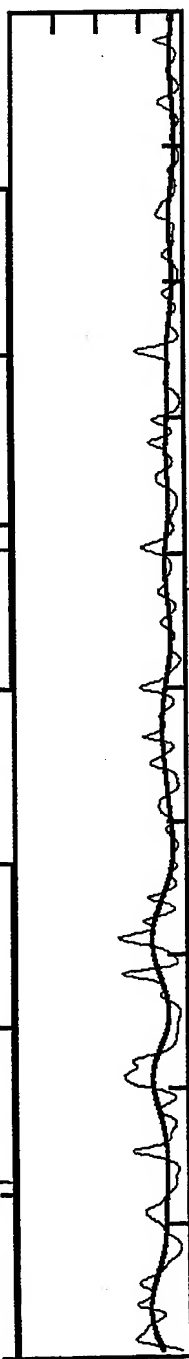


V2X1800, Window: .0 to 46.6 s V2X1600, Window: .0 to 34.7 s



Max = 257.29

30 sec



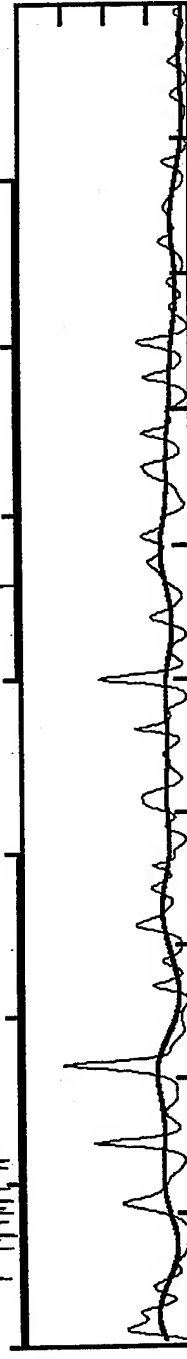
Max = 158.16

linear Scale: 0-8  
Radial Comp.



Max = 272.62

linear Scale: 0-8  
Vertical Comp.

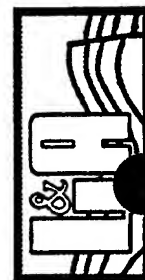


linear Scale: 0-8  
Transverse Comp.

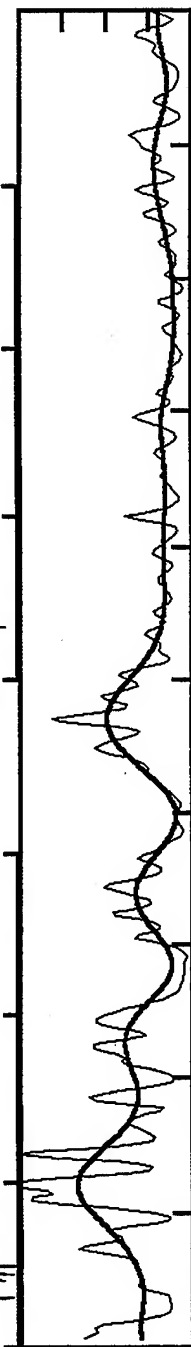
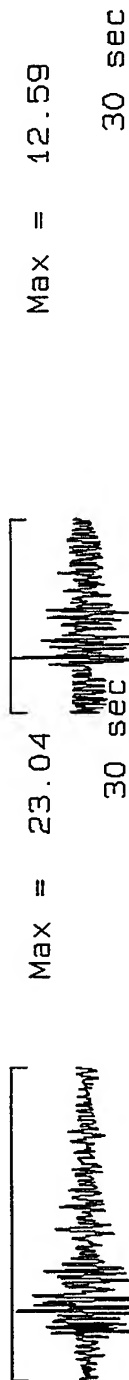
20 Hz



**VortexRock Consultants, Inc.**  
11434 Alder Creek Rd, Corona, CA 91720  
Tel - Fax (714) 692-1443, E-Mail: mahdyiar@coda.usc.edu



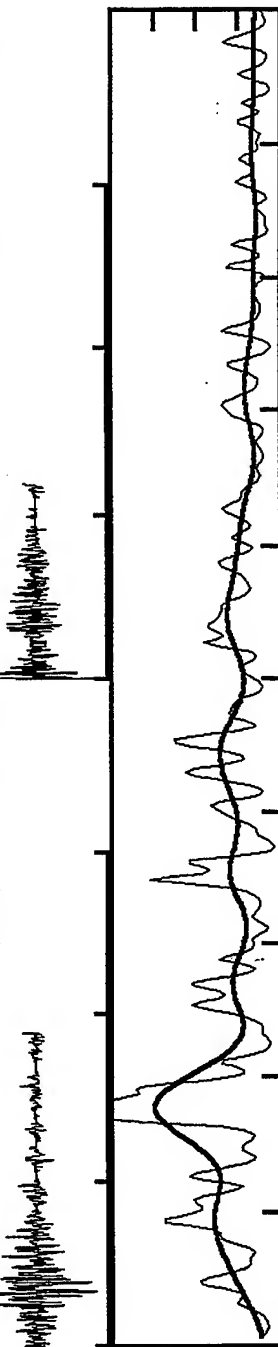
V2X1304, Window: .0 to 18.9 s V2X1602, Window: .0 to 11.8 s



linear Scale: 0-8  
Radial Comp.

Max = 15.83

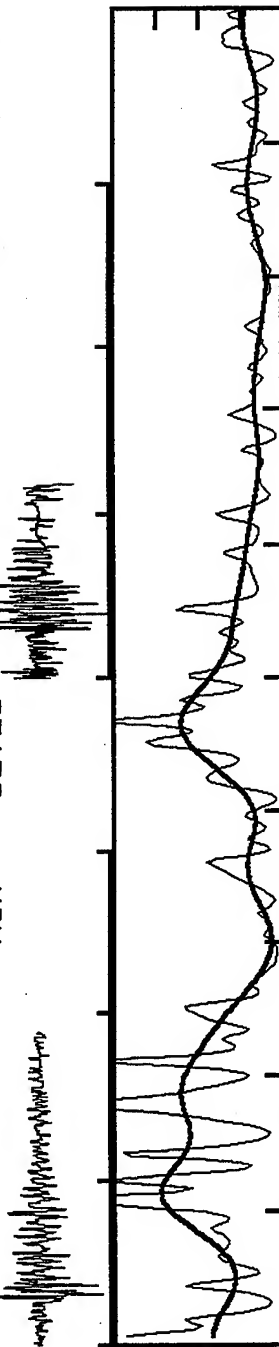
Max = 12.51



linear Scale: 0-8  
Vertical Comp.

Max = 10.49

Max = 10.49

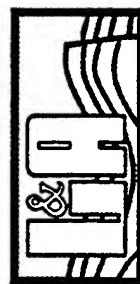


linear Scale: 0-8  
Transverse Comp.

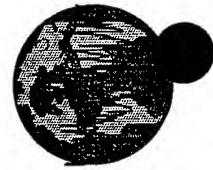
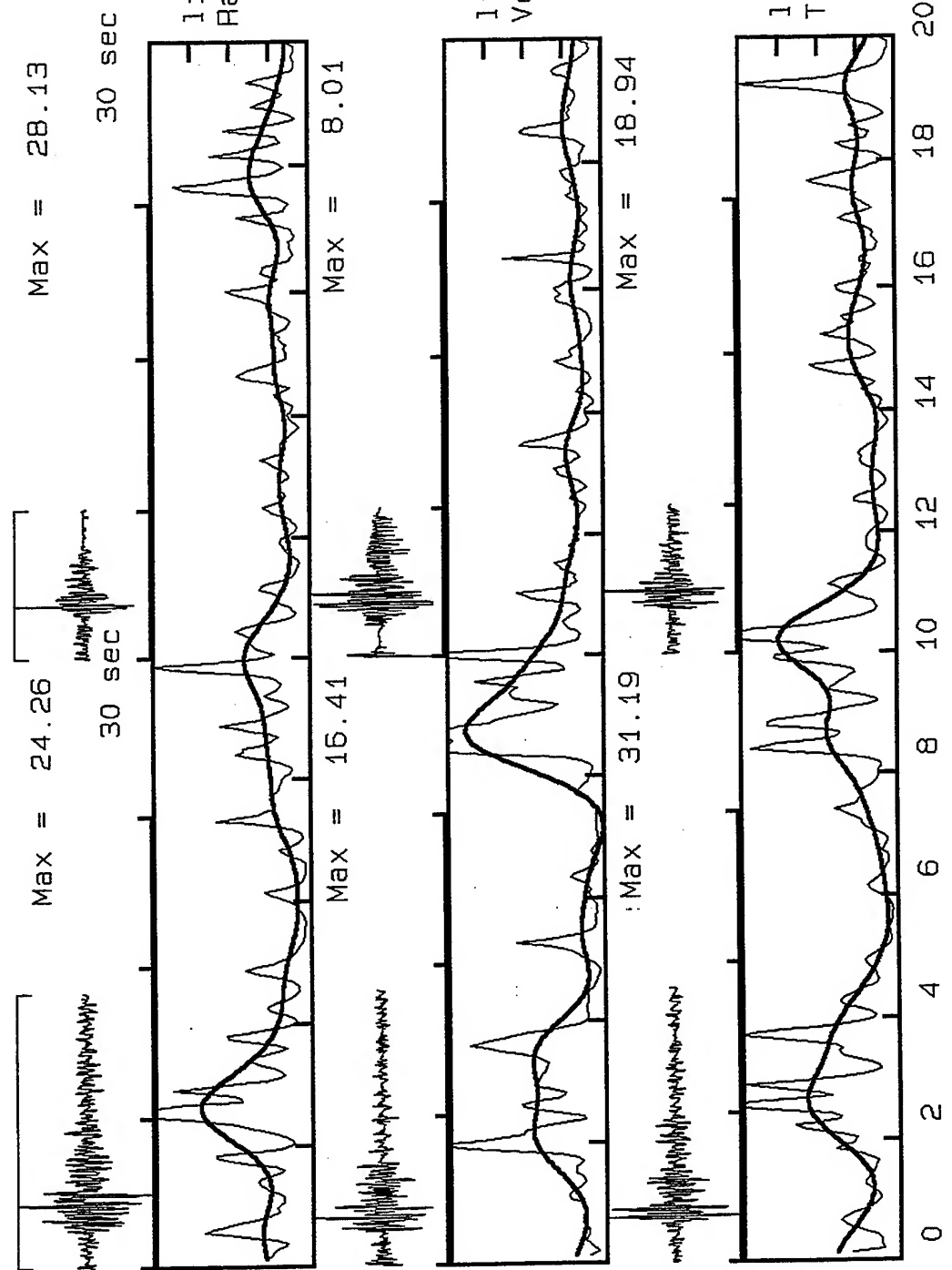
0 2 4 6 8 10 12 14 16 18 20 Hz



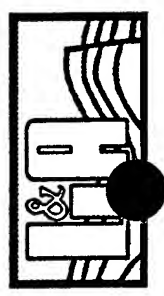
**VortexRock Consultants, Inc.**  
11434 Alder Creek Rd, Corona, CA 91720  
Tel - Fax (714) 692-1443, E-Mail: mahdyiar@coda.usc.edu



V2X1310, Window: .0 to 18.4 s V2X1603, Window: .0 to 10.1 s

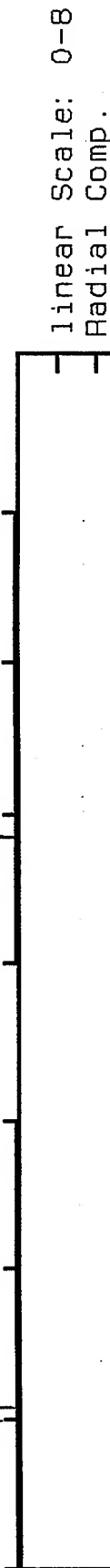
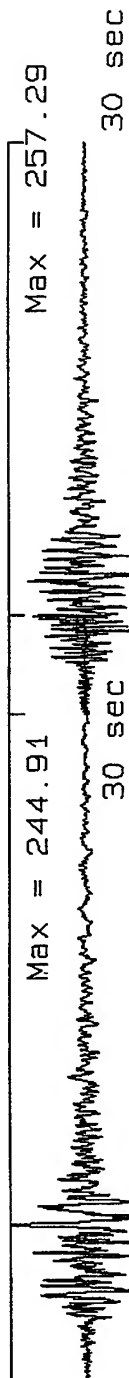


**VortexRock Consultants, Inc.**  
 11434 Alder Creek Rd, Corona, CA 91720  
 Tel - Fax (714) 692-1443, E-Mail: mahdyiar@coda.usc.edu





V2X1800, Window: .0 to 46.6 s V2X1600, Window: .0 to 34.7 s

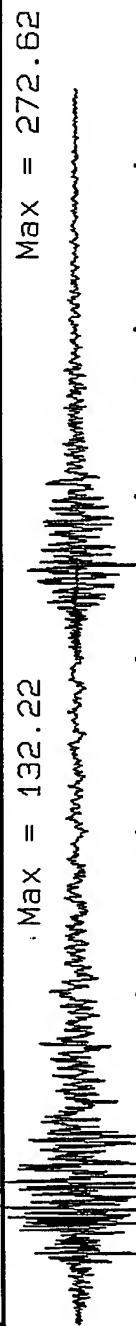


linear Scale: 0-8  
Radial Comp.



Max = 158.16

linear Scale: 0-8  
Vertical Comp.



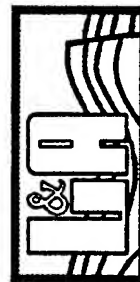
Max = 272.62

linear Scale: 0-8  
Transverse Comp.

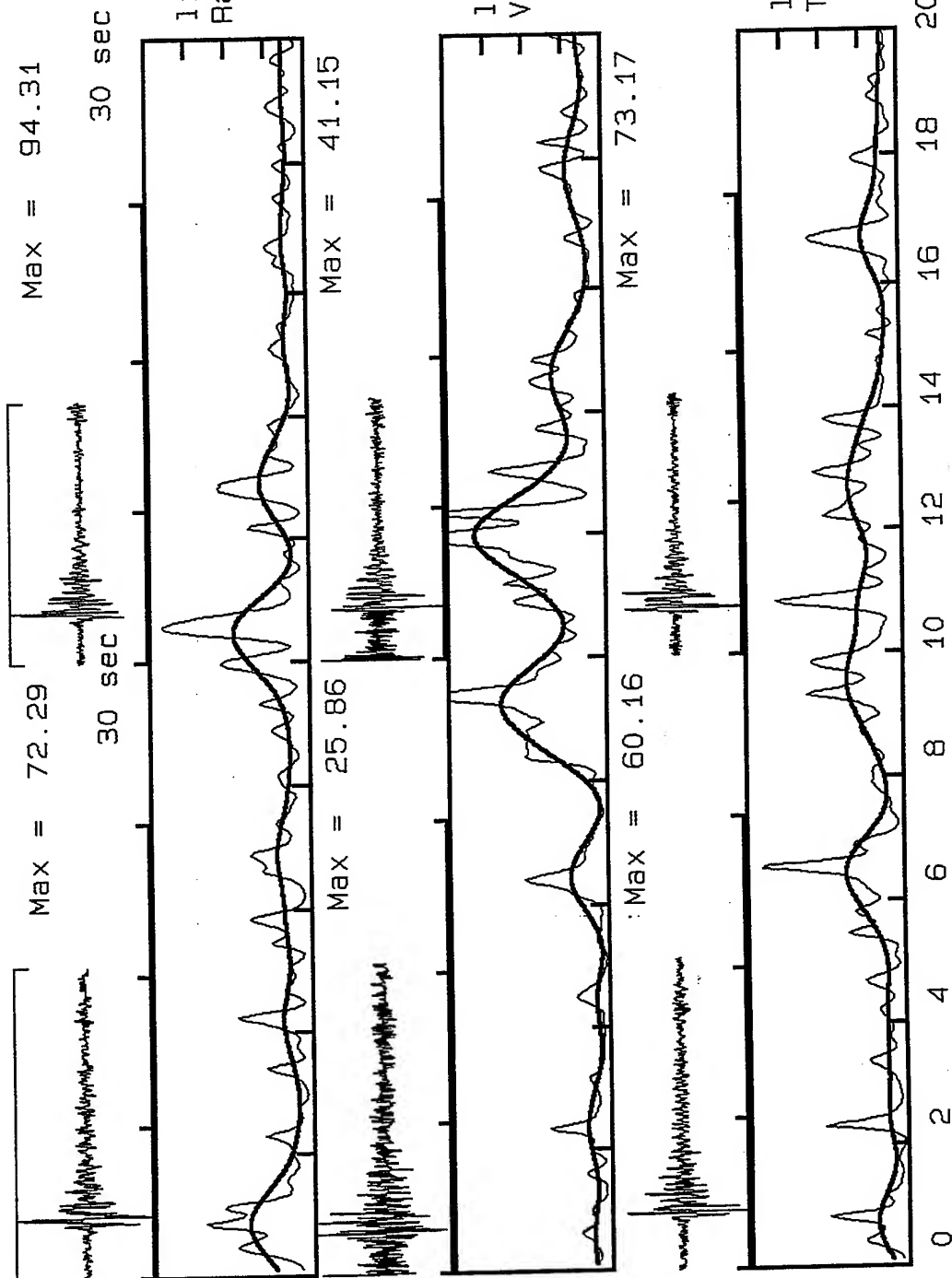
0 2 4 6 8 10 12 14 16 18 20 Hz



**VortexRock Consultants, Inc.**  
11434 Alder Creek Rd, Corona, CA 91720  
Tel - Fax (714) 692-1443, E-Mail: mahdiyar@coda.usc.edu



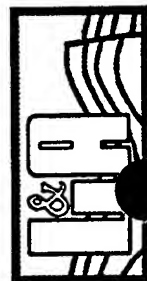
V2X1801, Window: .0 to 20.7 s V2X1601, Window: .0 to 17.3 s



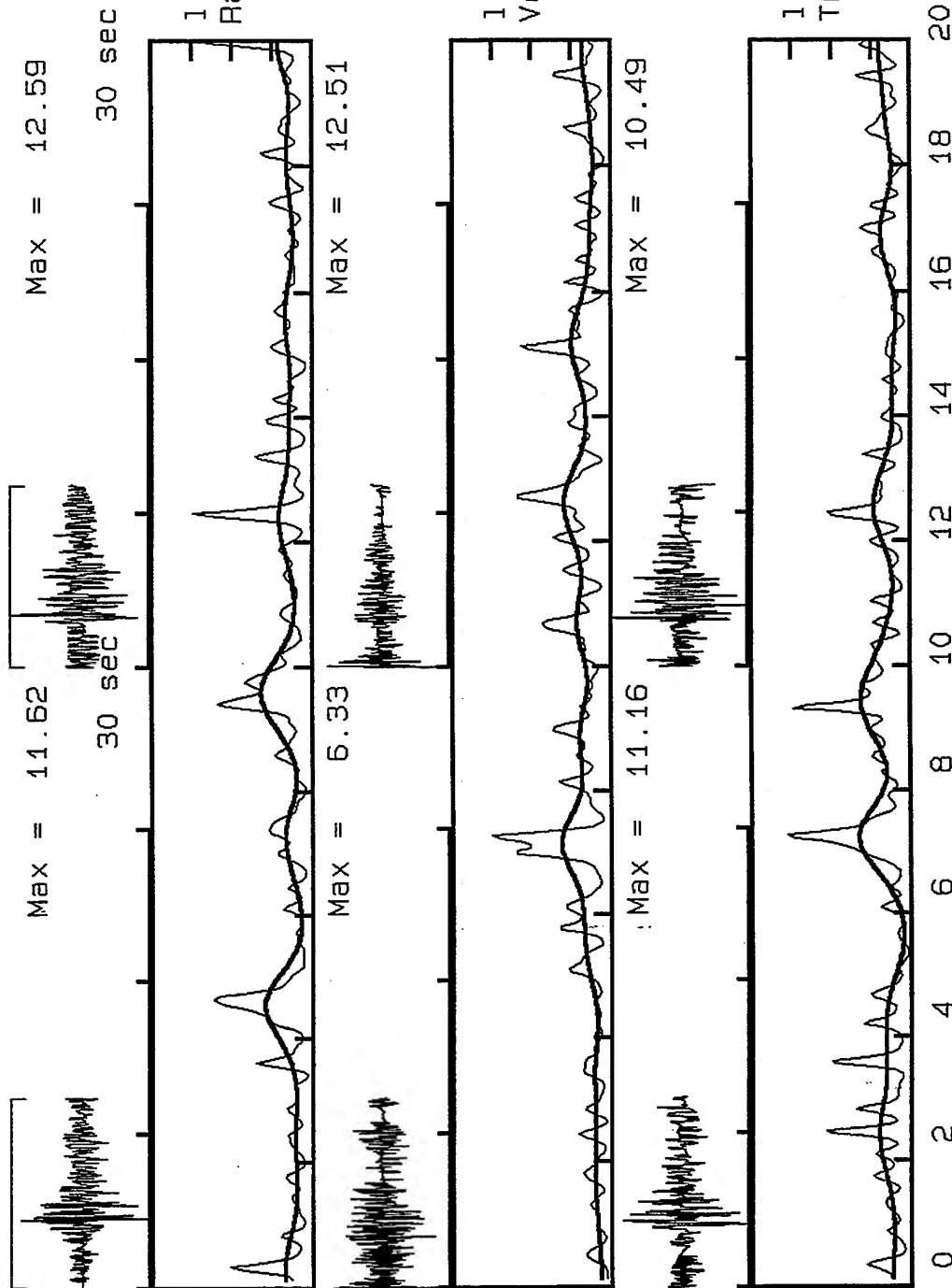
**VortexRock Consultants, Inc.**

11434 Alder Creek Rd, Corona, CA 91720

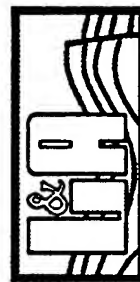
Tel - Fax (714) 692-1443, E-Mail: mahdyiar@coda.usc.edu



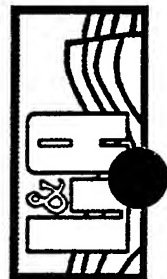
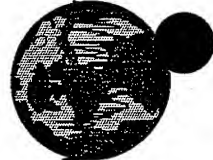
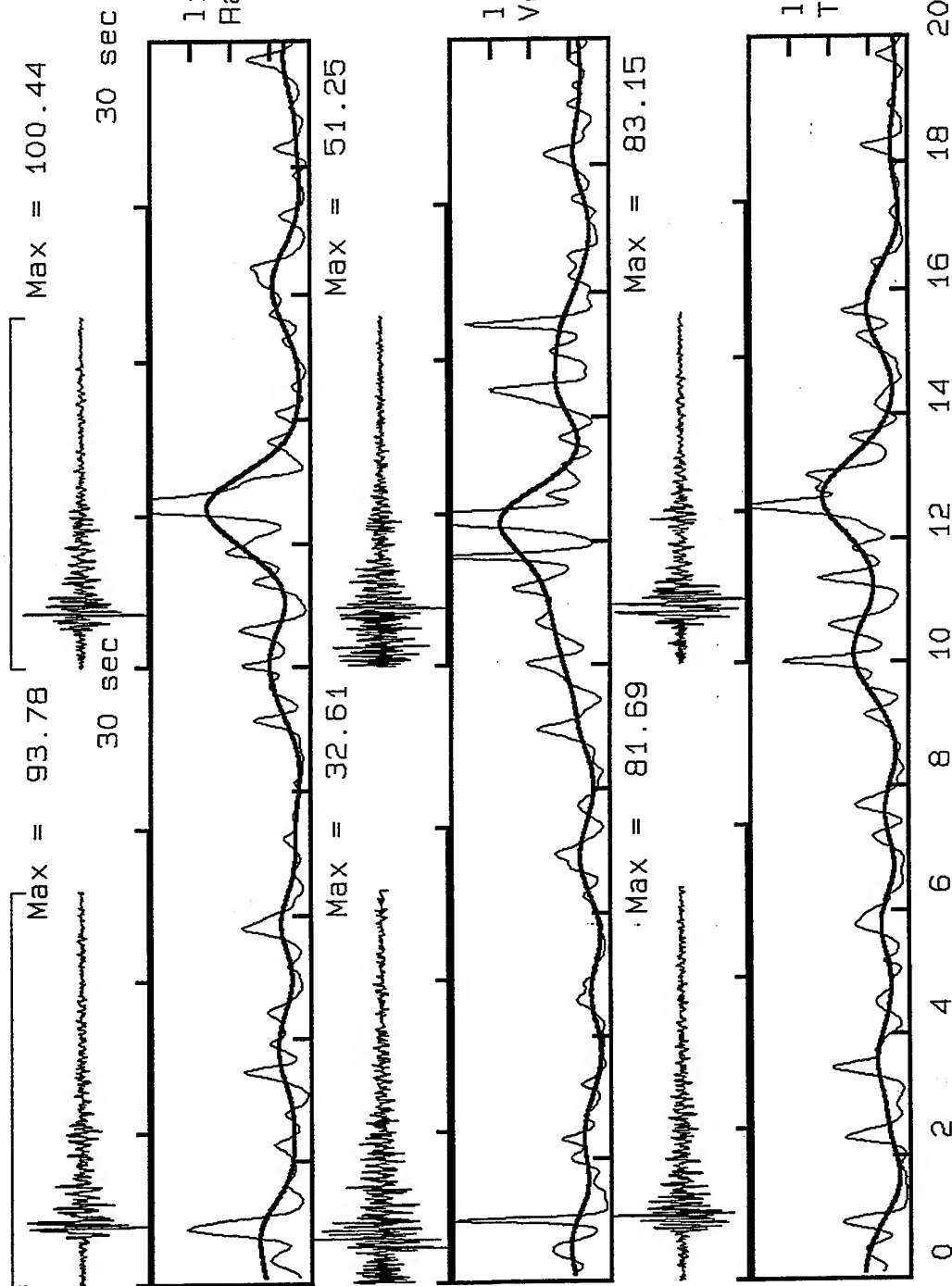
V2X1802, Window: .0 to 12.3 s V2X1602, Window: .0 to 11.8 s



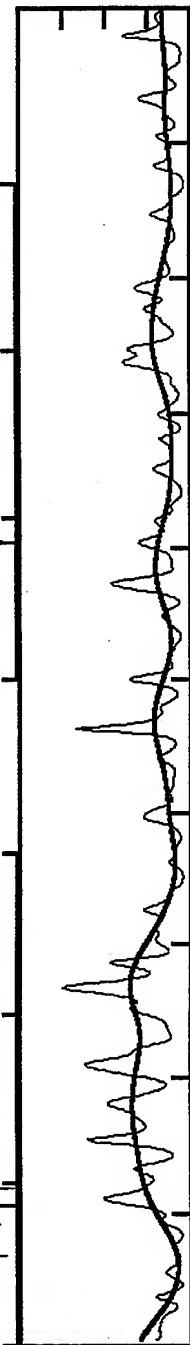
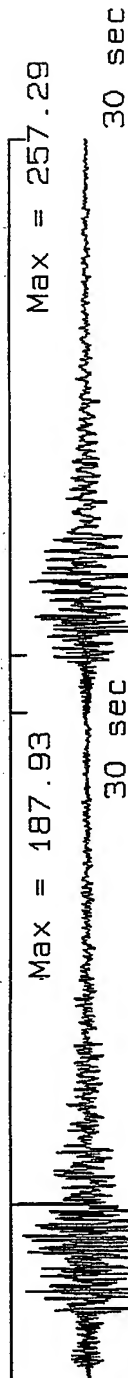
**VortexRock Consultants, Inc.**  
 11434 Alder Creek Rd, Corona, CA 91720  
 Tel - Fax (714) 692-1443, E-Mail: mahdian@codi.usc.edu



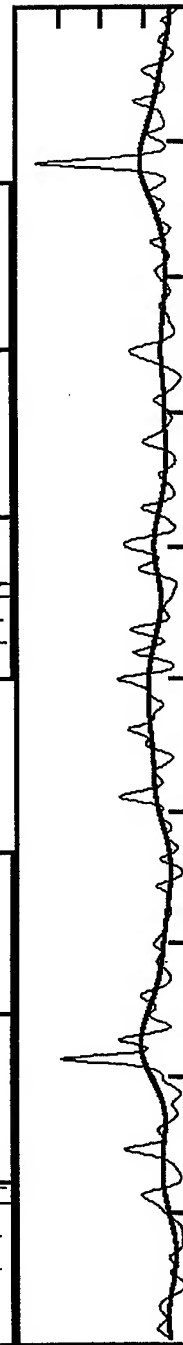
V2X1809, Window: .0 to 26.0 s V2X1609, Window: .0 to 22.9 s



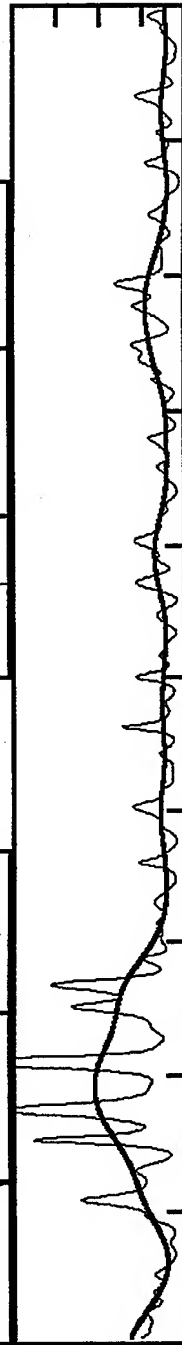
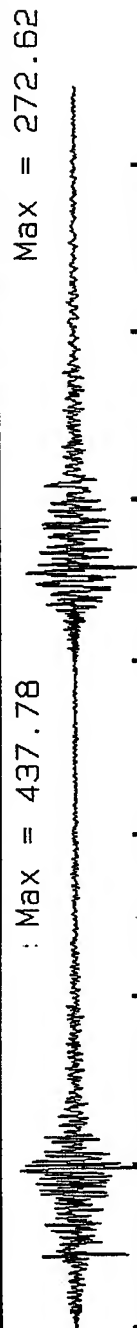
V2X4900, Window: .0 to 44.2 s V2X1600, Window: .0 to 34.7 s



linear Scale: 0-8  
Radial Comp.



linear Scale: 0-8  
Vertical Comp.

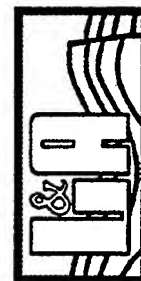


linear Scale: 0-8  
Transverse Comp.

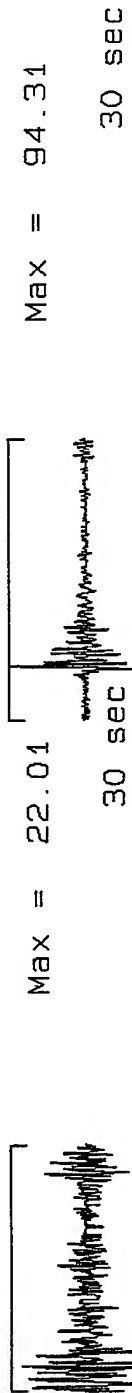
0 2 4 6 8 10 12 14 16 18 20 Hz



**VortexRock Consultants, Inc.**  
11434 Alder Creek Rd, Corona, CA 91720  
Tel - Fax (714) 692-1443, E-Mail: mahdyiar@coda.usc.edu

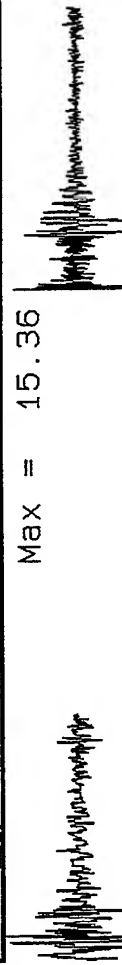


V2X4901, Window: .0 to 15.1 s V2X1601, Window: .0 to 17.3 s



linear Scale: 0-8  
Radial Comp.

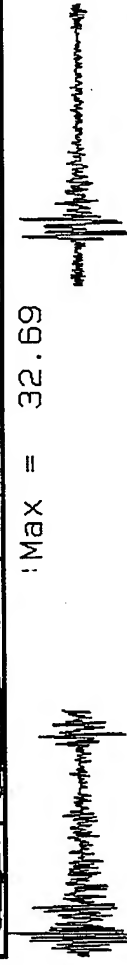
Max = 15.36



linear Scale: 0-8  
Vertical Comp.

Max = 32.69

Max = 73.17



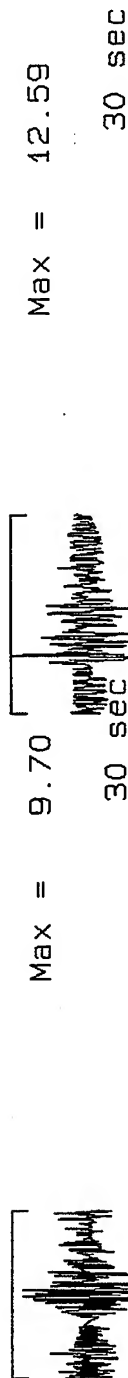
linear Scale: 0-8  
Transverse Comp.

0 2 4 6 8 10 12 14 16 18 20 Hz

**VortexRock Consultants, Inc.**  
11434 Alder Creek Rd, Corona, CA 91720  
Tel - Fax (714) 692-1443, E-Mail: mahayiar@coda.usc.edu



V2X4902, Window: .0 to 10.1 s V2X1602, Window: .0 to 11.8 s



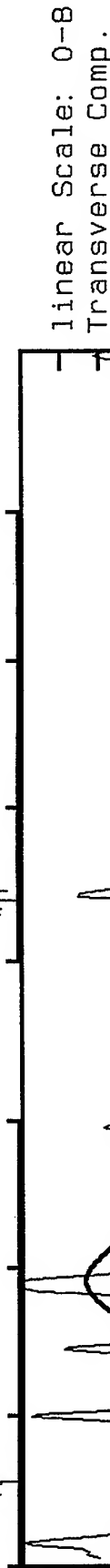
Max = 7.38

Max = 12.51



linear Scale: 0-8  
Vertical Comp.

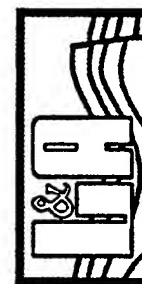
Max = 10.49



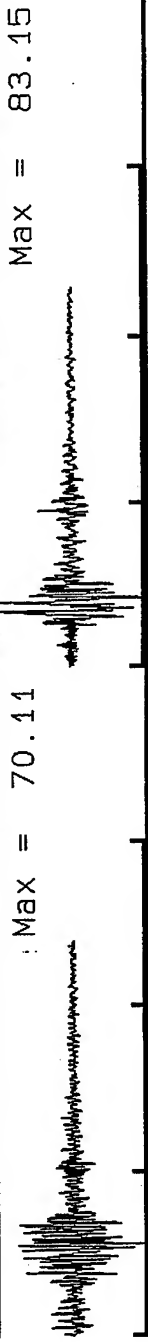
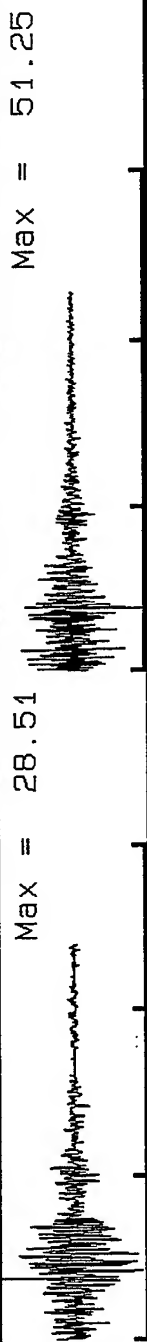
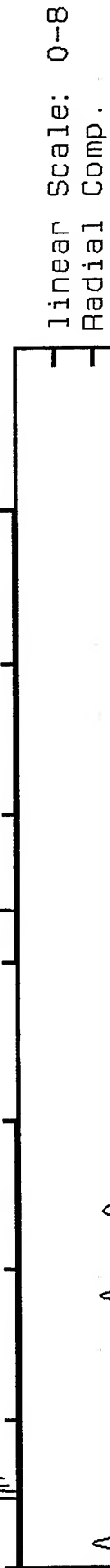
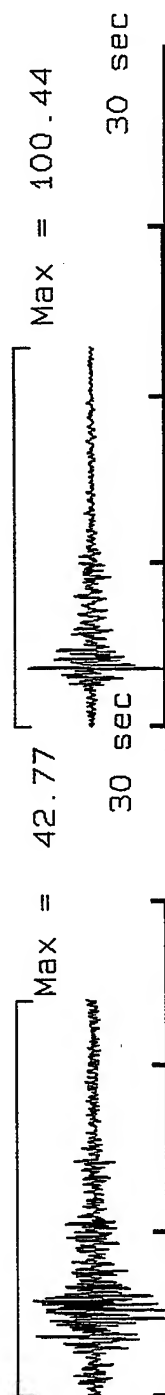
0 2 4 6 8 10 12 14 16 18 20 Hz



**VortexRock Consultants, Inc.**  
11434 Alder Creek Rd, Corona, CA 91720  
Tel - Fax (714) 692-1443, E-Mail: mahdiyari@coda.usc.edu



V2X4912, Window: .0 to 24.0 s V2X1609, Window: .0 to 22.9 s



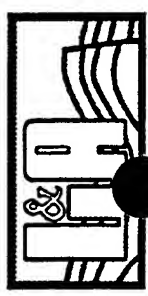
linear Scale: 0-8  
Radial Comp.

linear Scale: 0-8  
Vertical Comp.

linear Scale: 0-8  
Transverse Comp.

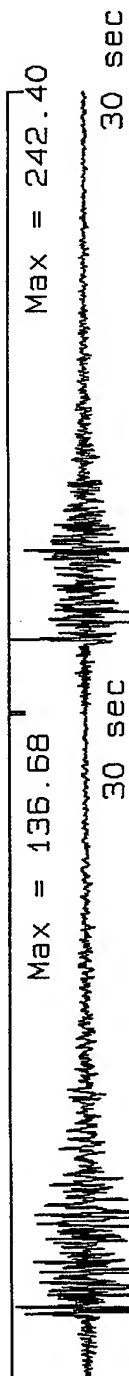
0 2 4 6 8 10 12 14 16 18 20 Hz

**VortexRock Consultants, Inc.**  
11434 Alder Creek Rd, Corona, CA 91720  
Tel - Fax (714) 692-1443, E-Mail: mahdyiar@coda.usc.edu





V2X6000, Window: .0 to 40.7 s V2X6100, Window: .0 to 37.7 s



linear Scale: 0-8  
Radial Comp.

Max = 149.23

linear Scale: 0-8  
Vertical Comp.

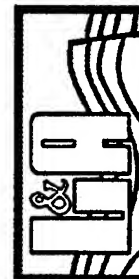
Max = 161.71

linear Scale: 0-8  
Transverse Comp.

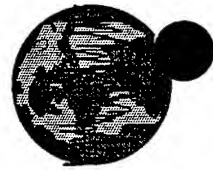
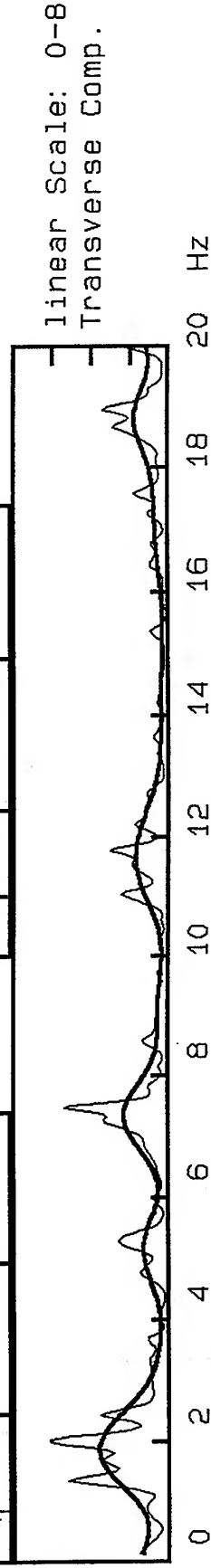
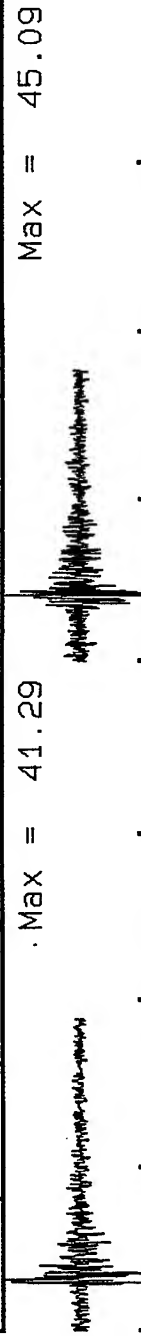
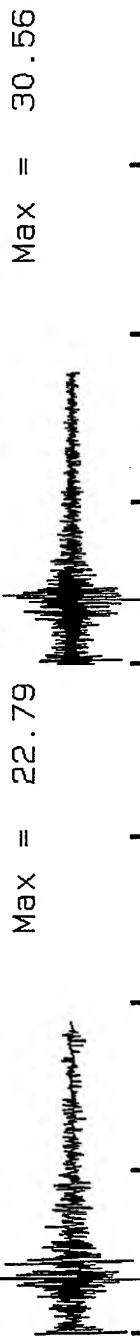
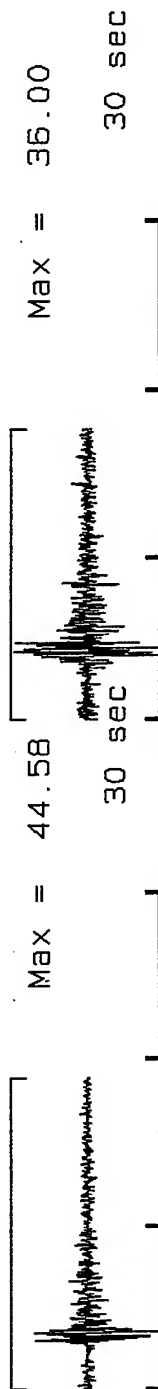
20 Hz



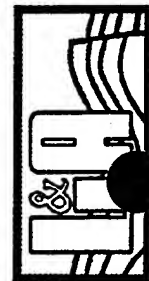
**VortexRock Consultants, Inc.**  
11434 Alder Creek Rd, Corona, CA 91720  
Tel - Fax (714) 692-1443, E-Mail: mahdyar@coda.usc.edu



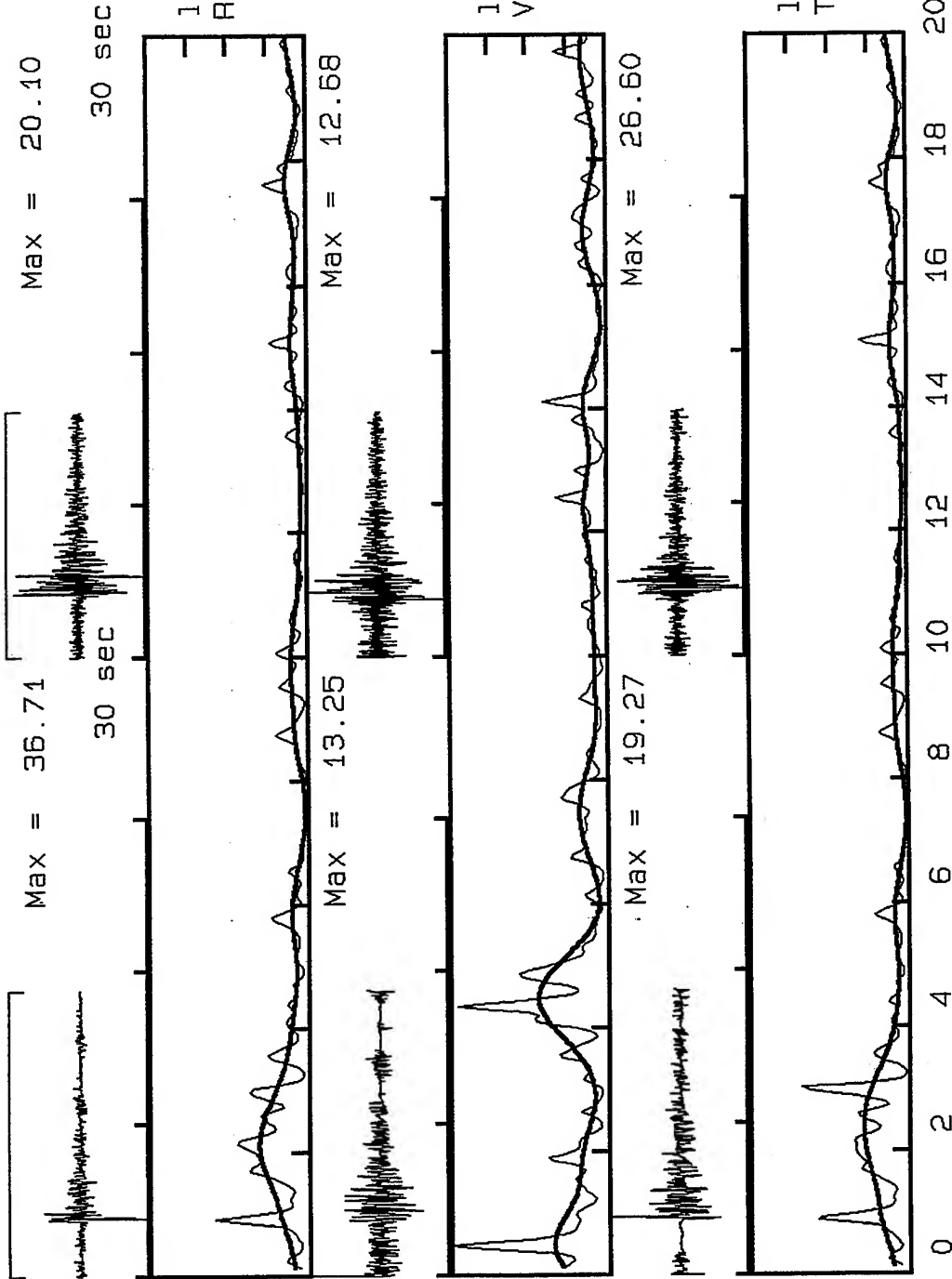
V2X6001, Window: .0 to 18.9 s V2X6101, Window: .0 to 17.7 s



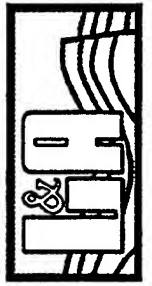
**VortexRock Consultants, Inc.**  
11434 Alder Creek Rd, Corona, CA 91720  
Tel - Fax (714) 692-1443, E-Mail: mahdyiar@coda.usc.edu



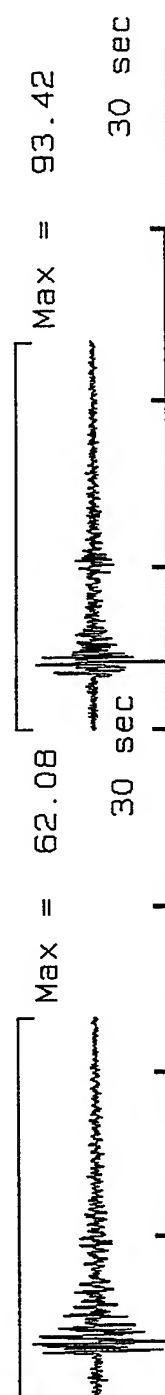
V2X6009, Window: .0 to 18.7 s V2X6107, Window: .0 to 16.2 s



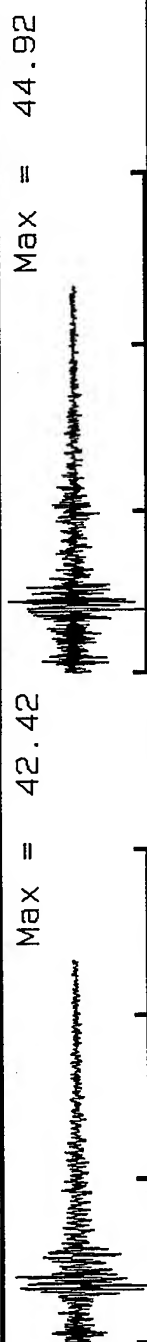
**VortexRock Consultants, Inc.**  
11434 Alder Creek Rd, Corona, CA 91720  
Tel - Fax (714) 692-1443, E-Mail: mahdyiar@coda.usc.edu



V2X6012, Window: .0 to 23.4 s V2X6110, Window: .0 to 23.4 s



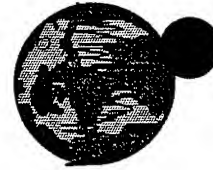
linear Scale: 0-8  
Radial Comp.



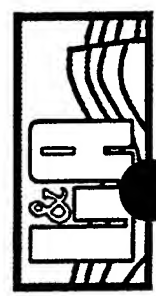
linear Scale: 0-8  
Vertical Comp.



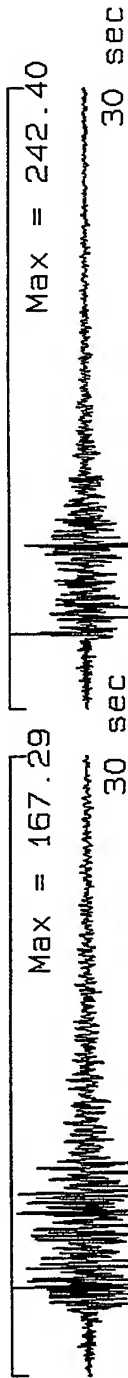
linear Scale: 0-8  
Transverse Comp.



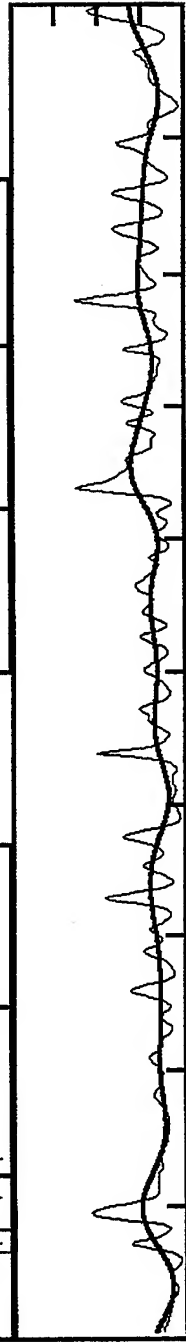
**VortexRock Consultants, Inc.**  
11434 Alder Creek Rd, Corona, CA 91720  
Tel - Fax (714) 692-1443, E-Mail: mahdyiar@coda.usc.edu



V2X6300, Window: .0 to 37.8 s V2X6100, Window: .0 to 37.7 s



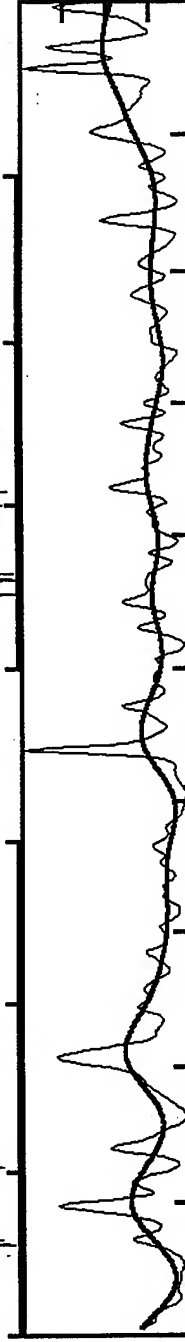
linear Scale: 0-8  
Radial Comp.



linear Scale: 0-8  
Vertical Comp.



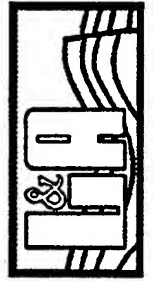
linear Scale: 0-8  
Transverse Comp.



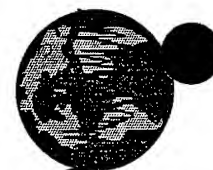
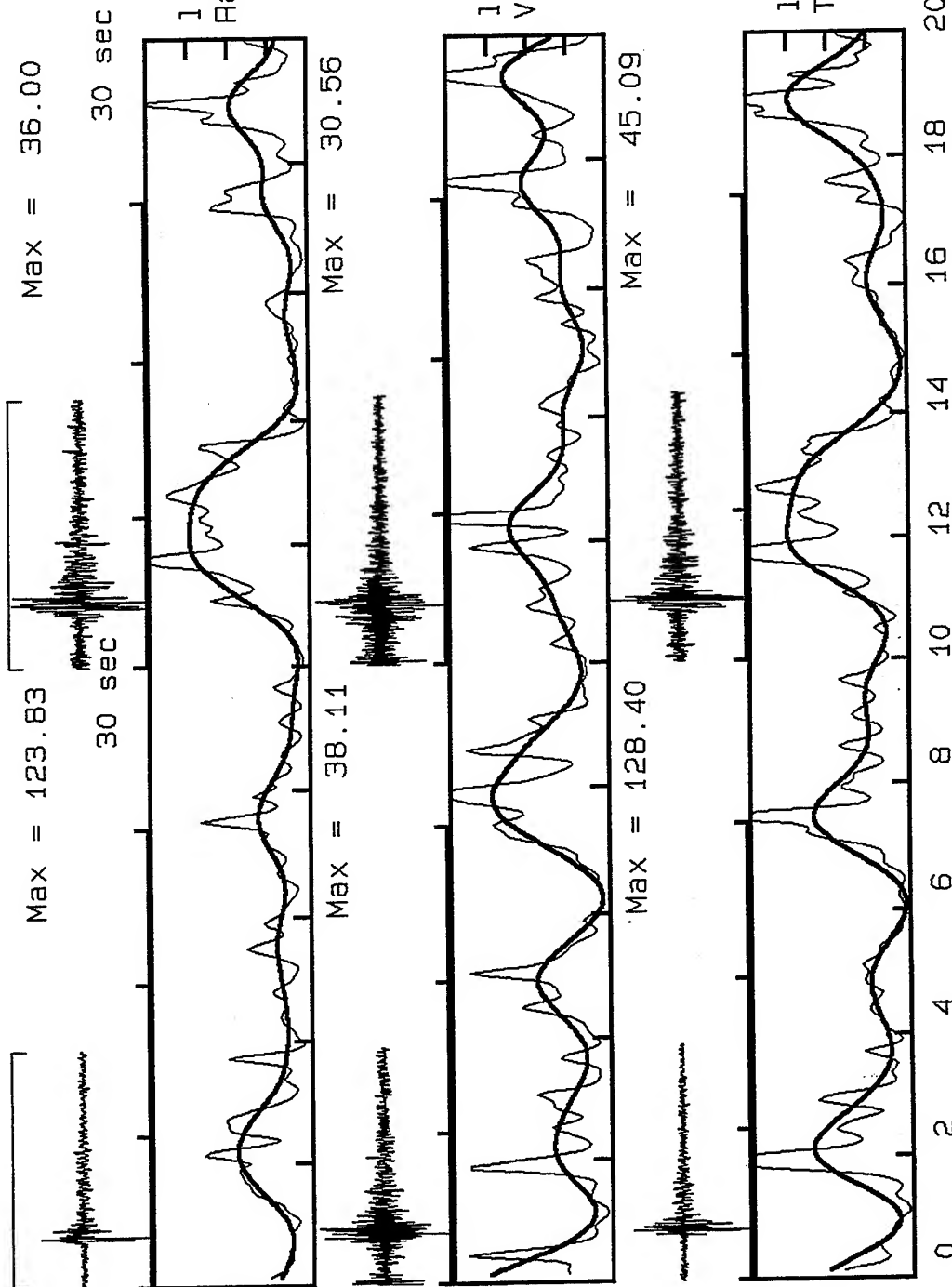
0 2 4 6 8 10 12 14 16 18 20 Hz



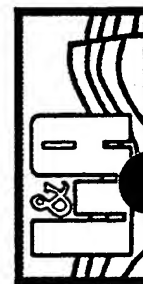
**VortexRock Consultants, Inc.**  
11434 Alder Creek Rd, Corona, CA 91720  
Tel - Fax (714) 692-1443, E-Mail: mahdyiar@coda.usc.edu



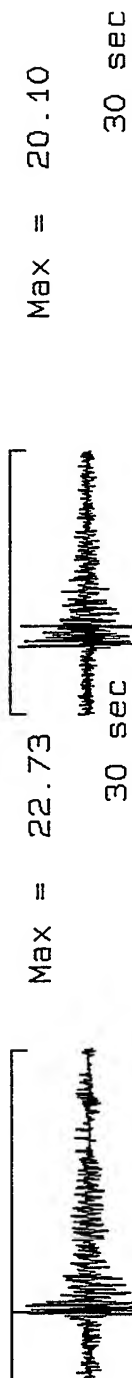
V2X6301, Window: .0 to 15.7 s V2X6101, Window: .0 to 17.7 s



**VortexRock Consultants, Inc.**  
 11434 Alder Creek Rd, Corona, CA 91720  
 Tel - Fax (714) 692-1443, E-Mail: mahdylar@coda.usc.edu

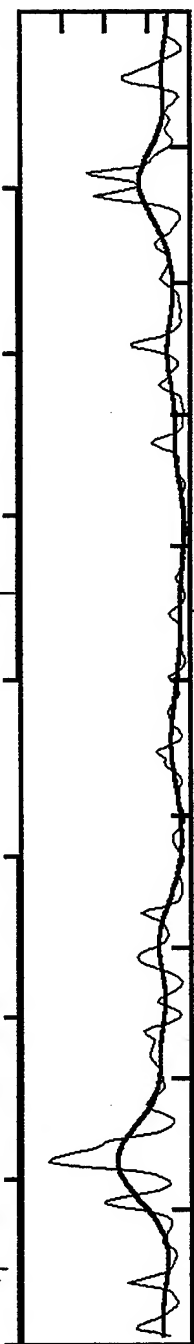


V2X6312, Window: .0 to 20.1 s V2X6107, Window: .0 to 16.2 s



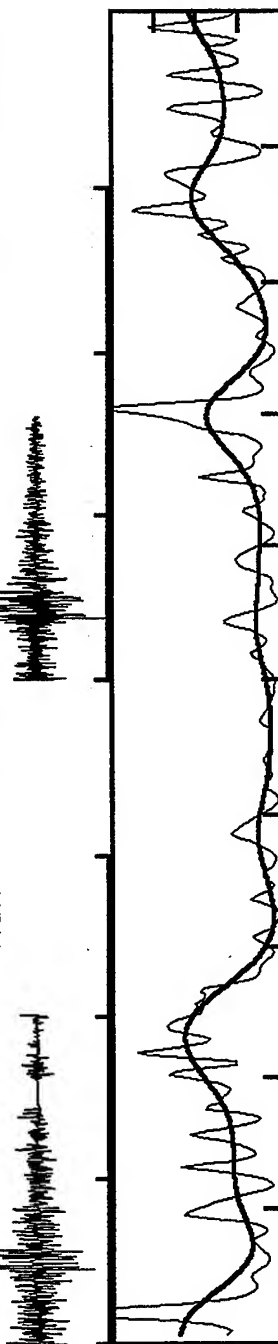
Max = 20.10

30 sec



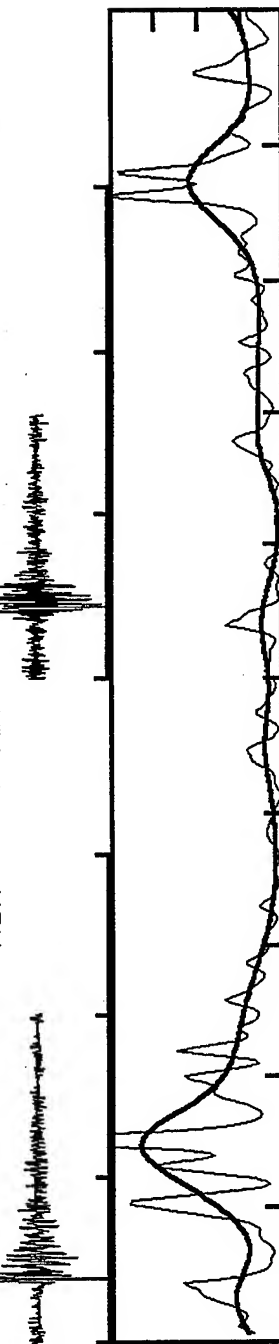
linear Scale: 0-8  
Radial Comp.

Max = 12.68



linear Scale: 0-8  
Vertical Comp.

Max = 26.60

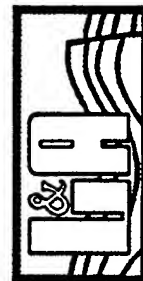


linear Scale: 0-8  
Transverse Comp.

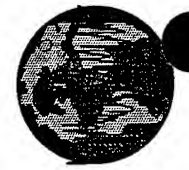
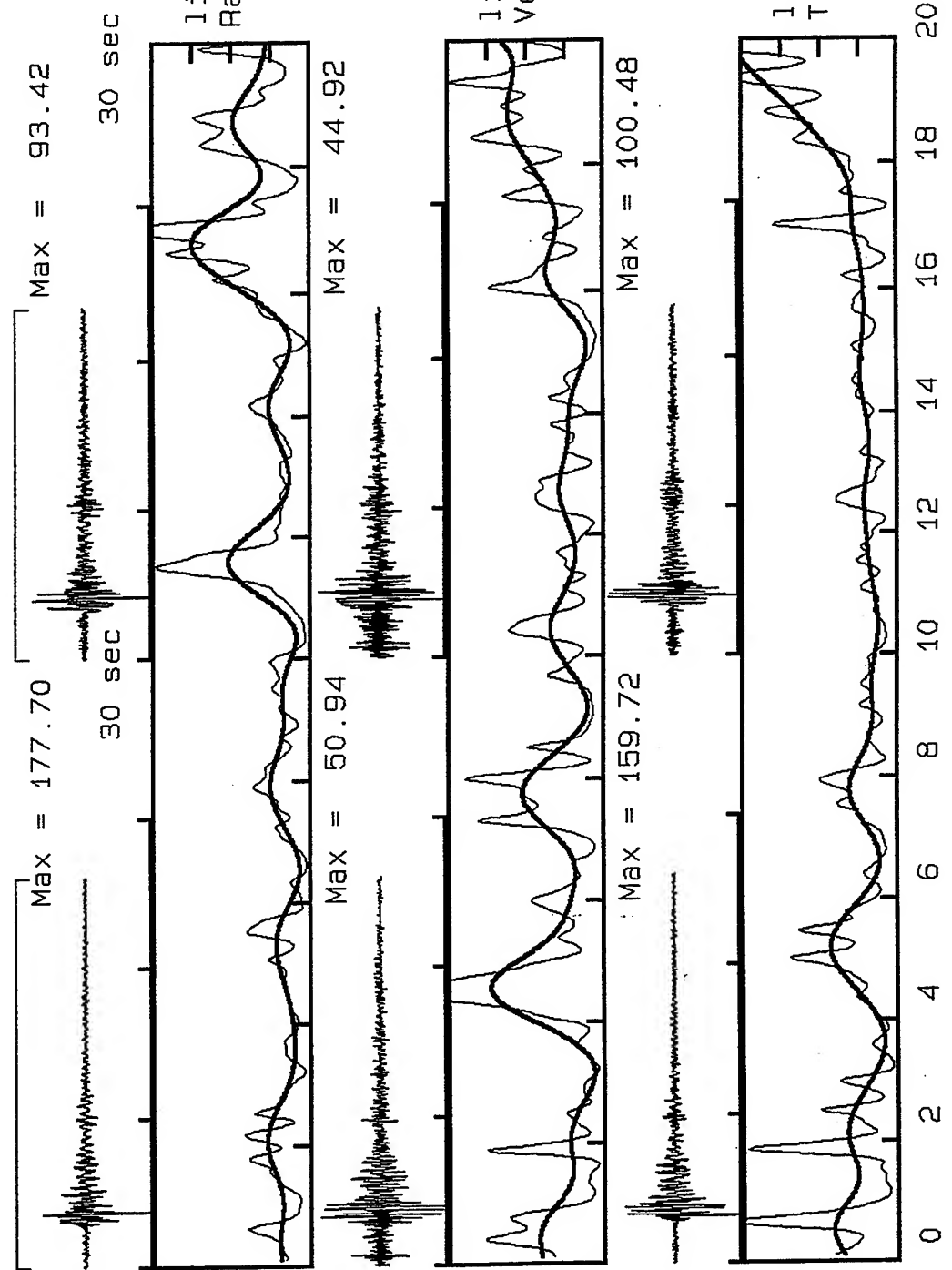
20 Hz



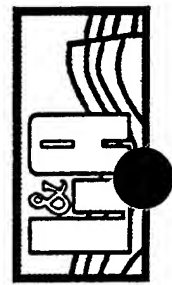
**VortexRock Consultants, Inc.**  
11434 Alder Creek Rd, Corona, CA 91720  
Tel - Fax (714) 692-1443, E-Mail: mahdylar@coda.usc.edu



V2X6316, Window: .0 to 26.0 s V2X6110, Window: .0 to 23.4 s

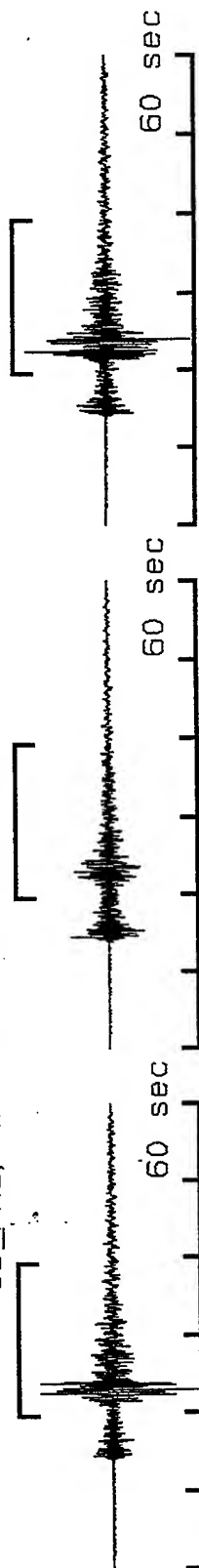


**VortexRock Consultants, Inc.**  
 11434 Alder Creek Rd, Corona, CA 91720  
 Tel - Fax (714) 692-1443, E-Mail: mahdyar@coda.usc.edu

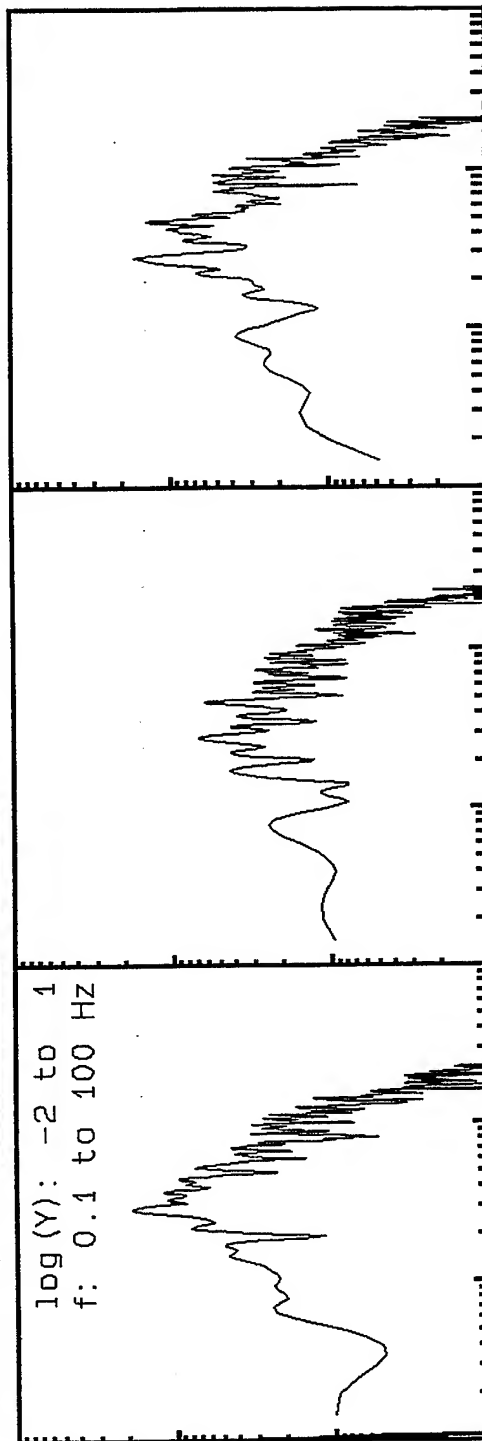




19\_PAS, Window: 19.6 to 39.2 s

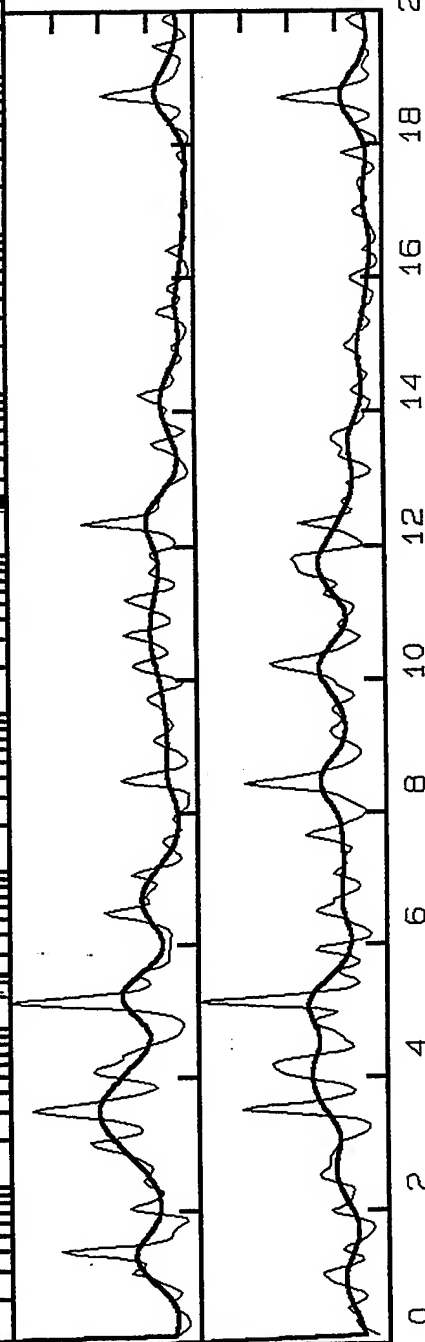


log (Y): -2 to 1  
f: 0.1 to 100 Hz

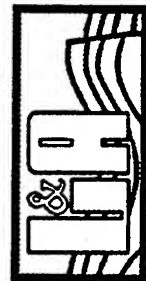


Radial/Vertical  
Linear Scale 0-8

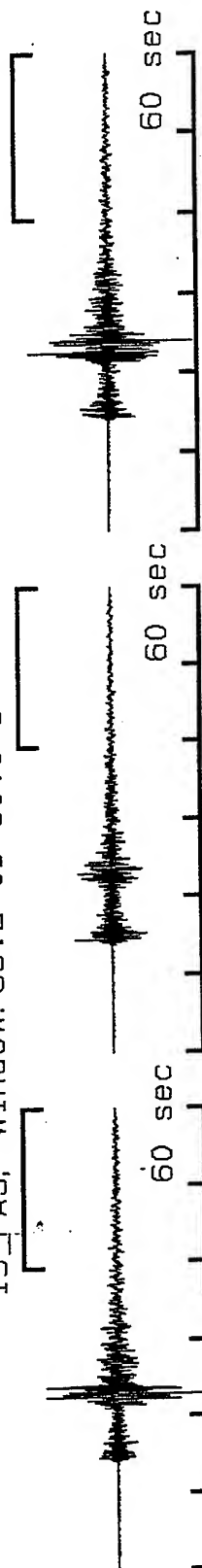
Transvers/Vertical:  
Linear Scale 0-8



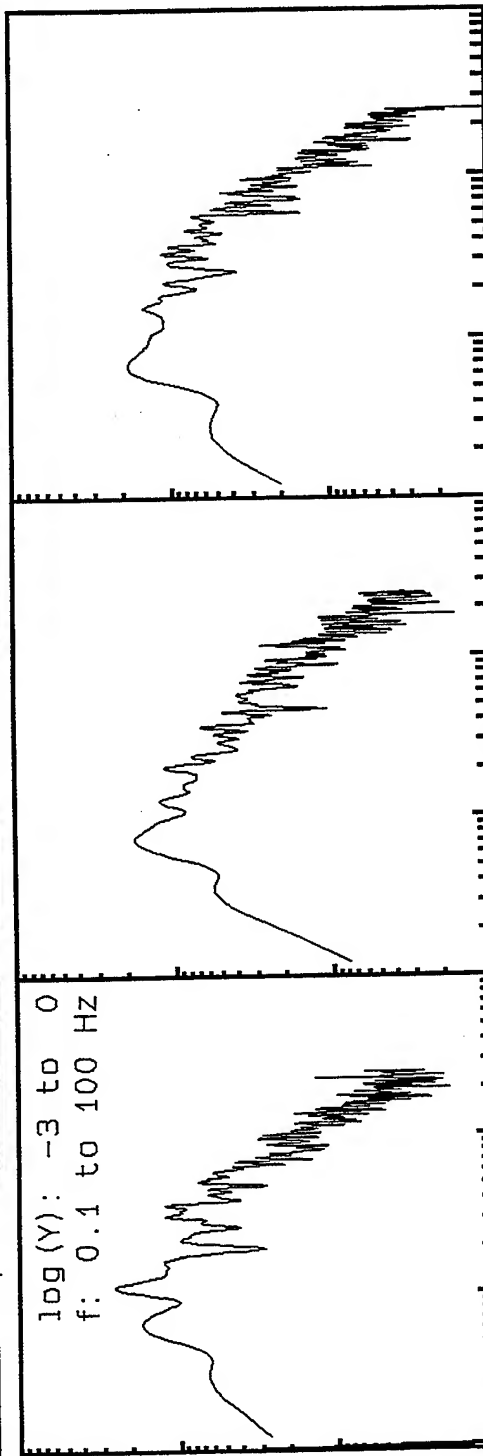
**VortexRock Consultants, Inc.**  
11434 Alder Creek Rd, Corona, CA 91720  
Tel - Fax (714) 692-1443, E-Mail: mahdyiar@coda.usc.edu



19\_PAS, Window: 39.2 to 60.0 s

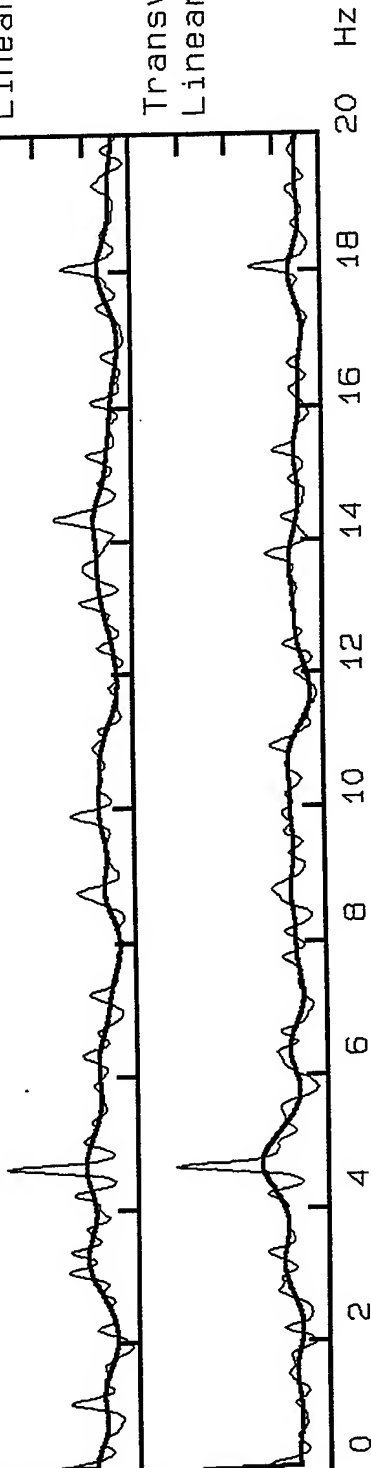


log(Y): -3 to 0  
f: 0.1 to 100 Hz



Radial/Vertical  
Linear Scale 0-8

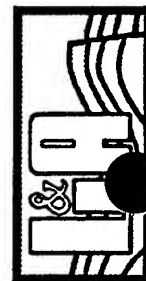
Transvers/Vertical:  
Linear Scale 0-8



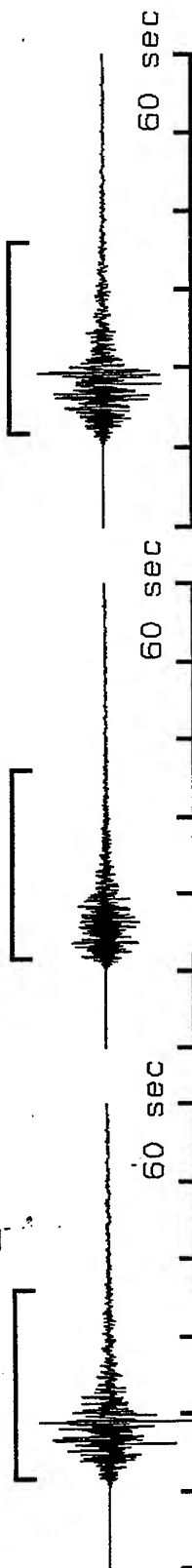
**VortexRock Consultants, Inc.**

11434 Alder Creek Rd, Corona, CA 91720

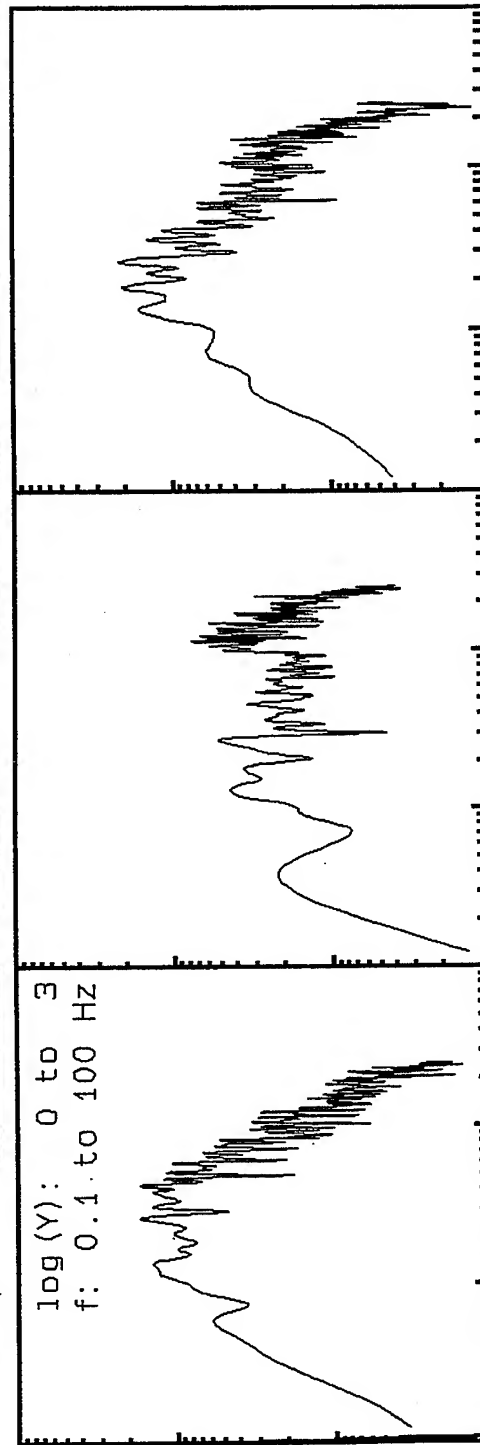
Tel - Fax (714) 692-1443, E-Mail: mahdyiar@coda.usc.edu



21\_la00, Window: 11.6 to 36.0 s

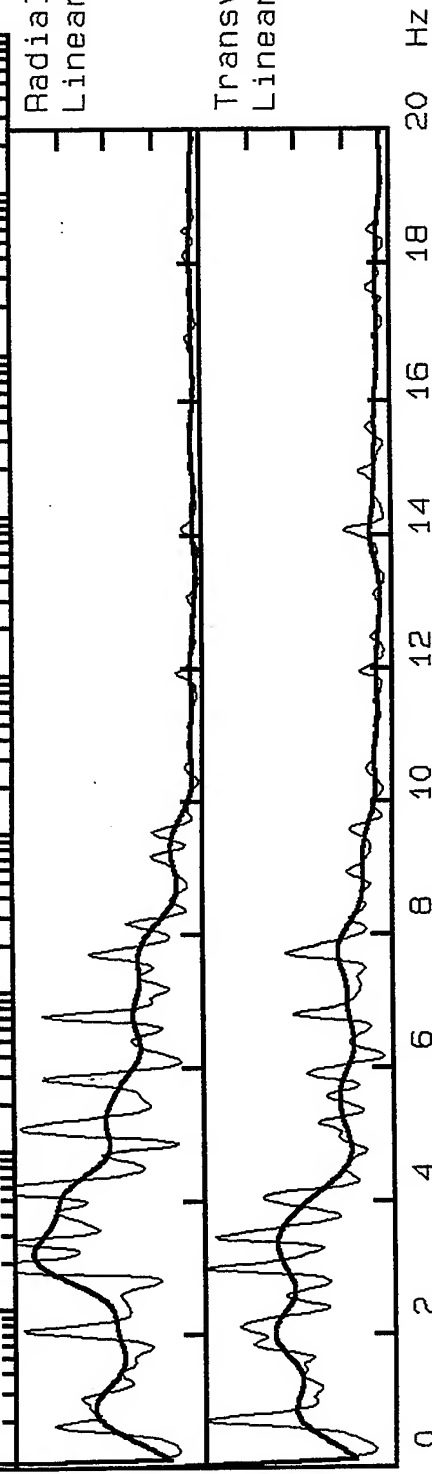


log(Y): 0 to 3  
f: 0.1 to 100 Hz



Radial/Vertical  
Linear Scale 0-8

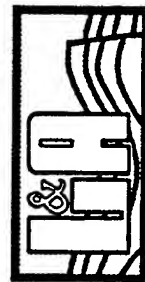
Transvers/Vertical:  
Linear Scale 0-8



**VortexRock Consultants, Inc.**

11434 Alder Creek Rd, Corona, CA 91720

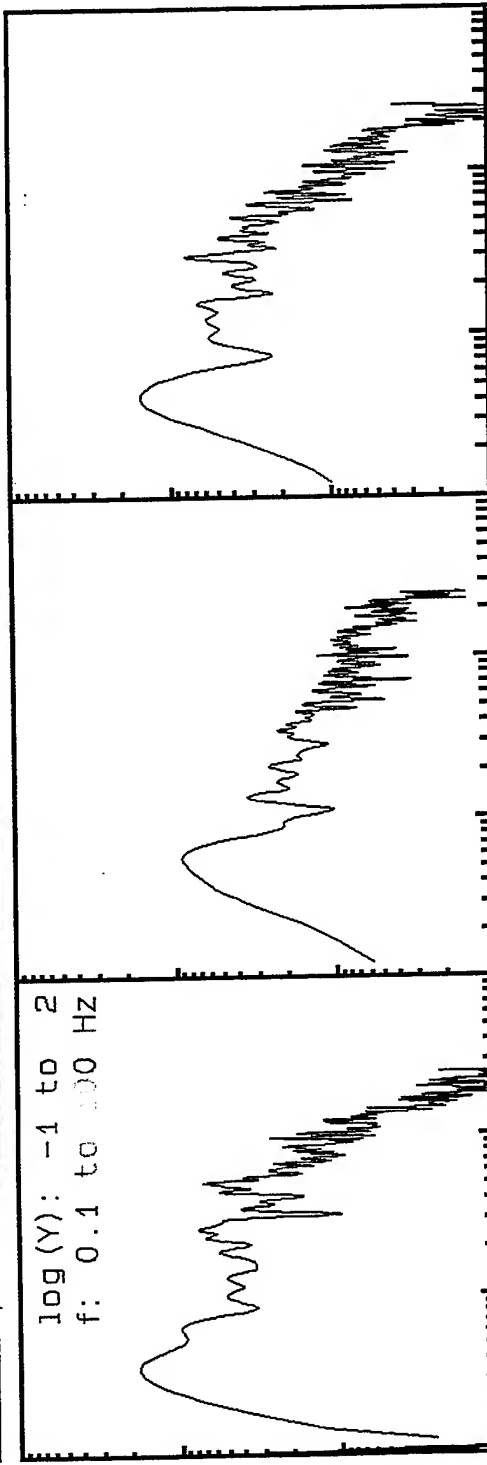
Tel - Fax (714) 692-1443, E-Mail: mahdyiar@coda.usc.edu



21\_1a00, Window: 36.0 to 60.0 s

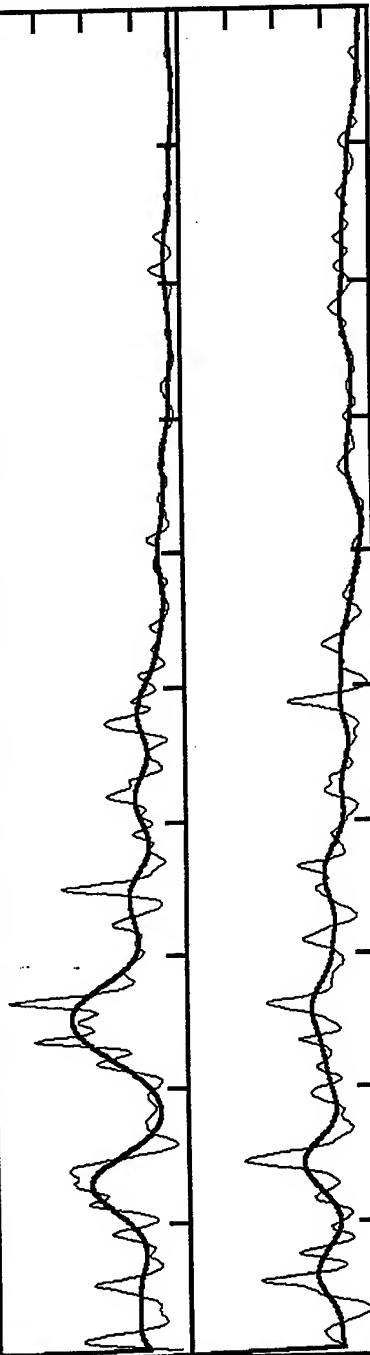


log (Y): -1 to 2  
f: 0.1 to 100 Hz



Radial/Vertical  
Linear Scale 0-8

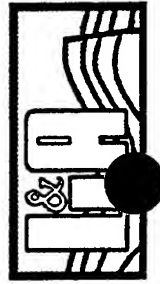
Transvers/Vertical:  
Linear Scale 0-8



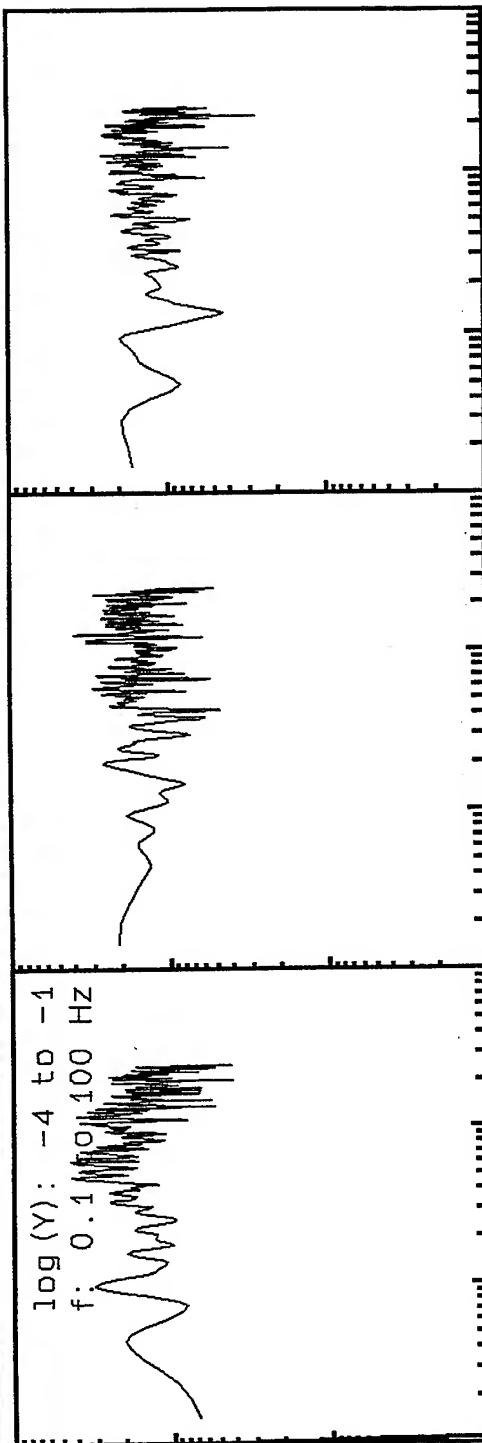
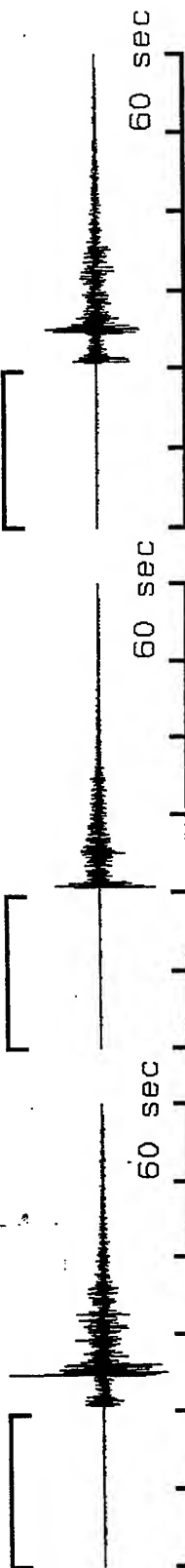
20 Hz



**VortexRock Consultants, Inc.**  
11434 Alder Creek Rd, Corona, CA 91720  
Tel - Fax (714) 692-1443, E-Mail: mahdyiar@coda.usc.edu

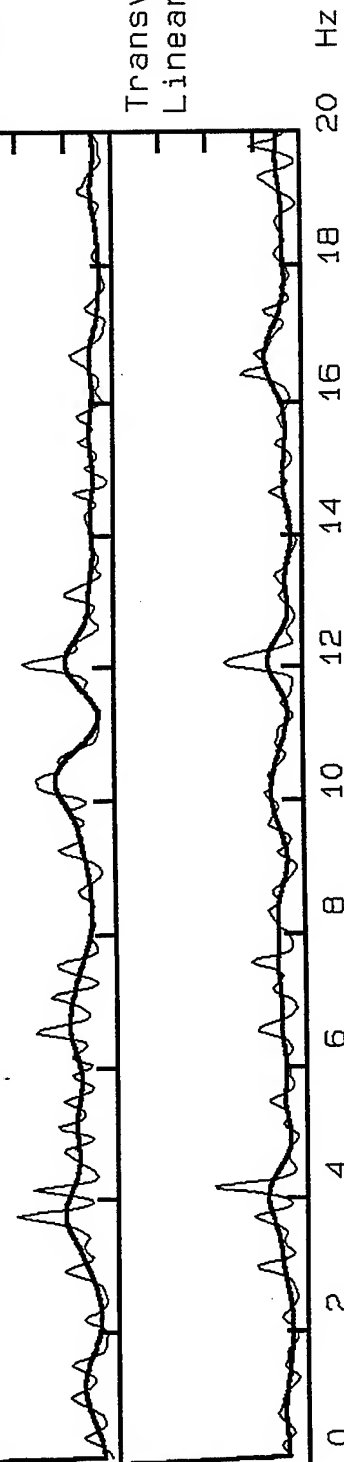


23\_la00, Window: .0 to 19.6 s

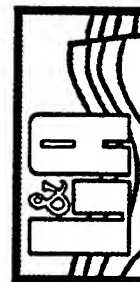


Radial/Vertical  
Linear Scale 0-8

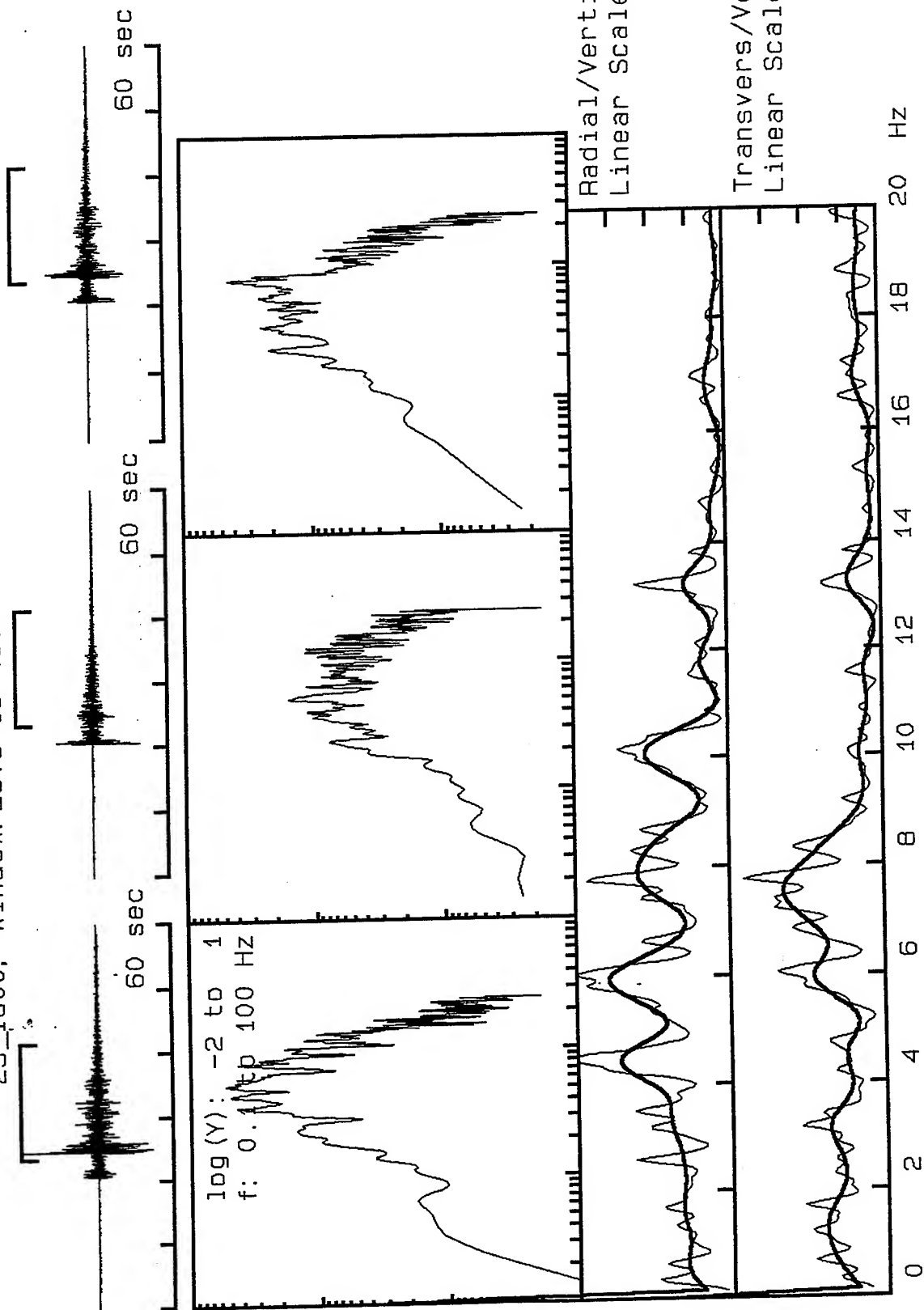
Transvers/Vertical:  
Linear Scale 0-8



**VortexRock Consultants, Inc.**  
11434 Alder Creek Rd, Corona, CA 91720  
Tel - Fax (714) 692-1443, E-Mail: mahdyar@coda.usc.edu



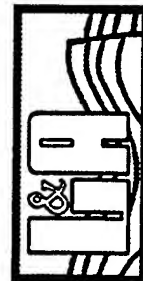
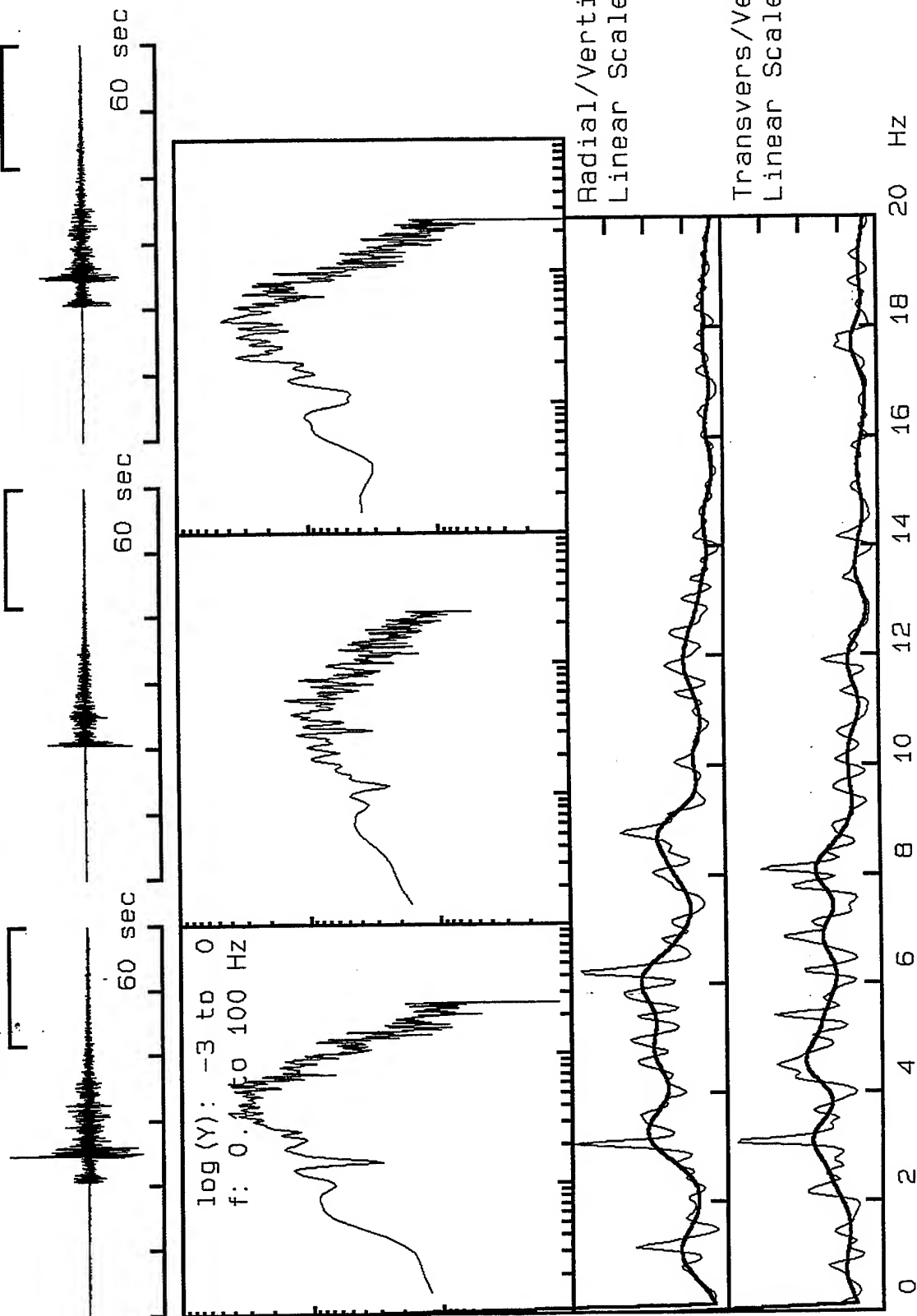
23\_1a00, Window: 23.6 to 41.6 s



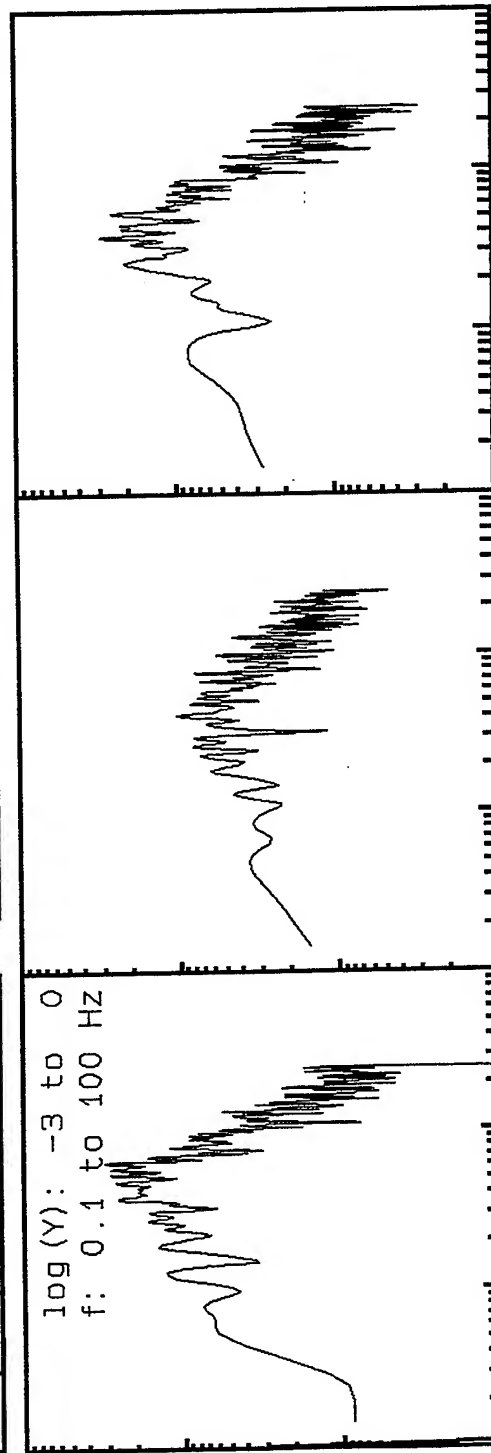
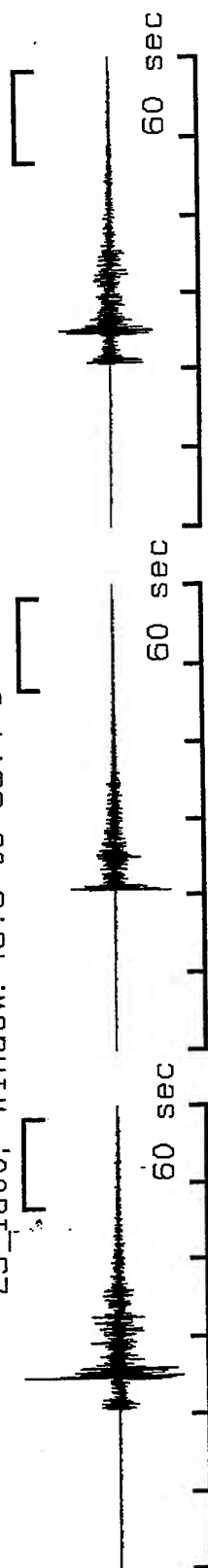
**VortexRock Consultants, Inc.**  
 11434 Alder Creek Rd, Corona, CA 91720  
 Tel - Fax (714) 692-1443, E-Mail: mahdytar@coda.usc.edu



23\_la00, Window: 41.6 to 60.0 s

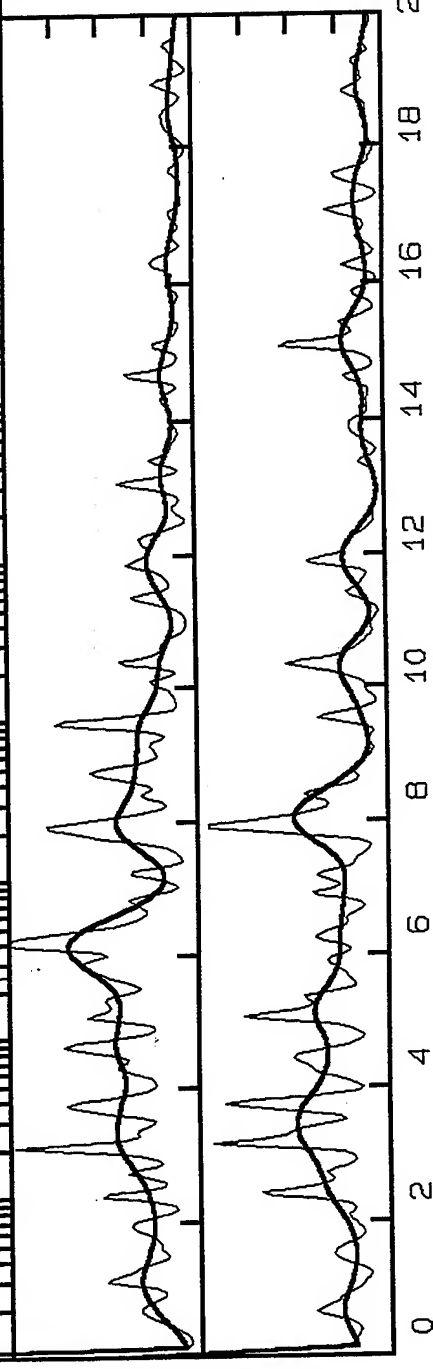


23\_la00, Window: 46.8 to 58.4 s

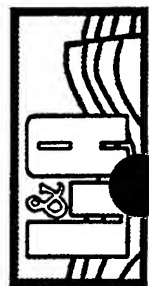


Radial/Vertical  
Linear Scale 0-8

Transvers/Vertical:  
Linear Scale 0-8

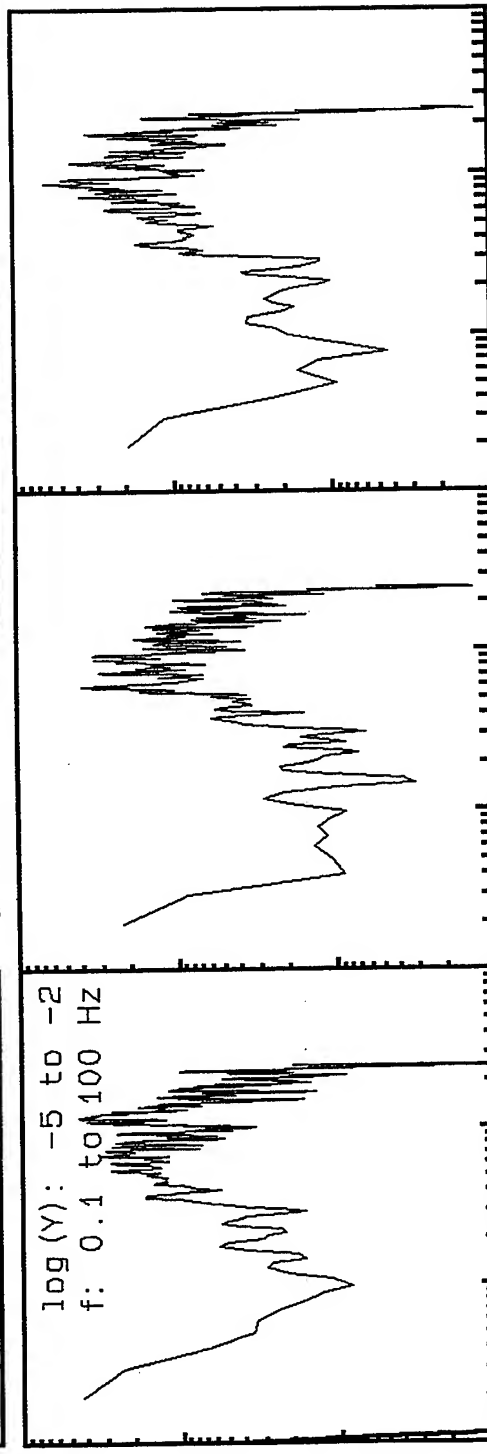
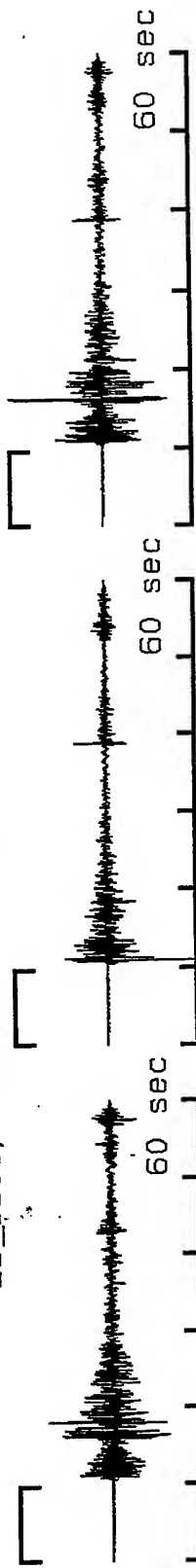


**VortexRock Consultants, Inc.**  
11434 Alder Creek Rd, Corona, CA 91720  
Tel - Fax (714) 692-1443, E-Mail: mahdyiar@coda.usc.edu



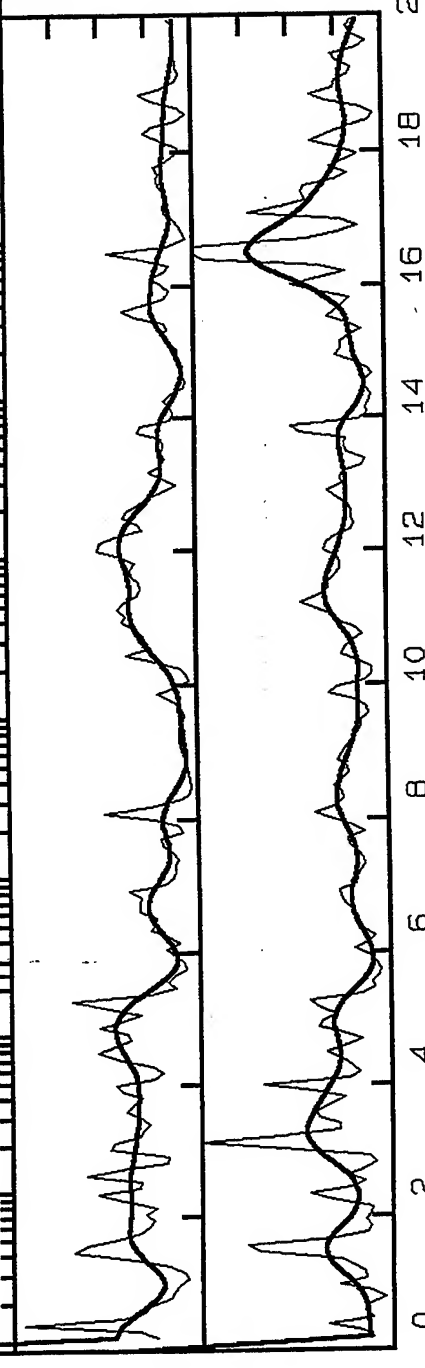


25\_1a00, Window: .0 to 9.6 s

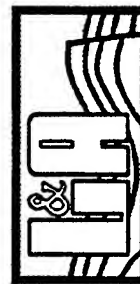


Radial/Vertical  
Linear Scale 0-8

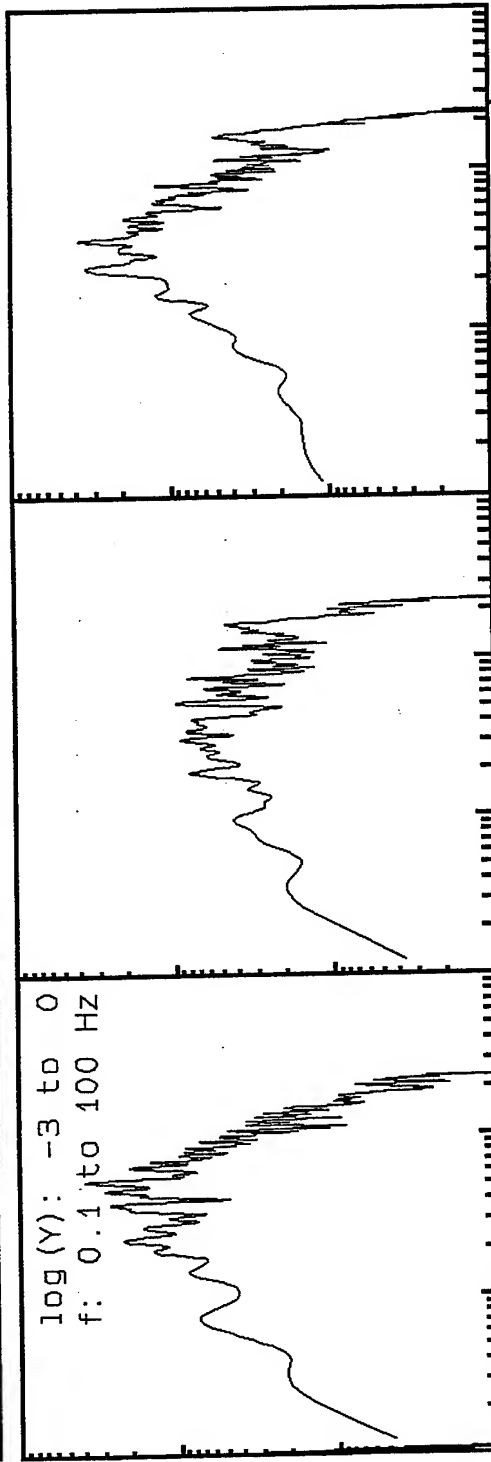
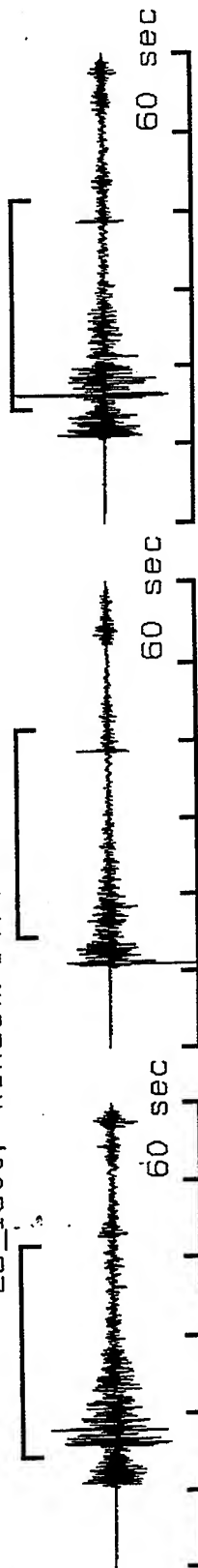
Transvers/Vertical:  
Linear Scale 0-8



**VortexRock Consultants, Inc.**  
11434 Alder Creek Rd, Corona, CA 91720  
Tel - Fax (714) 692-1443, E-Mail: mahdyar@coda.usc.edu

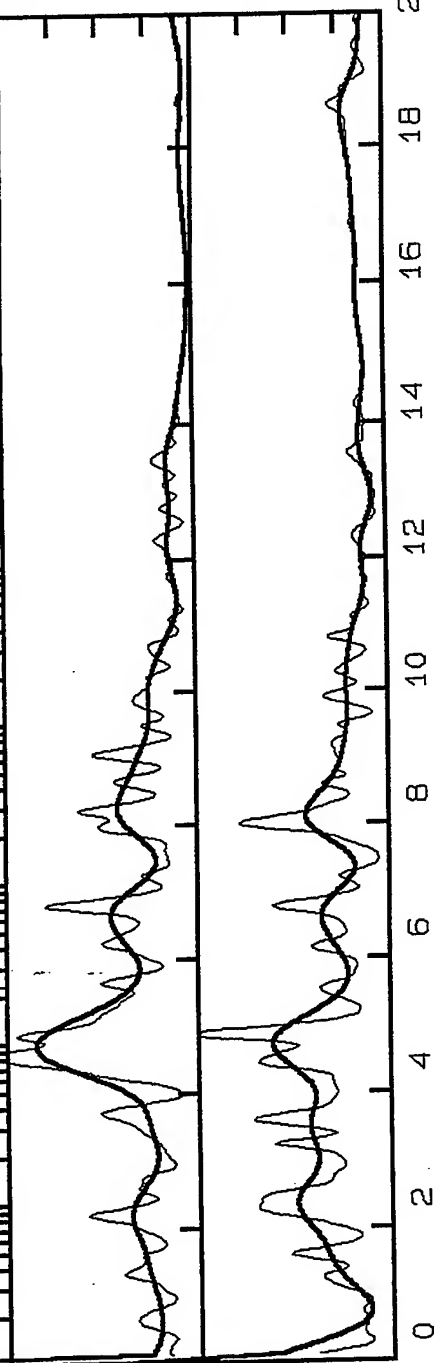


25\_la00, Window: 14.4 to 41.6 s



Radial/Vertical  
Linear Scale 0-8

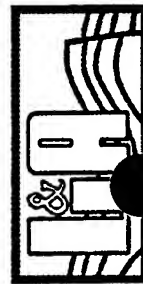
Transvers/Vertical:  
Linear Scale 0-8



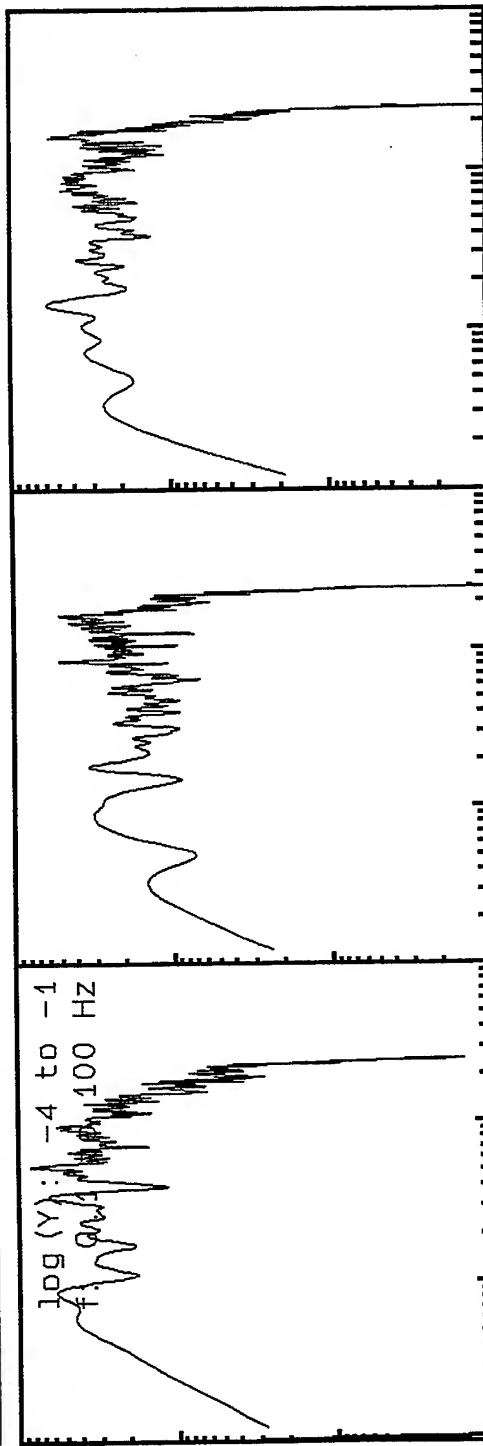
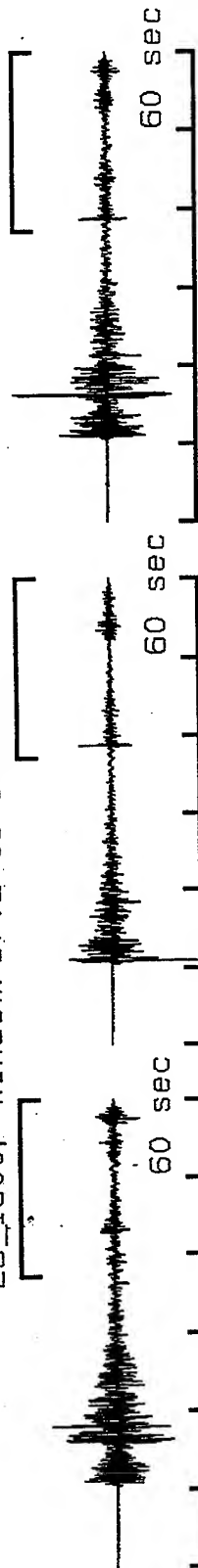
**VortexRock Consultants, Inc.**

11434 Alder Creek Rd, Corona, CA 91720

Tel - Fax (714) 692-1443, E-Mail: mahdyiar@coda.usc.edu

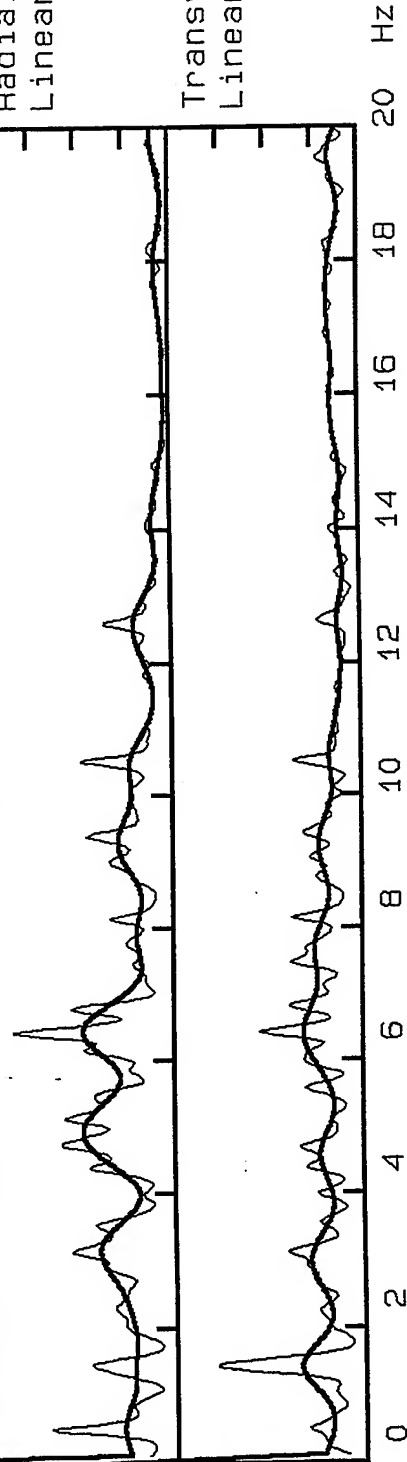


25\_la00, Window: 37.2 to 60.0 s



Radial/Vertical  
Linear Scale 0-8

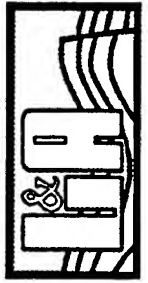
Transvers/Vertical:  
Linear Scale 0-8

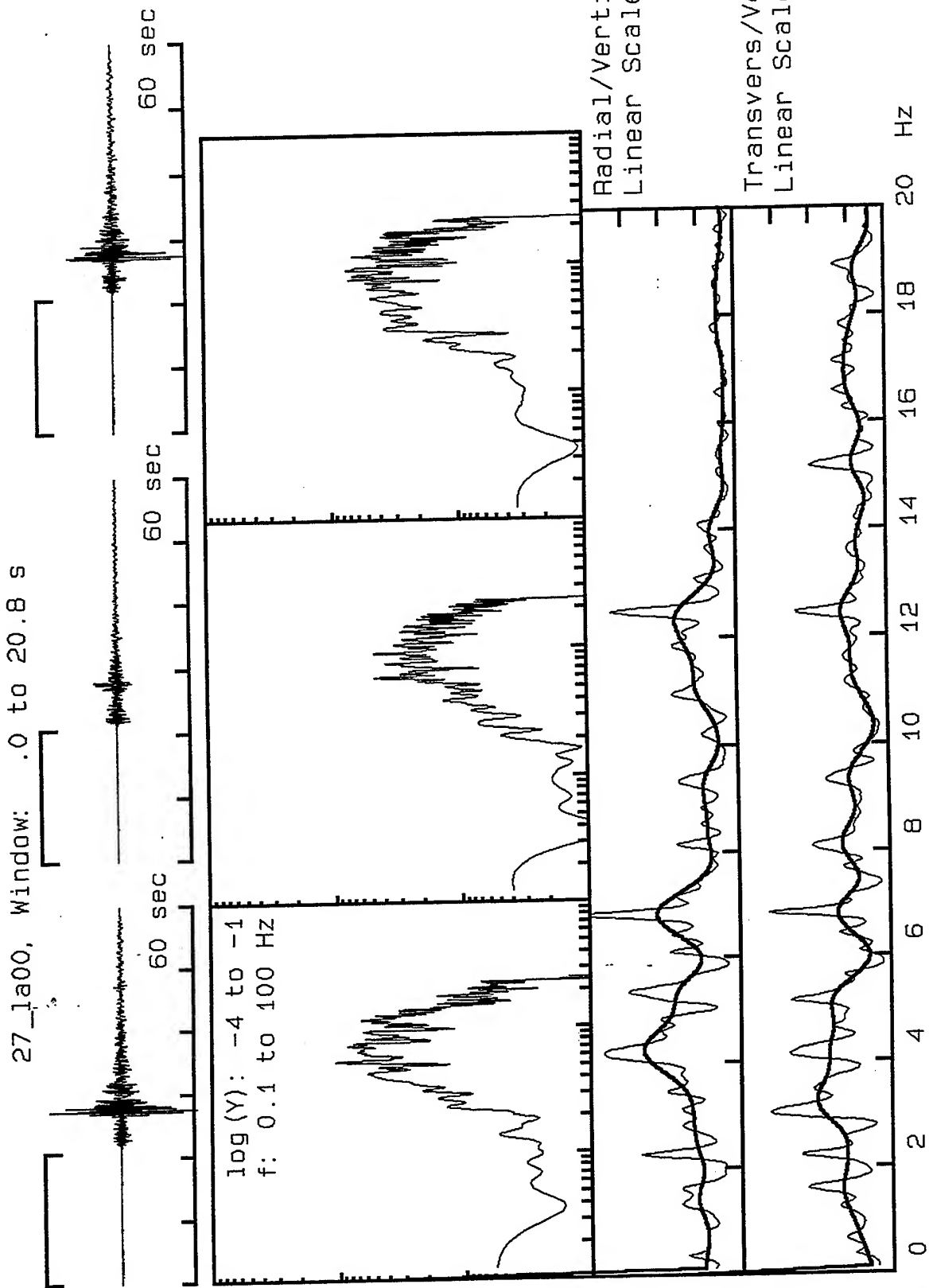


**VortexRock Consultants, Inc.**

11434 Alder Creek Rd, Corona, CA 91720

Tel - Fax (714) 692-1443, E-Mail: mahdyiar@coda.usc.edu





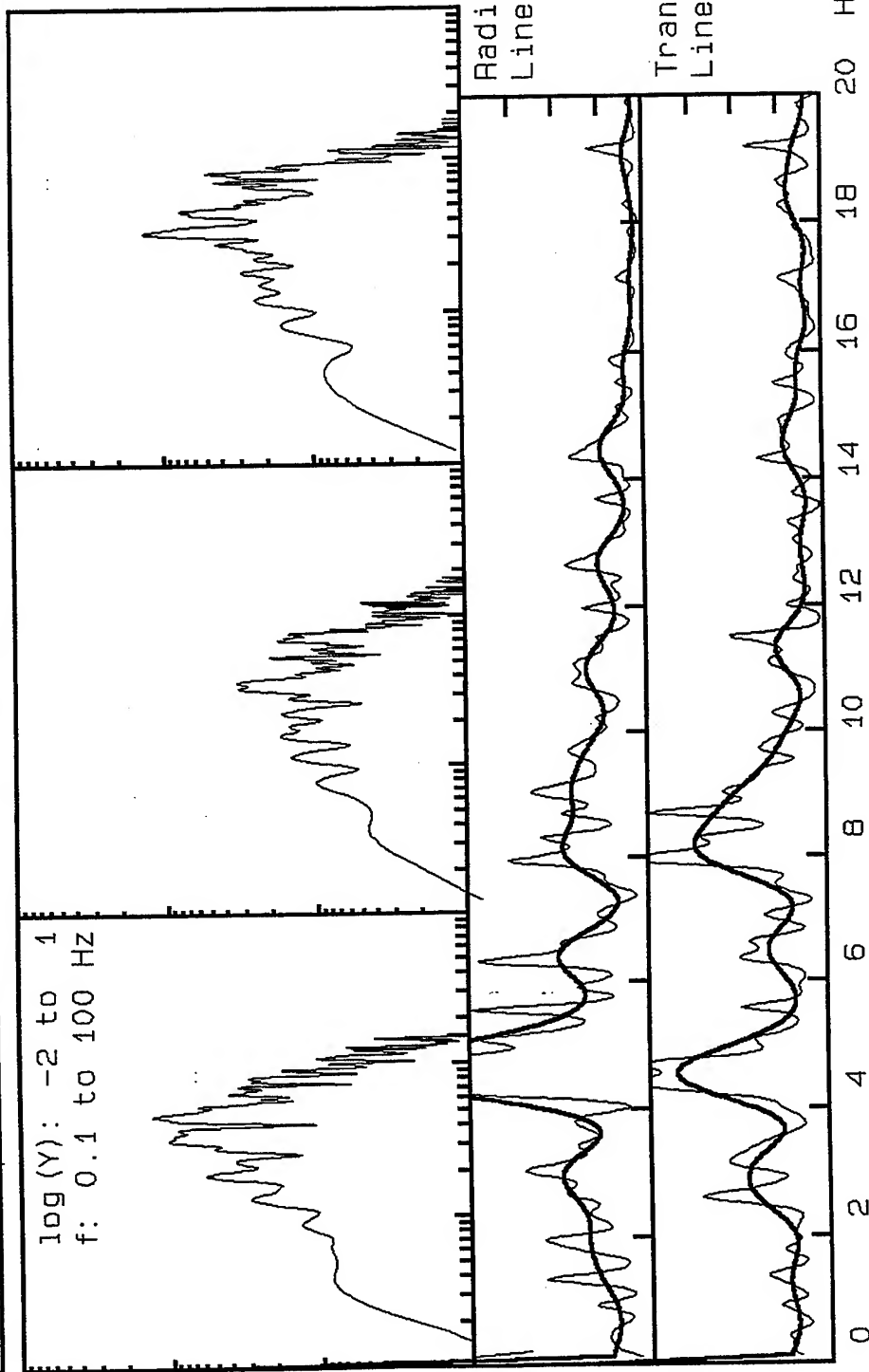
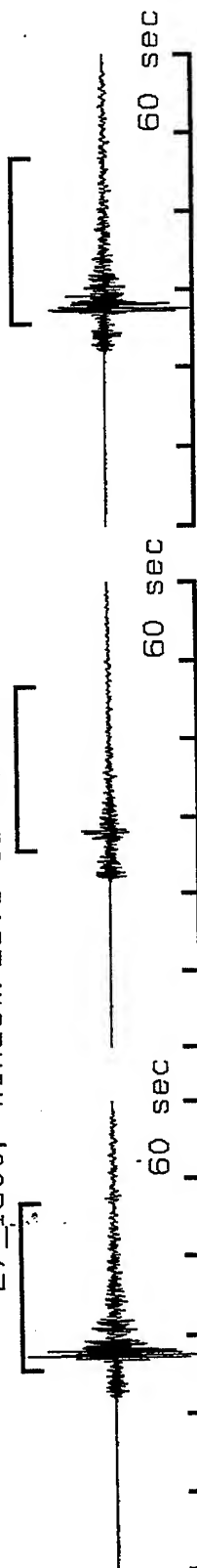
G-12



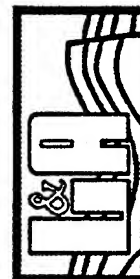
**VortexRock Consultants, Inc.**  
11434 Alder Creek Rd, Corona, CA 91720  
Tel - Fax (714) 692-1443, E-Mail: mahdyiar@coda.usc.edu

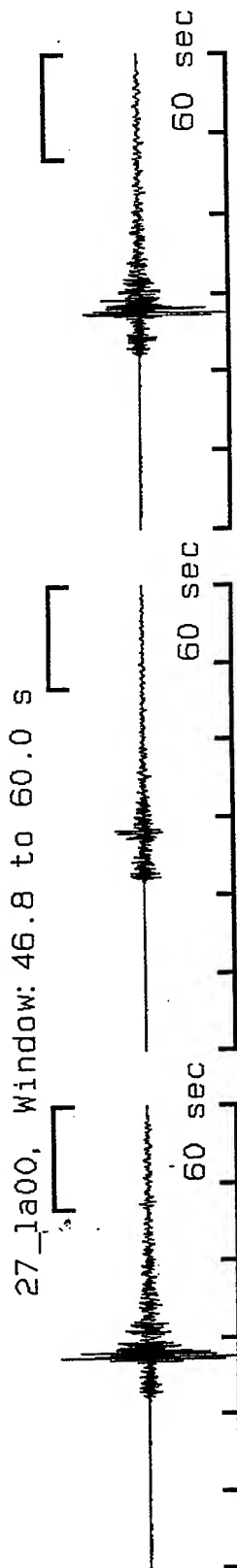


27\_la00, Window: 25.6 to 46.8 s

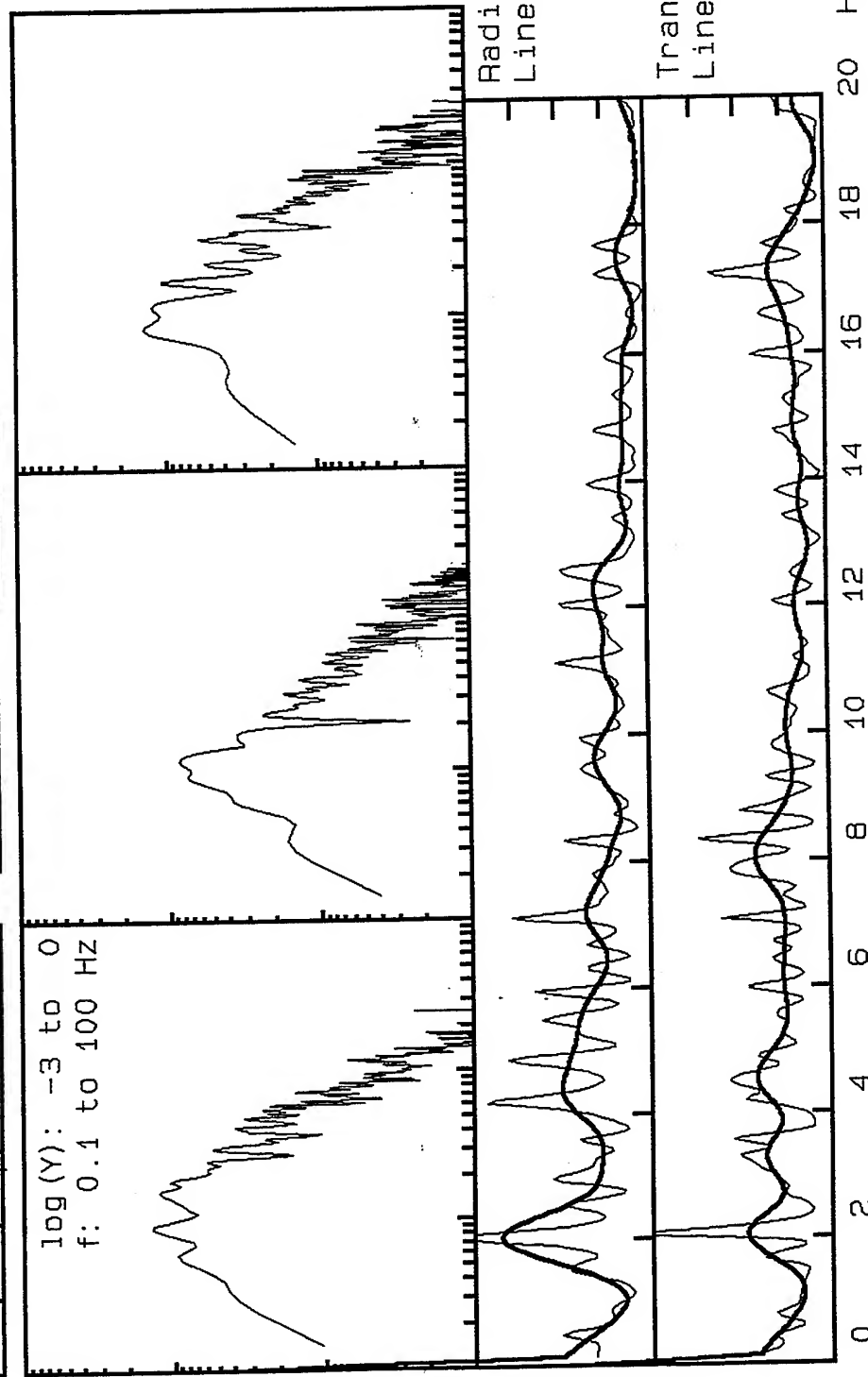


**VortexRock Consultants, Inc.**  
 11434 Alder Creek Rd, Corona, CA 91720  
 Tel - Fax (714) 692-1443, E-Mail: mahdyiar@coda.usc.edu

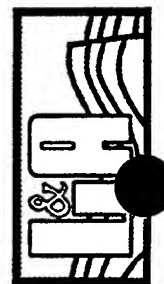




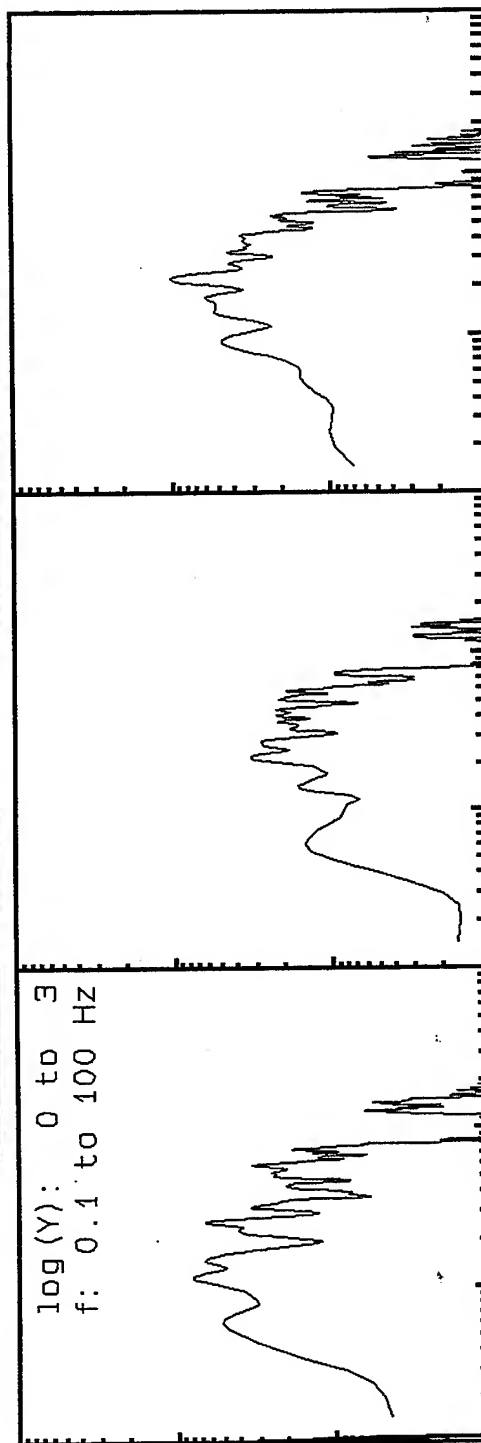
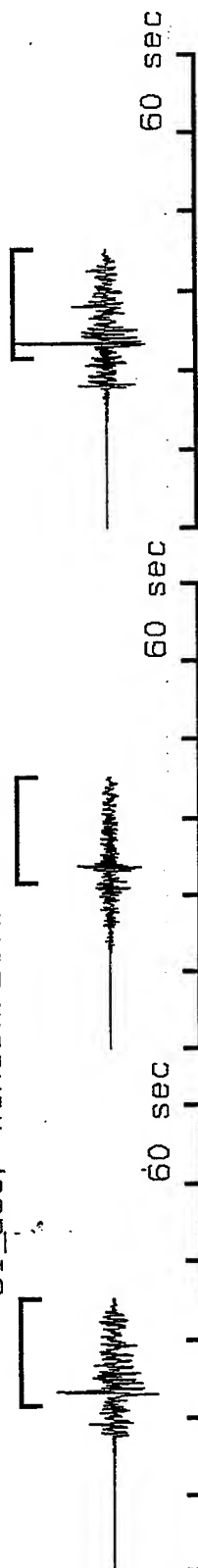
log(Y): -3 to 0  
f: 0.1 to 100 Hz



**VortexRock Consultants, Inc.**  
11434 Alder Creek Rd, Corona, CA 91720  
Tel - Fax (714) 692-1443, E-Mail: mahdyiar@coda.usc.edu

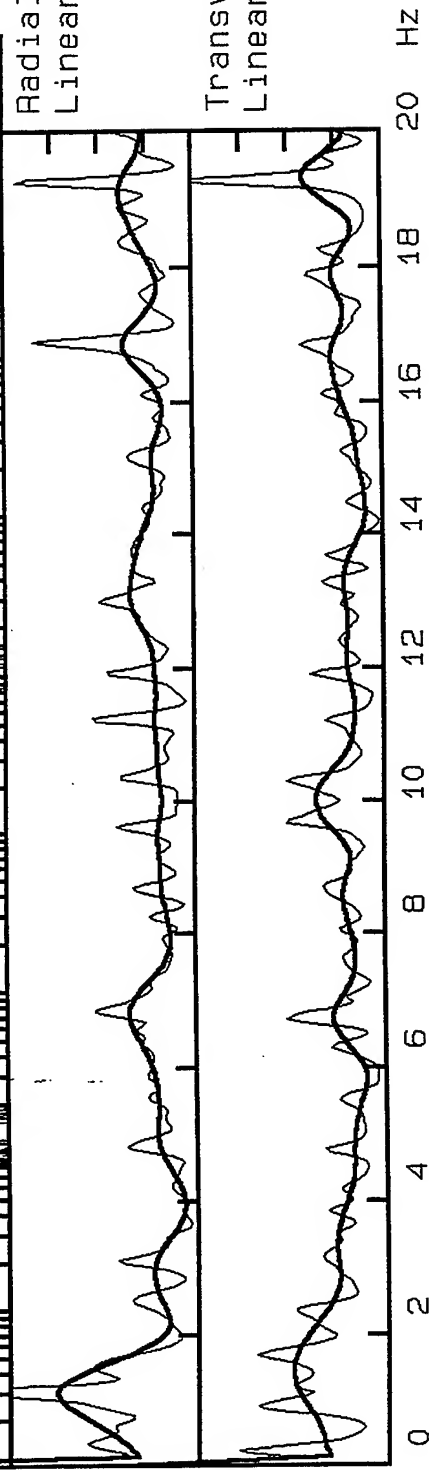


31\_usc, Window: 21.6 to 35.3 s



Radial/Vertical  
Linear Scale 0-8

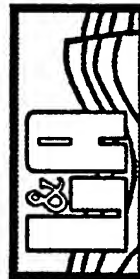
Transvers/Vertical:  
Linear Scale 0-8

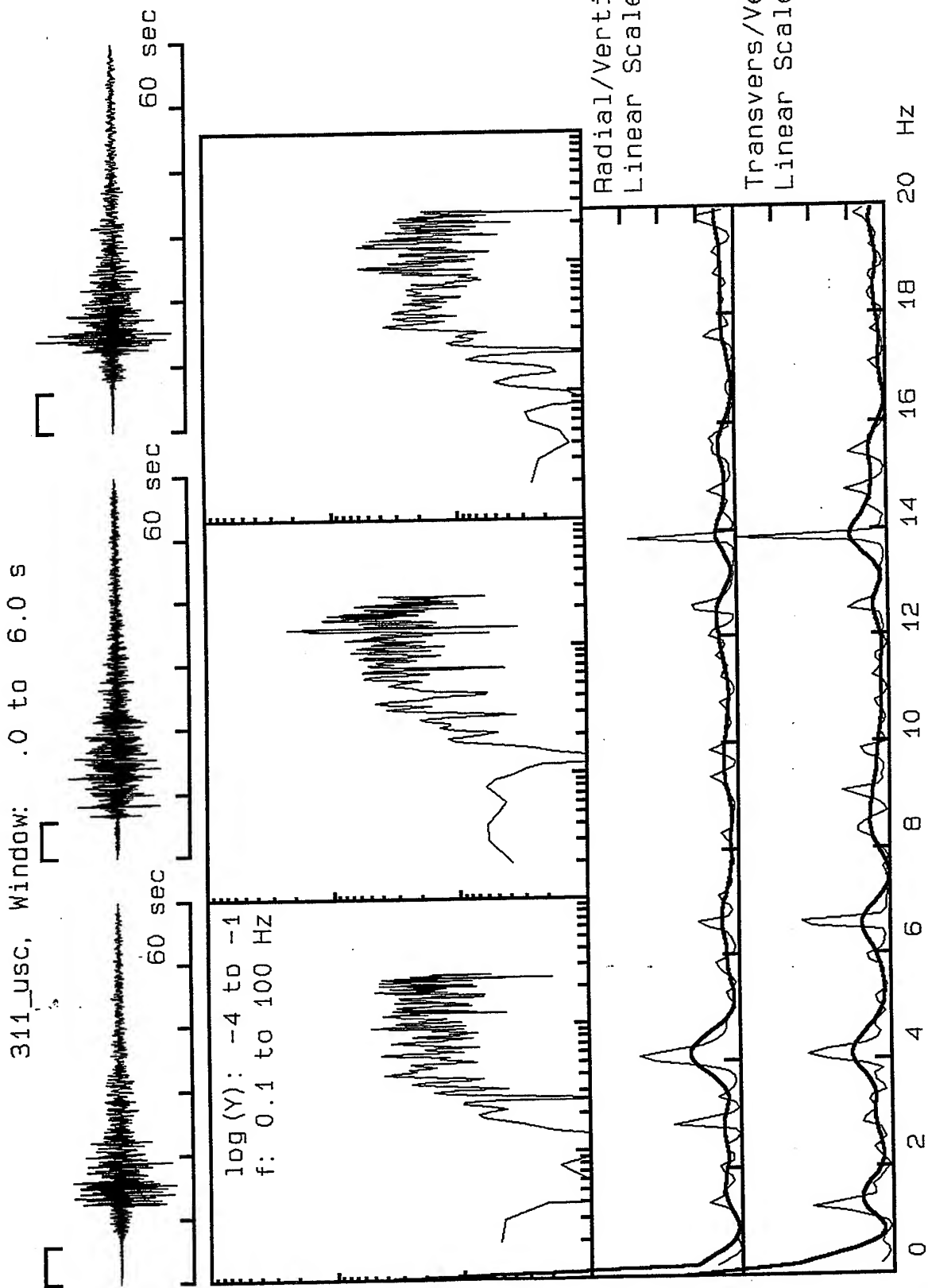


**VortexRock Consultants, Inc.**

11434 Alder Creek Rd, Corona, CA 91720

Tel - Fax (714) 692-1443, E-Mail: mahdyiar@coda.usc.edu

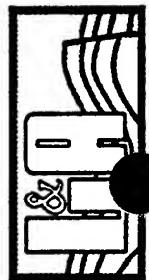




G-16

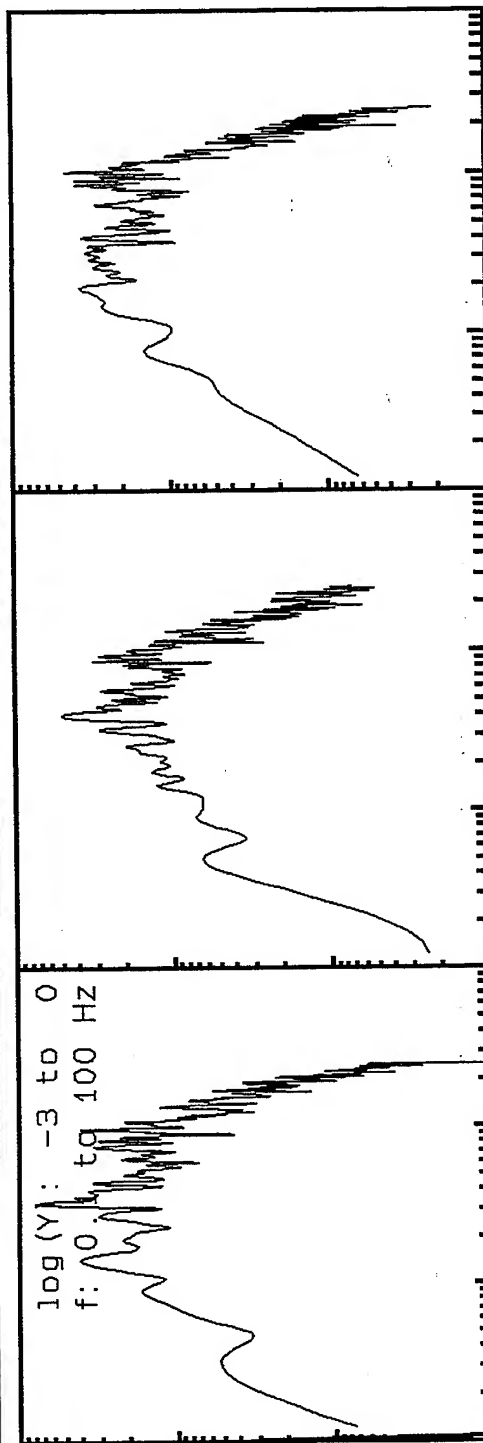
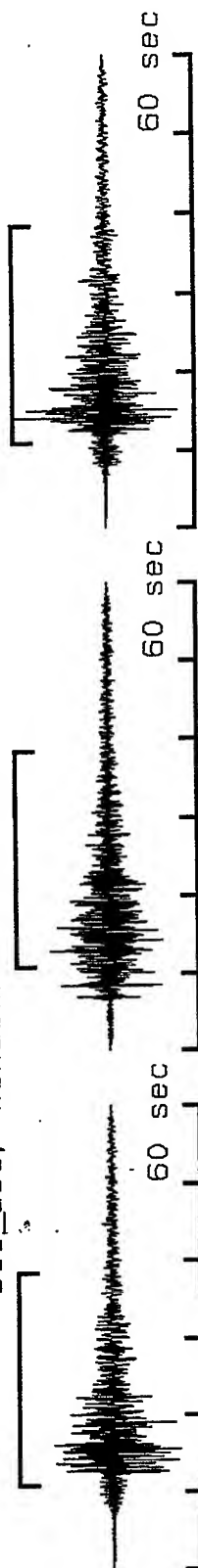


**VortexRock Consultants, Inc.**  
11434 Alder Creek Rd, Corona, CA 91720  
Tel - Fax (714) 692-1443, E-Mail: mahdyiar@coda.usc.edu



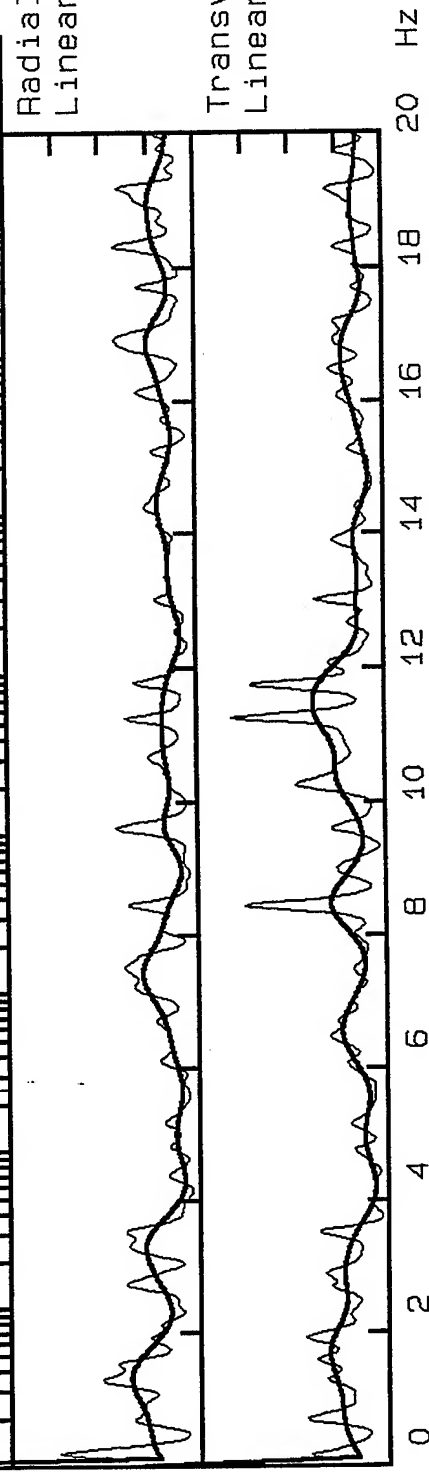


311\_usc, Window: 10.8 to 38.4 s



Radial/Vertical  
Linear Scale 0-8

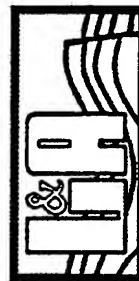
Transvers/Vertical:  
Linear Scale 0-8



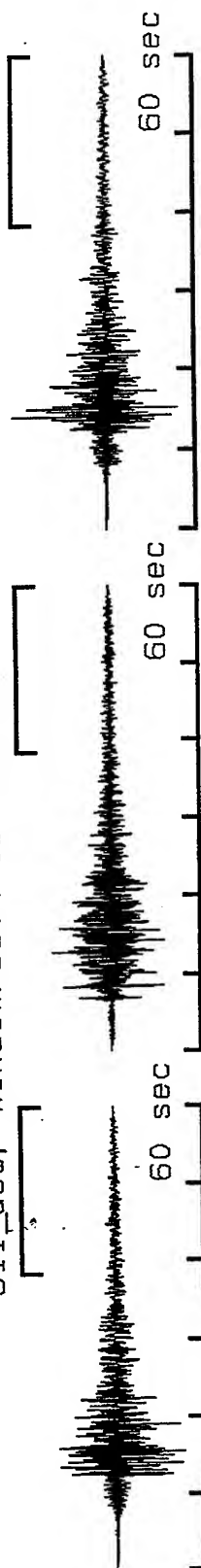
**VortexRock Consultants, Inc.**

11434 Alder Creek Rd, Corona, CA 91720

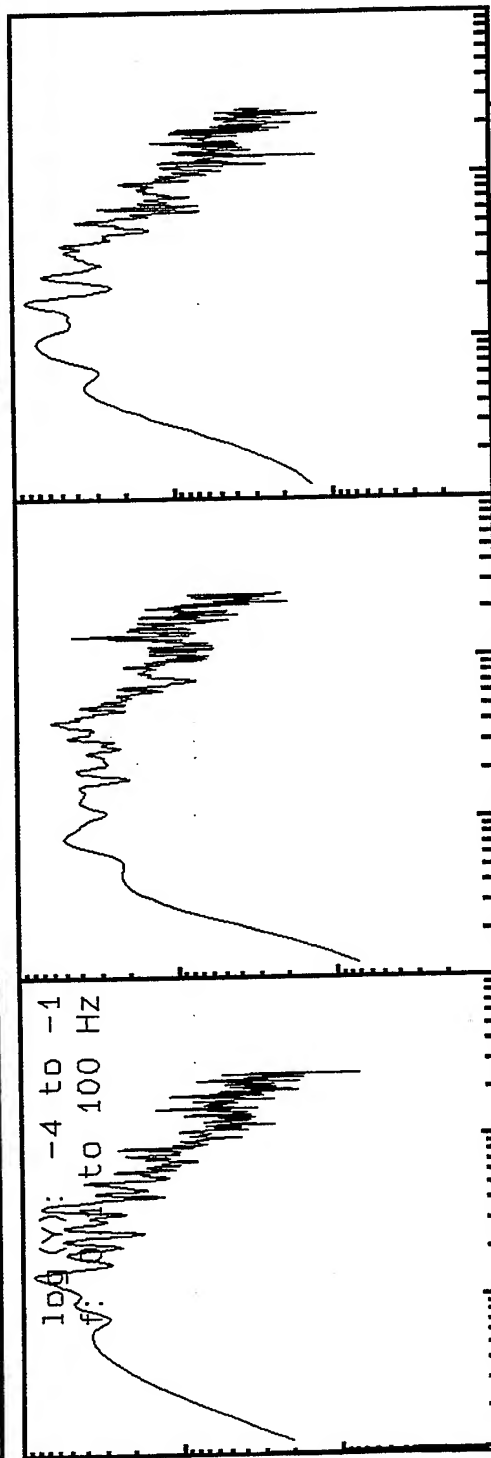
Tel - Fax (714) 692-1443, E-Mail: mahdyiar@coda.usc.edu



311\_usc, Window: 38.4 to 60.0 s

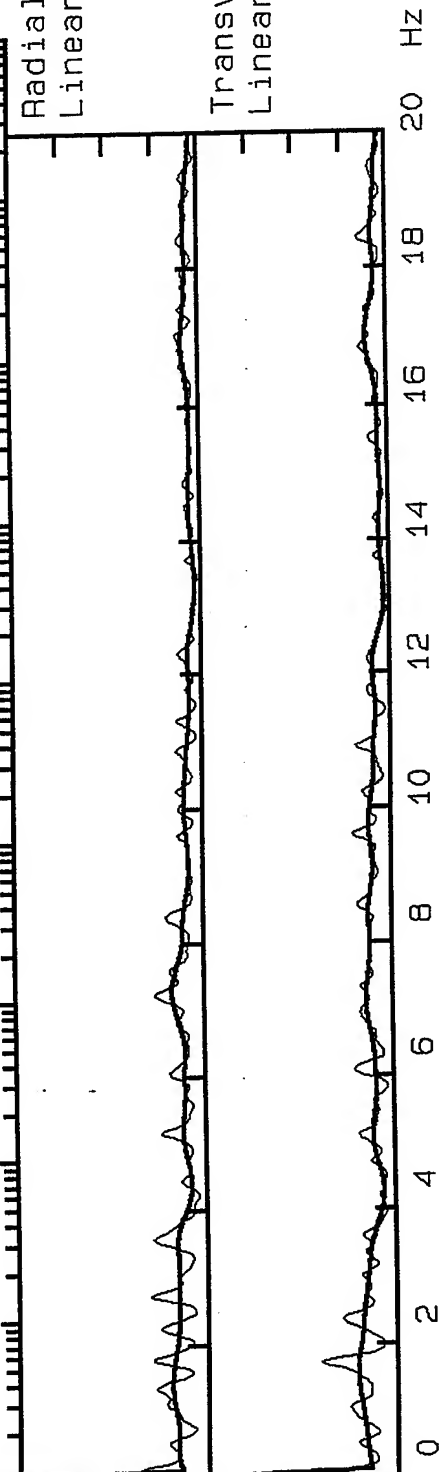


10A (Y): -4 to -1  
f: 10 to 100 Hz

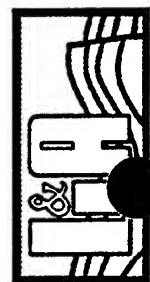


Radial/Vertical  
Linear Scale 0-8

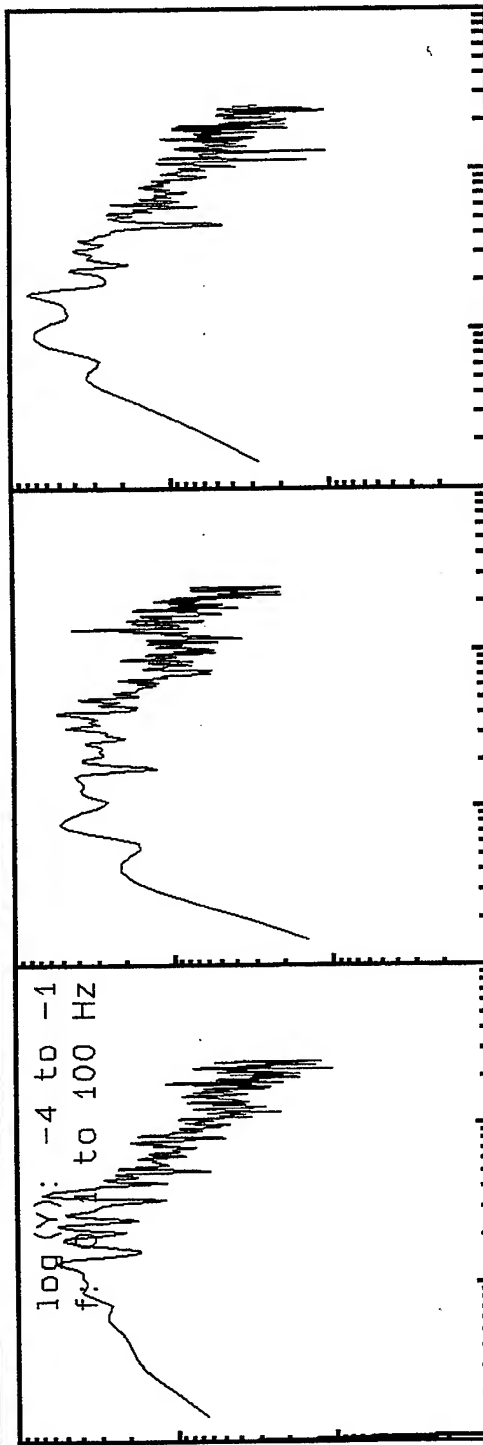
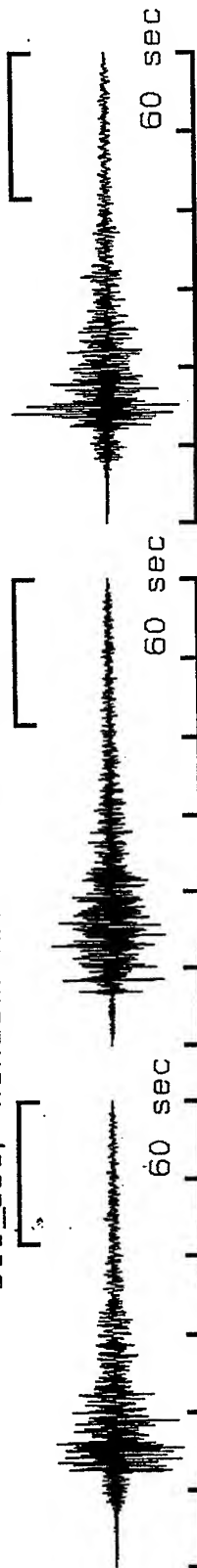
Transvers/Vertical:  
Linear Scale 0-8



**VortexRock Consultants, Inc.**  
11434 Alder Creek Rd, Corona, CA 91720  
Tel - Fax (714) 692-1443, E-Mail: mahdyar@coda.usc.edu



311\_usc, Window: 41.6 to 60.0 s



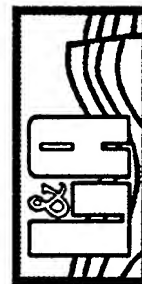
Radial/Vertical  
Linear Scale 0-8

Transvers/Vertical:  
Linear Scale 0-8

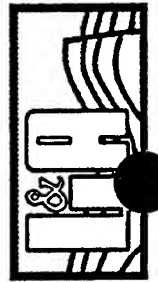
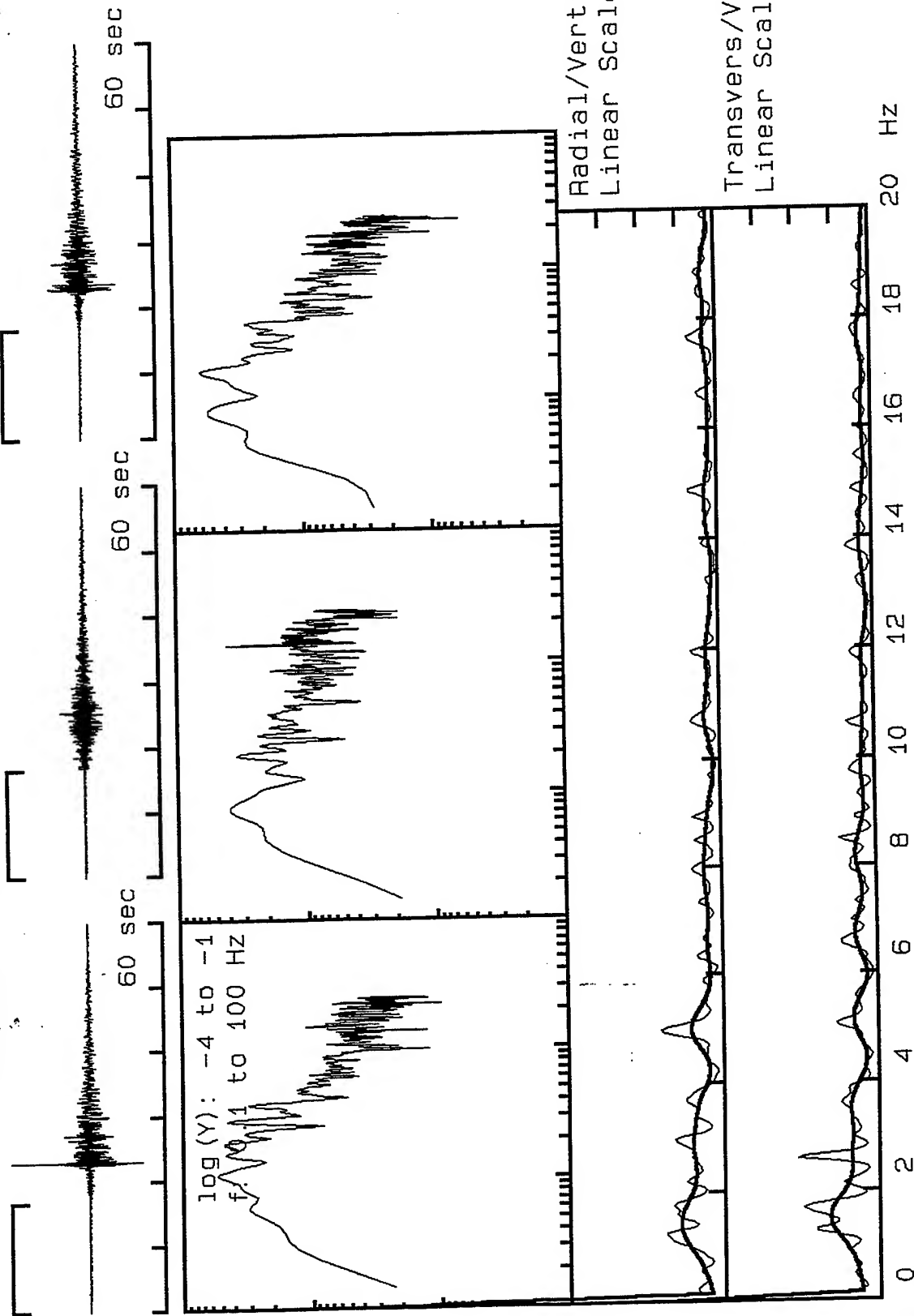
0 2 4 6 8 10 12 14 16 18 20 Hz



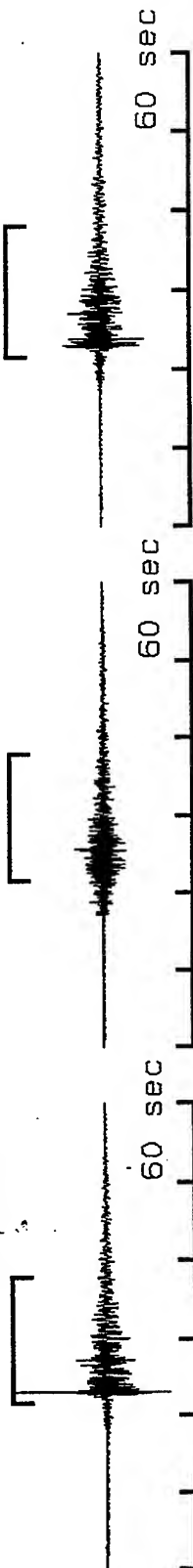
**VortexRock Consultants, Inc.**  
11434 Alder Creek Rd, Corona, CA 91720  
Tel - Fax (714) 692-1443, E-Mail: mahdyar@coda.usc.edu



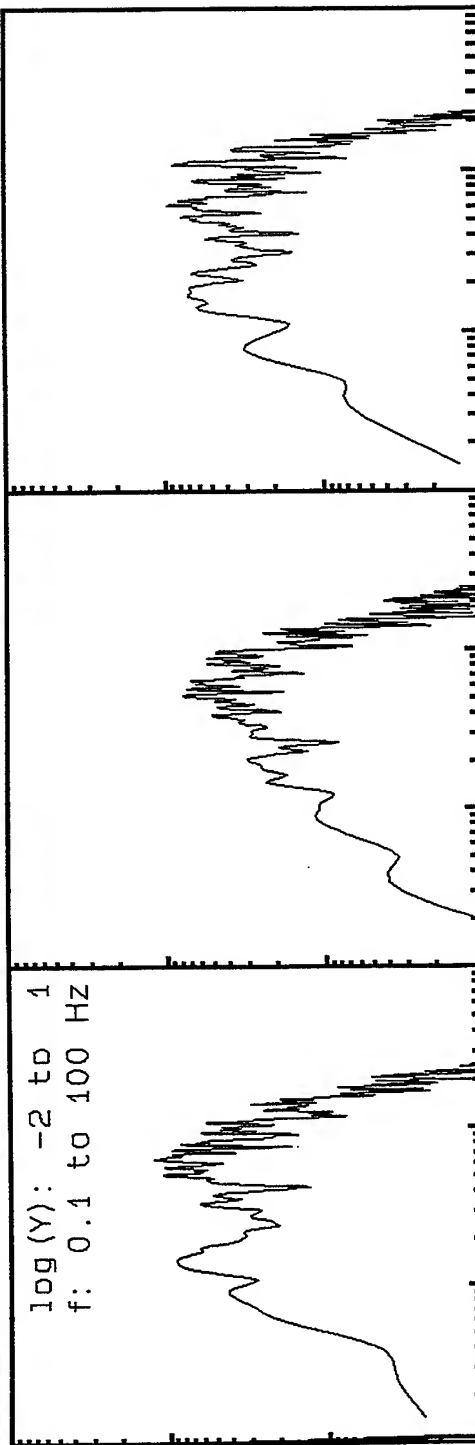
312\_usc, Window: .0 to 16.8 s



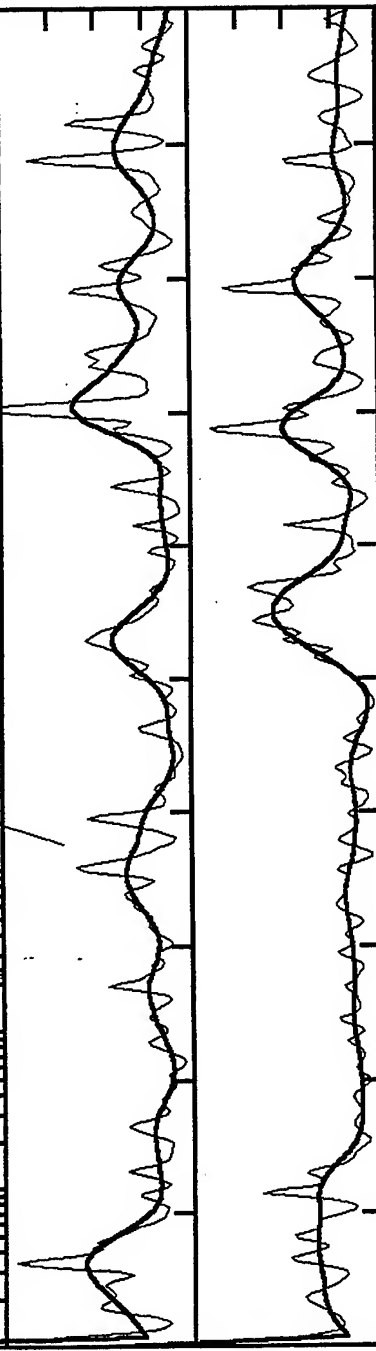
312\_usc, Window: 21.6 to 38.0 s



log(Y): -2 to 1  
f: 0.1 to 100 Hz



Radial/Vertical  
Linear Scale 0-8

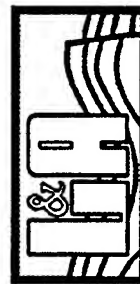


Transvers/Vertical:  
Linear Scale 0-8

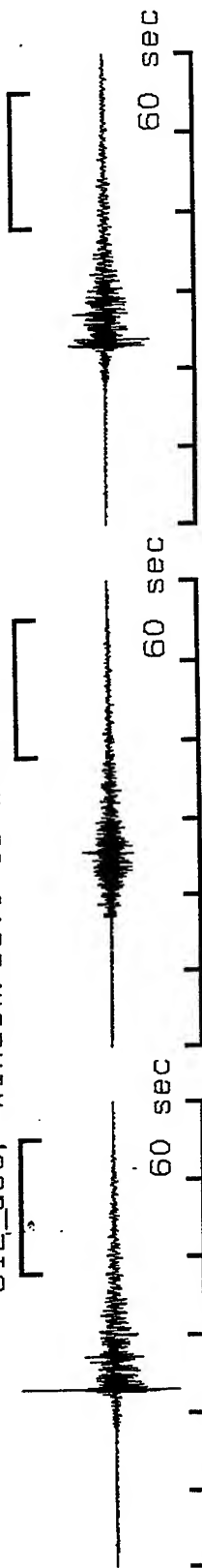
0 2 4 6 8 10 12 14 16 18 20 Hz



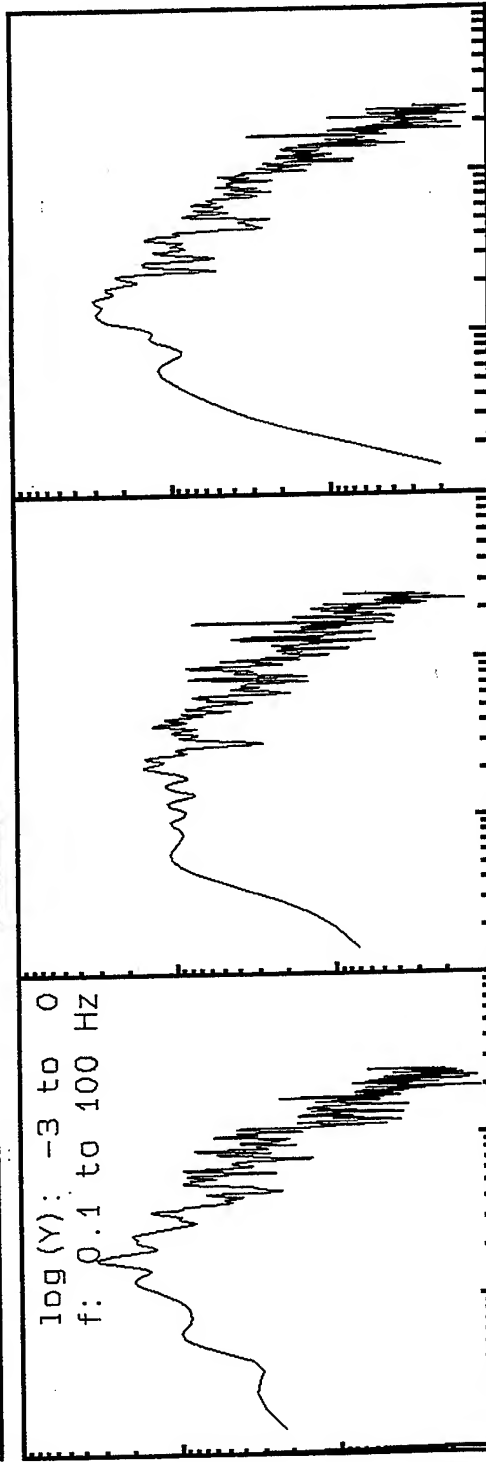
**VortexRock Consultants, Inc.**  
11434 Alder Creek Rd, Corona, CA 91720  
Tel - Fax (714) 692-1443, E-Mail: mahdyar@coda.usc.edu



312\_usc, Window: 38.0 to 55.2 s

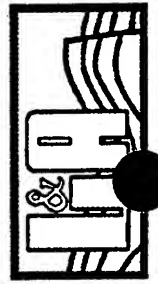
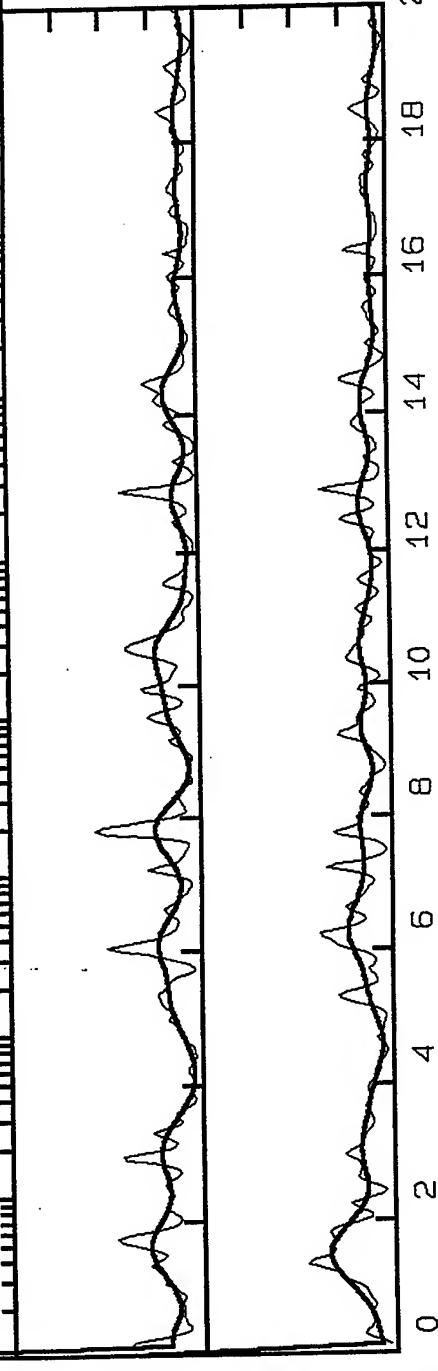


log(Y): -3 to 0  
f: 0.1 to 100 Hz

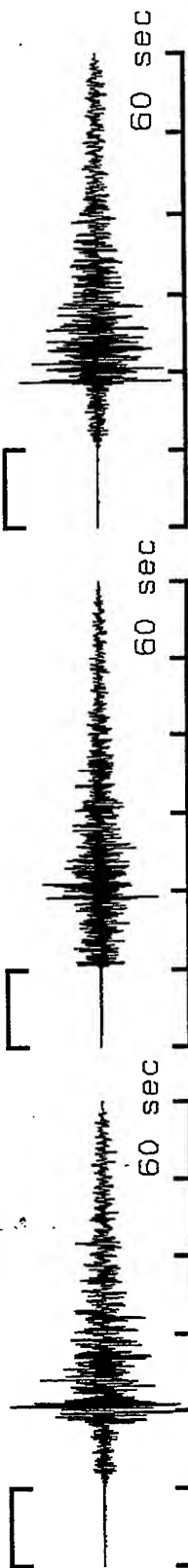


Radial/Vertical  
Linear Scale 0-8

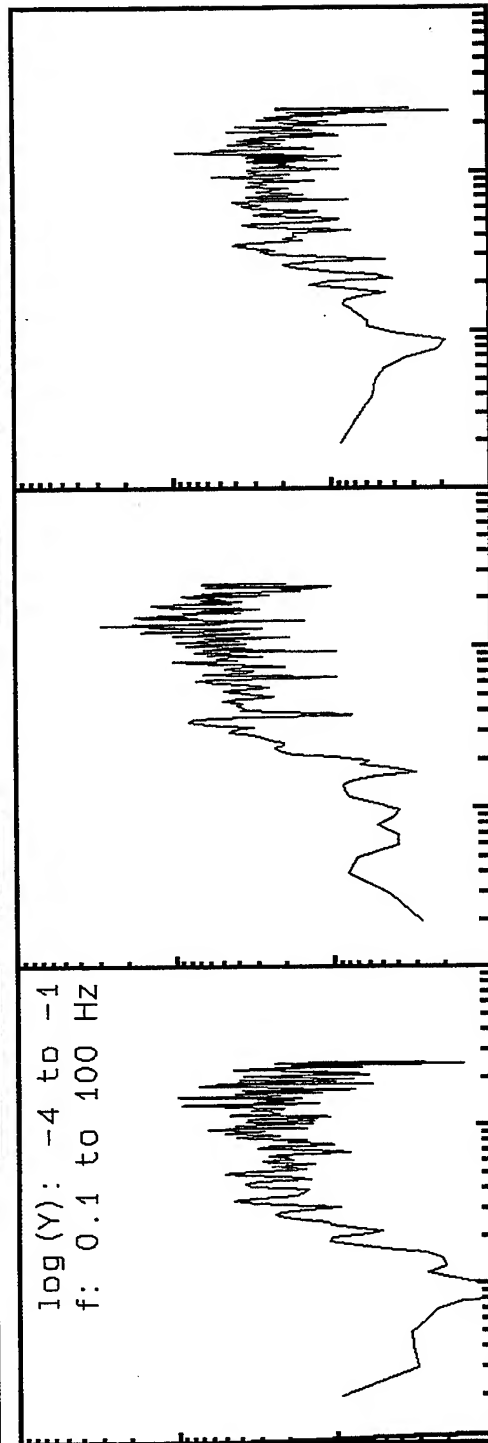
Transvers/Vertical:  
Linear Scale 0-8



39  $\mu$ sec, Window: .0 to 10.0 s



log (Y): -4 to -1  
f: 0.1 to 100 Hz



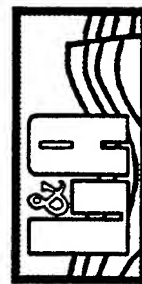
Radial/Vertical  
Linear Scale 0-8

Transvers/Vertical:  
Linear Scale 0-8

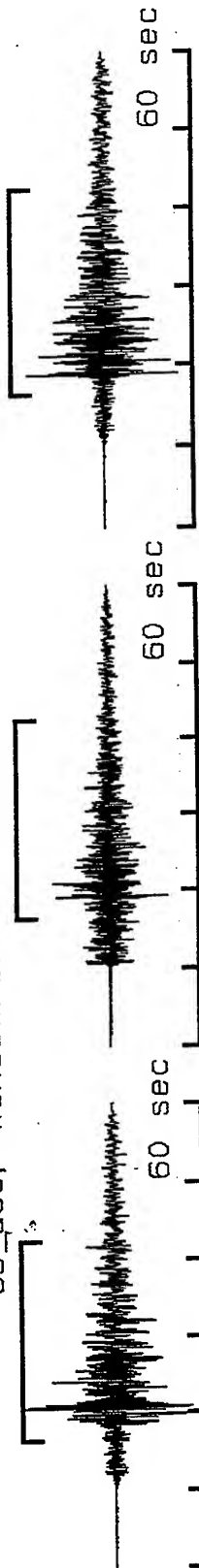
0 2 4 6 8 10 12 14 16 18 20 Hz



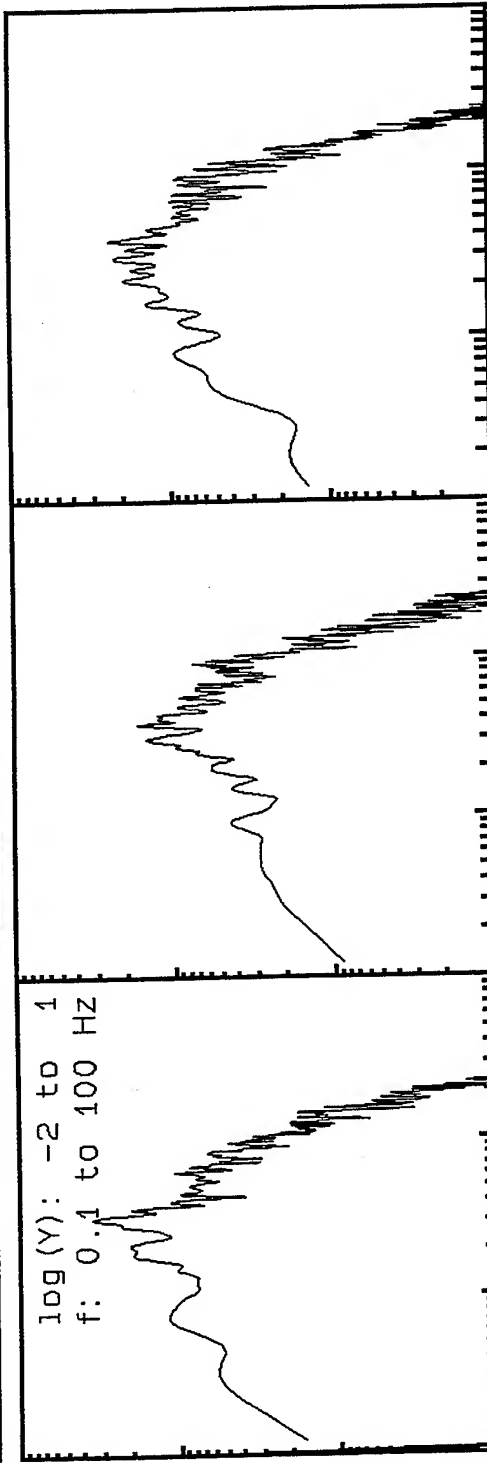
**VortexRock Consultants, Inc.**  
11434 Alder Creek Rd, Corona, CA 91720  
Tel - Fax (714) 692-1443, E-Mail: mahdyiar@coda.usc.edu



39\_usc, Window: 16.4 to 42.4 s

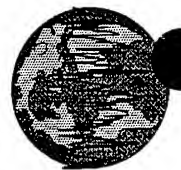
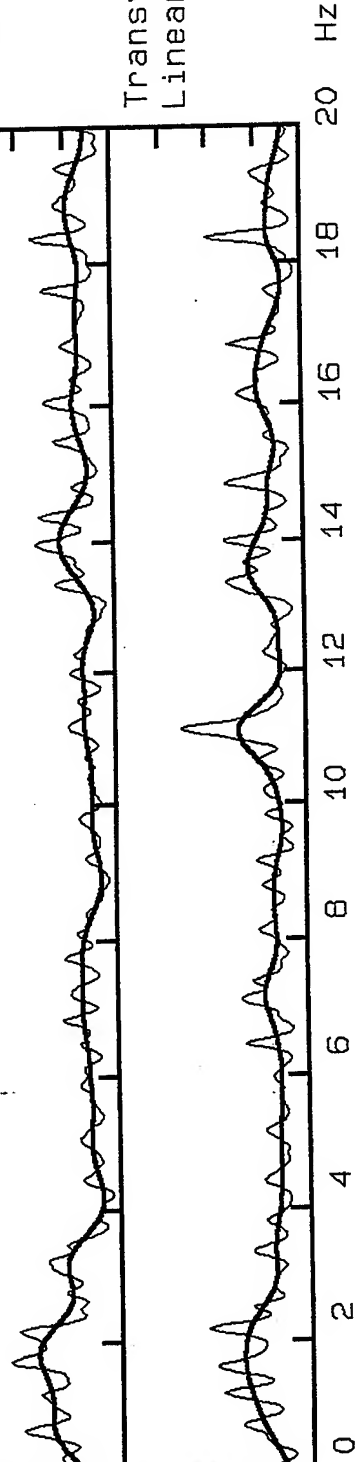


log (Y): -2 to 1  
f: 0.1 to 100 Hz



Radial/Vertical  
Linear Scale 0-8

Transvers/Vertical  
Linear Scale 0-8



**VortexRock Consultants, Inc.**

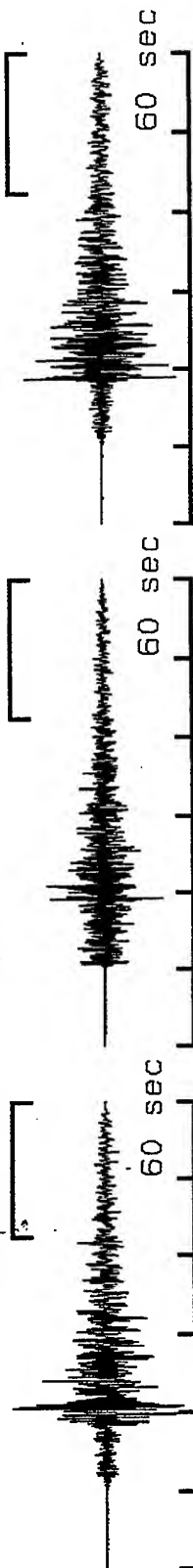
11434 Alder Creek Rd, Corona, CA 91720

Tel - Fax (714) 692-1443, E-Mail: mahdyiar@coda.usc.edu

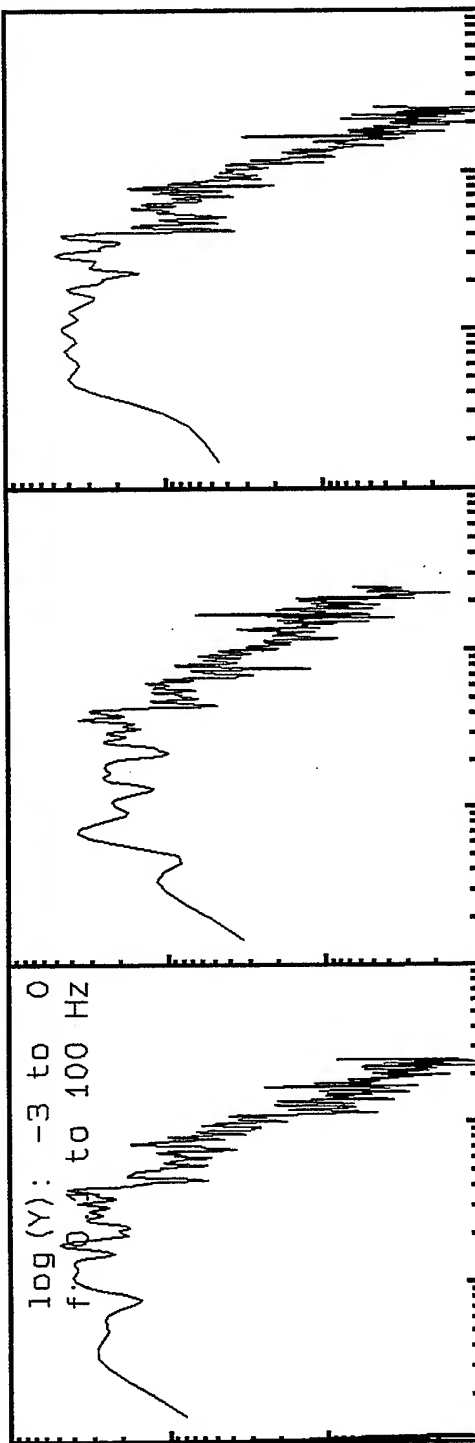




39\_usc, Window: 42.4 to 60.0 s

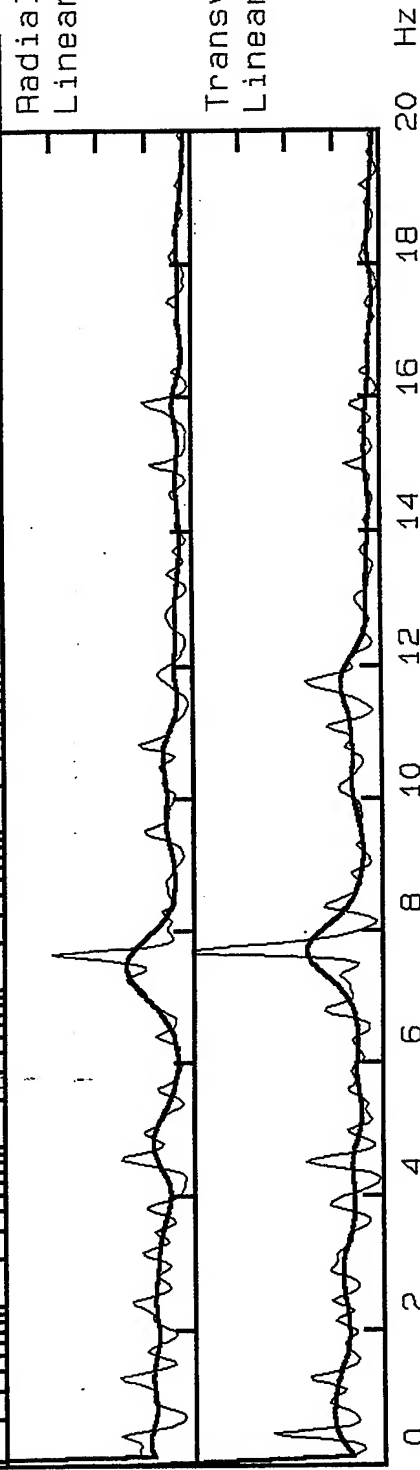


log (Y): -3 to 0  
f: 0 to 100 Hz



Radial/Vertical  
Linear Scale 0-8

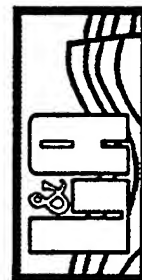
Transvers/Vertical:  
Linear Scale 0-8

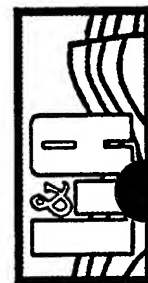
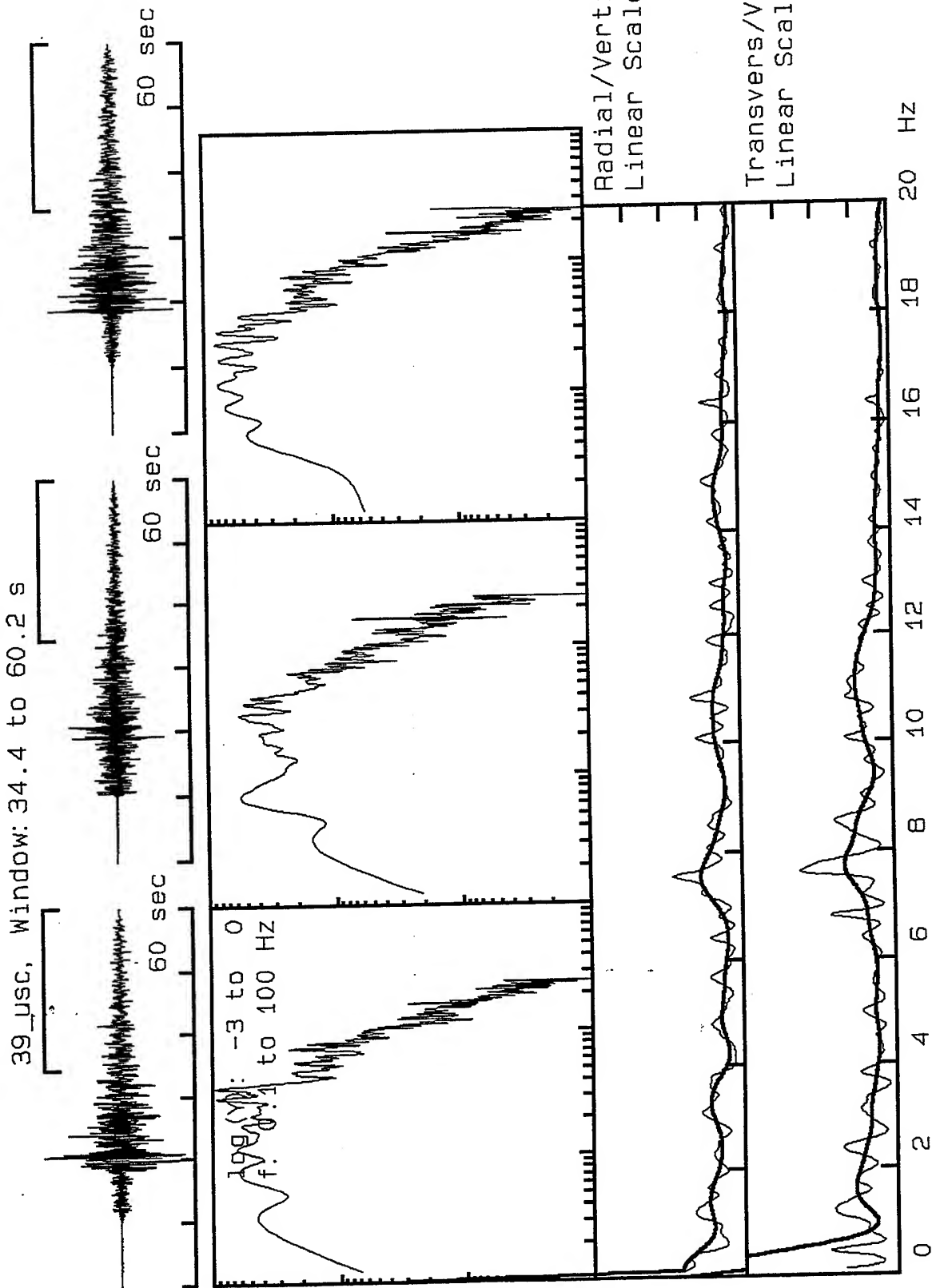


**VortexRock Consultants, Inc.**

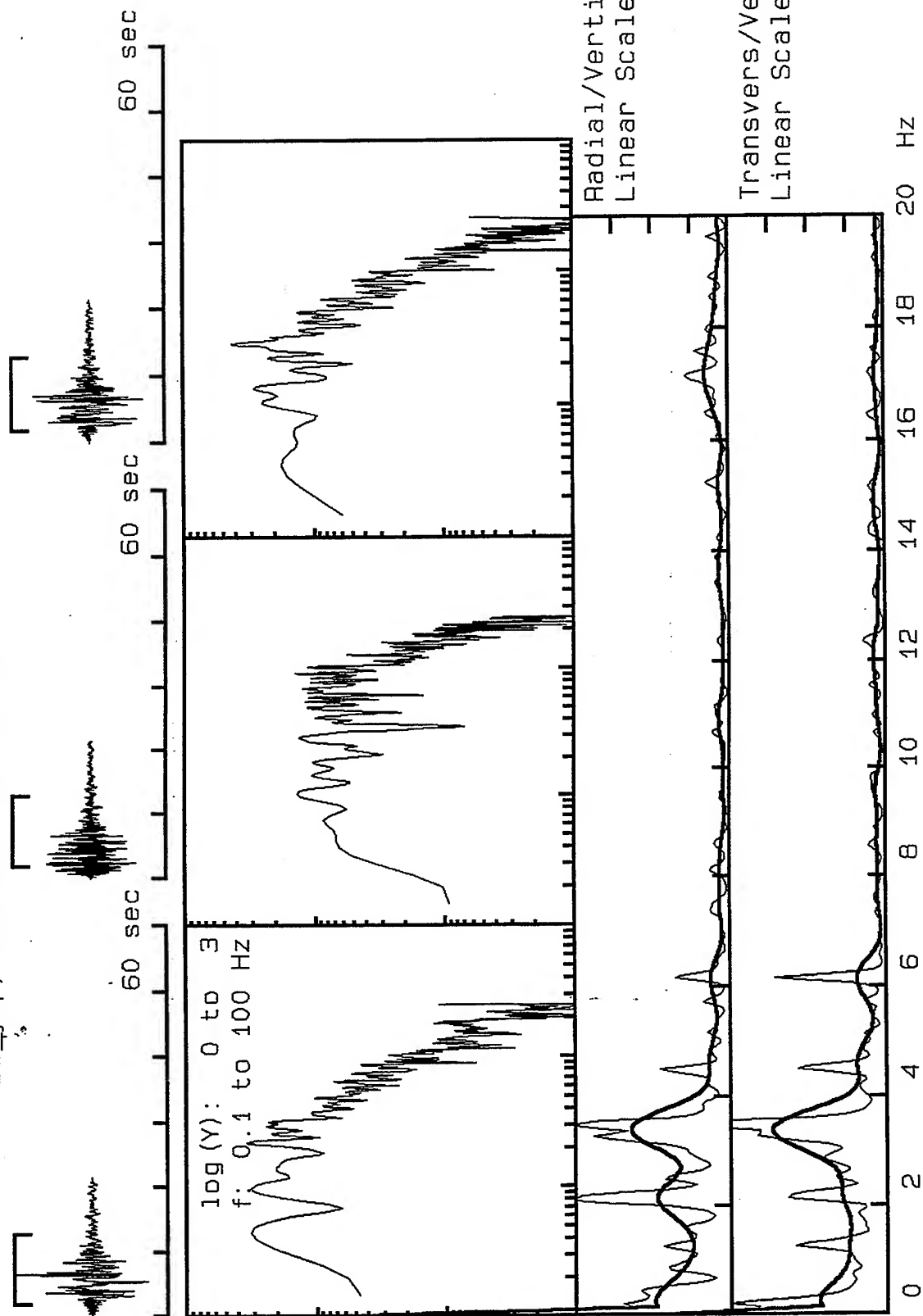
11434 Alder Creek Rd, Corona, CA 91720

Tel - Fax (714) 692-1443, E-Mail: mahdyiar@coda.usc.edu

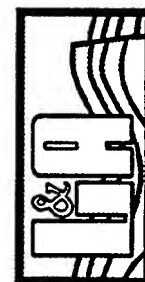




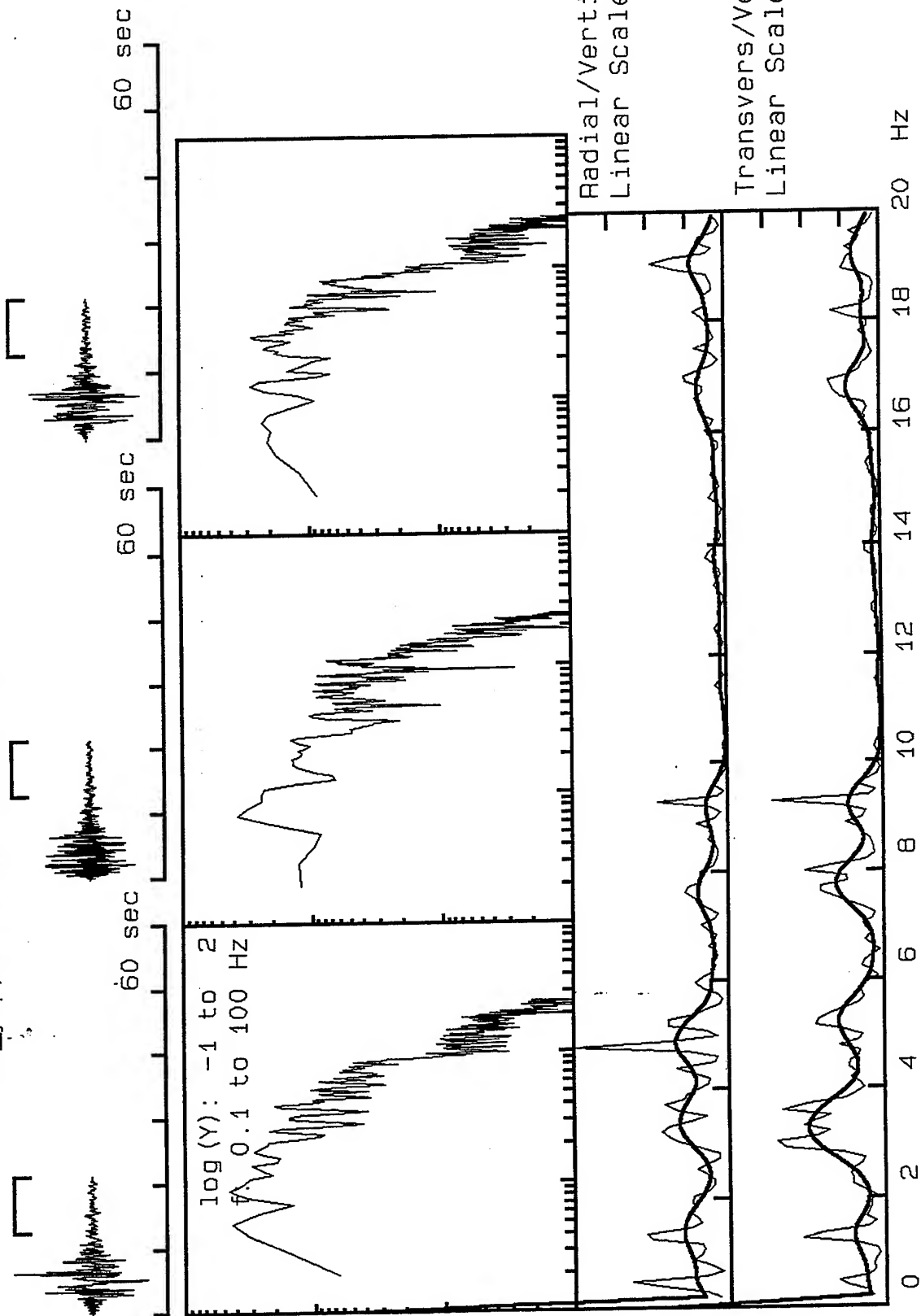
51\_jfp, Window: 2.0 to 12.8 s



**VortexRock Consultants, Inc.**  
11434 Alder Creek Rd, Corona, CA 91720  
Tel - Fax (714) 692-1443, E-Mail: mahdyiar@coda.usc.edu



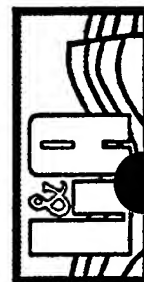
51\_jfp, Window: 12.8 to 21.4 s



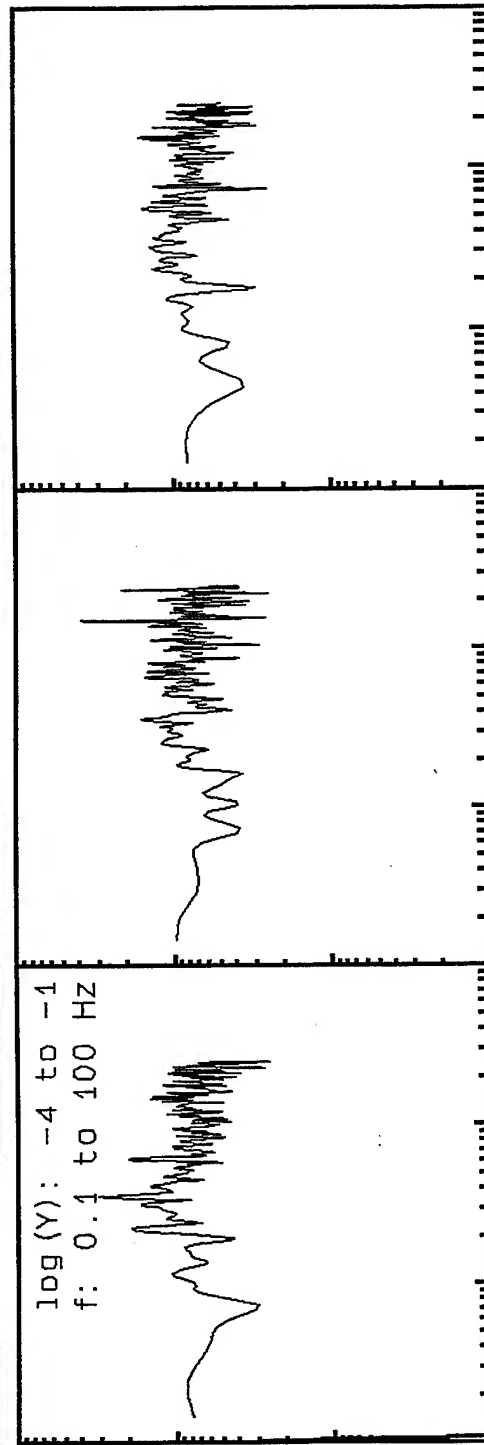
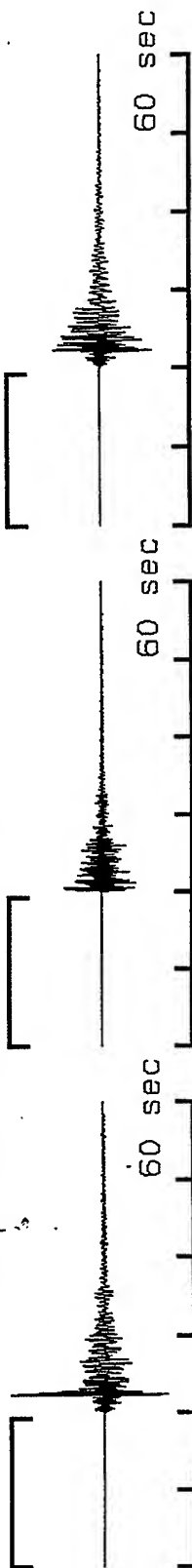
**VortexRock Consultants, Inc.**

11434 Alder Creek Rd, Corona, CA 91720

Tel - Fax (714) 692-1443, E-Mail: mahdyiar@coda.usc.edu

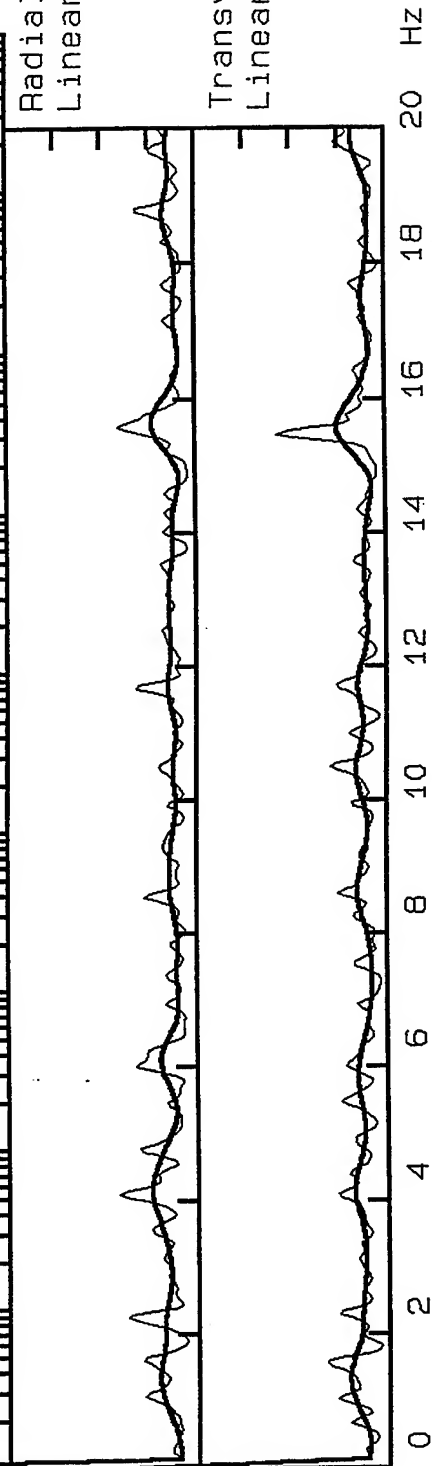


513\_jfpp, Window: .0 to 19.2 s

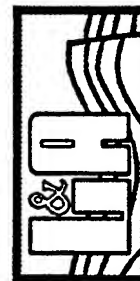


Radial/Vertical  
Linear Scale 0-8

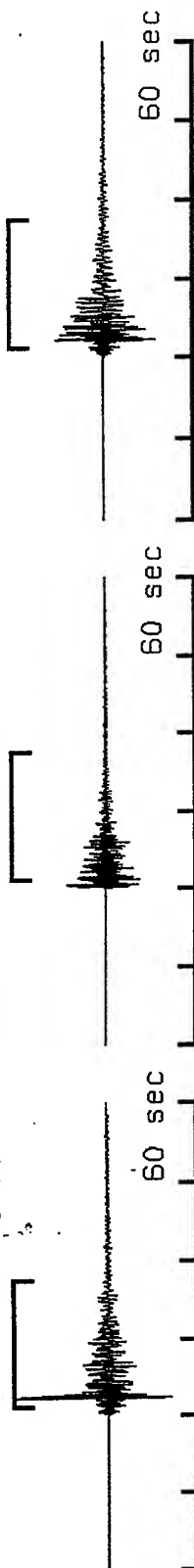
Transvers/Vertical:  
Linear Scale 0-8



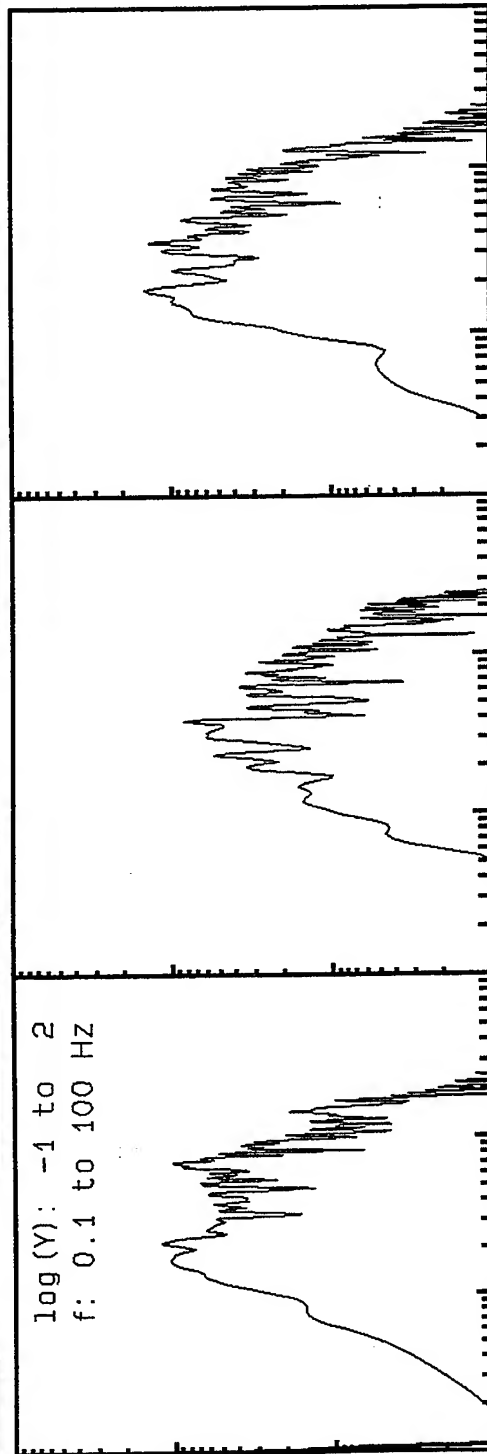
**VortexRock Consultants, Inc.**  
11434 Alder Creek Rd, Corona, CA 91720  
Tel - Fax (714) 692-1443, E-Mail: mahdyiar@coda.usc.edu



513\_jfpp, Window: 21.2 to 37.6 s

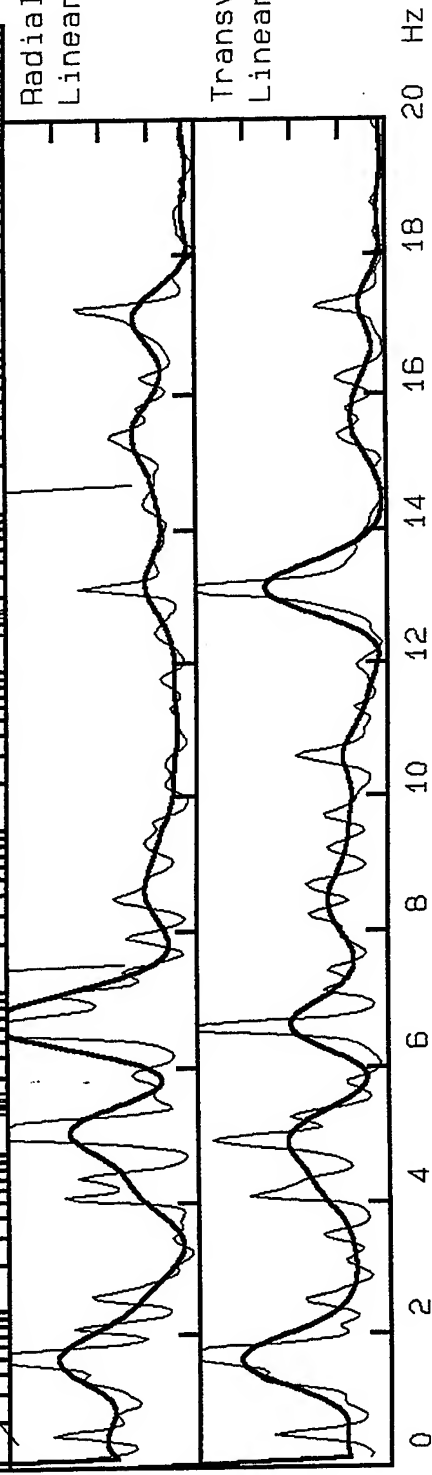


log (Y): -1 to 2  
f: 0.1 to 100 Hz

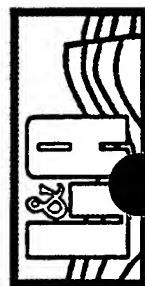


Radial/Vertical  
Linear Scale 0-8

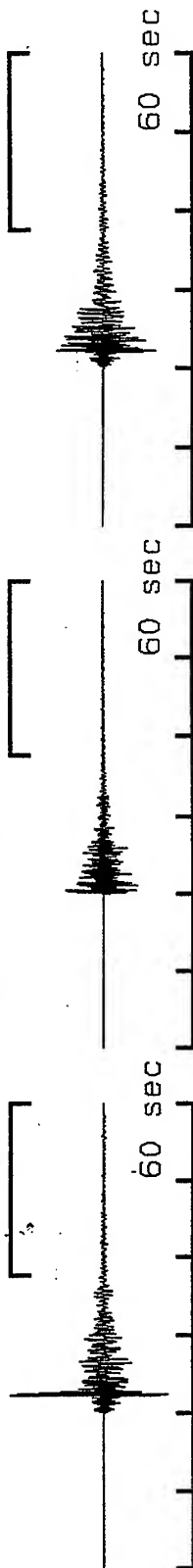
Transvers/Vertical  
Linear Scale 0-8



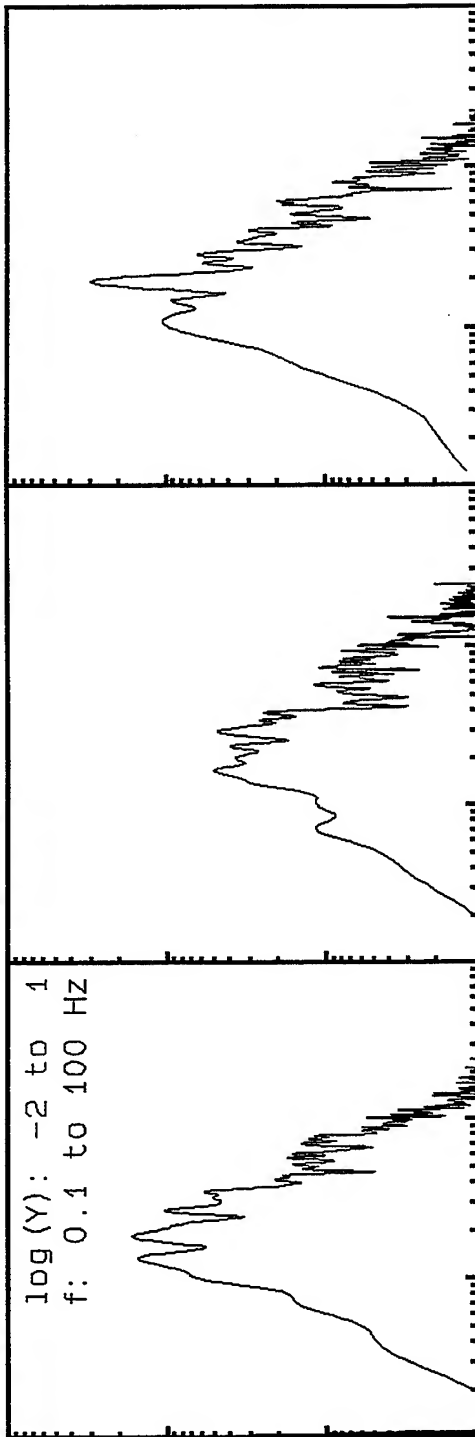
**VortexRock Consultants, Inc.**  
11434 Alder Creek Rd, Corona, CA 91720  
Tel - Fax (714) 692-1443, E-Mail: mahdyiar@coda.usc.edu



513\_jfpp, Window: 37.6 to 60.0 s

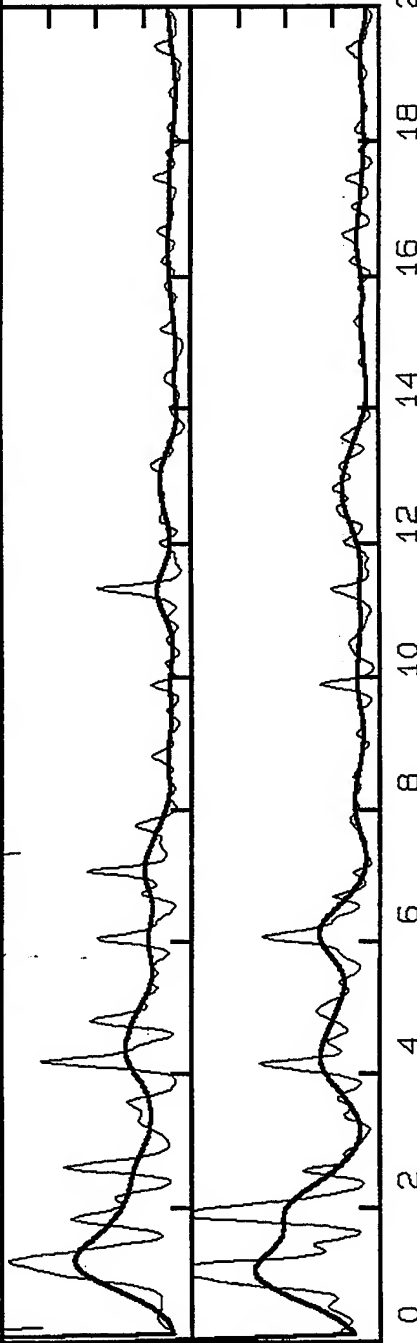


log (Y): -2 to 1  
f: 0.1 to 100 Hz

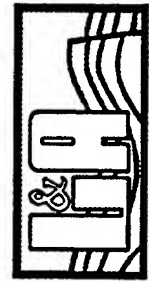


Radial/Vertical  
Linear Scale 0-8

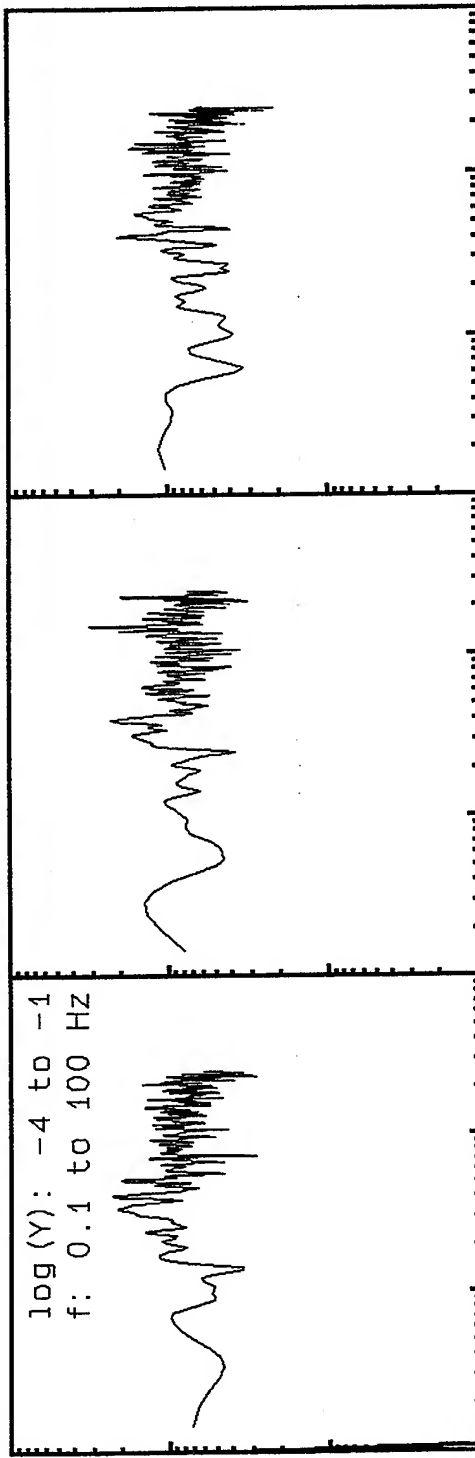
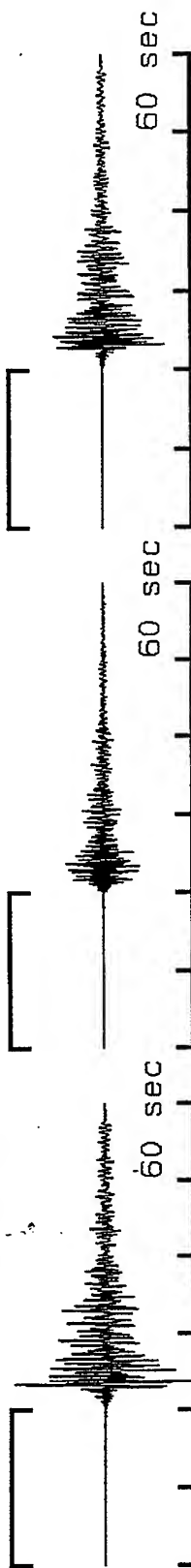
Transvers/Vertical:  
Linear Scale 0-8



**VortexRock Consultants, Inc.**  
11434 Alder Creek Rd, Corona, CA 91720  
Tel - Fax (714) 692-1443, E-Mail: mahdyiar@coda.usc.edu

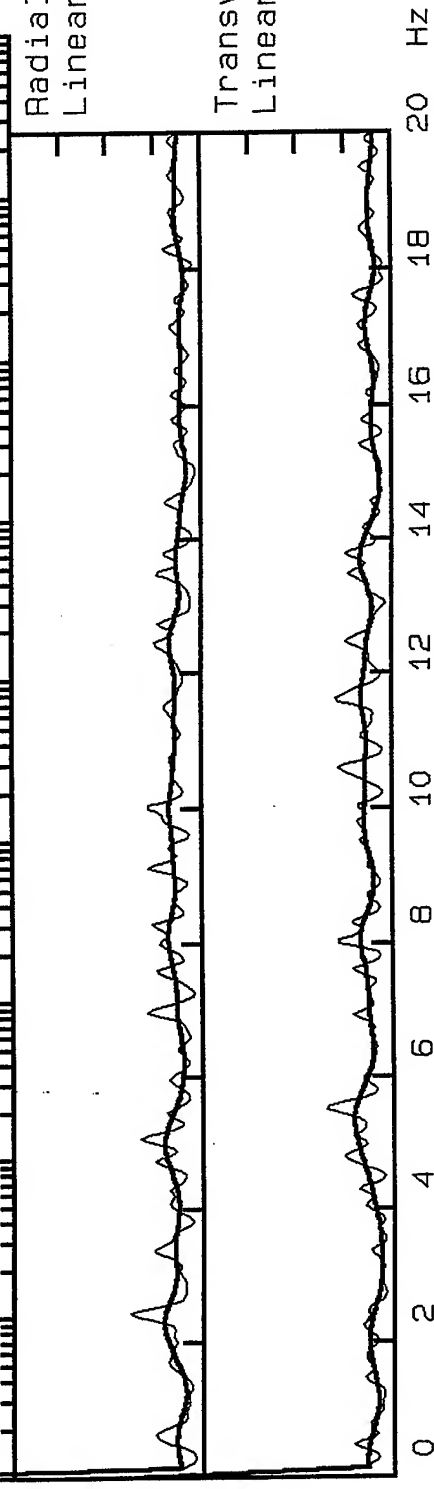


514\_jfpp, Window: .0 to 20.0 s



Radial/Vertical  
Linear Scale 0-8

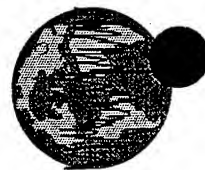
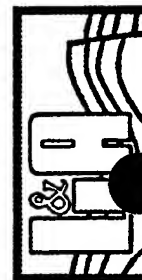
Transvers/Vertical:  
Linear Scale 0-8



**VortexRock Consultants, Inc.**

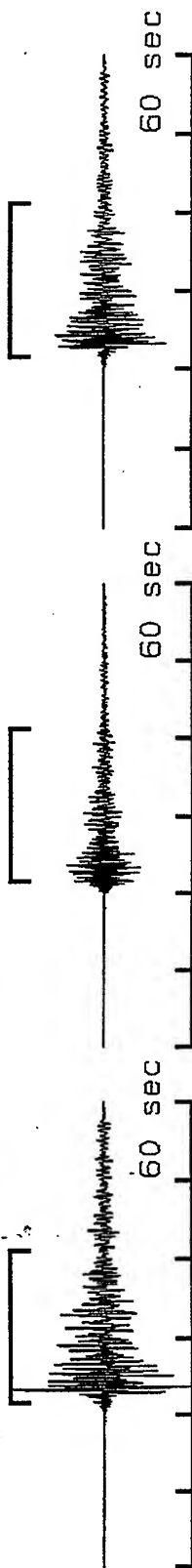
11434 Alder Creek Rd, Corona, CA 91720

Tel - Fax (714) 692-1443, E-Mail: mahdyiar@coda.usc.edu

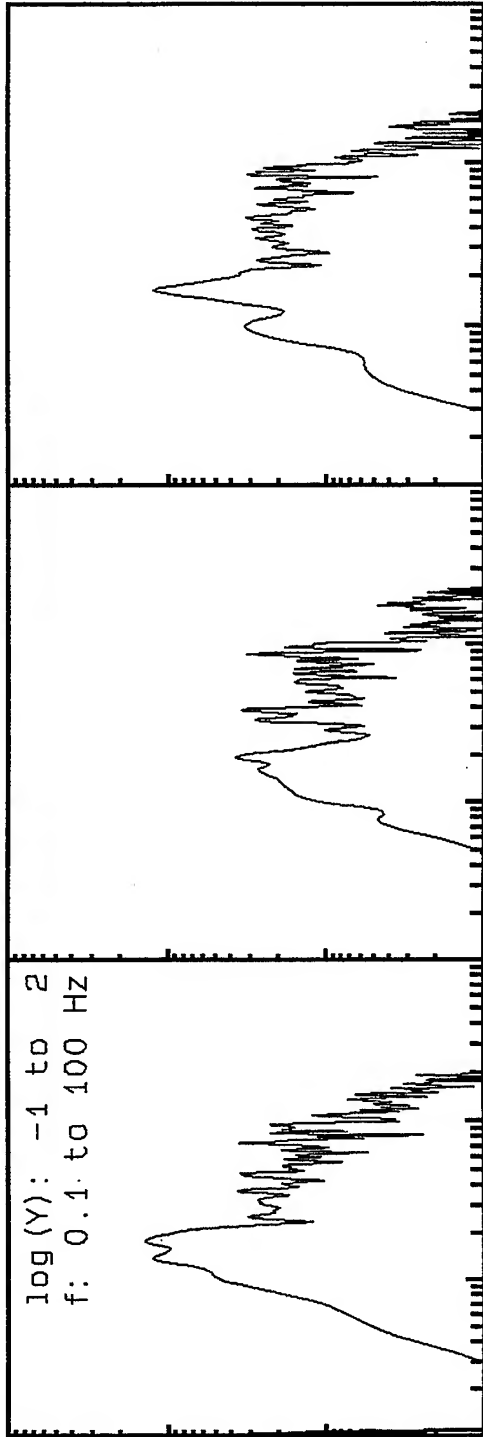




514\_jfpp, Window: 21.6 to 41.2 s

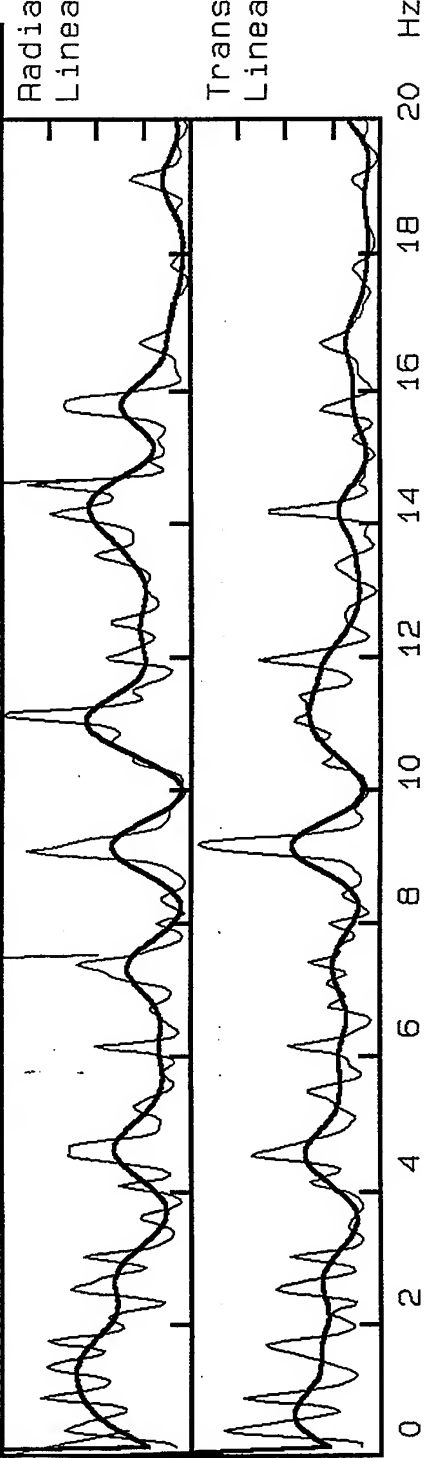


log (Y): -1 to 2  
f: 0.1 to 100 Hz

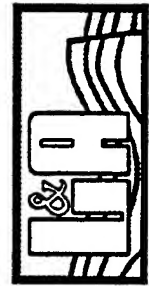


Radial/Vertical  
Linear Scale 0-8

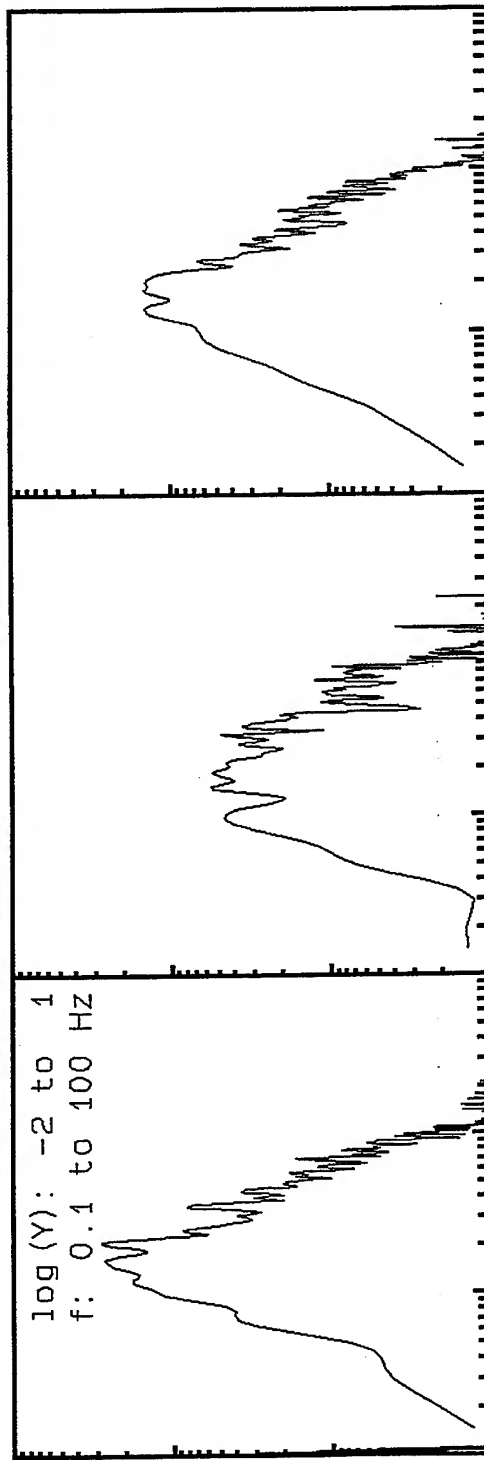
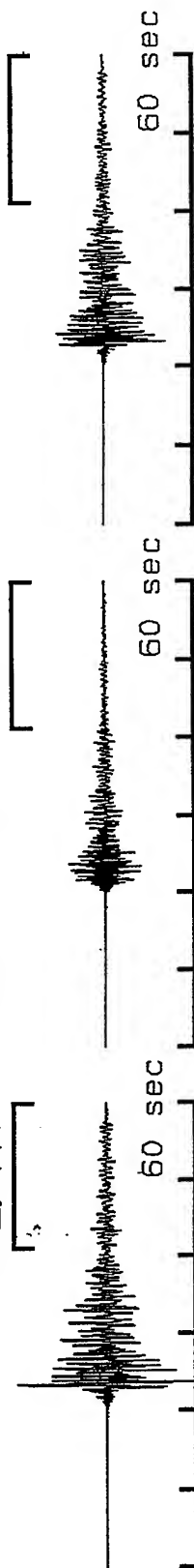
Transvers/Vertical  
Linear Scale 0-8



**VortexRock Consultants, Inc.**  
11434 Alder Creek Rd, Corona, CA 91720  
Tel - Fax (714) 692-1443, E-Mail: mahdyiar@coda.usc.edu

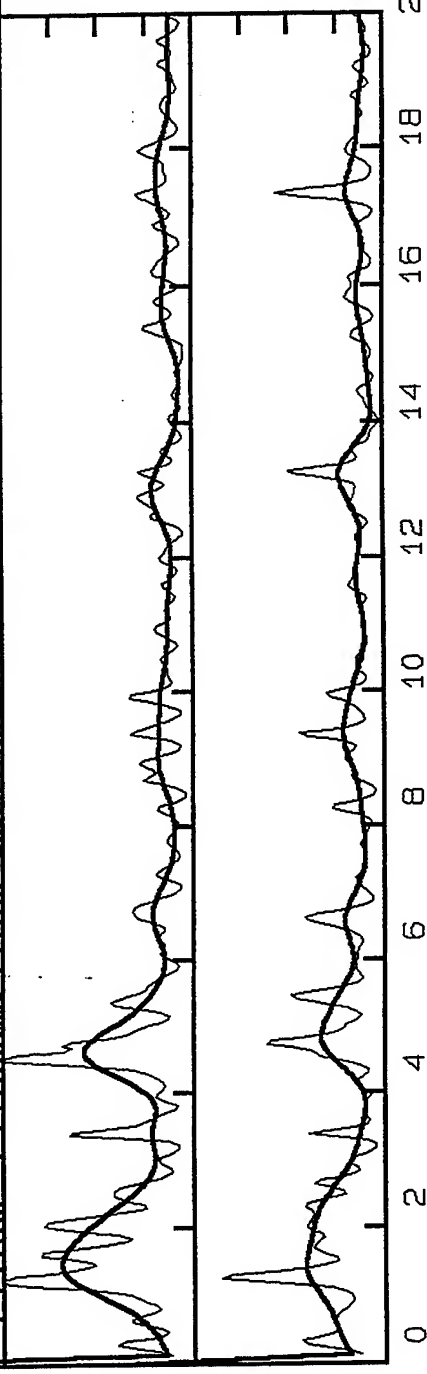


514\_jfpp, Window: 41.2 to 60.0 s

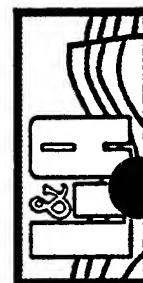


Radial/Vertical  
Linear Scale 0-8

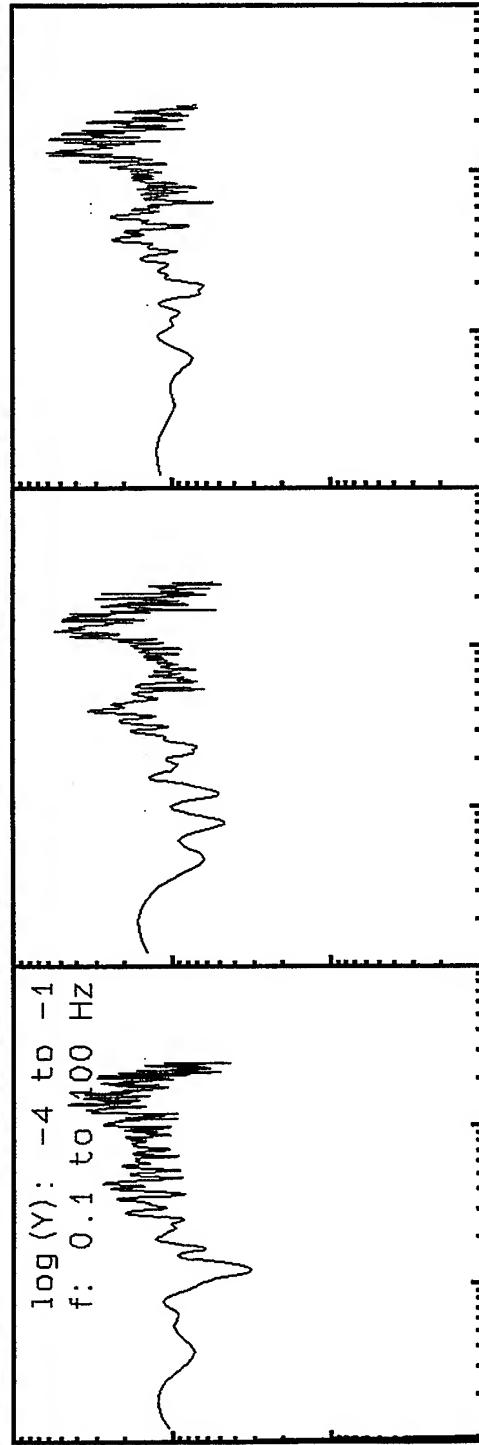
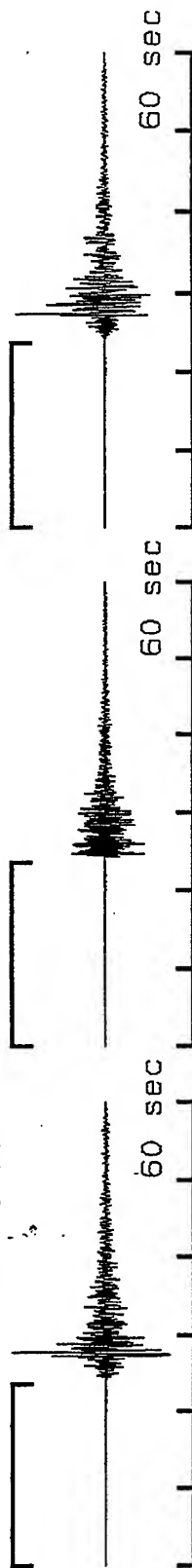
Transvers/Vertical  
Linear Scale 0-8



**VortexRock Consultants, Inc.**  
11434 Alder Creek Rd, Corona, CA 91720  
Tel - Fax (714) 692-1443, E-Mail: mahdyiar@coda.usc.edu



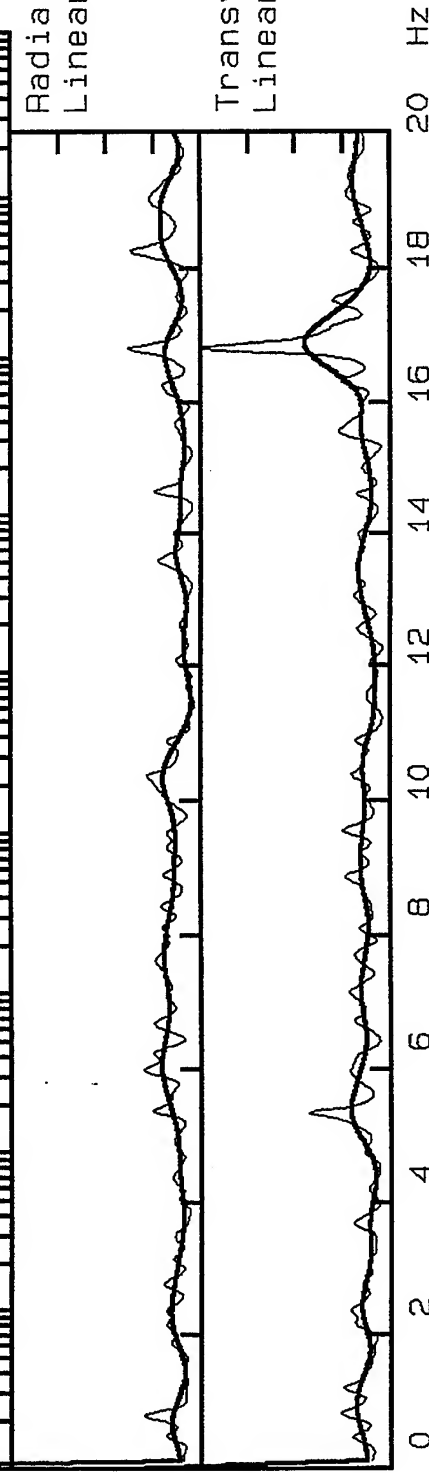
515\_jfpp, Window: .0 to 23.6 s



log (Y): -4 to -1  
f: 0.1 to 100 Hz

Radial/Vertical  
Linear Scale 0-8

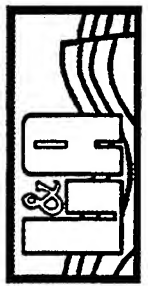
Transvers/Vertical:  
Linear Scale 0-8



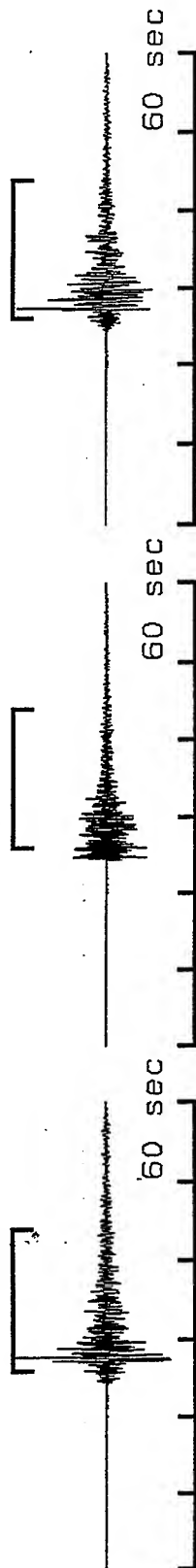
**VortexRock Consultants, Inc.**

11434 Alder Creek Rd, Corona, CA 91720

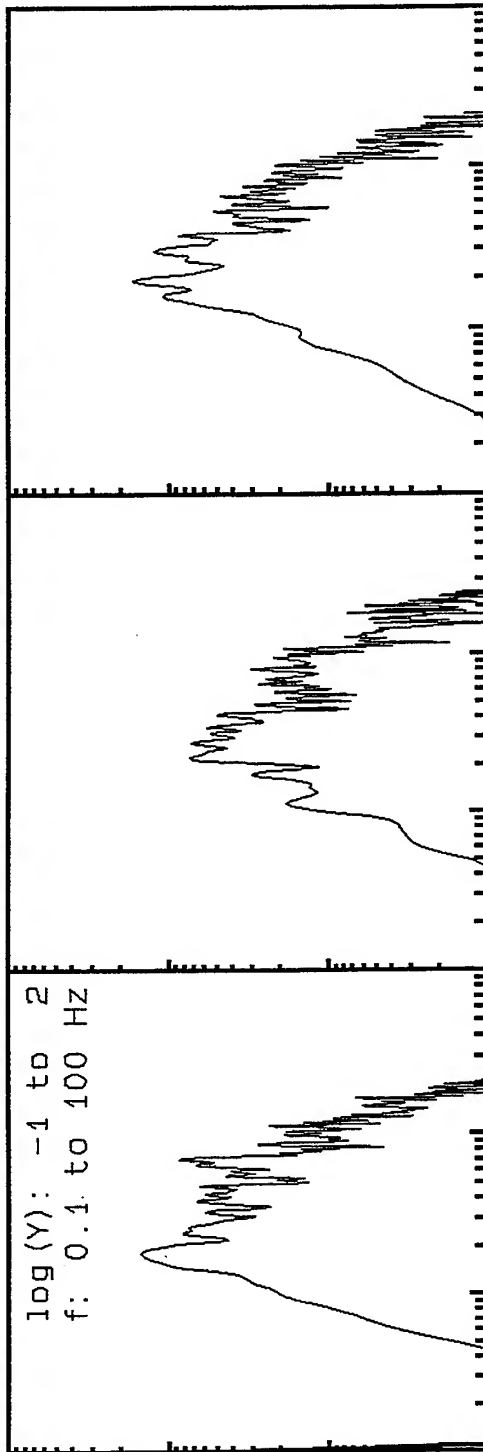
Tel - Fax (714) 692-1443; E-Mail: mahdyiar@codia.usc.edu



515\_jfpp, Window: 26.0 to 44.0 s



log (Y): -1 to 2  
f: 0.1 to 100 Hz



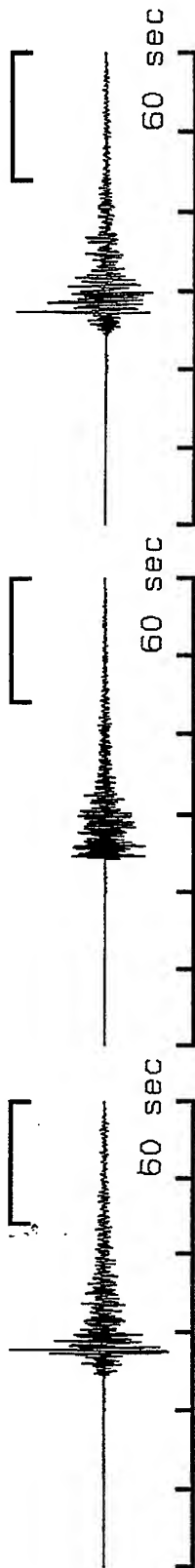
Radial/Vertical  
Linear Scale 0-8

Transvers/Vertical:  
Linear Scale 0-8

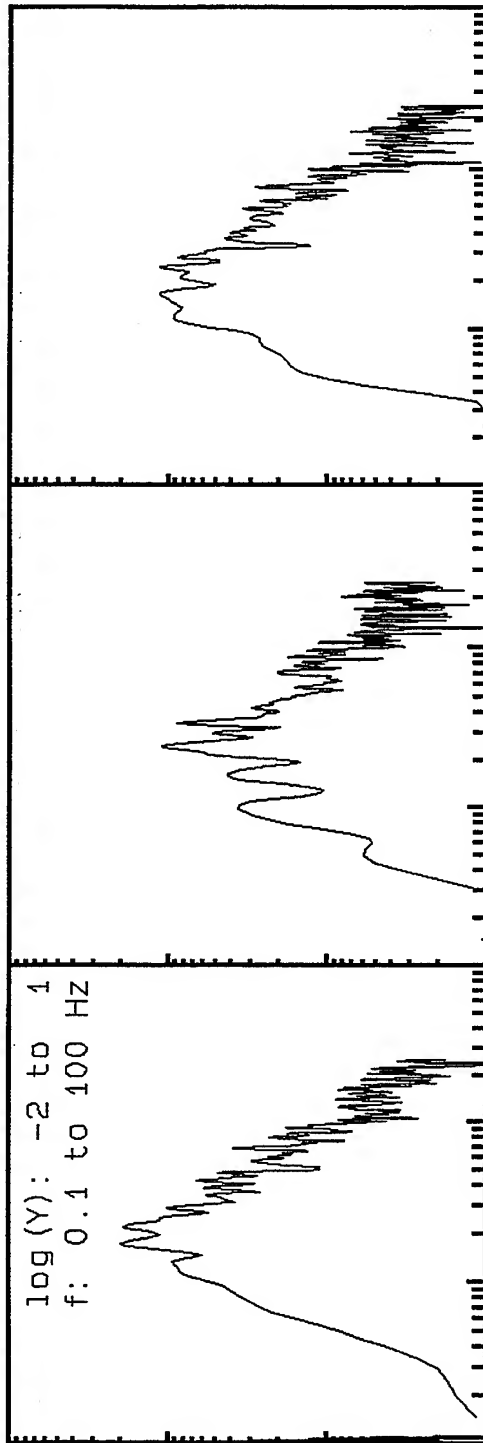
0 2 4 6 8 10 12 14 16 18 20 Hz



515\_jfpp, Window: 44.0 to 60.0 s

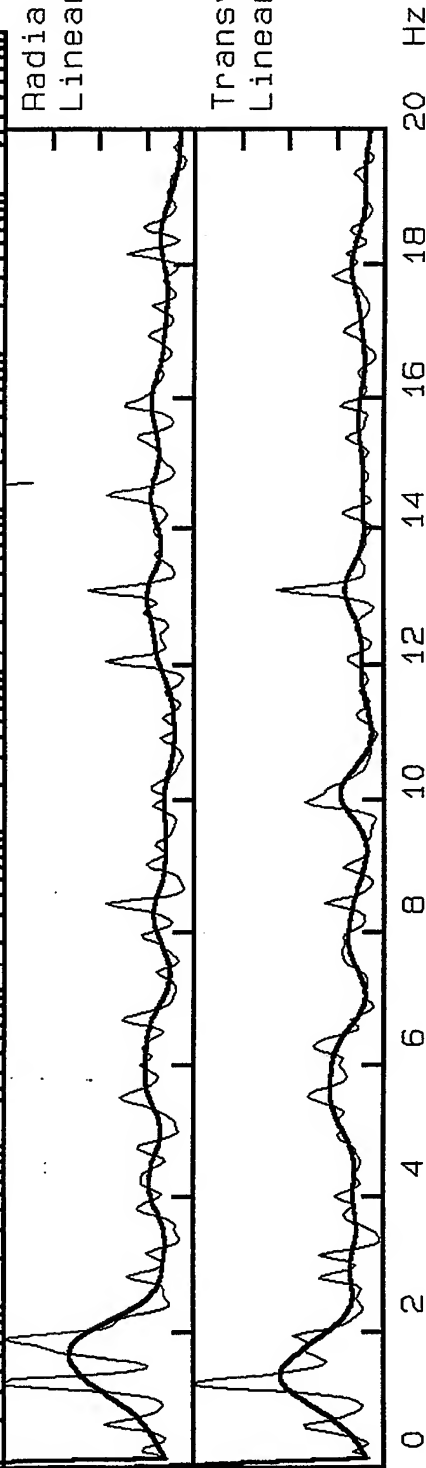


log (Y): -2 to 1  
f: 0.1 to 100 Hz

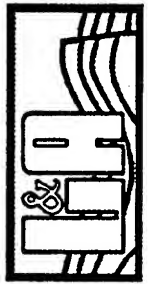


Radial/Vertical  
Linear Scale 0-8

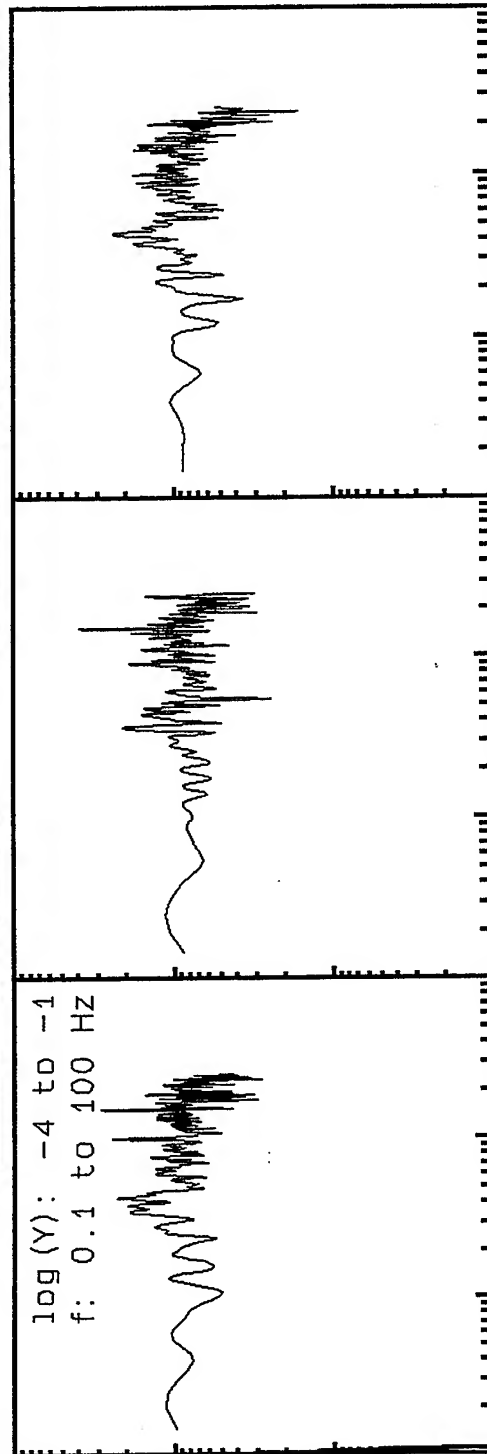
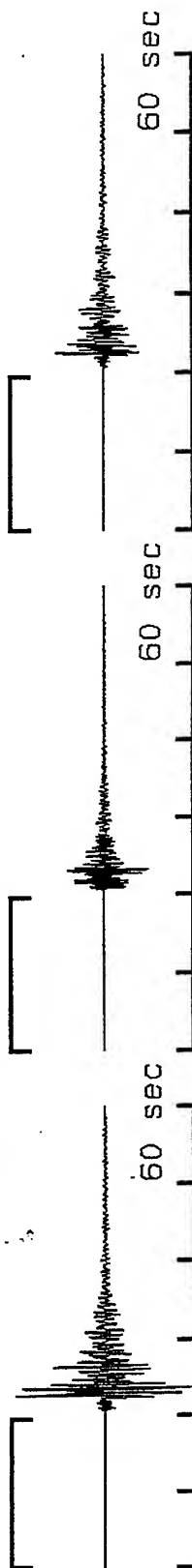
Transvers/Vertical:  
Linear Scale 0-8



**VortexRock Consultants, Inc.**  
11434 Alder Creek Rd, Corona, CA 91720  
Tel - Fax (714) 692-1443, E-Mail: mahdyar@coda.usc.edu

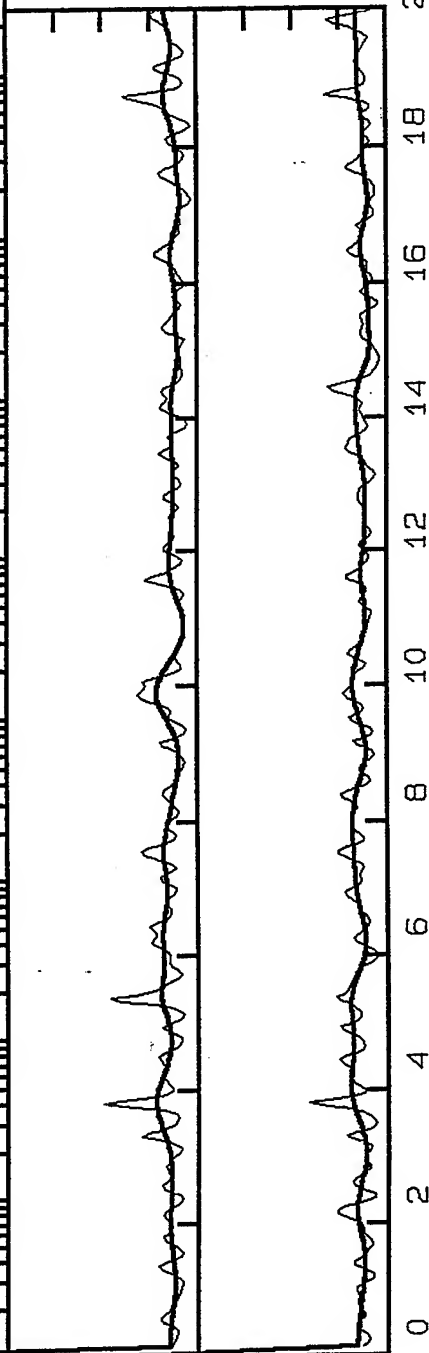


516\_jfpp, Window: .0 to 19.6 s

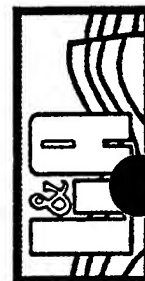


Radial/Vertical  
Linear Scale 0-8

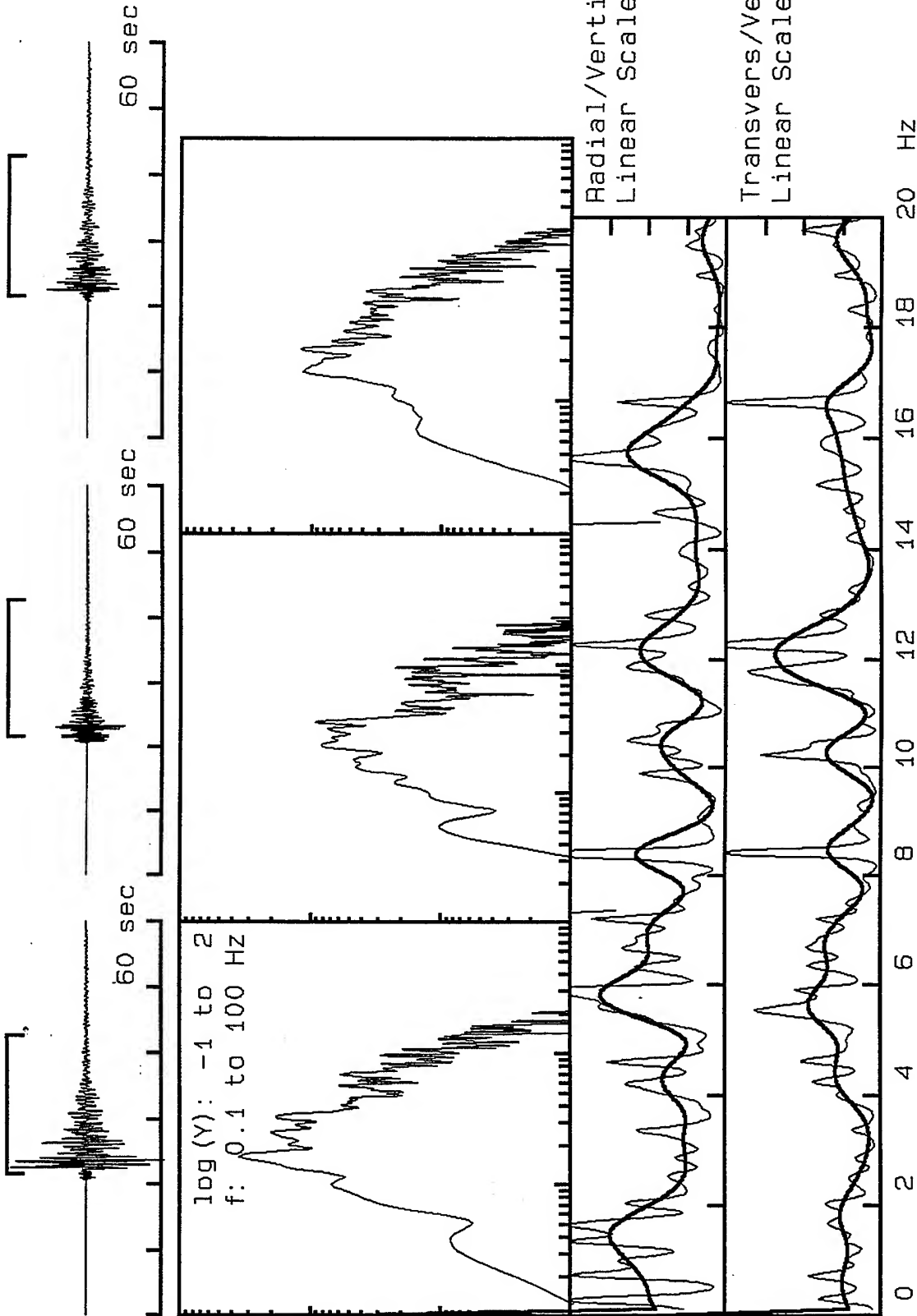
Transvers/Vertical:  
Linear Scale 0-8



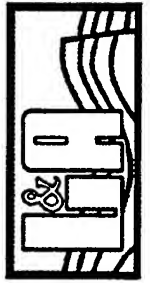
**VortexRock Consultants, Inc.**  
11434 Alder Creek Rd, Corona, CA 91720  
Tel - Fax (714) 692-1443, E-Mail: mahdyar@coda.usc.edu



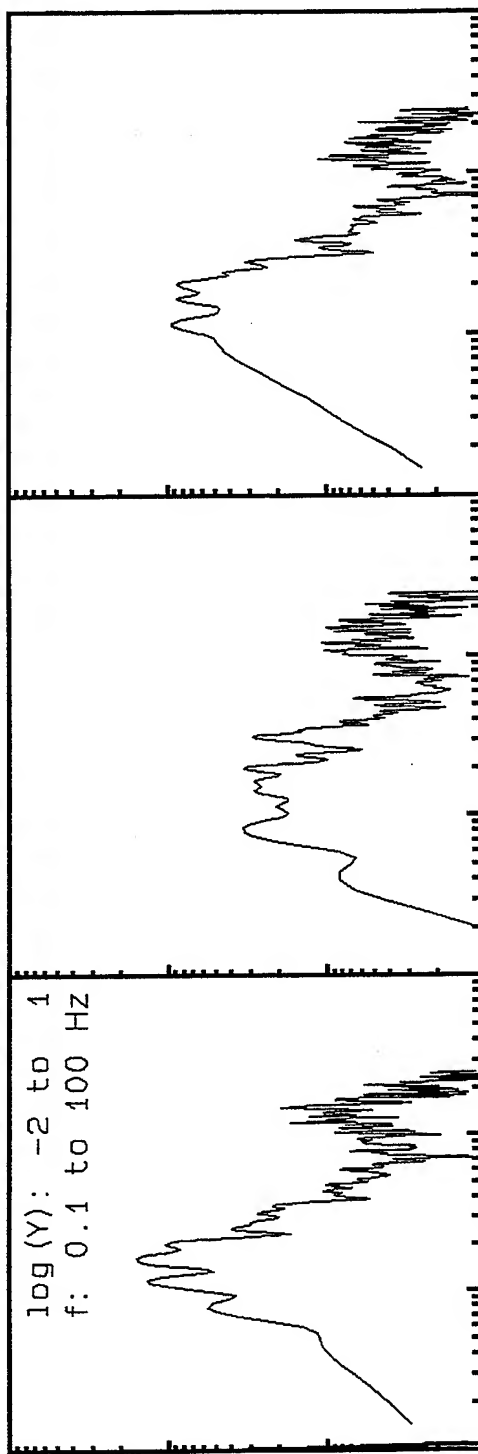
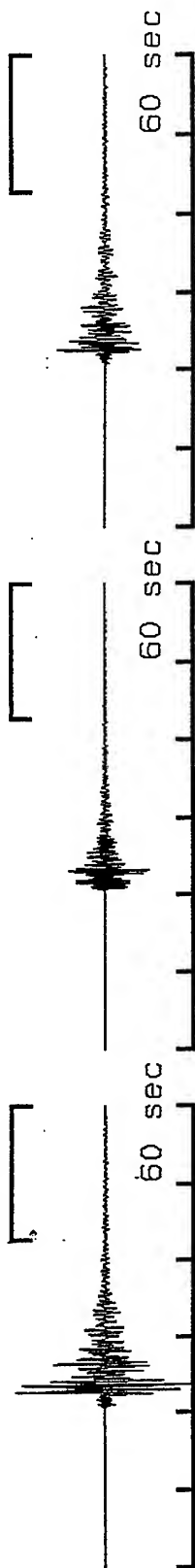
516\_jfpp, Window: 21.6 to 42.8 s



**VortexRock Consultants, Inc.**  
11434 Alder Creek Rd, Corona, CA 91720  
Tel - Fax (714) 692-1443, E-Mail: mahdyar@coda.usc.edu

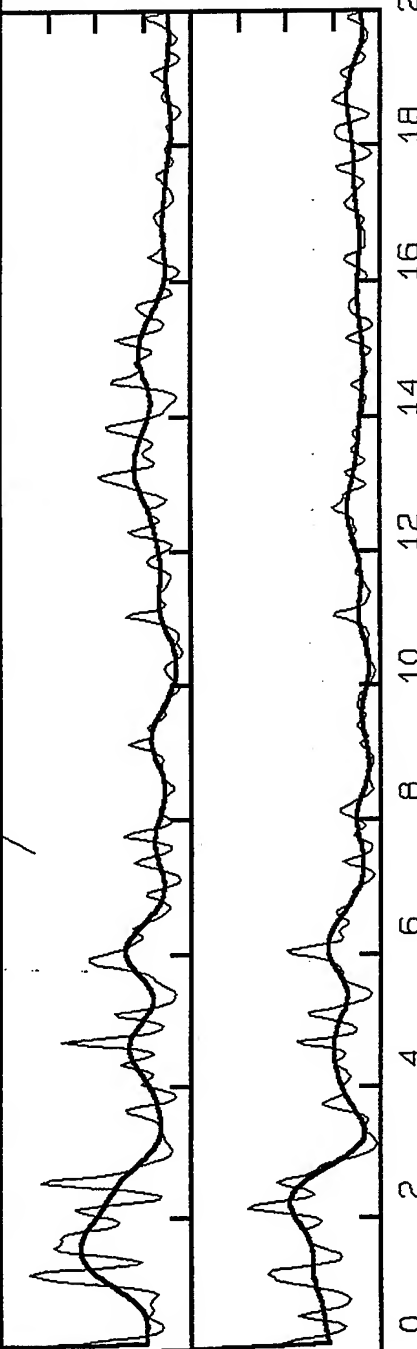


516\_jfpp, Window: 42.8 to 60.0 s

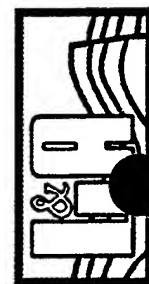


Radial/Vertical  
Linear Scale 0-8

Transvers/Vertical:  
Linear Scale 0-8

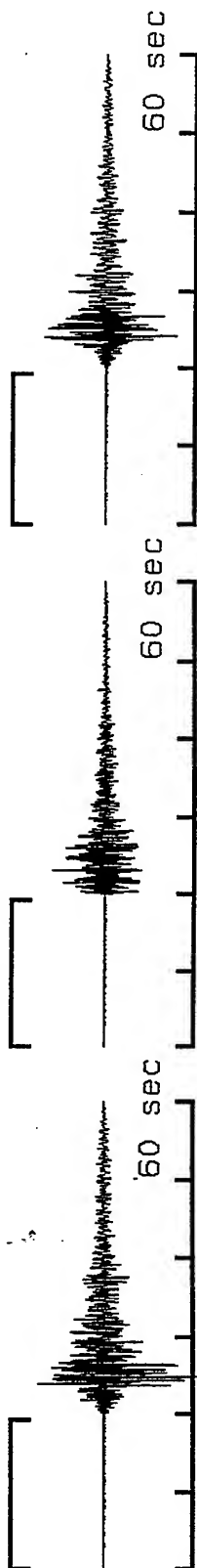


**VortexRock Consultants, Inc.**  
11434 Alder Creek Rd, Corona, CA 91720  
Tel - Fax (714) 692-1443, E-Mail: mahdyiar@coda.usc.edu

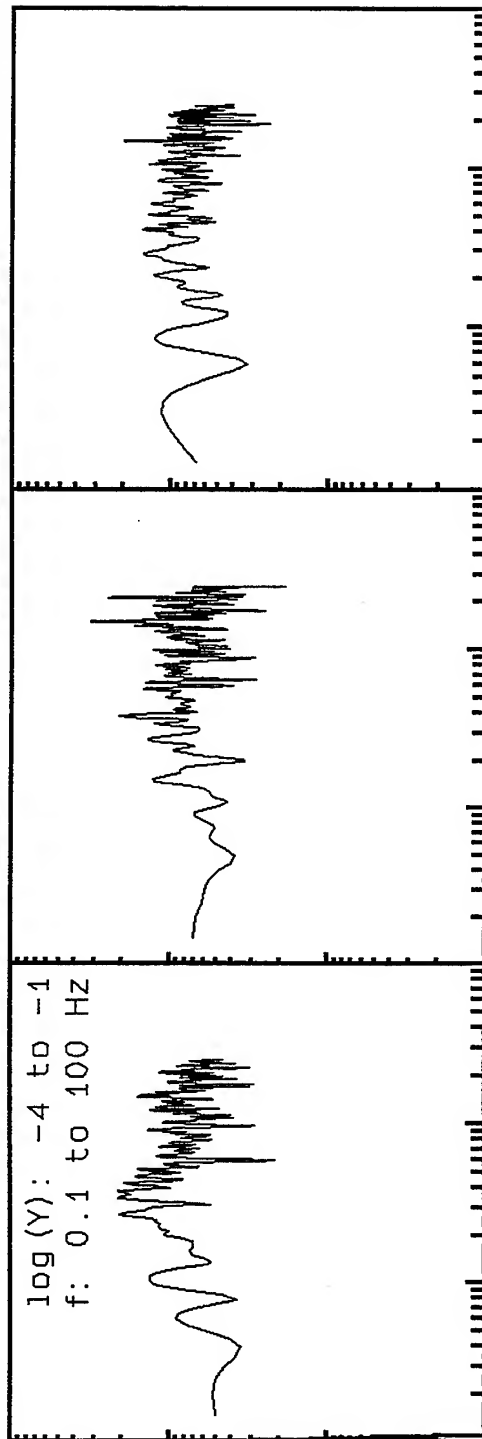




518\_jfpp, Window: .0 to 19.2 s



log (Y): -4 to -1  
f: 0.1 to 100 Hz



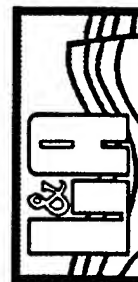
Radial/Vertical  
Linear Scale 0-8

Transvers/Vertical:  
Linear Scale 0-8

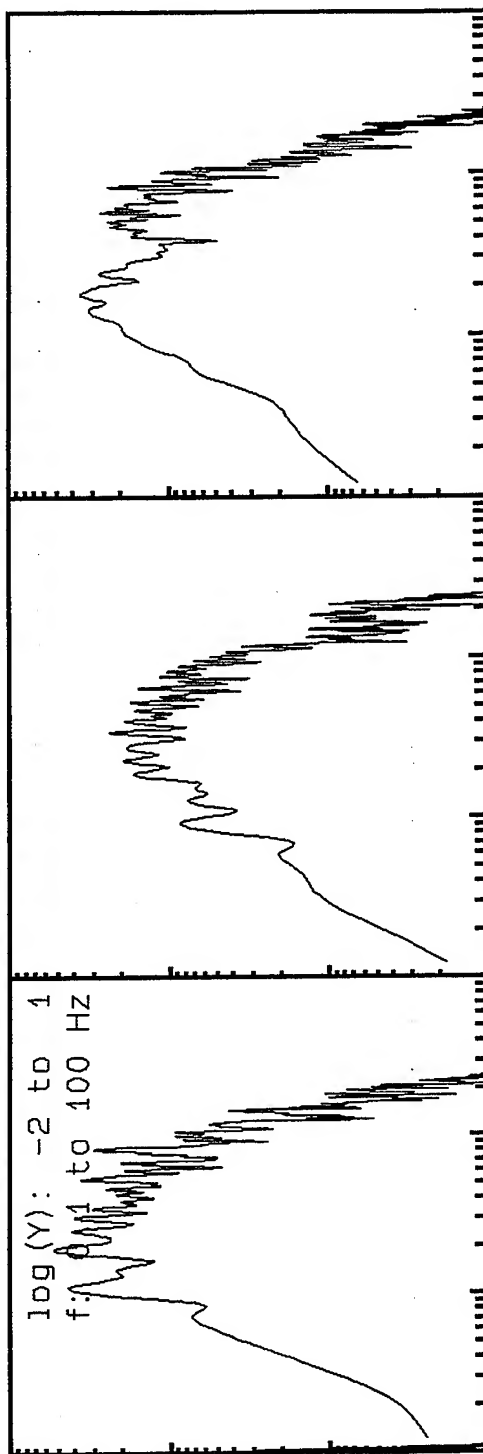
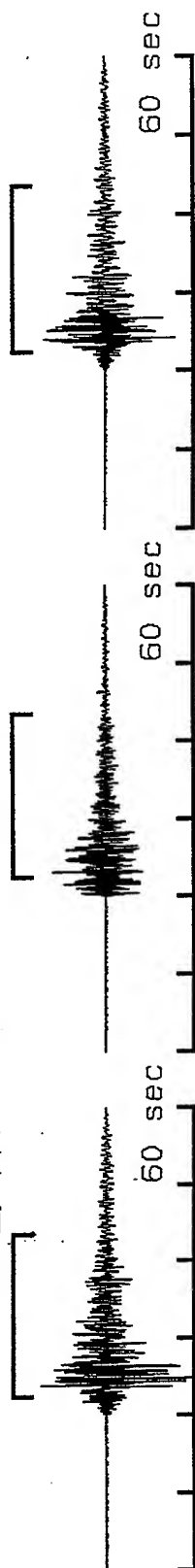
0 2 4 6 8 10 12 14 16 18 20 Hz



**VortexRock Consultants, Inc.**  
11434 Alder Creek Rd, Corona, CA 91720  
Tel - Fax (714) 692-1443, E-Mail: mahdytar@coda.usc.edu

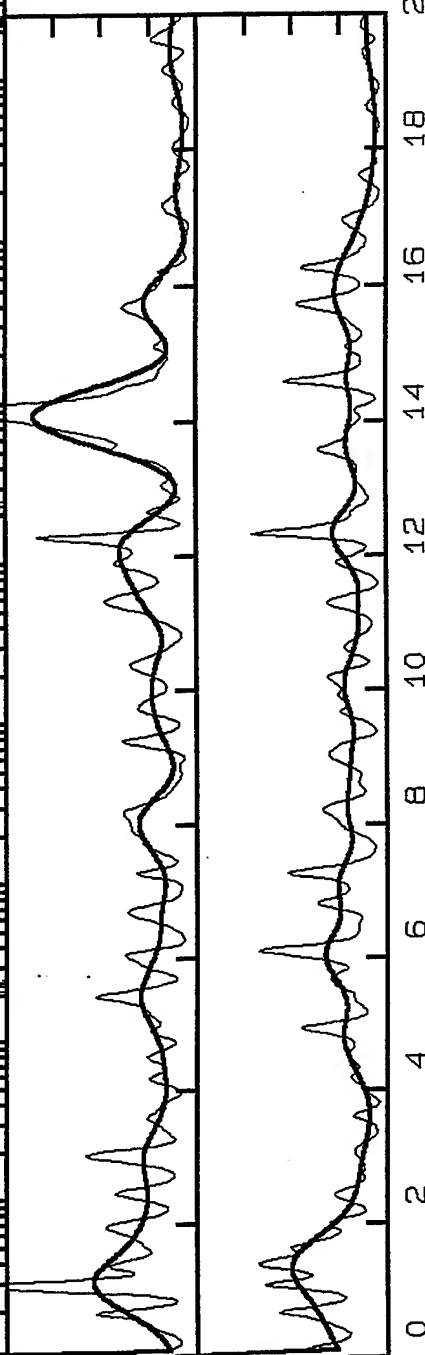


518\_jfpp, Window: 22.4 to 43.6 s



Radial/Vertical  
Linear Scale 0-8

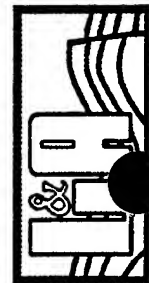
Transvers/Vertical:  
Linear Scale 0-8



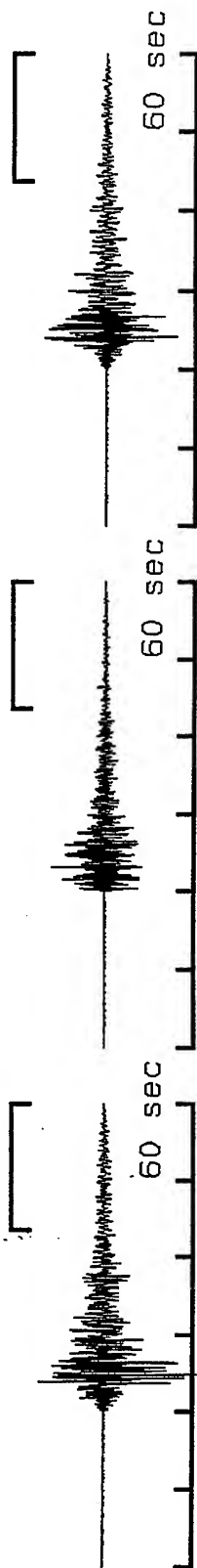
**VortexRock Consultants, Inc.**

11434 Alder Creek Rd, Corona, CA 91720

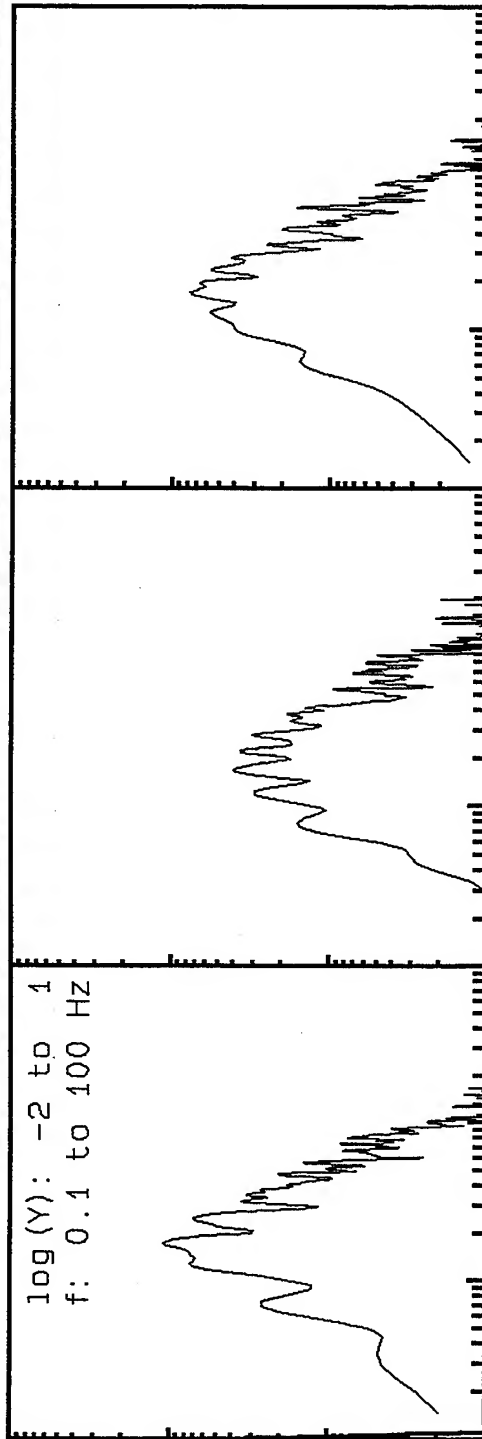
Tel - Fax (714) 692-1443, E-Mail: mahdyar@coda.usc.edu



518\_jfpp, Window: 43.6 to 60.0 s

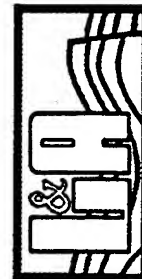
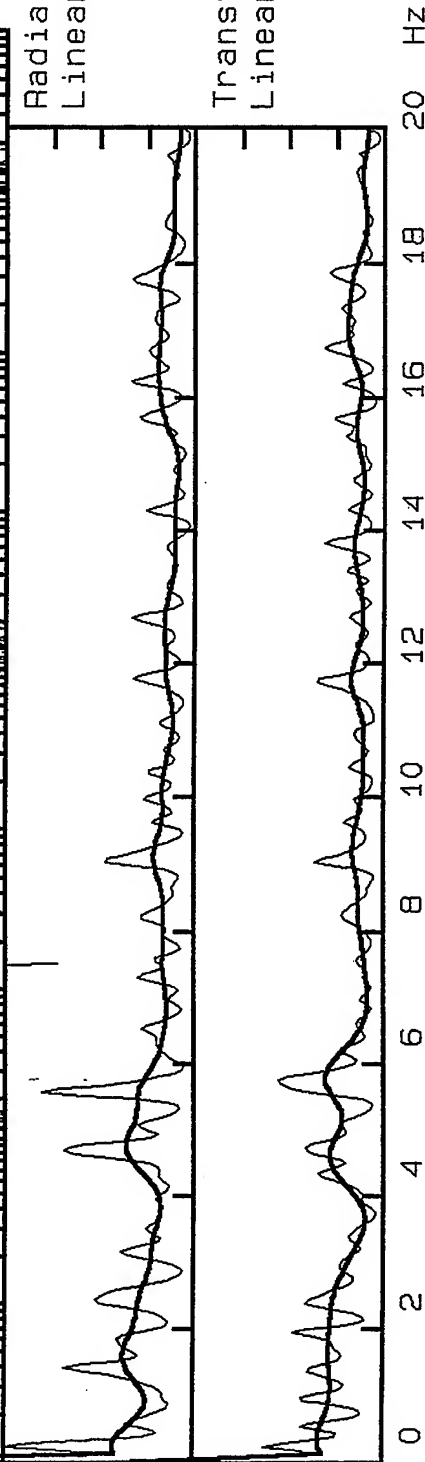


log (Y): -2 to 1  
f: 0.1 to 100 Hz

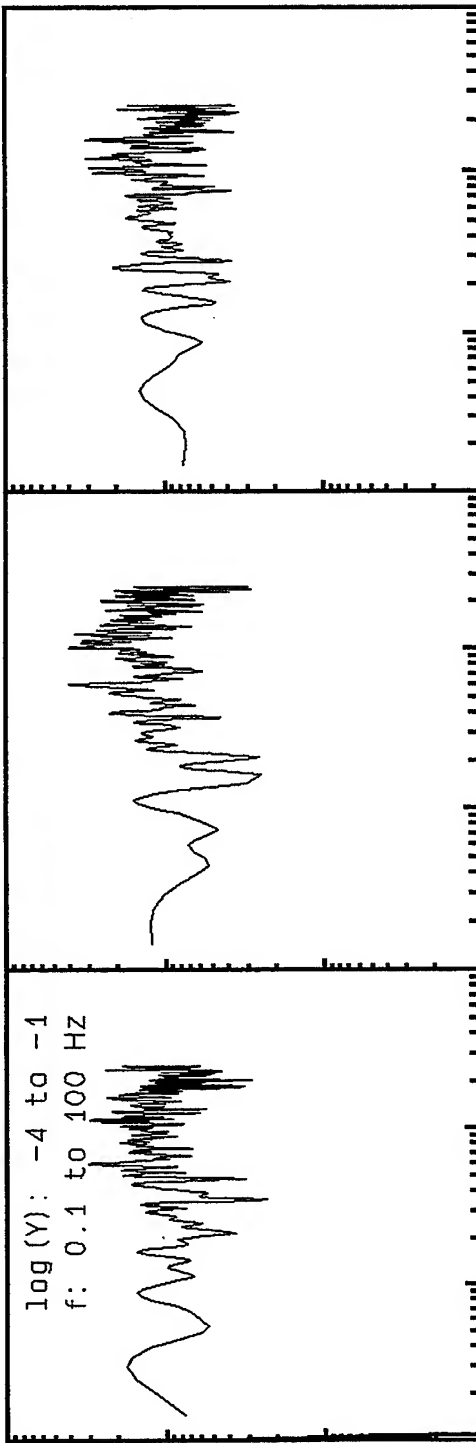
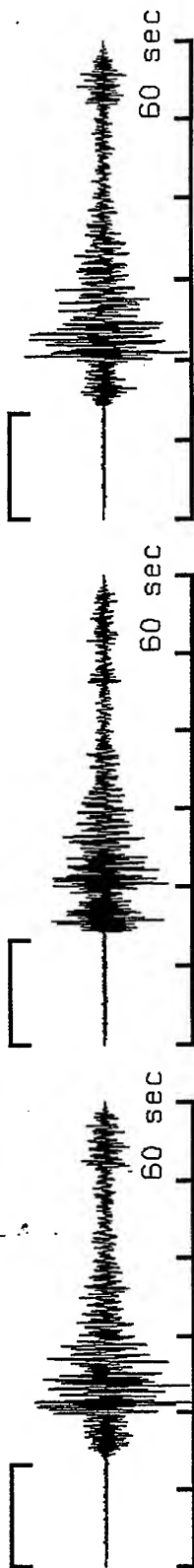


Radial/Vertical  
Linear Scale 0-8

Transvers/Vertical:  
Linear Scale 0-8

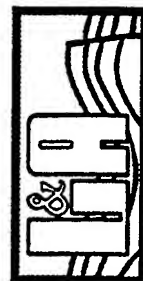
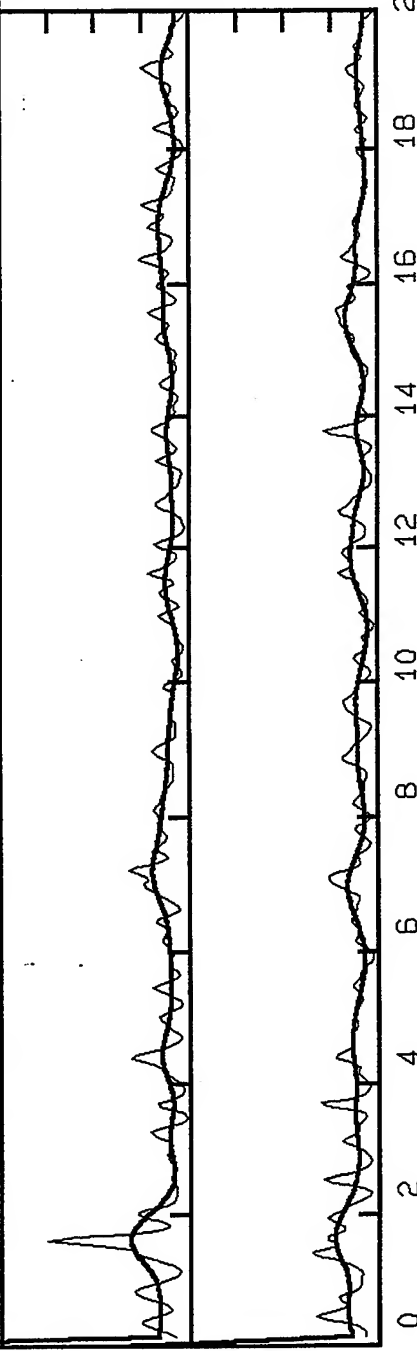


110\_la04, Window: .0 to 13.2 s

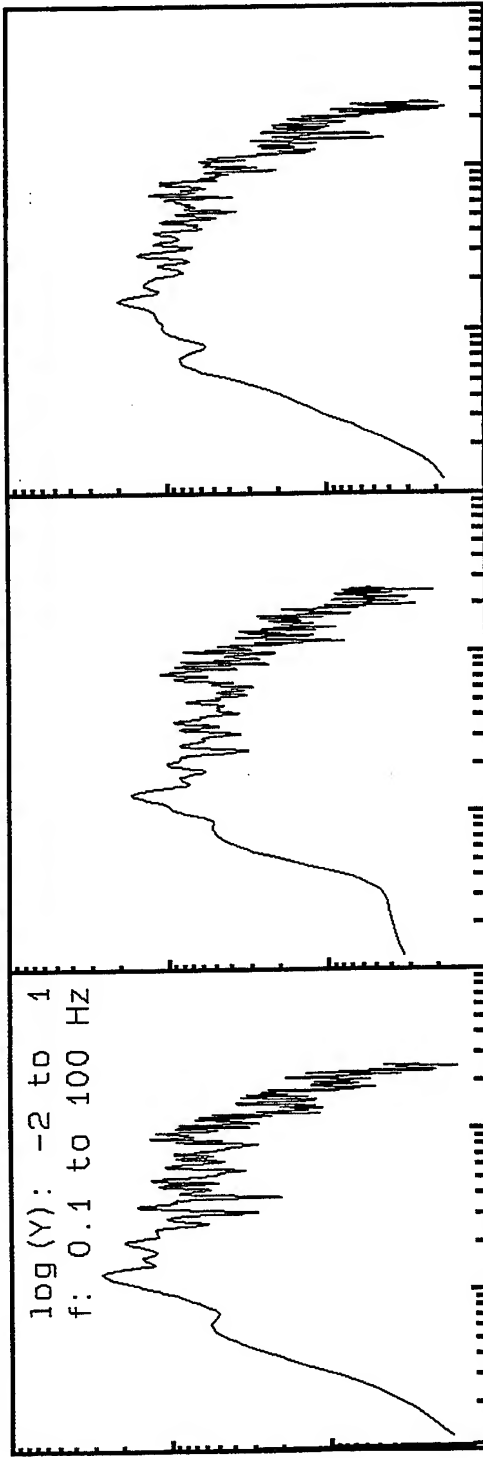
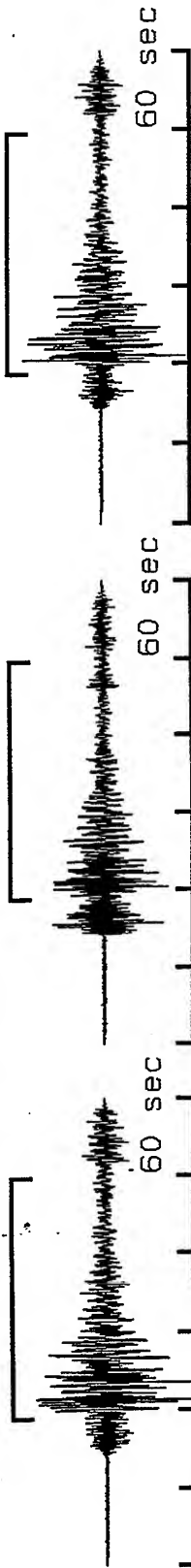


Radial/Vertical  
Linear Scale 0-8

Transvers/Vertical  
Linear Scale 0-8

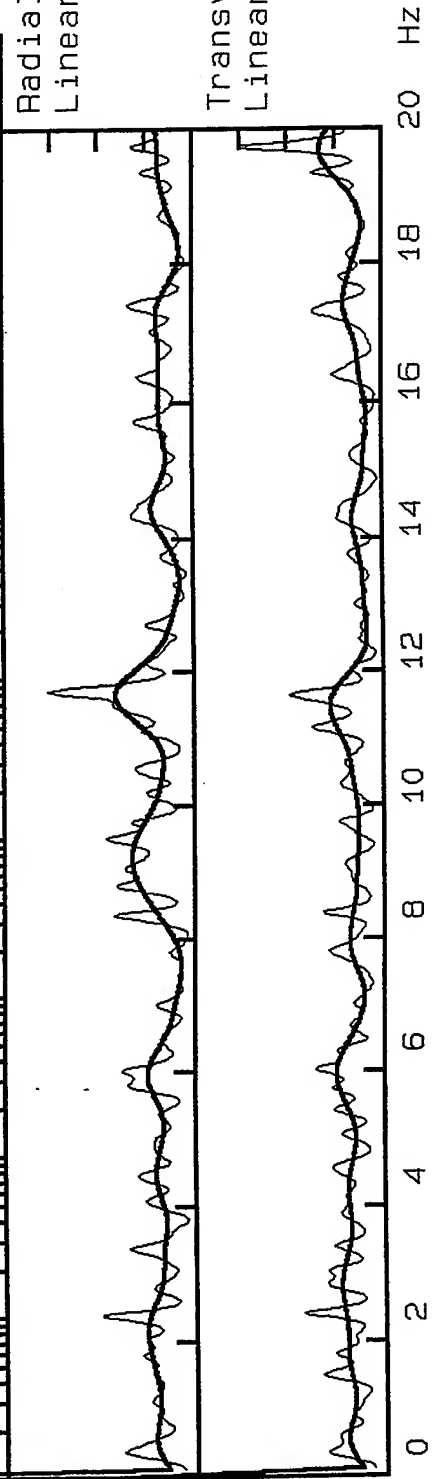


110\_la04, Window: 18.8 to 49.6 s

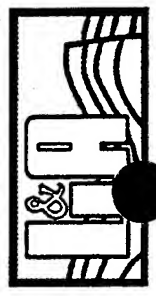


Radial/Vertical  
Linear Scale 0-8

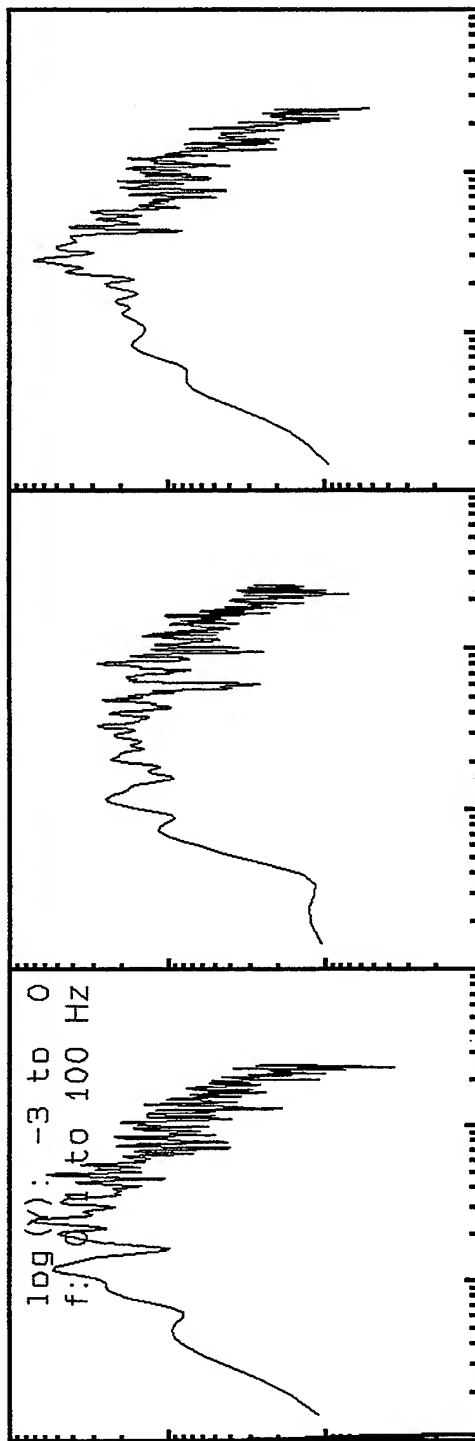
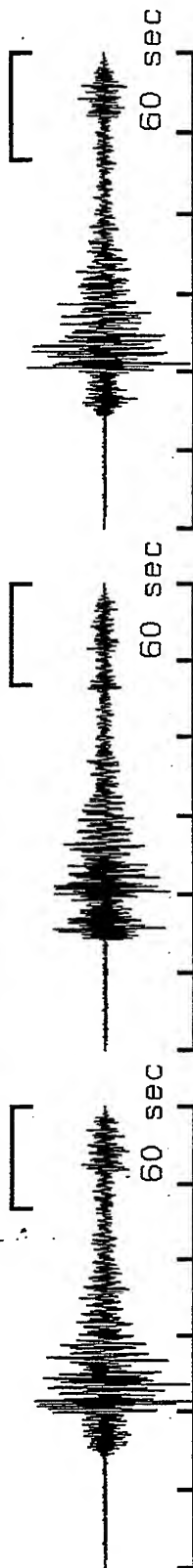
Transvers/Vertical:  
Linear Scale 0-8



**VortexRock Consultants, Inc.**  
11434 Alder Creek Rd, Corona, CA 91720  
Tel - Fax (714) 692-1443, E-Mail: mahdyiar@coda.usc.edu

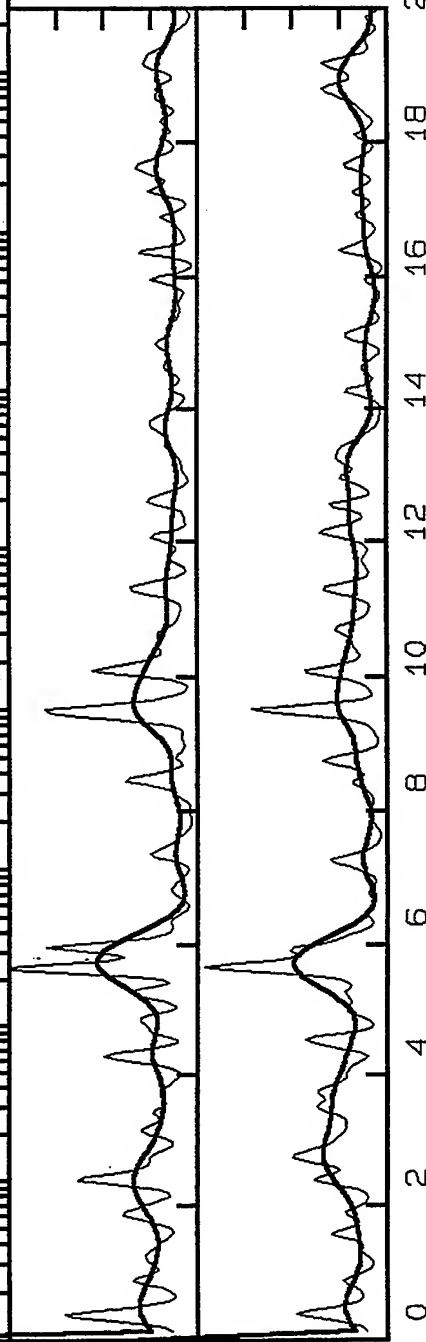


110\_la04, Window: 46.8 to 60.0 s

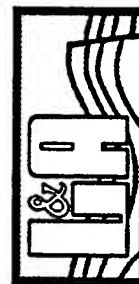


Radial/Vertical  
Linear Scale 0-8

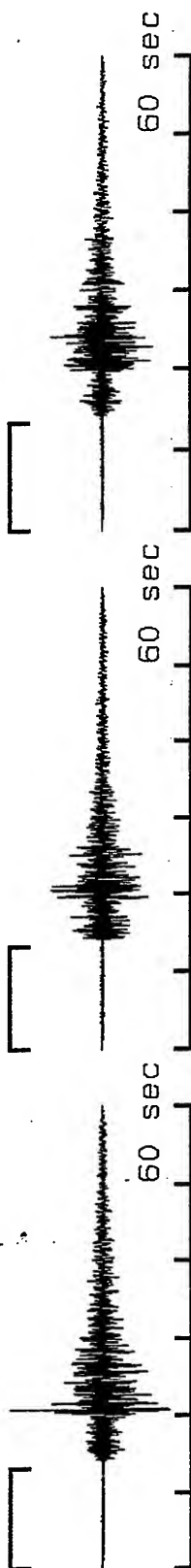
Transvers/Vertical:  
Linear Scale 0-8



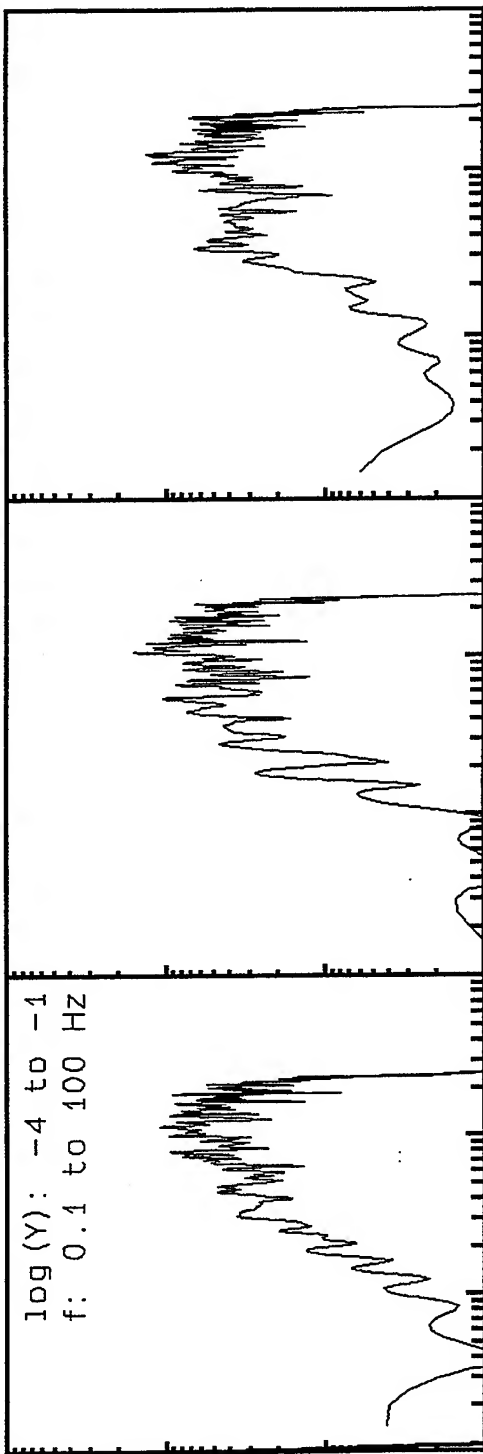
**VortexRock Consultants, Inc.**  
11434 Alder Creek Rd, Corona, CA 91720  
Tel - Fax (714) 692-1443, E-Mail: mahdyiar@coda.usc.edu



111\_la04, Window: .0 to 13.2 s

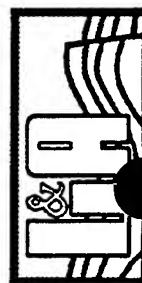
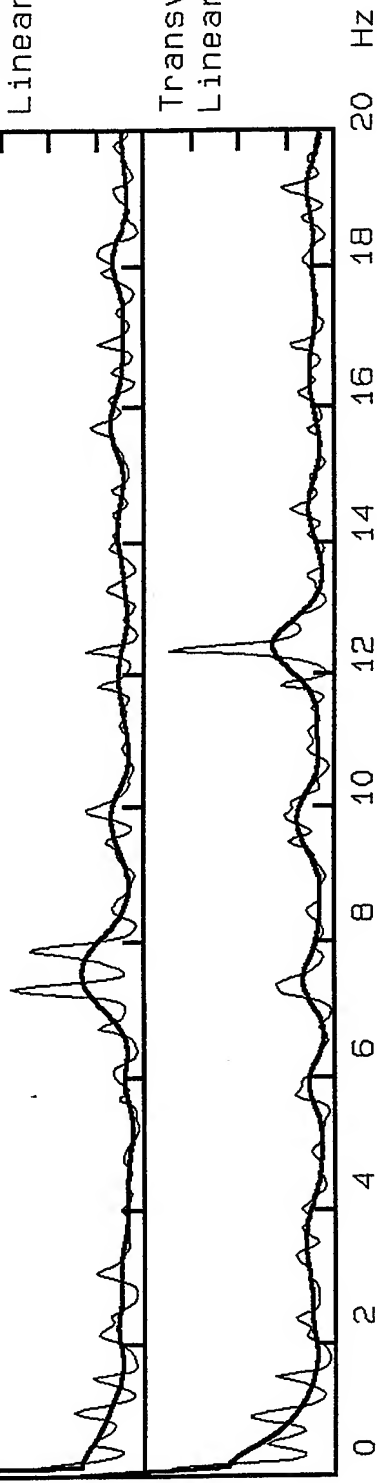


log(Y): -4 to -1  
f: 0.1 to 100 Hz

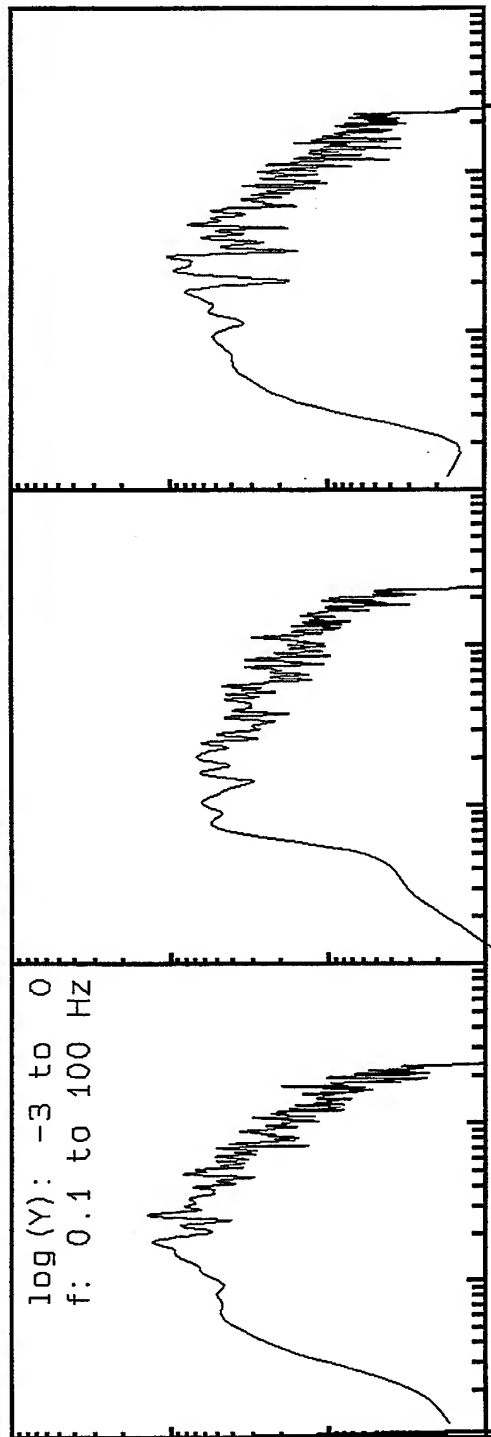
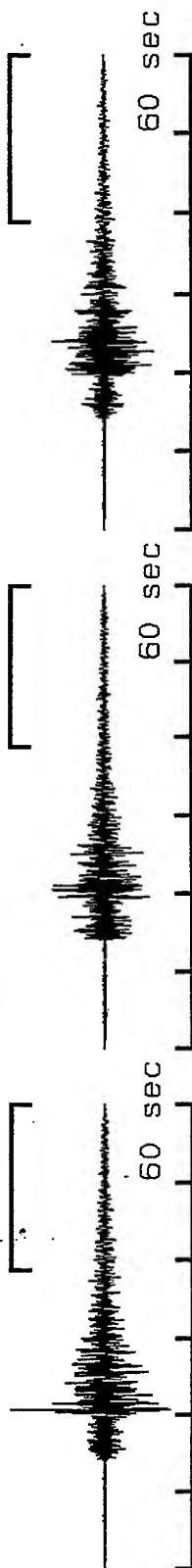


Radial/Vertical  
Linear Scale 0-8

Transvers/Vertical:  
Linear Scale 0-8

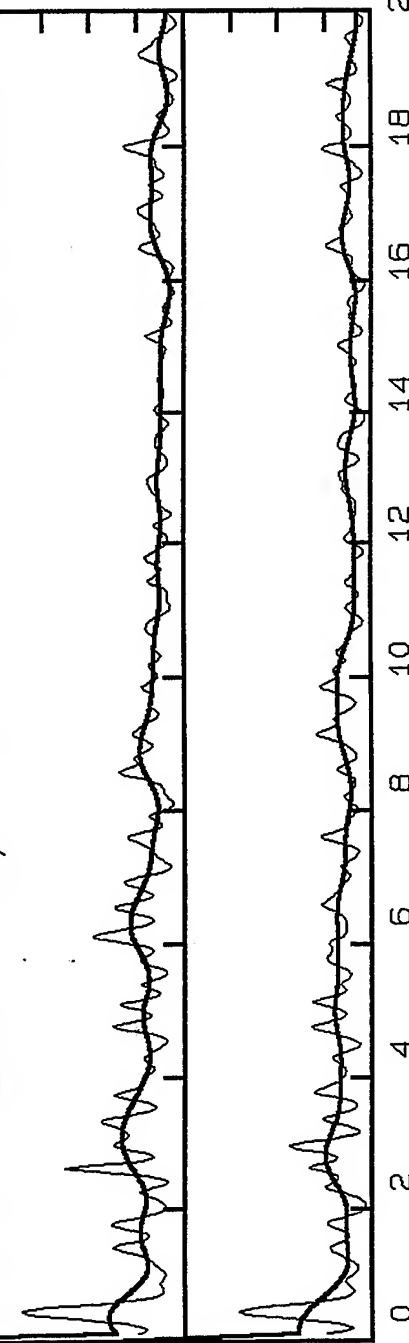


111\_1a04, Window: 38.8 to 60.0 s

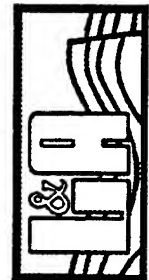


Radial/Vertical  
Linear Scale 0-8

Transvers/Vertical:  
Linear Scale 0-8

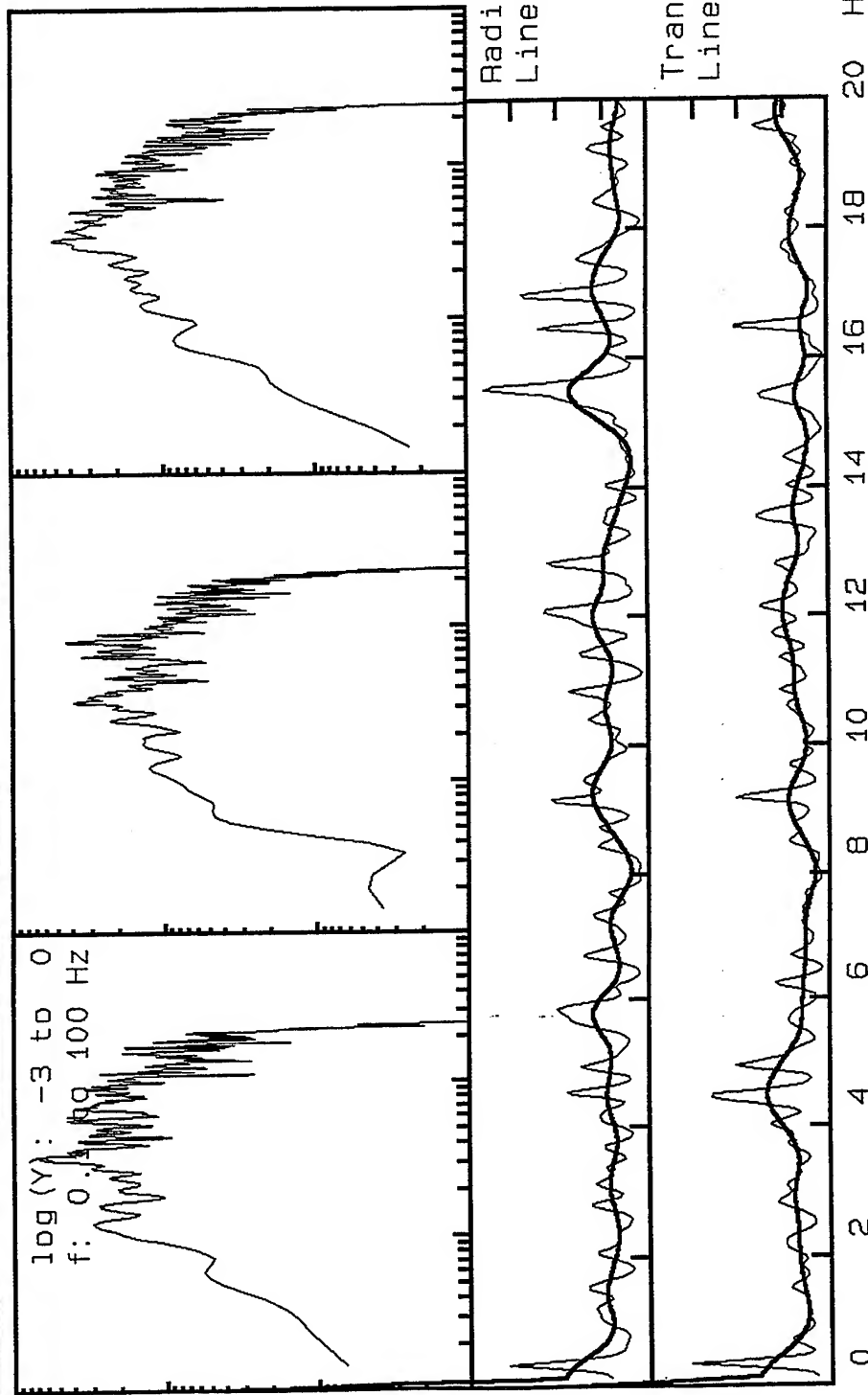
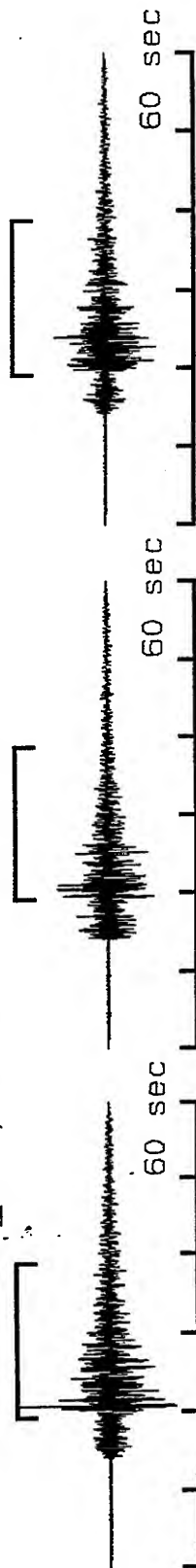


**VortexRock Consultants, Inc.**  
11434 Alder Creek Rd, Corona, CA 91720  
Tel - Fax (714) 692-1443, E-Mail: mahdyiar@coda.usc.edu

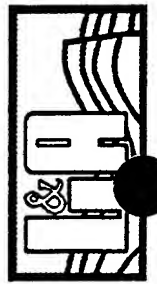




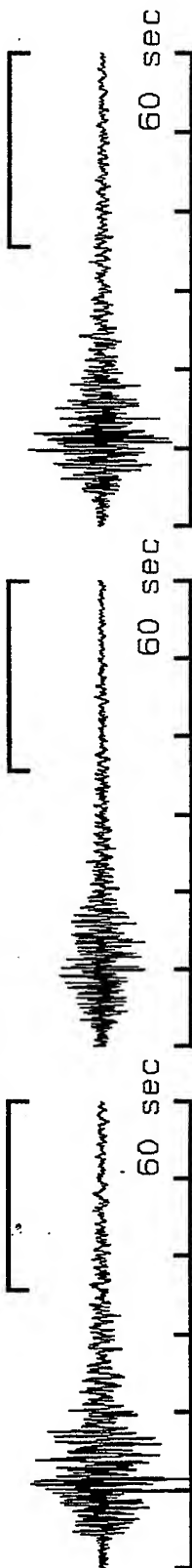
111\_la04, Window: 19.2 to 38.8 s



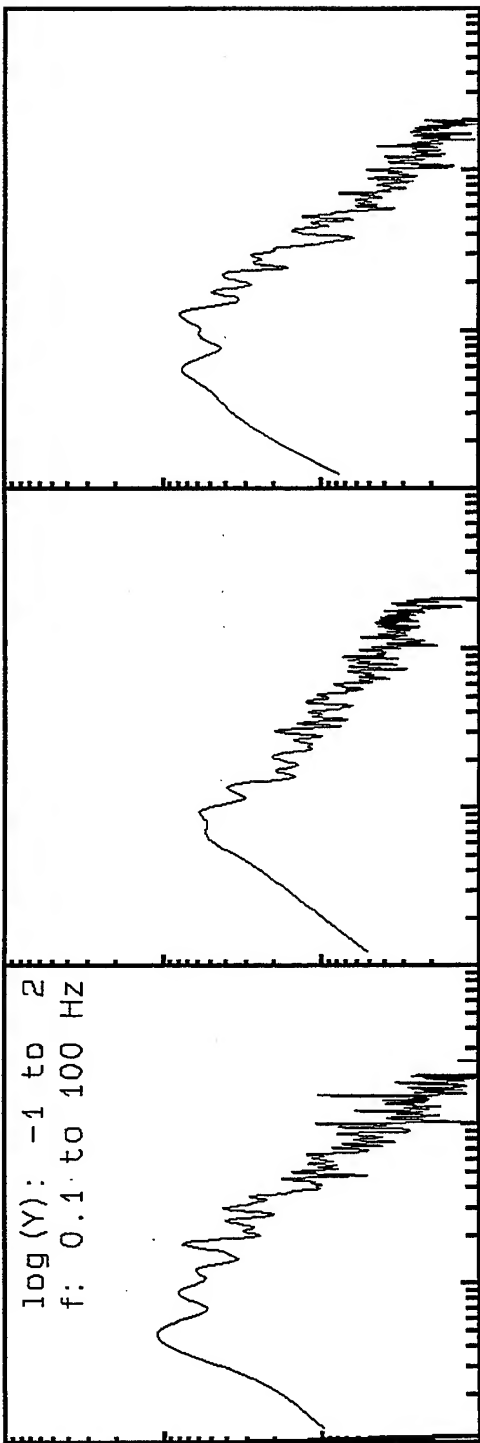
**VortexRock Consultants, Inc.**  
11434 Alder Creek Rd, Corona, CA 91720  
Tel - Fax (714) 692-1443, E-Mail: mahdyiar@coda.usc.edu



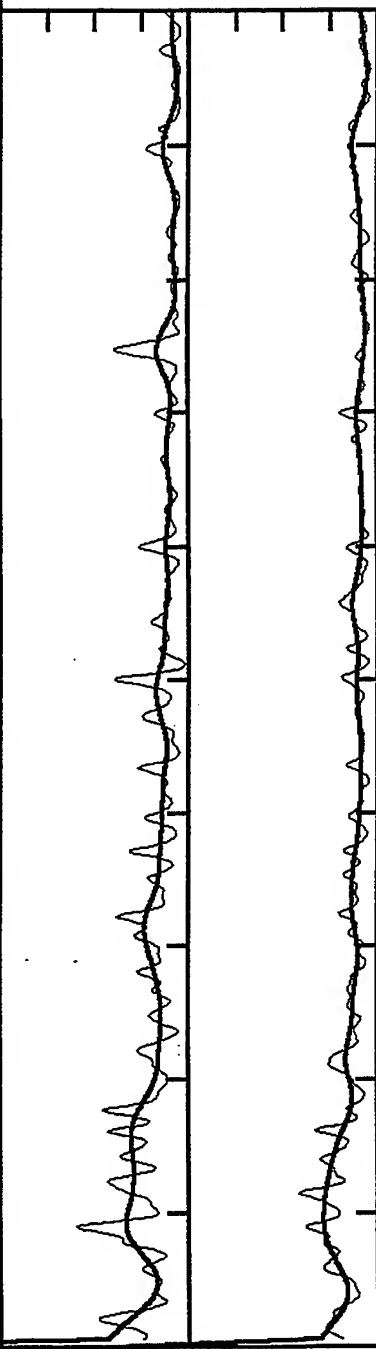
11\_alpha, Window: 35.6 to 60.0 s



log (Y): -1 to 2  
f: 0.1 to 100 Hz



Radial/Vertical  
Linear Scale 0-8

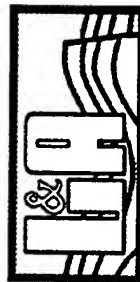


Transvers/Vertical:  
Linear Scale 0-8

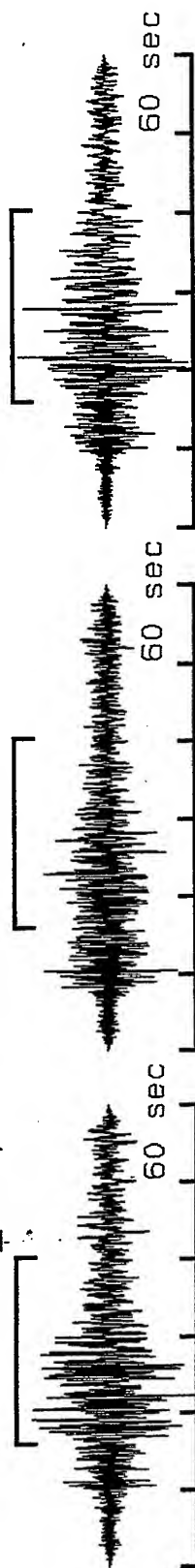
0 2 4 6 8 10 12 14 16 18 20 Hz



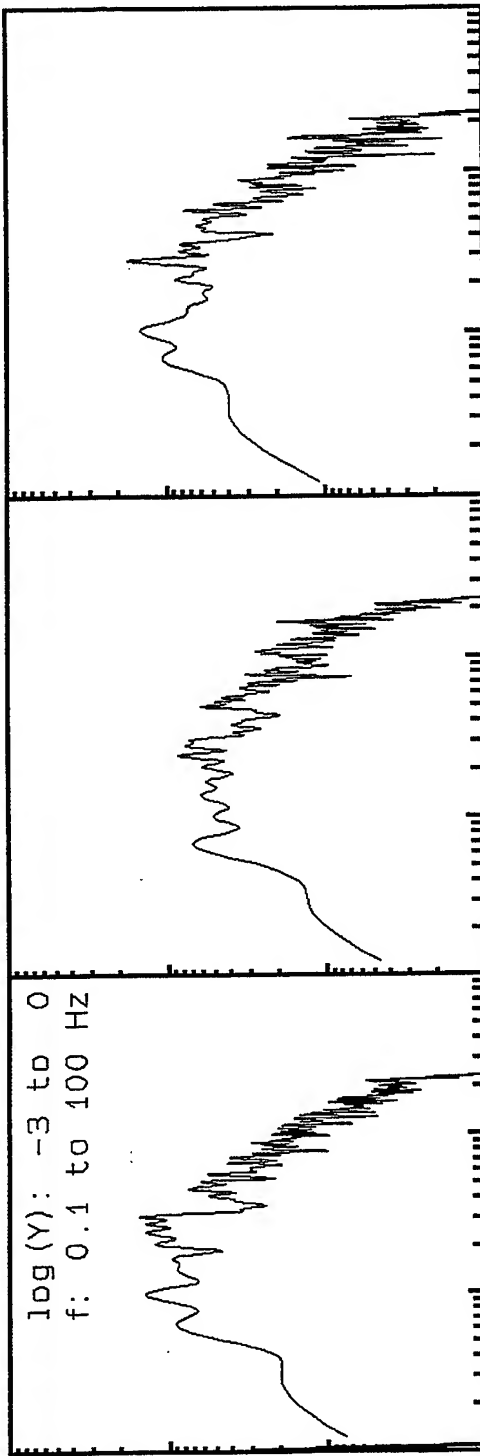
**VortexRock Consultants, Inc.**  
11434 Alder Creek Rd, Corona, CA 91720  
Tel - Fax (714) 692-1443, E-Mail: mahdiyari@coda.usc.edu



15\_la04, Window: 16.0 to 40.4 s

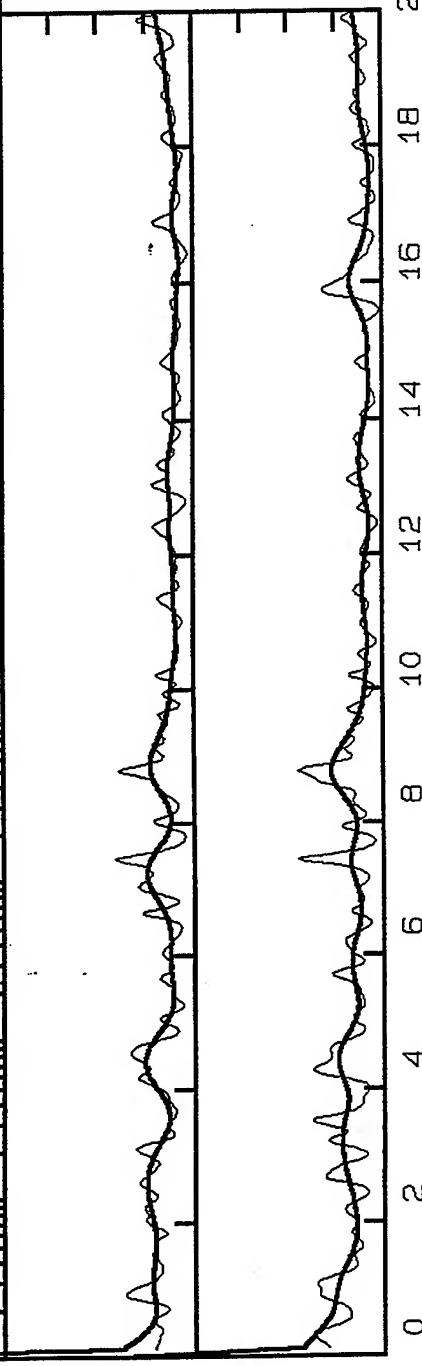


log (Y): -3 to 0  
f: 0.1 to 100 Hz

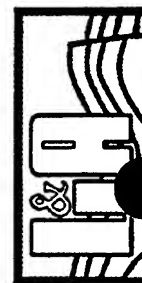


Radial/Vertical  
Linear Scale 0-8

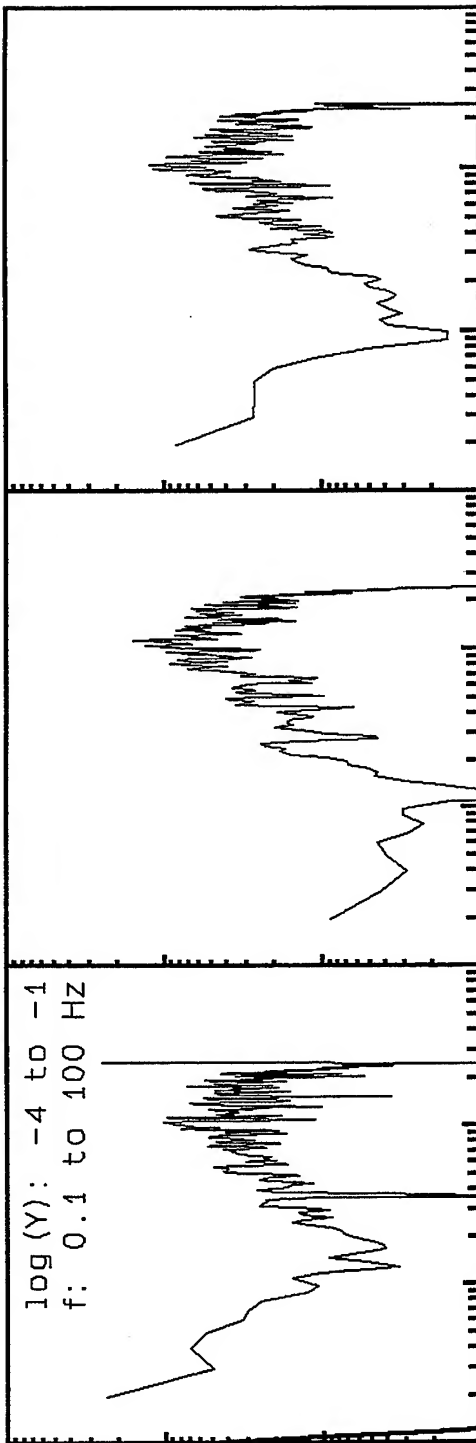
Transvers/Vertical:  
Linear Scale 0-8



**VortexRock Consultants, Inc.**  
11434 Alder Creek Rd, Corona, CA 91720  
Tel - Fax (714) 692-1443, E-Mail: mahdyiar@coda.usc.edu

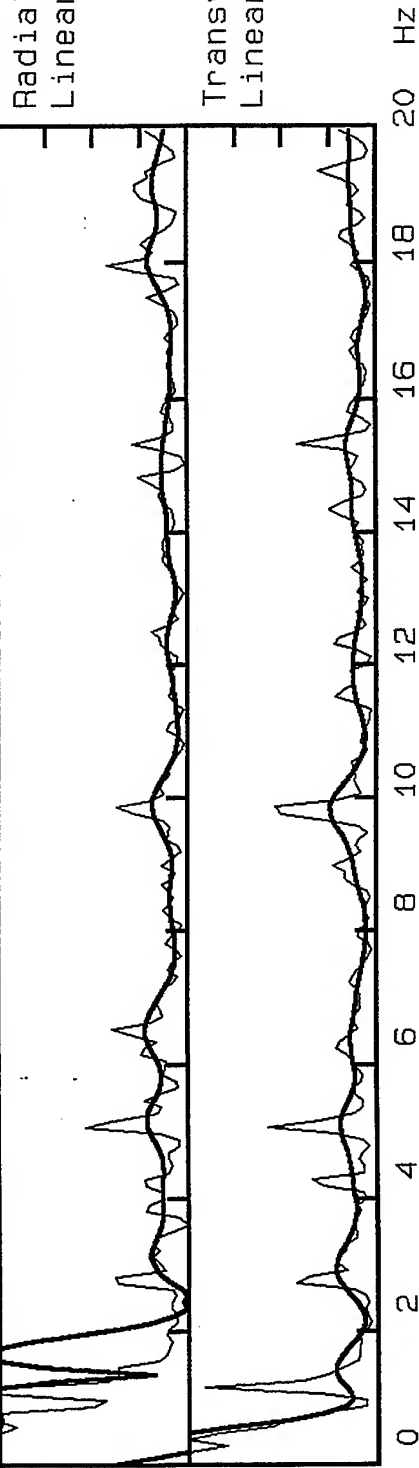


18\_1a04, Window: .0 to 8.4 s

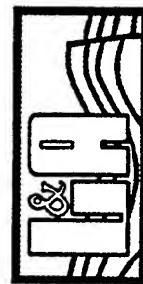


Radial/Vertical  
Linear Scale 0-8

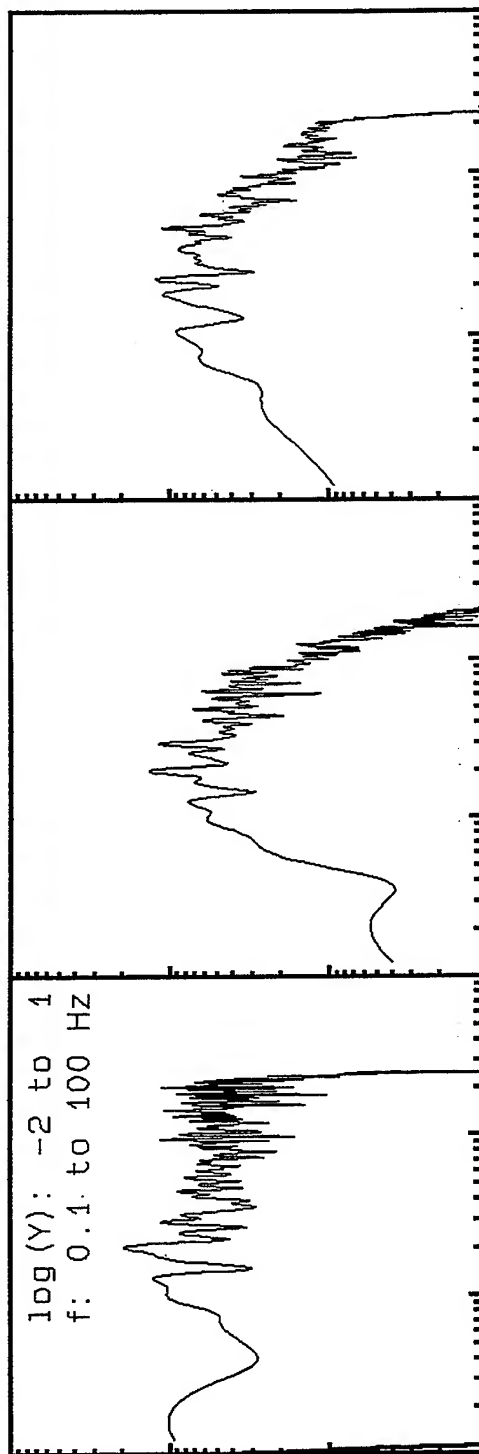
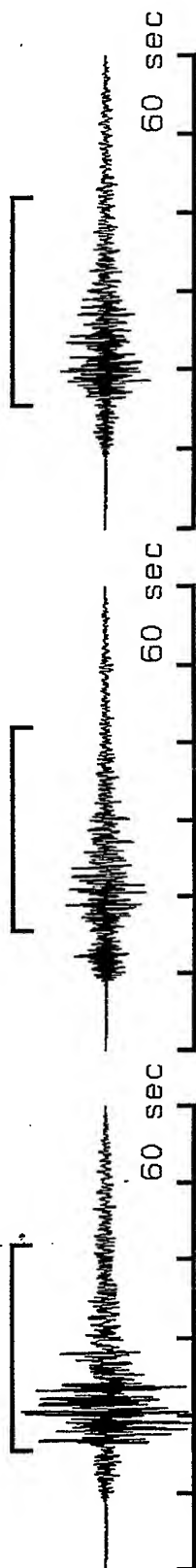
Transvers/Vertical:  
Linear Scale 0-8



**VortexRock Consultants, Inc.**  
11434 Alder Creek Rd, Corona, CA 91720  
Tel - Fax (714) 692-1443, E-Mail: mahdyiar@coda.usc.edu



18\_la04, Window: 15.6 to 42.0 s



Radial/Vertical  
Linear Scale 0-8

Transvers/Vertical:  
Linear Scale 0-8

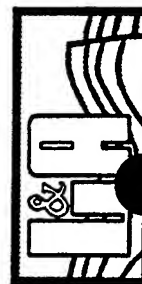
0 2 4 6 8 10 12 14 16 18 20 Hz



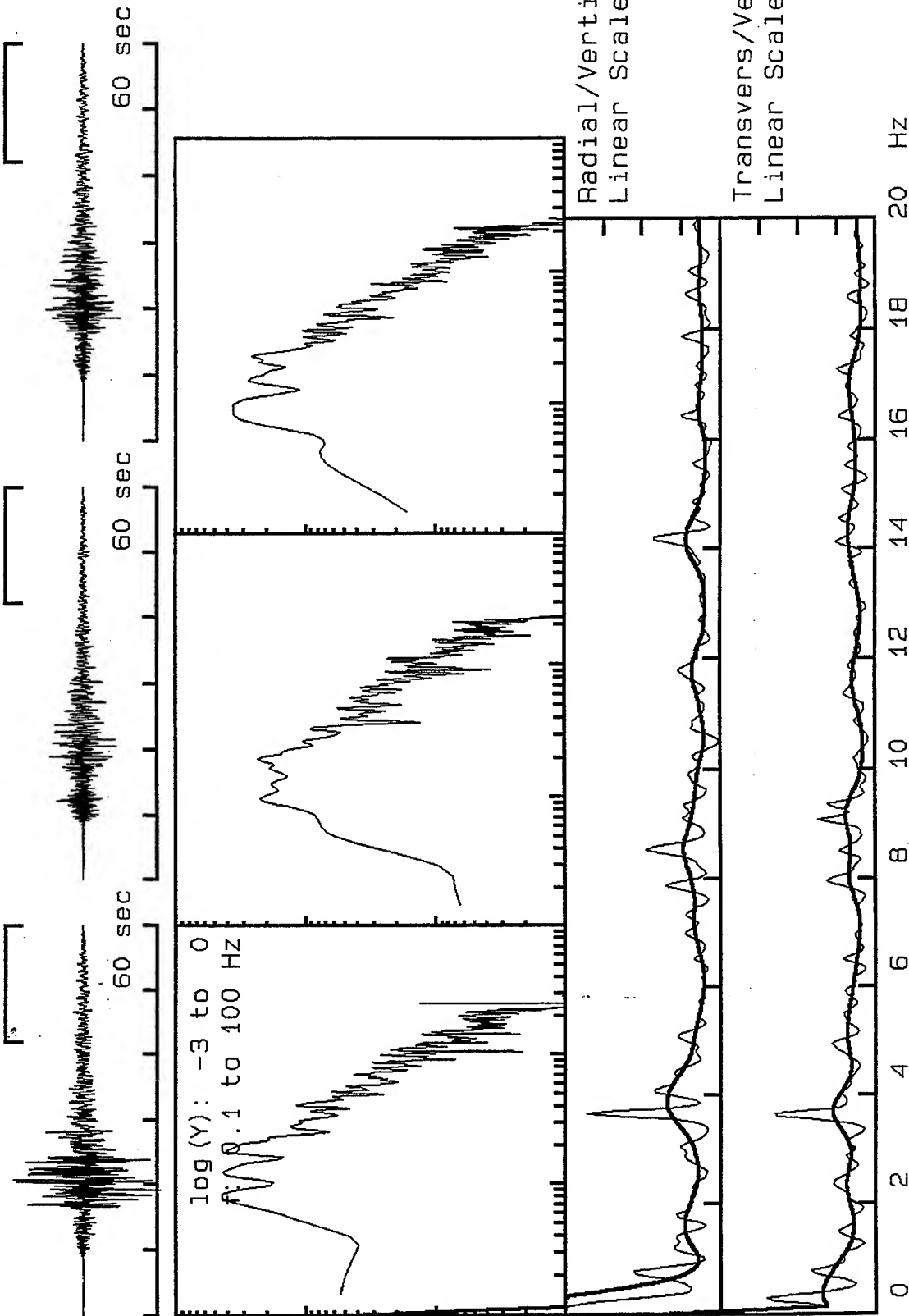
**VortexRock Consultants, Inc.**

11434 Alder Creek Rd, Corona, CA 91720

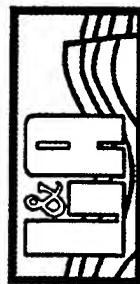
Tel - Fax (714) 692-1443, E-Mail: mahdyiar@coda.usc.edu



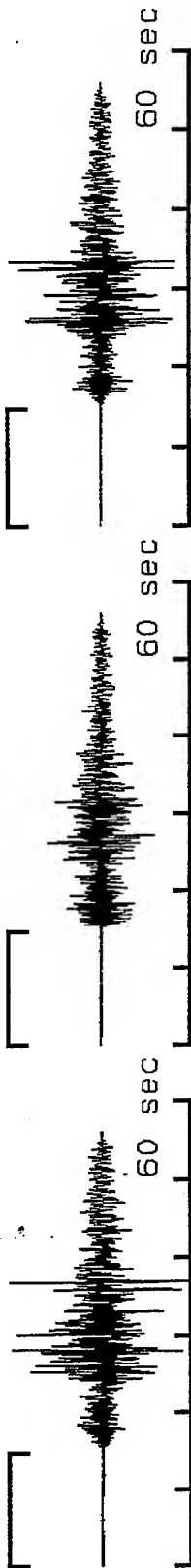
18\_la04, Window: 42.0 to 60.0 s



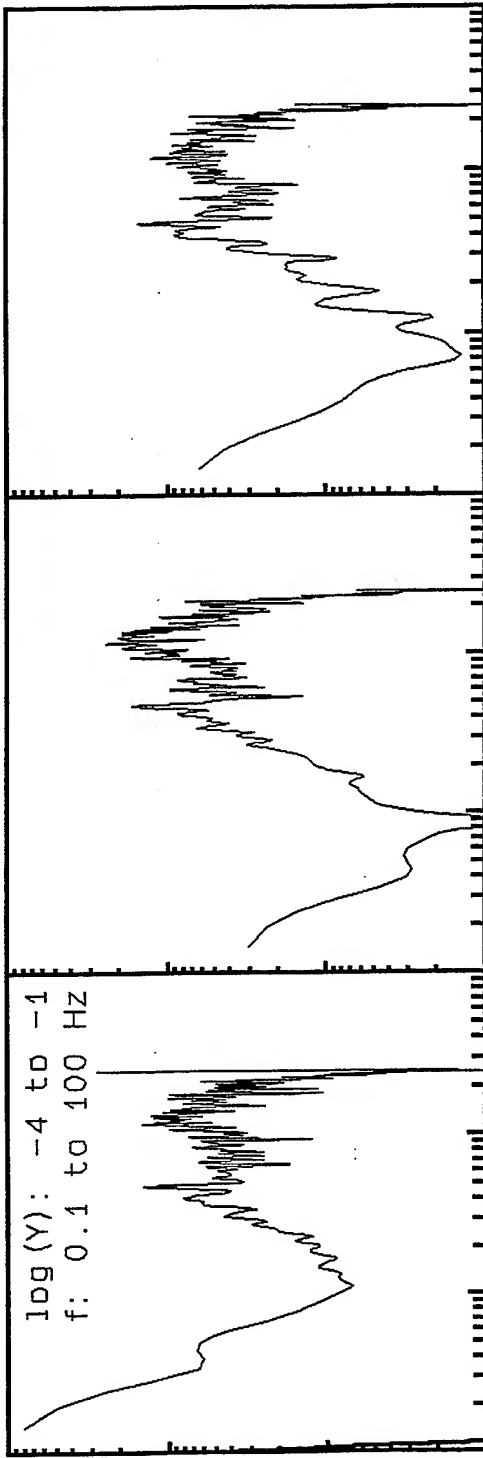
**VortexRock Consultants, Inc.**  
11434 Alder Creek Rd, Corona, CA 91720  
Tel - Fax (714) 692-1443, E-Mail: mahdyiar@coda.usc.edu



19\_la04, Window: .0 to 14.8 s

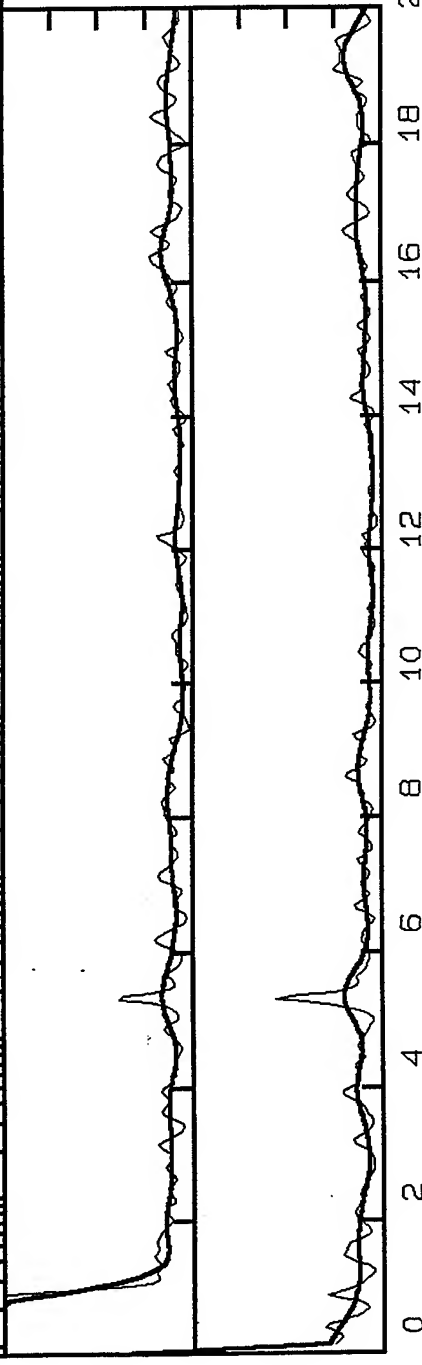


log(Y): -4 to -1  
f: 0.1 to 100 Hz

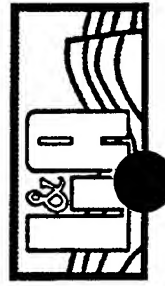


Radial/Vertical  
Linear Scale 0-8

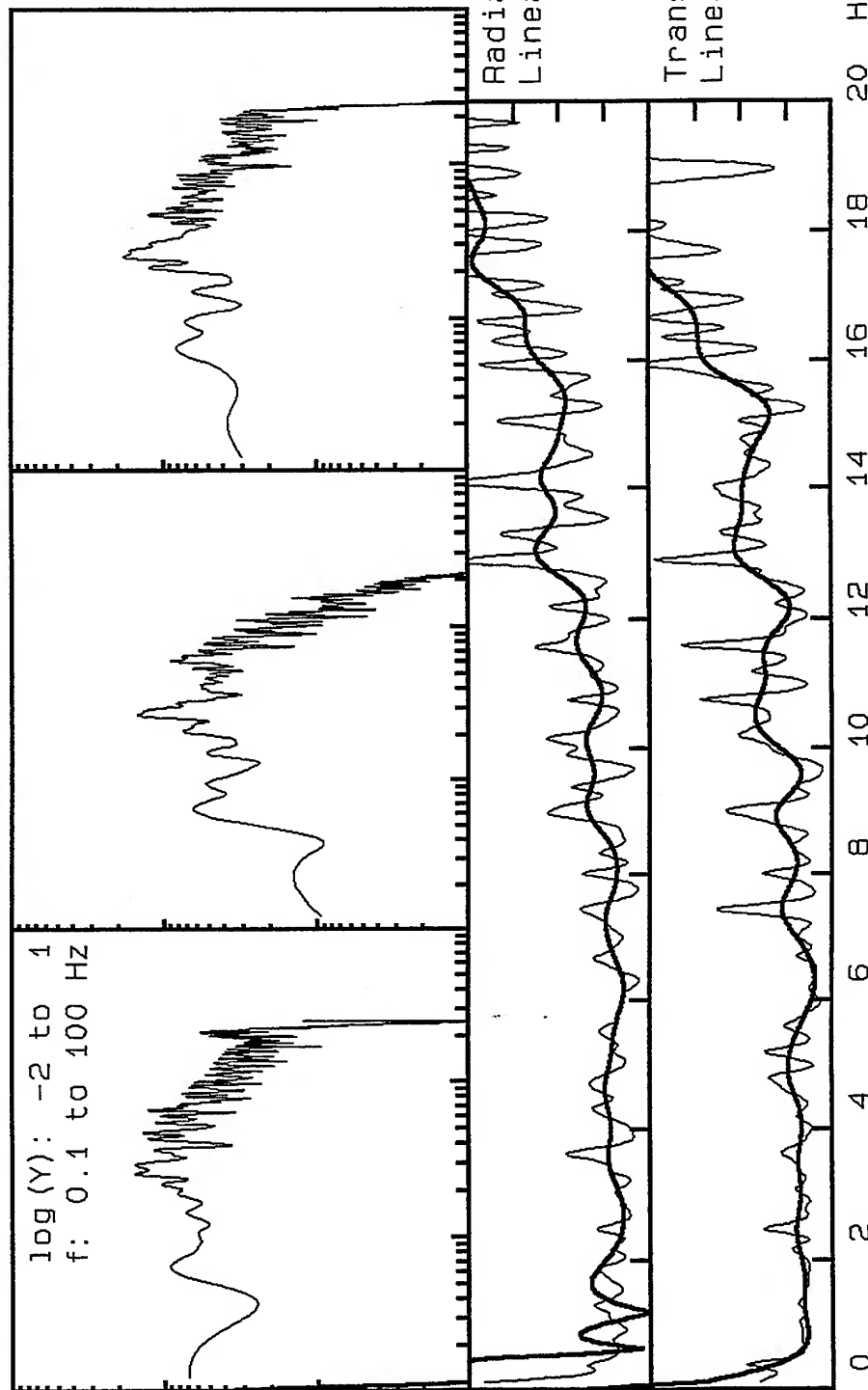
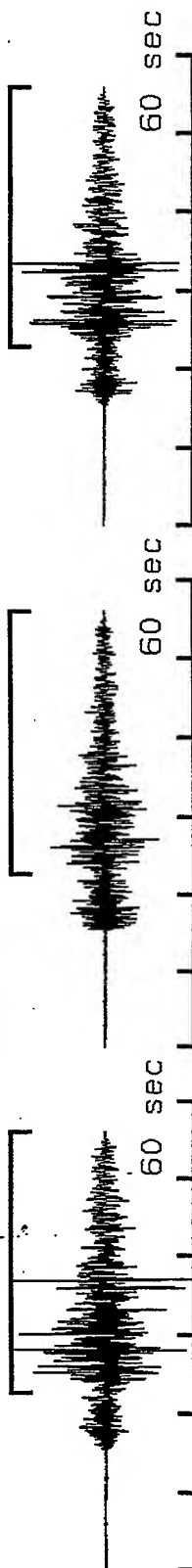
Transvers/Vertical:  
Linear Scale 0-8



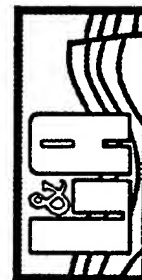
**VortexRock Consultants, Inc.**  
11434 Alder Creek Rd, Corona, CA 91720  
Tel - Fax (714) 692-1443, E-Mail: mahdytar@coda.usc.edu



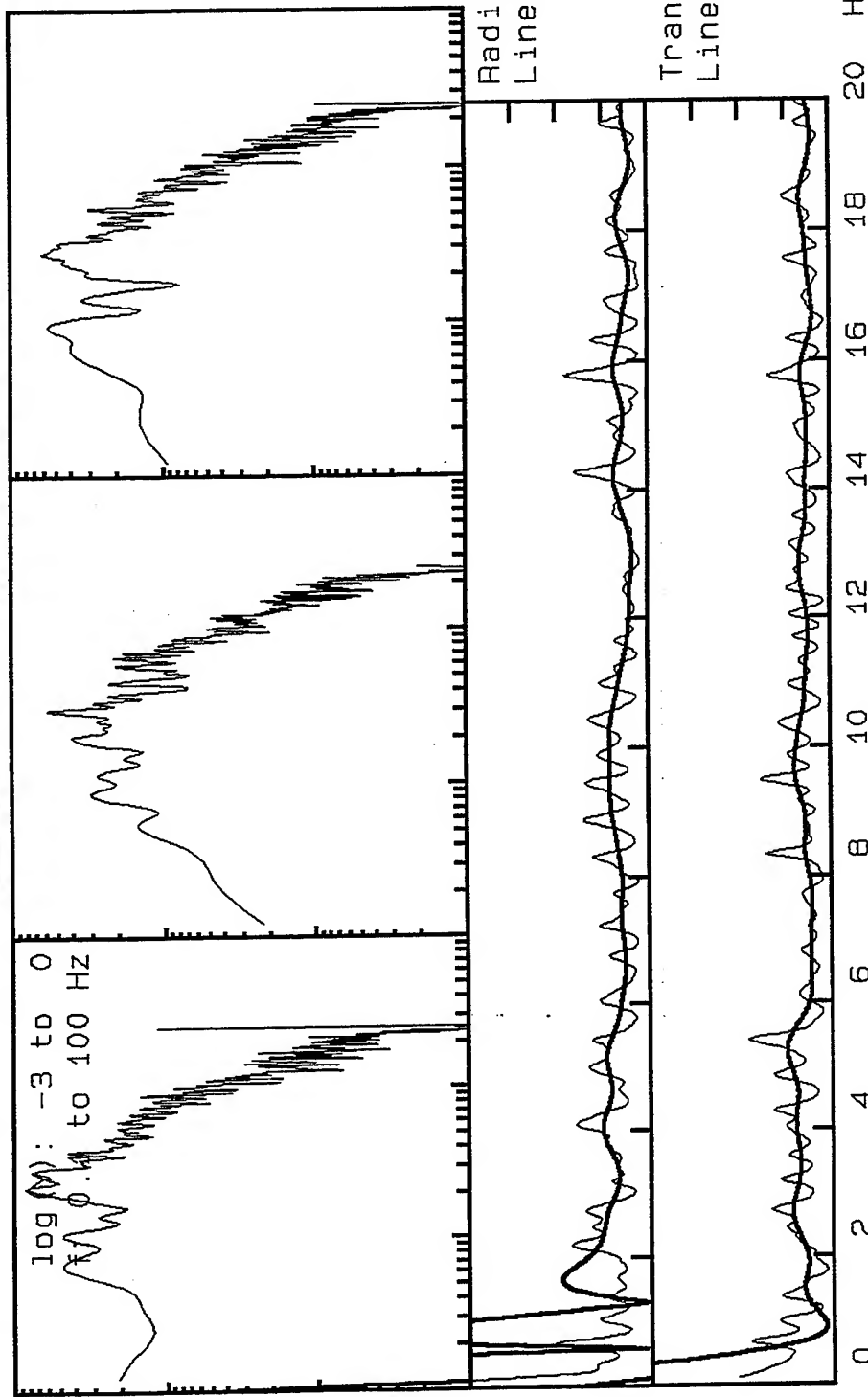
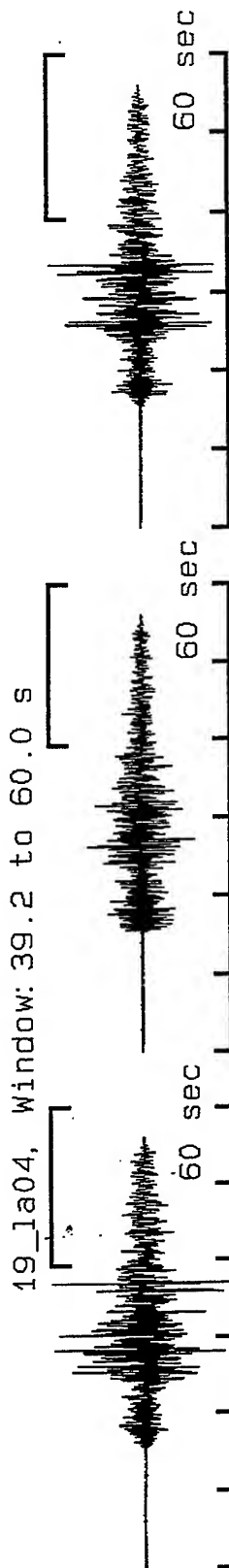
19\_1a04, Window: 22.8 to 56.0 s



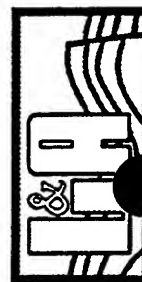
**VortexRock Consultants, Inc.**  
 11434 Alder Creek Rd, Corona, CA 91720  
 Tel - Fax (714) 692-1443, E-Mail: mahdyar@coda.usc.edu



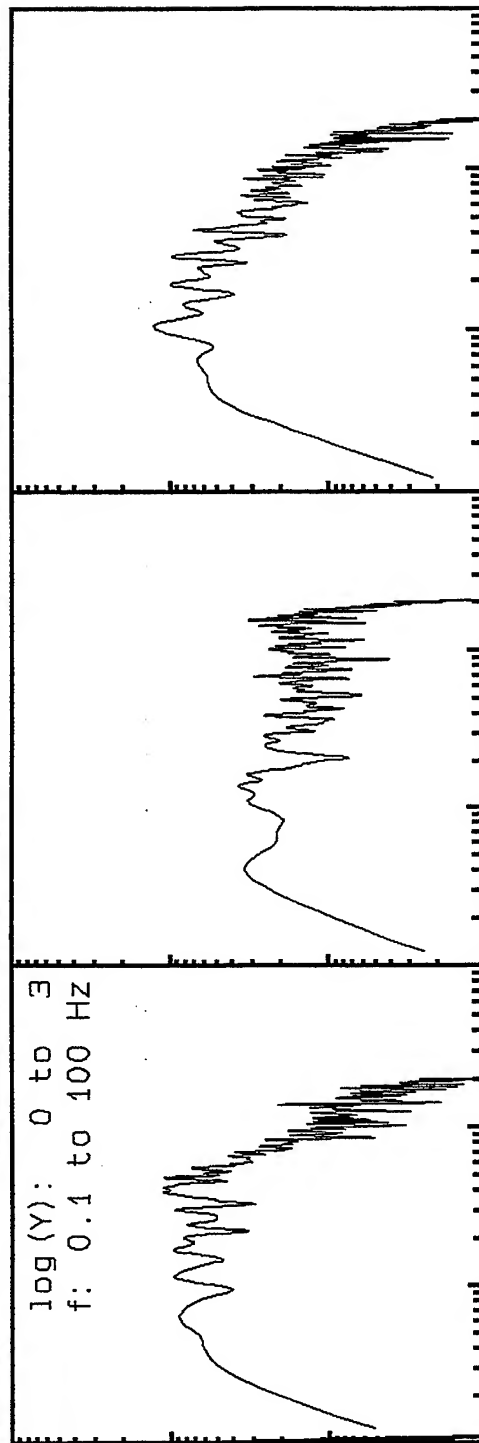




**VortexRock Consultants, Inc.**  
11434 Alder Creek Rd, Corona, CA 91720  
Tel - Fax (714) 692-1443, E-Mail: mahdyiar@coda.usc.edu

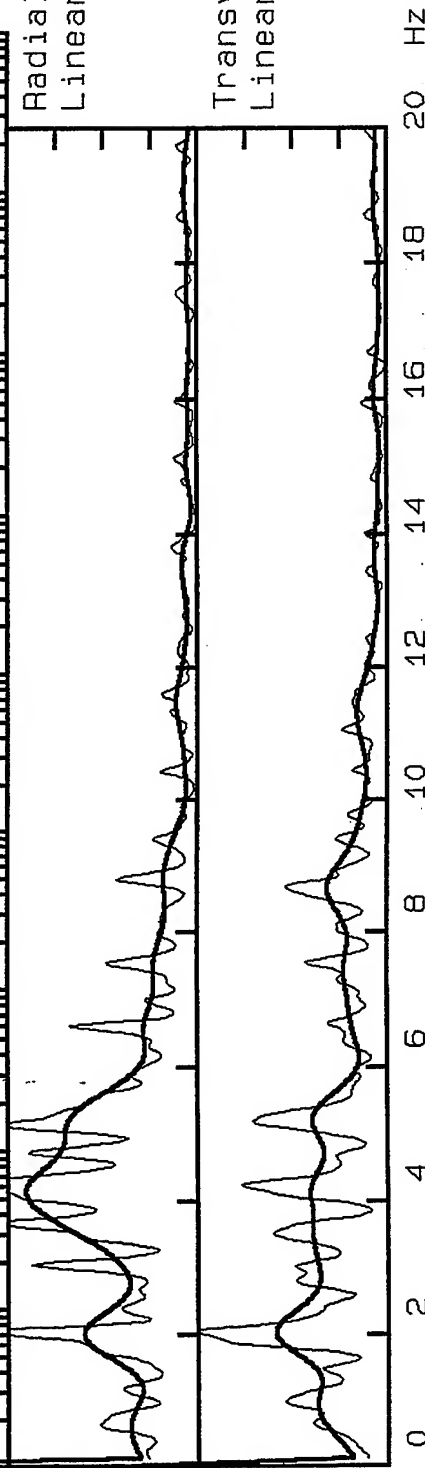


21\_LA02, Window: .0 to 30.8 s

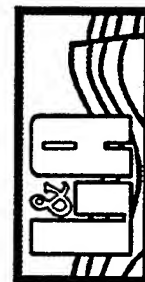


Radial/Vertical  
Linear Scale 0-8

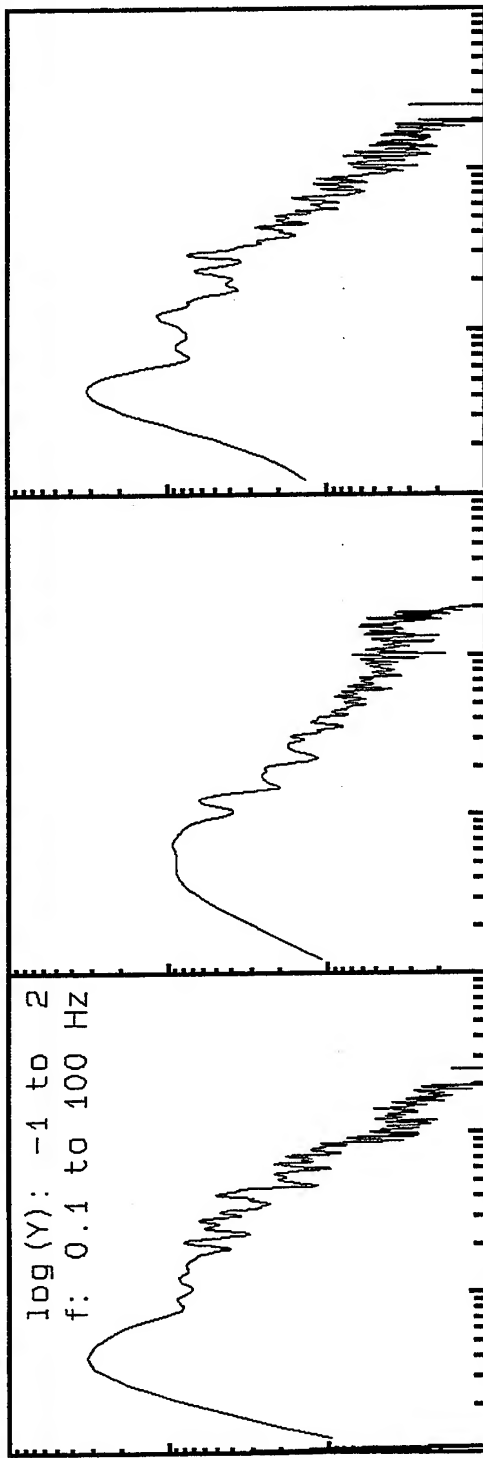
Transvers/Vertical:  
Linear Scale 0-8



**VortexRock Consultants, Inc.**  
11434 Alder Creek Rd, Corona, CA 91720  
Tel - Fax (714) 692-1443, E-Mail: mahdytar@coda.usc.edu



21\_LA02, Window: 30.8 to 60.0 s



Radial/Vertical  
Linear Scale 0-8

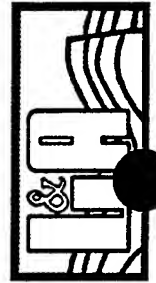
Transvers/Vertical:  
Linear Scale 0-8

20 Hz

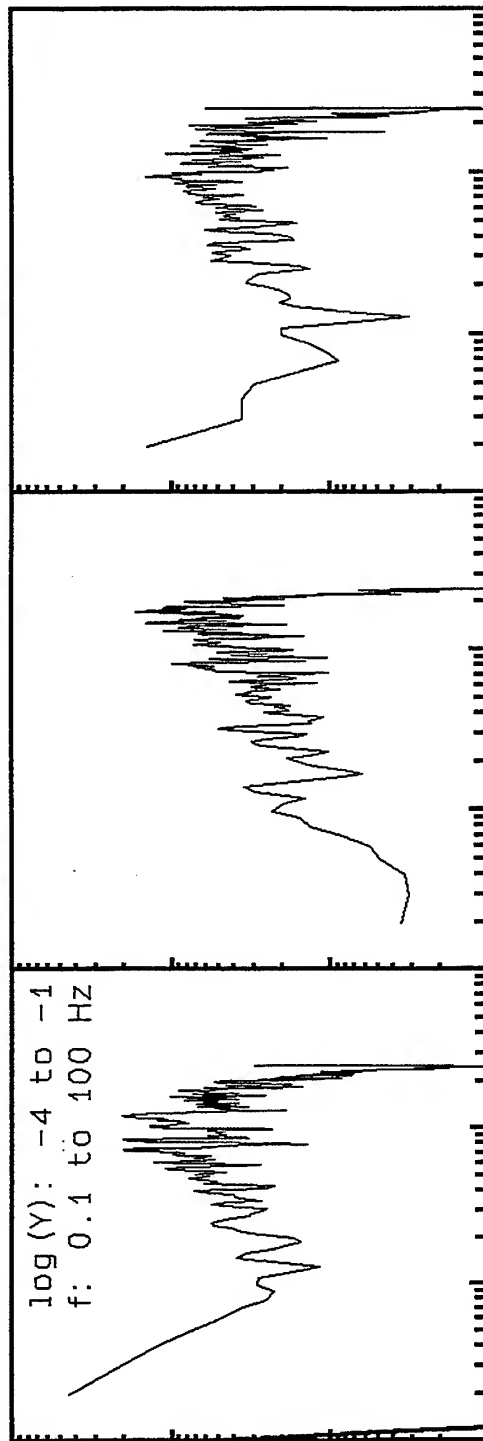
**VortexRock Consultants, Inc.**

11434 Alder Creek Rd, Corona, CA 91720

Tel - Fax (714) 692-1443, E-Mail: mahdyiar@coda.usc.edu

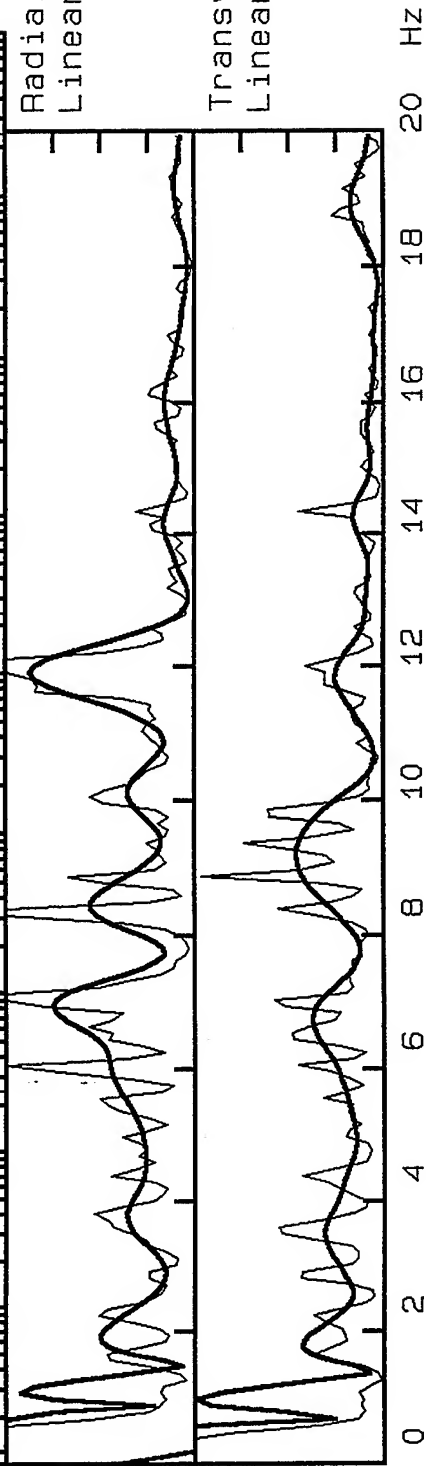


23\_LA02, Window: .0 to 9.6 s

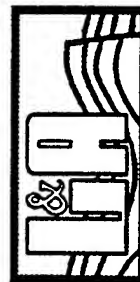


Radial/Vertical  
Linear Scale 0-8

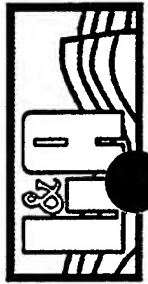
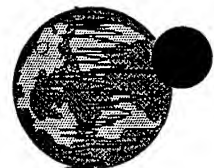
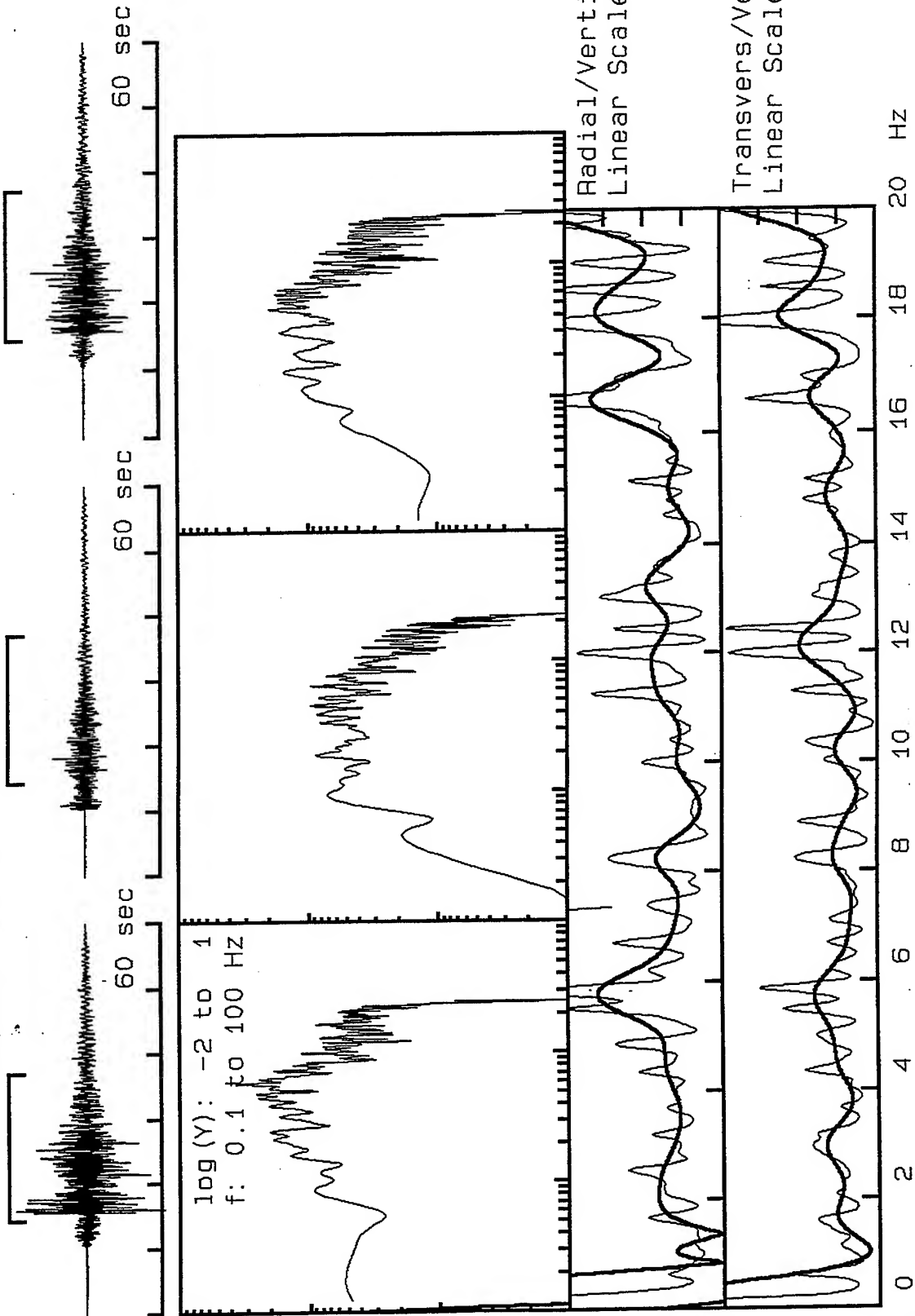
Transvers/Vertical:  
Linear Scale 0-8



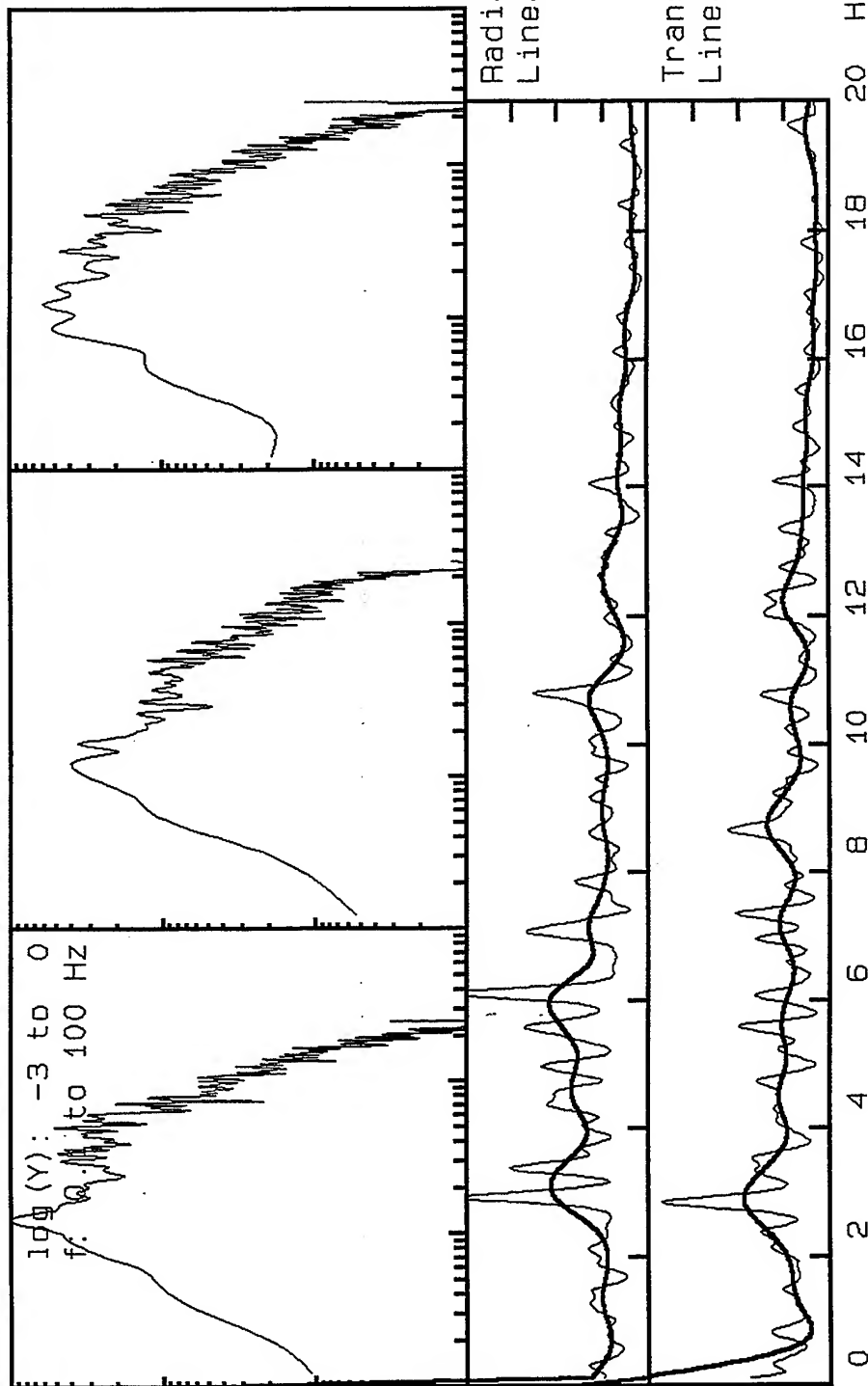
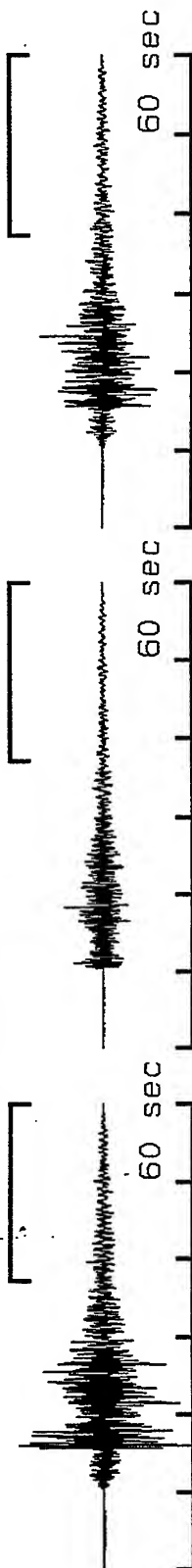
**VortexRock Consultants, Inc.**  
11434 Alder Creek Rd, Corona, CA 91720  
Tel - Fax (714) 692-1443, E-Mail: mahdyiar@coda.usc.edu



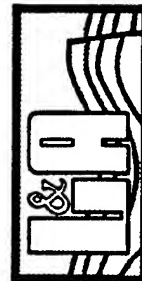
23\_LA02, Window: 14.4 to 37.2 s



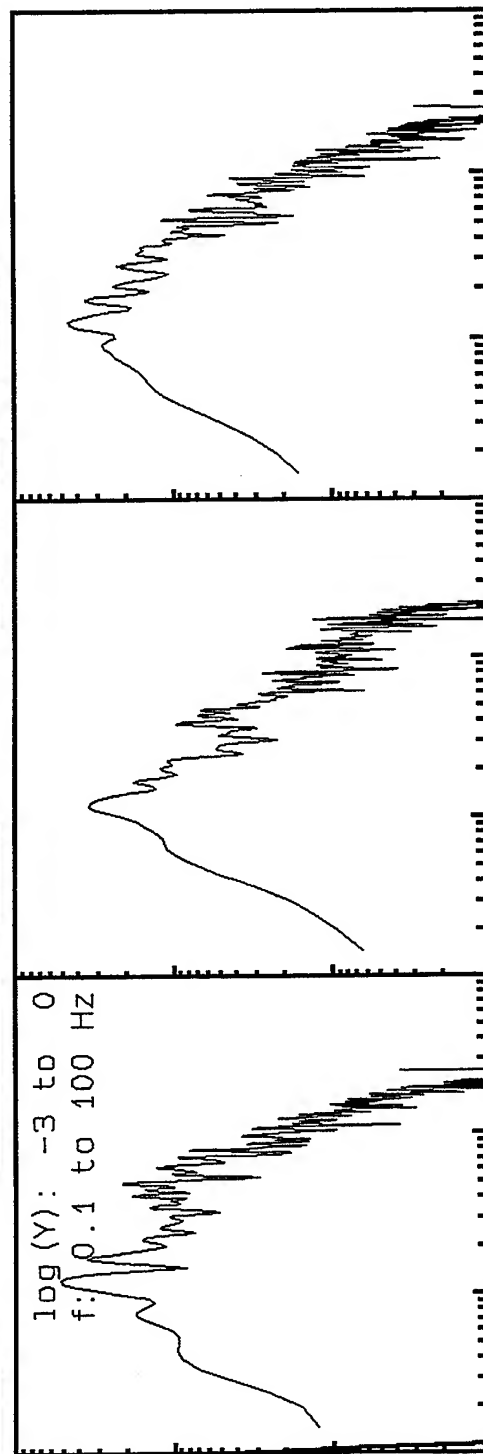
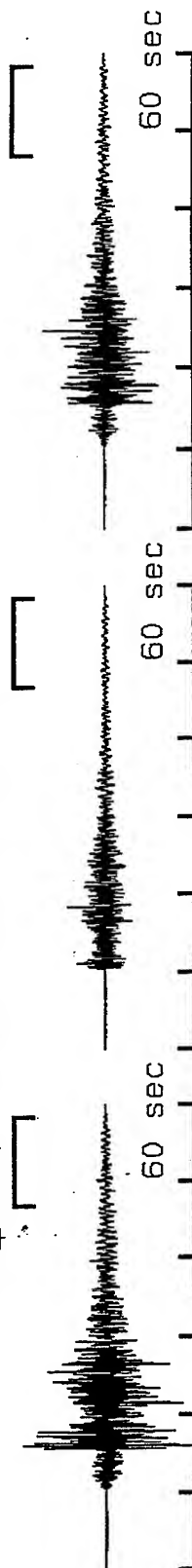
23\_LA02, Window: 37.2 to 60.0 s



**VortexRock Consultants, Inc.**  
 11434 Alder Creek Rd, Corona, CA 91720  
 Tel - Fax (714) 692-1443, E-Mail: mahdyar@coda.usc.edu

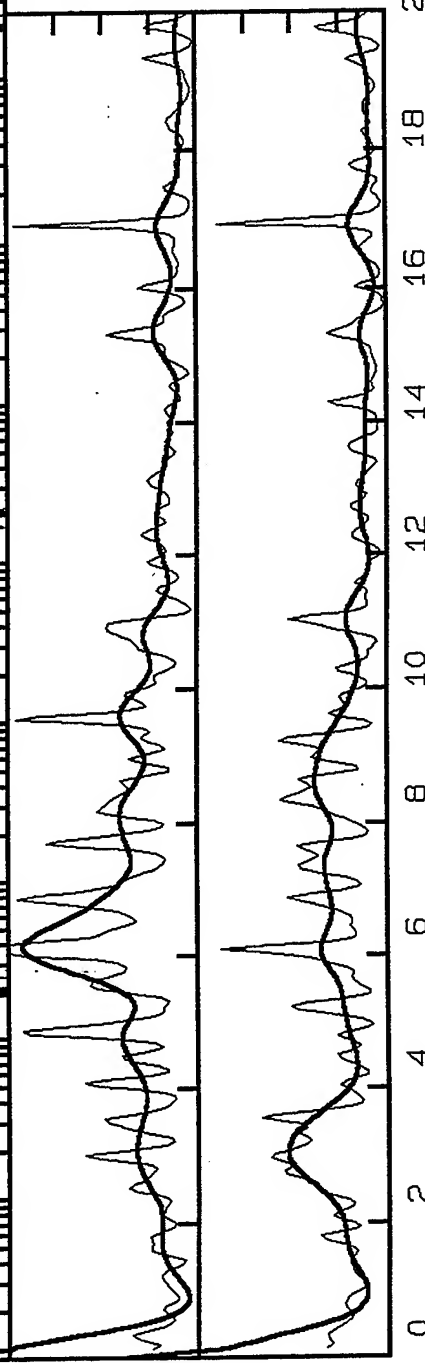


23\_LA02, Window: 46.8 to 58.4 s



Radial/Vertical  
Linear Scale 0-8

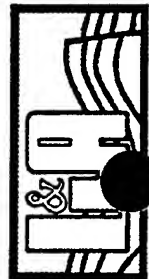
Transvers/Vertica:  
Linear Scale 0-8



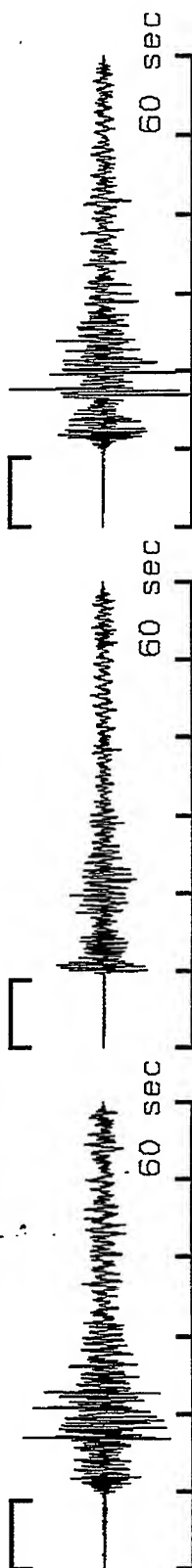
**VortexRock Consultants, Inc.**

11434 Alder Creek Rd, Corona, CA 91720

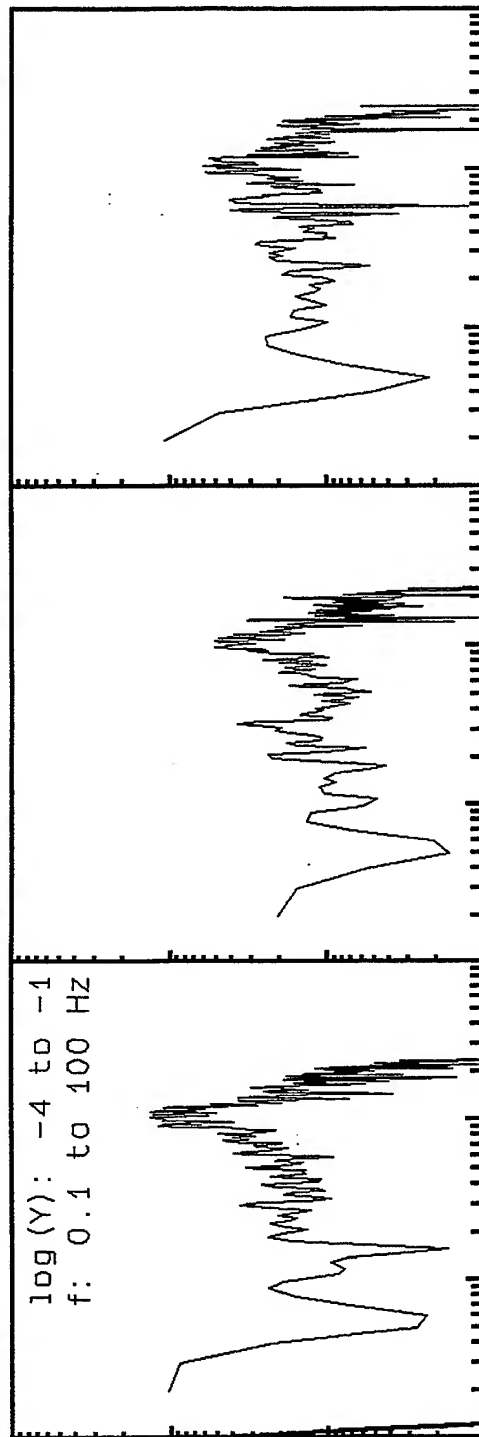
Tel - Fax (714) 692-1443, E-Mail: mahdyiar@coda.usc.edu



25\_LA02, Window: .0 to 8.8 s



log(Y): -4 to -1  
f: 0.1 to 100 Hz



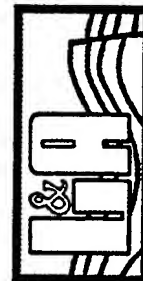
Radial/Vertical  
Linear Scale 0-8

Transvers/Vertica:  
Linear Scale 0-8

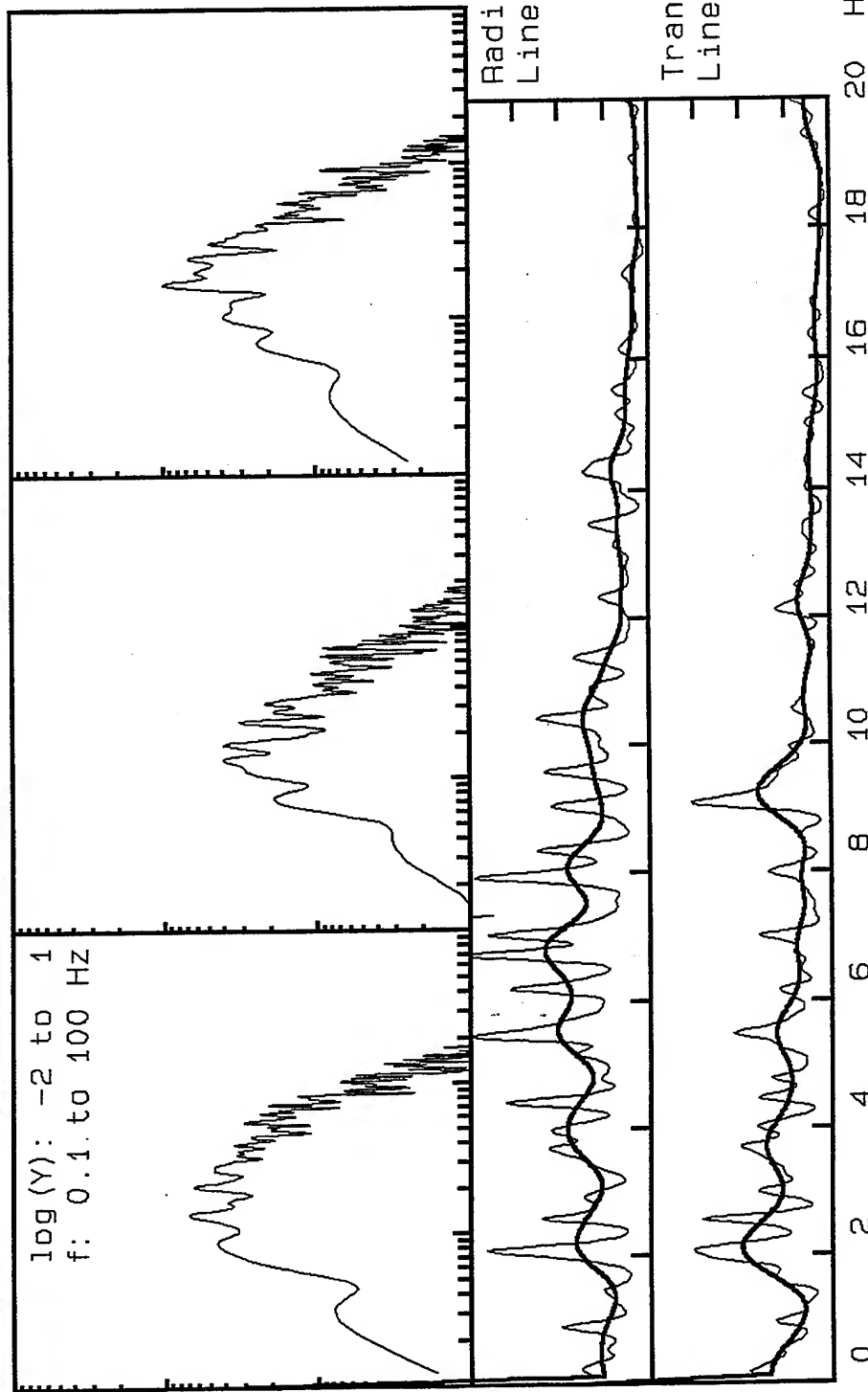
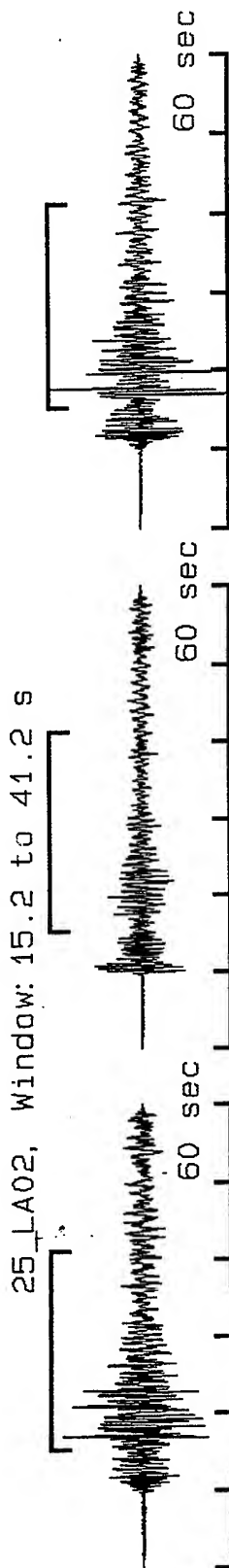
0 2 4 6 8 10 12 14 16 18 20 Hz



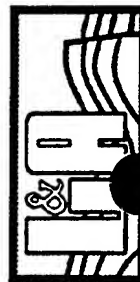
**VortexRock Consultants, Inc.**  
11434 Alder Creek Rd, Corona, CA 91720  
Tel - Fax (714) 692-1443, E-Mail: mahdyar@coda.usc.edu



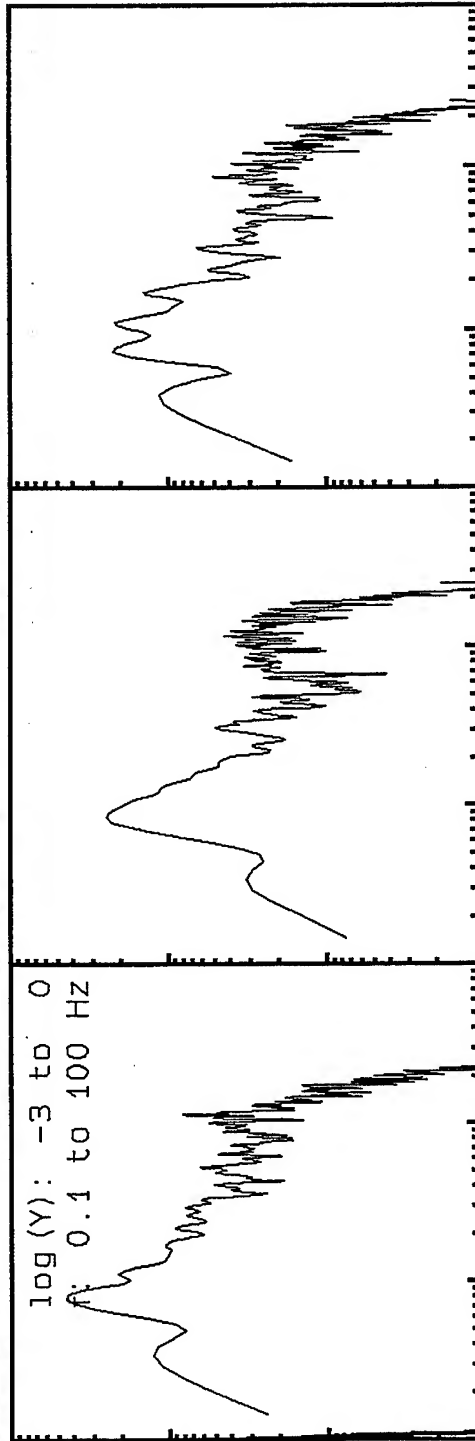
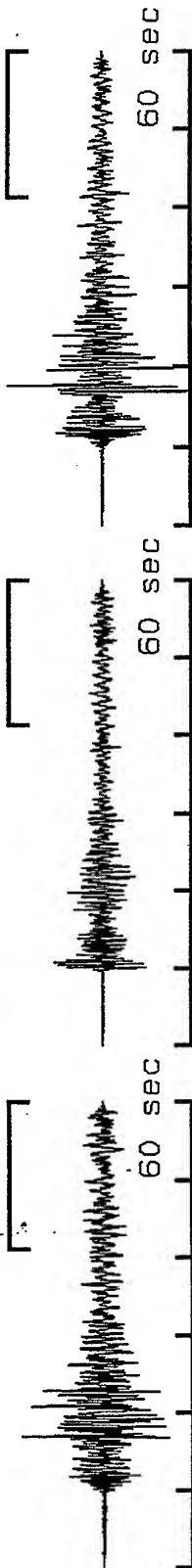




**VortexRock Consultants, Inc.**  
11434 Alder Creek Rd, Corona, CA 91720  
Tel - Fax (714) 692-1443, E-Mail: mahdyiar@coda.usc.edu

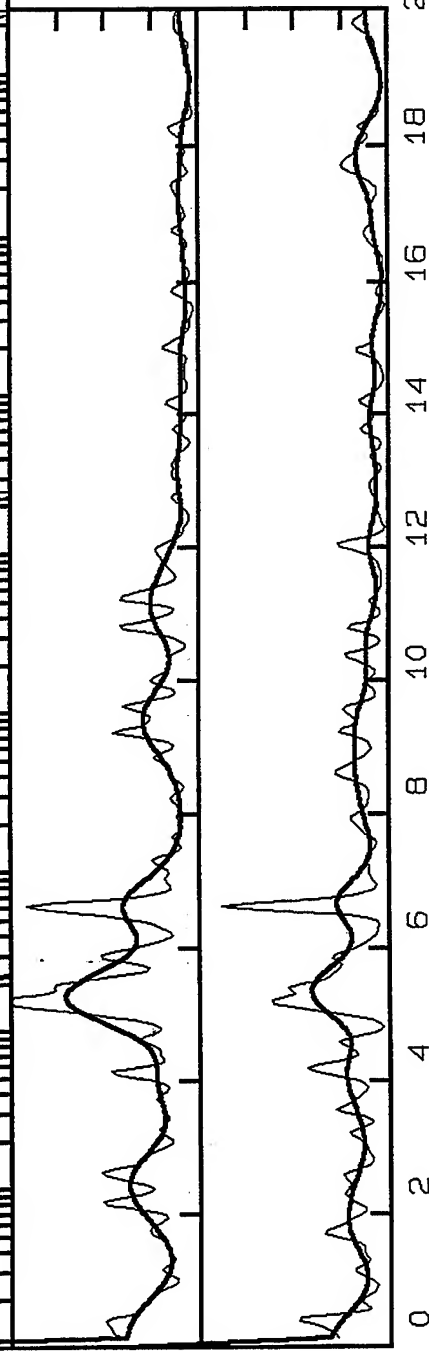


25\_LA02, Window: 41.2 to 60.0 s

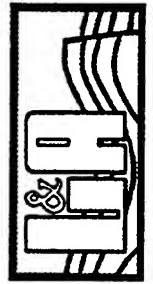


Radial/Vertical  
Linear Scale 0-8

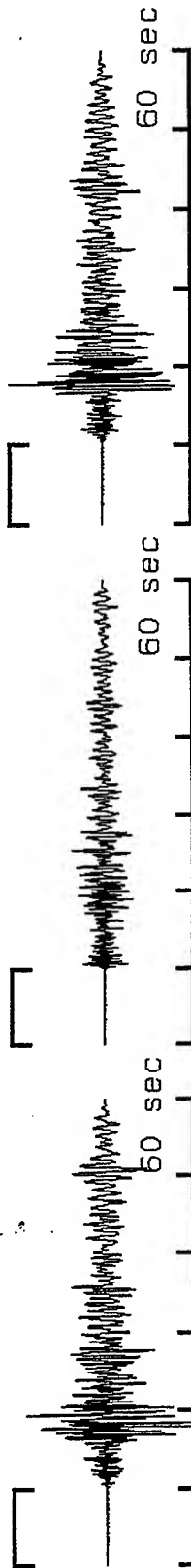
Transvers/Vertical:  
Linear Scale 0-8



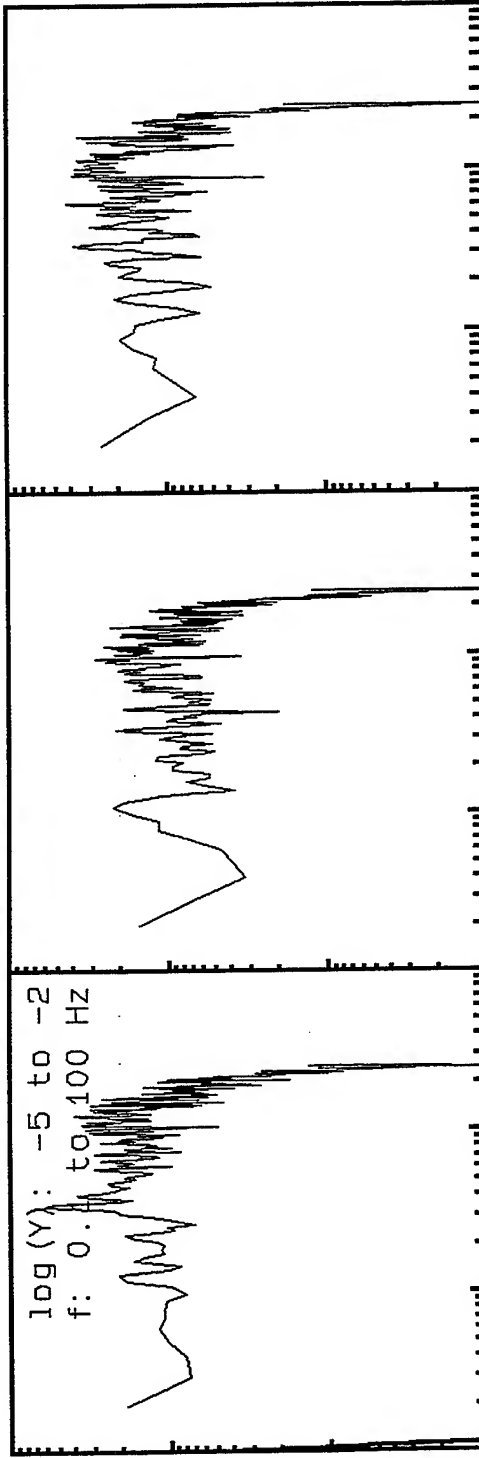
**VortexRock Consultants, Inc.**  
11434 Alder Creek Rd, Corona, CA 91720  
Tel - Fax (714) 692-1443, E-Mail: mahdyiar@coda.usc.edu



27\_LA02, Window: .0 to 10.0 s



log(Y): -5 to -2  
f: 0.1 to 100 Hz



Radial/Vertical  
Linear Scale 0-8

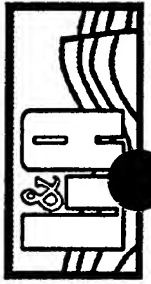
Transvers/Vertical:  
Linear Scale 0-8

0 2 4 6 8 10 12 14 16 18 20 Hz

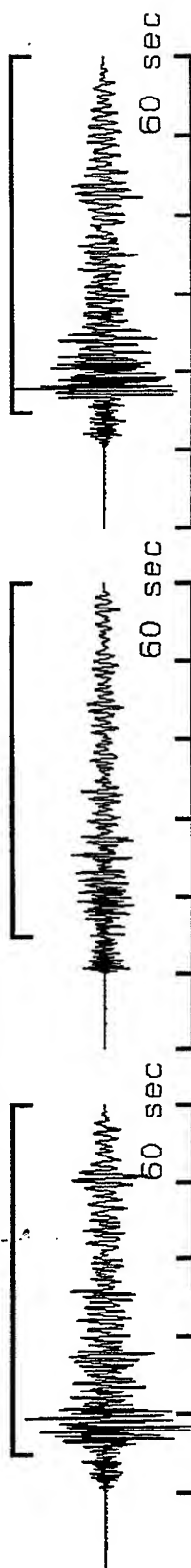
**VortexRock Consultants, Inc.**

11434 Alder Creek Rd, Corona, CA 91720

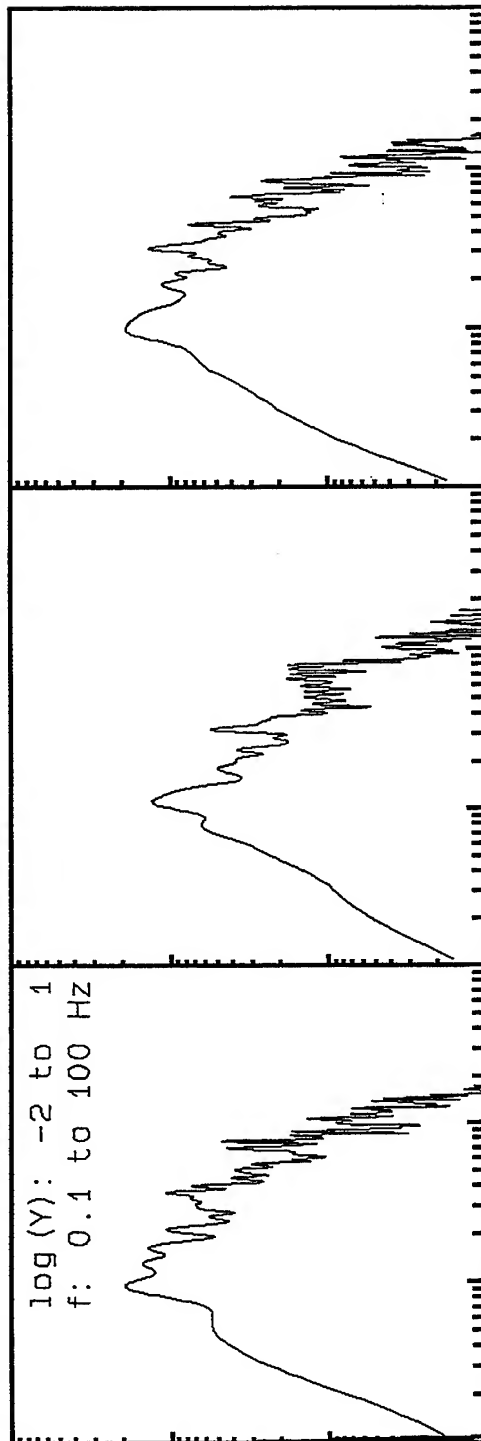
Tel - Fax (714) 692-1443, E-Mail: mahdiyari@coda.usc.edu



27\_LA02, Window: 14.8 to 60.0 s

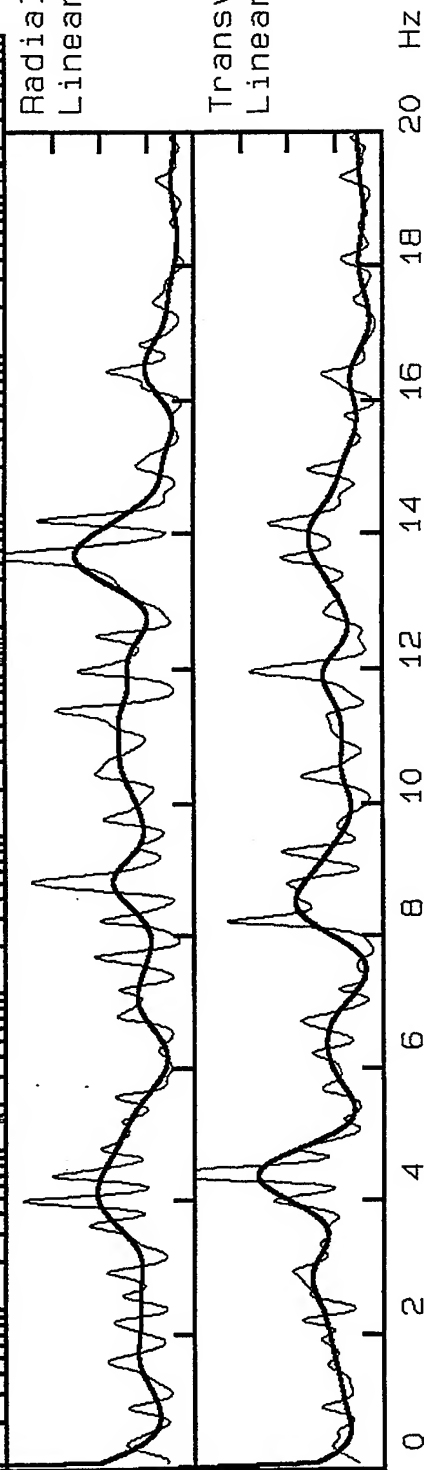


log (Y): -2 to 1  
f: 0.1 to 100 Hz



Radial/Vertical  
Linear Scale 0-8

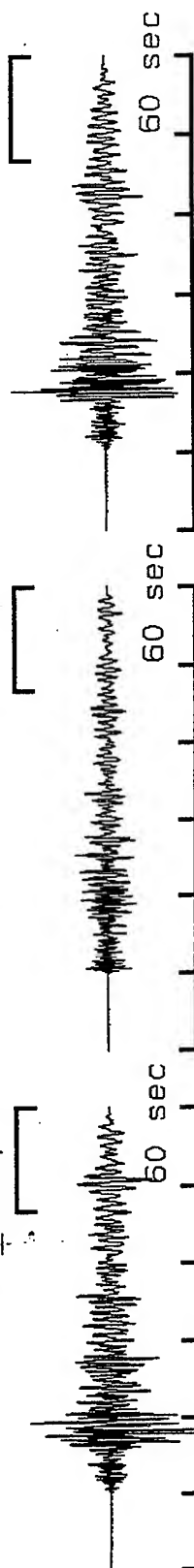
Transvers/Vertical:  
Linear Scale 0-8



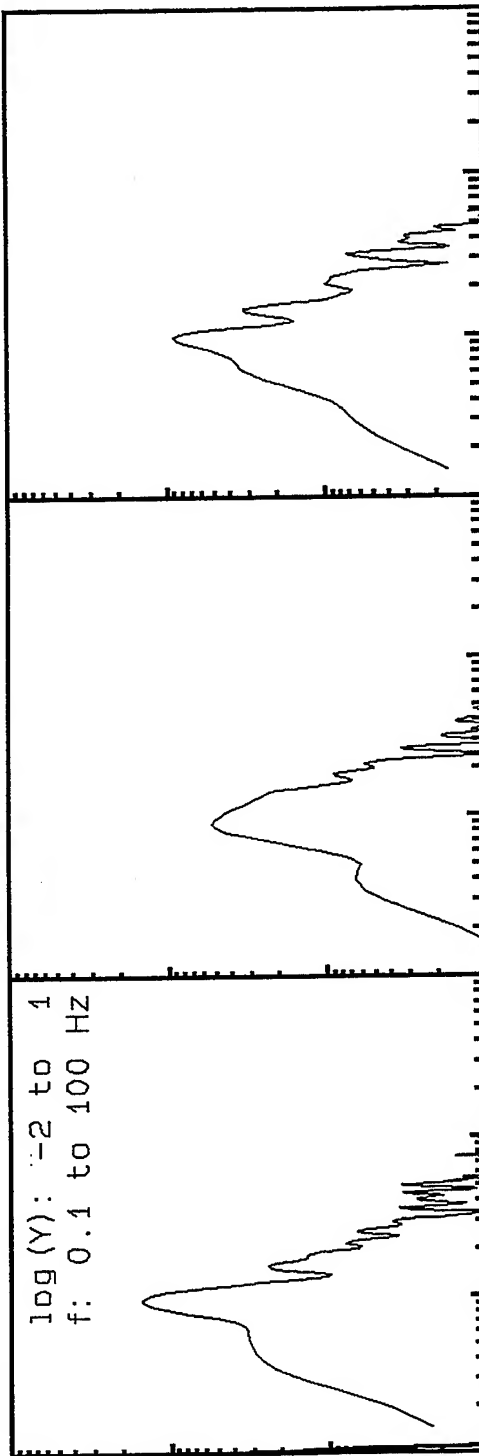
**VortexRock Consultants, Inc.**  
11434 Alder Creek Rd, Corona, CA 91720  
Tel - Fax (714) 692-1443, E-Mail: mahdyiar@coda.usc.edu



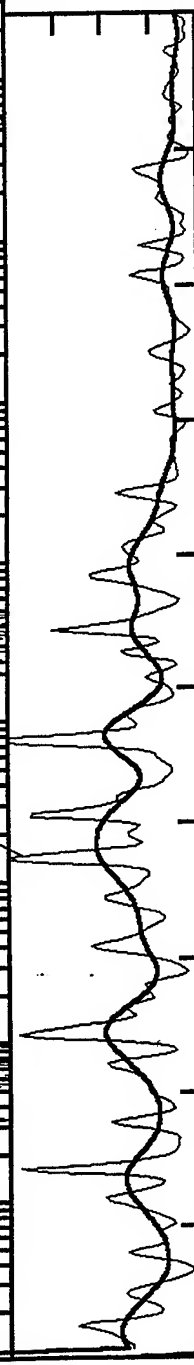
27\_LA02, Window: 46.8 to 60.0 s



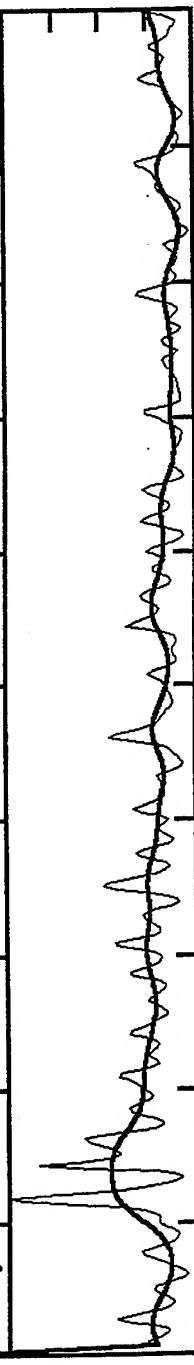
log (Y): -2 to 1  
f: 0.1 to 100 Hz



Radial/Vertical  
Linear Scale 0-8



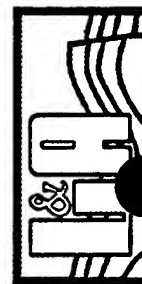
Transvers/Vertical:  
Linear Scale 0-8



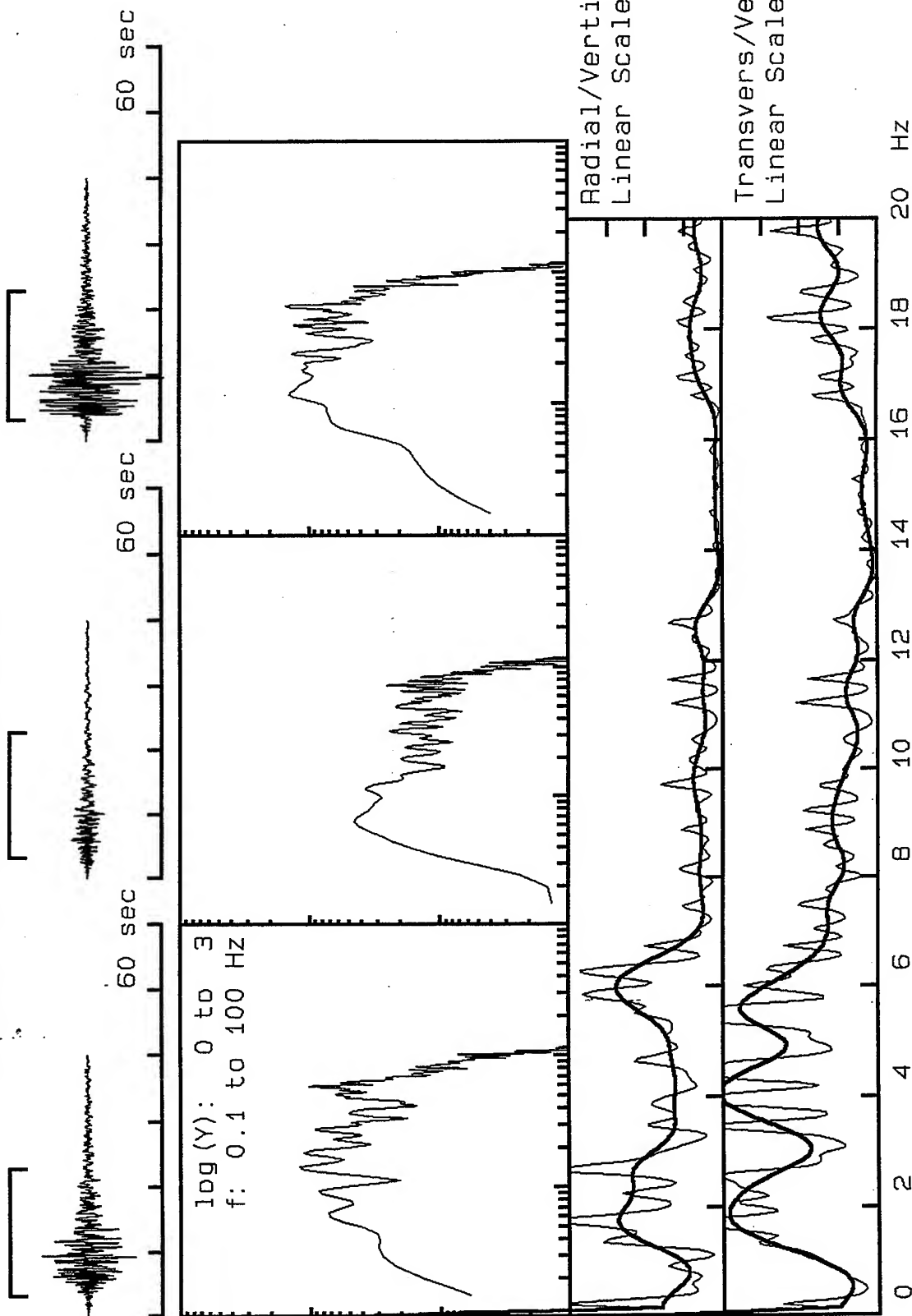
0 2 4 6 8 10 12 14 16 18 20 Hz



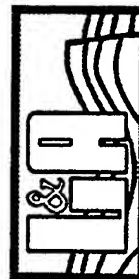
**VortexRock Consultants, Inc.**  
11434 Alder Creek Rd, Corona, CA 91720  
Tel - Fax (714) 692-1443, E-Mail: mahdytar@coda.usc.edu



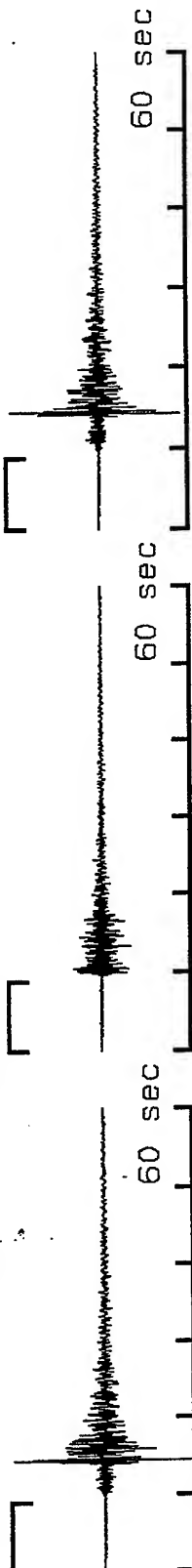
31\_LAHQ, Window: 3.2 to 22.8 s



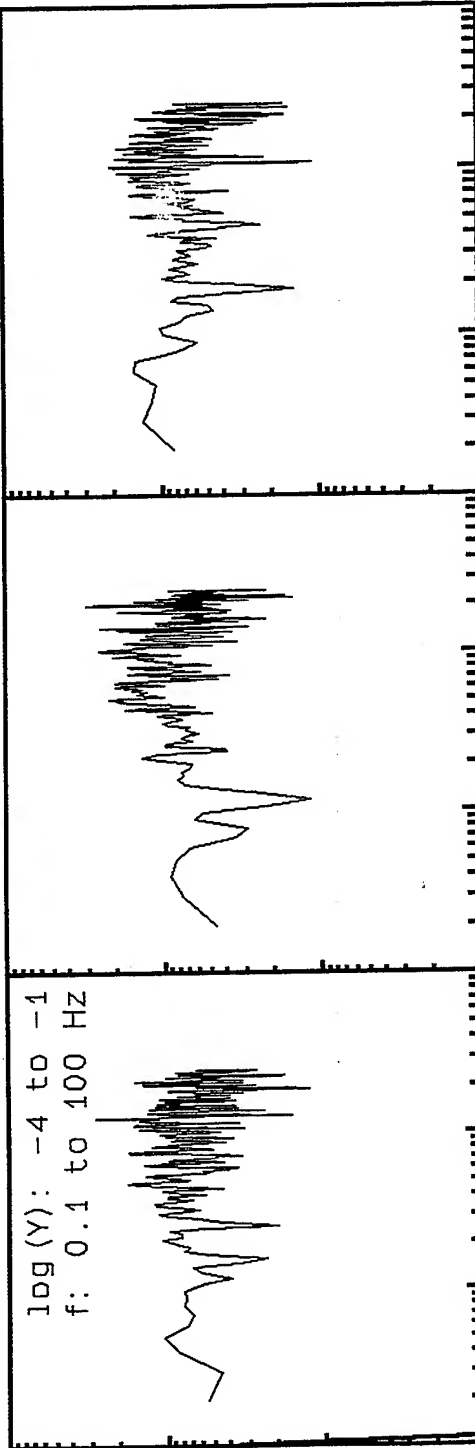
**VortexRock Consultants, Inc.**  
11434 Alder Creek Rd, Corona, CA 91720  
Tel - Fax (714) 692-1443, E-Mail: mahdyiar@coda.usc.edu



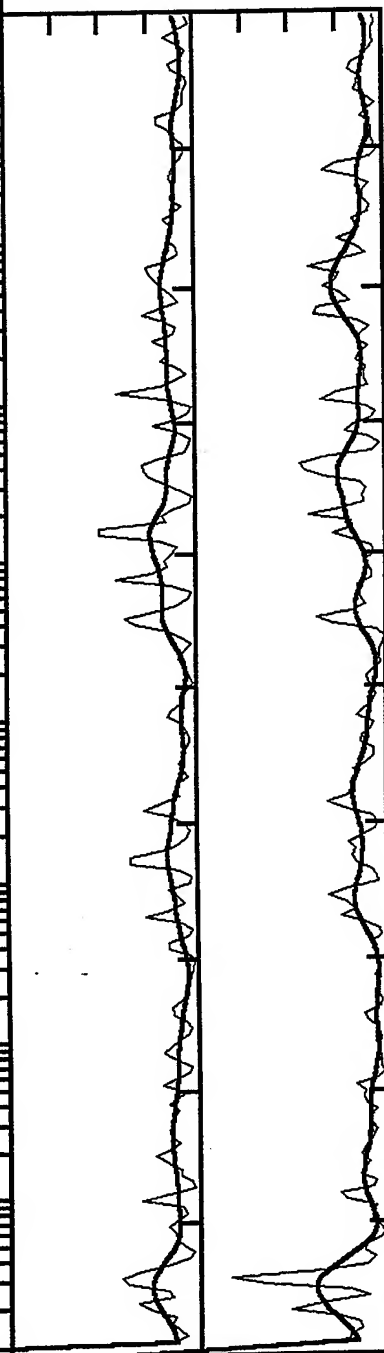
3111\_LA03, Window: .0 to 8.8 s



log(Y): -4 to -1  
f: 0.1 to 100 Hz



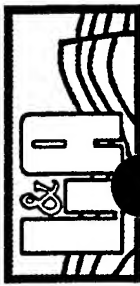
Radial/Vertical  
Linear Scale 0-8



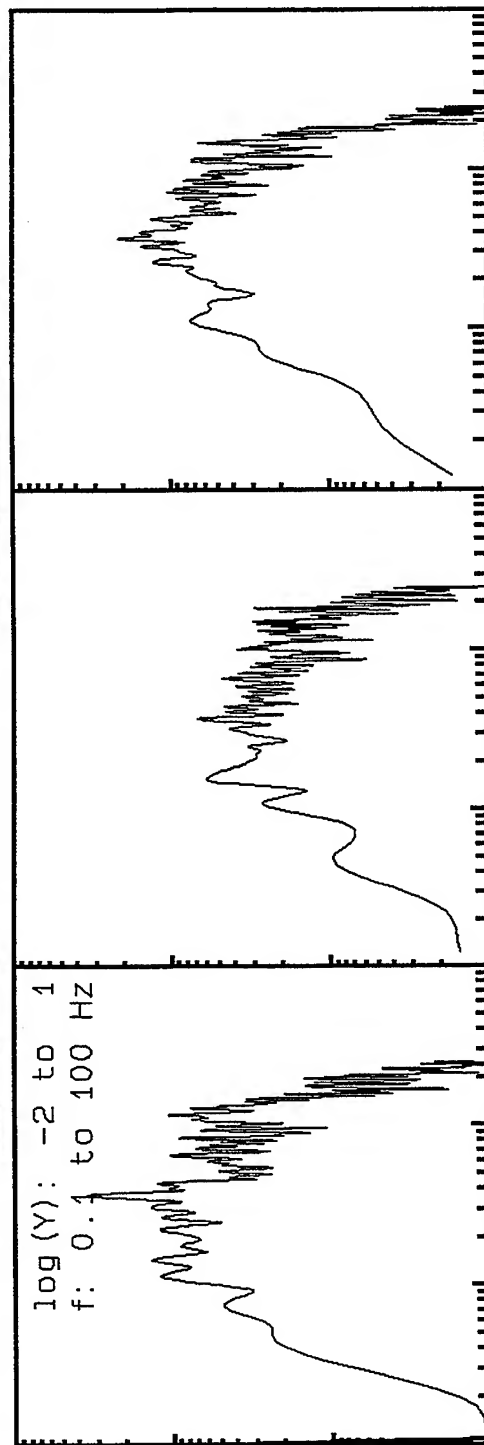
Transvers/Vertical:  
Linear Scale 0-8



**VortexRock Consultants, Inc.**  
11434 Alder Creek Rd, Corona, CA 91720  
Tel - Fax (714) 692-1443, E-Mail: mahdyiar@coda.usc.edu

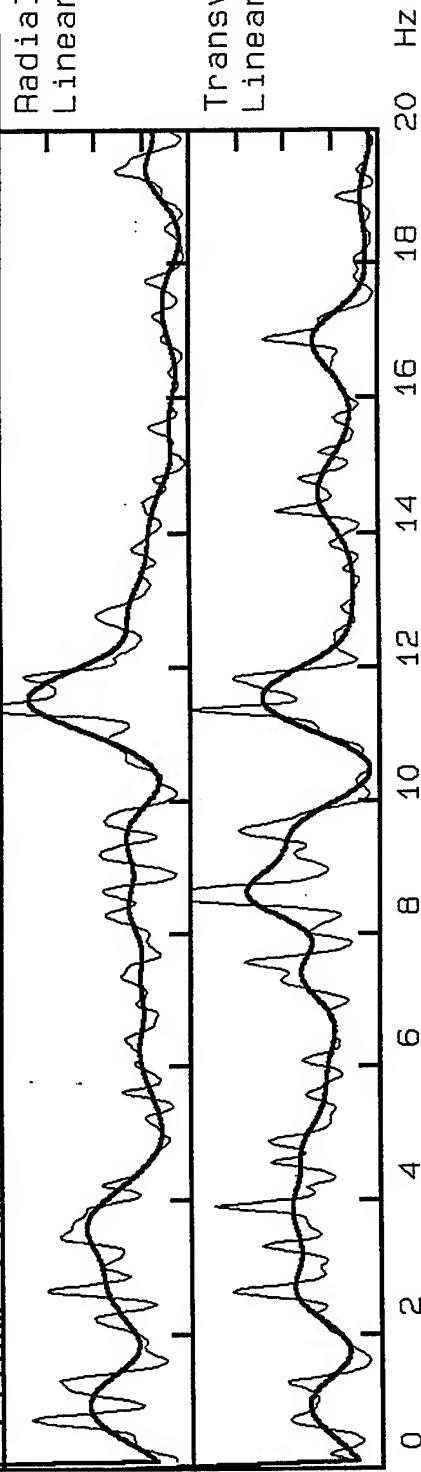


311\_LAO3, Window: 12.8 to 35.6 s

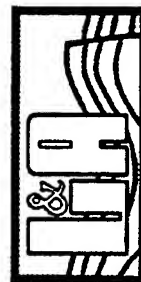


Radial/Vertical  
Linear Scale 0-8

Transvers/Vertical:  
Linear Scale 0-8

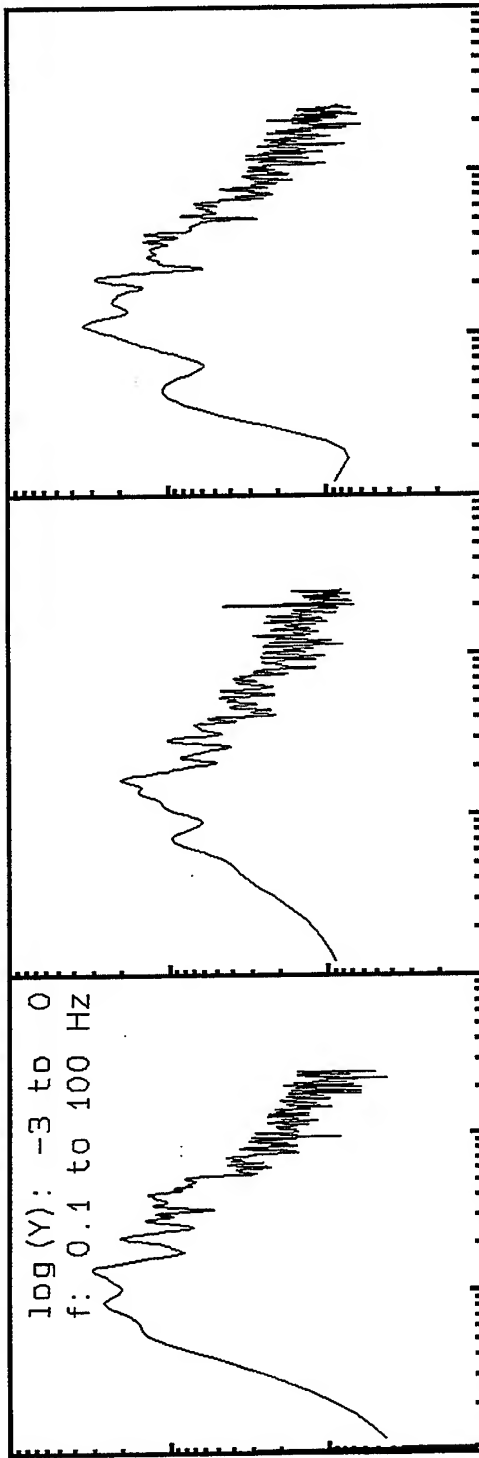
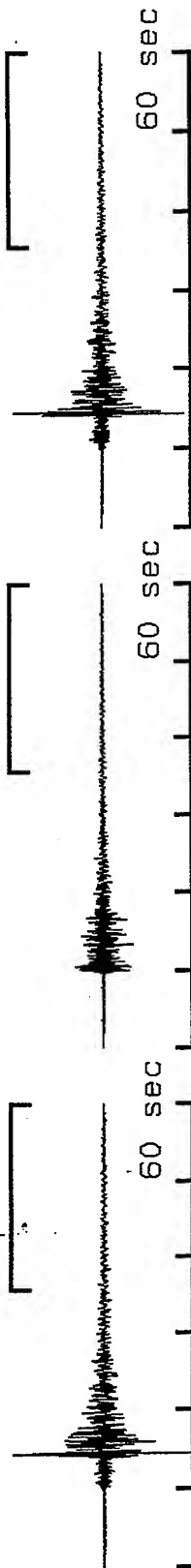


**VortexRock Consultants, Inc.**  
11434 Alder Creek Rd, Corona, CA 91720  
Tel - Fax (714) 692-1443, E-Mail: mahdyiar@coda.usc.edu



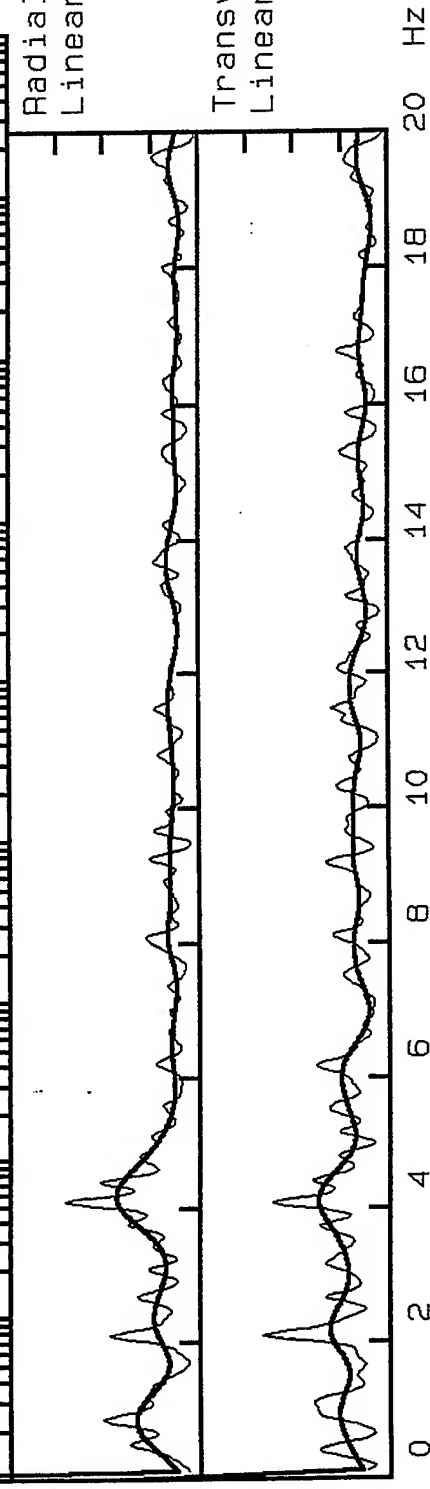


311\_LA03, Window: 35.6 to 60.0 s



Radial/Vertical  
Linear Scale 0-8

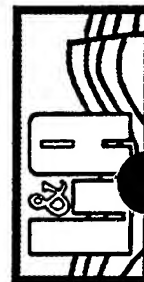
Transvers/Vertical:  
Linear Scale 0-8



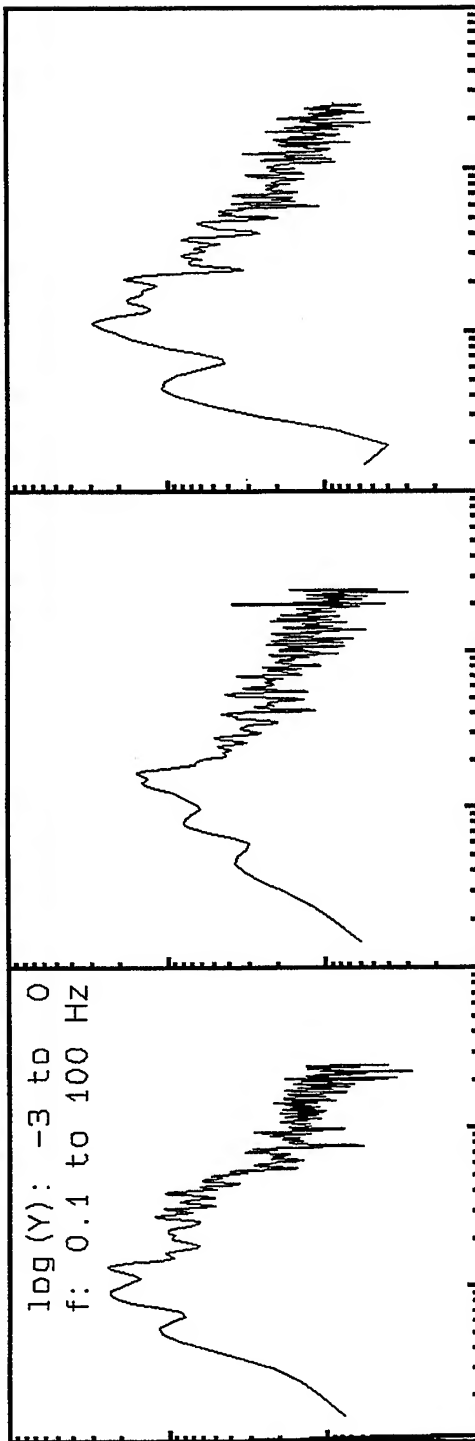
**VortexRock Consultants, Inc.**

11434 Alder Creek Rd, Corona, CA 91720

Tel - Fax (714) 692-1443, E-Mail: mahdiyari@coda.usc.edu

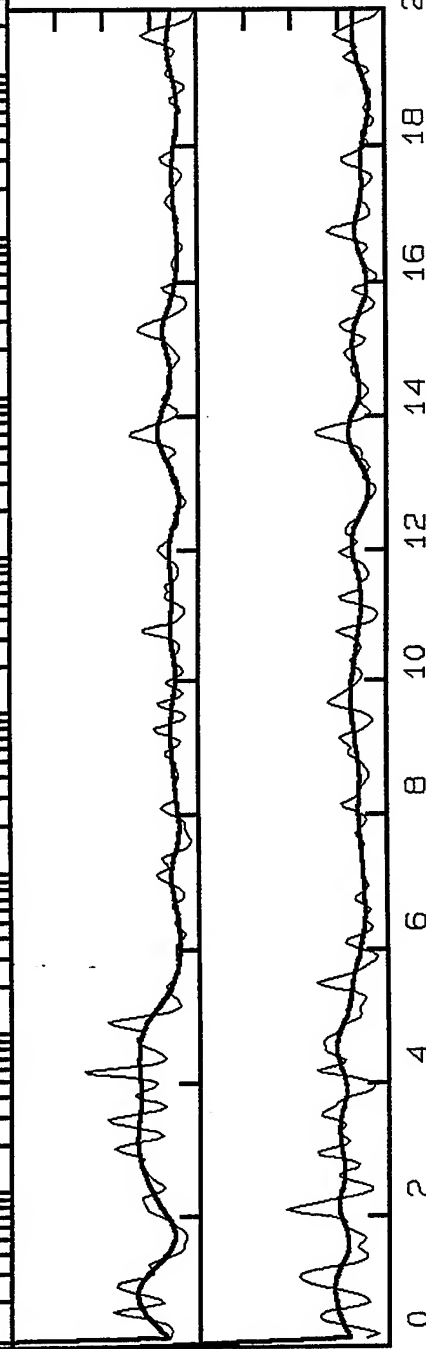


311\_LA03, Window: 41.6 to 60.0 s

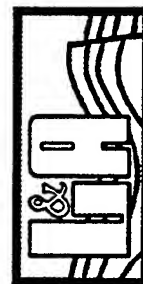


Radial/Vertical  
Linear Scale 0-8

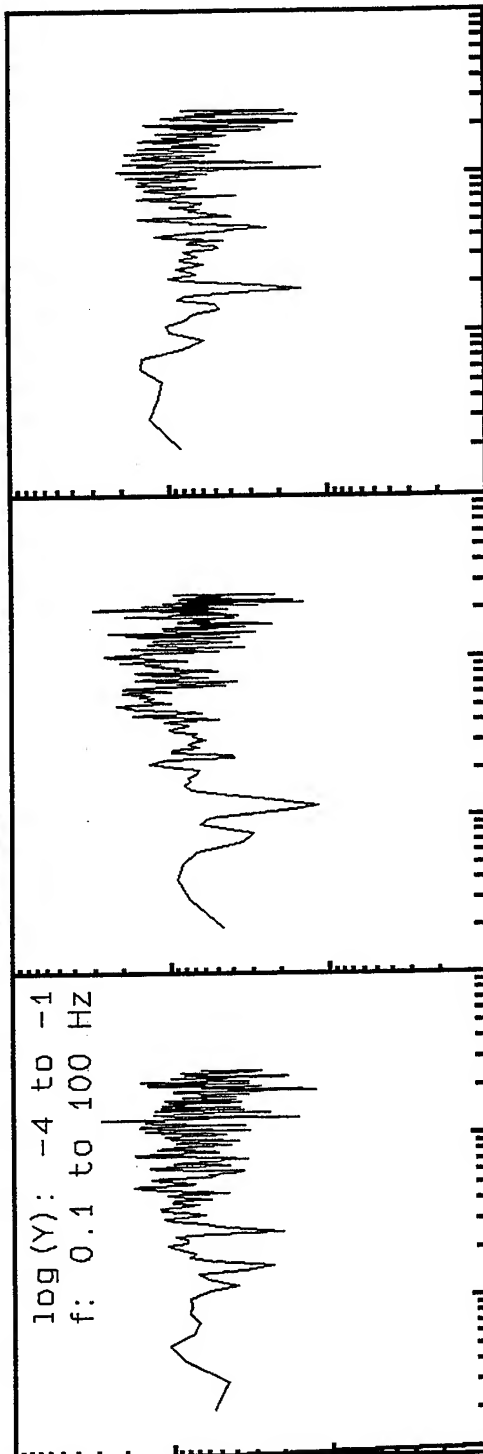
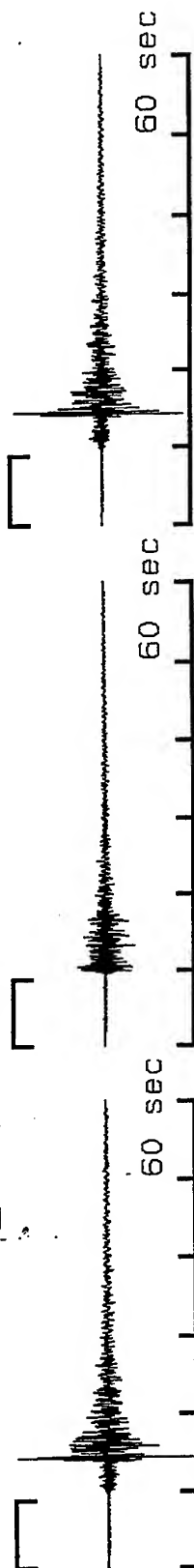
Transvers/Vertical:  
Linear Scale 0-8



**VortexRock Consultants, Inc.**  
11434 Alder Creek Rd, Corona, CA 91720  
Tel - Fax (714) 692-1443, E-Mail: mahdyiar@coda.usc.edu

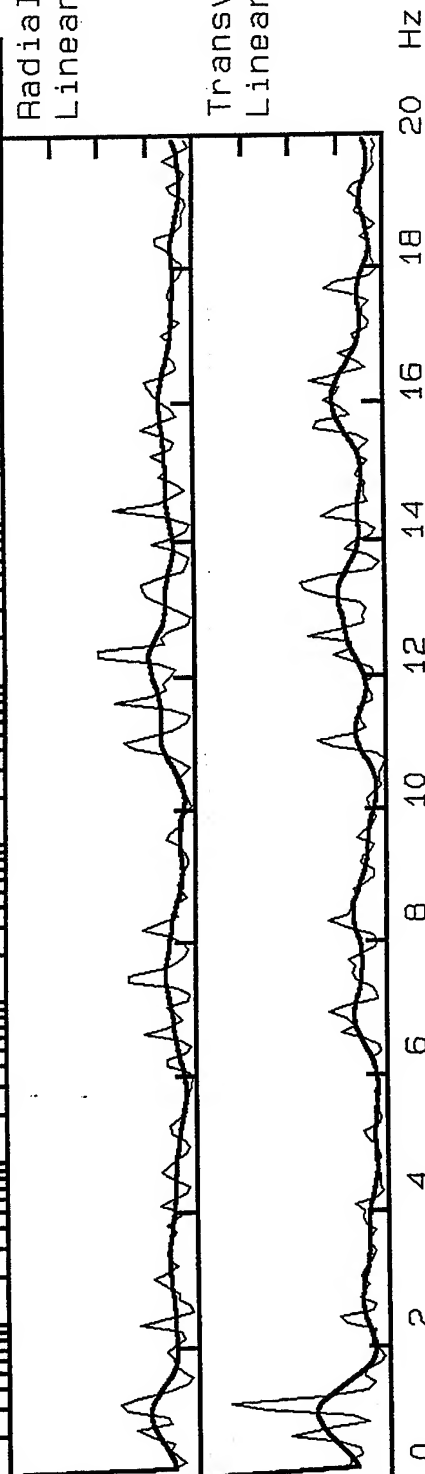


312\_LA03, Window: .0 to 8.8 s

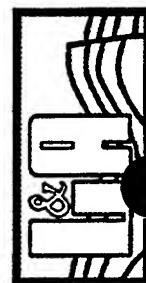


Radial/Vertical  
Linear Scale 0-8

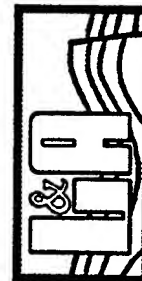
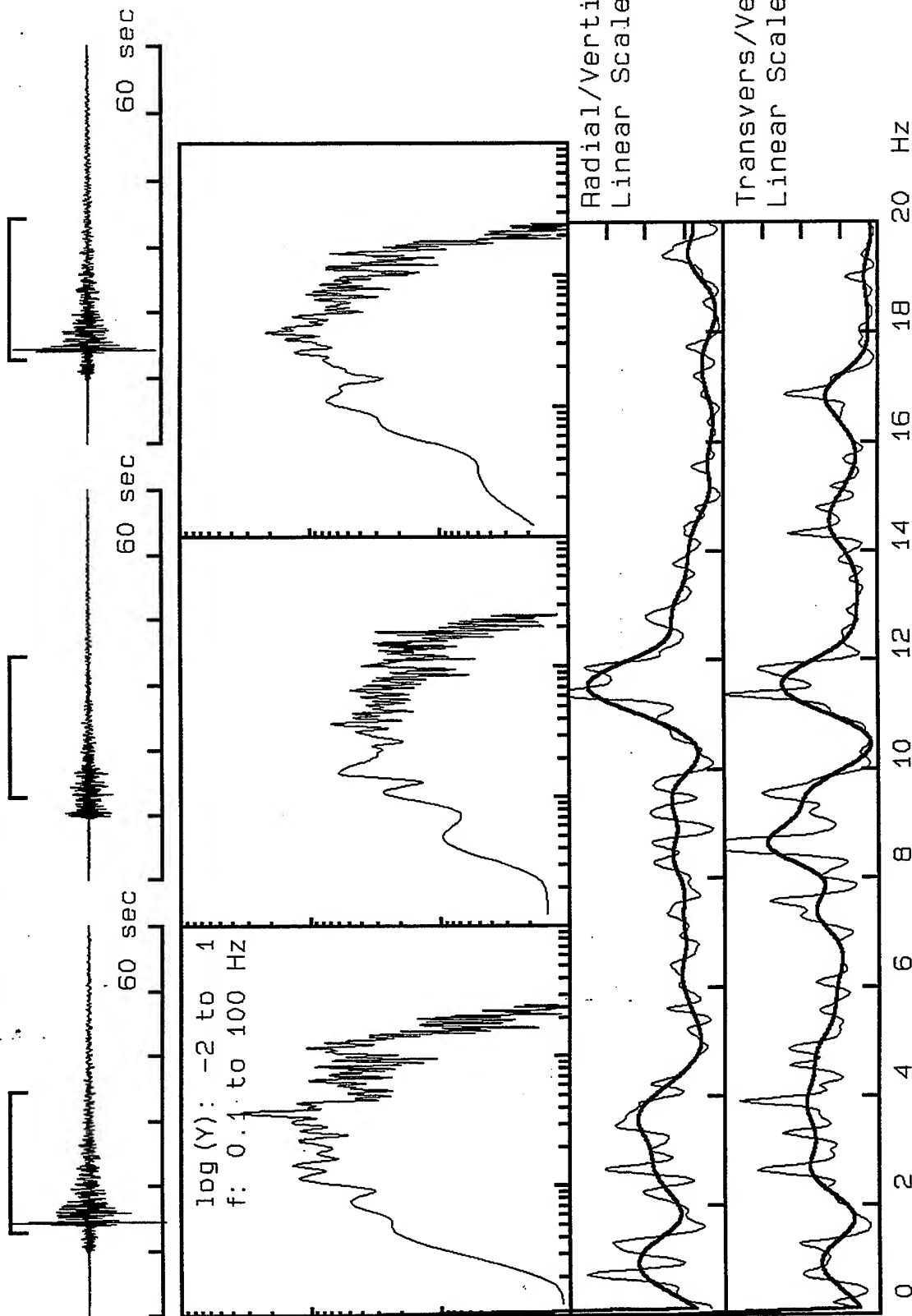
Transvers/Vertical:  
Linear Scale 0-8



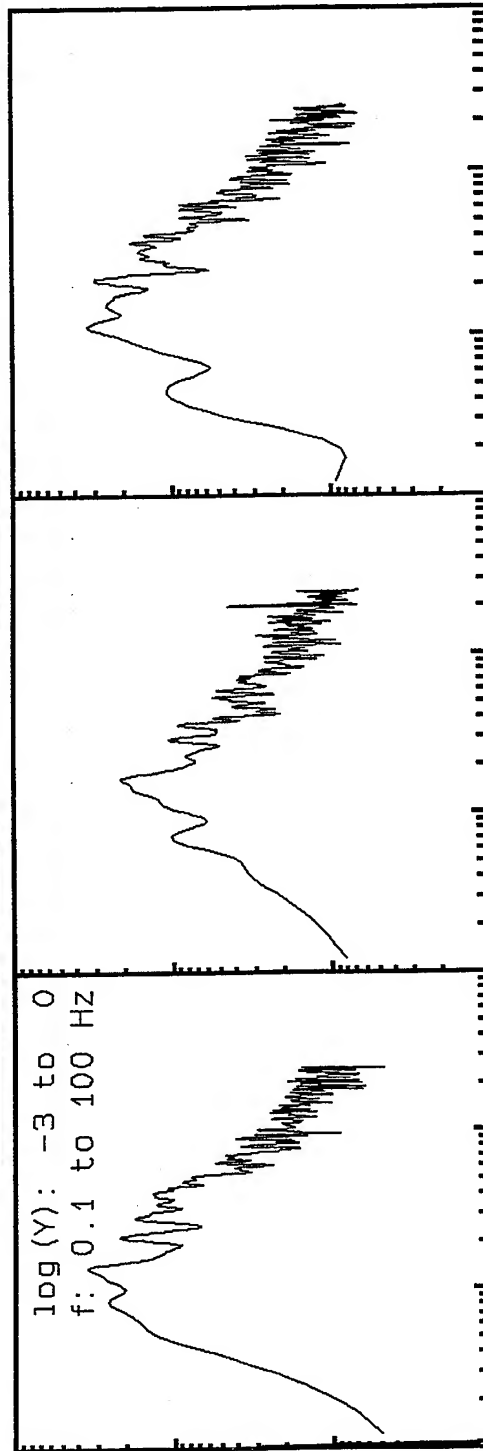
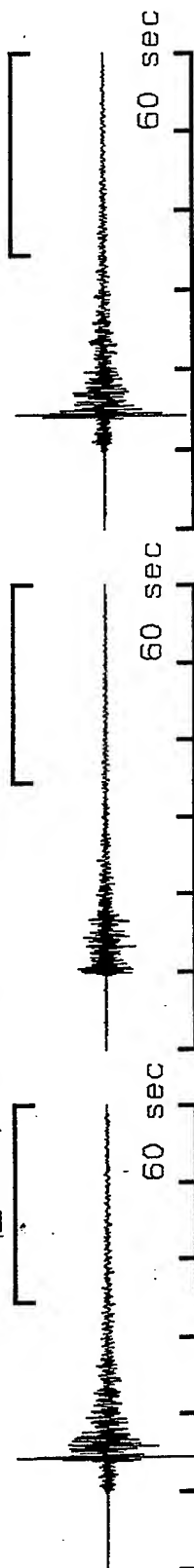
**VortexRock Consultants, Inc.**  
11434 Alder Creek Rd, Corona, CA 91720  
Tel - Fax (714) 692-1443, E-Mail: mahdyiar@coda.usc.edu



312\_LA03, Window: 12.8 to 34.4 s

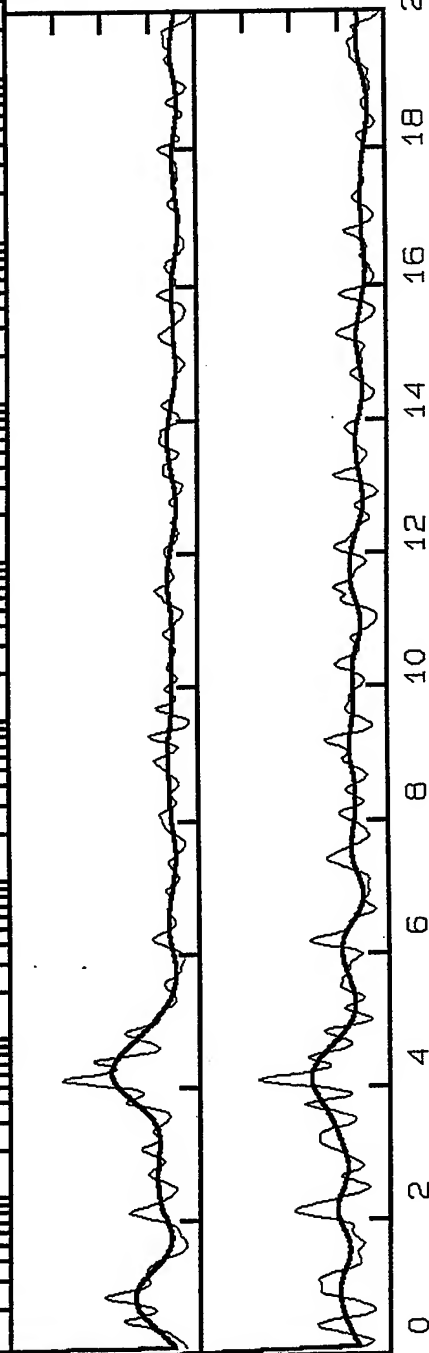


312\_LA03, Window: 34.4 to 60.2 s

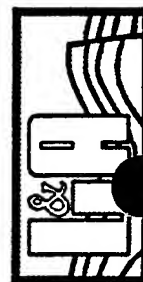


Radial/Vertical  
Linear Scale 0-8

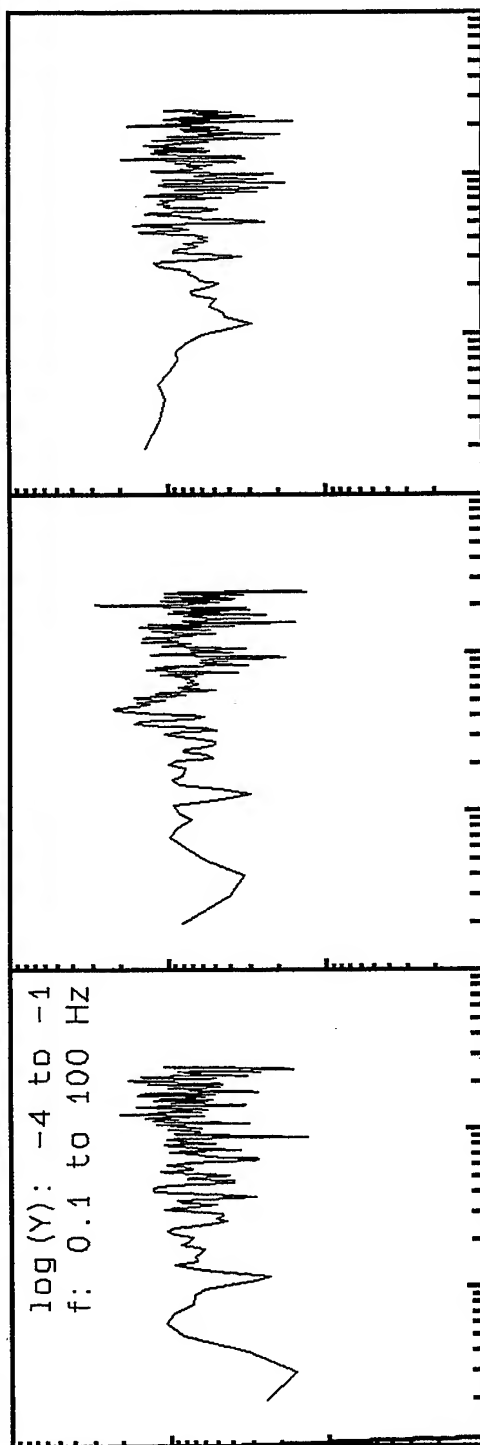
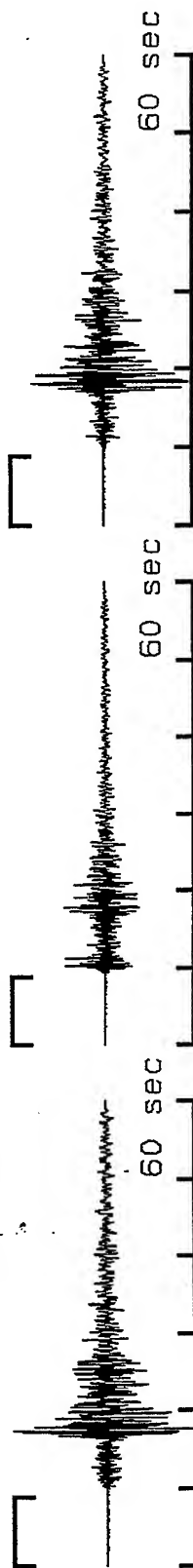
Transvers/Vertical:  
Linear Scale 0-8



**VortexRock Consultants, Inc.**  
11434 Alder Creek Rd, Corona, CA 91720  
Tel - Fax (714) 692-1443, E-Mail: mahdyiar@coda.usc.edu

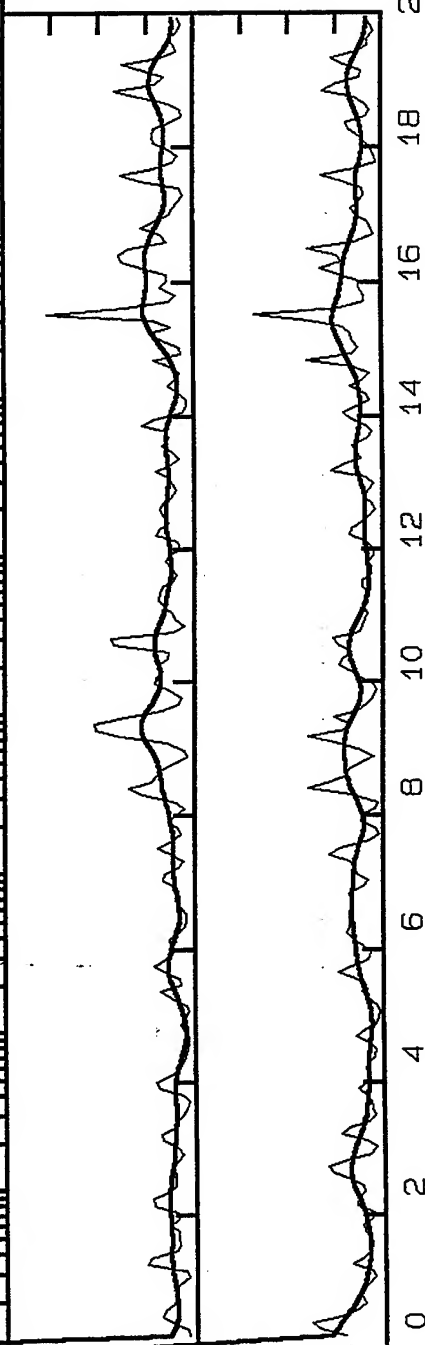


39\_LA03, Window: .0 to 8.8 s

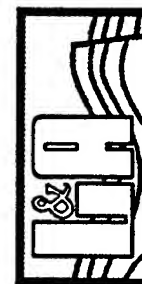


Radial/Vertical  
Linear Scale 0-8

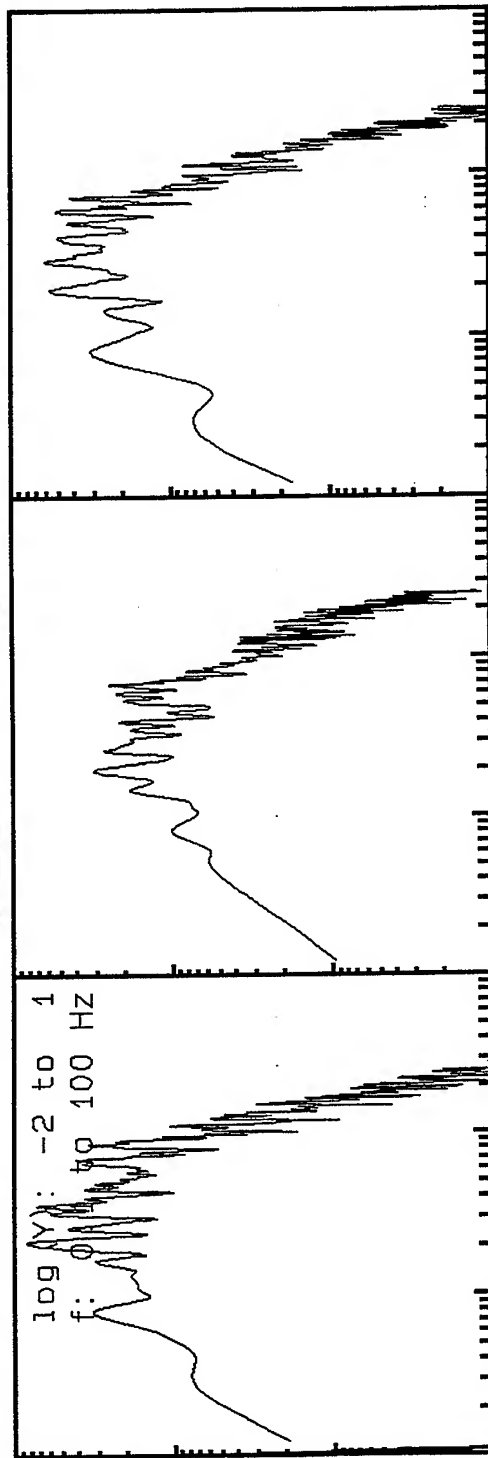
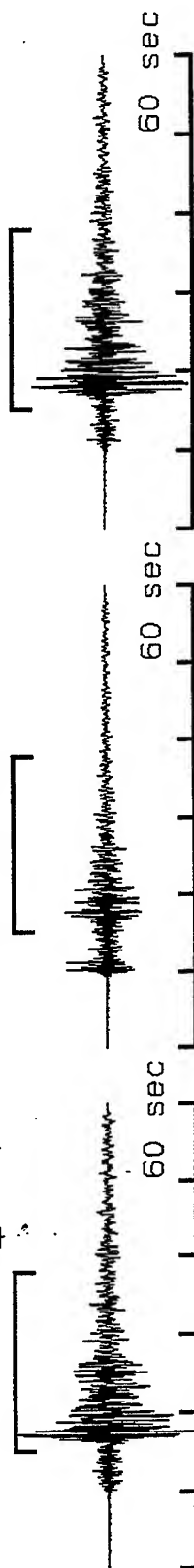
Transvers/Vertical:  
Linear Scale 0-8



**VortexRock Consultants, Inc.**  
11434 Alder Creek Rd, Corona, CA 91720  
Tel - Fax (714) 692-1443, E-Mail: mahdyiar@coda.usc.edu

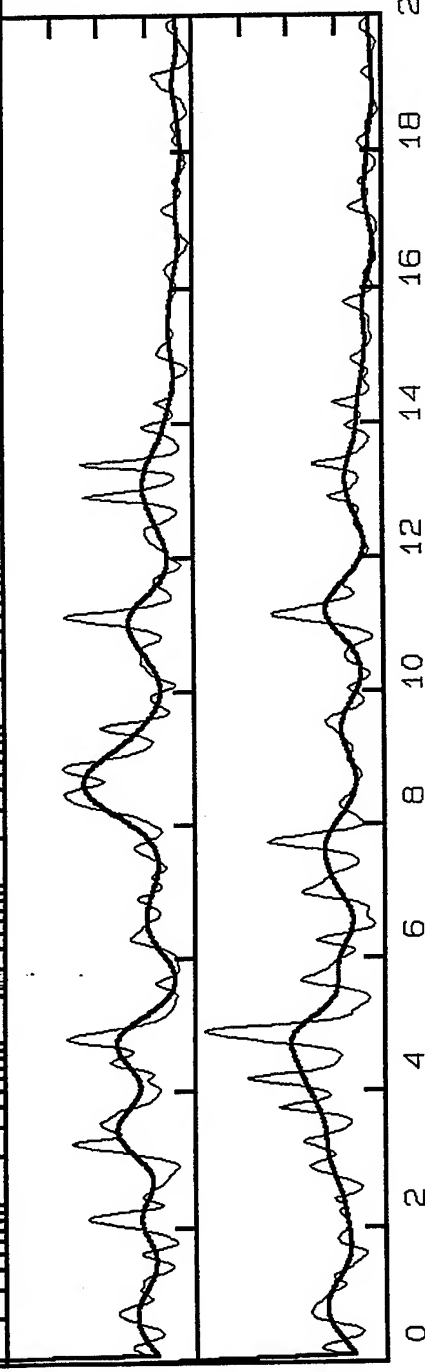


39\_LA03, Window: 15.2 to 38.0 s

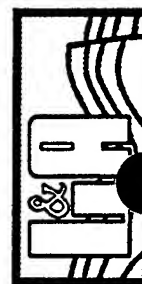


Radial/Vertical  
Linear Scale 0-8

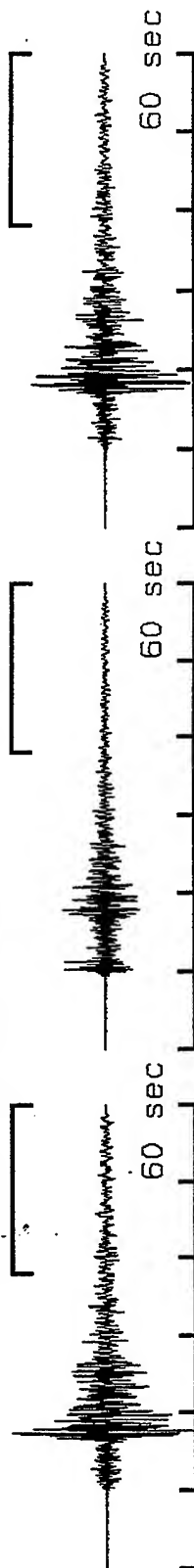
Transvers/Vertical:  
Linear Scale 0-8



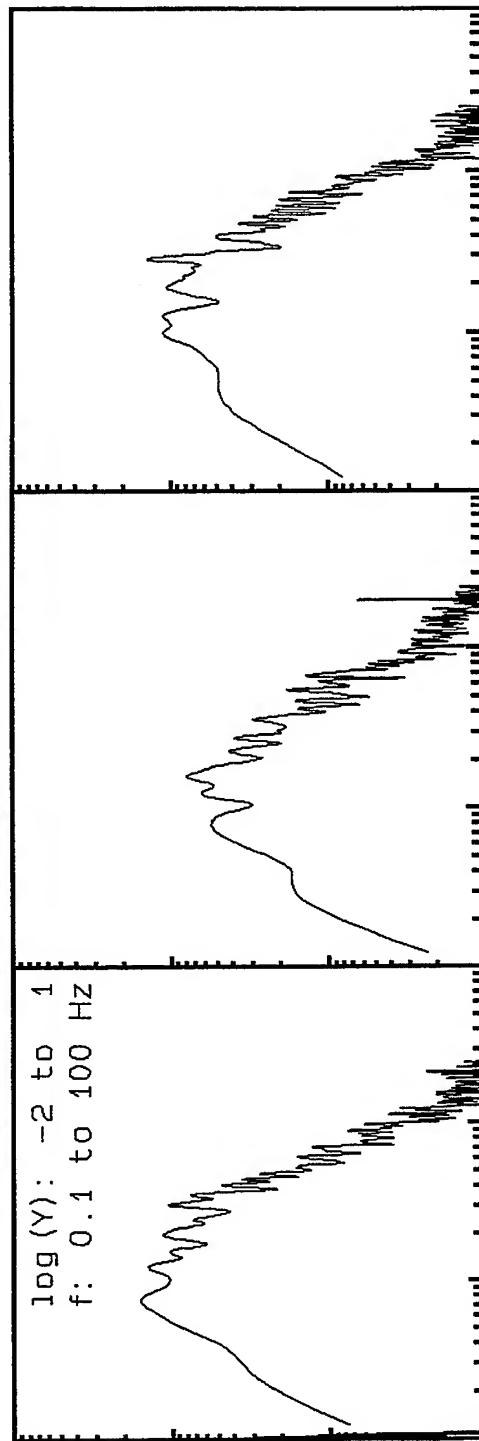
**VortexRock Consultants, Inc.**  
11434 Alder Creek Rd, Corona, CA 91720  
Tel - Fax (714) 692-1443, E-Mail: mahdyiar@coda.usc.edu



39\_LA03, Window: 38.0 to 60.0 s



log (Y): -2 to 1  
f: 0.1 to 100 Hz



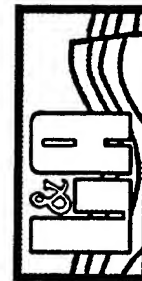
Radial/Vertical  
Linear Scale 0-8

Transvers/Vertical:  
Linear Scale 0-8

20 Hz

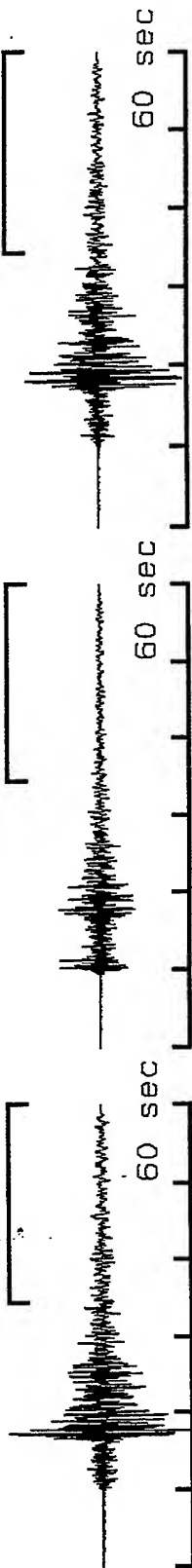


**VortexRock Consultants, Inc.**  
11434 Alder Creek Rd, Corona, CA 91720  
Tel - Fax (714) 692-1443, E-Mail: mahdyar@coda.usc.edu

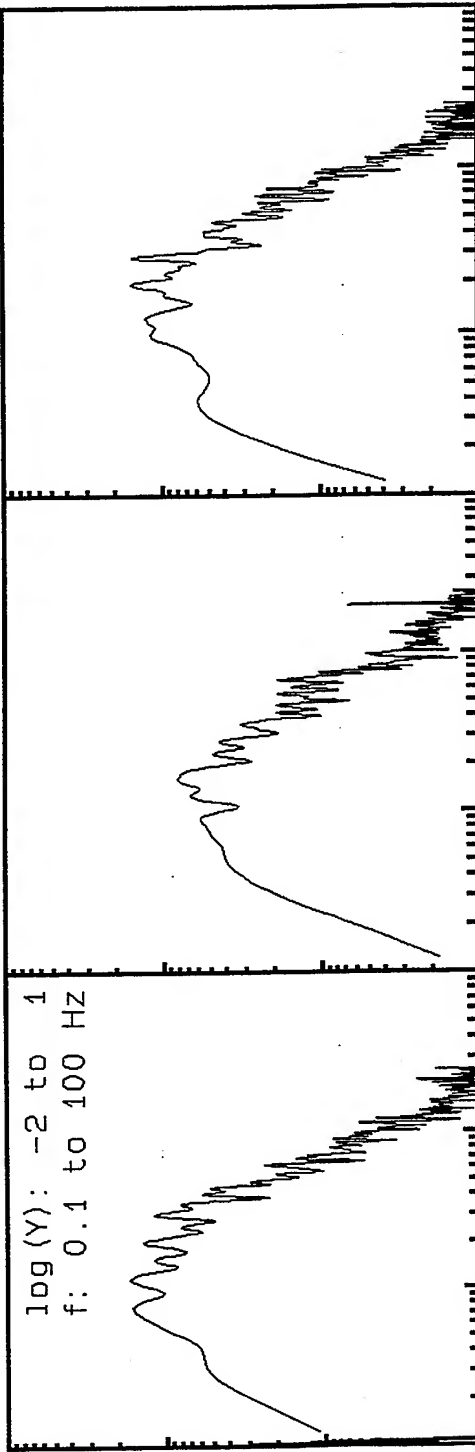




39\_LA03, Window: 34.4 to 60.2 s

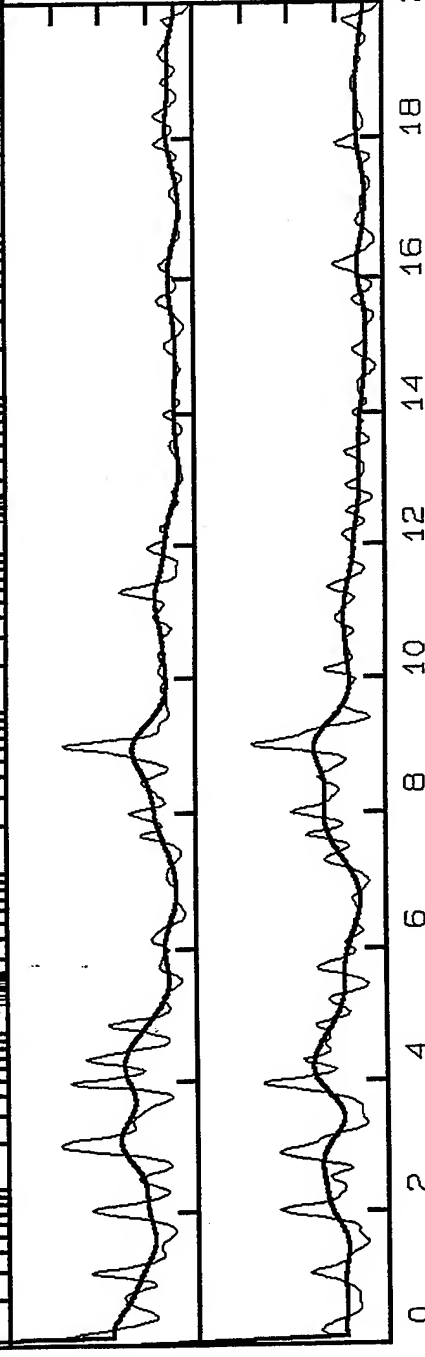


log(Y): -2 to 1  
f: 0.1 to 100 Hz

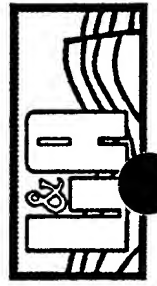


Radial/Vertical  
Linear Scale 0-8

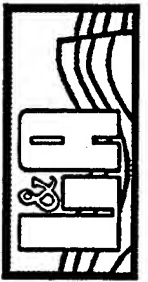
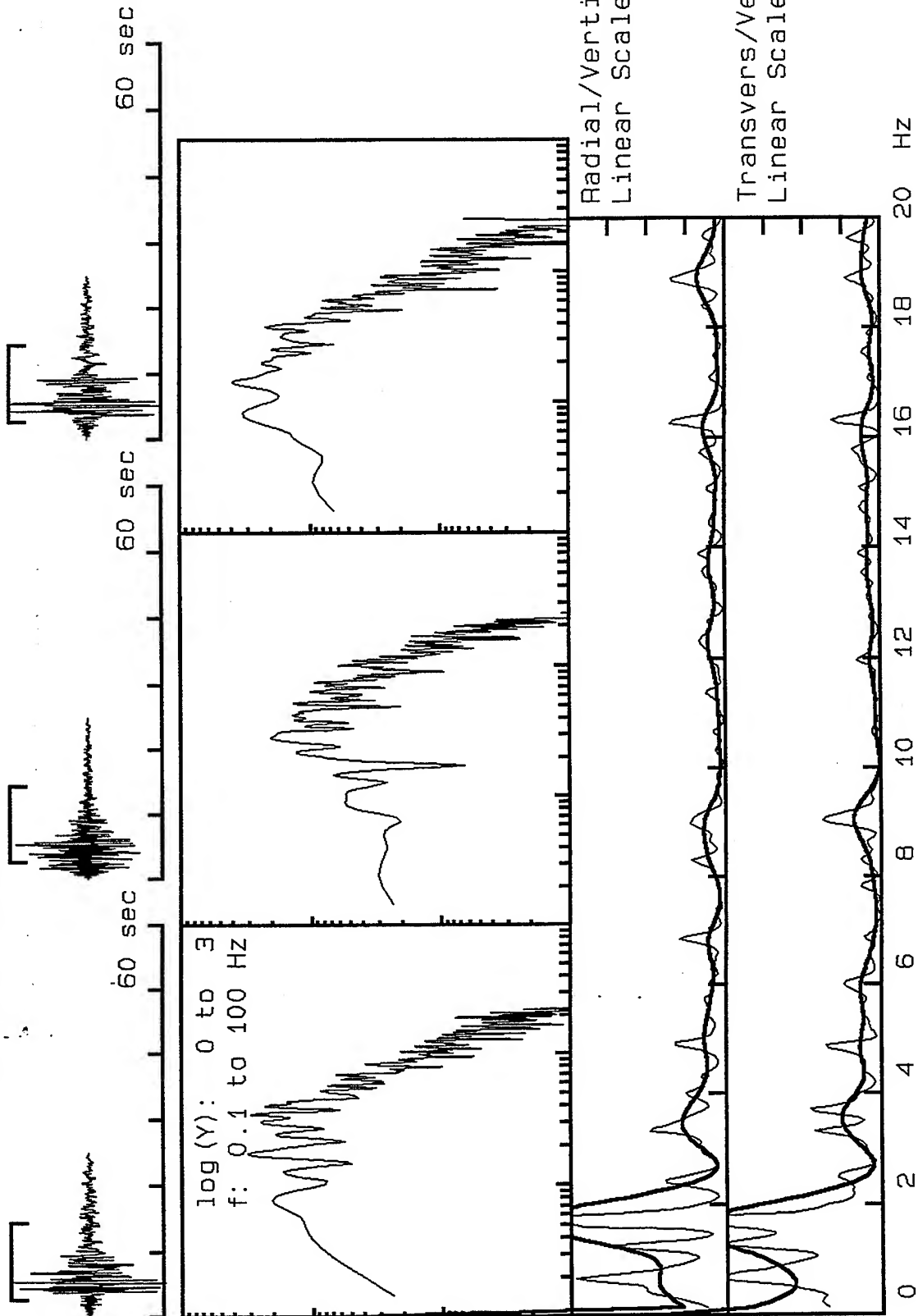
Transvers/Vertical:  
Linear Scale 0-8



**VortexRock Consultants, Inc.**  
11434 Alder Creek Rd, Corona, CA 91720  
Tel - Fax (714) 692-1443, E-Mail: mahdyar@coda.usc.edu



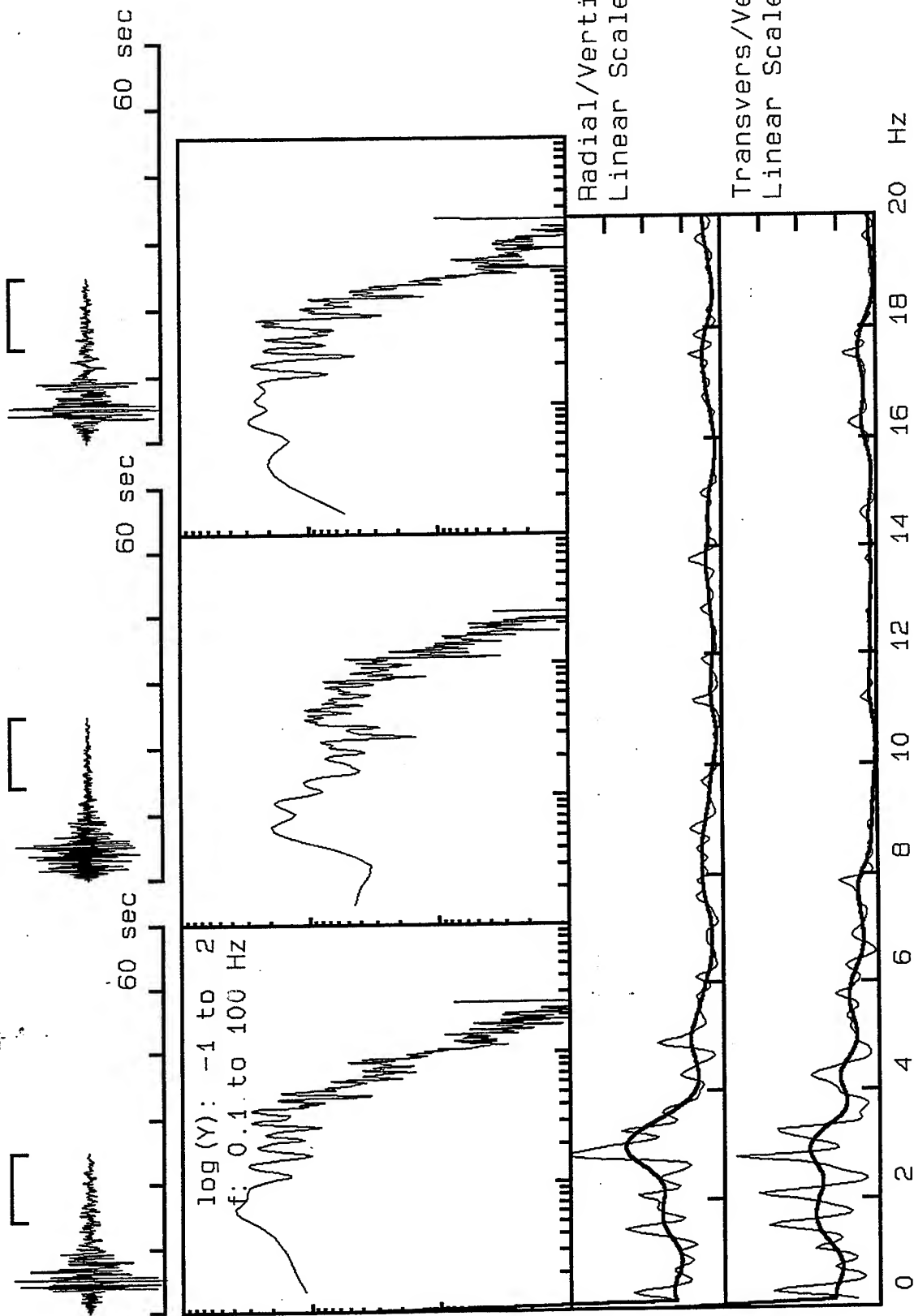
51\_NEWH, Window: 2.8 to 14.4 s



**VortexRock Consultants, Inc.**  
11434 Alder Creek Rd, Corona, CA 91720  
Tel - Fax (714) 692-1443, E-Mail: mahdyiar@coda.usc.edu



51\_NEWH, Window: 14.4 to 25.0 s



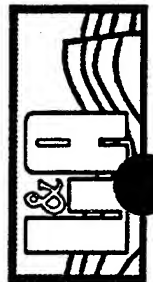
H-41



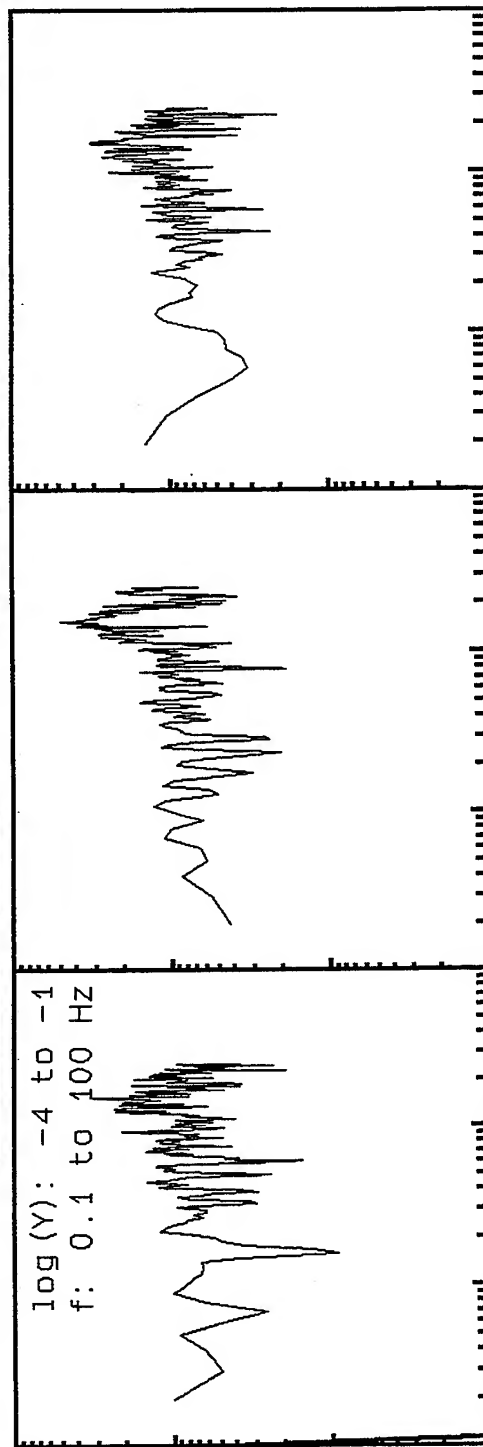
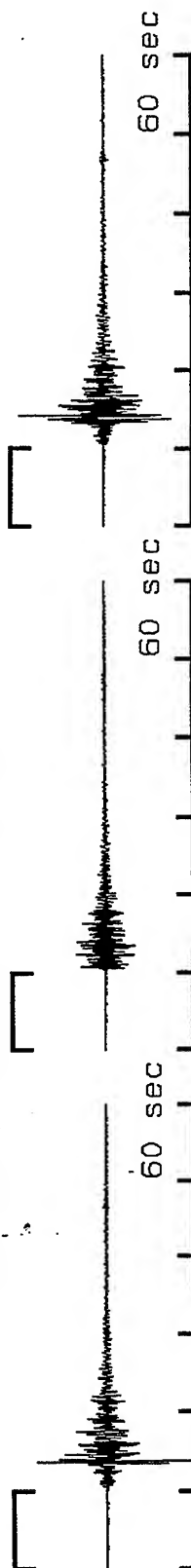
**VortexRock Consultants, Inc.**

11434 Alder Creek Rd, Corona, CA 91720

Tel - Fax (714) 692-1443, E-Mail: mahdyiar@coda.usc.edu

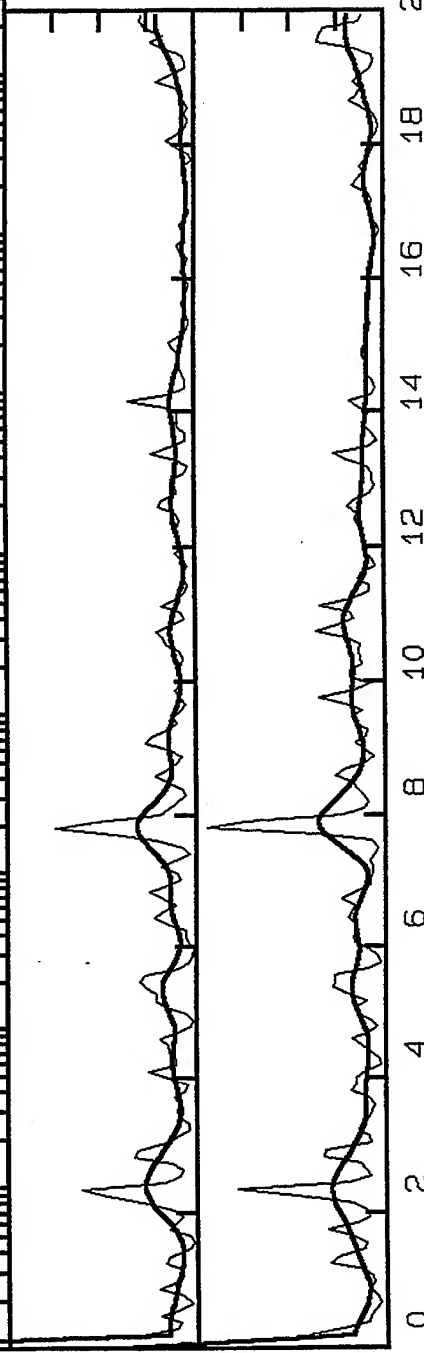


513\_NWHP, Window: .0 to 10.0 s

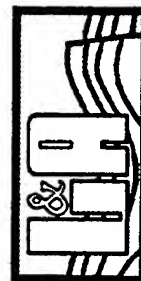


Radial/Vertical  
Linear Scale 0-8

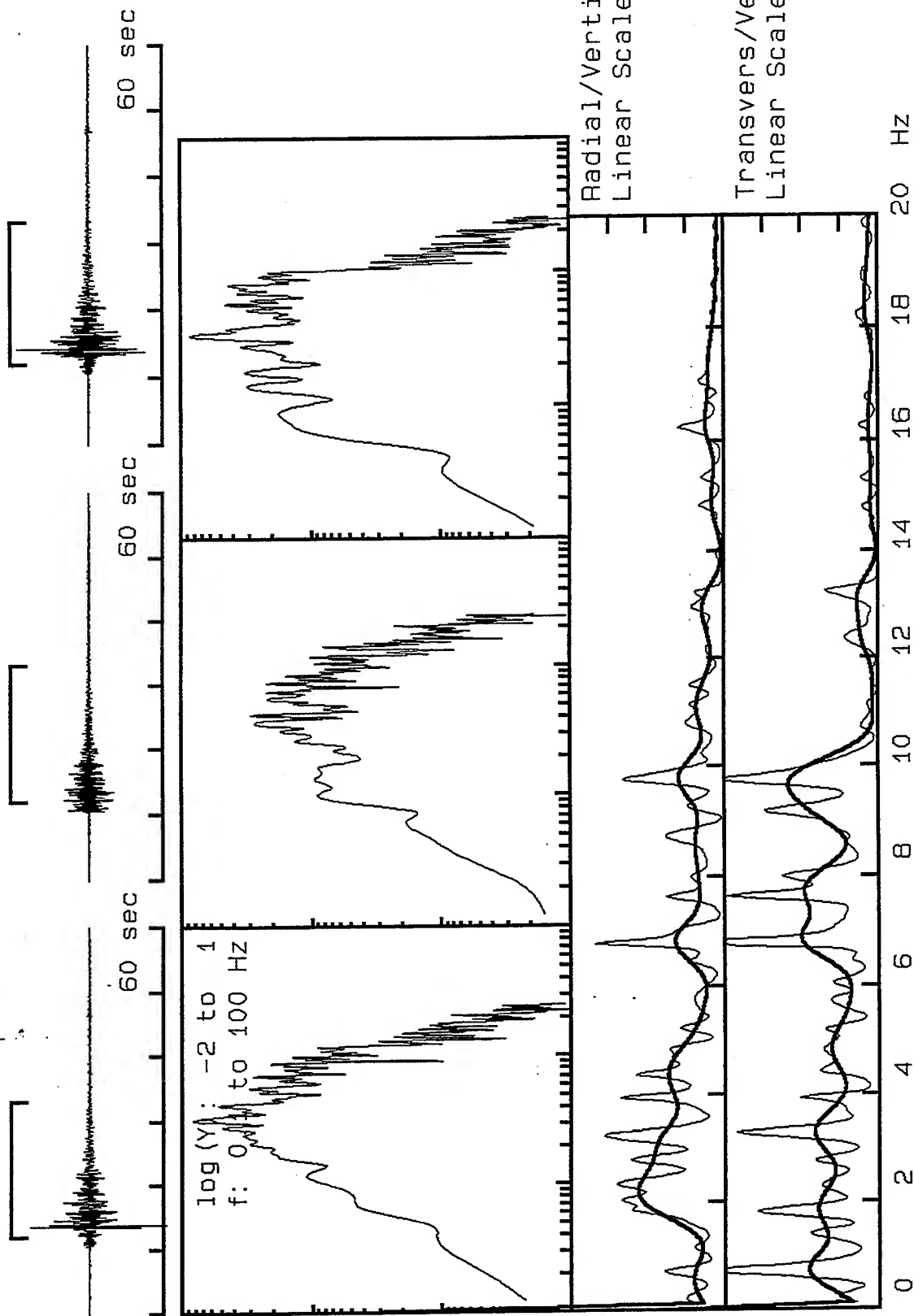
Transvers/Vertical:  
Linear Scale 0-8



**VortexRock Consultants, Inc.**  
11434 Alder Creek Rd, Corona, CA 91720  
Tel - Fax (714) 692-1443, E-Mail: mahdyiar@coda.usc.edu



513\_NWHP, Window: 12.0 to 33.2 s

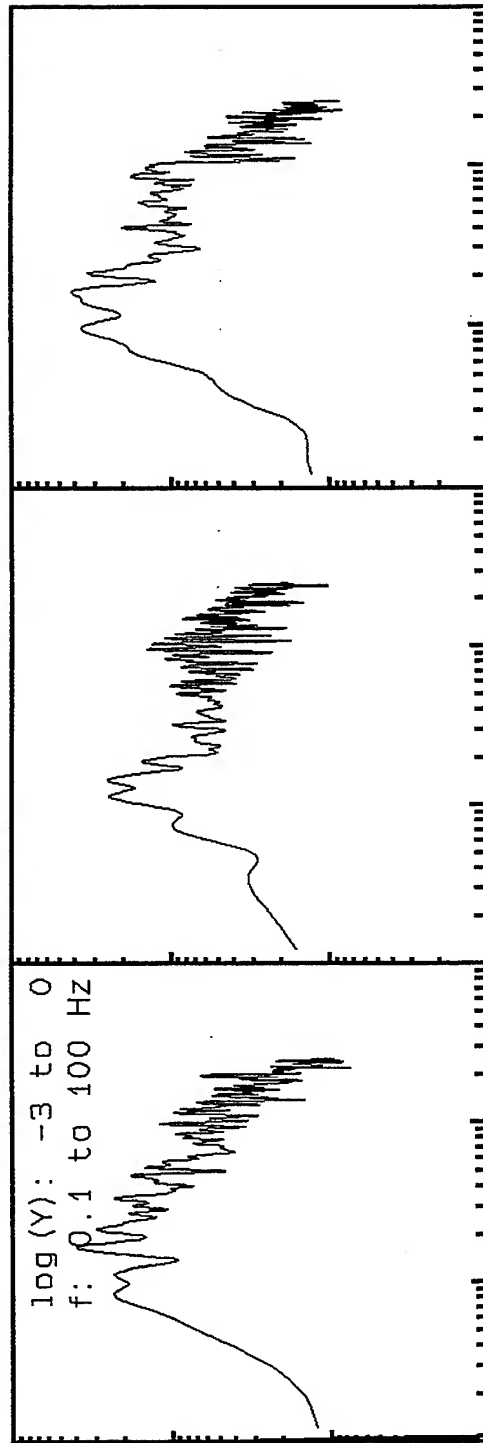
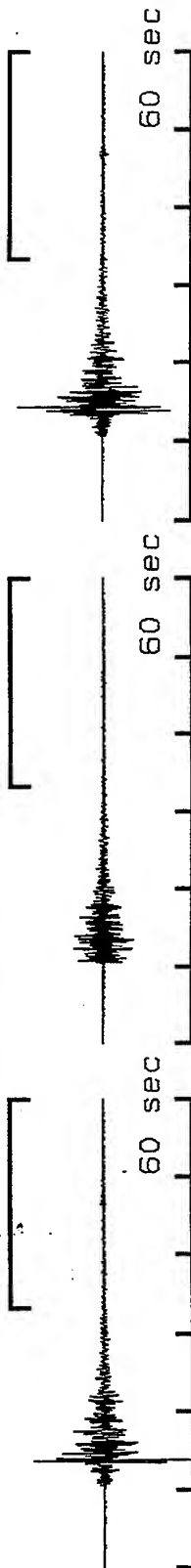


**VortexRock Consultants, Inc.**

11434 Alder Creek Rd, Corona, CA 91720

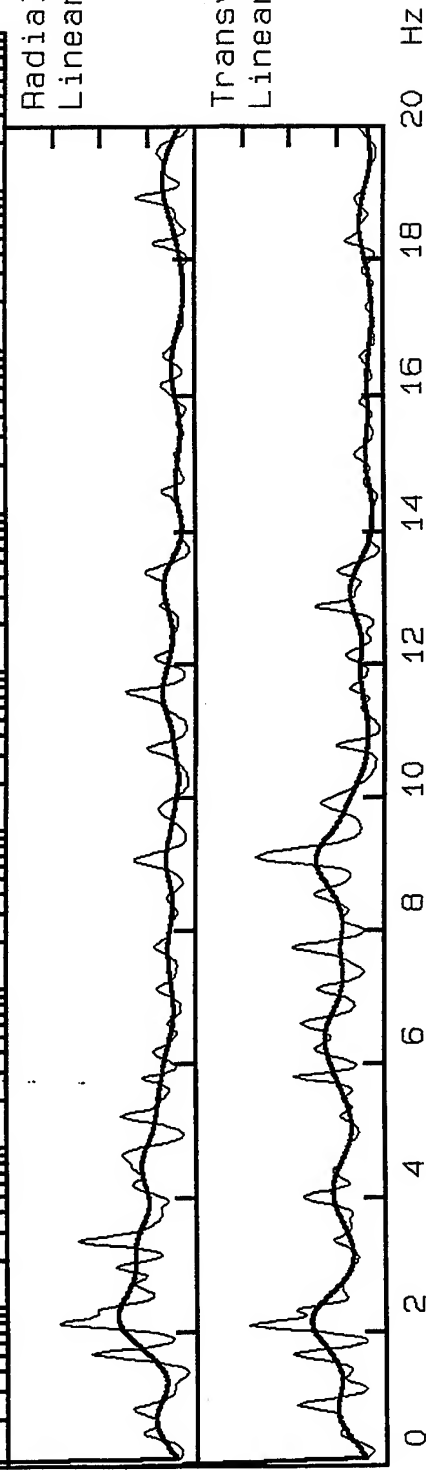
Tel - Fax (714) 692-1443, E-Mail: mahdyiar@coda.usc.edu

513\_NWHP, Window: 33.2 to 60.0 s

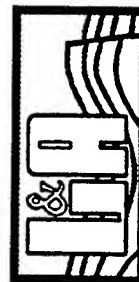


Radial/Vertical  
Linear Scale 0-8

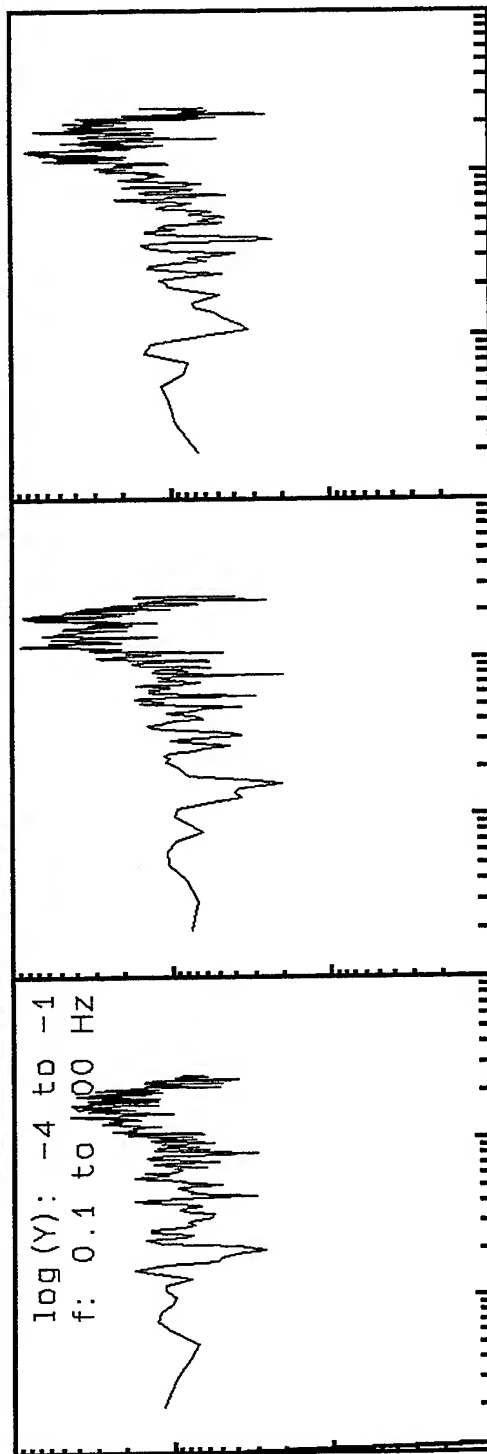
Transvers/Vertical:  
Linear Scale 0-8



**VortexRock Consultants, Inc.**  
11434 Alder Creek Rd, Corona, CA 91720  
Tel - Fax (714) 692-1443, E-Mail: mahdiyari@coda.usc.edu

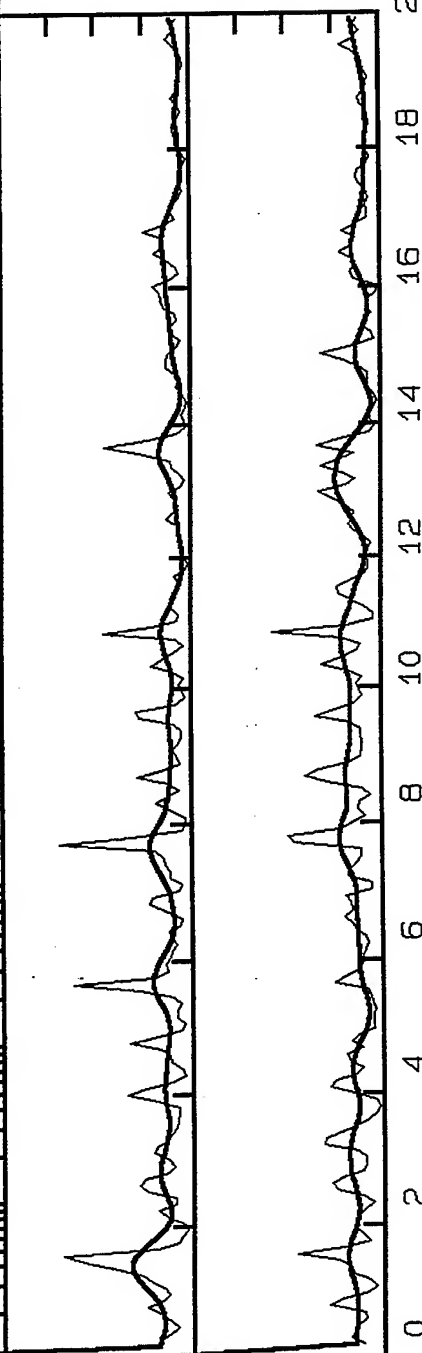


514\_NWHP, Window: .0 to 9.6 s



Radial/Vertical  
Linear Scale 0-8

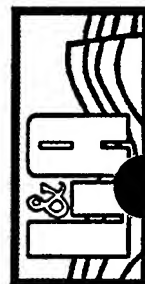
Transvers/Vertical:  
Linear Scale 0-8



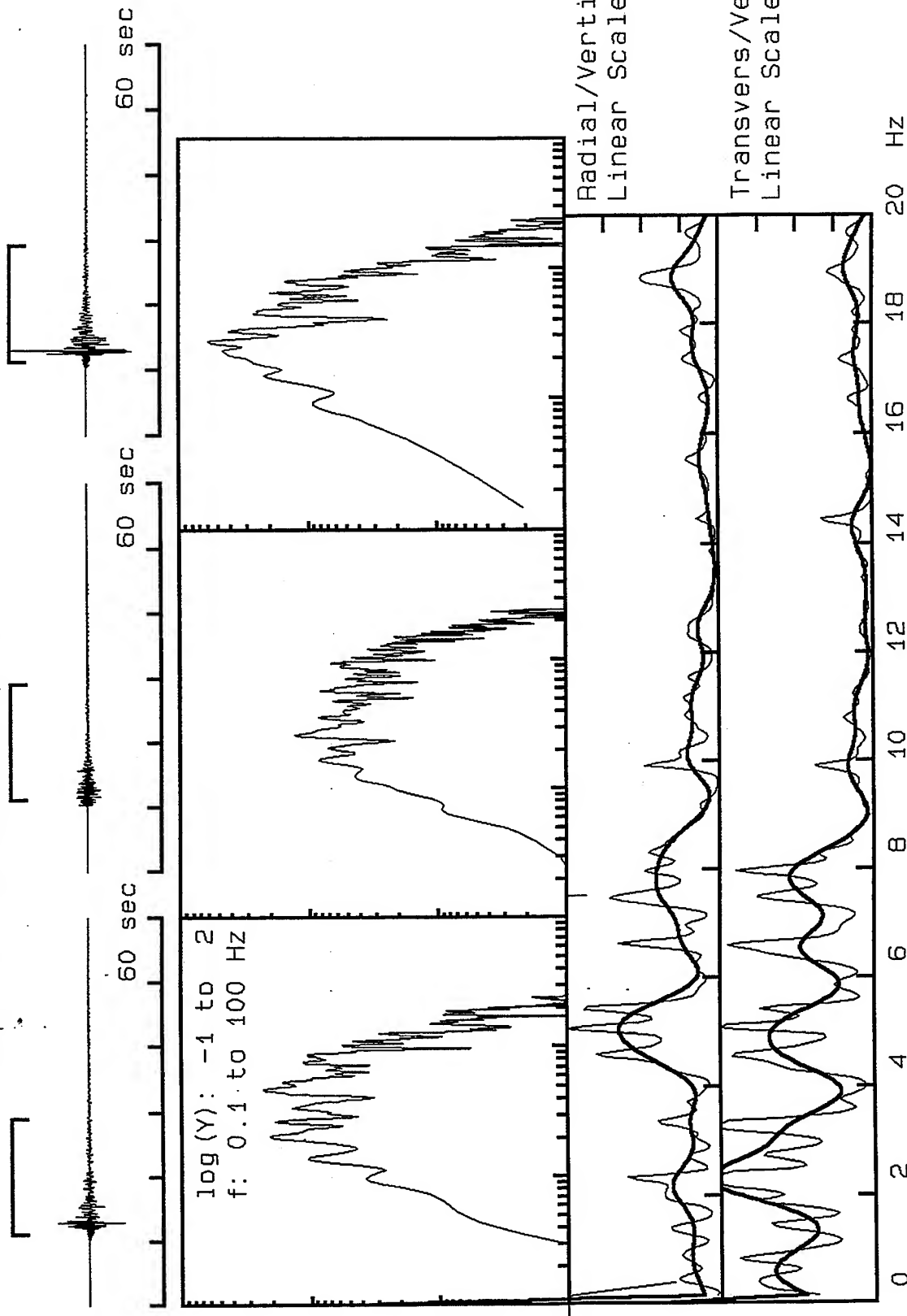
**VortexRock Consultants, Inc.**

11434 Alder Creek Rd, Corona, CA 91720

Tel - Fax (714) 692-1443, E-Mail: mahdyiar@coda.usc.edu



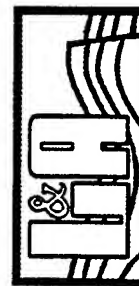
514\_NWHP, Window: 11.2 to 29.2 s



H-46

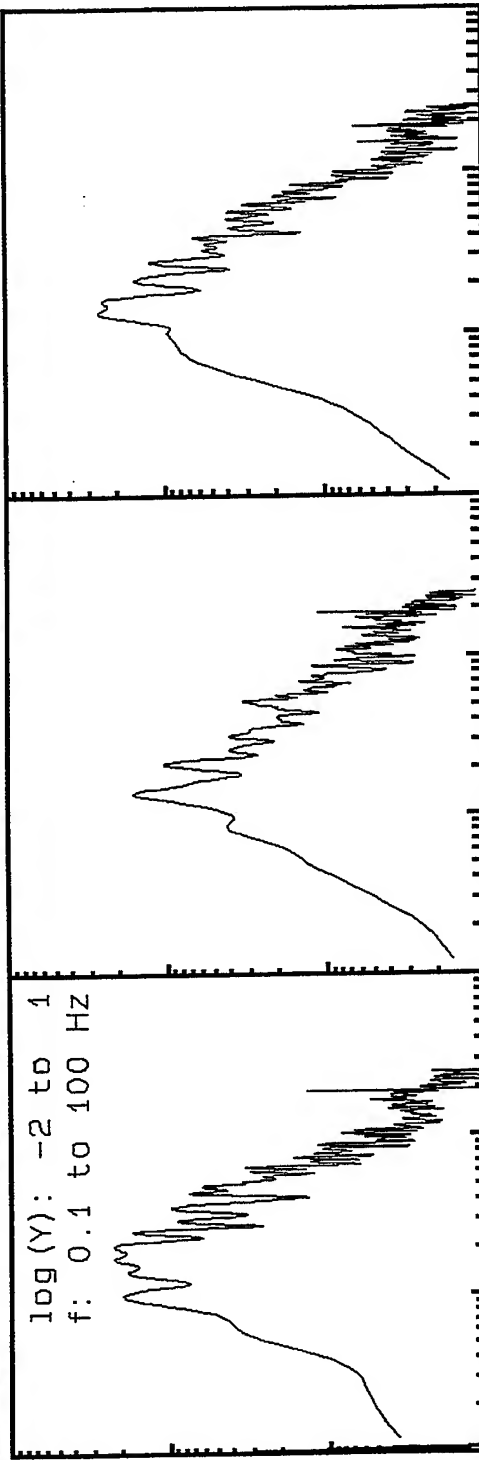
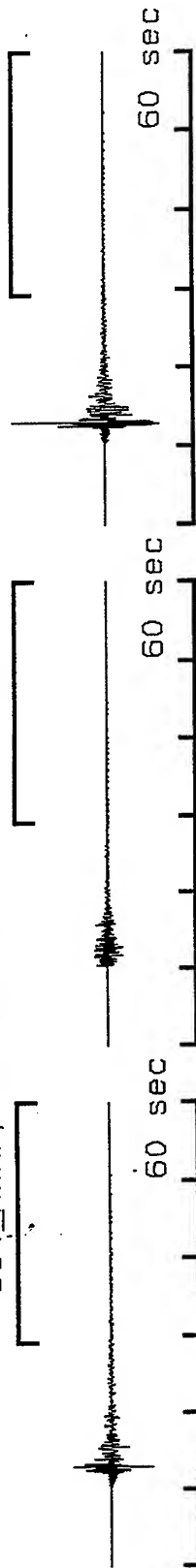


**VortexRock Consultants, Inc.**  
11434 Alder Creek Rd, Corona, CA 91720  
Tel - Fax (714) 692-1443, E-Mail: mahdyiar@coda.usc.edu



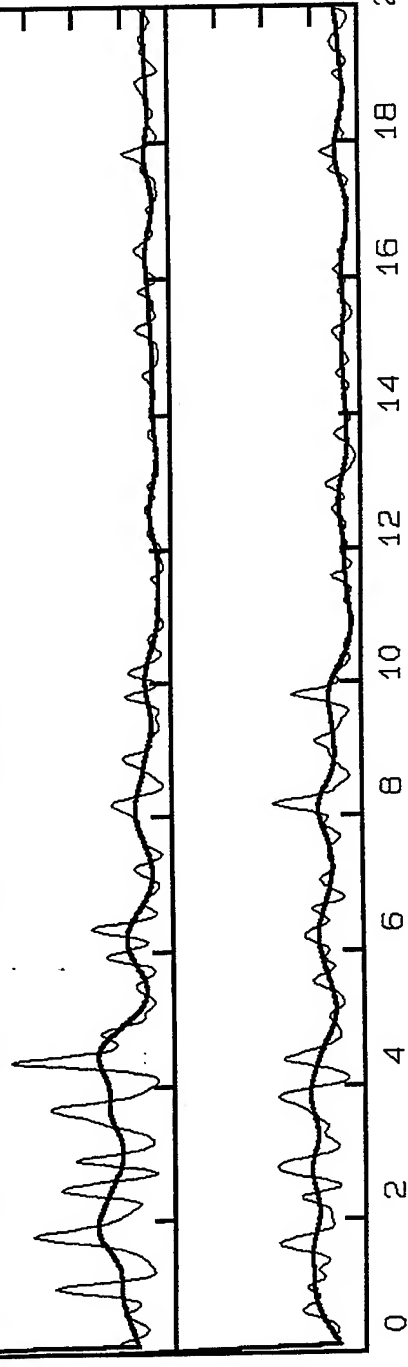


514\_NWHP, Window: 29.2 to 60.0 s

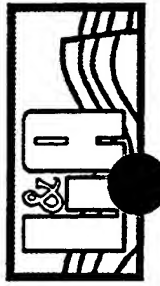


Radial/Vertical  
Linear Scale 0-8

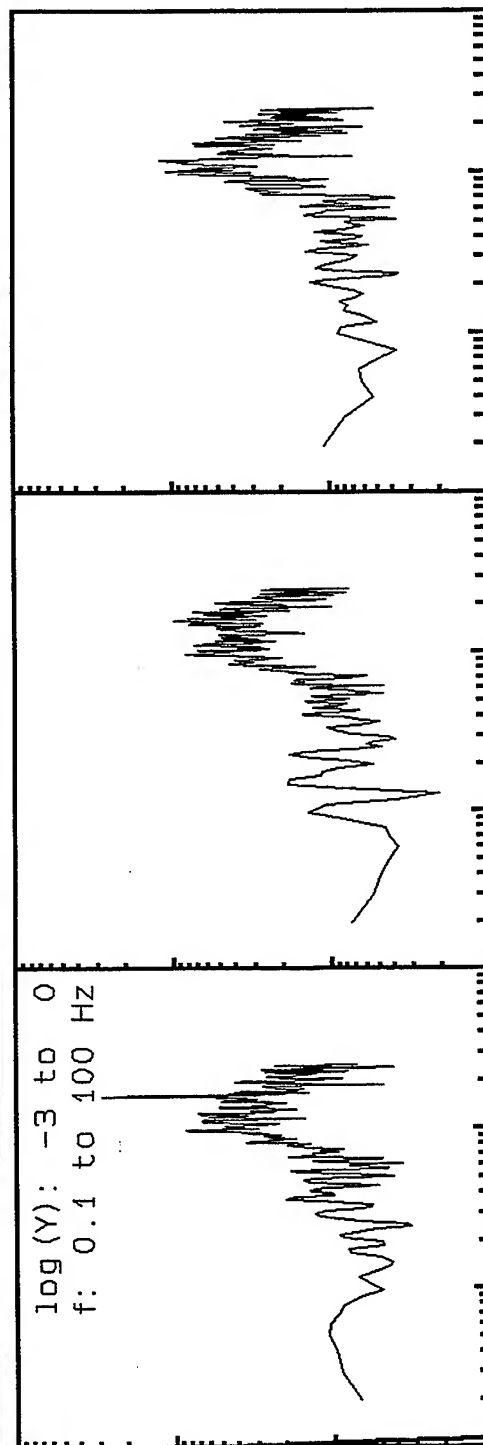
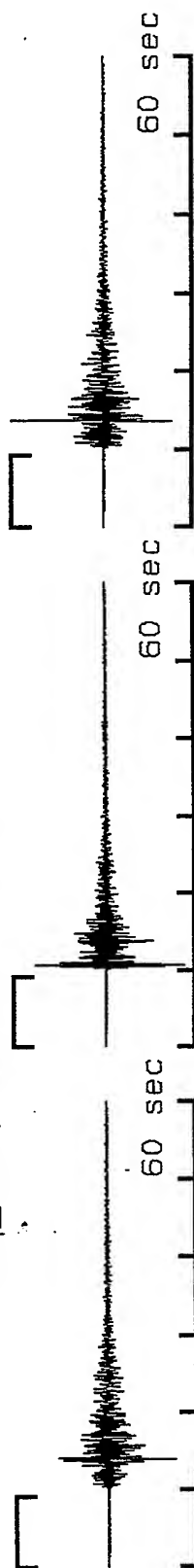
Transvers/Vertical:  
Linear Scale 0-8



**VortexRock Consultants, Inc.**  
11434 Alder Creek Rd, Corona, CA 91720  
Tel - Fax (714) 692-1443, E-Mail: mahdyar@coda.usc.edu

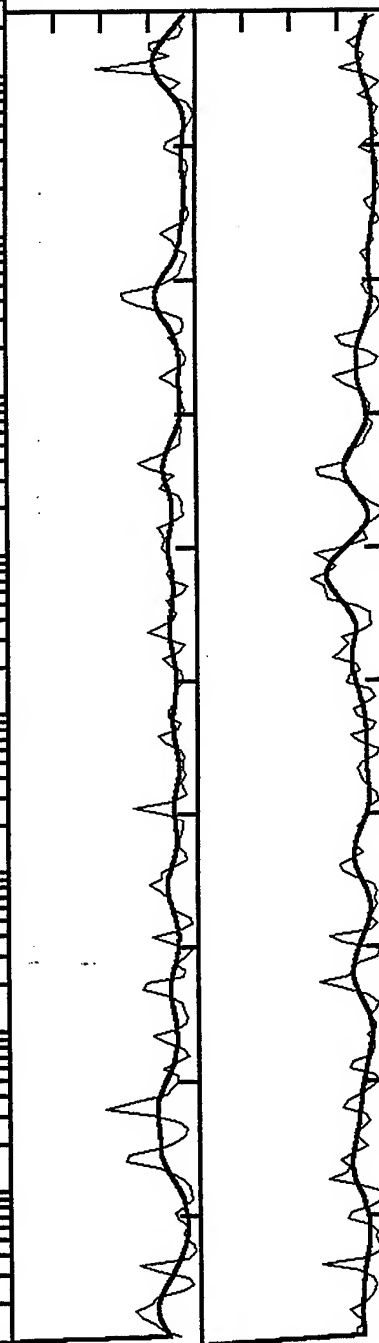


515\_NWHP, Window: .0 to 9.2 s



Radial/Vertical  
Linear Scale 0-8

Transvers/Vertical:  
Linear Scale 0-8

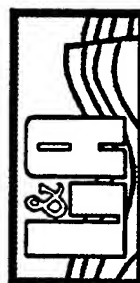


20 Hz

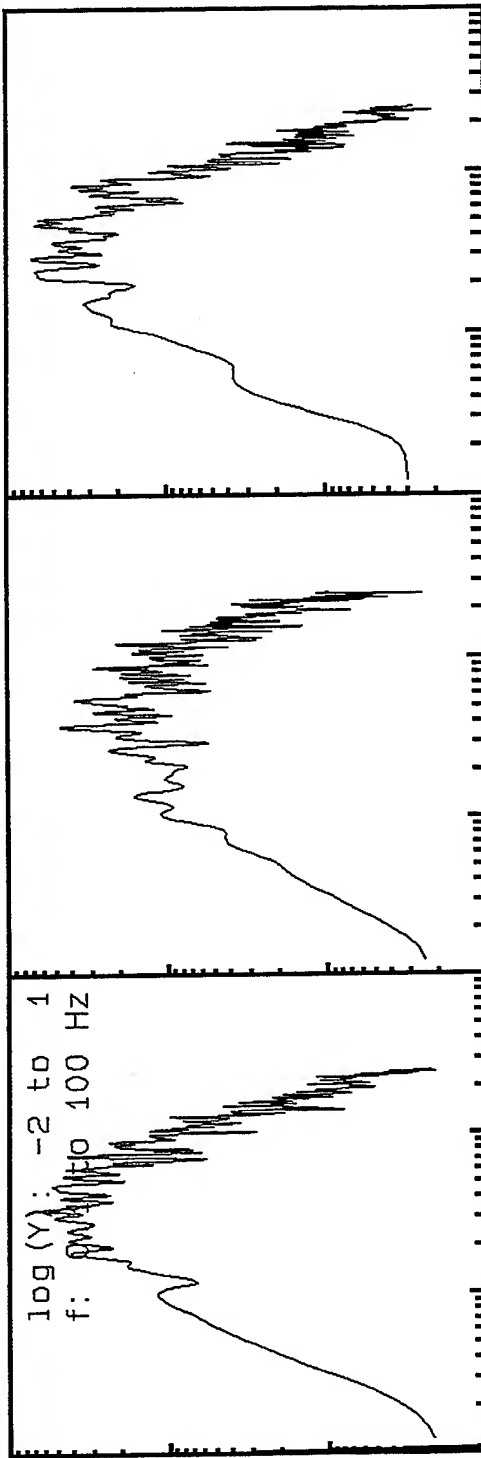
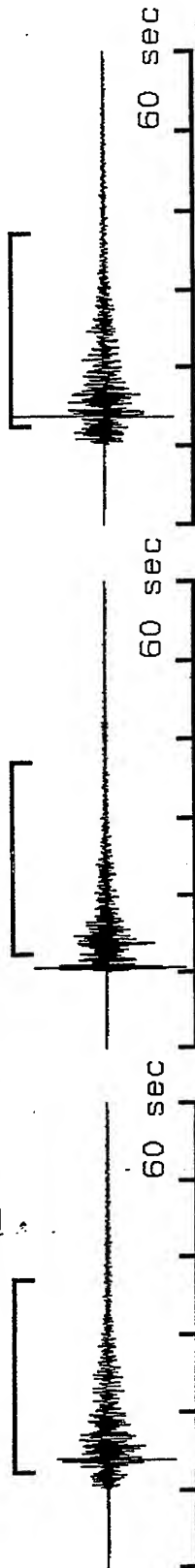
**VortexRock Consultants, Inc.**

11434 Alder Creek Rd, Corona, CA 91720

Tel - Fax (714) 692-1443, E-Mail: mahdyiar@coda.usc.edu

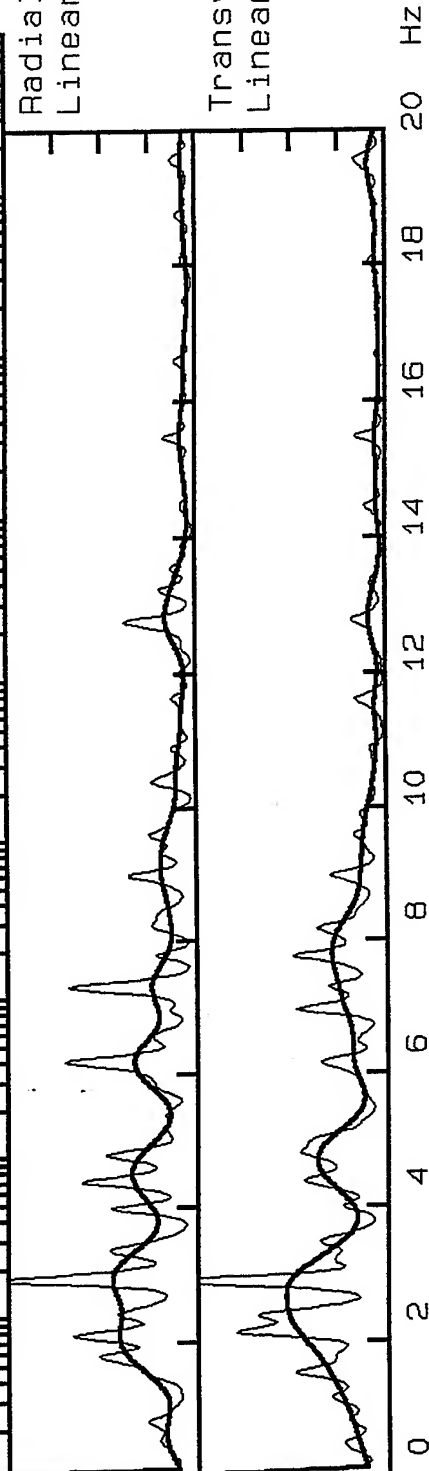


515\_NW Window: 12.4 to 37.2 s

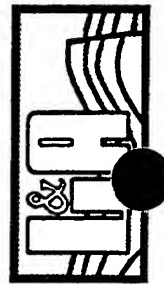


Radial/Vertical  
Linear Scale 0-8

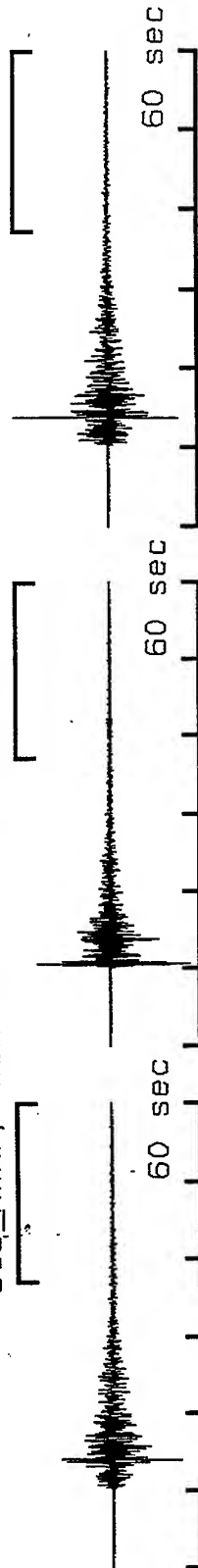
Transvers/Vertical:  
Linear Scale 0-8



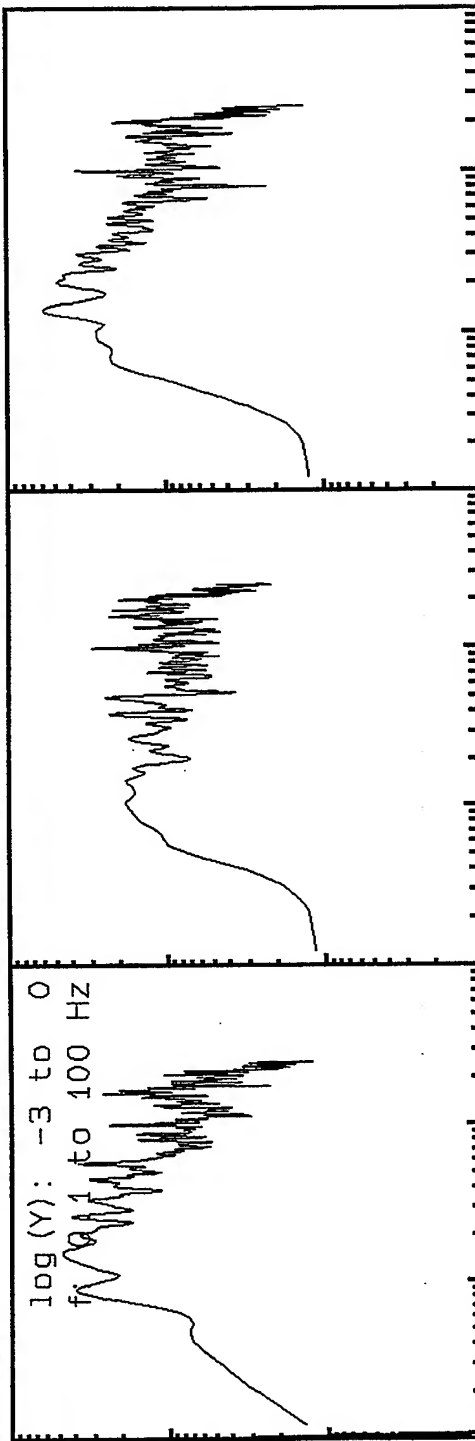
**VortexRock Consultants, Inc.**  
11434 Alder Creek Rd, Corona, CA 91720  
Tel - Fax (714) 692-1443, E-Mail: mahdyiar@coda.usc.edu



515\_NWHP, Window: 37.2 to 60.0 s

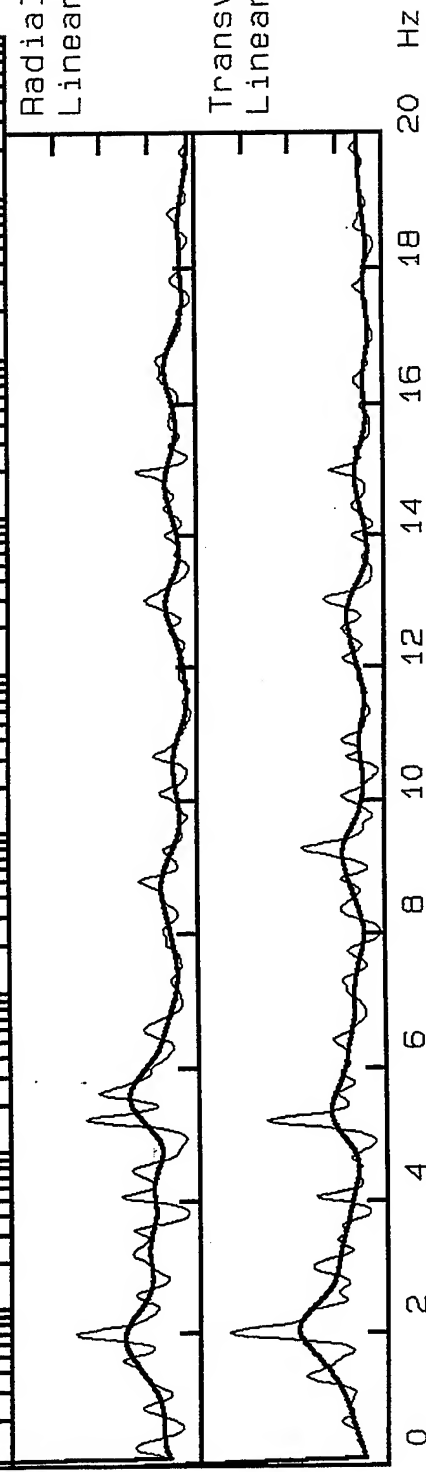


log(Y): -3 to 0  
f: 0.1 to 100 Hz

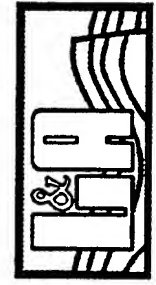


Radial/Vertical  
Linear Scale 0-8

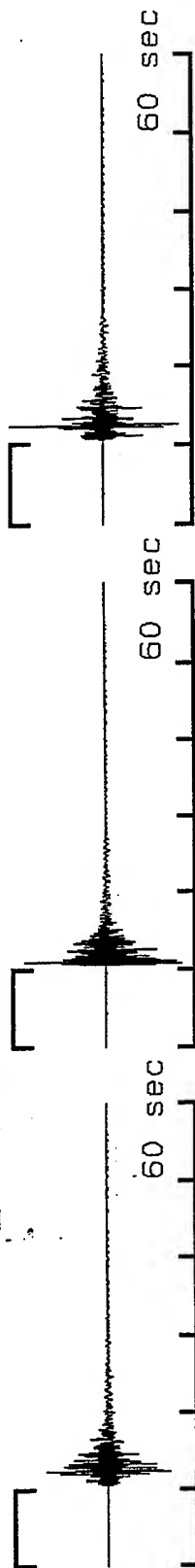
Transvers/Vertical:  
Linear Scale 0-8



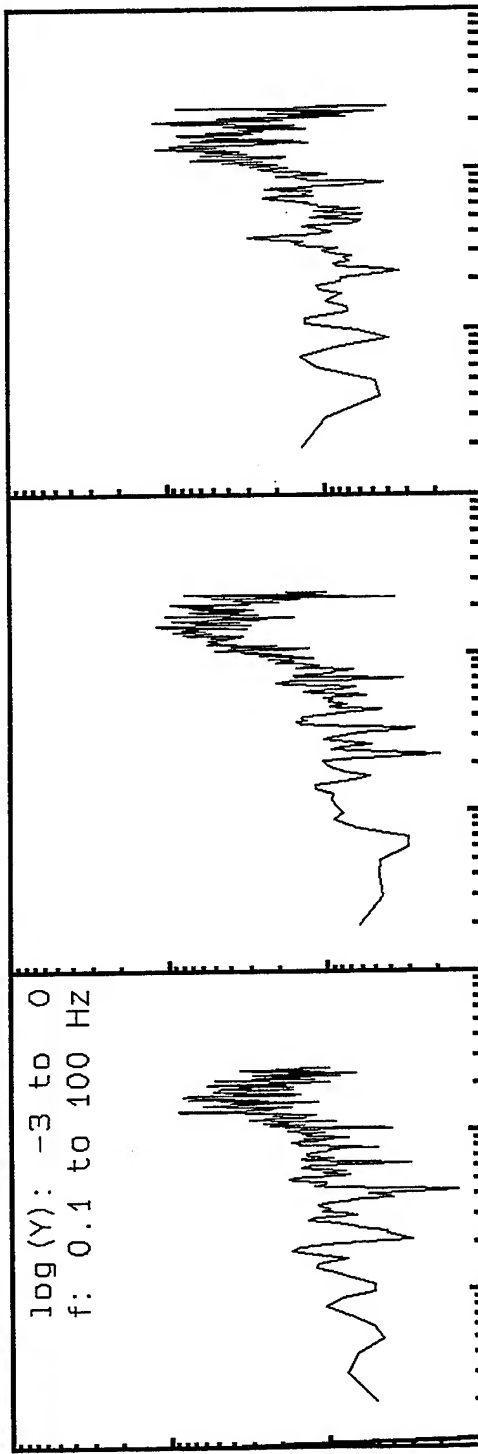
**VortexRock Consultants, Inc.**  
11434 Alder Creek Rd, Corona, CA 91720  
Tel - Fax (714) 692-1443, E-Mail: mahdyiar@coda.usc.edu



516\_NWHP, Window: .0 to 10.0 s



log (Y): -3 to 0  
f: 0.1 to 100 Hz



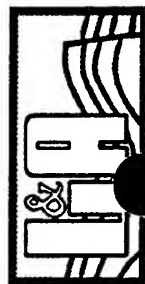
Radial/Vertical  
Linear Scale 0-8

Transvers/Vertical:  
Linear Scale 0-8

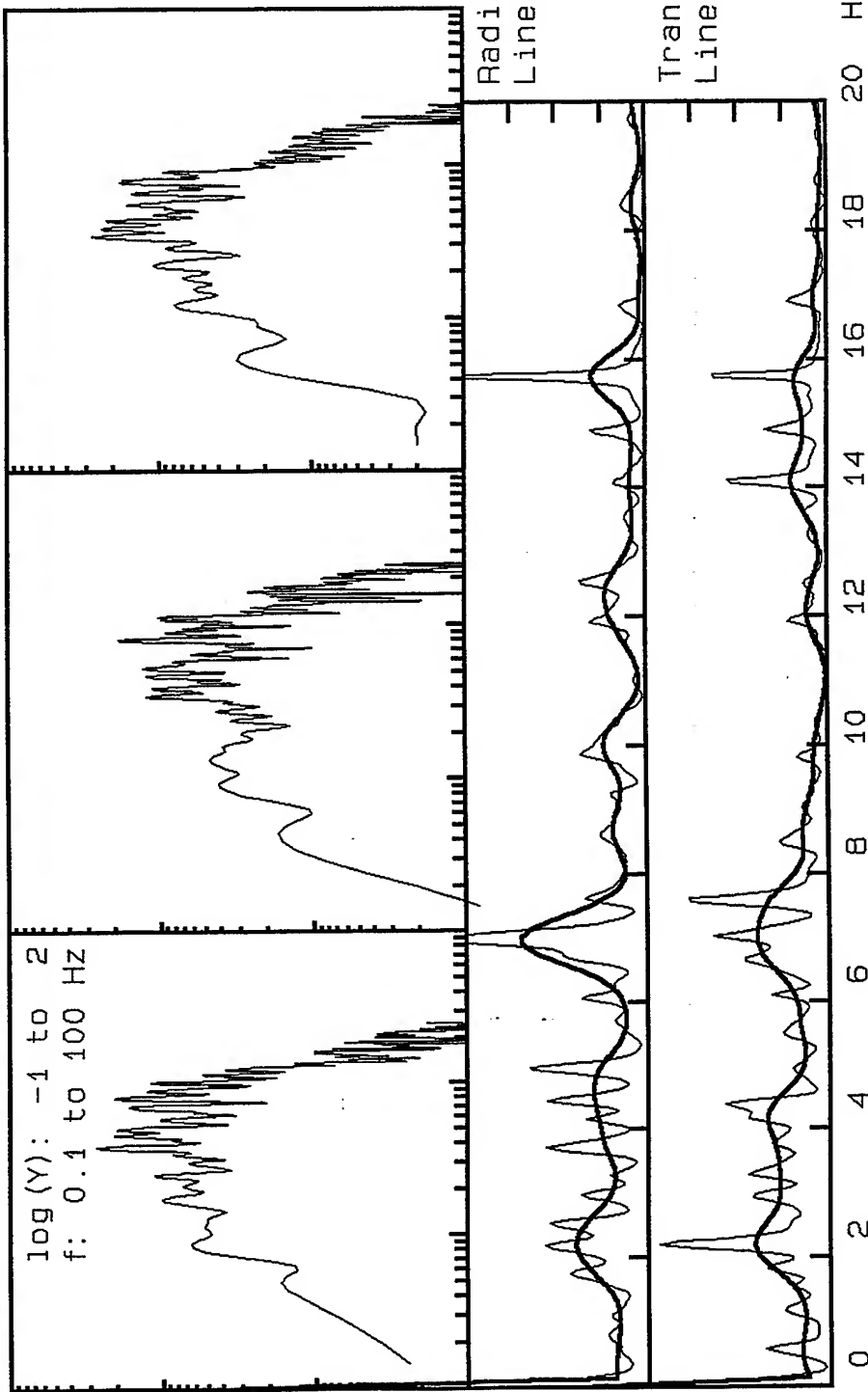
0 2 4 6 8 10 12 14 16 18 20 Hz



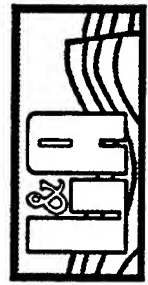
**VortexRock Consultants, Inc.**  
11434 Alder Creek Rd, Corona, CA 91720  
Tel - Fax (714) 692-1443, E-Mail: mahdyiar@coda.usc.edu



516\_NWHP, Window: 11.2 to 30.8 s



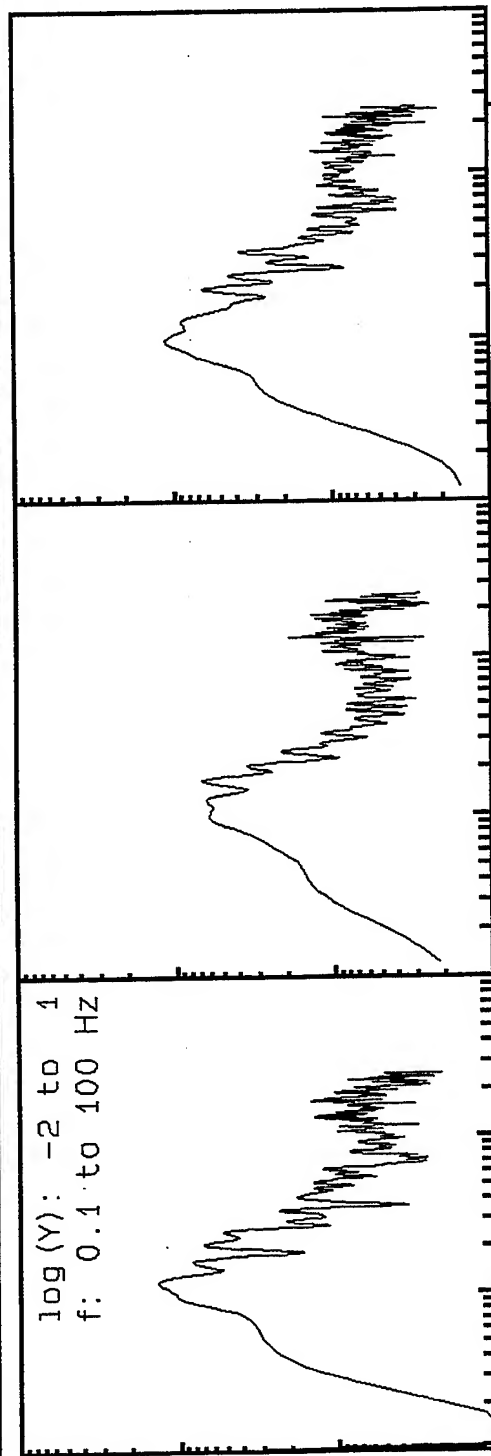
**VortexRock Consultants, Inc.**  
 11434 Alder Creek Rd, Corona, CA 91720  
 Tel - Fax (714) 692-1443, E-Mail: mahdyiar@coda.usc.edu



516\_NWHP, Window: 30.8 to 60.0 s

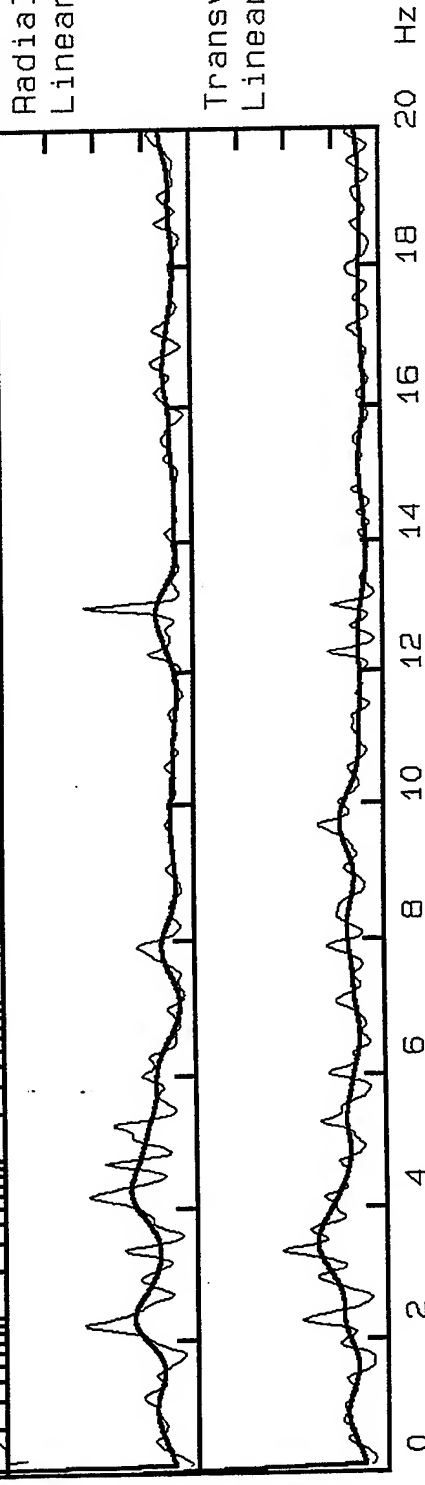


log(Y): -2 to 1  
f: 0.1 to 100 Hz

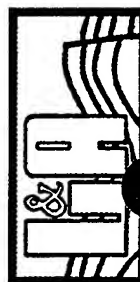


Radial/Vertical  
Linear Scale 0-8

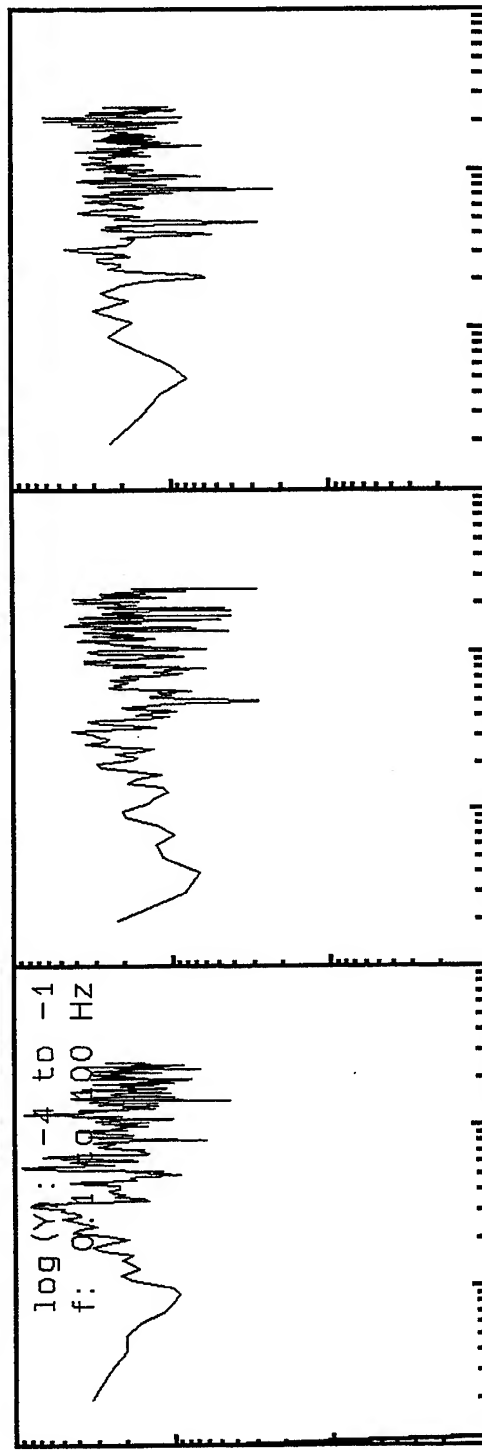
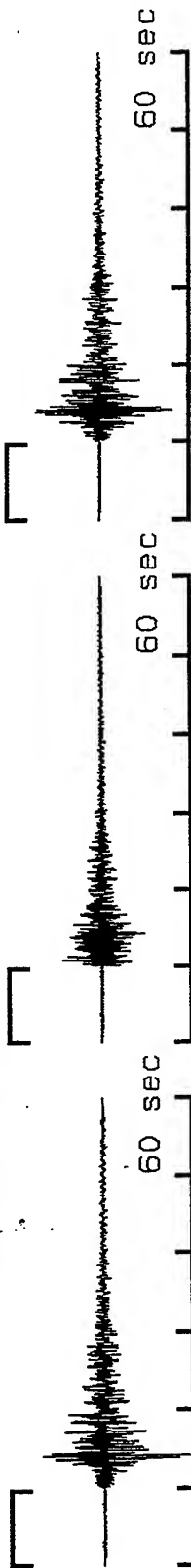
Transvers/Vertical:  
Linear Scale 0-8



**VortexRock Consultants, Inc.**  
11434 Alder Creek Rd, Corona, CA 91720  
Tel - Fax (714) 692-1443, E-Mail: mahdyiar@coda.usc.edu

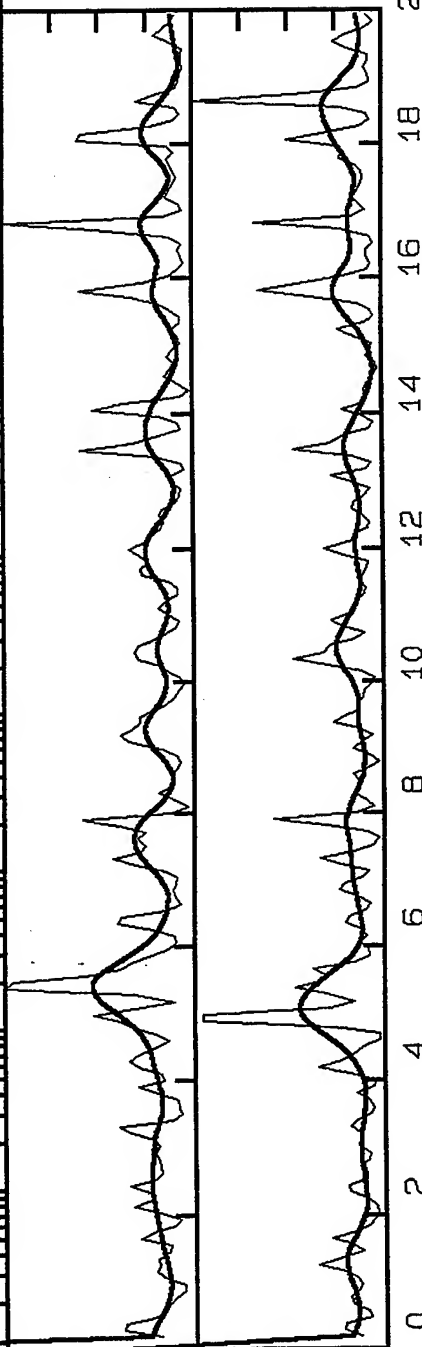


518\_NWHP, Window: .0 to 9.6 s

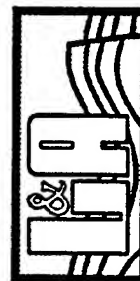


Radial/Vertical  
Linear Scale 0-8

Transvers/Vertical:  
Linear Scale 0-8

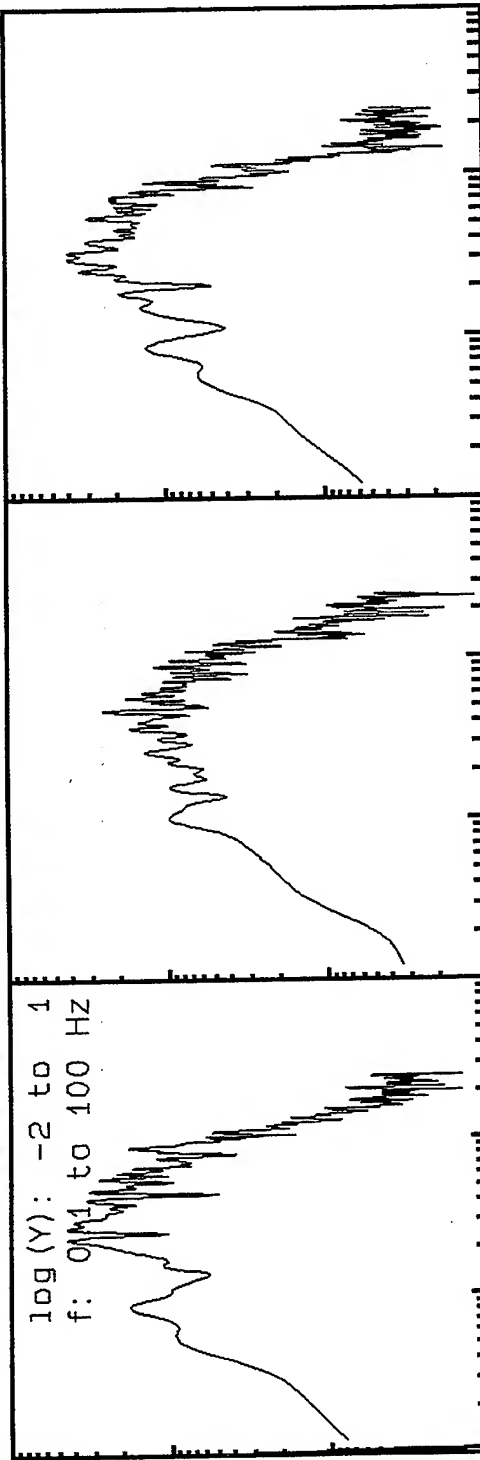
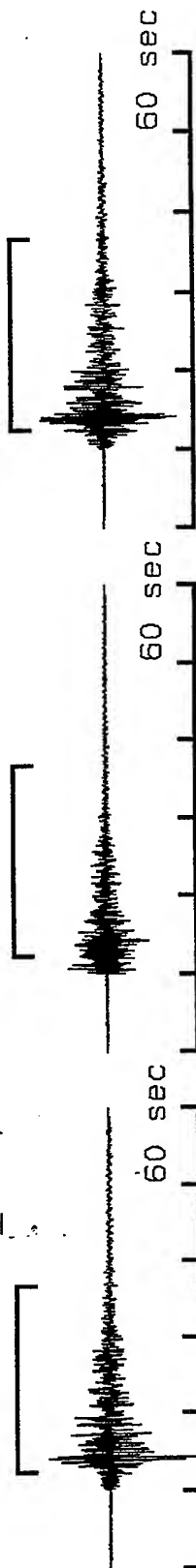


**VortexRock Consultants, Inc.**  
11434 Alder Creek Rd, Corona, CA 91720  
Tel - Fax (714) 692-1443, E-Mail: mahdyiar@coda.usc.edu





518\_NWHP, Window: 12.4 to 36.8 s



Radial/Vertical  
Linear Scale 0-8

Transvers/Vertical:  
Linear Scale 0-8

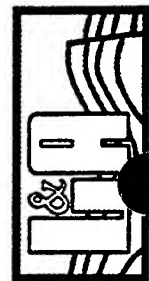
0 2 4 6 8 10 12 14 16 18 20 Hz



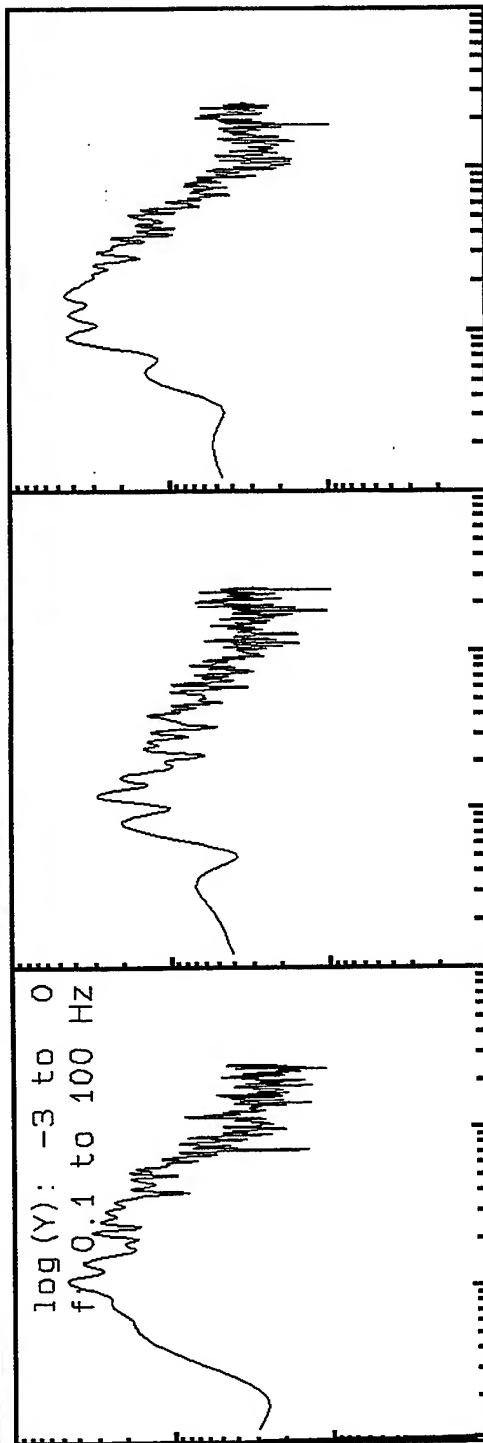
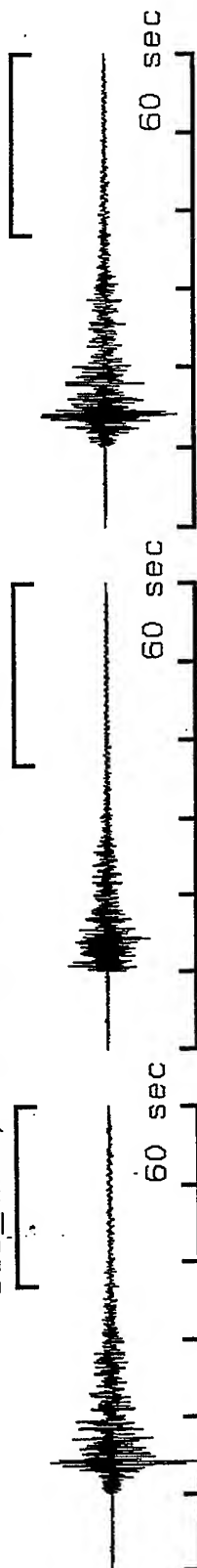
**VortexRock Consultants, Inc.**

11434 Alder Creek Rd, Corona, CA 91720

Tel - Fax (714) 692-1443, E-Mail: mahdyiar@coda.usc.edu

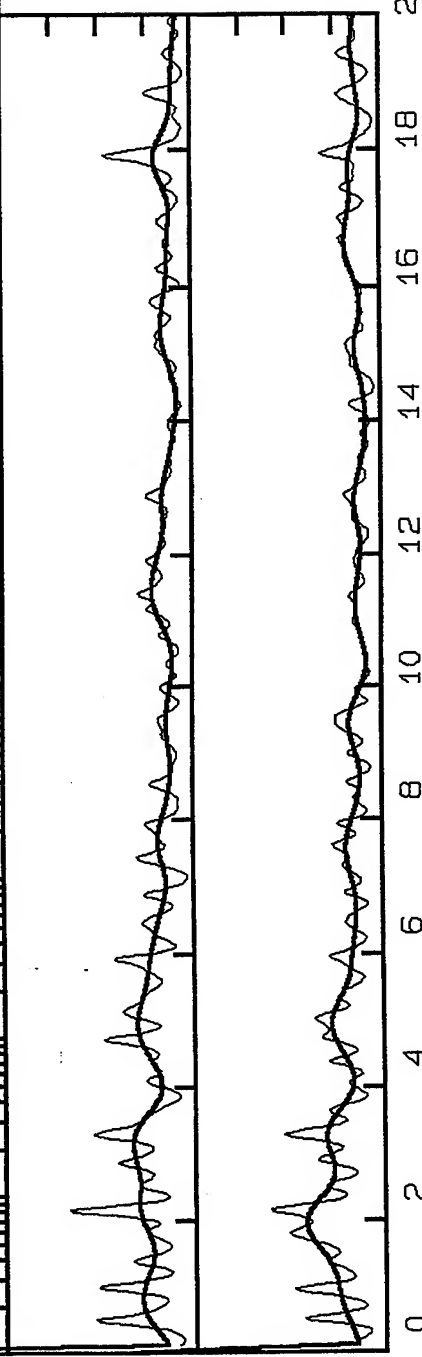


518\_NWHP, Window: 36.8 to 60.0 s

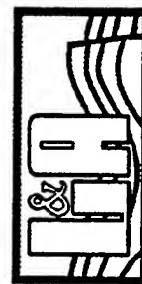


Radial/Vertical  
Linear Scale 0-8

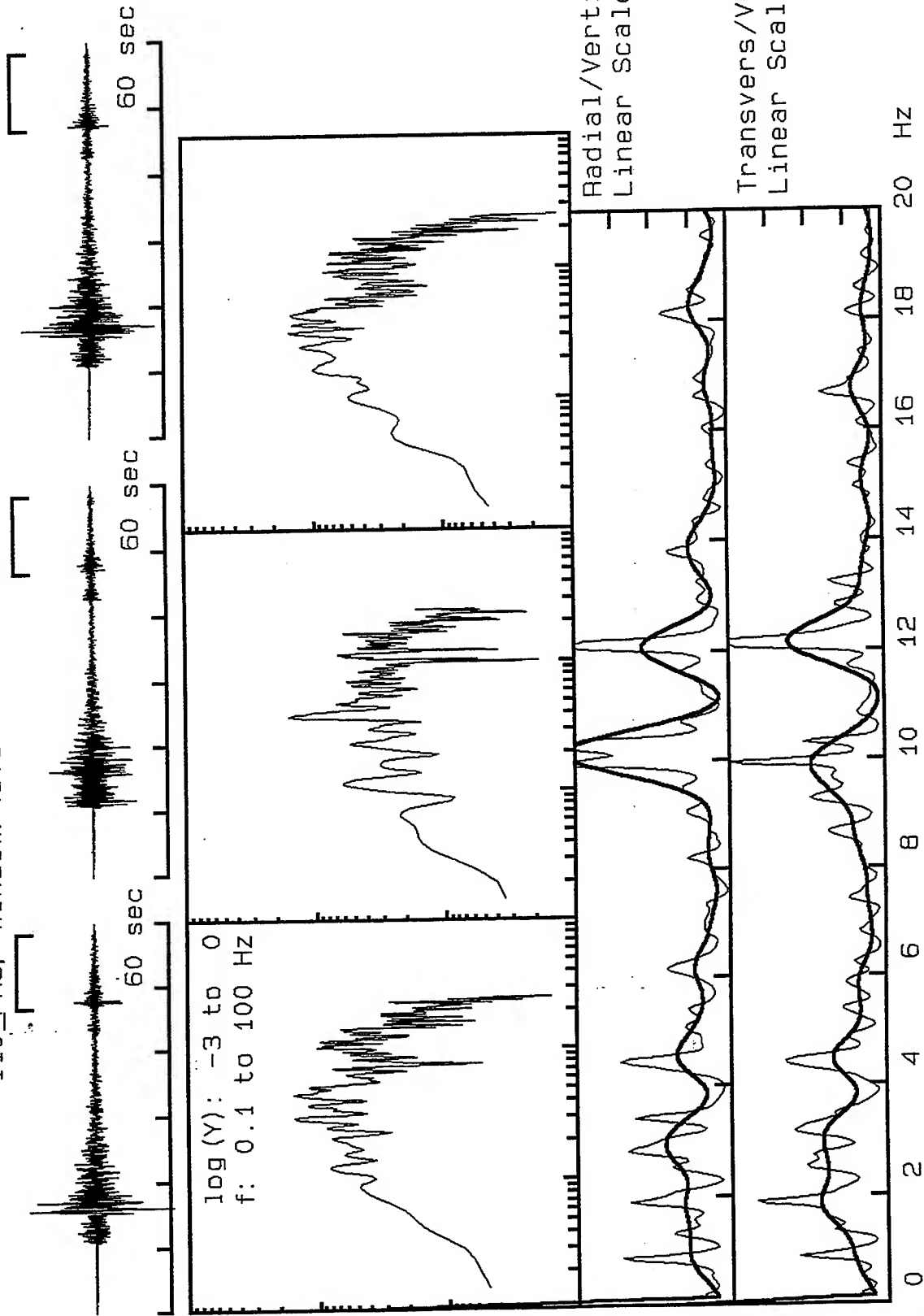
Transvers/Vertical:  
Linear Scale 0-8



**VortexRock Consultants, Inc.**  
11434 Alder Creek Rd, Corona, CA 91720  
Tel - Fax (714) 692-1443, E-Mail: mahdyiar@coda.usc.edu



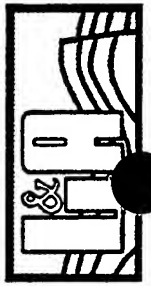
110\_PAS, Window: 46.8 to 58.4 s



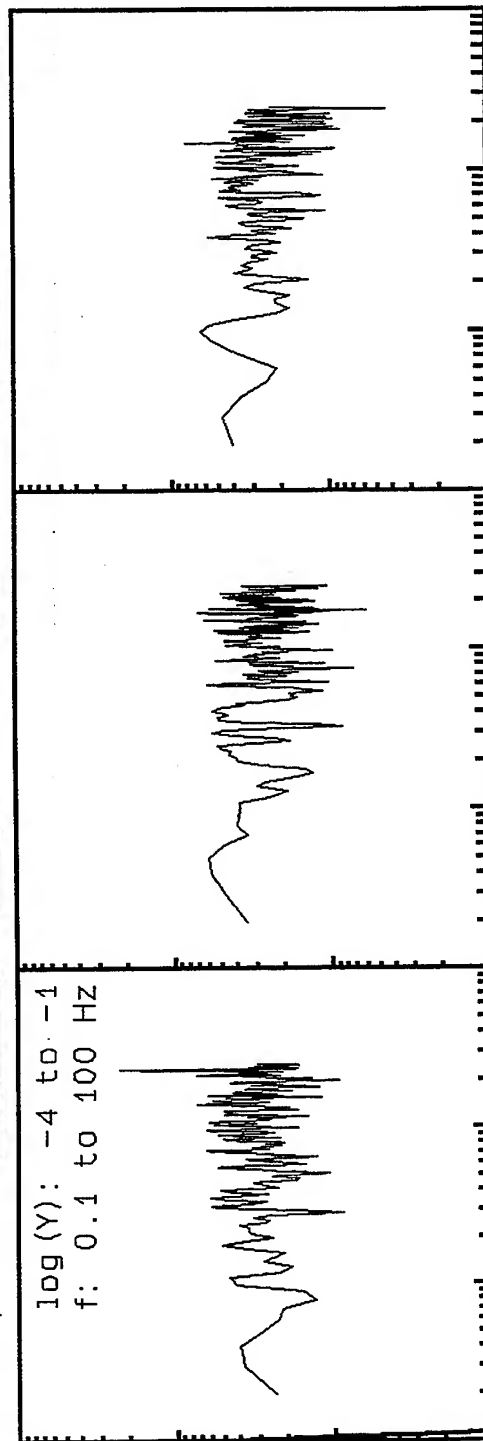
**VortexRock Consultants, Inc.**

11434 Alder Creek Rd, Corona, CA 91720

Tel - Fax (714) 692-1443, E-Mail: mahdyiar@coda.usc.edu

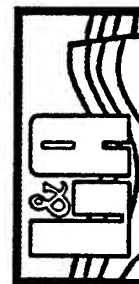
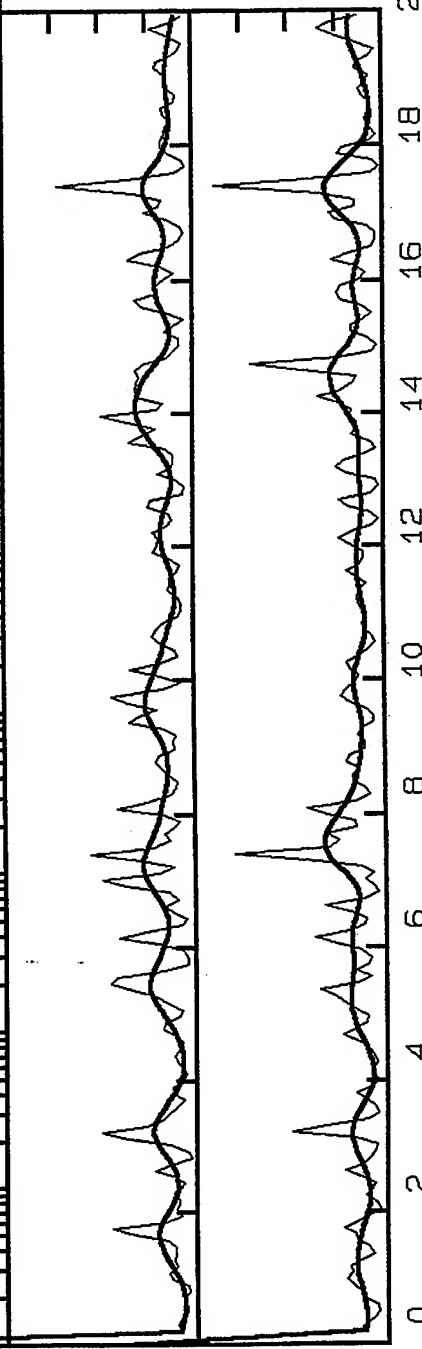


110\_PAS, Window: .0 to 10.0 s

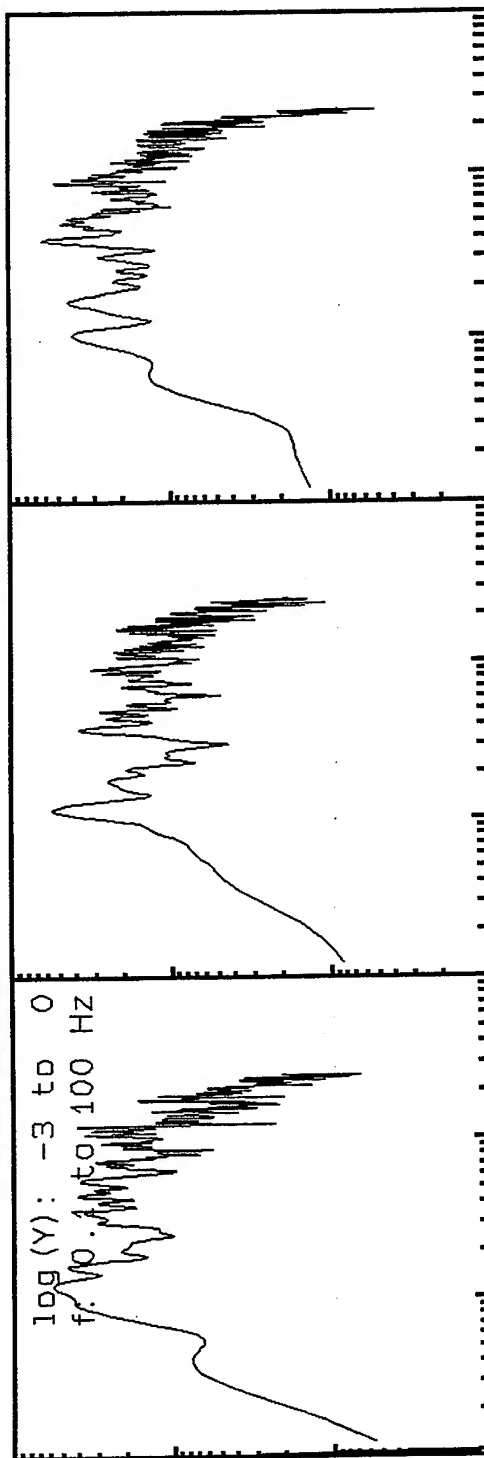
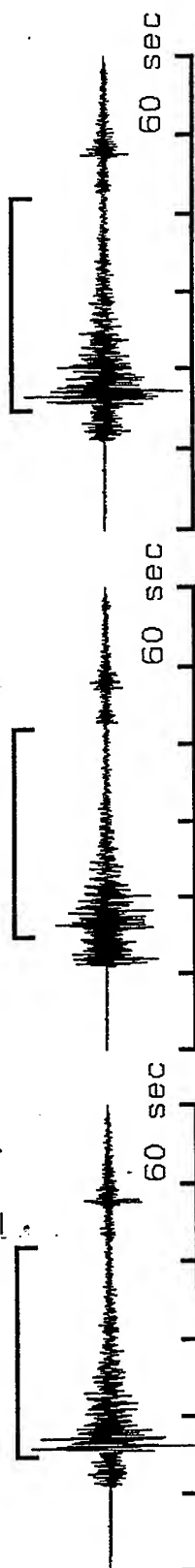


Radial/Vertical  
Linear Scale 0-8

Transvers/Vertical  
Linear Scale 0-8

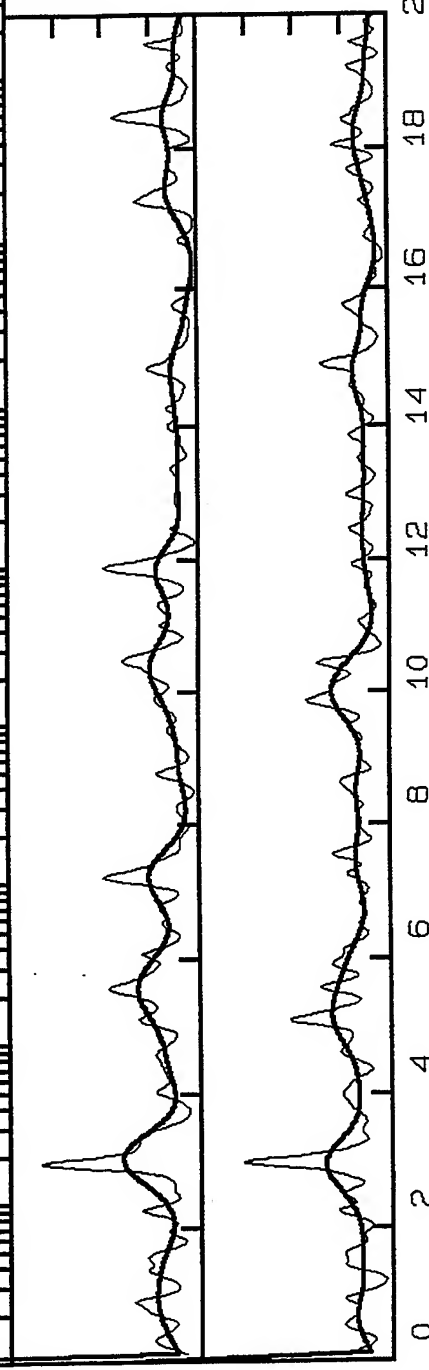


110\_PAS, Window: 14.8 to 42.0 s



Radial/Vertical  
Linear Scale 0-8

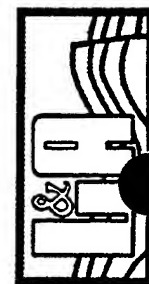
Transvers/Vertical:  
Linear Scale 0-8



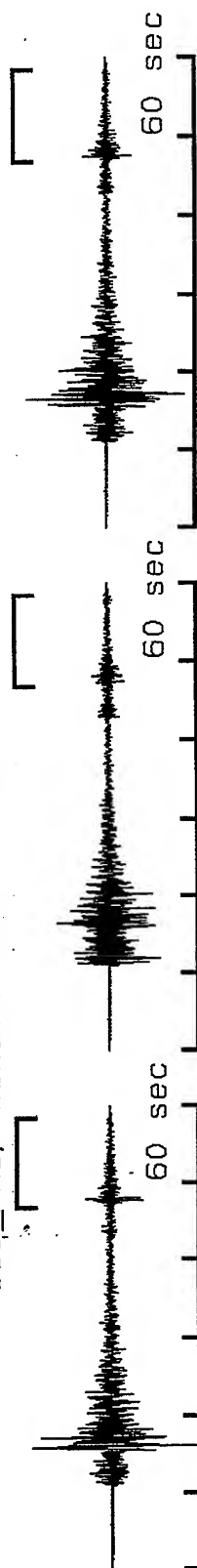
**VortexRock Consultants, Inc.**

11434 Alder Creek Rd, Corona, CA 91720

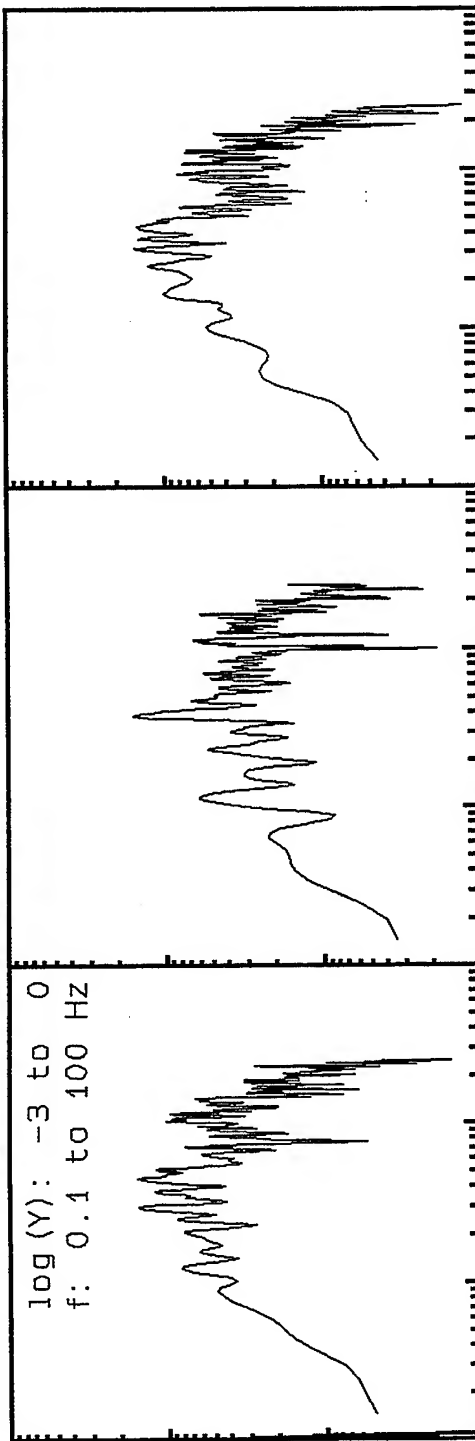
Tel - Fax (714) 692-1443, E-Mail: mahdyiar@coda.usc.edu



110\_PAS, Window: 46.8 to 58.4 s

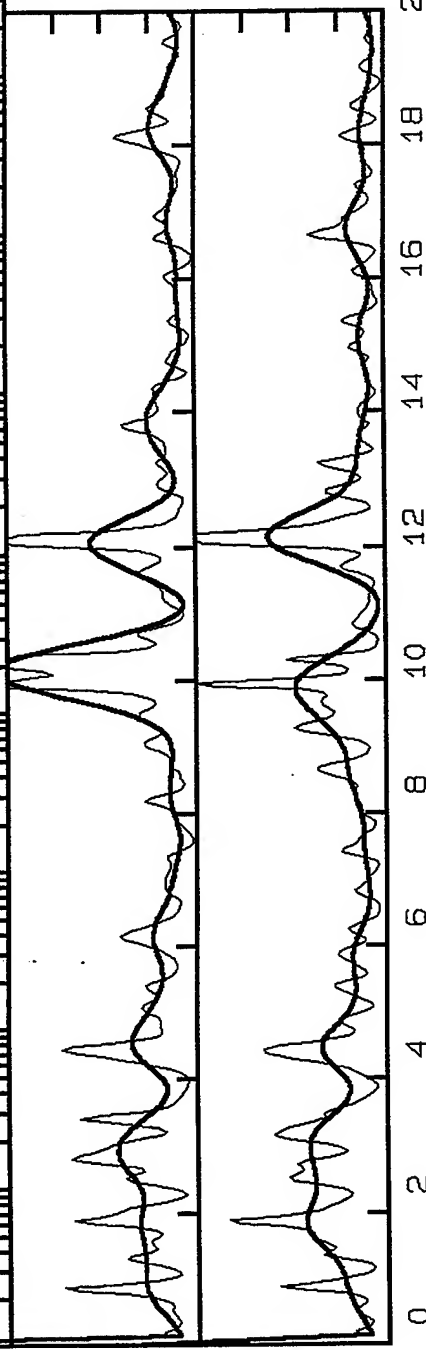


log (Y): -3 to 0  
f: 0.1 to 100 Hz

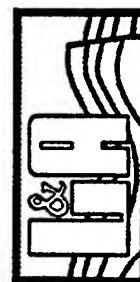


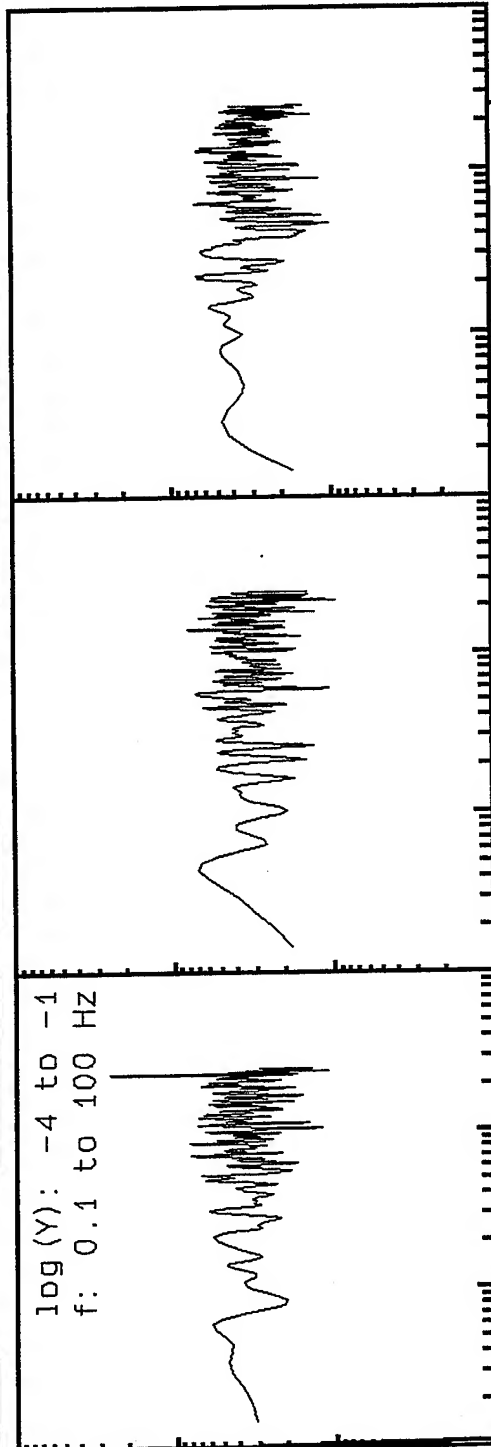
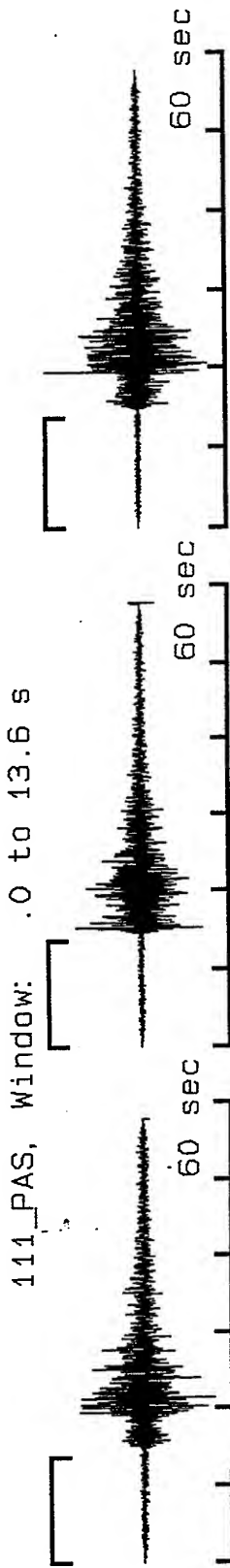
Radial/Vertical  
Linear Scale 0-8

Transvers/Vertical:  
Linear Scale 0-8



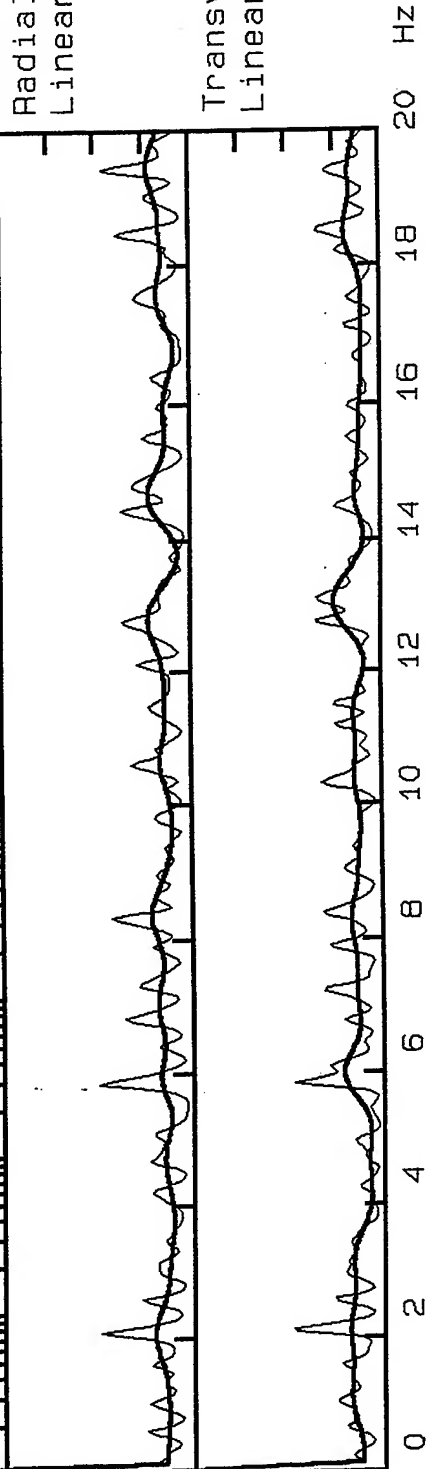
**VortexRock Consultants, Inc.**  
11434 Alder Creek Rd, Corona, CA 91720  
Tel - Fax (714) 692-1443, E-Mail: mahdyiar@coda.usc.edu



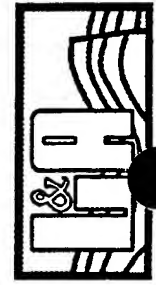


Radial/Vertical  
Linear Scale 0-8

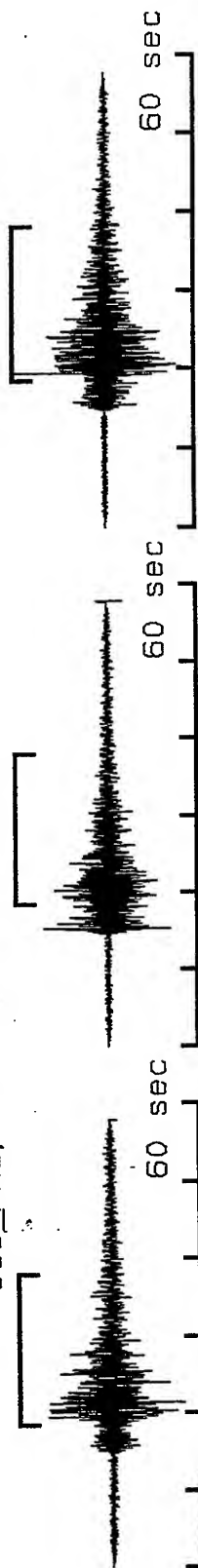
Transvers/Vertical:  
Linear Scale 0-8



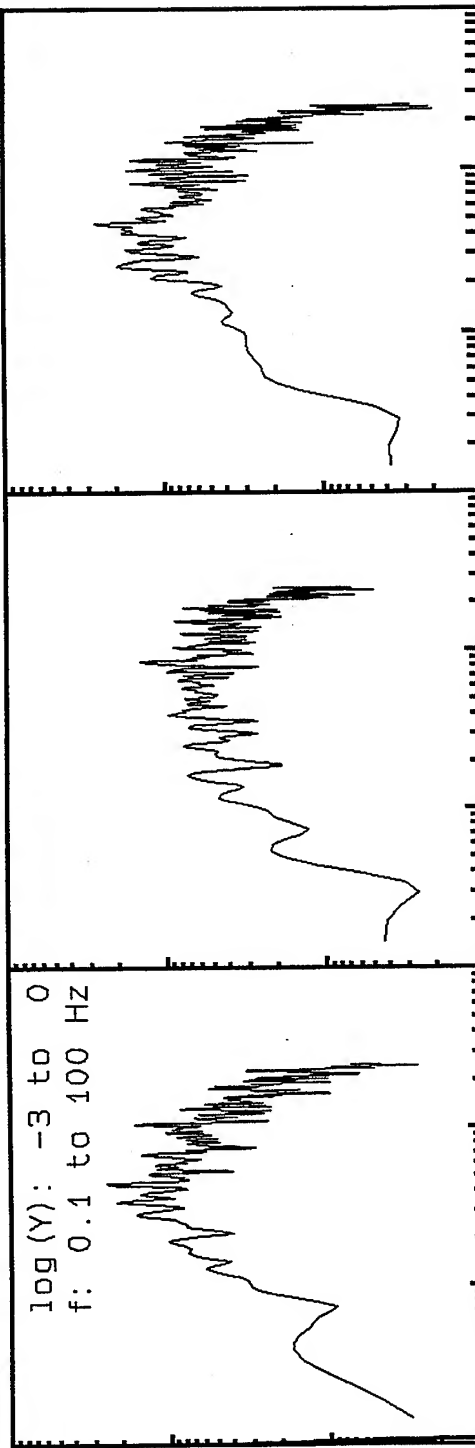
**VortexRock Consultants, Inc.**  
11434 Alder Creek Rd, Corona, CA 91720  
Tel - Fax (714) 692-1443, E-Mail: mahdyiar@coda.usc.edu



111\_PAS, Window: 18.4 to 38.0 s

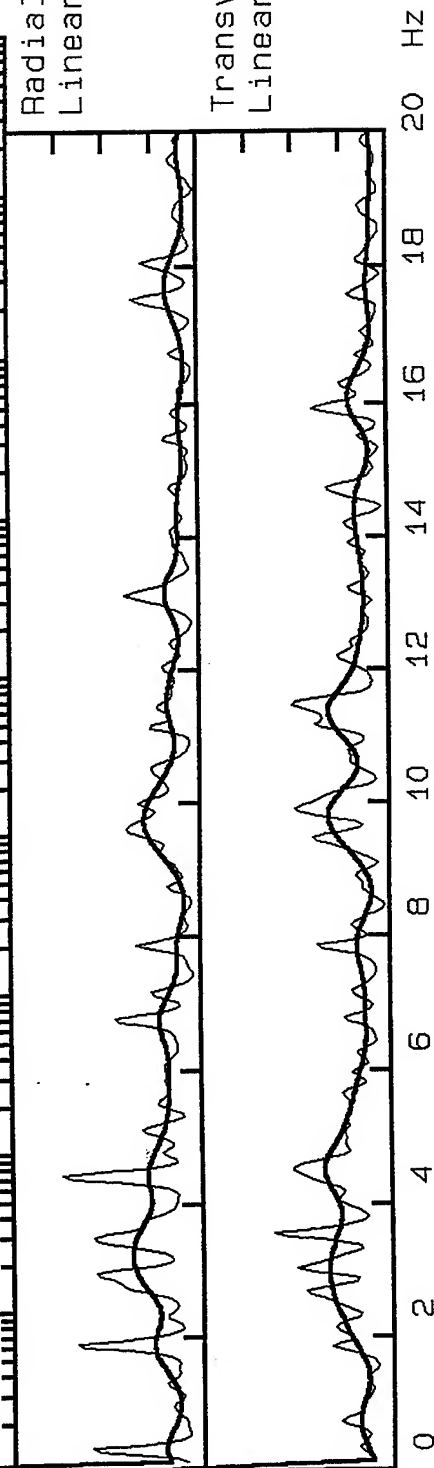


log (Y): -3 to 0  
f: 0.1 to 100 Hz

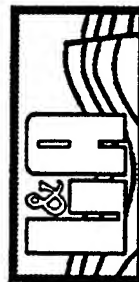


Radial/Vertical  
Linear Scale 0-8

Transvers/Vertical:  
Linear Scale 0-8

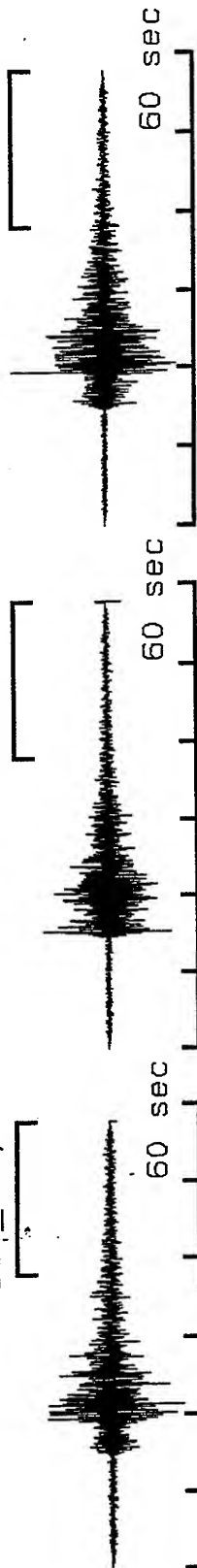


**VortexRock Consultants, Inc.**  
11434 Alder Creek Rd, Corona, CA 91720  
Tel - Fax (714) 692-1443, E-Mail: mahdyiar@coda.usc.edu

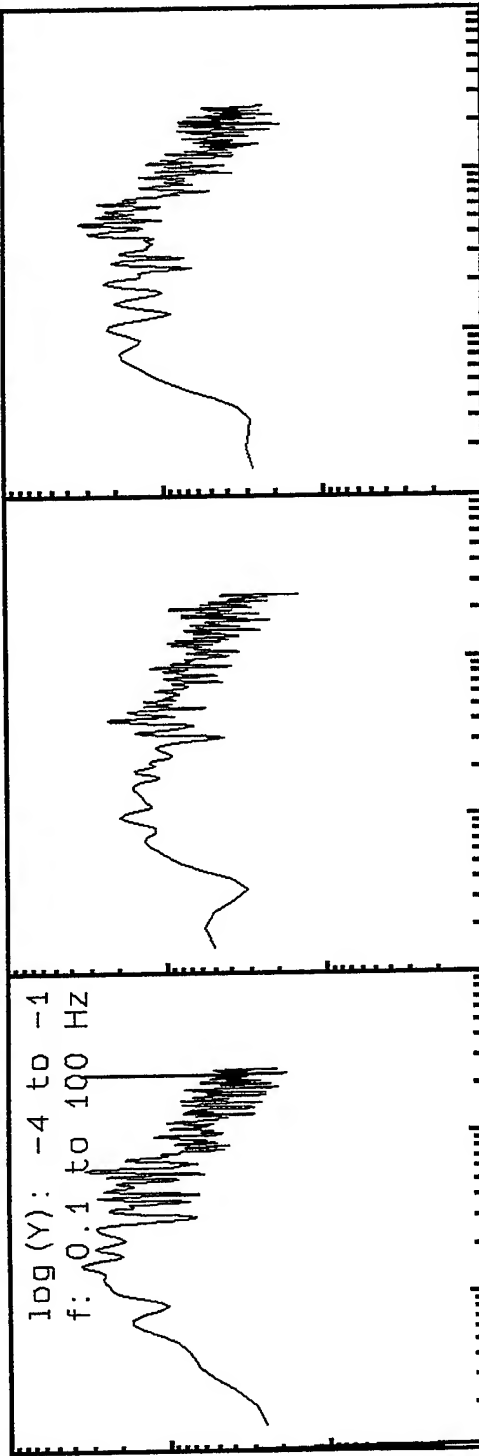




111\_PAS, Window: 38.0 to 57.8 s

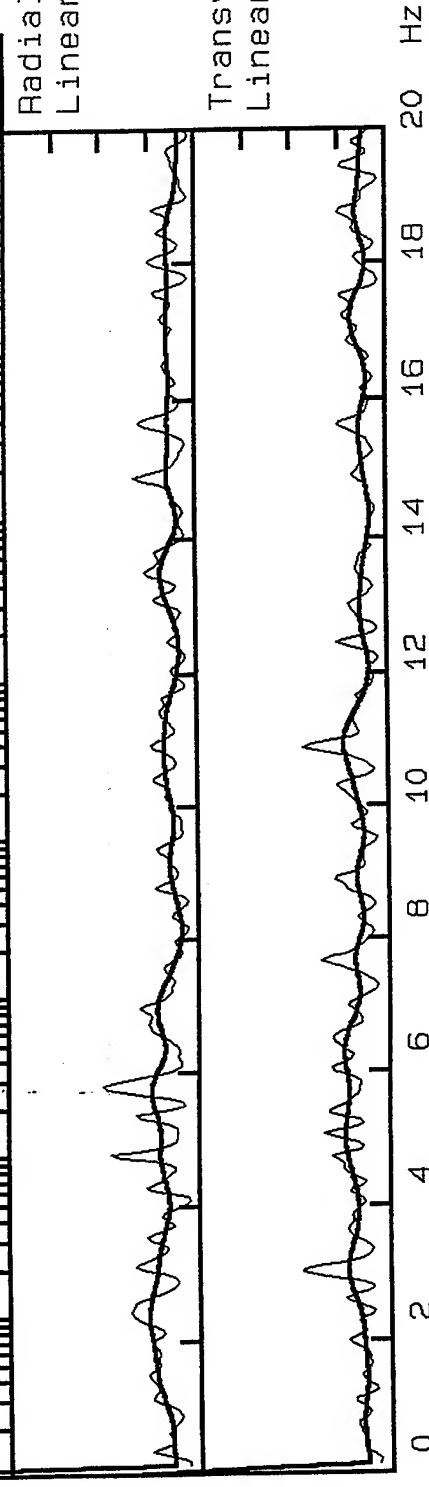


log(Y): -4 to -1  
f: 0.1 to 100 Hz

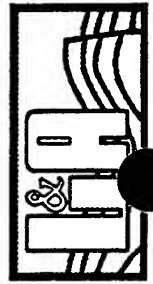


Radial/Vertical  
Linear Scale 0-8

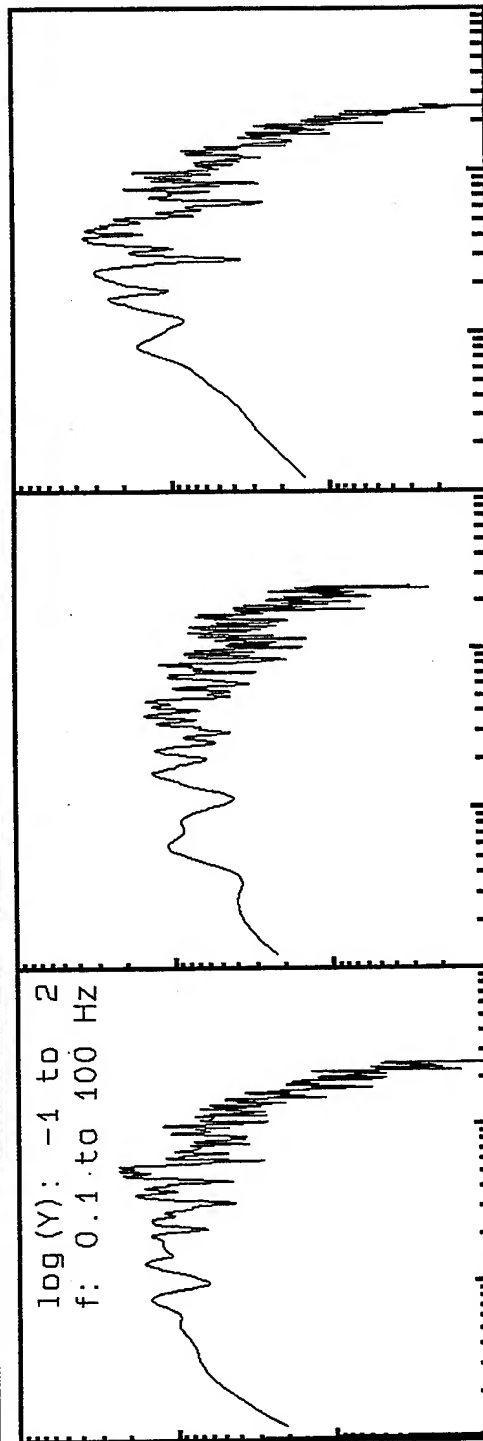
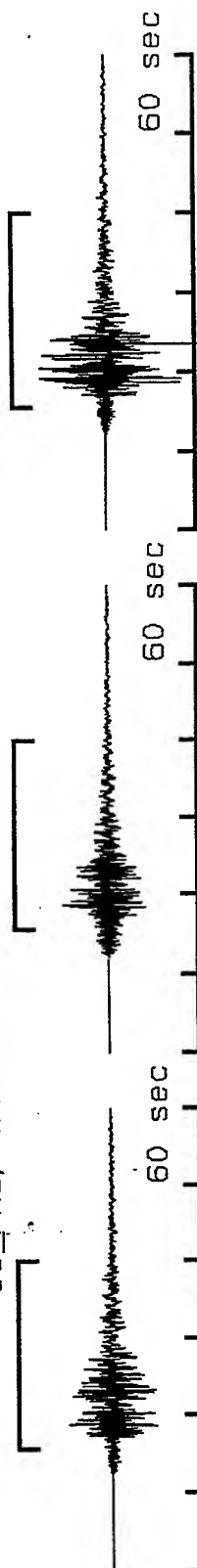
Transvers/Vertical:  
Linear Scale 0-8



**VortexRock Consultants, Inc.**  
11434 Alder Creek Rd, Corona, CA 91720  
Tel - Fax (714) 692-1443, E-Mail: mahdyar@coda.usc.edu

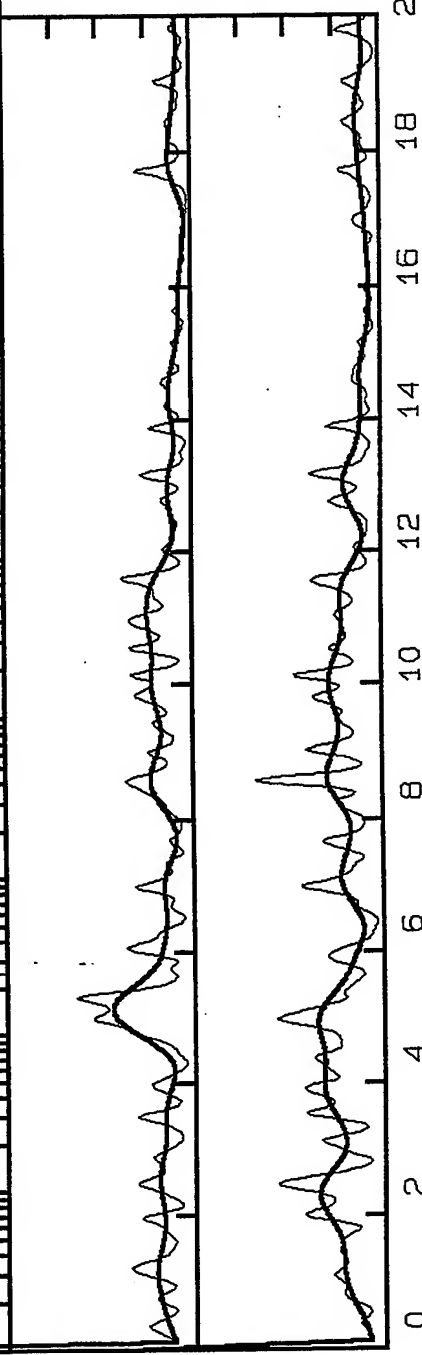


11\_PAS, Window: 15.6 to 40.0 S

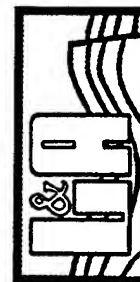


Radial/Vertical  
Linear Scale 0-8

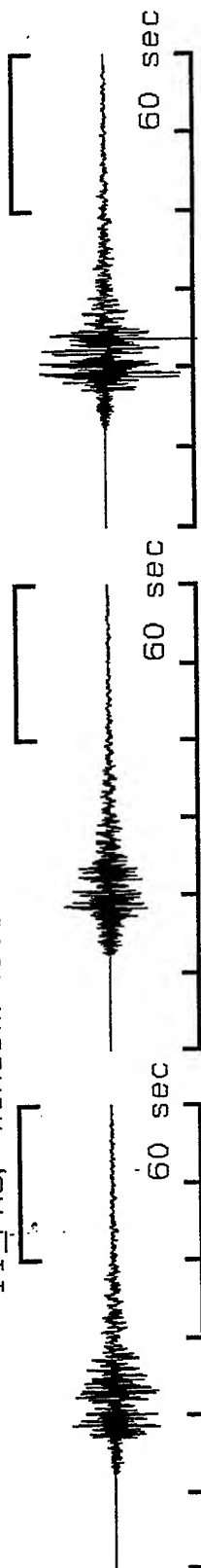
Transvers/Vertical:  
Linear Scale 0-8



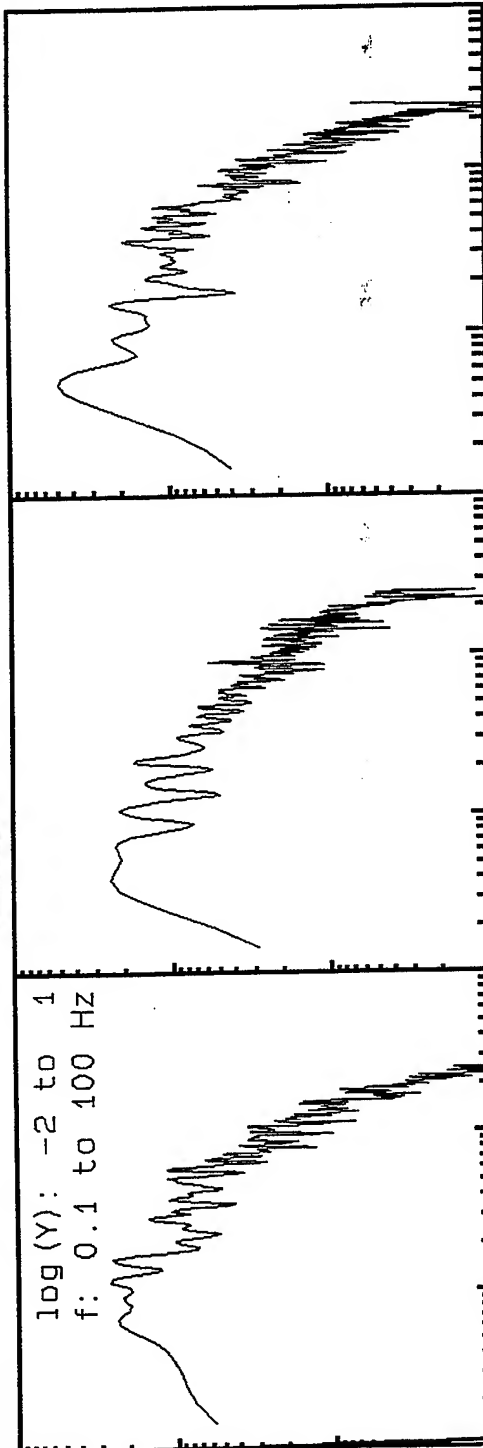
**VortexRock Consultants, Inc.**  
11434 Alder Creek Rd, Corona, CA 91720  
Tel - Fax (714) 692-1443, E-Mail: mahdyar@coda.usc.edu



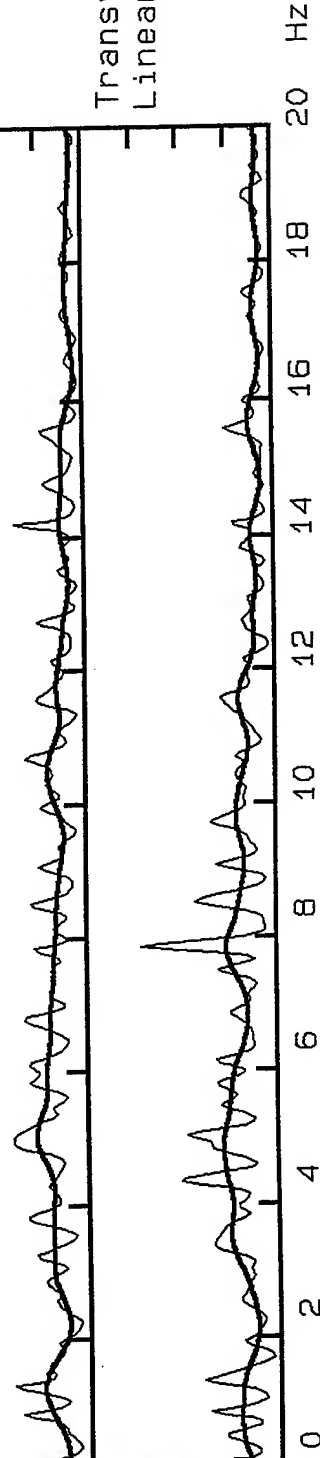
11\_PAS, Window: 40.0 to 60.0 s



log(Y): -2 to 1  
f: 0.1 to 100 Hz



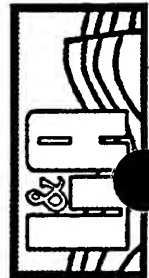
Radial/Vertical  
Linear Scale 0-8



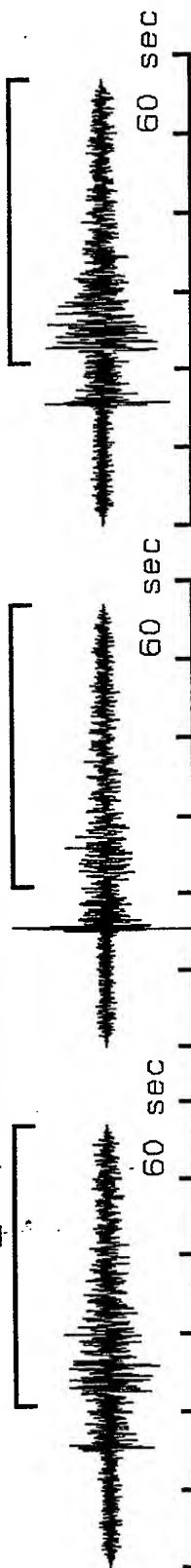
Transvers/Vertical:  
Linear Scale 0-8



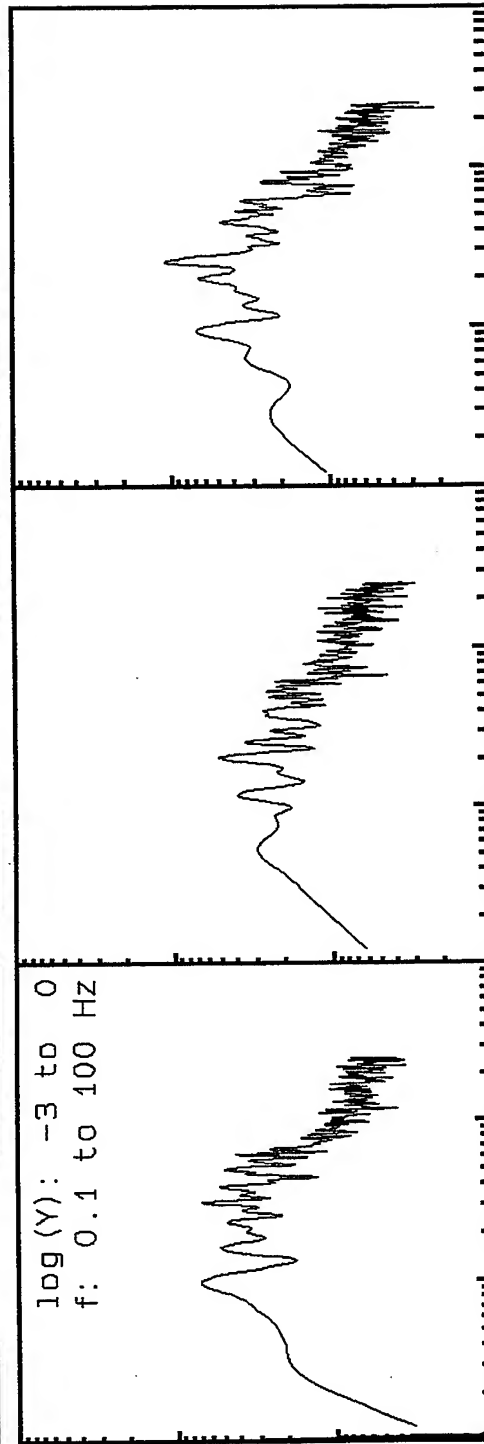
**VortexRock Consultants, Inc.**  
11434 Alder Creek Rd, Corona, CA 91720  
Tel - Fax (714) 692-1443, E-Mail: mahdyar@coda.usc.edu



15\_PAS, Window: 20.8 to 57.0 s



log(Y): -3 to 0  
f: 0.1 to 100 Hz



Radial/Vertical  
Linear Scale 0-8

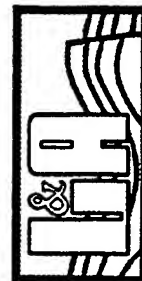
Transvers/Vertical:  
Linear Scale 0-8



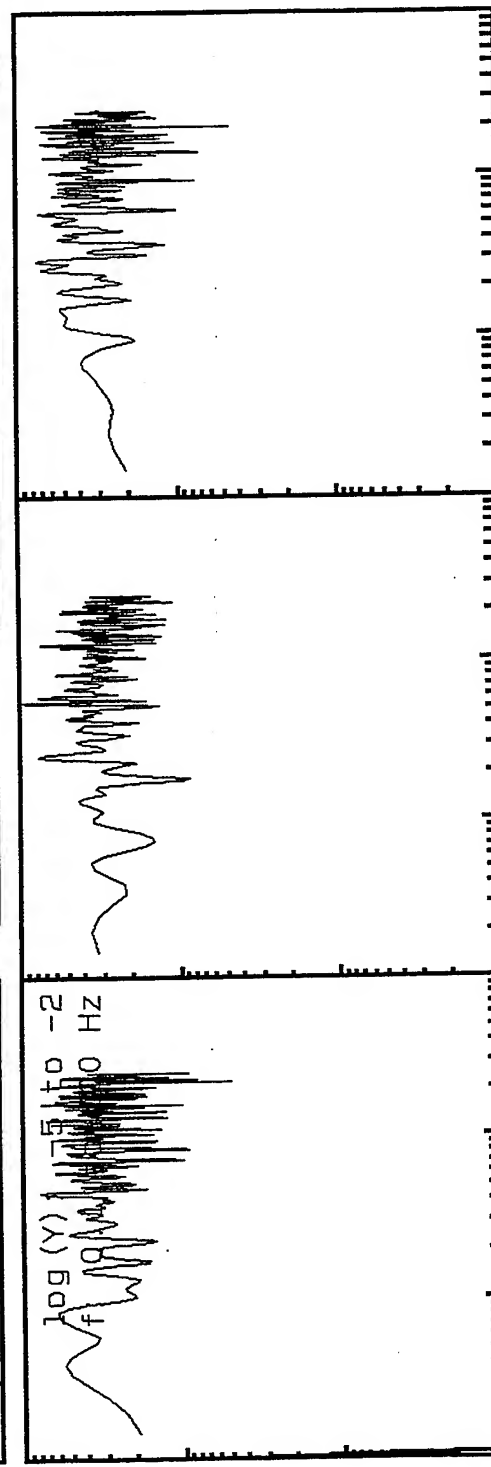
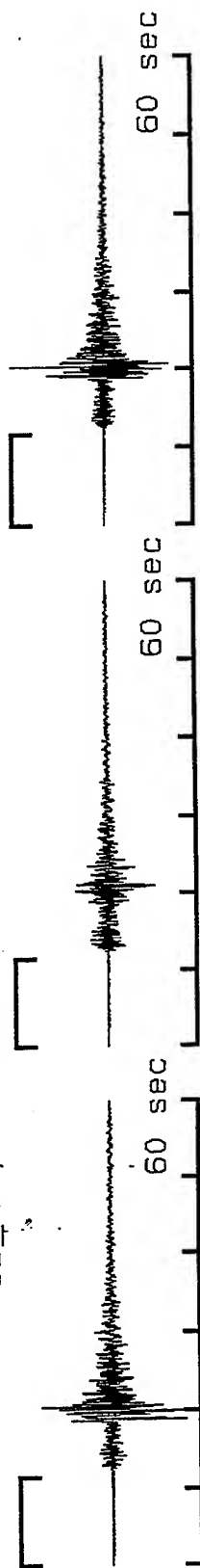
0 2 4 6 8 10 12 14 16 18 20 Hz



**VortexRock Consultants, Inc.**  
11434 Alder Creek Rd, Corona, CA 91720  
Tel - Fax (714) 692-1443, E-Mail: mahdyiar@coda.usc.edu

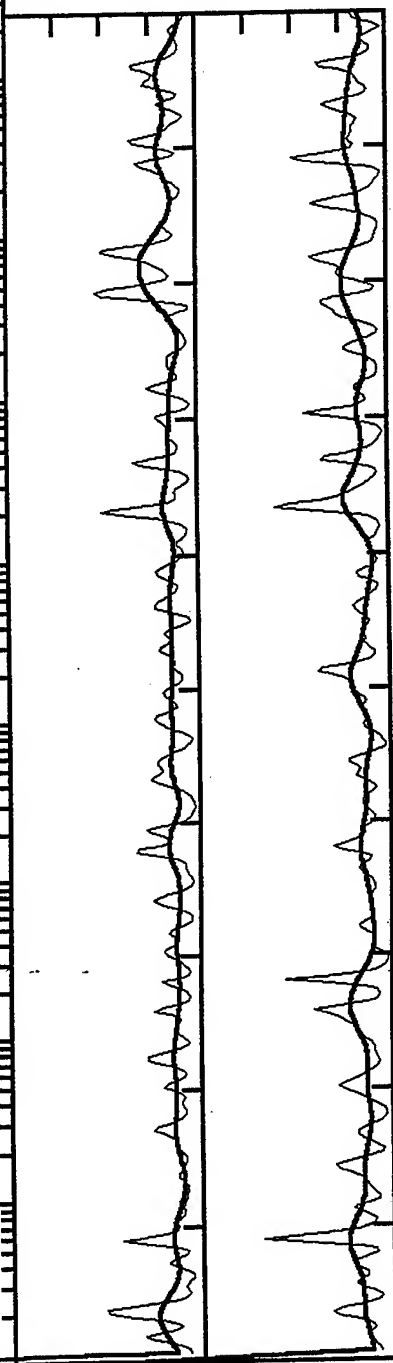


18\_PAS, Window: .0 to 11.6 s



Radial/Vertical  
Linear Scale 0-8

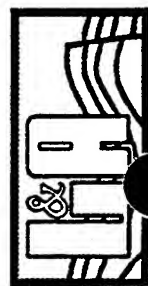
Transvers/Vertical:  
Linear Scale 0-8



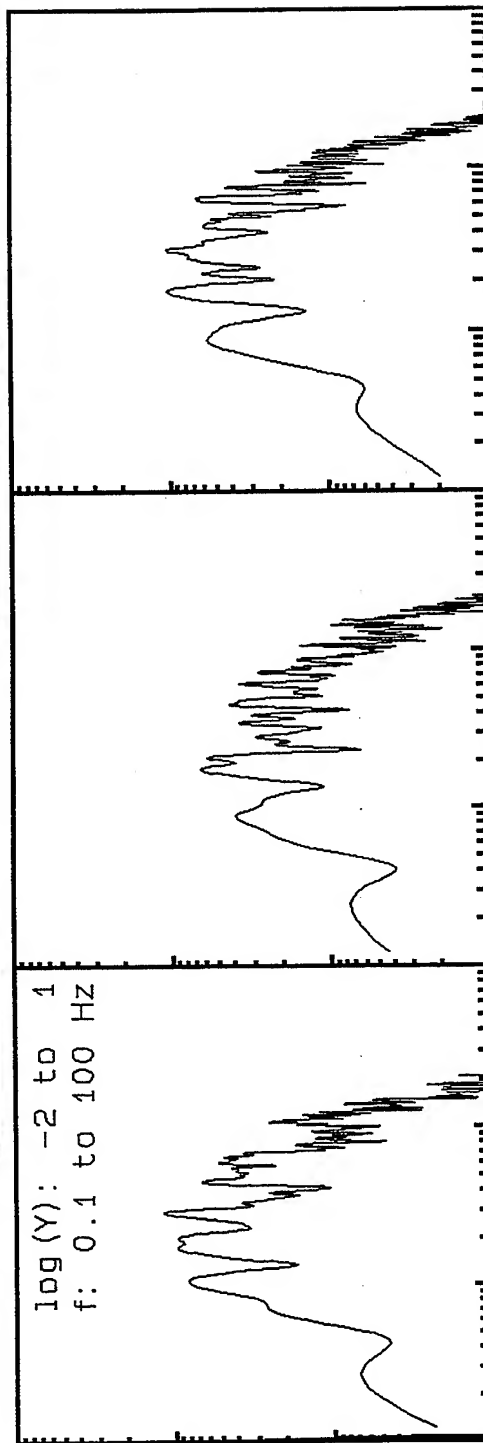
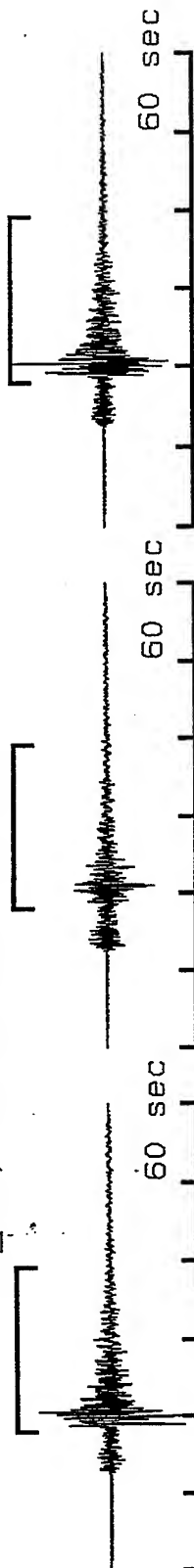
20 Hz



**VortexRock Consultants, Inc.**  
11434 Alder Creek Rd, Corona, CA 91720  
Tel - Fax (714) 692-1443, E-Mail: mahdiyar@coda.usc.edu

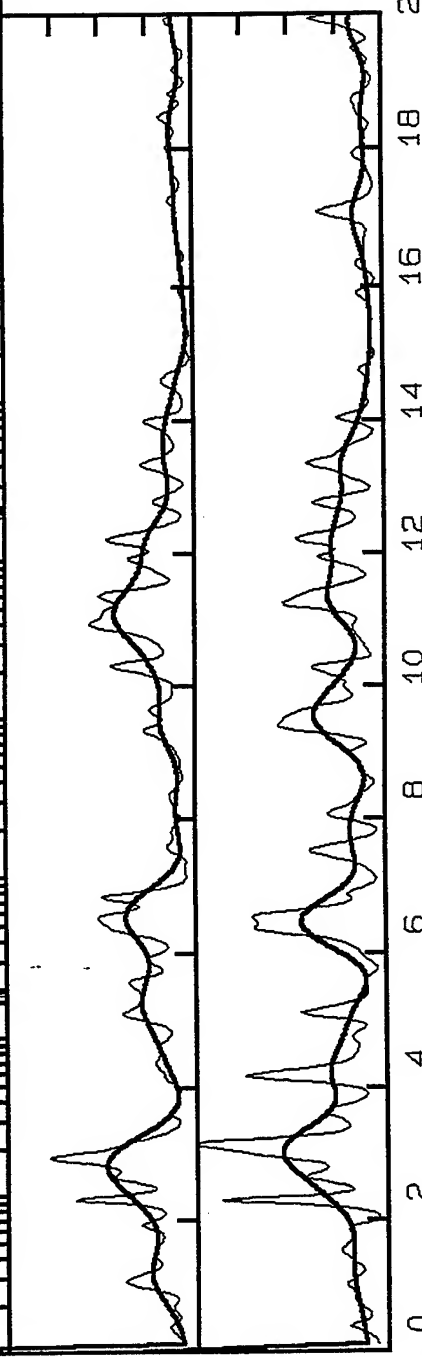


18\_PAS, Window: 18.0 to 39.2 s

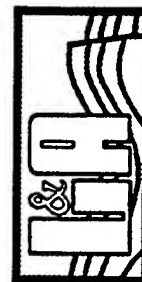


Radial/Vertical  
Linear Scale 0-8

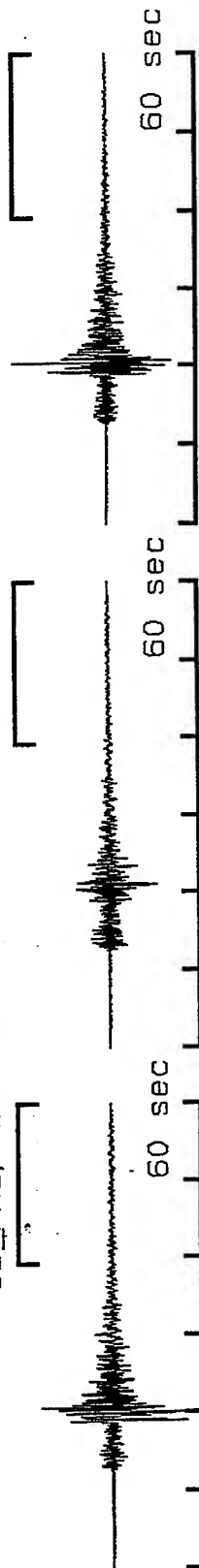
Transvers/Vertical:  
Linear Scale 0-8



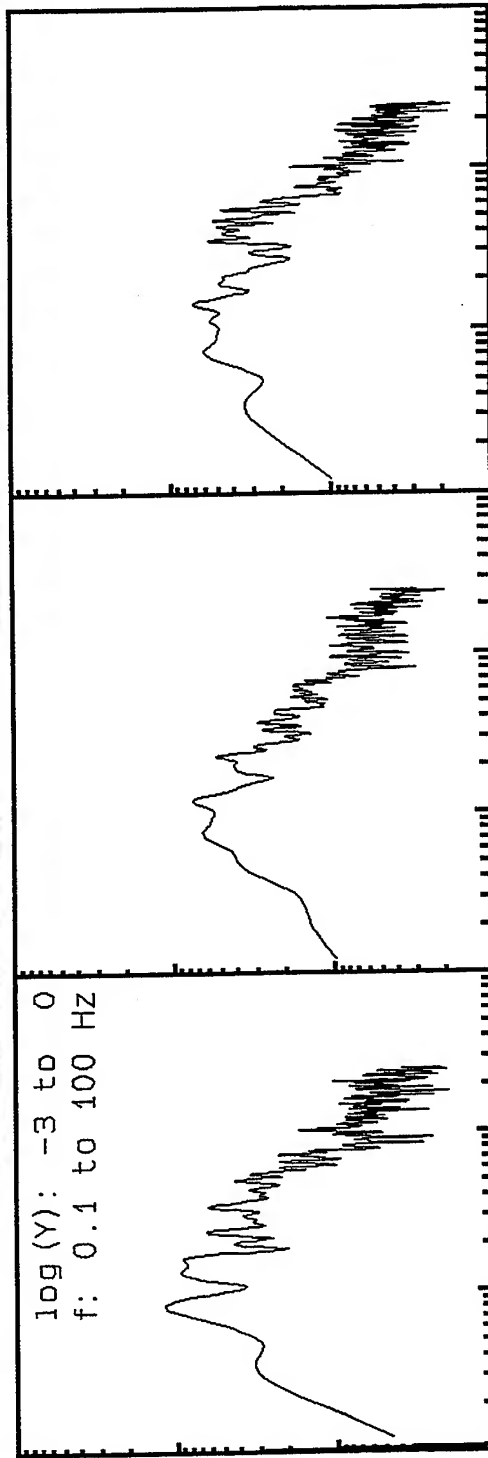
**VortexRock Consultants, Inc.**  
11434 Alder Creek Rd, Corona, CA 91720  
Tel - Fax (714) 692-1443, E-Mail: mahdyiar@coda.usc.edu



18\_PAS, Window: 39.2 to 60.0 s

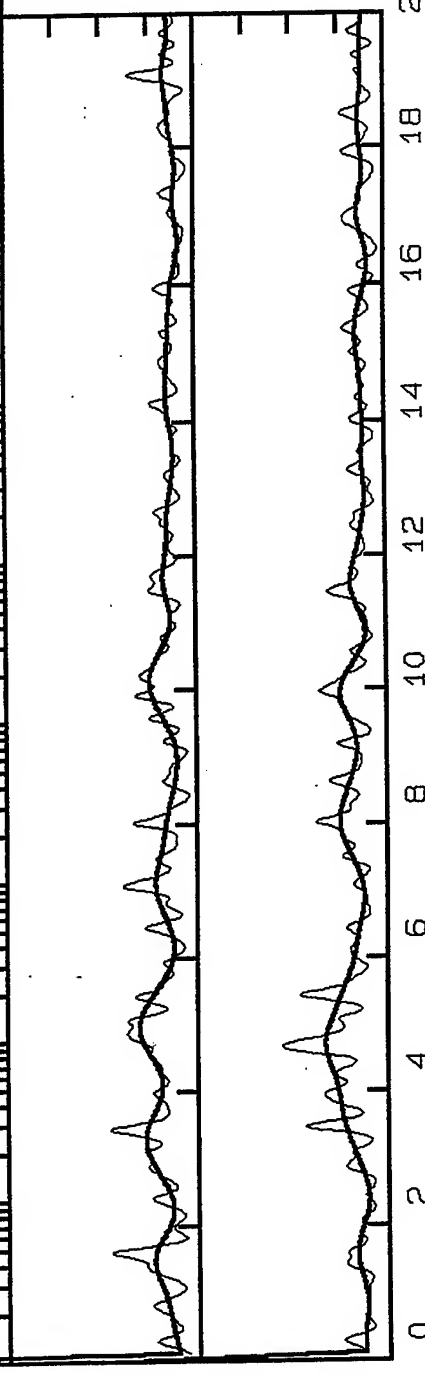


log(Y): -3 to 0  
f: 0.1 to 100 Hz

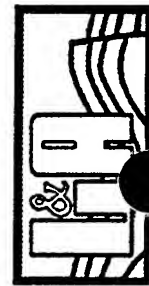


Radial/Vertical  
Linear Scale 0-8

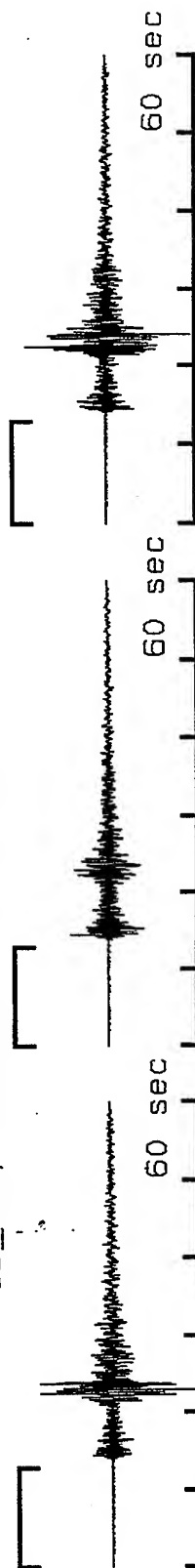
Transvers/Vertical:  
Linear Scale 0-8



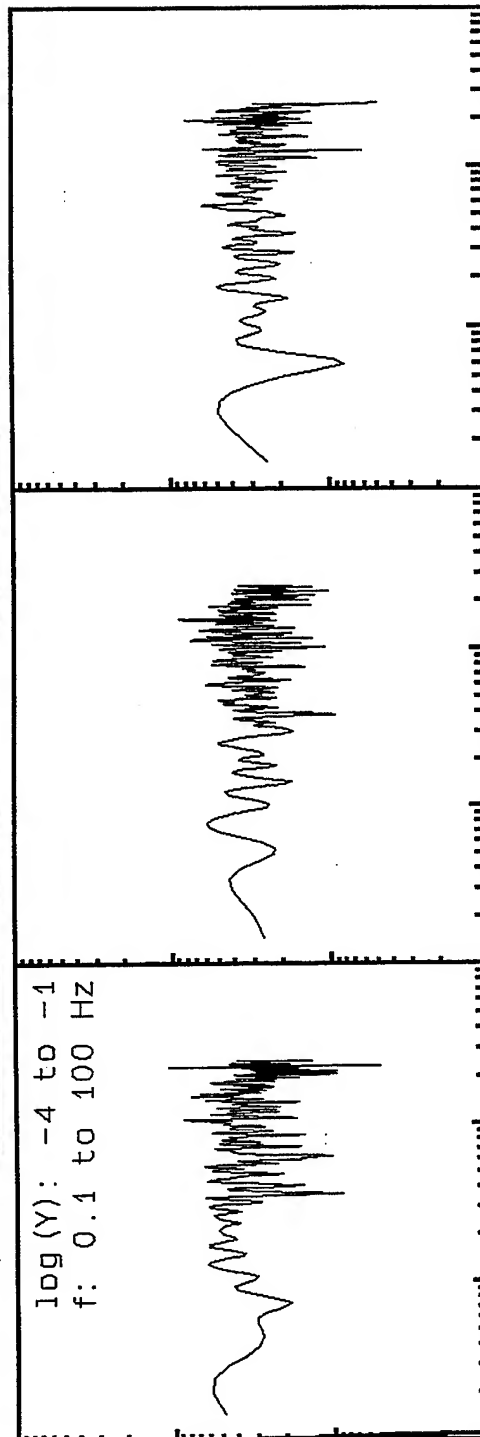
**VortexRock Consultants, Inc.**  
11434 Alder Creek Rd, Corona, CA 91720  
Tel - Fax (714) 692-1443, E-Mail: mahdyiar@coda.usc.edu



19\_PAS, Window: .0 to 12.8 s



log(Y): -4 to -1  
f: 0.1 to 100 Hz



Radial/Vertical  
Linear Scale 0-8

Transvers/Vertica:  
Linear Scale 0-8

0 2 4 6 8 10 12 14 16 18 20 Hz



**VortexRock Consultants, Inc.**  
11434 Alder Creek Rd, Corona, CA 91720  
Tel - Fax (714) 692-1443, E-Mail: mahdyiar@coda.usc.edu

